

PROCEEDINGS OF SPIE



SPIE—The International Society for Optical Engineering

Photonics Technology into the 21st Century: Semiconductors, Microstructures, and Nanostructures

Seng Tiong Ho
Yan Zhou
Weng W. Chow
Yasuhiko Arakawa
Chairs/Editors

1-3 December 1999
Singapore

Sponsored by
SPIE—The International Society for Optical Engineering
Nanyang Technological University, Singapore

Cosponsored by
SPIE Singapore Chapter
Institute of Physics, Singapore
United States Air Force Asian Office of Aerospace Research
and Development (AFOSR/AOARD)
United States Army Research Office-Far East (ARO-FE)

DISTRIBUTION STATEMENT A
Approved for Public Release
Distribution Unlimited

20000526 115



Volume 3899



PROCEEDINGS OF SPIE
SPIE—The International Society for Optical Engineering

Photonics Technology into the 21st Century: Semiconductors, Microstructures, and Nanostructures

**Seng Tiong Ho
Yan Zhou
Weng W. Chow
Yasuhiko Arakawa**
Chairs/Editors

**1–3 December 1999
Singapore**

Sponsored by
SPIE—The International Society for Optical Engineering
Nanyang Technological University, Singapore

Cosponsored by
SPIE Singapore Chapter
Institute of Physics, Singapore
United States Air Force Asian Office of Aerospace Research
and Development (AFOSR/AOARD)
United States Army Research Office-Far East (ARO-FE)

Cooperating Organizations
National University of Singapore
SPIE Hong Kong Chapter
SPIE India Chapter
SPIE Japan Chapter
SPIE Korea Chapter
SPIE Taiwan Chapter



Volume 3899

SPIE is an international technical society dedicated to advancing engineering and scientific applications of optical, photonic, imaging, electronic, and optoelectronic technologies.



The papers appearing in this book comprise the proceedings of the meeting mentioned on the cover and title page. They reflect the authors' opinions and are published as presented and without change, in the interests of timely dissemination. Their inclusion in this publication does not necessarily constitute endorsement by the editors or by SPIE.

Please use the following format to cite material from this book:

Author(s), "Title of paper," in *Photonics Technology into the 21st Century: Semiconductors, Microstructures, and Nanostructures*, Seng Tiong Ho, Yan Zhou, Weng W. Chow, Yasuhiko Arakawa, Editors, Proceedings of SPIE Vol. 3899, page numbers (1999).

ISSN 0277-786X
ISBN 0-8194-3501-5

Published by
SPIE—The International Society for Optical Engineering
P.O. Box 10, Bellingham, Washington 98227-0010 USA
Telephone 360/676-3290 (Pacific Time) • Fax 360/647-1445

Copyright ©1999, The Society of Photo-Optical Instrumentation Engineers.

Copying of material in this book for internal or personal use, or for the internal or personal use of specific clients, beyond the fair use provisions granted by the U.S. Copyright Law is authorized by SPIE subject to payment of copying fees. The Transactional Reporting Service base fee for this volume is \$10.00 per article (or portion thereof), which should be paid directly to the Copyright Clearance Center (CCC), 222 Rosewood Drive, Danvers, MA 01923. Payment may also be made electronically through CCC Online at <http://www.directory.net/copyright/>. Other copying for republication, resale, advertising or promotion, or any form of systematic or multiple reproduction of any material in this book is prohibited except with permission in writing from the publisher. The CCC fee code is 0277-786X/99/\$10.00.

Printed in the United States of America.

Contents

xi *Conference Committee*

PLENARY SESSION I

- 2 **Future technology and business opportunities in photonics: a view from the Optoelectronics Industry Development Association (OIDA) [3899-201]**
A. A. Bergh, Optoelectronics Industry Development Association (USA)
- 12 **Oxide-confined verticle-cavity surface-emitting lasers, quantum dots, and the Purcell effect: can scaling the mode size improve laser performance? [3899-202]**
D. G. Deppe, D. L. Huffaker, H. Huang, L. A. Graham, Univ. of Texas/Austin (USA)

PLENARY SESSION II

- 24 **Optical nonlinearities in semiconductors [3899-203]**
S. W. Koch, T. Meier, Philipps-Univ. Marburg (Germany)
- 36 **Advances in missile technology: impact of photonics [3899-204]**
A. S. Pillai, Defence Research and Development Organisation (India)

SESSION 1 NITRIDES

- 46 **Piezoelectric Franz-Keldysh effect in a GaN/InGaN/AlGaIn multilayer structure [3899-02]**
Y. T. Hou, K. L. Teo, M. F. Li, National Univ. of Singapore; K. Uchida, Univ. of Electro-Communications (Japan); H. Tokunaga, N. Akutsu, K. Matsumoto, Nippon Sanso Co./Tsubuka Labs. (Japan)
- 54 **Structural and optical properties of GaN materials grown on Si by metalorganic chemical vapor deposition [3899-03]**
J. L. Chen, National Univ. of Singapore; Z. C. Feng, Institute of Materials and Research Engineering (Singapore); X. Zhang, National Univ. of Singapore; S. J. Chua, Institute of Materials and Research Engineering (Singapore) and National Univ. of Singapore; Y. T. Hou, J. Lin, National Univ. of Singapore
- 63 **Luminescence, morphology, and x-ray diffraction features of InGaIn materials grown on sapphire by metalorganic chemical vapor deposition [3899-04]**
P. Li, National Univ. of Singapore; S. J. Chua, National Univ. of Singapore and Institute of Materials Research and Engineering (Singapore); Z. C. Feng, W. Wang, M. S. Hao, Institute of Materials Research and Engineering (Singapore); T. Sugahara, S. Sakai, Univ. of Tokushima (Japan)
- 73 **Common deep level in GaN [3899-05]**
T.-C. Wen, S.-C. Lee, W.-I. Lee, J.-D. Guo, M.-S. Feng, National Chiao Tung Univ. (Taiwan)
- 79 **Atomic force microscope study of GaN films grown by hydride vapor phase epitaxy [3899-07]**
H. Fang, Y. K. Wang, R. Y. Tsai, C. F. Chu, S. C. Wang, National Chiao Tung Univ. (Taiwan)

- 84 **Comparative investigation of high-resolution transmission electron microscopy and Fourier transform infrared spectroscopy for GaN films on sapphire substrate [3899-08]**
K. Li, Institute of Materials Research and Engineering (Singapore); Y. T. Hou, National Univ. of Singapore; Z. C. Feng, Institute of Materials Research and Engineering (Singapore); S. J. Chua, Institute of Materials Research and Engineering (Singapore) and National Univ. of Singapore ; M. F. Li, E. W. P. Lau, National Univ. of Singapore; A. T. S. Wee, Institute of Materials Research and Engineering (Singapore) and National Univ. of Singapore
- 92 **Stimulated emission from organic semiconductor [3899-09]**
L. Wang, Lab. of Excited State Processes (China); X. Liu, Y. Ning, Y. Liu, S. Wu, D. Wu, J. Zhao, C. Jin, Changchun Institute of Physics (China); L. Wang, X. Jing, F. Wang, Changchun Institute of Applied Chemistry (China)

SESSION 2 MEMS

- 98 **Improved silicon micromachined 3D mirror for acceleration sensing using an extrashort external-cavity laser self-mixing interferometer [3899-11]**
F. A. Chollet, A. Q. Liu, Institute of Materials Research and Engineering (Singapore); L. Zheng, A. K. Asundi, Nanyang Technological Univ. (Singapore); L. Lin, Univ. of Michigan (USA)
- 109 **Modeling of the optical torsion micromirror [3899-12]**
X. M. Zhang, F. S. Chau, C. Quan, National Univ. of Singapore; A. Q. Liu, Institute of Materials Research and Engineering (Singapore)
- 117 **Micromirror actuation with electrostatic force and plate bending [3899-13]**
S. Han, H. Park, J. Pak, Korea Univ.
- 124 **High-performance-readout integrated circuit for surface-micromachined bolometer arrays [3899-14]**
Y.-L. Chin, Chung Yuan Christian Univ. (Taiwan); T.-P. Sun, National Chi Nan Univ. (Taiwan); J.-C. Chou, National Yunlin Univ. of Science and Technology (Taiwan); Y.-C. Chin, Y.-C. Chou, Chung Shan Institute of Science and Technology (Taiwan); W.-Y. Chung, S.-K. Hsiung, Chung Yuan Christian Univ. (Taiwan)

SESSION 3 QUANTUM DOTS

- 134 **Quantum dot active regions for extended-wavelength (1.0 μm to 1.3 μm) GaAs-based heterostructure lasers and vertical-cavity surface-emitting lasers (Invited Paper) [3899-15]**
D. L. Huffaker, G. Park, Z. Zou, O. B. Shchekin, D. G. Deppe, Univ. of Texas/Austin (USA)
- 147 **Photoluminescence characteristics of GaAs/AlGaAs quantum dot arrays fabricated by dry and dry-wet etching [3899-16]**
X. Wang, A. Song, J. Liu, W. Cheng, G. Li, C. Li, Y. Li, J. Yu, Institute of Semiconductors (China)
- 153 **Effect of shape of quantum dots on strains: a finite element study [3899-17]**
G. Muralidharan, Institute of Microelectronics (Singapore)

SESSION 4 QUANTUM WELLS

- 162 **Fabrication of bandgap-tuned lasers in GaAs/AlGaAs structure using sol-gel SiO₂-induced quantum well intermixing [3899-18]**
L. H. Lee, O. Gunawan, B. S. Ooi, Y. Zhou, Y. C. Chan, Y. L. Lam, Nanyang Technological Univ. (Singapore)
- 168 **Photonic integration of InGaAs-InGaAsP laser using low-energy-implantation-induced quantum well intermixing [3899-19]**
H. S. Lim, B. S. Ooi, Y. L. Lam, Y. C. Chan, Y. Zhou, Nanyang Technological Univ. (Singapore); V. Aimez, J. Beauvais, J. Beerens, Univ. de Sherbrooke (Canada)
- 176 **Phase modulation of polariton in a GaAs quantum well waveguide [3899-20]**
K. Hosomi, M. Shirai, T. Katsuyama, Hitachi, Ltd. (Japan)
- 183 **InGaAlAs/InAlAs multiple quantum well structures grown by molecular beam epitaxy for long-wavelength infrared detection [3899-21]**
D. H. Zhang, W. M. Zhang, P. H. Zhang, T. Osotchan, S. F. Yoon, X. Shi, Nanyang Technological Univ. (Singapore); R. Liu, T. S. Wee, National Univ. of Singapore
- 191 **Influence of (001) vicinal GaAs substrates on the optical properties of defects in low-temperature-grown GaAs/AlGaAs multiple quantum wells [3899-23]**
M. H. Zhang, Y. F. Zhang, J. M. Sun, Q. Huang, C. L. Bao, J. M. Zhou, Institute of Physics (China)
- 196 **Optical Gunn effect in n-doped GaAs at mid- and far-IR wavelengths [3899-24]**
J. H. Stiens, Vrije Univ. Brussel (Belgium); G. N. Shkerdin, Institute of Radio Engineering and Electronics (Russia); F. Marest, R. A. Vounckx, Vrije Univ. Brussel (Belgium)

SESSION 5 MICROCAVITY AND NANO/MICROSTRUCTURES

- 210 **Nanophotonics: recent advances (Invited Paper) [3899-25]**
M. K. Chin, Nanovation Technologies, Inc. (USA); S. T. Ho, Northwestern Univ. (USA)
- 215 **Mode emission properties of semiconductor microdisk and microring lasers [3899-26]**
T.-D. Lee, P.-H. Cheng, J.-S. Pan, K. Tai, Y. Lai, K.-F. Huang, National Chiao Tung Univ. (Taiwan)
- 224 **Optical properties of InGaN multiple quantum well microdisks [3899-27]**
L. Dai, B. Zhang, Y. Zhang, R. Wang, X. Zhu, Peking Univ. (China); J. Y. Lin, H. X. Jiang, Kansas State Univ. (USA)
- 232 **InGaAlP quantum well microcavities of circular or deformed disks and disks with microstructures [3899-28]**
B. Zhang, G. Wang, Y. Chen, L. Dai, W. Fang, D. Wang, Y. Shen, Y. Qian, S. Xu, Z. Lai, X. Zhu, R. Wang, Peking Univ. (China); X. Y. Ma, Institute of Semiconductors (China)
- 239 **Eigenmode confinement in semiconductor microcavity lasers with an equilateral triangle resonator [3899-29]**
Y.-Z. Huang, Institute of Semiconductors (China)

- 247 **High-energy photon lithography for fabrication of photonic devices** [3899-30]
S. Lee, Nanyang Technological Univ. (Singapore); V. Kudryashov, Microelectronics Technology Institute (Russia); P. Lee, M. Liu, T. L. Tan, Nanyang Technological Univ. (Singapore)

SESSION 6 PHOTONIC BANDGAPS

- 258 **3D silicon infrared photonic lattices (Invited Paper)** [3899-32]
J. G. Fleming, S.-Y. Lin, Sandia National Labs. (USA)
- 268 **GaAs/Al_xO_y photonic bandgap material fabrication and characterization (Invited Paper)** [3899-33]
P. K. Bhattacharya, W. Zhou, J. Sabarinathan, D. Zhu, Univ. of Michigan (USA)
- 278 **Two-dimensional superconductor-dielectric photonic crystal** [3899-34]
C. H. R. Ooi, T. C. A. Yeung, T. K. Lim, C. H. Kam, Nanyang Technological Univ. (Singapore)

SESSION 7 OPTICAL COMMUNICATIONS

- 290 **1.2- μ m GaInAs/GaAs lasers: are they useful for high-capacity single-mode fiber datacom?** [3899-36]
F. Koyama, D. Schlenker, T. Miyamoto, Z. Chen, K. Iga, Tokyo Institute of Technology (Japan)
- 297 **Performance of a serial-search synchronizer for fiber-based optical CDMA systems in the presence of multiuser interference** [3899-37]
M. M. Mustapha, R. F. Ormondroyd, Cranfield Univ. (UK)
- 307 **New DS/WH encoding/decoding scheme for optical CDMA** [3899-38]
C. Yu, Beijing Univ. of Posts and Telecommunications (China); Q. Yang, Telecommunication Planning Research Institute of MII (China); W. Qin, Beijing Univ. of Posts and Telecommunications (China)
- 315 **Switching efficiency of ultrafast nonlinear interferometer as an optical time division demultiplexer** [3899-39]
X. Chen, M. Yao, M. Chen, J. Zhang, L. Xu, Y. Gao, Tsinghua Univ. (China)
- 319 **Optical switch and interconnect techniques based on semiconductor optical amplifiers** [3899-40]
D. Liu, X. Hu, D. Huang, Huazhong Univ. of Science and Technology (China)
- 326 **Normal-incident SiGe/Si MQW photodetectors operating at 1.3 μ m** [3899-42]
B. Cheng, C. Li, Q. Yang, H. Wang, L. Luo, J. Yu, Q. Wang, Institute of Semiconductors (China)
- 330 **Mechanism for erbium luminescence in silicon at 1.54 μ m** [3899-43]
M. Q. Huda, S. A. Siddiqui, M. N. Islam, M. S. Islam, Bangladesh Univ. of Engineering and Technology
- 335 **All-optical scheme for digital matrix multiplication** [3899-44]
P. Ghosh, D. N. Das, S. Mukhopadhyay, Vidyasagar Univ. (India)

SESSION 8 OPTICAL STORAGE

- 344 **Surface-emitting lasers for optical near-field data storage (Invited Paper) [3899-45]**
F. Koyama, S. Shinada, Tokyo Institute of Technology (Japan); K. Goto, Tokai Univ. (Japan); K. Iga, Tokyo Institute of Technology (Japan)
- 351 **Diffraction property of volume grating in Ce:KNSBN with differently polarized reading beam [3899-47]**
Z. Wang, B. Liang, G. Mu, J. Guan, H. Liu, R. Fu, Nankai Univ. (China)
- 359 **Test system for embossed information characteristics of 4X-density magneto-optical disk [3899-49]**
Z. Zhou, H. Chen, Huazhong Univ. of Science and Technology (China)
- 367 **650-nm AlGaInP quantum well lasers for the application of DVD [3899-50]**
L. Chen, X. Y. Ma, L. Guo, Institute of Semiconductors (China); J. Ma, H. Ding, Huayang Industrial Co. Ltd. (China); Q. Cao, L. Wang, G. Zhang, Y. Yang, G. Wang, M. Tan, Institute of Semiconductors (China)

SESSION 9 NONLINEAR OPTICS

- 376 **Optical nonlinearity of surface-modified PbS and $\text{Cd}_x\text{Pb}_{1-x}\text{S}$ nanoparticles in the femtosecond regime [3899-51]**
H. Li, Nanyang Technological Univ. (Singapore); B. Liu, National Univ. of Singapore; C. H. Kam, Y. L. Lam, W. X. Que, Nanyang Technological Univ. (Singapore); L. M. Gan, C. H. Chew, G. Q. Xu, National Univ. of Singapore
- 384 **Hyper-Rayleigh scattering and multiphoton fluorescence of nanoscale CdS colloids in water [3899-52]**
X. Wang, Y. Zhang, D. Fu, Z. Lu, Y. Cui, Southeast Univ. (China)
- 390 **Two-wave mixing in stark geometry photorefractive quantum wells under a magnetic field [3899-53]**
Y. F. Zhang, J. M. Sun, M. H. Zhang, Z. G. Zhang, Q. Huang, J. M. Zhou, Institute of Physics (China)
- 396 **Soliton stability and compression in a system with nonlinear gain [3899-54]**
S. C. V. Latas, M. F. S. Ferreira, Univ. of Aveiro (Portugal)
- 406 **Self-focusing, self-trapping, and optical limiting of light beams in photorefractive $\text{Bi}_{12}\text{SiO}_{20}:\text{Fe}$ crystal [3899-55]**
S. P. Aithal, Physical Research Lab. (India); P. P. Kiran, N. D. Rao, Univ. of Hyderabad (India)
- 417 **Spectra distribution properties of ultraweak photon emission from a biological system and its applications in the 21st Century [3899-56]**
Y. Zhu, South China Normal Univ.; Z. Zhu, Sony Semiconductor of America; Z. Guo, J. Ma, S. Li, South China Normal Univ.; Z. Bao, C. Bao, Zhejiang Univ. (China)

SESSION 10 POSTER SESSION

- 428 **Amorphous SiCN films prepared by ECR-CVD technique for photoconductive detectors** [3899-59]
D. H. Zhang, Y. Gao, Nanyang Technological Univ. (Singapore); J. Wei, Gintic Institute of Manufacturing Technology (Singapore)
- 434 **Aligned $\text{In}_{0.5}\text{Ga}_{0.5}\text{As}$ quantum dots on laser-patterned GaAs substrate** [3899-60]
S. K. Park, C. K. Hyon, B. D. Min, H. J. Kim, S. M. Hwang, E. K. Kim, Korea Institute of Science and Technology; H. K. Lee, C. Lee, Inha Univ. (Korea); Y. Kim, Donga Univ. (Korea)
- 440 **Taguchi optimization for SU-8 photoresist and its applications in microfluidic systems** [3899-61]
J. Zhang, K. L. Tan, L. J. Yang, H. Q. Gong, G. D. Hong, X. D. Wang, L. Q. Chen, Nanyang Technological Univ. (Singapore)
- 448 **Dynamics of diode-pumped microchip laser passively Q-switched with Cr:YAG** [3899-62]
W. Wang, M. Gong, G. Jin, Tsinghua Univ. (China)
- 455 **Pulse control of passively Q-switched microchip laser with cw pumping modulation** [3899-63]
W. Wang, M. Gong, G. Jin, Tsinghua Univ. (China)
- 462 **Quantum scale structures of nanocrystalline silicon films** [3899-64]
H. Y. Lin, Beijing Institute of Technology (China); Y. N. Gao, Peking Univ. (China); B. Liao, Y. Z. Guo, J. H. Liu, Beijing Institute of Technology (China); Y. X. Li, Peking Univ. (China)
- 468 **Holographic storage property of In:Fe:LiNbO_3** [3899-66]
W. Xu, R. Wang, M. Li, Y. Xu, Harbin Institute of Technology (China)
- 475 **Optical limiting properties of neutral nickel dithiolenes** [3899-67]
W. L. Tan, W. Ji, National Univ. of Singapore; J. L. Zuo, J. F. Bai, X. Z. You, Nanjing Univ. (China); J. H. Lim, S. S. Yang, D. J. Hagan, E. W. Van Stryland, CREOL/Univ. of Central Florida (USA)
- 483 **Nonlinear optical response of inorganic metal clusters $(\mu_3\text{-MoSe}_4)_X(\text{PPh}_3)_3\text{Cl}$ ($X = \text{Cu, Ag}$)** [3899-68]
Y. Xiong, National Univ. of Singapore; Q. Zhang, X. Xin, Nanjing Univ. (China); W. Ji, National Univ. of Singapore
- 489 **Dynamics of the $A^3\Pi_{0^+}$, $B^3\Pi_{1^+}$, and $C^1\Pi_1$ states of InCl by laser-induced fluorescence** [3899-69]
Y. Li, M. Lin, W. Zou, B. Zhang, W. Chen, Nankai Univ. (China)
- 497 **Plane wave quantity and its measurement of plate working surface** [3899-70]
J.-Q. Liu, Y.-N. Liu, Xi'an Institute of Optics and Precision Mechanics (China); L. Cao, Northwestern Polytechnical Univ. (China); X. Zhao, Xi'an Institute of Optics and Precision Mechanics (China)
- 503 **Image converter tube use in VUV.UV.visible light** [3899-71]
X. Zhang, L. Niu, M.-X. Gong, Y.-X. Zou, J.-Q. Liu, Xi'an Institute of Optics and Precision Mechanics (China)
- 508 **Optical refractive synchronization: bit error rate analysis and measurement** [3899-73]
J. R. Palmer, SilkRoad, Inc. (USA)

- 523 **Optical refractive synchronization: bidirectional information transport over a single wavelength/single laser for distances > 100 Km: analysis and measurement [3899-74]**
J. R. Palmer, SilkRoad, Inc. (USA)
- 550 *Author Index*

Conference Committee

Conference Chairs

Seng Tiong Ho, Northwestern University (USA)
Yan Zhou, Nanyang Technological University (Singapore)
Weng W. Chow, Sandia National Laboratories (USA)
Yasuhiko Arakawa, University of Tokyo (Japan)

Program Committee

Girish S. Agarwal, Physical Research Laboratory (India)
Hiroshi Amano, Meijo University (Japan)
Mee Koy Chin, Nanovation Technologies, Inc. (USA)
Hiroyuki Fujita, University of Tokyo (Japan)
Yong-Zhen Huang, Institute of Semiconductors (China)
Chen Liang Hui, Institute of Semiconductors (China)
Stephan W. Koch, Philipps-Universität Marburg (Germany)
Fumio Koyama, Tokyo Institute of Technology (Japan)
Yinchieh Lai, National Chiao Tung University (Taiwan)
Fong Yau Li, Institute of Materials and Research Engineering (Singapore)
Ming Fu Li, National University of Singapore
Jeff Y. Tsao, Sandia National Laboratories (USA)
Yi-Jen Diana Tsou, Industrial Technology Research Institute (Taiwan)
S. C. Wang, National Chiao Tung University (Taiwan)
Baoxi Xu, Data Storage Institute (Singapore)
Bei Zhang, Peking University (China)

Session Chairs

- 1 Nitrides
 S. C. Wang, National Chiao Tung University (Taiwan)
 Yong-Zhen Huang, Institute of Semiconductors (China)
- 2 MEMS
 Fong Yau Li, Institute of Materials and Research Engineering (Singapore)
- 3 Quantum Dots
 Yasuhiko Arakawa, University of Tokyo (Japan)
- 4 Quantum Wells
 Yan Zhou, Nanyang Technological University (Singapore)
- 5 Microcavity and Nano/Microstructures
 Bei Zhang, Peking University (China)

- 6 Photonic Bandgaps
 Yinchieh Lai, National Chiao Tung University (Taiwan)
- 7 Optical Communications
 Mee Koy Chin, Nanovation Technology, Inc.
 Fumio Koyama, Tokyo Institute of Technology (Japan)
- 8 Optical Storage
 Baoxi Xu, Data Storage Institute (Singapore)
- 9 Nonlinear Optics
 Girish S. Agarwal, Physical Research Laboratory (India)

SPIE and Nanyang Technological University wish to thank the following for their contribution to the success of this conference:

- United States Air Force Asian Office of Aerospace Research and Development (AFOSR/AOARD)
- United States Army Research Office-Far East (ARO-FE)

Plenary Session I

Future Technology and Business Opportunities in Photonics: A View from the Optoelectronics Industry Development Association (OIDA) *

Dr. Arpad A. Bergh

Optoelectronics Industry Development Association, 2010 Massachusetts Avenue, NW, Suite 200,
Washington, DC 20036, P:202-785-4426, F: 202-785-4428, email: aboida@osa.org

ABSTRACT

The “optoelectronics industry” is a collection of six or more distinct industries that all depend on OE technology. The major markets are in communication, imaging, storage and displays. This paper gives a brief overview of the anticipated paradigm shifts, the potential markets and the promising new technologies in various OE markets.

Keywords: optoelectronics industry, optical communications, imaging, optical storage

1. INTRODUCTION

The dictionary defines Optoelectronics as “a branch of electronics that deals with electronic devices for emitting, modulating, transmitting, and sensing light”.

Today Optoelectronics has a broader meaning. It also incorporates Electro-optics, a branch of physics that deals with the effects of an electric field on light transversing it (e.g. gas and solid state lasers), and Photonics, a branch of physics that deals with the properties and applications of photons, especially as a medium for transmitting information. It also increasingly overlaps with many facets of Optics, a science that deals with light, its genesis and propagation.

This relatively new branch of science and engineering interchangeably deploys electrons and photons, to take advantage of their best attributes. It has already laid the foundation of the technology that enables the information age. Optoelectronics enables all functions of the information industry. It is essential in gathering the information (imaging), as well as in transporting and displaying it. It also has a role, along with other technologies, in storing and processing information. Due to their increasingly important role optoelectronics components already represent a substantial worldwide market exceeding by a factor of three the market for traditional optics, Fig 1.

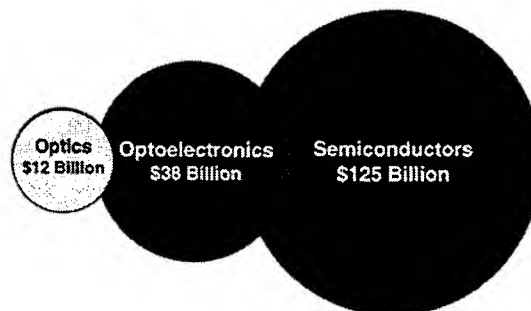


Figure 1. Worldwide Component Markets 1998

This is indeed remarkable when we consider that these elementary particles were only discovered in this Century.

Discovery of the electron:

It was in 1887, when J. J. Thomson working in the Cavendish laboratory at Cambridge measured the ratio of the charge e of an electron to its mass m by observing its deflection in both electric and magnetic fields. The discovery of electron is usually said to date from this historic experiment.

*Also published in *Proc. of SPIE* Vols. 3896, 3897, and 3898

Discovery of the Photon.

The discovery of the photon dates back to Planck's experiments in 1900 on the energy of photo-electronics leading to h , the Planck constant, 6.6254×10^{-27} erg sec. This was followed in 1905 by the famous Planck-Einstein equation:

$$E = h\nu,$$

Where h is the Planck constant and E is the energy of a quantum of light (called photon by others at a later date).

Some of the major attributes of the two particles explain their application domains and are compared in the following table:

Attributes	Electrons	Photons
wavelength	3 cm – 30 m	500 nm
Frequency	10 MHz – 10 GHz	500 THz
Energy	40 neV – 40 μ eV	2 eV
Propagation loss	High (in copper wire)	Low (in optical fiber)
Particle interaction	High	None

There are certain functions that can be uniquely provided by optoelectronics. In other areas OE competes with other technologies or assumes a supporting role as shown in the following table.

The Role of Optoelectronics in the Information Age Technologies

Dominant Enabling Technology	Competing with Other Technologies (Market Share)	Supporting Role Dominated by Electronics
Transmission	Sensors	Logic functions
Display	Storage	Processing
Imaging	Lighting	

2. OPTOELECTRONICS INDUSTRY

There is no single optoelectronics industry. It is, in fact, a combination of several industries supported by common technology and common infrastructure as shown in Fig. 2

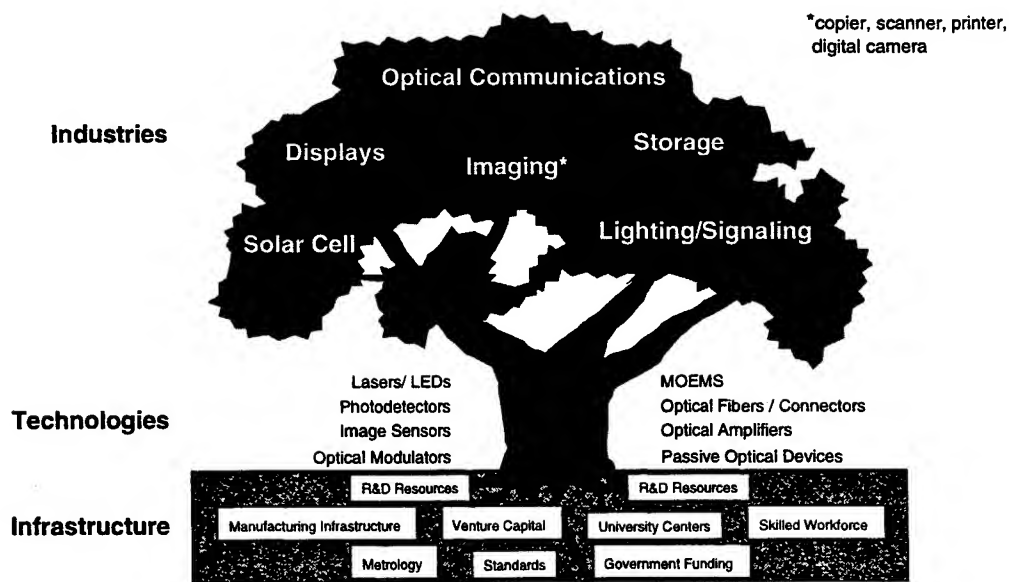


Figure 2. Optoelectronics Industries

Of the industry segments depicted in this figure communications, imaging, storage and displays have a large worldwide market, Fig 3 Emerging markets in optoelectronics are energy related and will have an increasingly important role as the world's known energy sources are depleted. Solar cells produce environmentally clean energy and solid state lighting has the promise of providing more efficient and environmentally benign replacement for the currently used incandescent and fluorescent light sources.

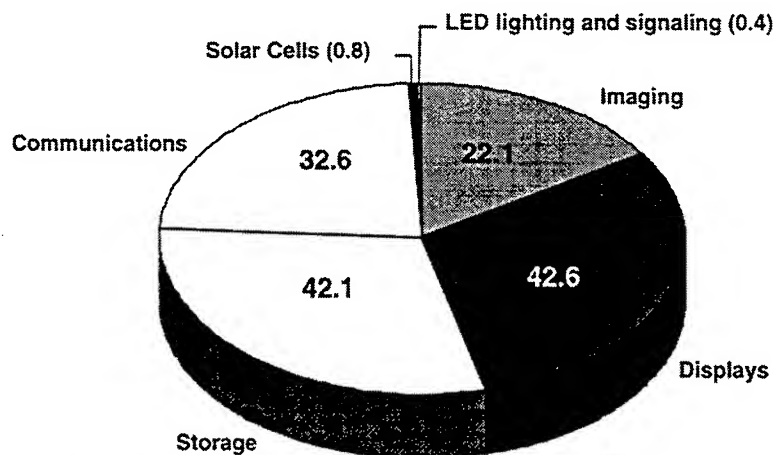


Figure 3. World OE Production (\$B) 1998 (Total: \$140.6 B, North America Estimate: \$42.8B)

This paper gives a brief overview of the anticipated paradigm shifts, the potential markets and the promising new technologies in various OE markets.

3. OPTICAL COMMUNICATION

Driven by Internet and data services, the evolution of information networks continues at an unprecedented pace. The traditional telephone architecture is rapidly changing:

- Transmission is moving to all-digital before the end of the next decade
- Voice services are increasingly augmented by multi media (incl. imaging)
- Voice, relative to data, becomes insignificant part of transmission bandwidth
- Intelligence is moving from the central office to the perimeter of the network
- The stationary telephone is replaced by the mobile telephone
- Telecom and datacom networks converge.

All these changes are made possible by the evolution of the electronic and optoelectronic technologies. Multi-Gb/s SONET/SDH and WDM transmission, resulting in capacities in excess of one Terabit/sec on a single fiber meet the explosive demand for bandwidth. Simultaneously, the increasing dominance of Internet, Web and data services is causing a conversion from voice- to data-centric networks, with a need for high-speed and broadband transmission at the lowest-possible cost.

In addition to the ongoing research and development at universities and industry the government has also played a significant role in this evolution. Some of the fruits of DARPA sponsored technologies are being implemented commercially and are changing the communications landscape. On the service level there is the Internet, on the system level WDM is reaching all segments of the network and on the device level VCSELs promise to lower costs, facilitate the integration of electronic and photonic components and render optical networks more affordable. Simultaneously the 1996 Telecommunication Act is unleashing competition among service providers and the consumer is left with a bewildering array of options. The streets of major cities are under attack from competing carriers laying new cable, and mobile phones are spreading faster than before.

OIDA's roadmapping in optical communication started in 1992. The most recent studies took place in 1998 and 1999. The 1998 study concentrated on the anticipated demand on communication systems that can deliver the required services. The predicted growth rate of the various communication services is shown in Fig 4.

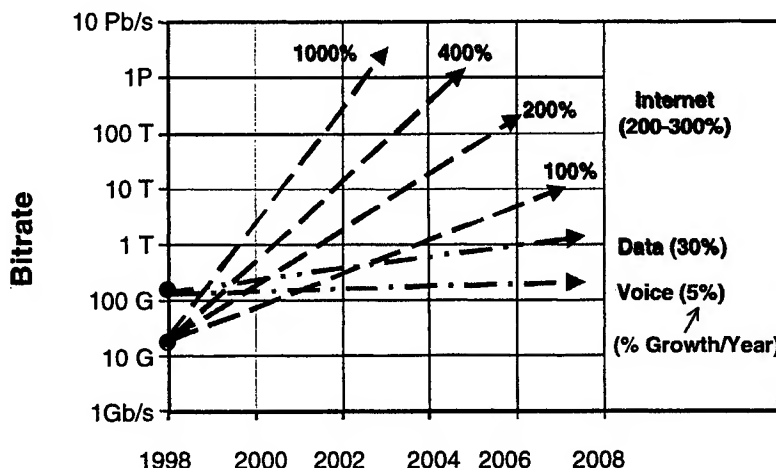


Figure 4. Growth Rate of Communication Services

This amazing growth rate is fueled by the evolution of the communication bandwidth which got a major boost in the mid-nineties from the commercial implementation of wavelength division multiplexing (WDM). To keep up with this growth and to deploy all the technology that has been demonstrated to date many practical and commercial issues must be addressed. The migration of the optical technology from the high performance backbone networks toward the high volume access network requires a drastic cost reduction of the OE components. The relentless cost reduction in the transmission network expressed in bit-km is shown in Fig 5.

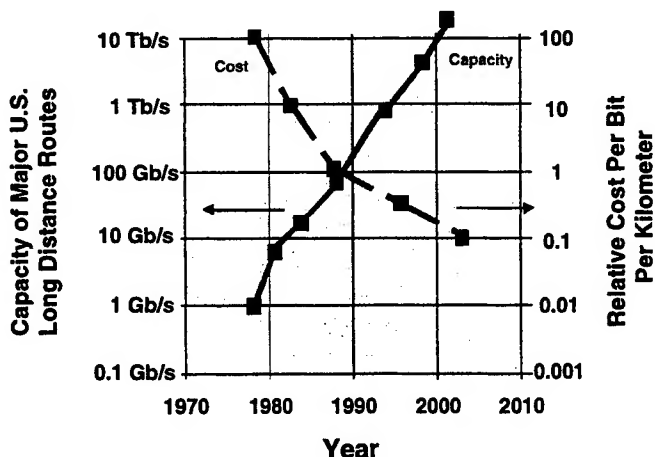


Figure 5. Transmission Cost Erosion, Ref. Yanming Liu, Corning

When the study was initiated two years ago it was obvious that communication would expand exponentially. It was also obvious that communication is segmented into several markets with sometimes overlapping and other times with divergent requirements.

The main areas of applications of the key OE components are:

- Long-Distance,

- Metro/Interoffice,
- Enterprise and Metro/Access,
- Local Area Network/Wide Area Network,
- Local Access Networks, and
- Backplane/Building Wiring.

In developing a roadmap estimates are made of the potential market volumes of the components in these various network segments, along with the key performance parameters and price targets as function of time. It is, however, exceedingly difficult to make predictions on the growth of the market volume of specific optoelectronic components. Nevertheless, using trend curves, latest technology developments and input from industry sources and analysts, a roadmap is constructed with the proviso that the predictions must be updated as data on actual equipment deployments and network applications become available.

The 1999 OIDA Roadmap Report delineated the OE components that require major industry efforts for their commercial realization. The following is a sample of key components required for optical networks with significant near term (1 to 4 years) market potential:

- Optical Crossconnects
- Optical Switches
- Optical Add-Drop Multiplexers
- Tunable Lasers
- Optical Amplifiers
- Optical Transceivers

An overriding requirement of these products is the simultaneous improvement in performance and ongoing cost reduction. The cost of components on the other hand depends on the volume of production. It is difficult to build high volumes when there is a proliferation of products for a given function. Optical switching for instance is one of the most desired functions but there are at least nine different approaches in which this can be accomplished. It will take several years and several generations of equipment before commonality is reached and standards are developed. In the meantime one can expect a steady increase in component performance with ongoing price erosion as shown in the next OIDA roadmap chart, Fig 6.

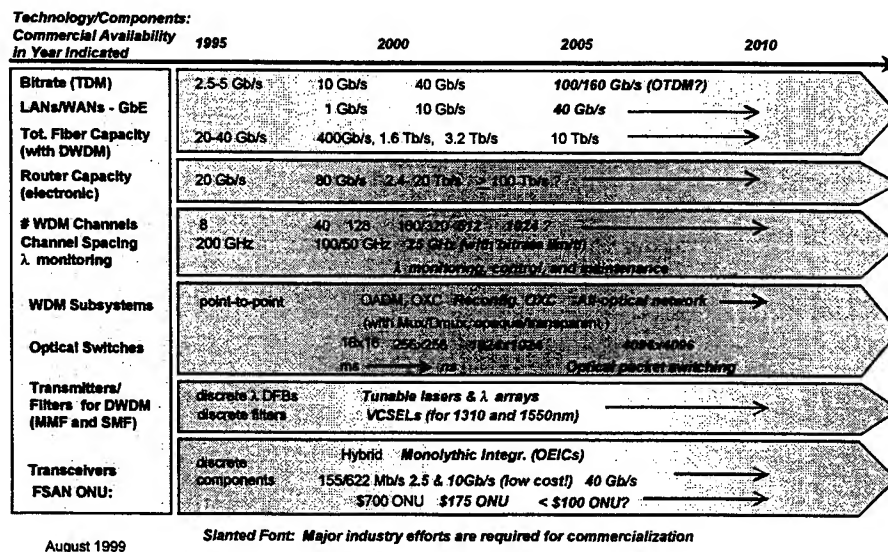


Figure 6. OIDA Communications Roadmap – 1999

All this activity will fuel the growth of the optoelectronic communications market, which in 1997 has already reached \$ 30 billion worldwide. As indicated in Fig 7 this market is expected to double by 2001 with no saturation in site for many years to come.

1997 Communications Market \$30.

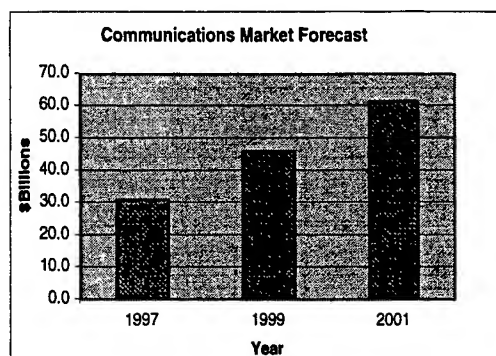
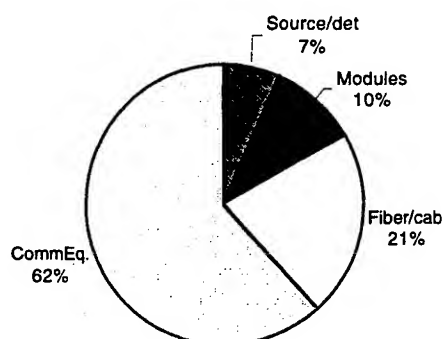


Figure 7. Optoelectronic Communications Market

4. IMAGING

Growth in the market value of the imaging industry has significantly lagged other technology sectors of the economy over the last five years as evidenced by the aggregate stock performance of imaging companies compared to the performance of the S&P 500 index. The Salomon Smith Barney Imaging Composite (SSIC), a weighted index of 50 imaging companies, widely used to track industry trends was up only 12%, versus more than 25% for the S&P 500 index.

The SSIC is composed of 5 sectors with Diversified Imaging/Photo and Document Processing companies representing 90% of the value of the composite. This Sector actually declined 4% last year, since many products in this sector are "mature" and experienced rapid price declines and decelerating volumes. Companies in this sector are looking to Advanced Imaging Applications as key growth drivers for future earnings.

Imaging companies are looking to Advanced Imaging Applications as key growth drivers for future earnings.

Advanced Imaging refers to the extension of conventional imaging products such as photographic film and cameras, video, copiers etc. as well as enabling entirely new capabilities through the application of digital technology. In the image capture area for example, electronic still cameras are replacing instant photography for scientific, insurance and real estate applications. Last year in Japan digital camcorders outsold both 8mm and VHS analog models. Worldwide digital camcorder sales totaled over \$3B. In 1998, it is estimated that 1.1 million digital cameras were sold in the U.S., up from 740,000 the prior year. Those figures should expand rapidly as PC based imaging becomes more user friendly and photo-realistic digital printers are able to interface directly to digital cameras.

Also, digitization is expected to provide significant growth for traditional film-based imaging companies and photofinishers. Digitization refers to high-resolution scanning and digital printing of film images and photographs. While commercial labs and motion picture special effects houses have transitioned to a digital infrastructure over the last 10 years, minilabs and wholesale photofinishers are just now beginning to install equipment that allows in line digitization of film with minimal impact on workflow.

When this digital infrastructure is in place and broadband internet access is widely available, it will enable a wide range of internet based imaging products and services. Also, new partnerships and joint ventures between film companies, internet companies and chip manufacturers are expected to increase growth. Many advanced imaging applications will be enabled by the wide spread access of broadband communication to the internet, greater microprocessor performance and highly integrated optoelectronic components.

Once optical networks enable broadband access to the internet, a major beneficiary will be imaging with many opportunities for instant transfer of still and motion picture images.

While the potential market for military and industrial imaging applications at \$3 to \$5 billion is much smaller than digital photo-finishing and networked imaging services (\$15 to \$20 billion), the technology demands will be an important driver for advanced imaging capabilities. Current market forecasts are based on extrapolations and are probably too conservative.

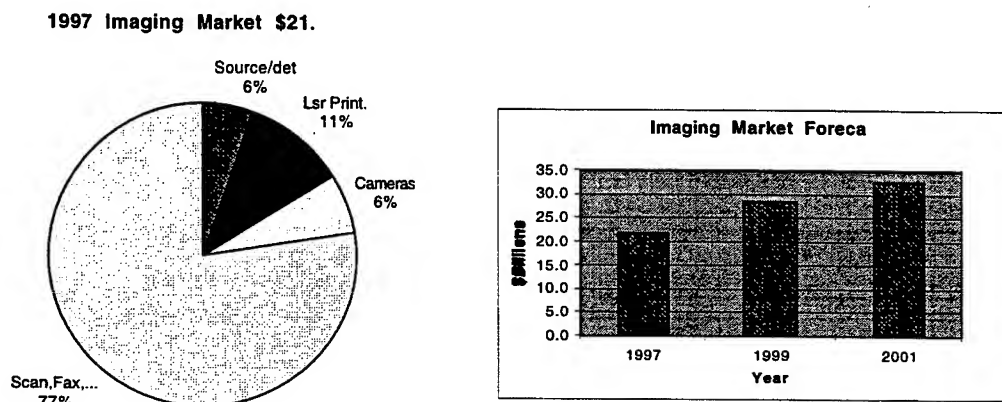


Figure 8. Optoelectronics Imaging Market

Typical areas of growth in imaging will benefit from

- Digital image format
- Digital signal processing with a great latitude of manipulating images
- Intelligent image capture/tracking
- Improved image sensor technology expanding the spectral and spatial resolution at an affordable cost
- Miniaturization, increasing portability and lowering power
- Fiber to the home, and
- Increased Small Office – Home Office use of imaging equipment.

Expanded Vision refers to the ability to outperform human vision.

Expanded Vision Characteristics are:

- Wider Field of View
- Broader Spectral Range (Uncooled detector)
- Increased Spatial Resolution
- Increased depth of field

These attributes are achieved by using advanced image sensors and by electronically processing the gathered information, such as in image fusion. In the future images acquired from multiple detectors will be combined using image fusion algorithms with integrated optoelectronics hardware systems to provide enhanced performance over a much broader spectral range than products are currently capable of delivering.

Night Vision Products

Night vision products have a long history dating back to the '60s. Refined military applications developed in the last two decades leading to many advanced products.

Currently military and law enforcement applications represent the largest segment of the night vision equipment market. In 1998 the market size for this segment exceeded \$3B. However, in the 2003 –2005 time frame, automotive, surveillance and home security applications are expected to approach the size of the current military /law enforcement segment. Optoelectronic products are estimated to be roughly 1/3 the total market size for these applications.

Miniaturization in Imaging – “The Micro Camera”

Many of the applications for micro cameras are similar to those identified for digital cameras, which are currently enjoying double digit growth in the marketplace. The acceptance of digital cameras as solutions for advanced imaging applications has been paced by the ability of the technology to meet market needs better than existing technology i.e. traditional photography. Micro camera characteristics include:

- Significantly Smaller Size
- Higher Spatial Resolution (In Color!)
- Lower Power

Today, micro cameras are used largely by law enforcement, military and private security agencies for surveillance and home security applications. In total these represent a market size of \$1B/yr. As digital cameras become a common peripheral for desktop and notebook PCs, demand for micro cameras for notebooks PDAs and other portable appliances will drive significant demand. In the 2003 –2005 time frame, these applications will represent the largest market segment followed by surveillance and inspection systems. In the table below, the optoelectronic products are estimated to be about 20% of the total market.

Intelligent Image Capture

The intelligent image capture system addresses the technology associated with the integration of a complex imaging system capable of automatically recognizing, isolating and tracking a target or object of interest in a scene in real time. Imaging applications identified for intelligent image capture also drive significant demand for digital image processing hardware as system complexity increases. The required image processing speeds for future systems might outpace Moore's Law.

Although many of the key enabling technologies for Intelligent Image Capture are algorithm based, the integrated systems designed for most applications drive significant demand for optoelectronic components.

Market Potential for Tracking Systems

Application	Estimated Total Market for Application in 2003	Estimated Market Size for OE Products
Weapons/Guidance Target Tracking	\$5B	\$1B
Surveillance / Security	\$100M	\$20M
Automotive	\$1B	\$200M
Consumer Web Camera	\$500M	\$100M

5. OPTICAL STORAGE

Data storage is an area where the optical approach competes with other technologies, such as magnetic hard disc, magnetic tape, semiconductor memory, etc.

Optical storage offers a reliable and removable storage medium with excellent archival lifetime at a low cost. Both optical recording and readout can be performed with a head positioned relatively far from the storage medium, unlike magnetic hard drive heads. This allows the medium to be reliable and removable, but the heavier head also leads to slower access time compared to hard disk drives. Consequently optical storage is limited to applications requiring reliability and removability, such as archival storage, software distribution, medical imaging, storing digital photographs, etc.

The market for disc storage exceeded \$60 B/year in 1996 with a small fraction attributed to optical storage as shown in Fig 9

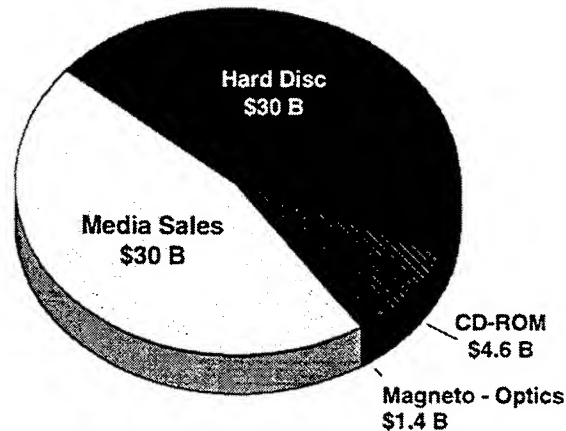


Figure 9. Worldwide Storage Market - 1996

With the rapid expansion of the Internet, server-based applications will emerge. Electronic commerce, medical imaging, libraries and corporate networks require modest access time (<10 ms) but very large storage capacities and reasonable transfer rates. These applications might give a further boost to the optical disc market. Optical disk market is also expected to grow for computer applications with the new DVD format gaining market share as shown in Fig 10

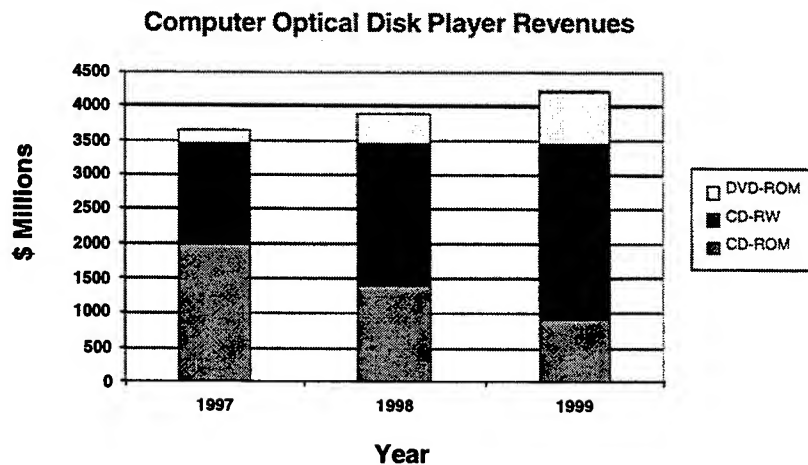


Figure 10. Optical Storage for Computers, Source: OITDA

It should be noted that storage technology is facing the same cost reduction pressure than all other market segments. Similar to the charts shown for communication, storage has a history of steady improvement in performance with a decline in unit price. For optical storage to maintain its position and increase its market share it must outperform competing technologies on both counts.

6. FUTURE TRENDS IN OPTOELECTRONICS

Future opportunities in optoelectronics will come in three areas:

- Improvements in technology – new breakthroughs
- Low cost, high volume manufacturing, and
- Integration with other technologies.

The first two items require no explanation. Integration requires the vertical integration of traditional academic disciplines. It should be a natural extension of optoelectronics which itself was created from the integration of optics and electronics. Future opportunities will rise from the integration with electronics, electronic processing (including software), micromechanics, etc as depicted in Fig 11

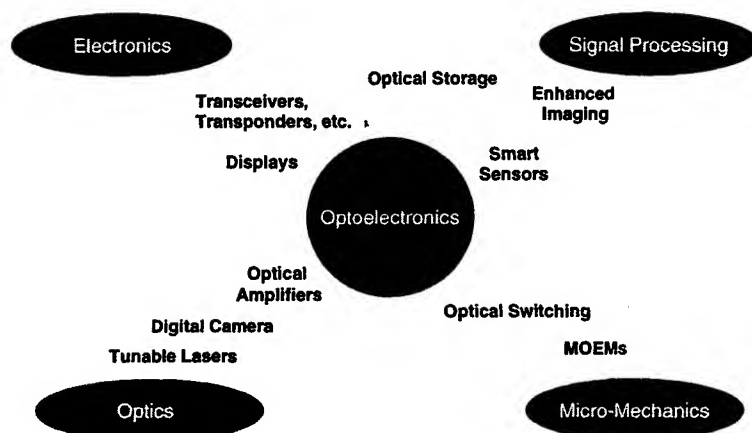


Figure 11. OE Centered Technology Integration

These are exciting times to be in optoelectronics. Our research and products will have major impact in many application areas from communication to transportation, medicine, biotechnology, electronic commerce, entertainment, etc. It will also support the leading technologies of the 21st Century, Fig 12.

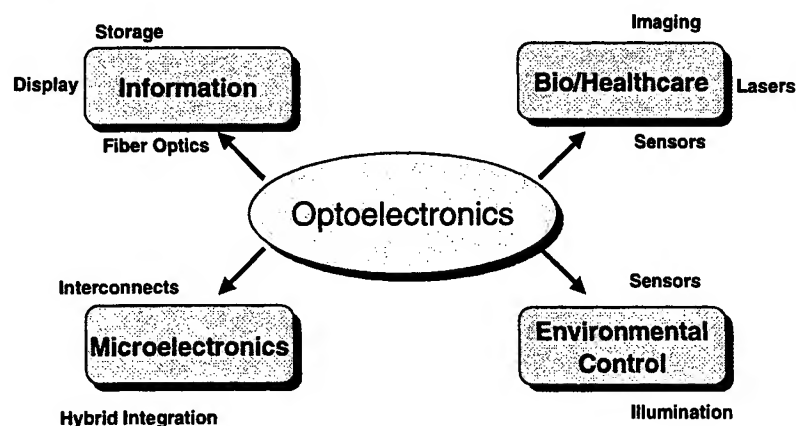


Figure 12. Leading Technologies for the 21st Century

Oxide-Confined Vertical-Cavity Surface-Emitting Lasers, Quantum Dots, and the Purcell Effect: Can Scaling the Mode Size Improve Laser Performance? *

D.G. Deppe, D.L. Huffaker, H. Huang, and L.A. Graham

Microelectronics Research Center
Department of Electrical and Computer Engineering
The University of Texas at Austin, Austin, Texas 78712-1084

ABSTRACT

The development of vertical-cavity surface-emitting lasers (VCSELs) has led to new types of low power, high efficiency light sources for data communication. The small size, low power, and surface-normal emission of VCSELs has enabled relatively dense two-dimensional arrays for highly parallel data communication and optical signal processing. In this paper we examine the issues of device scaling on VCSEL performance. We look specifically at what benefits may be derived from continued scaling of the active volume down to minimum sized dimensions, and what device schemes may be required to obtain the scaling. Laser rate equations are used to show that when the VCSEL mode volume is reduced to wavelength cubed dimensions, a significant improvement in modulation speed is predicted based on the radiative lifetime change due to the Purcell effect. However, several parasitic effects must be controlled in order to realize these benefits. Most important are control of the optical loss due to diffraction or scattering, and control of the electronic losses due to carrier diffusion and surface effects. Novel optical confinement schemes based on oxide-apertures, photonic bandgaps, and/or closely coupled two-dimensional arrays may be useful for controlling optical loss, while self-assembled quantum dots are attractive for controlling electronic diffusion to dimensions within the minimum optical mode volume.

Keywords: Semiconductor lasers, VCSELs, microcavities, cavity design, quantum dots, controlled spontaneous emission, high speed modulation.

1. INTRODUCTION

Vertical-cavity surface-emitting lasers (VCSELs) have emerged as one of the most important semiconductor lasers for low power optical interconnects.¹ Most commercial VCSELs are presently based on proton implantation to control the current injection into a small area of the optical cavity.² The optical mode volume is then defined by gain-guiding. This fabrication scheme has numerous proven advantages for manufacturing VCSELs including photolithographic patterning of the active area, planar processing, high device reliability, and high yield. On the other hand, in many ways devices based on gain-guiding have inferior performance to index-confined VCSELs, especially oxide-confined VCSELs.³ For gain-guided VCSELs, diffraction loss from the optical mode limits scaling the active volume to very small sizes, and can lead to instabilities in the VCSEL threshold and operating characteristics due to thermally induced index-guiding. Because of this there is a wide-spread industrial research effort in developing commercial VCSELs based on oxide confinement, for which these thermal effects are reduced or eliminated by the built-in index guide of an oxide-aperture. As compared to proton implanted VCSELs, oxide-confined VCSELs have low threshold currents and lower threshold current densities,³⁻⁹ higher wall-plug efficiency,¹⁰⁻¹² higher modulation speed,^{13,14} and improved mode characteristics for both multi-mode and single-mode operation.^{15,16} The lower power operation is crucial for two-dimensional arrays for reducing thermal cross-talk and increasing the VCSEL packing density. Oxide-confined VCSELs also have greatly improved scaling behavior. While gain-guided VCSELs that operate at 0.85 μm or 0.98 μm begin to show diffraction loss effects when the optical mode is reduced below $\sim 10 \mu\text{m}$ diameter, oxide-confined VCSELs show good scaling behavior down to $\sim 3 \mu\text{m}$ diameter. The improved scaling behavior is due to control of the diffraction loss by the oxide aperture.^{17,18}

In this paper we examine the impact of scaling the VCSEL optical mode to even smaller sizes than that presently achieved, ultimately to volumes approaching a cubic wavelength. If such small optical modes can be achieved new VCSEL characteristics are predicted, especially for the modulation response. Simply scaling the active volume to small size can greatly reduce the lasing threshold current, since fewer electronic states must be inverted to achieve optical gain. This may be of interest for realizing extremely low threshold VCSELs for new ultralow power operations, such as for optical interconnects for dense focal plane arrays.¹⁹ As we discuss below, though, a potentially more interesting result is the decreased radiative

*Also published in *Proc. of SPIE* Vols. 3896, 3897, and 3898

lifetime that results due to the Purcell effect, which can lead to high speed VCSEL operation even for bias levels at or below lasing threshold. High speed bias-free operation may then be possible, greatly improving VCSEL array performance and further reducing power consumption. Although the maximum power from such a small optical mode is reduced over today's commercial VCSELs, this power limitation can in principle be eliminated by using microarrays of Purcell enhanced VCSELs.

At present there are two serious device constraints that prevent the scaling of VCSELs to small optical modes. The first is optical loss. Depending on the mode confinement scheme, either diffraction or scattering loss usually accompanies a reduction in the optical mode size, and this is a major scaling limitation in today's VCSELs. In principle diffraction or scattering loss may be eliminated through lateral confinement using either very short cavities along with oxide apertures or photonic bandgaps for lateral confinement, or perhaps more simply by diffractively coupling the elements of a microarray. However, if optical loss is not controlled the gain required for lasing threshold in the small mode volume can exceed the maximum available from the active material. The second constraint is in the electronic confinement. Planar quantum well active regions can lead to lateral carrier diffusion lengths of several microns at room temperature, while electrons and holes must effectively be confined to the optical mode volume in order to realize the Purcell effect. Actually, the Purcell effect can reduce the diffusion length by shortening the recombination time, but it would be more effective to achieve tight lateral electronic confinement to sub-micron optical mode sizes. This can be obtained using quantum dot (QD) light emitters, for which lateral electronic confinement is "built-in" due to the self-organization of highly strained epitaxial films. The recent advances in QD lasers,²⁰⁻²⁴ including QD VCSELs,²⁵⁻²⁹ shows that this approach appears viable. Note that the diffusion problem is not of such a concern for infrared lasers, for which the optical wavelengths are a few microns within the semiconductor material.

Below we discuss the Purcell effect in oxide-confined VCSELs in detail. Experimental results on QD and planar quantum well microcavity light emitters and lasers aimed at characterizing the Purcell effect are described. Rate equations are used to predict the impact of the Purcell effect on VCSELs, both for lasing threshold and modulation response.

2. PURCELL EFFECT IN AN APERTURED-MICROCAVITY

It is well-known that an emitter's spontaneous emission rate is controlled by the volume and Q (loss rate) of the optical modes to which it's coupled.^{30,31} Recently it was shown that the spontaneous lifetime can be controlled in apertured-microcavities³²⁻³⁴ similar to those used for very low threshold VCSELs. Although Purcell's original arguments were brief and based on an ideal single mode cavity,³⁰ the VCSEL cavity typically contains many optical modes that exist within the emitters optical bandwidth. However, despite the existence of many optical modes, aperture confinement (or an etched pillar) can lead to one or two highly confined optical modes with sufficient Q to dominate the microcavity emission characteristics. This is illustrated in Fig. 1 for a VCSEL-type cavity based on distributed Bragg reflectors (DBRs). Each high index layer of the microcavity forms waveguide modes propagating in the plane of the layer, while apertured modes also exist that propagate back and forth vertically to the mirrors.

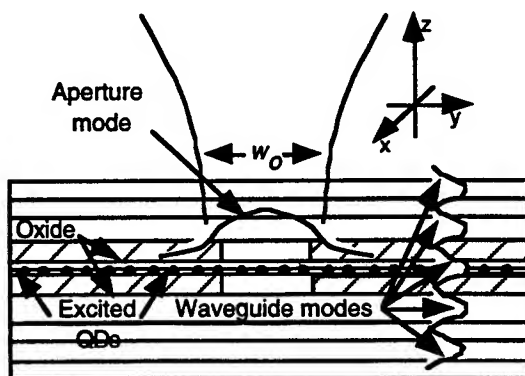


Fig. 1 Schematic illustration of an oxide-apertured microcavity based on QD light emitters and DBRs. Resonant optical modes exist due to the high index layers of mirrors and due to the double oxide apertures. However, for very small apertures the combined effects of Q and mode volume can lead to nearly 100% of the spontaneous emission being coupled into the aperture modes. (After Ref. [34])

When QD light emitters are used within the microcavity their coupling to the electromagnetic field depend on their positions within the cavity. Those QD emitters lying within the oxide-aperture interact with both the waveguide modes and the apertured-modes, while those QD emitters that lie outside the aperture interact with only the waveguide modes. We model the

QD light emitters as two-level systems. When only spontaneous emission is important for QD level decay, the total spontaneous from an emitter depends on the summation over all optical modes as given by

$$\frac{dN_2}{dt} = -\frac{2q^2\omega_d^2}{\hbar^2} \sum_m |\mathbf{d} \cdot \mathbf{A}_m(\mathbf{r}_d)|^2 \frac{(\gamma_d + \frac{\omega_m}{2Q_m})}{(\omega_d - \omega_m)^2 + (\gamma_d + \frac{\omega_m}{2Q_m})^2} N_2(t). \quad (1)$$

In Eq. (1), N_2 is the upper level population, m labels each cavity mode, q is the electronic charge, ω_d is the resonant frequency of the 2-level emitter, ω_m is the resonant frequency of mode m , V is the normalization volume of the cavity, \mathbf{d} is the dipole vector strength, $\mathbf{A}_m(\mathbf{r}_d)$ is the normalized vector strength of the cavity field at the QD position, $\frac{\omega_m}{2Q_m}$ is the photon loss rate from mode m , and γ_d is the QD dephasing rate. The vector strength of the cavity field is normalized such that $\int_V d^3\mathbf{r} \epsilon(\mathbf{r}) |\mathbf{A}_m(\mathbf{r})|^2 = \hbar/(2\omega_m)$, where $\epsilon(\mathbf{r})$ is the material permittivity at \mathbf{r} .

The collection of the cavity emission can be restricted to the apertured-modes using the spectral dependence of the emission from the cavity. These apertured-modes have frequencies that increase with the transverse mode number. By making very small apertures, higher order transverse modes can be eliminated from the bandwidth of the QD emitters, so that only the two lowest order transverse modes collect significant emission. The spontaneous photon number in these lower-order modes satisfy the rate equation

$$\frac{dn_o}{dt} = -\frac{\omega_o}{Q} n_o + \sum_{n=1}^{N_{ov}} \frac{2q^2\omega_n^2}{\hbar^2} |\mathbf{d}_n \cdot \mathbf{A}_o(\mathbf{r}_n)|^2 \frac{(\gamma_n + \frac{\omega_o}{2Q}) N_{2,n}(t)}{(\omega_n - \omega_o)^2 + (\gamma_n + \frac{\omega_o}{2Q})^2} \quad (2)$$

where the subscript n labels each emitter. We approximate the apertured-modes as Gaussian, and the QD emitters as having randomly oriented dipole moments. The coupling strength for these modes [Eqs. (1) or (2)] then becomes

$|\mathbf{d}_n \cdot \mathbf{A}_o(\mathbf{r}_n)|^2 = \frac{|\mathbf{d}|^2 \hbar e^{-(x_n^2 + y_n^2)/w_o^2}}{3\epsilon\omega_o\pi w_o^2 L_z}$, with a mode volume given by $V = \pi w_o^2 L_z$ where w_o is the mode radius and L_z is an effective cavity length. It has previously been estimated that when an oxide-apertures is not present, 80 to 90% of the spontaneous emission is coupled to waveguide modes (see Fig. 1), and this emission is approximately independent of the aperture. In terms of the dipole moment, the spontaneous emission rate of the QD embedded in bulk material is $\frac{1}{\tau_{sp,o}} = \frac{q^2\omega_n^3 n^3 |\mathbf{d}|^2}{3\pi\epsilon\hbar c^3}$, where n is the refractive index and c is the speed of light in vacuum. This means that for frequencies

close to that of the lowest order apertured-mode, the position dependent summation over emitter positions given from Eq. (1) can be expressed by

$$\frac{1}{\tau_{sp}(x_n, y_n, \omega_n)} = \frac{1}{\tau_{sp,o}} + \frac{1}{\tau_{sp,o}} \frac{4c^3/n^3}{\omega_o\omega_n w_o^2 L_z} \frac{(\gamma_n + \frac{\omega_o}{2Q}) e^{-(x_n^2 + y_n^2)/w_o^2}}{(\omega_n - \omega_o)^2 + (\gamma_n + \frac{\omega_o}{2Q})^2}, \quad (3)$$

where the first term on the right in Eq. (3) reflects the fact that the summation over the waveguide modes leads to a spontaneous emission rate nearly independent of the cavity, and the second term is due to the Purcell enhancement by the apertured modes. For large apertures the fraction of spontaneous emission actually captured by the apertured modes is negligible, while for small apertures the enhancement into the apertured modes can dominate the spontaneous lifetime. On

resonance the second term in brackets becomes $\frac{(\lambda_o^3/n^3)Q}{\pi^2(\pi w_o^2 L_z)}$ which is very nearly the mathematical form of the enhancement

described by Purcell for a single mode cavity.³⁰ Aside from constant factors, the cavity field intensity decay measured at frequency ω_n after a short-pulse excitation is given by

$$\frac{\omega_o}{Q} n_o(\omega_n, t) \propto \int_0^{\infty} d\rho_n \rho_n \frac{(\gamma_n + \frac{\omega_o}{2Q}) e^{-\rho_n^2/w_o^2} e^{-\frac{t-t_o}{\tau_{sp}(\rho_n, \omega_n)}}}{(\omega_n - \omega_o)^2 + (\gamma_n + \frac{\omega_o}{2Q})^2}. \quad (4)$$

The QD heterostructure has been used to characterize the Purcell effect for a micron sized oxide-apertured microcavity consisting of an 18 pair GaAs/AlAs DBR, an AlGaAs $\lambda/2$ cavity spacer, and a single upper $\lambda/4$ GaAs layer. The cavity spacer is $\text{Al}_{0.97}\text{Ga}_{0.03}\text{As}$ at the center of which is grown a single $\text{In}_{0.50}\text{Ga}_{0.33}\text{Al}_{0.17}\text{As}$ QD active region, with 100 Å GaAs layers and 135 Å grading layers immediately adjacent on either side. The apertured-microcavity is fabricated by patterning 5 μm squares in photoresist and reactive ion etching to a depth of 2900 Å to form mesas exposing both $\text{Al}_{0.97}\text{Ga}_{0.03}\text{As}$ layers of the cavity spacer. Lateral oxidation³⁵ is performed at 450 °C, after which a 5 pair ZnSe/MgF₂ DBR is deposited to complete the microcavity. The microcavity is measured at 10 K, for which the QD ground state emission wavelength is ~ 9700 Å with a spectral width of ~ 600 Å. Time resolved measurements are performed using a mode-locked Ti-Sapphire laser beam (pulse rate reduced to 5 MHz) focused with a microscope objective to a 5 μm diameter spot on the microcavity. Photoluminescence is collected through the same objective and time resolved using a grating spectrometer and photon counting module with rise and fall times of ~ 300 ps. The InGaAlAs/GaAs QDs have radiative lifetimes of ~ 2 ns and are conveniently used to obtain high sensitivity in the photodetection. Larger InGaAs/GaAs QDs that emit at longer wavelengths ranging from ~ 1.2 to ~ 1.3 μm at room temperature show shorter radiative lifetimes ranging from ~ 400 psec to ~ 800 psec. The longer wavelengths and shorter spontaneous lifetimes make these larger QDs of interest for fast VCSELs. The longer lifetimes and shorter wavelengths of the InGaAlAs/GaAs QDs make them convenient for characterizing the cavity effects.

Figure 2 shows photoluminescence decay for wavelengths around resonance for the 1 μm diameter apertured-microcavity. Curves (a) and (c) show off-resonance decays taken at 9800 and 9950 Å, while curve (b) shows the on-resonance decay for the lowest order mode at 9860 Å. There is a factor of ~ 2.3 increase in the emission rate at 9860 Å as compared to off-resonance wavelengths. The fact that wavelengths both shorter and longer than resonance show similar slower decays clearly indicates that the increased rate at resonance is due to the microcavity. Considering the first 2 ns of decay, the on-resonance lifetime [curve (b) in Fig. 1] is 0.9 ns, compared with the off-resonance lifetimes of 2.2 ns at 9950 Å and 1.9 ns at 9800 Å. The off-resonance lifetimes are close to the 2.1 ns lifetime measured for the epitaxial sample before processing. Therefore, the spontaneous emission rate is increased for the spatially averaged emitter positions by a factor of ~ 2.3 , with little inhibition off-resonance. Figure 3 shows spontaneous spectra and decay rates plotted versus wavelength for the 1 μm apertured-microcavity. The inset shows the emission over a greater wavelength range. The longer wavelength spectral peaks at 9860 Å

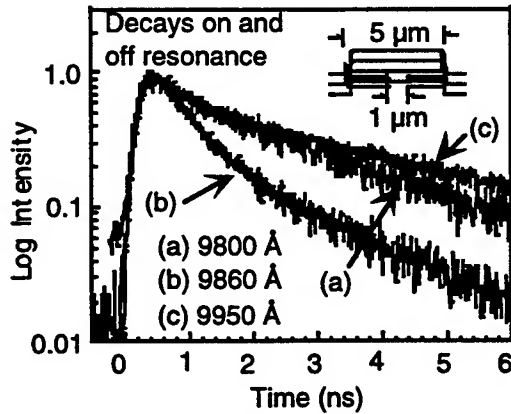


Fig. 2 Measured decay curves for a 1 μm apertured microcavity containing QD light emitters. Curve (a) for 9800 Å is for a wavelength shorter than resonance, curve (b) for 9860 Å is for a wavelength at resonance, and curve (c) for 9950 Å is for a wavelength longer than resonance.

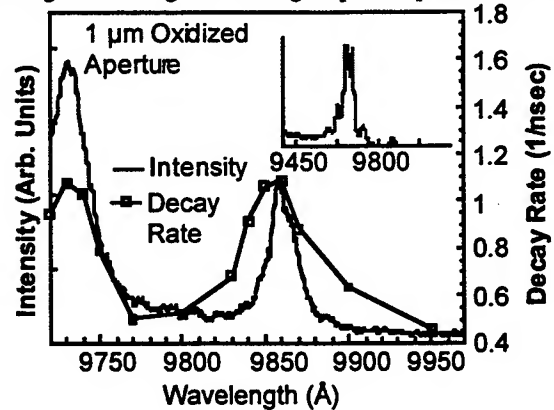


Fig. 3 Plot of measured decay rates versus wavelength and intensity versus wavelength for the 1 μm apertured microcavity.

and 9730 Å correspond to apertured-microcavity modes. The larger emission peaks starting at 9687 Å and visible to 9600 Å are due to emission from the oxide region (blue-shifted as compared to apertured modes) within the 5 μm mesa (see Fig. 1). Figure 3 shows that the spontaneous decay rate is enhanced at the lowest and next lowest order apertured-mode wavelengths of 9860 Å and 9730 Å. The spectral separation between the lowest and next lowest order modes depends on the mode area. The aperture-mode frequencies are approximately set by $\omega_m = (c/n)\sqrt{(\zeta_m/w_o)^2 + k_z^2}$, where the wavevector component k_z is

fixed by the mirrors. Bessel function modes satisfy the cylindrical symmetry of the cavity, so that we take $\zeta_0 = 4.810$ and $\zeta_1 = 7.664$ for Bessel functions of the first kind. From Figs. 2 and 3, $\omega_0 = 1.912 \times 10^{15}$ rad/s and $\omega_1 = 1.937 \times 10^{15}$ rad/s, and the mode diameter is estimated to be $w_0 = (c/n) \sqrt{(\zeta_1^2 - \zeta_0^2)/(\omega_1^2 - \omega_0^2)} \approx 1.8 \mu\text{m}$. The linewidth of the lowest order mode under continuous wave excitation is $\Delta\lambda = 15 \text{ \AA}$ which gives a $Q = \lambda_0 / \Delta\lambda = \omega_0 / (2\gamma_0) \approx 650$. Measurements to date suggest that electronic dephasing rates in the QDs can be $< 10^{11} \text{ s}^{-1}$, and we assume $\gamma_d < \frac{\omega_0}{Q}$ is satisfied.

From Eq. (4) we can also calculate the mode size required to achieve the spontaneous emission enhancement of 2.3 for the on-resonance wavelength. $\frac{\lambda_0^3 Q}{\pi^3 n^3 w_0^2 L_z} \approx 3.1$ provides a good match with the experimental data in Figs. 2 and 3. Given $\lambda_0 = 0.986 \mu\text{m}$, $Q = 650$, an assumed value of $n = 2.95$ for the refractive index of the cavity spacer, and an effective cavity length of $L_z = 0.75 \mu\text{m}$, the estimated mode size is $w_0 = 0.7 \mu\text{m}$. This Gaussian mode diameter of $2w_0 = 1.4 \mu\text{m}$ is in rough agreement with the $1.8 \mu\text{m}$ diameter estimated from the spectral separation of the transverse modes assuming Bessel functions. From the calculations, the spontaneous emission rate enhancement for emitters placed at the center of the optical mode is then a factor of 3.1 compared to the factor of 2 for the emission rate averaged over emitter positions. This dependence on the emitter position can lead to spatial hole burning of the QD emitters at the mode center. It was noted in the introduction that diffraction loss can decrease the mode Q for very small optical modes. For the experimental data of Figs. 2 and 3 we expect that a larger enhancement of the emission rate can be obtained with an increased Q, but only slightly higher Q's have been achieved in similar cavities with more DBR pairs.

Although the scaling behavior of selectively oxidized VCSELs with planar quantum well active regions has been studied extensively and gives some information on the cavity loss rate for small apertures, the actual optical loss dependence on mode size can be difficult to extract from the experiment. Generally, the threshold current density increases as the oxide aperture is decreased and can prevent lasing for very small apertures. However, the increase in threshold current density is not only due to a reduction in the mode Q, electronic losses can also play a role. Even a relatively small diffusion coefficient of $10 \text{ cm}^2/\text{sec}$ will lead to a diffusion length of $\sim 1.7 \mu\text{m}$. Ideally, if optical loss does not increase for the small aperture then neither should the threshold carrier density. On the other hand, the entire pumped area must be supplied through the small aperture, so that the current density through the aperture must increase to maintain the same carrier density. In addition, electronic losses often increase under and around the oxide aperture due to nonradiative recombination. These electronic effects due to diffusion make it difficult to clearly separate optical losses from electronic losses. However, a general trend is that the threshold current density is not so dependent on the aperture size as it is on the optical mode size. This is consistent with both the optical loss and electronic losses depending on the optical mode size, and for small apertures the larger optical mode both decreases the diffraction loss and increases the optical overlap with the injected carriers that suffer diffusion.

A more straightforward way to directly measure the optical loss dependence due to aperture and mode size is to measure the spontaneous linewidth dependence on the optical mode size. Care must also be taken using this approach to avoid stimulated emission or absorption effects that narrow or broaden the "cold-cavity" linewidth. We have made such measurements for oxide-apertured VCSEL-type cavities that contain either QD or planar quantum well active regions. The measured results are shown in Fig. 4. The number of upper MgF/ZnSe DBR pairs are either five or seven. The QD cavities are undoped and measured in photoluminescence, while the cavities containing planar quantum wells are lightly doped and excited with current injection. An interesting trend is that the Q's for similar type cavities depend on the type of active region used. This suggests that absorption intrinsic to the planar quantum well active region may in fact limit the Q for high reflectivity. In Fig. 4 the measured Q's for the QD cavity with seven MgF/ZnSe DBR pairs exceeds 5000 for aperture sizes greater than $4 \mu\text{m}$ diameter, while it is only ~ 2000 for the planar quantum well active region. A similar reduction from ~ 3000 to ~ 1200 is found for five pairs. For each of the cavity types the Q drops significantly for aperture sizes smaller than $3 \mu\text{m}$ in diameter. The $3 \mu\text{m}$ diameter is also the size for which VCSEL threshold current densities begin to sharply rise with reducing aperture size. This shows that diffraction loss must indeed be considered for small apertures, but also shows that the VCSEL Q may contain subtleties that we do not yet understand.

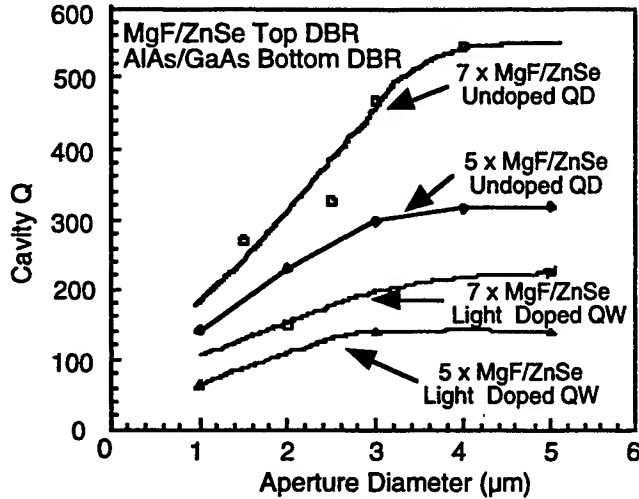


Fig. 4 Plot of Q versus aperture diameter for oxide-confined microcavities containing either QD or planar quantum well light emitters.

3. PURCELL EFFECT AND VCSEL CHARACTERISTICS

There has been a great deal of speculation about how laser thresholds will scale when the optical mode size is reduced due to microcavity confinement, with predictions that "zero-threshold" lasing will be obtained. However, the basis for some of these predictions are that the light versus current curve from the source can ideally be linear with 100% slope efficiency. This in itself is not the basis for a laser. A perfect "integrating sphere" would presumably give 100% spontaneous coupling efficiency from an emitter to a detector coupled through an emitting port, but this would not necessarily constitute a zero-threshold laser. The same is true for an ideal microcavity that can provide 100% spontaneous coupling efficiency to a detector, but with a Q that is insufficient to obtain lasing. Under extreme conditions the oxide-apertured microcavity that also uses strong QD electronic confinement such as shown in Fig. 1 can lead to nearly 100% spontaneous coupling efficiency. However, this microcavity emitter may not be a laser at all.

On the other hand, the increase in the spontaneous emission rate due to an oxide-apertured VCSEL-type cavity with a small enough volume to cause the Purcell effect can greatly improve the modulation rate of either a microcavity light emitting diode or a VCSEL. An interesting modification to the threshold also occurs, but the threshold current density is actually increased due to the increase in the spontaneous emission rate. Still the threshold current for very small optical modes and ideal electronic confinement such as provided by QDs can be very low, reaching sub-microamps. The very low threshold current is due to the small transparency current of the QD active region, while the optical gain can exceed that of a planar quantum well if inhomogeneous broadening is eliminated. The homogeneous linewidth from a QD emitter is measured to be $\leq 100 \mu\text{eV}$ at cryogenic temperatures, and is predicted to be ~ 2 to 3 meV or less at room temperature. While scaling the mode size has been studied for VCSELs, the impact on laser performance of changing the spontaneous emission rate by using a small mode volume has not yet been addressed. One reason is that experimentally, diffraction loss in part limits performance in single element VCSELs and is in itself an important scaling issue. Another reason though is that the VCSEL rate equations have not been put in a form that accurately accounts for the spontaneous lifetime dependence on the optical mode size.

A QD VCSEL microarray can be used to obtain milliwatt output powers typical of today's commercial VCSELs. Diffraction loss may also then be controlled through inter-element coupling. Below though we consider that the optical scattering losses are eliminated through strong lateral optical confinement, and consider the emission characteristics of a single element. From Fig. 1 we assume that the Gaussian optical mode has a free space wavelength $\lambda_o = 1.3 \mu\text{m}$, an effective mode area of πw_o^2 , an effective length of L_z , and a photon loss rate of ω_o/Q . To maintain resonance L_z must depend on w_o with $L_z(w_o) = L_z(\infty) / \sqrt{1 - \lambda_o^2 / (\pi^2 n^2 w_o^2)}$, and we take $L_z(\infty) = 0.59 \mu\text{m}$ and the cavity's average refractive index as $n = 3.3$. We hold $\omega_o/Q = 2 \times 10^{11} \text{ sec}^{-1}$ to isolate the effect of enhanced emission on laser performance.

The emitters are assumed to have a Gaussian density distribution with an effective area πw_{QD}^2 and a peak density $n_{QD} = 1.5 \times 10^{10} \text{ cm}^{-2}$. The spontaneous emission rate $1/\tau_{sp,o}$ is that which would occur without the cavity and for unity state

occupation by electrons and holes. $1/\tau_{sp,o} = 2.5 \times 10^9 \text{ sec}^{-1}$ is consistent with the radiative lifetime recently measured for 1.3 μm QDs.³⁷ The average population inversion of QD states is given by $2\sqrt{x} - 1$ with the upper state excitation given by x , where $0 \leq x \leq 1$. The \sqrt{x} dependence assumes equal probabilities of electron and hole occupation in the QD ground state levels with random capture. We consider that ideally the QD emitters will be homogeneously broadened with a linewidth of $2\gamma_d$ due to dephasing. The QD VCSEL will likely require high Q, so that the adiabatic approximation $\gamma_d \gg \omega_o/Q$ will be valid. For this case the QD spontaneous emission rate depends on the mode volume, dipole dephasing rate, and QD position within the mode, but not on the mode Q. Averaging over the emitter positions and retaining only leading terms gives the lasing mode's photon number rate equation as

$$\frac{dn}{dt} = -\left[\frac{\omega_o}{Q} - \frac{2\pi w_{QD}^2 w_o^2 n_{QD}}{w_{QD}^2 + w_o^2} \frac{\Omega^2}{\gamma_d} (2\sqrt{x} - 1)\right]n + \frac{2\pi w_{QD}^2 w_o^2 n_{QD}}{w_{QD}^2 + w_o^2} \frac{\Omega^2}{\gamma_d} x \quad (5)$$

with the emitter population x driven by a current source $\frac{I}{q}$ given as

$$\frac{I}{q} = 2\pi w_{QD}^2 n_{QD} \frac{dx}{dt} + \left(\frac{2\pi w_{QD}^2 n_{QD}}{\tau_{sp,o}} + \frac{4\pi w_o^2 w_{QD}^2 n_{QD}}{w_{QD}^2 + w_o^2} \frac{\Omega^2}{\gamma_d}\right)x + \frac{2\pi w_o^2 w_{QD}^2 n_{QD}}{w_{QD}^2 + w_o^2} \frac{\Omega^2}{\gamma_d} (2\sqrt{x} - 1)n \quad (6)$$

and

$$\Omega = \sqrt{\frac{c\lambda_o^2}{2\pi n^3 \tau_{sp,o} \pi w_o^2 L_z}} \quad (7)$$

We assume that the elements are designed so that $w_{QD}^2 = w_o^2$. The two spontaneous emission terms in Eq. (7) (in parenthesis and multiplying x) account separately for emission radiated into waveguide modes and into the aperture, just as above in Eq.

(3). A modified Purcell effect (with $\gamma_d \gg \omega_o/Q$) doubles the total spontaneous emission rate when $w_o = \frac{(\lambda_o/n)}{2\pi} \sqrt{\frac{(c/n)}{\gamma_d L_z}}$.

The threshold characteristics and the modulation response are calculated for a range of values of the mode diameter $2w_o$ and two different values of γ_d . We assume that the QD emitters are limited in linewidth only by homogeneous broadening, so that the spontaneous full-width at half-maximum energy spread is $2\hbar\gamma_d$ with $2\hbar\gamma_d = 6.6 \text{ meV}$ or $2\hbar\gamma_d = 1.3 \text{ meV}$. Figure 5 shows the calculated thresholds for mode diameters ranging from $5 \mu\text{m} \geq 2w_o \geq 0.6 \mu\text{m}$, and for the two different values of $2\hbar\gamma_d$. Threshold is taken as the pump rate needed to obtain a stimulated emission rate equal to the photon loss rate. Curves

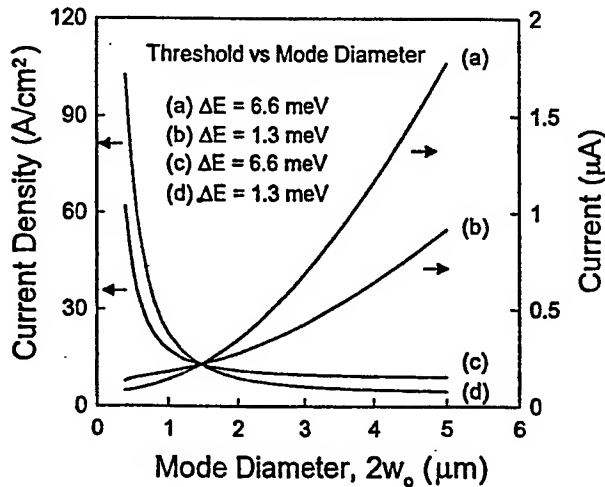


Fig. 5 Calculated threshold current and current density versus mode size for the QD VCSEL. The threshold currents versus mode diameter, $2w_o$, are shown in curve (a) for $\Delta E = 6.6 \text{ meV}$ and (b) for $\Delta E = 1.3 \text{ meV}$, and the current density versus mode diameter is shown in curve (c) for $\Delta E = 6.6 \text{ meV}$, and (d) for $\Delta E = 1.3 \text{ meV}$. The other laser parameters held fixed are $\omega_o/Q = 2 \times 10^{11} \text{ /sec}$, $\tau_{sp,o} = 400 \text{ psec}$, $n_{QD} = 1.5 \times 10^{10} \text{ /cm}^2$, $\lambda_o = 1.3 \mu\text{m}$, $n = 3.3$, $L_z = 0.59 \mu\text{m}$, and $w_{QD}^2/(w_o^2 + w_{QD}^2) = 0.5$.

(a) and (c) are the threshold current and current density for $2\hbar\gamma_d = 6.6 \text{ meV}$, and (b) and (d) are for $2\hbar\gamma_d = 1.3 \text{ meV}$. For modes with $2w_o < 2 \mu\text{m}$ the threshold current density increases as the mode size decreases due to the increased spontaneous

emission rate. For our parameter values, the mode sizes for which $2w_o = \frac{(\lambda_o/n)}{\pi} \sqrt{\frac{(c/n)}{\gamma_d L_z}}$ are $0.7 \mu\text{m}$ for $2\hbar\gamma_d = 6.6 \text{ meV}$, and $1.6 \mu\text{m}$ for $2\hbar\gamma_d = 1.3 \text{ meV}$. Curves (c) and (d) show that for mode diameters $2w_o > 1.5 \mu\text{m}$ the threshold is less for $2\hbar\gamma_d = 1.3 \text{ meV}$, but for $2w_o < 1.5 \mu\text{m}$ the threshold is less for the larger linewidth of $2\hbar\gamma_d = 6.6 \text{ meV}$. The transition occurs because the current density required for a fixed population inversion increases as the spontaneous emission rate increases. Since the spontaneous rate enhancement increases as the spontaneous linewidth decreases, the threshold for a given population inversion increases. For $2w_o = 5 \mu\text{m}$ the calculated threshold current densities are 9.0 A/cm^2 for $2\hbar\gamma_d = 1.3 \text{ meV}$, (c), and 4.7 A/cm^2 for $2\hbar\gamma_d = 6.6 \text{ meV}$, (d). These are close to the experimental values for $1.3 \mu\text{m}$ QD edge-emitting lasers.³⁶

The calculated small signal modulation responses from Eqs. (5) and (6) for different mode diameters at a bias level of twice threshold are shown in Fig. 6. The response curves in Fig. 3 are for $2w_o = 5 \mu\text{m}$, $2 \mu\text{m}$, or $0.6 \mu\text{m}$. The spontaneous linewidth in (a) is $2\hbar\gamma_d = 6.6 \text{ meV}$, and in (b) it is $2\hbar\gamma_d = 1.3 \text{ meV}$. Both the mode volume and linewidth impact the VCSEL's modulation response through the cavity coupling Ω^2/γ_d . As $2w_o$ is reduced the relaxation oscillation peak is reduced in amplitude and the 3 dB bandwidth increases. Decreasing the spontaneous linewidth also decreases the relaxation oscillation amplitude and increases the 3 dB bandwidth.

Calculated bias-free pulse responses are shown in Fig. 7. The responses are for current pulses of unit step functions 500 psec long with amplitudes of either the steady-state transparency current value ($x = 0.25$) or twice the steady-state threshold value,

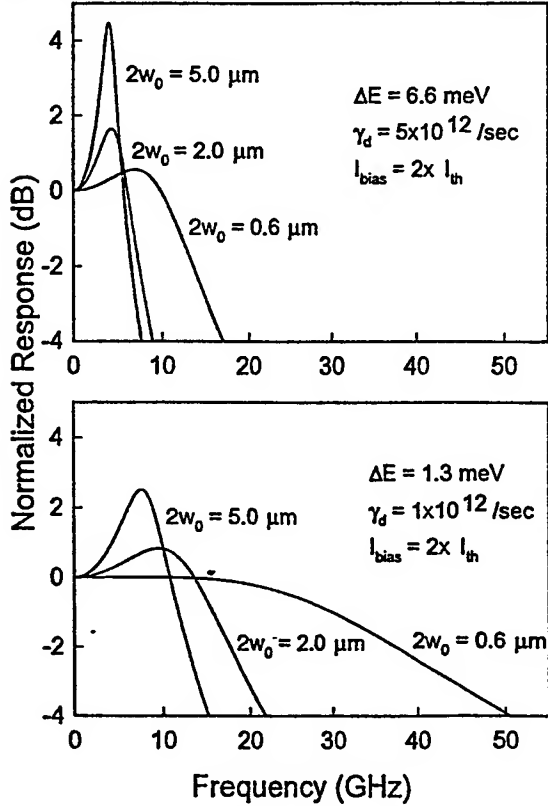


Fig. 6 Calculated small signal modulation responses for three different mode sizes of $2w_o = 5.0 \mu\text{m}$, $2.0 \mu\text{m}$, and $0.6 \mu\text{m}$. (a) shows the responses for $\Delta E = 6.6 \text{ meV}$, and (b) shows the responses for $\Delta E = 1.3 \text{ meV}$. The other laser parameters are given in the Fig. 2 caption.

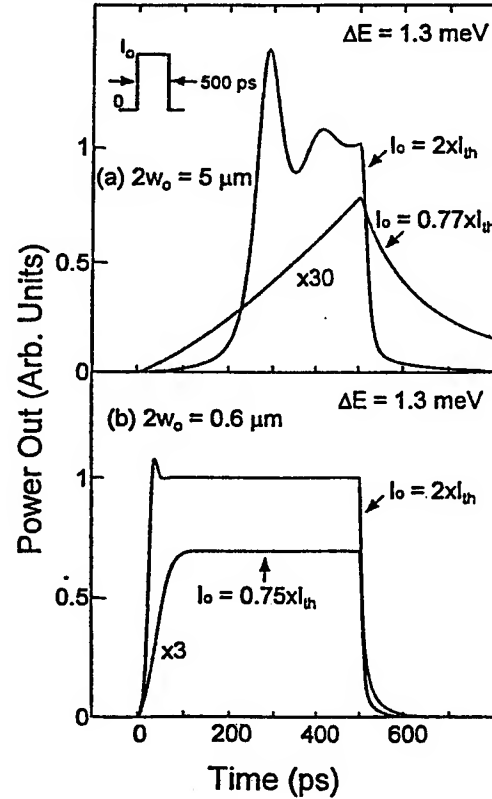


Fig. 7 Calculated bias-free responses for a 500 psec long current excitation pulse and $\Delta E = 1.3 \text{ meV}$, with the current amplitude equal to either transparency or twice the threshold current. (a) shows the responses for $2w_o = 5.0 \mu\text{m}$, and (b) shows the responses for $2w_o = 0.6 \mu\text{m}$. The other laser parameters are given in the Fig. 2 caption.

and two different mode sizes with $2w_0$ equal to either (a) 5 μm or (b) 0.6 μm . The spontaneous linewidths are held equal at $2\hbar\gamma_d = 1.3$ meV to study only those effects due to mode size changes. From Fig. 7 (a) and (b) we see that for current pulses of $\sim 0.7xI_{th}$ (transparency) the smaller mode size of $2w_0 = 0.6$ μm greatly improves the spontaneous pulse response, even allowing multi-gigabit data transmission. For current pulses of twice threshold the turn-on delay of ~ 250 psec for $2w_0 = 5$ μm in (a) is reduced to ~ 31 psec for $2w_0 = 0.6$ μm in (b). It's clear that the Purcell effect can have a major impact on the modulation response for microcavity QD VCSELs, especially around at bias levels around threshold.

4. SUMMARY

Scaling of the optical mode size has been examined for VCSELs. In order to take full advantage of the cavity effects strong lateral confinement must be achieved for both photons and electrons. The strong lateral confinement can be achieved using etched-pillars or oxide-apertures, but scattering and diffraction losses must be controlled to obtain high Q for micron-sized optical modes. Quantum dots are attractive for obtaining electronic confinement, but inhomogeneous broadening should be eliminated to take full advantage of cavity effects. For small sized QD VCSELs, the Purcell effect can greatly improve the modulation characteristics, perhaps even allowing high speed bias-free operation. Similar improvements in the modulation speed can be obtained using photonic bandgap cavities, but in many cases the microcavity QD VCSEL can be a direct replacement for today's commercial VCSELs.

ACKNOWLEDGMENTS

Various aspects of this work have been supported by the DARPA/Ultraphotonics program monitored by the AFOSR, and the DARPA supported Univ. of New Mexico OptoCenter.

REFERENCES

1. K. Iga, F. Koyama, and S. Kinoshita, "Surface emitting semiconductor lasers," *IEEE J. Quant. Electron.* **24**, pp. 1845-1855, 1988.
2. Y.H. Lee, B. Tell, K. Brown-Goebeler, J.L. Jewell, C.A. Burrus, J.M. Van Hove, "Characteristics of top-surface-emitting GaAs quantum-well lasers," *IEEE Phot. Tech. Lett.* **2**, pp. 686-688, 1990.
3. D.L. Huffaker, D.G. Deppe, K. Kumar, and T.J. Rogers, "Native-oxide defined ring contact for low threshold vertical-cavity lasers," *Appl. Phys. Lett.* **65**, pp. 97-99, 1994.
4. D.G. Deppe, D.L. Huffaker, T.-H. Oh, H. Deng, and Q. Deng, "Low-threshold vertical-cavity surface-emitting lasers based on oxide-confinement and high contrast distributed Bragg reflectors," *IEEE J. Quant. Electron.* **3**, pp. 893-904, 1997.
5. K.D. Choquette, R.P. Schneider, Jr., K.L. Lear, and K.M. Geib, "Low threshold voltage vertical-cavity lasers fabricated by selective oxidation," *Electron. Lett.* **30**, pp. 2043-2044, 1994.
6. Y. Hayashi, T. Mukaiharu, N. Hatori, N. Ohnoki, A. Matsutani, F. Koyama, and K. Iga, "A record low threshold index-confined InGaAs/GaAlAs vertical-cavity surface-emitting laser with a native oxide confinement structure," *Electron. Lett.* **31**, pp. 560-561, 1995.
7. G.M. Yang, M.H. MacDougall, and P.D. Dapkus, "Ultralow threshold current vertical-cavity surface-emitting lasers obtained with selective oxidation," *Electron. Lett.* **31**, pp. 886-887, 1995.
8. B.J. Thibeault, E.R. Hegblom, P.D. Floyd, R. Naone, Y. Akulova, and L.A. Coldren, "Reduced optical scattering loss in vertical-cavity lasers using a thin (300Å) oxide aperture," *IEEE Phot. Tech. Lett.* **8**, pp. 593-595, 1996.
9. E.R. Hegblom, D.I. Babic, B.J. Thibeault, and L.A. Coldren, "Scattering losses from dielectric apertures in vertical-cavity lasers," *IEEE J. Sel. Top. Quant. Electron.* **3**, pp. 379-389, 1997.
10. K.L. Lear, K.D. Choquette, R.P. Schneider, Jr., S.P. Kilcoyne, and K.M. Geib, "Selectively oxidized vertical cavity surface emitting lasers with 50% power conversion efficiency," *Electron. Lett.*, vol. 31, 208 (1995).
11. R. Jager, M. Grabherr, C. Jung, R. Michalzik, G. Reiner, B. Wieg, and K. Ebeling, "57 % wallplug efficiency oxide-confined 850 nm wavelength GaAs VCSELs," *Electron. Lett.* **33**, pp. 330-331, 1997.
12. B. Wieg, M. Grabherr, G. Reiner, and K.J. Ebeling, "High efficiency selectively oxidized MBE grown vertical-cavity surface-emitting lasers," *Electron. Lett.* **32**, pp. 557-558, 1996.
13. K.L. Lear, A. Mar, K.D. Choquette, S.P. Kilcoyne, R.P. Schneider, Jr., and K.M. Geib, "High-frequency modulation of oxide-confined vertical-cavity surface-emitting laser," *Electron. Lett.* **32**, pp. 457-458, 1996.
14. B.J. Thibeault, K. Bertilsson, E.R. Hegblom, E. Strzelecka, P.D. Floyd, R. Naone, and L.A. Coldren, "High-speed characteristics of low-optical loss oxide-apertured vertical-cavity lasers," *IEEE Phot. Tech. Lett.* **9**, pp. 11-13, 1997.
15. B. Wieg, M. Grabherr, R. Michalzik, G. Reiner, and K.J. Ebeling, "High power single-mode selectively oxidized vertical-cavity surface-emitting lasers," *IEEE Phot. Tech. Lett.* **8**, pp. 971-973, 1996.

16. M. Grabherr, R. Hager, R. Michalzik, B. Weigl, G. Reiner, and K.J. Ebeling, "Efficiency single-mode oxide-confined GaAs VCSEL's emitting in the 850 nm wavelength regime," *IEEE Phot. Tech. Lett.* **9**, pp. 1304-1306, 1997.
17. G. R. Hadley, "Effective index model for vertical-cavity surface-emitting lasers", *Opt. Lett.* **20**, pp. 1483-1485, 1995.
18. D.G. Deppe, T.-H. Oh, and D.L. Huffaker, "Eigenmode confinement in the dielectrically apertured Fabry-Perot microcavity," *IEEE Phot. Tech. Lett.* **9**, 713-715, 1997.
19. W.B. Veldkamp, "Wireless focal planes 'On the road to amacronic sensors'," *IEEE J. Quant. Electron.* **29**, pp. 801 - 813, 1993.
20. N. Kirkstaedter, N. Ledentsov, M. Grundmann, D. Bimberg, V. Ustinov, S. Ruvimov, M. Maximov, P. Kop'ev, Zh. Alferov, "Low threshold, large To injection laser emission from (InGa)As quantum dots," *Electron. Lett.* **30**, pp. 1416-1417, 1994.
21. K. Kamath, P. Bhattacharya, T. Sosnowski, T. Norris, and J. Phillips, "Room temperature operation of In_{0.4}Ga_{0.6}As/GaAs self-organized quantum dot lasers," *Electron. Lett.* **32**, pp. 1374-1375, 1996.
22. H. Shoji, Y. Nakata, K. Mukai, Y. Sugiyama, M. Suagawara, N. Yokoyama, and H. Ishikawa, "Room temperature CW operation at the ground state of self-formed quantum dot lasers with multi-stacked dot layer," *Electron. Lett.* **32**, pp. 2023-2024, 1996.
23. R. Mirin, A. Gossard, and J. Bowers, "Room temperature lasing from InGaAs quantum dots," *Electron. Lett.* **32**, pp. 1732-1733, 1996.
24. Q. Xie, A. Kalburge, P. Chen, and A. Madhukar, "Observation of lasing from vertically self-organized InAs three-dimensional island quantum boxes on GaAs (001)," *IEEE Phot. Tech. Lett.* **8**, pp. 965-967, 1996.
25. H. Saito, K. Nishi, I. Ogura, S. Sugov, and Y. Sugimoto, "Room-temperature lasing operation of a quantum-dot vertical-cavity surface-emitting laser," *Appl. Phys. Lett.* **69**, pp. 3140-3142, 1996.
26. D.L. Huffaker, O. Baklenov, L.A. Graham, B.G. Streetman, and D.G. Deppe, "Quantum dot vertical-cavity surface-emitting laser with a dielectric aperture," *Appl. Phys. Lett.* **70**, pp. 2356-2358, 1997.
27. J.A. Lott, N.N. Ledentsov, V.M. Ustinov, A.Yu. Egorov, A.E. Zhukov, P.S. Kop'ev, Zh.I. Alferov, and D. Bimberg, "Vertical cavity lasers based on vertically coupled quantum dots," *Electron. Lett.* **33**, pp. 1150-1151, 1997.
28. D.L. Huffaker, H. Deng, and D.G. Deppe, "1.15 μ m Wavelength Oxide-Confined Quantum Dot Vertical-Cavity Surface-Emitting Laser," *IEEE Phot. Tech. Lett.* **10**, pp. 185-187, 1998.
29. Z. Zou, D.L. Huffaker, S. Csutak, and D.G. Deppe, "Ground State Lasing From a Quantum Dot Oxide-Confined Vertical-Cavity Surface-Emitting Laser," *Appl. Phys. Lett.* **75**, pp. 22-25, 1999.
30. E.M. Purcell, "Spontaneous emission probabilities at radio frequencies," *Phys. Rev.* **69**, p. 681, 1946.
31. K.H. Drexhage, "Interaction of light with monomolecular dye layers," in *Progress in Optics*, edited by E. Wolf (North-Holland, Amsterdam, 1974), Vol. XII, Chap. IV.
32. Q. Deng and D.G. Deppe, "Spontaneous lifetime change in a dielectrically-apertured Fabry-Perot microcavity," *Optics Express* **2**, pp. 157-162, 1998.
33. L.A. Graham, D.L. Huffaker, S.M. Csutak, Q. Deng, and D.G. Deppe, "Spontaneous lifetime control of quantum dot emitters in apertured microcavities," *J. Appl. Phys.* **85**, pp. 3383-3385, 1999.
34. L.A. Graham, D.L. Huffaker, and D.G. Deppe, "Spontaneous lifetime control in a native-oxide-apertured-microcavity," *Appl. Phys. Lett.* **74**, pp. 2408-2410, 1999.
35. J.M. Dallesasse, N. Holonyak, Jr., A.R. Sugg, T.A. Richard, and N. El-Zein, "Hydrolization oxidation of AlGaAs-AlAs-GaAs quantum well heterostructures," *Appl. Phys. Lett.* **57**, pp. 2844-2846, 1990.
36. L. Zhang, T.F. Boggess, D.G. Deppe, D.L. Huffaker, O.B. Shchekin, and C. Cao, "Dynamic response of 1.3 μ m wavelength InGaAs/GaAs quantum dots," unpublished.
37. G. Park, D.L. Huffaker, Z. Zou, O.B. Shchekin, and D.G. Deppe, "Temperature Dependence of Lasing Characteristics for Long-Wavelength (1.3 μ m) Quantum Dot Lasers," *IEEE Phot. Tech. Lett.* **11**, pp. 301-303, 1999.

Plenary Session II

Optical Nonlinearities in Semiconductors*

S. W. Koch and T. Meier

Department of Physics and Material Sciences Center,
Philipps University, Renthof 5, D-35032 Marburg, Germany

ABSTRACT

A microscopic many-body theory for the nonlinear optical response of semiconductors is reviewed. The importance of Coulomb interaction induced carrier correlations is demonstrated in excitonic pump-probe spectra. The influence of excitonic and biexcitonic contributions to coherent pump-induced absorption changes at the exciton frequency are discussed. Absorption changes induced by incoherent exciton and unbound electron-hole populations are studied.

Keywords: optical nonlinearities, many-body theory, Coulomb correlations, excitonic pump-probe

1. INTRODUCTION

The study of optical nonlinearities in semiconductors and semiconductor heterostructures is a field of active theoretical and experimental research. Microscopic theoretical descriptions of optical nonlinearities in semiconductors generally have to deal with the different relevant quasiparticles and their interactions. In this paper we mainly focus on the important influence of the many-body Coulomb interaction on near-bandgap optical nonlinearities in semiconductors.

One subject of particular interest that has been investigated intensively already in the 1980s and is still receiving considerable attention are nonlinear absorption and refractive index changes induced by the presence of an electron-hole plasma. In the theoretical description of such nonlinearities many-body effects were included microscopically on a non-perturbative level.¹⁻⁵ This approach gives a good basic understanding of the weakening (bleaching) of excitonic absorption with increasing plasma density, the appearance of optical gain (negative absorption), as well as the corresponding dispersive nonlinearities caused by the presence of uncorrelated electron-hole pairs. These nonlinear population-induced absorption changes can be attributed to the effects of Pauli blocking (also called phase-space filling), as well as genuine many-body effects such as band-gap renormalization (electronic self energies) and screening of the Coulomb interaction potential.

Typically in optically excited semiconductors the quasi-particle scattering processes which govern the dephasing of optical excitations can be characterized by typical interaction times in the picosecond to sub-picosecond range. Hence, investigations of the coherent nonlinear optical response of semiconductors, which requires laser pulses shorter than the dephasing time, became generally possible only after the development of femtosecond laser sources in the late 1980s.

In the early ultrafast coherent pump and probe experiments particular attention was paid to the dynamical optical Stark effect of excitons in semiconductors.⁶⁻⁸ To investigate this Stark effect, a strong pump pulse is tuned below the lowest excitonic transition and the resulting absorption changes are monitored by a weak probe pulse.⁵ Analogous to atomic systems the experiments revealed that for large detuning the pump pulse leads to a blueshift of the excitonic resonance.⁶⁻⁸ In a two-band semiconductor model and for relatively large detuning below the exciton, the experimentally observed blueshift could be well described on the basis of the semiconductor Bloch equations (SBE) in the time-dependent Hartree-Fock (TDHF) approximation.^{4,5,9,10}

Generally, the TDHF-SBE are surprisingly successful in the analysis of coherent nonlinear optical effects in semiconductors and semiconductor nanostructures. With improved sample quality and experimental techniques, however, it became evident that many-body Coulomb correlations, i.e. many-body effects beyond the TDHF approximation, can lead to characteristic signatures in semiconductor nonlinearities that cannot be described with the TDHF-SBE.

Further author information: (Send correspondence to S. W. Koch)

S. W. Koch: E-mail: Stephan.W.Koch@physik.uni-marburg.de

T. Meier: E-mail: Torsten.Meier@physik.uni-marburg.de

*Also published in *Proc. of SPIE* Vols. 3896, 3897, and 3898

For example, the relevance of such correlations was clearly shown by analyzing the dependence of the measured signatures on the polarization directions of the incident pulses. Such experiments provided evidence for excitation-induced dephasing processes¹¹ and two-exciton (biexciton) contributions.¹²⁻¹⁶

To calculate the nonlinear optical response of semiconductors including two-exciton resonances it is necessary to include not only two-point functions, but also higher-order correlation functions in the theoretical description. For arbitrary excitation conditions this would mean that due to the many-body Coulomb interaction an infinite hierarchy of equations of motion has to be solved. One way to restrict this hierarchy to a finite number of correlation functions is to limit the theoretical analysis to a finite order in the optical field. Hence, only a finite number of interactions between the semiconductor and the light field takes place and thus only a finite number of electron-hole pairs is generated.^{17,18}

In order to describe four-wave mixing and pump-probe experiments one needs to consider at least processes up to the third-order in the light field ($\chi^{(3)}$). In the coherent limit, where interaction with other quasiparticles, for example phonons, are neglected, it is sufficient to consider just two quantities (density matrices). These two are the single-exciton amplitude p and the two-exciton amplitude B , which describes the evolution of two interacting electron-hole pairs.^{17,18} Nevertheless, solutions of the full coherent $\chi^{(3)}$ -equations are computationally quite demanding since effectively a quantum mechanical four-body problem has to be solved. Thus, one often restricts the numerical analysis to one-dimensional model systems,¹⁹⁻²² where however the parameters are chosen to represent realistic quantum-well configurations. Fully two-dimensional calculations are possible,¹⁵ however, they require rather involved computational analysis and cannot conveniently be used for extended model studies in which dependencies of the results on large numbers of system parameters are investigated. In the coherent $\chi^{(3)}$ -limit for excitation at and below the exciton resonance, the one- and two-dimensional results predict qualitatively similar absorption changes at the exciton which are in good agreement with experiments.¹⁵

Beyond the coherent limit additional occupation-type dynamical variables need to be considered. Up to third-order one then has to deal with four relevant variables, i.e. besides the coherences p and B also the pair occupation N and the exciton to two-exciton transition Z contribute.¹⁹ Since Z is a six point function, solutions of the coupled equations for these four density matrices are numerically even more demanding, such that up to now only few such calculations have been reported. In Ref. 20 it has been shown that in the presence of low-density incoherent occupations N also the six point function Z is significant in order to describe exciton bleaching and to account for transitions from incoherent single- to two-exciton states.

In this paper we review some of our recent results made towards the understanding of nonlinear optical processes in semiconductors including many-body correlations, see Refs. 15 and 20-24. After a brief description of the theoretical approach in Section 2, we focus on the discussion of numerical results on excitonic absorption changes in different situations. Resonant and off-resonant excitation are discussed in Sections 3 and 4, respectively. In both cases we find distinct signatures induced by many-body correlations. In Section 5 absorption changes induced by incoherent populations are analyzed and a brief summary is presented in Section 6.

2. THEORY

To theoretically model correlation effects relevant in coherent two pulse experiments such as pump-probe and four-wave mixing spectroscopy, see Fig. 1(a), we compute the nonlinear optical response in the coherent $\chi^{(3)}$ -limit.^{14,17,18} This is done by numerically solving the relevant equations of motion for the single-exciton amplitude p and the correlated part of the two-exciton amplitude \bar{B} , see Ref. 21. Omitting the various sums and indices the basic structure of the equations of motion is given by

$$\frac{\partial}{\partial t} p = i [\omega_p p + \mu E (1 - 2p^* p) + V p^* p p + V p^* \bar{B}], \quad (1)$$

$$\frac{\partial}{\partial t} \bar{B} = i [\omega_B \bar{B} + V p p]. \quad (2)$$

Here, ω_p and ω_B are energies of a single- and a two-exciton state, respectively, μ is the transition dipole, E the external laser field, and V the Coulomb interaction potential. In Refs. 15 and 21 we have numerically solved the microscopic versions of Eqs. (1) and (2), both for a fully two-dimensional model of the quantum-well structure²⁵ and for a simplified, quasi one-dimensional system. As shown in Ref. 15 the spectra obtained for both models are in good

qualitative agreement and explain correlation-induced signatures in the experimental differential absorption of high quality quantum wells.

Within our model we include the two spin-degenerate electron and heavy-hole bands using the circularly-polarized dipole matrix elements describing the optical interband transitions.^{13,16} Besides the heavy holes also light-hole transitions can be incorporated.²³ The monopole-monopole Coulomb interactions between particles at sites i and j are given by V_{ij} . In our one-dimensional model,^{15,21} the spatial variation is given by a regularized potential: $V_{ij} = U_0 d / (|i - j|d + a_0)$, where d is the distance between the sites and U_0 and a_0 are parameters characterizing the strength of the interaction and the spatial variation taken as $U_0 = 8meV$ and $a_0/d = 0.5$, respectively. In our numerical study we use a tight-binding model with electron and heavy-hole couplings of $J_e = 8meV$ and $J_{hh} = 0.8meV$ between neighboring sites. These system parameters result in an exciton binding energy of $8meV$ and a biexciton binding energy of $1.4meV$.¹⁵

The theory allows us to identify three types of optical nonlinearities.^{15,21} The total differential absorption signal is the sum of a *Pauli-blocking term* ($\propto \mu E p^* p$ in Eq. (1)) and *Coulomb-induced many-body nonlinearities*, which can further be separated into a first-order term ($\propto V p^* p p$ in Eq. (1)) and higher-order correlations ($\propto V p^* B$ in Eq. (1)), see Refs. 15 and 21. Thus the total differential absorption $\delta\alpha$ can be written as the sum of three contributions^{15,21}

$$\delta\alpha(\omega) = \delta\alpha_{pb}(\omega) + \delta\alpha_{CI,1st}(\omega) + \delta\alpha_{CI,corr}(\omega), \quad (3)$$

where pb denotes the optical nonlinearity induced by Pauli-blocking. The terms denoted with CI are Coulomb-interaction-induced nonlinearities. $CI, 1st$ is the first-order (Hartree-Fock) term, and $CI, corr$ the higher-order correlation contribution. The lineshape is different for each of the three terms in Eq. (3) which therefore introduce distinct signatures in the differential absorption spectra.^{15,21}

Besides the coherent response, we also analyze the importance of Coulomb correlations in situations where incoherent occupations are present. We focus on the fully incoherent situation and analyze absorption changes induced by incoherent occupations \bar{N} . Omitting the various sums and indices, which can be found in Ref. 20, the basic structure of the equations relevant in this case is given by

$$\frac{\partial}{\partial t} p = i [\omega_p p + \mu E (1 - 2\bar{N}) + V p \bar{N} + V \bar{Z}], \quad (4)$$

$$\frac{\partial}{\partial t} \bar{Z} = i [(\omega_B - \omega_p) \bar{Z} + V p \bar{N}]. \quad (5)$$

As before, we can also here distinguish between the different types of optical nonlinearities. Therefore the absorption changes induced by incoherent occupations \bar{N} are given by the sum of a *Pauli-blocking term* ($\propto \mu E \bar{N}$ in Eq. (4)) and *Coulomb-induced many-body nonlinearities*, which can again further be separated into a first-order term ($\propto V p \bar{N}$ in Eq. (4)) and higher-order correlations ($\propto V \bar{Z}$ in Eq. (4)), see Ref. 20. This allows us to write the total differential absorption $\delta\alpha$ as the sum over the three contributions as given by Eq. (3).

3. RESONANT EXCITATION

The differential absorption spectrum for resonant excitation at the exciton resonance with co-circularly polarized pump and probe pulses ($\sigma^+ \sigma^+$) with a time delay of $\tau = 2ps$ is shown in Fig. 1(b). The differential absorption $\delta\alpha(\omega)$ is strictly negative in the vicinity of the exciton resonance corresponding to a pump-pulse-induced bleaching of the exciton resonance. Positive contributions to $\delta\alpha(\omega)$ appearing well above the exciton are related to excited state absorption induced by exciting unbound two-exciton states. Besides the total signal, Fig. 1(b) also displays the three optical nonlinearities according to Eq. (3) separately. It is shown that $\delta\alpha_{pb}$ is weak and corresponds purely to a bleaching of the exciton resonance. $\delta\alpha_{CI,1st}$ is very strong and is antisymmetric around the exciton resonance. The dispersive shape of the differential absorption corresponds to a blueshift of the exciton. $\delta\alpha_{CI,corr}$ is also mainly dispersive around the exciton resonance, but with opposite sign compared to $\delta\alpha_{CI,1st}$, i.e. this term yields a redshift. Besides contributions with resonances at the exciton energy, $\delta\alpha_{CI,corr}$ also includes terms having resonances at the transition energies to unbound two-exciton states. Therefore it is not completely antisymmetric around the exciton resonance. Including all three contributions to obtain the total signal via Eq. (3), strong cancellations occur between $\delta\alpha_{CI,1st}$ and $\delta\alpha_{CI,corr}$ and the resulting differential absorption shows a predominantly absorptive spectral shape around the exciton resonance. It can be inferred from Fig. 1(b) that the bleaching at the exciton resonance is dominated by Coulomb-induced nonlinearities $\delta\alpha_{CI,1st} + \delta\alpha_{CI,corr}$ and only weakly enhanced by $\delta\alpha_{pb}$.

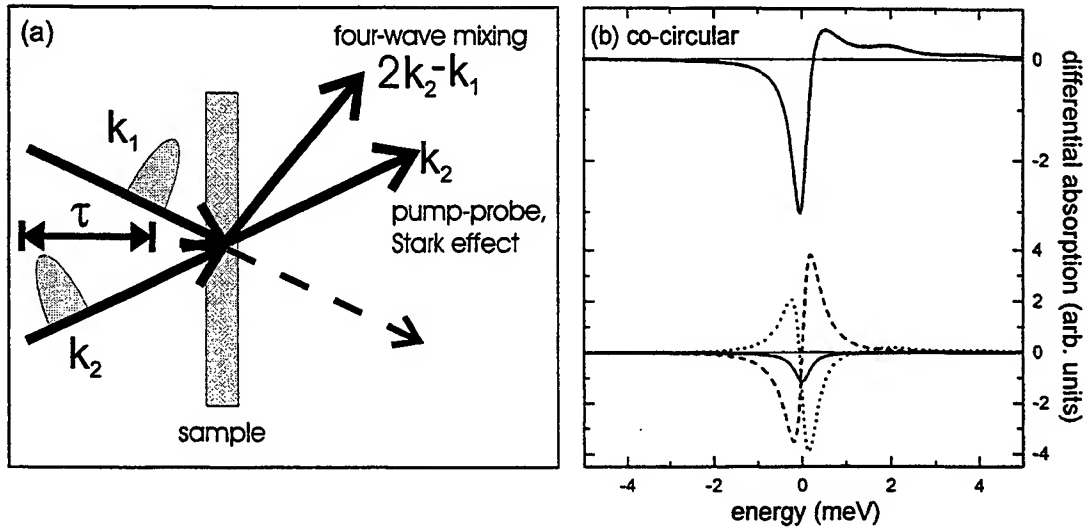


Figure 1. (a) Schematic illustration of nonlinear optical four-wave mixing and pump-probe experiments performed by excitation with two optical laser pulses having a time delay τ . (b) Total differential absorption spectrum $\delta\alpha(\omega)$ for resonant excitation at the exciton resonance and a time delay of $\tau = 2ps$ for co-circularly polarized pump (σ^+) and probe (σ^+) pulses. Also displayed in the lower part are $\delta\alpha_{pb}$ (solid), $\delta\alpha_{CI,1st}$ (dashed), and $\delta\alpha_{CI,corr}$ (dotted). The zero of the energy scale is chosen to coincide with the 1s-exciton resonance. The pump pulse has a duration of 1.18ps (full width at half maximum of pulse intensity). For further parameters see text.

Differential absorption spectra for time delays of $\tau = 2ps$, $0ps$, and $-2ps$ are displayed in Fig. 2 for both co-circularly ($\sigma^+\sigma^+$) and opposite-circularly ($\sigma^+\sigma^-$) polarized pump and probe pulses. As is shown in Ref. 21, for $\sigma^+\sigma^+$ excitation similar compensations among the Coulombic nonlinearities as displayed in Fig. 1(b) arise for all time delays. Within the coherent limit the signal amplitude is strongest for small delays and decreases with both increasing positive and negative delay, see Fig. 2. Apart from the change in strength, for $\sigma^+\sigma^+$ excitation the lineshapes are very similar for 0 and 2ps delay. The main visible difference between these two cases is that for $\tau = 0ps$ there is weak induced absorption appearing energetically below the exciton. This feature is reminiscent of the coherent spectral oscillations,⁴ which dominate the spectra for negative delays, see dotted line in Fig. 2(a) for $\tau = -2ps$. For negative time delays the probe arrives before the pump pulse. With calculations performed in the limit of ultrashort pulses it can be shown that in this case the differential polarization $\delta P(\omega, \tau)$ which determines the absorption changes is multiplied by the phase factor $\exp(i(\omega_p - \omega)\tau)$, where ω_p is the exciton frequency. Since the differential absorption $\delta\alpha(\omega, \tau)$ is determined by the imaginary part of $\delta P(\omega, \tau)$ the phase factor introduces $\sin((\omega_p - \omega)\tau)/(\omega_p - \omega)$ -like spectral oscillations of $\delta\alpha(\omega, \tau)$ around ω_p .^{4,21}

If only heavy-hole transitions are important, $\sigma^+\sigma^-$ polarized excitation makes it possible to analyze pure correlations effects.^{15,21,23} This is due to the fact, that for this geometry $\delta\alpha_{pb}$ vanishes, and also $\delta\alpha_{CI,1st}$ vanishes as long as the system is homogeneous, since neither of these contributions introduces any coupling between the subspaces of different spin states.^{21,22} Differential absorption spectra for $\tau = 2ps$, $0ps$, and $-2ps$ and $\sigma^+\sigma^-$ excitation are displayed in Fig. 2(b). For zero and positive time delays also in this configuration the spectra show bleaching at and some excited state absorption above the exciton resonance. Since with opposite-circularly polarized pump and probe pulses also a bound biexciton is excited, we see in Fig. 2(b) additional strong induced absorption below the exciton resonance. The energetic difference between the maximum of this induced absorption and the bleaching is just the biexciton binding energy. For negative delays also in this polarization configuration which is entirely induced by Coulombic correlations the spectra are characterized by coherent spectral oscillations.²¹ The presence of the oscillations in the correlation terms is in agreement with simplified analytical calculations presented in Ref. 21.

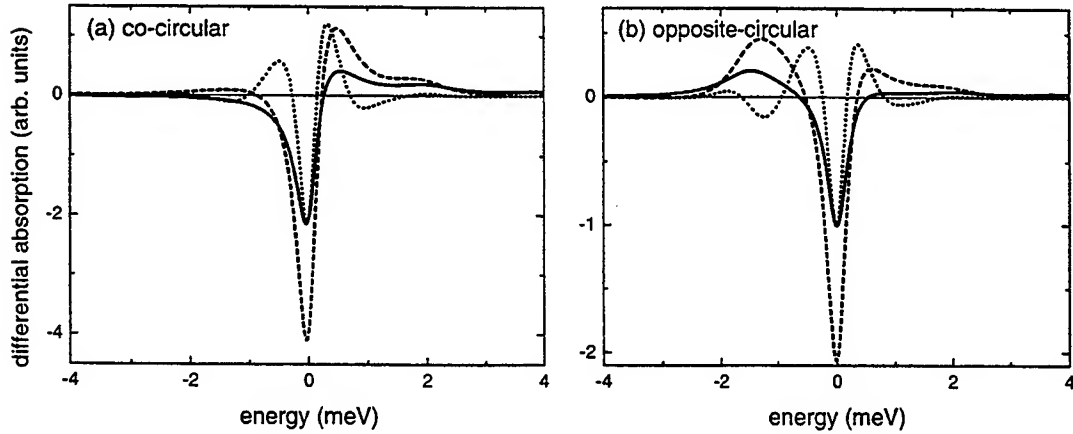


Figure 2. Total differential absorption spectra $\delta\alpha(\omega)$ for resonant excitation at the exciton resonance and a time delay of $\tau = 2ps$ (solid), $0ps$ (dashed), and $-2ps$ (dotted). (a) for co-circularly polarized ($\sigma^+\sigma^+$) and (b) for opposite-circularly polarized ($\sigma^+\sigma^-$) pump and probe pulses.

4. OFF-RESONANT EXCITATION

Here we investigate the influence of correlations on the excitonic optical Stark effect by tuning the pump pulse below the exciton resonance. Fig. 3 shows the resulting differential absorption spectra for co-circularly polarized excitation and various detunings of the central pump-pulse frequency below the exciton energy. The higher detunings ($5meV$ and $7.5meV$) exceed both the spectral width of the pump pulse and the homogeneous width of the exciton resonance. The solid line gives the full $\delta\alpha$, whereas the dashed line gives the result within TDHF where correlations are neglected, i.e. $\delta\alpha_{HF} = \delta\alpha_{pb} + \delta\alpha_{CI,1st}$. With increasing detuning the amplitude of the signal decreases and the bleaching at the exciton resonance develops into a dispersive shape corresponding to a blue-shift.^{4,21} Fig. 3 directly shows that the importance of the carrier correlations diminishes rapidly with increasing detuning. We thus conclude that the time-dependent Hartree-Fock approximation provides a good description for this polarization configuration as long as off-resonant excitation is considered.

An interesting effect induced by the dynamics of Coulomb correlations is found by analyzing for a fixed detuning the polarization-dependence of the Stark effect. We choose the detuning of the pump pulse as $4.5meV$ below the exciton resonance and investigate the absorption changes for the various polarization configurations. Fig. 4(a)-(d) displays the theoretical results for $\sigma^+\sigma^+$, xx , xy , and $\sigma^+\sigma^-$ excitation. Whereas for the three cases (a), (b), and (c) the differential absorption corresponds to a blueshift, for $\sigma^+\sigma^-$ clearly a redshift appears. Since for $\sigma^+\sigma^-$ excitation both the Pauli blocking and the first-order Coulomb-induced nonlinearities, i.e. the Hartree-Fock contribution, vanish identically, the redshift of the differential absorption is purely induced by Coulomb correlations.¹⁵

The physical origin of the redshift can be analyzed in more detail by looking at the individual contributions to the signal, as displayed on the right panels in Fig. 4. For $\sigma^+\sigma^+$, xx , and xy polarization both the Pauli blocking and the first-order Coulomb terms always induce a blueshift, whereas the Coulomb correlations always correspond to a redshift, see Fig. 4(a)-(c). The fact that also for $\sigma^+\sigma^+$ excitation, where no bound biexcitons are excited, the correlation term alone corresponds to a redshift indicates that the correlation-induced reversal of the direction of the shift is not directly related to the existence of a *bound* biexciton. For $\sigma^+\sigma^+$, xx , and xy polarization, however, the influence of correlations is rather small and its redshift is always overcompensated by the Pauli blocking and the first-order Coulomb terms resulting in a net blueshift.¹⁵

To substantiate the claim that the existence of a bound biexciton is not necessary to obtain a correlation-induced redshift, we have performed additional calculations of the differential absorption spectra for $\sigma^+\sigma^-$ configuration. As discussed in Ref. 15, the bound biexciton contribution has been eliminated by artificially dropping the six terms containing the attractive and repulsive Coulomb terms between the two electrons and two holes appearing in the homogeneous part of the equation of motion for the two-exciton amplitude \tilde{B} . In this case, also for $\sigma^+\sigma^-$ excitation no bound biexcitons exist. The approximation of neglecting the Coulomb terms that lead to the formation of bound

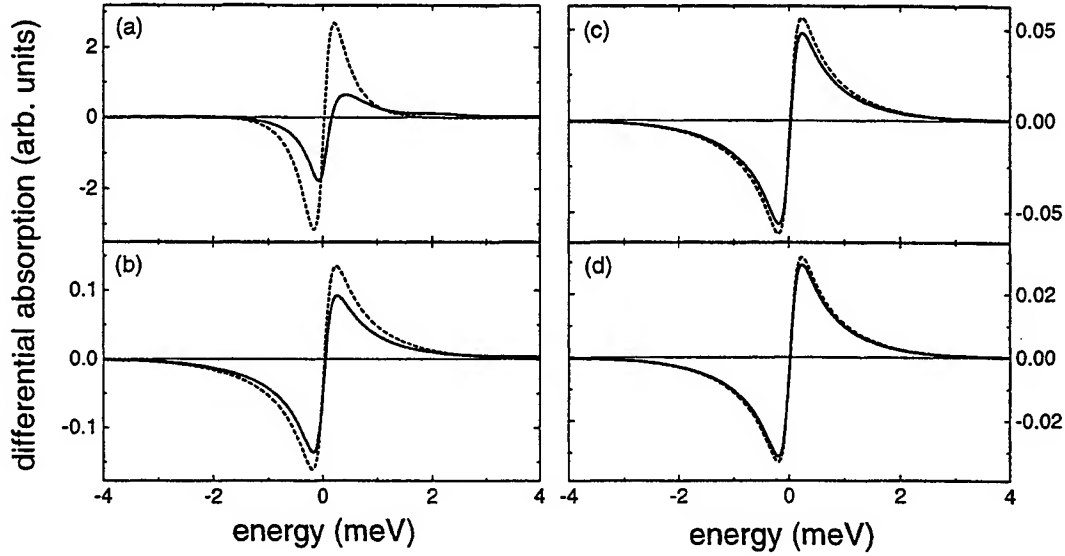


Figure 3. Differential absorption spectra for various detunings of the pump pulse below the exciton resonance with co-circularly polarized pump and probe pulses for time delay $\tau = 0ps$. The central frequency of the pump pulse is chosen (a) $1meV$, (b) $3meV$, (c) $5meV$, and (d) $7.5meV$ below the energy of the $1s$ -exciton. The solid line gives the full $\delta\alpha$, and the dashed line the result of a Hartree-Fock calculation ($\delta\alpha_{pb} + \delta\alpha_{CI,1st}$) neglecting correlations ($\delta\alpha_{CI,corr}$).

two-exciton states is identical to the second Born-approximation (SBA), since only terms up to second-order in the Coulomb interaction are retained in the signal.^{25,26} By solving a dynamic equation for \bar{B} , Coulomb memory effects are still included on this level.¹⁵ The resulting spectrum displayed in Ref. 15 shows that in the SBA the signal amplitude is somewhat reduced, however, the redshift clearly persists. Further calculations performed for the SBA in Markov approximation did not reproduce the redshift. This allows us to conclude that it is clearly the *dynamics* of Coulomb correlations that is responsible for the presence of a redshift.¹⁵ Our numerical results on the polarization-dependence of the optical Stark effect are in good agreement with experiments performed on high-quality InGaAs quantum wells with spectrally very narrow exciton linewidth, see Ref. 15.

In order to show that the redshift depends crucially on the energetic separation between heavy- and light-hole excitons and on the detuning we now extend our model to include both types of valence bands using the typical selection rules and the three to one ratio of the oscillator strengths.²³ The in-plane dispersion of the valence band structure in quantum wells is modeled by considering heavy- and light-hole masses according to the Luttinger-Hamiltonian. For GaAs parameters we get $m_{hh} = m_0/(\gamma_1 + \gamma_2) = 0.112m_0$ and $m_{lh} = m_0/(\gamma_1 - \gamma_2) = 0.211m_0$. Further band-mixing effects are neglected here for simplicity. For the conduction band electrons we use $m_e = 0.0665m_0$ and take the same coupling of $J_e = 8meV$ as used above. The valence band masses then enter into the model by taking the nearest-neighbor coupling to be inversely proportional to the mass, which yields $J_{hh} = J_e m_e / m_{hh} = 4.75meV$ and $J_{lh} = J_e m_e / m_{lh} = 2.52meV$. The site energies for the light-holes are chosen relative to the heavy-holes to have an adjustable splitting between the heavy- and light-hole excitons. Within our model the heavy- and light-hole transitions are coupled by sharing a common electronic state and via the Coulomb coupling.

Fig. 5 shows calculated differential absorption spectra for co-circularly and opposite-circularly excitation for various splittings between the heavy- and light-holes excitons (a) and (b), as well as for various detunings (c) and (d). Considering a detuning of $4.5meV$ below the $1s$ heavy-hole exciton and a splitting of $15meV$ between the heavy- and light-hole excitons (which is the splitting present in the InGaAs quantum well sample investigated in Ref. 15) we reproduce the blueshift for $\sigma^+\sigma^+$ and the redshift for $\sigma^+\sigma^-$ excitation, see Fig. 5(a) and (b). For reduced heavy-light splitting the blueshift for $\sigma^+\sigma^+$ excitation remains unchanged. However, for $\sigma^+\sigma^-$ excitation the amplitude of the redshift strongly decreases with decreasing splitting. For a splitting of $1meV$ and less the redshift even changes

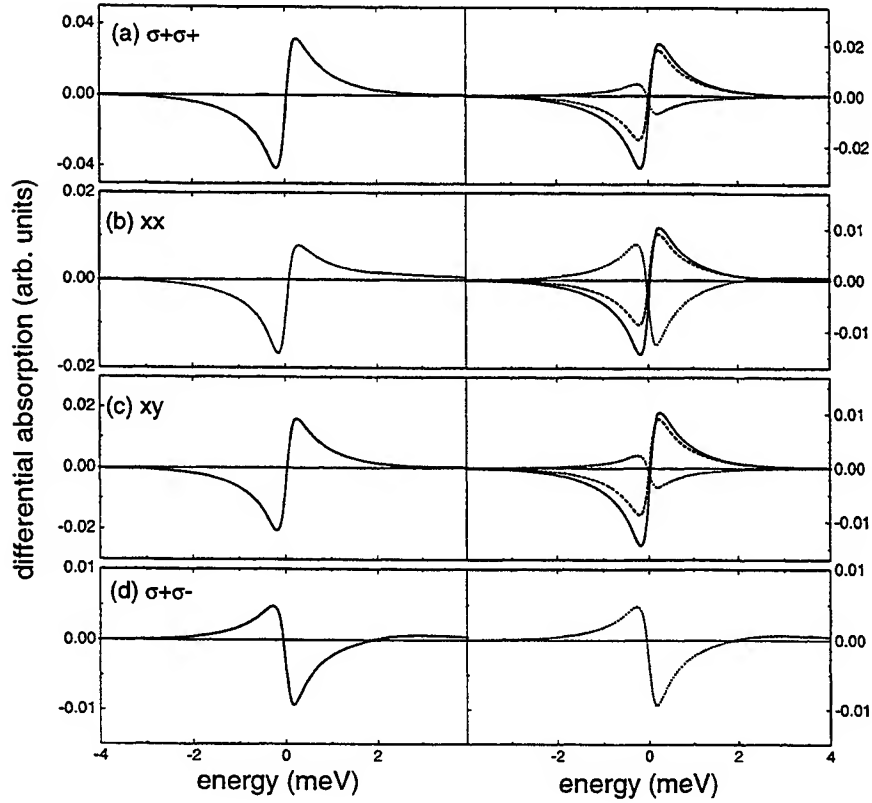


Figure 4. Differential absorption spectra for excitation 4.5 meV below the exciton and time delay $\tau = 0\text{ ps}$. (a) Co-circularly ($\sigma^+\sigma^+$), (b) linear parallel (xx), (c) linear perpendicular (xy), and (d) opposite-circularly ($\sigma^+\sigma^-$) polarized pump and probe pulses. The left panels show the full results, whereas the right panels show the three contributions to the signal: Pauli blocking (solid), first-order Coulomb (dashed), and Coulomb correlations (dotted).

into a blueshift. We thus conclude that the redshift should be well pronounced only in samples with a significant heavy-light splitting. For small splittings the coupling between heavy- and light-hole excitons leads to a blueshift which overcompensates the correlation-induced redshift of the heavy-hole exciton alone.

For a fixed heavy-light splitting taken as 15 meV in Fig. 5(c) and (d) the differential absorption spectra depend strongly on the detuning. For co-circularly excitation the blueshift present for a detuning of 4.5 meV survives also for larger detunings and is only reduced in amplitude with increased detuning. For opposite-circular excitation, however, besides a strong reduction in amplitude also the direction of the shift changes with increasing detuning. For very large detuning we again obtain a switch over from red- to blueshift. The reason for this behavior is that for very large detuning, heavy- and light-hole excitons are both off-resonant and we enter the regime of complete adiabatic following where the frequency dependent optical response decays only weakly with increasing resonance frequency.²⁷ Thus with increasing detuning the *relative* weight of the light-hole exciton increases, which then due to heavy-hole light-hole coupling induces the blueshift at the heavy-hole exciton.

The results presented in Fig. 5 clearly demonstrate that the Coulomb memory induced redshift for opposite-circularly polarized excitation is very sensitive to both the heavy-hole light-hole splitting and the pump detuning. Thus it should only be observable in samples with sufficiently large exciton splittings and only in a certain detuning range,²³ as was the case in the experiments presented in Ref. 15. The exact detuning and splitting ranges that allow to observe the redshift depend on the heavy- and light-hole masses and on the ratio of their oscillator strengths.

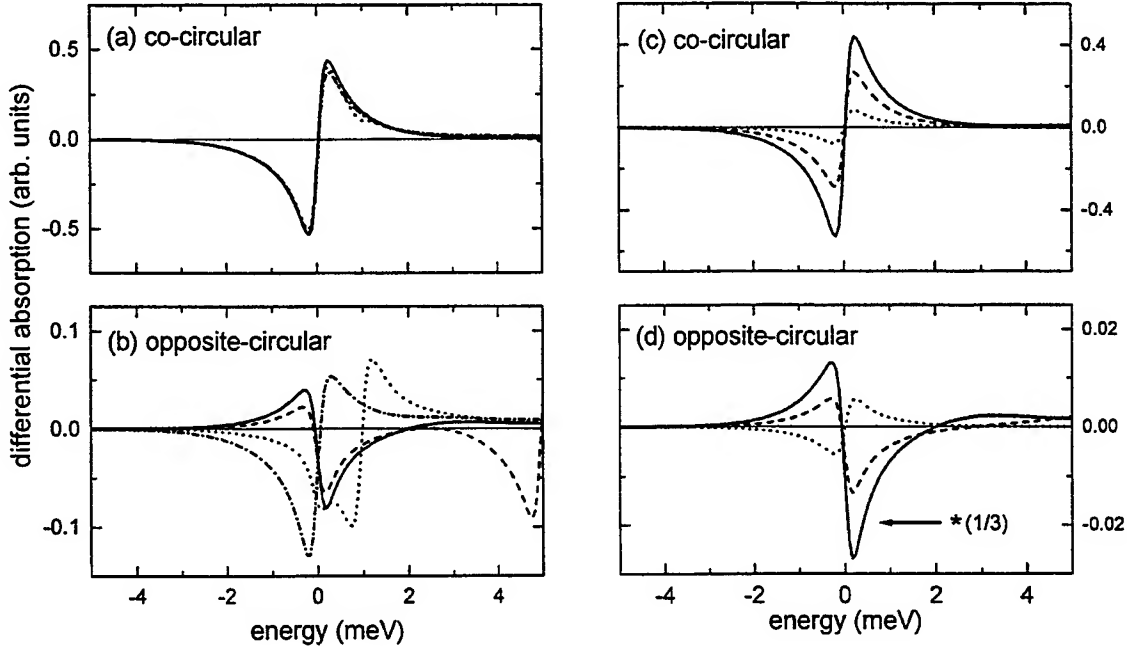


Figure 5. Differential absorption spectra including heavy- and light-holes for time delay $\tau = 0$ ps. (a) Co-circularly and (b) opposite-circularly polarized pump and probe pulses, respectively, for a fixed detuning of 4.5 meV below the $1s$ hh-exciton resonance and various splittings between the heavy- and light-hole excitons: 15 meV (solid), 5 meV (dashed), 1 meV (dotted), and 0 meV (dashed-dotted). (c) Co-circularly and (d) opposite-circularly polarized pump and probe pulses, respectively, for a fixed splitting between the heavy- and light-hole excitons of 15 meV and various detunings below the heavy-hole exciton resonance. 4.5 meV (solid), 6.75 meV (dashed), and 18 meV (dotted).

5. ABSORPTION CHANGES DUE TO INCOHERENT OCCUPATIONS

Numerical results on the absorption changes induced by incoherent exciton as well as electron-hole pair populations \bar{N} have been presented in Ref. 20, where the full Eqs. (4) and (5) have been solved numerically for our model. The homogeneous part of the equation of motion of \bar{N} contains the difference of energies of two single excitons. Thus \bar{N} describes pair occupations and coherences.^{19,28} As outlined in Ref. 20, the pair occupation can be expanded using the complete set of excitonic eigenstates Ψ_α , which are the eigenstates of the homogeneous part of the equation of p . For low-densities (non-degenerate limit) and in thermal equilibrium we assume that \bar{N} is given by a summation over thermally populated exciton states, i.e. schematically

$$\bar{N} = \sum_{\alpha} \frac{\exp(-\epsilon_{\alpha}/k_B T)}{A} \Psi_{\alpha}^* \Psi_{\alpha} \quad , \quad (6)$$

with

$$n = \frac{1}{L} \sum_{\alpha} \frac{\exp(-\epsilon_{\alpha}/k_B T)}{A} \quad , \quad (7)$$

where ϵ_{α} is the energy of Ψ_{α} , L the length of the system, and A is a constant determining the total density n .²⁰ In Eq. (6) we have assumed that no coherences between different exciton states are present and that excitons of both optically coupled pairs of degenerate electron and heavy-hole subbands are equally populated.

Besides assuming that initially thermally populated excitons are present, we can also consider the situation where unbound electron-hole states are populated. To model this situation we simply replace the exciton wavefunctions Ψ_{α} in Eq. (6) by the complete set of single-particle eigenstates Φ_{α} with energies $\tilde{\epsilon}_{\alpha}$, which are the eigenstates of the homogeneous part of the equation of p if the electron-hole Coulomb attraction V is neglected. For generating the thermal electron-hole-pair occupation \bar{N} we then use Eq. (6), where Ψ_{α} is replaced by Φ_{α} and ϵ_{α} by $\tilde{\epsilon}_{\alpha}$.²⁰

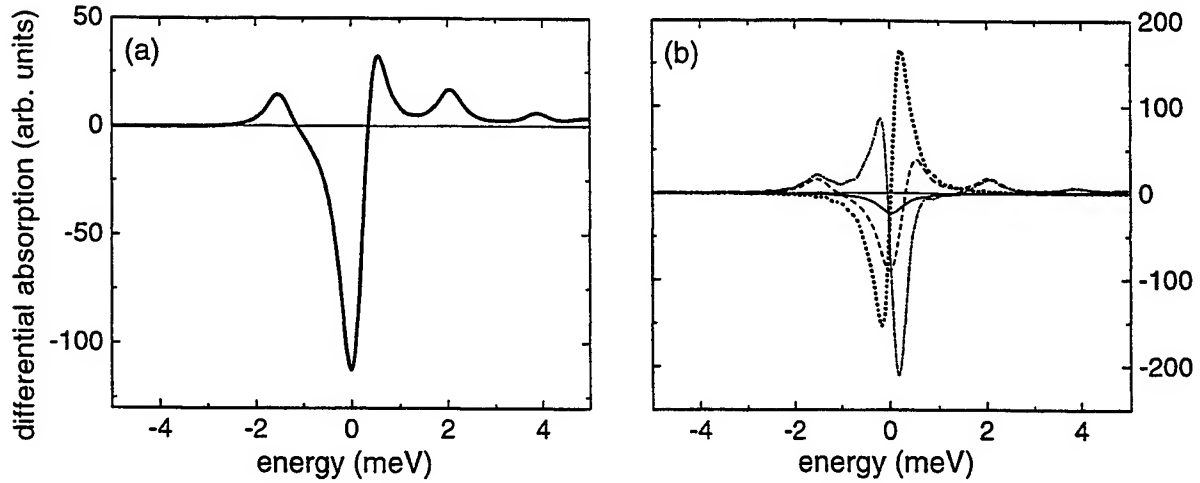


Figure 6. Differential absorption spectra induced by an incoherent occupation of the lowest exciton state. (a) total signal and (b) Pauli blocking (solid), first-order Coulomb terms (dotted), higher-order Coulomb-correlations (dashed-dotted), and sum of the two Coulomb terms (dashed). Dephasing times of $2ps$ for p and \bar{Z} have been considered.

We start our numerical analysis with the low temperature limit. At $T = 0K$ only the energetically lowest exciton state, i.e. the optically active $1s$ -exciton, is initially populated, and we calculate the differential absorption induced by an incoherent occupation \bar{N} of this exciton viewed by a circularly polarized probe pulse. Fig. 6 show the numerically calculated differential absorption spectra at $T = 0K$. Besides the total signal displayed in Fig. 6(a) also the three contributions due to Pauli blocking and first- and higher-order Coulomb-interactions, as well as the sum of the two Coulomb terms are shown separately in Fig. 6(b). We see that Pauli blocking induces a pure and rather small bleaching of the exciton, whereas the first-order Coulomb-term has a dispersive shape at the exciton corresponding to the well-known blueshift.^{10,29} As for the resonant coherent excitation, this blueshift is strongly compensated by the higher-order Coulomb-term ($\propto V\bar{Z}$), which besides excited-state absorption induced by exciton- to two-exciton transitions shows a redshift at the exciton resonance,²⁰ see Fig. 6(b). Adding the contributions we find that the total signal shows no net shift but bleaching of the exciton resonance, see Fig. 6(a). This bleaching of the exciton is mainly induced by the strong Coulomb-interaction-induced terms, and the Pauli blocking introduces only weak additional bleaching. Furthermore, we obtain excited state absorption above and below the exciton which is induced by unbound and bound biexcitonic two-exciton states, respectively. The results displayed in Fig. 6 clearly demonstrate that for a proper description of both exciton bleaching and excited-state absorption higher-order Coulomb correlations represented by the six-particle density matrix \bar{Z} are important and should not be neglected.²⁰ The Pauli blocking- and Coulomb-interaction-induced signatures in the differential absorption including strong cancellation between the first- and higher-order Coulomb-terms and the dominance of the Coulomb-terms over the Pauli blocking in the presence of incoherent occupations²⁰ are very similar to the signatures obtained in the analysis of coherent pump-induced differential absorption changes, see Refs. 15 and 21.

Fig. 7 displays the differential absorption induced by (a) thermalized excitons and (b) thermalized electron-hole pairs for two temperatures of $T = 2K$ and $100K$. As shown in Ref. 20, also at elevated temperatures for both excitons and electron-hole pairs the different signatures of the three nonlinearities as discussed above remains. Fig. 7(b) shows that with raising the temperature of an occupation of unbound electron-hole pairs both the bleaching of the exciton as well as the amplitude of the excited state absorption decrease. The result obtained for thermalized exciton occupations, Fig. 7(a), looks similar. At very low temperatures, where only the lowest exciton is populated, one sees clear signatures of the individual two-exciton states. These positive contributions become less structured at elevated temperatures due to the fact that for increased temperatures also energetically higher excitons are populated. Their transitions to two-exciton states, which occur at different frequencies, are added to the signal induced by the lowest exciton. The tail of the excited state absorption towards low energies appearing for elevated temperatures in the

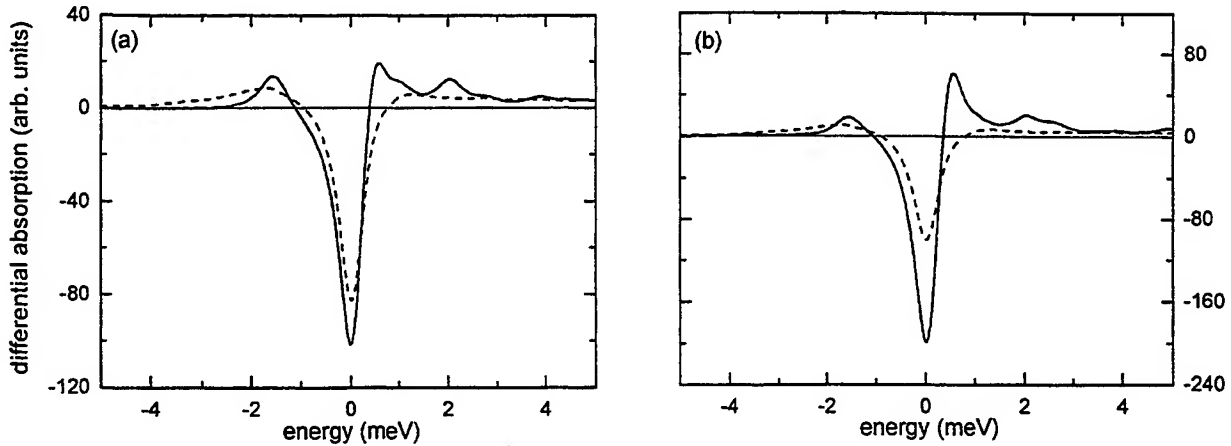


Figure 7. Differential absorption spectra for $T = 2K$ (solid) and $100K$ (dotted) induced by (a) thermally occupied excitons and (b) thermally occupied electron-hole states.

excited state absorption below the exciton directly shows that also energetically higher excitons are Coulombically-coupled to two-exciton states. Comparing the cases of unbound excitons and electron-hole pairs, Fig. 7(a) and (b), we note that for a fixed temperature the lineshapes of the differential absorption are quite similar. However, for thermalized electron-hole pairs the bleaching of the exciton resonance is stronger than for excitons. This stronger bleaching induced by electron-hole pairs compared to excitons means that there is stronger nonlinear coupling of low-energy electron-hole pairs to the $1s$ -exciton compared to the nonlinear coupling among the excitons themselves. For the Pauli-blocking these differences can be analyzed simply by using the exciton and electron-hole wavefunctions, as described in Ref. 29. If Coulomb-correlations are included in the description, on the other hand, due to the relevance of six particle correlations no such simple explanation is possible, since also two-exciton states (which can not be calculated analytically) are relevant. The temperature dependence of the bleaching induced by thermalized excitons and unbound electron and hole pairs obtained within our model has been investigated in detail in Ref. 20.

The dominance of the unbound electron-hole pair over the exciton contributions to the resonance bleaching is most likely the reason for the success of electron-hole plasma theories explaining experimentally observed exciton saturation at low temperatures.^{1,3,5,29} This trend is expected to be even more pronounced in systems with dimensionalities greater than one because of the reduction of the Coulomb-correlation effects with increasing dimensionality.

6. SUMMARY

A microscopic theory capable of describing coherent excitation effects in semiconductors including many-body Coulomb-induced carrier correlations is reviewed. The theory is applied to analyze polarization-dependent ultra-fast absorption changes at the $1s$ exciton resonance. For two-band semiconductors it is shown that the optical Stark effect may change from a blueshift for co-circularly polarized pump and probe pulses to a redshift for opposite-circularly excitation conditions. A theoretical analysis including heavy and light holes shows that the occurrence of the redshift for opposite-circularly polarized excitation depends sensitively on both the splitting between the heavy- and light-hole excitons and the pump detuning.

The theory is also applied to an incoherent situation. Whereas one could expect that correlations might not be important in this situation, strong correlation effects on the differential absorption induced by incoherent thermalized excitons and free electron-hole pairs are found. For low temperatures it is shown that populated free electron-hole pairs induce stronger bleaching at the exciton resonance than populated excitons of the same density.

In Ref. 21 the approach has been generalized to treat also effects of energetic disorder. Furthermore, the theory has been applied to excitons in microcavities,²¹ yielding numerical results on reflection changes that are in good qualitative agreement with recent experiments.³⁰ The theoretical approach has further been extended to include effects of higher intensities (coherent $\chi^{(5)}$ -limit) where it yields results on the excitonic differential absorption in good

agreement with experimental results.³¹ In addition, the theoretical approach has been used to clarify the relevance of a new coherent technique called "coherent excitation spectroscopy" which is based on partly nondegenerate four-wave mixing.²⁴ Work is in progress dealing with the analysis of disorder-induced dephasing in four-wave mixing spectroscopy, which can only be understood properly if both disorder and correlations are treated microscopically.²²

ACKNOWLEDGMENTS

We thank P. Thomas and our co-workers C. Sieh, F. Jahnke, and A. Knorr for many collaborations and valuable discussions. This work is supported by the Deutsche Forschungsgemeinschaft (DFG) through the Sonderforschungsbereich 383 and the Leibniz prize, and by the John von Neumann Institut für Computing (NIC), Forschungszentrum Jülich, Germany, through grants for extended CPU time on their supercomputer systems.

REFERENCES

1. H. Haug and S. Schmitt-Rink, "Electron theory of the optical properties of laser excited semiconductors," *Prog. in Quant. Electron.* **9**, pp. 3–100, 1984.
2. S. Schmitt-Rink, D. A. B. Miller, and D. S. Chemla, "Linear and nonlinear optical properties of semiconductor quantum wells," *Adv. in Phys.* **38**, pp. 89–188, 1989.
3. L. Bányai and S. W. Koch, "A simple theory for the effects of plasma screening on the optical spectra of highly excited semiconductors," *Z. Phys. B* **63**, pp. 283–291, 1986.
4. S. W. Koch, N. Peyghambarian, and M. Lindberg, "Transient and steady-state optical non-linearities in semiconductors," *J. Phys. C* **21**, pp. 5229–5249, 1988.
5. H. Haug and S. W. Koch, *Quantum Theory of the Optical and Electronic Properties of Semiconductors*, World Scientific, Singapore, 1994.
6. D. Fröhlich, A. Nöthe, and H. Reiman, "Observation of the resonant optical stark effect in a semiconductor," *Phys. Rev. Lett.* **55**, pp. 1335–1337, 1985.
7. A. Mysyrowicz, D. Hulin, A. Antonetti, A. Migus, W. T. Masselink, and H. Morkoc, "'Dressed excitons' in a multiple-quantum-well structure: Evidence for an optical stark effect with femtosecond response time," *Phys. Rev. Lett.* **56**, pp. 2748–2751, 1986.
8. A. V. Lehmen, D. S. Chemla, J. E. Zucker, and J. P. Heritage, "Optical stark effect on excitons in GaAs quantum wells," *Opt. Lett.* **11**, pp. 609–611, 1986.
9. S. Schmitt-Rink and D. S. Chemla, "Collective excitations and the dynamical stark effect in a coherently driven exciton system," *Phys. Rev. Lett.* **57**, pp. 2752–2755, 1986.
10. R. Binder, S. W. Koch, M. Lindberg, W. Schäfer, and F. Jahnke, "Transient many-body effects in the semiconductor optical stark effect: A numerical study," *Phys. Rev. B* **43**, pp. 6520–6529, 1991.
11. H. Wang, K. B. Ferrio, D. G. Steel, Y. Z. Hu, R. Binder, and S. W. Koch, "Transient nonlinear optical response from excitation induced dephasing in GaAs," *Phys. Rev. Lett.* **71**, pp. 1261–1264, 1993.
12. B. F. Feuerbacher, J. Kuhl, and K. Ploog, "Biexcitonic contribution to the degenerate-four-wave-mixing signal from a GaAs/Al_xGa_{1-x}As quantum well," *Phys. Rev. B* **43**, pp. 2439–2441, 1991.
13. K. Bott, O. Heller, D. Bennhardt, S. T. Cundiff, P. Thomas, E. J. Mayer, G. O. Smith, R. Eccleston, J. Kuhl, and K. Ploog, "Influence of exciton-exciton interactions on the coherent optical response in GaAs quantum wells," *Phys. Rev. B* **48**, pp. 17418–17426, 1993.
14. V. M. Axt and A. Stahl, "The role of the biexciton in a dynamic density matrix theory of the semiconductor band edge," *Z. Phys. B* **93**, pp. 205–211, 1994.
15. C. Sieh, T. Meier, F. Jahnke, A. Knorr, S. W. Koch, P. Brick, M. Hübner, C. Ell, J. Prineas, G. Khitrova, and H. M. Gibbs, "Coulomb memory signatures in the excitonic optical stark effect," *Phys. Rev. Lett.* **82**, pp. 3112–3115, 1999.
16. W. Schäfer, D. S. Kim, J. Shah, T. C. Damen, J. E. Cunningham, K. W. Goosen, L. N. Pfeiffer, and K. Köhler, "Femtosecond coherent fields induced by many-particle correlations in transient four-wave mixing," *Phys. Rev. B* **53**, pp. 16429–16443, 1996.
17. M. Lindberg, Y. Z. Hu, R. Binder, and S. W. Koch, " $\chi^{(3)}$ formalism in optically excited semiconductors and its applications in four-wave-mixing spectroscopy," *Phys. Rev. B* **50**, pp. 18060–18072, 1994.
18. V. M. Axt and A. Stahl, "A dynamics-controlled truncation scheme for the hierarchy of density matrices in semiconductor optics," *Z. Phys. B* **93**, pp. 195–204, 1994.

19. V. M. Axt, K. Victor, and A. Stahl, "Influence of a phonon bath on the hierarchy of electronic densities in an optically excited semiconductor," *Phys. Rev. B* **53**, pp. 7244-7258, 1996.
20. T. Meier and S. W. Koch, "Excitons versus unbound electron-hole pairs and their influence on exciton bleaching: A model study," *Phys. Rev. B* **59**, pp. 13202-13208, 1999.
21. C. Sieh, T. Meier, F. Jahnke, A. Knorr, F. Jahnke, P. Thomas, and S. W. Koch, "Influence of carrier correlations on the excitonic optical response including disorder and microcavity effects," *Europ. Phys. J. B*, in press.
22. S. Weiser, T. Meier, J. Möbius, A. Euteneuer, E. J. Mayer, W. Stolz, M. Hofmann, W. W. Rühle, P. Thomas, and S. W. Koch, "Disorder-induced dephasing in semiconductors," submitted.
23. S. W. Koch, C. Sieh, T. Meier, F. Jahnke, A. Knorr, P. Brick, M. Hübner, C. Ell, J. Prineas, G. Khitrova, and H. M. Gibbs, "Theory of coherent effects in semiconductors," *J. Lumin.*, in press.
24. A. Euteneuer, E. Finger, M. Hofmann, W. Stolz, T. Meier, P. Thomas, S. W. Koch, W. W. Rühle, R. Hey, and K. Ploog, "Coherent excitation spectroscopy on inhomogeneous exciton ensembles," *Phys. Rev. Lett.*, in press.
25. F. Jahnke, M. Kira, S. W. Koch, G. Khitrova, E. K. Lindmark, T. R. Nelson, D. V. Wick, J. D. Berger, O. Lynghes, H. M. Gibbs, and K. Tai, "Excitonic nonlinearities of semiconductor microcavities in the nonperturbative regime," *Phys. Rev. Lett.* **77**, pp. 5257-5260, 1996.
26. F. Jahnke, M. Kira, and S. W. Koch, "Linear and nonlinear optical properties of excitons in semiconductor quantum wells and microcavities," *Z. Phys. B* **104**, pp. 559-572, 1997.
27. R. Binder, S. W. Koch, M. Lindberg, N. Peyghambarian, and W. Schäfer, "Ultrafast adiabatic following in semiconductors," *Phys. Rev. Lett.* **65**, pp. 899-902, 1990.
28. G. Bartels, G. C. Cho, T. Dekorsy, H. Kurz, A. Stahl, and K. Köhler, "Coherent signature of differential transmission signals in semiconductors: Theory and experiment," *Phys. Rev. B* **55**, pp. 16404-16413, 1997.
29. S. Schmitt-Rink, D. S. Chemla, and D. A. B. Miller, "Theory of transient excitonic optical nonlinearities in semiconductor quantum-well structures," *Phys. Rev. B* **32**, pp. 6601-6609, 1985.
30. X. Fan, H. Wang, H. Q. Hou, and B. E. Hammons, "Biexcitonic effects in the nonperturbative regime of semiconductor microcavities," *Phys. Rev. B* **57**, pp. 9451-9454, 1998.
31. P. Brick et al., unpublished.

Advances in Missile Technology - Impact of Photonics*

Dr. A. Sivathanu Pillai

Chief Controller R&D, Defence Research and Development Organisation
B Wing, Sena Bhavan, New Delhi - 110 011

ABSTRACT

This paper discusses the role and impact of advancements in Photonics Technology on the performance enhancement of guided missile weapon systems with specific reference to the development of Indian guided missiles programme. India is emerging as a technologically strong nation with core competence in Space, Missile and Nuclear technologies, advanced computing including supercomputers and software. Based on the realisation of the fact that high technology strength is the key to economic prosperity and military strength, India is progressing several high technology areas that help in attaining the global competitiveness. Photonics is identified as one of the important areas in this direction and hence high priority has been accorded for Research & Development in Photonics. This paper reviews the current trends and developments in missile technology and highlights some of the important developments in Photonics that have a force multiplying effect on the performance enhancement of guided missile systems.

Key words: High technology in India, Guided Missiles Technology, Photonics

1. INTRODUCTION

A study of the evolution of war weaponry reveals that, over the years, guided missiles have evolved as a weapon of choice for the modern warfare. During the early days of warfare, the wars were fought using human and animal strength and the role of weapons were mainly to augment this physical strength. At that time the theatre of war was confined only to the land and sea. This trend continued up to the 18th century till the invention of gunpowder changed the nature of warfare. Rocketry made its beginning during the last quarter of the 18th century. A major milestone in the history of Rocketry occurred in 1792 AD, when the world's first war rocket was used by Tippu Sultan, Prince of Mysore, India, to defeat the British cavalry attack at Srirangapatnam, near Mysore in India. This has triggered the development of rocket as a war weapon. However, the real transformation happened almost 150 years later, towards the end of World War II, with the development of world's first guided missile - V2, by Germany. That was the beginning of revolutionary changes in the warfare that resulted in the development and use of a wide spectrum of guided missiles launched from multiple platforms and aided by variety of sensors. Gradually the theatre of war had extended to encompass the deep sea and outer space. High technology devices and intelligent and autonomous systems have emerged as the dominating features of the modern warfare. As a result of the transformation of the nature of warfare from being a human & animal warfare to weapon warfare to ultimately the high technology warfare, guided missile systems are at the core of this high technological warfare. There has been a continuous performance enhancement in every aspect of the guided missiles, as a result of the advancement of technologies in various fields. Photonics is one such area having significant impact on the performance enhancement of the guided missile weapon systems. This paper highlights some of the important developments in Photonics that have a force multiplying effect on the performance enhancement of guided missile systems.

*Also published in *Proc. of SPIE* Vols. 3896, 3897, and 3898

This paper is organised into three parts in the following sequence:

- A brief review of high technology growth in India, strength and core competence
- Integrated Guided Missile Development Programme, Missions, Technologies, and Global assessment
- Advances in Photonics and their impact on the performance enhancement of guided missile systems

2. TECHNOLOGY LEADERSHIP AND CORE COMPETENCE

A Nation is strong and gets its rightful place only if it has economic prosperity and comprehensive security. Realising that this can be achieved through technology, India has progressed several technological areas that helped the country to emerge as a technologically strong nation. During the last five decades, India has made an all round technological progress with many accomplishments. The green revolution and the operation flood made the country self sufficient in food production, milk, vegetables, fruits, cereals and other essential areas. The technology related to healthcare has resulted in increase of life expectance. The quest for tapping natural resources for generating power has given new impetus to the power sector. The nuclear tests in 1974 and in 1998 made India a nuclear weapon state, and India mastered harnessing of nuclear power to meet the growing demand for electricity. 500 MW fast breeder development and the target of 3000 MW power generation by 2000 are the immediate goals. By 2020 the nation is targeting 20000 MW nuclear power generation. India already has a 2 GFLOP super computer, which will reach 8 GFLOP by 2000 and teraflop speed by 2020. The nation is passing through a communication revolution towards reaching 20 million lines and soon to 100 million lines. With the established strength in computing systems, software and communication, large pool of talented software specialists, together, India is emerging as a strong nation in the area of information technology. India's current software export has already reached 1 billion US dollars.

The guided missiles Agni and Prithvi have demonstrated India's capability to develop high technology strategic systems without any help from outside. India made spectacular achievements in building its own launch vehicles, SLV-3, ASLV, and PSLV, and the GSLV which is getting ready will give India the capability to inject satellites into the geo-stationary orbit. The Indian satellites INSAT and IRS with 6 m resolution are among the best in the world. Recently PSLV launched German and Korean satellites providing cost effective launch services to the world. India is self-sufficient in space systems and their applications. In the area of aeronautics, the Indigenous light combat aircraft will take off very soon. India is dreaming of launching a reusable missile, deep penetration strike aircraft, and multipurpose aerospace vehicle - Hyperplane, harnessing the technological base established in aeronautics, space and missiles.

India is self-sufficient in production of all raw materials, special alloys, armour materials, electronic components and devices, computing systems and software for meeting the demands of the nation. Both public and private sector industries have been well knitted with R&D and academy to meet the demands. The Indian Defence R&D organisation, DRDO, achieved technology breakthrough in certain devices and computing systems, ASICs and MMICs, both Silicon and Gallium Arsenide based, PACE+ super computer, ANUPAMA microprocessor with state-of-the-art architecture to meet the requirements of strategic programmes. DRDO has developed core competence in many critical areas of armaments, combat vehicles, electronics and communications, aeronautics, missiles, life supporting systems and computing systems. This core competence is being used to develop state-of-the-art high technology systems for the armed forces.

India is blessed with abundance of manpower, natural resources and good value system. The R&D development cost varies from $1/10^{\text{th}}$ to $1/3^{\text{rd}}$ of the advanced nations depending on the type of programme. Also through various programmes, Indian specialists have learnt to work together with academic institutions and industries as partners, sharing each others strength to design, develop, and produce high technology systems in the country without any dependence from abroad.

3. INTEGRATED GUIDED MISSILE DEVELOPMENT

3.1 Mission & Technologies

The Integrated Guided Missile Development Programme (IGMDP) commenced in 1983 with an objective of design, development and leading to production of four types of missile systems namely, Prithvi, Trishul, Akash and Nag and technology demonstrator for long range system - Agni. Prithvi is a short range battlefield Surface to Surface missile launched from a mobile transporter. Prithvi uses liquid propellant rocket engines, light weight airframe, high accuracy strapdown inertial guidance system and electro-hydraulic control system. Trishul is a low level quick reaction surface to air missile system designed to defend the moving armoured columns from attacking aircraft and helicopters. The Naval version of Trishul is designed to defend the ships from the incoming sea-skimming missiles. Akash is a medium range surface to air missile with multi-target handling capability and ECCM features. Nag is a 3rd generation anti tank guided missile with a fire and forget and top attack capabilities. Nag has two state-of-the-art guidance systems, one using an Imaging Infra Red seeker and the other using a Millimetric wave active radar seeker. Agni is an Intermediate Range Ballistic Missile, which uses a specially developed carbon-carbon re-entry vehicle structure and re-entry guidance and control.

The technological goal of the IGMDP is to ensure that the systems are contemporary at the time of their induction into the Services. As a result, the technologies have been forecast 10 to 15 years in advance, concurrently developed, and channelled into the missile systems. The programme used several innovative management practices including the multi-institutional partnership, consortium, collaboration, technology empowerment, and developed all the critical technologies required for the programmes within the country using a network of R&D laboratories, academic institutions, public and private sector industries. The systems developed are of multi-user and multi-role in nature with contemporary performance.

3.2 Global Assessment

With a high supersonic manoeuvrable trajectory, high lethality, multiple field interchangeable warheads, and high accuracy, Prithvi is among the best in its class. With a quick reaction time of 6 sec, jamming proof Ka-band guidance, and anti-sea skimming missile capabilities, Trishul has contemporary performance in its class. The performance of Trishul is comparable to ADATS, CROTALE and BARAK. With multi-target engagement capability and modern homing guidance, Akash is state-of-the-art and comparable in performance to the PATRIOT. Nag is aiming to be the first of its kind in the world with fire & forget and top attack capabilities and a Tandem warhead capable of defeating composite and reactive armour.

3.3 Further advancements

Based on the above strength, India is working on several next generation technologies to enhance the performance of its guided missiles. The general directions of improvements include:

- (a) Faster speeds towards hypersonic missiles
- (b) Improved precision towards zero CEP
- (c) Intelligent systems like the Terminally Guided Sub-munitions
- (d) Capability of launching from multiple platforms
- (e) Enhanced stealth
- (f) Better ECM / ECCM capabilities

The above directions of improvement requires major technology advancements in the subsystems towards:

- (a) Lower weight
- (b) Less volume (Miniaturisation)
- (c) Lower power consumption

- (d) Better performance in terms of the processing efficiency, minimum errors, greater sensitivity and greater precision
- (e) Minimum aerodynamic interference and better integration with missile
- (f) Lower cost

It is interesting to note that many developments in Photonics could help in realising the above objectives. Some of them are discussed below.

4. ADVANCEMENTS IN PHOTONICS AND THEIR IMPACT ON PERFORMANCE ENHANCEMENT OF GUIDED MISSILES

4.1 Current applications of Photonics in Guided Missiles

Photonics has always been one of the important technologies used in various aspects of guided missiles. Some of the important areas where Photonics and related technologies play a crucial role in guided missiles include:

- (a) Missile guidance applications
 - Missile tracking sensors for command guidance
(Ex : IR plume trackers used in 2nd generation anti tank guided missiles and IR imaging sensors used in surface to air missiles)
 - Target tracking sensors for homing guidance
(Ex : IR homing seekers for air to air missiles, IR imaging sensors for 3rd generation anti tank guided missiles)
 - Inertial sensors for navigation systems used in surface to surface missiles and number of other applications
(Ex: Fibre optic gyros, ring laser gyros)
 - Imaging sensors for mid course guidance and terminal homing for long range missiles
(Ex : Imaging sensors for terrain contour matching and terminal guidance)
 - Illuminating source and homing sensors for semi-active homing applications, and range finders used in certain class of missiles
- (b) Proximity sensors for initiating warhead detonation
(Ex: IR Proximity fuzes used in anti sea skimmer missiles, altitude sensors used in surface to surface missiles)
- (c) Surveillance, target detection and target acquisition applications
 - Thermal sights for target acquisition in 3rd generation anti-tank guided missiles
 - Infra red search & tracking systems for naval applications
 - Space based sensors for detection of missile launch point for Ballistic Missile Defence Systems
 - Laser radars for precision tracking
- (d) Equipment for command, control & communications
 - Fibre optic communications
 - Display systems
- (e) Electro-optic counter measures & counter counter measure

- (f) Design aids for missile subsystems
(Ex: Experimental stress analysis tools, Laser anemometers used in wind tunnel testing applications)
- (g) Test & evaluation instrumentation for guided missiles
(Ex : Electro-optic tracking instruments used in missiles test ranges)
- (h) Manufacturing of precision missile components and quality control
(Ex : Laser welding, equipment for inspection and measurement, holography for NDT)

The above list indicates that Photonics is important at every phase of the guided missiles lifecycle. Therefore any development in this technology has a wide ranging impact on the missile systems performance.

4.2 Advancements in Photonics and their impact on guided missiles

4.2.1 Some of the important developments in Photonics and related technologies with potential applications for guided missile systems include:

- (a) Uncooled Imaging technology
- (b) Focal plane array technology
- (c) Conformal optics
- (d) Adaptive optics
- (e) Fiber optics technology
- (f) Micro-Opto-Electro-Mechanical Systems (MOEMS)
- (g) Optical Correlators
- (h) Multi-Spectral fusion (fusion of 3-5 μ and 8-12 μ images)
- (i) Multi-sensor Fusion (fusion of 3-5 μ and 8-12 μ images of IR and MM wave images)
- (j) Real-time Image Processing

4.2.2 Uncooled Imaging

Uncooled thermal imaging systems are very important for missile systems as these system offer significant operational advantages and saving of weight, space as well as cost associated with the cooling system. Towards this the resistive microbolometer technology, ferro-electric bolometer technology, uncooled thermo electric linear arrays are becoming more important. The research effort in uncooled infrared technology is directed towards several other military applications including reconnaissance, surveillance and weapon sighting capabilities as well as for precision munitions and dispenser system applications and anti armour submunition programmes.

4.2.3 Focal Plane Array Technology

Focal Plane Arrays technology is crucial for missile seekers and other imaging sensors. The focus is on developing larger size arrays, higher resolution and higher sensitivity focal planes. The current research is also focused on reducing the pixel size and increasing pixel sensitivity using advanced materials and micro electromechanical device structures. The advancement in FPA technology has a direct impact on the guided missile systems. For example, target detection and lock on range of a 3rd generation anti tank guided missiles can be significantly increased by enhancing the performance of the FPA.

4.2.4 Conformal optics

Conformal optics minimises the aerodynamic interference of the missile IR domes and windows by shaping the optics to minimise the aerodynamic drag coefficient. This will increase the aerodynamic efficiency of the missile and thus increase its range. However, the design, manufacturing and testing of the conformal optics and development of techniques & methods for dynamic aberration correction is a great challenge that is being addresses by the current research.

4.2.5 Adaptive optics

Adaptive optics compensates for the turbulence induced phase distortions of optical waves propagating through the atmosphere. Adaptive optic systems typically consist of a wavefront phase sensor, focusing optics, a spatial light modulator (SLM) for correcting phase errors, imaging sensors, and the control and processing electronics. These systems improve the image quality by reducing the phase aberrations introduced when the wavefront travels through turbulent atmosphere or aberrations introduced by the optical system itself. Adaptive optic system is a growing area of interest for the guided missiles. Advanced technologies are now becoming available to make these systems lightweight, low power, and compact. The technologies that are making this possible include highly integrated low power electronics, and new processing architectures for error sensing and control, flexible high density packaging, and Micro-Opto-Electro-Mechanical Systems.

4.2.6 Fibre optic technology

The advancement in Fibre optic technology has multiple implications for guided missile systems. The most beneficial development is the enhanced communication abilities of the fibre optics, which are important for command, control and communication applications. Fibre optic guided missile and track via missile systems are some of the important developments in this direction.

Another major application of fibre optic technology is in the area of sensors. Fibre optic gyro used in the inertial navigation units of missiles is an example for this. The Fibre Bragg grating sensors also called "Smart sensors" represent an exciting development in fibre-sensor technology. Fibre Bragg grating sensors can monitor the manufacture of a product or the condition of a structure in use by providing the real-time feedback by reflecting different wavelengths depending on the condition of the structure. Writing a periodic series of gratings (refractive-index modulations in the core of a single-mode fibre) using an ultraviolet beam generates a low-loss, highly reflective, wavelength-sensitive filter system. This non invasive process does not change the fibre's strength, electromagnetic-interference immunity or dielectric properties. Bragg grating sensors, when fabricated and annealed properly, have proven to be permanent, easily reproducible reflectors that can withstand high temperatures. The gratings respond to changes in temperature, compression and strain by changing the wavelength that they reflect, and their performance is not amplitude or intensity dependent. The sensors are small and can easily attached to surfaces to provide information on the structure's integrity. These sensors are very useful for monitoring the structural conditions during flight testing of guided missiles.

4.2.7 Micro- Opto-Electro-Mechanical Systems (MOEMS)

These systems represent another exciting development for missile and space applications. The saving in the weight, volume and power requirements are of great importance for the applications such as the terminally guided sub-munitions. Micro mirrors are the crucial enabling technology for these systems. Design techniques and fabrication processes for both individual micro mirrors as well as the arrays of micro mirrors are the focus of the current research efforts.

4.2.8 Optical correlators

Optical correlators relies on the Fourier transform property of a lens and a hologram of the Fourier transform of an object as viewed from a particular perspective, to establish a matching correlation coefficient. Optical correlators can be effectively used for automatic target recognition, missile guidance and tracking of the target scenes which do not have prominent features or high contrast with the background. The speed and innate parallel-processing capability of optics enable the correlator to simultaneously recognize and locate all objects in a scene almost instantaneously. These systems are very important for the missile guidance applications, especially the mid course and terminal guidance of long range surface to surface missiles.

4.2.9 Multi-Spectral fusion & Multi-Sensor fusion

The Multi-Spectral fusion methods greatly improve the detection and identification of low observable and camouflaged targets. Hence these methods are becoming more and more common for future applications. Missile seekers with two color detectors are already in operation. However for a battle field application, Multi-sensor fusion is emerging as a major technique to overcome limitations of IR and radar seekers, especially in a dense electronic / electro-optic counter measures environment. Dual mode missile seekers with both IR and radar imaging seekers are becoming important for future applications. Hence this is an important area for missile technology.

4.2.10. Real-time Image Processing

Due to the limitations imposed by the electronic processors for the real-time solutions to critical military application such as automatic target recognition, clutter rejection in infrared search and track (IRST) applications, vision-assisted piloting tasks in unmanned robotic vehicles (e.g., Remotely Piloted Vehicles, Unmanned Aerial Vehicles, or Unmanned Underwater Vehicles), and imaging Identification Friend of Foe, real-time image processing is an important technology. The intrinsic parallelism of optics is expected to circumvent these limitations in future. Towards this, the optronics processor holds a great promise for future real time applications for guided missiles.

4.2.11 The Indian scenario

India has already developed thermal Imagers based on 60 & 100 element linear arrays and 288x4 FPAs for MBT-FCS and Nag missile respectively. It is working on IRST system for Naval applications. A wide technology base exists within the country and also enough skilled manpower available in this field. Keeping in view the technology trends and the requirements of the country, DRDO is working in the development of several state-of-the-art systems including; Night Vision Devices based on Optical Amplification, Intelligent Search & Track system for Airborne platforms, High performance Thermal Imagers using staring FPAs/IR CCDs, Dual-bank/Bi-spectral 3-5 μm and 8-12 μm imagers, Thermal Imagers using uncooled detectors, Real time (on-line) image processing. Laser Instrumentation including Laser Designator/Range Finders using Laser diode pumped Nd:YAG laser, Eye-safe laser systems, Laser Range gated imaging, Laser proximity fuses, Blue-green lasers for underwater imaging, Coherent laser imaging, Sensors for smart ammunitions. Integrated Multi-spectral laser and Radar Warning systems and Autonomous EO Missile jammers with programmed auto-controls. Servo Control Systems will include LOS stabilization to an accuracy of 10 μ rad. Photonics includes EO tracking/guidance system based on optical correlation techniques, Helmet mounted display using wave-guide HOE, EO sensor using IO chips, Real-time imaging system through turbulent media. Optical Designs include design of light weight optical systems using GRIN/Binary optics. Special attention is being given to the development of non-linear materials, lasers, IR transmitting materials, thermal sensors, electro-optical devices and transducers, within the country.

Some of the identified focal areas for R&D include :

(a) Photonic Devices

- Optical amplifiers for night vision communication.
- Associated memory devices using neural network for recognition of targets.
- Correlator, convolver, pulse compressor and tuneable filters for signal processing.
- Gallium Arsenide based integrated optical components such as phase-shifters, modulators.
- A to D converter for optical computing applications.
- Distortion free optical recognition.

(b) Photonic Materials

- Laser host materials such as Nd, YAG, Er YAG, CNGG, Alexandrite, Ti Sapphire, Nd Glass.
- Laser non-linear materials such as Lithium Nichate, KTP, BBO, LBO for parametric devices, BSO, BGO and KNB for OPC applications.
- Organic and polymer materials such as Urea, MNA, POM, etc. for SHG applications, MNA/PMMA for guided wave applications, organic dyes for Q-switching and mode locking applications.
- Semiconductor materials such as GaAs, CdTe, CdZnTe, MCT, etc.
- IR materials such as ZnS, ZnSe and Chalcogenide glasses for IR optical components.

(c) Photonic Technologies

- OPC techniques
- Diode laser pumping for solid state lasers
- Optical parametric oscillator
- Er doped passive fibre optical amplifiers
- Real-time optical processing
- Integrated optical waveguide technology
- Holographic optical elements

(d) Sensors

- Optical & IR sensors and thermal imagers for IR detection and thermal imaging.
- Fiber optic sensors , Fiber Optic gyros (FOGs) and Ring-Laser gyros (RLG)
- Multi-spectral and multi-mode homing seekers

5. CONCLUSION

Advances in Photonics technology holds great promise for the performance enhancement of guided missile systems. Realising this potential, the Indian Defence R&D identified Photonics as one of the high priority areas for the research and development. In this context, this paper discussed the various important developments in Photonics and highlighted some areas related to guided missiles. It is clear from the above discussions that Photonics is a great force multiplier for guided missile technology. This paper also briefly outlined the Indian scenario in the area of Photonics and the thrust areas for R&D. With an established core competence in space, missile and nuclear technologies, and information technology, India is poised for greater technological advancement through the synergistic growth of Photonics and guided missile technology.

ACKNOWLEDGEMENT

The author gratefully acknowledges the contributions of several specialists from various DRDO laboratories, projects and partner organisations for their help in evolving the technology vision 2010 for DRDO, identifying the thrust areas in many critical technological areas including Photonics. This paper draws upon those inputs and highlighted some of these areas relevant to the guided missiles.

REFERENCES

1. *Technology Vision 2020*, Technology Information, Forecasting and Assessment Council (TIFAC), New Delhi
2. *Technology Vision 2010 for DRDO*, internal report of Defence Research & Development Organisation, New Delhi
3. R.S. Balcerak, "Uncooled IR imaging: technology for the next generation", *Infrared Technology and Applications XXV*, Proceedings of SPIE, Vol. 3698, USA, 1999
4. R.R. Shannon, "Overview of conformal optics", *Window and Dome Technologies and Materials VI*, Proceedings of SPIE, Vol. 3705, USA, 1999
5. Jeffrey A. Sloan and Donald W. Small, "Design and fabrication of a miniaturized optical correlator", *Optical Engineering*, , Vol. 32, No.12, pp. 3307-3315, 1993
6. Keith E. Drundin, "Fiber Optic Sensors: Smart Technology for Safety", *Photonics*, pp. 106-107, January 1996.
7. Deborah Jackson, *A Structural Approach to the Photonic Processor*, RAND Note N-3399-RC

SESSION 1

Nitrides

Piezoelectric Franz-Keldysh effect in a GaN/InGaN/AlGaN multilayer structure

Yong Tian Hou, Kie Leong Teo, Ming Fu Li

Center for Optoelectronics, Department of Electrical Engineering, National University of Singapore,
Singapore 119260

Kazuo Uchida

Department of Communications and Systems, The University of Electro-Communications, 1-5-1
Choufugaoka, Choufu, Tokyo 182, Japan

Hiroki Tokunaga, Nakao Akutsu and Koh Matsumoto

Nippon Sanso Co., Tsukuba Laboratories, 10 Ohkubo Tsukuba, Ibaraki, 300-26, Japan

ABSTRACT

Contactless electroreflectance (CER) of a GaN/InGaN/AlGaN multilayer structure grown on sapphire has been measured in the temperature range of 15 K and 450 K. Except for the GaN exciton structures, well-defined Franz-Keldysh Oscillations (FKO's) are observed above the AlGaN band gap. An electromodulational model based on complex Airy functions is used to analyse the FKO's line shape. The temperature dependence of transition energies is obtained both for GaN and AlGaN. The magnitude of the built in electric field in AlGaN layer is also determined. The temperature dependence of the electric field is found to be consistent with the variation of thermal strain in the epilayer. It is demonstrated that the built-in electric field can be identified to be due to the piezoelectric effect.

Key words: AlGaN, Contactless electroreflectance, Franz-Keldysh Oscillations, Piezoelectric effect

INTRODUCTION

III-nitride is a promising material for the development of optoelectronic devices in the blue and ultra-violet spectral regions.¹ High-efficiency blue and green light-emitting diodes (LEDs) and room-temperature laser diodes (LDs) based upon GaN and related materials have been achieved recently. This has encouraged the increasing efforts in the investigation of their fundamental properties in the recent years. For the lack of proper substrate, III-nitrides are usually grown on lattice mismatched and thermal incompatible foreign substrates. Sapphire is one of the most commonly used substrate. GaN epilayers grown on sapphire have been demonstrated to be under biaxial compressive strain. The influence of the strain on the valence band splitting and exciton recombination in III-nitrides has been studied extensively. The strain will also induce large piezoelectric fields in the epilayer for III-nitride materials having large piezoelectric constants. These piezoelectric fields have been reported to affect the optical and electrical performance of nitride materials and devices.³⁻⁷ However, understanding of the piezoelectric effect in III-nitrides is far to completeness, further investigation will be necessary.

Photorefectance (PR) and Contactless Electroreflectance (CER) are powerful nondestructive tools available for studying the optical properties of semiconductors. In the low field regime, the PR and CER displays sharp derivative-like features in the region of interband transitions.⁸ In the intermediate field regime, PR and CER exhibit Franz-Keldysh oscillations (FKO's), which can be used to determine the magnitude of the built-in electric fields.^{8,9} For III-nitrides, PR and CER have been performed extensively to study the exciton transitions and valuable information about the exciton fine structure has been obtained.¹⁰ However, most of the work are performed in the low field regime and the FKO's have only been observed in a few PR spectra for III-nitride system and lack detailed investigation.^{11,12} In comparison with PR, the CER method has a number of advantages for the study of wide-band-gap nitride materials. It does not require an UV laser as the pump beam and it also avoids the photoluminescence background due to this pump beam. In this paper, we report the

study of a GaN/InGaN/AlGaN multilayer structure by CER, clear FKO's associated with AlGaN layer are observed and the magnitude of the built-in electric field is determined. The built-in electric fields are also found to be temperature dependent and related to the thermal strain in the epilayer, which demonstrates its piezoelectric nature.

EXPERIMENTAL

The sample used in our experiment is a GaN/InGaN/AlGaN multilayer structure grown on the c-plane of sapphire substrate by metalorganic chemical vapor phase deposition (MOCVD). The sample consists of the following sequence: sapphire substrate/GaN(2.2 μ m)/AlGaN(0.1 μ m)/InGaN(0.39 μ m)/GaN(0.1 μ m) cap. The InGaN segment is a multiple quantum well with In concentrations of 20% and 2% in the well and barrier layer, respectively. The Al composition of AlGaN layer is 10%. All the layers are undoped. In the CER measurements, Xenon arc lamp of 150 W was used as the probe source and a 600 V peak to peak AC voltage was applied to the sample through a capacitor like electrodes as the modulation source. This value of the modulation voltage was sufficiently small so that the measured line shapes were independent of the modulation voltage. The modulation field is estimated to be near 3 kV/cm for a distance of about 1mm between the two electrodes. The signal was detected by an UV-enhanced Si photodiode. The sample was cooled with a closed-cycle refrigerator and measurements were performed in the temperature range of 15 K and 450 K.

RESULTS AND DISCUSSIONS

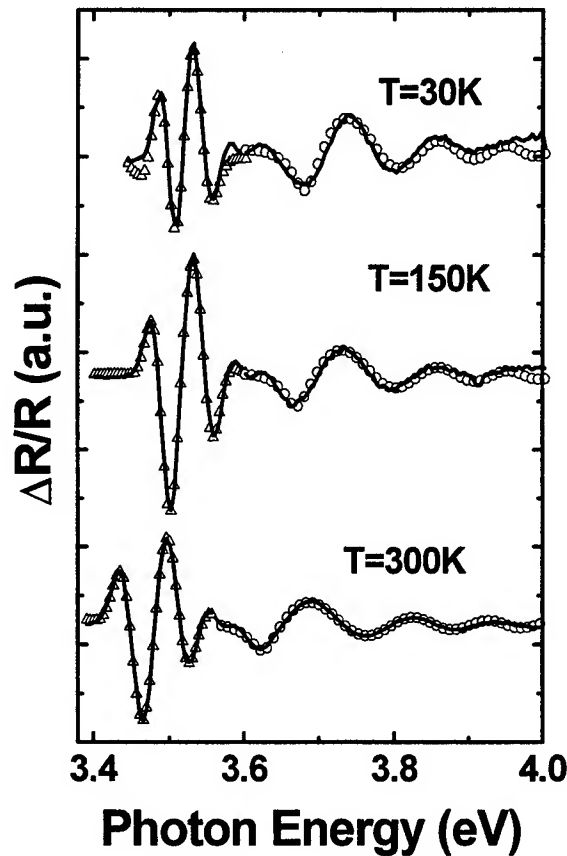


Fig.1: The CER of the sample at 30 K, 150 K and 300 K. Solid curves are experiments. Open triangles are the fit to the FDGFF form for GaN and open circles are the fit using the electromodulation model.

Figure 1 shows the CER of the sample measured at three typical temperatures (solid curves). From Fig.1, there are two portions of spectral structures observed obviously. From the observed absorption edges of GaN (3.44 eV) and AlGaIn (3.62 eV) layers by room temperature photovoltaic spectrum of the sample, the CER structures in Fig.1 can be identified from their energy positions.¹³ The sharp structures around 3.5 eV are from the GaN layer and the broad oscillation-like ones can be identified to be originated from the AlGaIn layer. The CER of the InGaIn segment is only observed as a weak structure (not shown) although emission from this layer dominates the photoluminescence spectra.¹⁴

For the sharp GaN spectral features in Fig.1, it is found the line shape is very similar with the previous report and they can be attributed to GaN excitonic absorption.¹⁵ The CER line shape due to excitons in the low field regime can be described by the first derivative of a Gaussian functional form (FDGFF). The modulated reflectivity $\Delta R/R$ can be expressed as:⁸

$$\frac{\Delta R}{R} = C_1 (1/\Gamma^2) \Phi(1, \frac{1}{2}, -\frac{1}{2}x^2) + C_2 (2x/\Gamma^2) \Phi(2, \frac{3}{2}, -\frac{1}{2}x^2) \quad (1)$$

where C_1 and C_2 are amplitudes, Γ a phenomenological broadening parameter. $\Phi(i, j, k)$ is the degenerate hypergeometric function, where x is related with the photon energy E and exciton transition energy E_0 by

$$x = (E - E_0) / \Gamma \quad (2)$$

The fundamental absorption edge in wurtzite GaN has three excitonic transitions, A, B and C related to the $\Gamma_9^V - \Gamma_7^C$, Γ_7^V (upper band)- Γ_7^C and Γ_7^V (lower band)- Γ_7^C interband transitions, respectively. The open triangles in Fig.1 is the least square fits to the first derivative of the Gaussian functional form (FDGFF) including the three exciton transitions of GaN.⁸ In our spectra, A and B features are not resolved because of the thermal or defect broadening although line shape fitting demonstrates two structures. The C exciton is separated by about 65 mV from A and B at room temperature. This value is very similar to that (70 meV) previously reported in CER of GaN.¹⁵

Above the band gap (3.6 eV) of AlGaIn, the spectrum shows clear oscillating behaviour. Since these oscillations occur at higher energy positions above GaN band gap, other possible mechanisms such as thickness interference fringes, piezoelectrical thickness variations, thermomodulation and electric field effects acting on a series of discrete electronic levels or on a continuum, can be excluded as all these effects will lead to oscillations below the GaN band gap. We thus identify them to be due to the FKO's.

We analyse the FKO's observed by a recently proposed electromodulation model based on complex Airy functions.^{16,17} From this model, if the effects of excitons and electric field non-uniformity are negligible, the CER response $\Delta R/R$ can be finally expressed as:^{16, 17}

$$\frac{\Delta R}{R} = \text{Re} \left[\frac{A e^{i\phi}}{(E - i\Gamma)^2} H(z) \right] \quad (3)$$

where ϕ is a phase factor, A the amplitude, E the photon energy and Γ represents collision broadening, the parameter z and the electro-optic energy $\hbar\theta$ are defined as:

$$z = \frac{(E_0 - E)}{\hbar\theta} + i \frac{\Gamma}{\hbar\theta} \quad (4)$$

$$(\hbar\theta)^3 = \frac{e^2 \hbar^2 F^2}{2\mu} \quad (5)$$

where e is the electronic charge, \hbar the Plank constant, F the magnitude of the electric field, E_0 the band gap energy, and μ the interband reduced effective mass in the field direction, given by

$$\mu = \left(\frac{1}{m_e} + \frac{1}{m_h} \right)^{-1} \quad (6)$$

where m_e is the electron mass and m_h the hole mass. Since the Al composition is small in our sample, we simply use the effective mass of GaN for $\text{Al}_{0.1}\text{Ga}_{0.9}\text{N}$ in the analysis, i.e., $m_e/m_0 = 0.22$ and $m_h/m_0 = 0.54$.¹⁸ where m_0 is the free electron mass.

For an isotropic three-dimensional critical point, the electro-optic function $H(z)$ is defined as a combination of the Airy function and its derivative.¹⁶

$$H(z) = 2\pi \left\{ e^{-i(\pi/3)} A_i'(z) A_i' \left[z e^{-i(2\pi/3)} \right] + z e^{-i(2\pi/3)} A_i(z) A_i \left[z e^{-i(2\pi/3)} \right] \right\} + i\sqrt{z} \quad (7)$$

where A_i is the Airy function and A_i' its derivative.

The open circles in Fig. 1 are the least square fits using Eq. (3) with a single Airy function. The good fit to the experimental line-shape supports our attribution of the observed structures to FKO's. From the line shape analysis, the magnitude of the built-in electric fields can be determined and the obtained values are in the range of 260 to 380 kV/cm for various temperatures. Under such high electric fields, excitons must be ionized and thus cannot contribute to the CER spectra. A numerical simulation of the carrier redistribution has shown that the maximum electric fields near the interface between GaN, InGaN and AlGaN interfaces are 80 kV/cm and it excludes the contribution of carrier redistribution to the

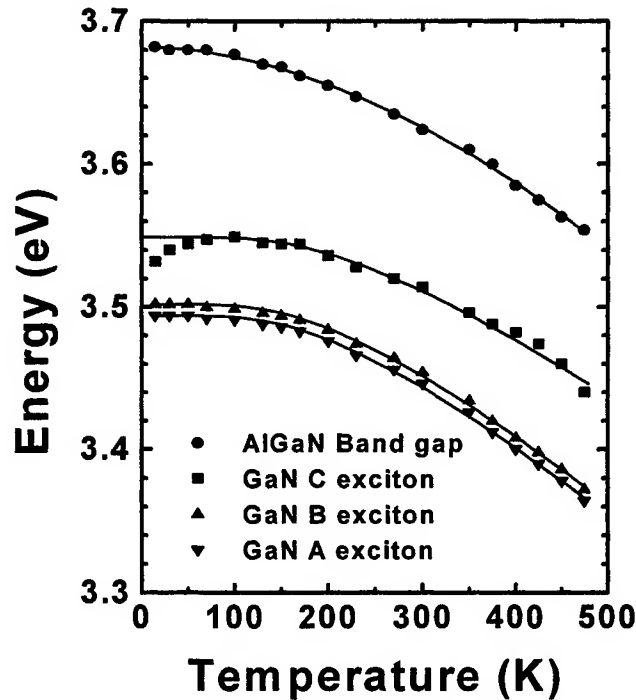


Fig.2: The temperature dependence of transition energies for GaN and InGaN (solid symbols). Solid line is the best fit to Varshni equation (AlGaN) and Bose-Einstein relation (GaN).

observed FKO's.¹³ The large electric field observed in the AlGaIn layer also cannot be possibly induced by photovoltaic effect, modulation field near the surface and interface, and therefore we identify it to be due to piezoelectric effect.

Fig.2 shows the obtained temperature dependence of GaN and AlGaIn transition energies. In the FDGFF fit to GaN CER, we have supposed that the B exciton has a fixed energy separation from A exciton (8 meV) and their broadening items are the same in order to reduce the adjustable parameters.

The temperature dependence of the interband transition energies of semiconductors can be described by the Varshni empirical relationship:¹⁹

$$E(T) = E(0) - \alpha T^2 / (\beta + T) \quad (8)$$

where $E(0)$ is the transition energy at 0 K, and α and β are Varshni coefficients.

The temperature dependence of interband transition energies for semiconductors also can be described by a Bose-Einstein-type relation:²⁰

$$E(T) = E(0) - 2a_B / [\exp(\theta_B/T) - 1] \quad (9)$$

where a_B represents the strength of the exciton-average phonon interaction, and θ_B corresponds to the average phonon temperature.

Best fits to the above Eq. (8) or (9) of the temperature dependence of transition energies for GaN and AlGaIn are shown in Fig.2 as solid lines.

For transition energies of AlGaIn, its temperature dependence can be better described by Varshni relationship of Eq. (8). Our obtained Varshni coefficients α and β are 12×10^{-4} eV/K and 1600 K, respectively. These values are close to those of GaN and $\text{Al}_{0.05}\text{Ga}_{0.95}\text{N}$ by CER.^{21, 22} The band gap at 0 K is obtained to be 3.682 eV. Using the AlGaIn band gap dependence of Al fraction,²³ the Al concentration in our sample is found to be 10.4 %, which is consistent with the growth Al composition (10%).

However, the Bose-Einstein-type relation is found to be more appropriate for the temperature dependence of GaN exciton energies. The a_B obtained is 140 meV and 150 meV for A and C excitons, respectively. Their average phonon

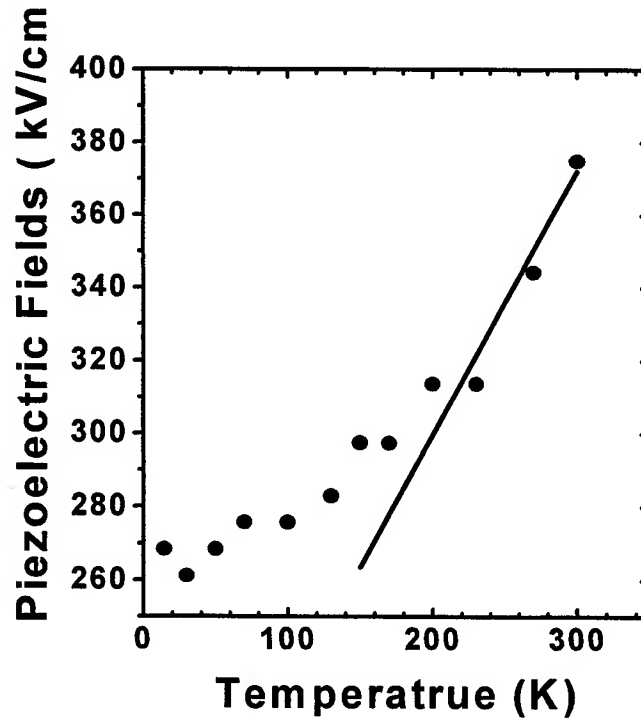


Fig.3: The temperature dependence of the obtained built-in electric fields (solid squares) and its calculation from the thermal strain (solid line).

temperature θ_B determined is 605 K for A exciton and 665 K for C exciton. These values are in good agreement with the previous results of GaN and $\text{Al}_{0.05}\text{Ga}_{0.95}\text{N}$ by CER.^{21, 22} As reported in ref. [21], a decrease of the energy separation between C exciton and A exciton at low temperature is also observed.

Figure 3 shows the obtained built-in electric fields at various temperatures. We exclude the data of temperatures higher than 300 K because the higher noise level diminishes the occurrence of the FKO's and leads to higher error in the determination of electric fields. From Fig.3, it is found that the built in electric field in AlGaIn layer has strong temperature dependence. As the temperature decreases, the magnitude of the electric field decreases. Furthermore, at temperature is lower than about 200K, the electric field decreases slower with temperature and it becomes almost temperature independent below 100K. The electric field will depend on the strain in the epilayer if it is due to piezoelectric effect. The above temperature dependence of electric field will reflect the variation of strain in the epilayer and a qualitative discussion will be given below.

For GaN grown on sapphire substrate, the lattice mismatch induced strain is believed to be almost completely relaxed at the growth temperature because of their large lattice mismatch (14%). Strain in the epilayer at lower temperatures is largely understood as a consequence of the difference in the thermal expansion coefficients between the nitride layer and substrate.^{25, 26} In our sample, the GaN layer is much thicker than other layers, so we treat our multilayer structure just as GaN/sapphire system in the estimation of the residue thermal strain. In the calculation, the difference of thermal expansion coefficient of GaN and AlGaIn are neglected because of our low Al fraction and very thin AlGaIn thickness. In order to calculate the thermally induced strain in the AlGaIn layer, we also assume the AlGaIn layer are pseudomorphically grown on the GaN layer. This assumption is reasonable for our sample with thin AlGaIn layer (0.1 μm) and low Al composition because it has been reported that AlGaIn can be pseudomorphically grown on GaN buffer up to thickness of 600 nm.²⁴

For GaN grown on sapphire substrate, the change of strain in the GaN layer can be calculated by:^{25, 26}

$$\Delta\epsilon_{xx} = \frac{a_{\text{GaN}}\alpha_{\text{GaN}} - a_{\text{sub}}\alpha_{\text{sub}}}{a_{\text{sub}}} \Delta T \quad (10)$$

where α is the thermal expansion coefficient, a the lattice constant, and ΔT the change of temperature. In Eq. (10), the in-plane lattice constant of GaN (a_{GaN}) and sapphire substrate (a_{sub}) are 3.189 Å and 4.758 Å, respectively. The thermal expansion coefficients of GaN (α_{GaN}) and sapphire (α_{sub}) at room temperature are 5.59×10^{-6} /K and 7.5×10^{-6} /K, respectively.²⁶ The larger thermal expansion coefficient of the sapphire substrate than the GaN layer indicates that a biaxial compressive strain will be built in the epilayer at room temperature after the cooling down from the growth temperature, which is in agreement with the experiments.^{25, 26} After the strain in GaN layer is determined, the strain in AlGaIn layer can be obtained by simply assuming the 0.1 μm AlGaIn layer has the same in-plane lattice constant as GaN in our sample.

After the strain in the AlGaIn layer is determined, the magnitude of piezoelectric field in the epilayer can be obtained using:³

$$F = \frac{2d_{31}}{\epsilon \epsilon_0} \left(c_{11} + c_{12} - \frac{2c_{13}^2}{c_{33}} \right) \epsilon_{xx} \quad (11)$$

where ϵ is the dielectric constant, ϵ_0 the vacuum permittivity, d_{31} the relevant piezoelectric constant, c_{ij} the elastic constants, and ϵ_{xx} the strain. The parameters used in Eq. (11) for $\text{Al}_{0.1}\text{Ga}_{0.9}\text{N}$ are calculated by linear interpolation between the corresponding parameters of GaN and AlN,³ and they are given in Table I.

The calculated piezoelectric fields of AlGaIn layer by Eq. (11), using the values of the thermal expansion coefficients for GaN and sapphire at room temperature, is shown as a solid line in Fig.3. Because the temperature dependence of thermal expansion coefficients is neglected, the calculation will only be applicable in the temperature range near 300K. From the calculation, it is found that the magnitude of the piezoelectric field in AlGaIn layer decreases linearly with the temperature and it qualitatively agrees with the experiment data near 300 K. The deviation of the theoretical calculation from the experiments at low temperatures is due to the simple assumption which neglects the temperature dependence of the thermal expansion coefficients. For semiconductors, the thermal expansion coefficient has strong temperature dependence below room temperature. The study of GaN/sapphire by X-ray diffraction has shown that the

thermal expansion of GaN and sapphire decrease as the temperature decreases from 300 K and become negligible below 100 K.²⁷ This can account for the observed slower rate of decrease in piezoelectric fields as temperature is decreased. Below 100 K, the electric field determined by FKO's is almost independent of temperatures, which indicates that the thermal expansion is actually negligible in this temperature region.

Table I: Values used for calculating strain induced piezoelectric fields.

	GaN	AlN	Al _{0.1} Ga _{0.9} N
d_{31} (cm/V)	-1.7×10^{-10}	-2.0×10^{-10}	-1.73×10^{-10}
ϵ (static)	10.0	8.5	9.85
C_{11} (GPa)	396	398	396
C_{12} (GPa)	144	140	144
C_{13} (GPa)	100	127	103
C_{33} (GPa)	392	382	391

Using Eq. (11), the strain in AlGaIn layer is estimated to be 0.14% from the piezoelectric field of 260 kV/cm at 15 K. If the AlGaIn is considered to be pseudomorphically grown on GaN, it corresponds to a compressive biaxial strain of about 0.11% in the GaN layer, which is in the region of strain values previous reported in GaN grown on sapphire.² The FDGFF fit to the GaN exciton structure at 15 K shows that the free exciton A is at 3.489 eV. By using the strain dependence of the excitation energy²², we obtain the strain in GaN layer to be about 0.13%. This indicates our assumption of AlGaIn pseudomorphically grown on GaN layer is reasonable.

CONCLUSION

In conclusion, exciton structures from the GaN and FKO's from the AlGaIn layer are observed in CER of a GaN/InGaIn/AlGaIn multilayer structure. The GaN CER features are analysed by the first derivative of a Gaussian functional form while an electromodulational model is used to fit the line shape of CER for FKO's in AlGaIn. The temperature dependence of their interband transition energies is studied in terms of Varshini and Bose-Einstein expressions. The magnitude of the built-in electric fields in AlGaIn layer is also determined at different temperatures. A qualitatively agreement can be obtained for the temperature dependence of the electric fields near 300 K. It is found that such temperature dependence is related to the thermal strain variation in the epilayer and we thus assign the large electric fields to be the piezoelectric fields.

ACKNOWLEDGEMENT

This work was supported by the Singapore NSTB RIC-University research funded project 681305.

REFERENCES

1. S. Strite and H. Morkoc, J. Vac. Sci. & Technol. **B10**, 1237 (1992); S. Nakamura, and G. Fasol, The blue Laser Diode: GaN Based Light Emitters and Lasers (Springer, Berlin, 1997).
2. B. Gil, O. Briot, and R. Aulombard, Phys. Rev. **B52**, R17028(1995).
3. G. Martin, A. Botchkarev, A. Rockett, and H. Morkoc, Appl. Phys. Lett. **68**, 2541 (1996).
4. E. T. Yu, G. J. Sullivan, P. M. Asbeck, C. D. Wang, D. Qiao, and S. S. Lau, Appl. Phys. Lett. **71**, 2794 (1997).
5. K. P. O'Donnell, T. Breitkopf, H. Kalt, W. Van der Stricht, I. Moerman, P. Demeester, and P. G. Middleton, Appl. Phys. Lett. **70**, 1843 (1997).
6. A. D. Bykhovski, B. L. Gelmont, and M. S. Shur, J. Appl. Phys. **81**, 6332 (1997).
7. A. D. Bykhovski, R. Gaska, and M. S. Shur, Appl. Phys. Lett. **73**, 3577 (1998).
8. F. H. Pollak, in *Handbook on Semiconductors*, vol. 2, edited by M. Balkanski (North-Holland, New York, 1994), p527.
9. H. Shen and M. Dutta, J. Appl. Phys. **78**, 2151 (1995).
10. F. H. Pollak, in *Group III Nitride Semiconductor Compounds*, Edited by G. Gil (Clarendon, Oxford, 1998), p.158, and references therein.
11. C. Wetzel, T. Takeuchi, S. Yamaguchi, H. Katoh, H. Amano, and I. Akasaki, Appl. Phys. Lett. **73**, 1994 (1998).
12. C. Wetzel, T. Takeuchi, H. Amano, and I. Akasaki, J. Appl. Phys. **85**, 3786 (1999)

13. W. Liu, K. L. Teo, M. F. Li, S. J. Chua, K. Uchida, H. Tokunaga, N. Akutsu, and K. Matsumoto, *J. Cryst. Growth*, **189-190**, 648 (1998).
14. K. L. Teo, J. S. Colton, P. Y. Yu, E. R. Weber, M. F. Li, W. Liu, K. Uchida, H. Tokunaga, N. Akutsu, and K. Matsumoto, *Appl. Phys. Lett.* **73**, 1697 (1998).
15. W. Krystek, F. H. Pollak, Z. C. Feng, M. Schurman, and R. A. Stall, *Appl. Phys. Lett.* **72**, 1353 (1998).
16. D. J. Hall, T. J. C. Hosea, and D. Lancefield, *J. Appl. Phys.* **82**, 3092 (1997).
17. R. A. Batchelor, A. C. Brown, and A. Hamnet, *Phys. Rev.* **B41**, 1401 (1990).
18. C. Merz, M. Kunzer, U. Kaufmann, I. Akasaki, and H. Amano, *Semicond. Sci. Technol.* **11**, 712(1996).
19. Y. P. Varshni, *Physica* **34**, 149 (1967).
20. P. Lantenschlager, M. Garriga, S. Logothetidis, and M. Cardona, *Phys. Rev.* **B35**, 9174 (1987).
21. C. F. Li, Y. S. Huang, L. Malikova, and F. H. Pollak, *Phys. Rev.* **B55**, 9251 (1997).
22. L. Malikova, Y. S. Huang, F. H. Pollak, Z. C. Feng, M. Schurman, and R. A. Stall, *Solid State Commun.* **103**, 273(1997).
23. D. Brunner, H. Angerer, E. Bustarret, F. Freudenberger, R. Hopler, R. Dimitrov, O. Ambacher, and M. Stutzmann, *J. Appl. Phys.* **82**, 5090 (1997).
24. T. Takeuchi, H. Takeuchi, S. Sota, H. Sakai, H. Amano, and I. Akasaki, *Jpn. J. Appl. Phys.* **36**, L177 (1997).
25. F. Hamdani, A. Botchkarev, W. Kim, H. Morkoc, M. Yeadon, J. M. Gibson, S.-C. Y. Tsen, D. J. Smith, D. C. Reynolds, D. C. Look, K. Evans, C. W. Litton, W. C. Mitchel, and P. Hemenger, *Appl. Phys. Lett.* **70**, 467 (1997).
26. D. Volm, K. Oettinger, T. Streibl, D. Kovalev, M. Ben-Chorin, J. Diener, B. K. Meyer, J. Majewski, L. Eckey, A. Hoffmann, H. Amano, I. Akasaki, K. Hiramatsu, and T. Detchprohm, *Phys. Rev.* **B53**, 16543 (1996).
27. H. Heinke, V. Kirchner, S. Einfeldt, U. Birkle, and D. Hommel, *J. Cryst. Growth* **189-190**, 375 (1998).
28. D. Volm, K. Oettinger, T. Streibl, D. Kovalev, M. Ben-Chorin, J. Diener, B. K. Meyer, J. Majewski, L. Eckey, A. Hoffmann, H. Amano, I. Akasaki, K. Hiramatsu, and T. Detchprohm, *Phys. Rev.* **B53**, 16543(1996).

Structural and Optical Properties of GaN Materials Grown on Si by Metalorganic Chemical Vapor Deposition

J. L. Chen^a, Z. C. Feng^{b,*}, X. Zhang^c, S. J. Chua^{b,c,#}, Y. T. Hou^c, J. Lin^a

^a Department of Physics, National University of Singapore, Singapore 119260.

^b Institute of Materials Research and Engineering, 3 Research Link, Singapore 117602.

^c Center for Optoelectronics, Department of Electrical Engineering, National University of Singapore, Singapore 119260.

Abstract

GaN thin films, undoped, Si- and Mg-doped, and InGaN-GaN multiple quantum well (MQW) structures have been grown on Si (001) substrates with specially designed composite intermediate layers consisting of an ultra-thin amorphous Si layer and a GaN/AlGaIn multilayered buffer by low pressure metalorganic chemical vapor deposition. The structural and optical properties of these new grown materials were studied. X-ray diffraction (XRD), Raman scattering and Fourier transform infrared reflectance measurements confirmed their wurtzite structure. Scanning electron microscopy exhibited the single crystalline grain size up to $\sim 2 \mu\text{m}$. Photoluminescence showed strong GaN near edge emission, with only very weak deep defect-related emissions, for GaN films, and strong MQW emissions. The film surface morphology and material properties are improved by adjusting the growth conditions and buffer layer structural design.

1. INTRODUCTION

GaN based materials attract much interest in recent years for its applications in blue-ultraviolet light emitting diode (LED), laser diode (LD) and other optoelectronics devices¹. Recently, the growth of high-quality GaN thin films on sapphire has been demonstrated^{2,3}. The growth of GaN on sapphire is usually difficult because of the large difference in lattice constant and thermal expansion coefficient between GaN and the sapphire substrate and the rigidity of sapphire substrate. GaN thin films have also been tried to fabricate on various other substrates, such as Si⁴, GaAs⁵, 6H-SiC⁶ etc. Silicon is an attractive substrate because of its high crystal quality, large area size, low manufacturing cost and the potential application in integrated devices. Therefore, GaN and related materials and structures grown on Si are possibly promising to develop new generation of devices by the combination of Si- and III-N based materials and technologies in the 21st century. However, due to the even larger difference in lattice constant and thermal expansion coefficient between GaN and the silicon substrate compared with that between GaN and sapphire, it is more difficult to grow high-quality GaN films and structures on Si substrates than on sapphire.

Buffer layers with structure constants between GaN and silicon have been tried to be grown between the GaN thin film and the silicon substrate to improve the quality of the GaN film. These include AlN⁷, carbonized silicon⁸, nitridized GaAs⁹, oxidized AlAs¹⁰, $\gamma\text{-Al}_2\text{O}_3$ ¹¹ and so on. Recently, we have successfully made efforts on the growth and characterization of GaN films on silicon substrate with special designed composite intermediate layers (CIL), and some good results, including enhanced photoluminescence (PL) emissions and LED applications, have been demonstrated^{12,13}.

In this paper, we present a study on the materials properties of these new grown materials. The GaN films are grown on silicon substrate with specially designed composite intermediate layers consisting of an ultra-thin amorphous Si layer and a GaN/AlGaIn multilayered buffer, by low pressure metalorganic chemical vapor deposition (MOCVD). The focus is on the structure and optical properties of these GaN films and structures

such as InGaN-GaN multiple quantum well (MQW) grown on Si (100). Various characterization techniques were employed in these studies, including X-Ray Diffraction (XRD), Scanning Electron Microscopy (SEM), Transmission Electron Microscopy (TEM), Fourier Transform Infrared (FTIR) spectroscopy, Raman scattering and photoluminescence (PL) spectroscopy. The results showed that good quality of wurtzite crystalline GaN films have been obtained. The film surface morphology and material properties are improved by adjusting the growth conditions and buffer layer structural design.

2. EXPERIMENT

2.1. Materials Growth

GaN epitaxy layers were grown on silicon(001) substrates by metalorganic chemical vapor deposition (MOCVD) at a low pressure environment, near 100Torr, in a vertical reactor. Trimethylgallium (TMGa), Trimethylaluminum (TMAI), and high purity ammonia (NH₃) were used as Ga, Al, and N precursors, respectively, and hydrogen-diluted silane (SiH₄) was employed for depositing thin amorphous silicon film. After a chemical cleaning process, the silicon(001) substrate was heated to 1030°C under hydrogen ambient for 10 min in order to produce a clean, oxide free surface. The silicon substrate was then cooled down to 525°C and an ultra-thin amorphous silicon film was deposited onto the silicon substrate, subsequently, a three period GaN/InGaN multilayer buffer (MLB) was grown on the top of the formed ultrathin amorphous silicon film to constitute the composite intermediate layers (CIL). Finally, the temperature was raised to 1000°C and a near 1 μ m thick unintentional doped GaN epitaxy layer was grown on the surface of the formed CIL. Mg-doped p-type GaN films and InGaN-GaN MQW structures were also successfully grown on Si (001) substrates with the CIL intermediate buffers.

2.2. Characterization Technology

After the growth, a series of materials characterization techniques, including X-Ray diffraction (XRD), scanning electron microscopy (SEM), transmission electron microscopy (TEM), Fourier transform infrared (FTIR), Raman scattering and photoluminescence (PL) spectroscopy, were used to assess the GaN films and structures. X-ray diffraction was measured using a Philips X'pert diffractometer with a Cu K α radiation source (1.54Å). The SEM image of the sample surface morphology is taken on a Philips XL 30 machine. The TEM image was taken on PHILIPS CM300 TEM system. TEM sample was prepared by traditional mechanical polishing, dimpling and Ar⁺ ion milling, cutting bars perpendicular to the Si(110) direction. Photoluminescence (PL) was measured with a Renishaw UV-2000 microscope system with a He-Cd laser 325 nm line for the excitation. Raman scattering measurements were performed employing a Renishaw visible-2000 microscope system and excited by the 514.5 nm line from an Ar⁺ ion laser. Fourier transform infrared (FTIR) reflectance spectra were measured using a PEKIN ELMER FT-IR system. All the measurements were performed at room temperature (RT).

3. STRUCTURAL CHARACTERIZATION

3.1. X-ray Diffraction

X-ray diffraction (XRD) θ -2 θ profile has been employed to characterize the MOCVD-grown GaN films over the CILs on Si (001) substrates. A typical XRD pattern is shown in Figure 1. It shows a strong Si (004) peak at $\sim 69^\circ$ from the substrate and (0001) oriented wurtzite GaN characteristic peaks at $\sim 34.6^\circ$ and $\sim 73^\circ$ due to the (0002) and (0004) diffractions of the wurtzite GaN, respectively. The full width at half maximum (FWHM) of

the (0002) GaN peak possesses a value as narrow as $\sim 0.17^\circ$. Such narrow value and the observation of the high order GaN (0004) diffraction peak confirm a good crystalline structural quality of the GaN film grown on Si.

Figure 1. XRD θ - 2θ scan for an undoped GaN/Si(100) with CILs, inserted is a narrow scan for the wurtzite GaN(0002) peak.

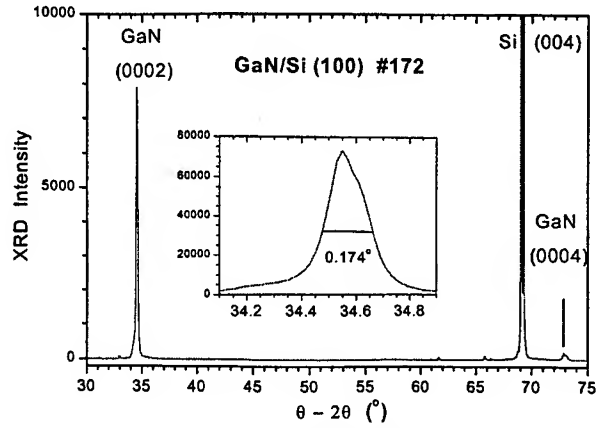
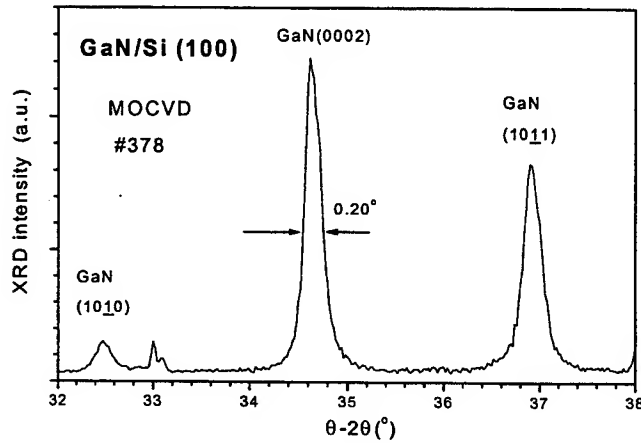


Figure 2. shows a XRD pattern of another MOCVD GaN/Si sample. The spectrum shows strong peaks at 32.4° and 36.9° , which are attributed to (10 $\bar{1}$ 0) and



(10 $\bar{1}$ 1) diffraction of wurtzite GaN, respectively¹⁴. The FWHM of the wurtzite GaN (0002) peak at 34.68° is about 0.20° . The surface morphology, examined by SEM and AFM, of this sample is superior than the one in Fig. 1. It is interesting to indicate that the GaN film with improved surface morphology showed strong XRD wurtzite GaN (10 $\bar{1}$ 1) and (10 $\bar{1}$ 0) peaks instead of only (0002) and (0004) patterns. This corresponds to the SEM observation in the next section.

Figure 2. XRD θ - 2θ scan for an undoped GaN/Si(100) with CILs

3.2. Scanning Electron Microscopy

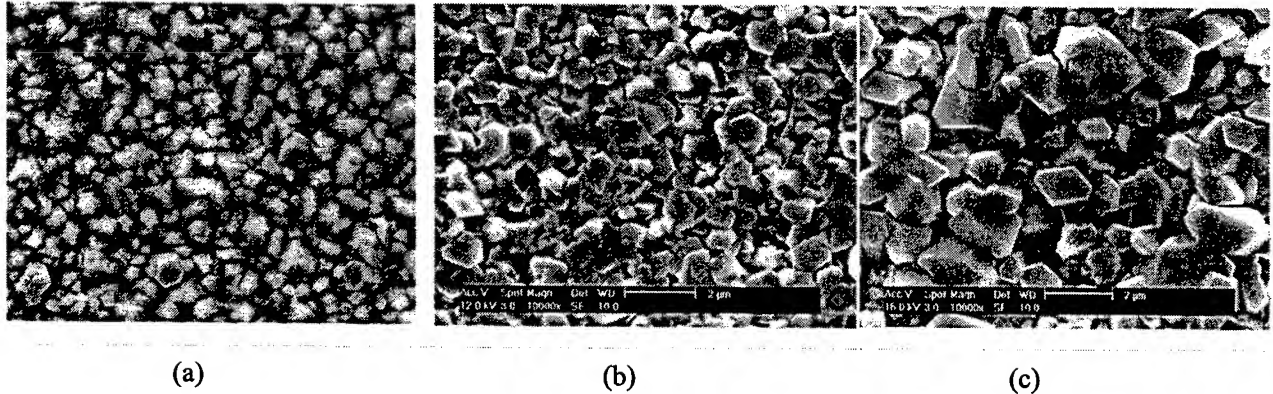


Figure 3. SEM plane-view of an undoped GaN/Si(100) with CILs. (a) 171, (b) 177 and (c) 205

Figure 3 shows the SEM plane-view image of three samples (a) 171, (b) 177, (c) 205, respectively. In Fig. 3 (a), the average size of the grains is estimated to be about $0.5 \mu\text{m}$, and they have not a clear, regular shape, indicating a not very good crystal structure of each grain. In Fig. 3 (b) the grain shows a crystal-like shape, which indicates a inner good crystal structure of each grain. The estimated average size of the grains is about

1 μm . In Fig. 3 (c), the picture shows the well-formed crystal-like grains stacking on the surface, with an estimated average size of about 1.5 μm and maximum grain size up to near 2 μm .

3.3. Transmission Electron Microscopy

The microscopic structure was investigated by TEM. Figure 4 shows the low magnification TEM cross section imaging of a sample. The figure shows a number of notable features. First, light region is seen at the interface of the Si substrate and the amorphous Si, a light region also appears at the GaN film/CIL buffer layer interface. These light regions are ascribed to the volume change accompany the conversion of Si to amorphous Si, InGaN to GaN respectively⁹. Secondly, we can see from the figure that the thickness of the CILs is about 0.12 micron, and it shows a stratum appearance, accordance to our expectation to grow CIL buffer layers. Thirdly, the GaN film shows a stack of disordered crystal-like grains, identical to the SEM result.

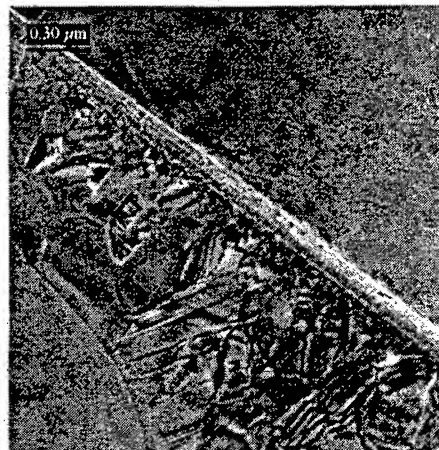


Figure 4. Low magnification TEM cross-section image of an undoped GaN/Si (100) with CILs.

Figure 5 shows the high magnification image of the sample on high resolution (HR) TEM, focusing on one grain. It shows a perfect single crystalline structure.

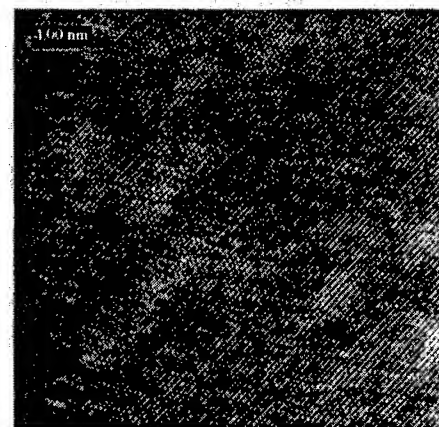


Figure 5. HR-TEM cross-section image of a un-doped GaN/Si (100) with CILs.

Combined with the XRD/SEM results obtained in the last two sections, we may get a preliminary structural picture for our MOCVD-grown GaN/Si with CILs. The grown GaN films possess a wurtzite polycrystalline structure, consist of crystalline grains. Good quality films can have the grain sizes up to 2 μm . Each grain is single crystalline wurtzite GaN. When most of grains are with the hexagonal c-axis along the substrate normal direction, XRD shows only GaN (0002) and (0004) wurtzite crystalline patterns. While the other wurtzite oriented patterns, such as (10 $\bar{1}$ 0) and (10 $\bar{1}$ 1), are also exhibited for some samples. This indicates that these samples have the wurtzite crystalline grains oriented with the hexagonal c-axes arbitrarily.

4. OPTICAL PROPERTIES

4.1. Raman Scattering

Figure 6. shows a Raman spectrum from a MOCVD-grown GaN/Si (001), with one magnified by a factor of 30. There shows a strong band at 520 cm^{-1} from the Si substrate, and a band at $\sim 300 \text{ cm}^{-1}$ due to the acoustic phonons of Si. There are three Raman bands representative to the wurtzite GaN: phonon modes of low E_2 at 141 cm^{-1} , high E_2 at 567 cm^{-1} and $A_1(\text{LO})$ at 736 cm^{-1} ^{15,16}. There are no phonon modes related to wurtzite phase GaN¹⁷ to be observed in our Raman spectra of GaN/Si samples. These provide a further confirmation together

with XRD measurements on the wurtzite structural nature of our MOCVD-grown GaN materials although they were grown on cubic structural Si substrates.

Figure 6. Raman spectra of a un-doped GaN/Si(100) with CILs, with one magnified by a factor of 30.

4.2. Fourier Transform Infrared Spectroscopy

Figure 7 (a) shows the measured FTIR spectrum of three samples: #198, #203 and #171. The dip at 737 cm^{-1} is characteristic of the wurtzite GaN $A_1(\text{LO})$ mode, corresponding to the Raman observation in Fig. 6. Another dip at $1,110\text{ cm}^{-1}$ is from the SiO_2 stretching mode due to the oxygen in the Si substrate or a partial oxidation of Si wafer. The peak at $\sim 567\text{ cm}^{-1}$ corresponds to the GaN phonon reststrahlen mode, close to the E_2 Raman mode, observed in the previous Fig. 6. The oscillation features beyond $1,200\text{ cm}^{-1}$ are due to the interference effects, which can be used to determine the GaN film thickness non-destructively. Further theoretical analysis of the FTIR reflectance from these GaN/Si can be applied to obtain further information on the structural features, similar to the FTIR analysis on GaN/sapphire systems^{18,19}.

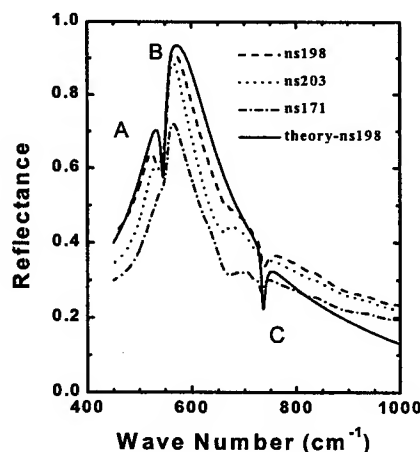
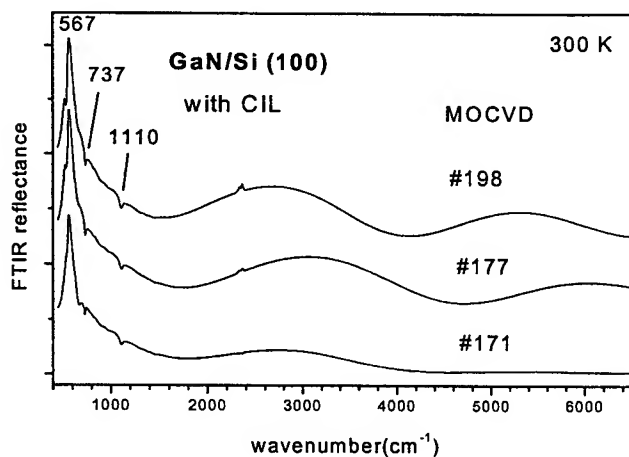
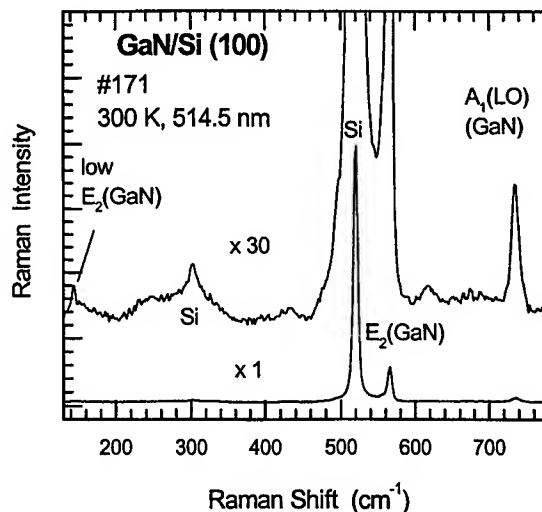


Figure 7 (a). FTIR reflectance spectra over the range of $400\text{--}6500\text{ cm}^{-1}$ of three MOCVD GaN/Si with CILs. (b). Phonon reststrahlen FTIR reflectance spectra of these three GaN/Si samples with a theoretical fit in solid line.

From Fig. 7(a), we can see that the oscillation features beyond 1200 cm^{-1} of the three samples are different each other. The #198 sample displays the strongest oscillation while #171 shows the weakest. These indicate a difference in the film/substrate interface properties, further detailed explanation is under pursuing.

There exist also obvious difference in the frequency region below 1000 cm^{-1} , i.e. the phonon reststrahlen band region. Spectra from these three samples in this frequency region are re-displayed in Figure 7 (b). There can be seen clearly two peaks A, B and a dip C in the spectra. The theoretical calculation of the reflectance of GaN on Si has performed by us²⁰. This is based on the GaN dielectric function of one layer model. In the calculation,

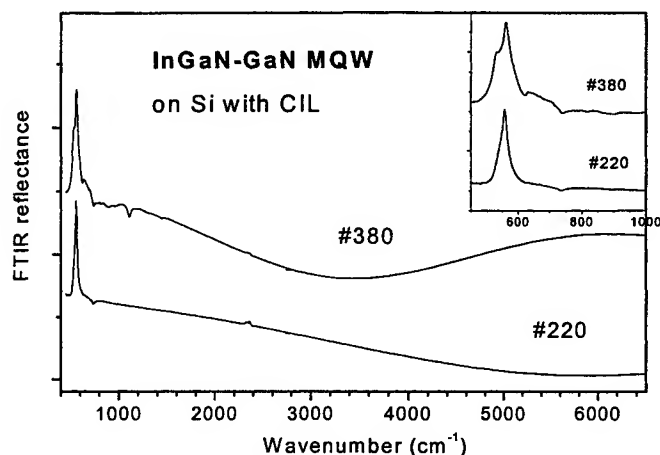
the phonon parameters from GaN grown on sapphire were used, based on which, the spectra of GaN on sapphire were fitted very well^{18,19}.

In the process of fitting, the following relation between the spectra and sample property parameters can be derived²⁰: the position of peak A depends on the film thickness and the dip between the peak A and B is caused by interference effect. The main peak B is due to the $E_1(\text{TO})$ phonon mode of GaN. The rising edge of peak B is affected by the $E_1(\text{TO})$ frequency, so $E_1(\text{TO})$ can be obtained through the fitting (557 cm^{-1}).

It could be observed from Fig.7 (b) that the experimental spectrum of GaN/Si #198 agrees best with the theoretical calculation, while fits are not so matched to other two spectra. Also some further difference between experiment and simulation can be seen. Comparing the spectra among the three samples, the reflectivity varies significantly both for the top of the reststrahlen band and the background outside the reststrahlen band. The background reflectance measured above 700 cm^{-1} is higher than that from the theory. This difference in background level is also revealed in IR of GaN grown on GaAs and GaP, which has been attributed to a possible (unexplained) experimental artifact²¹. These fits for the GaN/Si systems are far less good in comparison with the theoretical fits on the GaN/sapphire systems^{18,19}. The results of Fig. 8 (b) predict that the IR spectral shape depends on the detailed microstructure of the GaN film on Si.

Figure 8. FTIR reflectance spectra of two InGaN-GaN MQW on Si with CIL.

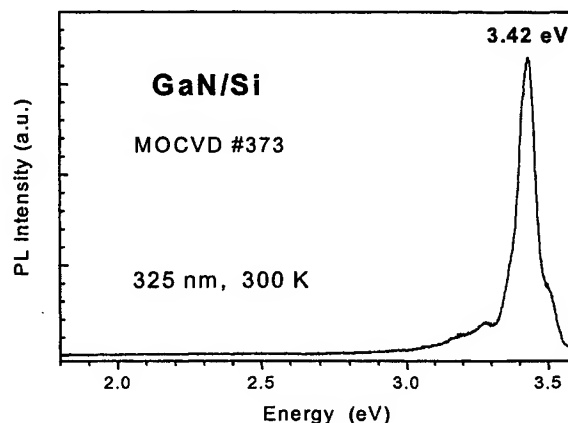
FTIR spectroscopy has also applied to analyze the multiple quantum well structures grown on Si substrates. Figure 8 shows the FTIR spectrum of two InGaN-GaN MQW samples. Compared with Figure 7(a), two features could be observed. First, the peak around 567 cm^{-1} , E_2 , of wurtzite GaN) in the MQW spectrum is sharper than that in the GaN film's. Secondly, the oscillation features beyond 1200 cm^{-1} of MQW is much weaker than that in the GaN, this might be due to the multiple interface structure in the InGaN-GaN MQWs, which weakens the interference effect.



4.3 Photoluminescence

Figure 9. RT PL spectrum of a un-doped MOCVD GaN/Si(100) with CILs.

Figure 9 shows the room temperature photoluminescence spectrum of a GaN/Si sample. RT PL of the GaN film grown over the CILs on Si (001) substrate possesses a strong luminescence emission peak around 3.4 eV, which is from the wurtzite crystalline GaN band edge emission. In the early-grown samples, there existed weak yellow-band emissions observed¹². An example can be further seen from Figure 10. It shows the RT PL spectra of a MOCVD GaN/Si with CILs(#171), measured under



different excitation power levels with different neutral density (NF) filters. When measured under NF=2, i.e. the lowest excitation power level, the defect related yellow band luminescence (YL) is very strong. With increasing the excitation power, the relative intensity of the YL emissions with respect to the GaN band edge 3.42 eV band decreases. This distinguishes the transition physics natures between these two types of emissions. There exists a third type of emissions spreading between 2.6-3.2 eV. Its dependence with the excitation power level is similar with the 3.42 eV GaN edge band. This band seems with the donor-acceptor-pair (DAP) transition nature.

With the improved design of the CIL structure and the optimization of the growth conditions, these defects-related yellow emissions were greatly depressed in the late growth runs, with almost no defects-related emissions detected in the energy region of 1.75-2.8 eV. This indicates a great improvement of the material quality of MOCVD-grown GaN on Si with CILs inter-structure.

Figure 10. RT PL spectra of a MOCVD GaN/Si with CILs(#172) under different excitation power levels with different neutral density (NF) filters.

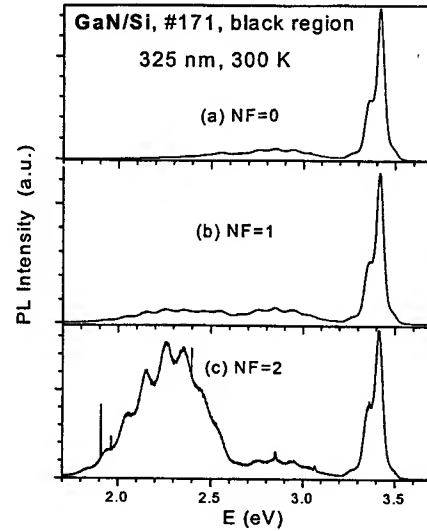
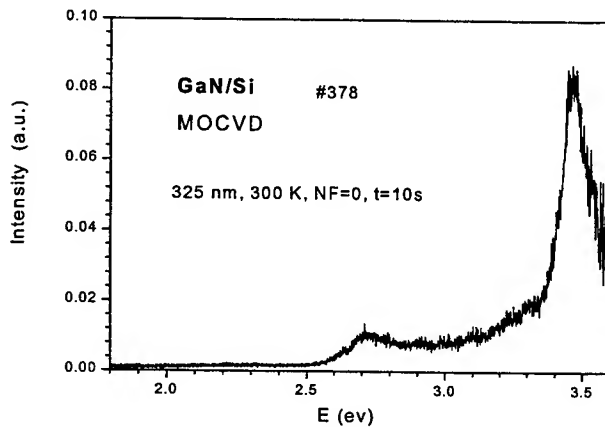
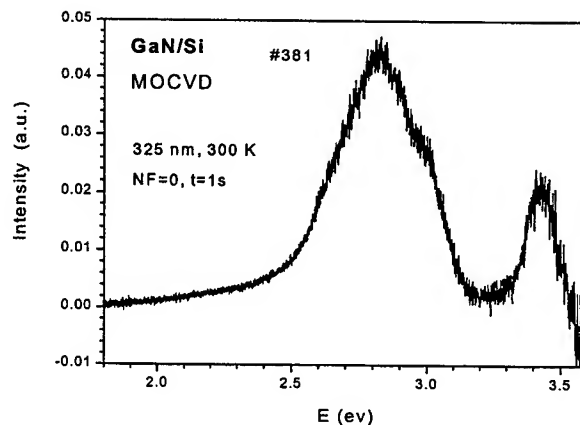


Figure 11 shows a RT PL spectrum from a p-type Mg-doped GaN film grown on Si (#378). Emissions appear below the GaN band edge emission band, spreading down to the 2.5 eV with a peak at 2.7 eV. These are due to the Mg acceptor or Mg-complexes in GaN. The appearance of these emissions indicates the activation of Mg-related acceptors in annealed p-GaN/Si.

Figure 11. RT PL spectrum of a MOCVD p-GaN/Si with CILs (#378).

Figure 12 shows a RT PL spectrum from an InGaN-GaN MQW with CILs grown on Si (#381). A strong band around 2.8 eV besides the 3.4 eV GaN edge band is seen, which is due to the transitions from the InGaN-GaN MQW structures. The quantum confinement effects have produced such strong emissions.

Figure 12. RT PL spectrum from an InGaN-GaN MQW on Si(100) with CILs (#381).



5. CONCLUSION

In conclusion, GaN thin films and multi-quantum wells(MQW) have been successfully grown on silicon(001) substrates with specially designed composite intermediate layers (CIL) consisting of an ultra-thin amorphous silicon layer and a GaN/Al_xGa_{1-x}N multilayered buffer by low pressure MOCVD. The structural and optical properties have been characterized by means of a variety of analytical techniques, including X-Ray Diffraction (XRD), Scanning Electron Microscopy (SEM), Transmission Electron Microscopy (TEM), Fourier Transform Infrared (FTIR), Raman scattering and photoluminescence (PL) spectroscopy. The TEM and SEM image proved a stratum structure buffer layer and a polycrystalline structure film composed of disordered crystalline grains. Scanning electron microscopy exhibited the single crystalline grain size up to ~2 μm. The XRD, Raman and FTIR spectrum identified the wurtzite crystalline structure nature of the grown GaN films. The narrow XRD GaN (0002) peaks indicate the good crystal quality of the films. For some GaN/Si samples, XRD patterns showed strong wurtzite GaN (10 $\bar{1}$ 1) and (10 $\bar{1}$ 0) peaks instead of only (0002) and (0004) patterns, which is related to the improved surface morphology. Photoluminescence on MOCVD-grown GaN/Si showed strong GaN near edge emission at 3.4 eV, related to the wurtzite crystalline GaN, and with only very weak deep defect-related emissions. The dependence of the emission intensity on the excitation power is different between the GaN edge band, the defect-related yellow emissions and a DAP transition. The quantum confinement enhanced strong PL emissions are obtained from the InGaN-GaN MQW structures grown on Si substrates. The film surface morphology and material properties are improved by adjusting the growth conditions and buffer layer structural design.

Reference:

1. S. Nakamura and G. Fasol, *The Blue Laser Diode*, Springer, Berlin, 1997.
2. S. Nakamura, M. Senoh, N. Iwana, and S. Nagahama, "High-brightness InGaN blue, green and yellow light-emitting diodes with quantum well structures," *Jap. J. Appl. Phys.* **34**, pp797-799, 1995
3. S. Nakamura, M. Senoh, S. Nagahama, N. Iwana, T. Yamada, T. Matsushita, H. Kiyoku, and Y. Sugimoto, "InGaN multi-quantum-well structure laser diodes grown on MgAl₂O₄ substrates," *Appl. Phys. Lett.* **68**, pp2105-2107, 1996
4. P. Kung, A. Saxler, X. Zhang, D. Walker, T.C. Wang, I. Ferguson, and M. Razeghi, "High quality AlN and GaN epilayer grown on (0001) sapphire, (100), and (111) silicon substrates," *Appl. Phys. Lett.* **66**, pp2958-2960, 1995.
5. A. Trampert, O. Brandt, H. Yang, and K.H. Ploog, "Direct observation of the initial nucleation and epitaxial growth of metastable cubic GaN on (001) GaAs," *Appl. Phys. Lett.* **70**, pp583-585, 1997
6. B.N. Sverdlov, G.A. Martin, H. Morkoc, and D. J. Smith, "Formation of threading defects in GaN wurtzite films grown on nonisomorphic substrates," *Appl. Phys. Lett.* **67**, pp2063-2065, 1995.
7. S. Guha and N. Bojarczuk, "Ultraviolet and violet GaN light emitting on Silicon," *Appl. Phys. Lett.* **72**, pp415-417, 1998.
8. A.J. Steckl, J. Devrajan, C. Tran, and R.A. Stall, "SiC rapid thermal carbonization of the (111) Si semiconductor-on-insulator structure and subsequent metalorganic chemical vapor deposition of GaN," *Appl. Phys. Lett.* **69**, pp2264-2266, 1996.
9. J. W. Yang, C. J. Sun, Q. Chen, M. Z. Anwar, M. A. Khan, S. A. Nikishin, G. A. Seryogin, A. V. Qsinsky, L. Chernyak, H. Temkin, C. Hu, and S. Mahajan, "High quality GaN-InGaN heterostructures grown in (111) silicon substrates," *Appl. Phys. Lett.* **69**, pp3566-3568, 1996.
10. N. P. Kobayashi, J. T. Kobayashi, P. D. Dapkus, W. J. Choi, A. E. Bond, X. Zhang, and D. H. Rich, "GaN growth on Si(111) substrate using oxidized AlAs as an intermediate layer," *Appl. Phys. Lett.* **71**, pp3569-3571, 1997.
11. L. Wang, X. Liu, Y. Zan, J. Wang, D. Wang, D. Lu and Z. Wang, "Wurtzite GaN epitaxial growth on a Si(001) substrate using γ -Al₂O₃ as an intermediate layer," *Appl. Phys. Lett.* **72**, pp109-111, 1998.

12. X. Zhang, S. J. Chua, P. Li, K. B. Chong, and Z. C. Feng, "Enhanced optical emission from GaN films grown on a silicon substrate," *Appl. Phys. Lett.* **74**, pp1984-1986, 1999.
13. X. Zhang, S.J.Chua, Z.C.Feng, P.li, K.B. Chong, and W. Wang, "Improved Mg-doped GaN films grown over a multilayered buffer," *Appl. Phys. Lett.* **73**, pp1772-1774, 1998.
14. A.J. Steckl, J. Devrajan, C. Tran, and R.A. Stall, "SiC rapid thermal carbonization of the (111) Si semiconductor-on-insulator structure and subsequent metalorganic chemical vapor deposition of GaN," *Appl. Phys. Lett.* **69**, pp2264-2266, 1996.
15. T. Azuhata, T. Sota, K. Suzuki and S. Nakamura, "polarized Raman spectra in GaN," *J. Phys.: Condensed Matter* **7**, pp129-133, 1995.
16. Z.C. Feng, M. Schurman, R.A. Stall, M. Pavloski & A. Whitley, "Raman scattering as a characterization tool for epitaxial GaN thin films grown on sapphire by turbo disk metalorganic chemical vapor deposition," *Appl. Optics* **36**, 2917-2922, 1997.
17. H. Siegle, G. Kaczmarczyk, L. Filippidis, A.P.Litvinchuk, A. Hoffmann, C. Thomsen, "Zone-boundary phonons in hexagonal and cubic GaN," *Phys. Rev. B.* **55**, pp7000-7004, 1997.
18. Z.C. Feng, Y.T. Hou, S.J. Chua & M.F. Li, "Infrared reflectance studies of GaN epitaxial films on sapphire substrate," *Surface & Interface Analysis* **28**, pp166-169, 1999.
19. Y.T. Hou, Z.C. Feng, K. Li, M.F. Li & S.J. Chua, "Influence of Si-doping on the characteristics of GaN on sapphire by infrared reflectance," *Appl. Phys. Lett.*, 1 Nov. 1999 issue.
20. Y.T. Hou, Z.C. Feng, J. Chen, X. Zhang, S.J. Chua, M.F. Li & J.Y. Lin, "Correlation between the infrared reflectance and microstructure of thin gallium nitride films grown on silicon substrates," *Appl. Phys. Lett.*, submitted.
21. G. Mirjalili, T. J. Parker, S. F. Shayesteh, M. M. Bulbul, and S. R. P. Smith, "Far-infrared and Raman analysis of phonons and phonon interface modes in GaN epilayers on GaAs and GaP substrate," *Phys. Rev. B.* **57**, pp4656-4663, 1998.

Luminescence, Morphology and X-ray Diffraction Features of InGaN Materials Grown on Sapphire by Metalorganic Chemical Vapor Deposition

P. Li^a, S. J. Chua^{*a,b}, Z. C. Feng^b, W. Wang^b, M. S. Hao^b, T. Sugahara^c and S. Sakai^c

^aCenter for Opto-electronics, Dept. of Electrical Engineering
National University of Singapore, SINGAPORE 119260

^bInstitute of Materials Research and Engineering, 3 Research Link, SINGAPORE 117602

^cDept. of Electrical and Electronics Engineering, The University of Tokushima,
2-1 Minami-Josanjima 770-8506, JAPAN

ABSTRACT

InGaN thin films were grown by low-pressure metalorganic chemical vapor deposition (MOCVD) and characterized by photoluminescence (PL) with variable excitation intensity and temperature, room-temperature cathodoluminescence (CL), high resolution X-ray diffraction (HRXRD), scanning-electron-microscopy (SEM) and atomic force microscopy (AFM). For PL, all the samples show dominant peaks at around 2.9 eV and extra peaks or shoulders at 2.8 eV at 6K. We concluded that the low energy peak is due to the localized near-band edge transition from the phase-separated InGaN mesoscopic structure with high In-content. The strong luminescence of the low energy peak at room temperature is due to the quantum confinement enhancement in the form of nanostructures or quantum dots. AFM images showed that phase-separated InGaN samples have inverted hexagonal pits which are formed by the In segregation on the (10 $\bar{1}$ 1) surfaces. Room temperature cathodoluminescence (CL) and images at wavelengths corresponding to the GaN band edge, the In-poor and In rich regions were studied. It was shown that phase separated In-rich regions formed at the periphery of the hexagonal pits.

Keywords: InGaN, phase-separation, MOCVD, photoluminescence, XRD, cathodoluminescence.

1. INTRODUCTION

The development of blue LEDs and laser diodes has attracted considerable research activities on the growth of GaN based III-V nitrides. The band gap of InGaN can be varied over nearly the whole spectral range from near UV to red, so it is usually used in active regions of these devices. The difficulty in the growth of high quality $\text{In}_x\text{Ga}_{1-x}\text{N}$ alloys is mostly due to the trade-off between the epilayer quality and the amount of InN incorporation into the alloy. Growth at the high temperatures of approximately 800°C typically results in high crystalline quality but the amount of InN in the solid is limited to low values because of the high volatility of In. Lowering the growth temperature results in an increase in the In content at the cost of reduced crystalline quality. The lattice mismatch and different thermal stability of the two constituents, InN and GaN, also complicate the growth of $\text{In}_x\text{Ga}_{1-x}\text{N}$. The lattice mismatch can lead to a miscibility gap¹, which causes the fluctuation of In content across the

* Correspondence: Email: elecjsj@nus.edu.sg; Tel:(65)-874-2264; Fax(65)-779-1103

film. Singh and co-workers^{2,3,4} provided strong evidence of phase separation in InGaN thick films grown by MBE. Other researchers reported phase separation in thick InGaN films grown by metalorganic chemical vapor deposition (MOCVD).^{5,6} Tran *et al.*⁷ showed that when phase-separation occurs, InGaN clusters with different indium compositions can coexist and that the high brightness in blue and green LEDs is due to radiative recombination in the In-rich InGaN clusters.

Recently it is discovered that $\text{In}_x\text{Ga}_{1-x}\text{N}$ layers with high In-content typically show an additional low energy luminescence peak⁸. The separation of this peak energy from the band-edge emission energy increases with increasing In-content. The deep transition responsible for the low energy peak dominates the PL spectra at room temperature. There is a possibility that the deep transition is caused by phase-separation. Another possibility is that the formation of mismatch dislocations may play an important role. These dislocations are formed due to the lattice mismatch between the $\text{In}_x\text{Ga}_{1-x}\text{N}$ layer and the underlying GaN layer, and they are increased with increasing In-content. The origin of the low energy peak is under intensive investigation.

Wu *et al.*⁹ reported that the V-defects initiate at the threading dislocations in one of the quantum wells from a Multiple Quantum Well (MQW) stack. The V-defect is correlated with the localized excitonic recombination centers that give rise to a long-wavelength shoulder in photoluminescence (PL) and cathodoluminescence (CL) spectra. Jahn *et al.*¹⁰ investigated the pinholes, dislocations and strain relaxation in InGaN. They found that part of the strain was reduced elastically by formation of hexagonally faceted pinholes. Misfit dislocations were observed to form at pinholes that reach the InGaN/GaN interface. Sugahara and Sakai¹¹ discussed the role of dislocation in InGaN phase separation. They showed that the dislocations in InGaN act as nonradiative recombination centers and confirmed that the phase separation in InGaN is caused by spiral growth due to mixed dislocations. They demonstrated that dislocations with the screw component favor the formation of In-rich regions. The extra combinations of the dangling bond in the dislocated areas can prevent the evaporation of InN during the InGaN growth.

In this paper, we report on an investigation of phase-separated InGaN thin films grown by low-pressure metalorganic chemical vapor deposition (MOCVD). Materials were studied by a variety of characterization techniques, such as photoluminescence (PL), cathodoluminescence (CL), high resolution X-ray diffraction (HRXRD), scanning-electron-microscopy (SEM) and atomic force microscopy (AFM). Various features from these measurements and spectral/morphology analyses were examined and correlated to the InGaN phase separation phenomena and mechanisms.

2. EXPERIMENTS

The four samples of $\text{In}_x\text{Ga}_{1-x}\text{N}$ films were grown by MOCVD (Emcore D125) on (0001) sapphire substrates. MOCVD was conducted using TMGa, TMIIn and NH_3 as precursors. A 2 μm thick undoped bulk GaN was first grown on the 250Å thick GaN buffer layer. The growth temperature was 530°C and 1050°C respectively for the GaN buffer and bulk layer. After deposition of the GaN bulk layer, the growth temperature was lowered down to about 700°C for the deposition of InGaN. The InGaN layer thickness was about 500Å. There was no cap layer on the top of InGaN. The carrier gas was H_2 and N_2 respectively for the growth of GaN and InGaN. The samples were analyzed by photoluminescence (PL) at different temperatures using He-Cd laser as excitation source as well as by cathodoluminescence

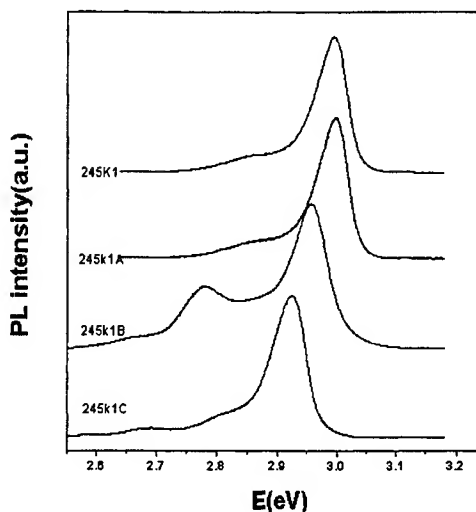
(CL) and Scanning Electron Microscopy (SEM) at room temperature (RT). CL measurements were performed with an acceleration voltage of 5 or 15kV using a JOEL 6400 SEM equipped with an Oxford Mono CL2. High resolution X-ray diffraction (HRXRD) 2θ - θ scan was performed with a Philips X'pert system. The surface morphology of samples was investigated by Digital Instrument III Atomic Force Microscopy (AFM).

3. RESULTS AND DISCUSSIONS

3.1. Photoluminescence

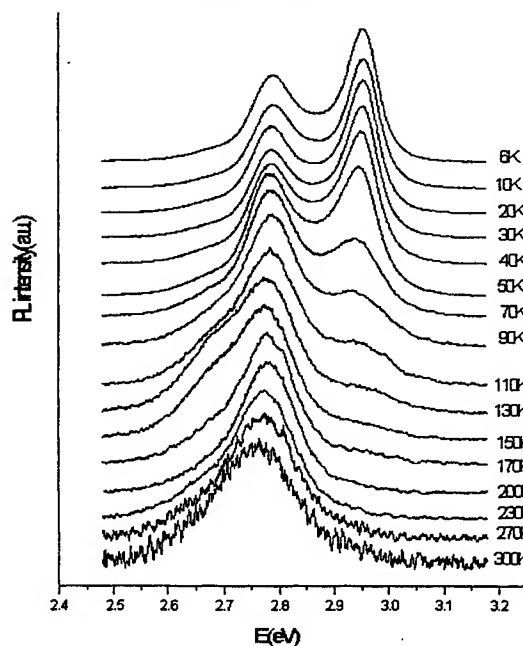
Figure 1 shows the low temperature PL of the four samples (245k1, 245k1A, 245k1B, 245k1C) at 6.6K. The In-contents determined by HRXRD are 16.19%, 16.42%, 19.53% and 20.02% respectively. All the samples exhibit a prominent peak at around 2.94 eV. The two samples, 245k1, 245k1A, have shoulders at 2.87, 2.86 eV, respectively. The sample 245k1B has a low energy peak at 2.8 eV and an even lower energy shoulder at 2.68 eV. The sample 245k1C has a low energy shoulder at 2.83 eV and a small peak at 2.68 eV.

Figure 1. Photoluminescence (6.6 K) of four MOCVD-grown $\text{In}_x\text{Ga}_{1-x}\text{N}/\text{GaN}/\text{sapphire}$ samples.



One possible mechanism that gives rise to the extra peaks or shoulders in some of the samples is the near-band-edge transition from the phase-separated InGaN mesoscopic structure with higher In-content. To elucidate the nature of the low energy peak, we varied the temperature of the sample 245k1B from 6.6 to 300 K. As seen in Figure 2, the low energy peak exhibits a rather complicated (red-shift, blue-shift, red-shift and blue-shift) temperature dependence which is similar to the S-shaped temperature dependence of the PL peak from InGaN epilayers and InGaN/GaN multiple quantum wells (MQWs), reported by Cho *et al.*^{12,13}.

Figure 2. Temperature-dependent PL of a MOCVD-grown $\text{In}_x\text{Ga}_{1-x}\text{N}/\text{GaN}/\text{sapphire}$ sample, 245k1B.

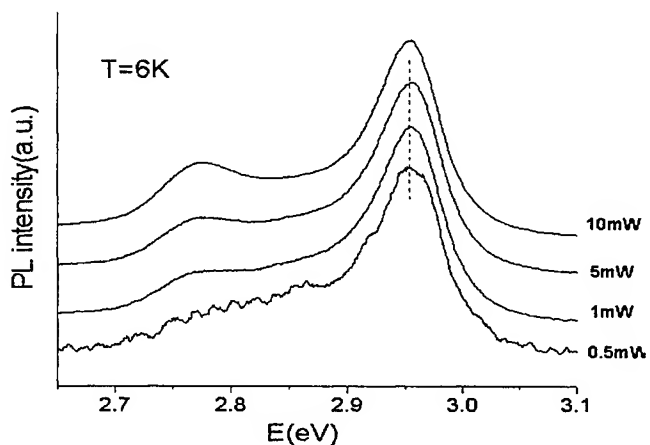


According to Cho *et al.*^{12,13}, the PL peak emission shift is correlated with a change in carrier lifetime with temperature. They demonstrated that the temperature-induced S-shaped PL shift is caused by the change in carrier recombination dynamics with increasing temperature due to inhomogeneities in the InGaN

structures. The behavior of the high energy peak of sample 245k1B, in contrast to that of the low energy peak, exhibits a red-shift and it quenches much faster than that of the low energy peak. There is a possibility that the carriers relax from regions with lower In content to regions with higher In content by means of emitting phonons or Auger electrons. At 300K, the low energy peak dominates the PL spectra while the high energy peak is not observable.

One may argue that the low energy peak may be due to the donor acceptor pair (DAP) transitions. To further clarify this question, the dependence of PL on excitation power was measured. With an increase of excitation power, both the low energy PL peak and high energy peak show no blue-shift which is expected for a DAP transition when the excitation power is increased as seen in Figure 3. Besides, the time-resolved photoluminescence (TRPL) measurements on these samples¹⁴ gives the lifetimes of the two peaks of several ns. The similar magnitude in lifetimes of the two peaks infers that the two peaks actually come from the same origin: the near-band-edge emissions from the two regions with different In contents. The low energy peak can not come from the DAP transition which usually has a relatively long lifetime of several microseconds.

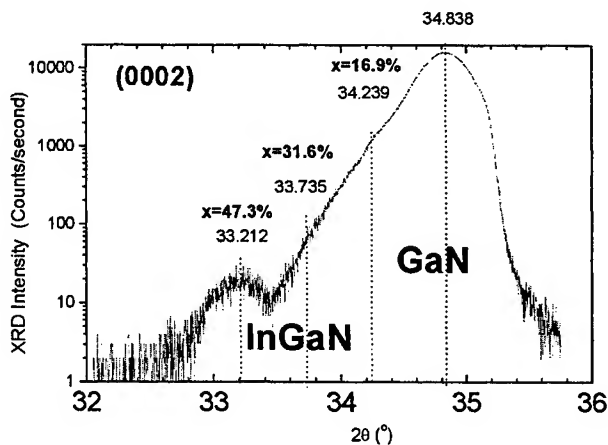
Figure 3. Excitation power dependent photoluminescence of a MOCVD-grown $\text{In}_x\text{Ga}_{1-x}\text{N}/\text{GaN}/\text{sapphire}$, 245k1B.



3.2. High Resolution X-ray Diffraction

To further prove the phase-separation of the sample, we performed the HRXRD 2θ scan of the sample which was shown in Figure 4. The peak at 33.212 degree corresponds to an In-content of 47.3%. From the excitation power dependent PL and HRXRD, we can confidently exclude the possibility that the DAP contributes to the lower energy peak of PL in InGaN.

Figure 4. XRD 2θ scan of a MOCVD $\text{In}_x\text{Ga}_{1-x}\text{N}/\text{GaN}/\text{sapphire}$, 245k1B.



3.3. Atomic Force Microscopy

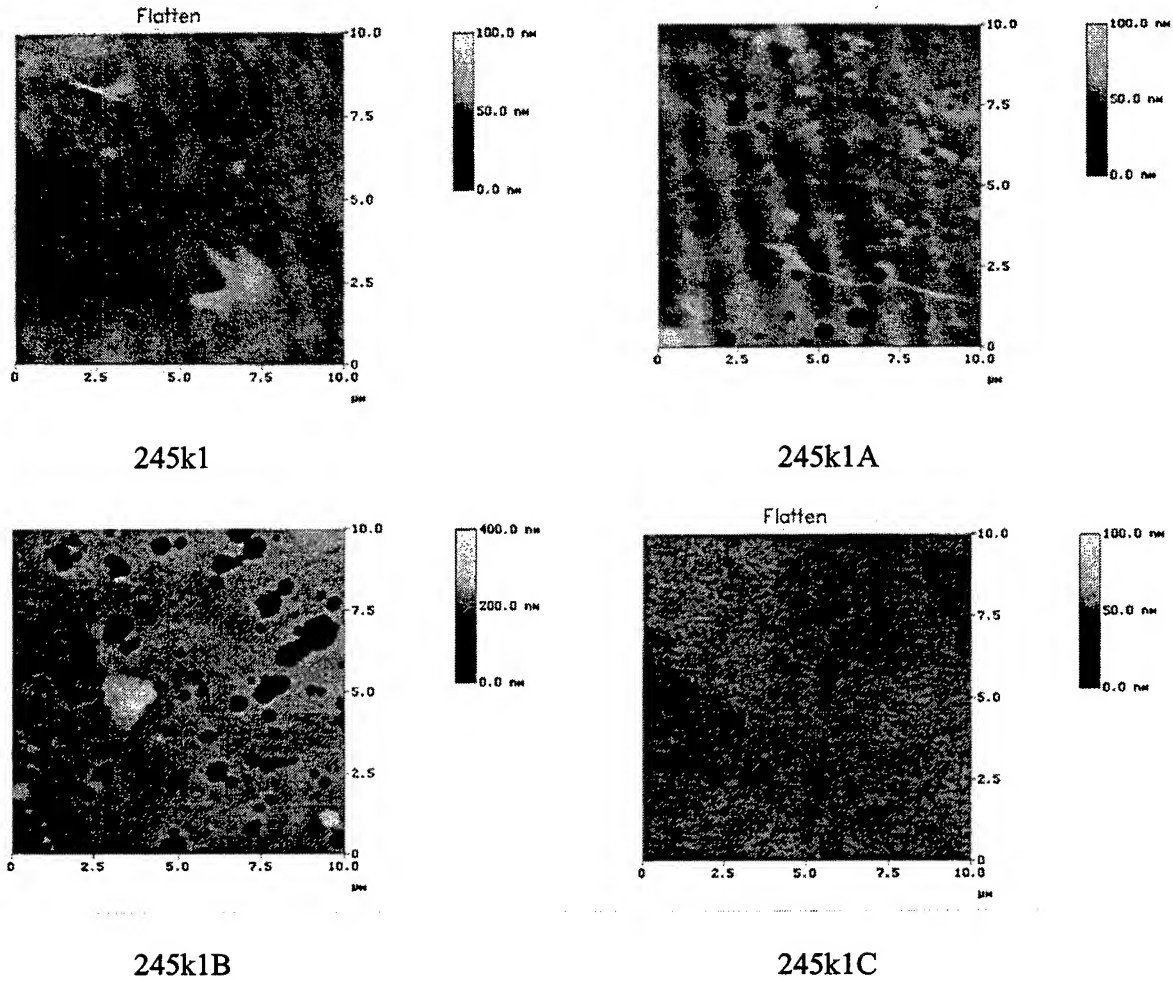


Figure 5. AFM images in tapping mode of four $\text{In}_x\text{Ga}_{1-x}\text{N}/\text{GaN}/\text{sapphire}$ samples.

Figure 5 shows the AFM images of the four MOCVD-grown $\text{In}_x\text{Ga}_{1-x}\text{N}/\text{GaN}/\text{sapphire}$ samples. The four samples exhibit different morphologies and all the samples have different degree of spiral growth mode. According to the spiral mode developed by Burton, Carbera and Frank (BCF model)¹⁵, the driving force, $\Delta\mu$, to grow a crystal is given by $\Delta\mu \approx \Omega\beta^2/K_B T$ where K_B and Ω are Boltzmann constant and the area per one molecule, respectively. And β (the free energy per unit length of a step) increases with decreasing temperature. The growth velocity of adhesive mode is proportional to $\Delta\mu$, but that of the spiral mode is linear to $(\Delta\mu)^2$. Therefore if the growth temperature decreases, spiral growth should be more dominant. The phase separation takes place only at low growth temperatures, and dislocation triggers nucleation of spiral growth.

The morphology of the sample 245k1 has undulation but it does not have “pits” which are “pinholes” formed at ends of the threading dislocations near the InGaN/air interface. The sample 245k1A has both large (diameter 700nm) and small (diameter 100nm) “hexagonal pits” which are inverted hexagonal pyramids formed at one end of TDs. The sides of the pits are $(10\bar{1}1)$ surfaces. The sample surface also

has undulations. The sample 245k1B does not have undulation but it has “rougher” surface morphology with higher density of both large and small “hexagonal pits” than the sample 245k1A. The sample 245k1C has very high density of tiny “black pits” which are formed by the termination of TDs.

Northrup *et al.*¹⁶ presented a first-principle calculation on the structure and energetics of the GaN(1011) surface, and various models of reconstruction. A strong preference for Indium surface segregation and occupation on specific surface sites is demonstrated. Their calculations indicate that in the absence of Indium, the equilibrium pit size is on the order of a few nanometers. However, the segregation of Indium on (1011) surfaces can provide a strong driving force to reduce the surface energy and thereby allow the formation of large inverted pyramid defects.

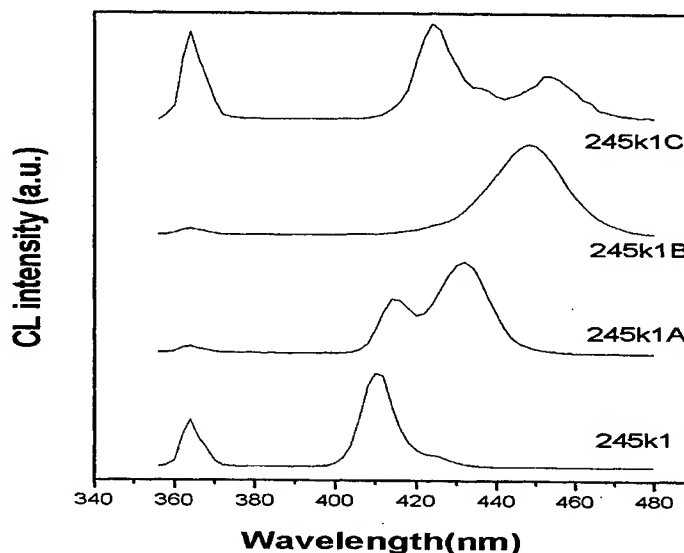
Comparing Fig. 1 with Fig.5, we found that the sample, 245k1B, has an obvious higher density of both large and small “pits”. This sample also has the strongest low energy peak which is attributed to the photoluminescence from the phase-separated In-rich region. Therefore, it is concluded that the sample, 245k1B, has the highest degree of phase-separation. Besides, our experimental results verify Northrup’s calculations.

3.4. Cathodoluminescence Spectrum

Recently, O’Donnell *et al.*¹⁷ reported a direct observation of phase separation in InGaN and showed that the phase separation, together with the quantum confinement enhancements, accounts for the surprisingly high efficiency of the InGaN-based diodes manufactured by Nichia Chemical Industries. The nanostructure, in the form of nearly pure InN quantum dots, occurs across a large range of average indium content in InGaN. In our experiments, the strong luminescence of the low energy peak at room temperature may be due to the quantum confinement enhancements in the form of nano-structures or quantum dots with high In-content which may not necessarily be pure InN dots but InGaN dots with high In content. The next question is the distribution of the In-rich QDs. Are they uniform or do they favor particular sites? To answer this question, we did the plan-view CL mapping.

Figure 6 shows the room temperature CL spectra of the four samples (245k1, 245k1A, 245k1B, 245k1C) by scanning the incident electron beam in relatively wide area ($10.6 \times 8.1 \mu\text{m}^2$). The CL spectra of sample 245k1C, and 245k1B exhibit two peaks. The peaks with longer wavelengths were attributed to band-edge related transitions in the In-rich region.

Figure 6. Room temperature CL of four MOCVD-grown $\text{In}_x\text{Ga}_{1-x}\text{N}/\text{GaN}/\text{sapphire}$ samples.



3.5. Scanning Electron Microscopy and Cathodoluminescence Image

Figure 7 shows plan-view SEM (SEM may not be taken at the same region as the AFM) and CL images for four sample 245k1, 245k1A, 245k1B, and 245k1C, respectively. CL images were taken at different wavelengths, corresponding to the GaN band edge (364nm), InGaN In-poor regions (410nm, 414nm, 424nm, and 424nm) and In-rich regions (424nm, 432nm, 448nm, and 454nm). In the SEM images, all the samples have “hexagonal pits” but with different size and density. Sample 245k1B has the highest density of “hexagonal pits” while sample 245k1C has the largest “pits” with a diameter of approximately 1 μm .

For any one of the four samples, the band-edge CL at 364nm is not uniform. The dark spots correspond to non-radiative recombination centers which were reported to be related with dislocations¹¹. The CL from the In-poor regions is also not uniform. The CL from In-rich region comes *only* from the periphery of the hexagonal pits. The situation is most clearly shown in the CL at 454nm of sample 245k1C where the CL from In-rich regions come from the periphery of the two hexagonal pits.

The conclusion is consistent with reference 18 in which a big difference in Indium inhomogeneity is found between InGaN layers grown on a dislocation-free homoepitaxi GaN and a dislocated GaN on sapphire. The assumption of higher indium incorporation rate at dislocation sites is reasonable, if the indium evaporation which is always happening at InGaN growth temperature is taken into account. Even if the deposition rate is uniform over the entire surface, the evaporation rate at the dislocation site must be slower due to the dangling bonds available at the dislocation sites.

4. CONCLUSIONS

In summary, to gain insight into the phase-separation in InGaN thin films, we studied the luminescence, morphology and X-ray diffraction features by means of PL, CL, SEM, AFM and HRXRD. The low energy peaks in low-temperature PL were attributed to the photoluminescence from the In-rich regions. The anomalous temperature-dependent behavior of the low energy peak was explained in terms of potential fluctuations from the In-rich region. The strong luminescence even at room temperature is explained by the near-band-edge emission from the nanostructures or dots formed in the phase-separated In rich regions. AFM shows that the sample with a higher density of inverted hexagonal pyramids also has a stronger photoluminescence from the phase-separated regions. The segregation of In on the (10 $\bar{1}$ 1) surfaces allow formation of large inverted pyramid defects. From the CL mapping, we found that the phase-separated In-rich regions formed *only* at the periphery of the “hexagonal pits”. To achieve blue, green, amber and even red LEDs, one way is to optimize the phase-separated In-rich region to have appropriate wavelengths and high brightness.

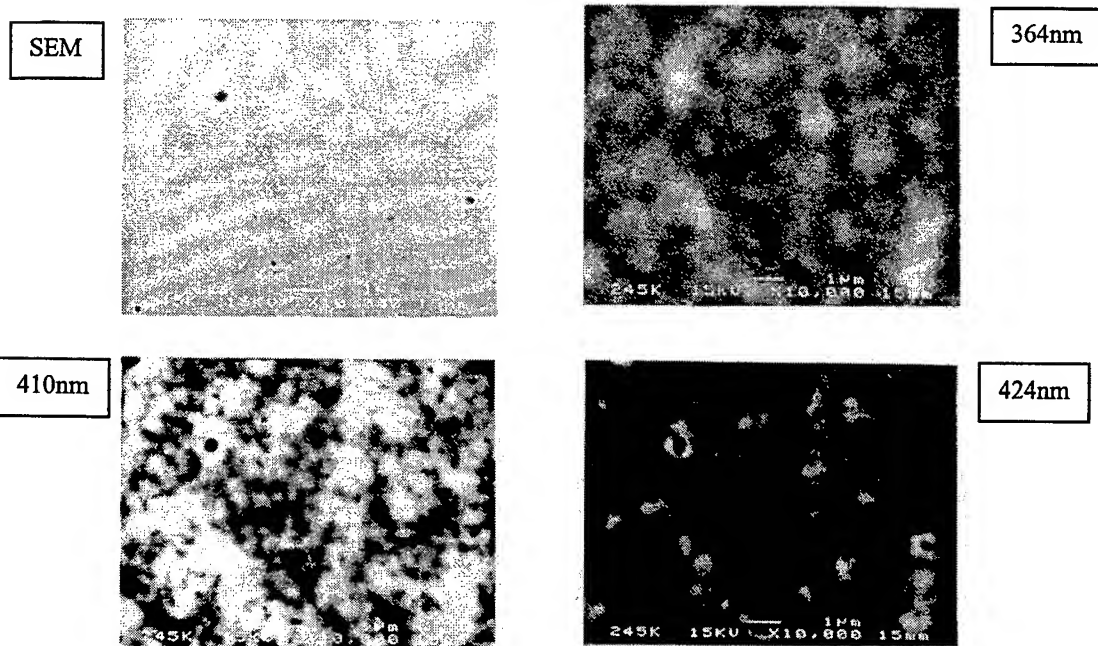


Figure 7-1. Top-view SEM and CL images of a MOCVD $\text{In}_x\text{Ga}_{1-x}\text{N}/\text{GaN}/\text{sapphire}$: 245K1.

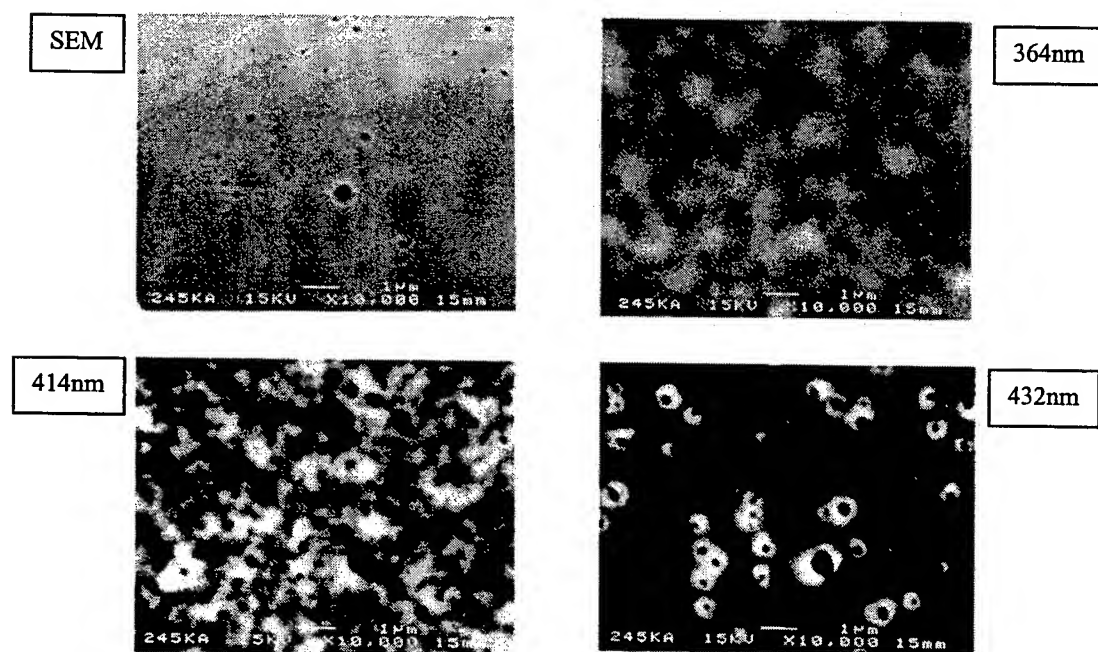


Figure 7-2. Top-view SEM and CL images of a MOCVD $\text{In}_x\text{Ga}_{1-x}\text{N}/\text{GaN}/\text{sapphire}$: 245K1A.

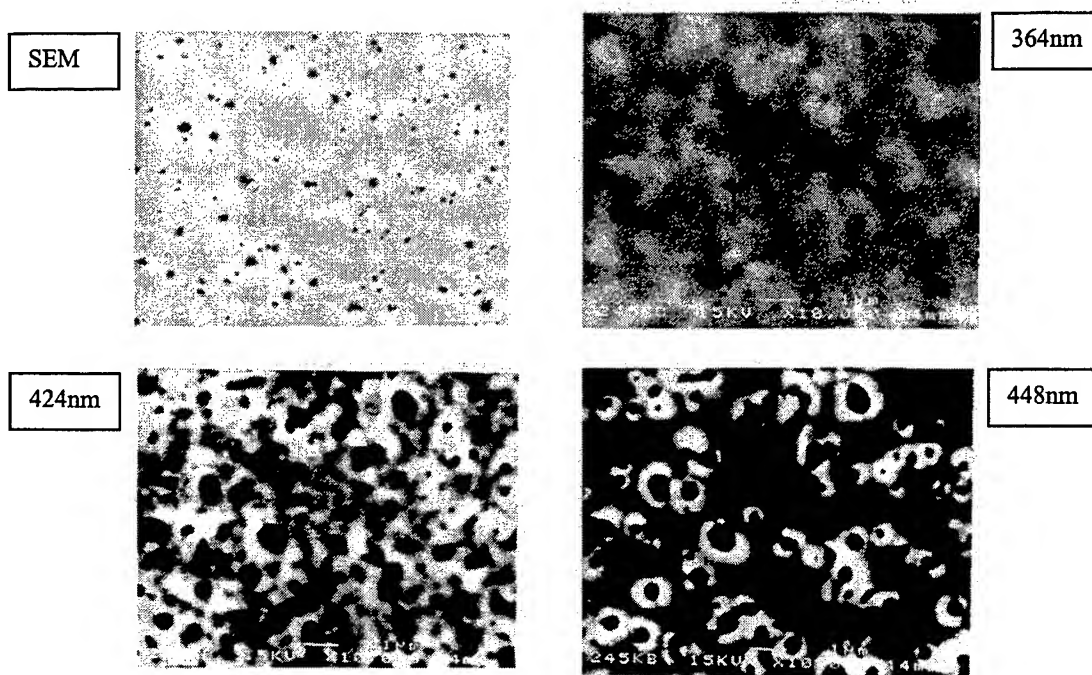


Figure 7-3. Top-view SEM and CL images of a MOCVD $\text{In}_x\text{Ga}_{1-x}\text{N}/\text{GaN}/\text{sapphire}$: 245K1B.

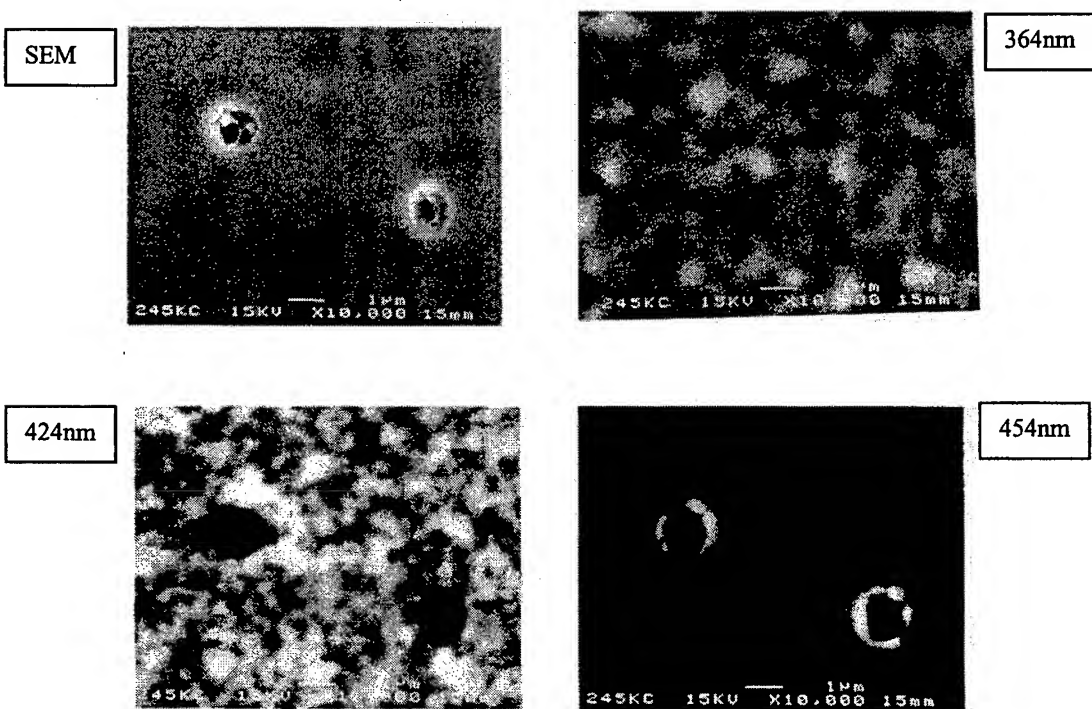


Figure 7-4. Top-view SEM and CL images of a MOCVD $\text{In}_x\text{Ga}_{1-x}\text{N}/\text{GaN}/\text{sapphire}$: 245K1C.

REFERENCES

1. I. Ho and G. B. Stringfellow, "Solid phase immiscibility in GaInN", *Appl. Phys. Lett.* **69**, pp. 2701-2703, 1996.
2. R. Singh, D. Doppalapudi, T. D. Moustakas, and L. T. Romano, "Phase separation in InGaN thick films and formation of InGaN/GaN double heterostructures in the entire alloy composition" *Appl. Phys. Lett.* **70**, pp. 1089-1092, 1997.
3. R. Singh and T. D. Moustakas, *Mater. Res. Soc. Symp. Proc.* **395**, pp. 163-168, 1996.
4. R. Singh, W. D. Herzog, D. Doppalapudi, M. S. Unlu, B. B. Goldberg, and T. D. Moustakas, *Mater. Res. Soc. Symp. Proc.* **449**, pp. 185-190, 1997.
5. A. Wakahara, T. Tokuda, X. Z. Dang, S. Noda, and A. Sasaki, "Compositional inhomogeneity and immiscibility of a GaInN ternary alloy", *Appl. Phys. Lett.* **71**, pp. 906-909, 1997.
6. N. A. El-Masry, E. L. Piner, S. X. Liu, and S. M. Bedair "Phase separation in InGaN grown by metalorganic chemical vapor deposition" *Appl. Phys. Lett.*, **72**, pp. 40-43, 1998.
7. C. Tran, R. Karlicek, M. Schurman, V. Merai, A. Osinsky, Y. Li, I. Eliashevich, M. Brown, J. Nering, T. DiCarlo, I. Ferguson, and R. Stall, "Growth and characterization of high-efficiency InGaN MQW blue and green LEDs from large-scale production MOCVD reactors" 2nd Inter. Symp. On Blue Laser and LEDs, pp. 246-249, Chiba, Sept. 29-Oct. 2, 1998.
8. A. Sohmer, J. Off, H. Bolay, V. Härle, V. Syganow, Jin Seo Im, V. Wagner, F. Adler, A. Hangleiter, A. Dörnen, F. Scholz, D. Brunner, O. Ambacher, and H. Lakner. "GaInN/GaN-Heterostructures and Quantum Wells Grown by Metalorganic Vapor-Phase Epitaxy", *MRS Internet Journal of Nitride Semiconductor Research*, Vol. 2, Article 14, 1998.
9. H. Wu, C. R. Elsass, A. Abare, M. Mack, S. Keller, P. M. Petroff, S. P. DenBaars, J. S. Speck, and S. J. Rosner, "Structural origin of V-defects and correlation with localized excitonic centers in InGaN/GaN multiple quantum wells", *Appl. Phys. Lett.* **72**, pp. 692-695, 1997.
10. B. Jähnen, M. Albrecht, W. Dorsch, S. Christiansen, H. P. Strunk, D. Hanser, and R. F. Davis, "Pinholes, Dislocations and Strain Relaxation in InGaN", *Internet Journal of Nitride Semiconductor Research*, Vol. 3, Article. 39, 1998.
11. T. Sugahara, M. S. Hao, T. Wang, D. Nakagawa, Y. Naoi, K. Nishino, and S. Sakai, "Role of Dislocation in InGaN Phase Separation", *Jpn. J. Appl. Phys.*, **37**, pp. 1195-1198, 1998.
12. Y. H. Cho, B. D. Little, G. H. Gainer, J. J. Song, S. Keller, U. K. Mishra, and S. P. Denbaars, Section G, GaN and related Materials, "Carrier dynamics of abnormal temperature-dependent emission shift in MOCVD-grown InGaN epilayers and InGaN/GaN quantum wells", *Internet Journal of Nitride Semiconductor Research* Vol. LS4, G2.4, 1999.
13. Y. H. Cho, G. H. Gainer, A. J. Fischer, J. J. Song, S. Keller, U. K. Mishra, and S. P. Denbaars, "S-shaped" temperature-dependent emission shift and carrier dynamics in InGaN/GaN multiple quantum wells", *Appl. Phys. Lett.* **73**, pp. 1370-1373, 1998.
14. S. J. Chua and G. Li, unpublished.
15. W. K. Burton, N. Cabrera, and F. C. Frank: *Philos. Trans. R. Soc. Ser. A* **243**, pp. 300, 1951.
16. J. E. Northrup, L. T. Romano and J. Neugebauer, "Surface energetics, pit formation, and chemical ordering in InGaN alloys", *Appl. Phys. Lett.*, **74**, pp. 2319-2322, 1999.
17. K. P. O'Donnell, R. W. Martin, and P. G. Middleton, "Origin of Luminescence from InGaN Diodes", *Phys. Rev. Lett.*, **82**, pp. 237-241, 1999.
18. H. Sato, T. Sugahara, Y. Naoi, and S. Sakai, "Compositional Inhomogeneity of InGaN Grown on Sapphire and Bulk GaN Substrates by Metalorganic Chemical Vapor Deposition" *Jpn. J. Appl. Physics*, **37**, pp. L341-344, 1998.

Study of a common deep level in GaN

Tzu-Chi Wen^{*a}, Shih-Chang Lee^a, Wei-I Lee^a, Jen-Da Guo^b, Ming-Shiann Feng^c

^aDepartment of Electrophysics and Microelectronics and Information Systems Research Center, National Chiao Tung University, HsinChu, Taiwan.

^bNational Nano Device Laboratory, National Chiao Tung University, HsinChu, Taiwan.

^cInstitute of Materials Science and Engineering, National Chiao Tung University, HsinChu, Taiwan.

ABSTRACT

A deep level with the activation energy around 0.45~0.6eV has persistently appeared in GaN samples grown by hydride vapor-phase epitaxy, organometallic vapor-phase epitaxy and molecular beam epitaxy. However, the origin of this deep level still remains unclear. In this study, we investigated this deep level trap E2 of GaN films by using deep level transient spectroscopy. The GaN films were grown by a conventional low pressure organometallic vapor-phase epitaxy technique with different V/III ratios. Frequency-dependent capacitance measurement was performed to determine the most proper frequency for capacitance measurements. Capacitance-voltage measurements were then applied to obtain the carrier concentrations. The carrier concentration became higher as the flow rate of NH₃ got lower. The deep level E2 is found in GaN samples grown with higher V/III ratios. The trap concentration of level E2 increased with increasing NH₃ flow rate. Compared with the theoretical prediction of the nitrogen antisite level in GaN, the level E2 was believed to be related to nitrogen antisites.

Keyword GaN, deep level, organometallic vapor-phase epitaxy, V/III ratios, frequency capacitance, antisite defect, DLTS

INTRODUCTION

Group III-V nitrides have wide bandgaps varied from 1.9eV, of InN, to 6.3eV, of AlN, and been promising materials for blue and ultraviolet optoelectronic devices¹, high temperature, and high power transistors^{2,3}, and solar-blind ultraviolet detectors.⁴ However, the progress of GaN technology has often been limited by material quality, such as high defect densities. Therefore, it is important to investigate the deep level traps in GaN. Deep-level transient spectroscopy (DLTS) and transient capacitance methods have been used to characterize the deep level traps in GaN grown by hydride vapor-phase epitaxy (HVPE), organometallic vapor-phase epitaxy (OMVPE) and molecular beam epitaxy (MBE). Several deep level centers in n-GaN with activation energies ranging from 0.14-1.63eV have been reported⁵⁻¹¹. Among them, a deep level with the activation energy around 0.45~0.598eV has been observed in samples grown by different techniques^{5,6,7,9,10}. The origin of this deep level still remains unclear. In the present study, we characterized deep level traps of two sets of GaN films by using deep-level transient spectroscopy (DLTS) and transient capacitance method.

EXPERIMENT

Two sets of n-type GaN film were discussed in this study. The set I, fabricated by AXTRON planetary reactor, contained about 4 μm thick Si-doped GaN layer (labeled R1). The set II were prepared by a conventional low pressure OMVPE, and the thickness of undoped GaN film was about 2 μm . The detail growth procedure had been described elsewhere.¹² The Set II, in brief, was grown by a conventional low pressure OMVPE reactor with trimethylgallium (TMG) as the column III precursor, and NH₃ as the column V precursor, respectively. A thin (500Å) GaN buffer layer was deposited on c-plane sapphire substrate at 525 °C using TMG and NH₃, and GaN film was then grown at 1050 °C. The GaN films, set II, was grown with different V/III ratios. The flow rate of NH₃ were 2500 sccm 2000 sccm 1500 sccm, labeled GaN2500 GaN2000 GaN1500.

Pt/Au and Au were used as Schottky contact metal on set I and set II, respectively. Aluminum was deposited a large area on the front surface as an ohmic contact. The current-voltage characteristic of Schottky diode at room temperature was well behaved. To determinate the most proper frequency of capacitance-voltage (C-V) and transient capacitance measurements, conventional capacitance-frequency (C-F) measurement were employed. Capacitance-voltage (C-V) measurements, to obtain the carrier concentration, were taken at different temperature to identify whether the carrier concentration was changing with temperature. A DLTS spectrometer by SULA Technology and a liquid-nitrogen cryostat operated in the temperature range between 90 and 530 K was used DLTS measurements. For the DLTS measurement, a 100 ms wide pulse at 0.3V was applied to fill the electron traps in GaN. A reverse bias of -3V was applied to remove electrons from the deep level in the depletion region, and the capacitance transient was detected by a 1MHz capacitance meter. The transient capacitance was measured by using a HP4194 impedance analyzer. The most proper measurement frequency used to do the transient capacitance measurements were indicated from C-F measurement.

RESULTS AND DISCUSSION

The response of parallel capacitance (C_p) to the frequency of GaN2500, at different temperature, is demonstrated in Fig.1. A Schottky diode can be simulated by a simple series RC alternating circuit. The charging and discharging of trap in low frequency can follow the input signal, while at higher frequency series resistance would affect on the result of capacitance. The abrupt increasing of capacitance at lower frequency, as shown from frequency-capacitance measurement, indicated that there are deep level traps in GaN films. According to Fig. 1 the range that the parallel capacitance do not vary with modulation frequency is around $10^3 \sim 10^4$ Hz. The most proper capacitance-voltage measurement frequency of GaN2000 GaN1500 are 5KHz 10KHz as suggested by C-F measurement. Figure 2 shows the carrier concentration of set II varies with measuring temperature. As the flow rate of NH_3 getting lower, the free carrier concentration became higher as indicated in Fig. 2. The large background carrier concentration is usually regarded to be caused by the large amount of nitrogen vacancy¹³. The carrier concentration of R1 is $1.184 \times 10^{17} \text{ (cm}^{-3}\text{)}$ from the similar measurement.

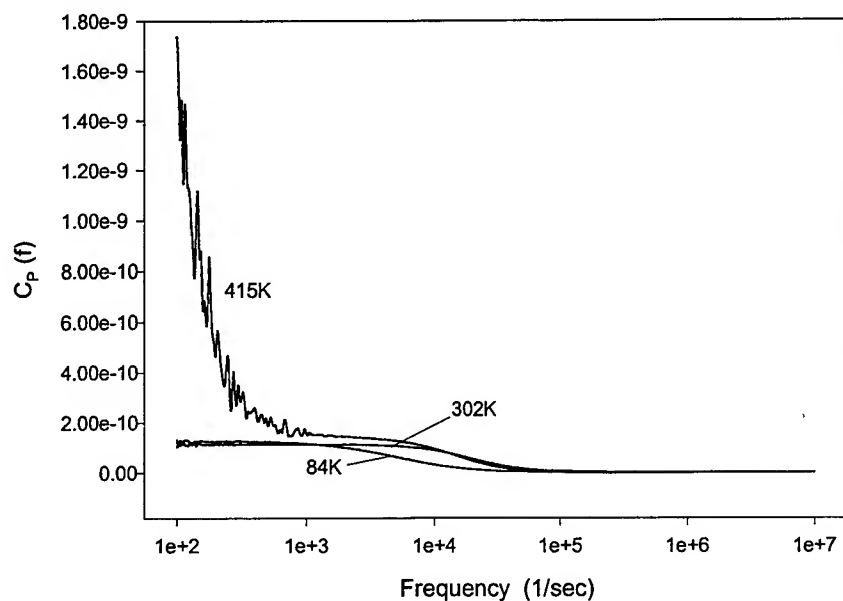


Fig. 1 The response of parallel capacitance to frequency of GaN2500 at different temperature. The abrupt increasing of C_p at lower frequency was caused by deep level traps in GaN films, and the proper measurement frequency of GaN2500 was around $10^3 \sim 10^4$ Hz.

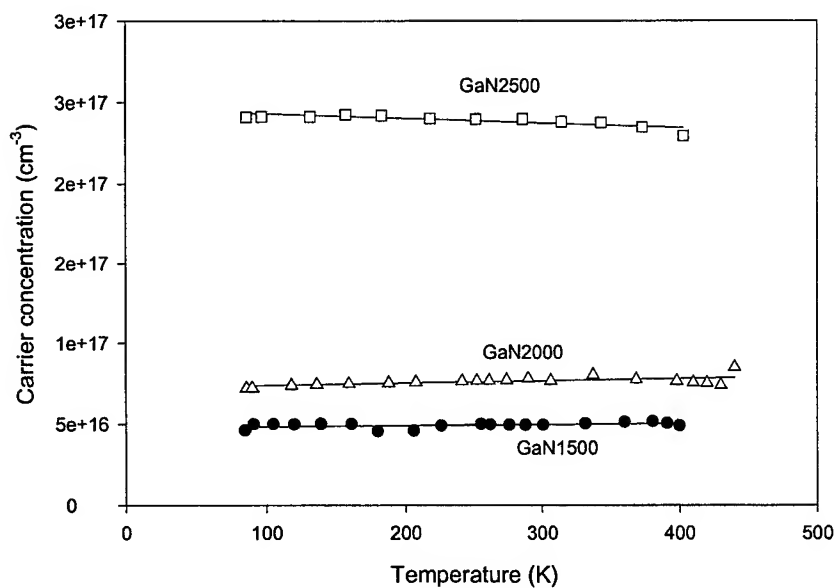


Fig. 2 Carrier concentration of set II varied with measurement temperature. Lower the NH_3 flow rate higher carrier concentration as indicated in Fig. 2. The large background carrier concentration is usually regard to cause by the big amount of nitrogen vacancy.

The results of DLTS spectra of R1 are presented in Fig.3 with the emission rate window which were set as 23.26 s^{-1} and 46.52 s^{-1} . Two distinct levels, labeled E_2 and E_4 , were clearly observed on R1. The activation energy, ΔE , and the electron capture cross section, σ , of each deep level traps were extracted from Arrhenius plots of $\log(T^2\tau)$ versus $1000/T$, where τ is the capacitance transient time constant deduced from the windows setting of the DLTS system and T is the corresponding temperature. A slop of linear least square fit to each set of data obtains the activation energy of each deep level. The characteristics of level E_2 and E_4 are listed in Table 1. Arrhenius plots reveal that level E_2 was closed to the level with activation energy of 0.49eV found by Götz *et al.*⁵, 0.58eV report by Hacke *et al.*⁶, 0.49eV reported by Lee *et al.*⁷, 0.598eV reported by Haase *et al.*⁹, and 0.578eV reported by Wang *et al.*¹⁰. Similarly, level E_4 was closed to 1.10eV reported by Chen *et al.*⁸, and the 0.961eV reported by Wang *et al.*¹⁰.

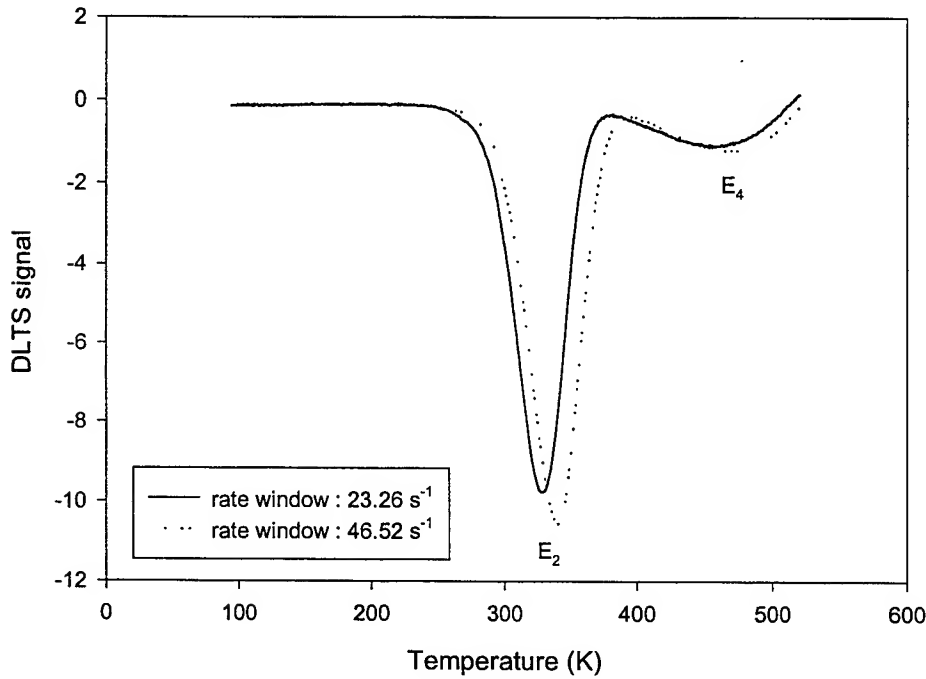


Fig. 3 DLTS spectrum measured on the sample R1 with emission rate windows of 23.26 s^{-1} and 46.52 s^{-1} .

Table 1. Characteristic of deep-level E_2 and E_4 measured by DLTS in the GaN sample Set I (R1)

Sample (Trap)	$N_d (\text{cm}^{-3})$	$N_t (\text{cm}^{-3})$	$\Delta E (\text{eV})$	$\sigma (\text{cm}^{-2})$
Set I, R1 (E_2)	1.184×10^{17}	$N_{E2} = 4.258 \times 10^{16}$	0.556	1.244×10^{-18}
(E_4)		$N_{E3} = 6.011 \times 10^{15}$	1.018	3.310×10^{-19}

To measure the transient capacitance, the reverse bias voltage of -2V was first employed to remove electrons from deep level traps in the depletion region. The capacitance was decreased immediately as the schottky diode was reverse biased, then the capacitance was increased exponentially to a constant value. To extract the time constants τ for a given temperature the least square fit of an exponential function was employed.⁸ Sample GaN1500 reveals only two levels, labeled as E_3 and E_5 . Three majority traps, labeled as E_2 , E_3 and E_5 , are observed in GaN2000. GaN2500 illustrate three deep level traps, i.e. E_1 , E_2 and E_3 , too. The activation energy and capture cross-section

for E_2 in sample GaN2000 is 0.554eV and $5.905 \times 10^{-16} \text{cm}^2$ which correspond to the defect level E_2 found in Set I as illustrate in Arrhenius plots. The activation energy and capture cross-section for E_3 of sample GaN2000 is 0.649eV and $7.169 \times 10^{-20} \text{cm}^2$. It close corresponded to 0.665eV reported by Hacke *et al.*⁶, 0.6eV measurement by Chen *et al.*⁸, 0.670eV found by Haase *et al.*⁹, 0.657eV found by Wang *et al.*¹⁰ and 0.62eV reported by Fang *et al.*¹¹. The activation energy ΔE and capture cross-section σ for E_5 in sample GaN1500 is 1.342eV and $1.759 \times 10^{-13} \text{cm}^2$. Level E_5 is similarly to the 1.44eV reported by Lee *et al.*⁷ and 1.27eV reported by Chen *et al.*⁸. The concentration of deep level traps, n_t , are obtains from the capacitance transient height, assuming uniform trap distribution. The traps concentration of set II is demonstrated in Table 2.

Table 2. The trap concentration of set II

	GaN 2500 (cm^{-3})	GaN 2000 (cm^{-3})	GaN 1500 (cm^{-3})
E_1	2.092×10^{15}	-	-
E_2	1.754×10^{15}	1.608×10^{14}	-
E_3	7.479×10^{15}	1.491×10^{15}	4.660×10^{15}
E_5	-	1.382×10^{15}	1.398×10^{16}

The fact that level E_2 appears in both samples grown by different MOCVD reactors, and different growth techniques, i.e. MOCVD, HVPE, and MBE, indicates that level E_2 is originated either from a native defect or a common impurity during the growth of GaN film. The trap concentration of level E_2 increases as raising the NH_3 flow rate. This increment implies that level E_2 is associated with either the increasing of nitrogen atoms or decreasing the gallium atoms. If level E_2 is associated with Ga vacancy, then the trap concentration of E_2 should be increased as the carrier concentration is decreased. It is contradictory with the results of C-V measurement. Dow and Jenkins¹⁴ calculated the deep level trap associated with Ga vacancy was acceptor like. However, the activation energy of E_2 is closed to conduction band, and it is donor like. The deep level traps for nitrogen substitution on Ga site below the conduction band 0.54eV, as indicated by Dow and Jenkins¹⁴, was close corresponding to the activation energy of E_2 . In addition, Haase *et al.*⁹ demonstrated that deep level E_2 could be generated by nitrogen implantation and subsequently removed by thermal annealing. Therefor, level E_2 is interpreted as a result of the N-antisite defect.

The defect level E_5 , which also found in samples grown by different techniques, indicated it might due to a native defect or a common impurity within the grown process. The broad photoluminescence emission band near 560nm¹⁵ and broad cathodoluminescence band near 520nm¹⁶ is thought as a result of oxygen in GaN. Chen *et al.*⁸ have suggest that level E_4 may be due to the oxygen impurities substitution on Ga site. The theoretical calculation the deep level of oxygen on Ga sites is 1.27eV, while it closed to the activation energy of E_5 . Thus level E_5 is believed to be related oxygen impurities on Ga site.

CONCLUSION

In summary, two different sets of GaN films, grown by different organometallic vapor phase epitaxy (OMVPE), are investigated in this study. DLTS and transient capacitance are utilized to characterize the deep center in GaN layer. Two distinct levels with activation energy $E_2=0.556\text{eV}$ and $E_4=1.018\text{eV}$ are clearly observed on sample Set I. Four majority-carried traps were found in sample set II, as mention above. Trap E_2 is believed to relate with nitrogen antisite defect, since the trap concentration increases as NH_3 flow rate increases.

ACKNOWLEDGMENTS

The authors would like to thank Dr. J.K. Ho at Industrial Technology Research Institute for crystal growth. This work was supported in part by the National Science Council of the R.O.C under Grant No. NSC89-2112-11-009-011

REFERENCES

1. S. Nakamura, M. Senoh, S. Nagahama, N. Iwasa, T. Yamada, T. Matsushita, H. Kiyoku and Y. Sugimoto, *Jpn. J. Appl. Phys., Part 2*, **35**, L74 (1996)
2. Z. Fan, S. N. Mohammad, O. Aktas, A. E. Botchkarev, A. Salvador, and H. Morkoc, *Appl. Phys. Lett.* **69**, 1229 (1996).
3. Q. Chen, M. A. Khan, J. W. Wang, C. J. Sun, M. S. Shur, and H. Park, *Appl. Phys. Lett.* **69**, 794 (1996).
4. M. Asif Khan, J. N. Kuznia, D. T. Olson, J. M. Van Hove, M. Blasingam, and L. F. Reitz, *Appl. Phys. Lett.* **60**, 2917 (1992).
5. W. Götz, N. M. Johnson, H. Amano and I. Akasaki, *Appl. Phys. Lett.* **65**, 463 (1994).
6. P. Hacke, T. Detchprohm, K. Hiramatsu, N. Sawaki, K. Tadamoto and K. Miyake, *J. Appl. Phys.* **76**, 304 (1994).
7. W. I. Lee, T. C. Huang, J. D. Guo and M. S. Feng, *Appl. Phys. Lett.* **67**, 1721 (1995).
8. Jenn-Fang Chen, Nie-Chuan Chen, Wen-Yen Huang, Wei-I Lee and Ming-Shiann Feng, *Jpn. J. Appl. Phys., Part 2*, **35**, L810 (1996).
9. D. Haase, M. Schmid, W. Kümer, A. Dömen, V. Härle, F. Scholz, M. Burkard and H. Scheizer, *Appl. Phys. Lett.* **69**, 2525 (1996).
10. C. D. Wnag, L. S. Yu, S. S. Lau, E. T. Yu, W. Kim, A. E. Botchkarev and H. Morkoc, *Appl. Phys. Lett.* **72**, 1211 (1998).
11. Z-Q Fang, D.C. Look, W. Kim, Z. Fan, A. Botchkarev and H. Morkoc, *Appl. Phys. Lett.* **72**, 2277 (1998).
12. C. F. Lin, G. C. Chi, M. S. Feng, J. D. Guo, J. S. Tsang, and J. M. Hong, *Appl. Phys. Lett.* **68**, 3758 (1996).
13. S. Strite and H. Morkoc, *J. Vac. Sci. & Technol. B* **10** 1237 (1992).
14. D. W. Jenkins and J. D. Dow, *Phys. Rev. B* **39** 3317 (1989).

Atomic force microscope study of GaN films grown by hydride vapor phase epitaxy

Huimei Fang, Y. K. Wang, R. Y. Tsai, C. F. Chu, and S. C. Wang

Institute of Electro-Optical Engineering, National Chiao Tung University, TAIWAN, R.O.C.

ABSTRACT

We report the results of the investigation of the structural, surface morphological, and optical properties of GaN films grown by hydride vapor phase epitaxy. These films were grown on sapphire substrate with no intentional dopings. These as-grown GaN film samples with thickness ranging from 5.58 μm to 14.9 μm were investigated under room temperature conditions. The surface morphology of these films was investigated using an atomic force microscopy (AFM). The root mean square (RMS) values of surface roughness range from 0.281 nm to 0.133 nm. The thicker films show lower defect counts with a defect density of about $2 \times 10^8 \text{ cm}^{-2}$. The structural property of these films was measured by double crystal X-ray diffraction (DC-XRD). The full width at half maximum (FWHM) of X-ray diffraction angle decreases as the film thickness increases with a lowest FWHM of about 265.5 arcsec. The optical properties of these films were investigated by photoluminescence (PL) measurement at room temperature. The results show a dominant near band-edge UV emission peak that increases with the film thickness with very weak yellow emission band.

Keywords: GaN, wide bandgap material, hydride vapor phase epitaxy, atomic force microscopy, photoluminescence

1. INTRODUCTION

The group-III-nitrides have received much attention recently. Many GaN-based light emitting devices such as blue light emitting diodes and blue laser diodes have been realized¹. These devices are commonly grown on foreign substrates such as sapphire and SiC because of the lack of availability of GaN substrate. However, due to the large mismatches of lattice constant and thermal expansion coefficient of these substrate and GaN, the GaN device wafer structure epitaxially grown on these foreign substrate generally have poor crystal quality such as high defect density and induced stress and bowing.² As a result the reliability of the devices fabricated on these substrates may be affected. For realization of reliable and high performance light emitting devices, it would be most desirable to use the GaN material as substrate. Although the bulk GaN material is not readily available because of the difficulty in the growth of GaN bulk crystal, thick films of GaN materials can be grown using Hydride Vapor Phase Epitaxy (HVPE) method. Therefore, there may be possibility of using HVPE grown thick GaN material as the substrate. In this paper, we report the results of our investigation of the structural, surface morphological, and optical properties of a series of HVPE grown GaN film samples with thickness ranging from 5.58 μm to 14.9 μm .

2. EXPERIMENTS AND RESULTS

We investigated the crystal quality of the GaN samples using the double crystal X-ray diffraction (DC-XRD) technique. The DC-XRD rocking curves were recorded and the full width half maximum (FWHM) of this curve was analyzed. Fig. 1 shows a typical rocking curve of a 7 μm thick GaN sample, which has a clean single peak with FWHM of 269.5 arcsec. The FWHM values of all the samples measured vary from 535 arcsec to 269.5 arcsec. The FWHM values show a general decreasing trend as film thickness increases indicating better crystal quality for the thicker film.

The surface morphological properties of GaN films were characterized using atomic force microscopy (AFM). The investigation was conducted under room temperature conditions. We used a Nanoscope multimode AFM with a Si_3N_4 tip. The AFM is operated under contact mode by measuring the forces between a probe and the sample. The surface topography is obtained by scanning the tip across the sample with a typical scan area of 1 μm square. Fig. 2 shows a typical AFM image of a 14.9 μm thick GaN sample. As shown in Fig. 2, the growing pattern of GaN film is clearly observable, so are the defects appearing as small dark circular dots. The defect densities estimated from the AFM image to be approximately $2 \times 10^8 \text{ cm}^{-2}$ for this sample.

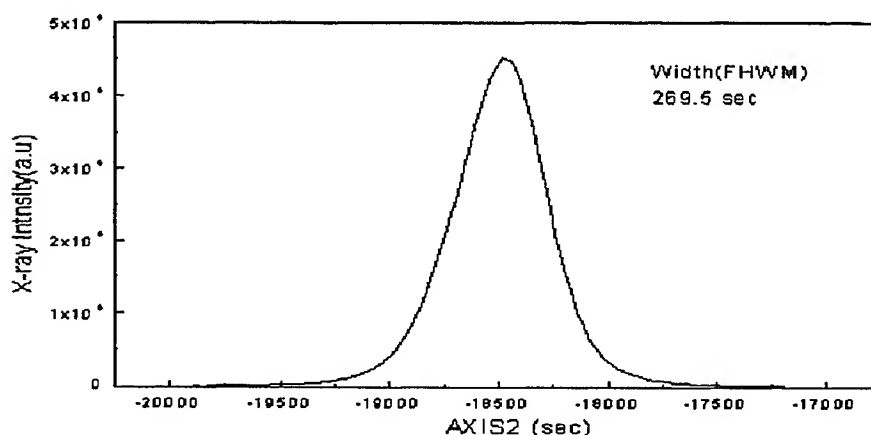


Fig. 1. A typical rocking curve of a 7 μm thick GaN sample.

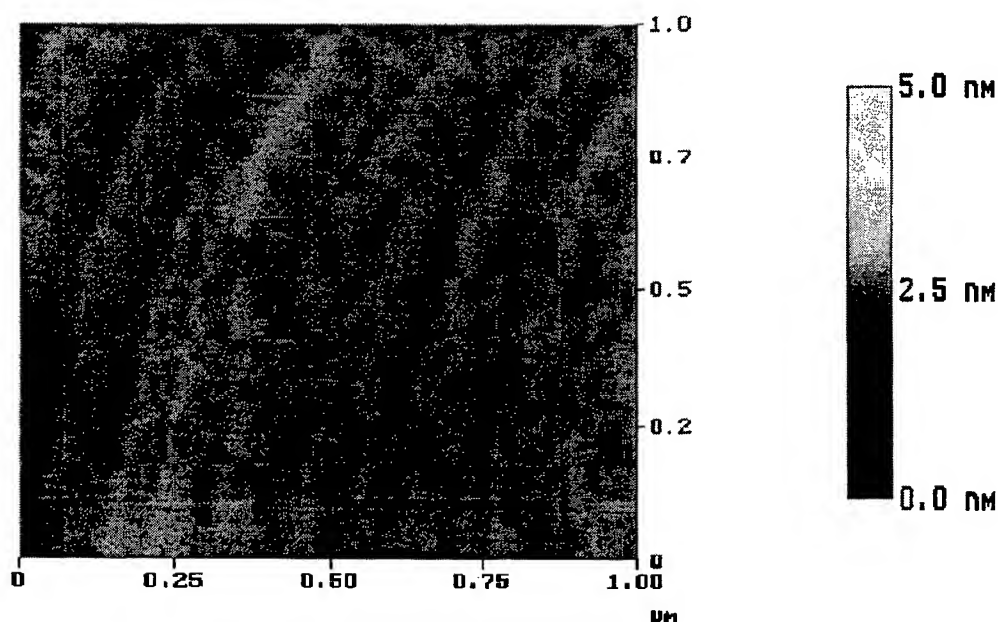


Fig. 2 Plan-view AFM image of a 14.9 μm thick GaN film.

From the AFM images of all the GaN samples, the estimated defect densities vary from $1.8 \times 10^9 \text{ cm}^{-2}$ to $2 \times 10^8 \text{ cm}^{-2}$ with lower defect density for the thicker films. These estimated defect densities are either lower or comparable with the reported typical defect density of 10^8 - 10^{10} cm^{-2} for the group-III-nitride epilayers.³⁻⁵

The section analysis was conducted along the surface growth pattern as depicted by the dark line drawn in the AFM image of Fig. 3. We selected the marker positions on the line to obtain the RMS of surface height variation between the two markers. Fig. 3 shows a typical section analysis data of a 7.0 μm thick film along with the AFM image. The RMS value for this sample is 0.16 nm.

Section analysis data were obtained for all different thickness samples and the AFM software performed both section analysis and roughness analysis of the measured data. The root mean square (RMS) values of the surface height roughness analysis and sectional analysis data were obtained for all samples. Fig 4 depicts the RMS variation with the sample thickness. The RMS values of sectional analysis fluctuate between 0.273 nm and 0.113 nm with no apparent correlation with film thickness. The 14.9 μm thick film has the lowest RMS value of 0.113 nm. While the RMS of surface roughness increases from 0.154 nm to 0.281 nm as the film thickness increases except for 14.9 μm thick film which has a lowest value of 0.133 nm.

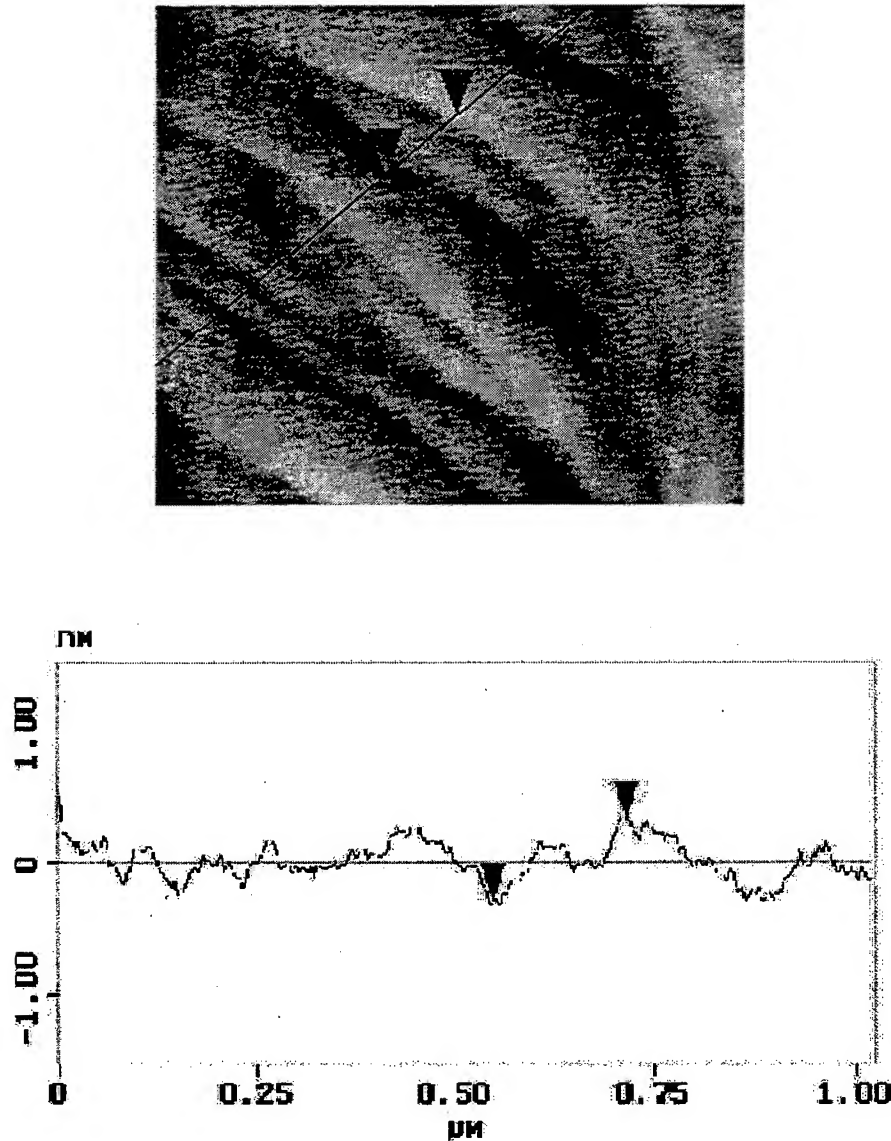


Fig. 3 The section analysis of 7.0 μm thick GaN film.

The optical properties of GaN film samples were investigated by ordinary photoluminescence (PL) at room temperature. A He-Cd 325-nm laser was used as the excitation light source and the experiment was conducted under room temperature conditions. The laser power incident on the sample was about 15 mW. Fig. 5 depicts the PL spectra of the GaN samples with film thickness ranging from 5.58 μm to 14.9 μm . The PL spectrum shows a strong UV emission line at 363.2 ± 0.5 nm and a weak 370.4 ± 0.9 nm line with phonon replicas,⁶ and a very weak yellow band fluorescence. The 363.2 nm line seems to correspond to the near-band-edge emission and the intensity of this line increases as film thickness increases. The 14.9 μm thick film almost has an intensity as least three times stronger than the other samples. The FWHM of the UV emission line varies from 4.73 to 7.44 nm with thicker film showing narrower linewidth. The yellow band emission band is very weak compared with the UV emission line indicating relatively good crystal quality of these films.

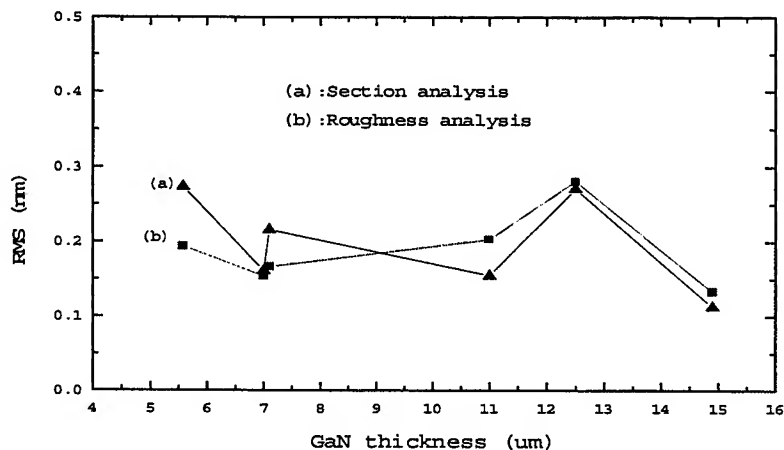


Fig. 4 Variation of RMS values with GaN film thickness.

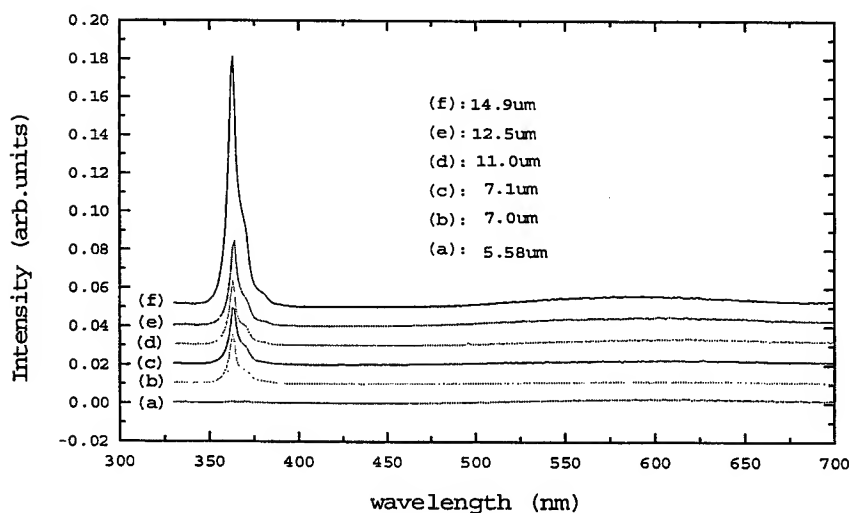


Fig. 5 Room-temperature PL spectra of the HVPE-grown undoped GaN samples.

3. CONCLUSION

In conclusion, we have investigated the crystal quality of HVPE grown GaN film samples with thickness ranging from 5.58 to 14.9 μm under room temperature conditions. From the AFM measurement we obtained the RMS values of surface height variation ranging from 0.113 nm to 0.273 nm with the lowest RMS value of 0.113 nm for 14.9 μm film. The RMS of surface roughness increases from 0.154 nm to 0.281 nm as the film thickness increases except for 14.9 μm thick film which has a RMS of 0.133 nm. We also estimated the defect densities of these films and found the thicker films have lower defect density with a defect density of $2 \times 10^8 \text{ cm}^{-2}$ for 14.9 μm thick film. From the double crystal X-ray diffraction measurement data, we observed that the thicker the film, the more perfect is the crystal quality of the film. All the samples show a dominant near-band-edge UV emission with very weak yellow emission band indicating relatively good crystal quality of these films. Based on these preliminary investigation results we found the HVPE grown GaN films possess relatively good crystal quality that could be a promising substrate material for epitaxial growth of GaN devices structures.

4. ACKNOWLEDGEMENTS

This work was supported by National Science Council of Republic of China in Taiwan. The authors would like to thank American Xtal Technology (AXT) for providing the HVPE grown GaN samples, and Dr. Herbert Cox of AXT for helpful technical discussion, and Dr. H. N. Lin of Precision Instrument Development Center for AFM measurement.

5. REFERENCES

1. S. Nakamura and G. Falso, *The Blue Laser Diodes*, (Springer-Verlag, Berlin, 1997)
2. M. K. Kelly, R. P. Vaudo, V. M. Phanse, L. Gorgens, O. Ambacher, and M. Stutzmann, *Jpn. J. Appl. Phys.* 38, L217-219 (1999)
3. G. M. Smith, J. M. Redwing, R. P. Vaudo, E. M. Ross, J. S. Flynn, and V. M. Phanse, *Appl. Phys. Lett.* 75, No. 1, 25 July 1999
4. A. Vertikow, M. Juball, and A. V. Nurmikko, *Appl. Phys. Lett.* 72, 2645 (1998)
5. K. Tachibana, T. Someya, and Y. Arakawa, *Appl. Phys. Lett.* 74, 383 (1999).
6. B. J. Pong, C. J. Pan, Y. C. Teng, G. C. Chi, W. H. Li, K.C. Lee, and C. H. Lee, *J. Appl. Phys.* 83, 5992 (1998).

Comparative investigation of high resolution transmission electron microscopy and Fourier transform infrared spectroscopy for GaN films on sapphire substrate

K. Li^{*a}, Y. T. Hou^b, Z. C. Feng^a, S. J. Chua^{a,b}, M. F. Li^b, E.W.P. Lau^c, and A.T.S. Wee^{a,c}

^a Institute of Materials Research and Engineering, 3 Research Link, Singapore 117602

^b Center for Optoelectronics, Department of Electrical Engineering, National University of Singapore, Singapore 119260

^c Department of Physics, National University of Singapore, Singapore 119260

ABSTRACT

A comparative study on GaN/sapphire has been performed by transmission electron microscopy (TEM) and infrared reflectance (IR). TEM observations reveal that both the undoped and Si doped GaN epilayers have large density of threading dislocations. Dislocations in the undoped GaN tend to form open core structure, while dislocation lines in the Si-doped GaN are very sharp and the strain contrast is much more confined. It is believed that Si-doping causes the increase in surface energy, resulting in the change of dislocation configurations from open core structures in undoped GaN to much more confined dislocation lines. Frank dislocation loops are also found lined up at a depth of about 110 ± 10 nm from the interface. High resolution TEM study also reveals that the GaN buffer layer grown at low temperature has transformed into its thermodynamically stable wurtzite structure during the high temperature post-buffer GaN epilayer growth process. The comparative infrared reflectance shows the corresponding behaviour. The interference fringes of the Si doped sample, compared with the undoped one, shows a contrast damping and reflectance reduction behavior, suggesting the presence of a transition/defect layer near the interface.

1. INTRODUCTION

With the progress in epitaxial growth techniques, intense research interest in recent years has been concentrated on III-V nitrides. These nitrides possess large direct bandgaps, extremely high hardness, very large heterojunction offsets, high thermal conductivity and high melting temperature. When grown in the form of ternary or even quaternary compounds, the bandgaps can also be tailored. Therefore, III-V nitrides, such as GaN, AlN, InN and their ternary compounds, are of significant technological importance for semiconductor device applications in the blue and UV wavelengths, such as light emitting diodes and semiconductor lasers, and they also promising candidates for high temperature and high power devices.¹⁻⁶ In recent years, GaN-based blue LEDs and, more recently, GaN-based lasers have been successfully fabricated.³⁻⁸

In spite of the great progress in III-nitrides growth, there are still some technical barriers lying ahead.⁹ One of the challenges is the lack of suitable substrate. Sapphire is currently the most commonly used substrate. All the difficulties in hetero-epitaxy exist in the growth of GaN on sapphire: different chemistry (GaN and Al_2O_3), different crystalline structure (wurtzite or sphalerite for GaN and corundum for sapphire), and large lattice mismatch (14%). The resulted density in GaN is very high (in the order of $10^{10}/\text{cm}^2$), even in high efficiency GaN-based device.^{10, 11} Obviously, it is of significant importance to characterize these defects so as to get a thorough understanding of the defect nature and formation mechanism. A thorough understanding will facilitate us in finding a way to reduce the defect density and increase the device performance. To achieve this goal, here we employ both high resolution TEM and FTIR to do a comparative study of the interface between GaN and sapphire, where most of the defects originate.

2. EXPERIMENTAL

GaN films were grown on (1000)-plane of sapphire substrate by metalorganic chemical vapor deposition (MOCVD). A GaN nucleation layer with a thickness of about 40 nm was first grown on substrate before the deposition of epilayer GaN. Monosilane (SiH_4) was used for n-type doping of GaN. The GaN films have a thickness ranging between 1.8 and 2.3 μm in this study.

TEM cross-section sample was prepared using the commonly adopted grinding-polishing-ion-milling method. First, two 2.5x1.5 mm² pieces of GaN were cut out from the sample and then glued together using G1 epoxy. The glued sample was then ground and polished from one side to a thickness of about 200 μm . After that, the polished sample was mounted to a Φ 3mm copper grid, with the polished side facing down. The sample was then further ground/polished to a thickness of about 80 μm . Following this, dimpling was applied until the sample was about 15 μm thick. Finally, the sample was ion milled in a Gatan PIPS, with the ion beam energy set at 4.5 kV and ion milling angle at $\pm 4^\circ$. The prepared sample is then observed in a field emission Philips CM300 with ultra twin objective lens design. Room temperature infrared reflectance spectra were measured at 1 cm⁻¹ resolution using a Fourier transform infrared spectrometer at near normal incidence.

3. RESULTS AND DISCUSSION

3.1 TEM investigation

The influence of dopant on dislocation structures is studied by TEM. Fig. 1 shows the bright field TEM images of the undoped GaN GN900 (Fig. 1 (a)) and Si-doped GaN GN654 (Fig. 1 (b)). Both images show high dislocation densities; the threading dislocation density in undoped GaN is about $9 \times 10^4/\text{cm}$, while the threading dislocation density in Si-doped GaN is lower; it is about $6 \times 10^4/\text{cm}$. The dislocation structure is obviously different in the undoped and Si-doped GaN. In the Si-doped GaN, the strain contrast caused by threading dislocation is much more confined and sharp dislocation lines can be clearly seen; while in the undoped GaN, the strain field caused by threading dislocations is much broader, and the dislocations tend to form open core structures. Small pits can be seen at film surface on top of some dislocations. This is supported by atomic force microscopy (AFM) observation of the film surface. The holes at the surface can be clearly seen in the AFM images (Fig. 2). There are more holes at the surface of undoped GaN than at the surface of Si-doped GaN, and the holes at the surface of undoped GaN are in average bigger than the holes at the Si-doped GaN surface.

According to Frank's energy competition theory,¹² whether an open core dislocation structure will be formed or not depends on the balance between the strain energy of a dislocation core and the extra surface energy when an open core structure is otherwise formed. In other words, an open core dislocation will be formed if there is a decrease in the total energy by replacing the highly strained dislocation core with an empty pipe. The essence of this theory is that open core dislocation

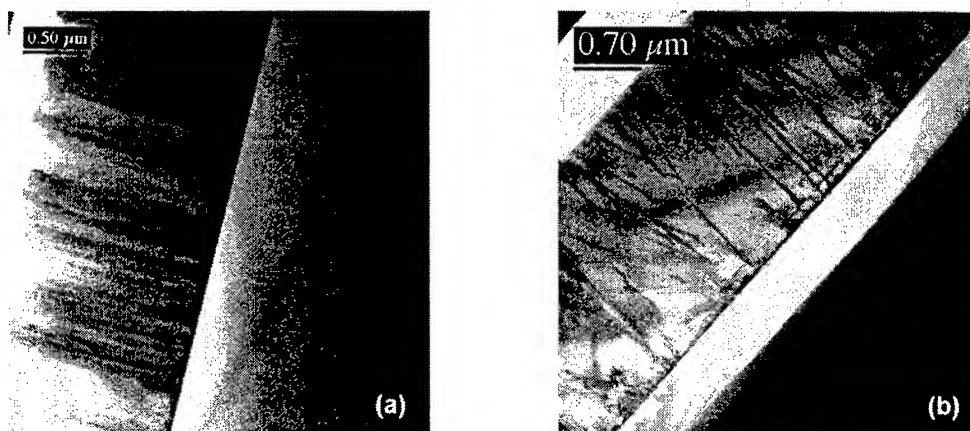


Fig.1 Bright field TEM images of (a) undoped GaN, and (b) Si-doped GaN.

structure is surface energy related. We have already found in our AFM study that different dopant can cause significant change in the surface morphology of GaN. It is well known different surface morphology is related to different growth mode, which is a result of different surface energy. Therefore, in the current case, we believe that Si doping causes the increase in surface energy of GaN, which results in the change from open core dislocation pipes to more confined dislocation lines.

It should also be noted that in Fig. 1 (b) there are Frank dislocation loops located at a distance of about 110 ± 10 nm from the interface, and the loops seem to form a secondary 'interface'.

The high resolution images of GaN/ Al_2O_3 interface are shown in Fig. 3. Similar to Fig. 1, the undoped GaN shows more obvious strain contrast, especially in the buffer layer region, than the Si-doped GaN. Careful examination of the stacking sequence of the atomic planes along the (0001) direction reveals that the thermodynamically unstable sphalerite structure

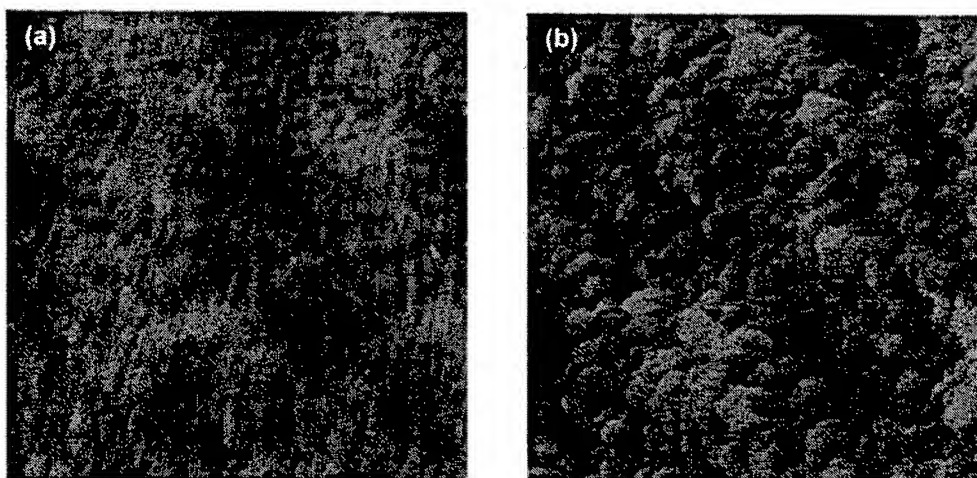


Fig.2 AFM images of (a) undoped GaN, and (b) Si-doped GaN.

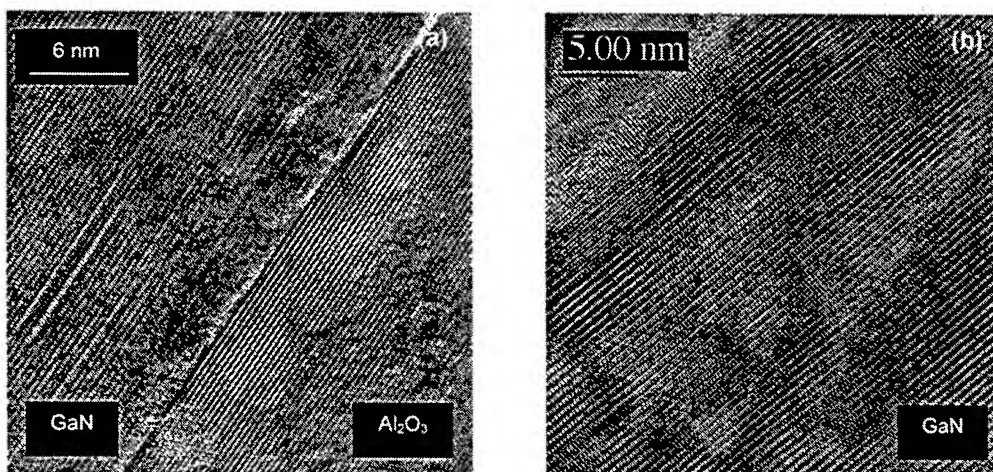


Fig. 3 High resolution TEM images of (a) undoped GaN, and (b) Si-doped GaN.

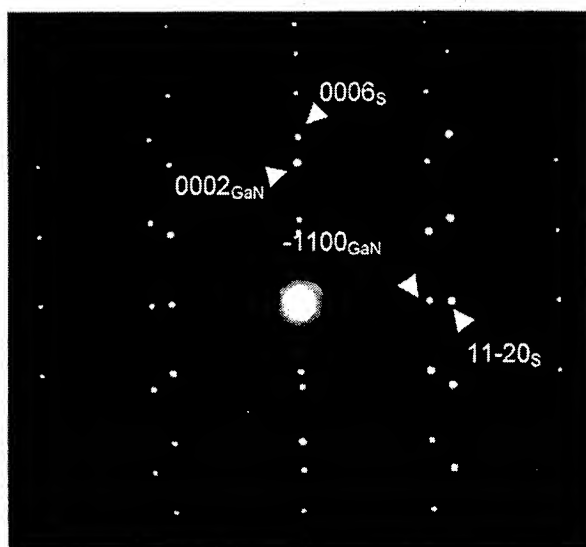


Fig. 4 Electron diffraction pattern from GaN/sapphire interface.

formed during low temperature (550 °C) buffer layer growth has transformed into thermodynamically stable wurtzite structure after the high temperature (1040 °C) epilayer growth; the stacking sequences of (0001) planes in the buffer layer is $\cdots\text{ABABAB}\cdots$ for wurtzite, rather than $\cdots\text{ABCABC}\cdots$ for sphalerite in both undoped and Si-doped GaN. Compared with the buffer layer, the crystallinity of epilayer is much better; there are fewer stacking faults in the epilayer. Two types of common stacking faults, extrinsic and intrinsic, can be easily found in the buffer layer region. The extrinsic stacking fault is formed through the insertion of half an atomic (0001) plane, where the stacking sequences changes from $\cdots\text{BABABABA}\cdots$ in perfect region to $\cdots\text{BABACBCB}\cdots$ in the faulted region, while the intrinsic stacking fault is formed through the extraction of half an atomic (0001) plane, where the stacking sequences changes from $\cdots\text{BABABABA}\cdots$ in perfect region to $\cdots\text{BABACACA}\cdots$ in the faulted region.

The corresponding electron diffraction pattern is shown in Fig. 4. Two sets of pattern from GaN and sapphire respectively can be easily distinguished. Since sapphire possesses a smaller lattice parameter than GaN, the spacing of its diffraction pattern in reciprocal space will be larger as compared with that of GaN. From the indexing of this diffraction pattern, it is clear that the electron beam is coming down along the $[11-20]$ direction of GaN or $[1-100]$ direction of sapphire. The orientation relationship between GaN and sapphire can also easily defined as $[11-20]_{\text{GaN}} \parallel [1-100]_{\text{sapphire}}$, and $[-1100]_{\text{GaN}} \parallel [11-20]_{\text{sapphire}}$.

3.2 FTIR investigation

We calculated the reflectance of layer/substrate system using the transfer matrix method, in which an arbitrary number of layers can be included and interference effects within the films are automatically included.¹³ The treatment of uniaxial films follows the method of Piro¹⁴ and all films are assumed to be oriented with their c-axes perpendicular to the surfaces and interfaces. This assumption is proven to be reasonable by X-ray diffraction which shows the characteristic (0002) and (0004) diffraction patterns of hexagonal GaN with c-axis of films being normal to the surface. We treated the substrate to be semi-infinite and neglected the internal reflections within the substrate. This is appropriate for our samples with non-polishing backside.

In order to minimize the influence of substrate reflectance, a Kramers-Kronig transformation from the experimental reflectance of sapphire is performed to accurately determine its dielectric function.¹⁵

For GaN, its dielectric function can be described by a single oscillator model:¹⁶

$$\varepsilon = \varepsilon_{\infty} \left(1 + \frac{\omega_{LO}^2 - \omega_{TO}^2}{\omega_{TO}^2 - \omega^2 - i\gamma_{TO}\omega} - \frac{\omega_p^2}{\omega(\omega + i\gamma_p)} \right) \quad (1),$$

where the second term is the dispersion due to phonons and the third term arises from free carriers. Here ε_{∞} is the high frequency dielectric constant, ω_{LO} and ω_{TO} are the frequency of LO and TO phonon, γ_{TO} is the damping factors of the transverse optic modes, ω_p is the plasma frequency and γ_p is the electron damping constant, respectively. For un-doped samples, the third term will be neglected.

Fig.5 shows the experimental IR spectra of the two samples GN900 and GN654 (open circles). The solid lines are the calculations with a simple film/substrate model. The parameters used in Equation (1) for the GaN film are listed in Table I.

For sample GN900, it can be found from Fig.5 that the simulation agrees well with the experiment for the whole spectral regions. This indicates the good crystalline quality of the film for this sample. The successful application of the simple film/substrate model also demonstrates that the interface of film and substrate is abrupt. This is in agreement with our TEM observations.

For sample GN654, fit to the IR reststrahlen band below 1200 cm^{-1} leads to a carrier concentration of $6.3 \times 10^{18} \text{ cm}^{-3}$, this value is very near to that by Hall measurement ($6.2 \times 10^{18} \text{ cm}^{-3}$). In this spectral region, the calculation shows poor fits to the top and falling edge of reststrahlen band for higher doping sample GN654. This "flat top" is also observed in SiC,¹⁷ the cause of which is not known yet.

However, in the spectral region beyond 1200 cm^{-1} , the calculation for sample GN654 shows significant deviation from the

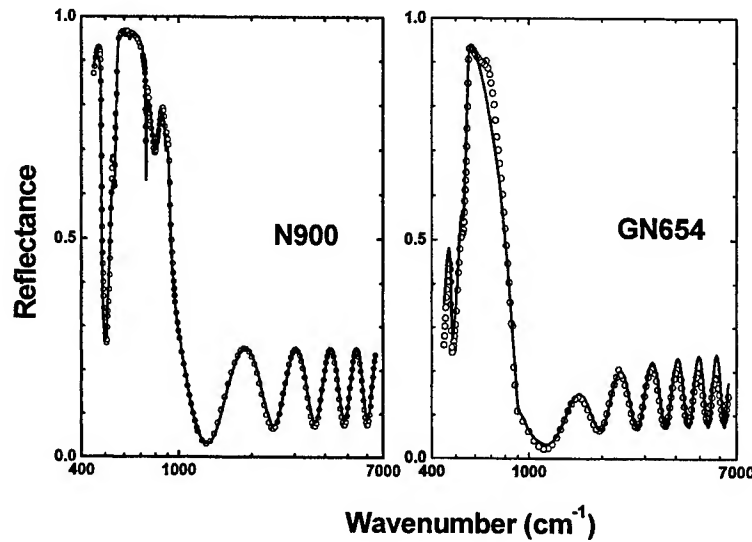


Fig.5 Infrared reflectance of samples N900 and GN654. Open circles are experiments and solid lines are simulations.

Table I Parameters used in Equation (1) for IR

	ϵ_{∞}	ω_{LO}	ω_{TO}	γ_{TO}	ω_p	γ_p
N900	5.2	742	560	5	0	0
GN654	5.2	742	560	5	700	400

experiment for the interference fringes. For the film/substrate system, the calculated reflectance values at the fringe maximum, R_{\max} , and minimum, R_{\min} , at higher photon frequency region far away from reststrahlen peaks are independent of photon frequency. However, for the spectrum of sample GN654 in Fig.5, the experimental interference fringes exhibit an intensity dependence of photon frequency even at far away from reststrahlen peaks. We plot in Figure 6a the fringe contrast, defined as $(R_{\max}-R_{\min})/(R_{\max}+R_{\min})$, of the two samples. It can be seen that the fringe contrast remains almost constant for sample N900, while it decreases with increasing frequency or fringe number for sample GN654.

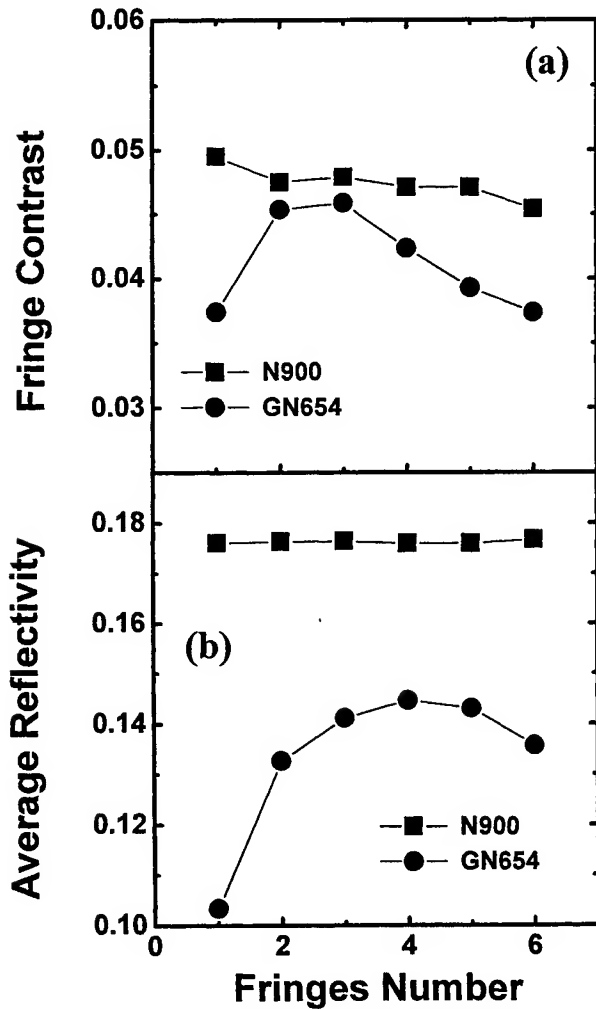


Fig.6 The interference fringes contrast and average reflectivity for sample N900 and GN654.

The damping behavior of the interference contrast can be explained by the presence of an interface layer. In the calculation, the interface layer has been considered simply as a mixture of GaN and voids, and their optical constants were obtained in the effective medium approximation using the Maxwell-Garnett model. Similar interface layer was also observed in reflectivity study of GaN on GaAs.^{18, 19} We interpret it as an effective optical transition layer induced by imperfections in epilayer near the interface.

Fig.6b shows the average reflectivity of the two samples along with calculation. The average reflectivity is defined as $(R_{\max}+R_{\min})/2$. As shown in Fig.6b, for sample GN900, the average reflectivity measured is independent of photon frequency (17.7%). However, for sample GN654, the average reflectivity at higher frequency decreases to 14.5%. This phenomenon indicates that a reflectivity loss mechanism also occurs in sample GN654. Atomic force microscopy (AFM) measurements on the surface roughness show that the roughness of our samples is all in several nanometers range. Such small roughness will not have considerable influence on IR, and the observed monotonically decrease of average reflectivity cannot arise from surface scattering. The contributing factor should still be voids related.

As observed in our TEM study, sample GN654 has many Frank dislocation loops lined up at a distance of about 110 ± 10 nm from the GaN/sapphire interface. Since Frank dislocation loops are formed through the

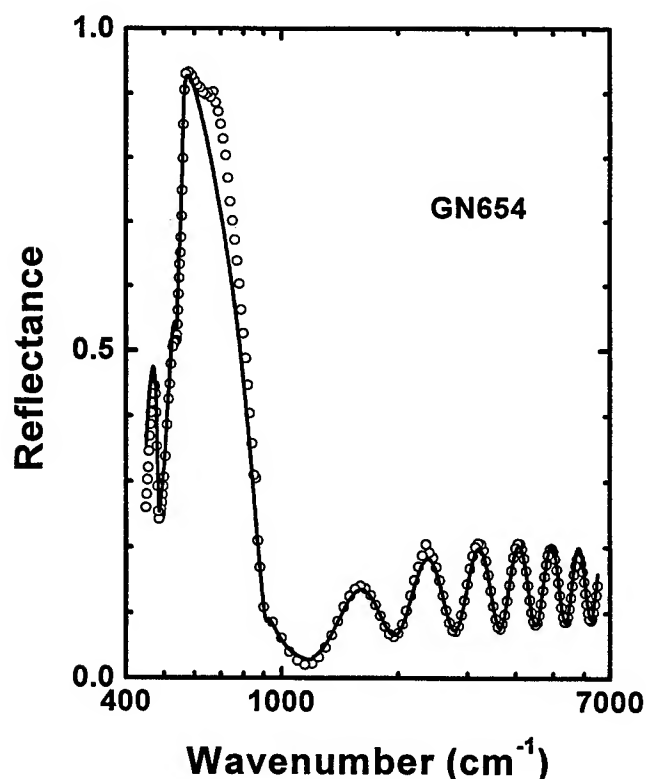


Fig. 7 Refitting of the IR reflectance spectrum of GN654 after an interface defect/void layer is assumed. Good fit is reached.

collapse of voids, our above void/GaN assumption is reasonable. After taking this assumption into the theoretical model and note that the refractive index of GaN is constant at regions away from reststrahlen bands, a good agreement with experiment is reached (Fig. 7). The GaN/sapphire interface characteristics can be obtained from the damping behavior of the interference fringe contrast. The percentage of voids in the interface layer is 15% and the thickness of interface layer obtained for sample GN654 is 0.09 μm , which is quite close to the depth of Frank dislocation loops observed in TEM. Recalling that the threading dislocation density is higher in the undoped sample GN900 than in the Si-doped sample GN654, the combination of FTIR and TEM results suggests to us that only the Frank dislocation loops, parallel to interface, are responsible for the damping and reflectance reduction behavior of Si-doped GaN, and the influence of the threading dislocations nearly perpendicular to the interface is insignificant.

4. CONCLUSIONS

The influence of dopant on the dislocation structure and its further influence on IR response of GaN are studied by TEM and FTIR. Comparative TEM and FTIR study demonstrates that both the undoped and Si-doped GaN have good film quality and abrupt GaN/sapphire interface. Dislocations in the undoped GaN tend to form open core structure, while dislocation lines in the Si-doped GaN are very sharp and the strain contrast is much more confined. In the Si-doped GaN, nearly continuous Frank dislocation loops are formed at a depth of about 110 ± 10 nm from the GaN/sapphire interface, and these Frank dislocation loops, which are parallel to the interface, are responsible for the damping and reflection reduction in the IR spectra of Si-doped GaN. In addition, the orientation relationship between GaN and sapphire is also determined by TEM.

5. REFERENCES

1. S. Strite, M. E. Lin and H. Morkoc, *Thin Solid Films*, **231**, p.197, 1993.
2. S. Nakamura, and T. Mukai, *Jpn. J. Appl. Phys.* **31**, p. L1457, 1992.
3. S. Nakamura, T. Mukai, and M. Senoh, *J. Appl. Phys.* **76**, p. 8189, 1994.
4. S. Nakamura, T. Mukai, and M. Senoh, *Appl. Phys. Lett.* **64**, p. 1687, 1994.
5. S. Nakamura, M. Senoh, and T. Mukai, *Appl. Phys. Lett.*, **62**, p. 2390, 1993.
6. T. Detchprohm, K. Hiramatsu, N. Sawaki, and I. Akasaki, *J. Crystal Growth*, **145**, p. 192, 1994.
7. S. Nakamura, *J. Crystal Growth*, **145**, p.911, 1994.
8. S. Nakamura, M. Senoh, S.I. NagaHama, N. Iwasa, T. Yamada, T. Matsushita, H. Hyyoku, and Y. Sugimoto, *Jpn. J. Appl. Phys.*, **35**, P. L74, 1996.
9. K. Li, A.T.S. Wee, J. Lin, Z.C. Feng, and E.W.P. Lau, *Surf. Interface Anal.*, **28**, pp.181-185, 1999.
10. S.D. Lester, F.A. Ponce, M.G. Craford, and D.A. Steigerwald, *Appl. Phys. Lett.*, **66**, p. 1249, 1995.
11. W. Qian, G.S. Rohrer, M. Skowronski, K. Doverspike, L. B. Rowland, and D. K. Gaskill, *Appl. Phys. Lett.*, **67**, p. 2284, 1995.
12. F.C. Frank, *Acta Crystallogr.*, **4**, p. 497, 1951.
13. Pochi Yeh, *Optical waves in layered media*, Wiley, New York, 1998.
14. O. E. Piro, *Phys. Rev.*, **B36**, p. 3427, 1987
15. J. A. Bardwell, M. W. C. Dharma-wardana, B. Leathem, S. Moisa, J. B. Webb, and B. Tam, *J. Electrochem. Soc.* in press.
16. A. S. Barker, Jr. and M. Ilegems, *Phys. Rev.*, **B7**, p. 743, 1973.
17. R. T. Holm, P. H. Klein, and P. E. R. Nordquist, Jr., *J. Appl. Phys.*, **60**, p.1479, 1986.
18. G. Mirjalili, T. J. Parker, S. F. Shayesteh, M. M. Bulbul, and S. R. P. Smith, *Phys. Rev.*, **B57**, p. 4656, 1998.
19. S. Shokhovets, R. Goldhalm, V. Cimalla, T. S. Cheng, and C. T. Foxon, *J. Appl. Phys.*, **84**, p.1561, 1998.

Stimulated emission from organic semiconductor

Lijun Wang^{a,*} Xingyuan Liu^b Yongqiang Ning^b Yun Liu^b
Shengli Wu^b Dongjiang Wu,^b Jiamin Zhao^b Changqing Jin^b
Lixiang Wang^c, Xiabin Jing^c, Fosong Wang^c

^a Lab. Of Excited State Processes, Chinese Academy of Science, Changchun, 130021,
P.R. China

^b Changchun Institute of Physics, Chinese Academy of Sciences, Changchun, 130021,
P.R. China

^c Changchun Institute of Applied Chemistry, Chinese Academy of Sciences,
Changchun, 130022, P.R. China

Abstract

Optically pumped surface emitting and edge emitting stimulated emission behaviors in organic semiconductor was demonstrated in this study. For the surface emitting device, the microcavity was formed by sandwiching a polymer film containing PVK, Alq and DCM between a DBR with a reflectivity of 99.5% and a silver film. The sample was optically pumped by the three harmonic of a mode-locked Nd:YAG laser with 300ps pulses at 2 Hz repetition rate. The lasing phenomenon was observed in DCM-doped PVK microcavity when pumped above the threshold intensity of 0.25MW/cm². The full width at half maximum (FWHM) was 0.6nm with the peak wavelength at 603nm. For the edge emitting device, a laser dye DCM doped Alq matrix was used as the gain medium. The sample was transversely pumped by the three harmonic output of the mode-locked Nd:YAG laser. The change of the emission spectra showed a clear threshold action and gain narrowing phenomenon when increasing the excitation intensity. The spectra narrowing observed results from the amplified spontaneous emission (ASE) in the gain material.

Keywords: organic semiconductor lasing, microcavity, optically pumped laser, surface emitting, edge emitting, stimulated emission, amplified spontaneous emission

1. Introduction

Since the first report of polymer lasers based on poly(*p*-phenylene vinylene) (PPV) with the microcavity by Friend's group¹ and on poly[2-(2'-ethylhexyloxy)-5-methoxy-1,4-phenylene vinylene] (MEH-PPV) film without the microcavity by Heeger's group² in 1996, organic semiconductor lasing has attracted much attention because of its academic interest and potential application in modern display technology and integrated optics field³⁻¹⁰. A variety of organic semiconductor materials including conjugated polymers and small-weight organic molecules have been reported to exhibit lasing behavior¹¹⁻¹⁵. In this paper, we present the optically pumped surface emitting and edge emitting lasing behaviors in organic semiconductor film.

2. Experimental

Two kinds of devices were fabricated. A microcavity structure was used in the surface emitting device. The microcavity is sandwiched between a distributed Bragg reflector (DBR) and a Ag metal reflective

*Email address: wslcip@public.cc.jl.cn

mirror, as shown in Fig.1. The film of blend of PVK, Tris(8-quinolinolato) aluminum (Alq) and DCM was used as the active layer. The DBR consists of one quarter-wavelength dielectric layers stack with alternating high and low index. The high-index material is TiO_2 with a refractive indices n_H of 2.0. The low-index material used here is SiO_2 with a refractive indices n_L of 1.46. The DBR mirror has a reflectivity of 99.5% at normal incidence with wavelength band from 580 to 620 nm. The DBR was electron-beam evaporated on the quartz substrate. A solution of 40mg PVK, 25wt% of Alq and 0.05wt% of DCM in 2ml of chloroform was spin-coated onto DBR to make the polymer film. The film thickness can be controlled through adjusting the solution concentration or turning speed of spin-coating machine. The thickness of the DCM:Alq:PVK film was about 200nm. Finally Ag metal layer of 300nm thick was deposited on the organic layer, which serve as the top reflector of the cavity.

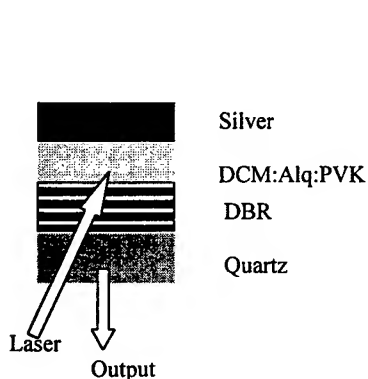


Fig.1. The structure of polymer surface emitting microcavity.

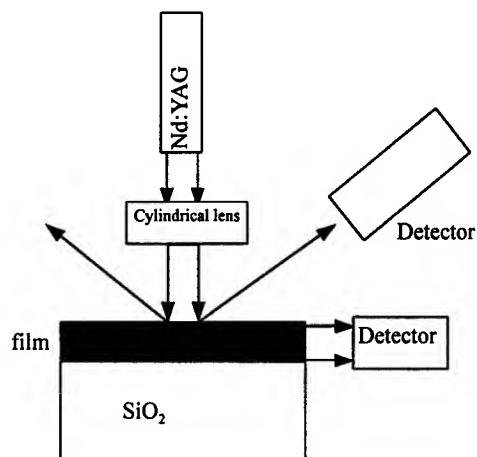


Fig.2. The experimental schematic setup of the edge emitting device.

For an edge emitting device, the film of laser dye DCM doped Alq matrix was used as the emissive layer. It was made by vacuum depositing Alq and DCM simultaneously on the quartz substrate in a vacuum of 1×10^{-3} Pa to form a noncavity film structure. The thickness of the DCM/Alq film was about 300nm. The experimental schematic setup of the edge emitting device is shown in Fig.2. The pump beam was focused onto the sample using a cylindrical lens ($f=10\text{cm}$) to obtain an excitation area of a $10 \times 0.2\text{mm}^2$ stripe. The emission of the film was detected from either the front or the edge of the film. The edges of the sample were polished to make the edge of the film smooth and sharp, which is very important for the output of the emission.

The photoluminescence (PL) and excitation emission spectra were recorded on a Hitachi Spectrophotometer F4500. The third harmonic output (355nm) of a mode-locked Nd:YAG laser was used as the excitation source. The pulse width was about 300ps. The repetition rate was 2Hz. The refractive index of the film was measured by prism coupling method. All these experiments were performed in the air at room temperature.

3. Results and discussion

3.1. Surface emitting device

Fluorescence spectrum of the DCM:Alq:PVK film and lasing spectrum obtained from the polymer surface emitting microcavity are shown in Fig.3 and Fig.4, respectively. Lasing phenomenon was observed when the monopulse pump intensity reached $0.25\text{MW}/\text{cm}^2$ (threshold intensity). When the

monopulse pump intensity go up to $0.34\text{MW}/\text{cm}^2$, the full width at half maximum (FWHM) of the lasing peak is 0.6nm with the peak wavelength at 603 nm . In the experiment, it was found that microcavity is the key structures for achieving high gaining. Such a structure will alter the emission properties of any emitter within the microcavity. The geometry of the microcavity alters the spontaneous emission rate of the emitting dipoles therein, allowing emission only at the resonance wavelengths of the cavity. This narrows the broad emission spectrum of conjugated polymer. This DCM-doped polymer film as a gain medium made it possible that polymer microcavity laser was realized.

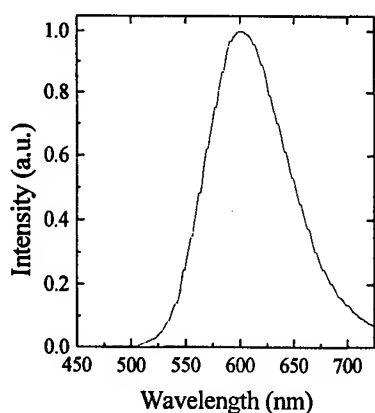


Fig. 3. Fluorescence spectrum of DCM:Alq:PVK film

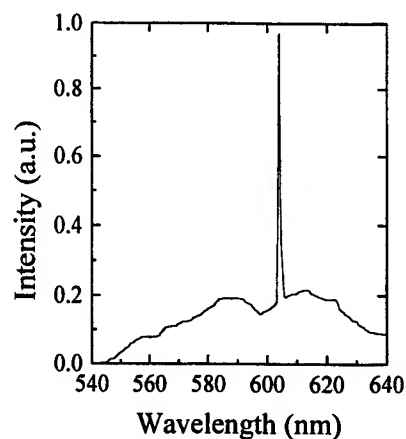


Fig.4 The lasing spectrum obtained from the surface emitting microcavity

3.2. Edge emitting device

The fluorescence and excitation spectra of the DCM/Alq film were achieved at a low excitation pulse energy of $0.1\mu\text{J}$, as shown in Fig.5. It was shown that the emission peak of the DCM/Alq film is located at about 620nm , which indicates that the emission of the DCM/Alq film results from that of the DCM molecules.

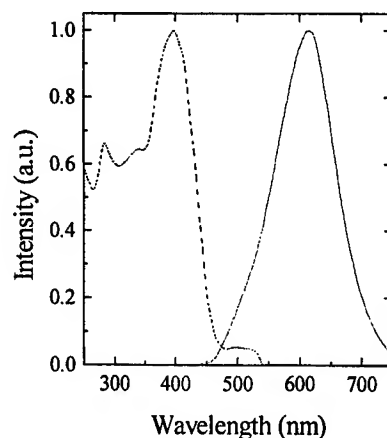


Fig.5 The Excitation (dash) and PL (line) spectra of the DCM/Alq film

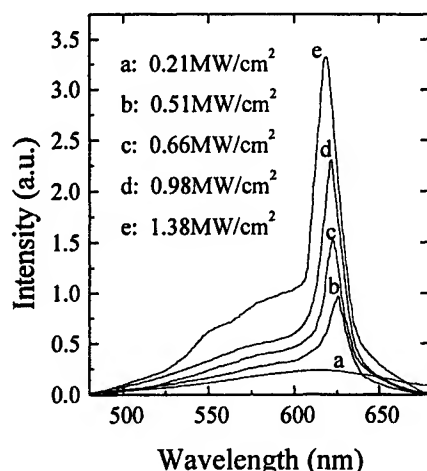


Fig.6 The edge emission spectra of the film of DCM/Alq at different excitation pulse intensity

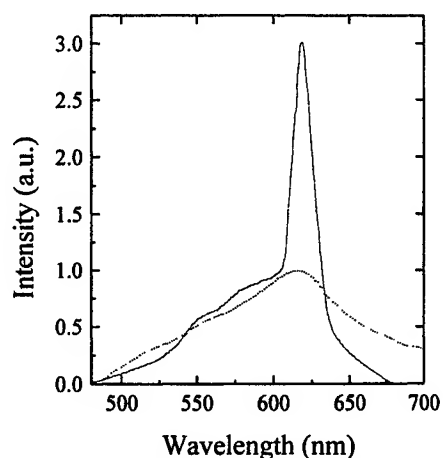


Fig.7 The edge emission (line) and surface emission (dash) spectra of the film of DCM/Alq at the excitation pulse intensity of 1.38 MW/cm^2 .

The emission spectra of the DCM/Alq film transversely pumped at different pulses intensities were illustrated in Fig.6. It shows that the emission spectrum of the sample comes from the spontaneous emission when pumped at a low excitation intensity. The peak at 618nm (curve b) became dominant at pump pulse intensity of 0.51 MW/cm^2 . Observing from the sides of the sample, a bright dot at the end of the pump stripe could be seen, which didn't exist at low excitation intensity. The spectra showed a dramatic narrowing when pump pulses intensity above this one. From the changes of the spectra detected at different pump energies, the excitation threshold intensity of gain narrowing was about 0.4 MW/cm^2 . At excitation pulse intensity of 1.38 MW/cm^2 , the spectrum was narrowed with the peak at 616nm, the FWHM of which was only 18nm. It was believed that the gain narrowing spectra illustrated in Fig.6 were due to the amplified spontaneous emission (ASE) guided in the blend film. The refractive indices of the substrate, the air and the film are 1.46, 1 and about 1.6, respectively. The refractive index of the film is greater than that of the surrounding media, so substrate/film/air actually constitutes an asymmetric planar waveguide. The emission light in accordance with waveguide modes can propagate in the film. During this process population inversion in the excitation area can be achieved if the pump pulses energy is high enough, then the spontaneous emission will be amplified along the stripe gain area. Consequently the spectrum will be enhanced and narrowed at the SE wavelength.

The emission spectrum of the DCM/Alq film detected from the film surface and from the edge at excitation pulse intensity of 1.38 MW/cm^2 is shown in Fig.7. The spectrum still exhibited the spontaneous emission properties when detected from the surface. So the spectral gain narrowing was observed only in the parallel direction of the film. This confirmed that the gain narrowing phenomenon shown in Fig.6 was due to the waveguided ASE in the film.

4. Conclusion

In conclusion, we have shown the optically pumped lasing phenomenon in DCM:Alq:PVK microcavity. The stimulated emission peak was located at the peak of 603nm with a linewidth of

0.6nm. The threshold pump intensity for lasing was estimated to be about 0.25MW/cm². A waveguide structure of quartz/DCM:Alq/air was employed for the edge emitting lasing. The change of the emission spectra showed a clear threshold action and gain narrowing phenomenon. The spectra narrowing observed is believed to be resulted from the ASE in the gain material.

Acknowledgements

This work was supported by National Natural Science Foundation of China and the Key Project of Chinese Academy of Sciences.

References

1. N. Tessler, G.J. Denton, R.H Friend, "Lasing from conjugated polymer microcavities", *Nature* **382**, pp. 695-697,1996.
2. F. Hide, M.A. Diaz-Garcia, B.J. Schwartz, M.R. Andersson, Q. Pei, and A.J. Heeger, "Semiconducting polymers: a new class of solid-state laser materials", *Science* **273**, pp.1833-1836,1996.
3. P.F. van Hutten, H.J. Brouwer,V.V. Krasnikov,T.A.Pham,R.E.Gill,and G.Hadziioannou, "Stimulated emission from films of conjugated polymers and oligomers", *SPIE* **3148**, pp.14-21,1997.
4. V.G. Kozlov,V. Bulovic,P.E.Burrows, and S.R. Forrest, "Laser action in organic semiconductor waveguide and double-heterostructure devices", *nature* **389**, pp.362-364,1997.
5. F. Hide, B. J. Schwartz, M. A. Diaz-Garcia, and A.J. Heeger, "Laser emissioon from sollutions and films containing semiconducting polymer and titanium dioxide nanocrystals", *Chem. Phys. Lett.* **256**, pp. 424-430, 1996.
6. R. Gupta, M. Stevenson, A. Dogariu, M.D. McGehee, J.Y. Park, V. Srdanov, A.J. Heeger, and H. Wang, "Low-threshold amplified spontaneous emission in blends of conjugated polymers", *Appl. Phys. Lett.* **73**, pp.3492-3494,1998.
7. S.V. Frolov, Z.V. Vardeny, and K. Yoshino, "Plastic microring lasers on fivers and wires", *Appl. Phys. Lett.* **72** , pp.1802-1804, 1998.
8. M.Berggren, A. Dodabalapur, and R.E. Slusher, " Stimulated emission and lasing in dye-doped organic thin films with Forster transfer", *Appl. Phys. Lett.* **71** , pp.2230-2232, 1997.
9. D. Moses, " High quantum efficiency luminescence from a conducting polymer in solution: a novel polymer laser dye" , *Appl. Phys. Lett.* **60** , pp.3215-3217, 1992.
10. G. Wegmann, H. Giessen, D. Hertel, and R.F. Mahrt, "Blue-green laser emission from a solid conjugated polymer", *Solid State Commun.* **104**, pp.759-762, 1997.
11. W. Holzer, A. Penzkofer, S.H. Hong, A. Bleyer, and D.D.C. Bradley, "Laser action in Poly(m-phenylenevinylene-co-2,5-diocetoxy-p-phenelenevinylene)", *Advanced Materials* **8**, pp. 974-977,1996.
12. S.V. Frolov, M. Ozaki, W. Gellermann, Z.V. Vardeny and K.Yoshino, "Mirrorless lasing in conducting polymer poly(2,5-diocetyloxy-p-phenylenevinylene) films", *Jpn.J.Appl.Phys.* **35** ,pp.L1371-L1373, 1996.
13. U. Lemmer, "Stimulated emission and lasing in conjugated polymers" , *Polym.Adv.Technol.* **9**, pp.476-487,1998.
14. V.G.Kozlov, G. Parthasarathy, P.E.Burrows, S.R. Forrest, Y. You and M.E. Thompson, "Optically pumped blue organic semiconductor lasers" *Appl. Phys. Lett.* **72** , pp.144-146, 1998.
15. V.G.Kozlov, V. Bulovic, and S.R. Forrest, "Temperature independent performance of organic semiconductor lasers", *Appl. Phys. Lett.* **71** , pp.2575-2577, 1997.

SESSION 2

MEMS

Improved silicon micromachined 3-D mirror for acceleration sensing using an extra-short external cavity laser self-mixing interferometer

Franck CHOLLET^a, LIU^a AiQun, ZHENG^b LuDi,
Anand ASUNDI^b and LIN^c LiWei

^aInstitute of Materials Research and Engineering (IMRE), Blk S7 lvl 3,
10 Kent Ridge Crescent, 119260 Singapore

^bNanyang Technological University (NTU), School of Mechanical and Production Engineering,
Nanyang drive, Singapore

^cUniversity of Michigan, Ann Arbor, MI, USA

ABSTRACT

We have designed a new type of folding suspended polysilicon micro-mirror, integrating a new type of precision position-lock (top lock), a new compact design for the hinges and a bi-directional electrostatic actuator to bias the position of the mirror. The mirror is intended to be used in a very short external cavity laser configuration ($\approx 10\mu\text{m}$) for acceleration/displacement sensing. An extensive theory has been build to guide the design and the fabrication of the sensor.

After probe assembly, the mirror has been actuated with a low-noise comb-drive actuator and the $\lambda/2$ range ($0.4\mu\text{m}$) required to bias optimally the external cavity laser, is obtained with a bit less than 10V, compatible with CMOS circuitry. The spring constant of the mirror suspension is about 0.38 N/m while the mass of the suspended mirror is slightly less than $2\mu\text{g}$, yielding a mechanical sensitivity to acceleration of about 50 nm/g.

Using the mirror in an external cavity configuration with a Fabry-Pérot laser diode at $0.8\mu\text{m}$ provides an intensity modulated signal with an expected displacement resolution of about 0.05 nm, limited by the mechanical structure. It will provide a sensitivity to acceleration in the μg range. We show theoretically that the linear range is about 3 orders of magnitude, but depends on the amount of light feedback in the laser cavity.

Keywords: optical MEMS, external cavity laser, ultra-short cavity, accelerometer

1. INTRODUCTION

Optical sensing of displacement, acceleration¹ or vibration² is an interesting application of microsystem technology. The existing product are mainly based on capacitive sensing of displacement, which require a state-of-the art electronics for the detection. In the other hand interferometric optical method may yield simple displacement detection by coding it in light intensity. An external cavity laser configuration, where the external mirror is movable, has shown here an advantage over standard arrangement by improving the displacement sensitivity. A massive device using this principle has shown a large linear range over about 5 orders of magnitude³ without feedback, a feat not attained by the capacitive detectors. This characteristic seems very interesting and calls to investigate the possibility to develop a rugged and compact version of the sensor using the MEMS technology.

A schematic of the basic structure is shown in Fig. 1. In order to obtain a simple device, we have chosen a silicon suspended flat mirror without external coupling optics. However, we will see that the sensitivity of the device is better with a stronger feedback, thus it needs a very short external cavity, where the diffraction loss will be small. Moreover the change of intensity induced by the displacement of the external mirror will be shown to present a periodicity of $\lambda_0/2$ and to posses a maximum in this range. Thus, to obtain the best sensitivity, the mirror should allow for

Further author information: (Send correspondence to F.C.)

F.C.: E-mail: fa-chollet@imre.org.sg

A.L.: E-mail: aq-liu@imre.org.sg

A.A.: E-mail: MASUNDI@ntu.edu.sg

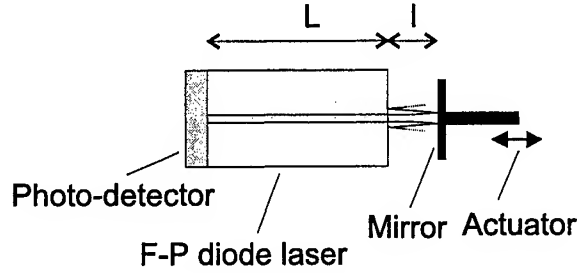


Figure 1. Schematic of an accelerometer based on an external cavity laser configuration. The mirror is suspended and the distance l change when an acceleration is applied to the support. The actuator applies a constant force to offset the position of the mirror to the laser facet.

an accurate displacement in a similar range. The standard mirror designs^{4,5} can not fulfil easily these targets. We have designed a new type of folding polysilicon mirror, integrating a new type of precision position-lock,⁴ the top lock, and a new compact hinge design⁶ to bring the mirror within $10 \mu\text{m}$ of the laser facet. Moreover, the mirror is integrated with a bi-directional electrostatic actuator to bias precisely its position, relaxing the constraint on the initial positioning of the diode laser.

2. SHORT-CAVITY COUPLED LASER ACCELEROMETER

2.1. Accelerometer

An accelerometer attached to an accelerating support is schematically represented in Fig. 2. The spring represents

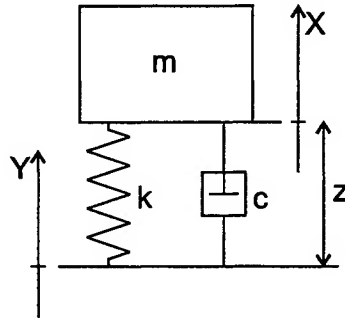


Figure 2. Mechanical schematic of an accelerometer attached to an accelerating support. Coordinate axes are in an inertial (non-accelerating) frame of reference.

the suspension of the mass linking the mass to the support while the dashpot includes all the damping forces existing in the system that are combined together using the principle of equivalent damping. We can then write the equation of motion of the mass as⁷:

$$m\ddot{x} = -c(\dot{x} - \dot{y}) - k(x - y), \quad (1)$$

where x and y are the displacement of the mass and the support with respect to an inertial reference frame. Introducing the relative displacement of the mass and the support $z = x - y$ we obtain the usual equation of motion, relating the acceleration of the support to the relative displacement between the mass and the support,

$$m\ddot{z} + c\dot{z} + kz = -m\ddot{y}. \quad (2)$$

Solving this equation for an harmonic excitation ($y = Y \sin(\omega t)$) we find the relationship between Z and the amplitude of acceleration $\ddot{Y} = \omega^2 Y$ given by:

$$Z = \frac{\ddot{Y}}{\sqrt{(\omega_0^2 - \omega^2)^2 + (\frac{\omega_0 \omega}{Q})^2}}, \quad (3)$$

where $\omega_0 = \sqrt{k/m}$ is the resonance frequency of the undamped system and $Q = m\omega_0/c$ the quality factor. When the system is used as an accelerometer we operate it at $\omega \ll \omega_0$ and we have

$$Z \approx \ddot{Y}/\omega_0^2. \quad (4)$$

We see that if we can measure Z we will know the acceleration of the support. Moreover this equation reveals that a trade-off exists, and a large sensitivity will be obtained at the expense of a small bandwidth. For a resonant frequency of 2 kHz, the mechanical sensitivity is about 62 nm/g, while if it is 1 kHz it increase four time to 250 nm/g. Studying the denominator appearing in eq. 3 it may be seen that for a linearity of about 1% the frequency range of an undamped system ($Q \approx \infty$) is about $0.1\omega_0$. However, for $Q \approx 0.75$ it may be increased above $0.5\omega_0$. The last important parameter that sets the ultimate sensitivity of the accelerometer is the thermo-mechanical noise. It is easily obtained by considering the mechanical-electrical analogy, where the dampers are replaced by an equivalent resistor and are the source of thermal noise.⁸ When $\omega \ll \omega_0$, the equivalent displacement density, $x_n(\Delta f)$, is given by

$$\|x_n(\Delta f)\| = \sqrt{\frac{4kT}{\omega_0 k Q}}, \quad (5)$$

where k is the Boltzmann constant, and T the absolute temperature. It can be seen that an increase of the spring constant or of the resonant frequency decreases the noise but also lowers the sensitivity. Moreover we observe here another trade-off, existing between a constant response in a large band of frequency ($Q \approx 0.75$) and a small thermo-mechanical noise ($Q \gg 1$). Still, increasing the resonance frequency will have a beneficial effect for this two parameters... but will decrease the sensitivity. For example, with a resonance frequency of 2 kHz, a spring constant of 0.15 N/m (or a mass of about 1 μ g) and a Q-factor of 5, we found a random displacement due to the thermal noise of about 1 pm/ $\sqrt{\text{Hz}}$ or 10^{-3} nm/ $\sqrt{\text{Hz}}$. Whatever could be the sensitivity of the optical detection, this value sets the resolution of the sensor to a value larger than about 0.01 nm (in a 10Hz band).

2.2. Laser coupled with an external short-cavity

The power delivered by a Fabry-Pérot semiconductor laser with the supplied current I is given by⁹

$$P = \eta_{ext} \frac{h\nu}{e} (I - I_{th}), \quad (6)$$

where η_{ext} is the external quantum efficiency of the laser above threshold and I_{th} the threshold current. Interestingly, this current changes with the reflectivity of the mirror facets according to

$$I_{th} = \frac{LW}{\beta} \left(\alpha + \frac{1}{2L} \ln \frac{1}{R_1 R_e} \right), \quad (7)$$

where LW is the junction area, R_1 and R_e are the power reflection coefficient at the laser facet, α the loss per unit length due to attenuation in the cavity and β the proportionality constant relating the gain in the cavity with the density of current in the junction. Typical values for these two parameters depend heavily on the material and the structure used for the laser. For GaAs double heterostructure laser they are about 1500 m^{-1} and $1.5 \cdot 10^{-4} \text{ m/A}$, respectively. Moreover the external efficiency (ie, the average number of photon generated for each electron-hole pair created in the junction that exits the laser) depends also on the mirror reflectivity,

$$\eta_{ext} = \eta_{int} \frac{\frac{1}{2L} \ln \frac{1}{R_1 R_e}}{\alpha + \frac{1}{2L} \ln \frac{1}{R_1 R_e}}, \quad (8)$$

with η_{int} the internal quantum efficiency exceeding 90% for the double heterostructure GaAs laser.

The presence of the external mirror can be accounted for by computing its effective reflectivity at the laser facet. We write the reflected field as the summation of all the field contributions reflected back into the active region of the photodiode. We have,³

$$\rho_e = \rho_2 - \frac{1 - R_2}{\rho_2} \sum_{n=1}^{\infty} C_n \left(-\rho_2 \rho_m \exp \left(j \frac{4\pi l}{\lambda} \right) \right)^n, \quad (9)$$

where ρ_2 ($R_2 = \|\rho_2\|^2 = 0.31$) and $\rho_m = \sqrt{0.97}$ are the complex reflectivities of the laser facet and the gold coated external mirror, respectively, C_n is the coupling factor at the n th reflection of the light on the mirror, taking into account beam diffraction and coupling with the laser aperture. There is no general analytic expression for this factor, because it is a general problem of diffraction and coupling from a mode with a complex transverse expression. However we may derive an approximate formula using classic diffraction theory by considering an elliptical Gaussian mode shape coupled back through a planar reflector. The distance between the laser facet and the mirror is the parameter that will set the applicability of Fresnel or Fraunhofer diffraction theory. The rule of thumb places the limit of near field when $d < a^2/\lambda$, where a is the largest dimension of the 'aperture' (ie, the laser spot at the facet) and d the distance between aperture and the plane of interest. For $\lambda_0 \approx 0.8\mu\text{m}$, and a typical lateral dimension of the laser mode at the output facet of about $2\mu\text{m}$, we found that Fraunhofer diffraction applies for l greater than $2.5\mu\text{m}$. This external cavity length will already be difficult to achieve with our technology and we may use Fraunhofer diffraction for our computation. However for large mode laser, the mode size may attain $4\mu\text{m}$ setting the limit on l at $10\mu\text{m}$, and thus may require the use of Fresnel diffraction for the coupling from the first reflexion. Subsequent reflexion will certainly fall in the case where Fraunhofer diffraction may be applied. In this case we have¹⁰

$$D_n = \frac{\pi}{4} \left(\frac{ab}{\lambda nl} \right), \quad (10)$$

where a and b are the transverse dimension ($1/e$) of the laser spot.

However this coupling coefficient considers only the effects of diffraction and neglects any angular misalignment, θ , that may exist between the mirror and the laser output facet. A very rough approximation of this effect may be obtained by considering that the mode profile have a Gaussian profile. Then, we can derive a formula using a similar formalism to the case of fiber* to fiber coupling¹² and after some algebra and simplification, allowed by the assumed small value of $\theta < 10^\circ$, we obtain,

$$\Gamma_n = \exp \left(-k_0^2 ab \frac{2(nl)^2 + k_0^2 a^2 b^2}{(nl)^2 + k_0^2 a^2 b^2} (n\theta)^2 \right), \quad (11)$$

where $k_0 = 2\pi/\lambda_0$ is the wave vector. We may note that the effect of the angular misalignment should be small if it remains much smaller than the far field Gaussian diffraction angles ($\lambda_0/\pi a$ and $\lambda_0/\pi b$).

Finally, in order to take into account the diffraction loss and the angular misalignment loss to compute the effective reflectivity, we have to take the product of the two individual effects, yielding the coupling factor that appears in Eq. 9,

$$C_n = D_n \cdot \Gamma_n. \quad (12)$$

Then, using eqs. (6-12), we plot in Fig. 3 the theoretical power output of the laser when the length of the external cavity is varied from $5\mu\text{m}$ to $45\mu\text{m}$. The sum appearing in eq. (9) is stopped when the term to be summed (ie, the feedback) is lower than 10^{-5} . We see that with a decreasing level of feedback (ie, an increasing length of the external cavity) the amplitude of the power variation decreases quickly, and simultaneously the slope of the curve decreases. Actually, this slope, representing the rate of change of the laser diode power with the external mirror displacement, is the optical sensitivity of the sensor. To obtain a better understanding of this factor we have plotted it in Fig. 4. The envelope of the sensitivity is decreasing rapidly with increasing cavity length. For example, a sensor with an external cavity length of $10\mu\text{m}$ is four time more sensitive than one with an external cavity length of $40\mu\text{m}$. By setting, somewhat arbitrarily[†], the minimum resolution of the intensity detector to about $2.5\mu\text{W}$, we find the resolution of the sensor to be 0.05 nm when the cavity length is about $10\mu\text{m}$. If the cavity length is larger the resolution will be smaller. We note that the sensitivity is a periodic function of the displacement, with a period of $\lambda_0/2$, which is more visible on the enlarged view in Fig. 5. This sets the practical range of micro-actuation for the mirror to a minimum value of about $\lambda_0/2$ to obtain a large sensitivity, considering that the laser diode may be placed at an arbitrary position. We show also in Fig. 5 the effect of tilting the mirror. We see that when the angle is increased the sensitivity drops and the curve becomes more and more sinusoidal. This may be understood is we look at the rank

*The fiber fundamental modes are not Gaussian either, but the model¹¹ used to describe their coupling losses also makes use of such approximation.

[†]The prediction of this value necessitates the investigation of the noise existing in the whole system, either using synchronous or direct detection, which is beyond the scope of this early paper.

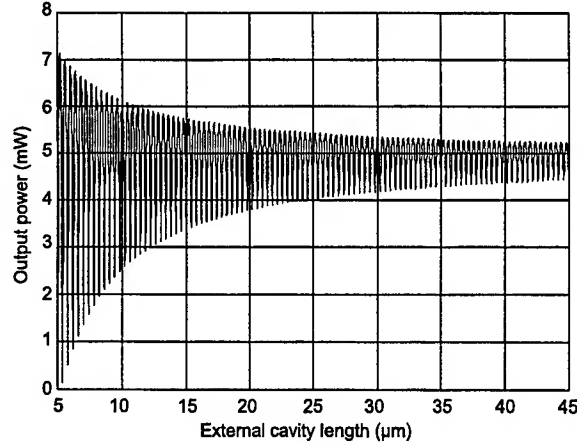


Figure 3. Theoretical output power of the external cavity laser for different external cavity length.

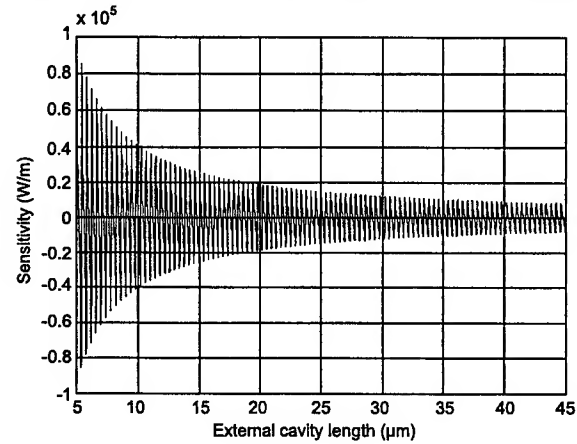


Figure 4. Theoretical sensor's optical sensitivity for different external cavity length.

where we stop the summation for the calculation of ρ_e in eq. (9). When the angle is 0° , the summation needs 727 terms before coming to a term lower than 10^{-5} , but, when the angle is 8° only 3 terms are needed. Thus as many more harmonics are added in the first case, the result is a non-regular function while in the latter case it is almost a sinusoidal function. Still it seems that the tolerance toward angular misalignment is not very bad and an accuracy of about 0.5° (9 mrad) will maintain adequate performance. It should be noted that when the length of the cavity is increased a similar effect appears, and the power fluctuation tends to be sinusoidal. The Figure 5 also shows that to maintain the sensitivity within 1% of the nominal value the displacement around the rest position should be in the order of 15 nm for a very strong feedback (highly non linear curve), but may be almost 100 nm if we accept the decrease by a factor of 6 in the sensitivity. In the first case, and considering the resolution of the sensor obtained previously, it means that the dynamic range of the sensor is about 3 order of magnitude while in the later case it is four order of magnitude. Obviously, a force feedback could enhance dramatically this figure, by at least one order of magnitude.

These simulations have provided us with an insight in the internal behaviour of the sensor, and have allowed us to extract most of the magnitude of the relevant physical parameters, allowing the fabrication.

3. MICROMACHINED EXTERNAL CAVITY MIRROR

The mirror has been fabricated using a standard micro-fabrication process, using two structural layers of polysilicon, a gold overcoat, one ground plane and two sacrificial layers of SiO_2 . Figure 6 is a general view of the mirror with

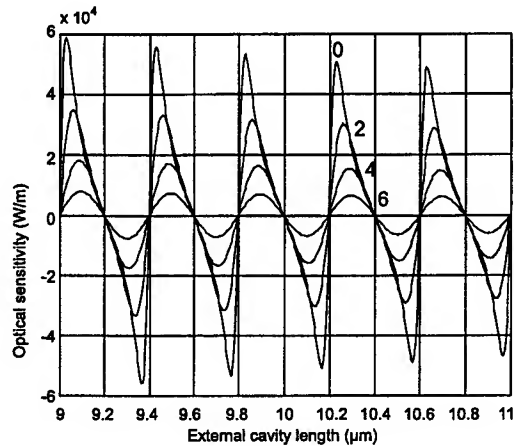


Figure 5. Theoretical sensor's optical sensitivity for the external cavity length around $10\mu\text{m}$. The parameter is the tilt angle of the external mirror in degree.

one of the precision lock engaged and the other still free. We can see the bi-directional actuator, at the rear, and the mirror suspension made of four folded-beam springs.

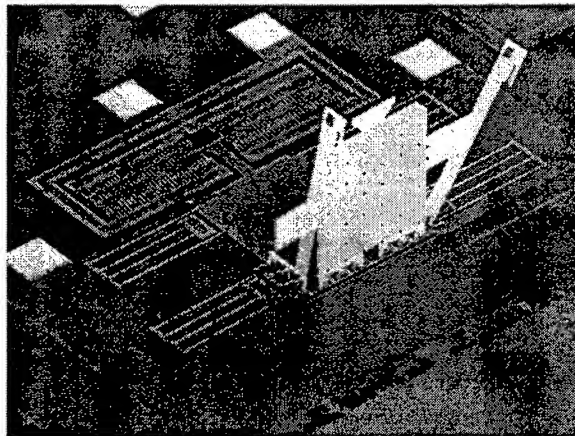


Figure 6. General view of the assembled 3D-mirror.

3.1. A 3D mirror

The structure is patterned in a stack of different layer and then is folded to its 3D shape with micro-probes under a microscope. The process layout rules limit the designer in his wishes and push him to find innovative, and sometimes involved, solution to satisfy the requisite of the design. The necessity to bring the mirror within $10\mu\text{m}$ of the laser facet (cf. Sect. 2.2) has necessitated the development of a new type of hinge, where, in contrast to the previously developed hinge,⁶ the beams used to constrain the axis (ie, the staple) are cantilevered and attached only on one side of the mirror. A close-up of the designed hinge is shown in Fig. 7. We can see that the distance between the plane of the mirror and the edge of the suspended structure is less than $10\mu\text{m}$, insuring the positioning of the laser diode without mechanical interference. It turns out that, in general, the microfabricated hinge behaviour is somewhat different from their macroscopic counterpart. In short, the centre of the axle is *not* the axis of rotation. Firstly, the axle doesn't have a round crosssection but, because of the anisotropic RIE etching, a square one. Thus it can not rotate freely in the staple but merely rotate around its edge, then, when the angle exceed 90° the axis of rotation needs to shift from one edge to the opposite. Secondly, in the case of a suspended hinge, the edges in question are *not* those of the axle, but those of the plate protruding over the two sides of the hinge. The existence

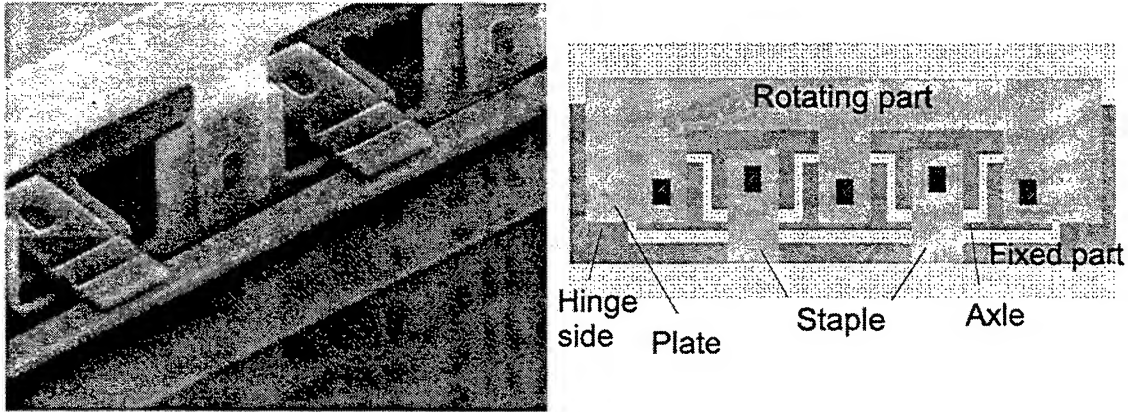


Figure 7. Close-up on the suspended hinge of the mirror and its typical layout.

of this pair of constraining structure (axle with staple constrain displacement upward, and plate with hinge side constrain displacement downward) is the result of the use of only two layers of structural material, where three are theoretically needed: we use a scissor arrangement.⁶ Thus a large friction at some special angle occurs that holds the rotating structure, as can be seen in the Fig. 6. This behaviour is not always a problem and may even be helpful. For example, when the axle is rotated 90° and the protruding plate rests on the hinge side, the rotated mirror stays erected, facilitating the engagement of the precision lock used to maintain it in place. An added advantage of the cantilevered staple, in the case of the suspended hinge we developed, is that it is more tolerant to misalignment between mask layers because it may slightly bend in the vertical direction during the rotation of the axle.

The precision lock on the side of the folded structure⁴ have been introduced to replace the initial spring lock⁶ that was much more clever but not accurate enough for most optical elements positioning. We found that the precision of positioning obtained with these lock would be greatly improved if instead of constraining the folded structure at its *side*, at about half the height of the plate, we constrained the *top* of the plate. Obviously for the same fabrication tolerance and clearance the incertitude angle is divided by two compared to the usual design. Figure 8 shows a close-up of the engaged lock positioning the folded mirror. Moreover, they have been designed in order that they do not protrude more than $10\text{ }\mu\text{m}$ from the mirror plane. The locking structure has been featured with dimples to define

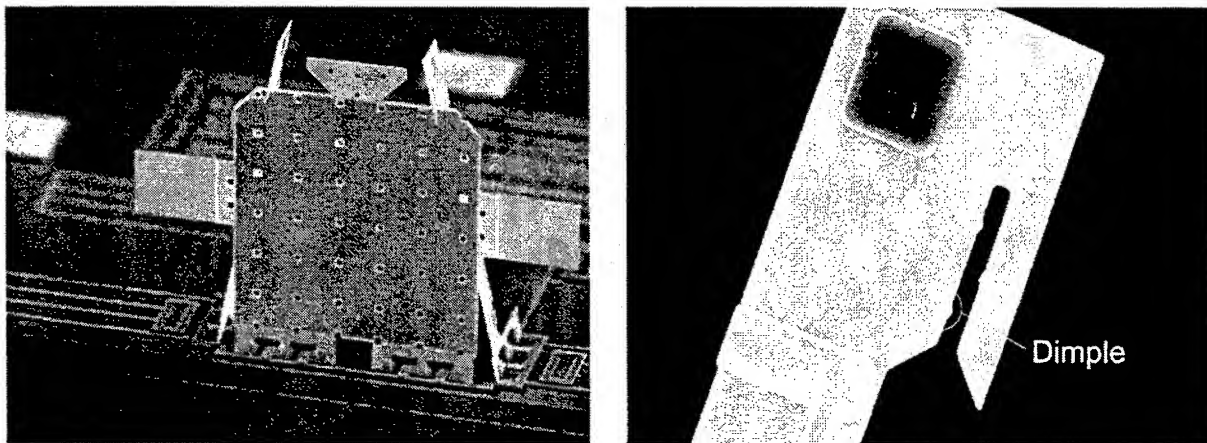


Figure 8. Close-up on the precision lock on top of the mirror with an enlargement of a locking structure (we can see the embossed shape of the spring in the plate that has a stiffening effect).

precisely the contact points with the mirror plate leaving a clearance of about $0.5\text{ }\mu\text{m}$ on each side of the mirror plate. Including the clearance at the hinge $\approx 0.75\text{ }\mu\text{m}$, corresponding to the thickness of the second sacrificial layer, we estimate the maximum error of angle than can be expected with this structure to about $\sin^{-1}((0.75 + 0.5)/300) \approx 4$

mrad (0.23°). This figure match the 9 mrad criterium established in Sect.2.2. Considering the current set of layout rules it seems that a completely passive alignment structure insuring a precision of about 1 mrad is an interesting challenge, that may be attained, for example, by increasing the height of the mirror to 1 mm, provided the gradient of stress in the deposited layer is well controlled.

3.2. A reflecting mirror

As we have seen in Sect. 2 we need a large effective reflectivity from the mirror to obtain the largest sensitivity to displacement. However, as we have seen in sect. 3.1, the estimated accuracy for the tilt of the mirror is about 4 mrad, without taking into account the possibility for the top lock to shift lateraly when it is folded up. Thus, the uncertainty in the tilt angle seems to be smaller than the maximum error allowed for the laser operation in a strong feedback configuration as estimated in Sect. 2.2. Still, owing to the crudeness of the model, we need a more accurate model to rule out with confidence a wide distribution of efficiency in the optical feedback arising from the actual value of the tilt angle.

Beside the tilt angle, there are other important factors that affect significantly the effective reflectivity of the mirror : the wavelength, the reflectivity of the mirror coating, the planarity and the roughness of the surface... The reflectivity of gold is still 97% at $\lambda_0 = 0.8\mu\text{m}$, but drops rapidly to 40% at $0.5\mu\text{m}$. If we plan to use a shorter wavelength laser (which would increase the optical sensitivity) we may think to us Ag as an alternative coating, provided it may sustain the hydrofluoric acid used during the release step of the structure. The Table 1 sums-up the measurement made on different architecture of mirror for the parameters affecting the reflectivity.

Mirror type	Radius of curvature ρ (mm)	Roughness RMS (Å)	Reflectance $ \rho_m ^2$ (Theoretical)	Transmittance (Theoretical)
3.5 μm thick poly with 0.5 μm Au	22	23	0.97	0.00
1.5 μm thick poly with 0.5 μm Au	1.9	26	0.97	0.00
2.0 μm thick poly	∞	35	0.35	0.01
1.5 μm thick poly	∞	32	0.35	0.03

Table 1. Measured radius of curvature and surface roughness of different mirror design with calculated reflectance and transmittance at $0.8\mu\text{m}$ for a perfect plane of specified thickness and material (neglecting interference effects).

The curvature of the mirror is due to the gradient of stress along its thickness because it is composed of different materials. It is important to maintain it as low as possible because it is related to a local tilt θ of the mirror by

$$\theta \approx \frac{x}{\rho}, \quad (13)$$

where x is the abscissa from the mirror centre (ie, where $\theta = 0$) and ρ is the radius of curvature. It should be noted that a bias tilt, resulting from the play in the hinge-lock structure or a tilt of the laser, will add algebraically with the local tilt resulting from curvature, moving the 'no tilt' spot on the mirror away from the centre ($x = 0$) to an arbitrary position ($x \neq 0$). Thus, aligning the reflection of the laser beam on the mirror at this exact spot will complicate substantially the assembly of the structure even if it would provide the strongest feedback. Finally, it may be thought to use the stress-induced curvature in order to obtain a cheap converging mirror, however the difficulty to control stress in the deposited layer (the manufacturer gives a range of 0-40 MPa tensile stress for the metal and 0-20 MPa compressive stress for the poly-Si...) makes it an unpractical solution. To increase further the radius of curvature of the mirror while taking benefit of a gold overcoat, it has been proposed to stiffen even more the mirror by leaving the sacrificial oxide layer between the two polysilicon layers. We are now investigating another approach which consists in creating a deep undulation at the edge of the mirror to act as a stiffener. The first results are quite interesting and it seems that we are able to obtain a radius of curvature of several cm with a plate of $1.5\mu\text{m}$ thick poly with a gold coating.

The roughness of the surface is very low (we have $R_{\text{RMS}} < \lambda_0/200$ and $R_t < \lambda_0/50$) and the reflectivity won't be affected significantly by this figure. It is an interesting point of the folded micro-mirror compared to an etched mirror. In our case, the surface of the mirror is controlled by the conformal deposition of layer onto an atomically flat substrate and not by an etching mechanism, which generally yield a rougher surface.¹³ When the radius of the

spot reflecting on the mirror exceed about $45 \mu\text{m}$, the effective reflectivity should take into account the existence of the hole used for the release process. They decrease the effective surface of the mirror and for a wide beam only 98.5% of the reflective surface will be gold coated, decreasing the reflectivity accordingly.

3.3. An actuated mirror

Section 2.2 has shown that the actuator should allow a range of about $\lambda_0/4$ to bring the mirror at the position where the sensitivity is the highest. However, the noise inherent to any power supply should not induce a motion larger than the signal to be detected!

Having chosen a folded-beam type of suspension, simple beam theory¹⁴ yields

$$k = \frac{8Ehw^3}{L_1^3 + L_2^3}, \quad (14)$$

for the spring constant of the the four springs suspension. E is the Young's modulus (170 GPa for the polysilicon), h the thickness of the layer ($2 \mu\text{m}$), w the width of the beam and $L_1 = 290 \mu\text{m}$ and $L_2 = 235 \mu\text{m}$ the length of the beams composing the elementary spring, yielding $k = 0.58 \text{ N/m}$ for $2 \mu\text{m}$ -wide beam. To obtain a resonant frequency between 2 and 3 kHz, the mass of the mirror has to be between 1.6 and $3.6 \mu\text{g}$.

The force delivered by the actuator is given approximately by¹⁵

$$F = N\epsilon_0 \frac{h}{g} V^2, \quad (15)$$

where $N = 59$ is the number of finger in the actuator, g is the air gap between the finger and V the applied voltage. Using this two parameters, we define the deflection constant a as

$$a = N\epsilon_0 \frac{h}{gk}, \quad (16)$$

yielding the simple relationship between voltage and displacement $x = aV^2$.

We have characterized the actuator and the mirror both in DC and AC for two types of mirror A and B with the same layout but fabricated on different wafer. They are chosen to represent the two extremes characteristics that were found on a batch of 7 wafers. Table 2 summarizes the main results. Using the layout dimension, measured

Mirror type		DC	AC	
	Beam width (μm)	Deflection constant ($\mu\text{m}/V^2$)	ω_0 (rad/s)	Q
A	2.0	$1.43 \cdot 10^{-3}$	17090 (2720 Hz)	4.8
B	1.75	$2.22 \cdot 10^{-3}$	13820 (2200 Hz)	4.5

Table 2. AC and DC experimental characteristics of the actuator for the assembled mirror.

layer thickness and assumed material density we computed the mass of the suspended mirror to be $1.95 \mu\text{g}$. We were able to check to some extent the validity of this value by measuring the resonant frequency of the mirror when the golded plate was present (and folded) and when it was removed. The resonant frequency changed by a factor of 1.72 corresponding to a change of mass by a factor of 2.9. This value compare well with the theoretical drop of mass from $1.95 \mu\text{g}$ to $0.69 \mu\text{g}$ corresponding to a factor of 2.8. We understand here the interest of using a gold mirror, the large density of the material (19.3 kg/m^3) yielding a substantial weight advantage. We also measured the Q factor when the mirror was assembled and when it was folded, but the difference was within the estimated margin of error and was not significant. It seems that the Couette's flow under the horizontal plate is the dominant loss factor, even if it seems that unfolding the mirror should result in increased air drag, decreasing the Q factor of the system.

The discrepancy between the two type of fabricated mirror with the same layout may be understood if we look at the 'Beam width' column in Tab. 2. We measured the actual width of beams that were $2 \mu\text{m}$ wide in the layout and found a quite large difference as reported. The action of this narrowing of the beam is twofold: on the one hand it decreases the spring constant of the suspension and on the other it decreases the electrostatic force of the

Beam Width (μm)	Analytical		IntelliCAD TM	
	Spring constant (N/m)	Deflection constant ($\mu\text{m}/\text{V}^2$)	Spring constant (N/m)	Deflection constant ($\mu\text{m}/\text{V}^2$)
2.0	0.58	$0.90 \cdot 10^{-3}$	0.59	$1.54 \cdot 10^{-3}$
1.75	0.38	$1.22 \cdot 10^{-3}$	0.39	$2.08 \cdot 10^{-3}$

Table 3. Theoretical characteristics of the actuator.

actuator by enlarging the gap. We have summarized in Tab. 3 the main point of the analysis using analytical formula and simulation using IntelliCADTM. We note that if the finite element analysis is pointless for determining the spring constant [†], the analysis of the electrostatic force using analytical formulation suffers from a systematic underestimation. The IntelliCADTM simulated value of the deflection constant differs by less than 7% with the experimental values, validating the model and the design of the actuator.

Thus to achieve the $0.4 \mu\text{m}$ displacement with the bi-directional actuator, it needs a voltage of less than 10 V, compatible with standard CMOS circuitry. As we have $\Delta x = 2 a V_0 \Delta V$, to observe a displacement due to the voltage noise of the power supply of the same order than the thermal noise displacement (0.01 nm) we need to keep the voltage noise below 0.35 mV for the largest offset voltage of 10V. In the worse case (ie, $V_0 = 10 \text{ V}$), a noise of 1 mV will induce a displacement of less than 0.03 nm, about half the expected resolution of 0.05 nm. We may reduce the sensitivity of the actuator to noise by lowering further the size of the comb-drive. Actually, the deflection constant a increase linearly with the number of fingers, N , while the offset voltage is divided by the square root of N . Thus the proportionality constant between noise and displacement changes as the square root of N . Dividing the actuator size by 4 will decrease the sensitivity to noise by a factor of 2, but also increase the offset voltage by the same factor.

4. CONCLUSION

We have presented a micro-actuated mirror that will be used in an external cavity configuration as an acceleration sensor. We have developed an extensive theory to predict his behaviour and proposed a new layout to fulfill its stringent requirements. The fabricated mirrors have been extensively characterized and were shown to behave essentially as predicted. We were able to explain a relatively wide dispersion of the experimental characteristics by taking into account the real width of the narrow beam used for the actuator and for the suspension.

The next phase of the project currently under way is the integration of the mirror with the LD at $0.8 \mu\text{m}$. The first results are encouraging, showing a sensitivity better than 1 nm but a more controlled environment is needed to increase the stability of the system. We expect a sensitivity of at least 0.05 nm, yielding accelerometer with a sensitivity better than 1 mg and with a dynamic (at 1% linearity) of about 10^3 to 10^4 . Future version will use smaller spring constant to increase the sensitivity while the integrated actuator will be used to provide a force feedback, extending substantially the dynamic of the sensor.

ACKNOWLEDGMENTS

We want to thanks Jr-Hung Taylor Tsai and the staff at Michigan University for merging efficiently the layout files and for the nice sub-dicing. The staff at the MicroMachine Laboratory (MML), Nanyang Technological University, is also acknowledged for his help during testing.

REFERENCES

1. F. Chollet, X. Tang, Y. Ha, A. Liu, L. Zheng, M. Li, and A. Asundi, "Surface micromachined shutter and low-voltage electronics for displacement/acceleration optical sensing," in *Proc. Transducer's 99*, pp. 1526-1529, IEEE, 7-10 June 1999.
2. C. Gorecki, F. Chollet, H. Kawakatsu, and H. Fujita, "Silicon-based integrated interferometer with phase modulation driven by surface acoustic waves," *Optics Letters* **22**(23), pp. 1784-1786, 1997.

[†]For our simple structure, the resonant frequency reveals also a difference of about 1% between the FEM simulation and the analytical formulation using the Rayleigh method.

3. R. Miles, A. Dandridge, A. Tveten, and T. Giallorenzi, "An external cavity diode laser sensor," *J. of Lightw. Technol.* **1**, pp. 81-93, 1983.
4. L. Lin, S. Lee, K. Pister, and M. Wu, "Micro-machined three-dimensional micro-optics for integrated free-space optical system," *IEEE Photon. Technol. Lett.* **6**, pp. 1445-1447, 1994.
5. M. Kiang, O. Solgaard, and R. Muller, "Silicon-micromachined micromirrors with integrated high-precision actuators for external-cavity semiconductor lasers," *IEEE Photon. Technol. Lett.* **8**, pp. 95-97, 1996.
6. K. Pister, M. Judy, S. Burgett, and R. Fearing, "Microfabricated hinges," *Sens. and Actuat. A* **33**, pp. 249-256, 1992.
7. W. Thomson and M. Dahleh, *Theory of Vibration with Applications*, ch. 3, pp. 74-81. Prentice-Hall, London, 5th ed., 1998.
8. T. Gabrielson, "Mechanical-thermal noise in micromachined acoustic and vibration sensors," *IEEE Trans. on Electron Dev.* **40**, pp. 903-909, 1993.
9. C. Chen, *Elements of Optoelectronics & Fibre Optics*, ch. 4, pp. 231-250. Irwin, Chicago, 1996.
10. L. Coldren and T. Koch, "External-cavity laser design," *J. of Lightw. Technol.* **2**, pp. 1045-1051, 1984.
11. S. Nemoto and T. Makimoto, "Analysis of splice loss in single-mode fibres using a gaussian field approximation," *Optical and Quant. Electron.* **11**, pp. 447-457, 1979.
12. C. Miller, *Optical Fiber Splices and Connectors*, ch. 4, p. 143. Marcel Dekker, New-York, 1986.
13. C. Marxer, C. Thio, M.-A. Grétilat, N. de Rooij, R. Bättig, O. Anthamatten, B. Valk, and P. Vogel, "Vertical mirrors fabricated by deep reactive ion etching for fiber-optic switching applications," *J. of Microelectromech. Syst.* **6**, pp. 277-285, 1997.
14. W. Jones, *Roark's Formulas for Stress & Strain*, ch. 7, p. 100. Mc Graw-Hill, Singapore, 6th ed., 1989.
15. W. Tang, T. Nguyen, and R. Howe, "Laterally driven polysilicon resonant microstructures," *Sens. and Actuat.* **20**, pp. 25-32, 1989.

Modeling of the optical torsion micromirror

X. M. Zhang^a, F. S. Chau^a, C. Quan^a and A. Q. Liu^b

^aDepartment of Mechanical and Production Engineering,
National University of Singapore, 10 Kent Ridge Crescent, Singapore 119260

^bMEMS Technology, Institute of Materials Research and Engineering (IMRE),
Block S7 level 3, National University of Singapore, Singapore 119260

ABSTRACT

Torsion micromirror devices have been widely used in many applications. This paper describes the modeling of a torsion beam micromirror based on the parallel plate capacitor model. First, a generalized and normalized equation that governs the static characteristics of the torsion micromirror device is derived. Henceforth the influence of the structural parameters of micromirror is discussed, and the snap-down effect and the capacitance variation of the micromirror are studied. Finally, a micromirror is designed and fabricated. However, the model has not yet been verified by experiment data as testing is in progress.

Keywords: Micromirror, Micro-optics, MEMS, Torsion beam, snap-down, MOEMS.

1. INTRODUCTION

With the development of micromachining techniques, micromirror devices have thrived and are now widely used. In recent years, various micromirror devices have been developed; they differ in structure, shape, material, machining, actuating and so on. They can be simply classified based on the type of support and movement, such as torsion beam micromirror, movable micromirror¹, flexure beam micromirror² and vertical-support beam micromirror³, etc. Compared with the other types, the torsion beam micromirror seems to be easy to fabricate and hence is used in many applications, for example, barcode reading systems, reading head for CD players, laser printers⁴, spatial light modulator^{5, 6}, optical switches⁷, and especially, digital projection displays⁸⁻¹².

For a torsion micromirror, the important parameters include its geometric dimension, its maximal rotation angle, its actuation curve (that shows the relation between the driving voltage and its angular deformation), reflection efficiency, and fill-factor (only for micromirror array, represents the ratio of the effective reflection area to the whole area). Generally, the maximum rotation angle and the actuation curve are among the aspects of most interest since a large rotation angle is critical for many applications. For instance, in digital projection display, the micromirror needs to be driven to rotate about 10 degrees⁸, and in optical switches, the maximum angle can be up to 45 degrees⁷. To be compatible with IC convention and to prevent electrical breakdown, the maximum driving voltage cannot be too high; it is generally less than 30V, typically less than 5V. Thus for a micromirror array integrated with some control circuits, it can directly use the power source of the integrated circuits if its driving voltage is not greater than 5V, resulting in a simpler design.

The electrostatic actuation of the torsion micromirror has been extensively studied in the literature, and several methods have been employed. One method is based on the parallel plate capacitor model to estimate the electrostatic torque between the micromirror surface and the electrodes, and then to use the elastic restoring torque caused by the beam torsion to reach equilibrium^{3, 6, 13, 14}. In addition, full finite element models have also been studied^{4, 15}. The first method, although simple, gives low accuracy. On the contrary, the FEM method is relatively accurate, but involves a large amount of calculation.

Many researchers have simplified and specialize parallel-plate model further for analysis convenience. For example, Degani et al¹³ studied specially the snap-down effect of the torsion micromirror by Taylor expansion, and Wetsel et al¹⁴ assumed the maximal rotation angle to be small in their works. In addition, the electrode size was assumed the same as that of the micromirror in some papers to simplify their analyses and results. However, in actual fact, the electrode cannot fully coincide with the micromirror, for example, the two electrodes under the micromirror should be separated by a gap for fear of electrical breakdown and unnecessary connection. Moreover, the electrode parameters greatly influence the micromirror behaviors as a result of the snap-down effect, as is shown later in this paper. Therefore, the electrode dimension should be taken into account in modeling. Under these circumstances, it has become significant to develop a generalized and normalized

equation, which represents the relation between the dimensions, the driving voltage, and the micromirror angular displacement.

In this paper, we take advantage of the parallel-plate model (due to its simplicity) to give out a generalized and normalized equation, to derive the relation between the driving voltage and the rotation angle (static characteristic). Subsequently, we discuss special topics such as the snap-down effect and the capacitance variation of the micromirror. Finally we describe the design and fabrication of a micromirror. However, no experiment data will be presented since the testing has not been completed up to now.

2. MODELING

In this section, the electrostatic torque is studied based on the parallel plate model; the equation governing the micromirror rotation is derived and discussed in detail. Finally, the results of the study of the snap-down effect and the capacitance variation are given.

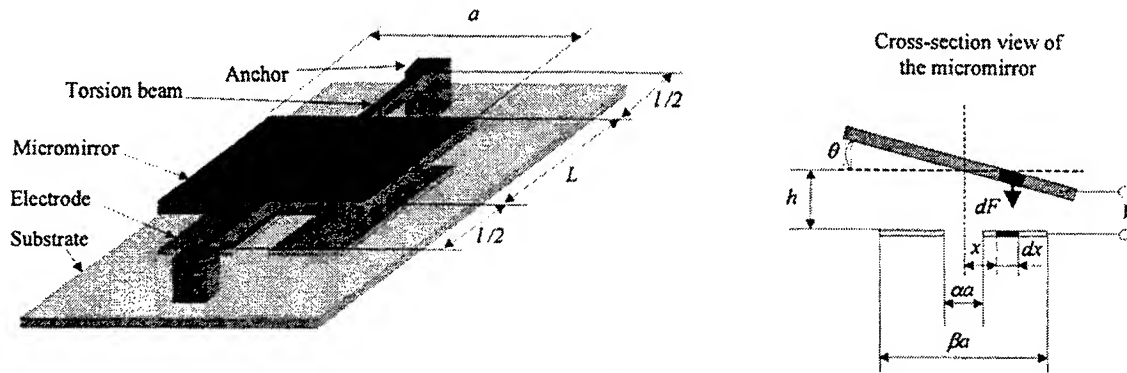


Fig. 1 Schematic diagram of the torsion micromirror

2.1 Electrostatic torque

Fig. 1 shows a schematic diagram of the torsion micromirror, and the cross-section view of the micromirror. The latter demonstrates the theorem of the parallel plate capacitor model. In Fig.1, L and a represents the width and length of the micromirror respectively (strictly speaking, L is the minimum of the micromirror length and the electrode length), l denotes the total length of the torsion beams, h is the gap between micromirror and electrode, and αa and βa define the size and position of the electrodes (normalized by the micromirror width a for later use). L , a , l , h , α and β , combined with the width w and the thickness t of the torsion beam, are the main structural parameters of the torsion micromirror.

When voltage V is added between the micromirror and one electrode, the electrostatic attraction causes the micromirror to rotate to a certain angle θ . Here we are interested in how to express the electrostatic torque. In the parallel plate capacitor model, the micromirror and the electrode are regarded as being composed of an infinite number of infinitesimal capacitors (Fig. 1). Therefore the electrostatic torque is given by

$$M_e = \int_{\frac{\beta a}{2}}^{\frac{\beta a}{2}} x dF = \int_{\frac{\beta a}{2}}^{\frac{\beta a}{2}} x \frac{\epsilon V^2}{2(h - x \tan \theta)^2} L dx$$

$$= \frac{\epsilon V^2 L}{2\theta^2} \left[\frac{1}{1 - \frac{\beta a}{2h} \theta} - \frac{1}{1 - \frac{\alpha a}{2h} \theta} + \ln \left(1 - \frac{\beta a}{2h} \theta \right) - \ln \left(1 - \frac{\alpha a}{2h} \theta \right) \right], \quad (1)$$

where M_e denotes the electrostatic torque, ϵ is the permittivity of air ($\epsilon \approx 8.85 \text{ pF/m}$), x and dx represents the position and the width of the infinitesimal capacitor used for integration. For simplicity, we normalize the rotation angle θ by

$$\Theta = \frac{\theta}{\theta_{\max}}, \quad (2)$$

where $\theta_{\max} = \frac{2h}{a}$ represents the maximum rotation angle. Substituting into Eq. (1),

$$M_e = \frac{\epsilon V^2 L}{2\theta_{\max}^2} \cdot \frac{1}{\Theta^2} \left[\frac{1}{1 - \beta \Theta} - \frac{1}{1 - \alpha \Theta} + \ln \left(\frac{1 - \beta \Theta}{1 - \alpha \Theta} \right) \right] \quad (3)$$

It is noted that in Eq. (3), all the structural parameters except for α and β contribute to M_e only as a coefficient. Moreover, the electrostatic torque M_e is proportional to the micromirror length L and the square of the driving voltage V . Therefore, M_e is very sensitive to the driving voltage.

2.2 Relation between driving voltage and rotation angle

When the micromirror is driven to rotate by electrostatic torque, the angular displacement of the torsion beams will initialize an elastic recovery torque. Therefore, the micromirror become steady only when these torques are equal (equilibrium condition).

The elastic recovery torque M_r , caused by the torsion beams can be expressed as

$$M_r = \frac{4GI_p}{l} \theta, \quad (4)$$

where G is torsion modulus ($G \approx 66 \text{ GPa}$ for polysilicon⁶), l is the total length of the two torsion beams, and I_p is the polar moment of inertia of the torsion beam expressed as¹⁶

$$I_p = tw^3 \left[\frac{1}{3} - 0.21 \frac{w}{t} \left(1 - \frac{w^4}{12t^4} \right) \right] \quad \text{for } t \geq w \text{ (} t \text{ and } w \text{ are the thickness and the width of torsion beam), and}$$

$$I_p = t^3 w \left[\frac{1}{3} - 0.21 \frac{t}{w} \left(1 - \frac{t^4}{12w^4} \right) \right] \quad \text{for } w \geq t. \quad (5)$$

For torque equilibrium, $M_e = M_r$, therefore

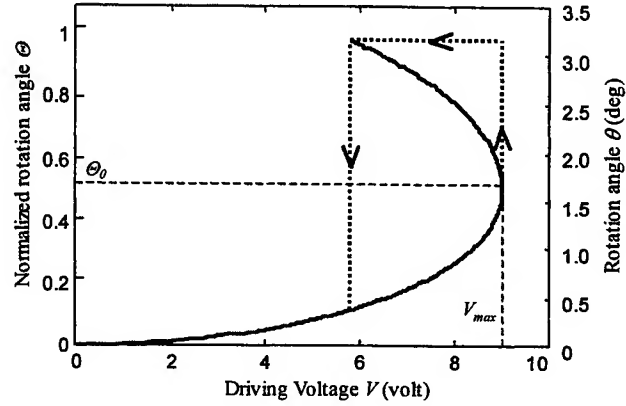
$$V = \left[\frac{8GI_p \theta_{\max}^3}{\varepsilon L l} \cdot \frac{\Theta^3}{\frac{1}{1-\beta\Theta} - \frac{1}{1-\alpha\Theta} + \ln\left(\frac{1-\beta\Theta}{1-\alpha\Theta}\right)} \right]^{1/2}, \quad (6)$$

This is the generalized and normalized equation representing the relation of the rotation angle, the driving voltage and all the structural parameters.

In practical uses, we require that the maximum value of V should not be too large. From Eq. (6), we can see the value of V is determined by two factors. The first is the Θ that requires the maximum driving voltage; this is governed by the second item in Eq. (6), which results in a snap-down effect that will be discussed in the next subsection. The other factor is the first item in Eq. (6), which comes from the structural parameters of micromirror.

Micromirror dimension	Mirror	
	Width a	$100 \mu m$
	Length L	$100 \mu m$
	Torsion beam	
	Length l	$130 \mu m$
	Width w	$2 \mu m$
	Thickness t	$1.5 \mu m$
	Electrode	
	α	0.1
	β	0.8
	Gap h	$2.75 \mu m$
	Max rotating angle θ_{\max}	3.2 degree

(a)



(b)

Fig. 2(a) The parameters of the micromirror, (b) The curve showing the relation between driving voltage and rotation angle

Eq. (6) shows that the driving voltage is directly proportional to $\theta_{\max}^{3/2}$ and $I_p^{1/2}$ and is indirectly proportional to $L^{1/2}$ and $l^{1/2}$. Since I_p is approximately directly proportional to t^3 and w (supposing $t < w$, as is true in most cases), $V \propto t^{3/2}, w^{1/2}$. As a result, 1) the driving voltage will increase to a very high value if the maximum rotation angle is designed to be large. This is one reason for the difficulty in achieving micromirror devices with large design rotation angles. 2) To minimize the driving voltage, it is more efficient to minimize the thickness of the torsion beam than to increase the lengths of the micromirror and the torsion beam, or to minimize the width of the torsion beam as well. 3) The micromirror width a and the gap h do not directly influence the actuation relation since they are combined into θ_{\max} . That is to say, if we want to design a micromirror whose maximum rotation angle has been selected, we cannot minimize the driving voltage by simply changing the micromirror width or the gap.

For a micromirror whose parameters are as shown in Fig. 2(a), the curve of driving voltage versus rotation angle is given in Fig. 2(b). This curve shows that initially the required driving voltage increases with rotation angle, and the increase of driving voltage is much more rapid than that of the rotation angle. As the rotation angle reaches a certain value θ_0 (or equivalently, θ_0), the required driving voltage reaches its maximum V_{\max} (This turning point in the curve and the angle can be named as snap-down point and snap-down angle respectively.). Thereafter, a smaller voltage is required to maintain the torque equilibrium. However, when the micromirror rotates beyond θ_0 , it will rapidly snap down until its edge touches the substrate since the voltage required to rotate further is smaller than the current driving voltage. This is the snap-down phenomenon. Consequently, after the snap-down point, the V - Θ relation will not follow the curve defined by Eq. (6) but be a straight-up line (dotted line in Fig. 2(b)). In the release procedure, the micromirror will not rotate back until the driving voltage is smaller

than a certain value. This hysteresis phenomenon is another property of the torsion micromirror, which is similar to the steady-state trigger circuit, and can be used in optical switches and digital displays, etc. to address^{6, 17} and self-lock¹⁸ the micromirror array.

2.3 Snap-down effect

The snap-down effect of the torsion micromirror is due to the non-linearity of the electrostatic force that is indirectly proportional to the square of the distance. When the torsion beam rotates and thus the gap between micromirror and electrode becomes smaller, the elastic torque increases linearly while the electrostatic torque increases rapidly, especially when the micromirror is near to the electrode. Finally, the torque equilibrium cannot be met.

The snap-down effect decreases the angle range that can be driven smoothly, which is bad for some applications where a large smooth driven angle is critical, such as laser printing, laser scanning and optical reading heads. Theoretically, we can get the

snap-down point by numerically solving $\frac{dV}{d\Theta} = 0$. From this point of view, it is easy to see that the first item in Eq. (6) has

no contribution to the position of the snap-down point and only the second item governs the snap-down effect. In the other words, the dimensions of the micromirror and the torsion beam have no influence on the snap-down effect. Conversely, it is only determined by the position and size of the electrodes.

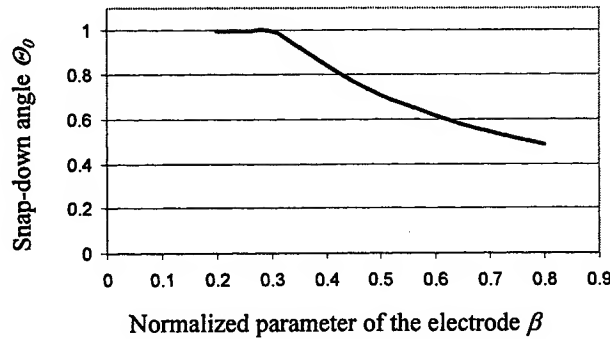


Fig. 3 Variation of snap-down angle with electrode parameter ($\alpha=0.1$)

Fig. 3 demonstrates the change of the snap-down angle with the electrode parameter. Here α and β are normalized parameters, αa denotes the gap between the two electrodes, and $\frac{(\beta - \alpha)a}{2}$ represents the width of each electrode. From Fig. 3 we can see that the snap-down angle is high when β is small, and become ~ 0.5 at large β .

If the torsion beam is located along the diagonal direction of the micromirror, the snap-down angle can be increased to ~ 0.8 . However, this improvement is at the price of the decrease of the maximum achievable rotation angle.

2.4 Capacitance of the micromirror

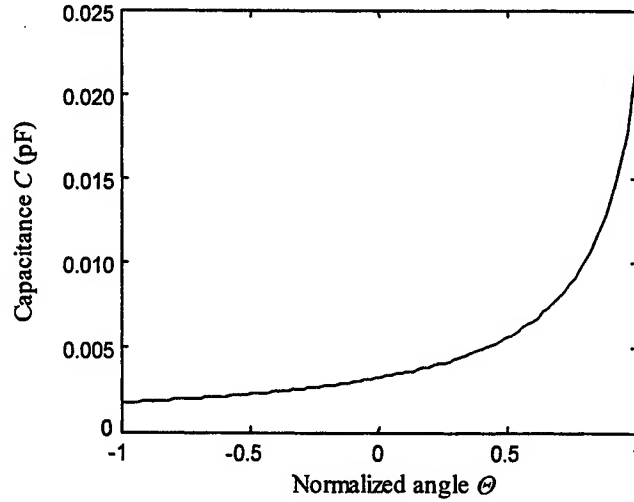


Fig. 4 The capacitance variation of the micromirror

Based on the parallel plate capacitor model, the micromirror and the electrode form a capacitor whose capacitance varies with the angle rotation. Similar to the calculation of electrostatic torque in section 2.1, the capacitance can be obtained by integration

$$C = \int dC = \frac{\epsilon L}{\theta_{\max}} \cdot \frac{1}{\Theta} \ln \frac{1 - \alpha\Theta}{1 - \beta\Theta} \quad (7)$$

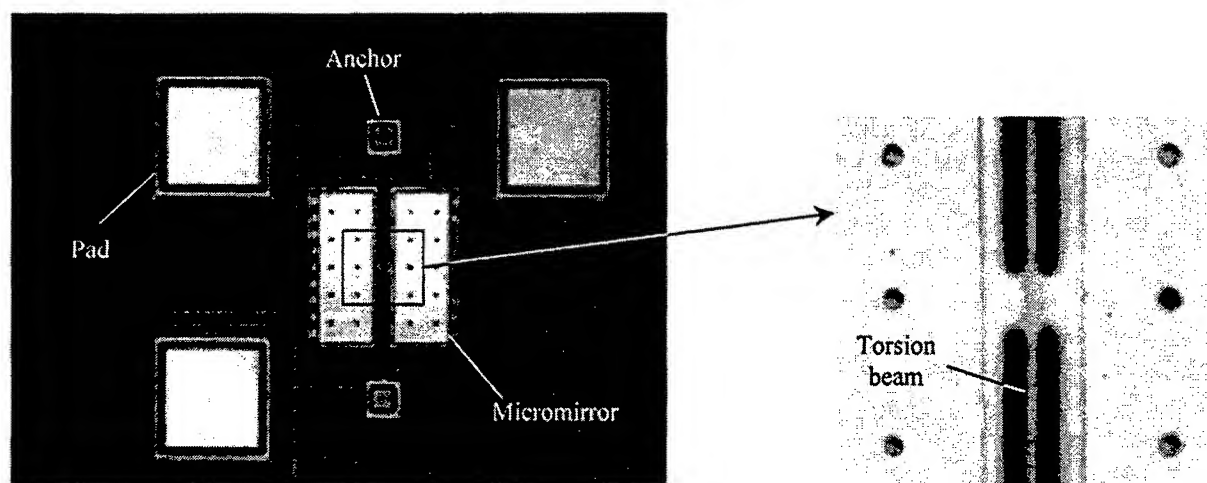
When $\Theta \rightarrow 0$, $C \rightarrow C_0 = \frac{\epsilon L(\beta - \alpha)}{\theta_{\max}}$. Fig.4 shows the variation of capacitance with angular position for the micromirror whose parameters are shown in Fig. 2(a).

Fig. 4 shows that the capacitance of the micromirror is insensitive when the rotation angle is negative (i.e. when the micromirror is driven by the other electrode to rotate to the other side) or small, and becomes sensitive only when the normalized rotation angle is relatively large (>0.5). Since the capacitance of the micromirror changes with the rotation angle, it can be employed to measure the angular displacement of the micromirror. Compared with the optical measurement methods^{1, 3, 4, 5, 13, 19, 20} that are most widely used, this method seems to be simpler and sufficiently accurate.

2.5 Design and fabrication of micromirror

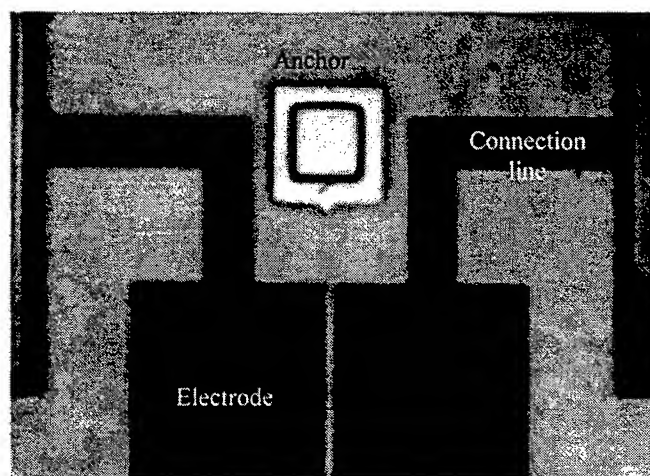
Based on the previous analysis, a micromirror with parameters as shown in Fig. 2(a) has been designed and fabricated. The main functional parameters are: (1) the maximum rotation angle $\theta_{\max}=3.2^\circ$, (2) the snap-down angle $\Theta_0=0.52$ ($\theta_0=1.7^\circ$), (3) the maximum driving voltage $V_{\max}=9.0V$, and (4) the natural frequency is about 100kHz.

The micromirror is fabricated using the three-layer polysilicon surface micromachining technology offered by the MEMS Technology Application Center at North Carolina (MCNC) under Multi-User MEMS Processes (MUMPS). Fig. 5 shows the micrographs of the micromirror. At the top, the micromirror is supported by two torsion beams (Fig.5 (b)), which are sequentially connected to and supported by two anchors (Fig. 5(a)). Beneath the micromirror lie two electrodes that are connected to the pads to input a driving voltage (Fig. 5 (c)). Additionally, one anchor is connected to another pad to ground the micromirror surface. In this design, the micromirror is divided into two parts connected by a $10\mu m \times 10\mu m$ bridge (Fig. 5 (b)) to increase the length of the torsion beam.



(a) Micrograph of the whole micromirror

(b) Close-up of the torsion beams



(c) View of the electrodes after removing the micromirror

Fig.5 the micrographs of the different parts of the micromirror

3. CONCLUSION

We have studied the electrostatic torque of the torsion beam micromirror based on the parallel plate capacitor model, and subsequently derived a generalized and normalized equation governing the static characteristics of the torsion micromirror. From this equation, we drew conclusions that (1) to minimize the driving voltage, the most efficient way is to minimize the thickness of the torsion beam, (2) the snap-effect is not influenced by the micromirror size or the torsion beam dimension, rather it is only determined by the size and position of the electrodes. The relation between the micromirror capacitance and the rotation angle was derived and discussed, resulting in a suggestion of a means of measuring the rotation angle through its capacitance. Based on the model used, a torsion beam micromirror has been designed and fabricated, and is currently being tested.

4. REFERENCES

1. N.C. Tien, O. Solgaard, M-H. Kiang, M. Danman, K.Y. Lau, R.S. Muller, "Surface-micromachined mirrors for laser-beam positioning", *Sensors and Actuators A*, 52, pp. 76-80, 1996.
2. Tsen-Hwang Lin, "Flexure-beam micromirror devices and potential expansion for smart micromachining", *SPIE*, Vol.2722, pp. 20-29, 1996.
3. Jong-Woo Shin, Seok-Whan Chung, Yong-Kweon Kim and Bum Kyoo Choi, "Design and fabrication of micromirror array supported by vertical springs", *Sensors and Actuators A*, 66, pp. 144-149, 1998.
4. F. Pan, J. Kubby, E. Peeters, J. K. Chen, O. Vitomirov, D. Taylor and S. Mukherjee, "Design, modeling and verification of MEMS silicon torsion mirror", *Proceedings of SPIE*, Vol.3226, pp. 114-124, 1997.
5. S. Kurth, R. Hahn, C. Kanfmann, K. Kehr, J. Mehner, V. Wollmann, W. Dotzel and T. Gessner, "Silicon mirrors and micromirror arrays for spatial laser beam modulation", *Sensors and Actuators A-Physical*, 66: (1-3), pp. 76-82, Apr 1998.
6. P. Jaechlin, C. Linder and N.F. de Rooij, J.M. Moret and R. Vailleamier, "Line-addressable torsional micromirrors for light modulator arrays", *Sensors and Actuators A*, 41-42, pp. 324-329, 1994.
7. Shi-Sheng Lee and Ming C. Wu, "Surface-micromachined vertical torsion mirror switches", *IEEE/LEOS IEEJ/SAMS International conference on optical MEMS and their applications MOEMS97 Technical Digest*, pp.115-118, Nara Japan, 1997.
8. Jack M. Younse, "Mirrors on a chip", *IEEE Spectrum*, pp.27-31, Nov 1993.
9. T.G. McDonald and L.A. Yoder, "Digital micromirror devices make projection displays", *Laser Focus world* 33: (8) S5-S8 Aug 1997.
10. J.B. Sampsel, "Digital micromirror device and its application to projection displays", *J. Vac. Sci. Technol. B* 12: (6), pp. 3242-3246, Nov-Dec 1994.
11. D.M. Monk and R.O. Gale, "The digital micromirror device for projection display", *Microelectronic Engineering*, 27: (1-4), pp. 489-493, Feb 1995.
12. M.A. Mognardi, "Digital Micromirror array for projection TV", *Solid state Technol.* 37: (7), pp. 63-67, Jul 1994.
13. Ofir Degani, Eran Socher et al., "Pull-in study of an electrostatic torsion microactuator", *Microelectromechanical systems*, 7 (4), pp. 373-379, Dec 1998.
14. Grover C. Wetsel, Jr., and Kirk J. Strozewski, "Dynamical model of microscale electromechanical spatial light modulator", *J. Appl. Phys.* 73 (11), pp.7120-7124, 1993.
15. M. Fischer, M. Giousouf, et al, "Electrostatically deflectable polysilicon micromirrors-Dynamic behavior and comparison with results from FEM modeling with ANSYS", *Sensors and Actuators A*, 67, pp. 89-95, 1998.
16. R.J. Roark and W.C. Young, "Formulas for stress and strain", McGraw-Hill Int. Edns., Singapore, 5th edn., Ch.7, 1976.
17. Brian T. Cunningham, Jonathan J. Bernstein, Don Seltzer, and David Hom, "Micromirror pixel addressing using electromechanical bistability", *Solid-state sensor and actuator workshop*, Hilton Head Island, South Carolina, pp.285-287, June 1998.
18. Larry J. Hornbeck, "Digital light processingTM and MEMS: reflecting the digital display needs of the networked society", *Micro-Optical Technologies for Measurement, Sensors, and Microsystems*, SPIE Vol.2783, Besancon, France, pp.2-13. June 1996.
19. S. Kurth, W. Dotzel, "Experimental adaptation of model parameters for microelectromechanical systems (MEMS)", *Sensors and Actuators, A* 62, pp.760-764.
20. Kirk J. Strozewski, Chih-Yu Wang, and Grover C. Wetsel, "Characterization of a micromechanical spatial light modulator", *J. Appl. Phys.*, 73(11), pp.7125-7128, 1993.

Micromirror actuation with electrostatic force and plate bending

Seungoh Han, Hojoon Park, and Jungho Pak
Micro-systems Laboratory, Dept. of Electrical Engineering, Korea University
1, 5-ka, Anam-dong, Sungbuk-ku, Seoul, 136-701, Korea

ABSTRACT

In this paper, a new method for actuating micro-mirrors, which utilizes bending of the micro-mirror plate, was proposed in order to increase the rotational angle without increasing the sacrificial layer thickness. The analytical model of the proposed actuating method was established and, based on the analytical model, the expected micro-mirror operation is presented. In order to confirm the expected operation surface-micromachined polysilicon micro-mirror was fabricated and tested. The bending of the micro-mirror plate, however, was not observed in the experiment with the fabricated micro-mirror. There are two possible reasons for this. One is the driving force reduction due to the decreasing of the voltage difference between the micro-mirror plate and underlying electrode caused by electrical conducting between the two. The other is the non-optimized design in the mechanical structure which causes the bending of the supporting beam before the plate starts to bend.

Keywords: MEMS, micro-mirror, electrostatic driving, plate bending

1. INTRODUCTION

Recently there has been a growing interest in the development of the micromachined mirror that can be used in optical applications such as the projection display. A typical micro-mirror consists of mirror plate, mechanical supporting part, and actuating part. The micro-mirrors are supported by either torsional flexures or bending arms and they provide a mechanical force to reset the micro-mirrors. The most common method for actuating micro-mirror is the use of an electrostatic force between the micro-mirror and underlying electrode because the electrostatic driving has many advantages such as low power consumption, easy fabrication, and bi-directional actuation.

The rotational angle of micro-mirrors is usually limited by the gap between the micro-mirror plate and the substrate and hence the sacrificial layer must be thick enough in surface micromachining technique. In this paper, a new method for actuating micro-mirrors, which utilizes bending of the micro-mirror plate, was proposed in order to increase the rotational angle without increasing the sacrificial layer thickness.

2. MICRO-MIRROR ACTUATION MECHANISM USING PLATE BENDING

2.1. Operation principle

Fig. 1 shows a schematic view of a micro-mirror including mirror plate, supporting beams, and driving electrode. When a small driving voltage is applied between the mirror plate and underlying electrode in micro-mirror configuration, the mirror plate is rotated due to the electrostatic force generated by the voltage difference between two electrodes. The rotational angle of the mirror plate is determined by balancing between the electrostatic force and mechanical torque of the supporting beams. In static equilibrium, the electrostatic force and the mechanical force are equal, resulting in a stable condition for the micro-mirror. As the driving voltage is increased higher than the stable condition, the electrostatic force increases and eventually overcomes the mechanical force, resulting in instability or a collapse condition, where one edge of the mirror plate contacts the substrate surface as shown in Fig. 1(a). The rotational angle of the micro-mirror, in this case, is limited by the gap between the mirror plate and underlying electrode.

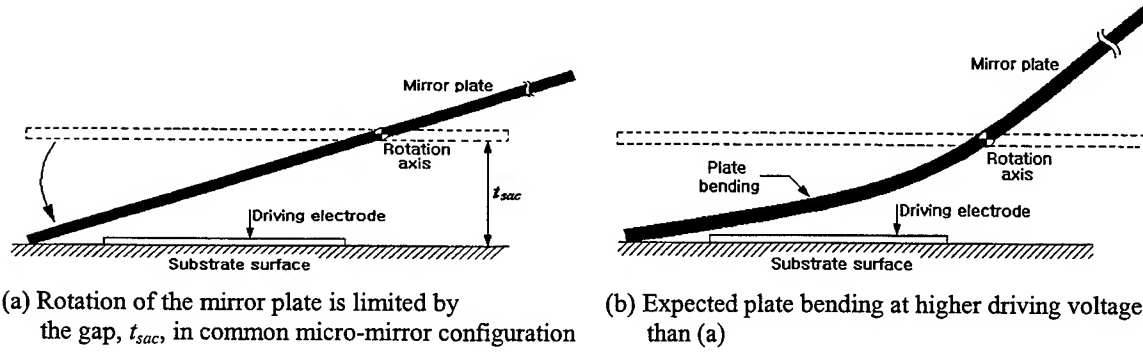


Fig. 1 Schematic diagram showing the bending mode operation in a micro-mirror

If the magnitude of the driving voltage is further increased, then the mirror plate would start to bend as shown in Fig. 1(b) and the rotational angle of the mirror plate will increase. Therefore, the limit in the rotational angle can be extended with identical sacrificial layer thickness(t_{sac}) when this bending of the mirror plate is used.

2.2. Analytical model

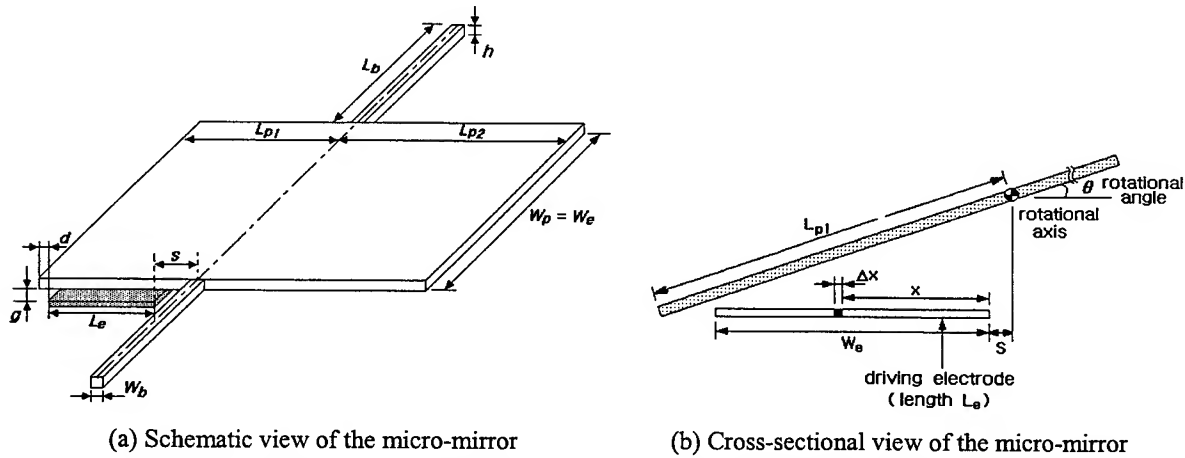


Fig. 2 Schematic view of the micro-mirror for the analytical modeling

A schematic view for the analytical description of the micro-mirror was sketched in Fig. 2. The capacitance in the incremental section Δx is given as

$$\Delta C = \frac{\epsilon L_e \Delta x}{g - (s + x) \tan \theta} = \frac{\epsilon L_e \Delta x}{g - t} \quad (1)$$

where ϵ is the permittivity in the vicinity between the mirror plate and underlying electrode and t is amount of gap reduction of an incremental section Δx , which is a function of x , $t(x)$. When the driving voltage with the magnitude of V is applied between the mirror plate and underlying electrode the electrostatic force is generated as follows.

$$\Delta F_e = \frac{\partial}{\partial t} \left(\frac{1}{2} \Delta C V^2 \right) = \frac{\epsilon L_e \Delta x V^2}{2} \frac{1}{(g - t)^2} \quad (2)$$

Thus the total electrostatic torque due to the electrostatic force can be obtained by integrating the contributions of all the plate elements as shown in equation (3).

$$T_e = \int_0^{w_e} \Delta F_e \cos \theta (s+x) = \frac{\epsilon L_e V^2 \cos \theta}{2 \tan^2 \theta} \left(\frac{g}{g - (s+W_e) \tan \theta} - \frac{g}{g - s \tan \theta} + \ln \frac{g - (s+W_e) \tan \theta}{g - s \tan \theta} \right) \quad (3)$$

The rotational angle of the mirror plate is determined by the balancing between the above electrostatic torque and mechanical torque given as¹

$$T_m = \frac{G\theta}{16L_b} w_b h^3 \left[\frac{16}{3} - 3.36 \frac{h}{w_b} \left(1 - \frac{h^4}{12w_b^4} \right) \right] \quad (4)$$

where $G = E/[2(1+\nu)]$ and E and ν are Young's modulus and Poisson's ratio, respectively. When the applied driving voltage is small, a stable condition, where the electrostatic torque is equal to the mechanical torque, is established and hence the rotational angle is determined. As the driving voltage increases the electrostatic torque becomes larger than the mechanical torque. Thus the stable condition doesn't hold any more and the plate starts to rotate more until one edge touches the substrate surface. The rotational angle is limited by the saturated value of $\theta_{sat} = \tan^{-1}(g/L_{pt})$. This behavior can be confirmed from Fig. 3 which shows the calculated electrostatic force and mechanical torque as a function of the driving voltage. Dimensions and constants used in the calculation are presented in Table 1.

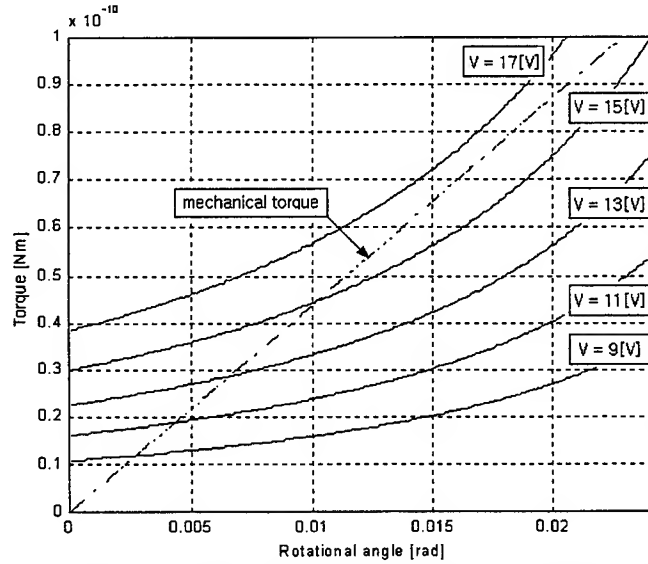


Fig. 3 The calculated electrostatic and mechanical torque as a function of the driving voltage

If the driving voltage is further increased, then the mirror plate would start to bend. For the simplicity in modeling, the driving voltage was divided into two portions: One portion generates the bending of the mirror plate and the other portion gives rise to the twisting of the supporting beams. The electrostatic force generating the bending of the mirror plate in the incremental section of Δx is calculated as

$$\Delta F_{e,bend} = \frac{\epsilon L_e \Delta x V_b^2}{2} \frac{1}{[g - (s+x) \tan \theta_{sat} - \delta(y) \cos \theta_{sat}]^2} \quad (5)$$

where V_b is the portion of the driving voltage that generates the bending of the mirror plate and $\delta(y)$ is the magnitude of the bending at the position y in the mirror plate.

Table 1. Dimensions and constants used in the calculation

Width of the driving electrode	W_e	40 μm
Length of the driving electrode	L_e	100 μm
Gap between the driving electrode and the rotational axis	s	10 μm
Gap between the mirror plate and the driving electrode	g	2 μm
Length of the supporting beam	L_b	70 μm
Width of the supporting beam	W_b	3 μm
Thickness of the structure	h	2 μm
Length of the mirror plate in the direction of the electrode	L_{p1}	55 μm
Young's modulus	E	160 GPa
Poisson's ratio	ν	0.23

Assuming the simply supported boundary condition $\delta(y)$ due to the $\Delta F_{e,bend}$ is obtained from²

$$\begin{aligned}\delta(y) &= \frac{\Delta F_{e,bend}(L_{p1}-a)y}{6EI L_{p1}} [L_{p1}^2 - (L_{p1}-a)^2 - y^2] & (0 \leq y \leq a) \\ &= \frac{\Delta F_{e,bend}(L_{p1}-a)y}{6EI L_{p1}} [L_{p1}^2 - (L_{p1}-a)^2 - y^2] + \frac{\Delta F_{e,bend}(y-a)^3}{6EI} & (a \leq y \leq L_{p1})\end{aligned}\quad (6)$$

where a is the position where the electrostatic bending force is applied and I is the second moment of an area given as $W_p h^3/12$. When the mirror plate is bent the bending angle of the mirror plate at the supporting point is given as²

$$\theta_{bend} = \int_0^{W_e} \frac{\epsilon L_e V_b^2}{12EI L_{p1}} \frac{a(2L_{p1}-a)(L_{p1}-a)dx}{[g - (s+x)\tan\theta_{sat} - \delta(y)\cos\theta_{sat}]^2} \quad (7)$$

Therefore the total rotational angle of the mirror plate is increased by the amount of θ_{bend} . The portion of the driving voltage generating the bending of the mirror plate is determined from the requirement that the electrostatic torque due to the extra portion of the driving voltage needs to be equal to the mechanical torque. If the driving voltage is further more increased the bending angle of the mirror plate at the position where the mirror plate contacts with the substrate is limited by the θ_{sat} . In this case the guided boundary condition must be used in equation (6) and therefore equations (6) and (7) are changed to equations (8) and (9), respectively.

$$\begin{aligned}\delta(y) &= \frac{R_B y^3}{6EI} + \frac{y}{2EI} [a^2 \Delta F_{e,bend} - (R_B - \Delta F_{e,bend})L_{p1}^2 - 2a\Delta F_{e,bend}L_{p1}] & (0 \leq y \leq a) \\ &= \frac{(R_B - \Delta F_{e,bend})y^3}{6EI} + \frac{a\Delta F_{e,bend}y^2}{2EI} - \frac{y}{2EI} [(R_B - \Delta F_{e,bend})L_{p1}^2 + 2a\Delta F_{e,bend}L_{p1}] + \frac{(R_B - \Delta F_{e,bend})L_{p1}^3}{3EI} + \frac{a\Delta F_{e,bend}L_{p1}^2}{2EI} & (a \leq y \leq L_{p1})\end{aligned}\quad (8)$$

$$\text{where } R_B = \Delta F_{e,bend} \left[1 + \frac{a(a^2 - 3L_{p1}^2)}{2L_{p1}^3} \right]$$

$$\theta_{bend} = \int_0^{W_e} \left(\frac{a^2 \Delta F_{e,bend}}{2} - \frac{(R_B - \Delta F_{e,bend})L_{p1}^2}{2} - a\Delta F_{e,bend}L_{p1} \right) \quad (9)$$

3. MICRO-MIRROR FABRICATION AND EXPERIMENTAL RESULTS

3.1. Micro-mirror fabrication

In order to confirm the analytical model, a micro-mirror was designed with dimensions shown in Table 1. The designed micro-mirror was fabricated by MEMS MPC service offered by Microsystem Technology Center where two polysilicon layers were used for both the driving electrode and mechanical structure, respectively.

Starting with silicon wafer, 500 nm silicon dioxide was grown by wet oxidation and then 1500 nm silicon nitride was deposited by LPCVD for the electrical isolation (Fig. 4(a)). For the electrical connection and driving electrode, 5000 nm thick LPCVD polysilicon was deposited and patterned (Fig. 4(b)), then 2 μm thick TEOS sacrificial layer was deposited and patterned to stick the structure to the substrate (Fig. 4(c)). After patterning the sacrificial TEOS layer, structural LPCVD polysilicon of 2 μm thickness was deposited and patterned as shown in Fig. 4(d). Finally, to release the fabricated micro-mirror structure, the sacrificial TEOS layer was wet etched and the sample was dried by the sublimation drying method with p-DCB to prevent the sticking problem. SEM photograph of the fabricated micro-mirror is presented in Fig. 5, which is the top view of the entire structure.

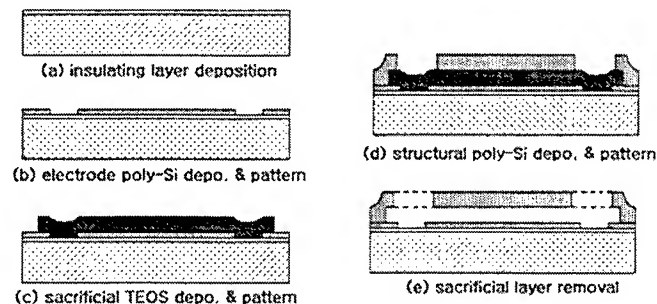


Fig. 4 Fabrication sequence of the micro-mirror

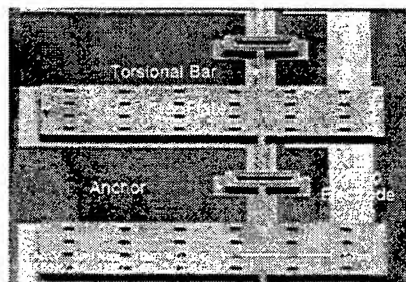
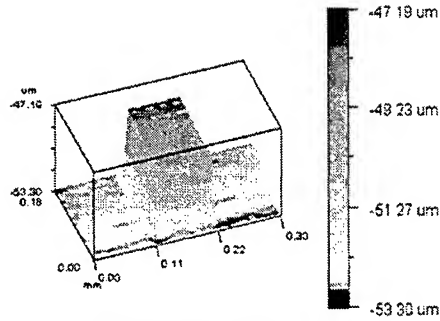


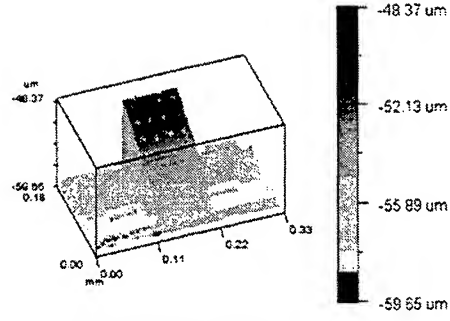
Fig. 5 SEM photograph of the fabricated micro-mirror

3.2. Experimental results

In order to obtain the relationship between the rotational angle and the driving voltage, the surface profile change of the micro-mirror due to the electrostatic torque was measured as a function of driving voltage using 3-dimensional profiler ACCURA1500 (manufactured by INTEC ENG. CO. LTD.). Two measured 3D profiles of the micro-mirror are shown in Fig. 6(a) and 6(b) where the driving voltage was 0V and 18V, respectively. With the measured 3D profiles, the rotational angle was calculated from the gradient of the mirror plate.

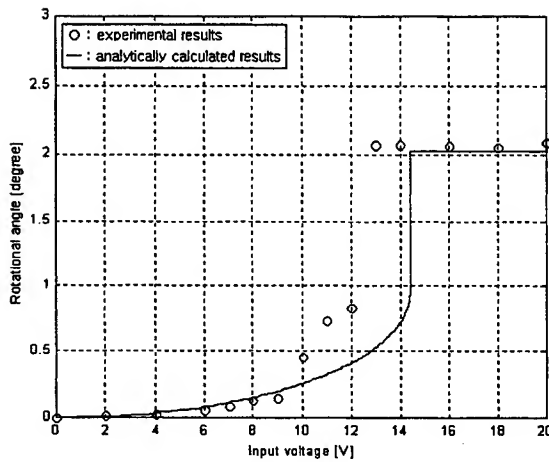


(a) Driving voltage = 0 V

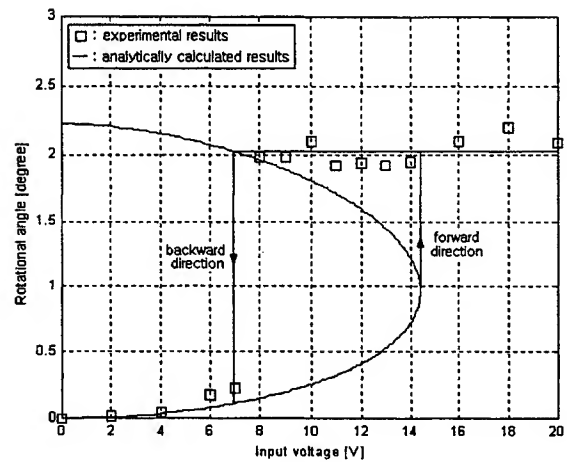


(b) Driving voltage = 18 V

Fig. 6 3D profiles of the micro-mirror when the driving voltages were 0 V and 18 V



(a) Rotational angle change in forward direction



(b) Rotational angle change in backward direction

Fig. 7 Experimental vs. calculated rotation angle as a function of the driving voltage

The rotational angle obtained from these 3D profiles is plotted in Fig. 7 as a function of driving voltage. In order to fit the analytical model with experimental results it was assumed that the $0.06 \mu\text{m}$ over-etch, $0.03 \mu\text{m}$ and $0.06 \mu\text{m}$ under-deposition in polysilicon and TEOS, respectively, and Young's modulus of 146 GPa . These fitting values are in the margin of each parameter³. As shown in Fig. 7, experimental data in the backward direction agreed quite well with the analytical curve but the data in the forward direction show little higher rotational angle in sub-saturation region and faster saturation than expected. These discrepancies in the forward direction may be due to a larger electrostatic force acting on the mirror plate than expected. A possible cause of the larger electrostatic force may come from the fringing field between the side and top of the mirror plate and the broad underlying electrode.

4. DISCUSSIONS AND CONCLUSIONS

The bending of the micro-mirror plate was not observed in measurement with the fabricated micro-mirror. There are two possible reasons for this. One is the driving force reduction due to the decreasing of the voltage difference between the micro-mirror plate and underlying electrode caused by the electrical conducting between the two. In order to prevent the electrical conducting problem it is necessary to insert an isolation layer between the micro-mirror structure and the underlying electrode. By doing so, however, the capacitance reduction due to the new series capacitor will decrease the electrostatic torque and thus increase the required driving voltage for rotating the mirror plate. The other is the non-optimized design in the mechanical structure which gives rise to the bending of the supporting beam before the plate starts to bend. The only possible solution to this problem is the time-consuming repetition of the design and simulation. The optimized mechanical

structure can be obtained from the iterated simulation and the analytical model presented in the previous section is expected to reduce the iteration number.

Most conventional micro-mirrors driven by electrostatic force need a thick sacrificial layer to obtain the required rotational angle. The thick sacrificial layer introduces the difficulties in the fabrication and increases the required driving voltage. A bending mode operation of the mirror plate was proposed in this paper. By using this driving method a large rotational angle can be obtained without increasing the sacrificial layer thickness. An analytical model for the bending motion of the mirror plate was established and in order to confirm the model micro-mirror with thin sacrificial layer was fabricated using a simple 2-polysilicon process and tested. The test results, however, didn't show the bending mode operation of the mirror plate. There are two possible reasons for this: one is the driving force reduction due to the electrical conducting between the mirror plate and underlying electrode and the other is the non-optimized design in the mechanical structure. In order to solve these problems an insulating layer needs to be inserted between the mirror plate and underlying electrode and the design of the mechanical structure must be optimized through the iterated simulation. When these problems are solved the proposed driving method using the bending mode operation of the mirror plate can be utilized and a micro-mirror with thin sacrificial layer can also be realized.

ACKNOWLEDGEMENT

The test micro-mirror was fabricated by the MEMS MPC service offered by Microsystem Technology Center in Korea. The authors would like to thank Minseok Song for his important contributions in the fabrication of the micro-mirror, Prof. Young Kweon Kim of Seoul National University for 3D profiler usage, and Prof. Ho Seong Kim for his helpful discussions in the measurement of the rotational angle.

REFERENCES

1. R. J. Roark and W. C. Young, *Formulas for stress and strain*, McGraw-Hill, 1975.
2. J. M. Gere and S. T. Timoshenko, *Mechanics of materials*, PWS Engineering, 1984.
3. Microsystem Technology Center, *2nd MEMS MPC report*, 1998.

High Performance Readout Integrated Circuit for Surface Micromachined Bolometer Arrays

Yuan-Lung Chin^a, Tai-Ping Sun^b, Jung-Chuan Chou^c, Yuan-Chung Chin^d

Yuan-Chin Chou^d, Wen-Yaw Chung^a, Shen-Kan Hsiung^a

^aInstitute of Electronic Engineering, Chung Yuan Christian University, Chung-Li, Taiwan 320, R.O.C.

^bDepartment of Electrical Engineering, National Chi Nan University, Nantou, Taiwan 545, R.O.C.

^cInstitute of Electronic and Information Engineering, National Yunlin University of Science and Technology, Touliu, Yunlin, Taiwan 640, R.O.C.

^dChung Shan Institute of Science and Technology, Material R&D Center, Lung-Tan, Taiwan 325, R.O.C.

ABSTRACT

In this paper, a high performance CMOS readout structure is proposed and applied for surface micromachined bolometer arrays. The silicon readout circuit is an important interface circuit for detector array and signal processing stages in the IR image system. Conventional readout configurations for thermal resistive sensors can be classified into four groups (1).Constant Temperature (CT) (2).Constant Current (CC) (3).Constant Voltage (CV) (4).Constant Bias(CB). To achieve a high performance readout and fit the working characteristics of IR detector material, new CMOS readout structures have been developed and fabricated. Based on the application of the proposed Constant Current (CC) input biasing technique, a new CMOS Bandgap Reference Constant Current (BRCC) readout structure is proposed and analyzed. The low power CMOS readout circuit is achieved using the reset switch techniques. By applying the proposed (BRCC) bias technique to improve low power, High linearity and low sensitivity of the resistive bolometer detectors and high performance readout interface circuit for the IR linear array is realized with a pixel size of $50 \times 50 \mu\text{m}^2$.

Keywords : Bolometer, CT , CC , CV , CB , BRCC , CMOS , IR linear array, Pixel Size

I. INTRODUCTION

The silicon sensor for radiant signals is considered to be the first silicon sensor ever produced. In recent years, the development of new technologies and improvements in the capabilities of existing technologies have led to new sensor structures. IR detectors are divided into two categories : photo detectors, which directly detect the IR photons, and thermal detectors, which detect the increase in temperature caused by the IR signal. Because the energy carried by photons in the infrared bandwidth is lower than the energy required for electrons to cross the silicon bandgap, silicon sensors for IR signals usually operate as thermal detectors. The main advantage of thermal detectors has been the ability to absorb radiation over a broad IR wave length range. They have found applications in infrared spectroscopy, burglar alarms, fire detection and thermal imaging in industry and medicine.

A 1×128 pixels bolometer infrared linear array array, using thin film polycrystalline silicon films was developed. The device is a monolithically integrated structure with a polycrystalline bolometer detector located over a high performance readout circuit. Since the thermal conductance of the polycrystalline bolometer detector is minimized, the temperature of the detector itself increases by applying the bias current. In this paper, a new readout circuit called the Bandgap Reference Constant Current(BRCC) is proposed to solved the above mentioned problems and improve the readout

performance. The BRCC readout circuit of the bolometer unit cell sensor under investigation, is composed of a bandgap reference circuit, source follower per detector, high gain amplifier, and reset switch. The BRCC readout chip was designed in $0.5\text{ }\mu\text{m}$ double poly double metal (DPDM) n-well CMOS technology in 1×128 . The high gain, low power, high sensitivity readout performances for the bolometer detector were achieved in a $50\times 50\text{ }\mu\text{m}^2$ pixel size.

II. 1×128 PIXEL POLYCRYSTALLINE BOLOMETER IR FRA

High-temperature superconducting microbolometer silicon microstructure infrared arrays offer the potential of lowest possible production cost combined with high performance for use in infrared imaging systems. Linear arrays employing thin films of polycrystalline have been prepared. The silicon Micro-Electro-Mechanical (MEM) can be divided into two categories: bulk and surface MEM¹, bulk MEM means the realization of micromachanical structures using the accurate machining of a relatively thick substrate. For example, membranes can be formed, by backside etching of silicon substrate using crystal orientation dependence^{2,3}. Nowadays, a number of firms successfully manufacture and market silicon transducers based on bulk processing. This requires construction of structures from stacked thin films. Their dimensions are generally one or two orders of magnitude smaller than those of bulk micromachined devices. Thus, miniaturization can be considerably increased. One particular advantage of surface micromachined devices is their easy integration with IC components, since the wafer surface is also the working area of IC elements. At present, most devices are still at their prototype stage. In this thesis, development of microelectromechanical thermal detectors that belong to the surface micromachining area was achieved.

The thermal isolation of the detector was realized by forming the detector onto a microbridge structure⁴. First, a sacrificial island is formed on each pixel. Next, a support layer is deposited to support the detector. The support layer is made of silicon nitride having a low thermal conductivity. A polysilicon resistor is then formed onto the support layer. An insulation layer is deposited on that. Etching windows are made at the edge of the sacrificial layer. Finally, an electrode pattern connects the resistor. SEM photograph of the single pixel and linear array pixel of bolometers are shown in Fig. 1. The procedures for the micro bolometer are shown in Fig.2. We have selected polysilicon as the bolometer material. Since polysilicon is commonly used in the conventional Si-VLSI process, we can manufacture the sensor using current Si-VLSI facilities.

The thermal isolation between the bolometer and the substrate is accomplished by forming the bolometer on the microbridge structure fabricated in each pixel using the surface micromachining technology since polysilicon is generally used in the conventional Si-VLSI process, this choice of detector material makes it possible to manufacture the image sensors using only existing Si-VLSI facilities, and realize a low cost uncooled infrared camera.

We fabricated microbolometers using surface micromachining techniques, which proved to be reliable microelectromechanical devices, in which the specific detectivity of constant-bias voltage circuit was attained. The incorporated features are that the polysilicon infrared detector is controlled by low stress LPCVD silicon nitride, thermal isolation structure in the pixel, and a wafer immersed in EDP and subsequently rinsed in ACE. The process yield reached 95%.

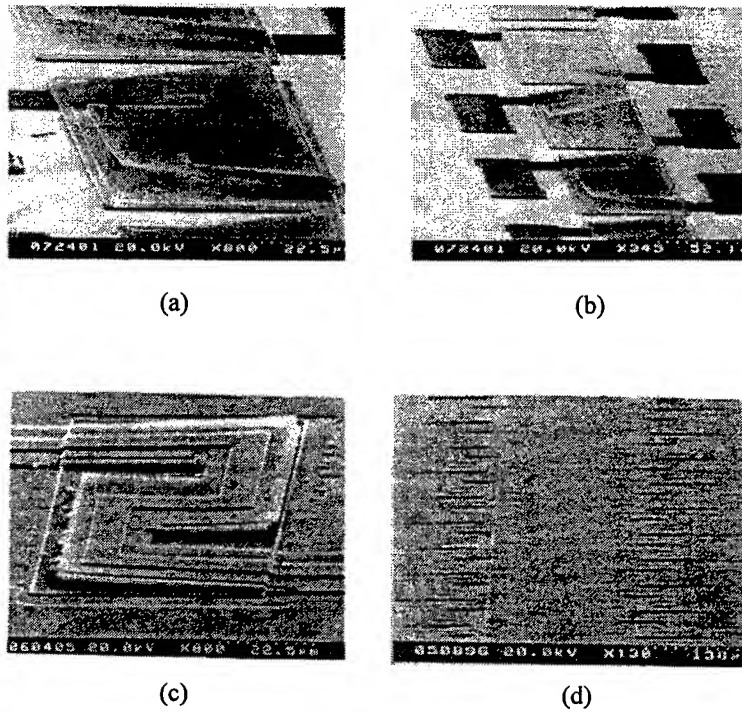


Fig. 1. SEM photograph of linear array bolometer

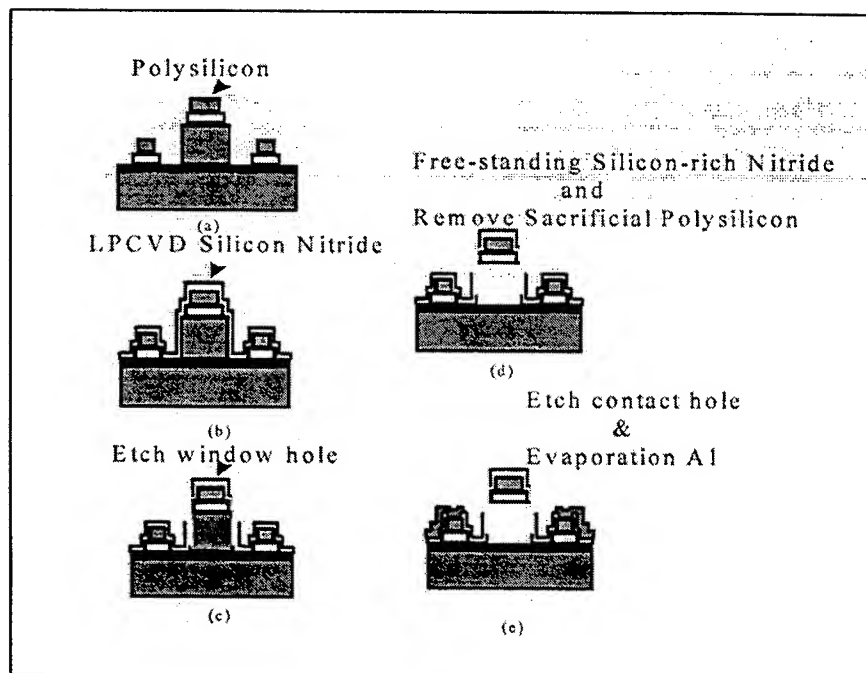


Fig. 2. Process flow to form bolometer

III. READOUT CIRCUIT DESCRIPTION

The 1x128 linear array BRCC readout structure is composed of four parts: the bandgap reference circuit, the unit cell input stage, the common output stage and the logic control function generator. The readout circuit configuration is shown in Fig. 3. Each cell has bolometer and BRCC readout circuit cell. Each column line also has MOSFETS. These MOSFETS serve as switches. Horizontal shift register to allow individual addressing of the pixel. The signal reading of each pixel was performed as follows: Sending data to the shift register turns on one time of cell MOSFETs. This applies a voltage pulse to the detector of the bolometer of each pixel, so that it is possible to read changes in the bolometer's resistor. The sample and hold circuits, composed of a capacitor and MOSFETs convert them into signals. This is done for each line in order, so the signals of all pixel can be read.

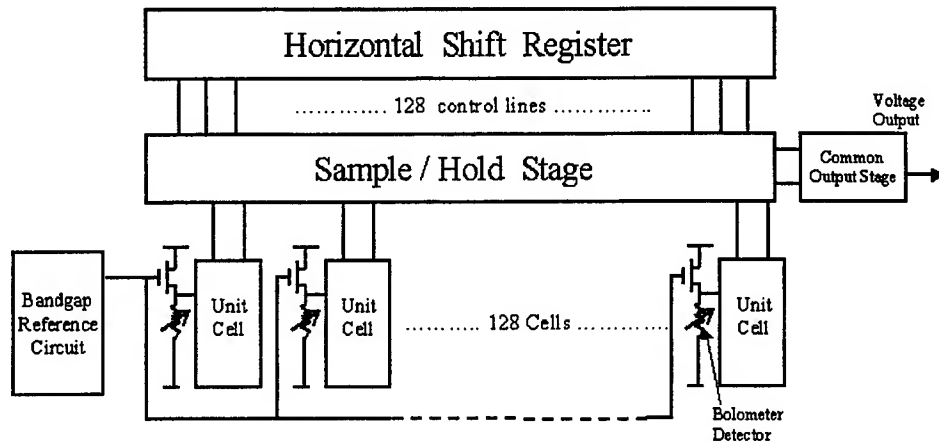


Fig. 3. Structure diagram of 1x 128 BRCC Linear Array

A. The bandgap reference circuit

The unit readout cells have constant current with a bandgap reference circuit. In order to reduce the effect caused by the operating temperature and power supply variations for amplifier applications, the bandgap reference generator was produced with the substrate bipolar PNP transistors in the standard CMOS fabrication process.

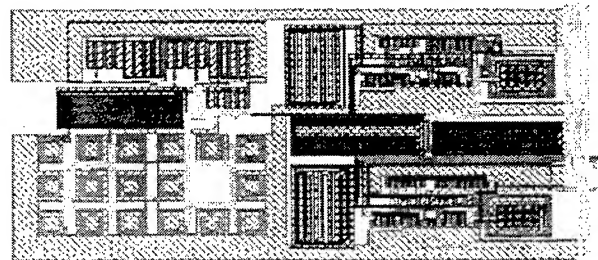
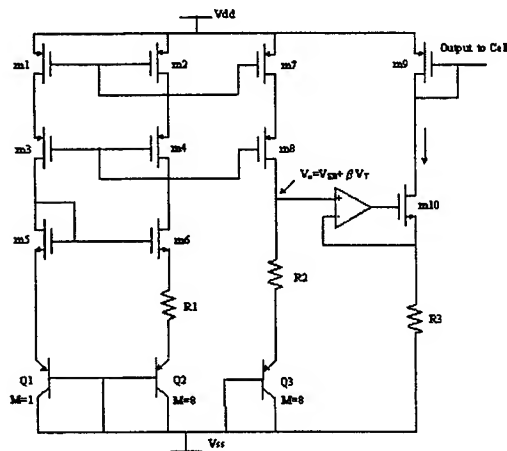


Fig. 4. Schematic and layout diagram of bandgap reference circuit.

B. The Unit-Cell Input Stage

The unit cell input stage was produced using a previously proposed SFD circuit and cascode amplifier. The UNC input circuit supports variable gain efficiency, good detector bias stability, low noise, good threshold uniformity, low power dissipation, and small-size input stage. The bolometer signal voltage is mirrored to the selected switch and a voltage gain is introduced using the cascode amplifier to improve the detection sensitivity, and noise coupling effect to the input stage. In the design of the BRCC input stage, a high-swing cascode voltage mirror is used to increase the output impedance and voltage accuracy. As shown in Fig. 5 the source follower is composed of M2 to M4 and cascode amplifier is composed of M5 to M7. The voltage gain is shown in Eq. 1.

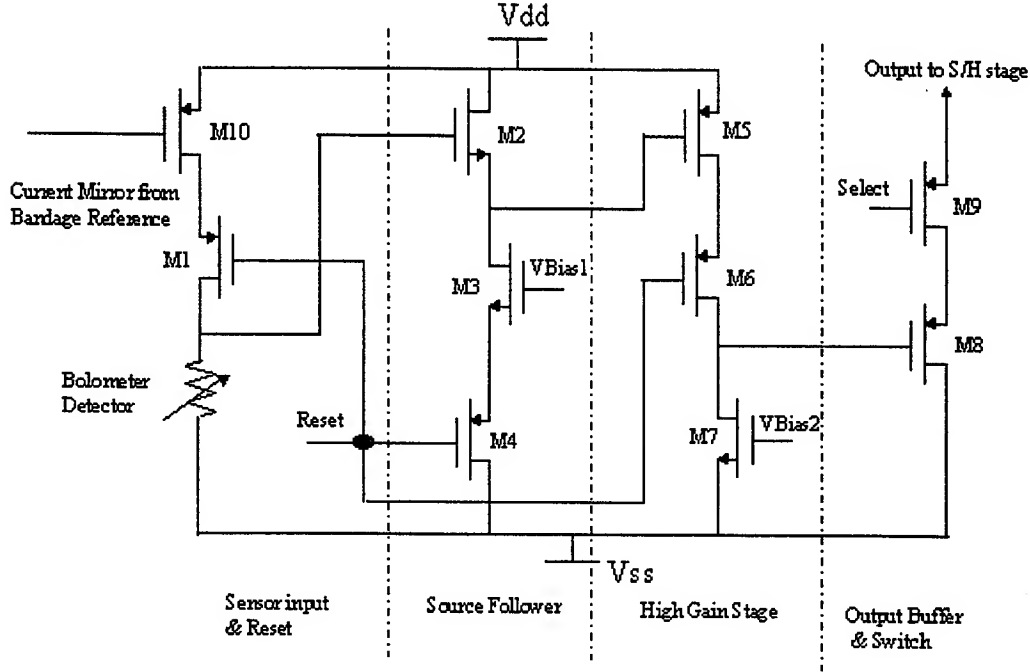


Fig. 5 BRCC readout schematic diagram of the unit cell of bolometer sensor

$$\frac{V_{out}}{V_{in}} = \frac{-g_{m5}(g_{ds6} + g_{m6} + g_{mbs2})}{g_{ds5}g_{ds6} + g_{ds5}g_{ds7} + g_{ds6}g_{ds7} + g_{ds7}(g_{m6} + g_{mbs6})} \approx \frac{-g_{m5}}{g_{ds7}} = -\left(\frac{2k'_sW_5}{L_5I_D\lambda_7^2}\right)^{1/2} \quad (1)$$

Using the reset switch technique to obtain low linear array power dissipation. The M4, M6 PMOS switch are closed when the control voltage is high (0V), and open when the control voltage is low (-5V). The switch is closed when the circuit is not in operation. This switch can reduce (N-1) times power dissipation. The source follower circuit associate of that M2, M3, M4 MOS. The M3 MOS as an active load. The gate voltage (V_{bias1}) can be controled to shift output DC level to satisfy cascode amplifier of the second stage working DC point. The M7 MOS is active load of the cascode amplifier. We can control gate voltage (V_{bias2}) to obtain voltage gain below the Eq. 1. The buffer M8 can be transfer voltage to current and output to sample and hold stage.

C. The Output Stage

In the common output stage, as shown in Fig. 6., the NMOS M14 with the dc gate bias $V_{bias3} = -2V$ is the current source active load of the output amp. The current be output when the switch M12 is ON. The difference voltage is coupled through to the common output stage. This eliminates the fixed pattern noise and $1/f$ noise in the multiplexing free. The sample and hold stage is achieved by the PMOS and capacitor. Using the TIA mode amp can be obtained output voltage as $V_{out} = i_{out} \cdot R_f$

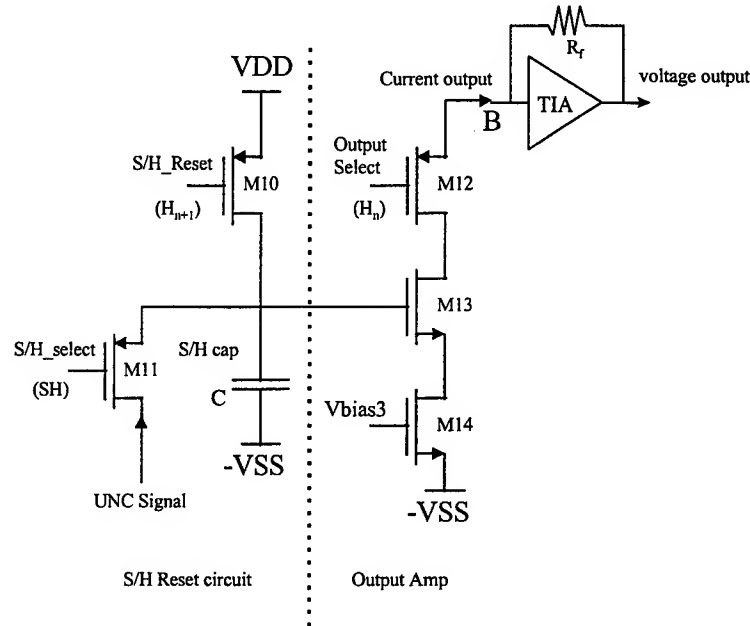


Fig. 6. BRCC readout schematic diagram of the S/H and output stage of bolometer sensor

D. The Multiplexer of BRCC Chip Operation

There are three bias voltages in the BRCC chip. Array them, the gate voltage V_{bias1} of source follower active load, the gate voltage V_{bias2} of cascode amp active load and the gate voltage V_{bias3} of output amplifier active load. Conversely, in order to monitor the internal current of the gate, external bias voltages must be applied.

The clock timing waveforms of the master clock M_Clk, Clk, and $H_1 \sim H_n$, select, reset with function generator. Where the clock signal has a high level of 0V and low level of -5V. The readout operation of the BRCC chip is described below. When the first the signal of select is low and the S/H is low and reset is low, the unit-cell input stage is switched to the sample and hold stage and signal to be output. After all pixels in the row have been read, the row is reset.

IV. SIMULATION and EXPERIMENTAL RESULTS

The responsivity of the detector is the ratio between the output signal and the detected radiant power. To measure the responsivity of the bolometer, the entire measurement system was set up as shown in Fig. 7. The bolometer was loaded into a dewar with a ZnSe window. The chamber of the dewar pressure is below 2×10^{-2} Torr. The ZnSe window has a high transmission in the $0.1 \sim 13 \mu\text{m}$ wavelength. The distance between the blackbody and bolometer is 10 cm. The black body is set at 800 K , and its aperture diameter is 0.64 cm.

Polysilicon resistances with different temperatures are shown in Fig. 8. The resistance and temperature coefficient of resistor (TCR) of polysilicon is strongly dependent upon the impurity concentration in polysilicon. Fig. 9. shows the measured dependence of the TCR on the resistivity of polysilicon. When the impurity concentration increase, both the resistance and TCR decrease.

The bandgap reference generator measurement presents a temperature coefficient of $250 \text{ ppm}/^\circ\text{C}$ over the temperature range from -20°C to 85°C . Both of circuit simulation and measured results of the bandgap reference biased operational amplifier are satisfied in this initial research, the results are shown in the Fig. 10. The linear analysis of BRCC readout circuit as show in Fig. 11.

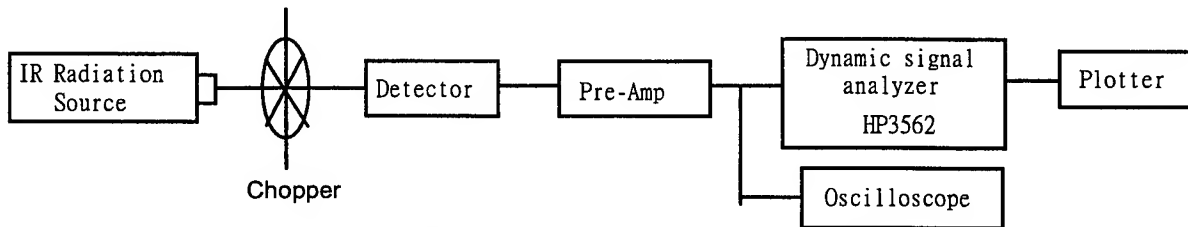


Fig. 7. Measurement structure of BRCC IR readout circuit

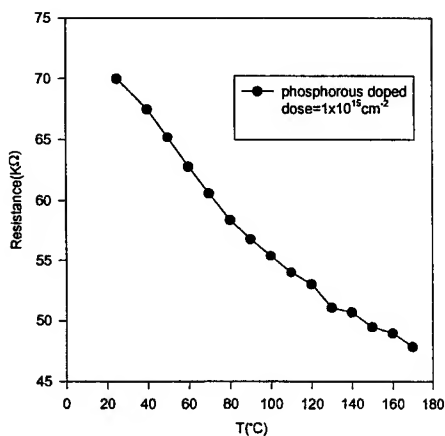


Fig. 8. Resistance of polysilicon with different temperatures

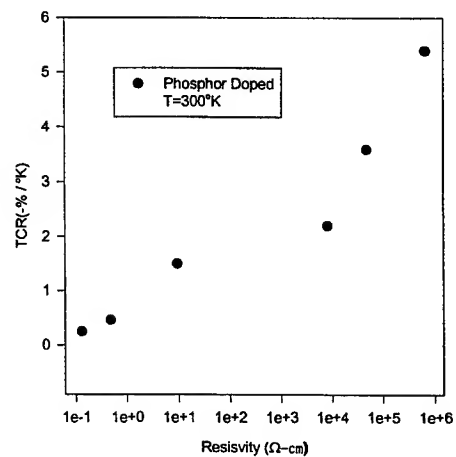


Fig. 9. Dependence of TCR on resistivity of polysilicon

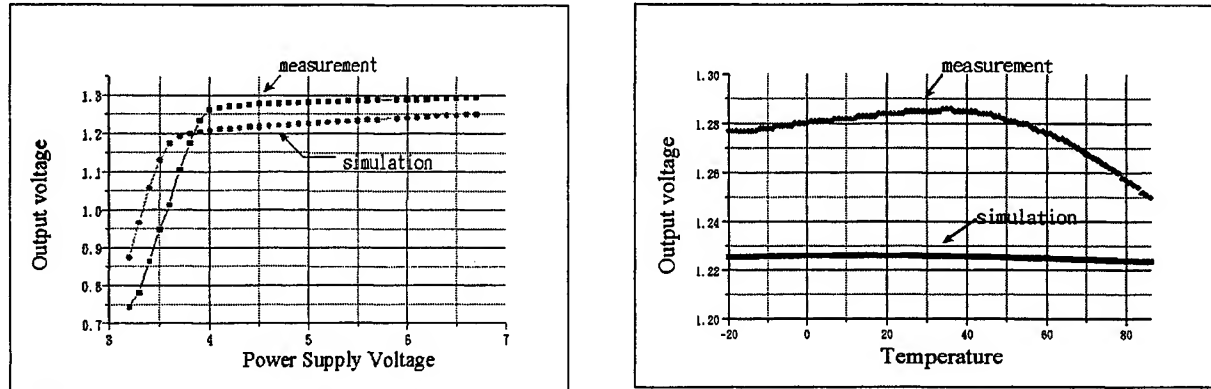


Fig. 10 Simulation and measurement different power supplied voltages and temperatures

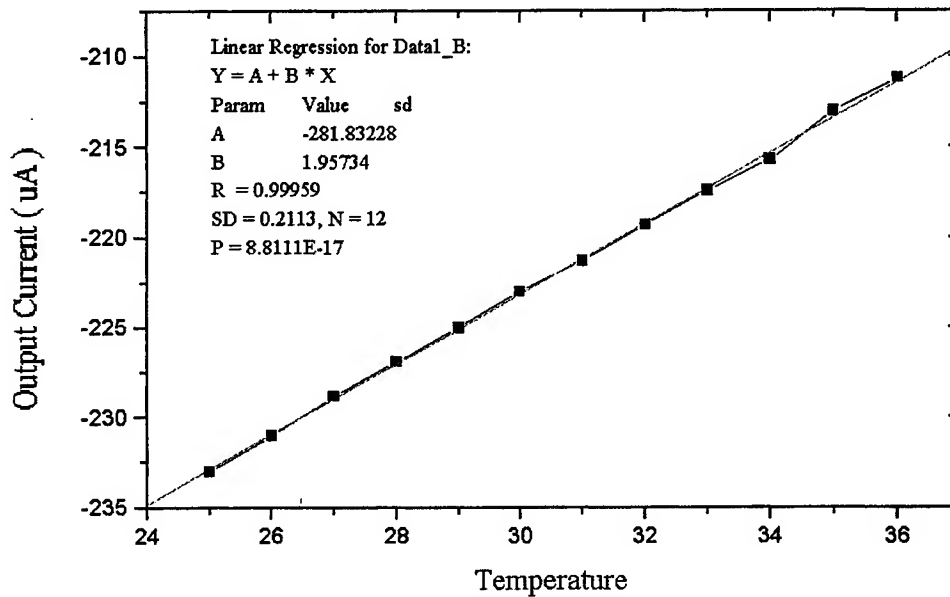


Fig. 11. Linearity of BRCC readout circuit

V. CONCLUTIONS

The measurement results of the fabricated readout chip at room temperature with VDD and VSS supplied voltages have successfully verified both the readout function and performance improvement. The readout circuits corresponding to thermal sensitive resistors using surface micromachined techniques at room temperature were approximately $65k\Omega$ with a resistance of polysilicon temperature coefficient film about $0.3\%/^{\circ}\text{C}$. The results of the bandgap reference biased satisfy the characteristic of linear resistive bolometer arrays. The fabricated chip has high gain ($>40\text{dB}$) and an active power dissipation ($<30\text{mW}$) sensor. The proposed CMOS bandgap Reference Constant Current (BRCC) structure can be applied to various IR FPAs.

REFERENCES

1. C. Lider, L. Paratte, M-a Gretillat, V.P. Jaecklin and N.F. de Rooij, "Review Surface Micromachining", J. Micromech Microeng. 2. PP.122-132,1992.
2. Kenneth E. Bean "Anisotropic Etching of Silicon " IEEE transaction on Electron Devives, Vol. ED-25, No. 10. pp. 1185-1193, October 1978.
3. D.B.Lee "Anisotropic Etching of Silicon "J. Appl . Phys Vol. 40, 45694574, October 1969.
4. C. H. Mastrangelo, Y. C. Tai, and R. S. Muller, "Thermophysical Properties of Low-Residual Stress Sillicon-rich , LPCVD Silicon Nitride Films "Sensor and Actuators A21-A23, pp. 856,1990
5. Akio Tanaka, Shouhei Matsumoto, Nanao Tsukamoto, Shigeyuki Itoh, Kazuhiro Chiba, Tsutomu Endoh, Akihiro Nakazato, Kuniyuki Okuyama, Yuuichi Kumazawa, Minoru Hijikawa, Hideki Gotog, Takanori tanaka, and Nobukazu Teranishi "Influence of Bias Heating on Titanium Bolometer Infrared Sensor ", SPIE Vol.3061, pp. 198-209, 1997.
6. S Middelhoek, A A Bellekom, U Dauderstadt, P J French, S R in 't Hout, W Kindt, F Riedijk and M J Vellekoop "Silicon Sensor " Meas. Sci. Technol. 6, pp. 1641-1658. 1995.
7. Eric R. Fossum and Bcdabrata Pain "Infrared Readout Electronics for Space Science Sensors: State of the Art and Future Directions" SPIE Vol.2020 Infrared Technology XIX, pp. 262-283. 1993.
8. Burgess R. Johnson and Paul W. Kruse "Silicon Microstructure Superconducting Microbolometer Infrared Arrays"SPIE Vol.2020 Infrared Technology XIX. pp. 2-11,1993.

SESSION 3

Quantum Dots

Quantum dot active regions for extended wavelength (1.0 μm to 1.3 μm) GaAs-based heterostructure lasers and vertical cavity surface emitting lasers

D.L. Huffaker¹, G. Park, Z. Zou, O.B. Shchekin, and D.G. Deppe

Microelectronics Research Center
Department of Electrical and Computer Engineering
The University of Texas at Austin, Austin, TX 78758

ABSTRACT

In this paper we discuss crystal growth, spontaneous emission characteristics and low threshold performance of 1.3 μm InGaAs/GaAs quantum dot heterostructure lasers grown using sub-monolayer depositions of In, Ga, and As. Oxide-confinement is effective in obtaining a low threshold current of 1.2 mA and threshold current density of 19 A/cm² under continuous-wave room-temperature operation. At 4 K a remarkably low threshold current density of 6 A/cm² is obtained. We also discuss ground state lasing at $\lambda=1.07 \mu\text{m}$ of a vertical cavity surface emitting laser in which a stacked and high dot density active region has been incorporated. The high QD density active region is achieved using alternating monolayers of InAs and GaAs. Lasing threshold conditions and gain parameters for a ground state quantum dot vertical cavity laser are also analyzed.

Keywords: quantum dots, InGaAs/GaAs, semiconductor lasers, surface emitting lasers

1. INTRODUCTION

The QD has advanced from a physical novelty to a material system with sufficient quality for use in laser diode active regions. Furthermore, the QD active region has potential applications in technology, such as extended wavelength (1.0 μm - 1.3 μm) operation of GaAs-based lasers¹⁻¹¹ and lateral electronic carrier confinement¹²⁻¹⁷ important for microcavity applications such as low power VCSELs and photonic bandgap defect lasers. As QD growth techniques and device designs mature, threshold current densities decrease and the QD GaAs-based laser wavelength increases. Early papers predict that the QD atomic-like density of states offer the potential for low threshold current, low current density^{18,19} and good temperature stability^{20,21} compared to quantum well devices. These assertions have been recently demonstrated experimentally with minimum CW, room temperature (300 K) threshold currents as low as 1.2 mA¹⁰, a threshold current density of 19 A/cm²¹⁰ and nearly temperature invariant threshold from 4 K to 250 K⁵.

Figure 1 shows the historical development of the InGaAs/GaAs QD GaAs-based laser using published threshold current densities and operating wavelengths. Major developments include the first demonstration of a QD diode laser ($J_{\text{th}} \sim 220$ A/cm², 77 K, pulsed) in 1994²¹. In 1996, the first 300 K QD laser is reported ($J_{\text{th}} = 650$ A/cm², pulsed)²³, followed by a very low threshold current density of $J_{\text{th}} < 100$ A/cm² (pulsed)²⁵. Later in 1996, the first CW, 300 K operation is demonstrated ($J_{\text{th}} \sim 3$ kA/cm²)²⁶. In 1998, the first 1.3 μm diode laser is reported ($J_{\text{th}} = 405$ A/cm², pulsed)¹ and in 1999, CW, 300 K operation at 1.3 μm is demonstrated ($J_{\text{th}} = 200$ A/cm²)⁴. To date, the lowest threshold current density measured for a QD laser is 19 A/cm² (300 K, CW)¹⁰ with a wavelength of 1.3 μm . The data points for Fig. 1 are found in the following references which are listed in order of publication date: Refs. 21-28, 1, 2, 4, 5, 6, 10. The present 1.3 μm laser performance is limited by nonradiative recombination and inhomogeneously broadened linewidth, and the effects of these parasitic current paths on lasing threshold have been studied theoretically^{7,29-31}.

The extended wavelength GaAs-based vertical cavity surface emitting laser (VCSEL) is of interest for applications in optical signal transmission. Especially important is the 1.3 μm wavelength regime for optical fiber communication, but new applications may also develop for VCSELs that operate at wavelengths where silicon is transparent or semi-transparent ($1.0 \mu\text{m} < \lambda < 1.3 \mu\text{m}$) due to the interest in hybrid integration with Si circuits. The benefit of high quality

¹electronic mail: dhuf@mail.utexas.edu

AlAs/GaAs distributed Bragg reflectors (DBRs) and selective oxidation processes make monolithic AlGaAs/GaAs VCSELs attractive. In addition, the QD active region is expected to generate new and interesting device physics when coupled with the AlAs/GaAs-based microcavity^{12,14,15,17}.

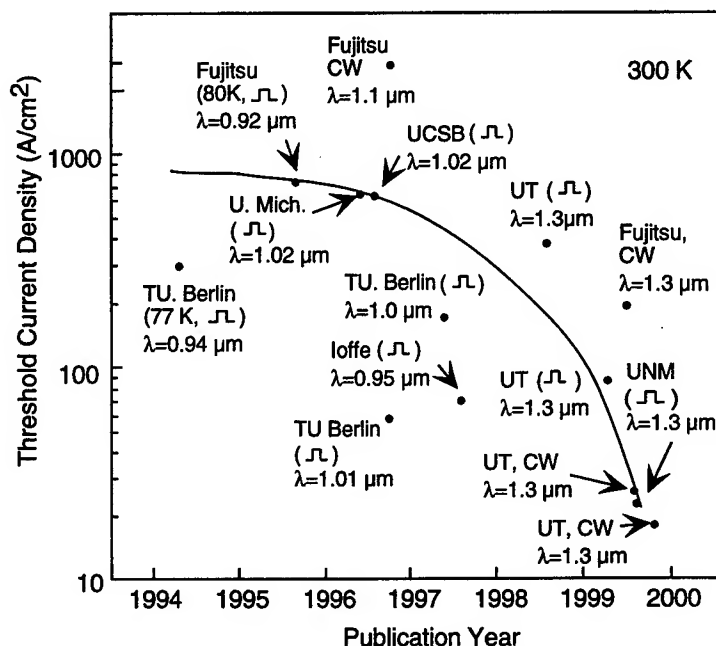


Fig. 1: The historical development of the InGaAs/GaAs QD GaAs-based laser showing published threshold current densities and operating wavelengths as a function of publication year.

Although 300 K ground state lasing has been demonstrated at 1.3 μm for GaAs-based edge emitters, QD VCSEL wavelengths have been similar to QWs^{13,32,33} or have corresponded to higher energy levels¹¹. The difficulty in extending the VCSEL wavelength past 1.0 μm out to 1.3 μm is due to the small gain in the ground state of a single QD layer. This problem is aggravated by effects of nonradiative recombination at 300 K and the inhomogeneously broadened linewidth. Stacking the QD layers has been used by many groups in order to increase the ground state gain.

In this paper, we review crystal growth and spontaneous electroluminescence characteristics at of 1.3 μm QDs along with low threshold current density lasing results. At the wavelength of 1.3 μm, we have achieved a 4.1 mA CW, 300 K threshold with an etched-stripe laser and 1.2 mA threshold with an oxide-defined stripe laser. The minimum threshold current density which we have achieved is 19 A/cm² (CW, 300 K) and 6 A/cm² (pulsed, 4 K) which we believe is very close to transparency. We also analyze threshold conditions for the ground state QD VCSEL and describe ground state lasing from a 1.07 μm VCSEL from a high dot density, stacked active region.

2. EPITAXIAL CRYSTAL GROWTH

Understanding the crystal growth has been essential in the advancement of the QD active region, although precise mechanisms controlling the QD formation are still not fully understood. Since Mukai and coworkers³⁴ initially demonstrated that InGaAs/GaAs QDs can achieve a high quality semiconductor energy gap corresponding to a 1.3 μm wavelength, much progress has been made. Already four groups have demonstrated 1.3 μm lasing from GaAs-based edge emitters^{1,2,4--8,10} and two groups have demonstrated CW, 300 K operation^{4,5,10}. Although the growth techniques vary, the most recent 1.3 μm laser demonstrations employ QD growth on a strained InGaAs buffer^{5,10} or QDs grown inside a strained InGaAs layer^{4,6,8}.

Using electroluminescence characteristics as a guide, our group has optimized a growth technique for achieving high quality 1.3 μm QDs which involves cycled and separate submonolayer deposition of In, Ga and As³⁵. The growth sequence is a 0.25 monolayer (ML) of In followed by a 5 sec. As flux, 0.25 ML Ga followed by a 5 sec. As flux. This

cycle is repeated 20 times for a total deposition of 10 ML of average composition $\text{In}_{0.50}\text{Ga}_{0.50}\text{As}$ QDs. The electroluminescence efficiency is sensitive to the thickness of each sub-ML deposition. We have found that 0.25 ML of In followed by 0.25 ML of Ga is the optimum thickness³⁵. Figure 2 shows an atomic force microscope (AFM) photograph of a $1\text{ }\mu\text{m} \times 1\text{ }\mu\text{m}$ surface directly after growth of 0.25 ML/0.25 ML QDs. The dot density is $\sim 10^{10}/\text{cm}^2$ and the dot diameter is $\sim 500\text{ }\text{\AA}$. We approximate the dot height to be $\sim 100\text{ }\text{\AA}$ from the AFM image. The In and Ga growth in the absence of As allows a larger surface migration of the column III atoms during QD formation, and favors larger QDs. Perhaps the easy migration also allows the QDs to form with an optimized In grading within the QDs themselves to minimize defects due to the strained material. The 300 K electroluminescence has a center wavelength of $1.32\text{ }\mu\text{m}$ and is significantly more efficient than the other growth sequences. For lasers, it is attractive to achieve the $1.3\text{ }\mu\text{m}$ wavelength with a minimum amount of indium in order to reduce strain and dislocations. The sub-ML growth method yields $1.3\text{ }\mu\text{m}$ emission with a total In content of 5 ML.

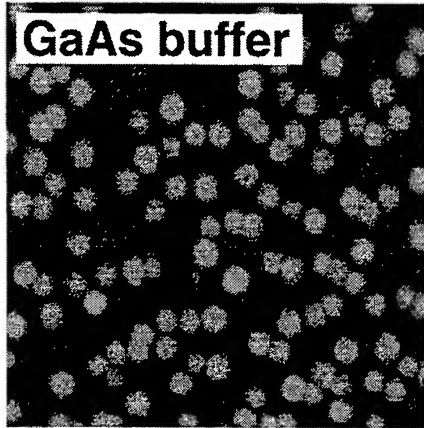


Fig. 2: Atomic force microscope image of epitaxial surface just after the formation of QDs from ten total MLs of InGaAs deposited using a sub-ML technique. A QD density of $1 \times 10^{10}\text{ cm}^{-2}$ is measured.

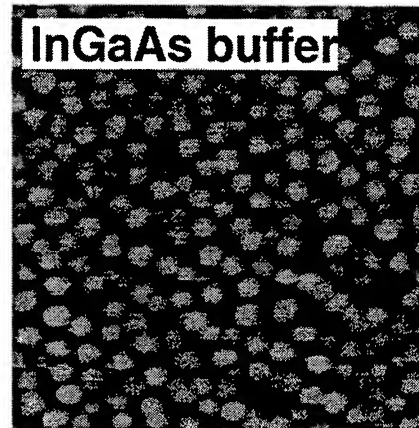


Fig. 3: Atomic force microscope image of epitaxial surface just after the formation of QDs from ten total MLs of InGaAs deposited using a sub-ML technique. The dots are formed on a 15 ML $\text{In}_{0.10}\text{Ga}_{0.90}\text{As}$ buffer layer. The resulting QD density is $\sim 2 \times 10^{10}\text{ cm}^{-2}$.

The current focus of many QD crystal growth studies is improving the QD size uniformity and reducing the non-radiative recombination that is present, seemingly due to strain effects. Both of these characteristics can have a large impact on lasing threshold. As we will discuss in the following sections, the nonradiative recombination rate increases for carriers in higher energy levels and radiative efficiency decreases for increasing current density. An increased QD density can increase radiative efficiency by keeping a larger fraction of the carriers in the ground state. Stacking QD layers can be effective for the same reasons^{4,8}. We have been able to increase the QD density by growing QDs on an InGaAs buffer layer. Figure 3 shows an AFM image of a $1\text{ }\mu\text{m} \times 1\text{ }\mu\text{m}$ square crystal surface where the $1.3\text{ }\mu\text{m}$ InGaAs QDs are grown on a 15 ML $\text{In}_{0.10}\text{Ga}_{0.90}\text{As}$ buffer layer using the sub-ML technique. The resulting QD density is $\sim 2 \times 10^{10}/\text{cm}^2$ which is a factor of two increase compared to the QDs grown on a GaAs buffer as in Fig. 2. If the QDs are grown on a thinner buffer layer ($<15\text{ ML}$) of $\text{In}_{0.10}\text{Ga}_{0.90}\text{As}$, the QD density remains $\sim 1 \times 10^{10}/\text{cm}^2$. A thicker buffer ($>15\text{ ML}$) will result in a constant density of $\sim 2 \times 10^{10}/\text{cm}^2$. Because the QD diameter remains $\sim 500\text{ }\text{\AA}$, independent of the QD density, the additional QD material must come from the InGaAs buffer layer and the wetting layer. Although the QD uniformity does not improve significantly, the increased QD density is critical since the gain from the $1.3\text{ }\mu\text{m}$ QD ensemble is not too much greater than distributed loss rates for present laser cavities.

Figure 4 shows a cross-sectional transmission electron microscope (TEM) photograph³⁶ of a QD ensemble grown under similar conditions to that shown in Fig. 2, with the exception that the QDs are covered with $100\text{ }\text{\AA}$ of GaAs followed by AlGaAs. From the TEM photograph, the QDs are $\sim 300\text{ }\text{\AA}$ in diameter and $\sim 150\text{ }\text{\AA}$ in height. The difference in QD diameters measured by AFM compared to TEM may be due to variations in growth, as the ground-state photoluminescence wavelength of the TEM sample is $1.27\text{ }\mu\text{m}$, or it may be due to effects of GaAs overgrowth on the size and shape of the QDs. We can approximate the height of the QD during overgrowth using the reflection high energy electron diffraction (RHEED) pattern. As the QDs form, the RHEED pattern goes from streaky to spotty. Similarly, as

the QDs are covered and the growth surface planarizes, the RHEED pattern changes from spotty to streaky. In high quality 1.3 μm QDs, this change occurs during deposition of 80 \AA and 120 \AA of overgrowth material.

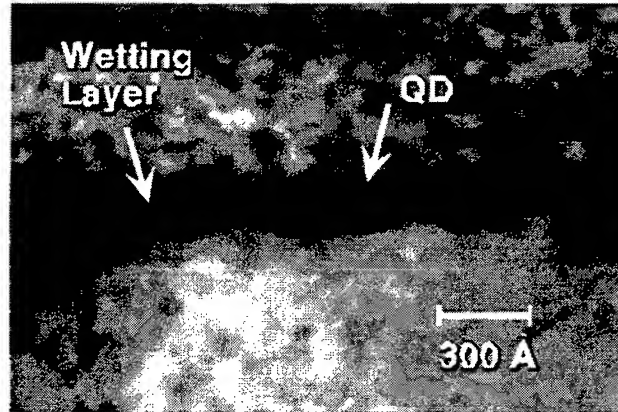


Fig. 4: Cross-section transmission electron microscope image showing a 10 ML total deposition of 0.25 ML/0.25 ML sub-ML QDs surrounded by GaAs.

3. TEMPERATURE CHARACTERISTICS OF SPONTANEOUS ELECTROLUMINESCENCE

We have studied spontaneous emission characteristics as a function of temperature to determine mechanisms controlling the threshold temperature dependence for edge-emitting QD lasers. We find that nonradiative recombination is the dominant limitation. The electroluminescence data shown in Figs. 5,6 and 7 are measured from short edge-emitters in which lasing is inhibited by end loss. A single QD layer active region is grown using the 0.25 ML/0.25 ML technique described in Section 2 with a total of 10 MLs deposited. The QDs are surrounded by a 200 \AA GaAs barrier on either side and centered in a thick $\text{Al}_{0.20}\text{Ga}_{0.80}\text{As}$ layer.

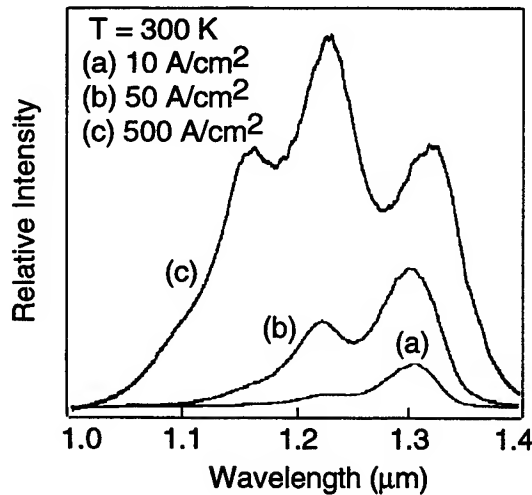


Fig. 5: Spontaneous emission spectrum measured from 1.1 mm long device at 300K for several different current densities.

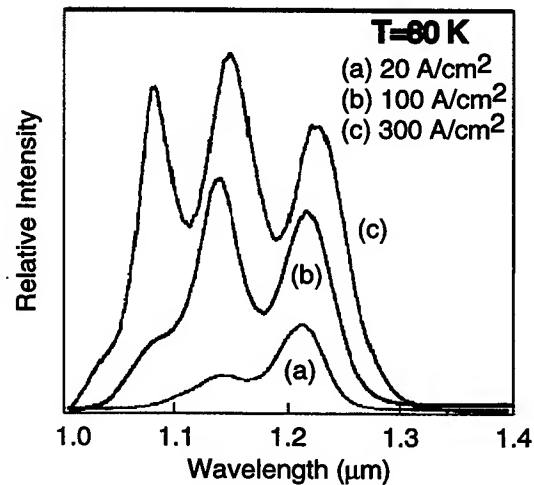


Fig. 6: Spontaneous emission spectrum measured from 1.1 mm long device at 80 K at several different current densities.

Figure 5 shows the QD spontaneous emission spectra at 300 K for several current densities. At the lowest current density of 5 A/cm^2 (spectra not shown), only the ground state is excited at the 1.31 μm wavelength with a FWHM of 40 meV. With increasing current density (10 A/cm^2 , 50 A/cm^2 and 500 A/cm^2), emission from three energy levels is

apparent. These transitions correspond to the 1.31 μm wavelength for the ground state, 1.23 μm for the first excited state and 1.16 μm for the second excited state. At 80 K these transitions correspond to 1.22 μm , 1.14 μm and 1.09 μm wavelength as shown in Fig. 6). At both 80 K and 300 K, the higher energy levels begin to fill before the ground state is saturated.

The electroluminescence output power for the 1.1 mm cavity is measured versus current and converted to efficiency versus current density at several temperatures. The results are shown in Fig. 7. At 80 K, the peak efficiency is 0.5 % at 5 A/cm^2 which corresponds to ground state emission. We believe based on collection efficiency that the internal quantum efficiency is well over 50 %. With increased current density and subsequent increased level filling (Fig. 6) the efficiency drops to 0.20 % at 100 A/cm^2 . This trend indicates that an increased nonradiative recombination rate exists for carriers in higher energy levels even at low temperatures. At 160 K, the peak efficiency drops to 0.34 % at 5 A/cm^2 and again decreases smoothly with increasing current density. At 250 K and 300 K, the peak efficiencies are 0.11 % and 0.04 % at current densities of 10 A/cm^2 and 40 A/cm^2 , respectively. The drop in peak efficiency at low current density as the temperature is increased indicates that temperature dependent nonradiative recombination centers are present in the QDs. Furthermore, we see that the radiative efficiencies vary among samples which are grown under similar conditions. Room temperature electroluminescence efficiencies as high as 0.20 % have been measured³⁵. Therefore, we attribute the nonradiative recombination to point defects on the QD surface or within the QD bulk that can be eliminated by optimized crystal growth.

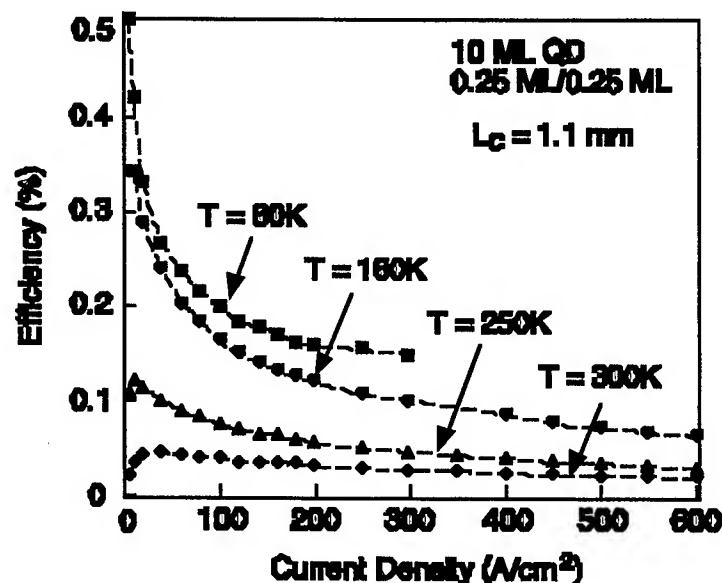


Fig. 7: Spontaneous emission efficiency of a 1.1 mm long device measured at several temperatures as a function of current density. Two trends are observed. The ground state efficiency decreases with increasing temperature and the efficiency at each temperature decreases with increasing current density.

From this data we see two important aspects of the nonradiative recombination. First, at all temperatures, as the excitation level increases, so does the nonradiative recombination. This can be explained by the existence of selection rules which govern radiative transitions between different electron-hole levels, but that do not exist for nonradiative recombination⁷. As more electrons and holes are added to each QD, the possible nonradiative recombination paths between an electron and multiple holes increase. In contrast, for radiative transition, each electron level is coupled to only one hole level. Second, the nonradiative transition rate is sensitive to temperature and increases for increasing temperature. Both effects influence lasing threshold. Therefore, it is important to operate the QD lasers at the lowest possible threshold current and current density in order to reduce these nonradiative effects.

4. LOW THRESHOLD 1.3 μm EDGE-EMITTING LASERS

We have studied both etched-stripe and oxide-confined edge emitters with very similar epitaxial design. The oxide-confined aperture allows a smaller device width to be realized without incurring significant lateral waveguide loss. A

schematic of the oxide-confined laser structure is shown in Fig. 8. The inset shows the QD active region centered in the waveguide along with material compositions and layer thicknesses within the waveguide. The laser heterostructure is grown on an n-type GaAs substrate using molecular beam epitaxy¹⁰. The temperature of the growth is 610 °C, except for the QD region. The undoped waveguide consists of $\text{Al}_{0.05}\text{Ga}_{0.95}\text{As}$ and is 0.194 μm thick. A 300 Å $\text{Al}_{0.98}\text{Ga}_{0.02}\text{As}$ layer is grown 0.35 μm both above and below the active region. Short period superlattices (200 Å thick) composed of alternating layers of $\text{Al}_{0.85}\text{Ga}_{0.15}\text{As}$ and GaAs to gradually change aluminum composition from 85% to 5% are grown at the interfaces between the waveguide and cladding layers to smooth the heterointerfaces. The Si and Be doping is decreased to $\sim 10^{16} \text{ cm}^{-3}$ within 0.5 μm of the $\text{Al}_{0.85}\text{Ga}_{0.15}\text{As}$ layers surrounding the waveguide, and at $\sim 2 \cdot 10^{17} \text{ cm}^{-3}$ in the remaining $\text{Al}_{0.85}\text{Ga}_{0.15}\text{As}$. A p^+ GaAs contact layer caps the structure.

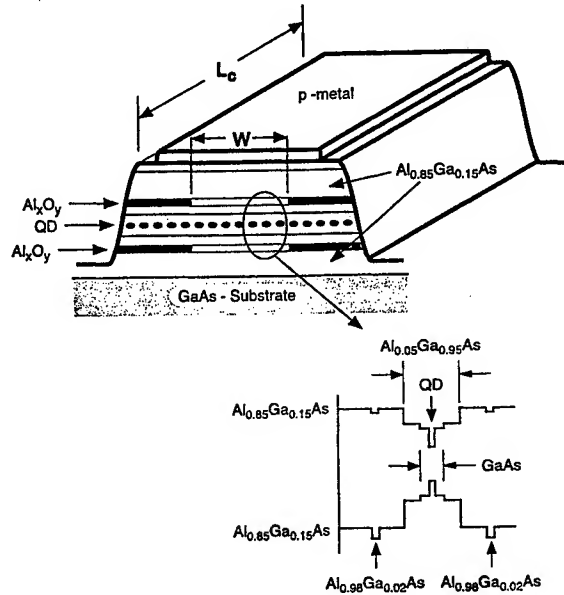


Fig. 8: Schematic cross-section of oxide-confined stripe laser. Inset shows material compositions in the waveguide region.

The single layer QD active region is grown at 510 °C. A 150 Å GaAs barrier is grown before the QD active region at 610 °C then the temperature is reduced to 510 °C. A 15 ML buffer layer of $\text{In}_{0.09}\text{Ga}_{0.91}\text{As}$ is grown followed by the QD deposition using the cycled sub-ML epitaxy sequence described above. The 12 ML deposition has an average composition of $\text{In}_{0.50}\text{Ga}_{0.50}\text{As}$ and the QDs are covered with 150 Å of GaAs. Atomic force microscope images of the crystal surface with the growth halted just after the 12 ML deposition shows a QD density of $n_{\text{QD}} \sim 2 \times 10^{10} \text{ cm}^{-2}$ with lateral sizes of ~ 500 Å similar to that shown in Fig. 3. The QD ground states radiate with an ensemble FWHM energy spread of $\hbar\Delta\omega \approx 30 \text{ meV}$.

The oxide-confined stripe lasers are fabricated by wet etching ridge waveguides through the upper cladding layer, active region and partially into the lower cladding layer to expose both $\text{Al}_{0.98}\text{Ga}_{0.02}\text{As}$ layers. The $\text{Al}_{0.98}\text{Ga}_{0.02}\text{As}$ layers are converted to oxide³⁷ in a steam environment at 470 °C for ~ 4 min. forming stripe apertures ranging from 5 μm to 20 μm . Cavity lengths that range from 420 μm to 1130 μm are formed by cleaving which is followed by depositing 5 or 6 pairs of MgF/ZnSe high reflectivity (HR) coatings on the end facets. The reflectivity of this mirror stack is >0.99 . The etched-stripe lasers are fabricated by wet etching shallow ridge waveguides through most of the upper cladding layer. The stripe widths range from 4 μm to 59 μm wide. Cavity lengths that range from ~ 1 mm to ~ 5 mm are formed by cleaving, and HR coatings consisting of 4 pairs of MgF/ZnSe are deposited on some of the lasers. The reflectivity of this mirror stack is >0.95 . The stripe lasers are mounted p-up on copper blocks.

Figure 9 shows lasing characteristics for a 5 $\mu\text{m} \times 870 \mu\text{m}$ oxide-confined laser and a 9 $\mu\text{m} \times 1020 \mu\text{m}$ etched-stripe laser under CW, 300 K operating conditions. The etched-stripe laser has 4 pairs of HR coatings on both facets (4 pairs/4 pairs), the oxide-confined has 5 pairs on one side and 6 pairs on the other side (5 pairs/6 pairs). The threshold current is 4.1 mA (45 A/cm²) for the etched-stripe laser with a threshold voltage of ~ 5.5 V and a very low 1.2 mA (27 A/cm²) for

the oxide-confined laser with a threshold voltage of ~ 5.0 V. To the best of our knowledge, this is the lowest threshold current yet reported for a QD laser. The dissipated power at threshold is ~ 6 mW for the oxide-confined laser and ~ 23 mW for the etched-stripe laser. In previous studies^{2,7}, we have shown that 300 K operation is limited by heating which results in increased upper level occupation and nonradiative recombination.

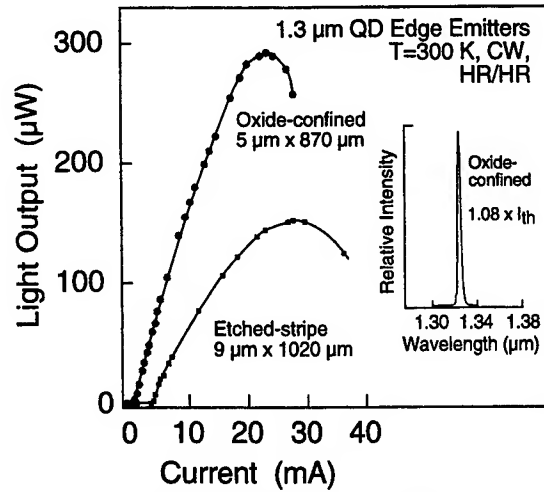


Fig. 9: Light versus current for both an oxide-confined laser (5 $\mu\text{m} \times 870 \mu\text{m}$, 5 pairs/6 pairs) and an etched-stripe laser (9 $\mu\text{m} \times 1020 \mu\text{m}$, 4 pairs/4 pairs) under CW, 300 K operation. Lasing threshold for the oxide-confined laser is 1.2 mA and 4.1 mA for the etched-stripe laser. The inset shows the lasing spectra for the oxide-confined laser just above threshold peaked at 1.33 μm .

Increased heat dissipation seems to trigger a cyclic "runaway" process which causes increased upper energy level population and nonradiative recombination which then lead to a higher threshold current. In this study, we have reduced the size of the active region by a factor of 2.1 which results in a lasing threshold current reduced by 3.4 as well as a threshold current density reduced by a factor of 1.7. The scaling of threshold current density to device size is due to reduced heating and nonradiative recombination in the smaller oxide-confined device. The external quantum efficiency just above threshold is only $\sim 2\%$ for both devices and decreases with increasing current. The decrease of the slope efficiency suggests that the device performance is still affected by the heating.

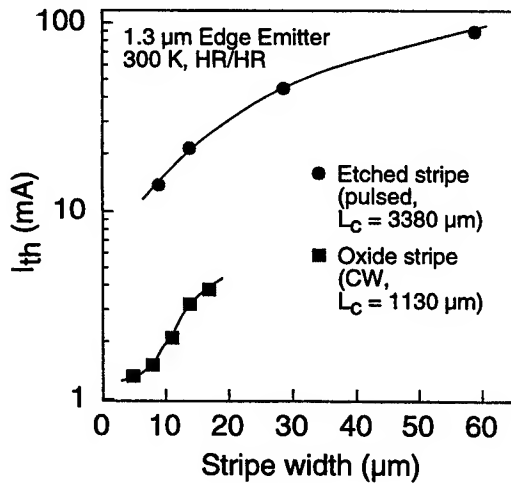


Fig. 10: Threshold current plotted as a function of stripe for the etched-stripe (pulsed, $L_c = 3380 \mu\text{m}$) and the oxide-confined laser (CW, $L_c = 1130 \mu\text{m}$).

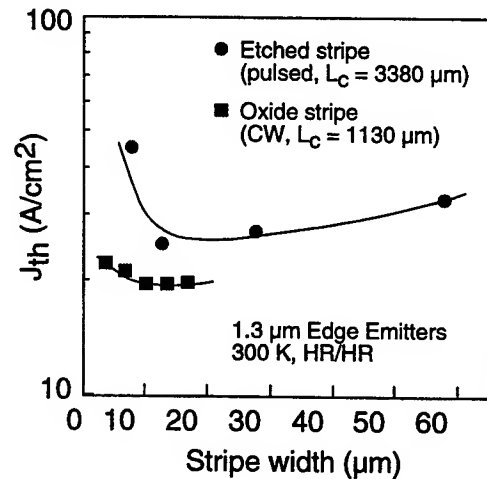


Fig. 11: Threshold current density plotted as a function of stripe width for the etched-stripe (pulsed, $L_c = 3380 \mu\text{m}$) and the oxide-confined laser (CW, $L_c = 1130 \mu\text{m}$).

The lasing wavelengths are $\lambda \sim 1.32 \mu\text{m}$ (not shown) for the etched-stripe laser and $\lambda \sim 1.33 \mu\text{m}$ for the oxide-confined laser which is shown in the inset spectrum. The maximum output power is $290 \mu\text{W}$ at 24 mA for the oxide-confined laser and $\sim 160 \mu\text{W}$ at 30 mA for the etched-stripe laser.

Figure 10 and 11 compare the 300 K threshold current and threshold current density as a function of stripe width for an etched-stripe laser ($L_c = 3380 \mu\text{m}$, 4 pairs/4 pairs, pulsed) shown by circles and the oxide-confined laser ($L_c = 1130 \mu\text{m}$, 5 pairs/5 pairs, CW) shown by squares. In Fig. 10, the minimum threshold current for the oxide-confined laser is 1.3 mA for a $5 \mu\text{m}$ wide aperture and threshold increases to 3.8 mA for a $17 \mu\text{m}$ wide device. The minimum threshold for the etched-stripe is $\sim 14 \text{ mA}$ for a $9 \mu\text{m}$ wide laser and increases to 89 mA for a $59 \mu\text{m}$ wide device. A combination of end loss and heating is responsible for the factor of seven difference in lasing threshold current between the $14 \mu\text{m}$ oxide-confined laser (3.2 mA) and the $14 \mu\text{m}$ etch-stripe laser (21.2 mA).

A comparison of threshold current density is shown in Fig. 11. The minimum threshold current density is 19 A/cm^2 (CW, 300 K) measured for an $11 \mu\text{m}$ wide oxide-confined laser. To our knowledge, this is the lowest 300 K threshold current density yet reported for a QD laser. For the etched-stripe laser, measured under pulsed condition, the threshold current density has a minimum of 25 A/cm^2 for the $14 \mu\text{m}$ wide stripe laser. For both types of lasers, the threshold current density increases with increasing stripe width, again indicating that the threshold is sensitive to heating even for pulsed operation. It is likely that the oxide-confined lasers are more sensitive to end loss than heating since shorter laser stripes ($L_c = 870 \mu\text{m}$, not shown) have consistently higher threshold current density and shorter devices yet ($L_c = 420 \mu\text{m}$, not shown) do not lase on the ground state. Waveguide scattering loss significantly increases the threshold current density for etched-stripes smaller than $14 \mu\text{m}$ and to a lesser degree for the oxide-confined lasers smaller than $11 \mu\text{m}$.

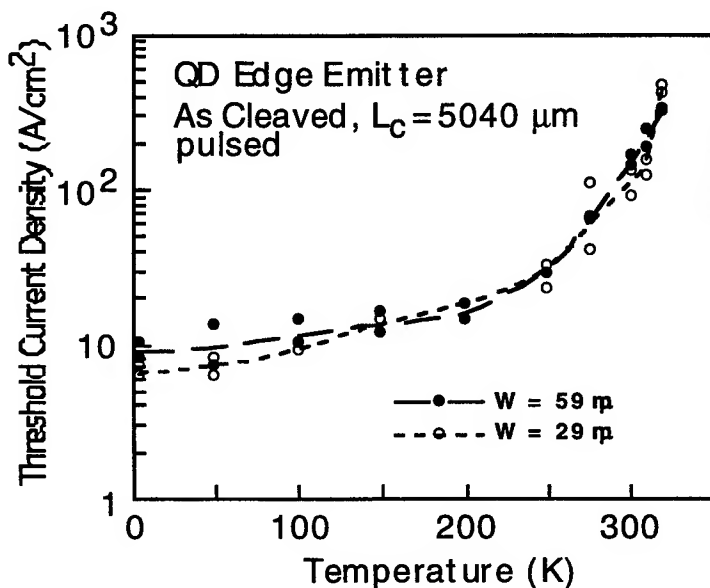


Fig. 12: Threshold current density versus temperature under pulsed operation. A minimum threshold current density of 6 A/cm^2 is measured at 4 K .

Figure 12 shows threshold current density dependence on temperature for two different etched-stripe devices with stripe widths of either 59 or $29 \mu\text{m}$ and cavity lengths of 5.04 mm (uncoated facets). A remarkably low threshold current density of 6 A/cm^2 is obtained at 4 K for the $29 \mu\text{m}$ wide stripe laser. In general, the threshold current density increases for increasing temperatures. However, at $\sim 150 \text{ K}$ the threshold increases less steeply. This is the temperature for which thermal QD coupling through the wetting layer occurs^{28,38}. Above $\sim 250 \text{ K}$ the threshold increases more steeply due to increasing nonradiative recombination that accompanies significant population of the QD upper energy levels and wetting layer.

The remarkably low threshold current density of 6 A/cm^2 at 4 K for the 5.04 mm cavity length shows that the transparency current of this single layer QD ensemble is small. For 4 K and low excitation we assume that nonradiative

recombination is negligible and arrive at a gain estimate for the QD ensemble. For the QD density of $2 \times 10^{10} / \text{cm}^2$, a degeneracy of two for the ground state levels, and a recombination time that we estimate to be ~ 640 ps, the transparency current is $J_{\text{trans}} = qn_{\text{QD}} / \tau_{\text{rec}} \approx 5 \text{ A/cm}^2$, with the maximum ground state gain obtained for a current density twice that at 10 A/cm^2 (in the absence of gain clamping due to stimulated emission.) The reduced density of states at the ground state peak energy is given by $\rho_{\text{red}}(\omega_g) = 4 \sqrt{\frac{\ln(2)}{\pi}} \frac{n_{\text{QD}}}{\Delta\omega} \approx 8.3 \times 10^{-4} \frac{\text{states}}{\text{cm}^2(\text{rad/sec})}$. The inversion factor, $(f_e - f_h)$, for laser operation can then be found from the threshold condition given by

$$\frac{\omega_c}{Q} = v_g \left[\alpha + \frac{1}{L} \ln\left(\frac{1}{R}\right) \right] = \sqrt{\frac{\ln(2)}{\pi}} \frac{c \lambda_c^2 \Gamma(f_e - f_h)_{\text{th}} n_{\text{QD}}}{\Delta z n^3 \tau_{\text{sp}} \Delta\omega} \quad (1)$$

where n is the refractive index (approximated to be ≈ 3.4), c is the speed of light in open space, v_g is the optical group velocity (approximated to be $\approx 6.7 \times 10^7 \text{ m/sec}$), L is the cavity length, R is mirror reflectivity product ($= \sqrt{R_1 R_2}$), λ_c is the free space wavelength of the cavity resonance, α is the waveguide loss, and $\Gamma/\Delta z$ is the waveguide confinement factor normalized by the active region thickness. For our waveguide we calculate $\Gamma/\Delta z = 3.57 \times 10^6 \text{ m}^{-1}$. The maximum modal gain from the QD ensemble ground state is then estimated from Eq. (1) to be $\sim 23 \text{ cm}^{-1}$. The threshold gain of 6 A/cm^2 would correspond to a modal gain of $\sim 5 \text{ cm}^{-1}$, so that the end loss of $\frac{1}{L} \ln\left(\frac{1}{R}\right) \approx 2.5 \text{ cm}^{-1}$ would require that $\alpha \approx 2.5 \text{ cm}^{-1}$ as well. With HR coatings of ≥ 0.95 reflectivity, the end loss is readily made negligible as compared to the internal waveguide loss. Along with heating, this leads to the low external differential slope efficiency shown in Fig. 9.

5. QUANTUM DOT VCSELS

In this section we discuss ground state lasing in a QD VCSEL operating at $1.07 \mu\text{m}$ and analyze the QD gain parameters. The VCSEL structure has been designed for very low optical losses therefore the lower 33 of 35 pairs of AlAs/GaAs DBRs are undoped. The first two pairs under the undoped $\text{Al}_{0.13}\text{Ga}_{0.87}\text{As}$ full-wave cavity are n-doped. An intercavity n-contact is used. The single upper p-DBR is lightly doped. Heavily doped AlGaAs/GaAs contact layers are grown on top of the p-type quarter-wave layers but are selectively etched from the VCSEL cavity region. The QDs are formed from five MLs of alternating InAs and GaAs. Each of the InGaAs QD layers are separated by 150 \AA of GaAs with 300 \AA of GaAs on either side of the 3-stack active region. A schematic is shown in Fig. 13³⁹.

Selective etching is used to form a trench stopping at the n-type GaAs layer of the first AlAs/GaAs bottom DBR pair. The n-type contact metallization is formed by evaporation/liftoff and alloying. Selective oxidation³⁷ is used to form aperture sizes ranging from $10 \mu\text{m}$ to $2 \mu\text{m}$ in diameter. After oxidation, the top contact layers are selectively etched from the optical cavity and p-contacts are deposited. The top DBRs (not shown in Fig. 13) are six pairs of MgF/ZnSe. Broad area edge emitters are also fabricated with $60 \mu\text{m}$ stripes to study the QD spontaneous emission while minimizing the filtering effect of the VCSEL cavity. Figure 14 shows electroluminescence from the wafer edge at a current density of 5 A/cm^2 . The ground state emission is centered at $1.07 \mu\text{m}$ with an inhomogeneously broadened linewidth of 76 meV . Two VCSEL resonances, one at $1.027 \mu\text{m}$ and one at $1.041 \mu\text{m}$ are also apparent.

Figure 15 shows CW, room temperature lasing characteristics from a $2 \mu\text{m} \times 2 \mu\text{m}$ square aperture. The lasing wavelength is $1.07 \mu\text{m}$ and by comparison with Fig. 14 is from the ground state transition of the QD ensemble. Threshold current is $268 \mu\text{A}$ and threshold voltage is 2.6 V . An uncalibrated Ge detector is used to measure the output intensity. The high threshold current density (6.7 kA/cm^2) is a factor of five greater than we would expect for a QW VCSEL of the same size⁴⁰. The high threshold current density is in part due to optical losses associated with the small aperture, but we also attribute it to a high nonradiative recombination loss rate described in Sections 3 and 4. A $10 \mu\text{m}$ device (LI not shown) has a threshold of $703 \mu\text{A}$ (895 A/cm^2) under CW, 300 K conditions.

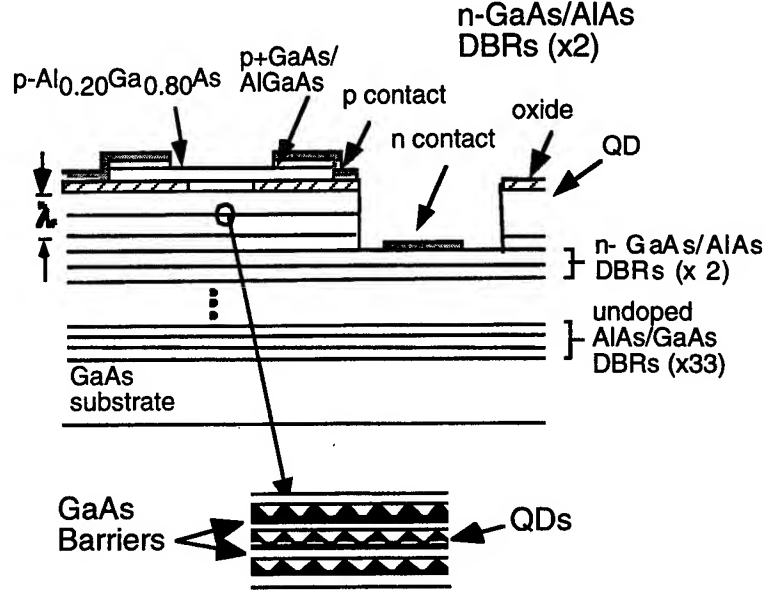


Fig. 13: Schematic cross section of the QD oxide-confined VCSEL device with intracavity contact. A 3-stack QD active region is centered in a full-wave cavity.

We have also analyzed the threshold condition for this QD VCSELs from the requirement of the round trip gain balancing the mirror loss as^{7,38}

$$\ln\left(\frac{1}{\sqrt{R_T R_B}}\right) = \sqrt{\frac{\ln(2)}{\pi}} \frac{8\pi^2 c^2}{n^2 \omega_o^2 \tau_{sp}} \frac{n_{QD}}{\Delta\omega} \quad (2)$$

where c/n is the speed of light in the cavity, ω_o is the cavity resonant frequency, τ_{sp} is the spontaneous lifetime of the QD exciton, R_T is the upper mirror reflectivity and R_B is the bottom mirror reflectivity. For the QD layers studied here $c/n=9 \times 10^7$ m/s, $n_{QD} \sim 5 \times 10^{10}$ /cm², $\omega_o = 1.75 \times 10^{15}$ rad/s and $\Delta\hbar\omega \sim 76$ meV and τ_{sp} is measured under nonresonant excitation at low temperature to be ~ 800 ps. For these conditions, we find that a three stack active region requires $\sqrt{R_T R_B} \geq 0.9983$ in order to satisfy threshold conditions. It is important to note that the actual size of τ_{sp} is unknown. Our value of $\tau_{sp} \sim 800$ ps is consistent with other nonresonant pumping measurements in which a lifetime of 880 ps was reported for In_{0.50}Ga_{0.50}As/GaAs QDs⁴¹. However, a spontaneous lifetime of ~ 380 ps was measured under resonant pumping conditions for InP/In_{0.48}Ga_{0.52}As QDs⁴². In this work it was emphasized that resonant pumping more accurately measures the Einstein coefficient for spontaneous emission. For a $\tau_{sp} \sim 400$ ps, the reflectivity requirements are reduced to a more realistic $\sqrt{R_T R_B} \geq 0.9966$. An important effect for 1.3 μ m QD VCSELs is that the QD spontaneous lifetime is predicted by superradiance theory to decrease as the dot size increases⁴²⁻⁴⁴. We have recently measured the spontaneous lifetime of 1.3 μ m QDs under nonresonant pumping conditions at 4 K to be $\tau_{sp} < 400$ ps⁴⁵.

To estimate the actual reflectivity of the our VCSEL cavity, we have measured the spontaneous linewidth at very low current density. The lowest order transverse modes consist of two closely spaced orthogonal polarizations separated by ~ 2.2 Å, but the longer wavelength polarization is more intense for each aperture size. We estimate the linewidth of the single lowest order mode between 30 A/cm² and 60 A/cm² to be ~ 1.9 Å for the 10 μ m, which gives a Q of ~ 5600 . Since we believe that the Q is limited by the upper MgF/ZnSe DBRs, we have calculated linewidths for several reflectivities based on this assumption. Previously, we have calculated the bottom DBRs to have a reflectivity of $R_B = 0.9997$ ⁴⁰. Holding this value constant, we calculate linewidths of 1.1, 1.8 and 2.4 Å for values of distributed losses in the upper MgF/ZnSe DBRs of 100, 200 and 300 cm⁻¹, respectively. These losses correspond to reflectivities of $R_T = 0.9959, 0.9931$ and 0.9903 , respectively.

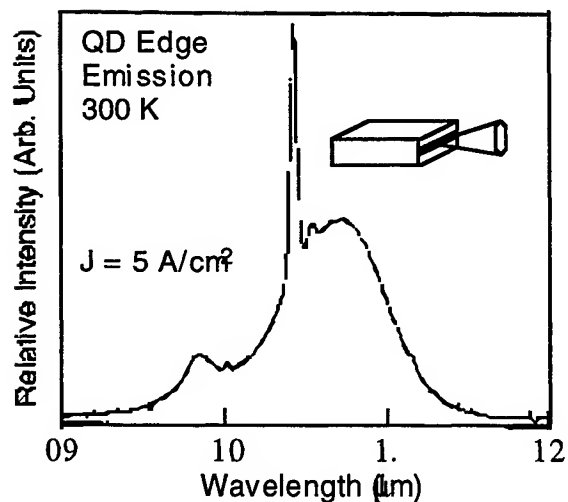


Fig. 14: Spontaneous electroluminescence spectrum from a QD edge emitter at a low current density of 5 A/cm² showing ground state emission wavelength of 1.07 μm.

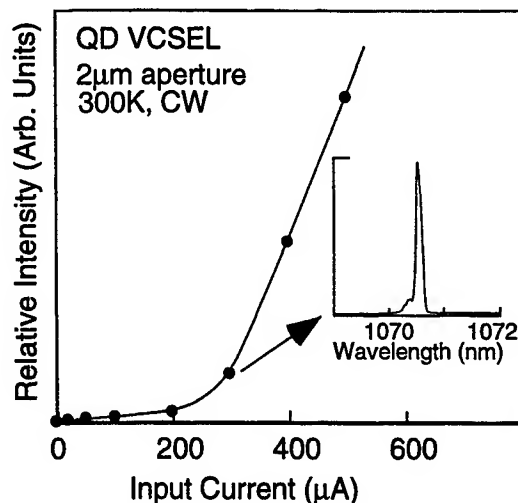


Fig. 15 Light versus current curves for a 2 μm x 2 μm square device at room-temperature, continuous-wave operation. The inset shows lasing spectrum at 300 μA.

The distributed loss of 200 cm⁻¹, although it seems rather high, agrees not only with the measured linewidth but also the differential efficiency measured on quantum well VCSELs of the similar design⁴⁰. The estimated reflectivity product is then $\sqrt{R_T R_B} \approx 0.9964$ which requires from equation (2) that the $\tau_{sp} \sim 350$ ps in order to achieve lasing. This value is considerably shorter than our nonresonant pumping measurements indicate, but in the range indicated by resonant pumping measurements⁴². If this is correct, then the stimulated emission rate of the three stack active region is a factor of two greater than that inferred from the nonresonantly pumped spontaneous lifetime.

6. SUMMARY

Quantum dot material quality continues to improve and QD lasing threshold continues to decrease. At the same time, the lasing wavelength is increasing and now lasers have been demonstrated by several groups at the technologically important 1.3 μm wavelength. In this paper, we have described materials studies for optimizing the sub-ML deposition technique for growth of QDs to achieve good electroluminescence efficiency at 1.3 μm. Temperature dependence of electroluminescence shows that nonradiative recombination increases with temperature, is present in the ground state transition and increases for higher energy states. Growing this active region on an InGaAs buffer allows an increased QD density and the demonstration of a low threshold CW room temperature operation of 4.1 mA. Temperature characteristics of these lasers indicate that nonradiative recombination effects due to heating strongly affect threshold with increasing temperature. However, at 4 K, where nonradiative recombination is not a factor, we measure a very low threshold current density of 6 A/cm². To reduce the heating effects at room temperature, we have introduced an oxide current aperture into the waveguide region to reduce the device width. This allows a 1.2 mA (CW, 300 K) threshold from a 5 μm stripe and a 19 A/cm² current density from an 11 μm stripe.

Also of technological importance is the extended wavelength (1.0 μm- 1.3 μm) GaAs-based VCSEL. The QDs are an attractive way to achieve this with the primary challenge being a small QD ground-state gain compared with the present VCSEL cavity loss. We have demonstrated low threshold (268 A/cm²) ground state lasing at 1.07 μm wavelength using a 3-stack active region in a low loss cavity. The wavelength just beyond 1.0 μm may be useful for VCSEL integration with Si integrated circuits due to the Si transparency. Analysis of the threshold conditions for the QD VCSEL suggests a spontaneous lifetime which is shorter than that measured under nonresonantly pumped conditions and further implies that superradiance may be important in QD lasers as predicted by theory.

ACKNOWLEDGMENTS

This work is supported by the Texas Advanced Research Program and the National Science Foundation under grant ECS-9734829.

REFERENCES

1. D.L. Huffaker, G. Park, Z. Zou, O.B. Shchekin, and D.G. Deppe, "1.3 μm room temperature GaAs-based quantum dot laser," *Appl. Phys. Lett.* **73**, pp. 2564-2566, 1998.
2. G. Park, D.L. Huffaker, Z. Zou, O.B. Shchekin, and D.G. Deppe, "Temperature dependence of lasing characteristics for long-wavelength (1.3 μm) GaAs-based quantum dot lasers," *IEEE Phot. Tech. Lett.* **11**, pp. 301-303, 1999.
3. L.F. Lester, A. Stintz, H. Li, T.C. Newell, E.A. Pease, B.A. Fuchs, and K. J. Malloy, "Optical characteristics of 1.24 μm InAs quantum-dot laser diodes," *IEEE Phot. Tech. Lett.* **11**, pp. 931-933, 1999.
4. S. Mukai, N. Ohtsuka, H. Shoji, M. Sugawara, N. Yokoyama, and H. Ishikawa, "1.3 μm CW lasing of InGaAs/GaAs quantum dots at room temperature with a threshold current of 8 mA," *IEEE Phot. Tech. Lett.* **11**, 1999, to be published.
5. G. Park, O.B. Shchekin, S. Csutak, and D.G. Deppe, "Room-temperature continuous-wave operation of a single-layered 1.3 μm quantum dot laser," *Appl. Phys. Lett.*, accepted for publication.
6. G. T. Liu, A. Stintz, H. Li, K.J. Malloy, and L. F. Lester, "Extremely low room-temperature threshold current density diode lasers using InAs dots in an $\text{In}_{0.15}\text{Ga}_{0.85}\text{As}$ quantum well," *Electron. Lett.* **35**, pp. 1163-65, 1999.
7. D.G. Deppe, D.L. Huffaker, S. Csutak, Z. Zou, G. Park, and O.B. Shchekin, "Spontaneous emission and threshold characteristics of 1.3 μm InGaAs/GaAs quantum dot GaAs-based lasers," *IEEE J. Quant. Electron.* **35**, pp. 1238-1246, 1999.
8. Y.M. Shernyakov, D.A. Bedarev, E. Y. Kondrat'eva, P.S. Kop'ev, A.R. Kovsh, N.A. Maleev, M.V. Maximov, S.S. Mikhlin, A.F. Tsatsul'nikov, V.M. Ustinov, B.V. Volovik, A.E. Zhukov, Zh.I. Alferov, N.N. Ledentsov and D. Bimberg, "1.3 μm GaAs-based laser using quantum dots obtained by activated spinodal decomposition," *Electron. Lett.* **35**, pp. 898-900, 1999.
9. A. E. Zhukov, A. R. Kovsh, V. M. Ustinov, Yu. M. Shernyakov, S. S. Mikhlin, N. A. Maleev, E. Yu. Kondrat'eva, D. A. Livshits, M. V. Maximov, B. V. Volovik, D. A. Bedarev, Yu. G. Musikhin, N. N. Ledentsov, P. S. Kop'ev, Zh. I. Alferov, D. Bimberg, "Continuous wave operation of long-wavelength quantum dot diode laser on a GaAs substrate," accepted for publication *IEEE Phot. Tech. Lett.* 1999.
10. G. Park, O.B. Shchekin, D.L. Huffaker, and D.G. Deppe, "Low threshold oxide-confined quantum dot laser," submitted to *IEEE Phot. Tech. Lett.*
11. D.L. Huffaker, H. Deng, and D.G. Deppe, "1.15 μm wavelength oxide-confined quantum dot vertical-cavity surface-emitting laser," *IEEE Phot. Tech. Lett.* **10**, pp. 185-187, 1998.
12. J.M. Gerard, D. Barrier, J.Y. Marzin, R. Duszewicz, L. Manin, E. Costard, V. Thierry-Mieg, and T. Rivera, "Quantum boxes as active probes for photonic microstructures: The pillar microcavity case," *Appl. Phys. Lett.* **69**, pp. 449-451, 1996.
13. D.L. Huffaker, L.A. Graham, and D.G. Deppe, "Low-threshold continuous-wave operation of an oxide-confined vertical-cavity surface-emitting laser based on a quantum dot active region and half-wave cavity," *Electron. Lett.* **33**, pp. 1225-1226, 1997.
14. J.M. Gerard, B. Sermage, B. Gayral, B. Legrand, E. Costard, and V. Thierry-Mieg, "Enhanced spontaneous emission by quantum boxes in a monolithic optical microcavity," *Phys. Rev. Lett.* **81**, pp. 1110-1112, 1998.
15. L.A. Graham, D. L. Huffaker and D.G. Deppe, "Spontaneous lifetime control in a native-oxide-apertured microcavity," *Appl. Phys. Lett.* **74**, pp. 2408-2410, 1999.
16. J.K. Kim, T.A. Strand, R.L. Naone and L.A. Coldren, "Design parameters for lateral carrier confinement in quantum dot lasers," *Appl. Phys. Lett.* **74**, pp. 2752-2754, 1999.
17. D.G. Deppe and H. Huang, "Quantum dot vertical cavity surface emitting laser based on the Purcell Effect," submitted to *Appl. Phys. Lett.*
18. Y. Arakawa and A. Yariv, "Quantum well lasers - gain, spectra, dynamics," *IEEE J. Quantum Electron.* **QE-22**, pp. 1887-1897, 1986.
19. M. Asada, Y. Miyamoto, Y. Suematsu, "Gain and threshold of three-dimensional quantum box lasers," *IEEE J. Quantum Electron.* **QE-22**, pp. 1915-1921, 1986.
20. Y. Arakawa and H. Sakaki, "Multidimensional quantum well laser and temperature dependence of its threshold current," *Appl. Phys. Lett.* **40**, pp. 939-941, 1982.
21. N. Kirstaedter, N.N. Ledentsov, M. Grundmann, D. Bimberg, V.M. Ustinov, S.S. Ruvimov, M.V. Maximov, P.S. Kop'ev, Zh.I. Alferov, U. Richter, P. Werner, U. Gosele, and J. Heydenreich, "Low threshold, large T_0 injection laser emission from InGaAs quantum dots," *Electron. Lett.* **30**, pp. 1416-1417, 1994.
22. H. Shoji, K. Mukai, N. Ohtsuka, M. Sugawara, T. Uchida, and H. Ishikawa, "Lasing at three-dimensionally quantum-confined sublevel of self-organized $\text{In}_{0.50}\text{Ga}_{0.50}\text{As}$ quantum dots by current injection," *IEEE Photon. Techn. Lett.* **7**, pp. 1385-1387, 1995.

23. K. Kamath, P. Bhattacharya, T. Sosnowski, T. Norris, and J. Phillips, "Room-temperature operation of $\text{In}_{0.40}\text{Ga}_{0.60}\text{As}/\text{GaAs}$ self-organized quantum dot lasers," *Electron. Lett.* **32**, pp. 1374-1375, 1996.
24. R. Mirin, A. Gossard, and J. Bowers, "Room temperature lasing from InGaAs quantum dots," *Electron. Lett.* **32**, pp. 1732-1733, 1996.
25. N.N. Ledentsov, V.A. Shchukin, M. Grundmann, N. Kirstaedter, J. Bohrer, O. Schmidt, D. Bimberg, V.M. Ustinov, A.Y. Egorov, A.E. Zhukov, P.S. Kop'ev, S.V. Zaitsev, N. Yu. Gordeev, Zh. I. Alferov, A.I. Borovkov, A.O. Kosogov, S.S. Ruvimov, P. Werner, U. Gosele, and J. Heydenreich, "Direct formation of vertically coupled quantum dots in Stranski-Krastanow growth," *Phys. Rev. B* **54**, pp. 8743-8750, 1996.
26. H. Shoji, Y. Nakata, K. Mukai, Y. Sugiyama, M. Sugawara, N. Yokoyama and H. Ishikawa, "Room temperature CW operation at the ground state of self-formed quantum dot lasers with multi-stacked dot layer," *Electron. Lett.* **32**, pp. 2023-2024, 1996.
27. F. Heinrichsdorff, M.-H. Mao, N. Kirstaedter, A. Krost, and D. Bimberg, "Room-temperature continuous-wave lasing from stacked InAs/GaAs quantum dots grown by metalorganic chemical vapor deposition," *Appl. Phys. Lett.* **71**, pp. 22-24, 1997.
28. A.E. Zhukov, V.M. Ustinov, A. Yu. Egorov, A.R. Kovsh, A.F. Tsatsulnikov, N.N. Ledentsov, S.V. Zaitsev, N. Yu. Gordeev, P.S. Kopev, and Z.I. Alferov, "Negative characteristic temperature of InGaAs quantum dot injection laser," *Jap. J. Appl. Phys.* **36**, pp. 4216-4218, 1997.
29. L.V. Asryan and R.A. Suris, "Inhomogeneous linewidth broadening and the threshold current density of a semiconductor quantum dot laser," *Semicond. Sci. Technol.* **11**, pp. 554-567, 1996.
30. D. Bimberg, N. Kirstaedter, N.N. Ledentsov, Zh.I. Alferov, P.S. Kop'ev, and V.M. Ustinov, "InGaAs-GaAs quantum dot lasers," *IEEE J. Select. Top. Quant. Electron.* **3**, pp. 196-205, 1997.
31. L.V. Asryan and R.A. Suris, "Temperature dependence of the threshold current density of a quantum dot laser," *IEEE J. Quant. Electron.* **34**, pp. 841-850, 1998.
32. Saito, H., Nishi, K., Ogura, I., Sugov, S., and Sugimoto, Y., "Room-temperature lasing operation of a quantum-dot vertical-cavity surface-emitting laser," *Appl. Phys. Lett.* **69**, pp. 3140-3142, 1996.
33. J.A. Lott, N.N. Ledentsov, V.M. Ustinov, A.Yu. Egorov, A.E. Zhukov, P.S. Kop'ev, Zh.I. Alferov, and D. Bimberg, "Vertical cavity lasers based on vertically coupled quantum dots," *Electron. Lett.* **33**, pp. 1150-1151, 1997.
34. K. Mukai, O. Nobuyuki, S. Mitsuru, and S. Yamzaki, "Self-formed $\text{In}_{0.5}\text{Ga}_{0.5}\text{As}$ quantum dots on GaAs substrates emitting at 1.3 μm ," *Jpn. J. Appl. Phys.* **33**, pp. L1710-L1712, 1994.
35. D.L. Huffaker and D.G. Deppe, "Electroluminescence efficiency of 1.3 μm wavelength $\text{InGaAs}/\text{GaAs}$ quantum dots," *Appl. Phys. Lett.* **73**, pp. 520-522, 1998.
36. S. Krishna, J. Xu, D. Zhu, K. Linder, O. Qasaimeh, P. Bhattacharya, and D.L. Huffaker, "Structural and luminescence characteristics of cycled submonolayer InAs/GaAs quantum dots with room temperature emission at 1.3 μm ," submitted to *Appl. Phys. Lett.*
37. J.M. Dallesasse, N. Holonyak, Jr., A.R. Sugg, T.A. Richard, and N. El-Zein, "Hydrolization oxidation of AlGaAs-AlAs-GaAs quantum well heterostructures," *Appl. Phys. Lett.* **57**, pp. 2844-2846, 1990.
38. Z. Zou, D.L. Huffaker, S. Csutak, and D.G. Deppe, "Ground state lasing from a quantum dot oxide-confined vertical-cavity surface-emitting laser," *Appl. Phys. Lett.* **75**, pp. 22-25, 1999.
39. Z. Zou, O.B. Shchekin, G. Park, D.L. Huffaker, and D.G. Deppe, "Threshold temperature dependence of lateral cavity quantum dot lasers," *IEEE Phot. Tech. Lett.* **10**, pp. 1673-1675, 1998.
40. D.L. Huffaker and D.G. Deppe, "Intracavity contacts for low-threshold oxide-confined vertical-cavity surface-emitting lasers," *Appl. Phys. Lett.*, **11**, pp. 934-936, 1999.
41. G. Wang, S. Fafard, D. Leonard, J.E. Bowers, J.L. Merz, and P.M. Petroff, "Time-resolved optical characterization of $\text{InGaAs}/\text{GaAs}$ quantum dots," *Appl. Phys. Lett.* **64**, pp. 2815-2817, 1994.
42. A. Kurtenbach, W.W. Ruhle, and K. Eberl, "Intrinsic radiative lifetimes of $\text{InP}/\text{In}_{0.48}\text{Ga}_{0.52}\text{P}$ quantum dots," *Solid State Comm.* **96**, pp. 265-269, 1995.
43. E. Hanamura, "Rapid radiative decay and enhanced optical nonlinearity of excitons in a quantum well," *Phys. Rev. B* **38**, pp. 1228-1234, 1988.
44. M. Sugawara, "Theory of spontaneous-emission lifetime of Wannier excitons in mesoscopic semiconductor quantum disks," *Phys. Rev. B* **51**, pp. 10,743-10,754, 1995.
45. T. Boggess, L. Zhang, D.G. Deppe, D.L. Huffaker, O.B. Shchekin, and C. Cao, "Dynamic response of 1.3 μm wavelength $\text{InGaAs}/\text{GaAs}$ quantum dots," submitted to *Appl. Phys. Lett.*

Photoluminescence Characteristics of GaAs/AlGaAs Quantum Dot Arrays Fabricated by Dry and Dry-Wet Etching

Xinghua Wang¹, Aimin Song, Jian Liu, Winchao Cheng, Guohua Li,
Chengfang Li, Yuexia Li and Jinzhong Yu*

National Laboratory for Superlattices and Microstructures
Institute of Semiconductors, Chinese Academy of Sciences, Beijing 100083

*National Key Laboratory for Integrated Optoelectronics
Institute of Semiconductors, Chinese Academy of Sciences, Beijing 100083

ABSTRACT

GaAs/AlGaAs quantum dot arrays with different dot sizes made by different fabrication processes were studied in this work. In comparison with the reference quantum well, photoluminescence (PL) spectra from the samples at low temperature have demonstrated that PL peak positions shift to higher energy side due to quantization confinement effects and the blue-shift increases with decreasing dot size, PL linewidths are broadened and intensities are much reduced. It is also found that wet chemical etching after reactive ion etching can improve optical properties of the quantum dot arrays.

Keywords: GaAs/AlGaAs, Quantum dot array, Etching method, Photoluminescence

1. INTRODUCTION

Low dimensional structures, such as quantum well (QW), quantum wire (QWR) and quantum dot (QD) were attracted much attention in recent years¹. Both fabrications of low dimensional quantum structure systems and their fundamental optoelectronic properties become active frontier subjects.

There are various methods for fabrication of QD arrays, for example, conventional self-organization epitaxial growth and chemical crystallization. In addition, QD arrays were made by combining epitaxial growth with microfabrication techniques together^{2, 3}. They were formed on MBE-grown QW wafers by means of micro-fabrication techniques, such as electron beam lithography (EBL), reactive ion etching (RIE) and wet chemical etching. For the QD arrays made by this way, the dot sizes are more homogenous, patterns can be well reproducible. During the processes of the reactive ion etching, however, high-energy ion gave rise to surface damage at the outsides of the dots. If wet chemical etching is applied after reactive ion etching, the surface damage will be decreased and the qualities of the QD arrays can be improved greatly.

2. PREPARATION OF THE QUANTUM DOT ARRAYS

¹ E-mail address: wangxh@red.semi.ac.cn; Telephone: 86-10-62339254; Fax: 86-10-62322388

Two types of GaAs/AlGaAs quantum well structure wafers, samples No.702 and No.706, were grown by MBE. As shown in figure 1, their structures are very similar. The structure of Sample No.702 is as following:

The substrate is a Si doped n^+ -GaAs, the impurity density is $2 \times 10^{18} \text{ cm}^{-3}$. After growth of 1 μm GaAs buffer layer, the successively following layers were grown: 1) 400 nm AlGaAs layer, 2) 6 nm GaAs quantum well, 3) 2 nm AlGaAs layer, 4) 2nd 6 nm GaAs quantum well, 5) 150 nm AlGaAs layer, 6) 100 nm GaAs top cover layer. All the epitaxial layers are undoped and Al composition in AlGaAs layers is 0.3, The structure of the sample No. 702 was shown in Fig. 1(a).

GaAs	100 nm
AlGaAs	150 nm
GaAs	6 nm
AlGaAs	2 nm
GaAs	6 nm
AlGaAs	400 nm
GaAs buffer	$\sim 1 \mu\text{m}$
n^+ — GaAs substrate	

(a) No. 702

GaAs	70 nm
AlGaAs	86.5 nm
GaAs	19.5 nm
AlGaAs	30 nm
GaAs	4.2 nm
AlGaAs	86.5 nm
GaAs buffer	300 nm
n^+ — GaAs substrate	

(b) No. 706

Fig 1. Structures of MBE-grown QWs

The QW structures were characterized by PL spectra at low temperature and other measurements in order to identify whether the quality is good enough or not, then the wafers with good quality were used for the next micro-fabrication processes. The cylindrical quantum dot arrays based on the original quantum well structures were fabricated by using electron beam lithography in combination with reactive ion etching, wet chemical etching and so on. The fabrication of the QD arrays is expressed by following processes:

1) resist on the wafer surface, 2) electron beam lithography (EBL), 3) development, 4) evaporation of NiCr alloy and metalization, 5) lift-off, 6) reactive ion etching (RIE) in electron cyclotron resonance (ECR) system (called dry etching), 7) wet chemical etching.

In our experiment, the two arrays with different dot sizes based on the sample No.702 were successfully

fabricated. The diameters of the quantum dots were measured by high-resolution scanning electron microscope (SEM) and were found to be 100 nm and 50 nm, respectively. The vertical etched highness of the cylindrical quantum dots is about 280 nm.

Another sample No.706 was also investigated in order to identify what role the wet chemical etching did play in fabrication processes. The sample structures and the qualities are similar to No.702. The sample No.706 with the double GaAs QWs was grown by MBE, as shown in Fig. 1(b). Thickness of the two well is 4.2 nm and 19.5 nm, respectively. The middle layer between the two QWs and their outsides are AlGaAs barrier layers. The three kinds of QD arrays on the sample No.706 wafer were fabricated by the processes mentioned above, but, without the wet chemical etching. The diameters of the three QD arrays formed after reactive ion etching are 130 nm, 75 nm and 46 nm, respectively.

In the paper, the qualities of the samples No.702 and No.706 as well as structures are almost similar, but their fabrication processes are different: after reactive ion etching, wet chemical etching was applied for sample No.702 (dry-wet etching) and was not used for No.706 (dry etching). The effect of wet chemical etching on optical properties of the QD arrays was identified from the PL spectra measured at low temperature.

It must be pointed out that the QD arrays can be fabricated directly by wet chemical etching after lift-off, without used reactive ion etching. However, it is difficult to form QDs because of isotropy of the chemical etching solution. Thus it is important to seek an ideal anisotropy solution.

3. RESULTS AND DISCUSSION

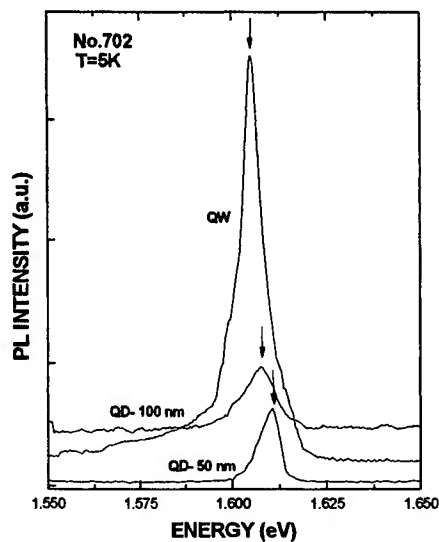
PL spectra of the sample No.702 and No.706, including the QD arrays and the two relative QWs, were investigated. The samples were placed in a Cryostat and the measurements were made at low temperatures. A light beam from Argon ion laser was used as an excitation light source. PL signals were analyzed by a bi-monochromator and detected by a photomultiplier with a cooled GaAs detector.

The PL spectra of the QD arrays with different sizes were measured as shown in Fig. 2. At the same time, PL spectra of MBE-grown QW wafer as the reference spectrum were also shown. The arrows represent the energy positions of the PL peak in the figure. Comparing PL spectra of the quantum dot arrays with these of the reference QW, the following results were obtained:

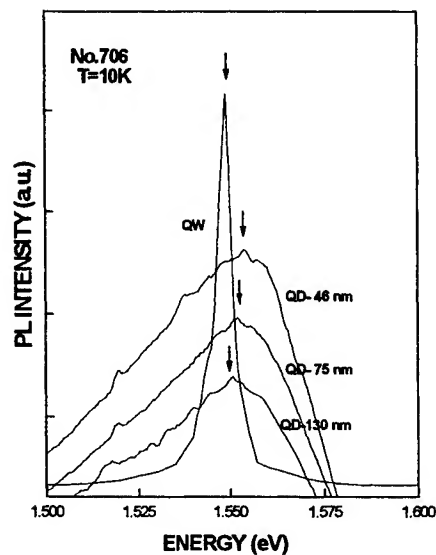
It is found from Fig. 2(a) that there is a very strong PL peak, its energy position is at 1.6050 eV, the full width at half maximum (FWHM) is 5 meV for the QW of the sample No.702. The PL spectra of the two quantum dot arrays, QD-100 nm and QD-50 nm, show two distinct emission peaks which are 1.6075 eV and 1.6105 eV at 5 K, respectively. Corresponding to the reference QW, the peak positions of the QD arrays shift towards higher energy, the blue-shift account is 2.5 meV and 5.5 meV, respectively. This is primarily due to quantum size effects: electrons and holes in a quantum dot are confined in three directions, the spatial confinements lead to heighten carrier subbands, thus it was observed experimentally that the emission from the QD arrays shifted to higher energy side. The smaller the diameter of quantum dots, the stronger the confinement effect and the larger the blue shift⁴.

The PL linewidths of the two quantum dot arrays, QD-100 nm and QD-50 nm, are broadened, FWHMs are 11 meV and 7 meV at 5 K, respectively. This is mainly caused by the inhomogeneity of the QD

dimensions, there are dot size fluctuations of a few nanometer within a quantum dot array, the increase of the emission linewidth should then be interpreted as the combined emission from dots with slight different sizes.



(a) No. 702



(b) No. 706.

Fig. 1. The PL spectra of samples No. 702 and No. 706. Here, the arrows represent the energy positions of the PL peak.

The PL intensities of the two QD arrays are much weakened in comparison with the reference QW. On the one hand, the reason can be explained as that in the QD arrays, the area excited by Ar⁺ laser is much smaller than that in QW, the shrinkage of the illumination area leads to weaken PL intensity. On the other hand, the reduction of PL intensities may be attributed to the influence of nonradiative recombination via the surface states and faults at the open sidewalls.

Besides, for the sample No.702, the peak energies emitted from QW and QD arrays are calculated using a simplified theoretical model and are compared with the experimental data. For the infinite barriers, the well-known expressions of the emission energy are given by following equations:

$$\text{For QW, } E = \frac{\hbar^2 \pi^2}{2m_e^*} \left(\frac{n}{L_z}\right)^2 + \frac{\hbar^2}{2m_e^*} (k_x^2 + k_y^2) \quad (1)$$

$$\text{For QD, } E = \frac{\hbar^2 \pi^2}{2m_e^*} \left[\left(\frac{n}{L_z}\right)^2 + \left(\frac{l}{L_x}\right)^2 + \left(\frac{m}{L_y}\right)^2 \right] \quad (2)$$

Corresponding to the reference QW, shifts of the peak position for QD-100 nm and QD-50 nm are 2.2 meV and 6.1 meV, respectively. The calculated value are almost close to the experimental data. It means that the experimental data are very reasonable and trustworthy.

PL spectra of another sample No.706 were investigated at 10 K as shown in Fig. 2(b). It is found from Fig. 2(b) that the peak energy of the QW with the well-width of 19.5 nm is 1.5492 eV and FWHM is 3 meV. Comparing with the reference QW, the PL blue-shifts for the three QD arrays (QD-130 nm, QD-75 nm and QD-46 nm) are observed experimentally to be 2.0 meV, 2.7 meV and 4.3 meV, respectively; the PL peaks at low energy side are broadened dramatically, FWHMs are about 50-60 meV and the intensities are weakened greatly.

As we mentioned above, the structures and qualities of the both samples No.706 and No.702 are nearly similar. Why the linewidths of the QD arrays based on sample No. 706 are much wider than these of the QD arrays based on samples No.702? It is know that the PL linewidth is caused by the fluctuations of the dot sizes, the dot inhomogeneity of the sample No.706 are nearly with No.702 and not very serious; so the peak widening is resulted from the difference of the fabrication process of the QD arrays. In the fabrication processes of the three QD arrays based on sample No.706, reactive ion etching was only used but not wet chemical etching, thus during the processes of the reactive ion etching, high-energy ion gave rise to surface damage at the open sidewalls. The PL peaks are widened enormously due to the influence of the recombination via the surface states and faults at the open sidewalls. The QD arrays were fabricated on the samples No.702 wafer by using dry-wet etching method, that is, wet chemical etching was applied after reactive ion etching, the surface damage was decreased greatly. In order to improve the quality of the QD arrays, the application of dry-wet etching method is very necessary and valid.

The luminescence signal of three QD arrays in respect to the QW with well-width of 4.2 nm was too weak to detect.

4. CONCLUSION

In the work, PL properties of the two different types of the QD arrays fabricated by etching were studied at

low temperature. The PL positions in comparison with these of the reference QW were observed to shift to higher energy side, no matter how the fabrication process is. The blue-shifts can be attributed to the spatial quantization size effects, and the smaller the diameter of the quantum dots, the larger the blue- shift.

In general, the PL linewidths of the QD arrays fabricated by etching are broadened, the PL peaks for the QD arrays based on sample No.702 (using dry-wet etching in the fabrication processes) are much more narrow than these for the QD arrays based on sample No.706 (only using dry etching). Our results demonstrate that in the fabrication processes of the QD arrays, wet chemical etching reduced the surface damage caused by high-energy ion in RIE process and improves the qualities of the QD arrays.

The QD arrays with the high quality afford us a possibility of the development and application of the optoelectronic devices made by the QD arrays. It is expected that the photoluminescence characteristics of the QD arrays will be improved dramatically by increasing resolution of electron beam lithography, enhancing dot density and homogeneity, decreasing etching energy of reactive ion, applying dry-wet etching method and so on.

REFERENCES

1. T. J. Thornton, "Ballistic transport in GaAs quantum wires— A short history", *Superlattices and Microstructures*, **23**, pp. 601-610, 1998.
2. K. H. Wang, A Pecher, E Hofling and A Forchel, "Low voltage electron-beam lithography based InGaAs/GaAs quantum dot arrays with 1 meV luminescence linewidths", *Journal of Vacuum Science & Technology B***15**, pp. 2829-2831, 1998.
3. M. Illing, G. Bacher, T. Kummell, A. Forchel, T. G. Andersson, D. Hommel, B. Jobst and G. Landwehr, "Lateral quantization effects in lithographically defined CdZnSe/ZnSe quantum dots and quantum wires", *Applied Physical Letter*, **67**, pp. 124-126, 1995.
4. Xinghua Wang, Guohua Li, Chengfang Li, Yuexia Li, Wenchao Cheng, Aiming Song, Jian Lui and Zhiming Wang, "Preparation of GaAs/AlGaAs quantum dots and their photoluminescence characteristics", *Chinese Journal of Luminescence*, **19**, pp. 202-210, 1998.

Effect of Shape of Quantum Dots on Strains: A Finite Element Study

G. Muralidharan

Institute of Microelectronics, 11 Science Park Rd., Science Park II, Singapore – 117685.

ABSTRACT

It is fairly well established that self-aligned quantum dots can form in strained epitaxial systems. One system that has been studied extensively is the InAs/GaAs system wherein the difference in lattice parameter is about 7.0%. Strains within the dot and the surroundings are known to influence the optical properties of the system. However, very little information is available on the strains in these quantum dots. In particular, the effect of shape of the initial shape of quantum dots and boundary conditions are not very well known. Strains in InAs quantum dots embedded in GaAs have been examined using the finite element method within a thermo-mechanical framework. The initial shape of the dot is assumed to be conical in 3-D with different width/height ratio typical of quantum dots. Modeling is accomplished using a 2-D axi-symmetric finite element model. Results of the simulation show that initially conical shaped dots become more rounded in shape and become lens-shaped. It has been shown that the width/height ratio is critical in determining the strains within the quantum dots. Results of the calculation are compared with the results of other calculations and experimental measurements of strains using the STM.

Keywords: InAs quantum dots, GaAs, Strains, finite element method

1. INTRODUCTION

Growth of hetero-epitaxial layers with a lattice parameter different from that of the substrate has shown that under certain conditions, 3-D island growth is possible in multi-layer strained systems. Such 3-D islands are also known to form well-aligned structures^{1,2}. Since no external lithography techniques are involved in the fabrication of these aligned nanometer-scaled structures, these are termed as self-aligned quantum dots. Study of self-aligned quantum dots is an exciting area of semiconductor physics. It is fairly well established that such self-alignment occurs due to long-range elastic strains induced by the presence of islands with a lattice parameter different from that of the substrate and the cap layer. It has been demonstrated that 3D islanding induced strain fields in the protective layer can extend upto distances of about 40 nm. It is also well known that the stresses and strains in the quantum dot influence the optical properties of the aggregate. It has been shown that in the InAs/GaAs system, the spectral position and the spectral width in 8K photoluminescence measurements depend upon the number of layers in the self-aligned system². It was concluded that inter-dot coupling was responsible for these observations. Hence, there is a significant interest in the study of the self-aligned quantum dots.

One of the issues that have been of interest is the spatial distribution and size of these quantum dots. It has been shown that it is desirable to have a well-controlled spatial distribution of these islands with a sharply peaked size. Since it is known that coherency strains control the growth of these dots, there has been interest in understanding the strains in these quantum dots and relating these to the growth and hence the optical properties. A variety of techniques have been used for the physical characterization of these quantum dots¹⁻⁸. Popular techniques used include high-resolution transmission electron microscopy (HRTEM)^{1,2,7-8}, Scanning Tunneling Microscopy (STM)/Atomic Force Microscopy (AFM)³⁻⁵ and high-resolution x-ray diffraction (XRD)⁸. Aspects of interest include shape, size and size distribution, spatial distribution including alignment, effect of growth conditions on the characteristics of the quantum dots and the strains in the quantum dots, substrate and the cap layers. In particular, the cross-sectional STM is a very popular tool for the study of the quantum dots since using this technique it is possible to cleave the wafers and study the shape of the quantum dots and to study the strains introduced due to the presence of the quantum dots. In the present study, further discussion will be focussed primarily upon the shape of the dots and the strains in the system.

Cross-sectional TEM and STM studies have shown that the shape of the self-aligned embedded quantum dots in this system is lens-shaped^{1,2,3}. Other studies using cross-sectional STM studies have shown a trapezoidal shape for quantum dots grown by MOCVD^{4,5}. However, the effect of cleaving on the shape of the quantum dots has not been addressed in these studies. Further, the change in strains due to the shape of the quantum dots is also not very well studied. Previous calculations have either focussed on pyramidal dots with a cap layer⁹⁻¹¹ or conical dots without a cap layer¹². It has been

discussed that the shape of the dot along with the boundary conditions can influence the strains in these dots. The subject of the current study is to examine the effect of the initial shape of the dots on the strains in these systems. This will partly help in understanding if the shape has any influence on the strains and hence the evolution of self-aligned quantum dots in these systems.

2. METHODOLOGY

In the current study, for illustration, we have used the case of an InAs quantum dot embedded in GaAs, with a buffer layer. The finite element method (ANSYS 5.5) is used for the calculations. 2-D axi-symmetric model has been used for the calculations. The difference in the lattice parameters of InAs and GaAs of 7.0 % is incorporated through a thermo-mechanical model. The InAs region and the GaAs region are assigned different thermal expansion coefficients such that the misfit is met at the interface. It has been fairly well established that the finite element method can be used to calculate strains in such systems^{11,12}. Comparison with calculations based on atomistic elasticity has clearly shown that discrepancy between the two techniques arises only in regions close to the interfaces¹⁰. The main emphasis in the current study is the effect of shape on the quantum dots. Hence, within the 2-D model, the shape of the free quantum dot is assumed to be a triangle. This represents a conical shaped dot in the 3-D model. Difference in shape is accommodated by changing the angles of the triangle. Isotropic material properties are used for the calculations as shown in Table 1. Rigid body displacement along the y-direction is constrained by applying null displacements along the y-direction to the node at the origin.

Figure 1 shows a schematic of the modeled region. As seen from the figure, the substrate GaAs has a thickness of 30 nm, the wetting layer is 1 nm thick and the cap layer extends up to a height of 30 nm from the buffer layer. Totally, three different shapes have been modeled in the present study. In the first model, the width of the dot (b) is taken to be 12 nm

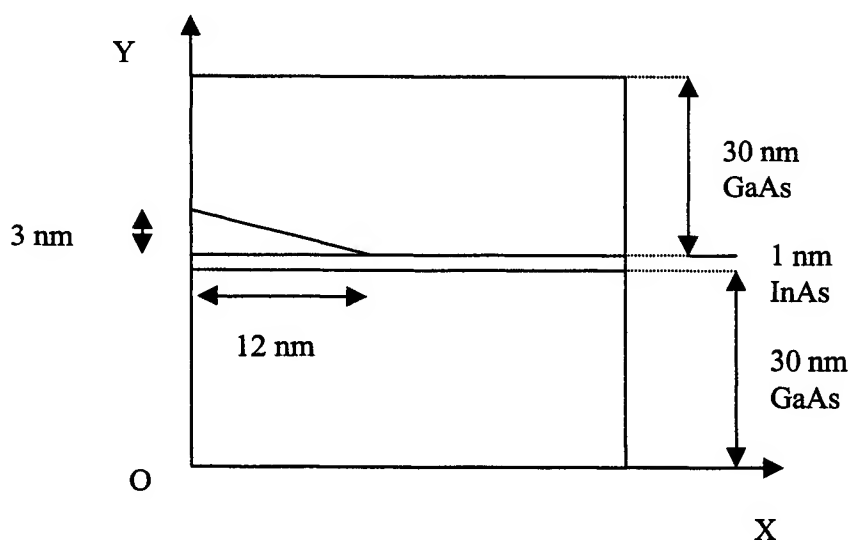


Figure 1. Schematic showing region used for the simulation. Region consists of 30 nm GaAs substrate layer, 1 nm InAs wetting layer and the InAs conical dot and the cap layer. Figure shows the dot with a base of length $b=12$ nm and height $h=3$ nm. Isotropy is assumed for the calculations. Translating to the physical model, the x-axis lies on the plane parallel to the interfaces while the y-axis is along the normal to the interfaces. O denotes the global origin for the calculations.

while the height (h) of the dot is assumed to be 3 nm. These dimensions are very similar to those observed in the earlier STM study. In the second model, the width of the dot is assumed to be 5 nm and the height is assumed to be 5 nm. These dimensions have been used in other studies aimed at calculating strains in these embedded quantum dots. The third model

Table 1. Elastic Properties of InAs and GaAs used for FEM calculations¹²

Material	E (GPa)	ν
GaAs	86.96	0.31
InAs	51.42	0.35

assumes a truncated cone. The width again is taken as 5 nm and the height is now assumed to be 2.5 nm. In the axisymmetric model, the axis of cylindrical symmetry is taken to be the y-axis.

3. RESULTS AND DISCUSSION

Figure 2 shows the results for the ϵ_{yy} (radial strain) and the resultant shape of the embedded quantum dot obtained from the simulation for the case when the b/h ratio is equal to 4. Note the large variation in strains within and around the quantum dot and the wetting layer. It should be recalled that the wetting layer is also assumed to consist of InAs. Note that the conical shape assumed for the dot has been modified into a more semi-ellipsoidal shape. The change in shape can be easily understood since in the radial direction, the dot is constrained by the presence of the GaAs substrate. However, both the GaAs cap layer and the InAs dot layers can expand in the y-direction perpendicular to the free surface with the only constraint being the compatibility between the InAs in the dot layer and the GaAs in the cap layer. Hence, the dot which was originally conical, becomes more rounded, resulting in a lens-shaped dot.

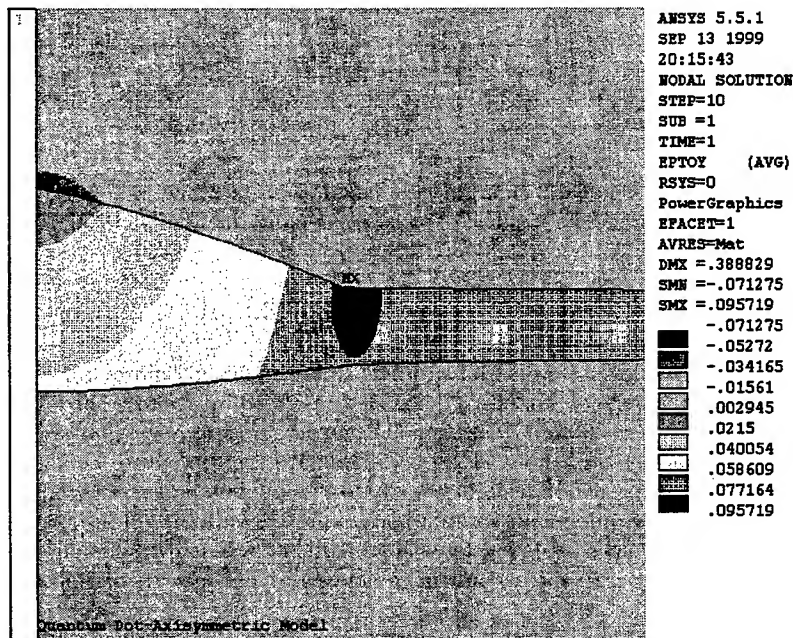


Figure 2. ϵ_{yy} as a function of position and the shape of the quantum dot for $h/b=4$.

Figures 3 to 6 show the variation in ϵ_{rr} (normal strain) as a function of position in the direction perpendicular to the interfaces along a line passing through the origin (y-direction). Three cases - where b/h is equal to 1, h/b equal to 4 and finally for the truncated cone with h/b equal to 1, respectively- are shown in the figures. The variation in strain (shape of curve) along the y- direction is very similar to that observed in previous calculations of strains in quantum dots⁸⁻¹⁰. The

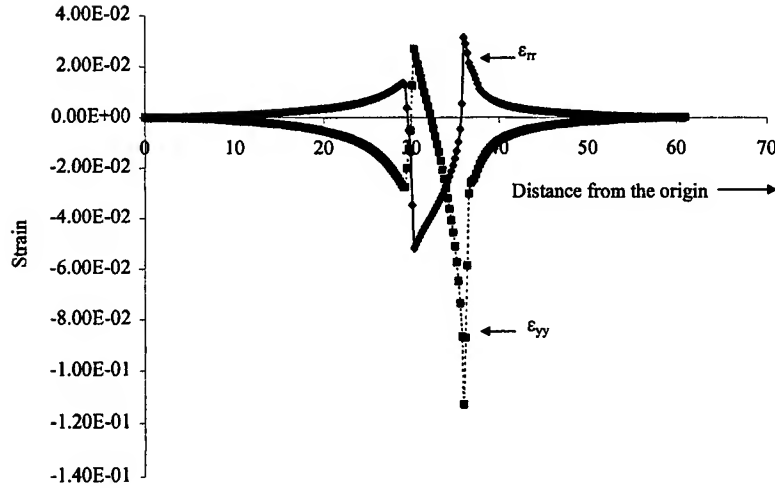


Figure 3. ϵ_{π} and ϵ_{yy} as a function of position along the line parallel to the y-axis and passing through the origin for the case when $b/h=1$.

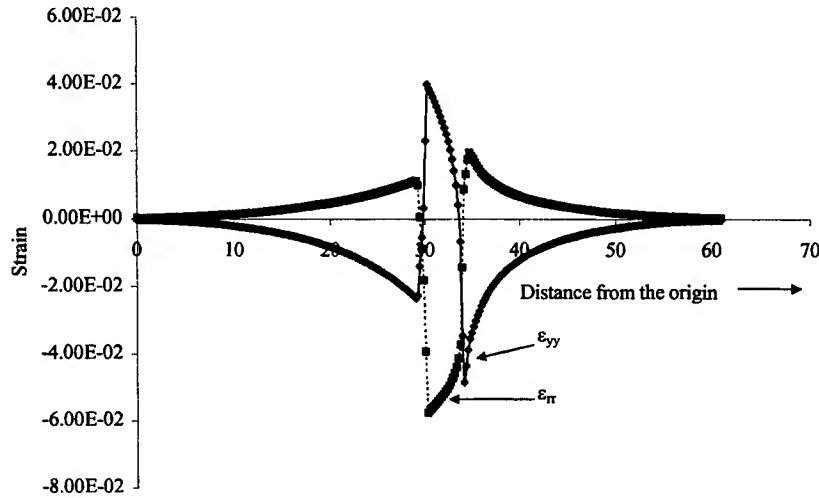


Figure 4. ϵ_{π} and ϵ_{yy} as a function of position along the line parallel to the y-axis and passing through the origin for the case when $b/h=4$.

major features of this curve are discussed below. As the wetting layer is approached from the substrate, note that the strain first becomes tensile. This is due to the lattice parameter of the InAs region (the wetting layer and the quantum dot) being larger than the substrate. Hence regions in the substrate that adjoin the layer with the larger lattice parameter are partially stretched to maintain continuity. Within the wetting layer and the dot itself, ϵ_{π} is essentially compressive, denoting that the quantum dot is constrained by the presence of the substrate. As the apex of the cone is reached, the situation is similar to that in the region near the wetting layer, with the substrate again experiencing a tensile ϵ_{π} strain.

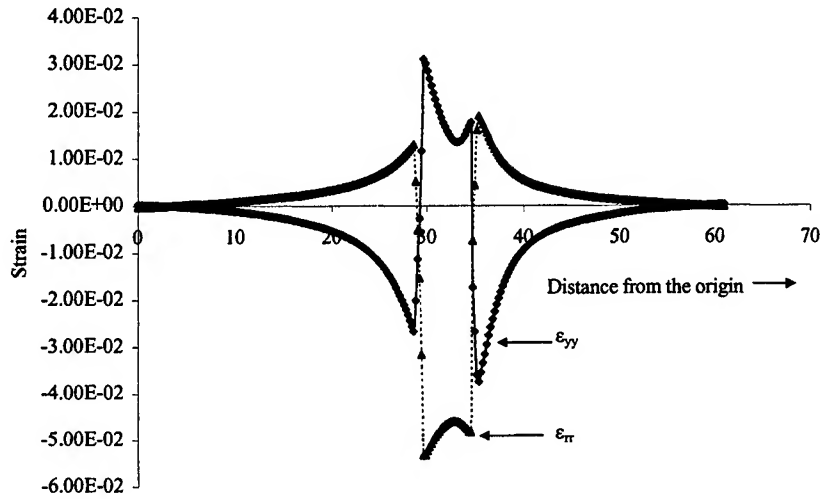


Figure 5. ϵ_{rr} and ϵ_{yy} as a function of position along the line parallel to the y-axis and passing through the origin for the case for a truncated cone with $b/h=1$.

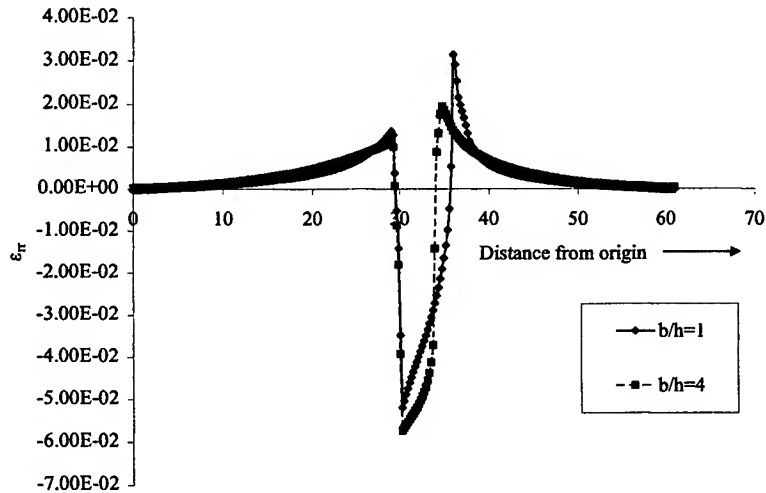


Figure 6. ϵ_{rr} as a function of position along the line parallel to the y-axis and passing through the origin for the case when $b/h=1$ and for $b/h=4$.

Also shown in the figures are the variations in ϵ_{yy} as a function of position along this line passing through the origin and parallel to the y-axis. Note that there is a compressive strain within the substrate near the wetting layer. Inside the quantum dot, ϵ_{yy} is initially tensile and then becomes compressive and within the substrate near the apex of the cone. This compressive strain has also been observed in the previous calculations for a pyramidal island with the same b/h ratio^{8,9}. The compressive strain in the substrate at the apex of the conical region and the bottom near the wetting layer is due to the Poisson expansion of the quantum dot along the y direction in response to the constraint introduced by the substrate in the radial direction. Note that this constraint was reflected in ϵ_{rr} being compressive within the quantum dot. As seen from figure

4 and figure 7, the magnitude of the compressive strains within the substrate at the top and bottom of the quantum dot are smaller when the b/h ratio and the height of the cone becomes smaller. This can be related to the size of the quantum dot along the y -axis. Note that for the case of b/h ratio equal to 1, the size of the island along the y -axis is 5 nm while it is only 3 nm when the b/h ratio is equal to 4. With the larger size along the y -axis, more displacement has to be accommodated along this direction with the result that the compressive strains in the substrate are larger on both the top and the bottom.

Figure 8 compares the radial strain in the quantum dot with a b/h ratio equal to 4 with that of the truncated quantum dot with b/h equal to 1. Note first that the maximum and minimum values in the strains are comparable for the two cases.

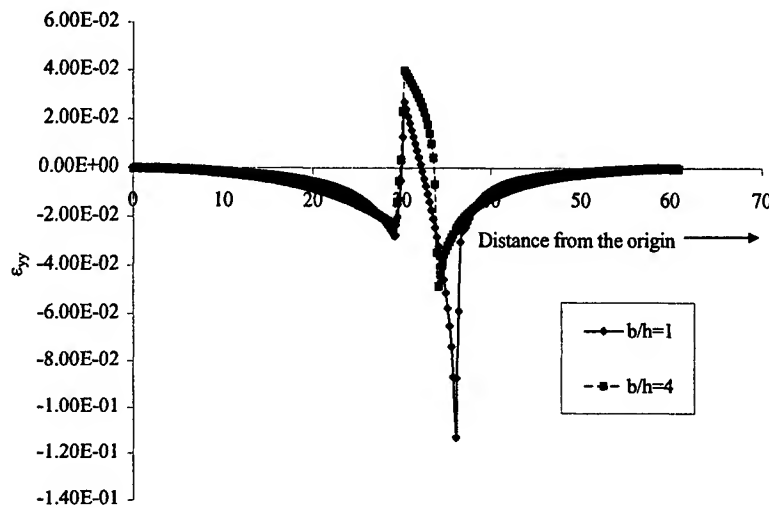


Figure 7. ϵ_{yy} as a function of position along the line parallel to the y -axis and passing through the origin for the case when $b/h=1$ and for $b/h=4$.

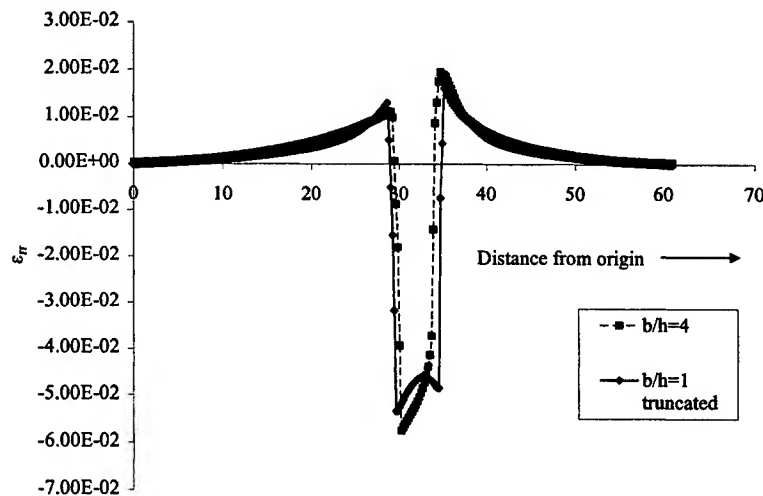


Figure 8. ϵ_{rr} as a function of position along the line parallel to the y -axis and passing through the origin for the case when $b/h=4$ and for a truncated cone with $b/h=1$.

This again is related to the fact that the size of the dot along the y-axis is 3 nm for the conical dot and 2.5 nm for the truncated conical dot. However, the shape of the strain is more flat for the truncated dot than that for the conical dot, consistent with previous calculations⁴. Thus, it has been shown clearly that the shape of the quantum dot can have a significant effect on both the radial strains and strains along the normal to the interfaces.

There are very few experimental studies that measure the highly non-uniform strains in these systems. In a recent study, the strains along the normal to the interfaces have been measured for InAs quantum dots in GaAs with a lens-shape using cross-sectional STM³. The size of the lens-shaped dot is very close to that of the quantum dot with b/h ratio equal to 4 used in our calculations. They found that the strains are first compressive (-14.0%) in the substrate close to the wetting layer, becomes tensile within the dot (about 7.0 %), then becomes highly compressive (-14.0%) again within the substrate at the top. Comparing this with the results of the calculations shown in figure 7 for b/h equal to 4 shows that the general trend is similar in that there are compressive strains on either side of the dot. However, the magnitudes of these strains are much smaller than that observed in the experimental study with the maximum compressive strain in the calculations reaching only about -5.0%. Within the quantum dot, tensile strains reach only about 4.0% and drops off fairly sharply in the calculations unlike in the experimental measurements wherein the strains stay around 7.0% within most of the quantum dot. It is tempting to attribute these discrepancies to the essentially 2-D nature of our model and the use of isotropic material properties. However, the results obtained from a full 3-D calculation¹³ are comparable to those obtained in the present study. It has also been shown that stress relaxation that occurs due to cleaving for the STM imaging may contribute to the observed discrepancy.

4. CONCLUSIONS

The finite element method has been used to calculate the effect of the shape of quantum dots on the strains within and outside InAs quantum dots in GaAs. Beginning with a conical quantum dot, it was shown that due to the constraints, the embedded quantum dot becomes lens-shaped, as is observed in experimental studies. Strains have been calculated for cone-shaped and truncated cone-shaped quantum dots using an axi-symmetric model. Results of these calculations compare well with other calculations of strains in pyramidal embedded quantum dots. However, discrepancies have been observed with experimental measurements of strains, which may partially be related to relaxation of strains during sample preparation.

ACKNOWLEDGMENTS

The author would like to thank Dr. John Wang for his support of the research outlined in this work. Thanks are also due to Mr. Tung Chih Hang and Mr. George T. T. Sheng for interesting discussions.

REFERENCES

1. Qianghua Xie, Anupam Madhukar, Ping Chen and Nobuhiko P. Kobayashi, "Vertically self-organized InAs quantum box islands on GaAs," *Phys. Rev. Lett.*, **75**, pp. 2542-2545, 1995.
2. G. S. Solomon, J. A. Trezza, A. F. Marshall and J. S. Harris, "Vertically aligned and electronically coupled growth induced InAs islands in GaAs," *Phys. Rev. Lett.*, **76**, pp. 952 - 955, 1996.
3. B. Legrand, B. Grandidier, J. P. Nys and D. Stievenard, J. M. Gerard, V. Thierry-Mieg, "Scanning tunneling microscopy and scanning tunneling spectroscopy of self-assembled InAs quantum dots," *App. Phys. Lett.*, **73**, pp. 96-98, 1998.
4. H. Eisele, O. Flebbe, T. Kalka and M. Dahne-Prietsch, "Cross-sectional STM study of InAs Quantum Dots for Laser Devices," *Surf. Interface Anal.*, **27**, pp. 537-541, 1999.
5. H. Eisele, O. Flebbe, T. Kalka, C. Preinesberger, F. Heinrichsdorff, A. Krost, D. Bimberg and M. Dahne-Prietsch, "Cross-sectional scanning-tunneling microscopy of stacked InAs quantum dots," *App. Phys. Lett.*, **75**, pp. 106-108, 1999.
6. O. Brandt, L. Tapfer, K. Ploog, R. Bierwolf, M. Hohenstein, F. Phillipp, H. Lage and A. Heberle, "InAs quantum dots in a single-crystal GaAs matrix," *Phys. Rev. B*, **44**, pp. 8043-8052, 1991.
7. O. Brandt, K. Ploog, L. Tapfer, M. Hohenstein, R. Bierwolf and F. Phillipp, "Formation and morphology of InAs/GaAs heterointerfaces," *Phys. Rev. B*, **45**, pp. 8443-8453, 1992.
8. A. A. Darhuber, V. Holy, G. Bauer, P. D. Wang, Y. P. Song, C. M. Sotomayor Torres and M. C. Holland, "Quantitative analysis of elastic strains in GaAs/AlAs quantum dots," *Physica B*, **227**, 11- 16, 1996.

9. M. Grundmann, O. Stier and D. Bimberg, "InAs/GaAs pyramidal quantum dots: Strain distribution, optical phonons and electronic structure," *Phys. Rev. B*, **52**, pp. 11969- 11981, 1995.
10. C. Pryor, J. Kim, L. W. Wang, A. J. Williamson and A. Zunger, "Comparison of two methods for describing the strain profiles in quantum dots," *J. Appl. Phys.*, **83**, pp. 2548-2554, 1998.
11. S. C. Jain, H. E. Maes, K. Pinardi and I. De Wolf, "Stresses and strains in lattice-mismatched stripes, quantum wires, quantum dots, and substrates in Si technology," *J. Appl. Phys.*, **79**, pp. 8145-8165, 1996.
12. T. Benabbas, P. Francois, Y. Androussi and A. Lefebvre, "Stress relaxation in highly strained InAs/GaAs structures as studied by finite element analysis and transmission electron microscopy," *J. Appl. Phys.*, **80**, pp. 2763-2767, 1996.
13. G. Muralidharan, "Strains in self-assembled InAs quantum dots in GaAs: A finite element study," To be presented at the MRS Fall Meeting, 1999.

SESSION 4

Quantum Wells

Fabrication of Bandgap Tuned Lasers in GaAs/AlGaAs structure Using Sol-Gel SiO₂ Induced Quantum Well Intermixing

L.H. Lee, O. Gunawan, B.S. Ooi*, Y. Zhou, Y.C. Chan, and Y.L. Lam

Photonics Research Group, School of Electrical and Electronic Engineering
Nanyang Technological University, Block S1, Nanyang Avenue, S639798, SINGAPORE

ABSTRACT

Quantum well intermixing (QWI) is a promising technology for the fabrication of photonic integrated circuits (PICs). In this paper, we report the development of a new QWI process using undoped and Er-doped SiO₂ dielectric caps prepared using sol-gel technique. A differential bandgap shift of as large as 83meV have been observed from samples intermixed with Er-doped and undoped SiO₂ respectively. Broad area gain guided lasers have been fabricated from the as-grown and samples with bandgap tuned to different degrees using undoped and Er-doped SiO₂. Lasers fabricated from the as-grown, undoped and Er-doped SiO₂ samples showed lasing wavelengths of 865nm, 850nm and 835nm respectively. Compared to the 865nm, the threshold current of the 850nm and 835nm wavelength lasers were found to increase by 5% and 9.5% respectively. The slope efficiencies from these lasers were found to exhibit only small change compared to the as-grown lasers. These results imply that the quality of the material remains relatively high after intermixed using sol-gel SiO₂ induced QWI technique.

Keywords: Quantum well Intermixing, photonic integrated circuits, sol-gel technique, GaAs/AlGaAs laser structure.

INTRODUCTION

Quantum well intermixing (QWI) using impurity free vacancy diffusion (IFVD) technique is one of the simplest and most versatile ways of controlling the bandgap of the quantum well (QW) after growth, particularly in GaAs-AlGaAs structures. This technique uses a SiO₂ dielectric cap to induce outdiffusion of Ga atoms during annealing, thereby generating group III vacancies in the underlying GaAs-AlGaAs material and hence promote interdiffusion between Ga and Al, which in turn, change of bandgap energy of the QW.

The SiO₂ cap for IFVD are typically coated on the GaAs/AlGaAs samples using Plasma enhanced chemical vapor deposition (PECVD) or sputtering. The sol-gel process is an interesting alternative to deposit SiO₂ on semiconductors. In recent years, the sol-gel method has gained considerable attention in the development of materials and devices for optical and PIC applications. SiO₂ deposition using sol-gel approach is simple and low cost. In addition, it allows the synthesis of very pure and homogeneous film on semiconductors. A key advantage of sol-gel process is the ease with which composition can be altered and dopants introduced. This is much more problematic for the competing PECVD methods. For these reasons, a wide range of novel materials could be prepared for PIC applications.

In this paper, we report the studying of IFVD effect on GaAs/AlGaAs laser structure using sol-gel derived SiO₂. In order to assess the quality of the intermixed materials, bandgap tuned lasers has been fabricated. From the lasing conditions of the lasers, the quality of the materials were found to remain high after intermixing.

*E-mail: cbsooi@ntu.edu.sg, Tel: (65)-7904517, Fax: (65)-7912687

EXPERIMENT

A GaAs-AlGaAs DQW laser structure was used in the experiments (Figure 1). This structure was grown by metal-organic vapor phase epitaxy (MOVPE) and was of the form of a separate-confinement heterostructure (SCH) DQW laser. The DQW region was undoped and consisted of two 10-nm-wide GaAs QW's, separated by a 10-nm $\text{Al}_{0.2}\text{Ga}_{0.8}\text{As}$ barrier. The top and bottom $\text{Al}_{0.2}\text{Ga}_{0.8}\text{As}$ layers were 0.1 μm thick to complete the waveguide core. Both the upper (0.9 μm thick) and the lower (1.5 μm thick) cladding layers were made of $\text{Al}_{0.4}\text{Ga}_{0.6}\text{As}$ and doped to a concentration of $5 \times 10^{17} \text{ cm}^{-3}$ using carbon and silicon, respectively. The top contact epitaxial layer consisted of 0.1 μm of GaAs doped with $5 \times 10^{18} \text{ cm}^{-3}$ of zinc. This material gave a 77-K photoluminescence (PL) peak at about 806 nm and a lasing wavelength from a broad-area laser at around 860 nm at room temperature.

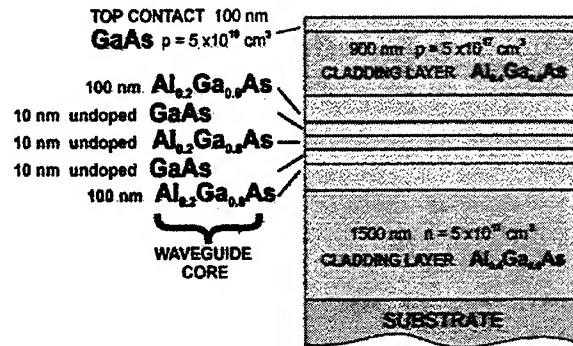


Figure 1 : Schematic diagram of the GaAs/AlGaAs structure used in the experiment.

The undoped SiO_2 sol-gel was prepared using a mixture of TEOS, $\text{C}_2\text{H}_5\text{OH}$ and H_2O were prepared in the molar ratio 1:10:12. This solution was for undoped film. For Er-doped films, the solution was mixed with 2% wt%, 5 wt% and 10 wt% erbium respectively. To obtain uniform and thin coating on the substrate, the solution was spun on the samples at a speed of 4000 rpm for 30 seconds. The gel was dried using a rapid thermal process at 600°C for 120 s.

The intermixing step was carried out in a RTP in a nitrogen atmosphere. The samples were placed faced down on a piece of fresh GaAs acting as a proximity cap and another piece of GaAs was placed over the back to provide an As overpressure during annealing. The chamber was vacuumed and purged with nitrogen to remove any undesirable contents. The samples were annealed at different temperature range from 850°C to 950°C , using nitrogen as process gas. PL were then carried out at 77 K to measure the bandgap after intermixing. This was carried out with the samples measured at 77 kelvin using liquid nitrogen.

The fabrication of band-gap tuned lasers from DQW material intermixed with different percentage of doped SiO_2 were done with samples (8 mm \times 8 mm size) spun with different sol-gel SiO_2 at 4000 RPM for 30 s. The intermixing process were done using the RTP at 900°C for 30 s. Then, PL measurement under 77 K using liquid nitrogen were carried out. Subsequently, the sol-gel were removed and Si_3N_4 (200 nm) were deposited for photolithography using mask aligner (50 μm stripe). Positive metal contact were deposited using Ti / Au (30nm / 150 nm). The substrate were then be thinned to 200 μm before depositing negative metal contact using Au / Ge / Au / Ni / Au (10 nm / 20 nm / 10 nm / 20 nm / 240 nm). Finally, the fabricated lasers were characterized using the semiconductor test kit. After the fabricating steps, the samples are cleaved into different cavity lengths of 500 μm , 700 μm , 900 μm and 1000 μm .

RESULTS AND DISCUSSIONS

Figure 2 shows the atomic force microscopy (AFM) images from samples deposited with different percentage of Er-doped SiO_2 . Measurements show that the root mean square (RMS) roughness increases with dopant concentration, i.e. from 0.3 nm to 1.1 nm for 10 % Er film. The results imply that undoped SiO_2 films produce a better and uniform film.

Different thickness of both undoped and Er-doped sol-gel films were deposited onto the DQW samples and annealed at different annealing conditions to study the effect of the SiO_2 thickness on the degree of intermixing. The number of layers to be deposited to achieve a given final multilayer thickness can be determined from Figure 3. The thickness of each layer were measured using thin film measurement technique. A thickness of about 120 nm was measured for the first layer, 130-140 nm for the second and third layers and about 170-200 nm for the fourth layers. The figure shows the consistency in all the different films. The thickness of sol-gel films gradually decreases with heating time, for a given temperature ^[1]. The difference in thickness between the fourth layer and first three layers can be explained since the latter has gone through annealing for repeated times.

Figure 4 give the degree of QWI as a function of RTP temperature for samples with 10% Er-doped SiO_2 . From Figure 4, it is observed that no significant wavelength shift has been obtained for different thickness. Similar trend has also been observed from samples intermixed with different percentage of erbium. The results in Figure 4 imply that the thermal stress effect is not the main factor in sol-gel intermixing since the flow temperature is relatively low ^[2].

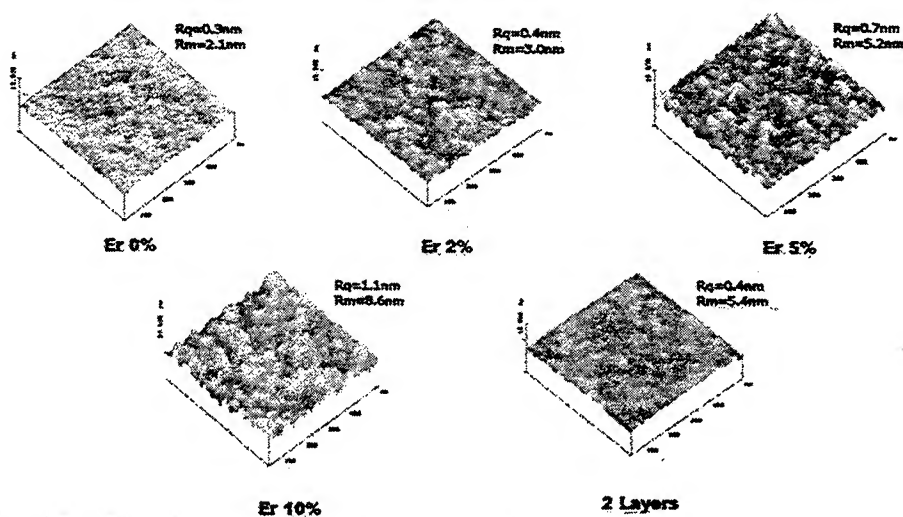


Figure2: Surface morphologies of the sol-gel SiO_2 doped with different Er concentration.

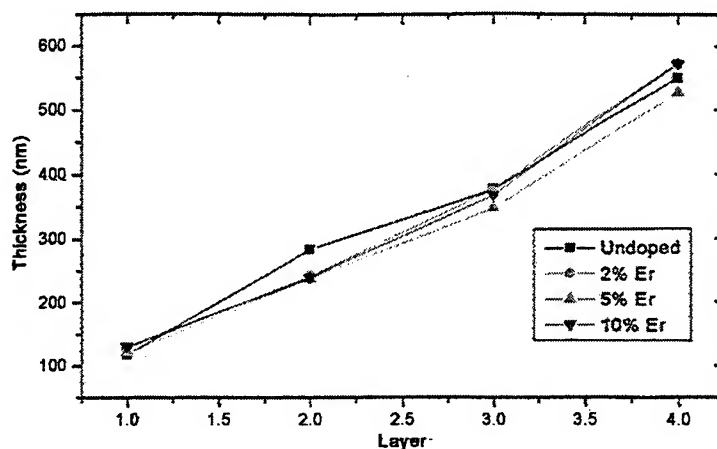


Figure 3 : Thickness of SiO₂ film as a function of number of layer

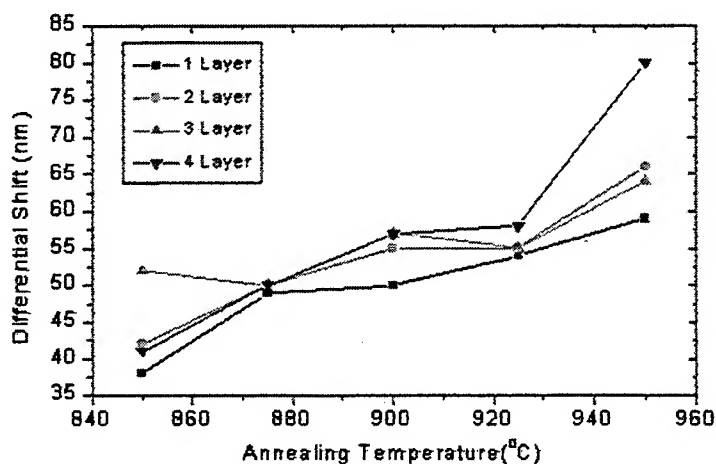


Figure 4 : Differential shift with reference to as-grown, as a function of RTP temperature for 10% Er doped sample

The as-grown samples and samples deposited with 200 nm of SiO₂ were intermixed at 900°C for 30 s. Figure 5 shows the PL spectra from the for as-grown, Er-doped and undoped samples. The SiO₂ layers deposited using sol-gel are highly porous and some of the bonding network of SiO₂ are believed to have been broken due to the stress gradient between the GaAs and SiO₂ films. This would enhance the diffusion of Ga atoms through the SiO₂ network. At the same time, As atoms would also diffuse into the SiO₂ during high temperature As overpressure annealing. However, Ga atoms would preferentially outdiffuse as the diffusion coefficient of As in SiO₂ is extremely low compared to Ga. At similar annealing temperatures, the effective diffusion rate of Ga has been found to be greater when using a short-rise-time RTP than using a conventional furnace. This observation suggests that stress induced at the SiO₂ - GaAs interface is responsible for enhancing outdiffusion of Ga, as RTP introduces greater stress at the SiO₂-GaAs interface than conventional furnace annealing^[3].

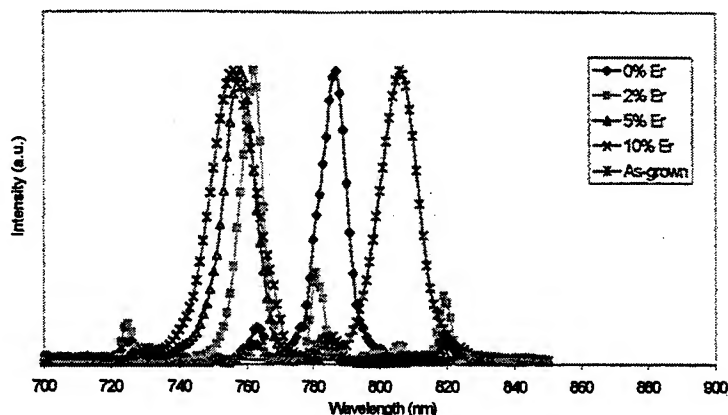


Figure 5 : PL spectra from the as-grown, undoped and doped samples

As shown in Figure 5, undoped SiO_2 seems to suppress intermixing compared to doped SiO_2 , with a differential shift of 30 nm under the same annealing condition. This is might be due to undoped SiO_2 film has a lower porosity network than Er-doped SiO_2 . Since impurity is added to the latter to cause the film to become more porous than the undoped film, it has resulted in promoting the Ga atoms from the GaAs layer to diffuse through the more porous network of the doped film and hence increasing quantum well intermixing.

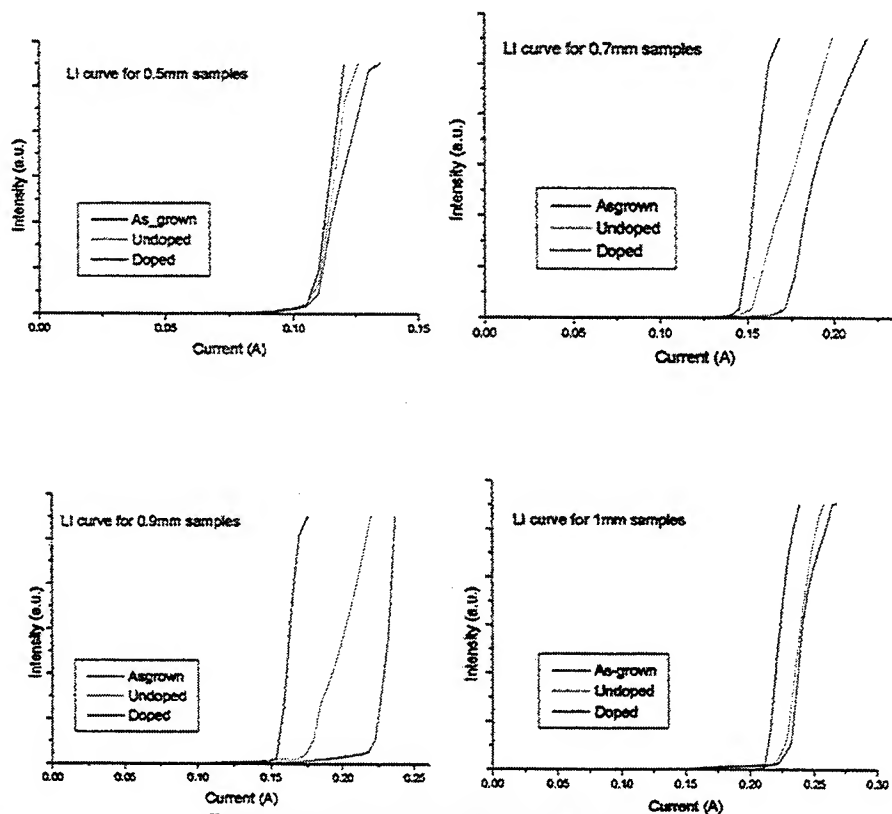


Figure 6 : LI curve for different cavity lengths

Bandgap tuned lasers have been fabricated from samples intermixed with different percentage of Er-doped SiO_2 . Comparing the samples for the same cavity length, the as-grown samples give lower threshold current I_{TH} . On the other hand, the I_{TH} of undoped samples are lower than the doped samples. The difference in threshold current is significant, comparing the doped and as-grown samples. This may be due to the loss of carrier confinement.

After obtaining the I-V curve and L-I curve, the optical spectral analyzer to the spectra emitted from the semiconductor lasers. From Figure 7, it clearly shows that the wavelength is successfully shifted after intermixing. These spectra were obtained from lasers with cavity length $700\ \mu\text{m}$ operated just above threshold. The peak wavelength of the as-grown, undoped and doped samples are at 865, 850 and 835 nm respectively. This indicated that the blue wavelength shift is greater comparing the doped sample against the undoped sample. This again illustrates that the QWI rate is greater due to the vacancies created by the dopant in the film.

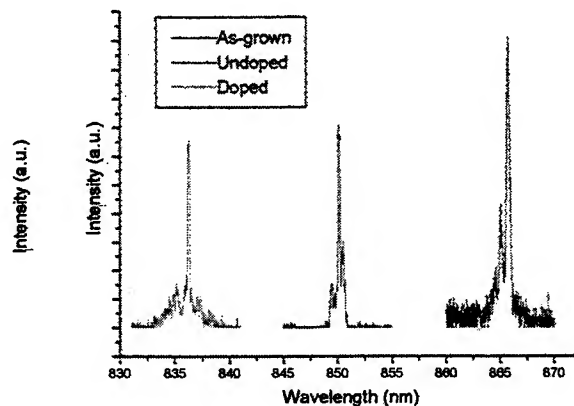


Figure 7 : Spectra of semiconductor lasers fabricated with cavity length of $700\ \mu\text{m}$.

CONCLUSION

QWI using sol-gel Er-doped and undoped SiO_2 films in GaAs/AlGaAs films have been developed. Bandgap tuned lasers, fabricated from the as-grown and intermixed samples have been demonstrated. The lasers fabricated from as-grown, undoped and doped samples give peak wavelength at 865, 850 and 835 nm. From the threshold current density, the intermixed lasers are found to be in good quality.

REFERENCES

1. R.M. Almeida, H.C. Vasconcelos, "Sol-gel technologies in thin film fabrication for integrated optic lasers and amplifiers", IEEE. J. Quantum Electron, CR 68, pp 172, 1995.
2. L.H. Lee, B.S. Ooi, Y.L. Lam, Y.C. Chan and C.H. Kam, "Quantum well intermixing in GaAs-AlGaAs laser structure using sol-gel SiO_2 dielectric cap", Photonics China, SPIE, V3547, pp 319, 1998.
3. I. Gontijo, Y.S. Tang, R.M. De La Rue, C.M. Sotomayor Torres and J. Marsh, " Photoreflectance and photoluminescence of partially intermixed GaAs-AlGaAs double quantum wells", J. Appl. Phys., V6, pp 76, 1994.

Photonic Integration of InGaAs-InGaAsP Laser Using Low Energy Implantation Induced Quantum Well Intermixing

Hwi Siong Lim, Boon Siew Ooi*, Yee Loy Lam, Yuen Chuen Chan, Yan Zhou
Photonics Research Group, School of Electrical and Electronic Engineering,
Nanyang Technological University, Singapore 639798

Vincent Aimez, Jacques Beauvais
Centre de Recherche en Physique du Solide and Département de Génie Électrique et Génie
Informatique, Université de Sherbrooke, Sherbrooke, Québec, Canada J1K 2R1

and J. Beerens
Centre de Recherche en Physique du Solide and Département de Physique, Université de Sherbrooke,
Sherbrooke, Québec, Canada J1K 2R1

ABSTRACT

Neutral impurity induced quantum well intermixing (QWI) is an attractive and promising postgrowth bandgap engineering process for the fabrication of photonic integrated circuits (PICs), as it introduces no additional electrical active dopants into the material system after intermixing. Here, we report the development of neutral impurity induced QWI processes in InGaAs-InGaAsP laser structure using low energy, i.e. 360keV, arsenic and phosphorous ion implantation. The samples were implanted at room temperature and 200 °C, with a dose range between 10^{12} and 10^{14} ions/cm². The QWI stage was carried out by annealing the implanted samples at 650 °C for 120 s. Samples implanted at 200 °C give higher degree of QWI. Compared to P implanted samples, larger bandgap shift was observed from As implanted samples after annealing. A differential PL bandgap shift as large as 93 nm (60 meV) was observed from samples implanted with 10^{14} ions/cm² of As. Bandgap tuned lasers fabricated from intermixed samples; the current threshold density of the intermixed lasers slowly increases with the amount of blueshift and is kept below 20% for the most blueshifted devices. The attractive device characteristics of the bandgap tuned lasers show that damage induced by the ion implantation can be almost fully treated after annealing. This implies that the material remains in good quality after QWI.

Keywords: Low energy ion implantation, quantum well Intermixing, InGaAs-InGaAsP, quantum well laser.

1. INTRODUCTION

Optoelectronics integrated circuits (OEICs) and photonics integrated circuits (PICs) are of considerable interest for the development of telecommunication system. The driving forces for PICs are to improve the complexity of next-generation optical communication links, networking architectures and switching systems, such as in the multichannel wavelength division multiplexer (WDM) and high speed time division multiplexer (TDM) system. In PICs, besides gaining from the low cost, size reduction, and increased packaging robustness, the main advantage is all the interconnections between the individual guided-wave optoelectronics devices are precisely and permanently aligned with respect to one another since the waveguides are lithographically produced.

In the integration process, complex devices are built up from components that are very different in functionality such as light emitter, waveguides, modulators and detectors. Each components need different material structures to achieve optimized performance. As a result, the ability to modify the bandgap energy and the refractive index of materials are important in order

* Correspondence: Email: ebsooi@ntu.edu.sg; Tel: (65)-7904517; Fax: (65)-7912687.

to realize OEICs and PICs. A number of techniques have emerged for this purpose, commonly used approaches are the growth and regrowth¹, selective area growth² and quantum well intermixing (QWI)³. Among the three techniques, QWI provides a postgrowth, simple and low-cost integration process.

QWI is based on the fact that a quantum well (QW) is inherently metastable system due to the large concentration gradient of atomic species across the QWs and barriers interface. Hence, this allows the modification of the bandgap of quantum well structures in selected regions by intermixing the quantum wells with the barriers to form alloy semiconductors. This technique offers an effective post-growth method for the lateral integration of different bandgap, refractive index and optical absorption within the same epitaxial layers. Current research has been focused on QWI using approaches such as impurity induced disordering (IFVD)⁴, photoabsorption induced disordering (PAID)⁵ and impurity induced disordering (IID)⁶.

Among all the QWI methods, IID is the only process which requires the introduction of impurities into the QW materials in order to realize the intermixing process. These impurities can be introduced through focus ion beam, furnace diffusion and also ion implantation. In this project, an ion implantation process was used not only to implant As and P impurities into the InGaAs-InGaAsP material, but also to create point defects in the material to promote higher degree of intermixing.

Low energy ion implantation IID is a relatively simple and highly reproducible intermixing process. It has the ability to provide high spatial resolution for the integration of small dimension devices and bandgap shifts can be controlled through the implantation parameters. This technique is commonly used to achieve lateral electrical and optical confinement in semiconductors such that low threshold current and single lateral-mode operation can be obtained⁶. Furthermore, the IID process is of considerable interest for the integration of WDM systems, such as the multiwavelength laser source, low-loss waveguide, modulator and even the detector.

During implantation, impurities as well as point defects such as Group III vacancies and interstitials are introduced into the materials in selected areas. It is noted that these impurities and point defects enhance the interdiffusion rate between the QWs and barriers and hence promote intermixing after annealing. During the interdiffusion process, the local bandgap increases but the corresponding refractive index decreases⁷. It is because under the influence of injected impurities, the compositional profile of QW is altered from a square to a nonsquare profile⁸. Thus provided that the annealing temperature is set below the thermal stability of the material, it is possible to obtain blueshifts solely in the desired regions which is a prerequisite to any PIC fabrication.

Neutral impurities As and P were used in this project as these species are matrix elements of the InGaAs/InGaAsP laser system. As compared to electrically active impurities, neutral impurities As and P exhibit less free carrier absorption loss. Besides, other reasons for choosing these neutral species is because As is not well studied in InGaAs/InGaAsP material system and P, which is commonly used, was chosen for the comparison of these two impurities towards the intermixing degree.

In this project, a low implantation energy at 360keV was chosen so that, 1) no extended defects are induced after QWI, 2) the damage to crystal can be minimized. At this low energy implantation, the process can be controlled such that the bombardment only occurs on the contact layers, as a result the crystalline quality of the cladding layers and QWs can be conserved. Furthermore, the implantation doses were chosen only up to 10^{14} ions/cm² to maintain the residual purity by introducing only insignificant doping and also to avoid the formation of amorphous epitaxial layers under higher dose.

2. EXPERIMENT

The lattice-matched InGaAs/InGaAsP single quantum well materials was grown by metal-organic vapor phase epitaxy (MOVPE) on a (100)-orientated n⁺-type S-doped InP substrates with an etch pit density less than 1000cm⁻². The geometry of the InGaAs/InGaAsP laser structure used in this experiment is shown in Fig. 1a. Fig 1b shows the bandgap structure profile at the active region. The InGaAs/InGaAsP laser structure consists of 55Å single In_{0.53}Ga_{0.47}As well with 120Å InGaAsP ($\lambda_g=1.26\mu\text{m}$, where λ_g is the wavelength corresponding to the bandgap) barriers. The active region was bounded by a stepped graded index (GRIN) waveguide core consisting of InGaAsP confining layers. The thickness and compositions of these layers (from the QW's barrier outward) were 500Å of $\lambda_g=1.18\mu\text{m}$ and 800Å of $\lambda_g=1.05\mu\text{m}$. The structure was completed by InP lower cladding of 1μm (with S-doping of $2.5 \times 10^{18}\text{cm}^{-3}$) and upper cladding of 1.4μm (with Zn-doped of $5 \times 10^{17}\text{cm}^{-3}$). The contact layers consist of 500Å InGaAsP (Zn-doped of $2 \times 10^{18}\text{cm}^{-3}$) and 1000Å InGaAs (Zn-doped of $2 \times 10^{19}\text{cm}^{-3}$). The

waveguide core was undoped, thus forming PIN structure with intrinsic region restricted to the QW and the GRIN layers. The samples gave a PL wavelength peak at 1.55 μ m at room temperature.

The samples were first implanted using an industrial Varian/Extrion DF-3000 implanter. The As and P implantation were carried out both at room temperature and at 200°C with doses varying between 1×10^{12} ions/cm² and 1×10^{14} ions/cm² using doubly charged ions at 360keV implantation energy. The samples were tilted 7° from the ion beam during implantation in order to reduce channeling effects.

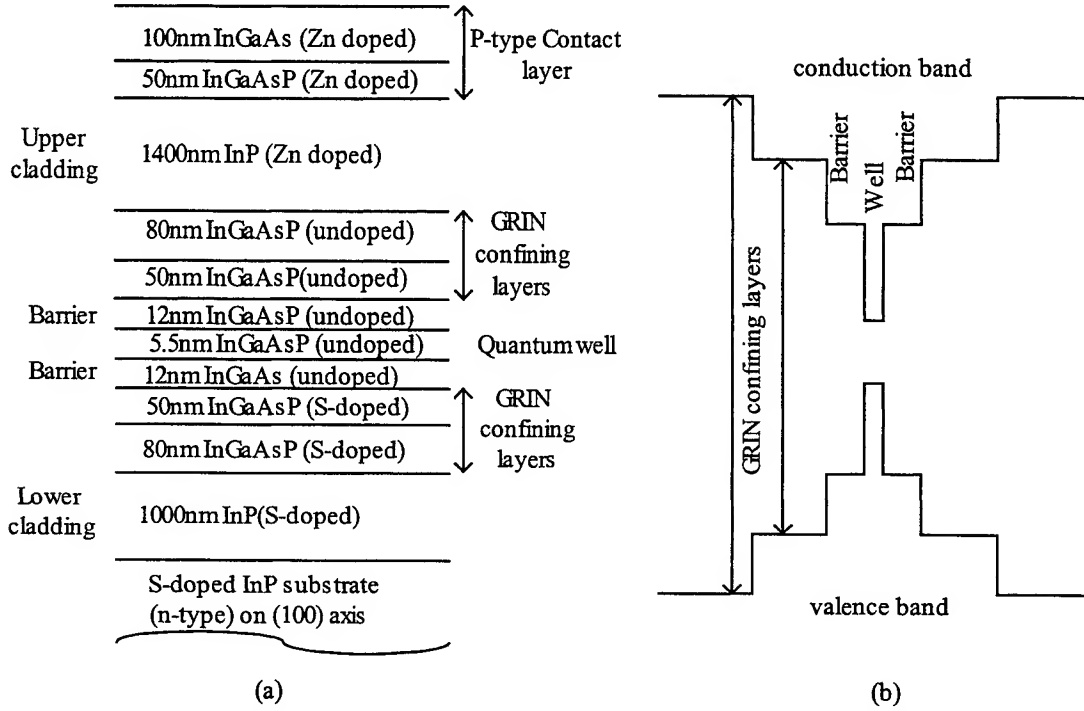


Figure 1. (a) The geometry of the InGaAs/InGaAsP single-quantum-well laser material structure used in this experiment, (b) Bandgap profile for the single quantum well InGaAs/InGaAsP material.

A subsequent annealing of the samples was carried out using a JetStar rapid thermal processor (RTP) under nitrogen-rich environment to avoid surface oxidation of the epitaxial layer. During annealing, the samples were face down onto a clean polished GaAs substrate as the proximity cap to prevent As out-diffusion⁸. Another GaAs cap was placed on top the sample to act as protection cap. The annealing process not only promotes QW intermixing but also to remove nonradiative recombination sites from the implantation process.

The intermixing step was carried out at two different temperatures, 600°C and 650°C, for 120s. Results from the thermal stability test show that the as-grown samples give no significant bandgap widening under these RTP conditions. Photoluminescence (PL) measurements at 77K were performed on the samples both before and after annealing to assess the degree of intermixing.

PL measurements indicates the amount of intermixing using As⁺⁺ and P⁺⁺ IID; following these results, bandgap tuned oxide stripe lasers were fabricated to evaluate the laser quality between the intermixed and the as-grown samples.

3. THEORETICAL IMPLANT SIMULATIONS

Theoretical calculation of the dosage and concentration of point defects after implantation was performed using TRIM⁹. The simulated As⁺⁺ and P⁺⁺ results for this experiment are shown in Figure 2. Implanting As⁺⁺ impurities at 360keV, the impurities are accumulated within the contact layers and the P⁺⁺ impurity peak extends into the upper cladding layer at more than 1μm above the active region (Fig 2a). These ion range distributions further confirm that no implantation damage is created in the QWs and the barriers. As can be seen from Fig 2b, due to the larger atomic number of As atoms, the amount of vacancies generated from the As-implantation is more than twice that of P-implantation. However, the As-generated vacancies are accumulated at 0.13μm from the surface (within the contact layers) and 1.56μm away from the bottom QW, whereas, P-generated vacancies are distributed evenly across one-quarter of the cladding layer from the surface. This implies that the concentration of defects is higher with As implants.

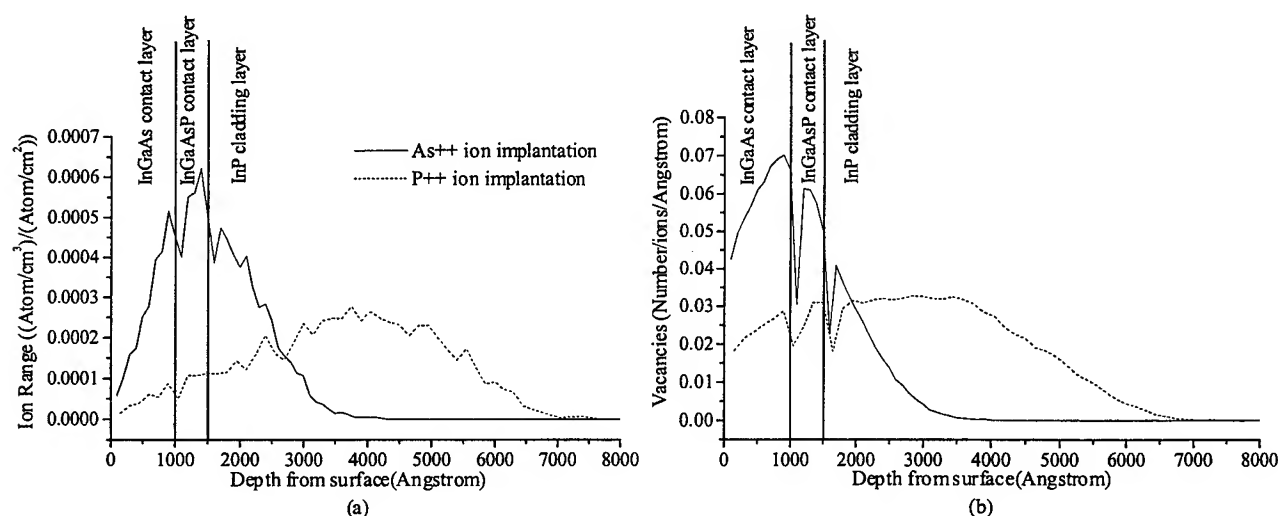


Figure 2. (a) TRIM simulation of As and P ion implantation impurity range distributions, (b) TRIM simulation of As and P ion implantation generated vacancies distribution. The simulations were performed at 360 keV with the ion angle tilted by 7°C for InGaAs/InGaAsP laser material system.

4. COMPARISON OF AS⁺⁺ AND P⁺⁺ INTERMIXING DEGREE

Unlike high energy implantation IID which introduced impurities and defects at the well and barrier region¹⁰, the PL emission for the low-energy implanted samples before going through RTP was still detectable and gave PL peak similar to the as-grown sample. This is because As and P ions were only implanted into the contact and cladding layers and the QW was not damaged and hence reduced the scattering loss (see Fig. 2).

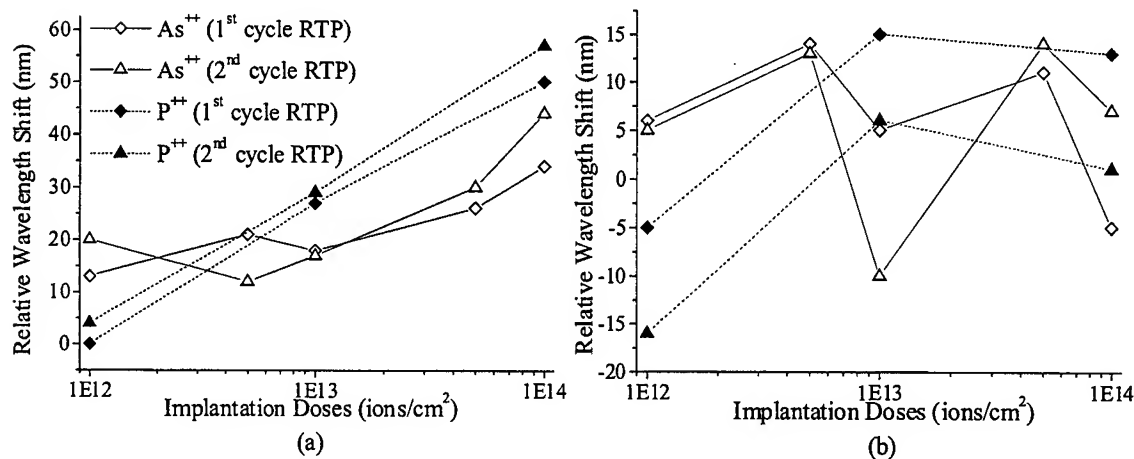


Figure 3. The 77 K wavelength blueshift relative to control sample versus different As and P implantation doses. (a) Samples implanted at 200 °C and (b) samples implanted at 20 °C. RTP annealing temperature was set to 600 °C and 2 minutes duration.

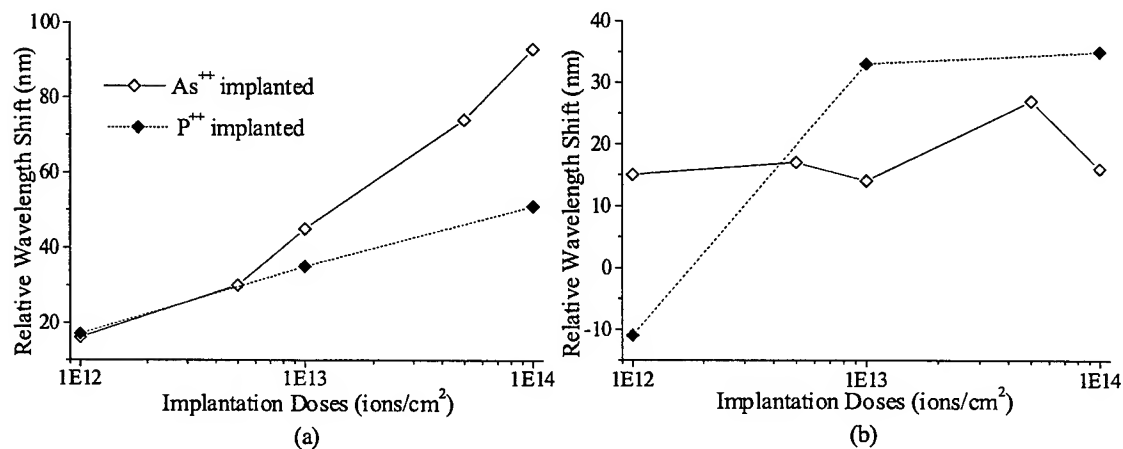


Figure 4. The 77K wavelength blueshift relative to control sample versus different As and P implantation doses. (a) Samples implanted at 200 °C and (b) samples implanted at 20 °C. RTP annealing temperature was set to 650 °C and each cycle of annealing was 2 minutes long.

Figure 3 shows the bandgap shift relative to the control samples, as a function of As and P implant doses for both samples implanted at 200 °C and room temperature respectively. The annealing temperature was set to 600 °C and gave insignificant thermal induced blueshift. Generally, it was found that the degree of QWI increases as a function of both the As and P implant doses for samples implanted at 200 °C (Fig. 3a). Under similar implant conditions, samples implanted at room temperature showed limited bandgap shifts (Fig. 3b and 4b). This phenomenon is in agreement with other workers¹¹ and can be attributed to the generation of aggregates with high diffusion activation energy during subsequent annealing¹² which appear at lower doses at room temperature. We can see that the formation of aggregates leads to a saturation in blueshifting for room temperature implants. Since the concentration of defects is higher with As ions than P ions from Fig. 4b, we can notice that As IID saturates for doses in the 10¹² ions/cm² range whereas P IID saturates for doses in the 10¹³ ions/cm² i.e. one order of magnitude higher. Because the amount of intermixing is closely linked to the quantity of defects that will diffuse through the wells during the rapid thermal annealing¹⁰, we can use higher doses and therefore obtain more blueshifting of the emission wavelength for implantation at elevated temperatures. The degree of intermixing was not found to be significantly

enhanced after the second annealing at the same temperature for 2 min for both room temperature and 200 °C implanted samples (Fig. 3a).

In order to verify the correlation between the intermixing degree and the amount of vacancies, the As and P were annealed at temperature slightly higher than the thermal stability, which was 650°C. For As implanted samples, differential wavelength shifts between the control and implanted samples ranging from 16nm (10meV) to 93nm (60meV) have been obtained with samples implanted at 200°C (Fig. 4a). These values are very interesting since such tunability of the bandgap energy allows the fabrication of multiple wavelength laser sources, quantum confinement stark effect (QCSE) modulators and low loss waveguides for photonic device integration. The observation of significant intermixing is confirming that defects are extremely mobile in InP based material systems¹⁰ since Monte-Carlo simulation performed with TRIM indicates that defects generated in samples implanted using these conditions are located at a relatively shallow depth of 0.13µm below the surface or well above the active region situated 1.5µm below (see Fig. 2b).

For P implanted samples, the relative blueshifts were of the same order for both annealing temperatures. This indicates that the diffusion of the point defects created during the ion implantation has been mostly treated even after the first 600°C annealing stage (Fig. 3a). For further intermixing, another implantation/anneal cycle could be performed¹³.

5. BANDGAP TUNED OXIDE-STRIPED LASERS

To access the quality of the material after QWI, broad area gain guided lasers were fabricated from as-grown sample (no implantation nor annealing), the control sample (no implantation but annealed), and the As and P implanted intermixed samples. In this experiment, multiple quantum well (MQW) InGaAs/InGaAsP laser heterostructure, which has the same epitaxial layer structure as the single quantum well (SQW) InGaAs/InGaAsP heterostructure (see Fig 1a) except for the addition of 4 wells and barriers, was used. The oxide stripe laser pattern with a contacted window of 30 or 50 µm width was used and the fabricated lasers were cleaved into 500 µm cavity length. The intensity versus current (L-I curves) and the spectrum of the laser emission were then measured and characterized. The results are shown in Fig. 6.

From Fig. 5a, we measured the threshold current density (J_{th}) for as-grown and control lasers to be 1.24kA/cm² and 1.28kA/cm² respectively. In the case of 1×10^{14} ions/cm² As and P implanted samples, we obtained J_{th} of 1.4kA/cm² and 1.48 kA/cm² respectively. The threshold current density for the 1×10^{12} ions/cm² As implanted sample is 1.28kA/cm², i.e. no noticeable increase in J_{th} (L-I curve not included for clarity since these devices had a 30µm wide contact window). The increase in J_{th} for highly intermixed samples is expected in part because of the QWs shape modification resulting in a loss of confinement after the intermixing process¹⁴. With only less than 20% increment of J_{th} for 140nm blueshifted lasers as compared to as-grown lasers, it implies that the surface damage from the IID process was mostly treated after annealing and that the optical quality of the material is conserved.

From Fig. 5b, the control samples and as-grown samples exhibit almost similar emission at 1.55µm, the 1×10^{12} ions/cm² As implanted samples emits at 1.51 µm and the 1×10^{14} ions/cm² As and P implanted samples are blueshifted more than 100nm to 1.447 µm and 1.410 µm respectively. These results show that low energy IID could be used to fabricate efficient WDM PICs with high quality multi-wavelength laser sources (small blueshifting) and low loss strongly blueshifted waveguides and QCSE modulators.

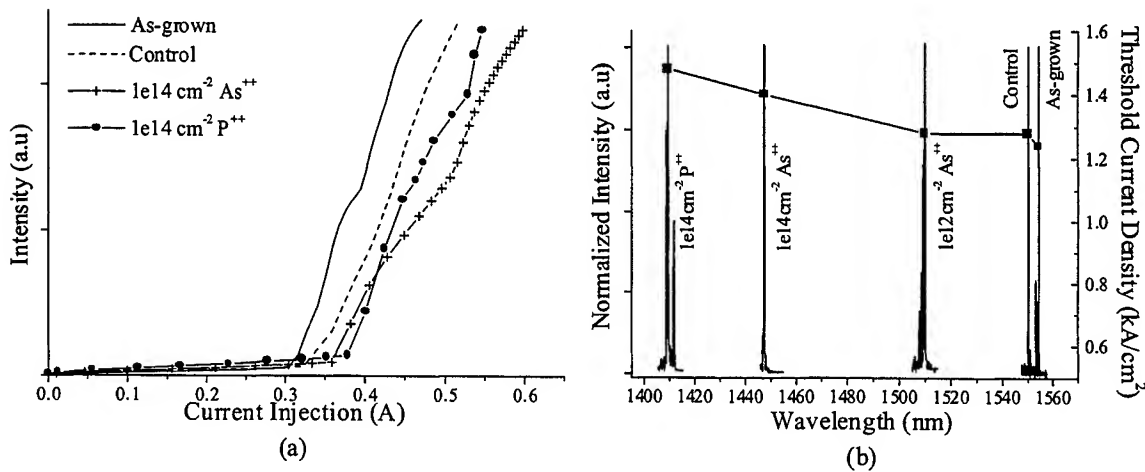


Figure 5. (a) Intensity versus Injection current (L-I) curves, (b) laser spectrum, for as-grown, control and As implanted InGaAs/InGaAsP MQW oxide stripe lasers.

6. CONCLUSIONS

We have successfully developed neutral IID process to control the degree of bandgap energy shift in InGaAs-InGaAsP quantum well laser structures using low energy, 360keV, As and P implantation at 200°C. Differential PL bandgap shifts between the unimplanted and implanted regions going up to 60meV (93nm) are reported for As implanted samples with a dose of 1×10^{14} ions/cm²; laser devices fabricated in this implanted material are shifted by 51meV (100nm) with no thermal shift for control lasers. To the best of our knowledge it is the largest degree of intermixing ever observed in InGaAs-InGaAsP laser structure using low energy arsenic implantation induced disordering. From the fabricated bandgap tuned lasers, we have observed that the surface damage created during implantation disappears for low doses and has been mostly treated after annealing with only 20% increase of threshold current density for 140nm blueshifted laser samples.

REFERENCES

1. E. S. Koteles, S. Charbonneau, P. Poole, J.J. Davies, M. Dion, G. Aers, Y. Feng, I. V. Mitchell and R.D. Goldberg, "Photonic integration using quantum well shape modification," *La Physique au Canada*, 1996, 251-254.
2. E. S. Koteles, "Techniques for Monolithically fabricating Photonic Integrated Circuits," in *Application of Photonics Technology*, G.A. Lampropoulos, J. Chrostowski, and R.M. Measures, Eds. New York: Plenum, pp. 413-418, 1995.
3. J. H. Marsh, "Quantum well intermixing," *Semicond. Sci. Technol.*, **8**, 1136-1155, 1993.
4. B.S. Ooi, K. McIlvaney, M.W. Street, A. Helmy, S.G. Ayling, A.C. Bryce, and J.H. Marsh, "Selective quantum well intermixing in GaAs-AlGaAs structures using impurity-free vacancy diffusion," *IEEE J. Quantum Electron.*, **33**, pp. 1784-1793, 1997.
5. A. McKee, C.J. McLean, G. Lullo, A.C. Bruce, R.M. De La Rue, J.H. Marsh, and C.C. Button, "Monolithic integration in InGaAs-InGaAsP multiple quantum well structures using laser intermixing," *IEEE J. Quantum Electron.*, **33**, pp. 45-55, 1997.
6. R.L. Thornton, R.D. Burnham, T.L. Paoli, N. Holonyak, Jr. and D.G. Deppe, "Low threshold planar buried heterostructure lasers fabricated by impurity-induced disordering," *Appl. Phys. Lett.*, **47**, pp.1239-1241, 1985.
7. P.D. Floyd, B.J. Thibeault, J. Ko, D.B. Young, L.A. Coldren, and J.L. Merz, "Vertical cavity lasers with Zn impurity-induced disordering (IID) defined active region," in *Proc LEOS'96*, **2**, pp. 207-208, 1996.
8. D.G. Deppe and N. Holonyak, Jr., "Atom diffusion and impurity-induced layer disordering in quantum well II-V semiconductor heterostructures," *J. Appl. Phys.*, **64**(12), 1998.

9. J.F. Ziegler, J.P. Biersack, and U. Littmark, *The stopping Range of Ions in Solids*, J.F. Ziegler Ed., New York: Pergamon, 1985.
10. P.J. Poole, S. Charbonneau, G.C. Aers, T.E. Jackman, M. Buchanan, M. Dion, R.D. Goldberg, and I.V. Mitchell, "Defect diffusion in ion implanted AlGaAs and InP: Consequences for quantum well intermixing," *J. Appl. Phys.*, **78**, pp. 2367-2371, 1995.
11. S. Charbonneau, E.S. Koteles, P.J. Poole, J.J. He, G.C. Aers, J. Haysom, M. Buchanan, Y. Feng, A. Delage, F. Yang, M. Davies, T.D. Goldberg, P.G. Piva, and I.V. Mitchell, "Photonics Integrated Circuits Fabricated using Ion Implantation," *IEEE J. Selected topics in Quan. Electr.*, **4**, pp. 772, 1998.
12. M. Paquette, V. Aimez, J. Beauvais, J. Beerens, P.J. Poole, S. Charbonneau, and A.P. Roth, "Blueshifting of InGaAsP-InP laser diodes using a low-energy ion-implantation technique: Comparison between strained and lattice matched quantum well structures", *IEEE J. Selected topics in Quan. Electr.*, **4**, 4, pp. 741, 1998.
13. P.J. Poole, P.G. Piva, M. Buchanan, G.C. Aers, A.P. Roth, M. Dion, Z.R. Wasilewski, E. S. Koteles, S. Charbonneau, and J. Beauvais, "The enhancement of quantum well intermixing through repeated ion implantation," *Semicond. Sci. Technol.*, **9**, pp. 2134-2137, 1994.
14. S. D. McDougall, O.P. Kowalski, C.J. Hamilton, F. Camacho, B. Qiu, M. Ke, R.M. De la Rue, A.C. Bryce, and J.H. Marsh, "Monolithic integration via a universal damage enhanced quantum-well intermixing technique", *J. Select. Topics Quant. Electron.*, **4**, 4, pp 636-646, 1998.

Phase Modulation of polariton in a GaAs quantum well waveguide

Kazuhiko Hosomi, Masataka Shirai, Toshio Katsuyama
Advanced Research Laboratory, Central Research Laboratory, Hitachi, Ltd.
1-280 Higashi-Koigakubo Kokubunji-shi, Tokyo 185-8601, Japan

ABSTRACT

In order to clarify the temperature dependence of the polariton phase change under electric field, an interferometric measurement was performed. The sample was a 400- μm -long polariton waveguide made of GaAs/AlGaAs layers with a p-i-n structure. A 7.5 nm GaAs single-quantum well is formed at the center of the core layer. The measured phase change at a lower temperature is about 10 times larger than that at a higher temperature, and the critical temperature is around 120 K. This critical temperature is remarkably high although the damping of the polariton usually occurs at a relatively low temperature. Such a high critical temperature indicates a possibility of a polariton device operation in a relatively high-temperature region.

Keywords: quantum well, waveguide, polariton, phase modulation, switching device

1. INTRODUCTION

There has recently been much interest in developing semiconductor optical-intensity modulators for applications in optical communication systems. Critical requirements for such modulators are low voltage operation and small size. In order to meet these requirements, we have developed a new type of opto-electronic device that uses propagation of an exciton polariton [1-4].

An exciton polariton is a composite quasi-particle formed by the coupling of an exciton and a photon. The polariton propagation is described by a specific energy vs. wavevector dispersion relation [5-8], which is shown in Fig.1. In this figure, the broken straight line represents the dispersion of an uncoupled photon and the broken parabolic curve indicates the dispersion relation of a single exciton. When the photon couples to the exciton, the dispersion curve of the resultant polariton splits into two different curves called the upper and lower branch, as shown in Fig. 1. The energy difference denoted by Δ_{LT} denotes the longitudinal-transverse (LT) splitting energy, i.e., the difference between the longitudinal exciton energy and transverse exciton energy. Note that the LT splitting energy is related to the oscillator strength. Our previous work showed that the LT splitting energy of the exciton in GaAs quantum well is 0.4 meV [3].

One of the most significant inherent features of exciton polariton is high sensitivity to an electric field, which is explained with a modified dispersion relation. As shown in Fig.2, since the slope of lower polariton branch is shallow around the resonant region, a small red shift of the resonance due to an electric field induces a large phase change (Δk) in a wave vector. Consequently, we can obtain a large phase shift with only a slight change in the electric field. We can make use of this highly sensitive response to achieve low-voltage operation in opto-electronic devices.

In addition, the characteristic wavelength of polariton propagation is much smaller than that of conventional light propagation. So it is possible to have a large effect in small device dimensions of only a few microns square, which means it is possible to fabricate extremely small optical devices. We therefore developed a directional-coupler-type device using polariton propagation and demonstrated its switching operation at the liquid-helium temperature [9].

In order to achieve a practical device that uses polariton propagation, higher temperature operation is a must. At present, the temperature dependence of the polariton effect has not been sufficiently studied. Accordingly, we performed the investigation on the temperature dependence of polariton phase change through an interferometric measurement. In this article, we describe the experimental procedure and discuss the results.

2. SAMPLE STRUCTURE

Figure 3 shows a schematic illustration of the sample structure, which consists of a 2- μm -wide GaAs/AlGaAs waveguide and a 400- μm -long electrode for applying the electric field. Figure 4 shows the cross-sectional structure of the waveguide, which is made of p-i-n GaAs/AlGaAs layers. A 1.8- μm -thick $\text{Al}_{0.13}\text{Ga}_{0.87}\text{As}$ core layer is sandwiched between $\text{Al}_{0.17}\text{Ga}_{0.83}\text{As}$ claddings. At the center of the core layer, a 7.5-nm GaAs single-quantum well (QW) is formed. The resonance wavelength of the QW is 790 nm.

We calculated the propagation constants and modal fields of the polariton waveguide described in Fig.4. The calculated field profile of the fundamental mode is shown in Fig. 5. The waveguide supports no higher mode, thus it is a single-mode. As shown in Fig. 5, the light propagating in the waveguide is well confined and interacts with an exciton in the QW, forming stable polariton propagation. The modal calculation yields a mode confinement factor of $\Gamma=4.5\text{E-}3$, which is defined as the overlap between the quantum wells and the optical mode.

The fabrication process of the devices was as follows. The epitaxial layers forming the waveguide were grown on a n-doped GaAs(100) substrate by using a conventional molecular-beam-epitaxy (MBE) system. The waveguide structure was fabricated by electron-beam (EB) lithography and subsequent electron-cycrotron-resonance (ECR) etching. The EB lithography was carried out with an ELS-3700 EB exposure system at an acceleration voltage of 30 kV. The wafers masked with EB resist were etched using ECR with SiCl_4 . Au electrodes were deposited onto the waveguide. The electrode pattern was patterned by EB lithography and subsequent ion milling with Ar.

3. EXPERIMENTAL PROCEDURE

The measurement setup is shown in Fig. 6. A tunable Ti-sapphire laser, excited by an Ar laser, was used as a light source. The tunable range of the Ti-sapphire laser was 770 - 870 nm and average power used for this measurement was 20 mW. The Ti-sapphire laser beam was transmitted with conventional optics and transformed to transverse-electric (TE) mode with a polarizer. In order to perform the interferometric measurement, the sample and a separate reference path formed a Mach-Zehnder interferometer. The TE-polarized beam was focused on the end face of a sample in a cryostat, which was inserted in one arm of the Mach-Zehnder interferometer. The interference pattern was observed with the CCD camera. The temperature of the sample was controlled by the temperature controller and was changed from liquid-helium temperature (LHeT) to a room temperature (RT). The phase change of the polariton was deduced from the fringe pattern change due to the applied electric field. Figure 7 gives the examples of the fringe pattern with and without an electric field.

4. RESULTS AND DISCUSSIONS

Figure 8 shows the measured V_π , the voltage required for change by π in the phase of the polariton propagation. Corresponding electric field required for π phase change is indicated by the right axis. As shown in the figure, V_π depends strongly on both the detuning wavelength and temperature.

Figure 9 shows the relation between phase shift per unit voltage and detuning wavelength, which is replotted from Fig.8. The phase shift rate, which is directly related with the refractive index change Δn , decreases monotonically with increase in the detuning wavelength. It should be noted that the detuning wavelength dependencies of the phase shift rate are classified into two groups corresponding to lower temperature (10 K- 80 K) and higher temperature (160 K-286 K).

If we focus our attention on temperature dependence, it is found that the phase shift rate at a lower temperature is considerably larger than for the higher temperature. For example, when the measured wavelength is detuned by 10nm from the resonant wavelength, the phase shift below 80 K is around π per unit voltage. On the other hand, at the temperature above 160 K, it is about $\pi/10$ per unit voltage. At the higher temperature, the $\Delta n/n/E$ is about $4\text{E-}10 \text{ cm/V}$ when $\Gamma=4.5\text{E-}3$, which roughly agree with the previous work on normal light propagation [10]. The critical temperature is around 120 K. This temperature dependence is shown more clearly in Fig.10, which shows the phase change rate at a detuning of 10 nm as a function of the measurement temperature.

Our experimental measurements show that the large phase shift can be obtained at least up to 120 K. On the other hand, as discussed in the introduction, the LT splitting energy defines the polariton stability with the temperature. The GaAs quantum well gives the LT splitting energy of 0.4 meV [3], which implies that a well defined polariton exists only up to 4.6 K. Accordingly, the critical temperature of 120 K obtained in the experiment is remarkably higher than expected from this criterion. Thus, the observed large critical temperature cannot be simply explained by the polariton stability as defined by the LT splitting energy. This indicates that the real part of the dielectric constant is influenced in a complex manner by the polariton effect.

In order to clarify such behavior, we studied the temperature dependence of the absorption spectra. Since the real part of the dielectric constant relating to the phase change is connected with the imaginary part relating to the absorption through the Kramers-Kronig transform [11], the absorption data provide a systematic understanding of phase change. Figure 11 shows the photocurrent spectra under several electric fields at (a) 5.1 K, (b) 80 K, (c) 120 K and (d) 160 K. Here, the photocurrent spectra roughly represent the absorption spectra. When the electric field is applied, large shift of the absorption edge to longer wavelength is clearly seen in each spectrum as a result of the quantum-confined Stark effect (QCSE). The extent of the shifted energy is about 0.06 eV under the electric field of 3.4×10^5 V/cm and it is independent of temperature. The significant temperature dependence, which may be related to the observed temperature dependence of the polariton phase change, does not appear in the spectra: not in shape, oscillator strength nor its electric field dependence. Therefore, we expect that only a slight change of absorption edge actually influences the phase shift. Further theoretical and experimental investigation is in progress, in order to clarify the physical origin of this critical temperature of 120 K.

SUMMARY

We investigated the temperature dependence of the polariton phase change under electric field, using interferometric measurement. The phase change rate at a lower temperature is considerably larger than that at a higher temperature. This large phase change rate remains up to 120 K. This critical temperature is much higher than that we had expected, and the physical mechanism is not clear at present. Such a high critical temperature indicates a possibility of a polariton device operation at a relatively high-temperature.

ACKNOWLEDGMENTS

This work was carried out by the Quantum Functional Devices Project under the management of FED (the R&D Association for Future Electron Devices) as a part of the MITI (Ministry of International Trade and Industry) R&D of Industrial Science and Technology Frontier program supported by NEDO (New Energy and Industrial Technology Development Organization).

REFERENCES

1. K. Ogawa, T. Katsuyama, and H. Nakamura, "Polarization dependence of excitonic-polariton propagation in a GaAs quantum-well waveguide," *Phys. Rev. Lett.*, **64**, pp.796, 1990.
2. T. Katsuyama, K. Hiruma, M. Shirai, K. Hosomi, M. Hatano, M. Yazawa, K. Ogawa, J. Shugeta, M. Matsui and T. Shimada, "Quantum function devices using polariton propagation," *14th Symp. Future Electron Devices*, **49**, 1995.
3. T. Katsuyama and K. Ogawa, "Excitonic polaritons in quantum-confined systems and applications to optoelectronic devices," *J. Appl. Phys.*, **75**, pp.7607-7625, 1994
4. T. Katsuyama, T. Sato, Y. Yamamoto and N. Sagawa, "Polariton propagation in coupled quantum wire waveguides," *Superlattices and Microstructure*, **20**, pp.59-63, 1996
5. E. I. Rashba and M. D. Sturge, in *Excitons*, Modern Problems in Condensed Matter Sciences, Vol. 2, edited by V. M. Agranovich and A. A. Maradum (North Holland, Amsterdam, 1982).
6. S. I. Pekar, *Zh. Eksp. Teor. Fiz.*, **6**, pp.1022-1036, 1958 [*Sov. Phys. JETP* **6**, pp.785-796, 1958]
7. J. J. Hopfield, *Phys. Rev.* **112**, 1555-1567, 1956
8. J. J. Hopfield and D.G. Thomas, *Phys. Rev.* **132**, pp.563, 1963
9. K. Hosomi, M. Shirai, J. Shigeta, T. Mishima and T. Katsuyama, "Light modulation by polariton directional-coupler-type devices" *IEICE Trans. Commun.*, **E82-B**, pp.1243-1247, 1999

10. J.E. Zucker and T.L. Hendrickson, "Electro-optic phase modulation in GaAs/AlGaAs quantum well waveguides," *Appl. Phys. Lett.* **52**, pp.945-947, 1988
11. F. Stern, *Solid State Physics*, Academic, New York, 1963

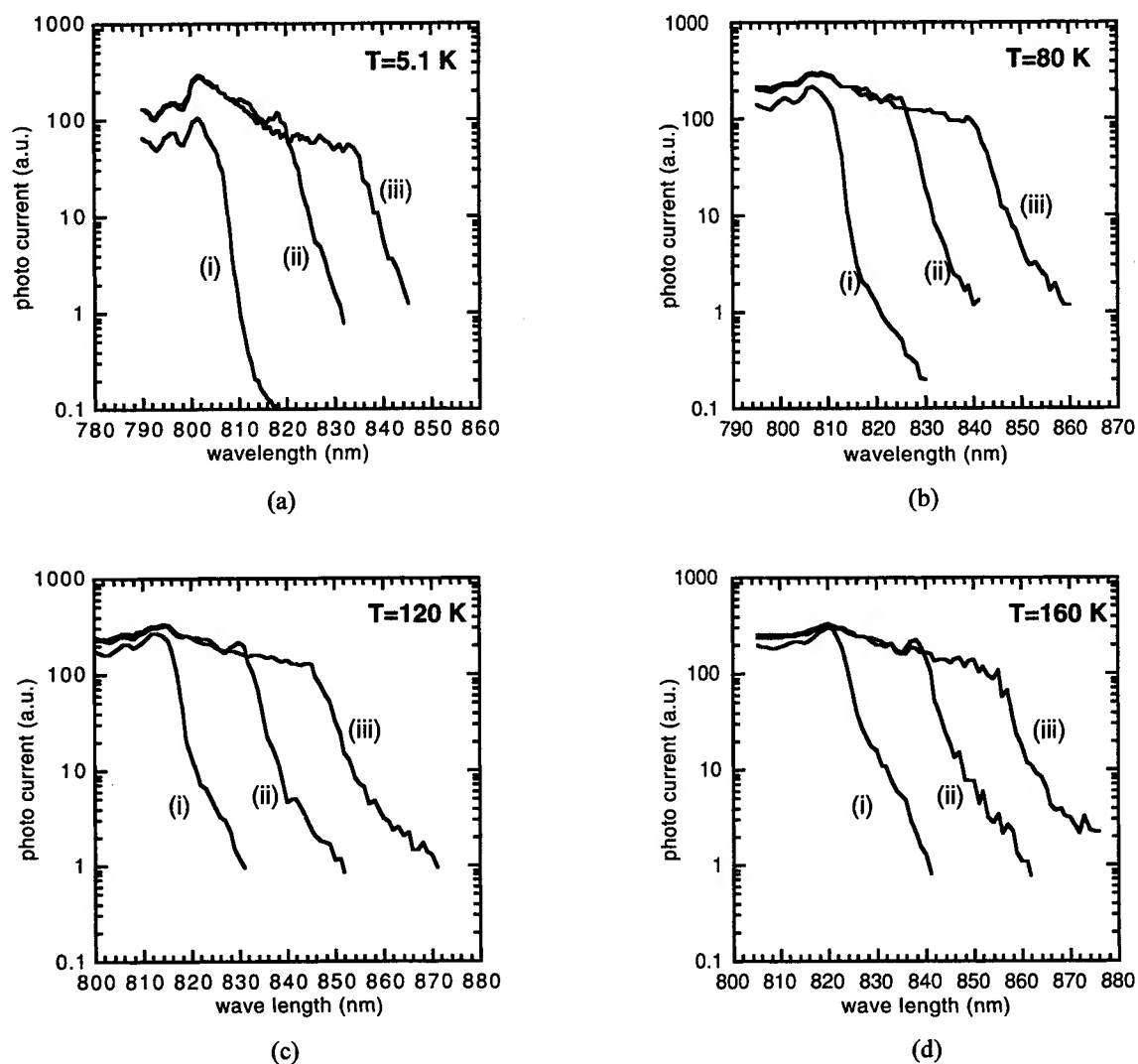


Fig. 11. Photo current spectrum of polariton waveguide under the electric field of (i) 0, (ii) 2.0×10^5 V/cm and (iii) 3.4×10^5 V/cm at various temperatures.

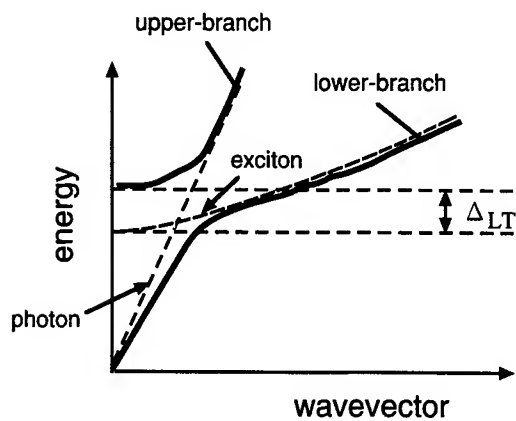


Fig. 1. Schematic dispersion relation (energy vs. wavevector) of an exciton polariton.

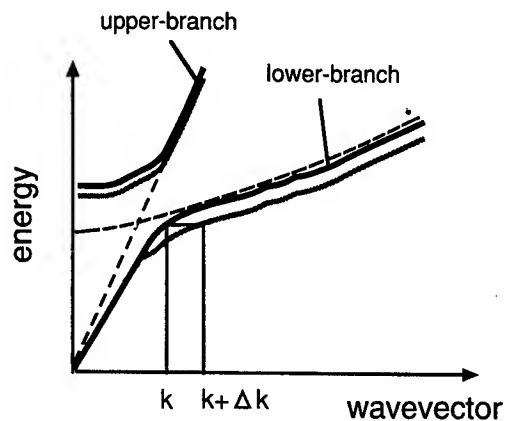


Fig. 2. Change in the dispersion curve caused by the shift of the resonant wavelength. The gray lines indicate the modified dispersion relation.

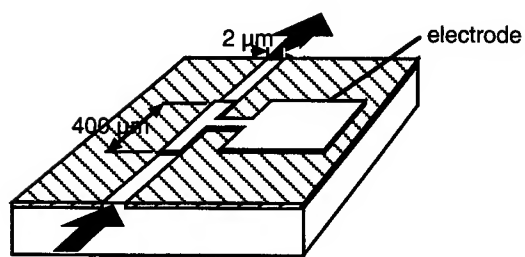


Fig. 3. Schematic illustration of the sample for interferometric measurement.

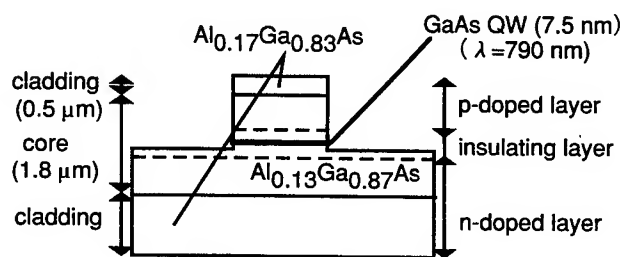


Fig. 4. Layer structure of the polariton waveguide.

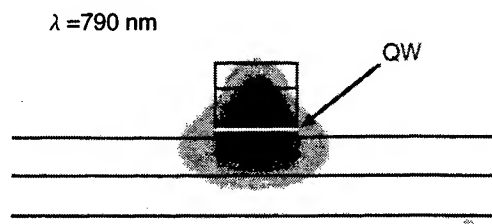


Fig. 5. The calculated field profile of the fundamental mode. The white line across the waveguide indicates the QW.

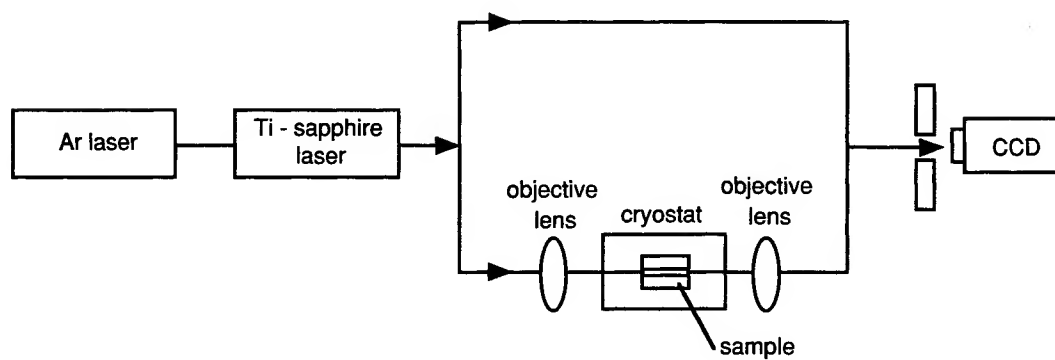


Fig. 6 Phase measurement system using a Mach-Zhender interferometer

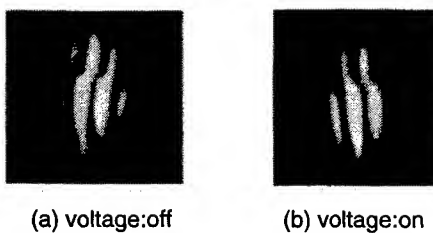


Fig. 7. The example of the interference pattern detected with a CCD camera.

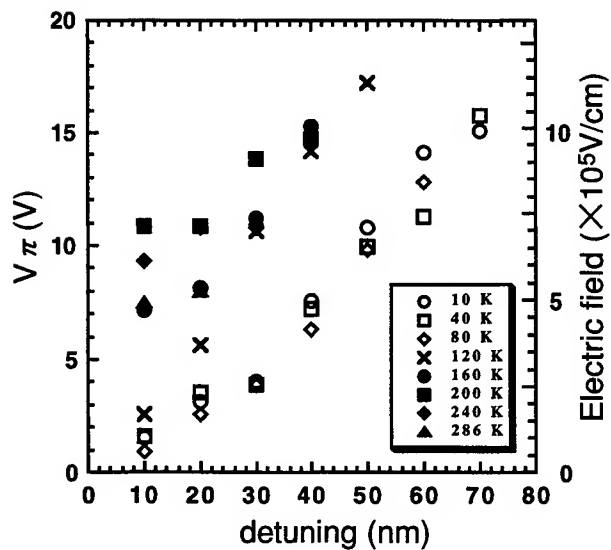


Fig. 8. The relation between $V\pi$ and detuning wavelength. Open and closed symbols correspond to low and high temperatures, respectively.

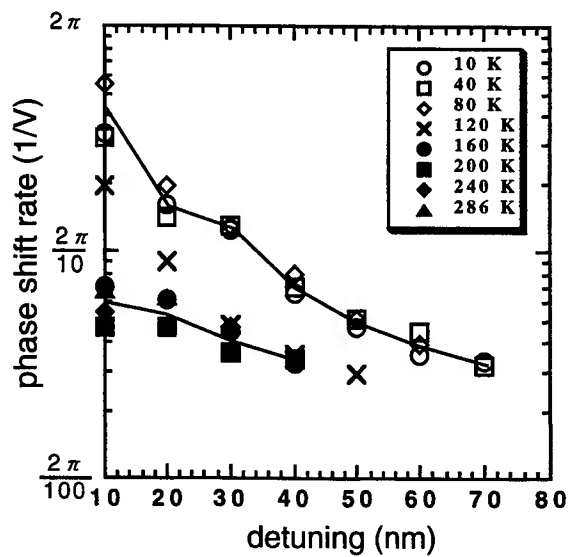


Fig. 9. Poraliton phase change per unit voltage under electric field.

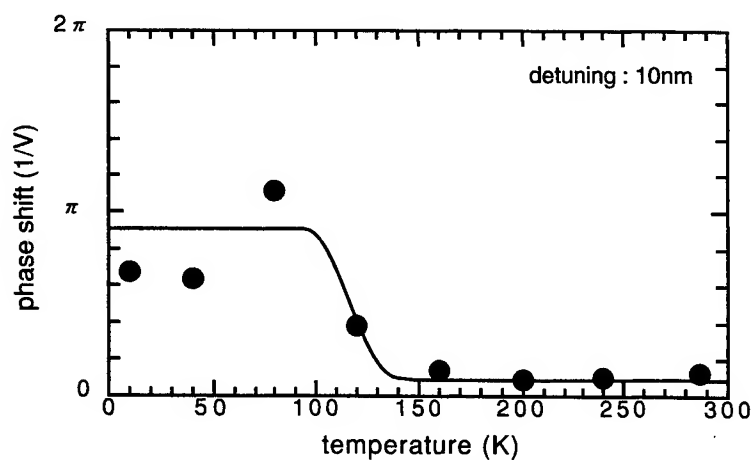


Fig. 10. Temperature dependence of the polariton phase change at a detuning of 10 nm. The solid line guides the eye.

InGaAlAs/InAlAs multiple quantum-well structures grown by molecular beam epitaxy for long wavelength infrared detection

D.H.Zhang^{*a}, W.M.Zhang^a, P.H.Zhang^a, T.Osotchan^a, S.F.Yoon^a, X.Shi^a, R. Liu^b and T.S. Wee^b

^aSchool of Electrical and Electronic Engineering, Nanyang Technological University, Singapore

^bDepartment of Physics, National University of Singapore, Lower Kent Ridge Road, Singapore 119260

ABSTRACT

We report the fabrication and characterization of the n-type *InGaAlAs/InAlAs* multiple quantum well structures, lattice-matched to *InP*, for the long wavelength infrared detection. It is found that strong absorption resulted from the intersubband transition in the quaternary material is observable and the wavelength of the absorption varies with the well width while the barrier width is kept unchanged. Our experimental results are in good agreement with the theoretical estimation based on simple finite barrier model and can be confirmed by the photoluminescence data.

Keywords: Intersubband absorption, Quantum well infrared photodetector (QWIP), quaternary semiconductor, Long wavelength infrared.

1. INTRODUCTION

An epitaxial growth of *InGaAlAs* quaternary compound at lattice match with *InP* allows an opportunity on bandgap engineering without suffering on the strain effect. The growth of *InGaAlAs* by molecular beam epitaxy (MBE) is relatively easier than that of *InGaAsP* quaternary compound since only one element in group V is involved and the three elements in group III have near unity sticking coefficients. The bandgap of the lattice matched *InGaAlAs* is varied from 0.74eV for *In_{0.53}Ga_{0.47}As* to 1.46eV for *In_{0.52}Al_{0.48}As*. The heterojunction between this quaternary compound exhibits the bandgap difference up to 0.72eV and conduction band discontinuity can be as high as 0.52eV¹. Moreover this quaternary alloy demonstrates superior electrical properties than that of *AlGaAs/GaAs* such as higher electron mobility, lower electron effective mass and higher electron saturation velocity.

Due to the high conduction-band discontinuity in *In_{0.53}Ga_{0.47}As/In_{0.52}Al_{0.48}As* lattice matched multiple quantum well (MQW), it allows a much shorter-wavelength operation than that in direct-gap of *GaAs/AlGaAs* quantum well infrared photodetector (QWIP). The first demonstration of intersubband absorption in the *In_{0.53}Ga_{0.47}As/In_{0.52}Al_{0.48}As* MQW with 50Å well width showed response wavelength peak at 4.4μm. Even shorter-wavelength absorption at 3.5μm was further developed by engineering the barrier to localize the electron wave function in the well layer at energies above the top of the barrier height².

However, an alternative long wavelength detector of the quaternary *InGaAlAs* compound has also a great interest due to the merit of material. The QWIP of lattice matched n-doped *InGaAlAs/InP* system was demonstrated with *AlAs* mole fraction of 0.0 to 0.15 and resulted in cutoff wavelengths of 8.5 to 19.4μm³. The typical sample of 0.10 *AlAs* mole fraction can achieve the detectivity of $3 \times 10^8 \text{ cmHz}^{1/2} \text{ W}^{-1}$ with cutoff wavelength of 13.3μm at 77K.

In this paper the n-type MQW structures of lattice matched *In_{0.53}Al_{0.17}Ga_{0.3}As/In_{0.52}Al_{0.48}As* were grown on *InP* by MBE with varied well widths. The intersubband absorption of the samples was measured on the mutipass waveguide. The quantum confined energy levels were verified by photoluminescence and theoretical calculation of finite barrier model.

* Correspondence: Email: edhzhang@ntu.edu.sg; Telephone: 65-7904841; Fax: 65-7920415

2. EXPERIMENTAL DETAILS

The $In_{0.53}Al_{0.17}Ga_{0.3}As/In_{0.52}Al_{0.48}As$ MQW structures were grown on semi-insulating (100) InP substrates in a solid source Riber MBE32 system. The InP substrates were degassed at 200°C for 30mins before transfer into the growth chamber. The process of native oxide desorption under arsenic overpressure was monitored by reflection high energy electron diffraction (RHEED). The transition from two-fold to four-fold pattern was observed at 510°C. The crystalline quality effects of the substrate temperature on the growth of this quaternary compound was reported in Ref. 4 and found that the optimum substrate temperature range is from 510 to 530°C. In this MQW growth the substrate temperature was maintained at 510°C. In order to grow this lattice matched quaternary epitaxy it found that the lattice match composition was relative insensitive to V/III flux ratio, however, the optimum flux ratio for a good crystal can be obtained in the range of 21-50 [2]. The group III flux was chosen by considering the lattice matched quaternary $InGaAlAs$ as a superimposition of two lattice matched ternary compounds $In_{0.53}Ga_{0.47}As$ and $In_{0.52}Al_{0.48}As$. Since the variation of aluminum content in the barrier and well is relatively large while the gallium source can be close and open for the barrier and well layers, the aluminum cell temperature was required to modify during the MQW growth. Therefore the short interrupt time of 70 seconds was adopted between the growth of well and barrier layers to accommodate the temperature difference of aluminum cell.

3000 Å $In_{0.53}Ga_{0.47}As$ doped cap-layer
4000 Å $In_{0.52}Al_{0.48}As$ undoped barrier
$In_{0.53}Al_{0.17}Ga_{0.3}As$ doped well
·
·
x30 MQWs
·
·
$In_{0.53}Al_{0.17}Ga_{0.3}As$ doped well
400 Å $In_{0.52}Al_{0.48}As$ undoped barrier
5000 Å $In_{0.52}Al_{0.48}As$ doped buffer
Semi-insulating InP Substrate

Fig. 1 Detail structure of lattice matched $In_{0.53}Al_{0.17}Ga_{0.3}As/In_{0.52}Al_{0.48}As$ MQW grown on InP substrate. Three different well width of 86, 120 and 150Å were grown on three samples with the same barrier thickness of 400Å. All doped layers are doped by silicon at $5 \times 10^{17} \text{cm}^{-3}$.

The grown MQW structures shown in Fig. 1 consist of 30 periods of $In_{0.53}Al_{0.17}Ga_{0.3}As/In_{0.52}Al_{0.48}As$ MQW on top of a 5000Å thick buffer layer of Si-doped $In_{0.52}Al_{0.48}As$. The thickness of undoped $In_{0.52}Al_{0.48}As$ barrier layer is maintained to be 400Å for all three MQW structures while the thickness of Si-doped $In_{0.53}Al_{0.17}Ga_{0.3}As$ well layer is varied in three samples which are 86, 110 and 120Å. The 3000Å thick cap-layer of Si-doped $In_{0.53}Ga_{0.47}As$ was also grown on top the MQW structures for further electrical contact. All Si-doped layers are doped with the doping concentration of $5 \times 10^{17} \text{cm}^{-3}$.

Table I. The response peak wavelength and spectrum line-width over the peak wavelength of the three MBE grown lattice matched $In_{0.53}Al_{0.17}Ga_{0.3}As/In_{0.52}Al_{0.48}As$ MQW structures with the varied the well width

Sample Number	Well Width (Å)	Peak Wavelength (μm)	$\Delta\lambda/\lambda_p$ (%)
M662	86	9.7	9.4
M676	120	14.5	12
M677	150	17.4	8

Since the intersubband absorption is relatively weak and for n-doped MQW it occurs only for some component of light incident parallel to the interface, the multipass waveguide with 45 degree fine polished is required to enhance the measurement. In order to shape multipass waveguide firstly the samples were cut into $12 \times 9 \text{ mm}^2$ and polish 45 degree at two opposite edges. Due to the internal multiple reflection this configuration allows multiple absorption of the MQW layer for about 31 times at the incidence angle of 45 degree. The infrared absorption was measured by Perkin Elmer Fourier transform infrared spectrometer model 2000 which has the wide spectrum range of 1.28 to $27 \mu m$. The four-beam condenser was utilized to focus the beam to the 45 degree polished edge at the right angle to the surface. The transmission was measured carefully and make sure that there is no other part of the light pass through. The transmission was normalized with the background transmission of pure nitrogen atmosphere and the absorption component originating from MQW was extracted by normalizing with the absorption of the bare InP substrate.

In order to investigate the energy levels in the MQW structures, the photoluminescence of the structures was examined at low temperature. The sample was placed in vacuum chamber in the closed cycle cryostat to enhance the radiative recombination process. The samples were excited by 514nm argon laser beam and the luminescence light was diffracted by 0.75 meter monochromator and detected by liquid nitrogen cooled germanium detector. In order to increase the signal to noise ratio the excited light was chopped and the photoluminescence signal was amplified by the lock-in amplifier system. At 4K the photoluminescence spectrum of the MQW structure with the doped cap-layer exhibits only the luminescence peak at low energy (lower than the band gap) from the doped layer. This is due to the cap-layer is thick and heavy doped. Therefore before the photoluminescence investigation of the MQW structures the cap-layer was removed by wet etching by mixture of 4 H_2SO_4 : 1 H_2O_2 : 35 H_2O which for our material system provides an isotropic etching rate of about 35 Å/sec .

The atomic concentrations in the well and barrier layers of the MQW structures were also determined by CAMECA Secondary Ion Mass Spectrometer (SIMS), model IMS-6f. The atomic concentrations of all three cation species can be derived from the number of ion at certain specific ion masses. In order to evaluate the variation of material composition within multilayers the cap-layer were partially removed by wet etching and atomic concentrations of all three cation species as a function of layer thickness were examined by sputtering through the MQW samples.

3. RESULTS AND DISCUSSION

In order to verify the variation of the structure compositions, the material composition depth profile measured by SIMS is illustrated for typical samples M676 in Fig. 2. The depth-profiles of three cation species including the peaks of ^{27}Al , ^{69}Ga and ^{115}In are displayed only in a part of MQW region with setting relative zero sputtering time. Since the indium content in both well and barrier layer material are almost the same i.e. mole fraction of 0.53 and 0.52, respectively, the ^{115}In profile shows slight variation with slight higher count rate in the well region. While aluminum mole fraction in the well and barrier are 0.17 and 0.48 respectively therefore the ^{27}Al profile is low in the well region and high in the barrier region. The profile of the ^{69}Ga has relatively large variation over the MQW region since there is no intended gallium in the barrier layer while the gallium content

in the well is 30 percent of the cation. Even the mole fraction difference of aluminum and gallium in the well and barrier regions is approximately equal, the variation of the profile in the logarithmic scale of the gallium looks more significant than that of the aluminum since the base gallium content in the barrier is zero. It can be noticed that the ^{69}Ga depth-profile has an opposite phase to the ^{27}Al profile. Although the well and barrier were intentionally grown with the abrupt interface, the depth profile display the smooth change due to the surface modification by sputtering and the resolution of the SIMS. From the period of the ^{69}Ga -peak profile and the intentional period value of the MQW the sputtering rate can be derived approximate $1.7\text{\AA}/\text{sec}$. The uniformity of the profile period can show the equal period of the grown MQW structure.

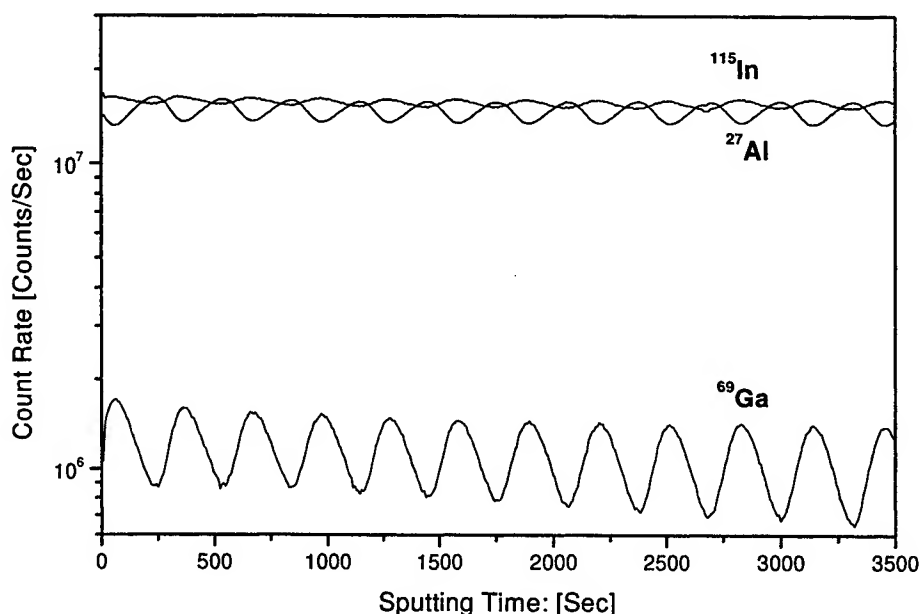


Fig. 2 Atomic concentration of three cations (^{115}In , ^{27}Al and ^{69}Ga) as a function of the sputtering time for the typical $\text{In}_{0.53}\text{Al}_{0.17}\text{Ga}_{0.3}\text{As}/\text{In}_{0.52}\text{Al}_{0.48}\text{As}$ MQW with the well width of 120\AA . The depth-profile displays only a part of the MQW region.

The infrared absorption of three MQW structures with the multipass waveguide at room temperature is shown in the Fig. 3a. Only the absorption peaks related to transition from the MQW are illustrated where the background peak was removed by comparing to the only substrate absorption with the same multipass configuration. The absorption peak wavelength and the peak width are also given in the Table I for three MQW structures. Since the well is n-doped by silicon with the doping concentration of $5 \times 10^{17} \text{cm}^{-3}$ and estimated Fermi energy level lies between the ground and first excited states, the absorption showed in Fig. 3a. probably originates from the intersubband absorption between the ground and first excited states in MQW of the conduction band. The peak wavelength corresponds to the energy difference between the ground and first excited states and from the measurement it increases as the well width increases because the energy difference is smaller when the well is wider. Since the spectrum line-width over the peak wavelength displayed in Table I for all three MQW structures has a value around 10 percent, this indicates that all the absorption peak possibly comes from the bound-to-bound transition.

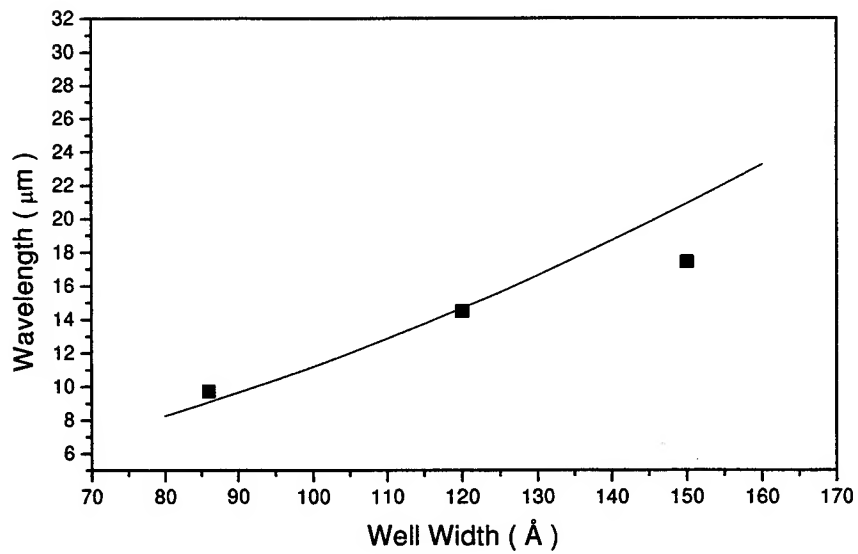
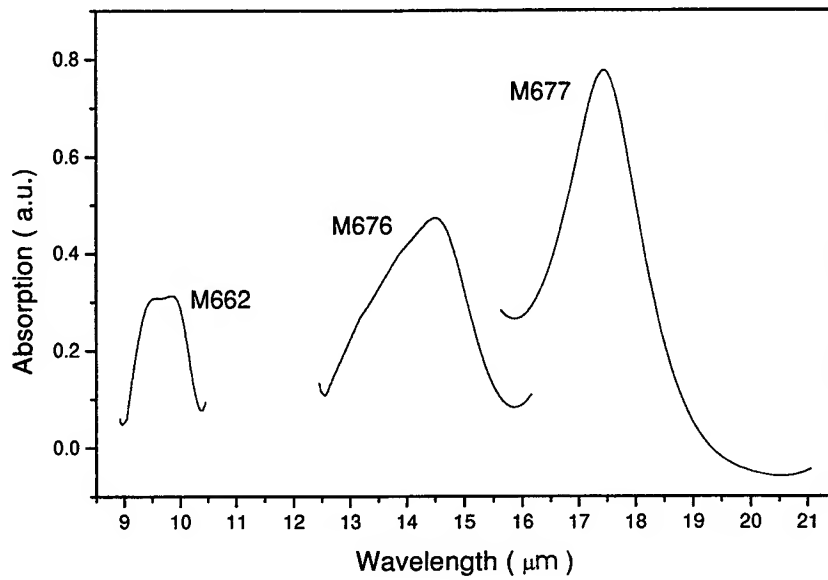


Fig. 3 a.) Measured intersubband absorption as a function of the wavelength of three $In_{0.53}Al_{0.17}Ga_{0.3}As/In_{0.52}Al_{0.48}As$ MQW structures with the well width of 86, 120 and 150 Å. b.) Intersubband transition wavelength from theoretical calculation as a function of the well width represented by solid line and the measured absorption peak wavelength represented by rectangular symbol.

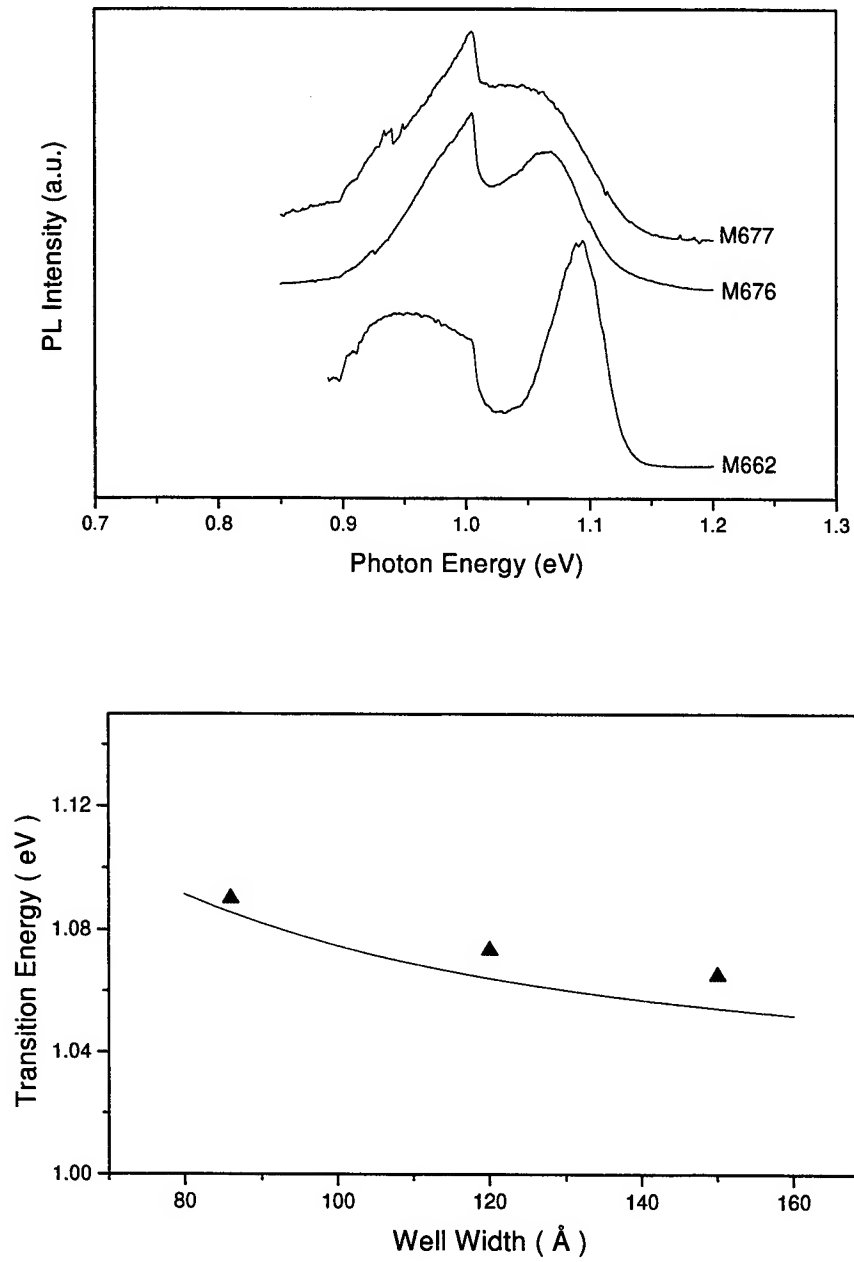


Fig. 4 a.) Photoluminescence intensity as a function of photon energy at 4K for three $In_{0.53}Al_{0.17}Ga_{0.3}As/In_{0.52}Al_{0.48}As$ MQW structures with the well width of 86, 120 and 150Å. b.) Interband transition energy from theoretical calculated as a function of the well width represented by solid line and the measured dominated photoluminescence energy peak represented by the rectangular symbol.

The origin of the absorption peak was also verified by theoretical calculation based on simple finite barrier model. For the MQW wavefunction calculation the mass difference in well and barrier layer was taken into account then the continuity of the probability current with different masses on each side of the interface was employed for the boundary condition. The electron effective mass of $In_{0.53}Al_{0.17}Ga_{0.3}As$ was used the linear interpolation between the known value of the lattice matched ternary compounds of $In_{0.52}Al_{0.48}As$ and $In_{0.53}Ga_{0.47}As$. The conduction band offset was derived from the 65 percent of the energy gap difference. The calculation showed that there are at least two bound states in the well when the well width is greater than 80Å. The response wavelength is evaluated from the energy difference between the ground and first excited states and the calculated result is plotted as a function of the well width and represented by the solid line in Fig. 3b. The measured values also shown in Fig. 3b by the rectangular symbol and demonstrates a good agreement with the calculated values.

In order to further investigate the energy levels in the MQW structures the samples were removed the cap-layer and measured the photoluminescence. The photoluminescence spectra for three MQW structures at temperature of 4K are shown in Fig. 4a. The spectra exhibit the dominated peak at 1.09, 1.07, and 1.06eV for the MQW with well width of 86, 120 and 150Å, respectively. The dominated peak decreases as the well width increases and possibly originates from the interband transition between the ground state of heavy-hole band to ground state of the conduction band. This is also confirmed by the MQW calculation of both valence and conduction bands. The ground bound state of heavy hole was estimated by the similar calculation of the single electron band with replacing electron effective mass and conduction band offset by the heavy hole effective mass and valence band offset. The transition energy was determined by the summation of the ground state energy of electron, ground state energy of heavy hole and energy band gap of the well material. The solid line in Fig. 4b shows the transition energy as a function of the well width and the rectangular symbol refers to the measured photoluminescence dominated peak energy. From the figure it shows that the measured points lie slightly above the calculated lines. This may be due to the parameter values used in the theoretical calculation is slightly shift from the real values in the grown MQW structures.

In addition to the photoluminescence dominated peak exhibiting at a high energy, the broad peak also appears at low energy for the narrow MQW structure. The peak energy at approximately 0.95eV is slightly lower than the energy band gap of the $In_{0.53}Al_{0.17}Ga_{0.3}As$ well layer therefore the low energy broaden peak most likely originates from the doping level in the well layer.

4. SUMMARY

The n-type MQW structures of lattice matched $In_{0.53}Al_{0.17}Ga_{0.3}As/In_{0.52}Al_{0.48}As$ were grown on InP by MBE with well width of 86, 120 and 150Å. The intersubband absorption of the samples exhibits the peak wavelength at 9.7, 14.5 and 17.4µm with the spectrum line-width over the peak wavelength of about 10 percent. The peak wavelengths are in good agreement with the theoretical calculation of intersubband transition between the ground and first excited states. The calculated energy levels were also verified by photoluminescence peak. The significant intersubband absorption peaks illustrated that these MQW structures are of great potential for long wavelength detector application.

ACKNOWLEDGEMENT

The authors would like to thank A/Prof. W.G. Zhu and Ms. M.M. Liu for their support in the absorption measurements.

REFERENCES

1. M.Levinshtein, S.Rumyantsev, M.Shur, *Handbook series on semiconductor parameters: volume 2 ternary and quaternary III-V Compounds*, World Scientific, Singapore, 1999.
2. B.F.Levin, "Quantum-well infrared photodetectors," *J. Appl.Phys.* **74**, pp. R1-R81, 1993.
3. C.Jelen, S.Slivken, V.Guzman, M.Razeghi, and G.J.Brown, "*InGaAlAs-InP* quantum well infrared photodetectors for 8-20 μ m wavelengths," *IEEE J. Quantum Electron.* **34**, pp. 1873-1876, 1998.
4. S.F.Yoon, P.H.Zhang, H.Q.Zheng, K.Radhakrishnan and S.Swaminathan, "Substrate temperature effects on the growth of *In*_{1-x}*y*Ga_xAl_yAs on *InP* substrates by molecular beam epitaxy," *J. Crystal Growth* **186**, pp. 315-321, 1998.
5. S.F.Yoon, P.H.Zhang, H.Q.Zheng, and K.Radhakrishnan, "The effects of arsenic pressure on the properties of *In*_{1-x}*y*Ga_xAl_yAs layers grown by molecular beam epitaxy," *J. Crystal Growth* **191**, pp. 24-30, 1998.

Influence of (001) vicinal GaAs substrates on the optical properties of defects in low-temperature grown GaAs/AlGaAs multiple quantum wells

M. H. Zhang*, Y. F. Zhang, J. M. Sun, Q. Huang, C. L. Bao, J. M. Zhou
*Institute of Physics, Center for condensed matter, Chinese Academy of Sciences, Beijing 100080,
People's Republic of China*

ABSTRACT

Photoluminescence (PL) spectroscopy and carrier lifetime measurement has been used to characterize optical properties of defects in the low-temperature (LT) grown GaAs/AlGaAs multiple quantum well structures. Two sets of samples were grown at 400 °C by molecular beam epitaxy on nominal (001) and miscut (4° off (001) towards (111) A) GaAs substrates, respectively. After growth, samples were subjected to 30 s rapid thermal annealing at 600-800 °C. It is found that after annealing, two defect-related PL features appear in the samples grown on miscut (001) GaAs substrates, but not in those grown on nominal (001) GaAs substrates. The carrier lifetimes are about 31 and 5 ps in as-grown samples grown on nominal and miscut (001) GaAs substrates, respectively. Optical transient current spectroscopy show different types of deep levels and their dependence on the annealing temperature. We found larger excitonic electroabsorption and stronger photorefractive effect in samples grown on miscut substrates.

Keywords: Low-temperature grown GaAs, deep-levels, photorefractive effect

1. INTRODUCTION

Recently, the low-temperature (LT) growth of photorefractive GaAs/AlGaAs multiple quantum well (MQW) structures has been demonstrated.¹⁻³ The photorefractive devices fabricated by these MQW structures combine the advantages of large excitonic electroabsorption with ultrafast lifetimes. LT growth can incorporate a great number of defects (due to excess As) into materials, leading to very short carrier lifetimes.^{4,5} Thus, the control of concentrations and types of defects in LT grown materials is very important to the performance of photorefractive MQW devices.

The properties of defects in LT-GaAs grown at 200-400 °C have been studied extensively. The dominant defects are As antisites (As_{Ga}), as has been verified by deep-level transient spectroscopy and other measurements.⁶ After annealing, excess As atoms group together to form As clusters. A great number of As antisites or clusters can change electrical and optical properties of GaAs strongly, for example, high resistivity and ultrafast carrier lifetimes in LT-GaAs.⁷ There are several factors to influence the properties of defects in LT grown GaAs. Among them, the substrate temperature,⁸ the As_4/Ga beam equivalent pressure (BEP) ratio,⁹ and the doping-level¹⁰ have been explored. However, to our knowledge, the effect of the miscuts of (001) GaAs substrates has not been investigated yet. At normal temperatures, the miscut (001) GaAs substrates give a step-flow growth mode, which is different from the nucleation growth mode on nominal (001) substrates. It is well known that the growth of InAs quantum dots on two kinds of GaAs substrates is very different.¹¹ We speculate that at low growth temperatures, the structures of defects incorporated into materials on two kinds of substrates may be different, too. This consideration leads us to study the LT growth of photorefractive GaAs/AlGaAs MQW structures on vicinal substrates.

Because the properties of the samples among the same set are similar, here we only give the results of two samples. Sample A and B with the same structure were grown at 400 °C on the nominal and miscut (4° off (001) towards (111) A) (001) GaAs substrates, respectively. During LT growth, an As_4/Ga BEP ratio of about 10 was used. The growth sequence consisted of 1 μm GaAs buffer layer, 50 nm AlAs layer, 150 nm $Al_{0.3}Ga_{0.7}As$ layer, and a 100-period GaAs/ $Al_{0.3}Ga_{0.7}As$ MQW structure. The AlGaAs barrier layer in the MQW structure was 4 nm in thickness, and the GaAs well layer was 7.5 nm. The two cladding AlGaAs layers and the MQW s were grown at 400 °C, while other layers grown at normal temperatures. After epitaxial growth, the wafers were cleaved into small pieces, and each piece was subjected to 30 s rapid thermal annealing (RTA) at 600-800 °C. To prevent As loss from the surface, each piece of sample was capped by a piece of GaAs substrate. Some annealed samples were cleaved further into 0.5 cm \times 0.5 cm pieces to measure photoluminescence (PL) spectra and

* Correspondence: Email: mhzhang@aphy.iphy.ac.cn; Fax: 86-10-62562605

carrier lifetimes. The epi-layers in other annealed samples were first removed from GaAs substrates by the lift-off in a dilute hydrofluoric acid, and then Van der Waals bonded to a glass slide. Finally two gold contacts with a spacing of 1 mm were deposited on the surfaces of the epi-layers by evaporation. Such fabricated samples were used to measure resistivity, transmission spectra and photorefractive properties under Frantz-Keldysh geometry.¹²

2. EXPERIMENTAL RESULTS AND DISCUSSIONS

Fig.1 (a) and (b) show PL spectra of sample A and B, respectively. All measurements were carried out at 77 K. It can be seen that the intensities of the band-edge PL for both of samples increase with annealing temperature. For sample A, two additional PL features appear at the lower energy side of the peak of the band-edge PL peak in the 600 and 700 °C-annealed pieces and disappear in the 800 °C-annealed piece. For sample B, these additional PL features can not be observed in all annealed pieces. It is a common phenomenon, which we also have observed in other samples. Therefore the difference of PL spectra is caused only by the different miscuts of (001) GaAs substrates. In the 600 °C-annealed piece of sample A, the band-edge PL peak, corresponding to the heavy-hole excitonic transition, is at 790 nm and the peaks of two additional PL features are at 794 and 797 nm, respectively. The energy differences between the excitonic PL peak and these two additional PL peaks are 8 and 14 meV, respectively. An effective mass calculation shows that in a 7.5 nm GaAs quantum well with $\text{Al}_{0.3}\text{Ga}_{0.7}\text{As}$ barrier at the same temperature, one-monolayer fluctuation in the well width only causes a 3 meV shift of the PL peak of the heavy-hole excitonic transition. Therefore the present observed additional PL features in sample A only could be ascribed to annealing-generated shallow defects. We will refer to these PL features as the defect-related PL features in the following.

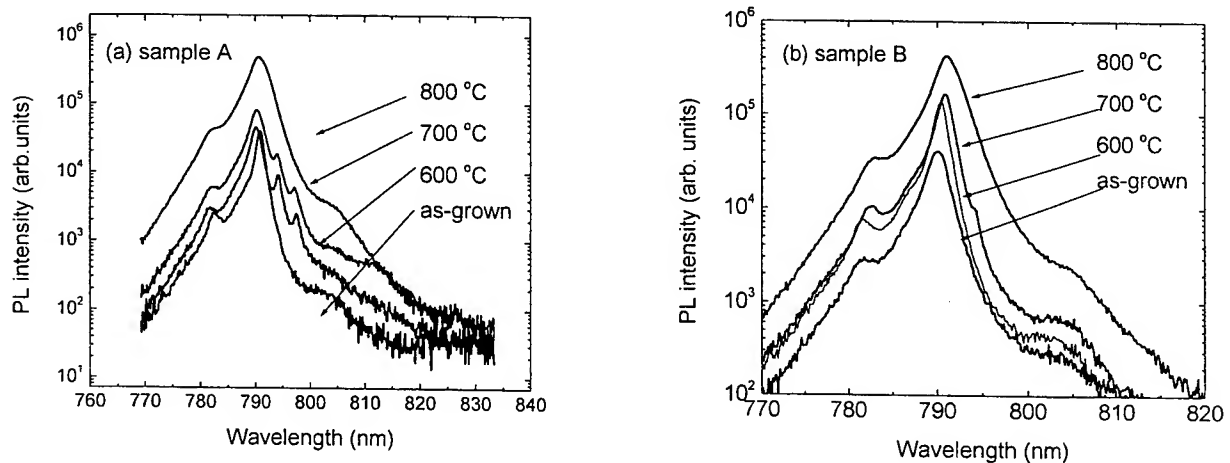


Fig.1 Photoluminescence spectra measured at 77 K: (a) sample A, (b) sample B. The samples were subjected to rapid thermal annealing at 600-800 °C for 30 s.

Fig 2 reports the resistivity dependence on annealing temperature for both sample A and B. For sample A, the resistivity of the as-grown sample is $2.0 \times 10^8 \Omega \cdot \text{cm}$. After annealing, it drops quickly to a very small value. The resistivity of the 800 °C-annealed piece is only $14 \Omega \cdot \text{cm}$. While for sample B, the resistivity of the as-grown piece is $6.3 \times 10^8 \Omega \cdot \text{cm}$. It drops slowly with the annealing temperature. The resistivity of the 800 °C-annealed piece is still $5 \times 10^5 \Omega \cdot \text{cm}$. The high resistivities of sample A and B before annealing are caused by As_{Ga} -like defects, which were incorporated into epitaxial layers during LT growth. After annealing, the atoms of excess As group together to form As clusters. Here we observed also another transformation channel of As_{Ga} -like defects in Fig.1 (a), which shows that two shallow defects are generated in annealed sample A. Hall measurement shows that its 800 °C-annealed piece is *n*-type, indicating that the shallow defects are donors. We propose that the structures of the As_{Ga} -like defects in two samples be different, which may be the reason of different annealing temperature dependence of PL spectra.

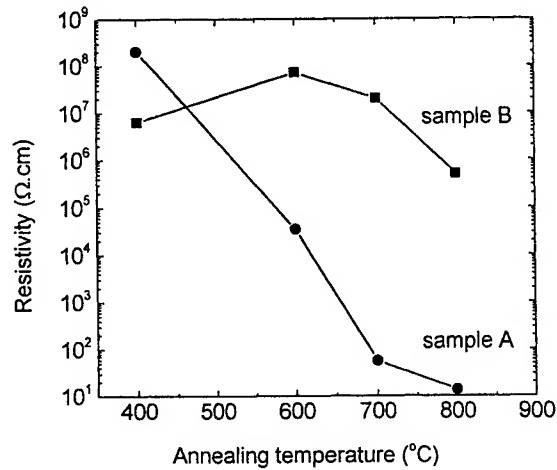


Fig.2 The resistivities of sample A and B versus the annealing temperature.

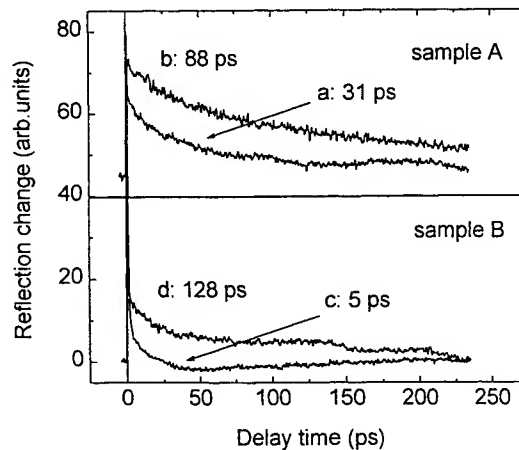


Fig.3 Carrier lifetimes measured by a pump-probe technique at room temperature and under the reflection geometry. Curve (a) and (b) are for as-grown and 700 °C-annealed sample A, respectively; curve (c) and (d) are for as-grown and 700 °C-annealed sample B, respectively.

The carrier lifetimes of two samples, shown in Fig. 3, were measured at room temperature and under the reflection geometry by a pump-probe technique. A 100fs Ti: sapphire laser chopped at a rate of 3.8 kHz was used and tuned at 820 nm, which is slightly above heavy-hole exciton energies of sample A at 834 nm and sample B at 836 nm, respectively. From Fig.2, it can be deduced that the concentration of defects in sample A should be larger than that in sample B before annealing. If the structures of As_{Ga} -like defects in two samples are the same, the carrier lifetime in sample A must be shorter than that in sample B before annealing. However, Fig.3 shows it is not the case. The carrier lifetimes in as-grown sample A and B are 31 and 5 ps, respectively. In addition, the pump-probe signal in sample A persists even at long delay time. Therefore we have the conclusion that the structures of As_{Ga} -like defects in two samples are indeed different. Fig.3 also shows that after

annealing at 700 °C, the carrier lifetimes in both of samples become longer, which are 88 ps in sample A and 128 ps in sample B, respectively.

In order to identify deep levels in sample A and B, we have performed the measurement of optical transient current spectroscopy (OTCS). In order to make electrodes contact the quantum well region easily, the upper AlGaAs cladding layers were etched. It was found that before etching, the OTCS signals from deep levels in quantum well region were very weak, but the deep level (the activation energy is 1.0eV) from the AlGaAs cladding layer can be measured easily. Because deep levels in AlGaAs layer have little influence on the photorefractive effect under Frantz-Keldysh geometry, so we focus our attention on deep levels from the quantum well region. Fig.4 (a) and (b) show deep levels in etched sample A and B after annealing at different temperatures. In the as-grown sample A, there is only deep level with the activation energy of 0.66eV. After annealing, this deep level disappears. In the 600°C- and 650°C-annealed sample A, the deep levels have the activation energies of 0.15 and 0.1 eV, respectively. For samples annealed at higher temperatures, we have not performed the measurement due to low resistivity. In the as-grown sample B, there are three deep levels with the activation energies at 0.68, 0.25, and 0.22eV, respectively. Up to the annealing temperature of 650°C, these three deep levels are stable. At the annealing temperature of 700°C, a new deep level with the activation energy of 0.19 eV appears. It means that deep levels in sample B are more stable than those in sample A against annealing. Before annealing, both the deep level at 0.66eV in sample A and that at 0.68 eV in sample B have the activation energy comparable to the reported value of As_{Ga} defect.⁹ On the other hand, the peak-temperatures of OTCS signals are different at the same rate window. According to the theory of deep levels, these two deep levels have different capture cross-sections. We also have observed stronger electroabsorption and photorefractive effect in as-grown sample B. Detail results will be reported elsewhere.¹³

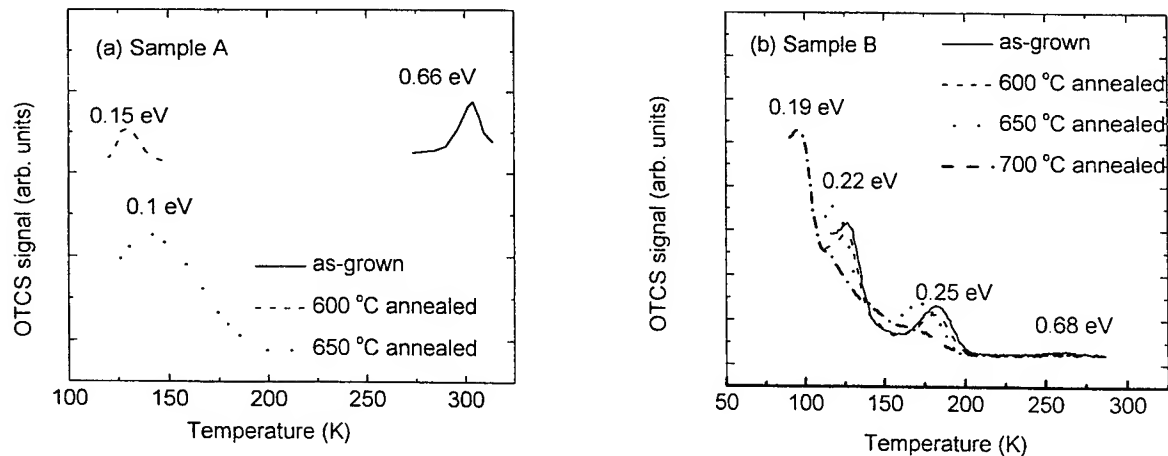


Fig.4 Deep levels in sample A and B versus annealing temperature.

3. CONCLUSIONS

In summary, PL spectroscopy and carrier lifetime measurement has been used to characterize optical properties of defects in LT grown GaAs/AlGaAs MQW structures. It is found that the structures of As_{Ga} -like defects in samples grown on nominal and miscut (001) GaAs substrates are different. After weak annealing, two defect-related PL features appear in samples grown on nominal (001) substrates, but not in those grown on miscut (001) substrates. We also find different carrier lifetimes and deep levels in two samples. Our measurement shows that in comparison with samples grown nominal (001) GaAs substrates, the as-grown samples grown on miscut (001) GaAs substrates have shorter carrier lifetime and stronger photorefractive effect.

ACKNOWLEDGMENTS

This work is supported by Chinese National Foundation of Natural Sciences under contract No. 69896260.

REFERENCES

1. I. Lahiri, K. M. Kwolek, D. D. Nolte, and M. R. Melloch, Appl. Phys. Lett. **67**, 1408 (1995).
2. W. Feng, Z. G. Zhang, Y. Yu, Q. Huang, P. M. Fu, and J. M. Zhou, J. Appl. Phys. **79**, 7404 (1996).
3. W. S. Rabinovich, S. R. Bowman, D. K. Katzer, and C. S. Kyono, Appl. Phys. Lett. **66**, 1044 (1995).
4. T. S. Sosnowski, T. B. Norris, H. H. Wang, P. Grenier, J. F. Whitaker, and C. Y. Sung, Appl. Phys. Lett. **70**, 3245 (1997).
5. G. Segsneider, T. Dekorsy, H. Kurz, R. Hey, and K. Ploog, Appl. Phys. Lett. **71**, 2779 (1997).
6. D. C. Look, Z.-Q. Fang, J. R. Sizelove, and C. E. Stutz, Phys. Rev. Lett. **70**, 465 (1993).
7. H. S. Loka, S. D. Benjamin, and P. W. E. Smith, IEEE J. Quantum Electron., **34**, 1426 (1998).
8. K. Mahalingam, N. Otsuka, M. R. Melloch, J. M. Woodall and A. C. Warren, J. Vac. Sci. Technol. B **9**, 2326 (1991).
9. A. Suda and N. Otsuka, Appl. Phys. Lett. **73**, 1529 (1998).
10. M. N. Chang, J.-W. Pan, J.-I. Chyi, K. C. Hsieh, and T.-E. Nee, App. Phys. Lett. **72**, 587 (1998).
11. R. Leon, C. Lobo, A. Clark, R. Bozek, A. Wyszomolek, A. Kurpiewski, and M. Kaminska, App. Phys. Lett. **84**, 248 (1998).
12. Q. Wang, R. M. Brubaker, D. D. Nolte, and M. R. Melloch, J. Opt. Soc. Am B **9**, 1626 (1992).
13. M. H. Zhang, Q. Huang, Y. F. Zhang, J. M. Zhou, Q. Li and Z. Y. Xu, Appl. Phys. Lett. **75**, 1366 (1999).

The optical Gunn effect in n-doped GaAs at mid and far IR-wavelengths

J. Stiens^{a*}, G. Shkerdin^b, F. Marest^a, R. Vounckx^a

^aVrije Universiteit Brussel, Lab for Micro and Optoelectronics, Electronics Department, Pleinlaan 2, B-1050 Brussels, Belgium.

^bInstitute of Radio Engineering and Electronics of RAS, Vvedensky Square 1, R-141120 Fryazino (Moscow Region), Russia

ABSTRACT

In this paper a rigorous quantum mechanical multi-valley model is developed to assess the optical equivalent of the electrical Gunn effect: a laser beam pumps free electrons from the central conduction band valley of n-doped bulk GaAs towards its satellite valleys. The computational complexities involve a central fully nonparabolic degenerated Γ -valley, an anisotropic L-valley of arbitrary degeneracy, impurity assisted, thermal and hot polar optical phonon assisted intravalley absorption mechanisms, and intervalley phonon assisted equivalent and nonequivalent intervalley absorption mechanisms. The influences of the doping concentration, electron temperature, optical power density and the equivalent LL-intervalley deformation potential (IDP) on the magnitude and relaxation time of the optical Gunn effect are discussed and compared with experimental results. We found that the optically induced nonlinear absorption and intervalley transfer strongly depend on the equivalent LL-IDP. The large scattering on the available data for LL-IDP (0.12 upto $1.0 \times 10^9 \text{ eVcm}^{-1}$) leads to large variations in the theoretical estimations. Under optimal plasma resonance conditions ($\lambda=10.6\mu\text{m}$, $N=7 \times 10^{18} \text{ cm}^{-3}$) we find an energy relaxation time in the L-valley of about 0.3 to 2.2 ps, a nonlinear refractive index n_2 of about 2.7 to $3.75 \times 10^{-8} \text{ cm}^2/\text{W}$ and e.g. a 10% electron transfer of about 1.8 to 3.2 MWcm^{-2} .

Keywords: Gunn effect, GaAs, intervalley, nonparabolicity, optical nonlinearity, free electron, L-valley

1. INTRODUCTION

In a semiconductor such as n-GaAs, the separation between the central Γ -valley and the satellite L-valley of the conduction band is appropriate to repopulate the valleys by optically heating the free carriers with a short and powerful mid- or far infrared light pulse^{1,2,3}. Because the conduction band shapes, the optical effective masses and the scattering probabilities of the free electrons in the two valleys are quite different, the population modulation induces changes in the dielectric function, expressed by the Drude relation, and hence an optical nonlinearity. This can be considered as the optical equivalent of the Gunn effect⁴. One fundamental difference is that the electrical Gunn effect is practical only possible in lightly doped semiconductors, whereas the optical equivalent is mostly pronounced for highly doped samples. The optical heating promotes carriers to higher states of the central valley (= intravalley transitions) and induces transitions to the satellite valleys (= nonequivalent intervalley transitions). The L-valley, consisting of four subvalleys also allows carrier jumps from one to another valley (=equivalent intervalley transitions). The heating of the carriers is most effective when light absorption is substantial. This can be effectuated by matching the frequency of the incident light with the plasma frequency of the multi-valley semiconductor. Such resonance condition can be fulfilled for the standard $10.6 \mu\text{m}$ wavelength of a CO_2 laser for a doping concentration of $7 \times 10^{18} \text{ cm}^{-3}$ in GaAs⁵. The aim of this paper is to develop a more fundamental theory of the optical Gunn effect and to estimate its implications on the involved optical nonlinearities. The nonlinearity is well understood, but too many sacrifices have been made to derive some general analytic formulas. A rigid theory describing the nonlinearities in a fundamental way is lacking due to the involved computational complications. More in particular, by focussing on the nonlinearities related to the band structure non-parabolicity and intervalley transfers, we found out step by step^{6,7} that conclusions drawn from approximative theories are not always correct when higher order corrections are introduced. In previous papers we proved that the nonlinear and even linear absorption in single valley approximations of nonparabolic semiconductors, if not rigorously treated, can lead to severe mistakes up to 100% . In this paper we extend our previously

* Correspondence: Email: jstiens@vub.ac.be; <http://etro.vub.ac.be/lami/jstiens/welcome.html> phone: (+32)2.629.23.97 ; fax: (+32)2.629.28.83

proposed multi-valley model to a more elaborated model in order to fully estimate the influence of the redistribution of the carriers between various extrema. Not much attention was paid before to the satellite valleys. In earlier efforts, the L-valley is only described by a too crude parabolic and isotropic model⁸. An important parameter in intervalley transfer devices is the intervalley deformation potential between equivalent L-valleys. However, experimental data found in literature for this deformation potential typically scatter over one order of magnitude⁹. The parameter value evaluation from experiments is usually difficult, controversial and inconsistent (e.g. normalisation factors). The paper is subdivided in the following sections. First we describe the modellisation used to calculate the free electron absorption coefficient. The intravalley and intervalley absorption contributions will be clearly distinguished in each valley. In the next section we derive the intensity dependent dielectric permittivity function. Afterwards, in section 4 numerical results are revealed and discussed. Comparison with experimental data are presented. The final conclusions are drawn in section 5.

2. CALCULATION OF THE FREE ELECTRON ABSORPTION COEFFICIENT

To treat the effect of the absorption of electromagnetic waves by free electrons in GaAs, we use a quantum mechanical approach. At medium infrared (IR) wavelengths electron transitions from the valence to the conduction band in GaAs are excluded so that we only need to take into account free electron absorption. As it is well known free electrons can absorb photons only by interacting with third particles such as optical or acoustic phonons, impurities or other imperfections (see, for example Ref. 6,8,10,11). Absorption by hot Γ -valley electrons in nonparabolic III-V semiconductors was studied before¹² taking into account only one Γ -valley of the semiconductor conduction band. In this paper we take into account the distribution of conduction electrons between the nonparabolic Γ - and the ellipsoidal L-valleys and consider absorption mechanisms connected with electron transitions between equivalent and nonequivalent valley energy minima. At medium infrared wavelengths we can neglect the small contribution of X-valley electrons. The contribution of Γ -L transitions in the absorption coefficient was already considered^{8,10} in the suggestion of an isotropic L-valley. As the L-valley of GaAs is represented by 4 strongly anisotropic energy minima it is not clear if the isotropic approximation can be used for calculation of the contribution of Γ -L transitions in the absorption coefficient.

In the Γ -valley we take into account free electron *intravalley* absorption mechanisms assisted by (hot) polar optical phonons and impurities and *intervalley* absorption mechanisms assisted by intervalley phonons resulting in electron transitions from the Γ - to the L-valley. In the L-valley we take into account besides the intravalley and intervalley absorption mechanisms existing in the Γ -valley, an additional absorption mechanism connected with L-valley electron transitions between equivalent L energy minima. We neglect the small contributions due to electron interactions with acoustic and non-polar optical phonons. To calculate the absorption coefficient we use an approach described in detail in ref⁶. In this paper we illustrate only the main results of our calculations.

By using Drude's model we can write down the expression for the dielectric permittivity ϵ_e at medium infrared wavelength:

$$\epsilon_e = \epsilon_1 \left(1 - \frac{\omega_{p,\Gamma}^2 + \omega_{p,L}^2}{\omega^2} + i \left(\frac{\omega_{p,\Gamma}^2}{\omega^3 \tau_\Gamma} + \frac{\omega_{p,L}^2}{\omega^3 \tau_L} \right) \right) \quad (1)$$

where $\omega_{p,\Gamma,L}^2 = \frac{4\pi n_{\Gamma,L} e^2}{m_{\Gamma,L} \epsilon_1}$, $n_{\Gamma,L}$ and $m_{\Gamma,L}$ are respectively the plasma frequency, the electron concentration and optical effective mass of the Γ - and L-valley, ω is the frequency of the incident electromagnetic wave, e is the electron charge, ϵ_1 is the permittivity of undoped GaAs at medium infrared wavelengths. The values $\tau_{\Gamma,L}$ are directly connected with the absorption coefficients by Γ - and L-valley electrons and can be determined as follows:

$$\tau_{\Gamma,L} = \frac{\omega_{p,\Gamma,L}^2 \epsilon_1}{\omega^2 \beta_{\Gamma,L}} \quad (2)$$

The values $\beta_{\Gamma,L}$ which can be interpreted as temporal absorption coefficients are defined as follows:

$$\beta_\Gamma = \sum_{\vec{p}, \vec{q}, L_i} (P_{op,\Gamma}^- D_{1op}^\Gamma + P_{op,\Gamma}^+ D_{2op}^\Gamma + P_{imp,\Gamma} D_{imp}^\Gamma + P_{\Gamma L_i}^- D_1^{\Gamma L_i} + P_{\Gamma L_i}^+ D_2^{\Gamma L_i}) \quad (3)$$

$$\beta_L = \sum_{\vec{p}, \vec{q}, L_i, j} (P_{op,L}^- D_{1op}^{L_i} + P_{op,L}^+ D_{2op}^{L_i} + P_{imp,L} D_{imp}^{L_i} + P_{L_i\Gamma}^- D_1^{L_i\Gamma} + P_{L_i\Gamma}^+ D_2^{L_i\Gamma} + P_{L_iL_j}^- D_1^{L_iL_j} + P_{L_iL_j}^+ D_2^{L_iL_j}) \quad (4)$$

These $\beta_{\Gamma,L}$ -values consist of several contributions. Every contribution is defined as the product of the transition probability P and the supply of electrons and scattering centres. As an example we give the full expression for the optical phonon assisted absorption mechanism.

$$D_{1op}^{\Gamma,L_i} = f_0(\varepsilon_p^{\Gamma,L_i}) [1 - f_0(\varepsilon_{p_1}^{\Gamma,L_i})] (1 + n_q) - f_0(\varepsilon_{p_1}^{\Gamma,L_i}) [1 - f_0(\varepsilon_p^{\Gamma,L_i})] n_q \quad (5)$$

$$P_{op,\Gamma}^{\pm} = \frac{\alpha_{op}}{\hbar^6 \omega^2} |\vec{e}_\kappa (\vec{\nabla}_p \varepsilon_p^\Gamma - \vec{\nabla}_{p_1} \varepsilon_{p_1}^\Gamma)|^2 \delta(\varepsilon_{p_1}^\Gamma - \varepsilon_p^\Gamma - \hbar\omega \mp \hbar\omega_0) \delta_{\vec{p}_1, \vec{p} \pm \vec{q}} \quad (6)$$

where $\alpha_{op} = \frac{2\pi e^2 \hbar^3 C_{op}}{\omega V}$, V is the crystal volume, $C_{op} = \frac{2\pi}{\hbar} |\langle \vec{p}_1 | \hat{H}_{e-op} | \vec{p} \rangle|^2$, \vec{e}_κ is the polarization vector, $f_0(\varepsilon_p^{\Gamma,L})$ is the electron distribution function, n_q , ω_0 are the distribution function and frequency of the polar optical phonons accordingly, \hat{H}_{e-op} is the operator of electron-polar optical phonon interaction, \vec{p}, \vec{q} are the wave vectors of electrons and phonons, the subscript 1 indicates the final state of the electron wave vector, $\varepsilon_p^{\Gamma,L_i}$ is the electron energy in Γ and L_i energy minima, $\delta_{\vec{p}_1, \vec{p} \pm \vec{q}}$ is the Kronecker symbol. For the other absorption mechanisms similar expressions can be derived. The terms containing $P_{L_iL_j}^{\pm}$ describe intervalley transitions of L -electrons between different equivalent energy minima (L_i and L_j) and the terms $P_{\Gamma L_i}^{\pm}, P_{L_i\Gamma}^{\pm}$ describe intervalley transitions between nonequivalent Γ and L_i energy minima. The terms containing $P_{op,L_i}^{\pm}, P_{imp,L_i}$ describe intravalley transitions of L -electrons within the same energy minimum. Expressions for $P_{op,L_i}^{\pm}, P_{imp,L_i}$ are the same as the equations (6) with the substitution $\Gamma \rightarrow L_i$. Expressions (1,2) can be used when $\text{Im} \varepsilon_e \ll \text{Re} \varepsilon_e$, in particular, if $\omega \tau_{\Gamma,L} \gg 1$.

The total absorption coefficient α_e by Γ and L -electrons is given by the following expression:

$$\alpha_e = 2 \frac{\omega}{c} \text{Im} \sqrt{\varepsilon_1 \left(1 - \frac{\omega_{p,\Gamma}^2 + \omega_{p,L}^2}{\omega^2} + i \left(\frac{\omega_{p,\Gamma}^2}{\omega^3 \tau_\Gamma} + \frac{\omega_{p,L}^2}{\omega^3 \tau_L} \right) \right)} \quad (7)$$

whereby c is the velocity of light.

In this paper we suggest that the electron distribution functions of both Γ and L -electrons can be described by the Fermi-Dirac function with a single electron temperature. For highly n -doped semiconductors electron-electron collisions are dominant. Hence this suggestion is justified. To proceed with the calculations we also have to know the dependencies of the electron energy spectrum in both valleys. For the L -valley we use the usual approximation of ellipsoidal energy minimum. For the nonparabolic Γ -valley we use the following approximate analytical expression (see, for example ref¹³):

$$\varepsilon_p = \frac{E_g}{2\alpha} \left(\sqrt{1 + \frac{2\alpha \hbar^2 p^2}{E_g m_0}} - 1 \right) \quad (8)$$

Here ε_p is the electron energy as a function of wave vector, E_g is the forbidden gap energy, m_0 is the effective mass of the electrons near the bottom of the conduction band (Γ -valley), α is the parameter of conduction band nonparabolicity.

Using the condition $n_\Gamma + n_L = n_0$ (n_0 is the total electron concentration) together with exps.(8) we find the following equation for Fermi level μ of the conduction electrons:

$$\frac{2N_{c,\Gamma}}{\sqrt{\pi}} \int_0^\infty \frac{dx \sqrt{x + \frac{\alpha T x^2}{E_g^2} \left(1 + \frac{2\alpha T x}{E_g} \right)}}{e^{\frac{x - \mu}{T}} + 1} + \frac{2N_{c,L}}{\sqrt{\pi}} \int_0^\infty \frac{dx \sqrt{x}}{e^{\frac{x + \frac{\Delta_{\Gamma-L} - \mu}{T}}{T}} + 1} = n_0 \quad (9)$$

where: $N_{c,\Gamma} = 2\left(\frac{m_0 T}{2\pi\hbar^2}\right)^{3/2}$, $N_{c,L} = 2\left(\frac{m_d T}{2\pi\hbar^2}\right)^{3/2}$, $m_d = N^{2/3}\sqrt{m_l m_t^2}$, $x = \frac{\epsilon_p}{T}$, $T = kt$, t is

electron temperature in Kelvin degrees, k is Boltzmann's constant, N is the number of equivalent energy minima in the L-valley ($N=4$), m_l, m_t are the longitudinal and transverse effective masses of the electrons in an ellipsoidal L-minimum, $\Delta_{\Gamma-L}$ is the energy separation between the minima of the Γ and L-valley. The optical effective mass of L-electrons m_L is given by the known expression: $(m_L)^{-1} = 1/3(m_l^{-1} + 2m_t^{-1})$, such that $m_L \approx 0.11m$ (m is the free electron mass). The expression used for the optical effective mass of the Γ -electrons is derived in ref ¹².

2.1 Absorption of electromagnetic waves by Γ -valley electrons.

The absorption mechanism in the Γ -valley can be subdivided between intravalley and intervalley ones. The main intravalley mechanisms in highly doped n-GaAs are connected with Γ -electron interactions with impurities and polar optical phonons. For electron-polar optical phonon interaction the value C_{op} can be written down as follows:

$$C_{op} = \frac{4\pi^2 e^2 \omega_0}{V q^2} \left(\frac{1}{\epsilon_\infty} - \frac{1}{\epsilon_0} \right) \frac{G_{\vec{p}, \vec{p} \pm \vec{q}}^{op}}{\left| 1 + \frac{1}{q^2 r_{op}^2} \right|^2} \quad (10)$$

Here r_{op} is the screening length of the electron-optical phonon interaction potential, $G_{\vec{p}, \vec{p} \pm \vec{q}}^{op}$ is the overlap integral of Bloch periodic wave functions between electron states $|\vec{p}\rangle$ and $|\vec{p} \pm \vec{q}\rangle$. In a parabolic valley the overlap integral is equal to 1, but for non-parabolic valleys the value of $G_{\vec{p}, \vec{p} \pm \vec{q}}^{op}$ is less than one and generally must be taken into account. This problem was already studied in other papers ^{6,13,14}. For the electron-impurity interaction a resembling value of C_{imp} is given by the expression

$$C_{imp} = \frac{32\pi^3 z^2 e^4 n_i}{V \epsilon_s^2 \hbar q^4} \frac{G_{\vec{p}, \vec{p} + \vec{q}}^{imp}}{\left(1 + \frac{1}{q^2 r_{imp}^2} \right)^2} \quad (11)$$

where r_{imp} is the screening length for the electron-impurity interaction, ϵ_s is the static dielectric permittivity of the semiconductor lattice, n_i and ze are the concentration and charge of the impurity centers, respectively and $G_{\vec{p}, \vec{p} + \vec{q}}^{imp}$ is the proper overlap integral for the electron-impurity interaction. The value n_i can be corrected when it is necessary for a doping compensation factor. These intravalley mechanisms were studied in the paper ⁶ for a nonparabolic Γ -valley. In that paper general expressions were deduced for the value of τ_Γ for the cases of absorption processes assisted by polar optical phonons (including the influence of the hot optical phonon effect), impurities and acoustical phonons (contribution of the last mechanism was shown to be very small). The general expressions are given by formulae (23, 37, 48) of that paper ⁶. These expressions are too cumbersome to be written down in this paper.

To calculate the absorption coefficient assisted by polar optical phonons and impurities we have to know the optical phonon distribution function and associated screening lengths of the interaction potentials. As both Γ - and L-valley electron contribute to these values we discuss this problem in the next part of the paper. For the electron-intervalley phonon interaction the value $C_{\Gamma L}$ can be written down as follows:

$$C_{\Gamma L} = \frac{\pi \Lambda_{\Gamma L}^2}{\rho \omega_{\Gamma L} V} \quad (12)$$

where $\Lambda_{\Gamma L}$ is the constant of intervalley Γ -L deformation potential, ρ is a crystal density.

The contribution of Γ -L intervalley transitions is described by the last 2 terms in Exp.(3). We denote the contribution of these terms in the value of τ_Γ as $\tau_{\Gamma-L}$. To calculate $\tau_{\Gamma-L}$ we suggest that in the main region of integration the constant of intervalley deformation potential is independent of the electron wave vector. With the help of this approximation we derived expressions for $\tau_{\Gamma-L}$

$$\frac{1}{\tau_{\Gamma-L}} = \frac{2N_{c,\Gamma}N_{c,L}\Lambda_{\Gamma L}^2 m_\Gamma}{3m_0 n_\Gamma \hbar \omega_{\Gamma L} \omega \rho} \beta_{\Gamma L} \quad (13)$$

The effect of the nonparabolicity of the Γ -valley is camouflaged in the $\beta_{\Gamma L}$ -value. As the intervalley phonon wave vector is very large (of the order of the reciprocal lattice vector) we neglect the screening effect of the electron-intervalley interaction potential. We see that the value $\tau_{\Gamma-L}$ depends on both the density (m_d) and the optical (m_L) effective masses of L-electrons. The difference between these values is tremendous ($m_d \cong 5m_L$) and the use of an isotropic L-valley approximation is totally unjustified.

2.2 Absorption of electromagnetic waves by L-valley electrons.

The L-valley of GaAs consists of 4 equivalent anisotropic (ellipsoidal) energy minima at the symmetry point $L \{\frac{1}{2}, \frac{1}{2}, \frac{1}{2}\}^{15}$. The absorption mechanisms in the L-valley are principally the same as in Γ -valley and can also be subdivided between intravalley and intervalley ones. The main intravalley mechanism for highly doped GaAs can be attributed to the electron interaction with impurities and optical phonons. We suggest that the value C_{op} for the electron-optical phonon interaction in the L-valley is the same as for Γ -electrons and is given by exp.(10). Rigorously speaking it is also necessary to take into account the overlap integrals for the L-electron wave functions^{13,14,16}, but for estimations we suggest that these overlap integrals are equal to 1. The L-electrons also interact with non-polar optical phonons but the contribution of this mechanism is very small and can be neglected. We also neglect the contribution of the L-electrons intravalley interaction with acoustic phonons. Hence to calculate the absorption coefficient assisted by intravalley transitions of L-electrons we take into account the first 3 terms in the Exp.(4). Expressions for $\tau_{op,L}$ and $\tau_{imp,L}$ were derived.

As it was mentioned above to calculate the absorption coefficient on the basis of Exp. (7) we have to know the polar optical distribution function n_q and the screening lengths of interaction potentials r_{op} and r_{imp} . The fact is that in order to cool down, the electron gas emits optical phonons and hence the optical phonon distribution function can be considerably disturbed^{6,17,18}. As it was shown⁷ the contribution of anisotropic L-valleys results in, although symmetric, but anisotropic dependencies of n_q and r_{op} , so both these values depend not only on modulus of \vec{q} but also on its direction in the Brillouin zone. The angular dependencies of these values induce cumbersome calculations of the absorption coefficient assisted by polar optical phonons. But in reality the angular dependencies of n_q and r_{op} are quite close to isotropic ones and for numerical calculations we may use the averaged values \bar{n}_q and \bar{r}_{op} given by Exp.(35) and Exp.(A5) of paper⁷. To derive such expressions we already suggested that the values n_q and r_{op} only depend on the modulus of \vec{q} , that means that in fact we used the averaged values \bar{n}_q and \bar{r}_{op} . The similar values of the screening length of impurity potential r_{imp} by Γ and L-valley electrons can be written down as follows:

$$\frac{1}{r_{imp}^2} = \frac{1}{r_{imp,\Gamma}^2} + \frac{1}{r_{imp,L}^2} \quad (14)$$

Here the values $r_{imp,\Gamma,L}$ are screening length of impurity potential by Γ and L valley electrons. Electron transitions from the Γ into the L-valley result in an increase of the screening effect for the case of nondegenerate L-electrons and degenerate Γ -electrons (this is the typical situation for highly doped n-GaAs with $n_0 > 2.10^{18} \text{ cm}^{-3}$). For the same electron concentration the screening length of the impurity interaction potential r_{imp} is smaller for a nondegenerate electron gas, when

$r_{imp}^2 \approx \epsilon_s T / (4\pi n e^2)$ than for a degenerate one. For example, for a strongly degenerate electron gas when $\mu \gg T$ it is known that $r_{imp}^2 \approx \epsilon_s \mu / (6\pi n e^2)$.

There are two main intervalley mechanisms of medium infrared absorption by L-electrons induced by interaction of L-electrons with L- Γ and L-L intervalley phonons. The contribution of these absorption mechanisms is described by the last 4 terms in Exp.(4). We denote the contribution of L- Γ and L-L transitions in the value of τ_L as $\tau_{L-\Gamma}$ and τ_{L-L} accordingly. To calculate $\tau_{L-\Gamma}$ and τ_{L-L} we suggest again that in the main region of integration the values of the intervalley deformation potential are independent on electron wave vector. As a result we find the following expressions for $\tau_{L-\Gamma}$ and τ_{L-L} :

$$\frac{1}{\tau_{L-\Gamma}} = \frac{2N_{c,\Gamma}N_{c,L}\Lambda_{\Gamma L}^2}{3n_L\hbar\omega_{\Gamma L}\omega\rho}\beta_{L\Gamma} \quad (15)$$

$$\frac{1}{\tau_{L-L}} = \frac{N_{c,L}^2\Lambda_{LL}^2}{2n_L\hbar\omega_{LL}\omega\rho}\beta_{LL} \quad (16)$$

To derive expression (16) we suggested that L-electrons are transferred from one L-energy minimum to the other 3 minima by absorbing or emitting intervalley phonons with the same frequency and the same L-L intervalley deformation potential. The total values of τ_Γ, τ_L are given by expressions (17) and (18):

$$\frac{1}{\tau_\Gamma} = \frac{1}{\tau_{op,\Gamma}} + \frac{1}{\tau_{imp,\Gamma}} + \frac{1}{\tau_{\Gamma-L}} \quad (17)$$

$$\frac{1}{\tau_L} = \frac{1}{\tau_{op,L}} + \frac{1}{\tau_{imp,L}} + \frac{1}{\tau_{L-\Gamma}} + \frac{1}{\tau_{L-L}} \quad (18)$$

When substituting exps.(17, 18) in exp.(7), we find the value of the total absorption coefficient by free Γ - and L-electrons at medium infrared wavelengths as a function of the electron temperature. It is necessary to note that Exps.(17, 18) describe the absorption coefficient by free electrons namely in the long wavelength region including medium infrared wavelength. To find the absorption coefficient of n-GaAs in the wavelength region $\lambda \leq 4\mu\text{m}$ it is necessary to take into account the so called indirect electron transitions between Γ - and L-valleys with intermediate states belonging to the higher conduction band ¹⁰.

3. NONLINEAR PERMITTIVITY OF n-GaAs AT MEDIUM INFRARED WAVELENGTHS

In order to calculate the permittivity dependence $\epsilon_e(W)$ on the intensity W we have to know dependencies of the electron concentrations $n_{\Gamma,L}$ and the electron temperature t on W . The shift of the electron temperature and the redistribution of the electrons in the Γ - and L-valleys with the EW intensity is mainly connected with the level of absorption by free electrons. This absorption leads to the heating of the electron gas and hence to transitions of Γ -electrons to the L-valley. The dependencies $n_{\Gamma,L}(T)$ can be found by solving eq.(9). To find the dependence $t(W)$ we have to solve the stationary energy balance equation (19). This enables to determine the required relationship $\epsilon_e(W)$.

$$\alpha_e W = P \quad (19)$$

Here P is the total power transferred to the lattice by the heated free electron gas during its energy relaxation process. The stationary regime in this paper is interpreted as the time scale where optical pulses are much longer than the relaxation times of the nonlinear mechanisms involved and shorter enough to avoid any thermal heating of the lattice. The heating time of the lattice is estimated to be tens of microsecond for these intensities.

There are several energy relaxation mechanisms: intravalley emission of optical phonons by Γ - and L-electrons, emission of L-L intervalley phonons by L-electrons when these electrons remain within the L-valley and emission of Γ -L intervalley phonons by Γ and L-electrons when these electrons are transferred from one (Γ - or L-) valley to another (Γ - or L-) valley. The value of P was calculated in paper⁷ where the contribution of the last mechanism (emission of intervalley Γ -L phonons) was neglected. In this paper we use the results of the same paper⁷ with the addition of the contribution of Γ -L

intervalley phonon emission. The contribution of the intravalley emission of optical phonons by Γ - and L-electrons with taking into account the influence of the hot optical phonon effect and emission of L-L intervalley phonons by L-electrons are given by Exps.(8, 17, 37, 38) of paper ⁷. The sum of these contributions we denote as P_{L-L} .

The contribution of Γ -L intervalley phonons emitted by Γ - electrons in the value of P ($P_{\Gamma-L}$) can be calculated on the basis of Exp.(20):

$$P_{\Gamma-L} = \sum_{\vec{q}, \vec{p}} \hbar \omega_{\Gamma L} C_{\Gamma L} \{ (n_{q\Gamma L} + 1) f_0(\epsilon_p^\Gamma) (1 - f_0(\epsilon_p^L - \hbar \omega_{\Gamma L})) - n_{q\Gamma L} f_0(\epsilon_p^L - \hbar \omega_{\Gamma L}) (1 - f_0(\epsilon_p^\Gamma)) \} \cdot$$

$$\delta(\epsilon_p^\Gamma - \epsilon_{\vec{p}-\vec{q}}^L - \hbar \omega_{\Gamma L}) = \sum_{\vec{q}} \hbar \omega_{\Gamma L} C_{\Gamma L} ((n_{q\Gamma L} + 1) A_{\Gamma L} - n_{q\Gamma L} B_{\Gamma L}) \quad (20)$$

Expressions for $A_{\Gamma L}$ and $B_{\Gamma L}$ can be found by direct comparison of left and right hand sides of Exp.(20).

In the case of thermodynamic equilibrium the value of $P_{\Gamma-L} = 0$. Hence in this case we have:

$$\frac{A_{\Gamma L} C_{\Gamma L}}{n_{q\Gamma L}(T)} = \frac{B_{\Gamma L} C_{\Gamma L}}{1 + n_{q\Gamma L}(T)} \quad (21)$$

The function $n_{q\Gamma L}(T)$ is given by the Bose-Einstein expression with the temperature equal to the electron temperature T .

Using the dispersion relation given by Exp.(8) for the nonparabolic Γ -valley we find by direct calculation the value $P_{\Gamma-L}$. As a result the total value of the power transferred to the lattice by the heated free electron gas distributed between Γ - and L-valleys is given by Exp.(22):

$$P = P_{L-L} + P_{\Gamma-L} + P_{L-\Gamma} \quad (22)$$

In these calculations we neglect the small contribution in the value of P connected with the L-valley electron-non-polar optical phonon interaction.

Substitution of Exp.(11) in Eq.(9) leads to the equation for the electron temperature dependence $t(W)$. Substitution of the dependence $t(W)$ in Exp.(1) gives us the dependence of dielectric permittivity on the electromagnetic wave intensity W .

4. RESULTS OF NUMERICAL CALCULATIONS AND DISCUSSIONS

Band edge effective mass m_0	0.063 m	Dielectric permittivity at λ 10.6 μm	10.72
Longitudinal L valley effective mass m_l	1.9 m	Density ρ (g/cm ³)	5.32
Transverse L valley effective mass m_t	0.075 m	Deformation Potential Λ_{LL} (eV/cm)	(1-0.12)x10 ⁹ [5,8,9]
Band gap E_g (eV)	1.42	$L - L$ intervalley phonon energy (eV)	0.029 [9]
Γ -L valley energy difference $\Delta_{\Gamma-L}$ (eV)	0.284	Deformation Potential $\Lambda_{\Gamma L}$ (eV/cm)	0.65 x10 ⁹ [8]
Γ valley nonparabolicity factor for α	0.82	$\Gamma - L$ intervalley phonon energy (eV)	0.031 [8]
Static dielectric permittivity ϵ_0	13.1	LO Phonon frequency ω_{LO} (eV)	0.036
HF dielectric permittivity ϵ_∞	10.9	Deacy time of LO-phonons τ_r (ps)	6.7

Table I. Material parameters of GaAs for $t_L=300K$ used in the numerical calculations. Data are taken from the following references ^{9,15,19-21,23,24}

Material parameters of GaAs, which were used for the numerical calculations are given in Table I. There is a large uncertainty in the values of the intervalley deformation potential. The values of $\Lambda_{\Gamma L}$ and Λ_{LL} given in different papers differ as much as one order of magnitude ^{9,19-21}. As the values of the relaxation times $\tau_{\Gamma-L}$, $\tau_{L-\Gamma}$ and τ_{L-L} are proportional to $\Lambda_{\Gamma L}^2$ and Λ_{LL}^2 , the uncertainties of $\Lambda_{\Gamma L}$ and Λ_{LL} values result in a much greater uncertainty in $\tau_{\Gamma-L}$, $\tau_{L-\Gamma}$ and τ_{L-L} values. In this paper we use values of $\Lambda_{\Gamma L}$, $\omega_{\Gamma L}$ found in reference ²⁰(see Table I). With the help of these values one can calculate that e.g. the

Γ -L valley transfer time is about 100 fs for Γ -electrons with 500meV kinetic energy and an L- Γ return time of about 2.2ps for L-electrons at the bottom of the L-valley for a parabolic Γ -valley²⁰ or about 1.6 ps for a nonparabolic Γ -valley.

As to the author's knowledge there is no exact information available concerning the Λ_{LL} -value, we show different simulations based on three different values of Λ_{LL} ($=1 \times 10^9$, 0.12×10^9 and 0.6×10^9 eV/cm) to show the influence of this parameter on the dependence $\epsilon_e(W)$. The first two values correspond respectively to the maximum and minimum values found in literature, and the last value is set equal to a common value of Λ_{GL} .

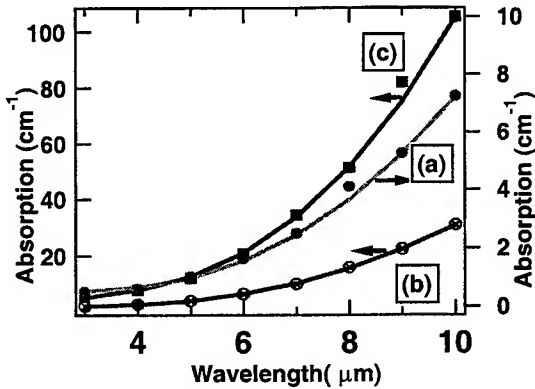


Fig.1 Comparison between theoretical and experimental dependences of the absorption coefficient α_e on the wavelength λ for three different doping concentrations in GaAs: (a) $n_0 = 0.13 \times 10^{18} \text{ cm}^{-3}$, (b) $n_0 = 0.49 \times 10^{18} \text{ cm}^{-3}$ and (c) $n_0 = 1.09 \times 10^{18} \text{ cm}^{-3}$ for $t = t_L = 296 \text{ K}$. The best fits are found for the following compensation factor $s = 8, 3.1, 3.05$, respectively.

As it was mentioned above it is necessary to take into account indirect Γ -L electron transitions to describe the experimental dependencies of the absorption coefficient versus wavelength. To test our model we fit three experimental absorption data²². These experimental and theoretical dependencies are presented in Fig.1. We found a satisfactory fit with the experimental results when the fit factor A related to the absorption mechanism assisted by indirect transitions between the Γ and L-valley, $A = 1.2 \times 10^{-9} T_1^2$ for $T_1 = 296 \text{ K}$. The compensation factors for fitting the experimental curves are indicated in the figure caption of figure 1. As we neglect transitions into the X-valley we restrict our model calculations of the absorption coefficient to wavelengths $\lambda > 3 \mu\text{m}$. The contribution of indirect electron transitions being very important for wavelengths $\lambda < 4 \mu\text{m}$, however evanesce very fast for larger wavelengths. At $\lambda \sim 8 \mu\text{m}$ this contribution is already reduced to 10% of the contribution given by direct Γ -L transitions and at the medium infrared wavelength $\lambda \sim 10 \mu\text{m}$, the contribution of indirect electron transitions in the absorption coefficient can be neglected.

In Fig. (2a,b) the contribution of the different absorption mechanisms to the total absorption coefficient are plotted versus the electron temperature for two different electron concentrations (a) $2 \times 10^{18} \text{ cm}^{-3}$ and (b) $7 \times 10^{18} \text{ cm}^{-3}$ and for a wavelength $\lambda = 10.6 \mu\text{m}$. All calculations were proceeded under the assumption that the free electron concentration is equal to the doping concentration. The contribution of L-L intervalley transitions in the absorption process is calculated at a moderate value of $\Lambda_{LL} = 0.6 \times 10^9$ eV/cm. The particular contributions of L-L and Γ -L intervalley transitions to the absorption coefficient and the resulting total absorption coefficients versus the electron temperature are shown in Figs.(3a,3b) for three different values of the intervalley deformation potential Λ_{LL} .

From Figs.(2a,2b,3a,3b) we see that the contribution of the intervalley transitions strongly increases with a growing electron concentration n_0 and electron temperature t . This is easy to understand taking into account that at these doping concentrations $n_0 > 2 \times 10^{18} \text{ cm}^{-3}$, the Γ -valley electron gas is degenerate and the Fermi energy increases with an increasing doping concentration. So for larger doping concentrations and electron temperature the number of electrons with energy $\epsilon \geq \Delta_{\Gamma-L} - \hbar\omega \pm \hbar\omega_{\Gamma-L}$ increases resulting in an increase of the contribution of Γ -L transitions to the total absorption coefficient. The contribution of Γ -L transitions at these concentrations is usually less than or about 15% of the total value of absorption coefficient. The relative contribution of this mechanism increases with an increase of the electron temperature. The contribution of L-L transitions in the value of the absorption coefficient strongly depends on the value of Λ_{LL} . At $\Lambda_{LL} = 1 \times 10^9$ eVcm⁻¹ this contribution results in a strong increase of the total absorption coefficient (=sum of all the contributions) with increasing electron temperature (see Figs.(3a,3b)) and exceeds the impurity contribution for $n_0 = 7 \times 10^{18} \text{ cm}^{-3}$ at $t = 900 \text{ K}$, and the combined impurity and optical phonon contributions for $n_0 = 2 \times 10^{18} \text{ cm}^{-3}$, and at $t = 900 \text{ K}$. On the other hand the contribution of L-L transitions is negligibly small for $\Lambda_{LL} = 0.12 \times 10^9$ eVcm⁻¹. At $\Lambda_{LL} = 0.6 \times 10^9$ eVcm⁻¹ and for an electron temperature $t > 700 \text{ K}$, the contribution of L-L transitions is already larger than the contribution of Γ -L transitions. It is important to mention that the total contribution of the intervalley transitions for highly doped n-GaAs results in an increase of the imaginary part of the dielectric permittivity and the absorption coefficient as a function of electron temperature (see

Figs[3a,3b]). On the contrary, the absorption coefficient related to the free electrons residing in the nonparabolic Γ -valley *only* of highly doped n-GaAs, *decreases* with an increase of the electron temperature¹².

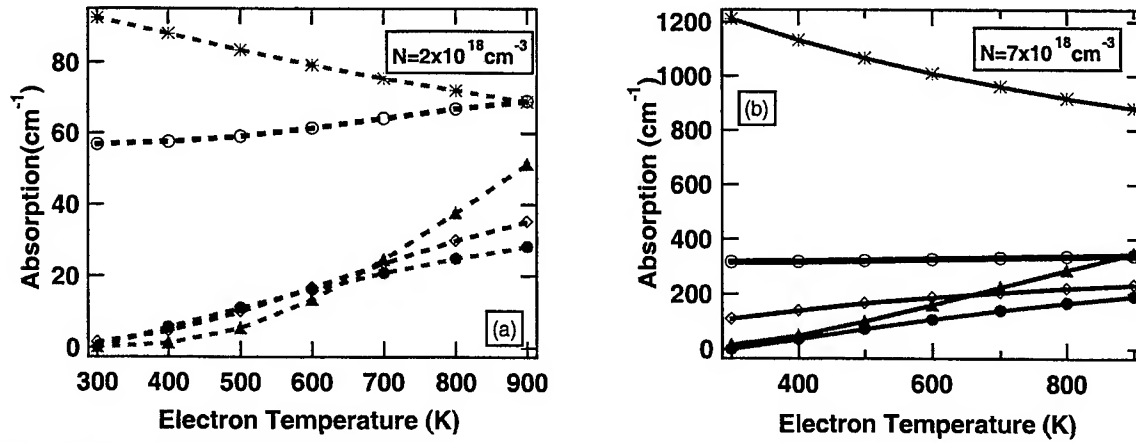


Fig.2 Dependences of different contributions to the absorption coefficient in GaAs on electron temperature t for two doping concentrations (a) $n_0 = 2 \times 10^{18} \text{ cm}^{-3}$, and (b) $n_0 = 7 \times 10^{18} \text{ cm}^{-3}$. Other parameters are $t_L = 300 \text{ K}$, $\lambda = 10.6 \mu\text{m}$, $\Lambda_{LL} = 0.6 \times 10^9 \text{ eV cm}^{-1}$: impurity contribution (*), contribution of thermal optical phonons (o), contribution of hot optical phonons (•), contribution of Γ -L intervalley transitions (◊), contribution of L-L intervalley transitions (▲).

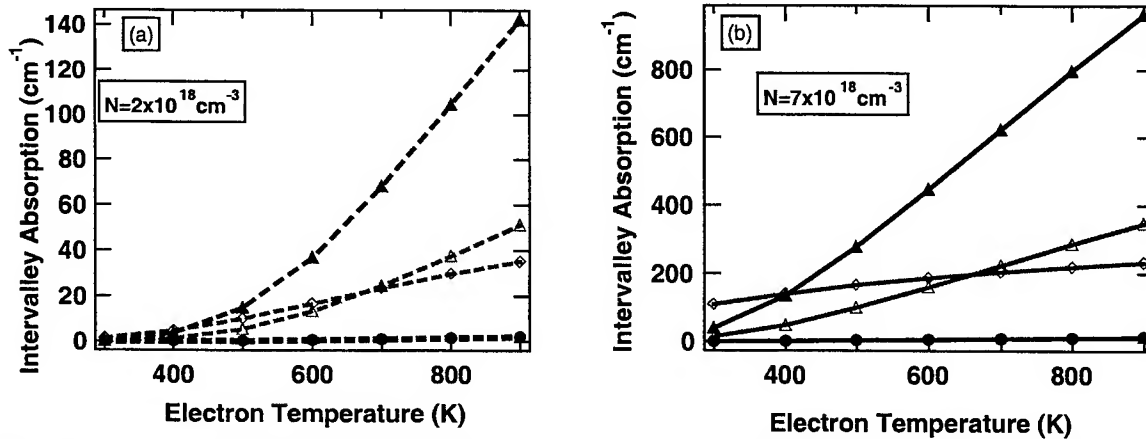


Fig.3 Dependences of contributions to the absorption coefficient in GaAs on electron temperature t for two doping concentrations (a) $n_0 = 2 \times 10^{18} \text{ cm}^{-3}$, and (b) $n_0 = 7 \times 10^{18} \text{ cm}^{-3}$. Other parameters are $t_L = 300 \text{ K}$, $\lambda = 10.6 \mu\text{m}$: contribution of Γ -L intervalley transitions (◊); contributions of L-L intervalley transitions at $\Lambda_{LL} = 0.12 \times 10^9 \text{ eV cm}^{-1}$ (•); $\Lambda_{LL} = 0.6 \times 10^9 \text{ eV cm}^{-1}$ (Δ); $\Lambda_{LL} = 1.0 \times 10^9 \text{ eV cm}^{-1}$ (▲).

The influence of L-L intervalley transitions is even more striking if we consider the dependencies of the electron distribution, absorption coefficient, or the index of refraction on the intensity of the incident electromagnetic wave. To find these dependencies we first have to calculate the dependence of the intensity W on the electron temperature t . The dependencies $W(t)$ for different values of n_0 are plotted in Fig. 4. As it is shown in this figure, the optical heating effect is stronger at smaller values of Λ_{LL} . This behavior of the $W(t)$ dependence is connected with the fact that the energy relaxation time of L-electrons τ_{eL} increases with a decrease of the value of Λ_{LL} . The dependencies of the L-electron energy relaxation time on electron temperature for different values of the intervalley deformation potential Λ_{LL} and doping concentrations are shown in Fig.5. We observe that the L-electron energy relaxation time increases from the values of about (0.3-0.45)ps at $\Lambda_{LL} = 1 \times 10^9 \text{ eV cm}^{-1}$ up to the values of about (1-2)ps at $\Lambda_{LL} = 0.12 \times 10^9 \text{ eV cm}^{-1}$ depending on the electron temperature and doping concentration. The value τ_{eL} is quite small at $\Lambda_{LL} = 1 \times 10^9 \text{ eV cm}^{-1}$ when the contribution of Γ -L transitions can be neglected but the contribution of Γ -L transitions has to be definitely taken into account at $\Lambda_{LL} = 0.12 \times 10^9 \text{ eV cm}^{-1}$ when the value of τ_{eL} strongly increases (the value Λ_{LL} was supposed to be equal to $0.12 \times 10^9 \text{ eV cm}^{-1}$ in paper⁴).

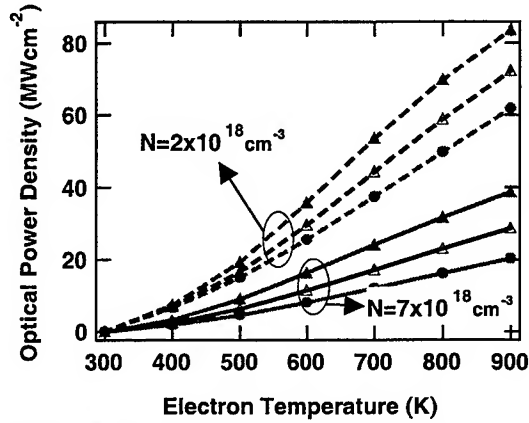


Fig.4 Dependences of the electromagnetic wave intensity W on the electron temperature t at $t_L=300\text{K}$, $\lambda=10.6\mu\text{m}$ for two different doping concentrations: $n_0=2 \times 10^{18}\text{cm}^{-3}$ (---) and $n_0=7 \times 10^{18}\text{cm}^{-3}$ (—) respectively and for three different values of $\Lambda_{LL}=0.12 \times 10^9\text{Vcm}^{-1}$ (●); $\Lambda_{LL}=0.6 \times 10^9\text{Vcm}^{-1}$ (Δ); $\Lambda_{LL}=1.0 \times 10^9\text{Vcm}^{-1}$ (▲).

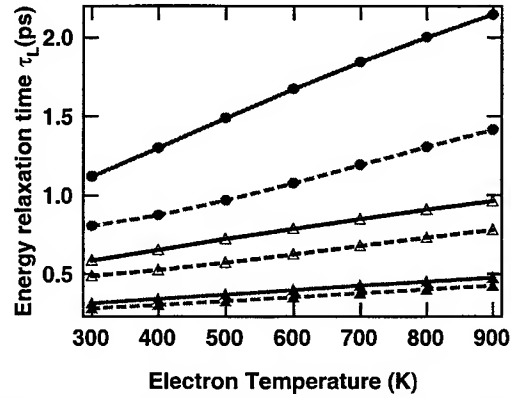


Fig.5 Dependences of the energy relaxation time of the L-valley electrons τ_{eL} on the electron temperature t for GaAs at a wavelength $\lambda=10.6\mu\text{m}$ and $t_L=300\text{K}$. Two different doping concentrations $n_0=2 \times 10^{18}\text{cm}^{-3}$ (---) and $n_0=7 \times 10^{18}\text{cm}^{-3}$ (—) are compared at three different values of $\Lambda_{LL}=0.12 \times 10^9\text{Vcm}^{-1}$ (●); $\Lambda_{LL}=0.6 \times 10^9\text{Vcm}^{-1}$ (Δ); $\Lambda_{LL}=1.0 \times 10^9\text{Vcm}^{-1}$ (▲).

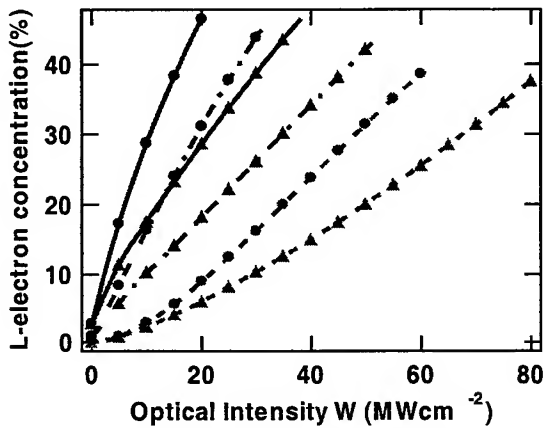


Fig.6 The relative electron concentration in the L-valley of GaAs versus the optical intensity at $t_L=300\text{K}$, $\lambda=10.6\mu\text{m}$ for two three different doping concentrations: $n_0=2 \times 10^{18}\text{cm}^{-3}$ (---), $n_0=5 \times 10^{18}\text{cm}^{-3}$ (-.-.-) and $n_0=7 \times 10^{18}\text{cm}^{-3}$ (—) respectively and for two different values of $\Lambda_{LL}=0.12 \times 10^9\text{Vcm}^{-1}$ (●); $\Lambda_{LL}=1.0 \times 10^9\text{Vcm}^{-1}$ (▲).

The evolution of the number of electrons, occupying the L-valley strongly increases with a growing doping concentration and optical intensity (see Fig.6) leading to a considerable increase of the contribution of L-L transitions in the absorption process. One observes that the lower the LL-IDP value the easier it is to populate the L-valley, although the smaller the absorption coefficient. One can conclude here that the optical Gunn effect is could be most efficient when the LL-IDP value is smallest. From fig.6 it is also clear that a smaller doping concentration ($5 \times 10^{18}\text{cm}^{-3}$) in combination with a small LL-IDP value is more preferable than a larger doping concentration when the LL-IDP value is large. This figure also shows that the for the highest doping concentrations the optical intensity can be limited to several MWcm^{-2} to induce a substantial electron transfer. The end of each curve of fig.6 ends where the electron temperature corresponds to 900K.

The dependences of the total absorption coefficient α_e at $n_0=7 \times 10^{18}\text{cm}^{-3}$ and the index of refraction $n_e(W) = \text{Re}\sqrt{\epsilon_e(W)}$ for different values of Λ_{LL} and doping concentrations are shown in Fig.8. One sees that the dependence $\alpha_e(W)$ is strongly influenced by the value of Λ_{LL} . In spite of the fact that the real part of dielectric permittivity given by Exp.(1) is independent of the value of Λ_{LL} , the dependence $n_e(W)$ is considerably influenced by the value of Λ_{LL} especially at larger doping concentrations (see Fig.8). For small intensities of the incident electromagnetic waves, the index of refraction can be written down as follows: $n_e = n_{e0} + n_2 W$. We find at $\lambda=10.6\mu\text{m}$, $t_L=300\text{K}$, and $n_0=2 \times 10^{18}\text{cm}^{-3}$ that $n_{e0} \approx 2.84$, n_2 is almost independent on Λ_{LL} and equal to $1.3 \times 10^{-9}\text{cm}^2/\text{W}$. On the other hand, we find at larger electron concentrations $n_0=7 \times 10^{18}\text{cm}^{-3}$, $\lambda=10.6\mu\text{m}$, $t_L=300\text{K}$ and at the value Λ_{LL} equal to 1×10^9 , 0.6×10^9 and $0.12 \times 10^9\text{eVcm}^{-1}$ that $n_{e0} \approx 1.38$, $n_2 \approx 2.7 \times 10^{-9}$, 3.3×10^{-9} , $3.75 \times 10^{-9}\text{cm}^2/\text{W}$, respectively. We observe that the influence of intervalley transitions and especially LL-transitions on the values of

the nonlinear absorption coefficient and the index of refraction at medium infrared wavelengths can be considerable for highly doped n-GaAs. In this case even the value of nonlinear refraction index n_2 depends considerably on the LL-IDP constant.

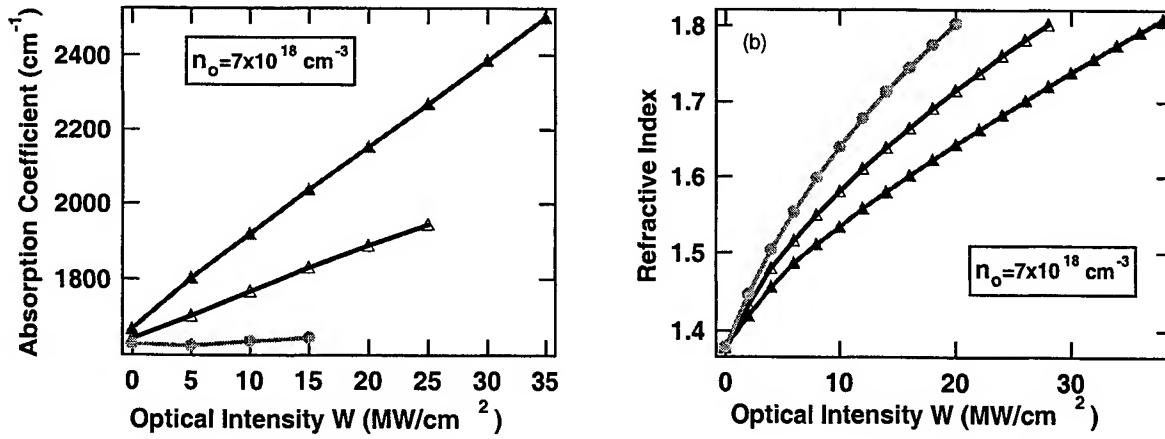


Fig.7 Dependences of the (a) total absorption coefficient α_e and the refractive index on the electromagnetic wave intensity W for GaAs at $n_0 = 7 \times 10^{18} \text{ cm}^{-3}$, at $\lambda = 10.6 \mu\text{m}$, $T_L = 300 \text{ K}$ and for three different values of $\Lambda_{LL} = 0.12 \times 10^9 \text{ eVcm}^{-1}$ (●); $\Lambda_{LL} = 0.6 \times 10^9 \text{ eVcm}^{-1}$ (Δ); $\Lambda_{LL} = 1.0 \times 10^9 \text{ eVcm}^{-1}$ (▲).

5. CONCLUSIONS

In this paper we have derived analytic quantum mechanical expressions for describing the optical Gunn effect at medium infrared wavelengths. Free electrons are heated and distributed between Γ - and L -valleys in GaAs taking into account the electron-optical phonon interaction (including hot optical phonons effect), electron-impurity interaction and the interaction of electrons with intervalley (ΓL and LL) phonons. The dependence of the absorption coefficient and the index of refraction on the optical power intensity have been derived by deriving an expression for the power transferred to the lattice from heated Γ - and L -valley conduction electrons. Emission of intervalley ΓL and LL phonons (i.e. intervalley ΓL and LL electron transitions) and optical phonons (intervalley Γ and L -electrons transitions) were considered as the main mechanisms of energy transfer from Γ - and L -valley electrons to the lattice. The anisotropy of the L -valley and the nonparabolicity of the Γ -valley have been rigorously taken into account.

It was shown that contributions of intervalley transitions in the absorption coefficient strongly depend on the electron concentration, temperature and intervalley deformation potential values and even exceed the contribution assisted by electron-impurity interaction for highly doped GaAs and high electron temperatures ($t \approx 900 \text{ K}$) if the value of the LL -intervalley deformation potential constant is about $1 \times 10^9 \text{ eVcm}^{-1}$. Contributions of intervalley transitions result in the dependence of the absorption coefficient on electron temperature t , increasing with the increase of t . On the contrary the absorption coefficient related to free electrons residing in the nonparabolic Γ -valley only decreases with increase of electron temperature.

Intervalley scattering to the Γ - and L -valleys plays an important role in the cooling of electrons. As a result the increase of electron temperature induced by optical absorption is greater for smaller values of the intervalley deformation potential constant Λ_{LL} . This behavior versus electron temperature is explained by the increase of the energy relaxation time of L -valley electrons τ_{eL} with the decrease of Λ_{LL} -value. It was shown that the L -electron energy relaxation time increases from the values of about $(0.3-0.45) \text{ ps}$ at $\Lambda_{LL} = 1 \times 10^9 \text{ eVcm}^{-1}$ up to the value of about $(1-2) \text{ ps}$ at $\Lambda_{LL} = 0.12 \times 10^9 \text{ eVcm}^{-1}$ depending on electron temperature and doping concentration. As a result absorption coefficient, dielectric permittivity and the index of refraction depend stronger on electromagnetic wave intensity for the case of smaller values of the intervalley deformation potential Λ_{LL} . It was shown that the value of nonlinear refraction index n_2 of highly n-doped GaAs considerably depends on the value of intervalley deformation potential constant Λ_{LL} at medium infrared wavelengths. Hence the experimental measurements of absorption coefficient and the index of refraction dependencies on electromagnetic wave intensity at medium infrared wavelengths would provide independent information about the values of intervalley deformation potential

constant Λ_{LL} . The combination of the small response time $((6-7)ps)$ and the quite great value of nonlinear refraction index n_2 ($n_2=2.7-3.75 \times 10^{-8} \text{ cm}^2/\text{W}$) at $n_0=7 \times 10^{18} \text{ cm}^{-3}$) also make this mechanism of dielectric permittivity modulation by medium infrared electromagnetic waves to be perspective for applications. The versatility of the intervalley transfer nonlinearity still offers opportunities for design and optimisation.

ACKNOWLEDGMENTS

This work was funded by the VUB-GOA (Concerted Research Actions), the IWT (Flemish Institute for the encouragement of Scientific-Technological Research in the Industry) and the European Innovation Project ULTIMOS IN30863I.

REFERENCES

1. K. Kash, P.A. Wolff, and W.A. Bonner, *Appl. Phys. Lett.* **42**, 173 (1983).
2. S. Y. Auyang, P.A. Wolff, *J. Opt. Soc. Am. B.* **6**(4), 595 (1989).
3. G. Shkerdin, A. I. Voronko, S.E. Kumekov, *Journ. Of Phot. and Optoelectronics* 1(N4), 193 (1993).
4. J.B. Gunn, *Solid State Commun.* **1**, 88 (1963).
5. J. Stiens, R Vounckx, *J. Appl. Phys.* **76**(6), 3526-3533 (1994).
6. G.Shkerdin, J.Stiens, R. Vounckx, *J. Appl. Phys.* **87**(7), 3792-3806 (1999).
7. G.Shkerdin, J.Stiens, R. Vounckx, *J. Appl. Phys.* **87** (7), 3807-3818 (1999).
8. Chin-Yi Tsai et al, *IEEE Journ. Quant. El.* **34**, 552 (1998).
9. S.Zollner, S.Gopalan, M.Cardona, *J. Appl. Phys.* **68**(4), 1682 (1990).
10. E. Haga, and H. Kimura, *Journ. of Phys. Soc. of Japan* **19**(9), 1596 (1964).
11. A.S. Jordan, *J. Appl. Phys.* **51**, 2218 (1980).
12. P.A. Wolff, S.Y. Yuen, K.A. Harris, J.W. Cook Jr., and J.F. Schetzina, *Appl. Phys. Lett.* **40**, 457 (1987).
13. Ehrenreich, *Journ. Phys. Chem. Solids* **2**, 131 (1957).
14. B.R. Nag, *Electron Transport in Compound Semiconductors*, Springer Series in Solid-State Sciences **11**, Springer-Verlag, Berlin (1980).
15. J.S. Blakemore, *J. Appl. Phys.* **53**(10), R123 (1982).
16. E.M.Conwell, *High Field Transport in Semiconductors*, Academic Press, New York and London, 1967.
17. S.E. Kumekov, and V.I. Perel, *Sov. Phys. JETP* **67**(1), 193 (1988).
18. J.C. Vaissiere, J.P. Nougier, M. Fadel, L. Hlou, P. Kocevar, *Phys. Rev. B* **46**(20), 13082 (1992).
19. S.Adachi, *J.Appl.Phys.* **58**(3), R1 (1985).
20. J.Shah, B.Deveaud, T.C.Damen, W.T.Tsang, A.C.Cossard, P.Lugli, *Phys. Rev. Lett.* **59**(19), 2222 (1987).
21. M.A.Littlejohn, J.R.Hauser, T.H.Glisson, *J. Appl. Phys.* **48**(11), 4587 (1977).
22. W.G.Spitzer, J.M.Whelan, *Phys.Rew.* **114**, 59 (1959).
23. M. Levinshstein, S. Rumyantsev, M. Shur, *Handbook on Semiconductor Parameters Vol.1*, World Scientific, London (1996).
24. S.Adachi, *Physical Properties of III-V Semiconductors and Compounds InP, InAs, GaAs, GaP and InGaAsP*, A Wiley-Interscience Publication, 1992.

SESSION 5

Microcavity and Nano/Microstructures

Nano-photonics: Recent Advances

M. K. Chin^{*a}, S. T. Ho^b

^a Nanovation Technologies, Inc., 1801, Maple Ave., Evanston, IL 60201, USA.

^b Dept. of Electrical and Computer Engineering, Northwestern University, Evanston, IL 60208.

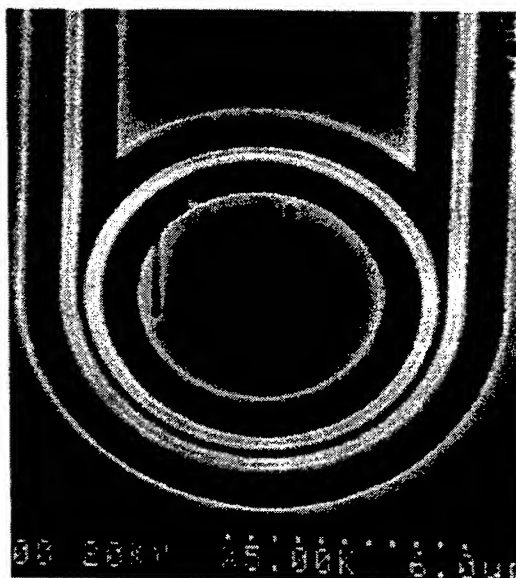
ABSTRACT

We have designed, fabricated and demonstrated ultra-compact directional couplers ($< 30 \mu\text{m}$) and "race-track" micro-resonators as nano-photonic building blocks for a range of WDM devices, including ultra-compact directional couplers, channel-dropping filters, $1 \times N$ demultiplexers and 2×2 crossbar switches.

Keywords: Nano-photonics, resonators, switches, waveguides, semiconductors, integrated optics, WDM.

Nanophotonics is an emerging field in photonics. It is an enabling technology that allows us to fabricate photonic devices on a much smaller scale and to realize photonic integrated circuits with much higher device-count and functional density. An example of nanophotonic device is the micro-ring resonator which has been used as the basis for a new class of Wavelength Division Multiplexing (WDM) devices that offers potential advantages in performance, size and cost. Waveguide-coupled microcavity ring and disk resonators in AlGaAs/GaAs material system with high finesse (> 100) and 22-nm free-spectral range (FSR) have been demonstrated [1]. These devices have also been demonstrated in other material systems [2]. The large FSR of these resonators results from their extremely small size ($\sim 10 \mu\text{m}$ diameter), which is made possible by the use of waveguides with a large lateral index contrast of 3.4 to 1. Such dimensions would conceivably enable realization of large-scale photonic integrated circuits, such as an optical cross-connect switching fabric, demanded by future dense WDM systems. We believe this technology will be one of very few viable options for realizing future high-density photonic integrated circuits that will become more prevalent with the advent of dense WDM communication systems.

The emergence of nano-scale photonic devices is triggered by advances in nanofabrication technology as well as in our understanding of low-dimensional quantized photonic and electronic structures. Historically in our group, our interest in low-dimensional photonic structures arose from an attempt to minimize the laser threshold power by maximizing the photon capture efficiency into the desired lasing cavity mode. This quantity, known as the spontaneous emission coupling factor (β), has a value of 10^{-5} at threshold for conventional laser diodes. It turns out that this value can be increased to nearly 1 (the theoretical limit) by using strongly guided two-dimensional dielectric waveguides with cross sectional dimensions smaller than a quarter of an optical wavelength in the material. In that case it is found that spontaneous emissions emitted in a certain polarization and in certain directions are greatly suppressed, and almost all spontaneous emissions are effectively channeled spatially into a particular desired direction and spectrally into one cavity mode. An example of such a photonic structure is shown in Fig. 1. It consists of a ring-shaped semiconductor cylindrical waveguide forming a ring cavity, coupled evanescently to a U-shaped waveguide forming the output. The ring waveguide



Photonic-Wire Laser Coupled to Nanoscale Waveguide

is bonded onto a glass substrate with a much lower refractive index. The waveguides have a cross section of only $0.2\text{ }\mu\text{m} \times 0.2\text{ }\mu\text{m}$. We call this a *photonic wire* laser as the optical confinement occurs strongly in both the transverse dimensions, in analogy to quantum wire which confines electrons in two directions. The total mode volume in the waveguide is only 0.3 cubic micrometer, making this one of the smallest lasers ever demonstrated.

Similarly, the photonic analog of quantum well would be a *photonic well*, which is simply a strongly guided waveguide with one of the transverse dimensions smaller than an optical wavelength. An example of such a waveguide that is useful for planar integrated circuits would be one that has strong lateral confinement (formed by a large index contrast) in the plane direction but the conventional layer structure of a weakly guided waveguide in the vertical direction. Because of the lateral confinement, this photonic well waveguide would be able to curve around sharply forming very compact cavities, bends, branches and crossovers, and, consequently, enabling integrated optic devices to be greatly miniaturized.

Fig. 2 shows a micro-ring resonator in GaAs/AlGaAs materials formed by the photonic well waveguide, coupled evanescently to two similar straight waveguides, across gaps of only 100 nm. The waveguides are formed by etching deep side trenches into the semiconductor using inductively coupled plasma reactive-ion etching (ICP-RIE). The patterns were defined by direct-write electron-beam lithography. ICP-RIE is a relatively new dry etching method and has not been widely utilized for etching of submicron structures. A principal advantage of ICP-RIE compared to conventional to RIE methods is the ability to independently control the ion energy and flux density. With ICP-RIE, we have achieved deeply etched nanometer-scale structures in GaAs/AlGaAs materials with aspect ratios as high as 30:1 and very smooth sidewalls with typical roughness less than 10 nm.

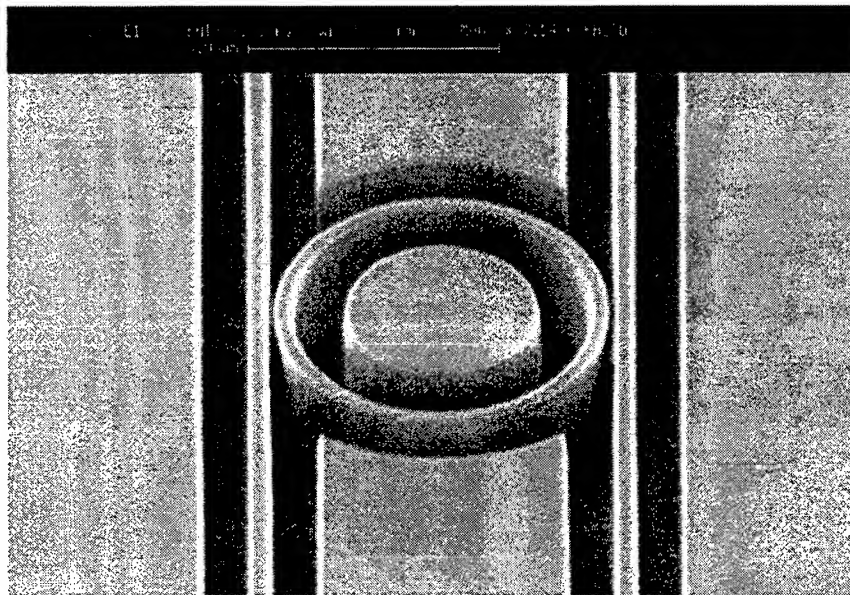


Fig. 2: A micro-ring resonator and two coupled waveguides. The diameter of the ring is $6\text{ }\mu\text{m}$, the width of the waveguide is $0.4\text{ }\mu\text{m}$, and the width of the gaps is $0.1\text{ }\mu\text{m}$.

The conventional ring resonators are coupled to input and output waveguides via a “point contact”, and therefore for sufficient coupling a very small gap of the order of 100 nm is required. As an alternative we and others have proposed a “race-track” resonator [3] which achieves the same desired coupling factor by trading off a longer coupling distance for a wider gap. We have found that as a result the fabrication is much more tolerant. Fig. 3 shows SEM pictures of a resonator-based channel dropping filter and the race-track resonator. Note that the waveguides are $0.4\text{ }\mu\text{m}$ wide but taper to $2\text{ }\mu\text{m}$ outside the resonator region for easier input coupling and to reduce optical loss.

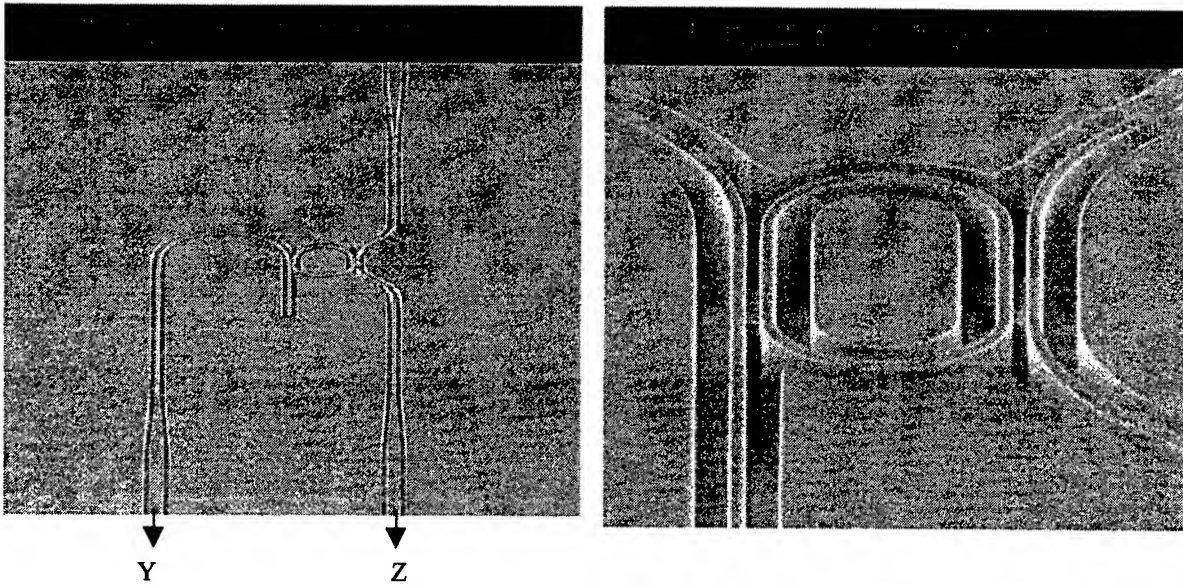


Fig. 3: (a) A race-track resonator coupled to two waveguides. (b) Close-up view of the race-track resonator.

The principle of operation which makes the microcavity resonator a versatile WDM device (a wavelength filter/switch, a multiplexer, even a modulator) is very simple, and is based on the concept of resonance. Essentially, the ring forms a Fabry-Perot interferometer with the two couplers forming the mirrors. The mirror reflectivities are determined by the coupling factors between the ring and the two coupled waveguides. The resonance wavelength (λ_m) is defined by the resonance condition: $l_{\text{eff}}n_{\text{eff}} = m\lambda_m$, where l_{eff} is the effective round trip length of the cavity, n_{eff} is the effective index of the waveguide, and m , an integer, is the order of the resonance. Hence, the free spectral range, defined as $\lambda_m - \lambda_{m+1}$, is large when the cavity length is small. In operation, input light (see Fig. 3a) will exit through port Y (called the reflection port) when the wavelength is off resonance, and exit through port Z (called the transmission port) when on resonance. Typical spectra from these ports for the race-track resonator device are shown in Fig. 4, where a switching efficiency of 80% was achieved. Resonance linewidth as small as 0.2 nm and cavity Q factors as high as 10,000 have also been obtained.

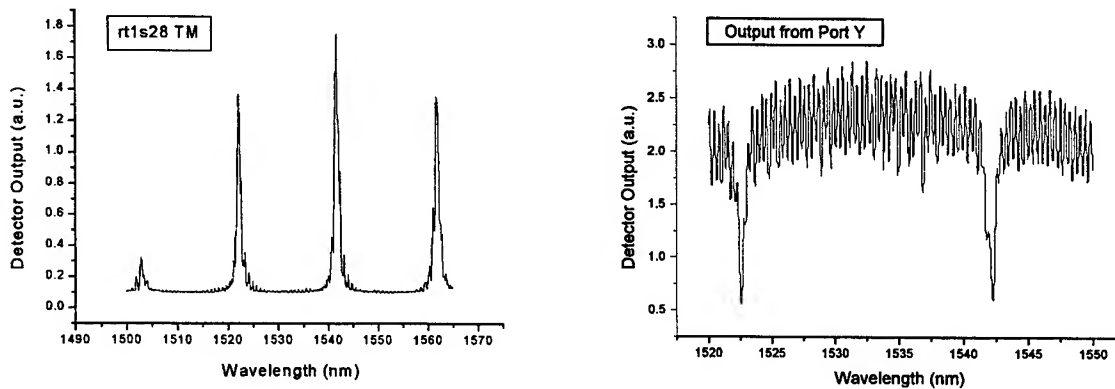


Fig. 4: (a) Reflection spectrum at output Y:
The oscillations are due to the Fresnel reflections.

b) Transmission spectrum at output Z.
Note the different wavelength range.

Using the race-track resonators as a building block, we have fabricated more sophisticated photonic integrated circuits such as 2 by 2 cross-bar switches and 1 by 8 and 1 by 16 wavelength multiplexer/demultiplexers. The SEM pictures of these devices are shown in Fig. 5. These devices illustrate the functional versatility and the size advantage of microcavity resonators. The $N \times N$ crossbar switch, for example, is a scalable add-drop matrix switch, an essential component for optical add-drop multiplexers (OADM) and optical cross-connects (OXC). The resonator-to-resonator spacing can be as small as $50 \mu\text{m}$, which means that the size of an $N \times N$ OXC fabric may be no more than $50N \times 50N \mu\text{m}^2$. In principle, optically transparent OXC can be achieved by incorporating optical amplifiers in the circuit to compensate for the propagation loss.

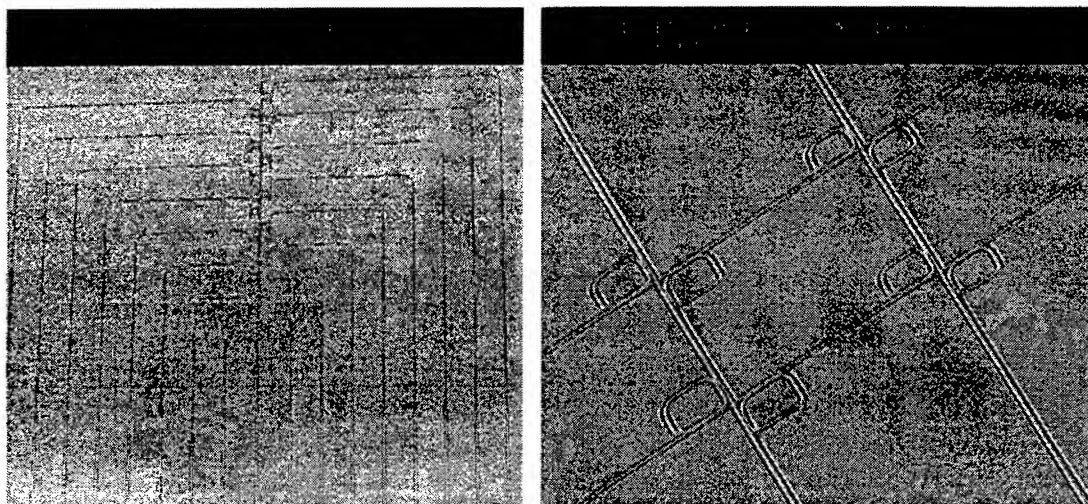


Fig. 5: (a) $1 \times N$ ($N = 16$) demultiplexer, (b) 2×2 crossbar switches

In multi-resonator devices, the resonators are designed to be slightly different in length according to the targeted resonance wavelengths. In practice, the resonance wavelengths are very sensitive to any variation or deviation in the cavity length and may need to be actively controlled, for example, by electro-optic tuning.

High density integrated optics for WDM requires a wide array of ultra-compact devices, not just filters and multiplexers (wavelength-sensitive devices), but also couplers and switches (broadband devices), as well as the ubiquitous curved waveguides and crossovers. In fact, in conventional integrated optics, the level of integration is limited by the size of curved waveguides as well as the active device dimensions. On the other hand, curves in nanophotonic waveguides is not an issue as amply evident in the microring resonators. Couplers and switches based

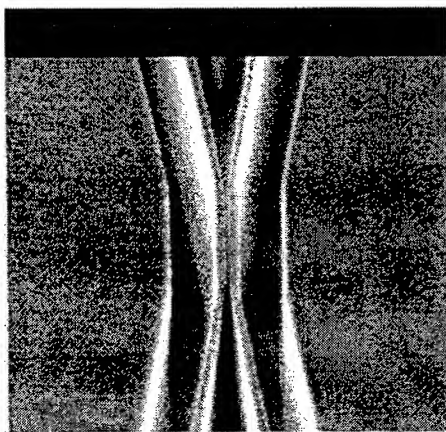
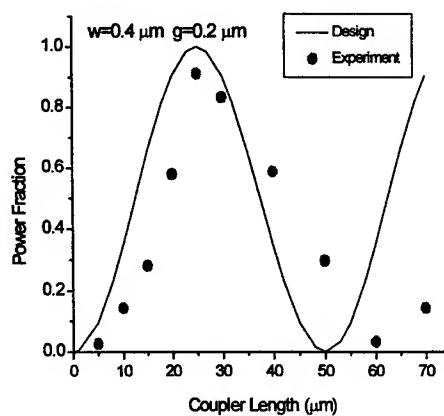


Fig. 6: (a) An SEM image of a coupler.



(b) measured results of power coupling.

on nano-photonic waveguides can be significantly smaller than the conventional devices, not only in the coupling region but more significantly in the input and output sections where curved waveguides, such as S-bends, are used. A fabricated coupler with a length of only 3 μm and a gap size of 0.15 μm is shown in Fig. 6(a). Fig. 6(b) shows the measured power transfer for different coupler lengths in the case of $w = 0.4 \mu\text{m}$ and $g = 0.2 \mu\text{m}$. Note that full power transfer occurs at $L_c = 25 \mu\text{m}$, making this probably the shortest directional coupler ever demonstrated.

In conclusion, we have designed and demonstrated ultra-compact directional couplers and race-track micro-resonators as nano-photonic building blocks for a range of WDM devices, including channel-dropping filters, $1 \times N$ demultiplexers and 2×2 crossbar switches.

References:

- [1] D. Rafizadeh, J. P. Zhang, S. C. Hagness, A. Taflove, K. A. Stair, S. T. Ho, "Waveguide-coupled AlGaAs/GaAs microcavity ring and disk resonators with high finesse and 21.6-nm free spectral range", *Optics Letts.*, vol. 22, pp. 1244-1246, 1997.
- [2] B. E. Little, J. Foresi, H.A. Haus, E. P. Ippen, W. Greene, and S. T. Chu, "Ultra-compact Si/SiO₂ micro-ring resonator channel dropping filter," *IEEE Photon. Technol. Lett.*, vol. 10, pp. 549-551, 1998.
- [3] M. K. Chin and S. T. Ho, "Design and modeling of waveguide-coupled single-mode microring resonators", *J. Lightwave Technol.*, vol. LT-16, pp. 1433-1446, Aug. 1998.

Mode emission properties of semiconductor micro-disk and micro-ring lasers

T.-D. Lee^a, P.-H. Cheng^a, J.-S. Pan^a, K. Tai^a, Y. Lai^{a*}, and K.-F. Huang^b

^aInstitute of Electro-Optical Engineering, National Chiao-Tung University, Hsinchu, Taiwan, ROC

^bDepartment of Electro-Physics, National Chiao-Tung University, Hsinchu, Taiwan, ROC

ABSTRACT

We have successfully fabricated optically pumped semiconductor micro-disk and micro-ring lasers under the InGaAsP/InGaAs system at the 1.5 μ m wavelength and under the InGaP/InGaAlP system at the 0.66 μ m wavelength. The spontaneous emission factor β of these micro-lasers is estimated directly from their output-pump curves and its dependence on the cavity volume is verified. Interesting phenomena regarding the far-field emission pattern and lasing linewidth of these micro-cavity lasers are experimentally observed and theoretically studied.

Keywords: Micro-cavity laser, Micro-disk laser, Micro-ring laser

1. INTRODUCTION

Semiconductor micro-disk and micro-ring lasers have attracted a lot of research interest recently due to their special properties including the high spontaneous emission factor β and the low lasing threshold¹⁻⁶. In such micro-structures with their size comparable to the optical wavelength, the emission property of excited dipoles can be greatly altered compared to the emission properties in the bulk. The underlying physical cause is the quantitative change of the photonic density of states due to strong optical confinement, which is analogous to the electronic counterpart in the presence of strong quantum confinement. Such modification of the emission properties due to optical confinement automatically leads to a cavity-volume dependent spontaneous emission factor β for any micro-cavity laser. In the mean while, the lasing modes of a semiconductor micro-disk laser are whispering-gallery-modes (WGMs) that propagate along the edge of the disk. Due to such a special resonant structure, the emission properties of micro-disk lasers exhibit many interesting differences compared to typical edge emitting lasers. The aim of this paper is to report our recent results on investigating these interesting properties.

We have successfully fabricated optically pumped semiconductor micro-disk and micro-ring lasers under the InGaAsP/InGaAs system at the 1.5 μ m wavelength⁷⁻⁹ and under the InGaP/InGaAlP system at the 0.66 μ m wavelength¹⁰. The micro-disks can be fabricated either by the pedestal-suspended method illustrated in figure 1(a) or by the epi-transferred method illustrated in figure 1(b). On the other hand, the micro-rings can only be fabricated by the epi-transferred method since the suspended pedestal can not be formed for a micro-ring. Figure 1(c) and (d) shows the SEM pictures of a typical pedestal-suspended micro-disk laser and a typical epi-transferred micro-ring laser fabricated in our lab. One advantage of the epi-transferred method is that one can simultaneously fabricate micro-disks and micro-rings of different sizes using a same wafer such that the comparison of their properties can be more meaningful and trustable.

The first subject of our study is to investigate the cavity volume dependence of the spontaneous emission factor β ^{8,11,12}. We have developed a method that can extract the value of β directly from the measured output-pump curve. By experimentally fabricating a series of micro-ring lasers with different ring-widths on the same wafer and using the epi-transfer method, we verify experimentally the inverse cavity volume dependence of the spontaneous emission factor and achieve a β value as large as 0.14. To clarify the obtained results, we derived a simple expression based on the classical mode counting method, which can give a rough estimate of the β value without requiring detailed cavity mode calculation. The predictions from this expression agree quantitatively with the experimental results for both the InGaAsP/InGaAs micro-lasers at the 1.5 μ m wavelength and the InGaP/InGaAlP micro-lasers at the 0.66 μ m wavelength.

The second subject of our study is to investigate the far-field emission patterns of semiconductor micro-disk lasers^{9,13}. Experimentally we fabricate pedestal-suspended micro-disk lasers along the wafer cleaved edge so that the reflected lights

* Correspondence: E-mail: yclai@cc.nctu.edu.tw; Fax:886-3-5716631; Tel:886-3-5913077

from the substrate will not deteriorate the measurement. The far-field distributions along both the θ and ϕ directions are then measured by a scanning detector. Interesting results including far-field emission angle narrowing along the θ direction and quasi-periodic distribution along the ϕ direction are observed. To explain the observed results, we have derived an expression for the far-field distribution in the cylindrical coordinate based on the scalar diffraction theory. The predictions from this expression agree very well with the measured data. Rigorous calculation based on the vector diffraction theory also yields similar results.

The third subject of our study is to investigate the lasing linewidths of a semiconductor micro-cavity laser under different pumping levels¹⁴. Interesting pump-power dependence of the lasing linewidths is observed for both the micro-disk and micro-ring lasers. We find that the usual theory of laser linewidth is not enough for explaining the results we observe.

The fourth subject of our study is to investigate the emission properties of non-circular micro-lasers¹⁵. We have successfully fabricated semiconductor micro-cavity lasers that have non-circular shapes (i.e., a pentagon shape micro-cavity laser). Optical lasing still can be achieved for these non-circular micro-cavity lasers. Again their far-field distributions are measured and are found to exhibit interesting properties.

In the following we shall present the details of our experimental and theoretical results on the above four subjects. We will also point out some unexplained phenomena that we observed.

2. THE SPONTANEOUS EMISSION FACTOR

The spontaneous emission factor β is defined as the fraction of the spontaneous emission that falls into the cavity mode^{11,12},

$$\beta \equiv \frac{\gamma_c}{\gamma_{sp}} \quad (1)$$

where γ_c is spontaneous emission rate into the cavity mode and γ_{sp} is the net spontaneous emission rate. For a monochromatic dipole, the Fermi golden rule gives the following expression for γ_c :

$$\gamma_c = \frac{2\pi}{\hbar^2} \mu^2 E^2(\vec{r}_a) \rho_c(\omega) \quad (2)$$

Here μ is the dipole moment, and $E(\vec{r}_a)$ is the vacuum field amplitude at the position of the dipole. Since

$$\int dV \epsilon E^2(\vec{r}) = \frac{\hbar\omega}{2} \quad (3)$$

As an estimate, one can assume

$$E^2(\vec{r}_a) = \frac{\hbar\omega}{2\epsilon_0 n^2 V_m} \quad (4)$$

with V_m being the cavity mode volume. In Eq.(2), ρ_c is the optical density of the state and can be simply estimated by:

$\rho(\omega) = 1/\Delta\omega_c$, with $\Delta\omega_c$ being the linewidth of the cold optical cavity. Practically the dipole will have a finite spontaneous emission linewidth $\Delta\omega_{sp}$. If $\Delta\omega_{sp} \ll \Delta\omega_c$, the dipole is effectively monochromatic and Eq.(2) is applicable. However, if $\Delta\omega_{sp} > \Delta\omega_c$, we need to multiply the spectral overlap factor $\Delta\omega_c / \Delta\omega_{sp}$ into Eq.(2) to take into account the spectral broadening effect. For our micro-disks and micro-rings, $\Delta\lambda_{sp}$ is about 30 nm and $\Delta\lambda_c$ is about 1 nm, therefore this spectral overlay factor is needed. Please also note that the mode volume V_c is not necessarily the cavity volume V_m . Actually $V_m \approx V_c w_R / R$ for a disk, where w_R is the width of the whispering gallery mode and R is the disk radius. To account for the spatial overlap effect between the mode field and the dipole distribution, we need to add a spatial overlap factor V_m / V_c in Eq.(2). Finally, it is reasonable to assume that the total spontaneous emission rate γ_{sp} for practical semiconductor micro-disks and micro-rings is roughly the same as the bulk value:

$$\gamma_{sp} = \gamma_b = \frac{\mu^2 \omega^3 n}{3c^3 \hbar \epsilon_0 \pi} \quad (5)$$

With these expressions, we finally obtain

$$\beta = \frac{\lambda}{8\pi\Delta\lambda_{sp}} \left(\frac{\lambda}{n}\right)^3 \frac{1}{V_c} \quad (6)$$

In getting Eq.(6), we have multiplied the result by a factor of 1/3 to account for the randomness in dipole orientation. Eq.(6) actually contains an interesting physical interpretation: the mode counting concept. If we define N_m as the number of mode that a cavity can support, then a reasonable estimate of N will be the bulk density of state times the cavity volume times the dipole emission linewidth. After some algebra, it is easy to find that the β factor in Eq.(6) is simply equal to the reciprocal of N :

$$\beta = \frac{1}{N_m} \quad (7)$$

With this interpretation, one can estimate the β value simply by counting the mode. As an example, let us consider a micro-disk with a diameter of 3 μm . By following the conformal transform and WKB analyses detailed in the literature, we find that there exist four modes in the span of the dipole emission spectrum. The four modes have similar field distribution and are of very high Q . Therefore the mode-counting method will predict the β value to be $1/8 = 0.125$. The additional factor of two is from the degeneracy of counterclockwise and clockwise traveling wave modes. When applying Eq.(7) directly, we obtain $\beta = 0.121$, where $\lambda = 1.5 \mu\text{m}$, $\Delta\lambda_{sp} = 30 \text{ nm}$, and $n = 3.4$ are used. The two values agree well with each other and also with the experimental result to be shown below. For a micro-ring, it supports fewer modes than a micro-disk of the same size and thus will have a larger β .

We now turn to the question about how to determine the β factor experimentally. From the rate equation model of a single-mode laser, the measured pumping power P_m and the measured lasing power P_L at the steady state satisfy the following expression⁸:

$$P_m = (c_1 / \beta) P_L (1 + \beta c_2 P_L) / (1 + c_2 P_L) \quad (8)$$

Here c_1 and c_2 are two unknown constants. By fitting the measured P_L versus P_m curve with this expression, one can determine the β value unambiguously. Figure 2(a) and (b) plot the obtained β values for micro-disk and micro-rings with different disk radius or ring widths. The inverse dependence of the β value on the disk radius or ring width is very obvious. The solid lines in both figures are the predictions from Eq.(6). The agreement is very excellent.

3. THE FAR-FIELD PATTERN IN THE θ DIRECTION

Figure 3(a) illustrates our experimental setup for measuring the far-field distribution. The measured distributions along the θ direction for micro-disks with two different radius are shown in figures 3(b) and (c). The symmetric distribution of the two figures indicates that the reflected lights from the substrate do not interfere our measurement. One special point about the two figures is that the far-field emission angle along the θ direction is much narrower than the prediction from the Fraunhofer diffraction formulation. The thickness of our micro-disk lasers at the 1.5 μm wavelength is 0.2 μm , which is much narrower than the optical wavelength. One would thus expect that the emission angle spreading along the θ direction will be very large according to the Fraunhofer diffraction formulation, but this is not what we observed in figures 3(b) and (c). In order to explain the observed results, we have developed a new far-field diffraction formulation in the cylindrical coordinate based on the scalar diffraction theory and the stationary phase approximation. The final far-field intensity distribution along the θ direction is given by⁹:

$$I(\theta) \propto \left| \frac{F(k \cos \theta)}{H_m^{(2)}(kR \sin \theta)} \right|^2 \quad (9)$$

where R is the disk radius and $F(k_r)$ is the inverse Fourier transform of the near-field distribution. Eq.(9) is to be compared with the result from the Fraunhofer diffraction formulation. The Fraunhofer diffraction theory is derived for a planar near-field distribution and the far-field intensity distribution is given by:

$$I(\theta) \propto \left| F(\sqrt{k^2 - k_y^2} \cos \theta) \right|^2 = |F(k_z)|^2 \quad (10)$$

The main difference between the two expressions is that an additional factor proportional to the inverse square of the Hankel function appears in Eq.(9). This additional factor signifies the geometry difference between a planar near-field distribution and a cylindrical near-field distribution. For practical micro-disks, this additional geometry factor in fact dominates in determining the emission angle θ_{FWHM} . Figure 3(d) shows the comparison between the theoretical predictions from Eq.(9) and the experimental results from figure 3(b) and (c). The agreement is very excellent. We have also performed another calculation based on the more rigorous vector diffraction theory. The obtained results are also similar, as also have been shown in figure 3(d). Our vectorial analysis also verifies that the polarization of the far-field is mainly along the ϕ direction, which again agree with experimental observations.¹⁶

4. THE LASING WAVELENGTHS AND LINEWIDTHS UNDER DIFFERENT PUMP LEVELS

In this section we present our experimental data on the pump power dependence of the single mode lasing wavelengths and linewidths for both micro-disk and micro-ring lasers. Figure 4 shows a series of experimentally measured single mode emission wavelengths versus the pumping power for 3, 5, 8 μm diameter micro-disks and a 5 μm diameter micro-ring. The horizontal axis is the pump power in unit of the threshold pump power, P_{th} . We notice that the emission wavelength is blue shifted as the pump increases. This is in accordance with the usual carrier dependent index effect. As the pump increases further, the wavelength becomes red shifted. Presumably this is due to the thermal effect. Figure 5 shows the corresponding emission linewidth versus pumping power for the same devices used to obtain figure 4. The data points are plotted in solid squares. Again, the horizontal axis is the pump power in unit of the threshold pump power, P_{th} . It is expected that the linewidth will decrease as the pump power increases from zero to the threshold value. The reduction by a factor of 10 is observed for the 8 μm diameter micro-disk at the vicinity of threshold. However, the linewidth remains almost unchanged as the pump increases further. This is different from the cases of conventional single mode semiconductor DFB and DBR lasers, which show the inverse proportionality with the output power when the lasers are pumped above the threshold. However, our observation agrees with the report of Mohideen et al¹⁴. They attributed this finding to strong interplay with the carrier dynamics when the spontaneous and stimulated emission rates at large β are comparable to the carrier equilibration rates. Theoretical calculation of the laser linewidth based on the single mode rate equation analysis gives a well-known expression for the laser linewidth:

$$\Delta\nu = \frac{1}{2\pi} [\gamma_c - \beta r_{sp} (N - N_0)] \quad \text{below threshold} \quad (11)$$

$$\Delta\nu = \frac{1}{2\pi} [\gamma_c - \beta r_{sp} (N - N_0)] \frac{(1 + \alpha^2)}{2} \quad \text{above threshold} \quad (12)$$

where α is the linewidth enhancement factor, N is the carrier number and N_0 is the transparent carrier number. Results from Eq.(11) and (12) are plotted in solid lines and are superimposed with the experimental data in figure 5. It is clear that the agreement is good only when the pump power is near or less than the threshold pumping value. Our study indicates that the analysis based on Henry and Schawlow-Townes linewidth formulation is not adequate for the semiconductor micro-disks or micro-rings. More sophisticated analyses are needed in order to explain these observed results.

5. NON-CIRCULAR MICRO-LASERS AND THE FAR-FIELD PATTERN IN THE ϕ DIRECTION

To investigate the possibility of obtaining highly directional output lights¹⁵, we have fabricated micro-cavity lasers of a pentagon shape under the InGaAsP/InGaAs system at the 1.55 μm wavelength. The fabrication procedures are the same as described in Section 1 except a pentagon mask pattern is used. Figure 6(a) shows the SEM of a 8 μm outer-diameter pentagon micro-laser right on the edge of the cleaved wafer. Optical lasing still can be achieved for this type of lasers. The lasing spectra as well as the output versus pump curve are shown in figure 6(b) and (c). The experimental results we observed do not give an obvious 5-peaks far-field distribution around the ϕ direction, as one might expect intuitively. Instead, the measured far-field emission distribution exhibits quasi-periodic distribution as shown in figure 6(d). Similar quasi-periodic distributions actually also exhibit in the measured results for circular micro-disks of different disk radius, as have been shown in figure 6(e) and (f). The period of the quasi-periodic distributions is a function of the disk radius and is not equal to the period of the standing wave pattern as one might expect. We are still searching for a reasonable explanation for these observed results.

6. CONCLUSIONS

We have presented the results of our recent investigation on semiconductor micro-disk and micro-ring lasers. Properties about the spontaneous emission factor and the far-field emission pattern of these micro-lasers have been clarified both experimentally and theoretically. Some interesting results about the lasing linewidth and the far-field distribution along the ϕ direction are experimentally observed and further studies are needed. We hope these results can serve as a basis for future investigation along this direction.

ACKNOWLEDGMENTS

This research was supported in parts by National Science Council of Taiwan, R.O.C.

REFERENCES

1. S. L. McCall, A. F. Levi, R. E. Slusher, S. J. Pearton, and R. A. Logan, "Whispering-gallery mode microdisk lasers," *Appl. Phys. Lett.* **60**, pp.289-291, 1992.
2. A. F. Levi, R. E. Slusher, S. L. McCall, T. Tanbun-Ek, D. L. Coblenz and S. J. Pearton, "Room temperature operation of microdisk lasers with submilliamp threshold current," *Electron. Lett.*, **28**, pp.1010-1011, 1992.
3. M. J. Rise, E. I. Chen, N. Holonyak, Jr., G. M. Iovino and A. D. Minervini, "Planar native-oxide-based AlGaAs-GaAs-InGaAs quantum microdisk lasers," *Appl. Phys. Lett.* **68**, pp.1540-1542, 1996.
4. M. Fujita, K. Inoshita and T. Baba, "Room temperature continuous wave lasing characteristics of GaInAsP/InP microdisk injection laser," *Electron. Lett.* **34**, pp.278-279, 1998.
5. B. Corbett, J. Justice, L. Considine, S. Walsh, and W. M. Kelly, "Low-threshold lasing in novel microdisk geometries," *IEEE Photonic Tech. Lett.*, **8**, p.855-857, 1996.
6. J. P. Zhang, D. Y. Chu, S. L. Wu, S. T. Ho, W. G. Bi, C. W. Tu, and R. C. Tiberio, "Photonic-wire laser," *Phys. Rev. Lett.*, **75**, pp.2678-2681, 1995.
7. T. D. Lee, P. H. Cheng, J. S. Pan, K. Tai and Y. Lai, "Mode emission characteristics of semiconductor micro-disk and micro-ring lasers," *Opt. Quant. Electron.* **28**, pp.1335-1341, 1996.
8. P. H. Cheng, T. D. Lee, J. S. Pan, Y. Lai and K. Tai, "Spontaneous emission factor versus cavity volume in low dimensional photonic micro-cavities," *Opt. Comm.* **142**, p.229-233, 1997.
9. T. D. Lee, P. H. Cheng, J. S. Pan, R. S. Tsai, Y. Lai, and K. Tai, "Far-field emission narrowing effect of micro-disk lasers," *Appl. Phys. Lett.* **72**, pp.2223-2225, 1998.
10. J. S. Pan, P. H. Cheng, T. D. Lee, Y. Lai, and K. Tai, "0.66 μ m InGaP/InGaAlP single quantum-well micro-disk lasers," *Japanese Journal of Applied Physics* **37**, pp.643-645, 1998.
11. M. K. Chin, D. Y. Chu, and S. T. Ho, "Approximate solution of the whispering gallery modes and estimation of the spontaneous emission coupling factor for microdisk lasers," *Opt. Comm.* **109**, pp.467-471, 1994.
12. M. K. Chin, D. Y. Chu, and S. T. Ho, "Estimation of the spontaneous emission factor for microdisk lasers via the approximation of whispering gallery modes," *J. Appl. Phys.*, **75**, pp.3302-3307, 1994.
13. B.-J. Li and P.-L. Liu, "Analysis of Far-Field Patterns of microdisk resonators by the finite-difference time-domain Method," *IEEE J. Quantum Electron.*, **33**, p.1489, 1997.
14. U. Mohideen, R. E. Slusher, F. Jahnke, and S. W. Koch, "Semiconductor microlaser linewidth," *Phys. Rev. Lett.* **73**, pp.1785-1788, 1994.
15. A. F. Levi, R. E. Slusher, S. L. McCall, J. L. Glass, S. J. Pearton, and R. A. Logan, "Directional light coupling from microdisk lasers," *Appl. Phys. Lett.* **62**, pp.561-563, 1993.
16. N. C. Frateschi, A. P. Kanjanmata, and A. F. Levi, "Polarization of lasing emission in microdisk laser diodes," *Appl. Phys. Lett.*, **66**, p.1859-1861, 1995.

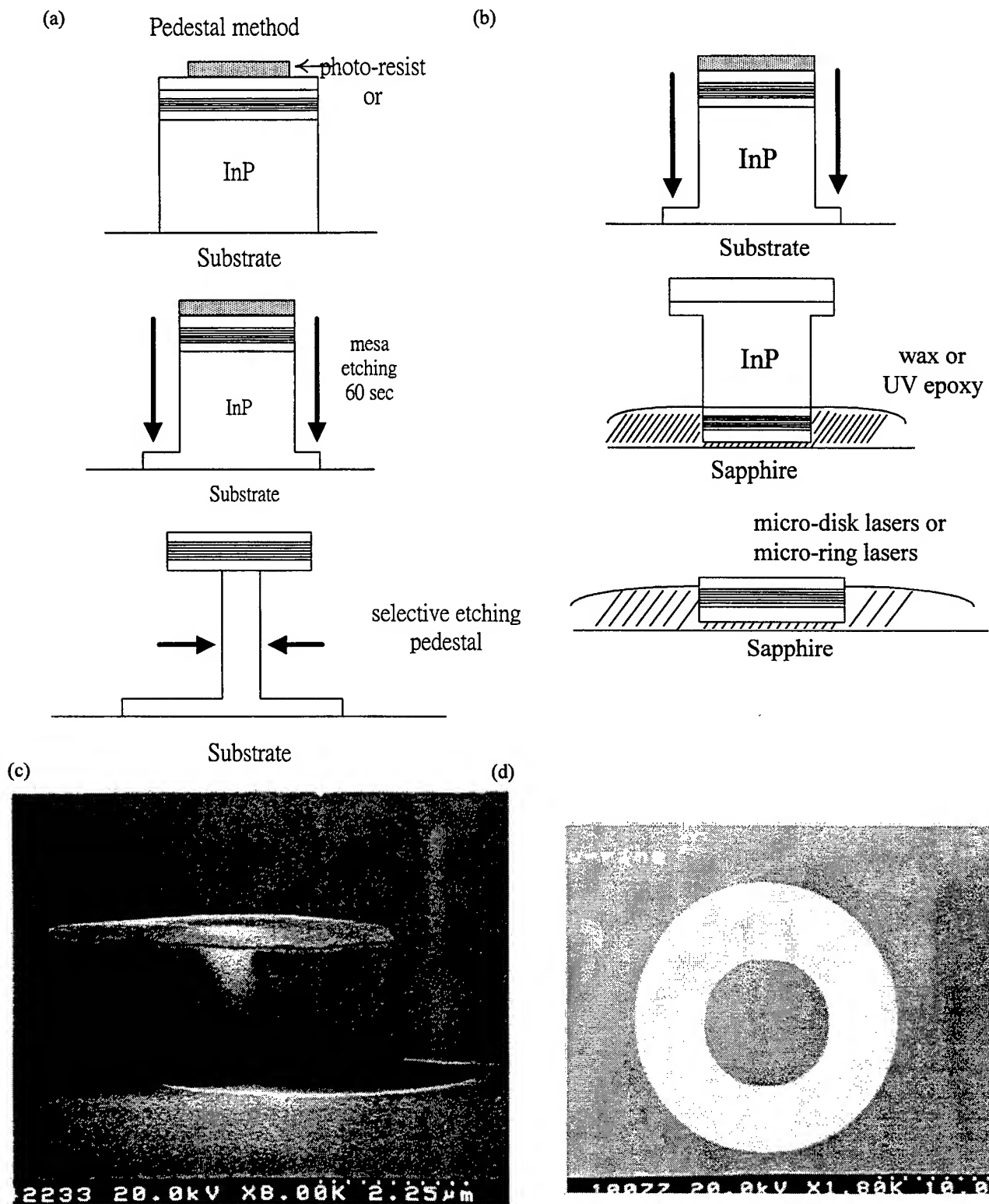


Figure 1: (a) Fabrication of pedestal suspended micro-disk lasers; (b) Fabrication of epi-transferred micro-disk or micro-ring lasers; (c) SEM of a pedestal suspended micro-disk; (d) SEM of a epi-transferred micro-ring.

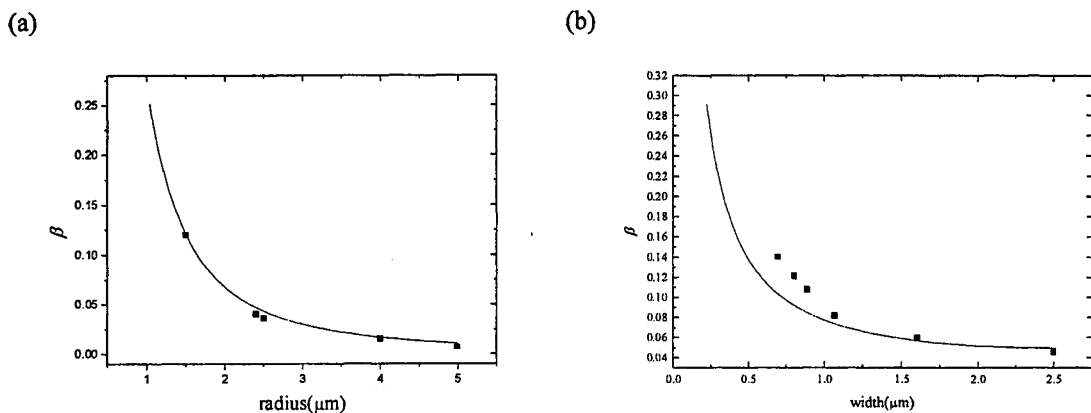


Figure 2: (a) The β values of micro-disk lasers with different radius; (b) The β values of micro-ring lasers with a same outer radius but different ring widths. Dot points: experimental data; Solid line: theoretical predictions.

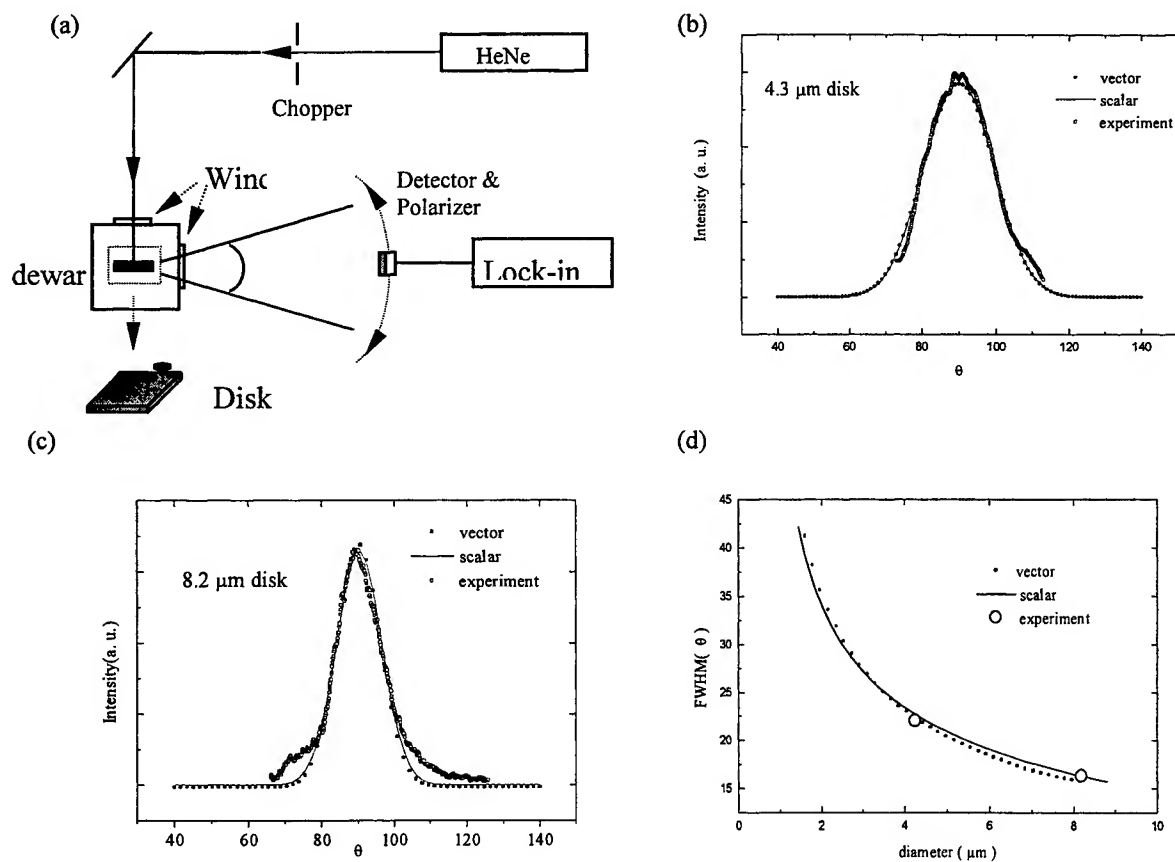


Figure 3: (a) Experimental setup for measuring the far-field pattern; (b) far-field pattern of a 4.3 μm micro-disk; (c) far-field pattern of an 8.2 μm micro-disk; (d) Comparison of theoretical predictions with the experimental data.

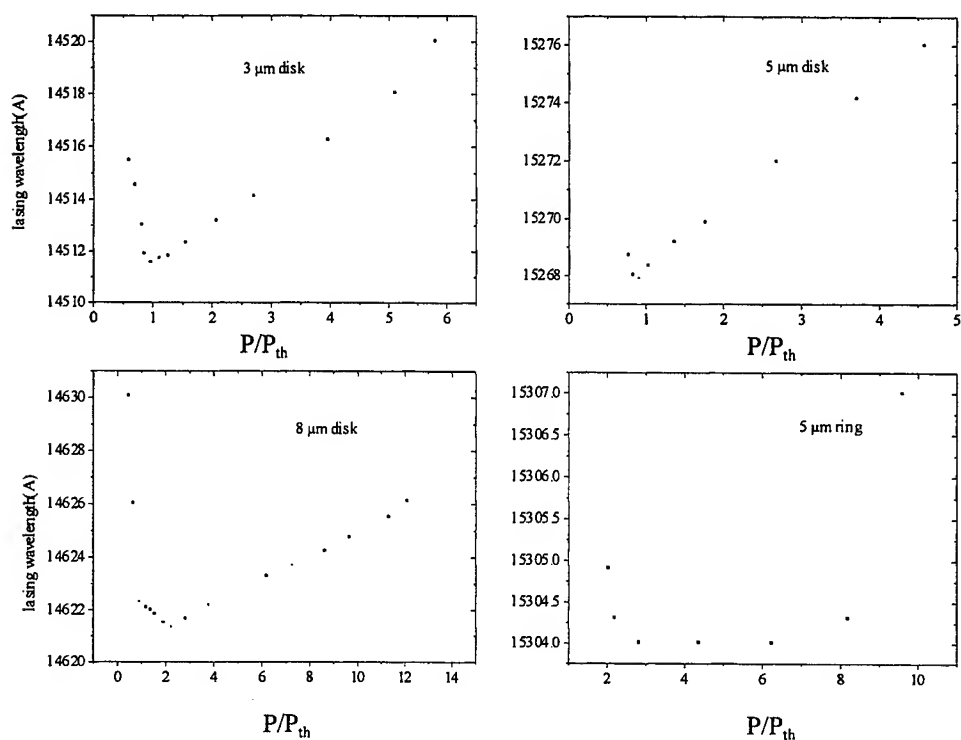


Figure 4: Lasing wavelengths of micro-disk and micro-ring lasers at different pump levels.

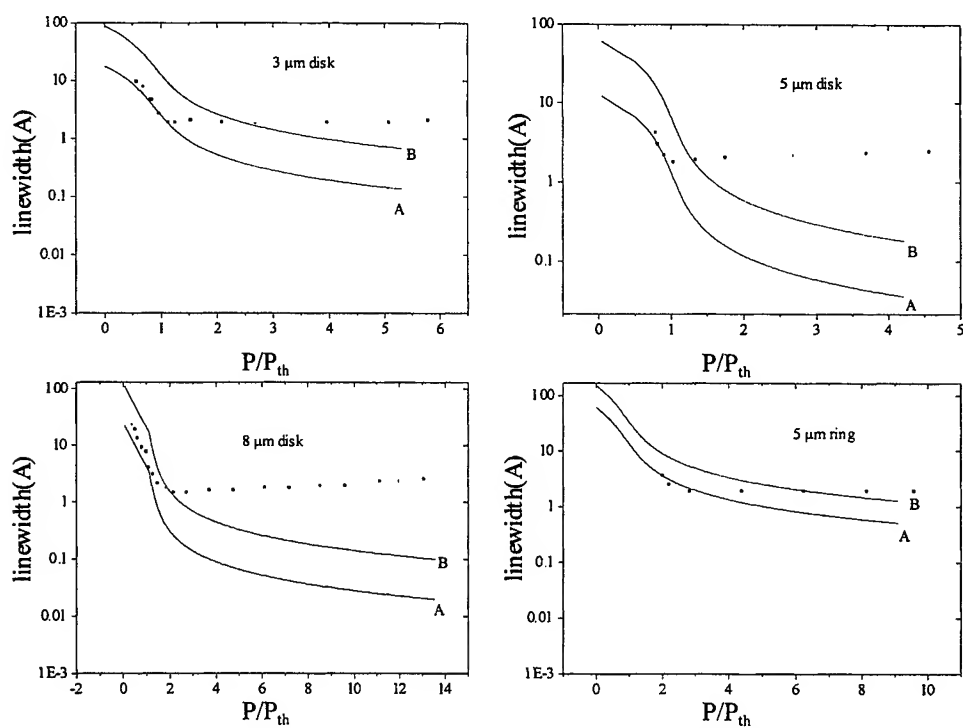


Figure 5: Lasing linewidths of micro-disk and micro-ring lasers at different pump levels. Dot points: experimental data; Solid line: theoretical predictions.

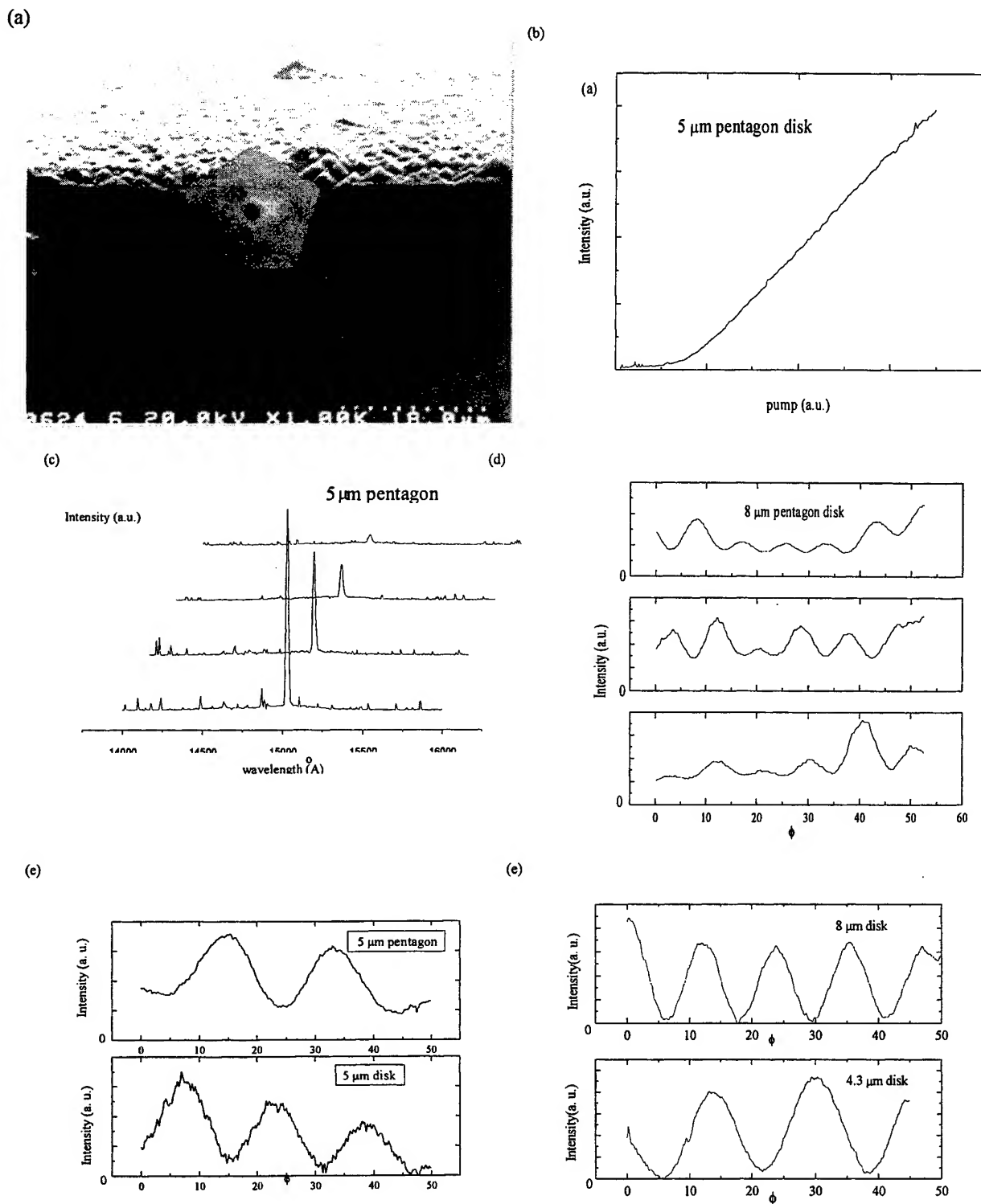


Figure 6: (a) SEM of a pentagon micro-laser on the wafer cleaved edge; (b) pump-output curve of a 5 μm pentagon micro-laser; (c) Lasing spectra of a 5 μm pentagon micro-laser; (d), (e), (f) far-field patterns along the ϕ direction for different micro-disk and micro-pentagon lasers.

Optical Properties of InGaN Multiple Quantum Well Microdisks

Lun Dai^a, Bei Zhang^{*a}, Yu Zhang^a, RuoPeng Wang^a, Xing Zhu^a, J. Y. Lin^b, and H. X. Jiang^b

a. Department of Physics and State Key Laboratory for Mesoscopic Physics,

Peking University, Beijing, 100871, China

b. Department of Physics, Kansas State University, Manhattan, KS 66506-2601, USA

ABSTRACT

$\text{In}_{0.22}\text{Ga}_{0.78}\text{N}/\text{In}_{0.06}\text{Ga}_{0.94}\text{N}$ multiple quantum well (MQW) microdisks with a size of 5.6 μm in diameter have been fabricated by photolithography and ion beam etching. Time-resolved photoluminescence (PL) has been employed to study optical transitions in MQW structure and microdisks. The dominant emissions from both MQW structures and microdisks were from localized exciton transitions. It was found in the microdisks that the low energy shoulder of the PL spectrum was quenched, and that the spontaneous emission line width was narrower while its intensity was enhanced with respect to that of the MQWs, which may be related to microcavity effects in the microdisks. A blue shift of the PL peak from the MQW microdisks compared with that in the MQW structures was also observed, and can be understood in terms of a reduced piezoelectric field due to strain relief in the microdisks. Microdisks with grating patterned micro-couplers around the disk edges were also fabricated by e-beam lithography to enhance light extraction from the microdisks. Near-field scanning optical microscopy (NSOM) was employed to map the near-field fluorescence images of the microdisks, which showed a strong emission preference in certain directions. The potential applications of III-nitride microdisks for optical interconnects and integration are also discussed.

Keywords: optical microcavity, optical microdisk, III-nitrides, InGaN MQW, photoluminescence, piezoelectric field, optical modes, NSOM, PL

1. INTRODUCTION

The study of optical microcavities is very important both in terms of fundamental physics as well as device applications^{1,2}. Since McCall et al demonstrated optically pumped semiconductor microdisk lasers in 1992³, the microdisk cavity has been widely studied⁴⁻⁷. Because of their small size and symmetry, microdisk lasers have advantages over edge emitting lasers, including strong optical confinement to the gain region, high quantum efficiency, high quality factor Q , and a low lasing threshold⁸⁻¹⁰. Significant improvements¹¹ in III-nitrides have led to rapid progress in their applications in optoelectronic and high-temperature/power electronic devices. InGaN alloys are important materials and attract special attention because of their applications in UV/blue light emitting diodes (LEDs) and laser diodes (LDs). The emission mechanisms in InGaN alloys and MQWs are currently under intensive investigations.

With many potential applications in optoelectronics, research on the III-nitride microcavity has become an intriguing field. Recently, several types of nitride microcavities have been fabricated and investigated¹²⁻¹⁷, including microdisks, microrings, and micropyramids^{13, 14}. Optical resonance modes have been observed in both GaN/AlGaIn and InGaIn/GaN MQW microdisks and microrings by optical pumping¹⁵⁻¹⁷. An enhancement of the intrinsic optical transition efficiency was also observed in the GaN/AlGaIn microdisks.

In this paper, we report the optical properties of $\text{In}_{0.22}\text{Ga}_{0.78}\text{N}/\text{In}_{0.06}\text{Ga}_{0.94}\text{N}$ multiple quantum well (MQW) microdisks with diameters of 5.6 μm . They were fabricated by UV photolithography and ion beam etching. Microcavity effects in these microdisks were observed and investigated. To enhance the light extraction from the microdisks, micro-couplers with grating patterns around the disk edges were fabricated by e-beam lithography. Preliminary results from these microdisks with micro-couplers measured by near-field scanning optical microscope (NSOM) are also presented.

2. MQW MICRODISKS

2.1 Experimental

The MQW structure was grown on a (0001) sapphire substrate by metal-organic chemical vapor deposition (MOCVD). It consists of a buffer layer, a 2.5 μm GaN epilayer, and an $\text{In}_{0.22}\text{Ga}_{0.78}\text{N}/\text{In}_{0.06}\text{Ga}_{0.94}\text{N}$ MQW structure with a total of four wells and

*Correspondence: E.mail: beizhang@ibm320h.phy.pku.edu.cn; Telephone: 086 010 62751739; Fax: 086 010 62751615

five barriers. The well and the barrier thicknesses are 20 Å and 100 Å, respectively. Photolithography and ion beam etching were employed to fabricate arrays of microdisks with diameters of 5.6 μm and spacings of 50 μm. The MQW structure was etched down to the sapphire substrate so that no III-nitride material was left between the microdisks.

Time-resolved PL spectra were measured for both $\text{In}_{0.22}\text{Ga}_{0.78}\text{N}/\text{In}_{0.06}\text{Ga}_{0.94}\text{N}$ MQW structures and the MQW microdisks. Excitation laser pulses with a pulse width of about 10 ps and a repetition rate of 9.5 MHz were provided by a cavity-dumped dye laser, which was pumped by an yttrium-aluminum-garnet (YAG) laser with a frequency doubler. The output from the dye laser was frequency doubled again by a second frequency doubler to provide tunability in the UV region. The laser output after the second doubler has an average power of about 20 mW and a tunable photon energy up to 4.5 eV. The laser wavelength chosen was 290 nm and had a spot size of about 0.3 mm. The PL detection system consists of a 1.33 m monochromator, a fast micro-channel plate photo-multiplier-tube (MCP-PMT), and a single photon counting system. It provides a spectral resolution of about 0.2 meV and an overall time response of about 25 ps.

2.2 Results

Fig. 1 is an SEM image of an $\text{In}_{0.22}\text{Ga}_{0.78}\text{N}/\text{In}_{0.06}\text{Ga}_{0.94}\text{N}$ MQW microdisk with a diameter of 5.6 μm. Fig. 2 is the low-temperature (10K) cw PL spectra of a MQW (a) structure and (b) microdisk under similar excitation conditions. The peak position of the dominant transition from the MQW structure was at 2.778 eV. Interference fringes located at the lower energy shoulder (2.683 eV and 2.573 eV) were also observed. In comparison, the low energy shoulder of the PL spectrum from the microdisks was quenched, and the line width was narrower. The PL peak position of the microdisks was at 2.831 eV, which was blue shifted by an amount of 53 meV with respect to that of the MQW structures. Taking into account the difference in the effective pumping areas between the MQW structures and the microdisks, the PL intensity in the microdisks was enhanced by a factor of 2.5 compared with that of the MQWs. The observed (i) enhanced quantum efficiency, (ii) blue-shift of emission peak position, and (iii) narrower line width in microdisks compared with those in MQW structure may be related to microcavity effects in the microdisks.

It should also be noted that a red-shift of the emission spectra was observed in the nitride MQW structure compared with that of epilayers, which is now understood to be due to lattice mismatch induced piezoelectric or crystal symmetry induced polarization field in MQWs¹⁸⁻²³.

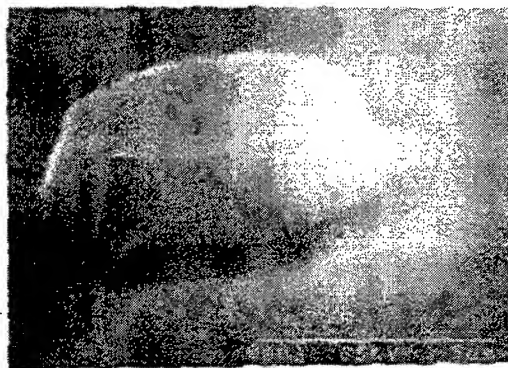


Fig. 1 SEM image of an $\text{In}_{0.22}\text{Ga}_{0.78}\text{N}/\text{In}_{0.06}\text{Ga}_{0.94}\text{N}$ MQW microdisk with a diameter of 5.6 μm.

Fig. 3 is a schematic diagram of the energy levels in $\text{In}_{0.22}\text{Ga}_{0.78}\text{N}/\text{In}_{0.06}\text{Ga}_{0.94}\text{N}$ MQWs (a) with a strain induced piezoelectric and (b) without a piezoelectric field. For the MQWs studied here, the localized exciton transition energy is determined by (a) the energy gap of the $\text{In}_x\text{Ga}_{1-x}\text{N}$ wells, where $E_g(\text{eV}) = 3.4(1-x) + 1.9x - 3.2x(1-x)$ for $\text{In}_x\text{Ga}_{1-x}\text{N}$,¹⁸ (b) the quantum confinement energies of the electron and hole, (c) the exciton binding energy, (d) the exciton localization energy, and (e) the piezoelectric field induced energy shift. As shown in Fig. 3(a), the energy level of the $\text{In}_{0.22}\text{Ga}_{0.78}\text{N}/\text{In}_{0.06}\text{Ga}_{0.94}\text{N}$ strained MQWs was decreased by the piezoelectric field, which reduces the transition energy of excitons in the MQWs and also increases the separation of the electron and hole ground-state wave functions, i.e., causes a reduced recombination rate.

A finite size MQW is required in order to sustain the lattice mismatch induced strain and the piezoelectric field. It is conceivable that strain relief would occur when the size of the MQW microdisk is smaller than a critical dimension. In that case, the piezoelectric field would be reduced and the transition energy of excitons would be increased, as is shown in Fig. 3(b). If this

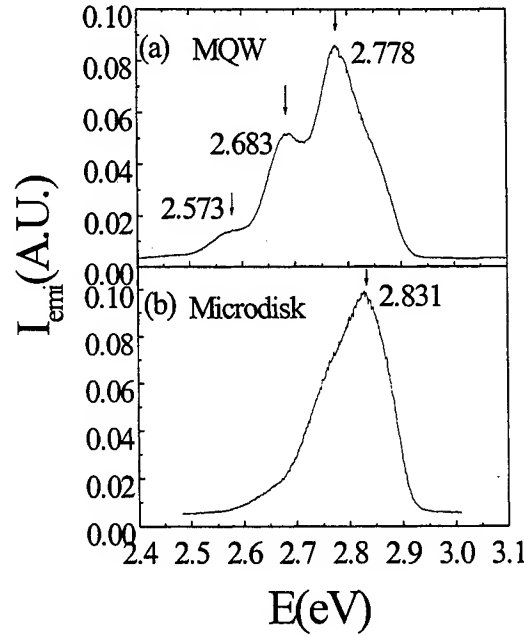


Fig.2. The cw PL spectra ($T=10\text{K}$) measured for (a) a MQW structure and (b) a MQW microdisk.

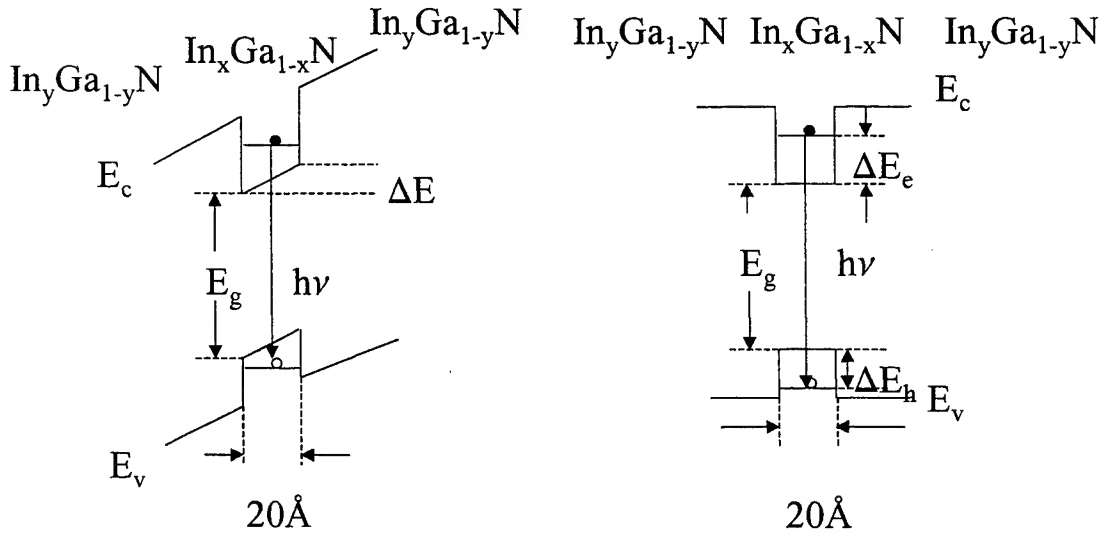


Fig. 3 Schematic diagram of energy levels in $\text{In}_{0.22}\text{Ga}_{0.78}\text{N}/\text{In}_{0.06}\text{Ga}_{0.94}\text{N}$ MQWs (a) with a strain induced piezoelectric field and (b) without a piezoelectric field.

is the case, the 53 meV blue shift observed in the microdisk (Fig. 2) corresponds to the amount of energy gained when strain was relieved in microdisks. The amount of the piezoelectric field in the $\text{In}_{0.22}\text{Ga}_{0.78}\text{N}/\text{In}_{0.06}\text{Ga}_{0.94}\text{N}$ MQW can thus be estimated as $53\text{ mV}/20\text{ Å}=0.27\text{ MV/cm}$. This value should represent the lower limit of the piezoelectric field strength in the $\text{In}_{0.22}\text{Ga}_{0.78}\text{N}/\text{In}_{0.06}\text{Ga}_{0.94}\text{N}$ MQW since most likely the strain is only partially relieved in the microdisks. However, this value is comparable to that reported previously¹⁸. This result clearly demonstrates that the optical properties of III-nitride MQW microdisks are quite different from those of MQW structures.

Figure 4 is the semi-logarithmic plots of the decay of PL measured at 10K for both a MQW structure and a microdisk at

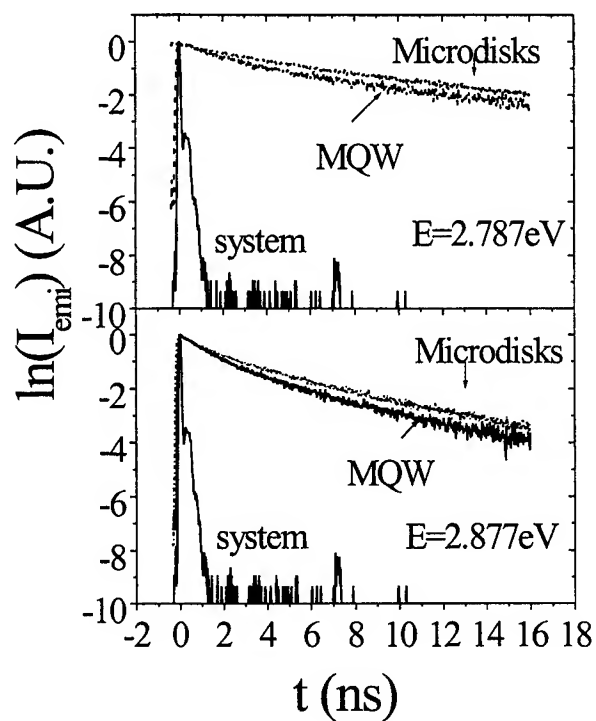


Fig. 4 Temporal response of the intrinsic exciton recombination measured at 10K for $\text{In}_{0.22}\text{Ga}_{0.78}\text{N}/\text{In}_{0.06}\text{Ga}_{0.94}\text{N}$ MQW and microdisks structure at emission energies of 2.787eV and 2.877eV, respectively. System response of about 25 ps is also indicated.

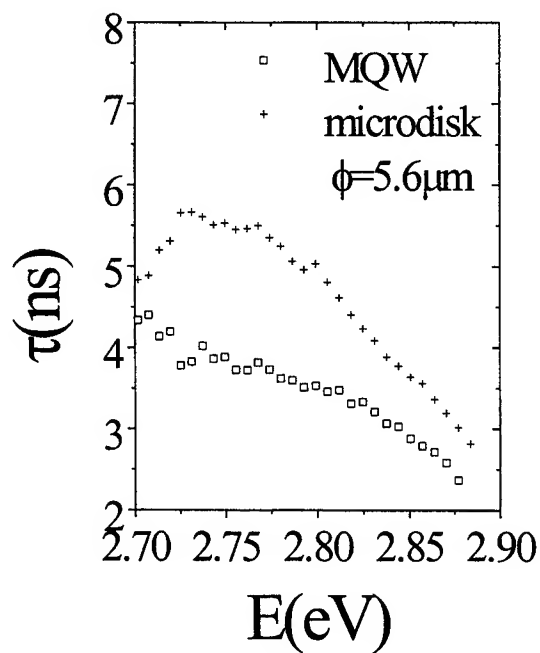


Fig.5. Emission energy dependence of PL decay lifetimes in $\text{In}_{0.22}\text{Ga}_{0.78}\text{N}/\text{In}_{0.06}\text{Ga}_{0.94}\text{N}$ MQWs and microdisks measured at $T=10$ K.

emission energies of 2.787 eV and 2.877 eV. The system response to the laser pulses (7ps width) is indicated as "system". The decays of both samples are single exponential, $I(t)=I_0\exp(-t/\tau)$, where τ defines the recombination lifetime. From Fig. 4, the decay of PL emission is slower in the MQW microdisks than that in MQW structures. The emission energy dependencies of the recombination lifetimes for both samples are plotted in Fig. 5. It was observed from Fig. 5 that the PL decay lifetimes, τ , are in the nanosecond and that they decrease with an increase of emission energy for both MQWs and microdisks. However, the decay lifetime is longer in microdisks than in MQWs for all emission energies. The decrease of decay lifetimes with emission energy, $d\tau/dE$, at the higher energy shoulder for microdisks is also larger than that of MQWs.

3. MICRODISKS WITH GRATING COUPLERS

3.1 Design and Experimental

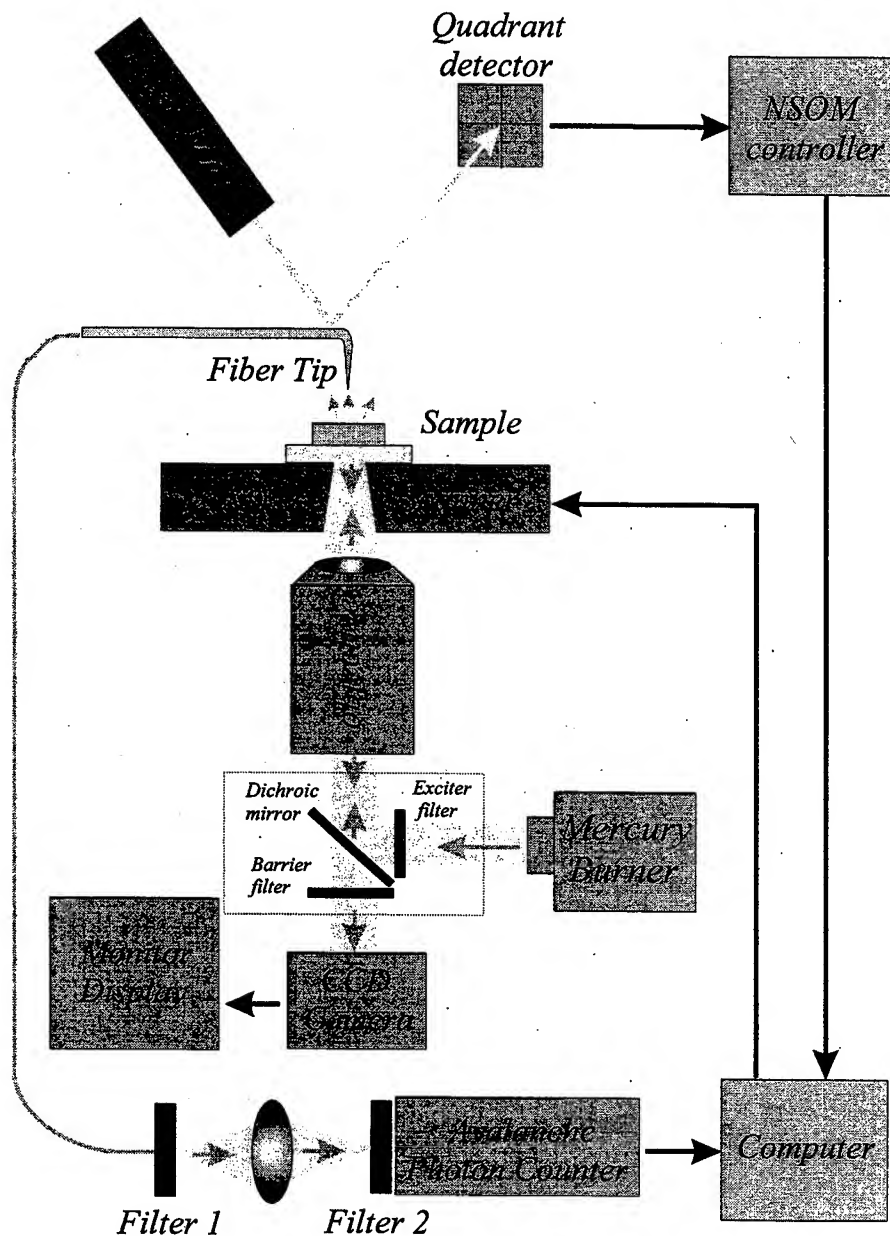


Fig.6 Schematic diagram of near-field scanning optical microscope (NSOM) in a transmission illumination mode.

An ideal circular microdisk laser emits radiation in a pattern with radial symmetry in the disk plane, which is also called a whispering-gallery (WG) mode microdisk laser. In this case, light emission is confined to a small angle centered on the disk plane³. However, it is necessary to control both the direction and intensity of the light output²⁴ for practical applications, such as in optical interconnects and integration.

In order to couple the light from WG mode microdisks directionally, we have investigated the possibility of fabricating micro-couplers on top of the microdisks. Our output coupler is patterned with a grating structure around the microdisk edge with a period of roughly 8 WG mode wavelengths. The coupler was patterned on the top of microdisks by using raster scan electron-beam lithography with PCMS negative resist material (thickness of 300 nm).

A commercial near-field scanning optics microscope (NSOM-100; RHK/Nanonics)²⁵ was employed to map the near-field fluorescence images of the microdisks both with and without micro-couplers. As shown in Fig. 6, the microdisk sample was located at the center of the flat xyz scanner. This system is capable of taking near-field images and normal force (contact mode or AC mode) atomic force microscopy images simultaneously using the same cantilevered tip. The flat scanner (Nanonics) has a scan range of 30 μm in the x, y, and z directions. The fiber probe used in this experiment was an Al-coated single mode fiber ($\lambda=630\text{nm}$), with a diameter of 100 nm. The optical signal was collected by a sensitive avalanche photon-detector (APD) module with a dark count of less than 100 counts per second. We used the transmission illumination offered by an inverted microscope (Olympus IX-70), since the sapphire substrate was transparent. The light source was a 100 W Hg lamp. A dichronic filter cube was used to provide a band-pass at 360-380 nm for the excitation as well as for transmission of fluorescence with wavelengths larger than 400 nm. Filters 1 and 2 in Fig. 4 were used to block out the 670 nm regulation laser and the 365nm excitation laser, respectively.

3.2 Results

Shown in Fig. 7 are the near-field fluorescent images of (a) a microdisk without a micro-coupler, (b) a plane view of a microdisk with a micro-coupler grating pattern, and (c) a perspective view at a constant height of a microdisk with a micro-coupler grating pattern. The near-field fluorescent images were acquired in constant-height mode. To prevent the tip from crashing into the disk edge, the fiber tip was engaged on the top surface of the disk under a long-working distance objective lens, and then retracted by adjusting the z-offset voltage. The excitation light was directly guided into the microdisk area with an output intensity of 15mW. The illumination laser beam was unfocused with a diameter of about 2-3 mm (Fig.6). For both plane view and perspective view, a bright illumination with ring features around the disk edge from the WG modes were observed.

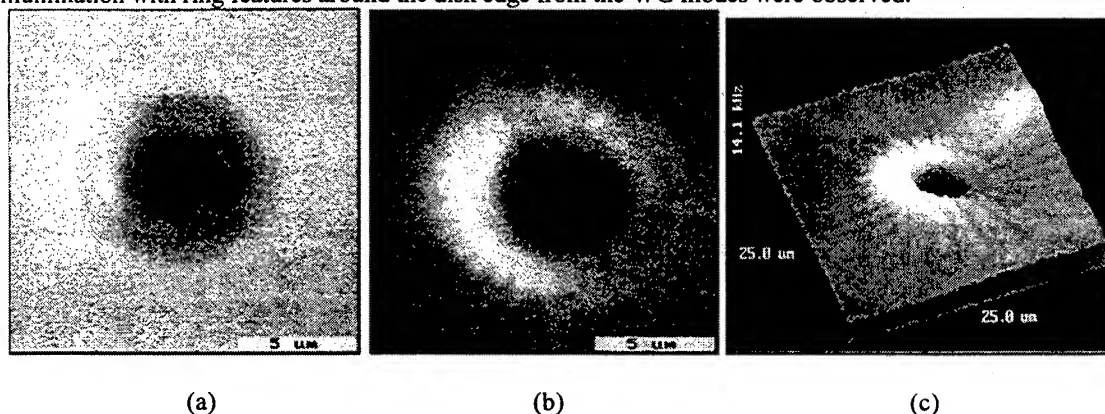


Fig.7 Near-field optical images of (a) a microdisk, (b) a microdisk with a grating coupler (plane view), and (c) a microdisk with grating coupler (perspective view at a constant height).

Near-field optical microscopy detects the non-propagating part of the wave spectrum and provides another view of the light distribution. In fact, the near-field probe acts as a tiny antenna to convert the non-propagating evanescent wave into a propagating one, which is subsequently guided to the APD detector. Hence, the bright rings in Fig. 7b at the disk edge represent the local evanescent-wave distribution, which cannot be observed by far-field microscopy.

Compared to the microdisks without micro-couplers, the microdisk with micro-couplers has a much brighter ring feature around the edge of the disk as well as some bright illumination along the radial directions of the microdisks. This indicates that the microdisks with micro-coupler grating patterns have a strong local evanescent-wave distribution both in the vertical direction as well as in certain directions where the guided structures are made on the sample surface. This result indicates that the micro couplers patterned on the top of the microdisks can modify and select radiation patterns without degradation of the Q value of the microdisks.

4. SUMMARY

In summary, the optical properties of $\text{In}_{0.22}\text{Ga}_{0.78}\text{N}/\text{In}_{0.06}\text{Ga}_{0.94}\text{N}$ MQWs microdisks have been investigated by picosecond time-resolved PL spectroscopy. By comparing to PL spectra from $\text{In}_{0.22}\text{Ga}_{0.78}\text{N}/\text{In}_{0.06}\text{Ga}_{0.94}\text{N}$ MQWs, our results have suggested that the elastic strain was relieved and thus the piezoelectric field was reduced in microdisks. An initial work of directional coupling of light from WG emitting modes from microdisks with micro-coupler gratings patterned on the top of microdisks was presented. Our results provide some useful information for the future III-nitride microdisk lasers, which have many potential applications in optoelectronics

ACKNOWLEDGEMENTS

The research at Peking University was supported by National Natural Science Foundation of China (NNSFC) projects of Nos. 69687007, 19774008, and 69686260, 19674004, the opening projects of State Key Laboratory for Mesoscopic Physics of China and State Key Laboratory for Integrated Electro-Optics of China. The research at Kansas State University is supported by NSF (INT-9729582).

REFERENCES

1. Serge Haroche and Daniel Kleppner, "Cavity Quantum Electrodynamics," *Physics Today*, pp. 24-30, 1989.
2. Yoshihisa Yamamoto and Richard E. Slusher, "Optical Processes in Microcavities," *Physics Today*, pp. 66-73, 1993.
3. S. L. McCall, A. F. J. Levi, R. E. Slusher, S. J. Pearton and R. A. Logan, "Whispering-gallery mode microdisk lasers," *Appl. Phys. Lett.* **60**, pp. 289-291, 1992.
4. D. Y. Chu, M. K. Chin, W. G. Bi, H. Q. Hou, C. W. Tu and S. T. Ho, "Double-disk structure for output coupling in microdisk lasers," *Appl. Phys. Lett.* **65**, pp. 3167-3169, 1994.
5. J. P. Zhang, D. Y. Chu, S. L. Wu, S. T. Ho, W. G. Bi, C. W. Tu and R. C. Tiberio, "Photonic-Wire Laser," *Phys. Rev. Lett.* **75**, pp. 2678-2681, 1995.
6. D. Rafizadeh, J. P. Zhang, S. C. Hagness, A. Taflove, K. A. Stair, S. T. Ho and R. C. Tiberio, "Waveguide-coupled AlGaAs/GaAs microcavity ring and disk resonators with high finesse and 21.6-nm free spectral range," *Optics Letters* **22**, pp. 1244-1246, 1997.
7. Bei Zhang, Ruopeng Wang, Xiaomin Ding, Lun Dai and Shumin Wang, "Observation of Laser Oscillation without Population Inversion in InGaAsP Microdisk Lasers," *Solid State Commun.* **91**, pp. 699-701, 1994.
8. A. F. J. Levi, R. E. Slusher, S. L. McCall, T. Tanbun-Ek, D. L. Coblenz and S. J. Pearton, "Room Temperature Operation of Microdisc Lasers with Submilliamp Threshold Current," *Electronics Letters* **28**, pp. 1010-1011, 1992.
9. A. F. J. Levi, S. L. McCall, S. J. Pearton and R. A. Logan, "Room Temperature Operation of Submicrometre Radius Disk Laser," *Electronics Letters* **29**, pp. 1666-1667, 1993.
10. A. F. J. Levi, R. E. Slusher, S. L. McCall, S. J. Pearton, and W. S. Hobson, "Room-temperature lasing action in $\text{In}_{0.51}\text{Ga}_{0.49}\text{P}/\text{In}_{0.2}\text{Ga}_{0.8}\text{As}$ microcylinder laser diodes," *Appl. Phys. Lett.* **62**, pp. 2021-2023, 1993.
11. Shuji Nakamura, "The Roles of Structural Imperfections in InGaN-Based Blue Light-Emitting Diodes and Laser Diodes," *Science* **281**, pp. 956-961, 1998.
12. K. C. Zeng, J. Y. Lin, H. X. Jiang and Wei Yang, "Optical properties of GaN pyramids," *Appl. Phys. Lett.* **74**, pp. 1227-1229, 1999.
13. S. Bidnyk, B. D. Little, Y. H. Cho, J. Krasinski, and J. J. Song, "Laser action in GaN pyramids grown on (111) silicon by selective lateral overgrowth," *Appl. Phys. Lett.* **73**, pp. 2242-2244, 1998.
14. H. X. Jiang, J. Y. Lin, K. C. Zeng and W. Yang, "Optical Resonance Modes in GaN Pyramid Micro-cavities," *Appl. Phys. Lett.* **75**, pp. 763-765, 1999.
15. R. A. Mair, K. C. Zeng, J. Y. Lin, H. X. Jiang, B. Zhang, L. Dai, H. Tang, A. Botchkarev, W. Kim, and H. Morkoc, "Optical properties of GaN/AlGaIn multiple quantum well microdisks," *Appl. Phys. Lett.* **71**, pp. 2898-2900, 1997.
16. R. A. Mair, K. C. Zeng, J. Y. Lin, H. X. Jiang, B. Zhang, L. Dai, A. Botchkarev, W. Kim, H. Morkoc, and M. A. Khan, "Optical modes within III-nitride multiple quantum well microdisk cavities," *Appl. Phys. Lett.* **72**, pp. 1530-1532, 1998.
17. K. C. Zeng, L. Dai, J. Y. Lin, and H. X. Jiang, "Optical Modes in InGaIn/GaN Multiple quantum well Microring Cavities," *Appl. Phys. Lett.*, accepted
18. Tetsuya Takeuchi, Shigetoshi Sota, Maki Katsuragawa, Miho Komori, Hideo Takeuchi, Hiroshi Amano and Isamu Akasaki, "Quantum-Confined Stark Effect due to Piezoelectric Fields in GaInN Strained Quantum Wells," *Jpn. J. Appl. Phys.* **36**, pp. 382-385, 1997.

19. Tetsuya Takeuchi, Hideo Takeuchi, Shigetoshi Sota, Hiromitsu Sakai, Hiroshi Amano and Isamu Akasaki, "Optical Properties of Strained AlGa_N and GaInN on GaN," *Jpn. J. Appl. Phys.* **63**, pp. 177-179, 1997.
20. Alexei Bykhovski, Boris Belmont, and Michael Shur, "The influence of the strain-induced electric field on the charge distribution in GaN-AlN-GaN structure," *J. Appl. Phys.* **74**, pp. 6734-6739, 1993.
21. Jin Seo Im, H. Kollmer, J. Off, A. Sohmer, F. Scholz, and A. Hangleiter, "Reduction of oscillator strength due to piezoelectric fields in GaN/Al_xGa_{1-x}N quantum wells," *Phys. Rev. B* **57**, pp. 9435-9438, 1998.
22. Marco Buongiorno Nardelli, Krzysztof Rapcewicz, and J. Bernholc, "Polarization field effects on the electron-hole recombination dynamics in In_{0.2}Ga_{0.8}N/In_{1-x}Ga_xN multiple quantum wells," *Appl. Phys. Lett.* **71**, pp. 3135-3137, 1997.
23. H. S. Kim, J. Y. Lin, H. X. Jiang, W. W. Chow, A. Botchkarev and H. Morkoc, "Piezoelectric effects on the optical properties of GaN/Al_xGa_{1-x}N multiple quantum wells," *Appl. Phys. Lett.* **73**, pp. 3426-3428, 1999.
24. Claire Gmachl, Federico Capasso, E. E. Narimanov, Jens U. Nockel, A. Douglas Stone, Jerome Faist, Deborah L. Sivco, Alfred Y. Cho, "High-Power Directional Emission from Microlasers with Chaotic Resonators," *Science* **280**, pp. 1556-1564, 1998.
25. X. Zhu, Y. Zhang, Y. Xin, G. Wang, R. Wang, Y. Ling, H. Zhou, Y. Yin, B. Zhang, L. Dai, G. Zhang and Z. Gan, "Near-field mapping of the emission distribution in semiconductor microdiscs," *Journal of Microscopy* **194**, pp. 439-444, 1999.

The InGaAlP Quantum Well Microcavities of Circular or Deformed Disks and Disks with Microstructures

Bei Zhang^a, GuoZhong Wang^a, YunQing Chen^a, Lun Dai^a, Wei Fang^a, Dajun Wang^a, Yumin Shen^a, Yi Qian^a, Shifa Xu^a, ZhiAn Lai^a, Xing Zhu^a, RouPeng Wang^a, XiaoYu Ma^b

^aDept. of Physics and State Key Laboratory for Mesoscopic Physics, Peking University, Beijing, 100871, China

^bThe Institute of Semiconductors, Chinese Academy of Sciences, Beijing, 100083, China

ABSTRACT

Optical microdisk is based on circularly symmetric micro-resonator and featured of the "whispering-gallery" modes with high quality of factor Q . However, the non-preferred directional emission and lack of high output from the disk are its drawbacks for application. Recently, a remarkable advance in the novel deformed microdisk laser at middle-infrared wavelength is highly attractive. In this report, as a preliminary try for microdisk at visible range, the InGaAlP quantum well (QW) circular cylindrical and deformed microdisks with radii about 2.5 to 10 μm emitting at wavelength of 0.62-0.67 μm were prepared by electron beam lithography and wet etching processing etc. The optical emission properties of these microdisks are studied by employing the scanning electron microscopy, atomic force microscopy, fluorescence image microscopy and scanning near-field optical microscopy etc. The preferential emission in these deformed microdisks was visually observed. When the cross section of microdisk was gradually deformed from circle, the change of fluorescence image from uniform ring towards 2 or 4 favorable emission along the circumference of microdisks was confirmed. The deformation could be caused by either the shape or etching profile of the disk waveguide. In addition, the microdisks patterned with some microstructures were proposed.

Keywords: Optical microcavity, Optical microdisk, Optical modes, InGaAlP QW, Deformed microdisks, whispering-gallery mode, fluorescence image

1. INTRODUCTION

Optical microdisk is a disk-like resonance cavity consisting of a thin layer of optical active medium with size of the order of optical wavelength. As one of the typical microcavities, it has been attracting special interest since the pioneer work of InGaAsP/InP microdisk laser by the group in AT&T Bell Lab in 1992¹⁻⁵. Due to the strong optical confinement to the gain region by the configuration of the waveguide, high quality factor Q could be achieved in microdisks. Optical microdisk is promising for making low threshold microlaser. Being distinct from the conventional Fabry-Perot (F-P) microcavity, the micro-fabrication of microdisk is relatively simplified since the sophisticated growth of distributed Bragg reflection (DBR) mirrors for F-P cavity can be avoided. However, the disk mode in microdisk is much more complicated than that in F-P cavity. The mode in microdisk is featured as "disk modes" composed of Whispering-Gallery modes and radial modes⁶⁻¹¹. They are realized by the total internal reflection of the light along the circular boundary by a larger difference of refractive index between the disk and its surrounding medium. The non-preferred symmetric radiation of the disk optical mode leads to lower output of the disk. It actually is a big problem in the applications of microdisk lasers. To get directional emission from microdisk should be one of the important projects on microdisk. There have been many attempts made by different research groups¹²⁻¹⁵. In particular, recently Gmachl etc. of Bell Labs and Yale scientists¹⁶ on the base of microdisk achieved a dramatic result. The directionality and power output were substantially improved by imposing a flattened quadrupolar deformation onto semiconductor microdisk lasers emitting at wavelength of mid-infrared 5 μm in temperature range from 40-100K. As they emphasized, the approach is applicable to other semiconductor microcavities at visible and near-infrared wavelength. Among various types of semiconductor microcavity, the microdisks emitting at visible wavelength is very

*Correspondence: E.mail: beizhang@ibm320h.phy.pku.edu.cn; Telephone: 086 010 62751739; Fax: 086 010 62751615

interesting. Recently, we have successfully fabricated InGaP thumbtack-like microdisks emitting at wavelength of $0.65\mu\text{m}$ ^{17,18,20} as well as III-nitrides cylindrical microdisks on short wavelength^{7-9,19}. The microcavity effects and disk modes in these microdisks were demonstrated.

In this report, we present our preliminary results on the InGaAlP/InGaP QW circular and deformed microdisks with radii about 2.5-10 μm emitting at visible red wavelength about 0.62-0.67 μm . They were prepared by micro-fabrication of electron-beam lithography and wet etching. Scanning electron microscope, atomic force microscope, fluorescence image microscope and scanning near-field optical microscope were employed to study the emission properties of the deformed microdisks at room temperature. Our preliminary results demonstrated that the disk emission properties were modified by the disk structure in three dimensions.

2. InGaAlP SQW CIRCULAR AND DEFORMED MICRODISKS

2.1 Epitaxial structures of InGaAlP quantum well (QW)

The wafers used to prepare microdisks were epitaxially grown by low-pressure metal-organic chemical vapor deposition (LP-MOCVD) on (100) n^+ -GaAs substrates. Two MOCVD single quantum well (SQW) wafers with different structures were adopted. The waveguide core of the wafer E contains a SQW of $\text{In}_{0.5}(\text{Ga}_{0.3}\text{Al}_{0.7})_{0.5}\text{P}/\text{In}_{0.5}(\text{Ga}_{0.75}\text{Al}_{0.25})_{0.5}\text{P}/\text{In}_{0.5}(\text{Ga}_{0.3}\text{Al}_{0.7})_{0.5}\text{P}$. The thickness of well and barrier is 5-6nm and 500nm, respectively. The SQW is sandwiched between a pair of cladding layers. The upper cladding layer is $\text{In}_{0.5}\text{Al}_{0.5}\text{P}$ with thickness about 0.1 μm and lower cladding layer is $\text{Ga}_{0.3}\text{Al}_{0.7}\text{As}$ about 0.35 μm . While the epitaxial structure of the wafer V contains a SQW of $\text{In}_{0.5}(\text{Ga}_{0.3}\text{Al}_{0.7})_{0.5}\text{P}/\text{In}_{0.5}\text{Ga}_{0.5}\text{P}/\text{In}_{0.5}(\text{Ga}_{0.3}\text{Al}_{0.7})_{0.5}\text{P}$ with the thickness of well and barrier 10nm and 100nm, respectively. The cladding layers in wafer V are the same of $\text{In}_{0.5}\text{Al}_{0.5}\text{P}$ with thickness about $\sim 0.3\mu\text{m}$ on the top and 0.8-1 μm at the bottom, respectively. Figure 1 is the scanning electron microscope (SEM) image of wafer V. The effective refractive index and electric field intensity profile in both wafers were calculated by the approximation of asymmetric multi-layer slab waveguide. The effective refractive index of both wafers is estimated to be 3.37-3.38. The numerical calculation profile indicated that a peak of electric field is located at the SQW region in the waveguide with the vertical optical confinement factor Γ about 0.96 and 0.72, respectively.

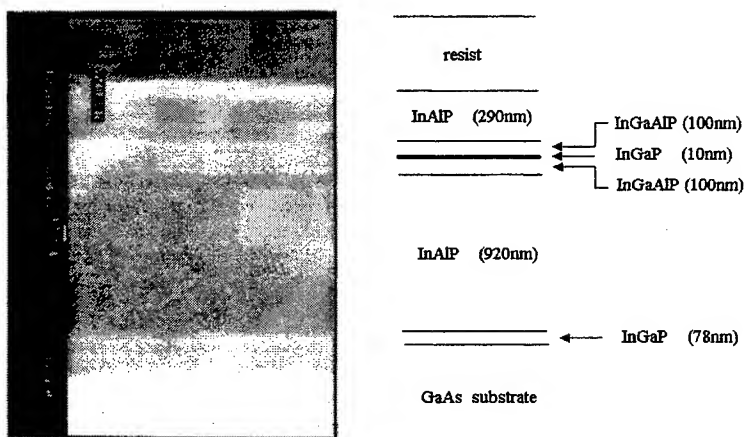


Figure 1 Scanning electron microscope (SEM) image of the cross section of MOCVD grown InGaAlP SQW wafer V.

2.2 Fabrications and the morphology of InGaAlP SQW circular and deformed microdisks

The circular and deformed mesa-like microdisks patterns were designed. In the cylindrical coordinate, the boundary of the deformed disk is described by the equation of $\rho(\phi) = \rho_0[1 + 2\epsilon \cos(2\phi)]^{1/2}$, which was the same as Gmachl's experiment¹⁶. Where $\rho(\phi)$ is the distance between original point to a point on the boundary, ϕ is the angle respect to the axis, ρ_0 is a constant, while ϵ is the deformation parameter. When $\epsilon=0$, the disk is a circular disk in shape. When ϵ is smaller than 0.15, it looks like an approximate ellipse, while ϵ is around 0.15-0.20, it looks like an "flattened" quadrupolar or a stadium. For

different ϵ but a fixed ρ_0 , the total area of the disk is the same. In our experiments, ρ_0 was chosen from 3-10 μm and ϵ was varied from 0 to about 0.2

In general, above microdisk patterns could be produced by conventional photolithography. Because of electron-beam lithography has the advantages of flexibly producing patterns by direct writing-on wafer by electron beam. It was adopted in this experiment for convenience not only for forming a variety of microdisk patterns with different size and configurations on a same MOCVD wafer but also for running simultaneous fabrication processing and making comparison of disk performance. The electron-beam exposure system is a modified scanning electron microscope system which is the model KYKY 1010 scanning electron microscope (SEM) attached a Beam Blanking Unit and connected to a personal computer by a model DA300 16-bit 4-channel D/A converter (DAC). A 2-dimensional pixel array of $2^{16} \times 2^{16}$ could be then produced by the electron-beam. The different patterns are obtained on the samples by the approaches of either "vector scan mode" or "raster scan mode" controlled by the patterning file. The resist PCMS was used as the negative electron beam resist. About 250-350 nm thick spun on and patterned PCMS film served as the etching mask to transfer the disk patterns on the same semiconductor InGaAlP SQW wafer. The mixture solution of Br_2 -methanol was used for wet etching. In some cases, Ar ion beam milling was used for dry etching. The etching procedure continued until the materials of SQW outside the pattern were etched off.

In our experiments, the cylindrical mesa-like microdisks (as distinguished from the thumbtack-like microdisks) with different size and shape were fabricated on both of MOCVD InGaAlP SQW wafers. Their depressed diameter and deformation parameter ϵ were varied from 5-20 μm and 0 to 0.2, respectively. During E-beam "writing" of disk-patterns, the deformed disks were produced with their elongated diameter oriented at 0° or 90° with respect to a cleaved edge of the wafer. Fig 2 is the SEM image of a typical InGaAlP SQW microdisk with the deformation parameter ϵ about 0.2. The morphology of the deformed microdisks was also measured by atomic force microscope (AFM) model Multimode SPM Nanoscope III A (Digital Instrument). The AFM and SEM results confirmed that the surface was flat and the boundary was smooth in most of the microdisks. The elongated (major) and depressed (minor) diameter of each deformed microdisk were measured by SEM and AFM. Deformation parameter ϵ was then estimated. The data obtained by both methods were reasonably comparable. However, in order to avoid the effects from AFM probe, the SEM data were adopted here.

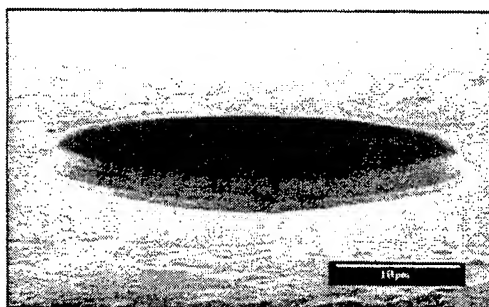


Fig 2 The SEM image of a typical InGaAlP SQW deformed microdisk.

2.3 Disk emission pattern

The fluorescence (FL) image of the InGaAlP microdisks was analyzed by a CCD mounted fluorescence microscope (Olympus BX60) system¹¹. A 100W mercury lamp is utilized as the light source. In this experiment, the excitation light was selected from the lamp in the green range of wavelength from 510-550 nm. The fluorescence image was viewed under the vertically incident excitation and collection through a fluorescence filter cube and a numerical aperture 0.90 microscope objective. A bright red fluorescence image of microdisk is clearly observed and recorded by computer through the CCD acquisition system. According to our previous study, the observed FL image of microdisk has relations to optical mode distributions in the microdisk. For the thumbtack-like InGaP microdisk, the bright red FL ring around the disk circumference demonstrated the dominant Whispering-Gallery mode in the disk. While in the cylindrical mesa-like microdisk, the uniform FL background on the surface of the disk revealed the co-existence of Whispering-Gallery mode and surface emission mode.

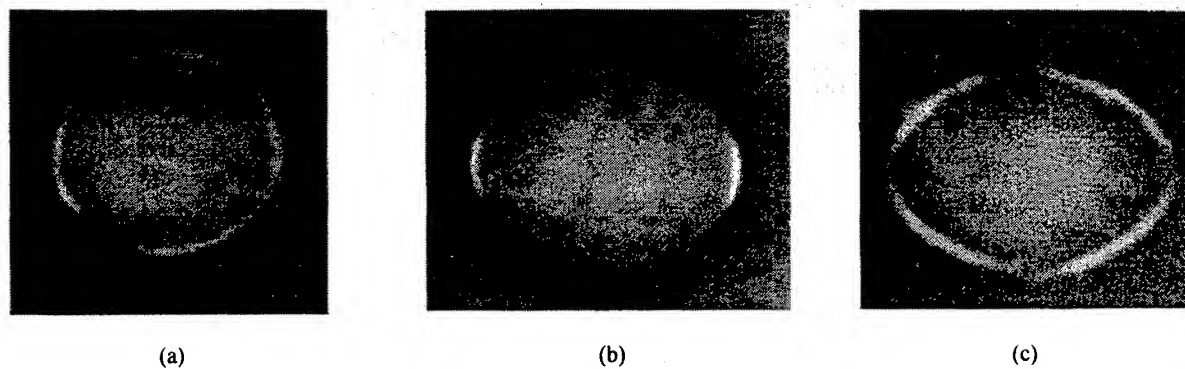


Fig. 3 Three different types of fluorescence (FL) image of the deformed microdisks on the wafer E

(a) $\epsilon=0.05$; (b) $\epsilon=0.14$; (c) $\epsilon=0.17$

Fig. 3(a),(b) and (c) illustrate three different types of fluorescence (FL) images observed from the deformed microdisks #ED1, #EA13 and #EB13 which fabricated on the wafer E, respectively. The orientation of their elongated diameter was parallel to one of the cleaved edge of the wafer. The deformation parameter ϵ of disks #ED1, #EA13 and #EB13 is about 0.05, 0.14 and 0.17, respectively. As distinct from the uniform bright and narrow red FL ring surrounding on the circular microdisk, it becomes not uniform and is broken to be some bright curved portions located at circumference of the deformed microdisk. For the FL image of slightly deformed disk with ϵ about 0.05 as shown in Fig. 3(a), the intensity of FL located at the edge of elongated diameter is getting stronger. In the FL image of disk #EA13 shown as Fig. 3(b), there is a pair of bright short curves located at the far ends on elongated diameter of the deformed microdisk oppositely. While in Fig. 3(c), the FL intensity of disk #EB13 from the boundary located near both of elongated diameter and depressed diameter is obviously vanished. Simultaneously, there are 4 bright red FL curves on the circumference symmetrically located in the vicinity of $\pm 45^\circ$ and $\pm 135^\circ$ respect to the elongated diameter. In this sample, since the orientation of the elongated diameter of the three disks were parallel to each other, the FL image characters for disk of different sizes are mainly depending on their deformation. Gmachl attributed their 45° peak emission from deformed microdisk laser ($\epsilon=0.16$) to the origination of bow-tie mode. Our observation in Fig. 3 provides interesting information on the similar deformed microdisks. It also indicated that the deformation parameter ϵ dominantly modified the FL emission pattern of deformed disks on wafer E. Our scanning near-field optical microscope fluorescence mapping on these microdisks is underway.

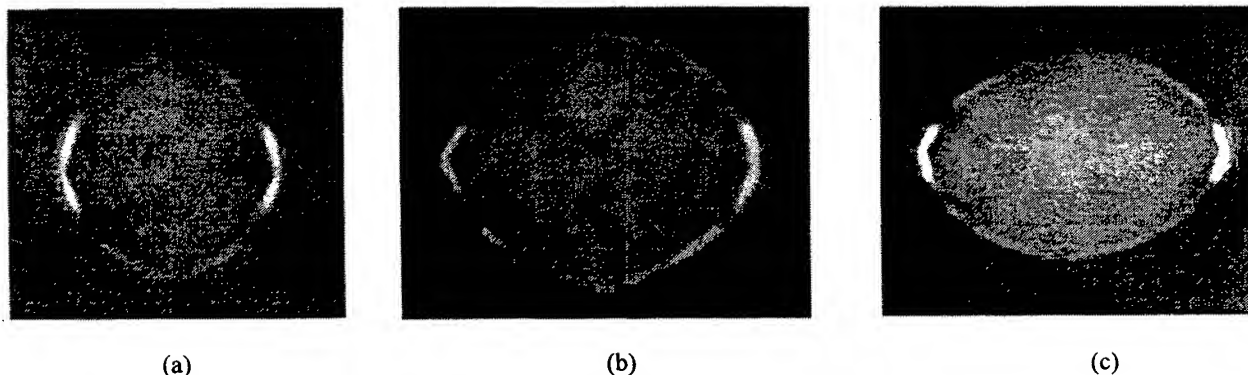


Fig 4 The FL images of deformed microdisks made on InGaAlP SQW wafer V
(a) disk #V-A21, $\epsilon=0.04$; (b) Disk #V-B21, $\epsilon=0.11$; (c) Disk #V-C-12, $\epsilon=0.20$

Fig 4 (a), (b) and (c) are the FL images of deformed microdisks of #V-A21, #V-B21 and #V-C12 made on another InGaAlP SQW wafer V, respectively. The elongated diameters of both disks #V-B21 and #V-C12 in Fig.4 (b) and (c) are parallel to one of the cleaved edge of wafer V, while the elongated diameters of disk #V-A21 in Fig. 4(a) is perpendicular to that cleaved edge. Therefore the depressed diameter of #V-A21 is parallel to the elongated diameters of the two other disks #V-

B21 and #V-C12. The deformation parameters ϵ of disks #V-A21, #V-B21 and #V-C12 are about 0.04, 0.11 and 0.20, respectively. It is very interesting to find out that the FL images of disks with different ϵ and/ or orientation made on same wafer V exhibit quite a similar feature of emission pattern. A pair of red bright curves located at the far-ends of diameter, apart 180°, occur in FL images of all the disks on wafer V. The axes on which the bright emitting pairs located are parallel to that cleaved edge mentioned above for all three disks, no matter the axes are parallel to elongated or depressed diameters of each disk. Furthermore they are accompanied with the 4-red less bright curves similar to Fig. 3(c). Additionally, a weak but uniformly red FL background on the surface of the microdisk can also be faintly observed.

The side view SEM images of the deformed microdisks are given in Fig 5. It may provide the evidence to explain the difference of the results on wafer E and V. Fig 5 (a)-(b) are the side view SEM images of the corner of the elongated diameter and depressed diameter of disk #E-B13 ($\epsilon \sim 0.17$) on wafer E, respectively. They are typical side-wall pictures of the disks shown FL image shown in Fig.3 (c). While Fig. 5 (c) and (d) are corresponding to the disks on wafer V.

Because of the anisotropy of the wet etching, it always leads to the different etching profiles on a semiconductor disk mesa from different direction for side view. As the results in Fig. 5(b) and (d), the side wall is a slope in both of the wafers E and V. They are the pictures corresponding to the region on depressed diameter of all the disks except the disk #V-A21 made on wafer E and V, respectively. The elongated diameter of disk #V-A21 and the depressed diameters of all the others on their wafer (V or E) are parallel each other, respectively. However, along the another direction which perpendicular to that cleaved edge, the etching profile is different between the two wafers. In Fig. 5 (a), The etching profile of disk is nearly vertical at the end of the elongated diameter of disk on wafer E. In contrast to wafer E, the undercutting of side wall appears on wafer V. In the disks on wafer V in our experiment, the side walls of depressed diameter for #V-A21 and elongated

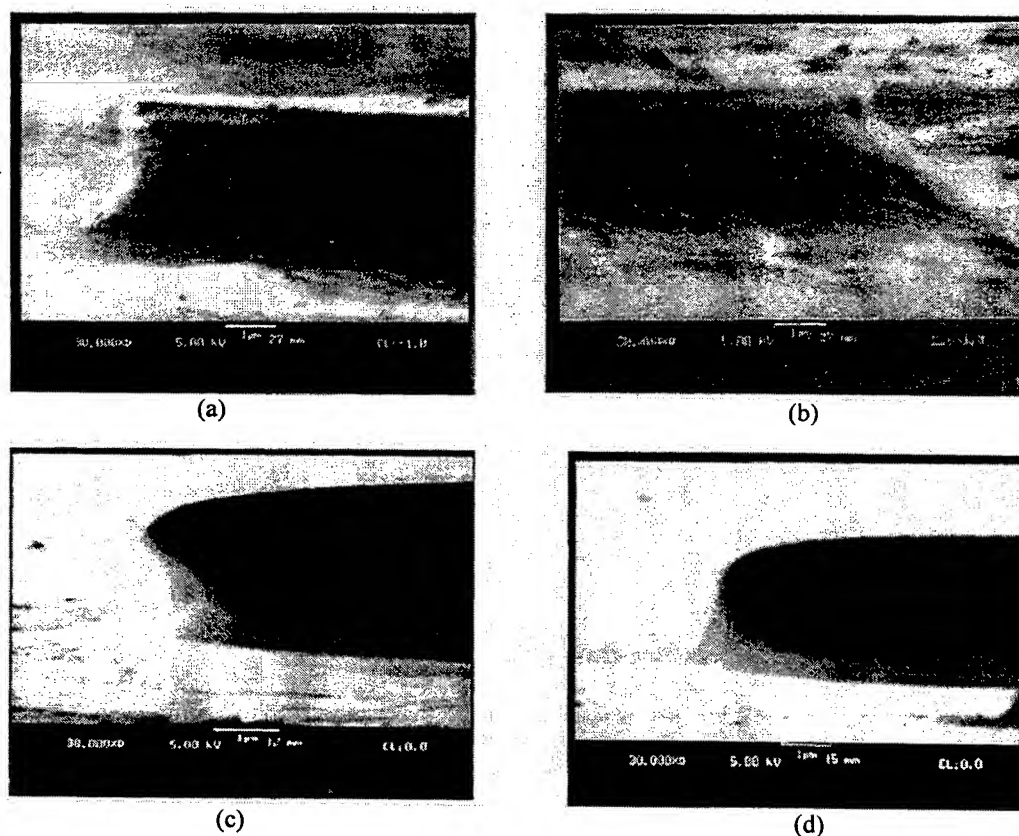


Fig.5 The side view SEM images of the deformed microdisks

- (a) part of disk #E-B13 at the elongated diameter (on wafer E)
- (b) part of disk #E-B13 at the depressed diameter (on wafer E)
- (c) part of disk #V-A21 at the depressed diameter (on wafer V)
- (d) part of disk #V-A21 at the elongated diameter (on wafer V)

diameter for #V-B21 and #V-C12 are all undercutting, while that of the elongated diameter for #V-A21 and the depressed diameter for #V-B21 and #V-C12 are slopes as shown in Fig.5 (c) and Fig. 5 (d), respectively. The results of Fig. 4 and Fig. 5(c) and (d) indicate that the pairs of bright FL curves are always located at the undercutting regions in wafer V.

The different etching profiles for these two wafers could be the effects of etching rates on GaAs substrate orientations and the quaternary materials with different compositions. In our experiment, the GaAs substrate of wafer V is mis-oriented 6° off the (100) towards the nearest (111), while wafer E tilts less. The composition and thickness of InGaAlP are also different in the two wafers. It means that in some cases, the etching profile becomes another important factor on the disk emission pattern.

3. DISCUSSIONS & CONCLUSIONS

In principal, in the case of microdisks, the optical field concentrates near the circumference of the disk by the totally internal reflection. The optical field distribution in the vertical direction of the disk is sensitive to the waveguide structure in the vicinity of their circumference. If the lower cladding layer under the active waveguide region is getting thinner or etched off by undercutting, the optical field profile will be changed. The vertical confinement factor in the upper cladding layer will be increased. As in our case, assuming the layered waveguide of wafer V is changed by wet etching, the thickness of lower cladding layer decreased to be 0.01 μm . The confinement factor in the upper cladding layer is approximated increased to be 1.8 times its previous value. As a result, the FL intensity near these undercutting region should be increased. The preferential FL emission was then mainly realized by the asymmetrical etch undercutting. However, due to the different structure of quantum well in wafer E, the effect of etching profile on the distribution of optical field intensity is relatively less, the deformed boundary shape of disk from circular is the dominant factor to the directional emission.

From the point view of the waveguide, microdisk is a 3-dimensional confined optical waveguide. Our preliminary results demonstrated that either the disk shape in the plane of the disk or the vertical structure of the disk waveguide could strongly modify the disk emission mode. Our results explicate that manifold deformations can be adopted to realize directional emission from a deformed microdisk in the visible wavelength material systems. Besides, more detailed investigation such as optimizing QW structure and technique procedure as well as disk mode measurement and analysis are in progress.

Based on the above preliminary results of deformed disk, we have proposed and designed microdisks with microstructure on the disk formed by putting symmetric or asymmetric dielectric medium or etching. The change on FL pattern is demonstrated.

ACKNOWLEDGMENTS

This work was supported by National Nature Science Foundation of China (NNSFC) projects of No.s 69687007, 19774008, 19674004 and 69686260, the Opening Projects of State Key Laboratory for Mesoscopic Physics of China and State Key Laboratory for Integrated Electro-Optics of China.

REFERENCES

1. S. L. McCall, A. F. J. Levi, R. E. Slusher, S. J. Pearton, R. A. Logan, "Whispering-gallery mode microdisk lasers," *Appl. Phys. Lett.*, **60**, pp. 289-291, 1992.
2. D. Y. Chu, M. K. Chin, N. J. Sauer, Z. Xu., T. Y. Chang, S. T. Ho, "1.5 μm InGaAs/InAlGaP quantum well microdisk lasers," *IEEE Photonics Technology Lett.*, **5**, pp. 1353-1355, 1993.
3. U. Mohideen, W. S. Hobson, S. J. Pearton, F. Ren, & R. E. Slusher, "GaAs/AlGaAs microdisk lasers," *Appl. Phys. Lett.*, **64**, pp. 1911-1913, 1994.
4. D. Y. Chu, S. T. Ho, X. Z. Wang, B. W. Wessels, W. G. Bi, C. W. Tu, R. P. Espindola, S. L. Wu, "Observation of enhanced photoluminescence in erbium-doped semiconductor microdisk resonator," *Appl. Phys. Lett.*, **66**, pp. 2843-2845, 1995.
5. B. Zhang, R. P. Wang, X. M. Ding, Z. Y. L. Dai, X. M. Cui, S. M. Wang, "The study on InGaAsP single quantum well semiconductor microdisk lasers," *Chinese J. Infrared Millimeter Waves (overseas edition)*, **14**, pp. 285-288, 1995.
6. N. C. Fratechi, A. F. J. Levi, "The spectrum of microdisk lasers," *J Appl. Phys.*, **80**, pp. 644-653, 1995.

7. R. A. Mair, K. C. Zeng, J.Y. Lin, H.X. Jiang, B. Zhang, L. Dai, H. Tang, A. Botchkarev, W. Kim, and H. Morkoc. "Optical properties of GaN/AlGa_N multiple quantum well microdisks", *Appl. Phys. Lett.* **71**, pp. 2898-2900., 1997
8. R. A. Mair, K. C. Zeng, J. Y. Lin, H. X. Jiang, Bei Zhang, Lun Dai, H. Tang, A. Botchkarev, W. Kim, H. Markoc "Photoluminescence properties of GaN/AlGa_N multiple quantum well microdisks", *Mat. Res. Soc. Symp. Proc* **482** " Nitride Semiconductors", pp649, 1997
9. R.A.Mair, K.C.Zeng, J.Y.Lin, H.X.Jiang, B.Zhang, L.Dai, A.Botchkarev, W.Kim, H.Morkoc, M.A.Khan, "Optical modes within III-nitride multiple quantum well microdisk cavities" *Appl. Phys. Lett.* **72**, pp1530-1532, 1998
10. R. P. Wang, M. M. Dumitrescu, "Theory of optical modes in semiconductor microdisk lasers," *J. Appl. Phys.*, **81**, pp. 3391-3397, 1997.
11. Y. Lin, B. Zhang, Y. Xin, C. H. Guo, L. Dai, D. J. Zhou, C. H. Huang, "Observation of disk mode pattern on organic microdisk," *Solid State Commun.*, **105**, pp. 445-448, 1998.
12. A. F. J. Levi, R. E. Slusher, S. L. McCall, L.J. Glass, S. J. Pearton, R. A. Logan, "Directional light coupling from microdisk laser", *Appl. Phys. Lett.*, **62**, pp. 561-563, 1993
13. D.Y.Chu, M.K.Chin, W.G.Bi, H.Q. Hou, C. W. Tu, S. T. Ho, "Double-Disk structure for output coupling in microdisk lasers", *Appl. Phys. Lett.*, **65**, pp31673169, 1994,
14. H. Deng, Q. Deng, D. G. Deppe, "Native-oxide laterally confined Whispering-gallery mode with vertical emission." *Appl. Phys. Lett.*, **69**, pp. 3120-3122, 1996.
15. J.P. Zhang, D.Y. Chu, S.L. Wu, W.G. Bi, R.C. Tiberio, C.W. Tu, S.T. Ho, "Directional light output from Photonic-wire microcavity semiconductor laser", *IEEE Photonics. Technol. Lett.*, **8**, pp968-,970, 1996.
16. C.Gmachl, F.Capasso, E.E.Narimanov, J.U.Nockel, A.D.Stone, J.Faist, D.Sivco and A.Cho, *Science*, **280**, pp1556-1564, 1998.
17. Xing Zhu, Yu Zhang, Yongchun Xin, Yong Ling, Ke Wu, Hetian Zhou, Yan Yin, Bei Zhang, Zizhao Gan, Feijun Son and Yu Wang, "Study of whispering-gallery mode of InGaP microdisks by using scanning near-field optical microscopy", *Proceedings of SPIE*, **3467**, pp231-240, 1998
18. Bei Zhang, Yongchun Xin, Guozhong Wang, Wanjin Xu, Zongju Xia, Yinhua Zou, Optical disk mode pattern of InGaP microdisks emitting at 0.65 μm , *Proceedings of SPIE*, **3547**, pp152-157, 1998.
19. Lun Dai, Bei Zhang, R. A. Mair, Kecai Zeng, Jingyu Lin, Hongxing Jiang, A. Botchkarev, W. Kim, H. Morkoc, M. A. Khan, "Optical properties and resonant modes in GaN/AlGa_N and InGa_N/Ga_N multiple quantum well microdisk cavities", *Proceedings of SPIE*, **3547**, pp158-163, 1998.
20. Xing Zhu, Yu Zhang, Yongchun Xin, Guozhong Wang, Ruopeng Wang, Yong Ling, Yan Yin, Bei Zhang, Guoyi Zhang, Zizhao Gan, "Near-Field Mapping of the Emission Distribution in Semiconductor Microdisks", *J. Microscopy*, **194**, Pt 2/3, pp439-444, 1999.

Eigenmode confinement in semiconductor microcavity lasers with an equilateral triangle resonator

Yong-Zhen Huang*

State Key Laboratory on Integrated Optoelectronics, Institute of Semiconductors,
Chinese Academy of Sciences, P.O. Box 912, Beijing 100083, P. R. China

ABSTRACT

We analyze the mode behaviors for semiconductor lasers with an equilateral triangle resonator by deriving the mode field distribution and the eigenvalue equation. The eigenvalue equation shows that the longitudinal mode wavelength interval is equivalent to that of a Fabry-Perot cavity with the cavity length of $1.5a$, where a is the side length of the equilateral triangle resonator. The transverse waveguiding is equivalent to as a strip waveguide with the width of $\sqrt{3}a/2$, and the number of transverse modes supported by the resonator is limited by the total reflection condition on the sides of the equilateral triangle. Semiconductor microcavity laser with an equilateral triangle resonator is suitable to realize single mode operation, and the mode wavelength can be adjusted by changing the side length.

Keywords: Resonant cavity, microcavity, semiconductor lasers, single-mode laser, optical resonance

1. INTRODUCTION

Semiconductor lasers with noncleaved mirrors and ultra-low threshold operation are required for realizing a large-scale photonic integration. Semiconductor micro-disk lasers, due to the small volume of the active region and the spontaneous emission control, have attracted a lot of attentions and significant breakthroughs have been achieved.¹⁻⁵ A photo-pumping microring laser with the cavity volume of only $0.27 \mu\text{m}^3$ was realized by photonic wire structure,³ a $2\text{-}\mu\text{m}$ -diameter GaInAsP microdisk injection laser was realized with the pulsed threshold current of 0.2 mA .⁴ However, the total internal reflection of the whispering-gallery modes greatly limits the output power and its directionality. Recently, high output power and highly directional semiconductor microlasers are achieved from a deformed cylinder resonator with bow-tie resonance modes,⁵ and the lasing threshold of GaAs microdisk lasers with holes pierced through the disk surface was reduced by up to 50 % compared to a disk without hole.⁶ Short-cavity edge-emitting lasers with deeply etched semiconductor/air distributed Bragg reflectors are also employed for the possible integration of the laser devices in photonic integrated circuits.⁷⁻¹⁰ A short-cavity laser with semiconductor/air distributed Bragg reflectors on both cavity ends is realized with the cavity length of $40 \mu\text{m}$.¹⁰

In this article, we manifest that semiconductor microcavity lasers with an equilateral triangle resonator are suitable for monolithic integration in photonic integrated circuits and a single mode operation. We derive the mode field distributions for the equilateral triangle resonator and the corresponding eigenvalue equation. The eigenvalue equation shows that the equilateral triangle resonator is suitable for realizing a single longitudinal mode operation, and the number of higher order transverse modes is limited by the total reflection on the sides of the triangle.

* Email: yzhuang@red.semi.ac.cn; Telephone: +86-10-62339217; Fax: +86-10-62322388

2. THEORETICAL ANALYSIS

For an equilateral triangle resonator with a uniform real refractive index $n > 2$ surrounded by the air, light rays propagating parallelly with the sides of the triangle will experience totally internal reflectivity. And the light ray will return to the starting point after six-time reflections on the sides with the path of the perimeter $3a$ of the triangle, where a is the side length of the triangle. We choose the $x - z$, the $x' - z'$, and the $x'' - z''$ coordinate system as shown in Fig. 1, with the z - axis, the z' - axis, and the z'' - axis parallel with one side of the triangle, respectively. The triangle resonator is formed by three points of $(x, z) = (\sqrt{3} a / 4, 0)$, $(-\sqrt{3} a / 4, -a/2)$, $(-\sqrt{3} a / 4, a/2)$ in the $x - z$ plane. The mode light

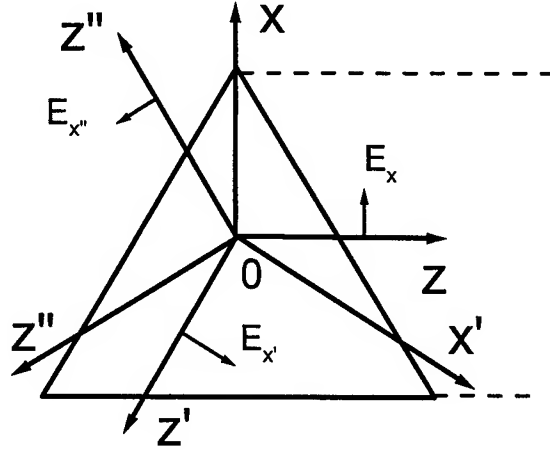


Fig.1 The schematic diagram of a triangle resonator with three sets of the coordinate system, the $x - z$, the $x' - z'$, and the $x'' - z''$ planes. The sides of the triangle resonator are $x = -\sqrt{3}(z - a/4)$, $x = -\sqrt{3}a/4$, and $x = \sqrt{3}(z + a/4)$. The electric fields E_x , $E_{x'}$, and $E_{x''}$ propagating in the three directions are also marked. The dashed lines shows the equivalent transverse strip waveguiding by unfolding the mode light rays.

rays propagate along the z -axis, the z' axis, and the z'' - axis, with nonzero electric fields E_x , $E_{x'}$, and $E_{x''}$ in the triangle resonator, and the fields experience total internal reflection at the sides of the triangle. We consider the field distribution in the $x - z$ plane for TE modes, and assume that the y -direction wavefunction $G(y)$ is already solved from a multilayer slab waveguide with the mode index of N . So the electric fields E_x , $E_{x'}$, and $E_{x''}$ inside the resonator satisfy the following wave equation

$$\left(\frac{\partial^2}{\partial x^2} + \frac{\partial^2}{\partial z^2} \right) E_x(x, z) + N^2 k_0^2 E_x(x, z) = 0, \quad (1)$$

with the free space wave number $k_0 = 2\pi / \lambda$. We express the wavefunctions as the waves propagate along the z , z' , and z'' directions in the corresponding coordinate systems:

$$E_x(x, z) = F(x) \exp(i\beta z), \quad (2)$$

$$E_{x'}(x', z') = F(x' - \sqrt{3}a/8) \exp(i\beta z' + i\phi_1), \quad (3)$$

$$E_{x''}(x'', z'') = F(x'' - \sqrt{3}a/8) \exp(i\beta z'' + i\phi_2). \quad (4)$$

The phase term $\sqrt{3}a/8$ in (3) and (4) is induced because the original points of the $x' - z'$, and the $x'' - z''$ planes are not

in the centers of the corresponding transverse waveguides, as shown in Fig. 1. The transverse wavefunction $F(x)$ is

$$F(x) = \begin{cases} \cos(\kappa x) & \text{even mode,} \\ \sin(\kappa x) & \text{odd mode,} \end{cases} \quad (5)$$

which is assumed strict confinement in the triangle resonator, i.e., $\cos \kappa x = 0$ and $\sin \kappa x = 0$ at the side $x = -\sqrt{3}a/4$. After the coordinate system transform, we get the electric fields $E_x(x, z)$, $E_x'(x', z')$ and $E_x''(x'', z'')$ as

$$E_x(x, z) = F(x) \exp(i\beta z), \quad (6)$$

$$E_x'(x, z) = F\left(\frac{\sqrt{3}z}{2} - \frac{x}{2} - \frac{\sqrt{3}a}{8}\right) \exp\left(-i\beta \frac{z}{2} - i\beta \frac{\sqrt{3}x}{2} + i\phi_1\right), \quad (7)$$

$$E_x''(x, z) = F\left(-\frac{\sqrt{3}z}{2} - \frac{x}{2} - \frac{\sqrt{3}a}{8}\right) \exp\left(-i\beta \frac{z}{2} + i\beta \frac{\sqrt{3}x}{2} + i\phi_2\right). \quad (8)$$

From Eqs. (5) and (6), we can find that $E_x(x, z)$ is composed of $\exp(i\kappa x + i\beta z)$ and $\exp(-i\kappa x + i\beta z)$, and the incident angles of the mode light rays $\exp(i\kappa x + i\beta z)$ and $\exp(-i\kappa x + i\beta z)$ on the side $x = -\sqrt{3}(z - a/4)$ are $\alpha_1 = 30^\circ - \tan^{-1}(\kappa/\beta)$ and $\alpha_2 = 30^\circ + \tan^{-1}(\kappa/\beta)$, respectively. The two light rays impinge the side at different incident angles, so they will have different total reflection phase shifts. The phase difference θ between the reflected wave and the incident wave for the TE mode, i.e., the electric field situated in the plane of incidence, satisfies¹¹

$$\tan\left(\frac{\theta}{2} - \frac{\pi}{2}\right) = \frac{\sqrt{N^4 \sin^2 \alpha - N^2}}{\cos \alpha}, \quad (9)$$

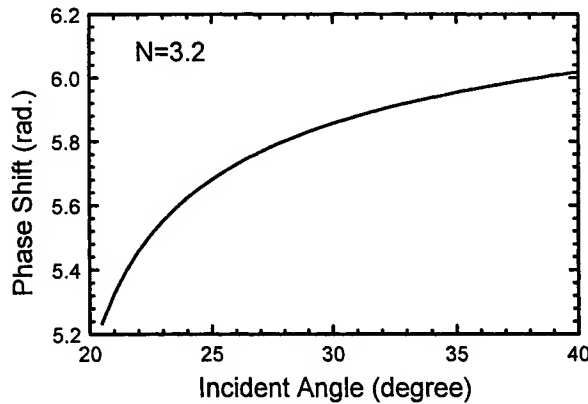


Fig. 2 The variation of the phase difference between the reflected and the incident waves is plotted as a function of the incident angle.

where α is the incident angle. Fig. 2 shows the phase shift θ as a function of the incident angle for the refractive index $N = 3.2$. The numerical results show that the variation of the phase shift with the incident angle is rather slow around the incident angle of the mode light rays of about $\alpha \approx 30^\circ$. Ignoring the reflection phase shift difference between the incident angles α_1 and α_2 , we obtain the following boundary conditions at the sides of the equilateral triangle:

$$E_x(x, z) \exp(i\theta_0) - E_x(x, z) = 0, \text{ at } x = -\sqrt{3}(z - a/4), \quad (10)$$

$$E_x(x, z) \exp(i\theta_0) - E_x(x, z) = 0, \text{ at } x = -\sqrt{3}a/4, \quad (11)$$

$$E_x(x, z) \exp(i\theta_0) - E_x(x, z) = 0, \text{ at } x = \sqrt{3}(z + a/4). \quad (12)$$

The average phase shift is taken to be

$$\theta_0 = (\theta_1 + \theta_2) / 2, \quad (13)$$

where θ_1 and θ_2 are phase shifts corresponding to the incident angle α_1 and α_2 , respectively. Substituted the wavefunction Eqs. (6)-(8) into the boundary conditions (10)-(12), we obtain an eigenvalue equation for the longitudinal propagation constant β , the phase terms ϕ_1 and ϕ_2 , which are dependent on the transverse mode distribution, as

$$3\beta_l a + 6\theta_0 = 2l\pi, \quad l = 2, 4, 6, \dots \quad (14)$$

$$\sqrt{3} \kappa_m a = 2m\pi, \quad m = 1, 3, 5, \dots \quad (15)$$

$$\phi_1 = 3\beta a / 8 + 2l_1\pi + \theta_0, \quad (16)$$

$$\phi_2 = 9\beta a / 8 + 2l_2\pi + 2\theta_0, \quad (17)$$

for the even transverse mode $\cos \kappa x$, and

$$3\beta_l a + 6\theta_0 = 2l\pi, \quad l = 1, 3, 5, \dots \quad (18)$$

$$\sqrt{3} \kappa_m a = 2m\pi, \quad m = 2, 4, 6, \dots \quad (19)$$

$$\phi_1 = 3\beta a / 8 + (2l_1 + 1)\pi + \theta_0, \quad (20)$$

$$\phi_2 = 9\beta a / 8 + 2l_2\pi + 2\theta_0, \quad (21)$$

for the odd transverse mode $\sin \kappa x$. l is the longitudinal mode index and m is the transverse mode index, $m = 1$ is correspondent to the fundamental mode, and l_1 and l_2 are inter numbers. Following the transmission of the mode light rays inside the equilateral triangle, we find that the incident angle at the sides interchanges between α_1 and α_2 . So we can expect that the approximation in the boundary conditions has little effect on the eigenvalue equation for the longitudinal propagation. From $N^2 k_0^2 = \beta_l^2 + \kappa_m^2$ and the above eigenvalue equations, we obtain the mode wavelength as

$$\lambda_{l,m} = 3Na / \sqrt{(l - 3\theta_0 / \pi)^2 + 3m^2}, \quad l + m = 3, 5, 7, \dots \quad (22)$$

Comparing the mode wavelength (22) with that of the Fabry-Perot resonator, we find that the longitudinal mode wavelength difference of the triangle resonator is equivalent to that of a Fabry-Perot resonator with the cavity length of $3a/2$. From the longitudinal mode wavefunction $\exp(i\beta z)$, we can construct two-fold degeneracy longitudinal wavefunctions of $\cos(\beta z)$ and $\sin(\beta z)$. According to the two-fold degeneracy in the longitudinal wavefunction and the constrain condition on the mode index of $l + m = 3, 5, 7, \dots$, we can expect that the mode number supported by the equilateral triangle resonator is equal to that of a Fabry-Perot resonator with the cavity length of $3a/2$ and the transverse strip width of $\sqrt{3}a/2$. However, an incident angle of the m th transverse mode at the side of the triangle resonator is $\alpha = 30^\circ - \sin^{-1}(\kappa/Nk_0)$, and the light rays of the transverse modes cannot be confined in the resonator if the incident angle α is less than the critical angle of total reflection $\alpha_c = \sin^{-1}(1/N)$. From $\alpha > \alpha_c$ and (15), we obtain the

number of transverse modes confined by the triangle resonator as

$$m < a[\sqrt{3(N^2 - 1)} - 3]/2\lambda. \quad (23)$$

3. NUMERICAL RESULTS

In Fig. 3, we plot the confined mode wavelength as functions of the side length a under $\theta_0 = 5.856$ and $N = 3.2$. The mode number is marked by the mode index of (l, m) in the figure. The first order transverse mode cannot be confined

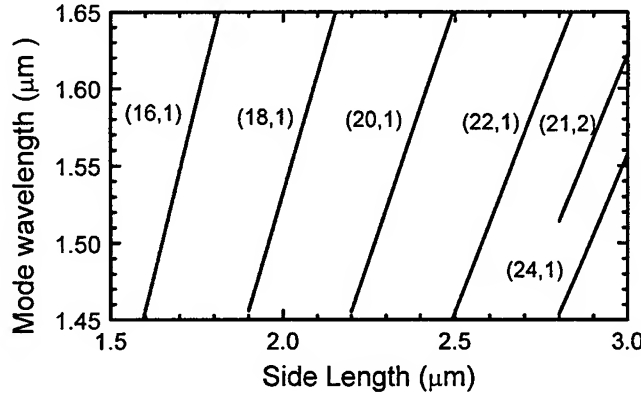
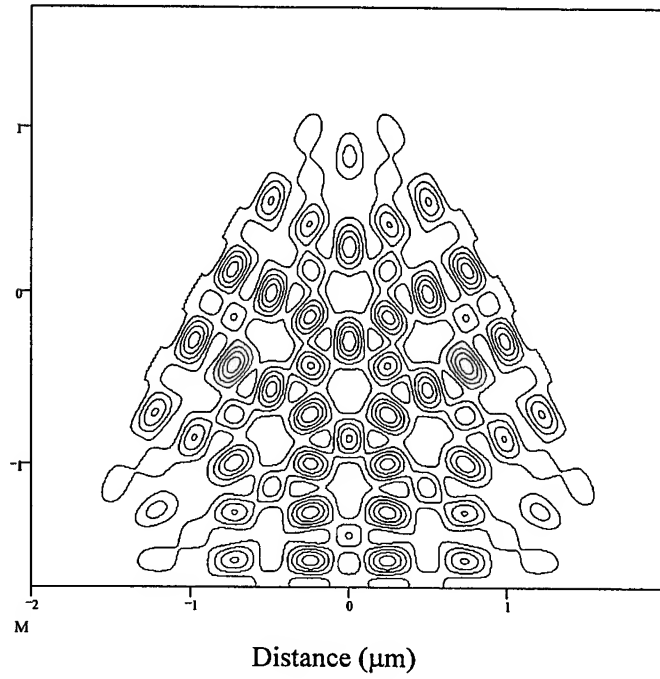


Fig. 3 The confined mode wavelength versus the side length of the equilateral triangle resonator with $N=3.2$. The longitudinal and transverse mode indexes are marked as (l, m) in the figure.

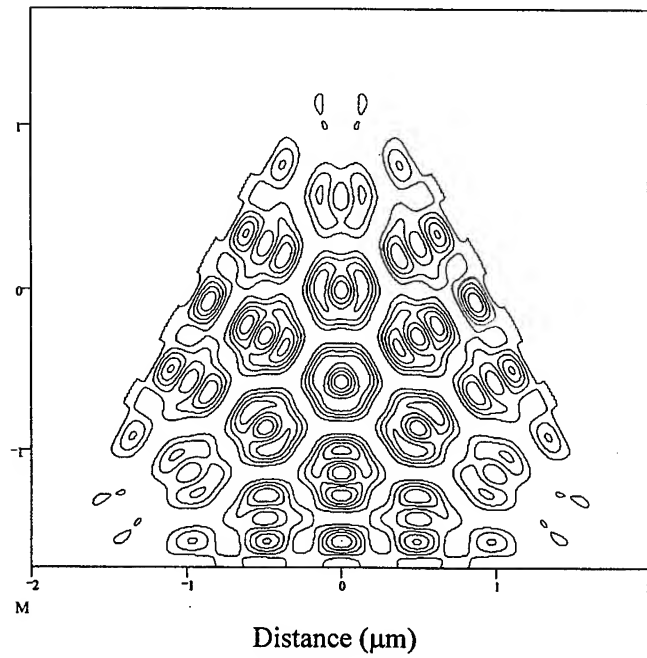
in the equilateral triangle resonator as the side length is less than $2.8 \mu\text{m}$. And the mode wavelength interval of different longitudinal modes is larger than 100 nm as the side length $a < 2.8 \mu\text{m}$, so semiconductor microcavity lasers with an equilateral triangle resonator are suitable for realizing single mode operation. For an equilateral triangle resonator with $a = 4 \mu\text{m}$, $N = 3.2$, and $\lambda = 1.55 \mu\text{m}$, Eq. (23) yields $m < 2.9$, i.e., we only have the fundamental and the first order transverse modes confined in the resonator around $\lambda = 1.55 \mu\text{m}$. The confined mode wavelengths are $\lambda_{30,1} = 1.5693 \mu\text{m}$, $\lambda_{29,2} = 1.6228 \mu\text{m}$, and $\lambda_{31,2} = 1.4975 \mu\text{m}$ with $\theta_0 = 5.856$. For the fundamental mode with the wavelength of $\lambda_{30,1} = 1.5693 \mu\text{m}$, the incident angles of the mode light rays on the sides of the triangle are 26° and 34° , and the corresponding phase shifts are $\theta = 5.727$ and 5.937 . The phase shift difference of the two incident angles is only 3.6% . So we can expect that the approximation boundary condition with the same phase shift is rather good, especially for a larger resonator. Considering the two-fold degeneracy in the longitudinal wavefunction, we have two modes with the same mode wavelength, i.e., the mode wavefunction $E_x(x, z) = \cos\kappa_1 x \cos\beta_{30} z$ and $\cos\kappa_1 x \sin\beta_{30} z$ for the fundamental mode $\lambda_{30,1} = 1.5693 \mu\text{m}$, and $E_x(x, z) = \sin\kappa_2 x \cos\beta_{31} z$ and $\sin\kappa_2 x \sin\beta_{31} z$ for the first order transverse mode $\lambda_{31,2} = 1.4975 \mu\text{m}$, respectively. The mode intensity distribution can be expressed as

$$\begin{aligned} M &= [E_x - (E_x' + E_x'')\sin 30^\circ]^2 + [(E_x' - E_x'')\cos 30^\circ]^2 \\ &= E_x^2 + E_x'^2 + E_x''^2 - E_x E_x' - E_x E_x'' - E_x' E_x''. \end{aligned} \quad (24)$$

The contour plots of the intensity distributions for the fundamental mode are plotted in Fig. 4 with the $E_x(x, z)$ of (a) $\cos\kappa_1 x \cos\beta_{30} z$ and (b) $\cos\kappa_1 x \sin\beta_{30} z$, and that of the first order transverse mode with the wavefunction of (a) $\sin\kappa_2 x \cos\beta_{31} z$ and (b) $\sin\kappa_2 x \sin\beta_{31} z$ are plotted in Fig. 5.



(a)



(b)

Fig. 4 The contour plots of intensity distributions for the fundamental modes in the equilateral triangle resonator with the side length of 4 μm are plotted with the wavefunction of (a) $E_x = \cos \kappa_1 x \cos \beta_{30} z$ and (b) $E_x = \cos \kappa_1 x \sin \beta_{30} z$.

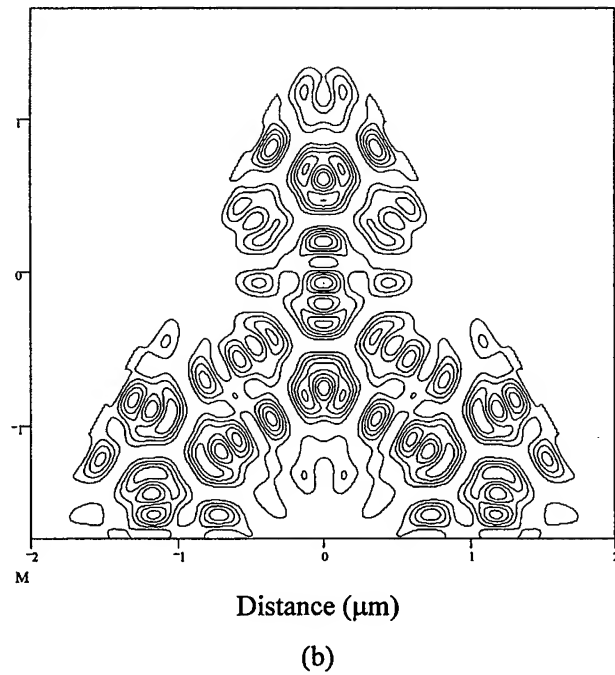
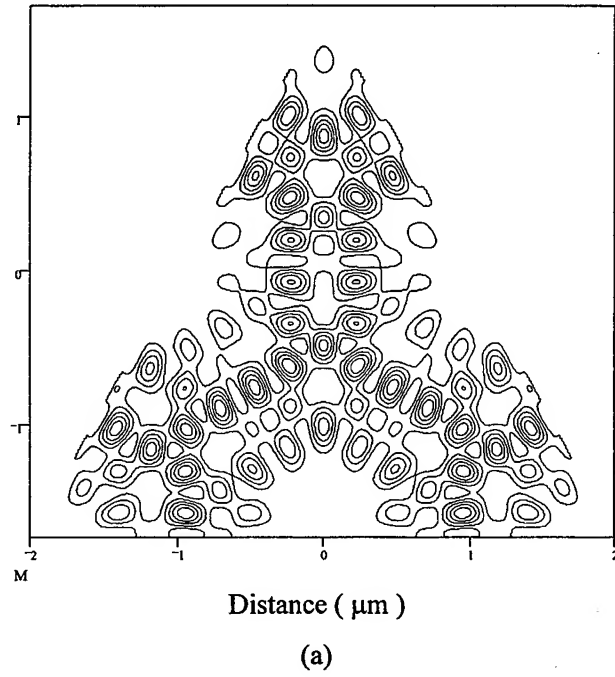


Fig. 5 The contour plots of intensity distributions for the first order transverse mode in the equilateral triangle resonator with the side length of $4 \mu\text{m}$ are plotted with the wavefunction of (a) $E_x = \cos\kappa_2 x \cos\beta_3 z$ and (b) $E_x = \cos\kappa_2 x \sin\beta_3 z$.

4. CONCLUSIONS

We have derived the eigenfunctions and eigenvalues for the modes confined in an equilateral triangle resonator. The results show that the semiconductor microcavity lasers with an equilateral triangle resonator are suitable for realizing a single mode operation, and equilateral triangle semiconductor lasers are an idea laser source in photonic integrated circuits. However, two degeneracy modes exist with the same mode wavelength.

ACKNOWLEDGMENT

This work was supported by the National Nature Science Foundation of China under grants No. 69688002 and 69896260, and the project of Chinese Academy of Sciences.

REFERENCES

1. S. L. McCall, A. F. J. Levi, R. E. Slusher, S. J. Pearton, R. A. Logan, "Whispering gallery mode microdisk lasers," *Appl. Phys. Lett.*, vol.60, pp.289-291, 1992.
2. A. F. J. Levi, R. E. Slusher, S. L. McCall, T. Tanbun-Ek, D. L. Coblenz, and S. J. Pearton, "Room temperature operation of microdisk lasers with submilliamp threshold current," *Electron. Lett.*, vol.28, pp.1010-1012, 1992.
3. J. P. Zhang, D. Y. Chu, S. L. Wu, S. T. Ho, W. G. Bi, C. W. Tu, and R. C. Tiberio, *Phys. Rev. Lett.* **75**, p. 2678 (1995).
4. T. Baba, M. Fujita, A. Sakai, M. Kihara, and R. Watanabe, "Lasing characteristics of GaInAsP-InP strained quantum-well microdisk injection layers with diameter of 2-10 μm ," *IEEE Photon. Technol. Lett.*, vol.9, pp.878-880, 1997.
5. C. Gmachl, F. Capasso, E. E. Narimanov, J. U. Noeckel, A. D. Stone, J. Faist, D. L. Sivco, A. Y. Cho, "High-power directional emission from microlasers with chaotic resonators," *Science*, vol. 280, pp.1556-1564, 1998.
6. S. A. Backes, J. R. A. Cleaver, A. P. Heberle, J. J. Baumberg, K. Köhler, "Threshold reduction in pierced microdisk lasers," *Appl. Phys. Lett.*, vol.74, pp.176-178, 1999.
7. K.-C. Shin, M. Tamura, A. Kasukawa, N. Serizawa, S. Kurihashi, S. Tamura, and S. Arai, "Low threshold current density operation of GaInAsP-InP laser with multiple reflector microcavities," *IEEE Photon. Technol. Lett.*, vol. 7, pp.1119-1121, 1995.
8. T. Baba, M. Hamasaki, N. Watanabe, P. Kaewplung, A. Matsutani, T. Mukaihara, F. Koyama, and K. Iga, "A novel short-cavity laser with deep-grating distributed Bragg reflectors," *Jpn. J. Appl. Phys.*, vol.35, pp.1390-1394, 1996.
9. Y. Yuan, T. Brock, P. Bhattacharya, C. Caneau, and R. Bhat, "Edge-emitting lasers with short-period semiconductor/air distributed Bragg reflector mirrors," *IEEE Photon. Technol. Lett.*, vol.9, pp.881-883, 1997.
10. T. Höfling, R. Werner, F. Schäfer, J. P. Reithmaier, and A. Forchel, "Short-cavity edge-emitting lasers with deeply etched distributed Bragg mirrors," *Electron. Lett.*, vol. 35, pp. 154-155, 1999.
11. J. P. Mathieu, *Optics*, pp55-57, Pergamon Press, Oxford, 1975 (English edition translated by J. W. Blaker).

High Energy Photon Lithography for Fabrication of Photonic Device.

S. Lee^{*a}, V.Kudryashov^b, P. Lee^a, M Liu^a and T.L.Tan^a

^aNanyang Technological University, National Institute of Education, 469, Bukit Timah Road, Singapore 259756.

^bMicroelectronics Technology Institute RAS, Chernogolovka, Moscow district, 142432, Russia

Photonic crystals and other photonic devices could be efficiently produced using relatively simple and cheap Plasma Focus Pinch x-ray point sources, similar to the NX2. With this point x-ray source, it was demonstrated that with a proximity printing scheme, feature sizes less than 100 nm could be reproduced in a 500 nm UV3 CAR layer.

Submicron lithography, x-ray lithography, e-beam lithography, chemically amplified resists, high aspect ratio structures, soft x-ray sources, Plasma Focus Pinch.

1. INTRODUCTION

The development of X-ray lithography was initiated by D.L.Spears and H.I.Smith in 1972 [1,2]. During the next 27 years all the main components of this technology such as powerful soft x-ray sources, long-life and accurate x-ray masks with critical dimensions down to 100 nm and high sensitivity chemically amplified resists were successfully developed. Nevertheless, for application of this novel technology to commercial production of VLS microelectronic devices, some complicated hence expensive, technical problems, still need to be solved. These are connected mostly with the alignment of layers, requiring an accuracy of 10% of the critical element linewidth over a relatively large area.

However, a recently developed class of photonic devices can be successfully fabricated using existing x-ray lithography technology. This is because a large part of these devices do not need precise alignment of layers. A big number of photonic devices could be built using artificial 2D and 3D photonic crystals with structural dimensions smaller than the wavelength of visible light [3].

Such photonic crystals could be efficiently produced using relatively simple and cheap Plasma Focus Pinch x-ray point sources, similar to the NX2 [4,5]. With this point x-ray source, it was demonstrated that feature sizes less than 100 nm could be produced in a 500 nm UV3 chemically-amplified resist (CAR) layer.

Small size but high accuracy optical elements such as computer generated holograms for a visible and infrared light and Fresnel zone plates have been successfully produced by e-beam and x-ray microlithography technology.

Even micromechanical switch technology for optical fiber devices was recently developed on the basis of high aspect ratio structure microfabrication technology.

Maximum resist thickness of 5 micron could be exposed with 1 nm wavelength soft x-rays from the Plasma Focus operated in neon. The quality of exposure depends on mask contrast and critical feature size since exposure decreases with depth in the resist.

This state of art is good enough for the commercial production of 2D optical crystal. Furthermore, x-ray lithography provides a unique possibility to produce sub-100nm structures with high aspect ratio; for example 70 nm width lines in a 2 micron resist [6]. It is possible to do exposure at an oblique angle to the resist surface.

Therefore modern x-ray lithography techniques could be efficiently used for commercial production of new classes of optical devices based on 2D and 3D artificial crystals, at critical dimensions not achievable with optical wavelengths.

* Correspondence: Email: slee@nie.edu.sg ; web site: <http://www.ssc.ntu.edu.sg:8000/ckplee/> ; Telephone: 65 4605300
Fax: 65 4698952

2. SUBMICRON STRUCTURES FORMATION IN RESIST LAYERS WITH X-RAY LITHOGRAPHY.

One of the most powerful technology which provides structure element dimensions to 100 nm and below with a relatively high output and low cost is conventional proximity x-ray lithography.

At the very beginning of its development it was demonstrated that at small gaps between x-ray mask and wafer exposed the diffraction and shadow blurring of the image transferred could be done much smaller than 100 nm for a precise submicron structures fabrication. PMMA based resists, widely used for demonstration experiments, have the intrinsic resolution better than 10 nm, but a very low sensitivity - of the order of 500 J/cm² of absorbed energy. Even simple soft x-ray tubes with electrical power only 300 W and copper anode producing 1.3 nm wavelength irradiation with a very low conversion efficiency of 2×10^{-5} provide a reasonable exposure time of several minutes at a 20 mm distance. To replicate a sub-100 nm elements, mask has to be brought to a close contact with resist to avoid a shadow blurring as the irradiation spot of this x-ray tube has a typical dimension of 1 mm.

This was done by an absorption element fabricated directly onto the resist surface. A half-micron photoresist layer was spun on PMMA, exposed with UV through photomask and developed. Then a heavy absorption material (lead) was evaporated at an oblique angle onto the photoresist structure sidewalls. The thickness of the evaporated layer was only 100 nm and since the walls were vertical, the thickness was also the width of masking element in x-ray exposure. The good test structure exposed in 1.6 micrometer PMMA resist layer to dose 1000 J/cm² and developed in 1 : 4 MEK- IPA mixture has been obtained.

Structures produced in resist have near vertical walls. As linewidth is only 70 nm, for 1.6 micron resist height it gives aspect ratio more than 20. This experiment demonstrates that it is easy to get sub-100 nm resolution for single standing lines, if the technology reproducibility and process cost are not under discussion.

For single standing lines it is even possible to vary its width by the proper choice of exposure and development parameters. For instance, for positive resists, overexposure and overdevelopment can lead to linewidth reduction.

The second advantage of x-ray lithography is the possibility to expose a relatively thick resist layer. Submicron resolution could be demonstrated for 5-10 micron resist layers, and structures with several micrometer feature size could be produced even in 200-500 micron resist layers. The main limitations for these thick resist layers exposure are connected with x-ray absorption in resist.

Potentially efficient and cheap x-ray lithography technology for sub-0.1 micrometer feature size devices can be realised already with a powerful plasma focus SXR source for applications not requiring precise alignment of layers. Examples of such devices include artificial optical crystals and single domain magnetic media, and 10-20 micron thick MEMS and micro-optical elements production with sub-micron accuracy to replace inaccurate photolithography.

This simple laboratory equipment (Figure 1) is used for more than 15 years for technology development in x-ray lithography and simple single layer test structures production.

Some results specific to x-ray lithography and very important from different applications point of view were demonstrated using this simple equipment.

X-ray lithography is really the only one technology (except evaporation and ion etching at oblique angles) which gives a possibility to work on an exposed wafer in a direction not perpendicular to its surface. Other submicron lithography technologies such as UV and e-beam do not provide this possibility because of a very small depth of focus.

In the case of x-ray lithography simple tilting of the mask and wafer assembly result in a tilted structure, as shown in Figure 2.

Such exposure at an oblique angle could be done with the same resist layer two or three times at different angles, to give a really three-dimensional net in resist bulk during development. As x-ray lithography has a submicron resolution and a very large (10 to 50 micron) depth of focus, this structures could work as an artificial 3D optical crystals. Photons have demonstrated the same behavior in such artificial photonic crystals, as electrons in solid state.

Numerous works were published recently on similar three dimensional structures production technology based on ion etching at oblique angles. But x-ray lithography poses a much higher throughput and so a lower cost. Really this artificial photonic crystals can be one of the main applications for single layer x-ray lithography technology.

A very large (to 5 – 500 micron, depending on wavelength) penetration depth of x-rays in resist gives a possibility to expose thick resist layers and multilayer resist systems. The last gives possibility to produce structures with undercut or slope sidewall profile if resist layers have a different sensitivity.

There is an x-ray lithography technology in which a two different sensitivity resist system is exposed through a special mask with two different pictures, formed in two separate masking layers. In this case different exposure takes place under different mask zones. Mask contrasts and resists sensitivities are chosen in such a manner, that after exposure and development, instead of a binary resist structure, an intermediate height structure is additionally formed.

SEM pictures of test structures produced in 2 and 3 layer resist systems by x-ray exposure are shown in Fig.3.

3. X-RAY MASK DESIGN AND TECHNOLOGY

X-ray mask design and technology is still under development. There are numerous technical problems to be solved for practical application of already existing masks for VLSI device production. These problems are connected mostly with alignment accuracy for large area exposure zones. Different kinds of mask distortion caused by tension in its layers during its production and usage, complicate these problems.

However, for single layer devices where high-precision element positioning is not critical, existing masks could be successfully used for a 0.1 micron feature size device fabrication.

Two types of x-ray masks (Figure 4) were used in our experiments. For thick resist layer exposure and for exposures in which we have to be sure that the gap between mask and resist does not exceed 2-3 microns, a polymer membrane with 0.5 – 0.8 micron gold masking layer on it was used. At the beginning of exposure, a mask gets an electrical charge because of photoelectrons emission from its surface and attracts to the resist due to electrostatic forces.

These masks have a several micrometer element positioning run-out, but are cheap, long life and could be useful for some applications. Test structures formed in thick resist layers, including multi-layer resist systems were produced using this type of masks as shown in Figure 5.

Another type of x-ray masks (Figure 4) was employed for high-resolution experiments and was designed in a conventional manner. Silicon wafers with 100 nm Si_3N_4 membrane windows from FASTEC, UK were covered with Cr-Au electroplating base. Positive type PMMA or negative AZPN114 resists were spun on this surface with film thickness from 0.3 to 0.7 micron and structure was exposed with 30 kV electron beam at JEOL 820 SEM modified for e-beam lithography experiments. Then gold was electroplated to thickness 150 – 500 nm using a conventional electroplating technique. SEM pictures of masks with resolution test structure and Frenzel zone plate are given in Fig. 6.

4. CHEMICALLY AMPLIFIED RESISTS IN X-RAY AND E-BEAM SUBMICRON LITHOGRAPHY.

The main progress in submicron lithography technology development in recent years is the result of Chemically Amplified Resists (CAR) development. These resists provide sub-100 nm resolution and have sensitivity 10-100 times higher than conventional PMMA resists.

CARs have much higher resistance to plasma-chemical etching and good thermal stability. The only one disadvantage of positive CARs is "T"-topping effect, caused by the neutralization of the acid produced during exposure by the airborne contamination in the upper resist layer. For negative CARs the main technological troubles are connected with its poor adhesion to substrate and some swelling during development if exposure is smaller than optimal.

CARs are very flexible from application point of view as could be spun with thickness from 40 nm to 0.5 mm, exposed with UV, e-beam and x-rays. The last makes possible mix-and-match technology application to CARs. Resists have good mechanical properties and could be used for good 3D structures production. Here we mean structures which have a significantly different resist thickness at different areas, of a complicated special profile of structures walls i.e undercut or slope. For micromechanics and optics applications, special self-supporting structures are very important. It was demonstrated that different type of self supporting structures could be easily produced in a relatively thick single layer AZPN114 CAR.

To produce a 3D structure in a single layer resist it is necessary to use two (or more) exposures with agents having a different penetration depth. For example, in experiments described in Ref [7], a 2 micron resist layer was exposed with 30 and 5 kV electron beams. The penetration depth of a 30 kV electron beam is more than 2 microns, so irradiation with this high energy electron beam produces a homogeneous exposure for the all resist depth. On the contrary, 5 kV electrons have a range in the resist of the order of 0.5-0.6 micron only, and with this energy e-beam exposure is produced in the upper resist layer only. After these two exposures, Post Exposure Baking (PEB) and development we get self-supporting structures. SEM pictures of this structures are given in Figure 7.

Self-supporting structures similar to those in the left picture (Figure 7), especially produced in a transparent media like resist, could be used as an optical microfibre or a 3D grating. A relatively large, flat structure connected to the supporting basic structure with its edge only, as it is shown in the right picture (Figure 7), could probably be used as a micromirror array for optical beam deflection or modulation.

This experiment with e-beam exposure just illustrates the general idea, how to produce 3D structures in a single layer resist – two (or more) exposures with different penetration depth are required. If structure has to be produced in a thicker resist layer (more than 5 micron) x-ray lithography has been used for whole thickness layer exposure. Electrons with different energies from 1 to 100 keV could be used for a structure production in the upper resist layer.

Irradiation with soft x-rays (0.8 – 4.4 nm) also could be used for a structure exposure in the upper resist layer. The thickness of the exposed layer will be determined in this case by the x-ray absorption coefficient, dose and resist sensitivity. Varying exposure it will be possible to adjust the thickness of the upper structure layer. This will provide an extra flexibility to the method.

Negative CARs have an additional useful property in optics application. After exposure and postbaking, the resist base is crosslinked. Usually it leads to a polymer free volume reduction and so to the increase of its density. Refractive index increases slightly in this case. For some optical applications this rise could be big enough to change optical properties of the media. Even without development it could be possible to produce some “flat” optical elements similar with lenses, gratings and waveguides.

5. APPLICATION OF A PLASMA FOCUS SOFT X-RAY SOURCE TO LITHOGRAPHY TECHNOLOGY.

Soft x-ray tubes, used in simple lithography possibilities demonstration experiments, have a very low x-ray output because of a low electron beam power to x-rays conversion efficiency.

For copper anode and acceleration voltage of 8 kV the efficiency is only 2×10^{-5} . For mask to resist gaps suitable for practical use (from 10 to 20 microns) and resolution better than 100 nm, distance between point x-ray source and mask has to be at least 10 cm. This leads to exposure time of several hours for conventional positive resists.

To put x-ray lithography in practice, it is necessary to use a high sensitivity Chemically Amplified Resists and more powerful soft x-ray sources. In our work we used a plasma focus device for x-ray lithography, and investigate CARs application to soft x-ray lithography.

Experiments in x-ray lithography technology were carried out at NTU using a specially designed plasma focus device NX2 [4,5], shown in Figure 8.

The NX2 is a plasma focus x-ray source operated in neon gas. The capacitor bank consists of 48 capacitors with a total capacity of 30 μF . The capacitors are charged to a maximum 11.5 kV by ALE model 802 chargers with a total power of 32 kW.

The short circuit rise time is 1 μs . The on-load current peaks at 400 kA at a repetition rate up to 16 shots per second.

The SXR from the plasma focus point source goes through the hole in the bottom of the anode and passes through a magnet trap, which deflects and absorbs the high energy electrons ejected from the pinch. Low energy and scattered electrons and UV radiation are blocked with a 10 μm Be foil located at an entrance aperture of the x-ray mask and wafer holder.

The NX2 produces maximum 20J of SXR per shot at 16 shots per second giving up to 300W of SXR power. For demonstration purposes even operation at the 50W level provides a required exposure dose in a reasonable time and reduces the anode overheating damage problems. The effective radiation source size is less than 0.5 mm. At a working distance from 20 to 40 cm and mask-to-wafer gap of 10 microns the shadow blurring is below 20 nm. Irradiation x-ray spectrum of the neon plasma is shown in Figure 9.

This wavelength range, 0.8 - 1.4 nm, with the strongest emission lines between 1 and 1.4 nm, provides mask contrast better than 10 for the 0.3 micron gold absorption layer. So, all the main parameters of NX2 such as radiation spectrum, source spot size and SXR power meet the technological requirements of the x-ray lithography for a laboratory application.

For demonstration, our test x-ray masks consist of 0.3 μm Au structure with lines to 0.2 μm and gaps below 0.1 μm electroplated on 0.1 μm Si₃N₄ membrane with Cr-Au (5 and 20 nm) electroplating base. Exposure was done with close contact between mask and resist, (no special extra spacer was used) to provide the highest possible resolution. Resists soft baking, post exposure baking and development were done in a conventional way [Figure 10]. We used UV3 CAR for this demonstration.

It is well known from experiments in e-beam lithography that both AZPN114 and UV3 have a resolution better than 0.1 μm for 0.3-0.5 μm layers and sensitivity 20 to 50 times higher than conventional PMMA.

The main problems for such high aspect ratio structures formation are the poor adhesion of negative resist and swelling during development, if exposure is not big enough, and a "T"-topping effect for positive resist.

Resist in gaps slightly below 0.1 μm is not removed completely at the groove bottom. It can be explained first of all by the gap dimension dependence of the dissolution mechanism - the narrower the gap, the slower the development of the resist and the slower the motion of the dissolved resist molecules.

But more likely this effect is connected with CAR nature of the resist. During x-ray exposure all lines despite of their width are irradiated with the same dose. Dose-on-linewidth correction is impossible. In our case the width of the exposed line is comparable with a diffusion length of the acid molecules produced during exposure. The concentration of the acid molecules can reduce significantly in the exposed zone because of their drift outside this zone. It leads to a linewidth dependant dissolution rate reduction for lines below 0.1 μm .

So, proximity exposure of thin positive CAR layers with SXR on NX2 plasma focus station provides resolution to 0.1-0.2 μm with a reasonable exposure time.

6. CONCLUSION

Although x-ray lithography is still not widely used for VLSI semiconductor device production, it can be very useful and competitive for a single layer device production. For application in optics this single layer structure could be made 3D even in one resist layer. For commercial applications relatively simple and low cost plasma focus stations could be used for highly efficient soft x-ray production. To increase the throughput, resists with chemical amplification have been used.

A big variety of optical devices could be produced by x-ray lithography – lenses and zone plates, gratings and waveguides, micromechanical optical fibers switches and connectors, flat panel deflectors and modulators. But the most promising application of the already existing x-ray lithography technology is artificial 3D optical crystals production.

7. REFERENCES

1. D.L.Spears and H.I.Smith "High-resolution pattern replication using soft x-rays" *Electron letters* **8**, pp 102-104, 1972.
2. D.L.Spears and H.I.Smith "X-ray lithography - a new high resolution replication process" *Solid State Technology* **15**, pp 21-26, 1972.
3. P.Villeneuve, J.Joannopoulos "Tricks of the light" *New Scientist* **26**, pp 26-28, 1995.
4. S.Lee, P Lee, G Zhang, A Serban, M Liu, V Kudryashov, X Feng, S V Springham, T K S Wong and C Selvam. "Powerful soft x-ray sources and high resolution lithography" *Sing.J.Phys.* **14**, No.1, 1-9, 1998.
5. S Lee, P Lee, G Zhang, X Feng, V Gribkov, M Liu and T K S Wong. "High rep rate, high performance plasma focus as a powerful radiation source" *IEEE Trans Plasma Science.* **26** (4), pp 1119-1126, 1998.
6. V.V.Aristov, V.A.Kudryashov, Yu.V.Krutenuk, "Structure Profiles in Positive X-Ray Resists" *Pros. Microcircuit Engineering 83* (Academic Press, London), pp 343-350, 1983.
7. V.A.Kudryashov, V.V.Krasnov, S.E.Huq, P.D.Prewett and T.J.Hall. "Electron beam lithography using chemically-amplified resist: resolution and profile control." *Microelectronic Engineering* **30** pp 305-308, 1996.

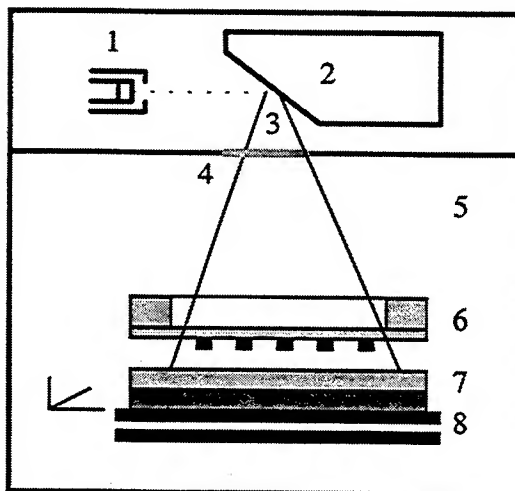


Figure 1. X-ray lithography system . 1- electron gun, 2- anode, 3- x-rays, 4- vacuum window, 5- exposure chamber, 6- x-ray mask, 7- substrate with resist, 8- X-Y-Z stage.

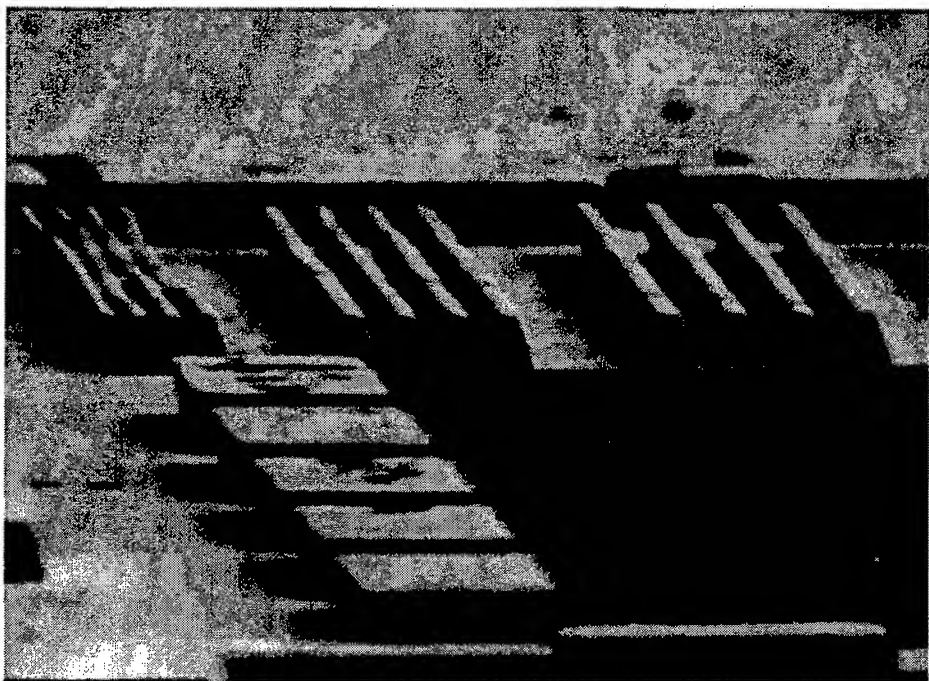


Figure 2. Tilted structures exposed in 3 um PMMA layer with polymer mask providing only 2 um masking layer – resist gap.

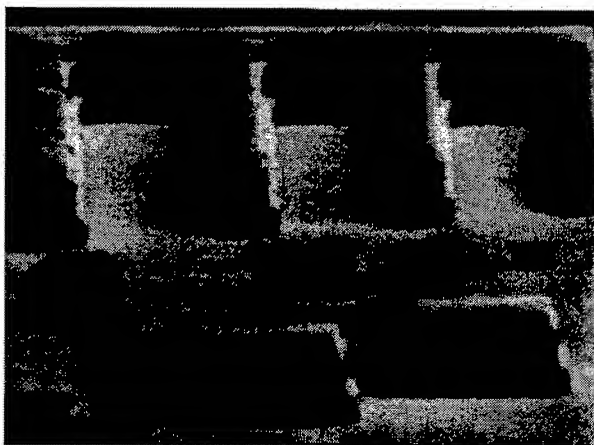
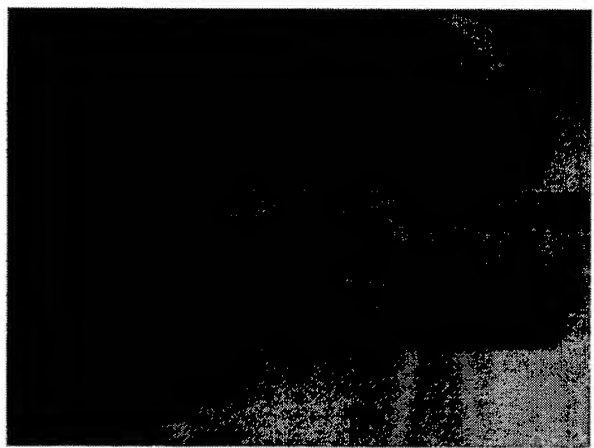


Figure 3. Test structures with undercut (left) and slope (right) sidewall profile produced by x-ray exposure in 2 and 3 layer resist systems.

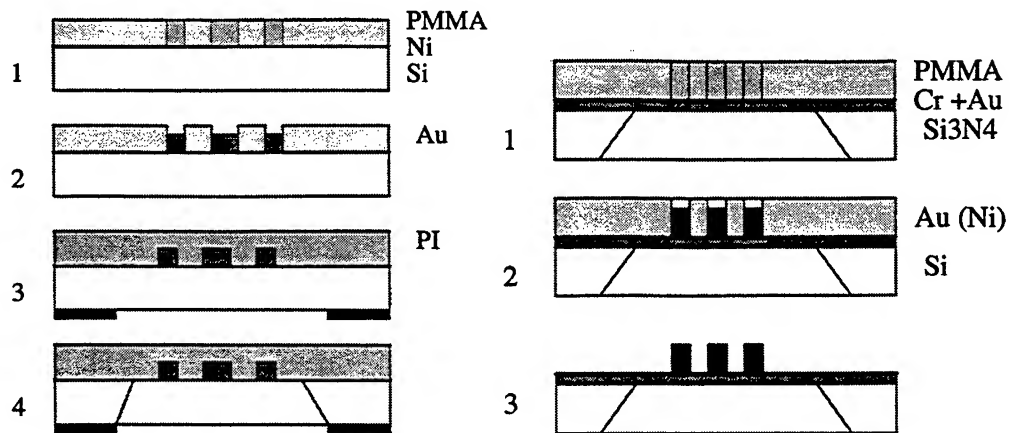


Figure 4. Schematic diagram of Polymer (left) and Si₃N₄ (right) membrane x-ray masks technology.

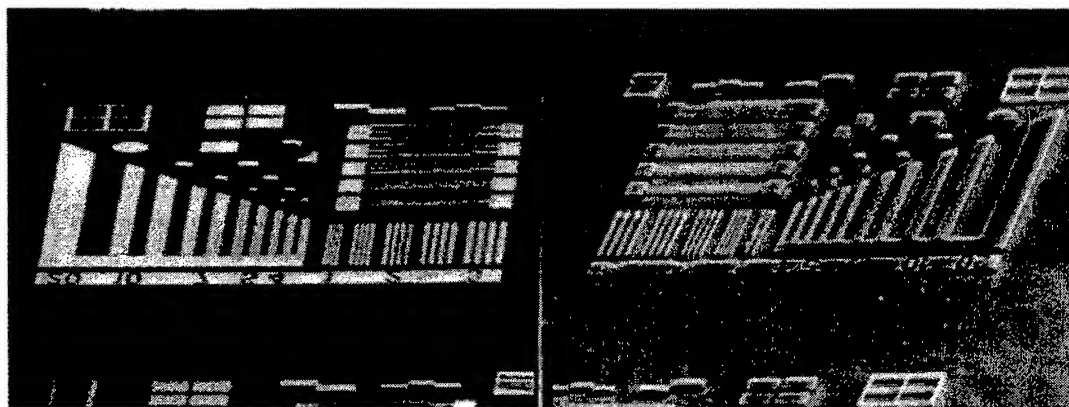


Figure 5. SEM picture of a masking layer for a polymer membrane x-ray mask and its replica in 4 um PMMA layer produced by Cu-anode 1.3 nm wavelength x-ray tube.

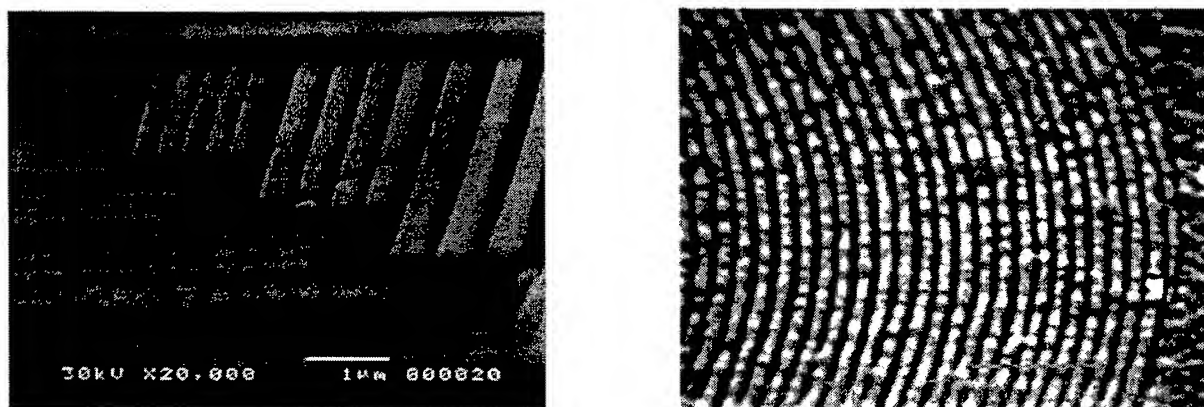


Figure 6. SEM pictures of gold masking structure formed on 100 nm Si₃N₄ membrane, left - resolution test structure with a minimal linewidth to 80 nm, right- zone plate structure with an outer zone width 60 nm.

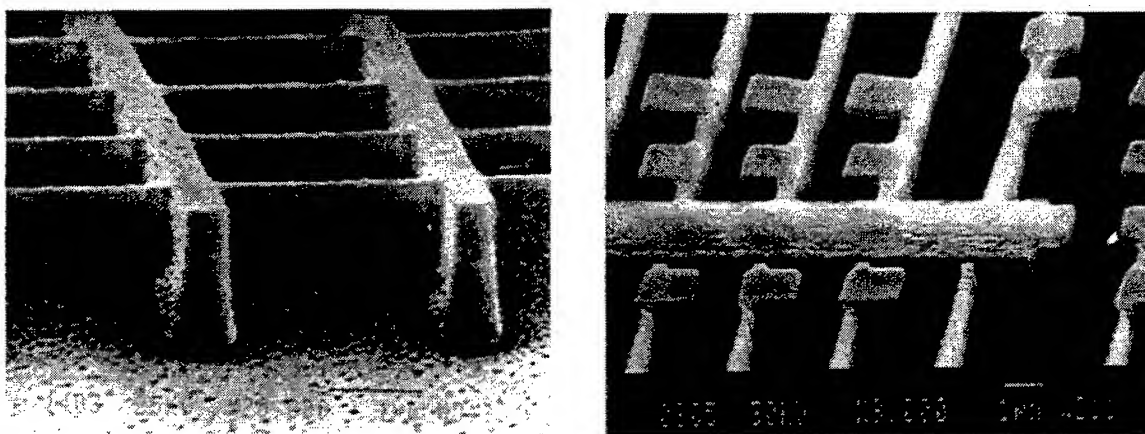


Figure 7. Self-supporting structures, produced in AZPN114 CAR with 5 and 30 kV e-beam exposure.

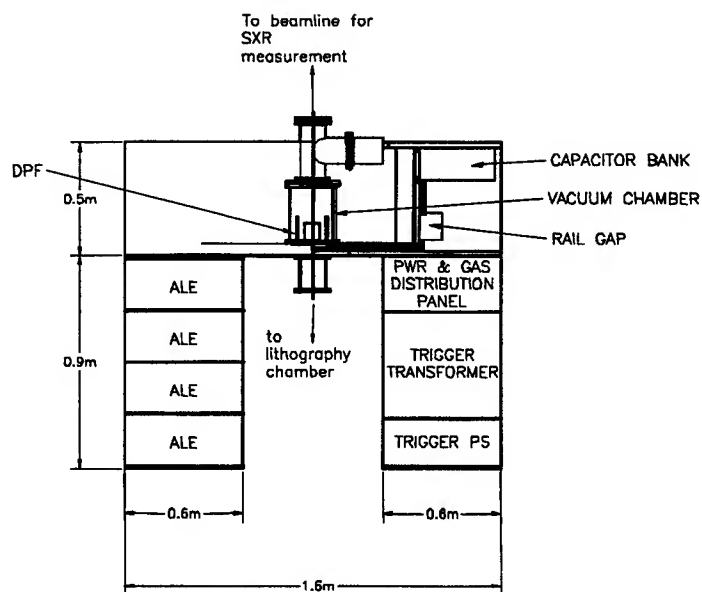


Figure 8. Schematic diagram of the NX2.

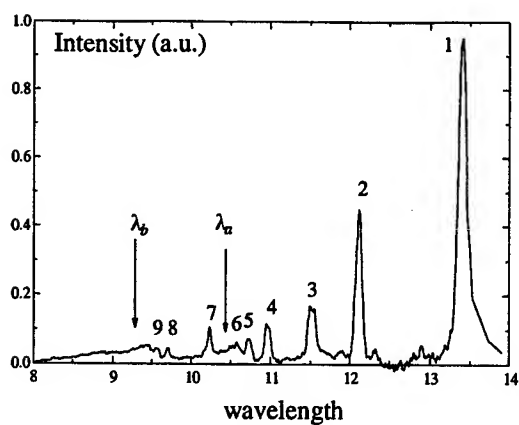


Figure 9. Neon plasma x-ray spectrum.

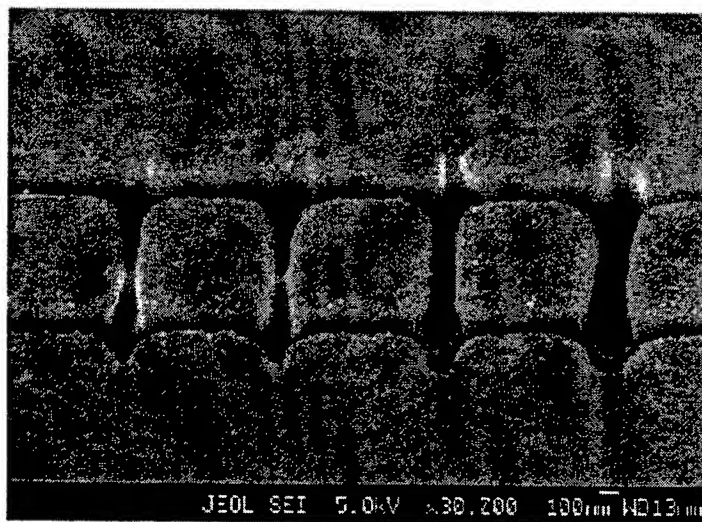


Figure 10. Test structure with sub 0.1 um gaps exposed with x-rays from NX2 in 0.5 um UV3 CAR.

SESSION 6

Photonic Bandgaps

3-D, Silicon, Infrared, Photonic Lattices

J.G.Fleming* and Shawn-Yu Lin**

*Org 1723, MS 1084

**Org 1712, MS 0603

Sandia National Laboratories,
P.O. Box 5800 Albuquerque NM 87185

ABSTRACT

Three-dimensional photonic lattices are engineered "materials" which are the photonic analogues of semiconductors. These structures were first proposed and demonstrated in the mid-to-late 1980's. However, due to fabrication difficulties, lattices active in the infrared are only just emerging. A variety of structures and fabrication approaches have been investigated. The most promising approach for many potential applications is a diamond-like structure fabricated using silicon microprocessing techniques. This approach has enabled the fabrication of 3-D silicon photonic lattices active in the infrared. The structures display bandgaps centered from 12μ down to 1.55μ , depending on pitch.

Keywords: Photonic lattice, Infrared, Photonic bandgap.

1. INTRODUCTION

The drive for miniature photonic devices has been hindered by our inability to tightly control and manipulate light. Moreover, photonics technologies are typically not based on silicon and, up till now, only indirectly benefited from the rapid advances being made in silicon processing technology. In this work, we overcome the disadvantage of silicon inherent in its electronic structure by using Si processing to create a 3-D silicon photonic lattice. This advance has been made possible through the use of a combination of IC (Integrated Circuit) fabrication technologies and may enable the penetration of Si processing into photonics.

The ability to confine and control light in three dimensions would have important implications for quantum optics and quantum-optical devices: the modification of black-body radiation, the localization of light to a fraction of a cubic wavelength, and thus the realization of single-mode light-emitting diodes, are but a few examples¹⁻³. Photonic crystals, the optical analogues of semiconducting crystals, provide a means of achieving these goals. The photonic band structure results when light encounters a well-defined repeating arrangement of materials with differing refractive indexes, see for example Figure 1.

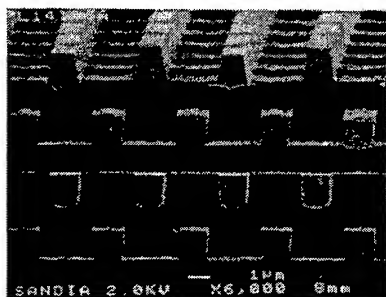


Figure 1: Oblique scanning electron micrograph showing a 7 layer photonic lattice fabricated in polysilicon with bandgap between 10 and 15μ .

This behavior is entirely independent of the electronic properties of the material making up the lattice, as long as it does not strongly adsorb. When correctly designed and fabricated, such structures can exhibit the property that photons with the bandgap energy cannot penetrate the lattice, regardless of their angle of incidence. The existence of photonic bandgaps was proposed over a decade ago ^{4,5} and was quickly demonstrated at millimeter wavelengths using macroscopic repeating structures made of machined rods ^{6,7}. However, since the critical dimensions of the lattice scale with the wavelength of the light, a reduction in wavelength to the infrared requires structures with minimum feature sizes on the order of a micron. As a result, until now, fabrication difficulties have stymied research in this area.

In this paper, we shall briefly summarize the various designs of 3-D photonic bandgap structures. We shall then outline the various fabrication approaches proposed to date, concentrating particularly on a silicon processing based approach which lends itself to integration with Si processing ^{8,9}. We will then provide experimental details of the properties of these artificial materials and outline their potential applications.

2. DESIGNS

Yablonovitch ⁴ and John ⁵ first proposed the photonic lattice concept in 1987. In general, the idea was to modulate photons in a manner similar to the way electrons are modulated in a semiconductor. This is achieved through a periodic variation in refractive index. A pseudo-gap was first demonstrated in a macroscopic FCC (face centered cubic) structure with spherical air-atoms ¹⁰. A design with a full bandgap based on diamond symmetry was proposed by Ho *et al.* of Iowa State University ^{6,7}. This design consists of a series of dielectric rods all aligned parallel to each other with a pitch equal to roughly half the wavelength of the mid point of the bandgap gap. The next layer is laid on top of, and orthogonal to, the first. The third level is aligned parallel with the first, but translated by a distance equal to half the pitch. The fourth level is parallel to the second, but is again translated by a distance of half the pitch. The structure then begins to repeat itself, Figure 1. This design mimics the way in which chains of atoms are lined up along the $\langle 110 \rangle$ directions in a diamond lattice. The resulting structure has a face-centered-tetragonal (FCT) lattice symmetry of which FCC is a special case. This design will be considered in most detail here since it lends itself to fabrication. A different design, which more closely mimics the arrangement of atoms in the diamond structure, but which is more difficult to fabricate has also been proposed ¹¹. Similar structures consisting of stacked rods, have been generically described as "wood-pile" structures ¹². Another structure with a full band gap has been proposed by workers at MIT and consists of a series of offset plates inter-attached by a series of columns ¹³. The simple cubic structure is also predicted to have a full gap ¹⁴. An interesting "triple-hole" structure has also been demonstrated ¹⁵ and will be considered in more detail below. We at Sandia have also proposed several structures, such as an inverse "stick figure" FCC structure, as well as inverse "stick figure" HCP and other high symmetry structures which demonstrate photonic band gaps at normal incidence, but which may not exhibit full bandgaps.

During the evolution of these structures a number of rules of thumb have been developed. Successful lattice designs have large contrast in refractive index, a high degree of symmetry, and interconnected regions of high index material. While the theory describing the properties of these structures has now been well developed, it will not be considered here. However, it should be noted that it is possible to completely describe these properties using Maxwell's equations. However, though the equations can be solved, the problems are of a complex vector form requiring detailed code and extensive computational capabilities. Because of these difficulties, most research groups tend to concentrate their efforts on a single structure for which they have developed and refined the code.

3. FABRICATION

Over the past decade, several of the designs proposed above have been fabricated. Since the dimensions of the lattice scale with the wavelength of light, it is possible to fabricate active millimeter regime structures using macroscopic processes. In this fashion the "Iowa" state structure has been demonstrated ^{6,7}. The problem in reducing the dimensions of the lattice to the more technologically interesting infrared is that the minimum feature sizes approach the micron regime.

The first approach to this problem was the "triple-hole" technique of Yablonovitch¹⁵. In this approach, a series of three holes are bored into the substrate through a surface mask. The holes are not perpendicular to the substrate; instead they are at an angle of 35 degrees from the normal, with each hole rotated 120 degrees one from another. The end result is a series of interconnecting holes with a high degree of symmetry. Since each hole is drilled through the same top-surface mask, only one photolithography level is required. Using e-beam techniques it is possible to obtain the minimum feature sizes required for the structure to be active in the infrared. However, while this approach was extremely innovative, it requires nonstandard processing and the performance of the structures did not meet expectations, possibly due to distortions of the hole shape and the gradual, cumulative, deviation from ideality inherent in such a approach.

Another fabrication approach demonstrated by Noda¹⁶ involves the use of wafer bonding. In this approach, etching, wafer bonding and selective etching build up the layers making up the structure. Alignment is achieved using interference techniques. The advantage of this unconventional approach is that it enables the use of traditional III-V materials. A completely different approach is the use of artificial opals. In this approach, close packed layers of mono-sized spheres are laid down to form either the structure or mold^{17,18}. The advantage of this approach is that large volumes of material should be achievable relatively cheaply. Yet other fundamentally different approaches have been the use of deep x-ray lithography to form a complex 3-D mold¹⁹, and the use of two-photon polymerization²⁰. The large variety of different fabrication techniques reflects both the difficulty of fabrication and the interest in these structures.

The approach we have taken in our work^{8,9} has been to employ the structure extensively studied in the millimeter regime by Iowa State University^{6,7}, and fabricate it using modified silicon integrate circuit fabrication processes. In the work described here, the width of the rods was targeted initially at 1.2μ , the height of the rods was targeted at 1.6μ and the pitch of the rods was targeted at 4.2μ . In our more aggressive structure the width was targeted at 0.18μ , the height at 0.22μ and the pitch at 0.65μ . We have also fabricated intermediate sized structures. The bandgap size is determined by the dielectric contrast of the two different materials that constitute the 3-D structure and by the filling fraction of the higher dielectric constant material. The index contrast in our case is between polysilicon and the surrounding air and is therefore $\sim 3.6:1$, or in the case where the sacrificial silicon dioxide has not been removed, $3.6:1.46$.

Two different processes were developed in the course of this work. The first process combined a series of mold definition, mold filling, and CMP (chemical mechanical polishing) steps to create parts with a minimum feature size of 1.2μ . The second process allowed us to fabricate parts with minimum feature sizes of 0.18μ . This was performed on a stepper with a 0.5μ limit of resolution and involved a complicated series of fillet processing, reactive ion etching and CMP. In both cases processing proceeded in a layer-by-layer fashion. The first process is schematically rendered in Figure 2.

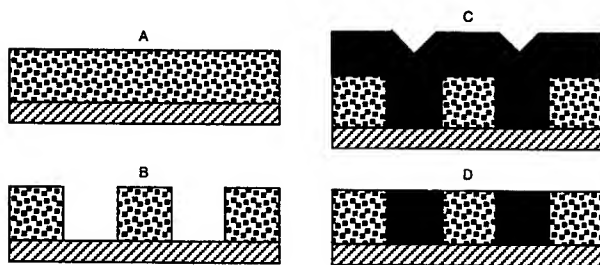


Figure 2: There are a number of possible modifications to this basic flow, for example the patterning of the as-deposited poly, or the filling of trenches between poly lines. In every case the elimination of previous level topography by CMP is critical.

There are alterations to the general process flow, depending upon the features, for example, the polysilicon thickness can be made equal to the layer thickness and then patterned to form the second layer. Gaps between the rods can then be filled with silicon dioxide, which is then planarized by CMP. The entire process can then be repeated to add additional layers. In all of the processes investigated, the use of CMP to

maintain planarity is critical. CMP ensures that topography introduced in one layer does not propagate into subsequent levels. In this manner, the number of levels is limited only by the generation of stress on the wafer. At the end of the process, the silicon dioxide can be selectively removed using a HF based solution to increase the refractive index contrast. Also, since the performance of the device only depends on a contrast in dielectric constants, the resistivity of the polysilicon and the contact resistance between layers are immaterial. Figure 1 shows a 7 layer structure fabricated using this process.

As examples of the flexibility of this approach we have used it to fabricate not just the "Iowa State" ^{6,7} structure, but also the "MIT" structure ¹³, the "90-degree" Iowa State structure, the simple cubic structure ¹⁴, an inverse FCC structure, an inverse HCP (hexagonal close packed) structure, the Wurtzite structure, as well as other less common structures. An example of the MIT structure (proposed by the group of Joannopoulos ¹³ at the Massachusetts Institute of Technology), fabricated using this approach is given in Fig. 3. In this case, the MIT design was broken up into its component slices and the slices were then fabricated sequentially, with CMP being used to ensure planarity. We have experimentally demonstrated that this structure also has a photonic bandgap. This particular structure is of sufficient complexity that it would be difficult to fabricate and test on a macroscopic scale. Another technologically interesting design is the "90-degree" Iowa State structure. One of the distinguishing characteristics of 3-D lattices is that the bandgap exists for all angles of incidence of light. This is predicted theoretically, however, it is experimentally difficult to demonstrate for the "zero degree" case, in which the incident light is parallel to the substrate surface. Furthermore, this structure can not be readily fabricated on the macroscopic scale and tested in the millimeter regime. However, using the layer-by-layer fabrication approach, it is possible to again break up the "90-degree" Iowa State structure into separate slices and then assemble them in a layer by layer fashion using the process outlined above. The end result is shown in Figure 4. Testing of this structure is experimentally straightforward and a gap is indeed found. Examples of other structures fabricated using the same process are given in Fig. 5.

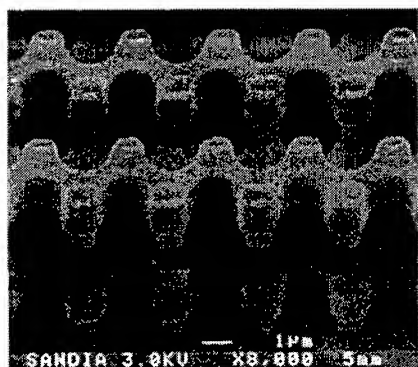


Figure 3: Oblique view cross section through the first three levels of the MIT structure ¹³ fabricated using the layer-by-layer technique. This complex structure would be difficult to fabricate using macro-machining techniques.

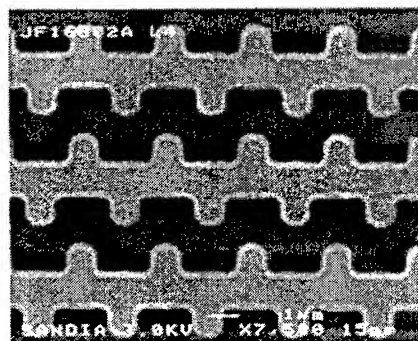


Figure 4: Top view scanning electron micrograph of a "Iowa State" structure ^{16,7} fabricated using the layer-by-layer approach. The fabrication of this structure enabled us to demonstrate experimentally the existence of a full 3-D photonic bandgap. Such a structure is difficult to fabricate on the macroscopic scale.

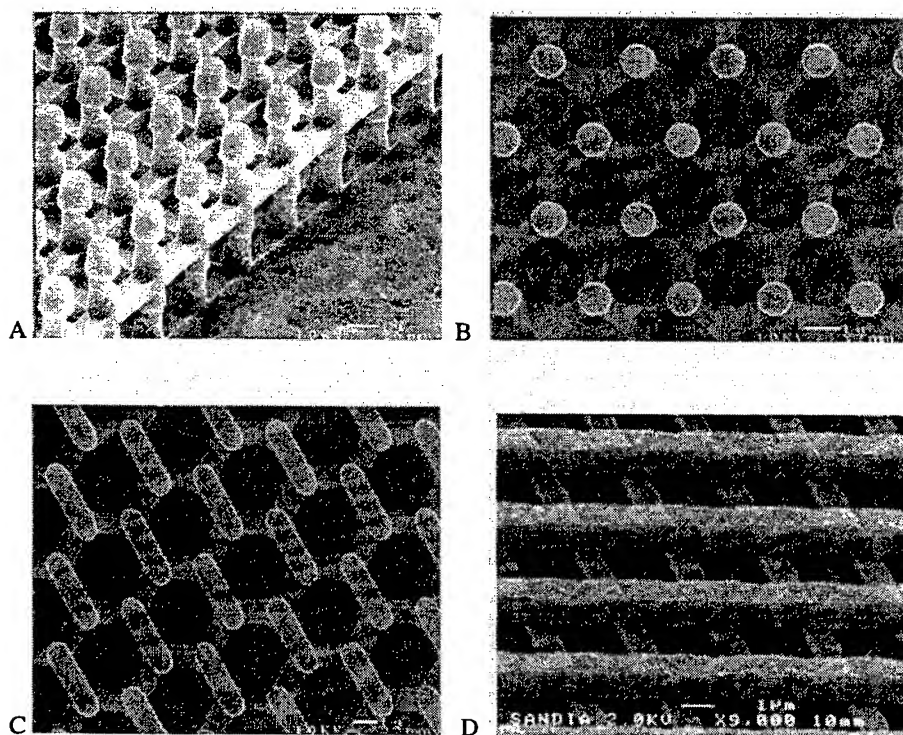


Figure 5: Examples of other structures fabricated using the mold approach. A is an example of the simple cubic structure. B shows the top view of a portion of the inverse FCC structure. C is the top view of a Sandia structure with a inverse HCP structure while D is an oblique view of a "woodpile" structure¹².

Our second, more aggressive, process relies on the use of fillet processing to obtain the minimum feature sizes required and is discussed in detail in Ref. 9. The process employed is considerably more complex, however, this complexity was driven by a lack of a stepper with sufficient resolution. Steppers with adequate resolution are now commercially available and the much simpler mold process can now be extended essentially to the band edge of Si. Figure 6 shows a part fabricated using the fillet process with a mid-gap of 1.5 microns.

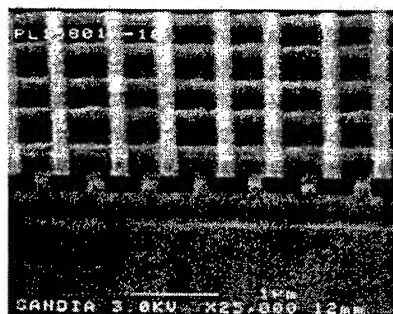


Figure 6: An oblique view of a cross section through a device formed by fillet processing. Due to the aggressive nature of the requirements on feature size and alignment the end result is not as well defined as the less aggressive part. However, as will be seen below, these defects had relatively little effect on the performance of the structure.

To date, we have found the performance of these devices to be relatively insensitive to most processing parameters. Level-to-level alignment can deviate by as much as 10%, as can layer width and height, without seriously compromising performance. However, care must be taken to ensure that neighboring levels make physical contact if the silicon dioxide is to be removed at the end of the process.

4. TESTING

The existence of a bandgap in these structures was determined from optical transmission and reflection measurements. Since light with the bandgap energy is forbidden, it is not able to penetrate the lattice and is instead reflected. To test the transmission properties of the 12μ mid-gap devices we used a standard, room temperature, Fourier-transform infrared measurement system with a broad spectral response from 2.5 to 25μ . The more aggressive device was tested with a similar system with a spectral range from 1 - 3μ . Before measurement, the back of the Si substrate was polished to a smoothness of better than 0.3 microns to avoid significant light scattering. The sampling beam was collimated to within a 10 degree divergence angle and had a spot size of $\sim 3\text{mm}$. Unless otherwise noted, the infrared light is incident along the stacking direction of the 3-D photonic crystal and was unpolarized. To find the absolute transmittance, a reference spectrum from a bare Si wafer coated was first obtained along with the signal spectrum taken from a wafer with a 3-D photonic crystal built on it. By ratioing the signal to the reference spectrum, the system's detector response was normalized, thereby eliminating the small unwanted absorption and other losses in the silicon substrate.

The absolute transmission and reflection spectra of light propagating along the $\langle 001 \rangle$ direction of the 3-D photonic crystal, that is, normal to the substrate, is plotted as a function of wavelength in Figures 7. Between 10 and 14μ , a strong transmittance dip is observed, signifying the existence of a photonic bandgap in the 3-D structure. Since light with these wavelengths can not penetrate the lattice it is reflected, indicated by an increase in the reflectance spectrum. A similar phenomenon is illustrated in Figure 8 for the transmittance through a crystal with midgap at 1.5 microns fabricated using the fillet process.

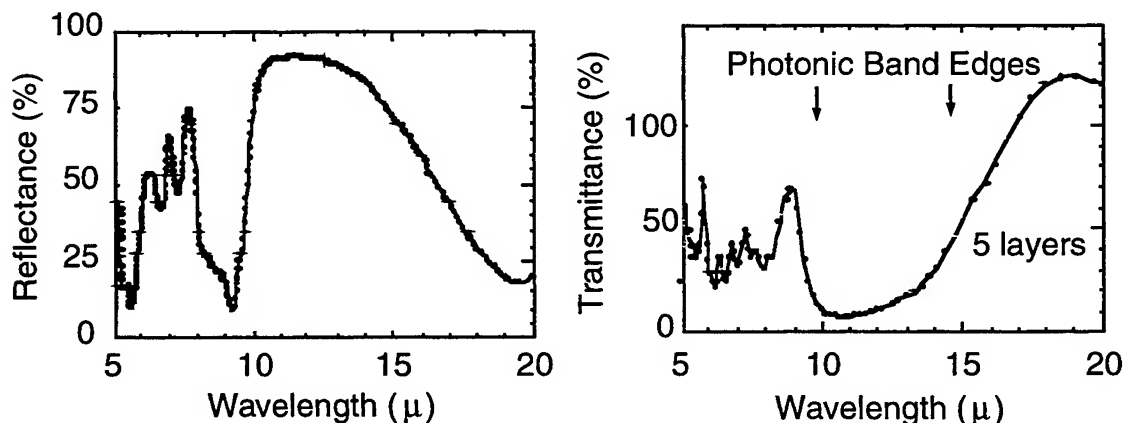


Figure 7: Plots of transmittance and reflectance through a 5 layer, 12μ midgap structure. There exists a dip in transmittance, which corresponds with an increase in reflection indicating the existence of the bandgap in the structure.

Figure 8 also shows the manner in which the bandgap develops with the addition of layers. To date the most layers we have fabricated are 12 for a structure with a midgap centered at 6μ . Figure 9 shows the transmission spectra of the 7-layer lattice shown in Fig. 1. In general, there appears to be roughly a factor of 2 reduction in transmission for every layer of lattice added.

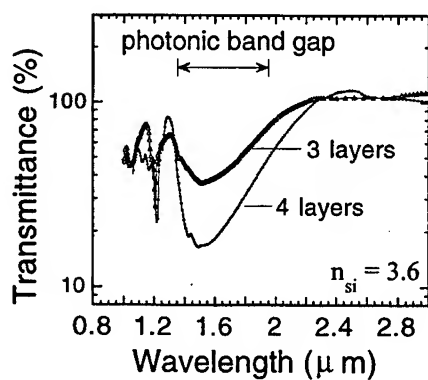


Figure 8: A plot of transmission as a function of wavelength for 3 and 4 layers of crystal with gap centered at 1.5μ . The development of the gap with the addition of layers can be clearly seen.

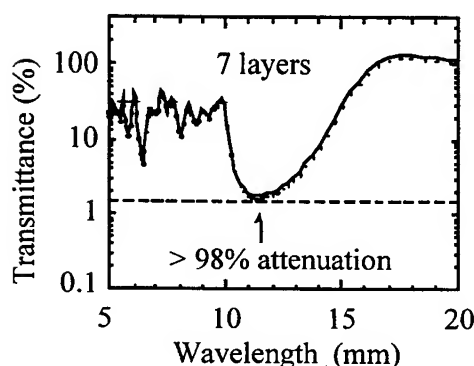


Figure 9: Plot of transmission amplitude as a function of wavelength for the structure shown in Fig.1. At a wavelength of 11μ there is ~98% attenuation. At this wavelength there is minimal absorption of light by the polysilicon. The lattice itself is only 10.5μ thick.

One of the distinguishing characteristics of the 3-D photonic lattice is that the bandgap is preserved regardless of the angle of incidence of light. This property is experimentally demonstrated in Figure 10.

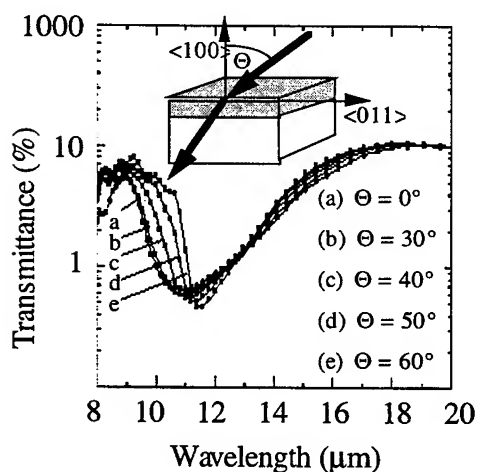


Figure 10: Plot of transmittance as a function of angle for a structure with mid-gap at 12m . Unlike a diffraction grating, the photonic band-gap exists for all angles of incidence.

As was mentioned above, the experimental determination of the gap at 90 degrees incidence is effectively impossible. However, this property was investigated by fabricating the lattice at 90 degrees (Fig. 4) and then determining the transmission, Fig. 11. It should be noted that the pitch of the 90 degree sample is different than that of the crystal in Fig. 1. The gap of a 2.5 unit cell MIT structure is given as is that of a 2 unit cell simple cubic structure. In both cases, spectra are taken with the beam orthogonal to the plane of the wafer. The angular dependence of the gap has not yet been determined, however, theory predicts that a full gap exists for the MIT structure¹³ as well as the simple cubic structure¹⁴. The 60 degree woodpile structure was also fabricated, Fig. 5d. However, a gap was not observed at 90 degrees for a structure with line pitches similar to those of the Iowa State structure. Another structure predicted to demonstrate a full gap is the inverse FCC structure¹⁵, Fig. 5b. In this structure, the atoms of a FCC lattice are replaced with empty space and visa-versa. This structure has been fabricated and the spectra obtained at 0 degrees is also shown given in Fig. 11.

All of the structures described above can be found in the literature. One of the advantages of the mold fabrication process is that it makes possible the simultaneous fabrication of a large variety of different structures. All of the examples described above were fabricated in a single lot, as well as several not found in the literature, which experimentally exhibit gaps at 0 degrees. Work is currently underway to determine which, if any, of these structures demonstrates full gaps.

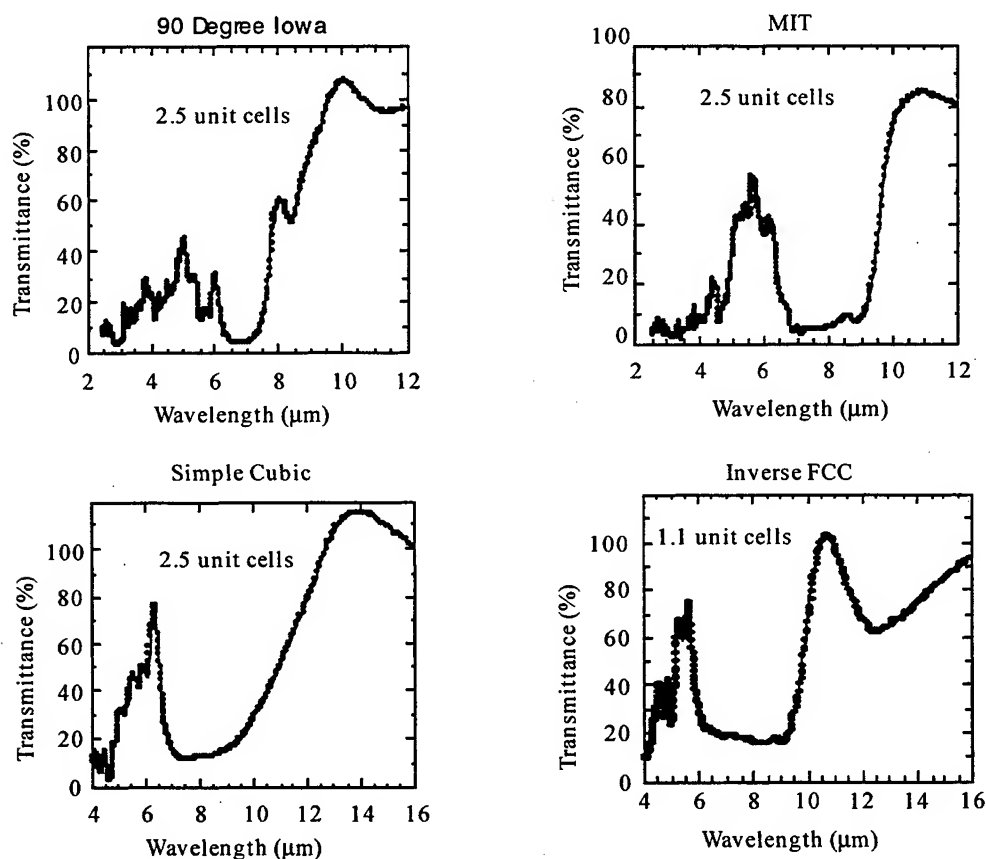


Figure 11: Transmission spectra of various different designs fabricated using the mold approach. In each case the spectra were obtained with an angle of incidence normal to the surface.

5. POTENTIAL APPLICATIONS

While still in its infancy, this technology has great potential. In our work we have demonstrated that the lattice building blocks can be fabricated in the infrared and optical ($1.5\ \mu$) wavelengths using widely available and supported Si fabrication equipment. Even these simple structures have interesting physical properties, they are efficient dielectric mirrors and they no longer demonstrate typical black body emission²¹. This property demonstrates that these structures exhibit truly different fundamental properties.

In this work we have also demonstrated the ability to fabricate cavities with volume less than one cubic wavelength²² this has potentially important implications for the fabrication of single mode LED's and lasers^{1,2}. These cavities are the result of intentional structural defects introduced into the lattice. The defects can either be additive, (the periodic addition of a line or line segment) or subtractive (the periodic removal of a line or a line segment). Fig. 12 gives examples of both types of cavity. Knowledge of the influence that such structural defects can have on the lattice can also be used to design efficient three-dimensional waveguides. In this application, the light propagates through the lattice by travelling along a string of intentionally introduced defects. This is a fundamentally different process than the traditional approach to waveguides, which relies on a gradation in refractive index and is restricted as to the maximum bending angle. Using the photonic lattice approach, 90 degree bends have been demonstrated in 2 dimensional structures at millimeter wavelengths,²³. While waveguides in 3-D photonic crystals have not yet been demonstrated, we are confident, based on the 2-D result, that such guides with 90 degree bends are possible.

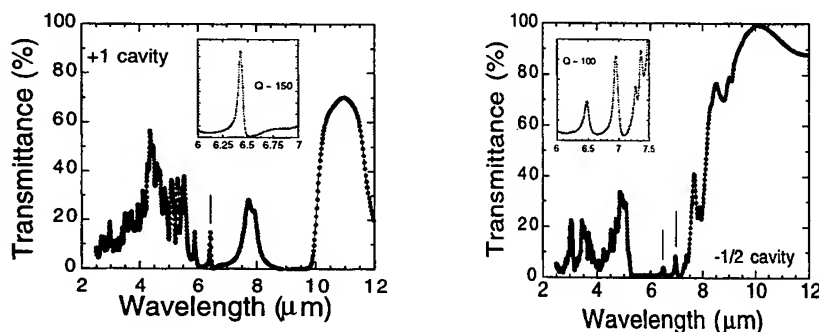


Figure 12: Transmission spectra of various cavity designs. In the first, extra material is added to the structure and in the second, material is removed from the structure.

The early work in this area^{4,5} was motivated by a desire to find a way to modify the spontaneous emission of light during various physical processes. This behavior is expected by theory and has been partially demonstrated by the modification of the black body emission spectra²¹. It may be possible to use this property to greatly increase the emission efficiency of a very narrow range of wavelengths in what would normally be a inefficient, broad band emission spectra, such as the emission of erbium in Si-based materials. If such a property can be demonstrated, it may lead to the development of silicon-based lasers and LED's, that are active at optical communication wavelengths. This could herald the evolution of low cost, complex, electronic and photonic components existing on a single chip and based upon a common set of materials and fabrication processes.

6. ACKNOWLEDGEMENTS

These parts were fabricated at Sandia National Laboratories Microelectronics Development Laboratory. The authors especially acknowledge the efforts of Tony Farino, Brad Smith, Dale Hetherington and Pat

Shea. This work was supported by the United States Department of Energy under contract DE-AC04-94AL85000. Sandia is a multiprogram laboratory operated by Sandia Corporation, a Lockheed Martin Company, for the United States Department of Energy.

7. REFERENCES

- ¹ E. Yablonovitch, Photonic band-gap structures. *J. Opt. Soc. Am. B* **10**, 283-295 (1993).
- ² J. Joannopoulos, R. Meade, & J. Winn, *Photonic Crystals*, (Princeton Press, New York, 1995).
- ³ J. Foresi, *et al*, Photonic band gap microcavities in optical waveguides, *Nature*, **390**, 143-145 (1997).
- ⁴ E. Yablonovitch, Inhibited spontaneous emission in solid-state physics and electronics. *Phys. Rev. Lett.* **58**, 2059-2062 (1987).
- ⁵ S. John, Strong localization of photons in certain disordered dielectric superlattices. *Phys. Rev. Lett.* **58**, 2486-2489 (1987).
- ⁶ Ho, K. *et al*, Photonic band gaps in three dimensions: new layer-by-layer periodic structures, *Solid State Comm.* **89**, 413-416 (1994).
- ⁷ Ozbay, E. *et al*, Measurement of three-dimensional photonic band gap in a crystal structure made of dielectric rods, *Phys. Rev. B* **50**, 1945-1948 (1994).
- ⁸ S.-Y. Lin *et al*, A three-dimensional photonic crystal operating at infrared wavelengths, *Nature*, vol. **394**, 251-253 (1998).
- ⁹ J.G. Fleming and S.-Y. Lin, A three-dimensional photonic crystal with stop band between 1.35 and 1.95 microns. *Optics Lett.* **24**, 49-51 (1999).
- ¹⁰ E. Yablonovitch and T.J. Gmitter, Photonic band structure: the face-centered cubic case, *Phys. Rev Lett.* **63**, 1950-1953 (1989).
- ¹¹ K.M. Leung, Diamondlike photonic band-gap crystal with a sizable band gap, *Physical Review B*, **56**, 3517-3519 (1997).
- ¹² Sozuer, H. & Dowling, J., Photonic band calculations for woodpile structures, *J. Modern Optics*, **41**, 231-239 (1994).
- ¹³ Fan, S. *et al*, Design of three-dimensional crystals at submicron lengthscales, *Appl. Phys. Lett.* **65**, 1466-1468 (1994).
- ¹⁴ M. Wada, Y. Doi, K. Inoue, J.W. Haus and Z. Yuan. A simple-cubic photonic lattice in silicon, *Appl. Phys. Lett.* **70**, 2966-2968 (1997).
- ¹⁵ C.C. Cheng, V. Arbet-Engels, A. Scherer and E. Yablonovitch, Nanofabricated three dimensional photonic crystals operating at optical wavelengths, *Physica Scripta.* **T68**, 17-20 (1996).
- ¹⁶ S. Noda, N. Yamamoto and A. Sasaki, New realization method for three-dimensional photonic crystal in optical wavelength region, *Jap. J. of Appl. Phys.* **35**, L909-912 (1996).
- ¹⁷ A. van Blaaderen, Opals in a new light, *Science*, **282**, 887-888 (1998).
- ¹⁸ A.A. Zakhidov, R.H. Baughman, Z. Iqbal, C. Cui, I. Khayrullin, S.O. Dantes, J. Marti and V.G. Ralchenko, Carbon structures with three-dimensional periodicity at optical wavelengths, *Science*, **282**, 897-901 (1998).
- ¹⁹ G. Feiertag, W. Ehrfeld, H. Freimuth, H. Kolle, H. Lehr, M. Schmidt, M.M. Sigalas, C.M. Soukoulis, G. Kiriakidis, T. Pedersen, J. Kuhl and W. Koenig, Fabrication of photonic crystals by deep x-ray lithography, *Appl. Phys. Lett.* **71**, 1441-1443 (1997).
- ²⁰ B.H. Cumpston *et al*, Two-photon polymerization initiators for three-dimensional optical data storage and microfabrication, *Nature*, **398**, 51-54 (1999).
- ²¹ Lin and Fleming, submitted for publication.
- ²² S.-Y. Lin and J.G. Fleming, Photonic band-gap microcavities in three dimensions, *Physical Rev. B*, **59**, 579-582 (1999).
- ²³ S.-Y. Lin, E. Chow, V. Hietala, P.R. Villeneuve and J.D. Joannopoulos, Experimental demonstration of guiding and bending of electromagnetic waves in a photonic crystal, *Science*, **282**, 274-276 (1998).

GaAs/Al_xO_y photonic bandgap material fabrication and characterization

Pallab Bhattacharya, Weidong Zhou, Jayshri Sabarinathan, Donghai Zhu

Solid State Electronics Laboratory, Department of Electrical Engineering and Computer Science,
University of Michigan, Ann Arbor, MI 48109-2122, USA

ABSTRACT

A relatively simple technique for fabrication of GaAs-based quasi-three-dimensional photonic crystals has been investigated. Selective impurity-induced layer disordering and wet oxidation techniques are utilized. The feasibility of this technique is successfully demonstrated and a photonic bandgap material with its bandgap around 1.18 μm has been fabricated. The electro-optic coefficients have been measured for the first time in such a medium. The process is reproducible and lends itself to integration with other optoelectronic and electronic devices on the same substrate, which might be required for pumping, electrical injection or other functions.

Key words: Photonic bandgap (PBG), light localization, quantum-well intermixing (QWI), wet oxidation, impurity-induced layer disordering (IILD)

1. INTRODUCTION

Photonic bandgap (PBG) crystals are materials possessing a periodic variation of permittivity. When the resulting distortion of the electromagnetic density of states within the material is such as to suppress propagation completely for a range of frequencies, the material is said to possess a full photonic bandgap.¹⁻³ Such photonic crystals are of great interest owing to the possibility of spontaneous emission control. Inhibited spontaneous emission could lead to thresholdless lasers or single mode light emitting diodes (LEDs), which may lower the power requirements and increase the efficiency and reliability. Enhanced spontaneous emission, on the other hand, would allow faster modulation speeds for optical interconnects. By tuning the photonic bandgap to overlap with the electronic band edge, electron-hole recombination can be controlled in a photonic bandgap crystal, leading to enhanced efficiency and reduced noise in the operation of various optoelectronic devices, such as low-loss resonators, optical transistors and optical switches, bandpass filters, and photonic integrated circuit (PIC), etc. By introducing "photonic defects" into the regular lattice of a photonic bandgap crystal, a localized state may be generated within the forbidden gap^{2,4,5} which can essentially be a tiny optical cavity and perhaps the core of a photonic bandgap disk laser.⁶ The optical properties may be tailor-made, leading to innovative optical devices in the up-coming future.

Unlike semiconductor crystals, photonic crystals do not occur naturally. There are, therefore, several seemingly insurmountable challenges: first and foremost, it would be desirable to realize the photonic crystals with III-V direct bandgap semiconductors, such as GaAs, AlGaAs, InP, InGaAsP, etc., in which the radiative efficiency is high. It is also desirable to create a three-dimensional (3D) medium. Second, the refractive index contrast needs to be large⁷, and the spacing of the dielectric scatterers should be of the order of λ/n in these materials, where λ is the vacuum wavelength and n is the refractive index of the material. Finally, for some of the applications described above, it may be desirable to delineate waveguides on which contacts, or electrodes, can be formed. Above all, the processing technique should be relatively simple and reproducible.

Many approaches have been investigated to fabricate the artificial photonic crystals, such as mechanically drilling air channels, chemically etching holes, e-beam patterned dry etching techniques and wafer bonding techniques, etc.⁸⁻¹³ Success in producing one-, two- and three-dimensional photonic bandgaps for microwave and millimeter-wave radiation, and for shorter optical wavelengths in one- and two-dimensional structures has been reported. Recently, photonic gaps have been demonstrated in silicon and GaAs-based nanometer scale 'woodpile' structures.¹⁴⁻¹⁷ The 3D photonic crystal fabrication techniques reported so far are either Si-based, where the low radiative efficiency due to indirect bandgap nature of silicon limits its application on optoelectronics, or involving multiple growth steps, which is cumbersome in terms of its compatibility to standard microfabrication process.

The compound semiconductor based processing technique that we will describe here is reproducible and by scaling down to small feature size and using e-beam lithography, it should be possible to tune the photonic gap from 1 to 15 μm . The fabrication process is a standard microelectronic fabricate technology by utilizing the traditional Zn diffusion technique and AlGaAs wet oxidation technique. Without etching or drilling air channels, which are the most dominant approaches in making current PBG crystals, the diffraction loss associated with the semiconductor-air interface is reduced significantly in this all-semiconductor structure. Light localization was verified by transmission experiment on different lengths of waveguide. Defects in our PBG crystals are created during the process, since our process incorporates the random nature of zinc diffusion induced disordering.

Fourier-transform infrared spectroscopy (FTIR) and transmission experiments were performed in the fabricated PBG materials. The electro-optic coefficients have been experimentally determined from the measurement of the TE-TM phase shift in a waveguide made with the medium.

2. FABRICATION

The photonic crystal is made with the heterostructure, shown in Fig. 1(a), grown by molecular beam epitaxy (MBE) on (001)-oriented GaAs substrate. After growing a 0.1 μm GaAs buffer layer, a 0.2 μm $\text{Al}_{0.98}\text{Ga}_{0.02}\text{As}$ etch stop layer, and a 0.5 μm GaAs etch protection layer, the active region is grown. It consists of a 1 μm thick layer of $\text{Al}_{0.98}\text{Ga}_{0.02}\text{As}$ followed by 6 periods of 0.18 μm of $\text{Al}_{0.8}\text{Ga}_{0.2}\text{As}$ and a multi-quantum-well (MQW) region. The latter consists of 20 pairs of 20 \AA GaAs and 150 \AA $\text{Al}_{0.8}\text{Ga}_{0.2}\text{As}$ layers. The total thickness of the active region is 3.14 μm . A protective 200 \AA GaAs cap layer is finally grown. The entire heterostructure is undoped.

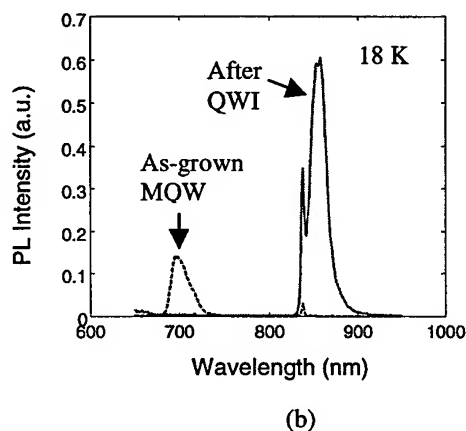
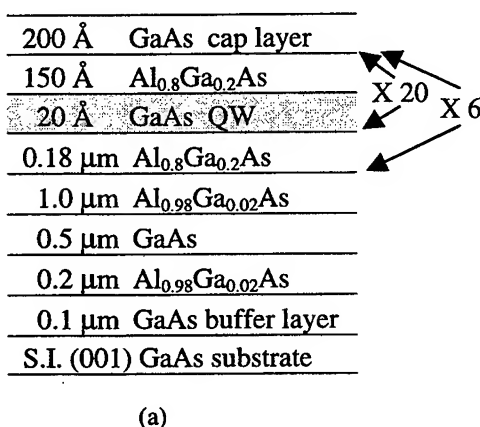


Figure 1 (a) GaAs-based heterostructure grown by molecular beam epitaxy and used to form the photonic bandgap (PBG) crystal; (b) Low-temperature (18K) photoluminescence (PL) spectra of the sample, showing the peak due to emission from the MQW regions disappears after IILD.

The processing steps to form the photonic crystal are outlined in Fig. 2. The key steps are a Zn-diffusion induced quantum well intermixing (QWI) of the MQW regions to form a uniform alloy¹⁸ -- known as IILD -- and a wet oxidation¹⁹ of epitaxially grown and intermixed AlGaAs alloy regions to form the stable oxide Al_xO_y with a refractive index of ~ 1.5 . Fig. 1(b) shows the low temperature photoluminescence spectrum peak originated from the MQW region in the as-grown sample disappeared after IILD or quantum-well intermixing (QWI).

A 0.1 μm thick layer of PECVD Si_xN_y is first deposited on the surface of the grown heterostructure and patterned into circular disks, to form a hexagonal close-pack form, by standard optical photolithography, as shown in Fig. 2(a). The center-to-center spacing a is $\sim 6 \mu\text{m}$. The relatively large diameter is chosen to minimize lateral diffusion of zinc. The deep zinc diffusion step is carried out with a ZnAs_2 source in an evacuated quartz ampoule at 575°C for 90 min. Impurity-induced layer disordering takes place selectively in the MQW regions through the openings between the Si_xN_y discs and converts it

into a uniform $\text{Al}_{0.71}\text{Ga}_{0.29}\text{As}$ alloy, left with different sizes of high index small MQW cylinders, as shown in Fig. 2(b). Ridges of width $35\text{ }\mu\text{m}$ are formed by standard optical lithography and a combination of reactive ion beam dry etching (RIE) and H_3PO_4 wet etching, as shown in Fig. 2(c). The etching is done down to the $0.5\text{ }\mu\text{m}$ GaAs layer. The sample is then inserted in an open-tube quartz furnace and wet oxidation is performed at 450°C for 15 hrs by flowing N_2 saturated with water vapor by bubbling it through a water bath held at 95°C . It is worthwhile to note that the relatively long oxidation time selected is due to the relatively low oxidation temperature chosen in order to minimize the zinc redistribution in the crystal. Both epitaxially grown $\text{Al}_{0.8}\text{Ga}_{0.2}\text{As}$ and intermixed $\text{Al}_{0.71}\text{Ga}_{0.29}\text{As}$ regions are uniformly oxidized to form the insulator Al_xO_y , as demonstrated in Fig. 2(d). It may be noted that under the hydrolysis conditions used, the thin $150\text{ }\text{\AA}$ $\text{Al}_{0.8}\text{Ga}_{0.2}\text{As}$ layers within the non-intermixed MQW regions are not oxidized.²⁰ We have now created a photonic crystal in which small MQW regions of average refractive index ~ 3.55 are embedded in an Al_xO_y medium of refractive index ~ 1.5 . The index contrast is therefore > 2.0 . A disadvantage of this process is the considerable lateral diffusion of zinc during the deep diffusion step. It is estimated that the scattering center radius r varies in the range of $0.15 - 1.5\text{ }\mu\text{m}$. The scanning electron microscope (SEM) image of the waveguide along with a schematic are shown in Fig. 3.

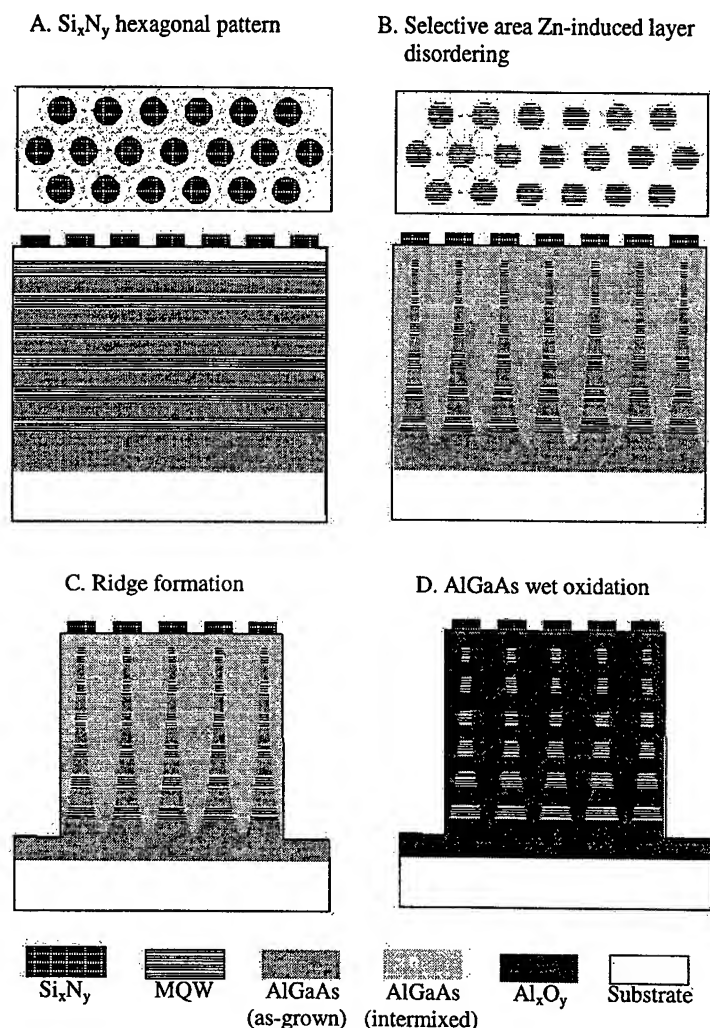
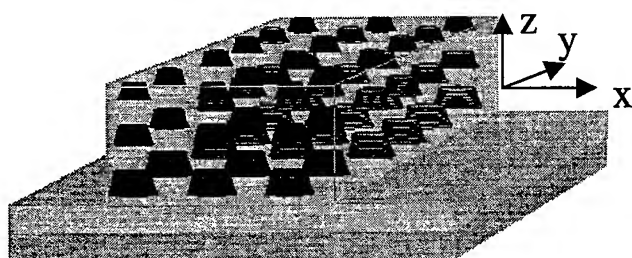
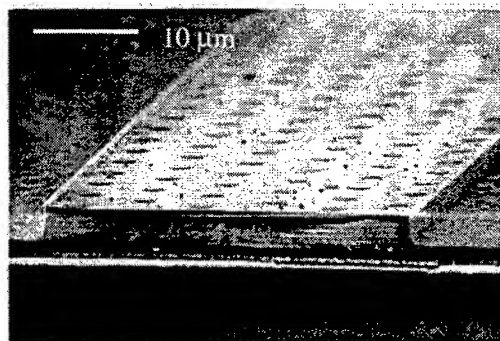


Figure 2 Process steps used to form PBG crystal. The key steps are the IILD of the MQW regions with zinc and the wet oxidation of AlGaAs regions to form Al_xO_y ($n \sim 1.5$).



(a)



(b)

Figure 3 (a) Schematic, and (b) scanning electron microscope (SEM) image of GaAs-based PBG waveguide made by conventional diffusion, wet-oxidation and etching techniques. The MQW scattering regions are faintly visible in the SEM image. Si_xN_y discs (reduced in size during processing) are seen on the top surface.

It is important to understand the nature of the fabricated crystal. If the diffusion was perfect (no lateral spreading), then the structure would be a set of centered hexagonal high-index rods, with periodic gaps, immersed in the low index Al_xO_y . However, because of the considerable lateral diffusion of Zn with depth, there is a variation in the size of MQW regions with depth. We therefore choose to describe our structure as a quasi-3D, weakly disordered, crystal. It may not have true 3D photonic bandgaps but should demonstrate stops bands.

The photonic bandgap crystal is cleaved with different waveguide lengths ranging from 0.6 to 1.8 mm and the GaAs substrate is removed by using lapping and the selective wet etching techniques, including a combination of NH_4OH and HF solution for selective etching of GaAs and AlGaAs layers. A black wax protection layer on top and SiO_2 anti-reflection (AR) coating on the waveguide facets are used prior to substrate etching in order to protect the photonic crystal and the waveguide cleaved facets. The yellowish transparent color of the waveguide after substrate removal can be seen under the microscope, which is one of the evidence of formation of AlGaAs alloy after intermixing.¹⁸ The final PBG waveguide is placed on a silica glass substrate for waveguide transmission experiment to avoid mode leakage into GaAs substrate.

The processed photonic crystal with ridges of width 15-35 μm are cleaved to lengths in the range of 0.6 - 2 mm for the electro-optic measurements. To avoid mode leakage into the GaAs regions, all the GaAs layers, including the substrate, are removed by selective wet etching. One is therefore left with the MQW regions embedded in Al_xO_y . A Pd/Zn/Pd/Au top contact layer and a Ti/Ge/Ti/Au bottom contact layer are deposited on the waveguide for application of bias. The total thickness of the device is 4.12 μm . Measurements, to be described below, are made by mounting the devices suitably on glass substrates. A typical device is shown schematically in Fig. 4. An identical Al_xO_y waveguide without MQW regions was also made as a calibration device.

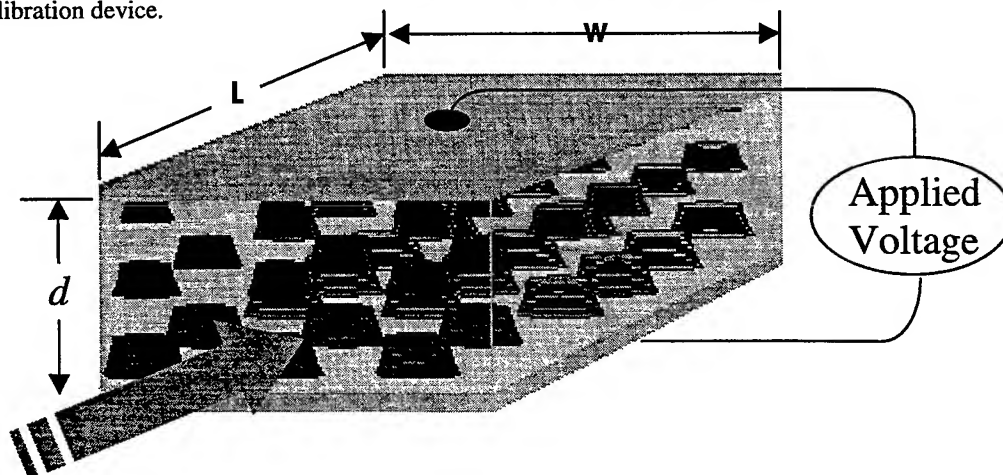


Figure 4 Experimental setup for EO measurement with the schematic of fabricated waveguide, the applied bias and the incident beam.

3. EXPERIMENTAL RESULTS

Low-temperature photoluminescence spectrum of the as-grown heterostructure reveals a peak at 702 nm (Fig. 1(b)), which originates from the MQW regions and confirms the high quality of the sample. Surface normal (z-direction) FTIR was performed at room temperature, in the wavelength range of 2.5 - 25 μm on samples in which the GaAs substrate was thinned down to 100 μm and polished. Since the beam size (~ 5 mm) is much larger than the waveguide width, samples with several parallel waveguides were used and normal incidence (from the top) was employed. The measured spectrum is shown in Fig. 5. The spectrum is normalized by the measured spectra of the GaAs substrate and Al_xO_y of thicknesses identical to those in the photonic crystals. A transmittance dip between 15-20 μm is observed, which fits reasonably well with the results²¹ of a 2D crystal scaled from the microwave measurements, with the parameters of our structure, using a simple scaling factor of 1146 (the ratio of center-to-center spacing of high index scatterers). This is also shown in Fig. 5. The smaller and wider transmission dip in our measured data compared to the reference results, could be due to the scatterer size non-uniformity in our crystal. Transmission spectroscopies on both surface normal (z-direction) and waveguide (y) direction were also done in the wavelength range of 0.9-1.6 μm with a photomultiplier or a Ge detector. Again, the measured data was normalized with respect to GaAs and Al_xO_y . The measured spectra are also shown in Fig. 5, with a 12 dB attenuation at 1.18 μm along z direction. A transmission peak is also noted within the stop band in the y-direction. The exact origin of the second gap at the lower wavelength is not fully understood, but its presence is confirmed with measurement in two orthogonal directions. As shown in Fig. 6, our calculation based on plane wave expansion technique²² has revealed a gap around 1.5 μm for an ideal 2D PBG structure with parameters same as our fabricated quasi-3D structure. Similar gaps have been theoretically calculated by Maystre *et al.* in photonic crystals composed of dielectric rods in air or air holes in dielectric medium²³ and have been attributed to grating effects due to Wood's anomalies. These authors²⁴ also observed that introduction of doping, or defects, in the lattice produced states in the gap, like the one observed by us. It must be remembered that we are presenting a technique which could potentially be useful for realizing semiconductor-based 3D photonic crystals. In the crystal reported here, the perfect periodicity is destroyed by process-induced non-uniformity of the scatterer size. These aspects are under investigation.

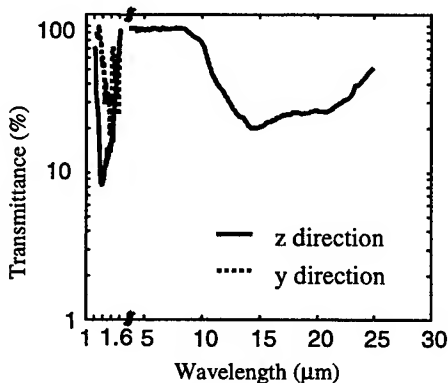


Figure 5 Transmission spectra shows a stop band between 15-20 μm along z-direction for a PBG material with $a=6.3$ μm , $r=0.15$ -1.5 μm and index contrast of 2.3. Also shown are the stop bands around 1 μm measured along the y- and z-directions and the calculated stop band around 17 μm .

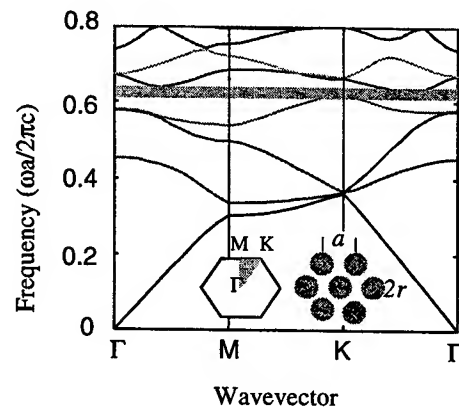


Figure 6 Calculated band structure based on expansion theory with $n_i=1.5$, $n_h=3.5$, $r=1.5$ μm , $a=6.3$ μm ; note a gap centered at 1.5 μm .

In order to investigate possible light localization due to the observed defect states, we have measured the transmission coefficient, T , as a function of waveguide length, L . The GaAs substrates were completely removed in these samples, in order to eliminate mode leakage into substrates. The cleaved facets of waveguides, varying in length from 0.6 mm to 1.8 mm, were end fired with TE polarized light from a 1.15 μm He-Ne laser and the guided (transmitted) power at the output was measured with a power meter. We did not observe any evidence of light leaking into the thin Al_xO_y supporting layer underneath. The measured data is shown in Fig. 7(a). A distinct exponential decay of the transmission with waveguide length is observed and assuming that the decay is $\sim \exp(-L/L_{\text{loc}})$, where L_{loc} is the localization length, a value of $L_{\text{loc}}=0.4$ mm is extrapolated. We have also fitted the same data with a $T \sim L^{-2}$ dependence in accordance with the scaling theory of localization at the localization

transition.^{4,5,25} The fit is shown in Fig. 7(b). For a $T \sim L^{-2}$ dependence, an average transport velocity $v = 3.81 \times 10^7$ cm/s is estimated, assuming an average mean free path of $1.73 \mu\text{m}$. The phase velocity for this device, derived from a geometrical optics estimation with a fill factor of 0.2, is about 1.54×10^{10} cm/s. Therefore, it can be said with some caution that light localization occurs in our samples, possibly due to the localized defect states, observed in the transmission experiments.

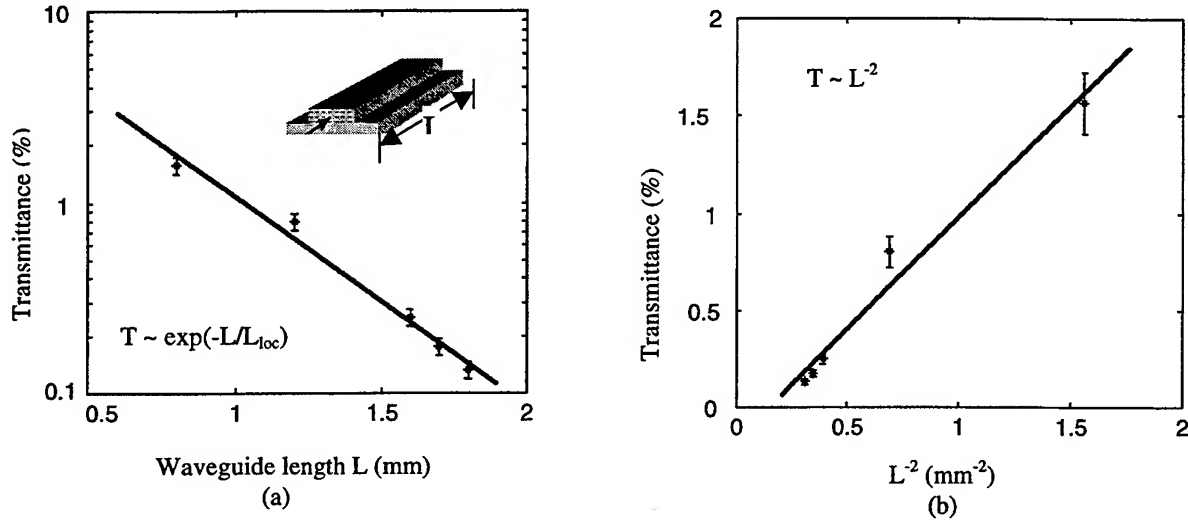


Figure 7 Measured transmission of end-fired $1.15 \mu\text{m}$ light through waveguides as a function of guide length. The polarization of the incident light is parallel to the heterostructure layers. The measured transmission is fitted to (a) exponential, and (b) quadratic variation with waveguide length. Both fits are good, indicating strong photon localization.

The PBG waveguide with top and bottom contacts was fabricated for measurement of the electro-optic properties. The measured current-voltage characteristics of the devices are shown in Fig. 8(b), wherein the high resistivity of the material is evident. Measurement of the E-O coefficients was carried out by coupling $1.15 \mu\text{m}$ light from a He-Ne laser onto one end of a waveguide with a focusing lens. Care was taken to make sure the focused spot size on the facet of the waveguide is less than $4 \mu\text{m}$ in diameter, so that maximum coupling into the waveguide is achieved. The latter is determined by the reflectivity of the input facet. The polarization of the light is oriented, through use of an input polarizer, at 45° to the direction of the electric field. The phase retardation of the transmitted light was measured with an analyzer and a power meter at the output end of the waveguide. The measured phase retardation and the refractive index change as a function of the applied voltage for the photonic waveguide structure, as shown in Fig. 8(b), are seen to vary with field in a nonlinear manner, while no observable phase shift is recorded for the Al_xO_y calibration structure. It is important to note that the waveguide geometry is required for these measurements. However, the dimensions of the waveguide are large enough so that the data reflect the electro-optic properties of the bulk photonic bandgap material. The error bars in the data are indications of measurement system error associated with the multiple optical alignment during many repeated experiment. It is clear, however, that the curve is distinctly concave downward. The linear and quadratic E-O coefficients are obtained by fitting the phase retardation with the relation:²⁶

$$\Delta\Phi = \pi L n_0^3 \lambda^{-1} (\Gamma_l r E \pm \Gamma_q s E^2) + \Delta\Phi_0 \quad (1)$$

Where r and s are the linear and quadratic E-O coefficients, respectively, $\Delta\Phi_0$ is the built-in birefringence induced phase shift, n_0 is the average refractive index of active region, E is the average electric field, Γ_l and Γ_q are the linear and quadratic confinement factors, L is the length of the waveguide and λ is the laser wavelength.

The results reported here were obtained with waveguides of length $L = 2 \text{ mm}$ and width $W = 35 \mu\text{m}$. In reality Eq. (1) is a summation over all regions over which the optical mode extends. In the following analysis we neglect any mode leakage outside the PBG guide. Equation (1) then relates to the measured effects in the embedded $\text{GaAs}/\text{Al}_{0.8}\text{Ga}_{0.2}\text{As}$ MQW regions. The value of n_0 in our samples is 3.48. The confinement factors Γ_l and Γ_q in our waveguide are essentially equal to the fill factor f since the E-O effect is only due to the MQW regions. The value of f is calculated by considering the progressive

change in the size of the MQW regions over the six periods. These are estimated from the measured diffusion and intermixing profiles in calibration samples. Thus $f = \frac{1}{6} \sum_{i=1}^6 f_i$, where, $f_i = 0.057 r_i^2$, and r_i is radius of the i^{th} MQW region, noting that $r_1 = 0.15 \mu\text{m}$ and the separation between the MQW regions is $0.18 \mu\text{m}$. We estimate a value of $f = 0.17$. Finally the electric field E , or the fractional voltage drop across the MQW regions is calculated by considering the boundary condition across dielectric regions with dielectric constants of 1.5 and 3.48. The field across the MQW regions is estimated to be given by $E = 0.31(V/d)$, where V is the applied bias and $d = 4.12 \mu\text{m}$ is the guide thickness. From the fitting of the data in Fig. 3, shown by solid curves, we estimate $r = 1.66 \times 10^{-12} \text{ m/V}$ and $s = -2.57 \times 10^{-19} \text{ m}^2/\text{V}^2$ and the built-in birefringence $\Delta n = 1.1 \times 10^{-5}$, due to the anisotropy in the medium.

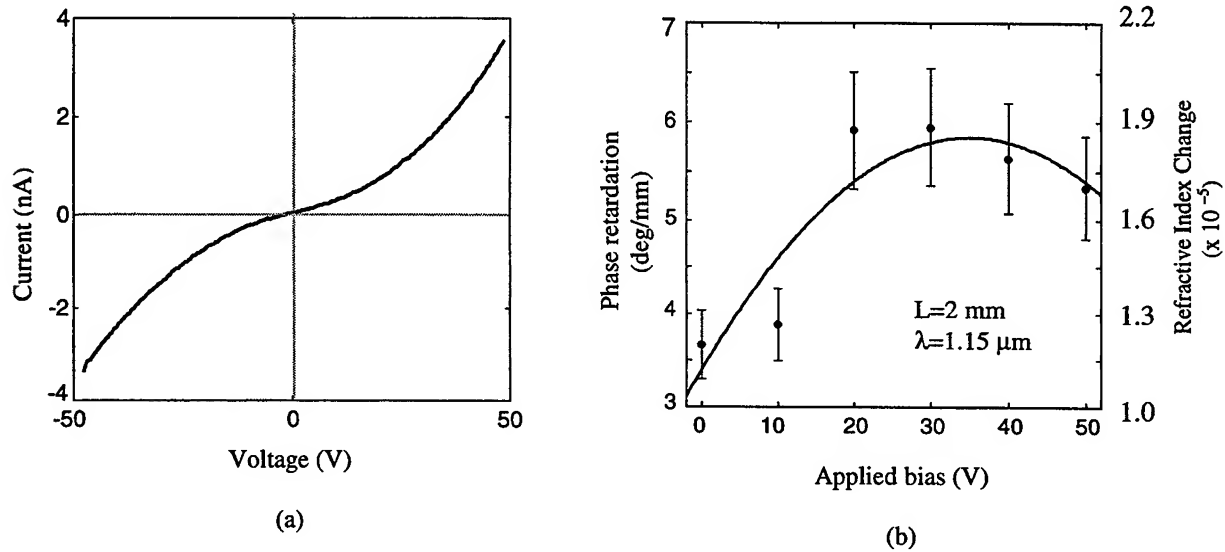


Figure 8 (a) current-voltage characteristics of the PBG waveguide shown in Fig. 4 with $L = 2 \text{ mm}$, $W = 35 \mu\text{m}$ and $d = 4.12 \mu\text{m}$; (b) measured phase retardation and refractive index change as a function of the applied voltage. The solid curve is a fit to the data.

It may be remembered that the energy of the guided light is $\sim 0.35 \text{ eV}$ below the bandgap of the GaAs regions of the MQW. Therefore the quantum confined Stark effect (QCSE) and associated phenomena can be presumed to be inoperative. The magnitude of the measured Pockels effect, indicated by the value of r , is almost exactly the same as that of GaAs or GaAs/AlGaAs MQW^{27,28}, which is not surprising. However, a strong non-linearity, with a sign opposite to that associated with the QCSE-type of Kerr effect^{26,27}, is observed in Fig. 3. Nonlinearity in photonic media has been predicted or calculated by several authors. Faist and Reinhardt^{29,30} have shown, theoretically and experimentally that phase modulation due to many-body effects in an electro-optic medium is quadratic with electric field and has an opposite sign to that for band-filling or other electroabsorption related effects. Therefore, with some caution, it may be presumed that the observed non-linear behavior is a consequence of many-body effects, remembering that the many-body effects arises from the pseudogap in the weakly disordered system and the consequent light localization. Our observation may be the first experimental evidence of many-body effects in a photonic bandgap medium.

4. DISCUSSION

4.1 Optimization of the epitaxial growth structure

A high content of aluminum of both epitaxial grown $\text{Al}_x\text{Ga}_{1-x}\text{As}$ barrier region and the intermixed $\text{Al}_x\text{Ga}_{1-x}\text{As}$ is desirable for a high oxidation rate. The oxidation rate of $\text{Al}_x\text{Ga}_{1-x}\text{As}$ decreases dramatically with decreasing the aluminum content.³¹ On the other hand, in order to effectively disorder the quantum well region through zinc induced disordering, a high zinc concentration in the order of 10^{19} cm^{-3} or above is required.³² While SIMS results show that the Zn solubility N_{Zn} in the Al_xGa_1 .

x As alloy is strongly dependent on the Al content x , as shown in Fig. 9. Fig. 10 shows the N_{Zn} decreases exponentially with increasing x . To satisfy the $N_{Zn} > 10^{19} \text{ cm}^{-3}$ requirement for disordering, the aluminum content in $\text{Al}_x\text{Ga}_{1-x}\text{As}$ must be less than 0.8. An optimized aluminum content x must be selected. Our final design uses $x=0.8$ for epitaxially grown $\text{Al}_x\text{Ga}_{1-x}\text{As}$ and $x=0.71$ for intermixed $\text{Al}_x\text{Ga}_{1-x}\text{As}$.

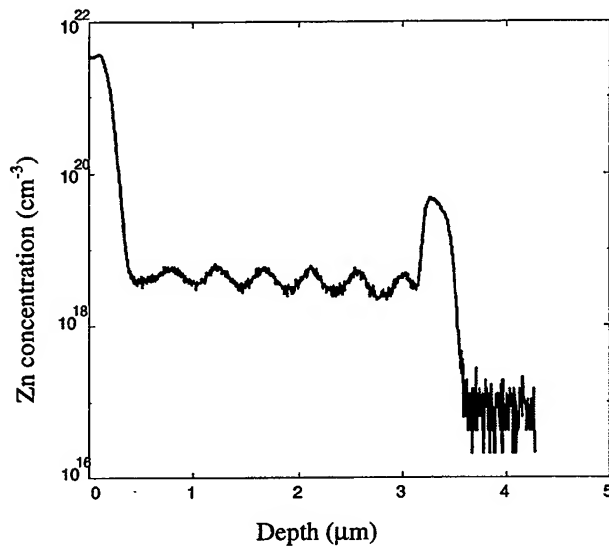


Figure 9 SIMS profile of Zn concentration along depth in the structure after IILD.

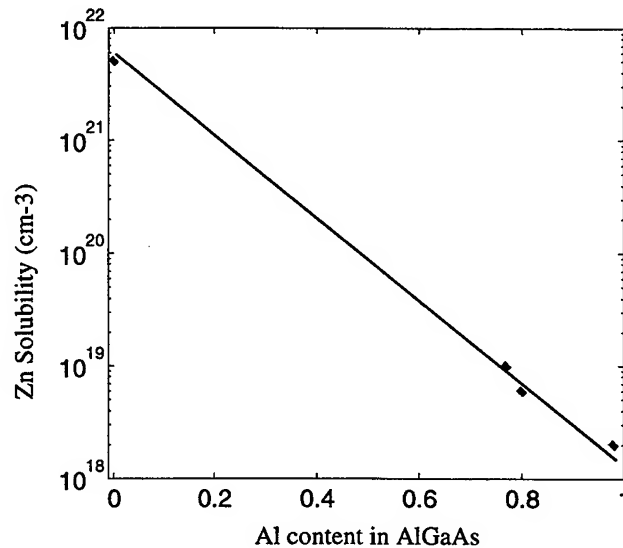


Figure 10 Zn solubility vs aluminum content x in $\text{Al}_x\text{Ga}_{1-x}\text{As}$ based on SIMS results.

4.2 Process reliability and limitations

Due to the relatively simple process comparing to other techniques, it is very reliable and compatible to the standard microfabrication process. The only disadvantage of this process is the considerable lateral diffusion of zinc during the deep diffusion step. We have determined that the lateral spread almost matches the depth for 1.4 μm diffusion, as shown in Fig. 11. However, this provides the randomness in the size and spacing of the MQW scatterers and helps us to realize a disordered photonic crystal. It is estimated that the size of the scattering centers varies in the range of 0.3 - 3 μm . By using well-controlled process to minimize the lateral spreading, the spacing can be further decreased.

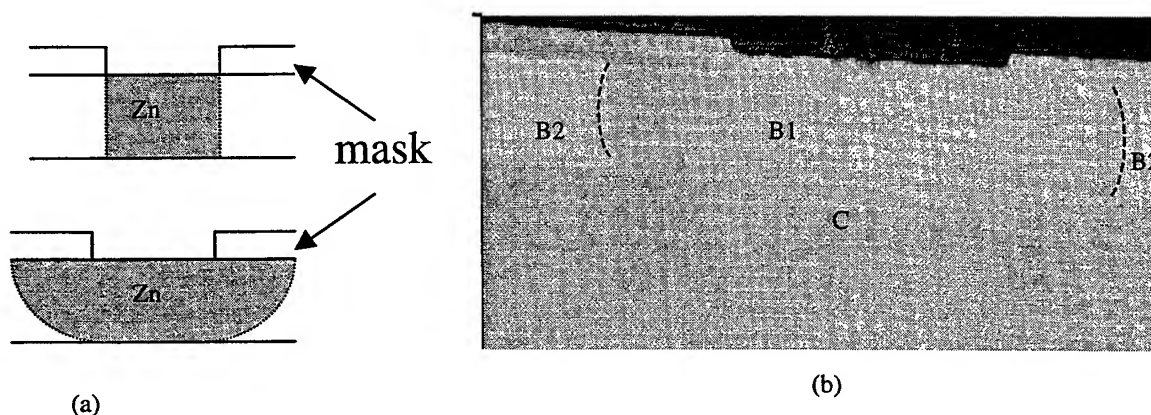


Figure 11 (a) Schematic illustration of ideal (top) and nonideal (bottom) diffusion process; (b) scanning capacitance measurement result shows the Zn lateral spreading along depth almost matches the depth for a 1.4 μm diffusion for a simple GaAs/AlGaAs MQW structure. The MQW region B is sandwiched in between the top Si_3N_4 pattern region A and the bottom GaAs region C, where region B1 (center darker area) is Zn diffusion region and B2 are undiffused areas.

5. CONCLUSION

We demonstrate here a processing technique with which we have created a quasi-three-dimensional photonic crystal. A stop band around 1.5 μm has been obtained both experimentally and theoretically. We have measured the electro-optic coefficients for the first time, with the linear E-O coefficient $r = 1.66 \times 10^{-12}$ m/V and the quadratic E-O coefficient $s = -2.57 \times 10^{-19}$ m²/V², respectively. The technique is versatile, such that photonic crystals of any dimension and shape can be created. Work is in progress to improve the size uniformity and scale down the scatterer spacing by using electron-beam lithography and better controlled disordering techniques.

ACKNOWLEDGMENTS

The authors acknowledge the help provided by Prof. J. Kanicki and Tong Li in performing the FTIR measurements. Useful suggestions made by H. Gebretsadik and O. Qasimeh are appreciated. The work was partially supported by the Army Research Office. One of us (PB) gratefully acknowledges the support provided by the John Simon Guggenheim award.

REFERENCES

- 1 E. Yablonovitch, "Inhibited spontaneous emission in solid-state physics and electronics," *Phys. Rev. Lett.* **58**, pp. 2059-2062, 1987.
- 2 S. John, "Strong localization of photons in certain disordered dielectric superlattices," *Phys. Rev. Lett.* **58**, pp. 2486-2489, 1987.
- 3 E. Yablonovitch, "Photonic band-gap structures," *J. Opt. Soc. Am B* **10**, pp. 283-295, 1993.
- 4 D. Wiersma, P. Bartolini, A. Lagendijk, and R. Righini, "Localization of light in a disordered medium," *Nature* **390**, pp. 671-673, 1997.
- 5 J. D. Joannopoulos, P. Villeneuve, S. Fan, "Photonic crystals: putting a new twist on light," *Nature* **386**, pp. 143-149, 1997.
- 6 R. K. Lee, O. J. Painter, B. Kitzke, A. Scherer and A. Yariv, "Photonic bandgap disk laser," *Electron. Lett.* **35**(7), 1999.
- 7 K. M. Ho, C. T. Chan, C. M. Soukoulis, R. Biswas and M. Sigalas, "Photonics band gaps in three dimensions: new layer-by-layer periodic structures," *Solid State Commun.* **89**, pp. 413-416, 1994.
- 8 C. C. Cheng, V. Arbet-Engels, A. Scherer, and E. Yablonovitch, "Nanofabricated three dimensional photonics crystals operating at optical wavelengths," *Phys. Scripta* **T68**, pp. 17-20, 1996.
- 9 K. M. Ho, C. T. Chan, and C. M. Soukoulis, "Existence of a photonic gap in periodic dielectric structures," *Phys. Rev. Lett.* **65**, pp. 3152-3155, 1990.
- 10 E. özbay, E. Michel, G. Tuttle, R. Biswas, M. Sigalas, and K. M. Ho, "Micromachined millimeter-wave photonic band-gap crystals," *Appl. Phys. Lett.* **64**, pp. 2059-2061, 1994.
- 11 T. F. Krauss, R. M. De La Rue, S. Brand, "Two-dimensional photonic-bandgap structures operating at near-infrared wavelengths," *Nature* **383**, pp. 699-702, 1996.
- 12 K. McIntosh, L. Mahoney, K. Molvar, O. McMAhon, S. Verghese, M. Rothschild, and E. Brown, "Three-dimensional metallodielectric photonic crystals exhibiting resonant infrared stop bands," *Appl. Phys. Lett.* **70**, pp. 2937-2939, 1997.
- 13 V. Berger, O. Gauthier-Lafaye, and E. Costard, "Fabrication of a 2D photonic bandgap by a holographic method," *Electron. Lett.* **33**, pp. 425-426, 1997.
- 14 S. Y. Lin, *et al.*, "A three-dimensional photonic crystal operating at infrared wavelengths," *Nature* **394**, pp. 251-253, 1998.
- 15 S. Noda, N. Yamamoto, and A. Sasaki, "New realization method for three-dimensional photonic crystal in optical wavelength region," *Jpn. J. Appl. Phys.* **36**, L909-912, 1996.
- 16 J. G. Fleming and Shawn-Yu Lin, "Three-dimensional photonic crystal with a stop band from 1.35 to 1.95 μm ," *Opt. Lett.* **24**, pp. 49-51, 1999.
- 17 S. Kawakami, "Autocloning of three-dimensional photonic crystals and their applications," in the 6th International Workshop on Femosecond Technology, TB-11, Makuhari Messe, Chiba, Japan, 1999.
- 18 W. Laidig, *et al.*, "Disorder of an AlAs-GaAs superlattice by impurity diffusion," *Appl. Phys. Lett.* **38**, pp. 776-778, 1981.

- 19 J. M. Dallesasse, N. Holonyak, Jr., S. R. Sugg, T. A. Richard, and N. El-Zein, "Hydrolyzation oxidation of $\text{Al}_x\text{Ga}_{1-x}\text{As}$ -GaAs quantum well heterostructures and superlattices," *Appl. Phys. Lett.* **57**, 2844-2846 (1990).
- 20 J.-H. Kim, D.H. Lim, K.S. Kim, G. M. Yang, K. Y. Lim, and H. J. Lee, "Lateral wet oxidation of $\text{Al}_x\text{Ga}_{1-x}\text{As}$ -GaAs depending on its structures," *Appl. Phys. Lett.* **69**, pp. 3357-3359, 1996.
- 21 V. Arbet-Engels, E. Yablonovitch, C. C. Cheng, A. Scherer, "Bandgap engineering of 3-D photonic crystals operating at optical wavelengths," in *Microcavities and Photonic Bandgaps*, Rarity & Weisbuch eds., pp. 125-131, Kluwer Academic Publishers, Netherlands, 1996.
- 22 M. Plihal, A. Shambrook, A. Maradudin, P. Sheng, "Two-dimensional photonic band structures," *Opt. Commun.* **80**, pp. 199-204, 1991.
- 23 D. Maystre, "Electromagnetic study of photonic band gaps," *Pure Appl. Opt.* **3**, pp. 975-993, 1994.
- 24 P. Sabouroux, G. Tayeb, D. Maystre, "Experimental and theoretical study of resonant microcavities in two-dimensional photonic crystals," *Opt. Commun.* **160**, pp. 33-36, 1999.
- 25 Z. Genack, and N. Garcia, "Electromagnetic localization and photonics," *J. Opt. Soc. Am. B* **10**, pp. 408-413, 1993.
- 26 J. Pamulapati, J. Loehr, J. Singh, P. Bhattacharya, M. Ludowise, "Refractive index and electro-optic effect in compressive and tensile strained quantum wells," *J. Appl. Phys.* **69**, pp. 4071-404074, 1991.
- 27 M. Glick, D. Pavuna, and F. K. Reinhart, "Electro-optic effects and electroabsorption in a GaAs/AlGaAs multiquantum-well heterostructure near the bandgap," *Electron. Lett.* **23**, pp. 1235-1237, 1987.
- 28 M. Bloemer and K. Myneni, "Electro-optic properties near the absorption edge of GaAs/AlGaAs multiple-quantum-well waveguides," *J. Appl. Phys.* **74**, pp. 4849-4859, 1993.
- 29 J. Faist and F.-K. Reinhart, "Phase modulation in GaAs/AlGaAs double heterostructures. I. Theory," *J. Appl. Phys.* **67**, pp. 6998-7005, 1990.
- 30 J. Faist and F.-K. Reinhart, "Phase modulation in GaAs/AlGaAs double heterostructures. II. Experiment," *J. Appl. Phys.* **67**, pp. 7006-7012, 1990.
- 31 K. D. Choquette, *et al.*, "Advances in selective wet oxidation of AlGaAs alloys," *IEEE J. Quantum Electron.*, pp.916-926, 1997.
- 32 D. G. Deppe and N. Holonyak, Jr., "Atom diffusion and impurity-induced layer disordering in quantum well III-V semiconductor heterostructures," *J. Appl. Phys.* **64**, pp. R93-R113, 1988.

Two Dimensional Superconductor-Dielectric Photonic Crystal

C.H. Raymond Ooi *, T.C. Au Yeung , T.K. Lim , C.H. Kam

School of Electrical & Electronic Engineering,

Nanyang Technological University, Singapore 639798

ABSTRACT

Two dimensional hexagonal lattice photonic crystal made of superconducting rods embedded in dielectric matrix and dielectric rods embedded in superconducting matrix are studied. We used two-fluid model to describe the electromagnetic response of the superconductor phase. The superconductor-dielectric photonic band structures are computed using the plane wave expansion method . We found a extremely large low frequency gap as due to the electric field expulsion in the superconductor . Qualitative explanations for the dependency low frequency gap size on dielectric constant , penetration depth and filling fraction are given . A smaller gap have been found at much higher lattice constant/wavelength ratio. We also found a fundamental mode with extremely localized electric field in the dielectric phase, similar to the localized mode in defective photonic crystal . This photonic crystal could be useful for superhigh-Q periodic resonant cavities .

Keywords : photonic crystal ,superconductor , two-fluid model , low frequency gap , resonant cavity

1. INTRODUCTION

Much work has been done on the computation¹ of the band-structures of electromagnetic waves propagating in two-and three-dimensional dielectric periodic structures since it was first shown² that these periodic structures can be designed to produce the required bandgaps. Photonic crystals were mainly fabricated from high contrast dielectric materials³, typically used in the semiconductor technology. Dielectric periodic structures can be designed to mold the propagation of light in an integrated semiconductor optoelectronics where electronic and optical signals coexist and transform between each other . Recently , combinations of various materials for the design of photonic crystals have been studied. Sigalas et. al.⁴ found a wider photonic band gaps when dielectric constant ϵ and relative permeability μ have their maximum values in different materials and suggested using magnetically tuned ferrite materials. Electric and magnetic fields dependent materials like ferroelectrics, ferromagnets and ferrimagnets were investigated in two-dimensional photonic crystals⁵. Frequency dependent dielectrics⁶ and metallics⁷ photonic crystals have been studied too. The wide range of materials that can be used to make photonic crystals provides vast avenues in the design and applications of novel photonic crystals devices for integration into the semiconductor optoelectronics system.

However, we foresee novel applications and interesting possibilities of incorporating the photonic crystals concept into superconducting devices. It is interesting to investigate new possibilities of merging superconducting electronics and photonics. From this motivation; in this paper, we study the band structure of two-dimensional non-dissipative superconductor-dielectric photonic crystal. We confine our study to E-polarization in a hexagonal lattice. In section 2, we describe the electromagnetic response of a typical non-magnetic superconductor using the two-fluid model^{8,9} via the complex conductivity. At sufficiently low and high frequencies, the complex conductivity approximates to imaginary conductivity, since we are interested in a non-dissipative superlattice. In section 3 , we decouple the Maxwell's equations in the absence of free charge and external applied current to obtain the differential equation in an eigenvalue form for E-polarization , valid in both dielectric and superconducting phases. Using the Bloch theorem and Fourier expanding all the periodic functions, we obtain the infinite size eigenvalue equations . Section 4 briefly describes the computation of the matrix eigenvalues using Matlab algorithms results we obtain in Section 5 .

* Email : PG427012@ntu.edu.sg. Fax : 7904161 (Photonics Lab)

2. FORMULATION OF THE COMPLEX CONDUCTIVITY

We consider the superconductor with local behaviour so that we can use the two-fluid model to describe the electromagnetic response of the superconductor below T_c . This model has proven successful in describing the performance of superconductive devices, especially at high frequency⁹. The complex electrical conductivity, $\sigma = \sigma_n + \sigma_s$ of a superconductor in the presence of electromagnetic fields is due to the total conduction electrons of density, $n = n_s + n_n$ which is composed of the unpaired-normal electrons and the paired-superelectrons of density n_n and n_s respectively⁸.

The conductivity of the normal electrons, from Drude model is

$$\sigma_n = n_n e^2 \tau / m (1 + j\tau\omega) = [1 - j\tau\omega] n_n e^2 \tau / m (1 + \tau^2\omega^2) \quad (1)$$

where τ is the relaxation time of the normal fluid and m is the effective mass of the normal electrons.

Using $\lim_{\tau \rightarrow \infty} \left[\int_{-\infty}^{\infty} \frac{\tau}{1 + \omega^2 \tau^2} d\omega = \tan^{-1} \omega \tau \right] = \frac{\pi}{2} \int_{-\infty}^{\infty} \delta(\omega) d\omega$ where $\delta(\omega)$ is the Dirac delta function and taking

τ to infinity, we have

$$\sigma_s = \lim_{\tau \rightarrow \infty} \sigma_n = (\pi n_s e^2 / 2m) \delta(\omega) - j n_s e^2 / m \omega \quad (2)$$

Then, the total complex conductivity is

$$\sigma = (e^2 / m) \left[(n_n \tau / (1 + \tau^2 \omega^2) + \delta(\omega) \pi n_s / 2) - j (\tau^2 \omega n_n / (1 + \tau^2 \omega^2) + n_s / \omega) \right] \quad (3)$$

For non-zero frequency, the complex conductivity becomes,

$$\sigma(\omega \neq 0) \Rightarrow (e^2 / m) \left[(n_n \tau / (1 + j\tau\omega)) - j n_s / \omega \right] \quad (4)$$

So far, the convention $\exp(j\omega t)$ has been adopted, as used in Ref. 8. Hereafter, we change convention to $\exp(-j\omega t)$, by simply changing j to $-j$. It should be mentioned that, the superelectron density, mass and charge are $n^* = n_s/2$, $m^* = 2m$ and $e^* = 2e$ respectively. Then, the original definition of London penetration depth¹⁰, $m^* / \mu_0 n_s^* e^{*2} = \lambda_L^2$ can be equivalently expressed as $m / \mu_0 n_s e^2 = \lambda_L^2$. We should note that τ , n_n and n_s are indirectly related by their temperature dependence.

The Gorter-Casimir result¹¹ gives the quantitative temperature dependency of superelectrons density $n_s^*(T)/n^* = 1 - (T/T_c)^4$, where $n^* = n_s(0)/2$. Combining this with the definition of London penetration depth, we have

$$\lambda_L(T) = \lambda_{L,0} / \sqrt{1 - (T/T_c)^4} \quad (5)$$

where $m / \mu_0 n e^2 = \lambda_{L,0}^2$.

In the case of $\tau\omega \gg 1$, Eq. 4 reduces to imaginary conductivity,

$$\sigma(\omega) = j e^2 n / m \omega = j / \omega \mu_0 \lambda_{L,0}^2 \quad (6)$$

In the case of $\tau\omega \ll 1$, Eq. 2 reduces to,

$$\sigma(\omega) = (e^2 / m) [n_n \tau + j n_s / \omega] \quad (7)$$

Furthermore, if $n_s \tau \ll n_s / \omega$ is satisfied¹², the complex conductivity can also approximate to imaginary conductivity, like in the high frequency case,

$$\sigma(\omega) = j e^2 n_s / m \omega = j / \omega \mu_0 \lambda_L^2(T) \quad (8)$$

In fact, the electrodynamic response of a superconductor at high frequency (where $\tau \omega \gg 1$) is essentially the same as that of a normal metal . As such, it may seem unnecessary using superconductor instead of metal . The need for incorporating photonic crystal into superconducting electronics is one of the reasons for using superconductor. Besides, for operation in low frequency regime¹², the band structure has non-linear temperature dependence (Eq. 5 & 8) especially near T_c .

3. FORMULATION OF EIGENVALUE EQUATIONS

Assuming that the superconductor is non-magnetic , with dielectric constant close to unity and has a linear free current response to the time-harmonic electric field. Then, the electromagnetic properties of dielectric /superconductor is written as

$$\nabla \times \mathbf{B} = \mu_0 \left[\frac{\partial}{\partial t} \mathbf{D} + \sigma \mathbf{E} \right] = \mu_0 \left[-j \omega \epsilon_0 \epsilon(\mathbf{r}) + j z(\mathbf{r}) / \omega \mu_0 \right] \mathbf{E} \quad (9)$$

where $\epsilon(\mathbf{r}) = 1$, $z(\mathbf{r}) = 1/\lambda^2$ in superconductor and $\epsilon(\mathbf{r}) = \epsilon$, $z(\mathbf{r}) = 0$ in dielectric.

With such simplistic assumptions, this formulation may not hold for exotic (organic,ceramic,magnetic) superconductors . However, the assumptions are necessary to effectively represent most metallic superconductors.

We study the two dimensional hexagonal (triangular) photonic crystal in x-y plane with each lattice point designated by the axis of an infinitely long cylindrical rod (parallel to z-axis), we call 'photonic atom' which can have either a superconducting phase (for 'superconducting atom') or a dielectric phase (for 'dielectric atom').

For E-polarization , Eq. 7 and $\nabla \times \mathbf{E} = - \partial \mathbf{B} / \partial t$ yield

$$\left[\frac{\partial^2 E_z}{\partial x^2} + \frac{\partial^2 E_z}{\partial y^2} \right] + f(x, y) E_z = 0 \quad (10)$$

where $f(x, y) = [(\omega/c)^2 \epsilon(x, y) - z(x, y)]$; $f = (\omega/c)^2 \epsilon$ (in dielectric) and $f = (\omega/c)^2 - (1/\lambda)^2$ (in superconductor)

Rearranging Eq.10 in the eigenvalue form, we have

$$\epsilon(x, y)^{-1} \left[\frac{\partial^2 E_z}{\partial x^2} + \frac{\partial^2 E_z}{\partial y^2} \right] - v(x, y) E_z + (\omega/c)^2 E_z = 0 \quad (11)$$

where $v(x, y) = z(x, y)/\epsilon(x, y) = 1/\lambda^2$ in superconductor and 0 in dielectric.

By using the Bloch function for E_z and Fourier expanding the periodic functions E_z , $\epsilon(x, y)^{-1}$ and $v(x, y)$, we have the eigenvalue problem

$$\sum_{\mathbf{G}'} [w(\mathbf{G}-\mathbf{G}')(\mathbf{k}+\mathbf{G}') \cdot (\mathbf{k}+\mathbf{G}') + v(\mathbf{G}-\mathbf{G}')] E_z(\mathbf{G}') = (\omega/c)^2 E_z(\mathbf{G}) \quad (12)$$

where $w(0) = \epsilon^{-1}_b + (\epsilon^{-1}_a - \epsilon^{-1}_b) f$, $w(\mathbf{G} \neq 0) = 2f(\epsilon^{-1}_a - \epsilon^{-1}_b) J_1(x)/x$, and $v(0) = v_b + (v_a - v_b) f$,

$v(G \neq 0) = 2f(v_a - v_b) J_1(x)/x$; where $x = Gd/2$, $f = \frac{\pi}{2\sqrt{3}} r^2$ (the filling fraction of an 'atom' per unit cell), $r=d/a$, d =diameter of 'atom' and a = lattice constant.

For the case of 'dielectric atom' embedded in superconductor (background), $\epsilon_a = \epsilon$, $\epsilon_b = 1$ and $v_a = 0$, $v_b = 1/\lambda^2$.
For the case of 'superconductor atom' embedded in dielectric (background), $\epsilon_a = 1$, $\epsilon_b = \epsilon$, and $v_a = 1/\lambda^2$, $v_b = 0$.

For H-polarization, we have

$$\left[\frac{\partial}{\partial x} \left(\frac{1}{f(x,y)} \frac{\partial H_z}{\partial x} \right) + \frac{\partial}{\partial y} \left(\frac{1}{f(x,y)} \frac{\partial H_z}{\partial y} \right) \right] + H_z = 0 \quad (13)$$

The Fourier expansion of Eq. 11 cannot be expressed in an eigenvalue form

$$\sum_{G'} g(G-G')(k+G) \cdot (k+G') H_z(G') = H_z(G) \quad (14)$$

where the Fourier components of $\frac{1}{f(x,y)}$ are $g(0) = g_b + (g_a - g_b)f$ and $g(G \neq 0) = 2f(g_a - g_b) J_1(x)/x$

For the case of 'dielectric atom', $g_a = 1/(\omega/c)^2 \epsilon$, $g_b = 1/[(\omega/c)^2 - 1/\lambda^2]$.

For the case of 'superconductor atom', $g_a = 1/[(\omega/c)^2 - 1/\lambda^2]$, $g_b = 1/(\omega/c)^2 \epsilon$.

4. COMPUTATION OF THE MATRIX EIGENVALUES

Equations 12 & 14, each forms a set of $N \times N$ size matrix, where $N \rightarrow \infty$. For each k in the first Brillouin zone, we use the Matlab command 'eig' to solve all the N eigenfrequencies ω/c for the case of E-polarization. Unfortunately, this approach cannot be used to solve for H-polarization, because Eq. 14 cannot be expressed in an eigenvalue form. We have to use the zero-determinant to find the solution for k , given each value of ω/c . Due to this difficulty; in this paper, we confined our study to the case of E-polarization. We have used $N=289$ plane waves for the computation of the band structures and field distributions results presented in Section 5. The axis of all figures are normalized in unit of $2\pi/a$. So the band structures are $\omega a/2\pi c$ versus $ka/2\pi$.

5. RESULTS AND DISCUSSIONS

The photonic band structures for dielectric-superconducting PC appear essentially the same (comparing Fig.1a & 1b) as the all-dielectric PC (where the superconductor is replaced by vacuum with $\epsilon = 1$) except for the existence of the bandgap from zero frequency. The higher bands are the product of the higher G terms in Eq. 12. We find that, the higher bands are up-shifted approximately $(1-f)/\lambda_L^2$ and f/λ_L^2 for dielectric and superconducting 'atom' respectively. The band structures appear to be up-shifted more for lower bands, thus creating a low frequency (LF) gap which size (ω_c) increases with inverse of the penetration depth ($1/\lambda_L$). However, the increment is not indefinite. Instead, it saturates for extremely low penetration depth for all values of dielectric constant ϵ and atom ratio, r (Fig. 2 & 3) when the expulsion of the electric field by the superconductor is maximum. The onset of saturation, defined as the point where $d^2\omega_c/d(1/\lambda_L)^2$ is maximum, occurs at $1/\lambda_L \sim 2$. The fact that superconductor acts as a field-forbidden medium while the dielectric acts as field-confining medium for frequency below $1/\lambda_L$ is clearly shown in Fig. 4 & 5. At frequency greater than $1/\lambda_L$, the field begins to penetrate more and more into the superconductor (Fig 4b & 5b). The electric field for the fundamental mode is tightly confined within 'dielectric background' (Fig.4a) and 'dielectric atom' (Fig. 5a) since the field is highly evanescent in the superconductor.

The LF gap size increases with the superconductor filling fraction, f_s (Fig. 6a) but decreases with the dielectric filling fraction $f_d (=1-f_s)$ (Fig. 6b) . The LF gap is maximum ($= 1/\lambda_L$) with bulk superconductor , as $f_d \rightarrow 0$ (Fig. 6b) . Creating large bandgap alone does not have much use. It is the flexibility of using photonic crystal to control the photonic bandgap for various purposes that makes it so useful and motivates the understanding of the mechanisms of bandgap . A frequency with a wavelength too large ($\lambda / 2 >$ field confining width) to fit into the dielectric region will be forbidden inside the PC . Figure 7a & 7b implies that the LF gap is slightly larger for fields confined to the background than the fields confined to the 'atom' even though the area of the background and the 'atom' are the same within a unit cell ($f=0.5$). Therefore, the LF gap size does not only depend on the field-confining/forbidden area, but also depend on the geometry of the area , since it is the geometry which determines the field-confining width . Figures 7a & b also show that the LF gap size decreases with dielectric constant ϵ for both superconducting and dielectric 'atoms'. The effect of increasing ϵ is equivalent to increasing the effective field confining width. The wavelength is simply squeezed more if ϵ is larger . This means that larger wavelengths can now fit into the field-confining width , thus reducing the LF gap.

The band structure of Fig. 8a is computed using optimized parameters , $\epsilon=1$, $1/\lambda_L=2$ and $r=0.9$ which maximized the LF gap for 'superconducting atom' ('dielectric atom'). One large bandgap exists in the band structure at a higher a/λ (~ 1.75). The width and frequency of this gap can be tuned . This property could be advantageous to the fabrication of dielectric-superconductor PC with higher precision operating in optical regime since the required lattice constant is larger . Normally, the bandgap for dielectric PC exists around $a/\lambda \sim 0.5$. The required small lattice constant makes the fabrication of a perfect PC in optical regime difficult .

A highly dielectric-localized fundamental mode with almost flat dispersion (Fig. 8b) divides the LF gap and another gap for 'dielectric atom' with optimized $1/\lambda_L=2$ and $r=0.1$ but a large dielectric constant $\epsilon=14$. We found that the frequency of the mode decreases with ϵ . This mode is ideal for use as a superhigh-Q resonant cavity . Operating at a frequency where the superconductor is perfectly field-repulsive (completely no absorption of photon) with very small fraction of dielectric phase ($r=0.1$) , the PC can be used to store up high EM energy density within the 'dielectric atoms', which form a periodic resonant cavities .

The typical relaxation time τ of the normal fluid ranges from 10^{-11} s (near 0 K) to 10^{-15} s (near T_c)¹⁴ . If the PC operates at optical regime , $\omega \sim 5 \times 10^{15} \text{ s}^{-1}$; then Eq. 6 is valid (since $\tau\omega \gg 1$) and the penetration depth $\lambda_{L,0}$ which determines the LF gap size is independent of temperature at below T_c . Suppose that we wish to make use of the localized mode in Fig. 8 using a superconductor with small $\lambda_{L,0}$ ($= 64 \text{ nm}$) like Nb_3Sn ¹⁵ . Then, the required lattice constant is about 0.8 micron and the resonant wavelength is about 500 nm , in the optical regime. For temperature dependent applications , the PC has to operate at low frequency regime and further conditions¹² have to be satisfied for the imaginary conductivity approximation to hold .

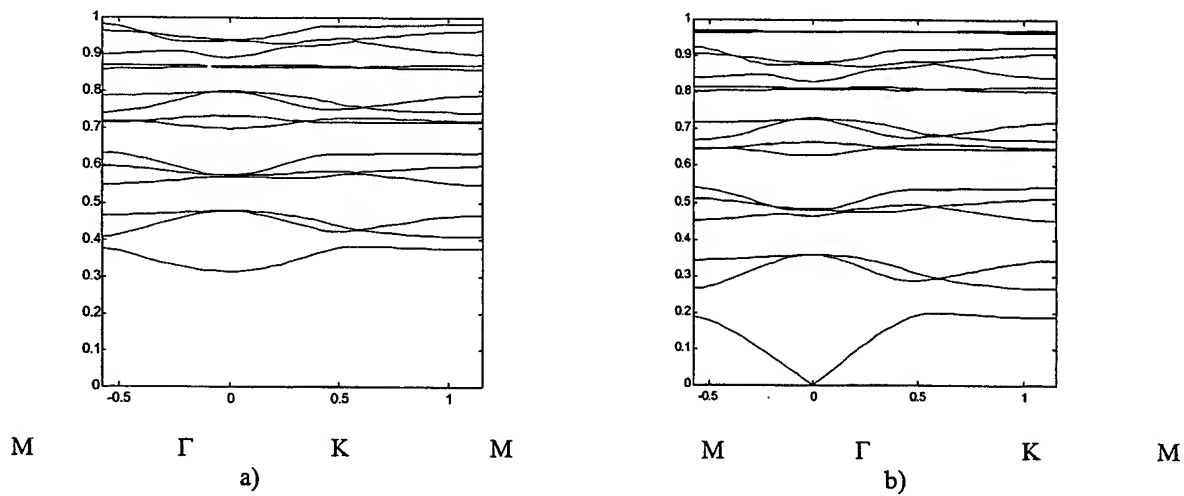
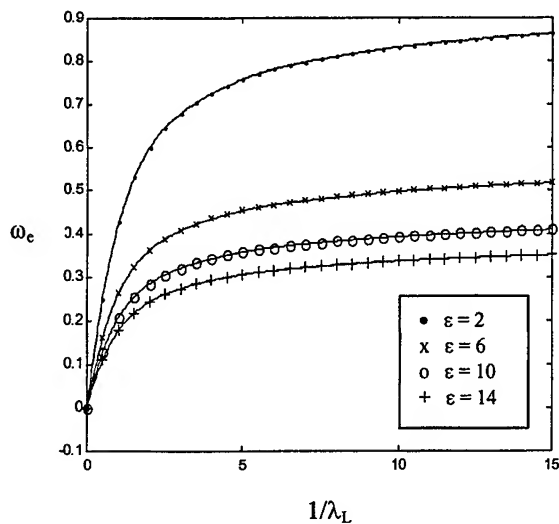
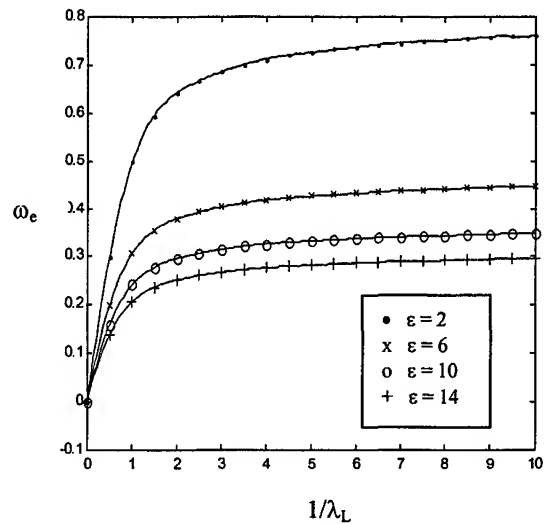


Figure 1: Band structures for E-polarization with $f = 0.431$, $\epsilon = 14$ and $1/\lambda_L = 0.5$.

a) dielectric 'atoms' in superconducting background , b) all-dielectric PC with background dielectric $\epsilon = 1$

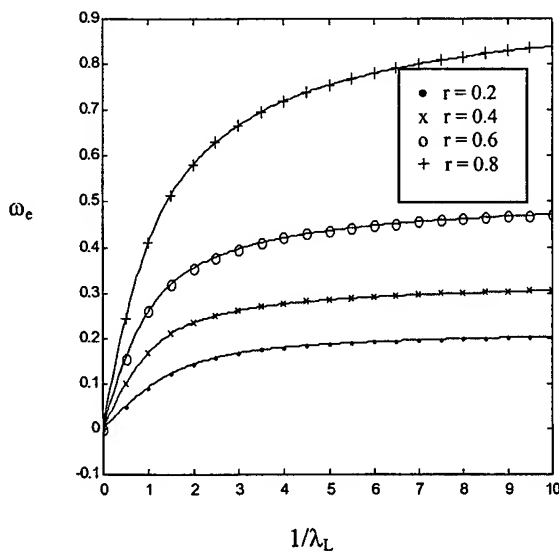


a)

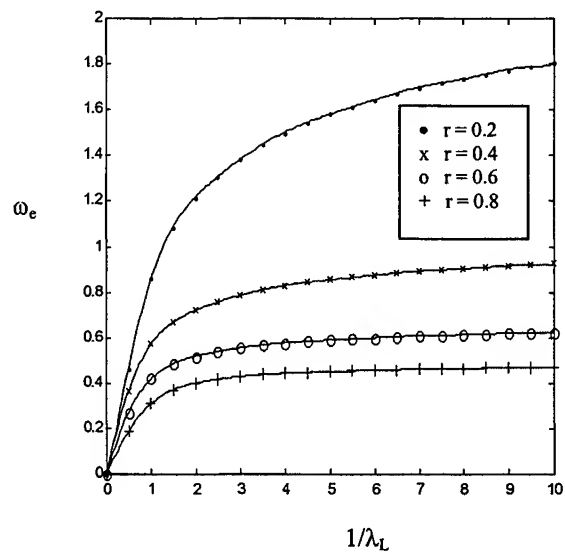


b)

Figure 2 : LF gap size versus $1/\lambda_L$ for different ϵ with $r = 0.68938$ a) 'superconducting atom' b) 'dielectric atom'.

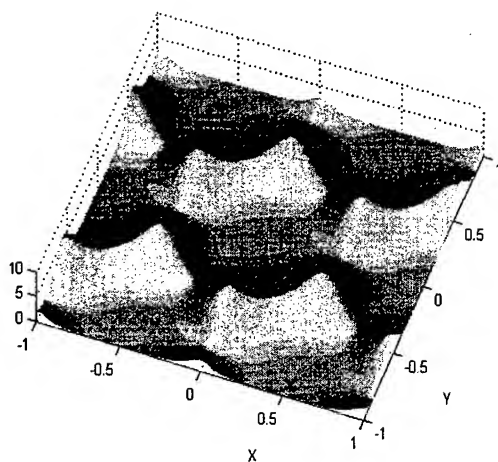


a)

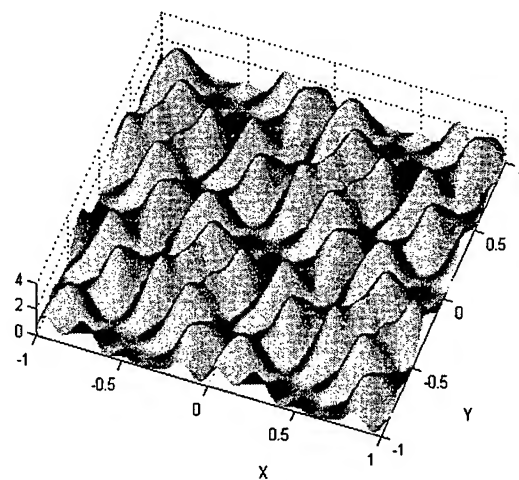


b)

Figure 3 : LF gap size versus $1/\lambda_L$ for different r with $\epsilon = 4$ a) 'superconducting atom' b) 'dielectric atom'

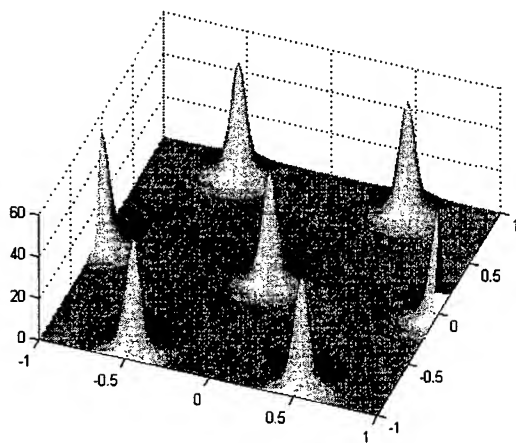


a)

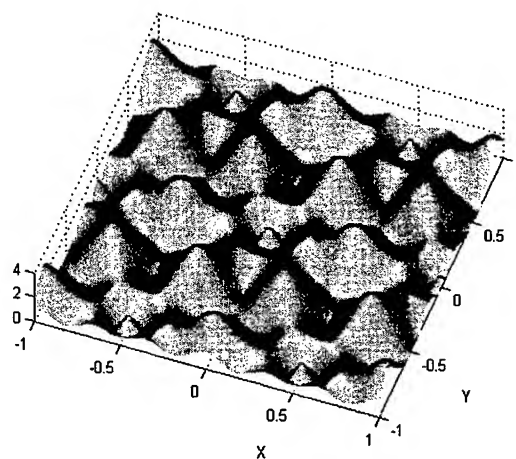


b)

Figure 4: Spatial distribution (in unit a) of E_z field intensity for 'superconducting atom' at point K with $\epsilon = 1$, $1/\lambda_L = 2$, $r = 0.9$ and a) $\omega/c = 1.4494$ (1st band) , b) $\omega/c = 3.1924$ (higher band)

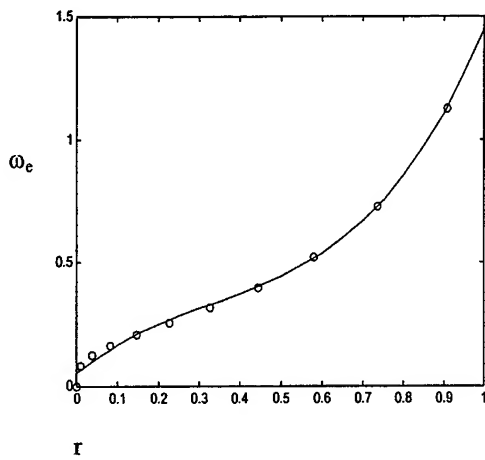


a)

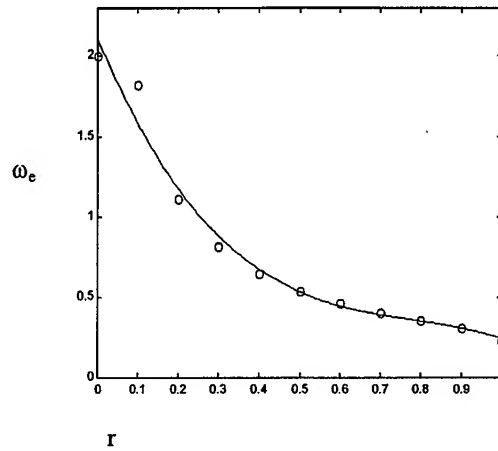


b)

Figure 5: Spatial distribution (in unit a) of E_z field intensity for 'superconducting atom' at point K with $\epsilon = 14$, $1/\lambda_L = 2$, $r = 0.1$ and a) $\omega/c = 1.5973$ (1st band) , b) $\omega/c = 3.1924$ (higher band)



a)



b)

Figure 6 : LF gap size versus $r = d/a$, with $\epsilon = 5$ and $1/\lambda_L = 2$ for a) 'superconductor atom' and b) 'dielectric' atom. The solid line is the cubic polynomial fit to the computed points 'o'.

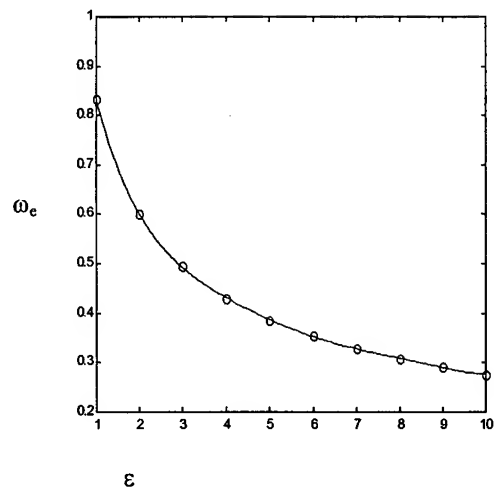
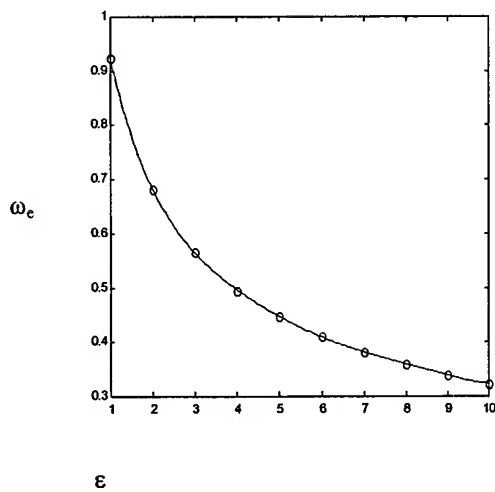


Figure 7 : LF gap size versus dielectric constant ϵ , with $f = 0.5$ and $1/\lambda_L = 2$ for a) 'superconductor atom' and b) 'dielectric' atom.

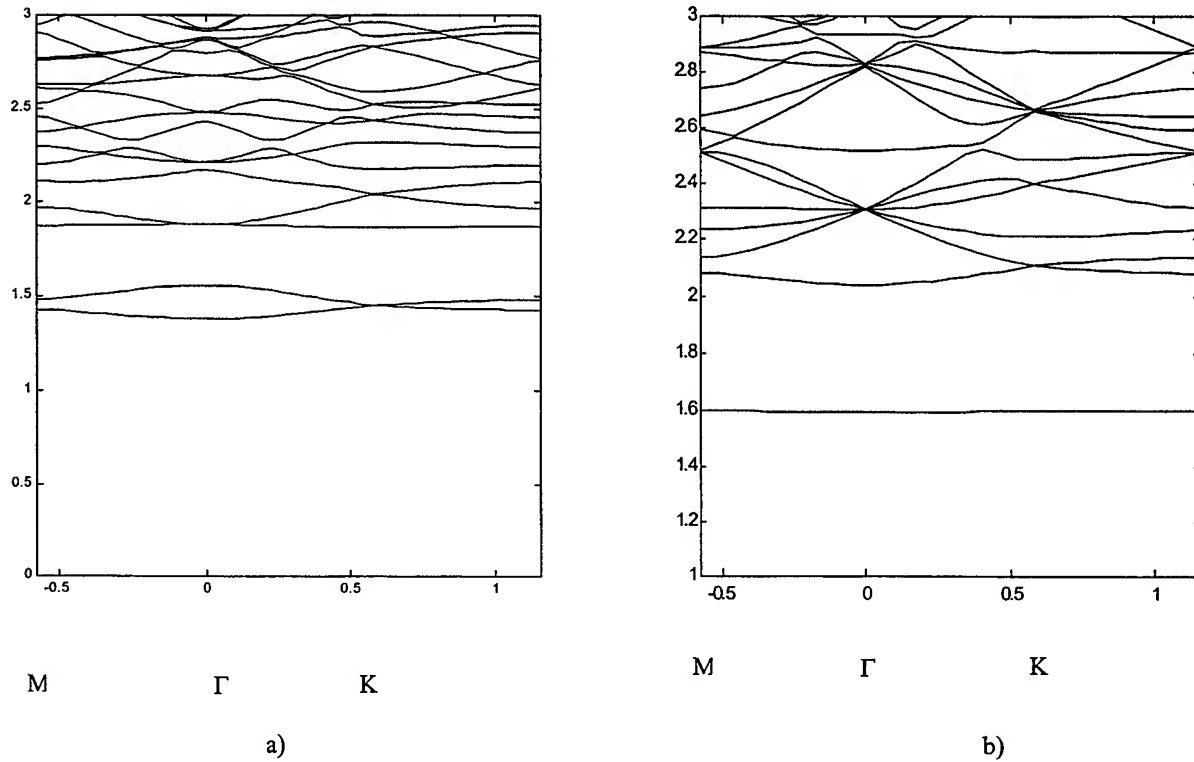


Figure 8: Band structures showing large LF gap a) $\epsilon = 1$, $1/\lambda_L = 2$ and $r = 0.9$ for 'superconducting atom'
b) $\epsilon = 14$ with $1/\lambda_L = 2$ and $r = 0.1$ for 'dielectric atom'

6. CONCLUSIONS

We have studied the photonic band structure and the electric field distribution in 2-D superconductor-dielectric photonic crystal using the plane wave expansion method and two fluid model. We found very large low frequency gap as due to the expulsion of the electric field from the superconductor. However, the field with frequency greater than $1/\lambda_L$ can propagate in the superconductor. Qualitative explanations for the dependency low frequency gap size on dielectric constant, penetration depth and filling fraction have been given. A smaller gap have been found at much higher lattice constant / wavelength ratio. We also found a fundamental mode with extremely localized electric field in the dielectric phase, similar to the localized mode in defective photonic crystal. This photonic crystal could be useful as superhigh-Q periodic resonant cavities, optical device in superconducting electronics and temperature tuned bandgap device.

ACKNOWLEDGEMENT

C.H. Raymond Ooi wishes to thank Prof. D.R. Tilley for fruitful discussions.

REFERENCES

1. Costas M. Soukoulis, *Photonic Band Gap Materials*, Proceedings of the NATO ASI on Photonic Band Gap Materials, Elounda, Crete, Greece, June 18-30, 1995 (NATO ASI Series, Kluwer Academic Publishers, The Netherlands, 1996).
Maradudin, A. A.; and McGurn, A. R., Out of plane propagation of electromagnetic waves in a two-dimensional periodic dielectric medium, *J. Mod. Optics* 41, 275 (1994). Ho, K. M.; Chan, C. T.; and Soukoulis, C. M., Existence of a photonic gap in periodic dielectric structures, *Phys. Rev. Lett.* 65, 3152 (1990).
2. E. Yablonovitch, *Phys. Rev. Lett.* 58, 2059 (1987).
3. Krauss, T. F.; De La Rue, R. M.; and Brand, S., Two-dimensional photonic-bandgap structures operating at near- infrared wavelengths, *Nature* 283, 699 (1996). Gourley, P. L., et al., Optical properties of two-dimensional photonic lattices fabricated as honeycomb nanostructures in compound semiconductors, *Appl. Phys. Lett.* 64, 687 (1994). Ho, K. M., et al., Photonic band gaps in three dimensions: New layer-by-layer periodic structures, *Solid St. Comm.* 89, 413 (1994).
4. Sigalas, M. M.; Soukoulis, C. M.; and Ho, K. M., Effect of the magnetic permeability on photonic band gaps, *Phys. Rev. B: Condensed Matter* 56, 959 (1997).
5. Alex Figotin, Yuri A. Godin and Ilia Vitebsky, Two dimensional tunable photonic crystals, *Phys. Rev. B* 57, 2841 (1998).
6. V. Kuzmaik, A.A. Maradudin and A. R. McGurn, Photonic band structures of two-dimensional systems fabricated from rods of a cubic polar crystal, *Phys. Rev. B* 55, 4298 (1997).
7. V. Kuzmaik & A.A. Maradudin, Photonic band structures of one-and two-dimensional periodic systems with metallic components in the presence of dissipation, *Phys. Rev. B* 55, 7427 (1997). Smith, D. R., et al., Experimental and theoretical results for a two-dimensional metal photonic band-gap cavity, *Appl. Phys. Lett.* 65, 645 (1994).
8. M. Tinkham, *Introduction to superconductivity*, 2nd. ed. (New York : McGraw Hill, c1996).
9. T. van Duzer, C.W. Turner, *Principles of superconductive devices and circuits*, p124-128. (London: Edward Arnold, 1981).
10. Kittel, Charles, *Introduction to solid state physics*, p.259 6th ed. (New York : Wiley, c1986).
11. Tilley, D. R. & Tilley, J., *Superfluidity and superconductivity*, (Hilger, Boston, c 1986).
12. C.H. Raymond Ooi, T.C. Au Yeung, T.K. Lim, C.H. Kam, Photonic bandgap in one dimension dielectric-superconductor (sent to *Phys. Rev. B*).
13. The number of plane waves used is sufficiently large that we have obtained converging results.
14. T. van Duzer, C.W. Turner, *Principles of superconductive devices and circuits*, p.28 (London : Edward Arnold, 1981).
15. Charles P. Poole, Jr., Horacio A. Farach, Richard J. Creswick, *Superconductivity* (San Diego : Academic Press, c1995.)

SESSION 7

Optical Communications

1.2 μm GaInAs/GaAs Lasers

- Are they useful for high capacity single mode fiber datacom ? -

Fumio Koyama, Dietmar Schlenker, Tomoyuki Miyamoto, Zibiao Chen and Kenichi Iga
Precision & Intelligence Laboratory, Tokyo Institute of Technology
4259 Nagatsuta, Midori-ku, Yokohama 226-8503, Japan
Tel: +81-45-924-5068, Fax: +81-45-924-5961, E-mail: koyama@pi.titech.ac.jp

ABSTRACT

Gigabit/s-LANs with 0.85 μm vertical cavity surface emitting lasers (VCSELs) are now going into the market. But, their link length is limited to be shorter than 500 m due to modal dispersion of employed multi-mode fibers and various modal problems should be considered in system design. The next step will be to develop long wavelength VCSELs matching to a single mode fiber with longer link lengths of several km and higher data rates. Long wavelength single mode fiber datacom should be advantageous because of avoiding modal noise and relaxing eye safe issues. Recently, we demonstrated a 1.2 μm wavelength highly strained GaInAs/GaAs quantum well (QW) edge emitting laser, which exhibits reasonably low threshold and excellent temperature characteristics. The threshold current is as low as 13 mA for an as-cleaved $5 \times 380 \mu\text{m}$ laser. A characteristic temperature T_0 under pulsed operation is as high as 140 K. This is the record high T_0 in 1.2 – 1.3 μm wavelength band. Even under "heatsink-free" cw operations, T_0 was much higher than that of conventional 1.3 μm GaInAsP/InP systems. We can avoid thermoelectric coolers as well as heatsink itself, thus, an all-plastic mold package without heatsink may give us a drastic cost reduction.

It is interesting to note that commercial standard single mode fibers are designed to locate a cut-off wavelength at around 1.2 μm for the purpose of production tolerance. A question arises: whether this 1.2 μm wavelength band can be utilized for single mode fiber datacom or not. We have demonstrated a 2 Gb/s-5km single mode fiber data transmission experiment using a fabricated 1.22 μm uncooled GaInAs/GaAs laser.

We believe that the VCSEL technology may drastically improve the transmitter performances at this new wavelength band and this 1.2 μm Gigabit LAN may become realistic by extensive developments. In this paper, we would like to discuss a possibility of high speed datacom using a newly developed 1.2 μm highly strained GaInAs/GaAs lasers.

Keywords: Long wavelength lasers, Strained quantum wells, Data link, Surface Emitting Lasers, Single mode fiber

1. INTRODUCTION

The optical technology is becoming inevitable for high speed local area networks (LANs) and computer interconnects. Gigabit/s-LANs with 0.85 μm vertical cavity surface emitting lasers (VCSELs) are now going into the market. But, their link length is limited to be shorter than 500 m due to modal dispersion of employed multi-mode fibers and various modal problems should be considered in system design. The next step will be to develop long wavelength VCSELs matching to a single mode fiber with longer link lengths of several km and higher data rates. Long wavelength single mode fiber datacom should be advantageous because of avoiding modal noise and relaxing eye safe issues. Figure 1 shows various materials for VCSELs in wide spectral ranges. There have been several approaches toward 1.3 μm VCSELs by using various materials on GaAs, such as GaInNAs/GaAs [1]-[3], GaAsSb/GaAs [4] and GaInAs/GaAs quantum dots [5]. On the other hand, high performance GaInAs/GaAs edge emitting lasers have been demonstrated, but their lasing wavelength has been limited below 1.1 μm [6]. Recently, we demonstrated a highly strained GaInAs/GaAs quantum well (QW) laser emitting at nearly 1.2 μm wavelength, which exhibits reasonably low threshold and excellent temperature characteristics [7]. If we are able to extend the lasing wavelength by using highly strained QWs, we can expect various benefits in the following:

- 1) Possibility for single mode fiber LANs with longer link length and higher data rate

- 2) Increased power level for eye safety
- 3) Reduced operating voltages for advanced CMOS circuits
- 4) Better sensitivity in GaInAs detectors
- 5) Performance improvements by high strain and deeper wells

Also, it is interesting to note that commercial standard single mode fibers are designed to locate a cut-off wavelength at around 1.2 μm for the purpose of production tolerance as shown in Fig. 2. In other word, the cut-off wavelength of roughly 50% of commercial single mode fibers is shorter than 1.2 μm . A question arises: whether this 1.2 μm wavelength band can be utilized for single mode fiber datacom or not. The solution may come from a laser availability at 1.2 μm wavelength band. In this paper, we like to present some lasing characteristics of 1.2 μm highly strained GaInAs/GaAs QW lasers and to discuss a possibility of single mode fiber data transmission by using a 1.2 μm uncooled laser.

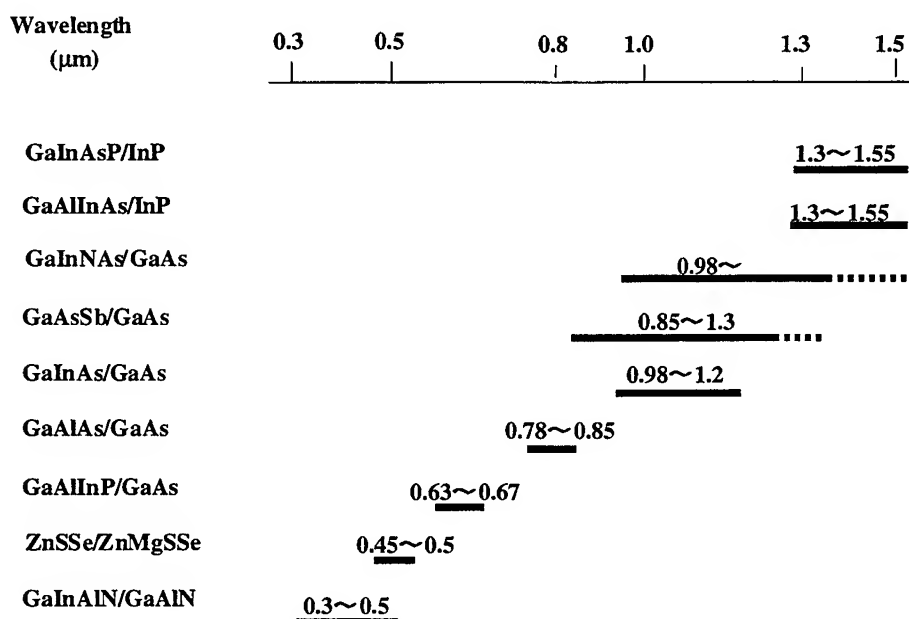


Fig.1 Materials for VCSELs in wide spectral range

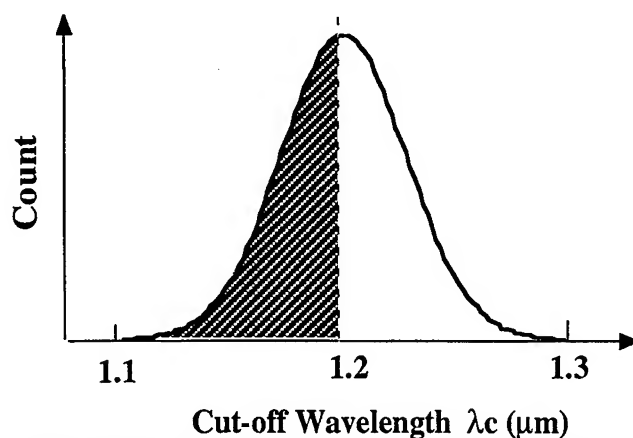


Fig. 2 Distribution of cut-off wavelength of standard single-mode fibers.

2. HIGHLY STRAINED 1.2 μm GaInAs/GaAs QUANTUM WELL LASER

We have developed highly strained GaInAs/GaAs QW lasers emitting beyond 1.2 μm in wavelength by growing wafers by metalorganic chemical vapor deposition (MOCVD). We realized good crystal quality for highly strained QWs by optimizing growth conditions in MOCVD and by using a strained buffer layer [7]. The active region consists of 7.5 nm thick $\text{Ga}_{0.62}\text{In}_{0.38}\text{As}$ wells and 19 nm thick GaAs barriers. The details are described in ref. [7]. The PL peak wavelength of a processed wafer was 1.17 μm , which can be extended to 1.2 μm without any penalties in crystal qualities. We fabricated 5 μm wide ridge waveguide stripe lasers as shown in Fig.3. Fabricated chips were tested on a copper plate without bonding, resulting in a high thermal resistance of about 1000 K/W. The device worked well even under such "heatsink-free operation". Figure 4 shows light output/current characteristics for various temperatures of sub-mount under "heatsink-free" cw operations. The lasing wavelength at 85 $^{\circ}\text{C}$ is 1.22 μm . Heating of the chip under cw operation increases the wavelength by about 20 nm. A threshold of 14 mA and a slope efficiency of 0.2 W/A are obtained for $5 \times 380 \mu\text{m}^2$ as-cleaved ridge waveguide lasers under room temperature pulsed operations. Some devices under high injection showed a lasing wavelength beyond 1.25 μm due to heating as shown in Fig. 5, which is the longest wavelength ever reported for GaInAs/GaAs systems. Figure 6 shows the temperature dependence of thresholds. A characteristic temperature T_0 under pulsed operation is as high as 140 K for as-cleaved 380 μm long devices. Even under "heatsink-free" cw operations, T_0 ($= 66\text{K} \sim 140\text{K}$) was higher than that of conventional 1.3 μm GaInAsP/InP systems. Technologies well-established on 0.85 μm or 0.98 μm VCSELs can be used for realizing 1.2 μm VCSELs. We could expect heatsink-free transmitter modules using such high performance long wavelength VCSELs. If we are able to avoid thermoelectric coolers as well as heatsink itself, an all-plastic mold package without heatsink may give us a drastic cost reduction.

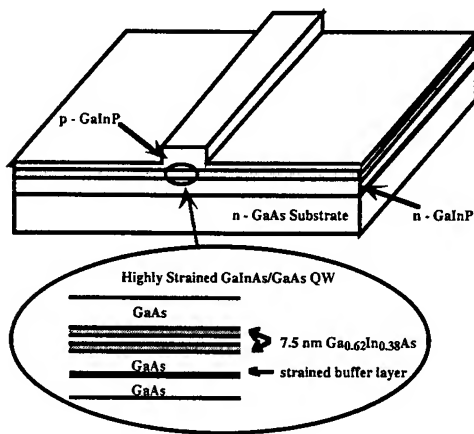


Fig.3 Schematic structure of 1.2 μm GaInAs/GaAs ridge waveguide laser.

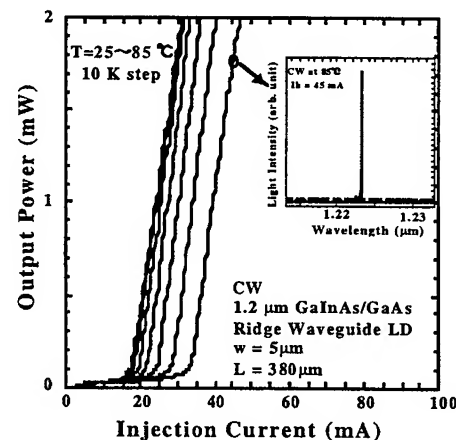


Fig. 4 Light output/current characteristics and lasing spectrum under heatsink-free cw operation.

3. SINGLE MODE FIBER DATA TRANSMISSION AT 1.2 μm

The most important issue is whether single mode fiber transmission is possible in 1.2 μm wavelength band or not. We carried out a 2 Gb/s data transmission experiment with a 5 km long standard single mode fiber by using a fabricated 1.2 μm laser. The fabricated laser was directly modulated using an NRZ pseudorandom bit sequence (PRBS) with a word length of $2^{15}-1$. The laser emission was coupled into a 5 km long single mode fiber with a cut-off wavelength of 1.16 μm . After transmission through the single mode mode fiber, the signal light was detected by a 8 GHz bandwidth PIN-FET receiver and the electrical signal was amplified and fed to an electrical sampling oscilloscope and a bit error detector (ANRITSU MP1762A). The bias current was 1.1 times the threshold. The bias current was carefully set to minimize the spectrum broadening of a modulated laser. The modulation current was 30 mA peak-to-peak. Figures 7 (a) and (b) show the spectrum under cw operation and under 2 Gb/s direct modulation, respectively. The peak wavelength of a modulated

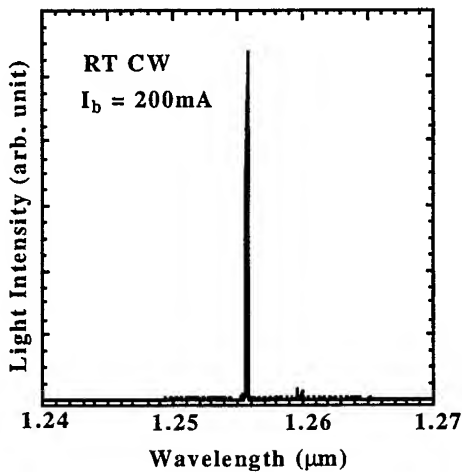


Fig. 5 Spectrum showing the longest emission wavelength under heatsink-free cw operation.

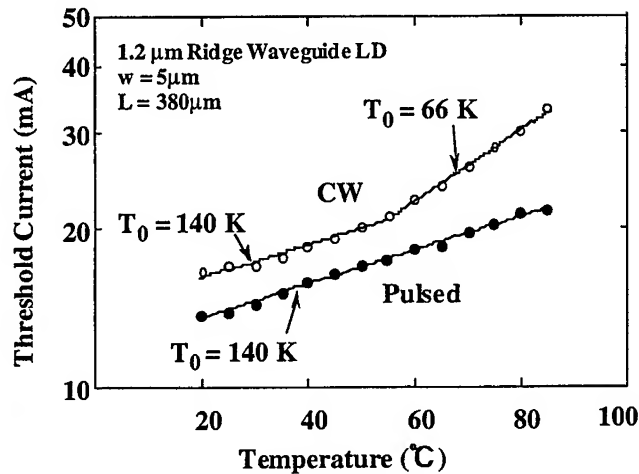


Fig. 6 Temperature dependence of thresholds under cw and pulsed operations

GaInAs/GaAs laser was 1.22 μm .

Figure 8 shows the bit error rate and eye patterns before and after the transmission of a 5 km long single mode fiber. Power penalty was below 1 dB. We also measured a small signal transmission bandwidth of the fiber by using a 1.22 μm GaInAs/GaAs QW laser modulated by a 10 GHz bandwidth LiNbO₂ external modulator as shown in Fig. 9. The result exhibits a potential bandwidth of higher than 10 GHz for a 5 km long fiber. The link length could be extended up to 10 km with a bit rate of 1 Gb/s.

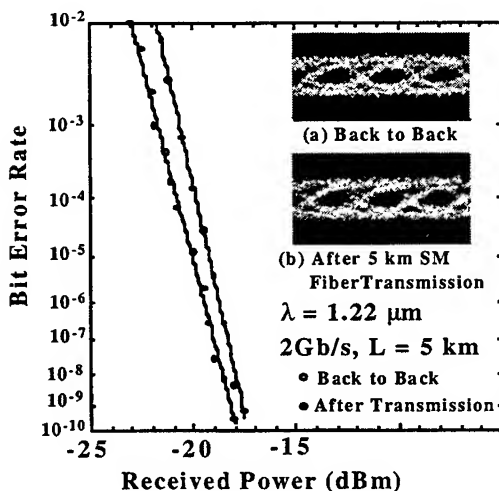


Fig. 8 2 Gb/s single mode fiber data transmission with 1.22 μm directly modulated GaInAs/GaAs QW laser.

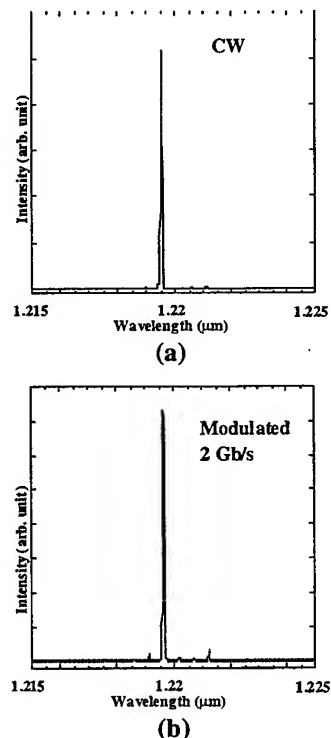


Fig. 7 Lasing spectrum under cw (a) and 2 Gb/s modulation (b).

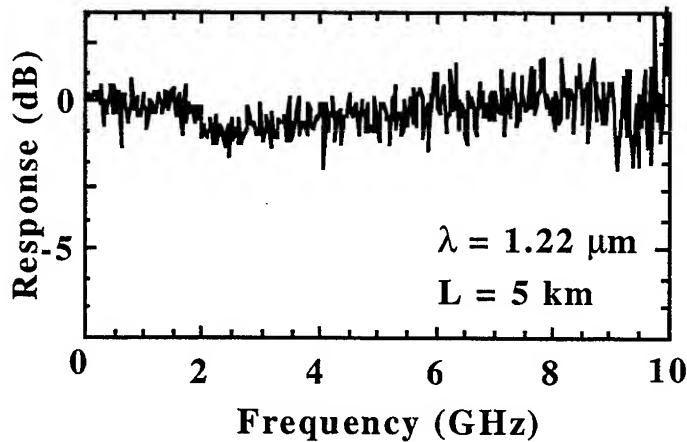


Fig. 9 Small signal frequency response of 5km long single mode fiber measured by using 1.22 μm GaInAs/GaAs laser and 10 GHz-bandwidth external modulator.

4. PROSPECTS of 1.2 μm SINGLE MODE FIBER LANS

A standard single mode fiber can guarantee single mode transmission at a wavelength of longer than 1.27 μm , although the cutoff wavelength of most of standard fibers is around 1.2 μm . Thus, two modes (LP_{01} and LP_{11} modes) still remain in the worst case at 1.2 μm . One possible solution is to select fibers with a cut-off wavelength shorter than 1.2 μm . It is not a big trouble increasing the cost, because 50 % of commercial single mode fibers may give us a cut-off wavelength of below 1.2 μm . Another simple way is to introduce a mode filter consisting of a fiber loop to eliminate the LP_{11} mode, which was recently demonstrated for single mode fiber transmission by using a 0.85 μm VCSEL [8]. Figure 10 shows the calculated loss of the fiber loop filter as a function of the loop radius [9]. Even if a modal dispersion may happen, we can easily avoid the LP_{11} mode by using the mode filter with a negligible power penalty for the fundamental LP_{01} mode. Also, the dispersion effect due to mode coupling between these two modes in installed fibers would be small at an operating wavelength near the cut-off wavelength.

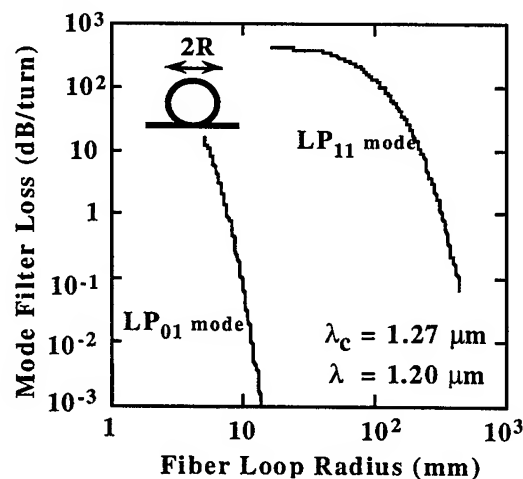


Fig. 10 Loss of fiber loop mode filter for LP_{01} and LP_{11} modes.

Figure 11 shows the calculated transmission bandwidth for VCSEL data links, exhibiting performances even better than that using 1.3 μm Fabry-Perot LDs. A slight increase in transmission loss and chromatic dispersion in comparison with a 1.3 μm wavelength band may not be a big issue. A higher transmission bandwidth can be expected because of the dynamic single mode operation of VCSELs.

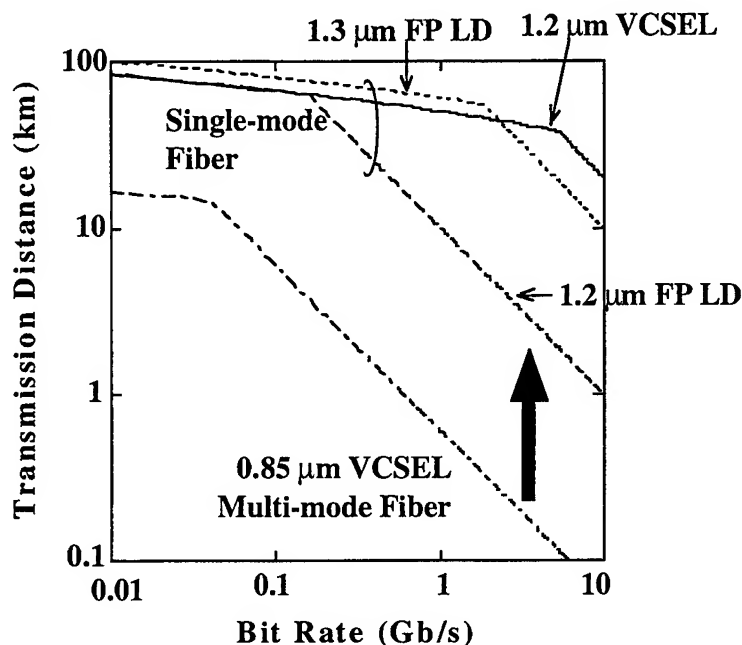


Fig.11 Transmission Bandwidth of VCSEL Datalink

5. CONCLUSION

We have demonstrated a 2 Gb/s single mode fiber data transmission experiment using a 1.22 μm highly strained GaInAs/GaAs laser with a high characteristic temperature of 140 K. We like to strongly suggest a "1.2 μm wavelength band" using high performance GaInAs/GaAs VCSELs for high speed single mode fiber LANs of several Gb/s or beyond. We believe that the VCSEL technology may drastically improve the transmitter performances at this new wavelength band and this 1.2 μm Gigabit LAN may become realistic by extensive developments.

ACKNOWLEDGMENTS

The authors acknowledge Dr. A. Matsutani and Mr. T. Sakaguchi for help in experiments. The authors also acknowledge Mr. M. Miyamoto of Fujikura Ltd. and Mr. T. Kunikane of Fujitsu Laboratories Ltd. for offering single mode fiber and LiNbO₂ external modulator, respectively. This study was supported by Grant-in-Aid for COE Research from the Ministry of Education, Science, Sports and Culture (#07CE2003, "Ultra-parallel Optoelectronics").

REFERENCES

- [1] M. Kondow, K. Uomi, A. Niwa, T. Kitatani, S. Watahiki and Y. Yazawa, "GaInNAs: A novel material for long-

- wavelength-range laser diodes with excellent high-temperature performance" , Jpn J. Appl. Phys., 35, pp. 1273-1275, 1996.
- [2] S. Sato, S. Satoh, "Room temperature continuous-wave operation of 1.24 μ m GaInNAs lasers grown by metalorganic chemical vapor deposition" , 16th IEEE International Semiconductor Laser Conference, PD-5, 1998.
 - [3] T. Miyamoto, K. Takeuchi, T. Kageyama, F. Koyama and K. Iga, "GaInNAs/GaAs quantum well growth by chemical beam epitaxy" , Jpn. J. Appl. Phys., 37, pp.90-91, 1998.
 - [4] T. Anan, K. Nishi, S. Sugou, M. Yamada, K. Tokutome and A. Gomyo, "GaAsSb: A novel material for 1.3 μ m VCSELs" , Electron. Lett., 34, pp.2127-2129, 1998.
 - [5] D.L. Huffaker, H. Deng and D.G. Deppe, "1.15- μ m wavelength oxide confined vertical cavity surface emitting laser diodes" , IEEE Photon. Technol. Lett., 10, pp.185-187, 1998.
 - [6] K. CZOTSCHER, E.C. LARKINS, S. WEISER, W. BENZ, J. DALEIDEN, J. FLEISSNER, M. MAIER, J.D. RALSTON and J. ROSENZWIG, "Uncooled high-temperature operation of InGaAs-GaAs multiple quantum-well lasers at 20Gb/s" , IEEE Photon. Technol. Lett., 9, pp.575-577, 1997.
 - [7] D. Schlenker, T. Miyamoto, Z. Chen, F. Koyama and K. Iga, " 'Long wavelength GaInAs/GaAs quantum well lasers" , International Conference on Indium Phosphide and Related Materials, WeP18, 1999.
 - [8] P. Schnitzer, R. Jager, C. Jung, R. Michlzik, D. Wiedenmann, F. Mederer and K.J. Ebeling, "Biased and bias-free multi-Gb/s data links using GaAs VCSELs and 1300-nm single-mode fiber" , IEEE Photon. Technol. Lett., 10, pp.1781-1783, 1998.
 - [9] D. Marcuse, "Curvature loss formula for optical fibers" , J. Opt. Soc. Am., 66, pp.216-220, 1976.

Performance of a Serial-Search Synchroniser for Fibre-based Optical CDMA Systems in the Presence of Multi-user Interference

Mazlyn Mona Mustapha and Richard F. Ormondroyd[†]
Communications and Wireless Networks Group,
Cranfield University, RMCS, Shrivenham,
Swindon, SN6 8LA, UK

ABSTRACT

This paper examines the performance of a serial-search synchronisation system in the presence of multiple access interference and receiver noise for a non-coherent fibre-based optical CDMA system using optically orthogonal codes. The synchronisation performance of two different optical CDMA systems, an on-off keyed system and an M -ary pulse-position modulation system with $M=2$, are compared. The effects of the dwell-time, the total number of users, the code weight, decision threshold and optical hard-limiters on the mean acquisition time of the synchroniser are examined. It is shown that an optimum dwell-time exists which minimises the mean acquisition time.

Keywords: optical CDMA, serial-search synchronisation, code acquisition

1. INTRODUCTION

In an optical CDMA system, the receiver must be able to synchronise to, and track, the code sequence contained within the received signal. This signal is generally buried in the multiple access interference (MAI) generated by the other CDMA users sharing the channel. The synchronisation process consists of two parts: initial coarse synchronisation, which is called acquisition, and the subsequent fine-tuning and the continuous tracking of the code sequence. In this paper, only the acquisition process is examined.

For a non-coherent optical CDMA system using the on-off keying (OOK) method with optical orthogonal codes (OOC) and optical tapped-delay-line receivers, the structure of the spread-spectrum signal is different from the conventional direct-sequence spread-spectrum signal used in wireless CDMA systems. This has an impact on the acquisition process. In conventional CDMA, the spreading code is modulo-2 added to the data bits, which is equivalent to multiplying the chips with the bits when they are represented as polar signals. In this case, synchronisation can be carried out by correlating the received signal with a locally generated replica signal. Maximum correlation generally indicates that the replica code is synchronised to the code in the received signal. For the OOK/OOC optical CDMA system, the chip sequence is effectively ANDed with the data bits. In this case, acquisition involves locating the wanted chip positions within the data bit period and rejecting the chips of the other-user codes that fall within the same data bit period. This is carried out using the passive optical delay line, but requires data bit synchronisation. To achieve chip and bit synchronisation within the same acquisition time requires that a training sequence of spread data bits is transmitted. The output from the optical tapped delay line is then compared with the required training sequence. The dwell-time of the correlation process for the optical CDMA system is now spread over the training sequence. This is a different process to that needed for a conventional CDMA system.

The importance attributed to the acquisition time, and hence the required system complexity, depends upon the intended application. In some situations, rapid acquisition may be required, such as for short bursts of data exchange. If the acquisition time is long, the data throughput is reduced. However, for applications where the data transfer period is relatively long, the time taken to synchronise is not a critical parameter and it is more important to ensure that synchronisation has been achieved reliably.

[†] Correspondence: Tel: +44 1793 785260; Fax: +44 1793 785902 Email: mustapha@rmcs.cranfield.ac.uk;
r.f.ormondroyd@rmcs.cranfield.ac.uk

Code acquisition for radio-based spread spectrum systems has been covered extensively in the literature^{1,2,3}. In 1990, Kiasaleh⁴ considered the problem of code acquisition for a spread spectrum system using on-off keying and pseudonoise (PN) codes over an optical channel. More recently, code acquisition for both coherent⁵ and non-coherent⁶ optical CDMA systems have been examined. In this paper, an analysis of the mean acquisition time of a serial search synchroniser used in a non-coherent optical CDMA system is presented using the flow graph technique. The synchronisation performance of two different optical CDMA systems, an OOK and an M -ary pulse-position modulation (PPM) with $M=2$, are compared. The effects of the dwell-time (i.e. training sequence length), the OOC code weight, the number of users, the detector decision threshold and the use of optical hard-limiters on the mean acquisition time are examined.

2. SYSTEM DESCRIPTION

The system investigated here is a fibre-based, non-coherent optical CDMA network utilising a star topology with optical tapped-delay line encoders and decoders⁷, as shown in Figure 1. Optical orthogonal codes⁸ are used to spread the data bits. The OOC used has a length of F chips and a code weight of K . It is assumed that all N users are sending data to the network continuously. Also, it is assumed that the target station already knows the OOC of the transmitting station, and that it is expecting to receive data from that station. Consequently, the target receiving station tries to synchronise itself with the OOC of the transmitting station continuously. Moreover, it is assumed that the system is chip synchronous, i.e. the chips are located at multiples of the chip width T_C .

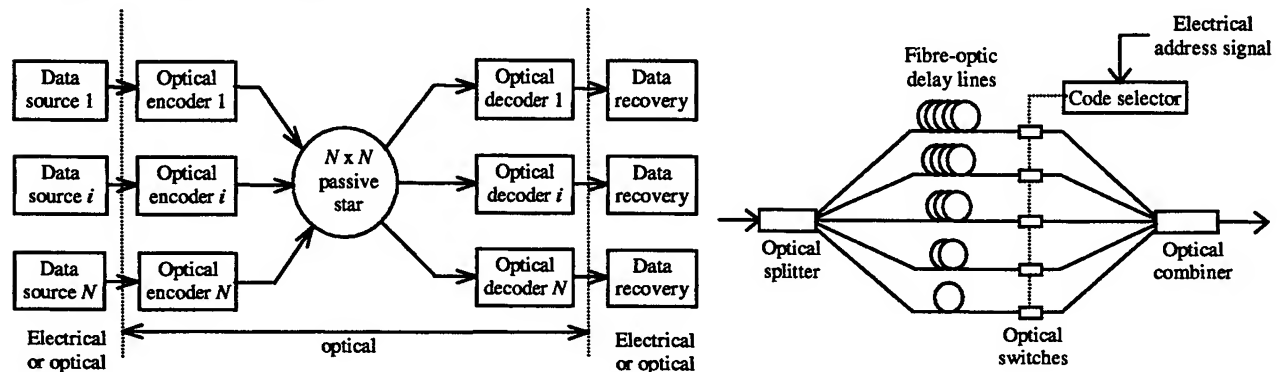


Figure 1(a): A star topology optical CDMA network and Figure 1(b): Fibre-optic tapped delay-line encoder

To assist in the search of the wanted chip location, a training sequence of length ℓ bits is sent by the transmitter. This training sequence must be known to the target station in order for the receiver to successfully retrieve it from the incoming signal. Also, it is assumed that the location of the training sequence within the data stream is known by the receiving station, although the precise chip location is unknown.

In an OOK system, when a data bit '1' is sent, a code sequence is transmitted, but when a data bit '0' is sent no signal is transmitted. Therefore, the first bit of the training sequence must be a data bit '1'. Although the training sequence starts with a '1' bit, it is assumed that the probability of a data bit '0' and a data bit '1' occurring in the training sequence is equal.

The receiver arbitrarily takes the first F chips into consideration. This is because the beginning of the initial training bit is unknown to the receiver. Then, each chip is examined to see if it exceeds the threshold. If the threshold is exceeded, which means that a '1' is detected, the location (within the data bit) of these chips, $X_1 = \{x_{i_0}, x_{i_1}, \dots, x_{i_t}\}$, is stored for comparison at a later stage. The stored elements in X_1 denotes the probable locations of the wanted chip. This process is repeated for the remaining $(\ell - 1)$ training bits. For the ℓ^{th} bit, each chip is compared with the threshold and if it exactly matches the training sequence in conjunction with the elements in $(X_1, X_2, \dots, X_{\ell-1})$ synchronisation is achieved. Otherwise, that particular chip location is disregarded and the next chip is examined. Using this search method, only the exact training sequence is detected. If an error occurs in detecting one bit of the training sequence, the receiver will not synchronise. As the length of the training sequence increases, the probability of making a synchronisation error decreases; however the

acquisition time increases as a direct consequence because the search rate has been reduced. Consequently, acquisition is a compromise between achieving a high enough probability of synchronisation and the search rate.

2.1. Optical Hard-Limiter

The use of optical hard-limiters⁹ reduces certain patterns of interference and this can reduce the bit error probability. In these simulations, an ideal optical hard-limiter is assumed whereby the input signal intensity is limited to v_f if it is equal to or greater than the threshold, otherwise, the hard-limiter output is zero. This is represented as:

$$g(y) = \begin{cases} v_f & y \geq y_{th} \\ 0 & 0 \leq y < y_{th} \end{cases} \quad (1)$$

where y_{th} is the threshold level. Within the system simulations, the optical hard-limiter precedes the receiver correlator.

2.2. M -ary Pulse-Position Modulation Encoding

If the number of consecutive zero bits within the training sequence is large it may lead to an increased probability of non-synchronisation. To reduce this effect, the use of M -ary pulse-position modulation (PPM) with $M = 2$ encoding is also examined. In this encoding technique, data bits '1' and '0' are represented by '10' and '01' bits respectively^{10,11}. This has the effect of doubling the training sequence length from ℓ bits to 2ℓ bits.

2.3. Receiver Noise

In previous work, it has been assumed that the photodetector in the receiver is noiseless. In this paper, the receiver noise is included in the performance analysis to achieve a more realistic system. Here, an avalanche photodiode (APD) is used. For the APD, the distribution of photocurrent is assumed to be Gaussian, and it is given by:

$$P_{APD}(x) = \frac{1}{\sqrt{2\pi\sigma^2}} \exp\left[-\frac{(x-\mu)^2}{2\sigma^2}\right] \quad (2)$$

where σ^2 is the variance and μ is the mean photocurrent. In this case, the variance includes shot noise and thermal noise components and is defined as:

$$\sigma^2 = 2eB(I_{ph} + I_D)M^{2+\gamma} + \frac{4kTBF_n}{R_L} \quad (3)$$

In this equation, the first term represents shot noise and the second term represents thermal noise, e is the electron charge, B is the bandwidth at the receiver front-end, I_{ph} is the generated photocurrent, I_D is the dark current, M is the multiplication factor, γ is the detector material constant, k is Boltzmann's constant, T is the absolute temperature, F_n is the detector amplifier noise figure and R_L is the detector circuit load resistance. The photocurrent, I_{ph} , is dependent upon the optical power incident upon the detector, Φ :

$$I_{ph} = \frac{\eta\Phi e\lambda}{hc} \quad (4)$$

where η is the detector quantum efficiency, λ is the wavelength, h is Planck's constant and c is the velocity of light in vacuum. In the simulation of the system, described in section 4, all optical losses due to the optical tapped delay line encoders and decoders and the star coupler, etc. are included when Φ is calculated. This equation indicates that the probability density function depends on the photon density input *via* the shot noise term.

2.4. Failed Synchronisation

The training sequence is retransmitted until the receiver has synchronised to the received signal. Termination of the training sequence could be *via* an acknowledgement signal sent from the receiving station back to the transmitting station, indicating that synchronisation has been achieved. Alternatively, because the optical CDMA system uses a star topology and data from every transmitter is broadcast to all users, it is possible for the transceiver at the sending-end to verify that the receiver

has been able to synchronise to the transmitted code sequence. This can be accomplished by allowing the transmitting station's receiver to attempt to synchronise itself with the transmitted code sequence. This method is feasible if the length of fibre from each station to the star coupler is approximately the same. If the sending station is unable to synchronise itself correctly with the transmitted signal, it is very likely that this is also the case at the target station.

3. MEAN ACQUISITION TIME

In practical applications, it is necessary to quantify the performance of a synchroniser. One such performance measure is the acquisition time. This is defined as the total time required to find the correct wanted chip locations within the data bit. The acquisition time is a random variable, and it is difficult to quantify. Consequently, the mean acquisition time, which is the expected value of the total search time, is calculated instead. The mean acquisition time is obtained by means of a state transition diagram of a flow graph process or a discrete-time Markov process¹².

The probability of a false alarm, P_{fa} , is the probability that synchronisation is indicated, but at the incorrect chip location. This occurs when the multi-access interference mimics the training sequence pattern and the receiver synchronises to this erroneous chip location. Conversely, the probability that the receiver synchronises correctly is called the probability of detect, P_D . Using both of these values, the mean acquisition time of the synchroniser can be calculated.

When a training sequence of length ℓ bits is used, then for a chip synchronous system, at least $a = F(\ell - 1)$ chips must be searched through before synchronisation is possible. Also, it is assumed that if the training sequence is located, the system verifies that the correct chip location has been obtained by means of a further longer correlation. If it is a false alarm, a penalty time $T_{fa} = bT_c$ is incurred, where $b = FL$ and L is the number of bits needed to establish that an error had occurred. On the other hand, if the correct chip location is detected, the search is completed.

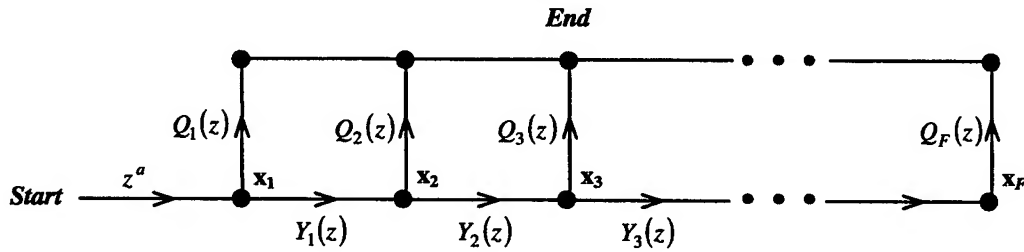


Figure 2: Generating Function Flow Graph for Acquisition Time

Figure 2 shows a simplified flow graph for the acquisition time. Here,

$$Q_n(z) = \frac{z(1-\beta)P_n}{1-\beta z^{a+1}\{H(z)\}^{F-1}} \text{ and } Y_n(z) = (1-P_n)H(z) \quad (5)$$

where $n = \{1, 2, \dots, F\}$, $H(z) = \alpha z^{a+b+1} + (1-\alpha)z$, $\beta = 1 - P_D$ and $\alpha = P_{fa}$.

$P_m = \frac{1}{F+1-m}$ is the *a priori* probability of a correct chip location, given that chips $\{1, \dots, m-1\}$ are incorrect.

From Figure 2, the flow graph generating function is:

$$\begin{aligned} U(z) &= z^a [Q_1(z) + Y_1(z)Q_2(z) + Y_1(z)Y_2(z)Q_3(z) + \dots + Y_1(z)Y_2(z)\dots Y_{F-1}(z)Q_F(z)] \\ &= \frac{(1-\beta)z^{a+1}}{1-\beta z^{a+1}\{H(z)\}^{F-1}} \times \{P_1 + (1-P_1)P_2H(z) + (1-P_1)(1-P_2)P_3[H(z)]^2 + \dots + (1-P_1)(1-P_2)\dots(1-P_{F-1})[H(z)]^{F-1}\} \end{aligned} \quad (6)$$

which can be simplified to:

$$U(z) = \frac{(1-\beta)z^{a+1}}{1-\beta z^{a+1}\{H(z)\}^{F-1}} \times \left\{ \frac{1}{F} + \frac{F-1}{F} \cdot \frac{H(z)}{F-1} + \frac{F-1}{F} \cdot \frac{F-2}{F-1} \cdot \frac{[H(z)]^2}{F-2} + \dots + \frac{[H(z)]^{F-1}}{F} \right\}$$

$$= \frac{(1-\beta)z^{a+1}}{1-\beta z^{a+1}\{H(z)\}^{F-1}} \times \frac{1}{F} \sum_{n=0}^{F-1} [H(z)]^n$$
(7)

When $z = 1$, $U(1) = 1$. The mean acquisition time is then:

$$\bar{T}_{acq} = \left. \frac{\partial}{\partial z} U(z) \right|_{z=1}$$

$$= T_C \left\{ 1 + a + \frac{(1-P_D) \{ (F-1) [P_{fa}(a+b)+1] + a+1 \}}{P_D} + \frac{F(F-1) [P_{fa}(a+b)+1]}{2F} \right\}$$

$$= T_C \frac{2P_D + 2P_D a + 2(a+1)(1-P_D) + 2(1-P_D)(F-1) [P_{fa}(a+b)+1] + P_D(F-1) [P_{fa}(a+b)+1]}{2P_D}$$

$$= T_C \frac{2(a+1) + (2-P_D)(F-1) [P_{fa}(a+b)+1]}{2P_D}$$
(8)

where T_C is included to translate the mean acquisition time from the unit time scale onto the real time scale.

4. DISCUSSION OF RESULTS

To obtain P_D and P_{fa} , the synchronising receiver system was simulated using different combinations of values of training sequence length (dwell-time), decision threshold for the data bits, th , code weight and number of users. The simulations were repeated until a sufficient number of samples were collected for reasonably accurate values of P_D and P_{fa} to be obtained. The mean acquisition time was then obtained using (8).

For the data transmitted by the interfering users, the data bits '1' and '0' occur with equal probabilities. Also, all the users are assumed to be bit asynchronous, i.e. they each have a random time delay, $T_D = \{0, T_C, \dots, (F-1)T_C\}$, with respect to each other. System simulations with and without optical hard-limiters were implemented. In the simulations that incorporated hard-limiters, the hard-limiters were placed at the input to the decoder. The hard-limiters clip the value of the chips to a normalised value of 1, and thus for a spreading sequence of code weight K , the maximum output of a hard-limited correlator is K . When receiver noise was added to the system, the receiver decision threshold was obtained by finding the optimum probability of error of the network by adjusting the APD gain. Two cases were compared, one where the optimum error probability was used, and another where the error probability was affected by the receiver noise. The main system parameters are listed in Table 1.

Parameters	Values	Parameters	Values
Chip period, T_c	10ns	Wavelength, λ	1.55 μm
Receiver bandwidth, B	100 MHz	Detector dark current, I_D	1 nA
Sequence length, F	1000 chips	APD material constant, γ	1
Penalty factor, L	10 bits	Ambient temperature, T	300 K
Detector quantum efficiency, η	0.8	Receiver noise figure, F_N	2.0
Optical input power	80 μW	APD bias resistor, R_L	50 Ω

Table 1: System parameters

4.1. Effect of Decision Threshold Variation

In the OOC/OOK optical CDMA system, the value of threshold used after the passive correlator to detect the data bits has a key role in determining the bit error probability. In the present method of synchronisation, this also has an impact on the mean acquisition time. The effect of threshold variation was examined by simulating the system with various thresholds. For the system using the optical hard-limiter, the maximum threshold is limited to the value of the code weight, K , for reasons described earlier. In the figures that follow, the mean acquisition time is obtained as a function of the synchroniser dwell-time. Increasing the number of bits in the training sequence lengthens the dwell-time. Referring to Figure 3(a), as the threshold of the OOK system is increased towards K , the mean acquisition time is reduced. This is because the probability of a bit error is reduced which leads to a reduction in the probability of a false alarm. However, once the threshold has exceeded K , the mean acquisition time increases, especially for larger values of dwell-time. When the threshold is larger than K , even a correctly correlated '1' data bit can be decoded as a '0' data bit because it does not achieve the required threshold value. The correlated '1' data bit can only be regarded as a '1' if the multi-access interference adds up with the wanted chips to the threshold value. The effect of this is that the probability of detection is reduced and this leads to an increased mean acquisition time.

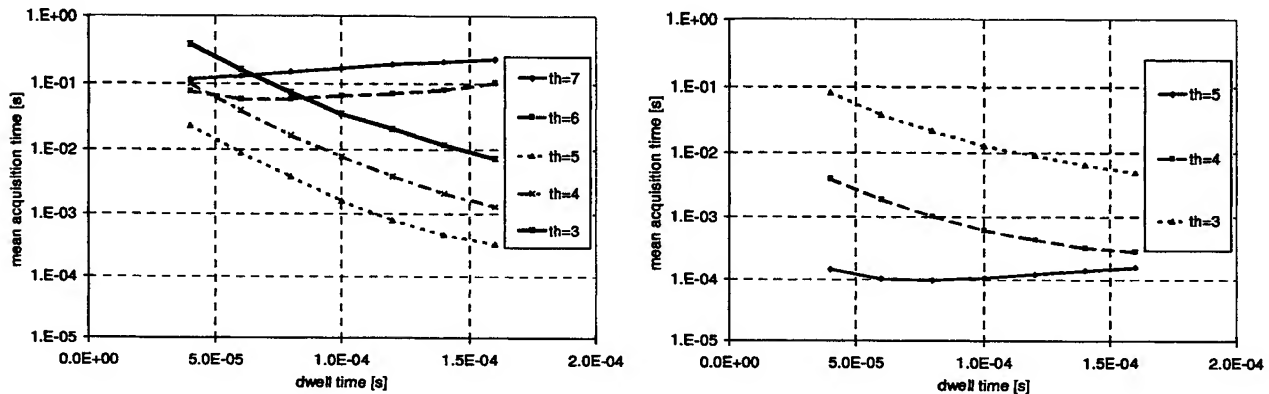


Figure 3: Effect of Threshold Variation for an Optical CDMA OOK System with $K=5$ and $N=30$
(a) without a hard-limiter and (b) with a hard-limiter

Using an optical hard-limiter, as shown in Figure 3(b), the mean acquisition time is reduced compared to a non-hard-limiter system with the same threshold. This is because the hard-limiter has removed certain patterns of interference. This reduces P_{fa} and increases P_D . Also note that an optimum dwell time exists where the mean acquisition time is a minimum. The reason for this is that for short dwell-times, P_{fa} is high and P_D may be low. For long dwell-times P_{fa} is significantly reduced and P_D is improved but the long dwell-time is now the dominant parameter determining the mean acquisition time.

For the PPM system with $M=2$, the effect of the threshold is shown in Figure 4 below.

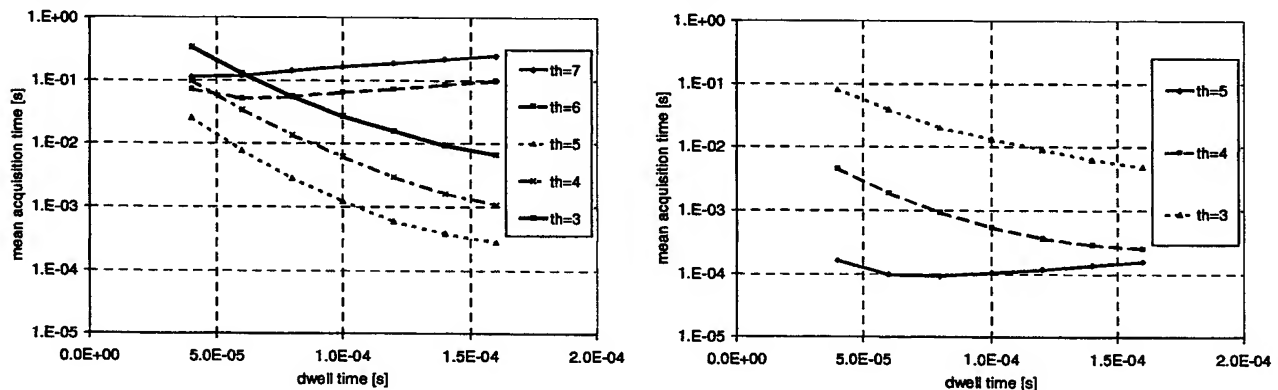


Figure 4: Effect of Threshold Variation for an Optical CDMA PPM System with $K=5$ and $N=30$
(a) without a hard-limiter and (b) with a hard-limiter

Figure 4(a) shows the results when the optical hard-limiter is not used and Figure 4(b) shows the case when a hard-limiter is used. Comparing Figures 3 and 4, it will be seen that there is a very slight improvement in the mean acquisition time when the PPM system is used, especially when the threshold is equal to or less than K .

4.2. Effect of Number of Users

For an OOK optical CDMA system which does not use an optical hard-limiter, the effect of the number of users, N , is shown in Figure 5(a). For short dwell-times, the impact of the multi-access interference is significant and the mean acquisition time increases as N is increased due to an increase in P_{fa} and a reduction in P_D . However, as the dwell-time is lengthened, the impact of N decreases significantly to an extent where N has little effect on the mean acquisition time. This is due to a reduction in P_{fa} and an improved P_D because the correlation with the wanted signal has been improved. As for the previous case, when the dwell-time is long, this is the dominant term in setting the mean acquisition time.

When an optical hard-limiter is used before correlation, it reduces certain patterns of interference. The result of this is shown in Figure 5(b) where it is seen that the mean acquisition time for low values of dwell-time is reduced when compared to the non-hard-limiter system for the same number of users. As for the earlier figures, an optimum dwell-time exists corresponding to minimum mean acquisition time.

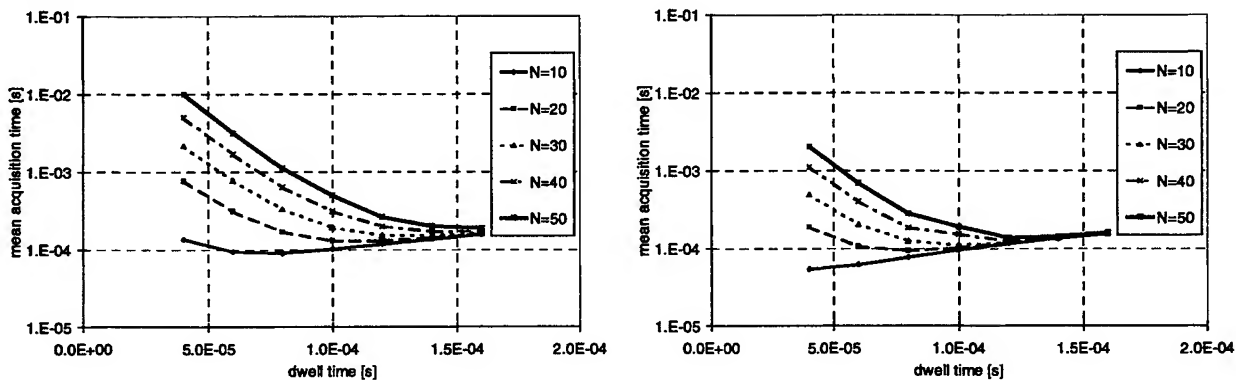


Figure 5: Effect of the Number of Users, N , for an Optical CDMA OOK System with $K=3$ and $th=3$ without a hard-limiter and (b) with a hard-limiter

The effects of user number variation in an optical CDMA using PPM without a hard-limiter is shown in Figure 6(a). In comparison with the OOK case, the PPM system has a lower mean acquisition time and this is more apparent for larger numbers of users at lower values of dwell-time. This reduction in mean acquisition time is the result of a reduced P_{fa} . One reason for the improved performance is that a string of consecutive '0' bits in the training sequence reduces the probability of achieving synchronisation. Using PPM with $M=2$, breaks up consecutive '0' bits and as a result, the probability of achieving synchronisation is improved.

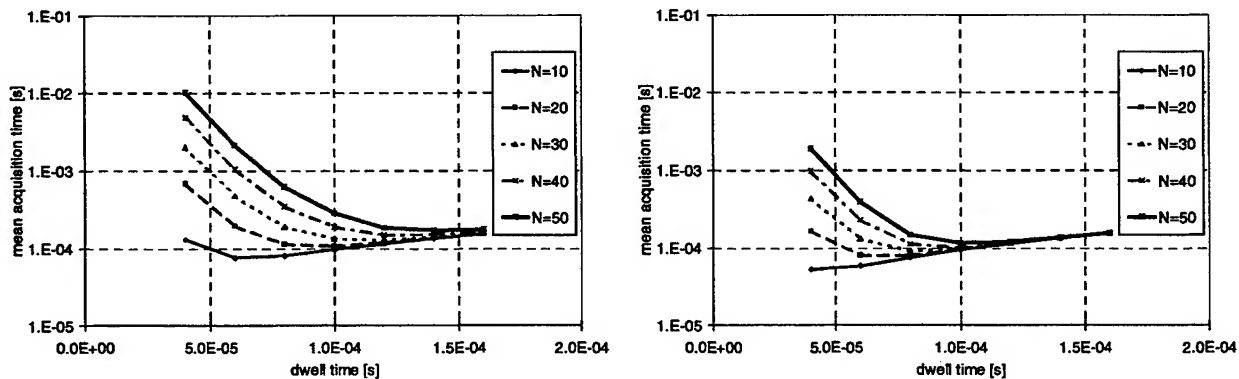


Figure 6: Effect of the Number of Users, N , for an Optical CDMA PPM System with $K=3$ and $th=3$ (a) without a hard-limiter and (b) with a hard-limiter

Figure 6(b) shows the effects of using an optical hard-limiter with an optical CDMA PPM system. The use of the hard-limiter results in a further reduction in mean acquisition time for low values of dwell-time. However, when comparison is made with the OOK optical CDMA system with a hard-limiter, the improvement is less significant.

4.3. Effect of Code Weight Variation

Figure 7 shows the effects of code weight variation in an optical CDMA system with and without a hard-limiter. For an OOK system with no hard-limiter, shown in Figure 7(a), at short dwell-times, the mean acquisition time is increased as the code weight is increased. This is because increasing the code weight increases the number of chips in the spreading sequence, for the same number of users, and this results in a higher incidence of 'hits' and hence a higher P_{fa} .

Referring to the graphs for a hard-limiting system, shown in Figure 7(b), the variation of mean acquisition time with code weight is significantly reduced. This is because of the hard-limiting properties that reduce some patterns of interference, and this reduces P_{fa} . Furthermore, the variation of mean acquisition time with dwell-time is also reduced.

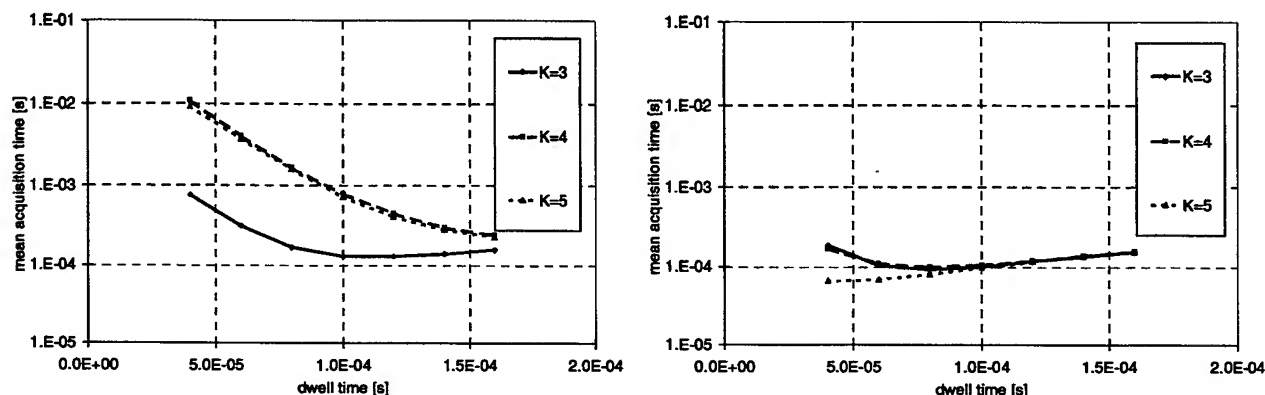


Figure 7: Effect of the Code Weight, K , for an Optical CDMA OOK System with $N=20$
(a) without a hard-limiter and (b) with a hard-limiter

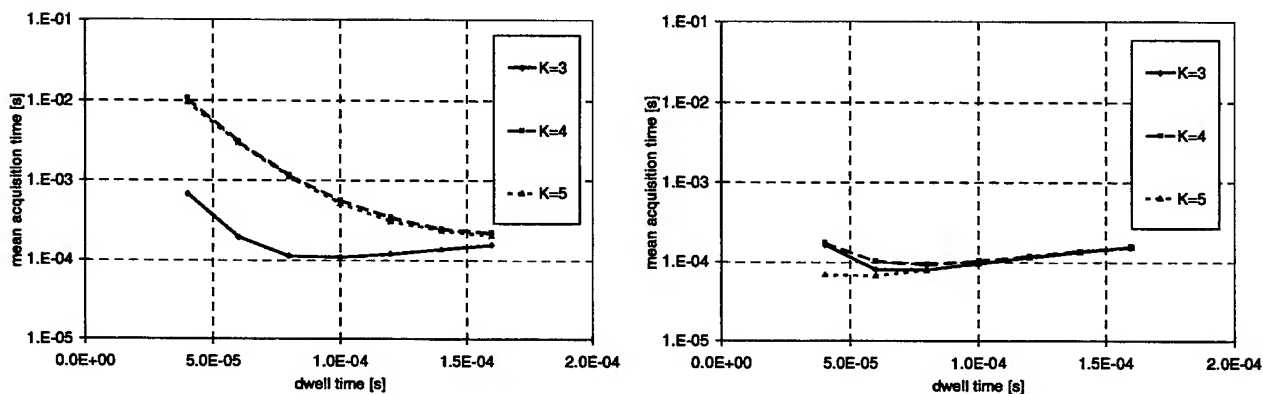


Figure 8: Effect of the Code Weight, K , for an Optical CDMA PPM System with $N=20$
(a) without a hard-limiter and (b) with a hard-limiter

The effect of code weight variation on an optical CDMA PPM system is shown in Figure 8. For a system without a hard-limiter, shown in Figure 8(a), the mean acquisition time is reduced when compared to a non-PPM system with the same code weight, because PPM spaces out consecutive '0' bits in the training sequence, and this reduces the effect of 'hits' and reduces P_{fa} . For the case of a hard-limiting system in Figure 8(b), the effect of the 'hits' at low values of dwell-time is

reduced further because some interference patterns are eliminated. Thus the mean acquisition time is reduced when compared to a non-hard-limiting system.

4.4. Effect of Receiver Noise

Figure 9 shows the effect of APD noise on an OOK optical CDMA system. When an optimum APD gain is chosen, i.e. the probability of a bit error is minimised, the mean acquisition time is marginally larger than that of its PPM counterpart, when no hard-limiter is used, as shown in Figure 9(a). With hard-limiting, for both cases, the overall mean acquisition time is reduced, particularly at lower values of dwell-time.

In Figure 9(b), the effect of APD noise is shown for a system with a non-optimum APD gain. There is a marked increase in the mean acquisition time when compared with the curves in Figure 9(a), especially at lower dwell-times. This is because of the effect of the receiver noise on the bit error rate. The use of an optical hard-limiter gives an overall reduction in the mean acquisition time, but the reduction is not as significant as in Figure 9(a).

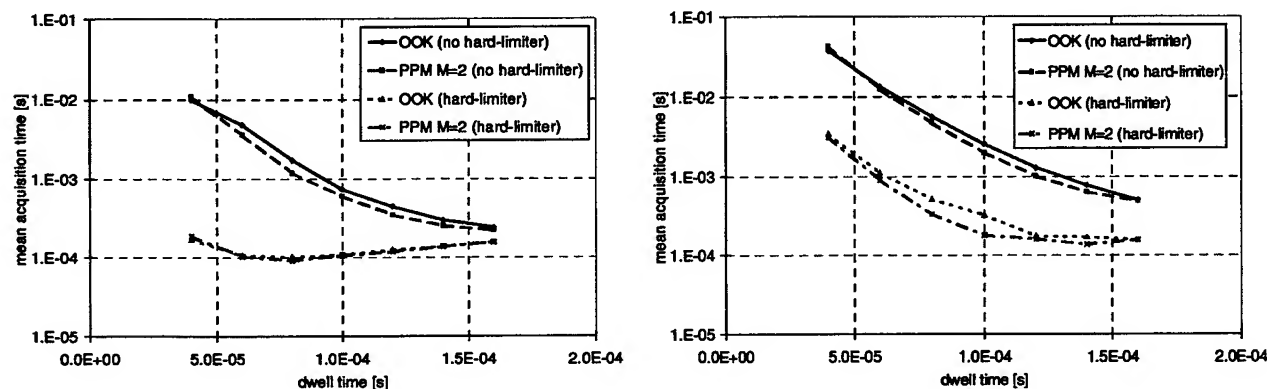


Figure 9: Effect of Receiver Noise in an Optical CDMA System with $K=4$ and $N=20$
(a) with optimum APD gain and (b) with non-optimum APD gain

When the APD gain produces the optimum bit error probability, the multi-access interference dominates the APD noise, and thus the results of Figure 9(a) are similar to that of a noiseless system. However, when the APD gain gives rise to a non-optimum bit error probability, the APD noise dominates the multi-access interference, and the bit error probability deteriorates. This causes an increase in the false alarm probability, and this leads to a higher mean acquisition time.

5. CONCLUSIONS

The effects of the key system parameters on the performance of a serial search synchroniser for an optical CDMA system have been examined. The results show that: (i) the optimum mean acquisition time is obtained at an optimum threshold of K , (ii) the mean acquisition time is increased when the number of users, N , and the code weight, K , is increased, (iii) optical hard-limiting reduces the probability of false alarm, P_{fa} , especially in systems with large multi-access interference, (iv) the use of optical PPM with $M=2$ reduces the probability of false alarms by breaking up the occurrences of strings of data bit '0' in the training sequence, and (v) operating at a non-optimum APD gain results in an overall increase in mean acquisition time, but this is eliminated when an optimum gain is chosen.

6. ACKNOWLEDGEMENTS

The authors are pleased to acknowledge the support of Tenaga Nasional Berhad for their kind provision of a postgraduate bursary.

7. REFERENCES

1. M. Pandit, "Mean acquisition time of active-correlation and passive-correlation acquisition-systems for spread-spectrum communication-systems", *IEE Proceedings: Part F: Radar and Signal Processing*, **128**, pp 211-214, 1981.
2. A. Polydoros, C. L. Weber, "Unified approach to serial search spread-spectrum code acquisition - Part I: General Theory", *IEEE Transactions on Communications*, **COM-32**, pp 542-549, 1984.
3. A. Polydoros, C. L. Weber, "Unified approach to serial search spread-spectrum code acquisition - Part II: A Matched-Filter Receiver", *IEEE Transactions on Communications*, **COM-32**, pp 550-560, 1984.
4. K. Kiasaleh, "PN code acquisition for the spread-spectrum optical on-off-keying communication system", *IEEE Transactions on Communications*, **38**, pp 1879-1885, 1990.
5. W. Huang, K. Kitayama, "Code acquisition in optical pulse CDMA utilizing coherent correlation demodulation", *Conference Record / IEEE Global Telecommunications Conference*, **1**, pp 265-269, 1997.
6. G. C. Yang, "Performance analysis for synchronization and system on CDMA optical-fiber networks", *IEICE Transactions on Communications*, **E77B**, pp 1238-1248, 1994.
7. P.R. Prucnal, M.A. Santoro, T.R. Fan, "Spread spectrum fiber-optic local area network using optical processing", *IEEE Journal of Lightwave Technology*, **LT-4**, pp 547-554, 1986.
8. J. A. Salehi, "Code division multiple-access techniques in optical fiber networks - Part I: Fundamental principles", *IEEE Transactions on Communications*, **37**, pp 824-833, 1989.
9. J. A. Salehi, C. A. Brackett, "Code division multiple-access techniques in optical fiber networks - Part II: Systems performance analysis", *IEEE Transactions on Communications*, **37**, pp 834-842, 1989.
10. I. Andonovic, L. Tancevski, M. Shabeer, L. Bazgaloski, "Incoherent all-optical code recognition with balanced detection", *Journal of Lightwave Technology*, **12**, pp 1073-1080, 1994.
11. H. M. H. Shalaby, "Performance analysis of optical CDMA communication systems with PPM signaling", *IEEE Global Telecommunications Conference*, **3**, pp 1901-1905, 1993.
12. J.K. Holmes, *Coherent Spread Spectrum Systems*, Robert E. Krieger Publishing Company, 1990.

Research of A New DS/WH En-/De-coding Scheme for Optical CDMA

Yu Chongxiu^{*a}, Yang Qifang^b, Qin Wenbiao^a

^aDept. of Electronics Engineering, Beijing Univ. of Posts & Telecommunications

P. O. Box 163, Beijing 100876, P. R. China

^bTelecommunication Planning Research Institute of MII, Beijing 100037, P. R. China

ABSTRACT

In this paper the direct spreading/wavelength hopping (DS/WH) en-/de-coding scheme for optical code-division multiple access (OCDMA) is proposed. The system structure is designed and analyzed. A new code sequence—wavelength hopping extended quadratic congruence for prime code (WH EQC/prime code)—is adopted. It is shown that the code capability can be increased by increasing the number of discrete wavelengths or by employing asymmetric systems with different prime numbers for spreading and hopping (p_s and p_h). The synchronous signal is designed and analyzed. It is very easy for user to decode synchronously. The performance of the system is investigated and it is shown that the en-/de-coding scheme and system structure are feasible.

Keywords: Optical CDMA, DS/WH, En-/De-coding, WH EQC/Prime Code, Multi-rate Data Stream, Synchronous Decoding

1. INTRODUCTION

In the optical fiber communication, the optical multiple access techniques include the optical time-division multiple access (OTDMA), the optical wavelength-/frequency-division multiple access (OW/FDMA) and the OCDMA. The OTDMA and the OW/FDMA have been researched for years and are applied in the optical fiber communication now. In comparison to OTDMA and OW/FDMA, The OCDMA have some advantages, such as delay free, highly security, working asynchronously or synchronously, allowing a simple protocol. So the OCDMA attracts much more attention¹⁻¹¹ and has been made some progress. R.A.Griffin et al researched coherence coding of optical pulse for CDMA⁵. P.R.Prucnal et al used optical processing in spread spectrum of fiber-optic local area network⁶. S.Betti et al studied OCDMA techniques based on polarization modulated coherent system⁷. L.Tancevski et al discussed the time spreading code in optical network⁸. J.A.Salehi et al proposed the holographic CDMA and so on. These researches form various en-/de-coding scheme called respectively as spread time, spread spectrum, correlation encoding and polarization modulating of coherent light etc. But in these researches the code structure and en-/de-coding scheme are not considered in detail. The code structure affects codes' correlation property and en-/de-coding techniques. The various en-/de-coding schemes affect performance of system while using the same code. For example, the parallel configuration as shown in Fig.1 used for encoding/correlating prime codes is

* Email: cxyu@noya.bupt.edu.cn; Telephone: 86-10-62282137

so bulky and loss that such a system is not realizable when the code length is very large.

Considering performance and number of active user in the OCDMA system, we take advantage of the resource of wavelength and bandwidth for en-/de-coding. The code sequence of each user is a unique wavelength-combination.

The code sequences of users are different not only in wavelength domain but also in time domain. And some

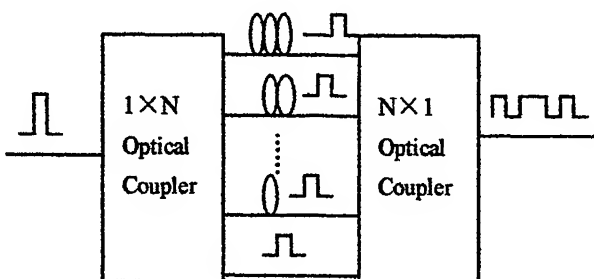


Fig. 1: Parallel configuration of an all-optical encoder for OCDMA

narrow-band filters are used for decoding at receiver. Thus we study the new mechanism of en-/decoding -- DS/WH and design a system structure. We adopt a combination code with wavelength hopping and extended quadratic congruence for prime code (EQC/prime code), i.e. it is composed of different wavelengths in different chips of EQC/prime code.

The WH EQC/prime code has great code capability. Thus the system can operate at a speed much lower than other spreading time system when their code length is same. It remains transparent to any input modulation format and to any rate of data stream. And it doesn't need the light source generating ultra-short light pulse. Usually every user has a code sequence, there is only a fixed transmitting speed in the system. According to requirements we can let user possess a few code sequences and en-/de-coding devices then the user can transfer by a few times of basic speed of data stream.

The developed electrical technologies and high-speed optic-electronic devices, computer techniques are also adopted in the OCDMA system. The principle, system structure and performance analysis of the new scheme are described in detail as follows.

2. OPTICAL WH EQC/PRIME CODE

Usually the user's signature sequence in spreading time is composed of code unit "0" or "1" which appears at different time slot and all code elements use a single wavelength. The code length for a large number of the user in the optical fiber communication system is very large. So the width T_s of each slot is very narrow, even closed to pulse width in the OTDMA system. This requires the light source generating ultra-short pulse. When a common light source is used in a system, the number of user is very few. So this kind of system is lack of utility.

Now the user's code sequence designed in our system is a combination code with multiple wavelengths and EQC/prime codes and we call it as WH EQC/prime code. The code is composed of different wavelength at different chip of EQC/prime code. For a given prime number p , EQC/prime code comprises p blocks of length $(2p-1)$ chips which are concatenated together to form the code sequence of length $p(2p-1)$ chips and each block has only one pulse and $(2p-2)$ zeros. The position of the pulse within every block is determined by the extended quadratic congruence placement operator :

$$a_{ij} = [i^{j(j+1)/2} / p] \quad i=1,2,3,\dots, p-1; \quad j=0,1,2,\dots, p-1 \quad (1)$$

where $[]$ represents operation modulo p . The total number of the code, which combine the EQC/prime code with multiple wavelengths, is therefore $p(p-1)^2$ when p is both the prime number used in the EQC/prime code generation and the number of wavelengths in symmetric system. In asymmetric system, different prime numbers p_s and p_h respectively

denote algorithm for the prime code and the number of wavelength hopping, then the total number of codes in the family is $p_h(p_h-1)(p_s-1)$. The WH EQC/prime code has very good auto-/cross-correlation properties². When we use prime number p_h wavelengths whether in symmetric or asymmetric system or not, the number of code and the security of the codes are substantially increased. Comparing the various codes with multiple wavelengths, the number of code (N) and their properties including auto-correlation sidelobe (A) and cross-correlation peak (C) are shown in Table 1.

For given the number of user, the code length of WH EQC/prime code is very short. So the width requirement for T_s can be reduced greatly. It is obvious that the WH EQC/prime code can en-/de-code at lower speed. It can get more spreading gain because of multiple wavelengths.

Table 1: Comparison Between Various codes: here A: MAXIMUM AUTOCORRELATION SIDELOBES; C: MAXIMUM CROSSCORRELATION PEAK; N: CODE CARDINALITY

Code	p_h	p_s	Code length	A	C	N
prime	31	31	$p_s^2=961$	3 0	2	$p_h p_s=961$
EQC	31	23	$p_s(2 p_s-1)=1035$	1	2	$p_h(p_s-1)=930$
Prime-hop	31	31	$p_s^2=961$	0	1	$(p_h-1)p_s=930$
EQC/prime	31	23	$p_s(2 p_s-1)=1035$	0	2	$p_h(p_h-1)(p_s-1)=27900$

3. PRINCIPLE AND STRUCTURE OF SYSTEM

We choose that an OCDMA system is a passive star-network. Its each user connects the center passive star ($N \times N$) coupler with two optical fibers as shown in Fig.2. Correspondingly there are the N transmitters and the N receivers which perform en-/decoding respectively. The signal power of every user is distributed equally to every receiver. The transmitter and receiver both include code generator and synchronous signal module. In addition to these, the transmitter has a data processing module and the receiver has some avalanche photodiodes (APD) and a logic circuit for decoding. There is the problem of synchronous acquisition and tracking of user sequence and it is prerequisite to correctly realizing en-/de-coding. So first we resolve the problem of the synchronous decoding by user's synchronous signal, then design the structures of transmitter and receiver.

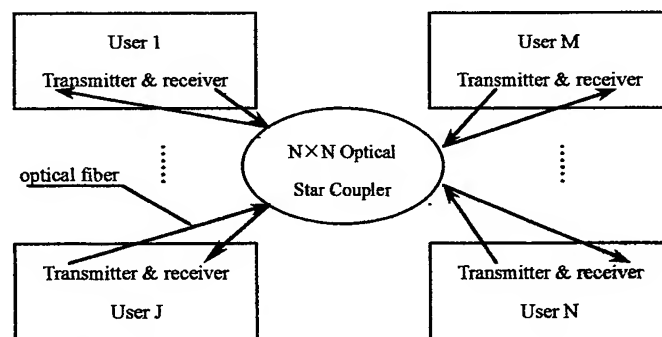


Fig.2: the Diagram of system structure

3.1 The user's Synchronous Signal

It is worthwhile resolving both the initial synchronization of code sequence and the lock-in synchronism of decoding at receiver. In the research of electric CDMA, the methods of resolving the problems are various such as the acquiring of phase following, the synchronous acquiring by delaying, the locked loop by baseband correlating and single correlator etc.

But they can't be transplanted to OCDMA because of the absence of optical devices of similar function. In some researches of OCDMA⁴⁻⁶, The synchronization problem of incoming signal and the local code isn't considered or is assumed to be synchronous decoding. So the optical synchronization of user's signal isn't also resolved well.

We research a new method of synchronous decoding by the optical coherence in optical CDMA system. If a length of optical fiber introduces at an arm of a Mach-Zehnder interferometer as shown in Fig.3(a), it will make the transmitted signal at the arm produce a time-delay τ which destroys the coherence. When a pulse signal $\varepsilon(t)$ is inputted, the output signals $\varepsilon_1(t)$ or $\varepsilon_2(t)$ is a signal having two pulses between which the time interval is τ , i.e.

$$\varepsilon(t) = A(t)e^{i\omega t} \quad (2)$$

$$\varepsilon_1(t) = \frac{1}{2} [A(t)e^{i\omega t} \otimes h(t) + A(t-\tau)e^{i\omega(t-\tau)}] \quad (3)$$

$$\varepsilon_2(t) = \frac{1}{2} [A(t)e^{i\omega t} \otimes h(t) - A(t-\tau)e^{i\omega(t-\tau)}] \quad (4)$$

where \otimes denotes convolution. We take $\varepsilon_1(t)$ as a synchronous signal which is transmitted together with encoded user signal. A matched Mach-Zehnder interferometer which has the same time-delay ($\tau_r = \tau_t = \tau$, τ_r and τ_t denote time-delay at the transmitter and the receiver respectively.) is used in the receiver. When it receives the transmitted signal $\varepsilon_1(t)$, at the output end the two pulses respectively from its two arms superpose and create an interferential signal at the time t_0 as shown in Fig.3 (b). The interferential signal is the maximum value and taken as a synchronous signal. Here a balanced detector is also needed to extract the synchronous signal. The electric current $i(t)$ from the detector

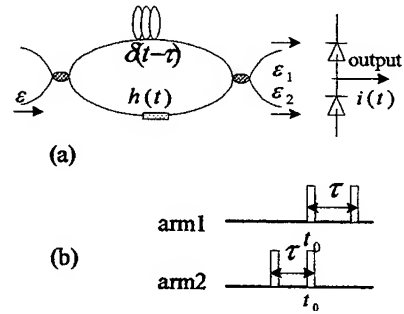


Fig.3: (a): the Mach-Zehnder interferometer having unequal arms; (b): the superposed output signal at the receiver

$$i(t) = i_1(t) - i_2(t) \cong RI_0 \operatorname{Re} [\gamma(\tau) \otimes h(\tau)] \quad (5)$$

where $I_0 = \Gamma(0)$, $\gamma(\tau) = \frac{\Gamma(\tau)}{I_0}$, $\Gamma(\tau) = \lim_{T \rightarrow \infty} \frac{1}{T} \int_{-\frac{T}{2}}^{\frac{T}{2}} \varepsilon^*(t) \varepsilon(t+\tau) dt$. The current signal can drive and decide the

local code generator at the receiver when to start to work.

By above principle, we design a synchronous signal module whose structure is as shown as Fig.3(a). It is independent of data channel at the transmitter and the receiver. The different users take the respective time-delay at the transmitter so that the coherent detection at the receiver may distinguish the synchronous signal of the different users. At the transmitter, the operation of synchronous signal module is controlled by user's data processing module and its output signal is coupled to coupler 1 as shown in Fig.4. At the receiver the synchronous signal module drives and judges the local code generator when to start to work. Thus the synchronous decoding at the receiver is implemented.

3.2 Transmitter

In order to realize the DS/WH encoding, the encoder designed by us includes the laser array, code generator, data processing module, optical couplers and synchronous signal module as shown as Fig.4. Where the synchronous signal module includes an E/O converter placed in the front of it. The laser array composed of many single wavelength lasers can provide multiple hopping wavelengths. The code generator is composed of an electrical shift register that produces a circulating code as a user's signature sequence. The data processing module packs user's data into frames. Each frame data has user data of constant bytes similar to cell of ATM. The data processing module adds an electrical synchronous signal at the front of each frame data and the error correction code (ECC) behind of each frame data. The transmitter is transparent to any data stream. The user's data and its ECC both are encoded by the local code generator. The encoded signal with code sequence drives and controls when and which laser to emit. The optical signals emitted from these lasers are coupled to coupler 1. An electrical synchronous signal from data processing module drives the synchronous signal module output an optical synchronous signal before transmitting each frame data. The synchronous signal and encoded signal from coupler 1 are again coupled at the coupler 2. It will be transmitted and broadcasted to all the receivers by the passive star ($N \times N$) coupler in the OCDMA system.

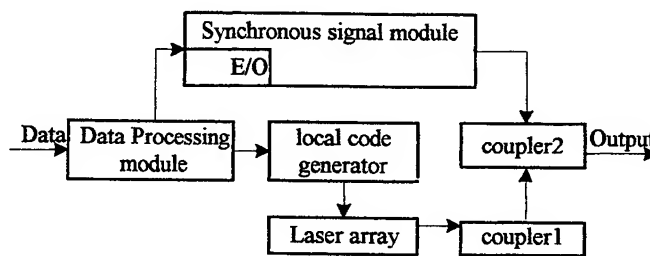


Fig.4: the structure of a transmitter

We let some users share a set of laser array to reduce number of lasers in whole network. The code sequence of every user is divided into p_h code sequences in which every one has only a single wavelength as shown as Fig.5. In the code generator of every user, these sequences of single wavelength are generated and registered into p_h register units. These code sequences of single wavelength drive corresponding wavelength laser emit light in the different time-slot. The process is called as DS/WH encoding. Because all users have the same clock frequency, the encoding speed is fixed and called as a basic speed. Usually a user only has a code sequence and only transmit at basic speed.

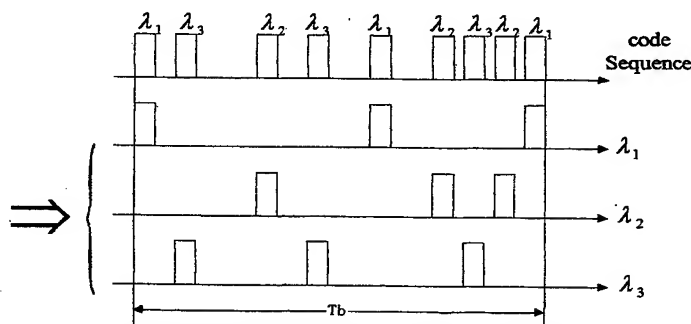


Fig.5: the divided code sequences of single wavelength

We can also let some users transmit data at multi-times basic speed. For a user, data processing module firstly divides user's data into some parallel frames and adds a synchronous signal at the front of these parallel frames. The data frames are loaded into their register units and every register unit uses a code sequence. If a user has j code sequences then the user encodes with j code sequences. The encoding speed of its data stream is j times of basic speed. This forms multi-rates signal stream in the OCDMA system

3.3 Receiver

The receiver is mainly composed of the filter-switch array, local code generator, synchronous signal module, APD and logic circuit as shown as Fig.6. Firstly the received signal is divided into the $(p_h + 1)$ paths. A signal from a path comes into the synchronous signal module and signals from other paths connect into filter-switch array. The synchronous signal module outputs a detectable current signal by balanced detection when the incoming signal matches synchronous signal from the module. And the current signal drives the local code generator to start to work. The local code generator generates circling code which decides when and which filter-switch to work. Behind every filter-switch, the APD detects the filtered optical signal and converts into electrical signal. The electrical signal has the highest intensity when the incoming encoded signal matches the local code sequence. The electrical signal level is closed to zero when incoming encoded signal mismatches the local code sequence. Accumulating all electrical signal from all wavelengths optical pulse, the logic circuit judges then recovers user's initial data. The process is called as synchronous decoding.

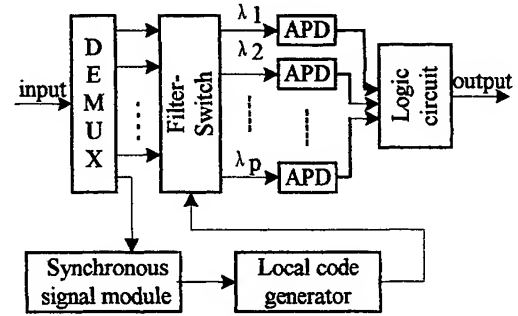


Fig.6: the structure of a receiver

Considered the probability of clock pulse excursion, the synchronous signal module always tracks incoming synchronous signal and compel local code sequence and incoming encoded signal to synchronize. The synchronous signal placed at front of each data frame adjusts the local code generator once a data frame.

For multi-rate receiving, a receiver has many local code generators, APDs and logic circuits whose number is decided by the transmitter. Many local code generators work simultaneously and are driven by same synchronous signal module because all parallel data frames share a synchronous signal at the transmitter. Then the decoded data are processed by a protocol that the transmitter and receiver both observe.

The above transmitter and receiver are used in the system shown in Fig.2. We can simultaneously en-/de-code for N users.

4. PERFORMANCE ANALYSIS

In order to illustrate the performances of the new system designed, we discuss some main parameters of system as follows.

4.1 The Spreading Spectrum Gain G

In general the anti-interference efficiency of an OCDMA system is explained by the spreading-spectrum gain G . For a DS system, it is defined by $G_D = B_2/B_1$, where B_1 and B_2 respectively denote the bandwidth of a user signal before and after direct spreading. And the other interference introducing to B_2 is eliminated in decoding. In the new system the WH effect is also considered. So here G is defined by

$$G = G_D \bullet G_H = G_D \bullet p_h = p_s(2p_s - 1)p_h \quad (6)$$

where G_H is the gain of wavelength hopping and decided by p_h . It is obvious that the DS/WH system designed by us is

greatly increased anti-interference efficiency due to $G > G_D$. It is at the cost of wavelength resource in the system.

4.2 The Signal-to-Noise Ratio (SNR)

At the receiver, a signal through synchronous decoding is represented by

$$D(t) = \sum_{i=1}^{p_h} e_i d_i(t) + n(t) \quad (7)$$

where e_i is the power of a required i th wavelength signal, $d_i(t)$ is the code of i th wavelength separated by WH EQC/prime code, $n(t)$ is the noise term which is composed of the white noise $n_0(t)$ and the interference noise $n_1(t)$ from the other codes of active users. We assume different wavelength signals have same power e and $d_i(t)$ ($i=1,2,\dots,p_h$) have same number of light pulse in the symmetric system. Neglecting $n_0(t)$, we can deduce the SNR of ste symmetric system is as fellows:

$$\begin{aligned} SNR &= \frac{P_h e}{\alpha \frac{e_N}{G_s}} \end{aligned} \quad (8)$$

where the coefficient α is the ratio of the noise power entering into the required signal to the total noise power e_N .

In comparison to DS OCDMA system, the SNR is increased due to α is the coefficient less than 1.

4.3 The Rate of Error Code (REC)

At the receiver, if the code chips k in a required signal is overlapped by ones in other user signals, the error bits occur. This case is a stochastic process. So the rate of error code is represented by its probability density $p(k)$, i.e.

$$p(k) = \binom{N-1}{k} \left(\frac{B^2}{2A}\right)^k \left(1 - \frac{B^2}{2A}\right)^{N-1-k} \quad (9)$$

Where N is the number of user in the system, A , B is the code length and the code weigh of user signature sequence respectively. Thus the rate of error code of single wavelength is written by

$$REC_s = \sum_k p(k) \left[\frac{1}{2} Q\left(\frac{I_1 - Z}{\sigma_n}\right) + \frac{1}{2} Q\left(\frac{Z - I_0}{\sigma_n}\right) \right] \quad (10)$$

Where I_0 , I_1 is the average power of the received bit data "0" and "1" respectively, Z is the threshold of decoding, σ_n is the root mean square of noise. $Q(x) = \text{erfc}(x) = \frac{1}{\sqrt{2\pi}} \int_x^\infty e^{-y^2/2} dy$.

For the designed system with p_h hopping wavelengths, we introduce a coefficient $\beta = M/p_h$ when M wavelengths are interfered. So the rate of error code in the system is increased by β times. Through derivation it is approximately equal to:

$$REC_{p_h} = \beta \cdot REC_s = \frac{M}{p_h} \cdot REC_s \quad (11)$$

From the equation (12), we see that the wavelength hopping system improved the REC because of $M/p_h < 1$.

5 CONCLUSION

The direct spreading/wavelength hopping en-/de-coding scheme for OCDMA system is designed and analyzed. A new code is composed of different wavelength in the different chips of EQC/prime code, i.e. user signature sequence is the function of both time and wavelength, so the security of system is increased greatly. In the en-/de-coding scheme, the optical synchronous signal of user's data is designed and detected by balance detection thus user can track synchronous signal easily and decode synchronously. The system has a good REC because of good auto-/cross-correlation properties of WH EQC/prime codes. This scheme is transparent to any rate of data stream by data processing module. In the system all users can access random, so the network management is simplified. And it is obvious that the number of code, REC and SNR are improved greatly. The result of research and design is shown that the new en-/de-coding scheme and the system structure are feasible.

ACKNOWLEDGMENTS

The work is supported by the National Natural Science Foundation of China under granted NNSFC 69677025.

REFERENCES

1. Jawad A. Salehi, "Code Division Multiple-Access Techniques in Optical Fiber Networks—Part I: Fundamental Principles", *IEEE Trans. On Commun.*, **37**, No.8, pp824-833, August 1989
2. L. Tančevski, I. Andonovic, M. Tur, J. Budin, "Massive Optical LAN's Using Wavelength Hopping/Time spreading with Increased Security", *IEEE Photonics Technology Letters*, **8**, No.7, pp935-937, July 1996
3. Rade Petrovic et al, "CDMA techniques in optical fiber LAN's", *Journal of Optical Communications*, **12**, No.3, pp101-106, 1991
4. W.C.Kwong et al, "Ultrafast all-optical code-division multiple-access network", *Proc. SPIE*, **1787**, pp121-132, 1992
5. R.A.Griffin et al, "Coherence coding for photonic code-division multiple access network", *IEEE Journal of Lightwave Technology*, **13**, No.9, pp1826-1837, 1995
6. P.R.Prucnal et al, "Spread spectrum fiber-optic local area network using optical processing", *IEEE Journal of Lightwave Technology*, **4**, No.3, pp547-554, 1986
7. S.Betti et al, "optical code division multiple access techniques based on polarization modulated coherent systems", *Journal of Optical Communications*, **14**, No.5, 1993, pp183-188
8. L.Tancevski et al, "Massive optical LAN's using wavelength hopping/time spreading with increased security", *IEEE Photonics Technology Letters*, **8**, No.7, pp935-937, 1996
9. A.J.Poustie et al, "All-optical circulating shift register using a semiconductor optical amplifier in a fiber loop mirror" *Electronics Letters*, **32**, No.13, pp1215-1216, 1996
10. W.C.Kwong, et al, "Performance comparison of asynchronous and synchronous code-division multiple access techniques for fiber optical local area network", *IEEE Trans. on comm.*, **39**, No.11, pp1625-1634, 1991
11. S.V.Maric et al, "multimedia transmission in fiber optic LAN's using optical CDMA", *Journal of Lightwave Technology*, **14**, No.10, pp2149-2153, 1996

Switching Efficiency of Ultrafast Nonlinear Interferometer as an optical time division demultiplexer

Xingzhong Chen*, Minyu Yao, Minghua Chen, Jianfeng Zhang, Lei Xu and Yizhi Gao

Department of Electronics Engineering, Tsinghua University, Beijing, 100084, China

ABSTRACT

All-optical time-domain demultiplexers are expected to play a major role in future ultrafast all-optical time division multiplexing (OTDM) systems to overcome the electronic bottleneck. Ultrafast nonlinear interferometer (UNI) is a good candidate for all-optical time-division demultiplexing. The switching efficiency of UNI is investigated numerically. We construct an analysis model of the UNI. In our analysis, the effects of control pulse parameters such as pulsewidth, power and jitter on the switching efficiency of UNI are considered. The required peak power of the control pulse to obtain maximum switching efficiency is found to decrease in as the width of the control pulse is increased. Jitter of control pulse reduces the switching efficiency. It is also noticed that the length of birefringent fiber is no contribution to the switching efficiency. However more than 90% switching efficiency could be reached when the control pulsewidth varied 40%, when pulse power is in 40% or when the jitter is about 3%.

Keywords: Optical time division multiplexing (OTDM), semiconductor laser amplifier (SLA), demultiplexer, ultrafast nonlinear interferometer (UNI), switching

1. INTRODUCTION

With the prospect of a multimedia society being established in the near future, it has become increasingly important to develop high-speed, long-distance optical communication systems. Although significant effects have been focused on the development of wavelength division multiplexing (WDM) solutions, impressive progress has also been made in the high-speed time division multiplexing (TDM) technology in spite of the apparent absence of suitable high-speed electronic components.

All-optical time-domain demultiplexers are expected to play a major role in future ultrafast all-optical time division multiplexing (OTDM) systems to overcome the electronic bottleneck. Nonlinear optical loop mirror (NOLM) and semiconductor light amplifier loop mirror (SLALOM) as all-optical demultiplexer were researched extensively in the near decade. NOLM require long fiber lengths to get adequate phase shifts for switching because of using optical fiber as the nonlinear media. As a result, these devices have high latency and no potential for integration. In SLALOM, the nonlinearity is perturbed on time scale equal to the inverse frame rate and not at the bit period of the aggregate stream.

Fig. 1 shows a diagram of UNI.

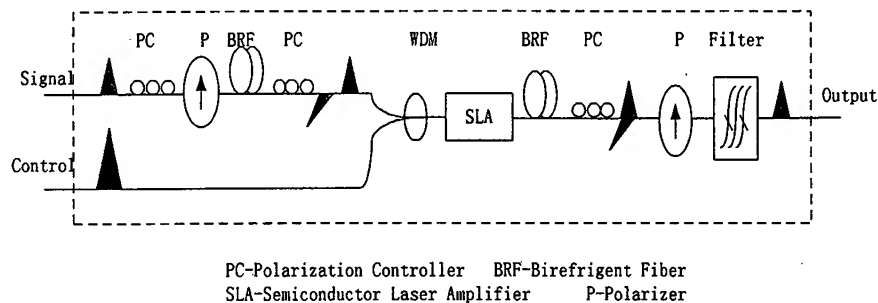


Figure 1 Schematic of UNI

* Email: xzchen@mail.cic.tsinghua.edu.cn; Telephone: 86 10 6277 2379; Fax: 86 10 6277 0317

The polarization state of data signals is set at 45° to the main axes of birefringence fiber by a polarizer, thus the input data pulses are split into two orthogonally polarized pulses separated by 60ps propagating through 25m BRF. Both the separated signal pulses in BRF are referred to as leading pulse and trailing pulse. The signal and co-propagating control pulses are injected into a SLA via a wavelength division multiplexer (WDM). The control pulse induces refractive index and gain nonlinearities in the SLA. Because the control pulse and the trailing signal pulse are temporally overlapped, it imparts a differential phase and amplitude modulation to the two signal components due to sub-picosecond components of the refractive index and gain nonlinearities. The trailing pulse gets π phase difference with the leading pulse. After the SLA the two signal components are re-timed to overlap in second BRF, which axis is orthogonally to the first section of BRF, and are interfered in a polarizer at 45° with respect to the orthogonal signal polarization. A tunable optical filter following the polarizer is used to cancel the control pulses.

2. BASIC EQUATIONS

The equation describing the response of a semiconductor laser amplifier can be written as

$$\begin{aligned}\frac{\partial G(N)}{\partial T} &= \frac{g_0 - G(N)}{\tau_c} - \frac{G(N)}{E_{sat}} P(z, T) \\ \frac{\partial P(z, T)}{\partial z} &= G(N)P(z, T) - \alpha_{int} P(z, T) \\ \frac{\partial \phi(z, T)}{\partial z} &= -\frac{\alpha G(N)}{2}\end{aligned}\quad (1)$$

where $g_0 = \Gamma a N_0 (I/I_0 - 1)$ is the small signal gain, N is the carrier density; N_0 is the transparency carrier density, a is the gain coefficient, Γ is the confinement factor, $P(z, T)$ and $\phi(z, T)$ are the power and phase, τ_c is the spontaneous carrier lifetime, $I_0 = qVN_0/\tau_c$ is the injected current required for transparency, E_{sat} is the saturation energy, q is the electron charge, V is the active volume, $G(N)$ is defined by

$$G(N) = \Gamma a (N - N_0), \quad (2)$$

To obtain the equation (2), it has been assumed that amplified spontaneous emission and internal loss can be neglected.

Assuming amplification function given as

$$h(z, T) = \int g(z_1, T) dz_1, \quad (3)$$

We can get the output power and phase,

$$\begin{aligned}P_{out}(z, T) &= P_{in}(z, T) e^{h(z, T)} \\ \phi_{out}(z, T) &= \phi_{in}(z, T) - \frac{1}{2} \alpha h(z, T)\end{aligned}\quad (4)$$

Equation (5) can be solved using the approach

The transfer function of UNI can be described by

$$H(t) = g_l(t)g_t(t) \cos^2 \left[\frac{\phi_l(t) - \phi_t(t)}{2} \right] + \frac{1}{4} [g_l(t) - g_t(t)]^2, \quad (5)$$

where $g(t)$ is the gain of SLA and $\phi(t)$ is phase shift due to SLA. The subscript l and t denote the leading and trailing pulse, respectively. $g(t)$ and $\phi(t)$ are constant if there is no time dependent external influences such as a control optical signal.

The dynamic gain and phase of SLA and the characteristics of UNI can be got by solving the above equations numerically.

3. RESULTS AND DISCUSSION

As a numerical example of the UNI, we considered the SLA with following parameters, which are listed in Table 1.

Table 1. Parameters of SLA used in calculations

Symbol	Value
L	300μm
τ_s	400ps
Γ	0.3
N_0	1.5×10^{-24}
α	6
a	1×10^{-20}
g_0	3.3×10^4
λ	1.5μm
v_g	8.5×10^7 m/s

We assume the Gaussian intensity envelope for the input signal pulse and control pulse.

$$\begin{aligned} I_s(t) &= I_s \cdot \exp(-4 \ln 2 \cdot (t/\Delta t_s)^2) \\ I_c(t) &= I_c \cdot \exp(-4 \ln 2 \cdot (t/\Delta t_c)^2) \end{aligned} \quad (6)$$

where I and Δt are the peak power and the full width at half maximum, respectively. The subscript s and c represents signal and control pulse, respectively.

The switching efficiency is defined as the ratio of demultiplexing output power to the amplified signal power without control pulse in UNI.

Fig. 2 shows the switching efficiency as a function of the control pulsewidth. With the normalized control pulse increased, the switching efficiency firstly increased, and the maximum of switching efficiency is up to 0.42. However, the switching efficiency will be decreased while control pulsewidth increased continually. We can obtain that more than 90% switching efficiency could be reached when the control pulsewidth varied 40%.

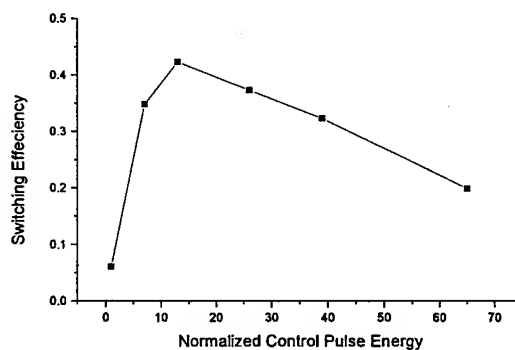
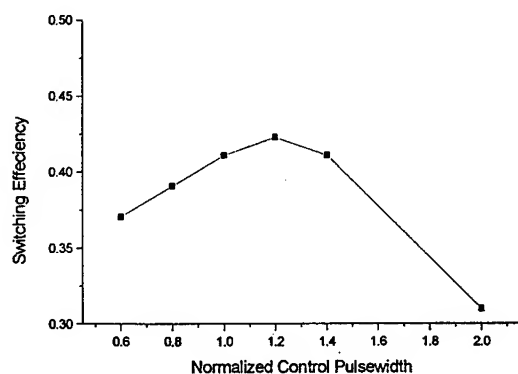


Figure 2. Switching efficiency vs. the control pulsewidth Figure 3. Switching efficiency against control energy

Fig. 3 gives the variation of switching efficiency for different control pulse energy. It shows that the switching efficiency increased with the normalized control pulse energy in the lower energy, and it reduced in the large energy. It also can achieve the 90% switching efficiency when control pulse energy changed 40%.

With the length of birefringent fiber changed, the switch efficiency has no obvious change. It results a wider switching window. Too wide the switching window will cause the crosstalk and power penalty, thus we should restrict the length to keep the polarization walkoff in the range of 2/3 base bit width.

The switching efficiency decreased with the increase of jitter between control pulse and signal pulse. Fig. 4 shows this relationship. We can conclude that the switching efficiency will be changed in 90% while jitter variation is limited by 3%.

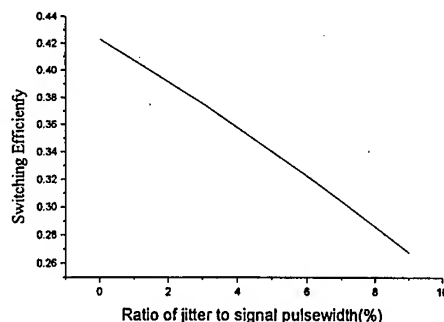


Figure 4. Switching efficiency vs. the jitter

Classic communication theory gives that bit error ratio of 10^{-9} is corresponding with the jitter less than 8.4%. In this circumstance, the switching efficiency will be about 80%.

4. CONCLUSIONS

The switching efficiency of UNI has been presented. The UNI mathematical model is established and the results show that more than 90% switching efficiency could be reached when the control pulsewidth varied 40%, when pulse power is in 40% or when the jitter is about 3%. It is obvious concluded that the jitter is a key factor which will affect the switching efficiency.

ACKNOWLEDGMENTS

This work is supported by National Nature Science Foundations of China (69682009, 69738010), National Key Laboratory of Integrated Optoelectronics of China and Huawei Foundations.

REFERENCES

1. N. S. Patel, K. L. Hall, and K. A. Rauschenbach, "40Gb/s demultiplexing using an ultrafast nonlinear interferometer (UNI)," *IEEE Photonics Technology Letters*, 8, pp.1695-1697, 1996
2. N. S. Patel, K. L. Hall, and K. A. Rauschenbach, "Interferometer all-optical switches for ultrafast signal processing," *Applied Optics*, 37, pp.2831-2842, 1998
3. Xingzhong Chen, Minyu Yao, and Yizhi Gao, "Ultrafast Nonlinear Interferometer (UNI)," *Chinese J. of Lasers*, B8, pp203-206, 1999
4. M. Eiselt, W. Pieper, and H. G. Weber, "SLALOM: semiconductor laser amplifier in a loop mirror," *J. Lightwave Technology*, 13, pp2099-2112, 1995
5. M. Jinno, and T. Matsumoto, "Nonlinear sagnac interferometer switch and its applications," *IEEE J. of Quantum Electronics*, 28, pp.875-882, 1992

Optical switch and interconnect techniques based on the semiconductor optical amplifiers

Deming Liu*, Xiaojun Hu, Dexiu Huang

Dept. of Optoelectronic Engineering, Huazhong Univ. of Science and Technology

ABSTRACT

In this paper the new progress in the researching fields of optical switch were reviewed. A compute model for calculating the switch speed, extinction ratio, noise figure, dynamic range as well as the switch gain was presented. The switch time, contrast ratio of SOA gate are calculated and evaluated. The methods to suppress the ASE noise are discussed. A novel and special method to extract optical route signal is presented. The results of the theoretical analysis showed that the optical gain of the SOA should be setup in optimum so as to obtain the best performances of the switch. An optical switch matrix using the polarization-insensitive strained quantum well SOAs and the optical couplers was fabricated and a novel and simplified method for extracting the logical control signal of the optical switch was specially designed, in which the optoelectronic integrated circuit (OEIC) techniques could be used to fabricate a compact, effect, high speed and low-cost optical switch matrix. It is shown that with the rapid improvement of OEIC techniques, the larger scale switch matrix based on SOA gate would be able to get into practice in the near future.

Keywords: SOA gate, switch time, contrast ratio, ASE noise, route signal, switch matrix

1. INTRODUCTION

Recently there has been growing demand in developing all-optical network (AON) to support the broadband integrated service digital network (B-ISDN). In 21st century, signal will not only be transmitted by fiber, but also be processed optically. Optical switch and interconnect techniques may be the key to constitute a real all-optical network. Various optical switch devices, such as optical switch based on semiconductor optical amplifiers (SOAs) gate, directional coupler switch, Mach-Zehnder interferometer switch, X or Y digital switch and free-space optical switch, are studied and improved rapidly over these years¹⁻⁴. Because of its special advantages⁵, optical switch based on SOA gate attracts considerable interest in the researching fields of optical switch. The superior performances of SOA gate switch include:

- high on/off speed
- high extinction ratio
- easy to be integrated with other semiconductor devices
- zero loss or gain

* Correspondence: Email: dmliu@mail.hust.edu.cn; Telephone/Fax: 0086-27-87543355

- polarization-independent

These performances are important in practice optical communication system. In this paper, switch gain, switch time, contrast ratio of SOA gate are analyzed. For switch array based on SOA gate in which a large number of SOA are cascaded, the accumulated ASE noise may deteriorate greatly the performances of the optical switch. How to suppress the ASE noise is also discussed. In addition, a novel and simplified method for extracting the logic control signal of the optical switch is presented in which the optoelectronic integrated circuit (OEIC) techniques could be used to fabricated a compact, effect, high speed and low-cost optical switch matrix.

2. PERFORMANCE ANALYSIS OF SOA GATE

2.1. Switch time and extinction ratio

The analysis on the SOA gate starts with the carrier rate equation:

$$\frac{\partial}{\partial t} N(z, t) = \frac{I(t)}{qV} - R(N) - \frac{g_m(N)}{h\nu A} \Gamma P(z, t) , \quad (1)$$

where $R(N)$ is the total spontaneous recombination rate which is generally expressed as $R(N) = AN + BN^2 + CN^3$, where A, B, C are the coefficients for the nonradiate recombination, the spontaneous emission and the Auger recombination, respectively. g_m is the material coefficient per unit length, which can be written as

$$g_m = a(N - N_0) . \quad (2)$$

In equation (1), it is assumed that the injection current is uniform spatially. The amplifier longitudinal nonuniformity related to the variation of the carrier is considered. $P(z, t)$ is amplified along active region of SOA, which can be expressed as

$$\frac{\partial}{\partial z} P(z) = (\Gamma g_m(z) - \alpha_s) P(z) . \quad (3)$$

With numerical computing, the output optical power, switch time and the contrast ratio of SOA gate in steady state can be got by solving the equation (1), (2) and (3). In the calculation, the active region of SOA is divided into 40 small sections to stimulate the nonuniformity of optical power along SOA waveguide. All the parameters used in the theoretical compute are listed in Table 1.

Table 1 the parameters used in the computing

$A=0.25/\text{ns}$	$\Gamma=0.3$	$\alpha=2.5 \cdot 10^{-16} \text{cm}^2$
$B=0.1 \cdot 10^{-18} \text{cm}^3/\text{ns}$	$V=1.2 \cdot 10^{-10} \text{cm}^3$	$N_t=1.0 \cdot 10^{18} \text{cm}^{-3}$
$C=0.94 \cdot 10^{-37} \text{cm}^6/\text{ns}$	$L=400 \mu\text{m}$	$\alpha_s=20 \text{cm}^{-1}$

Fig.1 (a), (b), (c) and (d) show the operation of switch under the injection current pulse of the step function and the 50 μ W input optical power. It is clear from Fig.1 (b) and (d) that the switch time (from state OFF to state ON) is shorter when the injection current is a three-step pulse. It is well known that the switch time depends on the carrier lifetime in SOA⁶. Optical switch based on quantum-well semiconductor optical amplifier (QW-SOA) gate has higher switch speed. Besides, the input optical power has also the influence on the speed slightly. The theoretically calculation shows however that certain transformation of the injection current controlling the SOA gate can also help to improve the switch speed effectively.

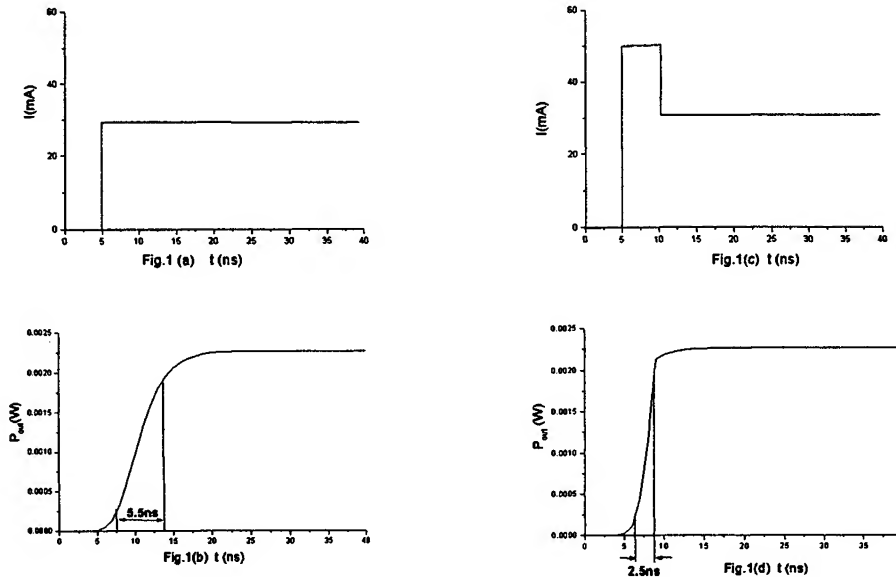


Fig.1 (a) The injection current pulse in SOA. (b) The optical power of the SOA gate as a function of time corresponding to (a). (c) The injection current pulse in SOA wit a three-step pulse. (d) The optical power of the SOA gate as a function of time corresponding to (c).

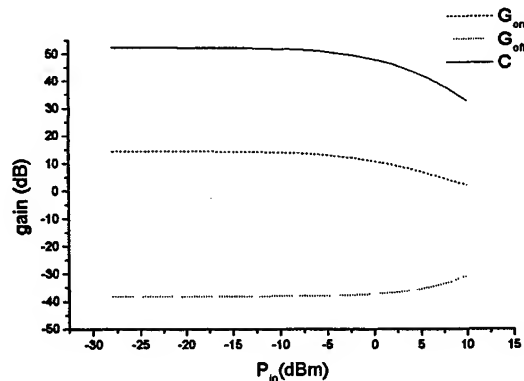


Fig. 2 Calculated result of the gain G_{ON} , G_{OFF} and the contrast ratio of SOA versus input optical power when the injection currents of ON-state and OFF-state are 60mA and 0mA respectively.

Contrast ratio C is defined as the ratio of gain at ON-state to gain at OFF-state. Fig.2 illustrates the theoretically calculated gains of SOA gate at steady ON-state and OFF-state versus input optical power for $I_{ON}=60\text{mA}$ and $I_{OFF}=0\text{mA}$, respectively. The corresponding contrast ratio C as the function of input optical power is therefore obtained. It is shown that the contrast ratio decreases with the increasing of input optical power (P_{in}) due to the gain saturation of ON-state and the saturated absorption of OFF-state. This result is consistent with the discussion reported before.

2.2 Optimization of signal-noise ratio

At ON-state, the gain of SOA gate compensates the fan-out and fan-in losses in switch arrays with the price of introducing the amplified spontaneous emission (ASE) noise. In the following calculation, it is shown that there are two ways to reduce ASE noise in switch arrays consisting of couplers and SOAs. One is to optimize the operation current of SOA gate on every stage; another is to design the special architecture of the switch matrix.

The noise figure of the switch decreases with the increasing of the optical signal-to-noise ratio when the input power and switch net gain is given. After repetitious attenuated and amplified the signal power comes to:

$$P_{out} = P_{ase} L_{in} L_1 G_1 L_2 L_k G_k L_{n-1} G_{n-1} L_{n+1} = P_{in} G_{tot}, \quad (4)$$

and the accumulated ASE noise is

$$P_{sp} = P_{ase} L_{n+1} \sum_{k=1}^n (G_k - 1) \prod_{m=k+1}^n L_m G_m, \quad (5)$$

where L_k and G_k is the front coupling loss and the gain of SOA gate at stage k , respectively. The maximization of signal-to-noise ratio is under the following conditions: the total gain of the switch equal to 1; the gain of SOA at every stage is not larger than saturation gain; input optical power is fixed to be a constant. So, the problem is simplified to be the minimization of P_{sp} with these constraints. Differential method is used to find the optimized gain of SOA at every stage.

$$\frac{\partial P_{sp}}{\partial G_k} = \frac{-P_{ase} G_n L_{n+1}}{G_k} \sum_{i=k+1}^n (1 - L_i) \prod_{j=i+1}^n G_{j-1} L_j < 0. \quad (6)$$

If $G_{1max} G_{2max} \dots G_{n-1max}$ is larger than the required gain, the last amplifier is not needed and the problem is simplified to be the optimization of the front $(n-1)$ -stage SOAs' gain. The optimization of optical signal-to-noise ratio is realized when maximizing the gain of the front stage SOAs and minimizing the gain of the rear stage SOA are reached at the same time.

On the other hand, assuming the operation current of every SOA is fixed, we can also analyze the relation between P_{sp} and L_k using the following equation:

$$\frac{\partial P_{sp}}{\partial L_k} = P_{ase} L_{n+1} G_k \sum_{i=1}^{k-1} (G_i - 1) \prod_{\substack{j=i+1, \\ j \neq k}}^n L_j G_j > 0 \quad (7)$$

Similar to the discussion of gain optimization, we can obtain the following conclusion: the noise of the switch in which the major loss is at the front stages is larger than that of the switch in which the major loss is at the rear stages. Choosing the architecture of an optical switch involves a lot of factors, such as the quantities of SOA gates and couplers, control complexity, switch speed and noise figure. Our analysis may help to choose the topology of optical switch based on SOA gate.

3. THE METHOD TO EXTRACT ROUTE SIGNAL

In a large-scale optical switch, the process of route optical signal is complex. The switch control complexity and state-setting time may decide a switch's system performance in practice. By now, in most optical switches, logic control signal is extracted from the optical channel by opto-electrical (OE) transformation. The process is to abstract a portion of signal power from the signal channel with an optical coupler, to convert the optical signal into electrical signal with PIN detector, to deal with the electrical signal and to use it to control optical switch array. Obviously, the optical coupler and detector degenerate the superiority of optical switch. Here, a special and simple method to extract the logic control signal of the optical switch based on SOA gate is presented. Experiment shows that the method works well.

In semiconductor optical amplifier, the interaction of photon and electron produces three optical phenomena namely stimulated absorption, spontaneous emission and stimulated emission. Under the zero bias current the stimulated absorption is dominant in the active region of SOA. The carrier density and the SOA junction voltage vary according to input optical power. When injection current increases and the carrier density is equal to the transparent carrier density, stimulated emission balances with stimulated absorption. At this threshold point, carrier density and SOA junction voltage do not vary with input optical power. If the injection current exceeds this threshold, stimulated emission becomes the major phenomenon in SOA. The carrier density and the SOA junction voltage vary reversely with the input optical power. Based on this phenomenon, a new method to extract optical route signal from optical channel is designed. If the injection current of SOA at ON-state is larger than the threshold point, the SOA junction voltage signal can be amplified directly and be treated as the route signal. Fig.3 shows the experimental result for the measurements of the SOA junction voltage versus the injection current in the SOA.

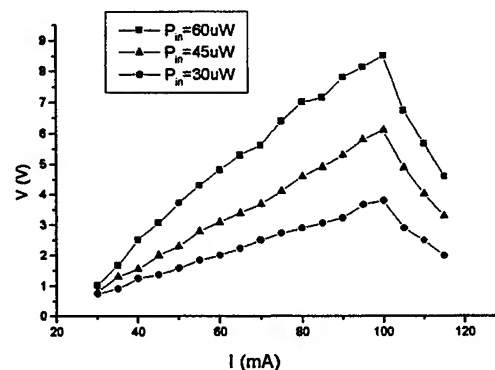


Fig.3 Measured amplified junction voltage amplitude of SOA gate versus the injection current in SOA

Clear step signal of the junction voltage is also observed with a common oscillograph when the input optical signal is a step-function wave. In an optical switch, SOA is always biased to be at the state of amplifying to give small-signal gain, so the phase of the junction voltage signal is reversed to the input optical signal. Note that, in Fig.3, the junction voltage of SOA decreases sharply after the injection current exceeds 100mA. It is because that when the injection current is larger than 100mA, the SOA tested in our experiment get into excited state. Injected carrier becomes to be depleted abundantly and the junction voltage is cut down.

With this simple method, it is not necessary to insert the OE transformation in the optical switch matrix based on SOA gate, which makes the switch cost lower. It is possible to be integrated packaged, because the route signal is extracted from the junction voltage of SOA directly. This method is superior than usual method referring to the fast switching of packet switch.

4. SWITCH MATRIX BASED ON SOA GATE

Fig.4 show a 1×2 semiconductor optical amplifier switch element with this method. The route signal is extracted from the first-stage SOA and processed to control the injection current of the second stage SOAs. From Fig.3 ,we can see that the junction voltage was affected by the injection current level greatly. It is coincident with the fact that carrier density depend on injection current mainly. In our experiments, the injection current of the SOA from which we extract the route signal keeps stable. It guarantees the steady operation of the switch element.

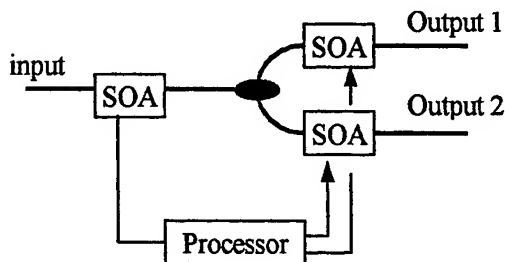


Fig.4 a 1×2 switch element based on SOA gate

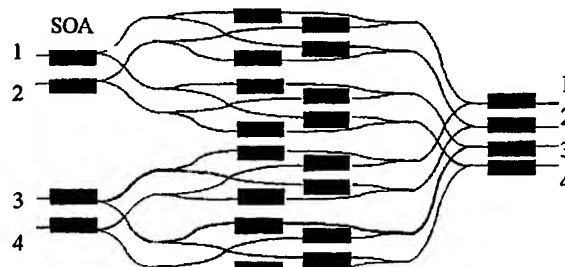


Fig .5 4×4 gate array based on SOA

Fig. 5 presents a 4×4 switch matrix based on SOA gate. The four amplifiers at the front-stage and at the back-stage, respectively, serve as booster amplifiers while the middle-stage SOA are used as switching gate. It is a complete nonblocking optical switch and supports both broadcast and point-to-point communication. In addition, it uses a minimum number of SOA gate. Our method is applicable in this switch matrix. Route signal is extracted from the booster amplifiers at the front-stage and controls the current injected in the SOA gates at the middle-stage. Monolithically integrated 4×4 semiconductor optical amplifier gate array of this architecture have been fabricated and improved gradually⁷. With the method demonstrated here, large scale switch matrix based on SOA gate would be able to get into practice in the near future.

5. CONCLUSION

This paper analyzed the switch time and contrast ratio of SOA gate. A possible way to improve the switch time of SOA gate is also presented. ASE noise is a limitation of semiconductor amplifier switch matrix. We discussed two methods to decrease the ASE noise of cascaded SOAs. In addition, a new and simple method to extract route signal of the optical switch is demonstrated. It is shown that, with this method, compact, high speed and low-cost optical switch matrix can be fabricated by monolithical integrating techniques.

ACKNOWLEDGMENTS

Authors should be greatly appreciated the funding support from the national foundation for High Technology Program of China and from the Shenzhen Huawei technology Co. (China).

REFERENCES

1. R.Fortenberry, A.J.Lowery, W.L.Ha, and R.S.Tucker, "Photonic packet switch using semiconductor optical amplifiers," *Electron.Lett.*, 27, pp. 1305-1307, 1991
2. G.Soulage, A.Jourdan, P.Doussiere, G.Da Loura, and M.Sotom, "Clamped-gain SOA gates as multiwavelength space switches," *Tech.Dig. Opt.Fiber Vommun.Conf.*, paper TuD 1, San Diego, CA, 1995.
3. A.Sneh, J.E.Zucker, B.I.Miller, and L.M.Stulz, "Polarization-insensitive InP-based MQW digital optical switch," *IEEE Photonics.Technol.Lett.* 9, pp. 1589-1591, 1997
4. P.Granstrand, et al, "pigtailed tree structure 8x8 Lithium niobate switch matrix with 112 digital optical switches", *IEEE Photonics. Tech. Lett.* 6, pp. 71-73, 1994,
5. Ito.T, et al, "Polarization independent semiconductor optical amplifier gate and its application in WDM system ", *IEICE Transactions on Electronics*, V E81-C No 8, August, 1998.
6. H.SOTO, et al, "Modelling and experimental measurements of the switching behavior of semiconductor optical amplifiers," *Optical and Quantum Electronics*, 28, pp. 669-681, 1996.
7. M.Gustavsson, B.Lagerstrom, L.Thylen, M.Janson, L.Lundgren, A.C.Morner, M.Rask and B.Stoltz, "Monolithically integrated 4x4 InGaAs/InP laser amplifier gate switch array," *Electron. Lett.* 28, pp. 2223-2225, 1992.

Normal-incident SiGe/Si MQWs Photodetectors Operating at 1.3 μ m

Buwen Cheng*, Cheng Li, Qinqing Yang, Hongjie Wang, Liping Luo, Jinzhong Yu, Qiming Wang

State Key Laboratory on Integrated Optoelectronics, Institute of Semiconductors,

Chinese Academy of Sciences, P.O.Box 912, Beijing 100083, China

ABSTRACT

A normal-incident SiGe/Si multiple quantum wells (MQWs) photodetector was reported. The structure and fabrication process of the photodetector were introduced. The photocurrent spectra measurement showed that the response spectra was expanded to 1.3 μ m wavelength. The quantum efficiency of the photodetector was 0.1% at 1.3 μ m and 20% at 0.95 μ m.

Keywords: SiGe/Si, MQWs, Photodetector

1. INTRODUCTION

Nowadays, most of the research on photodetectors and receivers for optical communication has successively utilized III-V compounds because of their superior performance to silicon technology. However, Si integrated circuit technology is mature, compact, cheap and reliable. The compatibility of Si-based materials with the Si process technology stimulates a great number of research efforts to exploit Si-based photodetectors. The spectral response of Si-based photodetectors was extended into the 1.3 μ m spectral region through the use of strained SiGe/Si heterostructures. These have opened the door for the realization of Si-based monolithic integrated photoreceiver for optical communication. Unfortunately, the indirect bandgap of SiGe results in a small absorption coefficient as compare with the direct bandgap materials. In order to achieve a high-quantum efficiency, in most of the SiGe/Si photodetectors, the incident light is coupled into the buried waveguide formed by the larger index of refraction of the strained superlattice layer sandwiched between layers of Si to have a sufficiently large absorption depth^{[1][2][3]}. The disadvantage is that it is difficult to couple with fiber and the coupling efficiency is low. In this paper, we introduce a normal incident SiGe/Si MQWs photodetector operating at 1.3 μ m.

2. STRUCTURE AND FABRICATION

The schematic structure of the SiGe/Si MQWs photodetector was shown in Fig.1. The materials were grown by MBE at 750°C. Starting from the n-Si (100) substrate, a 100nm intrinsic Si layer was grown as the buffer. On the buffer layer, the absorption layer of the photodetector which contains 20 periods of alternately stacked 10nm Si_{0.7}Ge_{0.3} and 30nm Si was grown. Then a 100nm intrinsic Si and a 100nm p⁺-Si contact layer were grown sequentially.

Devices were fabricated using standard photolithography and dry etching. Circular mesas were etched down to the substrate by SF₆+O₂. The diameter of the mesa was 1mm. Al was evaporated to form the top contact. The device was thinned to 100 μ m from backside and the bottom contact was formed by evaporating Aluminium. 500nm SiO_xN_y was used to passivate the device.

3. RESULT AND DISCUSSION

Fig.2 showed the I-V characteristic of the device. It was shown that the device has good electrical properties. The breakdown voltage was 12V. At a reverse bias of 11.5V, the leakage current is 0.002mA, corresponding to a current

* Correspondence: Email: cbw@red.semi.ac.cn; Tel: 10+62339551; Fax: 10+62322388

density of $0.064\text{mA}/\text{cm}^2$.

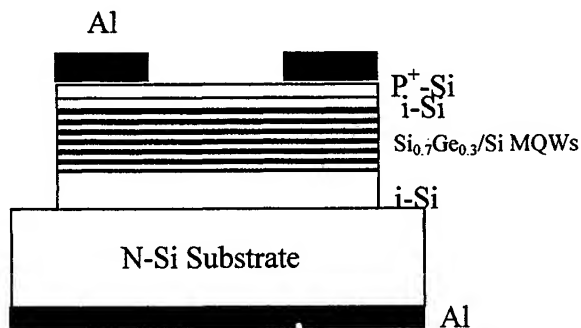


Fig.1 Schematic cross section of the normal incident SiGe/Si MQWs photodetector.

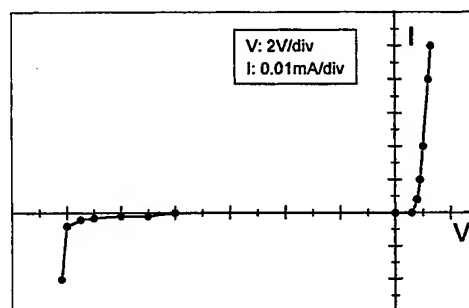


Fig.2 I-V characteristic of the Photodetector.

The photocurrent response of the device at different bias was shown in Fig.3. Tungsten lamp was used as light source. The spectrum was obtained by using a Fourier transform infrared spectrometer. It showed that there was a peak response at about $0.95\mu\text{m}$. The wavelength range for which the photodetector can response has been expanded to $1.3\mu\text{m}$ wavelength. The photocurrent increased with the increasing of the applied bias. But the response at $1.3\mu\text{m}$ changed only a little when the bias was increased.

The quantum efficiency of the photodetector was measured by a calibrated InGaAs photodetector. The result was shown in Fig.4 as dots. The external quantum efficiency of the device was $0.1\% \pm 1.3\mu\text{m}$ and 20% at $0.95\mu\text{m}$.

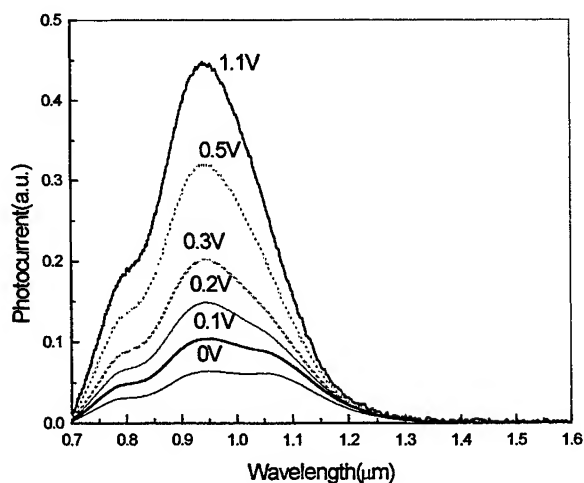


Fig.3 Photocurrent spectra of the photodetectors at various applied bias.

The external quantum efficiency is strongly dependent on the material absorption coefficient α . L. Naval *et al* developed an estimate of α for the strained SiGe alloy [4] based on the absorption data for unstrained (bulk) SiGe provided by Braunstein *et al* [5]. For low absorption levels, the room temperature curves are fitted to a simple one-phonon model for the fundamental absorption as follows:

$$\alpha = \begin{cases} 0 & h\nu \leq E_g - k\theta \\ A_a \frac{(h\nu - E_g + k\theta)^2}{\exp(\theta/T) - 1} & E_g - k\theta \leq h\nu \leq E_g + k\theta \\ A_a \frac{(h\nu - E_g + k\theta)^2}{\exp(\theta/T) - 1} + A_e \frac{(h\nu - E_g - k\theta)^2}{1 - \exp(-\theta/T)} & h\nu \geq E_g + k\theta \end{cases} \quad (1)$$

Where E_g is the indirect bandgap. T is the temperature. k is Boltzman constant, and θ is the phonon equivalent temperature. The parameters A_a and A_e weigh the phonon absorption and emission contributions, respectively. The external quantum efficiency of the device can get as follows:

$$\eta = (1 - R)(1 - e^{-\alpha(\lambda)d})$$

Where R is the reflectance of the device surface. d is the equivalent absorption depth. The calculated result of η was shown in Fig.4 as solid line.

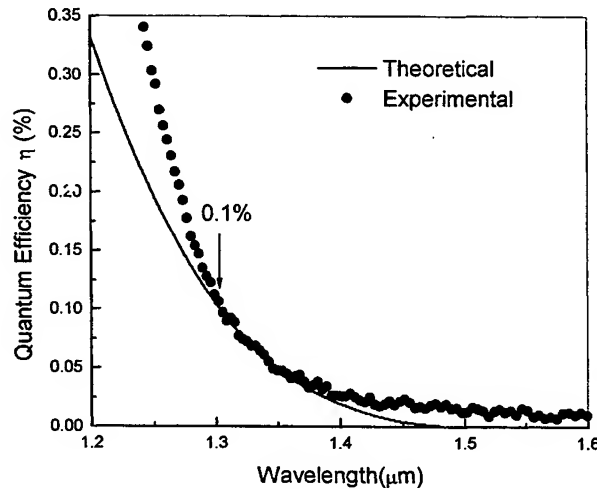


Fig.4 Measured external quantum efficiency of the photodetector by a calibrated InGaAs detector (dots) and theoretical results (solid line).

The 0.1% quantum efficiency at 1.3μm is too low for practical use. There are two main reasons that cause the low quantum efficiency. First, in this device, the Ge content x of the SiGe absorption layers is too low. The absorption coefficient of the $\text{Si}_{0.7}\text{Ge}_{0.3}$ layer is too little at 1.3μm wavelength. The other reason is that the thickness of the absorption layer was little.

There are several approaches that can be taken to increase the efficiency. First, The quantum efficiency will be increased if $\text{Si}_{1-x}\text{Ge}_x$ absorption layers with higher Ge mole fraction were grown. But because of the large lattice mismatch between Si and Ge, the thickness of the SiGe layer must be not above the critical thickness so that pseudomorphic, dislocation-free SiGe alloy layers can be grown on a silicon substrate. This thickness has a strong dependency on the Ge fraction, x . So, a compromise between x and the thickness of the absorption layer must be taken. Secondly, in order to settle the limitation of the thickness of the absorption layer, two kinds of materials can be chosen. One of them is SiGeC alloy. It has been found that SiGeC will be lattice match with Si substrate when the ratio of Ge content and C content equal to 9:1^[6]. Using this kind of SiGeC alloy as absorption layer, the thickness will not be limited due to the strain. One can grow more thick absorption layer to achieve high quantum efficiency. The other

material which can be chosen for absorption layer is strain compensated $\text{Si}_{1-x}\text{Ge}_x/\text{Si}$ MQWs. The $\text{Si}_{1-x}\text{Ge}_x/\text{Si}$ MQWs was grown on a relaxed $\text{Si}_{1-y}\text{Ge}_y$ alloy layer ($x>y$). The $\text{Si}_{1-x}\text{Ge}_x$ absorption layers will be compressed and the Si barrier layers are tensed. The total strain of the MQWs can be zero. Thirdly, using a resonant cavity structure, will effectively increase the absorbing length, therefore, increasing the quantum efficiency^{[7][8][9]}.

4. CONCLUSION

A normal-incident SiGe/Si MQWs PIN photodetector have been fabricated. The response spectrum was expanded to $1.3\mu\text{m}$ wavelength because of the strain-induced band-gap narrowing. An external quantum efficiency of 0.1% at $1.3\mu\text{m}$ has been obtained.

ACKNOWLEDGEMENT

The authors would like to thank Ph. D Zhuo Yu, Daizong Li and Changjun Huang for their helpful discussion. This work was supported by the "863" Research Plan under Grant No.863-307-15-4(03) and the National Natural Science Foundation of China under Grant No.69896260.

REFERENCES

1. H. Temkin, T. P. Pearsall, J. C. Bean et al, " $\text{Ge}_x\text{Si}_{1-x}$ Strained-layer superlattice waveguide photodetectors operating near $1.3\mu\text{m}$ ", Appl. Phys. Lett., **48**(15), pp.963~965, 1986
2. T. P. Pearsall, H. Temkin, J. C. Bean et al, "Avalanche gain in $\text{Ge}_x\text{Si}_{1-x}/\text{Si}$ infrared waveguide detectors", IEEE Electron Device Lett., **ED-7**(5), pp.330~332, 1986
3. A. Splett, T. Zinke, K. Petermann et al, "Integration of Waveguides and Photodetectors in SiGe for $1.3\mu\text{m}$ Operation", IEEE Photonics Technology Lett., **6**(1), pp.59~61, 1994
4. L. Naval, B. Jalali, L. Gomelsky et al, "Optimization of SiGe/Si Waveguide Photodetectors operating at $1.3\mu\text{m}$ ", J. of Lightwave technology, **14**(5), pp.787~797, 1996
5. R. Braunstein, A. R. Moore, and F. Herman, "Intrinsic optical absorption in germanium-silicon alloy", Phys. Rev., **109**(3), pp.695-710, 1958
6. P. Broucaud, C. Guedj, D. Bouchier, et al, Journal of Crystal. Growth, **157**, pp.410-413, 1995
7. R. T. Carline, V. Nayar, D. J. Robbins et al, "Resonant Cavity Longwave SiGe-Si Photodetector Using a Buried Silicide Mirror", IEEE Photonics Technology Lett., **10**(12), pp.1775~1777, 1998
8. Yukari Ishikawa and N. Shibata, "Epitaxy-ready Si/SiO₂ Bragg reflectors by multiple separation-by-implanted-oxygen", Appl. Phys. Lett., **69**(25), pp.3881~3883, 1996
9. D. C. Diaz, C. L. Schow, Jieming Qi, and J. C. Campbell, "Si/SiO₂ resonant cavity photodetector", Appl. Phys. Lett., **69**(19), pp.2798-2800, 1996

The mechanism for erbium luminescence in silicon at 1.54 μm

M. Q. Huda,* S. A. Siddiqui, M. N. Islam, M. S. Islam

Dept. of EEE, Bangladesh University of Engineering and Technology, Dhaka 1000, Bangladesh.

ABSTRACT

Origin of erbium luminescence at 1.54 μm , a prospective optical source in silicon based optoelectronics has been analyzed. Erbium atoms in silicon have been considered as recombination centers with specific values of capture and emission coefficients. Electron-hole recombination through these levels has been considered to be the origin of erbium excitation. At steady state of excitation, a certain fraction of erbium sites were found to remain occupied by electrons. Trapped electrons, which eventually recombine with holes in the valence band, provide the energy for $^4I_{15/2} \rightarrow ^4I_{13/2}$ transition of erbium atoms. It was however found that, even with 100% quantum efficiency of this energy transmission, not every electron-hole recombination corresponds to the excitation of an erbium atom. This wastage of recombination energy was attributed to the rather long lifetime of erbium decay. Capture and emission processes of photo generated excess carriers in the erbium related level have been equated for non-steady state conditions. It has been shown that the steady state erbium luminescence actually follows a transient rise, typically of the order of few hundred microseconds. The anomalous behavior of continuous rise of erbium luminescence after termination of short excitation pulses of 30 μs has been explained mathematically for the first time.

Keywords: Erbium, excitation, luminescence, Shockley-Read-Hall, defect level

1. INTRODUCTION

The rare earth element erbium has the interesting property of emitting at 1.54 μm , the wavelength for optical communication. Incorporation of erbium into silicon thus opens the possibility of complete optoelectronic functionality in silicon chips. Despite the fact that the silicon technology is now very much mature and economically viable, it has the serious shortcoming of not being radiative. There are different approaches like porous silicon, defect induced emission, etc. to achieve efficient light emitters in silicon, but the Si:Er technique till now seems to be the most promising option. Since the first demonstration of atomically sharp luminescence of erbium in silicon by Ennen et al.,¹ numerous work has been done on this field. Efficiency of erbium luminescence has been increased substantially by introducing co-dopants.² The problem related to limited solid solubility of erbium in silicon has also been solved by the technique of solid phase epitaxial recrystallization.³ Light emitting diodes working at room temperature have already been demonstrated few years ago.^{4,5}

The mechanism of erbium luminescence in silicon however is not fully understood. It is accepted that, erbium atoms are excited from the ground state to a higher energy state ($^4I_{13/2}$) through electron-hole recombination process. The excited atom relaxes from the $^4I_{13/2}$ state to the ground state either by a radiative or a non-radiative process.^{6,7} The former represents the emission of a photon at 1.54 μm . The exact mechanism of erbium excitation is still under investigation. It was suggested through a theoretical analysis that, a band to band Auger process can be a possible mechanism with the help of a localized defect state.⁸ Priolo et al, on the other hand, explained the excitation mechanism through excitons bound in erbium related defect states.⁹ This idea of exciton related mechanism was supported by others while trying to explain the behavior of erbium luminescence under short excitation pulses in photoluminescence measurements. For short excitation pulses of the order of 30 μs , it was found that the luminescence from erbium continues to increase for a certain duration even after the laser pulse has been terminated.^{10,11} In a recent publication, on the other hand, Taguchi *et al.* suggested that the observed behavior of erbium luminescence under short excitation pulses can result from a slower system response.¹² The proposed mechanisms, however, are ambiguous to some extent, and fail to explain the experimental results conclusively. The idea of exciton related mechanism is not very consistent with the fact of erbium luminescence at room temperature.

* Electronic Mail: qhuda@eee.buet.edu

In this paper, we develop a new approach for erbium excitation involving impurity states. Our model gives detail explanation of the origin of erbium luminescence in silicon. We also show for the first time that the observed behavior of erbium luminescence under short excitation pulses is real, and can be explained mathematically.

2. THE LUMINESCENCE MECHANISM

We propose that the erbium excitation is a process involving electron-hole recombination at the erbium site. The erbium atom has been considered to be an impurity center (Shockley-Read-Hall) in silicon. The corresponding defect level in the band gap, referred as erbium level from now on, has been assigned with values of thermal emission and capture coefficients for charge carriers.¹³ In accordance with experimental results in the literature,¹⁴ we have taken this erbium level to be situated 150 meV below the conduction band. Possible capture and emission processes of carriers in the erbium level are show in Figure 1. The electron trapped in the erbium level can either jump back to the conduction band, or it can capture a hole in the valence band. The later process corresponds an electron-hole recombination, and the resulting energy becomes available to the erbium atom for possible excitation. The excited atom decays to its ground state by the characteristic lifetime of decay. Radiative part of this ${}^4I_{13/2} \rightarrow {}^4I_{15/2}$ transition corresponds the light emission at 1.54 μm .

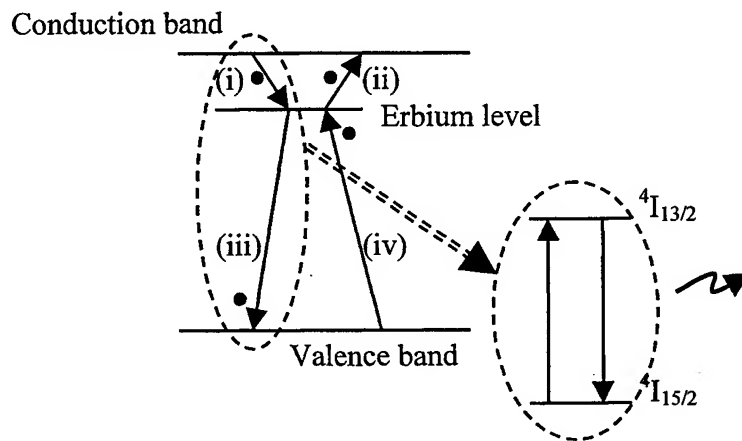


Figure 1. Schematic diagram of the processes involving erbium excitation: (i) electron capture, (ii) electron emission, (iii) hole capture, and (iv) hole emission. Destination of electron through a process is shown by a symbol on the arrowhead. Processes (i) and (iii) together correspond the excitation of an erbium atom from ground state to the higher energy state.

Let N_{Er} is the total number of active erbium sites per unit volume and n_{Er} of them are filled by electrons at a steady state of optical excitation. The process of capturing an electron or emitting a hole from the erbium level depends on the number of empty sites. Similarly, the process of electron emission or hole capture in the erbium level depends on the number of erbium sites being occupied. The balance between capture and emission of carriers in the erbium level is then given as:

$$e_n n_{Er} + c_p p n_{Er} = e_p (N_{Er} - n_{Er}(t)) + c_n n (N_{Er} - n_{Er}(t)), \quad (1)$$

where e_n , e_p are the electron and hole emission rates respectively with units of s^{-1} ; and c_n , c_p are the corresponding capture coefficients with units of $\text{cm}^3 \text{s}^{-1}$. The first term on the left hand side represents the rate of electron emission from the erbium level, whereas the second term represents the rate of hole capture. The two terms on the right hand side represents the rate of hole emission and electron capture respectively. The fraction of erbium atoms being occupied by electrons at steady state is then given as:

$$f_i = \frac{n_{Er}}{N_{Er}} = \frac{c_n n + e_p}{e_n + c_p p + c_n n + e_p}. \quad (2)$$

The number of erbium sites which are filled with electrons and are available for excitation is given by $f_i(N_{Er} - N_{Er}^*)$, where N_{Er}^* is the number of excited erbium ions in the steady state. Taking the assumption that the excited erbium ions do not change the electronic property of the corresponding defect levels, the rate of erbium excitation is given by:

$$f_i(N_{Er} - N_{Er}^*)c_p p = \frac{N_{Er}^*}{\tau_{Er}}, \quad (3)$$

where τ_{Er} is the decay time of the $^4I_{13/2}$ state of erbium to the ground state, taking the effect of radiative and non-radiative transitions. If the radiative lifetime of the excited erbium state is given by τ_{rad} then the luminescence strength from erbium is given by:

$$I \propto \frac{N_{Er}^*}{\tau_{rad}} = \frac{c_p p}{f_i c_p p + \frac{1}{\tau_{rad}}} \frac{f_i N_{Er}}{\tau_{Er}}. \quad (4)$$

3. INITIAL RISE OF THE LUMINESCENCE

When a laser pulse is applied to an erbium doped silicon sample, excess electron-hole pairs are generated. Recombination of these carriers through erbium sites results in 1.54 μm luminescence. However, rate of capture and emission of carriers through erbium centers is controlled by the corresponding emission and capture coefficients. As a result, a finite amount of time is needed for the erbium luminescence to reach the steady state. Equating the capture and emission rate of carriers from the erbium level as a function of time, we obtain,

$$\frac{dn_{Er}(t)}{dt} = (e_p + c_n n)(N_{Er} - n_{Er}(t)) - (e_n + c_p p)n_{Er}(t). \quad (5)$$

Solution of equation (5) gives the time function of electron occupied erbium sites as:

$$n_{Er}(t) = \frac{b}{a} N_{Er} (1 - e^{-at}), \quad (6)$$

where,

$$a = (e_p + e_n + c_n n + c_p p)$$

$$b = (e_p + c_n n)$$

The effect is shown in Figure 2 for a typical set of parameters. The electron occupancy of erbium levels is seen to be increasing exponentially to a steady level. The time variation of $n_{Er}(t)$ results in a variation in the capture and emission processes of carriers. The rate of electron-hole recombination through erbium levels is then given by $n_{Er}(t)c_p p$. However, even with a 100% quantum efficiency of coupling between the erbium level and the 4f shell electrons, not every recombination will be useful for exciting erbium atoms. Energy released by electron-hole recombination at sites where erbium atom is still in the excited state, would naturally be a wastage in terms of erbium luminescence. This fraction of

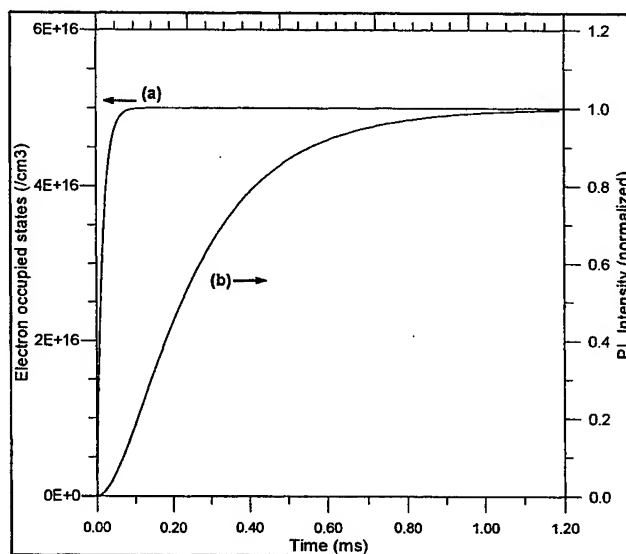


Figure 2. Time function of erbium luminescence after providing the laser excitation. (a) the exponential increase of electron occupied erbium sites (n_{Er}) to the steady value. (b) increase of PL intensity to the final value. A rise time of the order of few hundred microseconds is noticed.

recombination energy is likely to be a significant factor in determining erbium luminescence strength, as the lifetime of erbium decay is rather long. Taking assumption that the electronic property of an erbium level remains independent of the energy state of the corresponding atom, the net rate of excitation (pumping rate, $P(t)$) can be taken as,

$$P(t) = f_i(t)[N_{Er} - n_{Er}^*(t)]c_p P, \quad (7)$$

where, $n_{Er}^*(t)$ is the density of erbium atoms in excited state.

Equating the rate of erbium excitation with the rate of decay, we obtain,

$$\frac{d n_{Er}^*(t)}{dt} = f_i(t)[N_{Er} - n_{Er}^*(t)]c_p P - \frac{n_{Er}^*(t)}{\tau_{Er}}. \quad (8)$$

Luminescence strength from erbium atoms at any instant will be proportional to the concentration of excited atoms, and is given as: $I(t) \propto n_{Er}^*(t)/\tau_{rad}$.

Equations (5-8) represent the initial transient in erbium luminescence. The resulting time variation of luminescence is shown in Figure 2. It is interesting to see that, the luminescence from erbium takes a rather long time to reach the steady state. It has been found that, the rise time typically varies in the range of few hundred microseconds.¹³

4. SHORT EXCITATION PULSE

The pumping rate of erbium atoms, as given by equation (7), is a product of $f_i(t)$ and $(N_{Er} - n_{Er}^*(t))$. Thus the pumping rate goes through a peak value before reaching the steady state where pumping and decaying rates become equal with a consequence of constant luminescence. As soon as the laser excitation is terminated, the excess carrier density starts decaying exponentially with the carrier lifetime. The luminescence decay profile for this case follows the same equations (5-8) with proper boundary conditions.

If a laser excitation pulse can be made short enough, luminescence from erbium fails to reach the steady level at the time of termination of the pulse. The pumping rate, as a result, remains higher than the rate of erbium decay. Apart from that, the pumping action remains efficient due to less number of erbium atoms being in the excited state. As a result, termination of the laser excitation doesn't correspond an instant decay of luminescence. Instead, the trapped carriers, as well as a fraction of the excess carriers keep on pumping erbium atoms with a rate higher than that of their decay. The slow down process of the pumping action depends on capture cross-section, emission coefficient, carrier lifetime, etc., and follows equations (5),(7), and (8). The luminescence peak is achieved at a point where pumping rate of erbium atoms equals the rate of their relaxation to the ground state.

Using our model, we have been able to simulate both the experimental results reported on short excitation pulses.^{10,11} In fact, we put a wide variation of values regarding emission and capture coefficients, lifetimes, laser power, etc., and found the same anomalous effect for short excitation pulses. Figure 3 shows the fitting on the result of Shin et al.¹⁰ Same operating temperature of 9K was taken in our model. For this particular case, capture cross section for electron and hole was taken to be $2.2 \times 10^{-19} \text{ cm}^2$. Electron emission coefficient was taken as 10^{-3} s^{-1} ; and the emission coefficient for hole in accordance with this value was found to be negligible. To our understanding, estimation of optically active erbium atoms by electrical or optical measurements can only give approximated values. This is due to the fact that, the

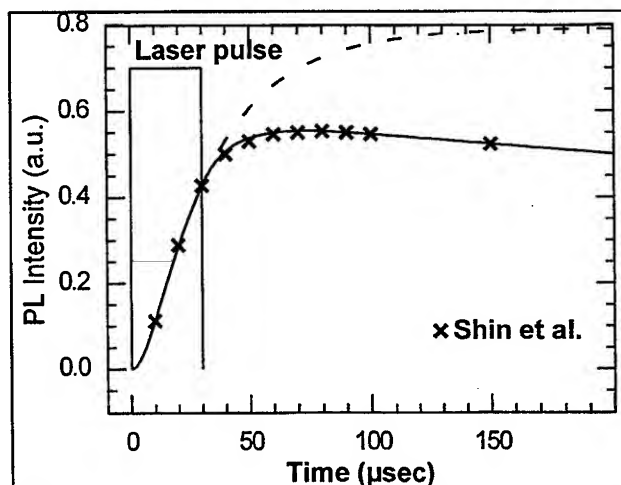


Figure 3. Calculated photoluminescence intensity from an erbium doped sample under a short excitation pulse of 30 μs . Symbols indicate the experimental results from Shin et al.¹⁰ The dotted line corresponds the gradual rise of PL to a steady state in case of a laser pulse of sufficient duration.

luminescence intensity is proportional to the excited erbium atoms, not the actual density of optically active atoms. Electrical activation of an erbium atom in the form of a donor or a trap level, on the other hand, can only be regarded as the first step towards optical activation. We therefore, have taken a value of $10^{17}/\text{cm}^3$ as the concentration of optically active erbium centers. This value is a factor of three less than that regarded in ref. 10 as the concentration of electrically and optically active erbium atoms. The lifetime for erbium decay was taken as 1.1ms. This varies from the approximated value of 800 μs by Shin et al., but in general is a good match with most of the reports on luminescence decay.^{6,7,15} Optical generation rate of carriers was taken to be $10^{22}/\text{cm}^3/\text{s}$, with a minority carrier lifetime of 15 μs . The simulated curve in this case fits remarkably well with the reported result. The prolonged rise of erbium luminescence, as observed by Przybylinska et al.¹¹ was of the order of 100 μs , with a 100% increase of luminescence during this period. We found that, the condition was originated mostly due to a longer carrier lifetime.¹³ This is reasonable, as the background concentration, as well as the implantation dose in their sample was considerably lower.

5. CONCLUSION

In conclusion, we have analyzed the mechanism of erbium luminescence in silicon in detail. Erbium sites were considered as Shockley-Read-Hall centers. Electron-hole recombination through these levels have been equated for the erbium excitation process. The proposed model explains the transient conditions of luminescence rise and decay. The anomalous behavior of erbium luminescence under short laser excitation pulses, as reported in literature, has been explained with the model.

REFERENCES

1. H. Ennen, J. Schneider, G. Pomrenke, and A. Axmann, "1.54- μm luminescence of erbium-implanted III-V semiconductors and silicon," *Appl. Phys. Lett.* **43**, pp. 943-945, 1983.
2. J. Michel, J. L. Benton, R. F. Ferrante, D. C. Jacobson, D. J. Eaglesham, E. A. Fitzgerald, Y. -H. Xie, J. M. Poate, and L. C. Kimerling, "Impurity enhancement of the 1.54- μm Er^{3+} luminescence in silicon," *J. Appl. Phys.* **70**, pp. 2672-2678, 1991.
3. A. Polman, J. S. Custer, E. Snoeks, and G. N. Van den Hoven, "Incorporation of high concentrations of erbium in crystal silicon," *Appl. Phys. Lett.* **62**, pp. 507-509, 1993.
4. B. Zheng, J. Michel, F. Y. G. Ren, L. C. Kimerling, D. C. Jacobson, and J. Poate, "Room-temperature sharp line electroluminescence at $\lambda=1.54 \mu\text{m}$ from an erbium-doped, silicon light-emitting diode," *Appl. Phys. Lett.* **64**, pp. 2842-2844, 1994.
5. G. Franzò, F. Priolo, S. Coffa, A. Polman, and A. Carnera, "Room-temperature electroluminescence from Er-doped crystalline Si," *Appl. Phys. Lett.* **64**, pp. 2235-2237, 1994.
6. Francesco Priolo, Giorgia Franzò, Salvatore Coffa, and Alberto Carnera, "Excitation and nonradiative deexcitation processes of Er^{3+} in crystalline Si," *Phys. Rev. B* **57**, pp. 4443-4455, 1998.
7. J. Palm, F. Gan, B. Zheng, J. Michel, and L. C. Kimerling, "Electroluminescence of erbium-doped silicon," *Phys. Rev. B* **54**, pp. 17603-17615, 1996.
8. I. N. Yassievich, and L. C. Kimerling, "The mechanisms of electronic excitation of rare earth impurities in semiconductors," *Semicond. Sci. Technol.* **8**, pp. 718-727, 1993.
9. F. Priolo, G. Franzò, S. Coffa, A. Polman, S. Libertino, R. Barklie, and D. Carey, "The erbium-impurity interaction and its effects on the 1.54 μm luminescence of Er^{3+} in crystalline silicon," *J. Appl. Phys.* **78**, pp. 3874-3882, 1995.
10. Jung H. Shin, G. N. van den Hoven, and A. Polman, "Direct experimental evidence for trap-state mediated excitation of Er^{3+} in silicon," *Appl. Phys. Lett.* **67**, pp. 377-379, 1995.
11. H. Przybylinska, G. Hendorfer, M. Bruckner, W. Jantsch, and L. Palmetshofer, "The role of oxygen in optical activation of Er implanted in Si," *J. Alloys. Comp.* **225**, pp. 555-558, 1995.
12. A. Taguchi, K. Takahei, M. Matsuoka, and S. Tohno, "Evaluation of the energy-transfer rate between an Er 4f shell and a Si host in Er-doped Si," *J. Appl. Phys.* **84**, pp. 4471-4478, 1998.
13. Saiful Anam Siddiqui, *Excitation Mechanism of Erbium in Silicon*, M.Sc. Thesis, Dept. of EEE, Bangladesh University of Engineering and Technology, Dhaka, 1999.
14. S. Libertino, S. Coffa, G. Franzò, and F. Priolo, "The effects of oxygen and defects on the deep-level properties of Er in crystalline Si," *J. Appl. Phys.* **78**, pp. 3867-3873, 1995.
15. S. Coffa, G. Franzò, F. Priolo, A. Polman, and R. Serna, "Temperature dependence and quenching processes of the intra-4f luminescence of Er in crystalline Si," *Phys. Rev. B* **49**, pp. 16313-16320, 1994.

An all-optical scheme for digital matrix multiplication

Partha Ghosh, Debendra Nath Das, Sourangshu Mukhopadhyay

Department of Physics and Technophysics,
Vidyasagar University, Midnapore, West Bengal, 721102, India.*

ABSTRACT

In optical computation matrix multiplication takes an important role for the purpose of digital data processing. Lot of proposals with various techniques on matrix-matrix multiplication have been seen in the last few decades. Here in this communication the authors propose a new concept of digital matrix multiplication scheme with fibre optic spatial maps.

Keywords: Matrix multiplication, fibre optic spatial maps, binary matrices.

1. INTRODUCTION

Optics has successful contribution in computation and arithmetic data processing and operations due to its inherent parallelism. Many schemes of arithmetic data processing are already reported by the scientists in last few decades.¹⁻¹² In parallel optical computation matrix-matrix multiplication has a major role for digital data processing. There are many proposals of matrix multiplications, which are implemented by optics.¹³⁻¹⁷ Uses of photorefractive media to develop systems for matrix multiplication were described by C. Gu et-al¹⁶ and B. Liu et-al¹⁷ in their individual contributions. C. Gu et-al proposed the method of matrix-matrix multiplication by the proper use of photorefractive media in the system, where the elements of the resultant matrix is expressed by the graded variation of light intensity. In an alternative approach B. Liu et-al proposed a scheme of Matrix-vector multiplication by the use of photorefractive crystal. There also the elements of the resultant matrix are expressed by the graded variation of light intensity. In such way we can see that there are many other proposals of matrix multiplications, which are published in the last decade. Here in this communication we report a completely newer approach for multiplication of two matrices, where each elements are represented by a bit either 1 or 0. The result of the whole multiplication operation comes also as a binary matrix, i.e. elements are represented either by 1 or by 0. For an example we take two different matrices

$$A = \begin{bmatrix} 1 & 0 & 1 \\ 1 & 1 & 1 \\ 0 & 1 & 1 \end{bmatrix} \text{ and } B = \begin{bmatrix} 1 & 1 & 0 \\ 0 & 1 & 1 \\ 1 & 1 & 0 \end{bmatrix}$$

The product of the two matrices is

$$P = A \times B = \begin{bmatrix} 1 & 0 & 1 \\ 1 & 1 & 1 \\ 0 & 1 & 1 \end{bmatrix} \times \begin{bmatrix} 1 & 1 & 0 \\ 0 & 1 & 1 \\ 1 & 1 & 0 \end{bmatrix}$$
$$= \begin{bmatrix} 1 + 0 + 1 & 1 + 0 + 1 & 0 + 0 + 0 \\ 1 + 0 + 1 & 1 + 1 + 1 & 0 + 1 + 0 \\ 0 + 0 + 1 & 0 + 1 + 1 & 0 + 1 + 0 \end{bmatrix}$$

* Correspondence : Email: root@viduni.ren.nic.in. Fax : (91) 03222 61009/64338.

The result P can be written as

$$P = \begin{bmatrix} 1 & 1 & 0 \\ 1 & 1 & 1 \\ 1 & 1 & 1 \end{bmatrix}$$

if it is considered that elements of the result are represented bitwise, i.e., either by 1 or 0.

2. OPTICAL IMPLEMENTATION OF MULTIPLICATION SCHEME OF TWO BINARY MATRICES

The optical implementation of the scheme is given in Figure 1. In this scheme we need parallel beam source for the multiplication operation. There are two parallel planes separated by a small distance selected for giving input signal. The first plane takes the input matrix A and the second plane does the same for B. For 3 x 3 matrix multiplication each of the input planes accommodates 27 square pixels or cells (9 x 3) made of either by optical shutters or by optically or electronically triggered spatial light modulators. Each of the cells has a triggering channel for addressing. The addressing signal may be an electronic/opto-electronic/optical signal depending on the material requirement. The character of the cells is that, when they get triggering signal 1 (presence of the proper triggering signal) they become transparent and at the time of withdrawal of the signal they become opaque. Here in the first input plane each cell takes that amount of the input triggering signal which is required for switching the elements of the A matrix. For example to give the inputs in the first plane the first cell in the first row here takes 1, the second cell takes 0 and the third takes 1 triggering signal.

In the same way 4th, 5th and 6th cells of the first row repeat like first, second and third cells respectively. After that 7th, 8th and 9th cells repeats also like first, second and third cells in respect. Following the same procedure each cell is transparent (i.e., 1) in the second row of the first input plane and cells in the third row of the first input plane take the triggering signals 0, 1, 1, 0, 1, 1, 0, 1, 1 respectively from first to last. The triggering signals of the cells in the first plane are given in such a way that the 3 x 3 A matrix comes three times side by side, where the elements (1 or 0) of the matrix A are signified by the transparencies of the cells in the A plane. So one can think, a matrix like

$$\begin{bmatrix} 1 & 0 & 1 & 1 & 0 & 1 & 1 & 0 & 1 \\ 1 & 1 & 1 & 1 & 1 & 1 & 1 & 1 & 1 \\ 0 & 1 & 1 & 0 & 1 & 1 & 0 & 1 & 1 \end{bmatrix}$$

Is appeared in the A plane to represent the input A matrix

$$\begin{bmatrix} 1 & 0 & 1 \\ 1 & 1 & 1 \\ 0 & 1 & 1 \end{bmatrix}$$

In such way any square matrix can be represented by the above process of repeating in series. Here each bit element of the matrix is represented by transparency (opaque or transparent) in the A plane. For example if our input A matrix is

$$\begin{bmatrix} 1 & 0 & 1 & 1 \\ 1 & 1 & 0 & 1 \\ 1 & 0 & 1 & 0 \\ 1 & 0 & 0 & 1 \end{bmatrix}$$

then its representation in A plane will be

$$\begin{bmatrix} 1 & 0 & 1 & 1 & 1 & 0 & 1 & 1 & 1 & 0 & 1 & 1 & 1 & 0 & 1 & 1 \\ 1 & 1 & 0 & 1 & 1 & 1 & 0 & 1 & 1 & 1 & 0 & 1 & 1 & 1 & 0 & 1 \\ 1 & 0 & 1 & 0 & 1 & 0 & 1 & 0 & 1 & 0 & 1 & 0 & 1 & 0 & 1 & 0 \\ 1 & 0 & 0 & 1 & 1 & 0 & 0 & 1 & 1 & 0 & 0 & 1 & 1 & 0 & 0 & 1 \end{bmatrix}$$

Now the procedure of giving 3 x 3 B matrix as input in the second plane of the system, described in figure 1, is a little different.

First 3 x 3 B is transposed.

$$\text{The transposed B is } \begin{bmatrix} 1 & 0 & 1 \\ 1 & 1 & 1 \\ 0 & 1 & 0 \end{bmatrix}$$

There are also 27 cells or pixels in B plane to represent the B matrix, where each cell is made of optical spatial light modulators or optical shutters.

Here 1, 0, 1, the first row elements of the transposed B matrix are given as input respectively to the triggering channels of the 1st, 2nd and 3rd cells of the 1st row, 2nd row and 3rd row in the 2nd plane respectively:

The 2nd row elements 1, 1, 1 of the transposed B matrix will go to the triggering channels of the 4th, 5th & 6th cells respectively in each rows of in the 2nd plane and finally 0, 1, 0, the third row elements of the transposed B matrix will go as inputs to the triggering channels of 7th, 8th and 9th cells respectively in all the rows of the 2nd input plane in figure 1. Thus triggering channels in the 1st, 3rd, 4th, 5th, 6th, 8th cells of all rows in the 2nd plane will get 1 and others will receive 0 to code this input plane properly in accordance to the elements of 3 x 3 B matrix. In such way any 4 x 4 or higher order matrix can be represented in B plane by proper coding of transparencies.

Now in the screen, which is also a parallel plane to the 1st & 2nd input plane, we get the result of the matrix multiplication between A and B. There are nine spots arrayed in 3 rows and 3 columns in the output plane. The 1st spot in 1st row and 1st column of output plane is connected by optical fibers with the optical outputs of 1st, 2nd and 3rd cells in the 1st row of 2nd input plane. Similarly 2nd and 3rd spots in the 1st row of the final output plane is connected with those of 4th 5th, 6th and 7th, 8th, 9th cells in the 2nd input plane respectively. In such way other cells of the output spots are connected. Here any output spot is the logical OR among respective three horizontal and consecutive optical signals from the 2nd input plane. For example spot 2 in the 2nd row and 2nd column of the output matrix gives the sum of light outputs from the 4th, 5th and 6th cells in the 2nd row of the 2nd input plane.

3. AN ALTERNATIVE APPROACH TO GET THE ACTUAL RESULT OF THE MATRIX-MATRIX MULTIPLICATION

The system described in figure 1 holds the output matrix in such a way that each element of the resultant matrix (coming from the product of two binary matrices) is a bit, i.e., either 1 or 0. This scheme can be modified to produce the actual result of the product of the two matrices in the output plane. If we take an example of two matrices

$$A = \begin{bmatrix} 1 & 0 & 1 \\ 1 & 1 & 1 \\ 0 & 1 & 1 \end{bmatrix} \text{ and } B = \begin{bmatrix} 1 & 1 & 0 \\ 0 & 1 & 1 \\ 1 & 1 & 0 \end{bmatrix}$$

then their actual product answer will be

$$P = A \times B = \begin{bmatrix} 10 & 10 & 00 \\ 10 & 11 & 01 \\ 01 & 10 & 01 \end{bmatrix}$$

To get this result we should take the graded level variation of the light intensity corresponding each element representing position in the final output plane. Following this principle if A and B are the two matrices as described above, in the output plane we will get no light (00) in the position of 1st row 3rd element, near about double intensity of light (10) in the position of 1st row 1st element in comparison to the intensity (01) obtained in the position of 3rd row 3rd element. In this modified scheme the element of the result is marked by 00 for no light, 01 for light with some prefixed intensity I_0 , 10 for light with the intensity near about $2I_0$, 11 for light with the intensity nearabout $3I_0$ and so. To get the actual result in the output screen by light intensity demarkation we need to ensure that each light beam carries same intensity to each cell in the A plane and the uniform loss character of the media. The modified scheme is shown in figure 2.

4. CONCLUSION

Here in this scheme of matrix multiplication if the output elements are expressed by 1 (presence of light) and/or 0 (absence of light signal). The result of multiplication will be represented as

$$P = A \times B = \begin{bmatrix} 1 & 1 & 0 \\ 1 & 1 & 1 \\ 1 & 1 & 1 \end{bmatrix}$$

for the product of the matrices taken in the example.

Otherwise if the elements of the output (resultant) matrix of the product are represented by their graded level intensity radiation we will get the exact result as

$$P = A \times B = \begin{bmatrix} 10 & 10 & 00 \\ 10 & 11 & 01 \\ 01 & 10 & 01 \end{bmatrix}$$

in the screen for the product of the matrices used in the example.

For multiplication between any two 3×3 matrices the system in fig. 1 can be used satisfactorily. The system can be extended horizontally and vertically for uses of multiplication of 4×4 or any higher order matrices. This type of matrix multiplication will be very much useful in pixel based digital image processing.

REFERENCES

1. J.N. Roy, and S. Mukhopadhyay, 'A minimization scheme of optical space-variant logical operations in a combinational architecture', opt. commn. **119**, pp. 499-504, 1995.
2. A.A. Sawchuck, and T.C. Strand, 'Digital Optical Computing', Proc. IEEE, **72**, pp. 758-779, 1984.
3. A. Huang, Y. Tsunoda, J.W. Goodman, and S. Ishihara, 'Optical Computation using residue arithmetic', Appl. Opt., **18**, pp. 149-162, 1979.
4. S. Mukhopadhyay, J.N. Roy, and S.K. Bera, 'Design of a minimized LED array for maximum parallel logic operations in optical shadow casting technique', opt. commn. **99**, pp. 31-37, 1993.
5. S. Mukhopadhyay, 'Binary optical data subtraction by using a ternary dibit representation technique in optical arithmetic problems, Appl. opt. **31**, pp. 4622-4623, 1992.
6. M.T. Fatehi, K.C. Wasmundt, and S.A. Collins, Jr., 'Optical flip-flops and Sequential logic circuits using a liquid crystal light valve', Appl. Opt. **23**, pp. 2163-2171, 1984.

7. P. Ghosh, D.N. Das, and S. Mukhopadhyay, 'All alternative approach of optical flip-flop with tristate logic', *Indian J. Pure. Appl. Phys.*, **36**, pp. 224-227, 1998.
8. W. Wu, S. Campbell, S. Zhou, and P. Yeh, 'Polarization encoded optical logic operations in photorefractive media', *opt. Lett.* **18**, pp. 1742-1744, 1993.
9. C. Denz, T. Dellwig, J. Lembeke, and T. Tschudi, 'Parallel optical image addition and subtraction in a dynamic photorefractive memory by phase code multiplexing', *opt. Lett.* **21**, pp. 278-283, 1996.
10. S. Mukhopadhyay, and D.N. Das, 'Image edge detection and enhancement by inversion operation', *Appl. Opt.* **37**, pp. 8254-8256, 1998.
11. S. Mukhopadhyay, P. Ghosh, and D. Dutta, 'A Conversion Scheme of decimal number to its residue for optical computation', *Indian J. Pure. Appl. Phys.* **30**, pp. 322-326, 1992.
12. A. Basuray, S. Mukhopadhyay, H.K. Ghosh, and A.K. Datta, 'A tristate optical logic system', *Opt. Commn.* **85**, pp. 167-171, 1991.
13. R.A. Athale, and W.C. Collins, 'Optical matrix-matrix multiplier based on outer product decomposition', *Appl. Opt.* **21**, pp. 2089-2092, 1982.
14. S. Cartwright, 'New optical matrix-reactor multiplier', *Appl. Opt.* **23**, pp. 1683-1686, 1984.
15. R.P. Bocker, S.R. Clayton, and K. Bromley, 'Electro-optical matrix multiplication using the twos complement arithmetic for improved accuracy', *App. Opt.* **22**, pp. 2019-2023, 1983.
16. C. Gu, S. Campbell, and P.Yeh, 'Matrix-matrix multiplication by using grating degeneracy in Photorefractive media', *opt. Lett.* **18**, pp. 146-148, 1993.
17. B. Liu, L. Liu, L. Shao, and H. Chen, 'Matrix-vector multiplication in a photorefractive crystal', *Opt. Commn.* **146**, pp. 34-38, 1998.

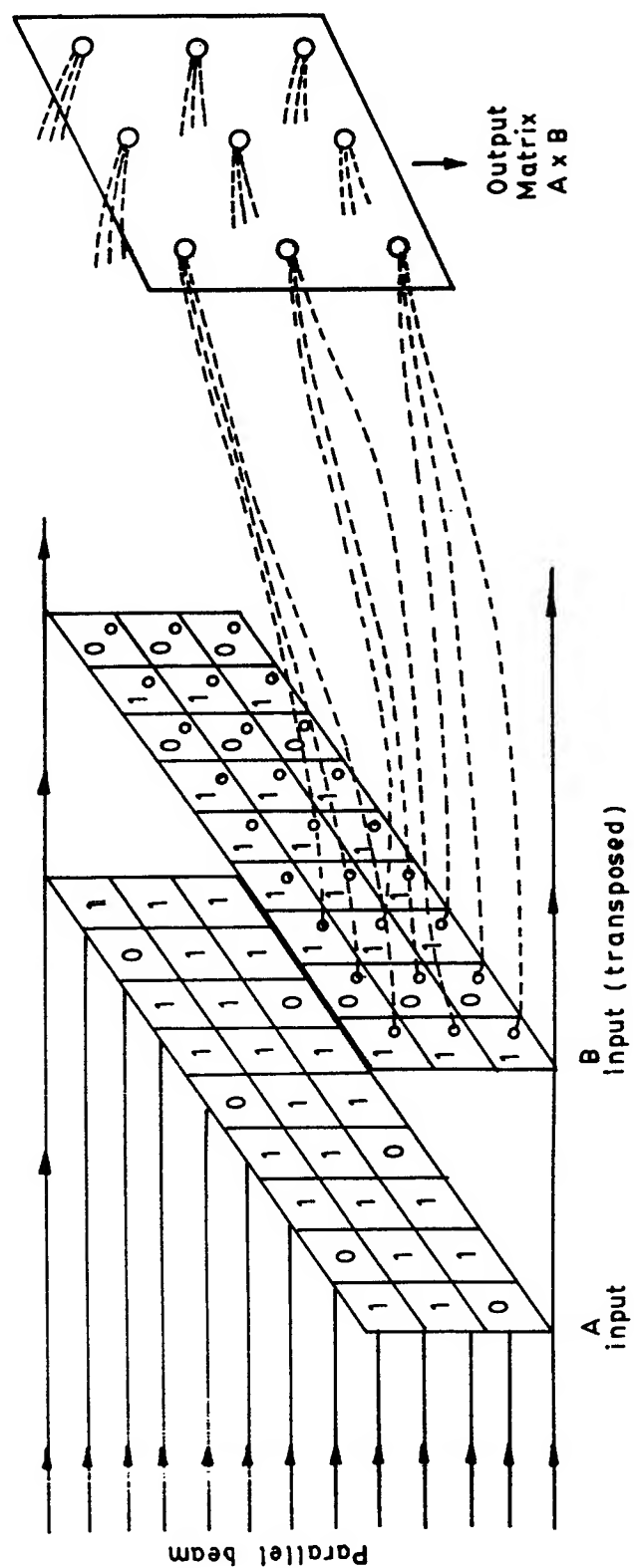


Fig. 1 : An optical (3x3) matrix multiplication system.

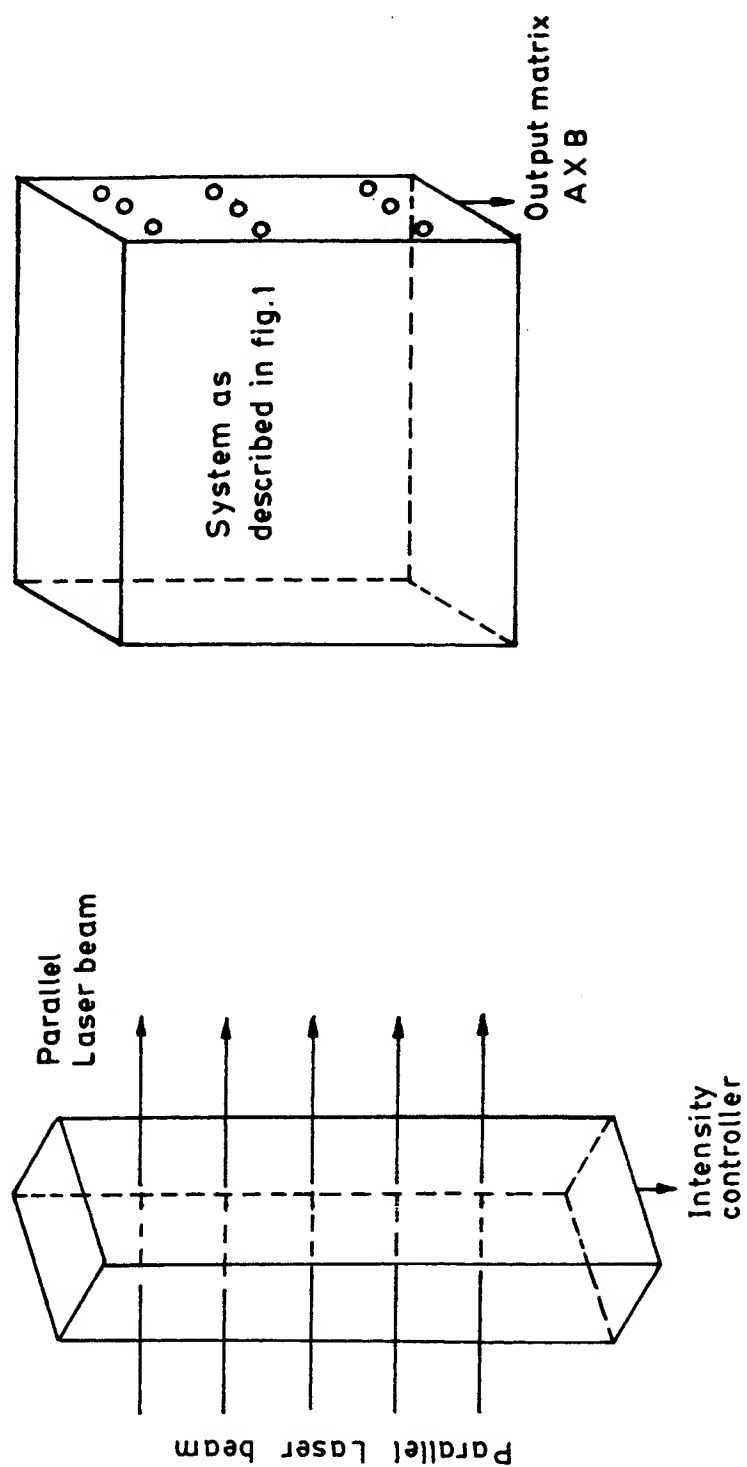


Fig. 2 : A modified scheme for 3 x 3 matrix-matrix multiplication

SESSION 8

Optical Storage

Surface Emitting Lasers for Optical Near-field Data Storage

Fumio Koyama^a, Satoshi Shinada^a, Kenya Goto^b and Kenichi Iga^a

^aPrecision & Intelligence Laboratory, Tokyo Institute of Technology
4259 Nagatsuta, Midori-ku, Yokohama 226-8503, Japan

Tel: +81-45-924-5068, Fax: +81-45-924-5961, E-mail: koyama@pi.titech.ac.jp

^bSchool of High-Technology for Human Welfare, Tokai University
Nishino 317, Numazu-city, Shizuoka 410-03, Japan

ABSTRACT

One of interesting applications of two dimensional VCSEL arrays is high density optical data storage. We proposed a micro-metal aperture VCSEL for producing optical near-field. The evanescent wave emitted from a small metal aperture formed on a VCSEL surface is irradiated to an optical disk, such as a phase change optical disk. We carried out a near-field analysis on the radiation from the metal micro aperture loaded on a VCSEL by using 2-dimensional finite element method (FEM), showing a possibility of a spot size of below 100 nm. We can recycle the reflected wave from the metal aperture, when we properly design the phase matching between the DBR mirror and the metal. We can expect an improvement in a power conversion efficiency of radiating near field light from the aperture by using a "photon recycling" effect. An expected efficiency and power density are discussed for 850 nm metal aperture VCSELs.

We have fabricated micro-metal aperture VCSELs by using focus ion beam etching. The size of the fabricated apertures ranges from 100 nm and 400 nm. We have realized sub-mA low threshold metal aperture VCSELs. The power density is estimated to be $\sim 6 \text{ kW/cm}^2$. We will be able to improve the power density by reducing the oxide aperture in the cavity. We also discuss on another way to increase the efficiency and the power density, such as using a surface plasmon effect of a small metal tip formed on the surface. We will discuss a possibility of optical near-field recording by using the proposed metal aperture VCSEL.

Keywords: semiconductor laser, surface emitting lasers, near field optics, optical data storage, optical disk

1. INTRODUCTION

An ultra-high density optical memory using near field optics has been attracting much interest for future Tera byte optical data storage¹. Betzig and coworkers demonstrated an optical recording by a near-field scanning optical microscope (NSOM) and suggested a possibility of Tera byte data storage². One of the authors (K. Goto) proposed a Tera byte optical memory system using a vertical cavity surface emitting laser (VCSEL) array³. The proposed optical disk system is based on an optical head consisting of a 2-dimensional VCSEL array. It is important to realize a high-efficiency VCSEL for near field optical heads by reducing the total power consumption in arrays. We proposed a micro-apertured VCSEL for producing optical near field with high efficiency and carried out two-dimensional finite element method (FEM) analysis for such a device^{4,5}. A VCSEL having a GaAs near-field probe was demonstrated by using a hybrid integration approach⁶. Also, near-field optical recording was demonstrated using a metal apertured edge emitting laser⁷.

In this paper, we carried out a near field analysis of a micro-aperture VCSEL by using 2-dimensional finite element method (2-D FEM). In addition, we fabricated a VCSEL with a micro-aperture on Au top surface by using focus ion beam etch. Reasonably low threshold operation was achieved and the radiated power from the micro-aperture was measured. Prospects of micro-metal apertured VCSELs will be described.

2. METAL APERTURE SURFACE EMITTING LASERS

Figure 1 shows the schematic view of a VCSEL optical writing head with a contact head technology^{3,8}. If we confine photons in a micro-cavity, optical near-field can be efficiently produced from a sub-wavelength sized aperture formed in the micro-cavity. The evanescent wave emitted from a small metal aperture formed on a VCSEL surface is irradiated to an optical disk, such as a phase change optical disk. The differential quantum efficiency of the present VCSEL reaches

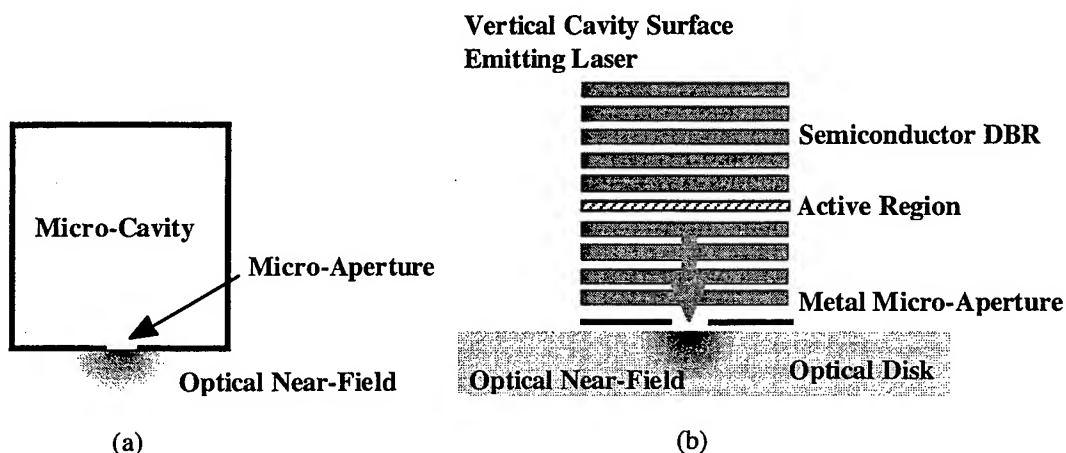


Fig. 1 (a) Generation of optical near-field from small-apertured micro-cavity
(b) Optical recording by using metal-apertured VCSEL

95 %, but a single mode output power has been limited below 5 mW⁹. Thus, the optical power density may not be enough for optical recording. The reflected wave from the metal surface can be coupled again to the laser cavity, when we properly design the phase matching between the DBR mirror and the metal aperture shown in Fig. 1(b). Thus, we can recycle photons confined in the micro-cavity. Figure 2 shows the calculated optical power density from the aperture as a function of the effective mirror reflectivity of the composite mirror. We assumed that the lasing wavelength is 850 nm, the internal absorption loss is 10 cm⁻¹ and the throughput at the micro-aperture is -10 dB. An increase in the power density can be achievable by using the "photon recycling" effect. A possibility of high efficient VCSEL optical heads using a micro-metal aperture is suggested.

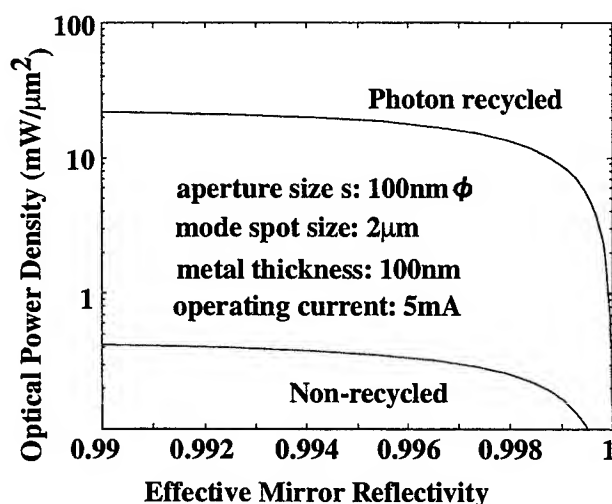


Fig. 2 Calculated optical power density of optical near-field at a micro-aperture.

3. NEAR FIELD ANALYSIS BY USING 2-D FINITE ELEMENT METHOD

Figure 3(a) shows a schematic structure of our proposed metal aperture VCSEL. The surface of a top emitting VCSEL is coated by a Au film and the optical near field radiates from a sub-wavelength size micro-aperture formed in this Au film. The n-type GaAlAs/AlAs distributed Bragg reflector (DBR) has typically 36.5 pair, and the p-type DBR is designed to consist of 11 pair, that is about a half of a conventional mirror design in VCSELs. When we design the phase matching between the top DBR mirror and the metal, the composite mirror of Au and the top DBR gives us a high reflectivity. The calculated reflectivity of the Au-film-loaded 11 pair DBR without the micro-aperture is 99.3%, which is comparable to that of a 22 pair DBR without metal terminating. An oxide confinement structure is also used for single transverse mode operation. The micro-aperture is placed at the center position of the Al oxide aperture. We have assumed that the wavelength is 850 nm. Note that the computed result can be available by scaling down the aperture with reducing the wavelength. This means that the micro-aperture can be reduced for shorter wavelengths.

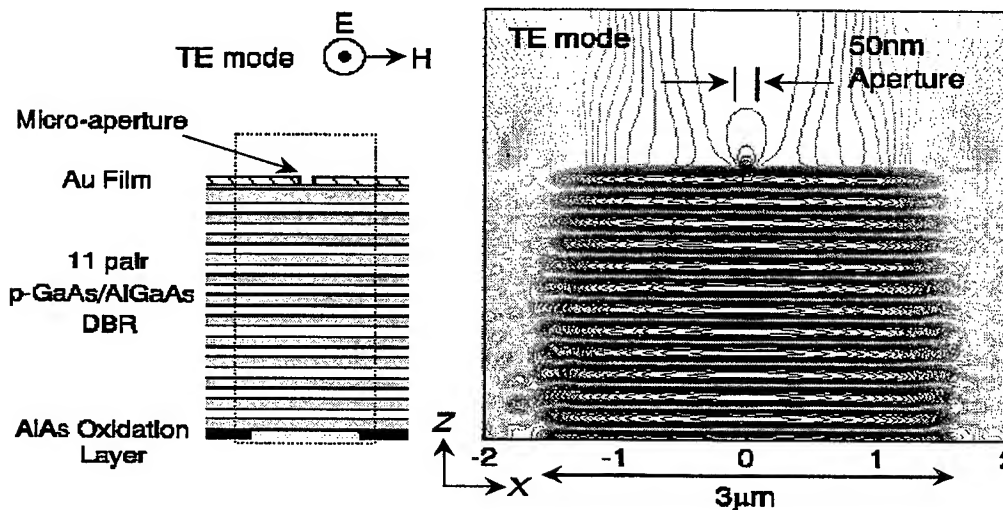


Fig. 1. (a) Schematic structure of a VCSEL with a metal micro aperture
(b) Intensity distribution calculated by 2-D FEM.

(thick Au film: 50 nm, micro-aperture width: 50 nm, oxide aperture width: 3 μm).

We calculated the intensity distribution in the part of the VCSEL surrounded by dashed line in Fig.3(a) by using a 2-D FEM⁵. Figure 3(b) shows the calculated intensity distribution by 2-D contour plot⁵. A thickness of Au film and a width of a micro-aperture are 50 nm. In this calculation, we have assumed that the electric field is perpendicular to the sheet. We define the electric field perpendicular and parallel to the sheet as TE and TM modes, respectively. The light is confined laterally by a 3 μm wide Al oxide aperture and the periodic distribution in the DBR shows a standing wave. An evanescent wave is produced in the air through the micro aperture. Figure 4 shows the calculated intensity distribution across the cavity at the center of the aperture for various aperture widths. The near-field intensity decreases with decreasing the micro-aperture width. A node position near the boundary between GaAs and Au slightly shifts to the DBR side with decreasing the aperture width, because of the effect of the boundary condition between GaAs and Au. The attenuation of the intensity in the 100 nm wide micro-aperture is 5 dB in comparison with a 3 μm wide aperture. We found the attenuation of TM modes is smaller than that of TE modes, because the boundary condition is different between electric and magnetic fields in the aperture. Also, we found that the attenuation can be reduced if we fill the inside of the micro-aperture with a material with high refractive index because the wavelength in the aperture becomes shorter equivalently. In case that a filling material is GaAs, the attenuation decreases to 1.5 dB at a 100 nm wide aperture.

Figure 5 shows the intensity profile of output through a 100 nm aperture for TE mode at the bound between Au and air. The spot size (FWHM) is as small as 99 nm comparable to the aperture width, which is much smaller than the wavelength.

Figure 6 shows the calculated spot size at the bound between Au and air as a function of the aperture width for TE and TM modes. Below 50 nm of aperture width for TE modes, the spot size increases because of penetrating light through the Au film. On the other hand, the spot size of TM modes decreases monotonically. The minimum spot size is about 70 nm at a 30 nm wide aperture for TM modes. Therefore, the proposed VCSEL structure can produce a locally confined light beyond the optical diffraction limit. It is noted that a VCSEL with a shorter wavelength will be able to make a smaller spot size.

The transverse mode control is also an important issue to realize efficient near-field radiation, because higher-order transverse modes have nodes at the position of the micro-aperture. We calculated the mode reflectivity of the micro-aperture loaded DBR for transverse modes, which are defined by the 3 μm wide oxide aperture. The mode reflectivity is defined as the ratio of reflected light coupling to the incident mode, which is defined in the $\text{AlAs}/\text{Al}_x\text{O}_y$ aperture. Figure 7 shows the calculated mode reflectivity depending on the metal aperture width. A reflectivity of more than 99% can be obtained at an aperture of less than 100 nm for the TE mode. The reflectivity of the first order mode becomes larger than the fundamental mode at a metal aperture of larger than 200 nm because the radiation from the aperture deteriorates the reflectivity of the fundamental mode. We expect that a fundamental mode operation can be maintained when the oxide aperture width is reduced less than 1 μm for stable transverse mode control.

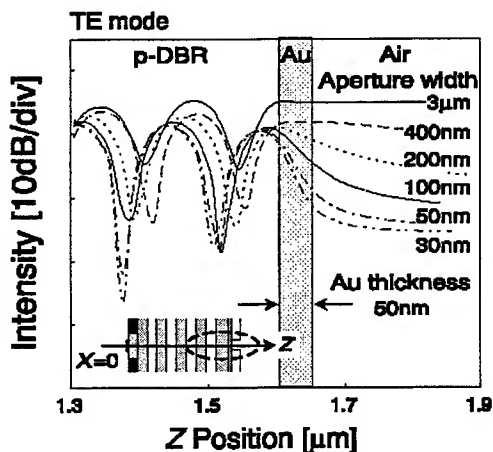


Fig. 5 Intensity profile of the output through 100 nm wide micro-aperture for TE mode⁵.

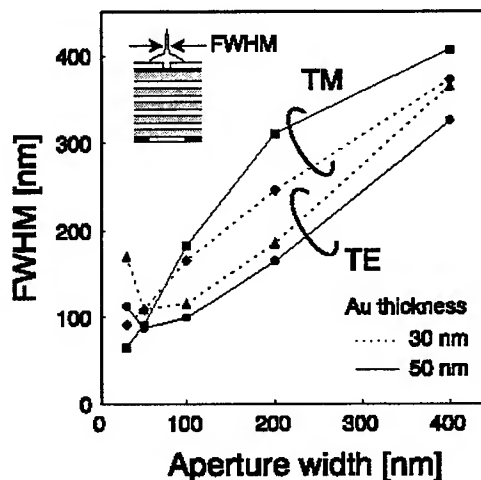


Fig. 6 The spot size (FWHM) as a function of the aperture width for TE and TM modes⁵.

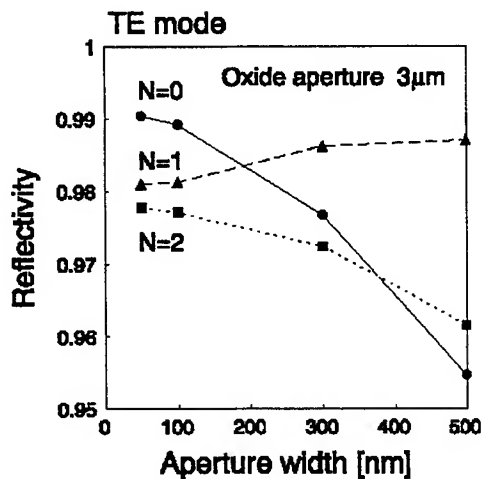


Fig. 7 Mode reflectivity versus micro-aperture width for various transverse modes. N shows the mode number in the figure⁵.

4. FABRICATION AND CHARACTERIZATION

We fabricated a Au-film loaded VCSEL prior to forming a micro-aperture¹⁰. The active region consists of GaAs/GaAlAs triple quantum wells. The active region (oxide aperture) diameter is 3~4 μm . The lasing wavelength of VCSELs is 850 nm. Figure 8 shows I-L characteristics of VCSELs with various thicknesses of Au film. Only spontaneous emission was observed for 10~20 nm thick Au film loaded devices. About 30 nm is a critical thickness for a laser oscillation, but its threshold current was high. A slope efficiency began to decrease because of absorption when the Au film thickness was more than 60 nm. This reduction of slope efficiency is in agreement with calculated differential efficiency depending on the Au absorption. The Au film thicker than 100 nm can block the emission light. We obtained a threshold current as low as $\sim 700 \mu\text{A}$ corresponding to 3 kA/cm^2 of threshold current density. It indicates that the composite mirror consisting of a Au thin film and small pair p-DBR can give us a high reflectivity for reasonably low threshold operations.

To fabricate metal micro-apertures, we used a focused ion beam (FIB) etch with Ga^+ ion sources. The fabricated micro-aperture was as small as 100 nm on a 100 nm thick Au film and its image observed by using atomic force microscope (AFM) is shown in Fig. 9. We fabricated and tested VCSELs having micro-apertures with diameters ranging from 100 nm to 1 μm on a 100 nm thick Au film terminating semiconductor. Figure 10 shows I-L characteristics of a VCSEL before and after forming a 400 nm micro-aperture¹⁰. This sample has a 8 μm oxide aperture and the threshold current is 1.7 mA, which almost unchanged. We measured the output power using a Si detector with $10 \times 10 \text{ mm}^2$ area separated by 3 mm from the device. We assumed that the radiation from the micro-aperture is spherical because the size of the aperture is smaller than a half of wavelength. Thus, we estimated that 50 percent of the total output power radiated from the aperture is detected. The output power from the 400 nm aperture is estimated to be 10 μW at 5 mA.

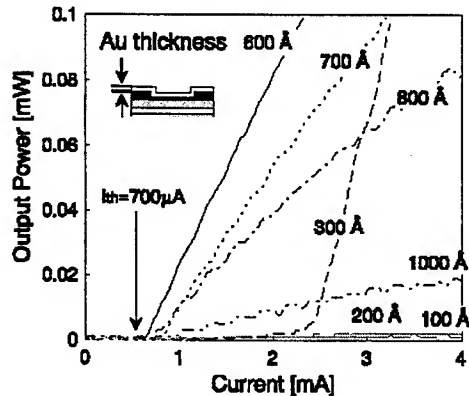


Fig. 8 I-L characteristics of Au film loaded VCSEL before fabricating a micro-aperture¹⁰.

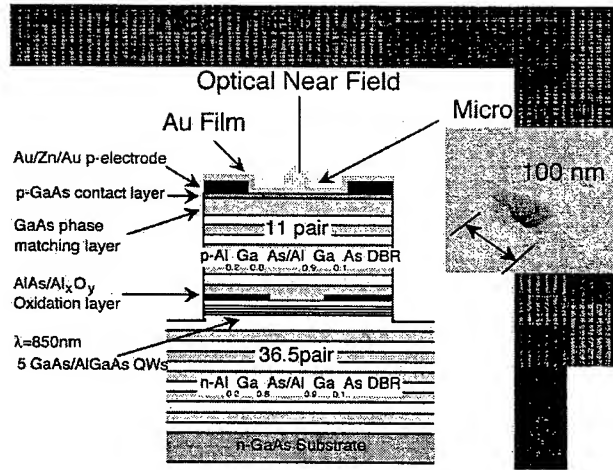


Fig. 9 Schematic structure of metal micro-aperture VCSEL¹⁰.

Figure 11 shows the intensity profile of near field patterns below the threshold for various aperture sizes between 100 nm and 1 μm ¹⁰. We measured these patterns by using a conventional optical microscope with a spatial resolution of about 1 μm . A broad emission with full width at half maximum (FWHM) of 7 μm is originated from light through the Au film. The peak shown on the center of emission light is attributed to the radiation from the aperture. Its FWHM is about 1 μm which is equal to the diffraction limit of the optical microscope we used in this measurement. It is also considered that the peak intensity may have been reduced by the diffraction-limited resolution. Thus, the real peak intensity should be much higher than that of the background light through the Au film. The output power density of a 400 nm-aperture VCSEL at a bias current of 5 mA is estimated to be $0.06 \text{ mW}/\mu\text{m}^2$, which is calculated from the differential power in Fig. 10 and the aperture size.

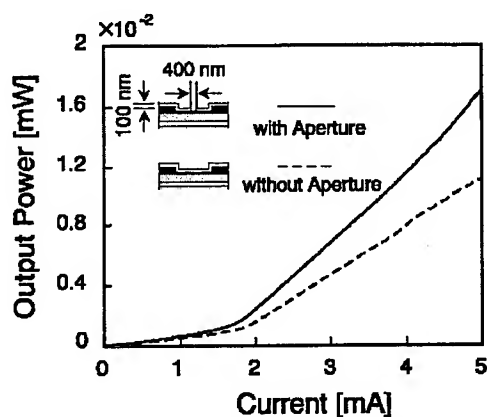


Fig. 10. I-L characteristics of a VCSEL with and without a 400 nm aperture. The Au thickness is 100 nm¹⁰.

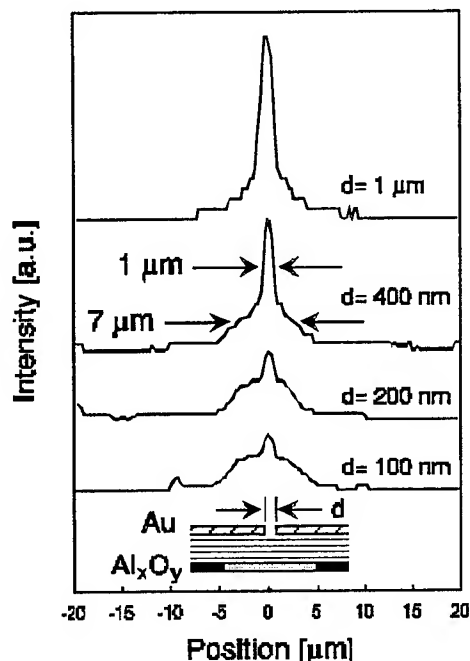


Fig. 11. Near field patterns of a VCSEL with various metal aperture sizes measured by a conventional microscope with a spatial resolution of 1 μm¹⁰.

The estimated power level may be insufficient for optical recording in disk memories. The power density in the present device is partly limited by its large oxide aperture ($\sim 8 \mu\text{m}$). One way to increase the power density is to reduce the oxide aperture in the cavity. For example, if $1 \times 1 \mu\text{m}$ small oxide apertures are used, the power density may be increased by a factor of more than 50. Also, the problem is that higher-order transverse modes appear above the threshold, which was observed in experimental devices. Higher order modes should significantly decrease the power density because these modes have nodes at the position of the micro-aperture. We have to realize a single mode operation for increasing the power density at the micro-aperture. Another possible way to increase the power density is to use surface plasmons¹¹, enhancing optical near field by putting a metal tip in the micro-aperture as shown in Fig. 12.

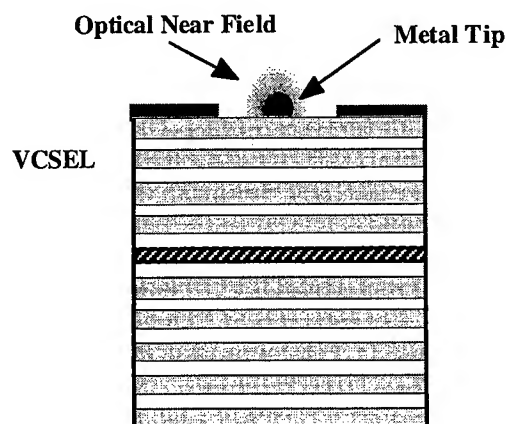


Fig. 12 Enhancement of optical near-field by using localized surface plasmon.

5. CONCLUSION

The modeling and experiment on micro-metal aperture VCSELs were presented. The photon recycling effect is helpful for increasing the device efficiency. The same concept may be useful for realizing a VCSEL reading optical head by integrating a photo-detector in the laser cavity. We presented the near field analysis of this novel VCSEL, which shows a possibility of producing a narrow spot of 100 nm beyond diffraction limit. Also, we fabricated a VCSEL with a metal micro-aperture. The metal and semiconductor DBR composite mirror provides a reflectivity of more than 99%, which resulted in a reasonably low threshold current density of 3 kA/cm² in fabricated devices. We fabricated a micro-aperture as small as 100 nm by FIB. We evaluated the output power radiated from the micro-aperture and discussed on the method for obtaining higher intensity. Further study may open up a new function of 2-D VCSEL arrays for use in high capacity data storage.

6. ACKNOWLEDGEMENTS

The authors thank A. Matsutani, N. Nishiyama and M. Arai for their help in experiment. This study was supported by Grant-in-Aid for COE Research from the Ministry of Education, Science, Sports and Culture (#07CE2003, "Ultra-parallel Optoelectronics").

7. REFERENCES

1. M. Ohtsu: "Near-Field Nano/Atom Optics and Technology," Spriger-Verlag, 1997
2. E. Betzig, J.K. Trautman, R. Wolfe, E.M. Gyorgy, P.L. Finn, M.H. Kryder and C.-H. Chang: Appl. Phys. Lett. **61**, p.142, 1992.
3. K.Goto: Jpn. J. Appl. Phys. **37**, Pt 1, No.4B, p.2274, 1998.
4. F. Koyama, K. Goto and K. Iga: OECC'98, 16D1-4, 1998.
5. S. Shinada, F. Koyama, K. Suzuki, K. Goto and K. Iga, CLEO-PR'99, ThD-4, 1999.
6. C. Mihalcea: NAIR/OITDA Workshop on Ultrahigh Density Data Storage, March, 1999.
7. A. Partovi, ISOM/ODS'99, ThC-1, 352, 1999.
8. H. Ukita, Y. Katagiri and S. Fujimori, Appl. Opt., **28**, pp.4360-4365, 1989.
9. R. Jager, M. Grabherr, C. Jung, R. Michalzik, G. Reiner, B. Weigl and K. J. Ebeling, Electron. Lett., **33**, pp.330-331, 1997.
10. S. Shinada, F. Koyama, N. Nishiyama, M. Arai, K. Goto and K. Iga, Extended Abstracts of 1999 International Conference on Solid State Devices and Materials, E-7-2, 1999.
11. U.C. Fischer and D.W. Pohl, Phys. Rev. Lett., **62**, p.458, 1989.

Diffraction property of Volume grating in Ce:KNSBN with different polarized reading beam

Zhaoqi Wang*, Baolai Liang, Guoguang Mu, Jiuhong Guan, Hongli Liu, Rulian Fu

(Opto-electronic Information Science and Technology Lab, E.M.C

Institute of Modern Optics, Nankai University, Tianjin 300071, P.R.China)

ABSTRACT

The diffraction efficiency of volume grating written by two-wave mixing in Ce:KNSBN photorefractive crystal as a function of the writing beam ratio for different polarized reading beam is experimentally studied. It is found that, the polarization and the incident direction of the reading beam strongly affect the diffraction efficiency. In the selected direction, the extraordinarily polarized reading beam obtains enhanced diffraction and achieves nearly fifteen times larger diffraction efficiency than the ordinarily polarized reading beam. The modified coupled-wave theory is used to fit the experimental data and the fitting results are coincident with the experimental results. We also theoretically examined the relation between the diffraction efficiency and the amplitude coupling constant κ of the reading beam and its diffracted beam. As $\kappa < 6\text{cm}^{-1}$, the diffraction efficiency has single maximum and the maximum diffraction efficiency increases as κ increases. As $\kappa > 6\text{cm}^{-1}$, the diffraction efficiency curves exhibit two peaks. But the central position of the curves does not change with the variation of κ .

Key word: Photoactivity, diffraction efficiency, volume grating, energy transfer,

1. INTRODUCTION

Since the discovery of the photorefractive effect, photorefractive materials have been regarded as the promising candidates for holographic storage and optical image processing applications.¹⁻⁴ Potassium sodium strontium barium niobate (KNSBN) crystals have received considerable attention because they are easy to prepare and have large photorefractive (PR) nonlinearities as well as suitable sensitive spectrum range.^{5,6} In addition, they have low degrees of lattice occupancies, PR species and hence PR responses can be controlled by introduction of dopants into their lattice sites.^{7,8} So far, two-beam coupling measurement and self-pumped phase conjugation for KNSBN crystals have been investigated.⁹⁻¹³ Recently the superior real-time holographic storage performance in Co:KNSBN has also been demonstrated.¹⁴

In the holographic applications, the diffraction behavior is the first important matter characterizing the performance merits of the PR crystal. But until now, the relation between the diffraction efficiency and the polarization of the reading beam for the volume grating in Ce:KNSBN crystal has not been reported yet. In this research, we experimentally studied the diffraction efficiency of the volume gratings in Ce:KNSBN versus the writing beam intensity ratio for different polarized reading beam. It is found that the diffraction efficiency strongly depends on the reading beam polarization and the readout direction. In the selected direction, the extraordinarily polarized reading beam obtains enhanced diffraction and achieves nearly fifteen times larger diffraction efficiency than the ordinarily polarized reading beam. Then we used the modified coupled-wave theory to fit our experimental data, and obtained satisfactory results. Finally we theoretically examined the relation between the diffraction efficiency and the amplitude coupling constant κ of the reading beam and its diffracted

* Correspondence: Email: wangzq@sun.nankai.edu.cn Tel: +86-22-23508332

beam. As $\kappa < 6\text{cm}^{-1}$, the diffraction efficiency has single maximum and the maximum diffraction efficiency increases as the κ increases. As $\kappa > 6\text{cm}^{-1}$, the diffraction efficiency curves exhibit two peaks. But the central position of the curves does not change with the variation of κ .

2. EXPERIMENTS

Experimental arrangement is shown in Fig. 1. The beam splitter BS split the Ar⁺ 514.5nm laser beam into two beams of equal intensity. One beam, passing through the reflector M1, the half wave plate HWP1 and the polarizer P1, incidents on the crystal as the writing beam I_p . The other beam, passing through the reflector M2, the half wave plate HWP2 and the polarizer P2, incidents on the crystal as the writing beam I_s . The bisector of I_p and I_s is normal to the c -axis of the crystal. The polarization and the intensity of I_p and I_s can be adjusted by the half wave plates and the polarizers. At the other side of the crystal, the He-Ne 632.8nm laser beam, passing through the half wave plate HWP3 and the polarizer P3, incidents on the crystal with Bragg diffraction angle θ as the reading beam I_r . The intensity and the polarization of I_r are also adjusted by the half wave plate and the polarizer. The diffracted beam I_D is captured by the detector. To satisfy with the weak readout beam condition and to eliminate the eration effect of the reading beam on the recorded grating, we kept $I_s + I_p \geq 80\text{mW/cm}^2$ and $I_r = 20\mu\text{W/cm}^2$. We carefully expended the writing and reading beams to reduce the error caused by not overlapping of the beams. The experiments were carried out on a sample of Ce:KNSBN crystal of dimensions $5 \times 5 \times 5.5\text{ mm}^3$ obtained from Shandong University, China.

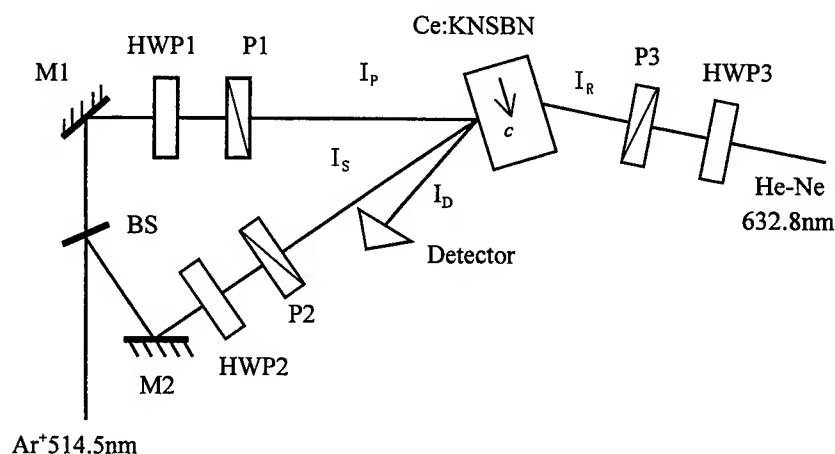
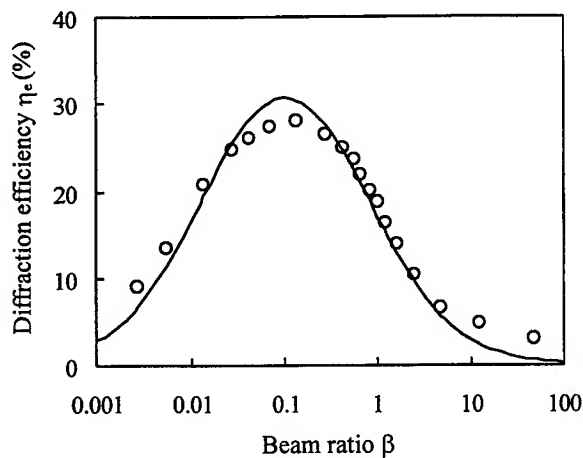
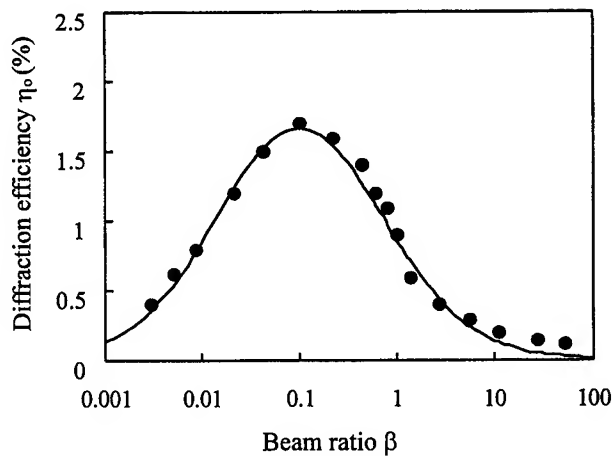


Fig.1. Scheme of experimental setup

Firstly we examine the relation between the diffraction efficiency and the writing beam ratio for the grating written by extraordinarily polarized beams. The experimental data are shown in Fig. 2 with small circles. (The solid curves are theoretically fitting results of Eq.5 in section 3.). Fig. 2(a) is for the case that the reading beam is of extraordinary polarization. It can be seen that the diffraction efficiency η_e increases monotonically from 9% as the beam ratio increases from $\beta=0.003$. As the beam ratio increases to $\beta=0.11$, the diffraction efficiency reaches its maximum value of 28%. Then the diffraction efficiency decreases monotonically as the beam ratio increases. As the beam ratio increases to $\beta=1$, the diffraction efficiency decreases to 19%. As the beam ratio increases to $\beta=50$, the diffraction efficiency falls to 3%. Fig.2 (b) is for the case that the reading beam is of ordinary polarization. It can be seen that the diffraction efficiency η_o increases

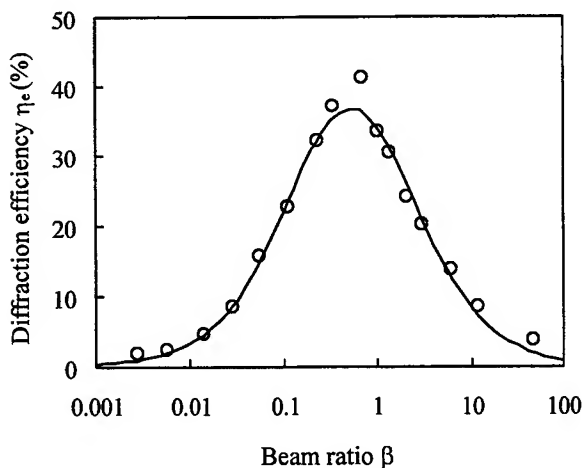


(a) for the extraordinarily polarized reading beam
(o: experimental data of η_e ; —: theoretical fitting curve).

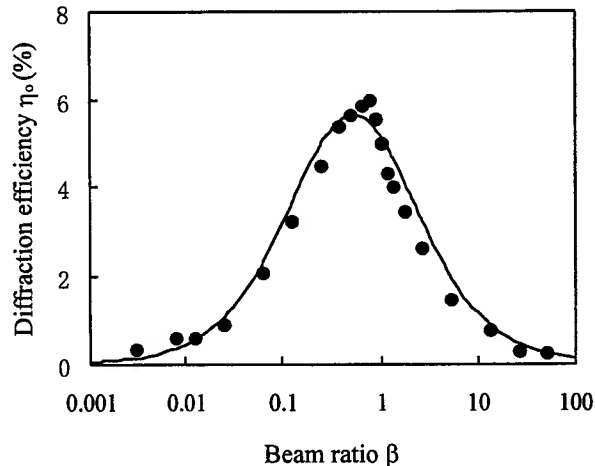


(b) for the ordinarily polarized reading beam
(•: experimental data of η_o ; —: theoretical fitting curve).

Fig.2. Diffraction efficiency η as a function of the beam ratio β for the grating writing by extraordinarily polarized beams.



(a) for the extraordinarily polarized reading beam
(o: experimental data of η_e ; —: theoretical fitting curve).



(b) for the ordinarily polarized reading beam
(•: experimental data of η_o ; —: theoretical fitting curve).

Fig.3. Diffraction efficiency η as a function of the beam ratio β for the grating writing by ordinarily polarized beams.

monotonically from 0.4% as the beam ratio increases from $\beta=0.003$. As the beam ratio increases to $\beta=0.11$, the diffraction efficiency reaches its maximum value of 1.8%. Then the diffraction efficiency decreases monotonically as the beam ratio increases. As the beam ratio increases to $\beta=1$, the diffraction efficiency decreases to 0.9%. As the beam ratio increases to $\beta=50$, the diffraction efficiency falls to $\eta_o=0.12\%$. It can also be seen in a comparison of Fig. 2(a) and Fig. 2(b) that the

maximum η_e is about fifteen times larger than the maximum η_o , but η_o and η_e both reach the maximum value at writing beam ratio $\beta=0.11$.

Secondly we examine the relation between the diffraction efficiency and the writing beam ratio for the grating written by ordinarily polarized beams. The experimental data are shown in Fig. 3 with small circles. (The solid curves are theoretically fitting results of Eq.5.). Fig. 3(a) is for the case that the reading beam is of extraordinary polarization. It can be seen that the diffraction efficiency η_e increases monotonically from 1.9% as the beam ratio increases from $\beta=0.003$. As the beam ratio increases to $\beta=0.67$, the diffraction efficiency reaches its maximum value of 41%. Then the diffraction efficiency decreases monotonically as the beam ratio increases. As the beam ratio increases to $\beta=1$, the diffraction efficiency decreases to 31%. As the beam ratio increases to $\beta=50$, the diffraction efficiency falls to $\eta_e=3.8\%$. Fig. 3(b) is for the case that the reading beam is of ordinary polarization. It can be seen that the diffraction efficiency η_o increases monotonically from 0.36% as the beam ratio increases from $\beta=0.003$. As the beam ratio increases to $\beta=0.67$, the diffraction efficiency reaches its maximum value of 6.1%. Then the diffraction efficiency decreases monotonically as the beam ratio increases. As the beam ratio increases to $\beta=1$, the diffraction efficiency decreases to 5%. As the beam ratio increases to $\beta=50$, the diffraction efficiency falls to $\eta_o=0.25\%$. The maximum η_e is nearly seven times larger than the maximum η_o , but η_o and η_e both reach the maximum value at $\beta=0.67$.

So no matter how the writing beam polarization are, the diffraction efficiency for the extraordinarily polarized reading beam is much larger than that for the ordinarily polarized reading beam. This enhancement is caused by the energy transfer between the reading beam and the diffracted beam. In the selected direction, extraordinarily polarized reading beam has much more energy transfer to the diffraction beam.

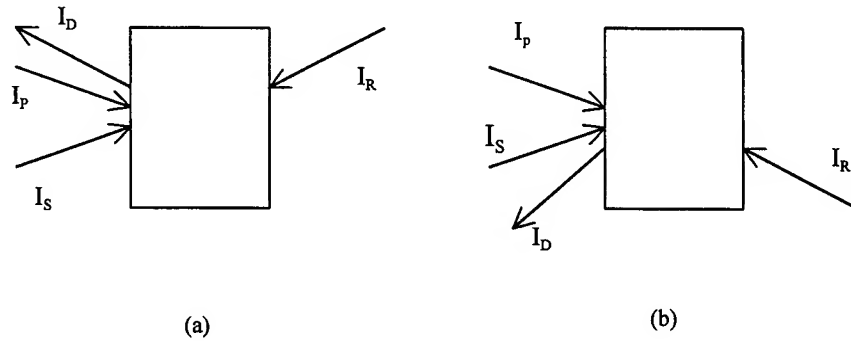


Fig.4. Different readout geometry

We experimentally verified it with the gratings written by the ordinary polarization beams. Firstly, we use extraordinarily polarized beam to read out the grating according to the geometry shown in Fig. 4(a) at $\beta=0.67$. The measured diffraction efficiency is equal to 3%. Then we change to the reading geometry shown in Fig. 4(b). The diffraction efficiency equal to 41%, which is enhanced nearly fifteen times and is coincident with our assumption. Secondly, we use ordinarily polarized beam to read out the grating according to the geometry shown in Fig. 4(a) at $\beta=0.67$. The diffraction efficiency is equal to 5%. Then we change to the reading geometry shown in Fig. 4(b). The diffraction efficiency is equal to 6.1%, which only increases slightly. This indicates a weak coupling effect between the reading and the diffracted beam with ordinary polarization.

3. THEORETICAL ANALYSIS

The diffraction efficiency of a volume grating with uniform index modulation is described by the Kogelnik formula¹⁵,

$$\eta = \sin^2(\pi \Delta n L / \lambda \cos \theta) \quad (1)$$

where Δn is the index modulation amplitude, L is the thickness of the grating, θ is the Bragg angle for the reading beam, and λ is the reading beam wavelength. However, the photorefractive grating is no longer uniform due to the coupling between the writing beams. Hence formula (1) should be modified. After considering the coupling effect of the writing beams, and assuming that the reading beam is satisfied with the weak readout condition, Yue et al and Hong et al respectively introduced the modified couple-wave theory to describe the diffraction efficiency of photorefractive gratings in SBN and BaTiO₃.^{16, 17}

By following standard methods for steady-state coupled-wave problems, using the slowly varying approximation for the amplitudes of the reading beam A_R and the diffracted beam A_D , and assuming that the reading beam is satisfied with the Bragg condition, we can obtain the coupled-wave equations,

$$\begin{aligned} \frac{dA_R}{dz} &= \frac{-\alpha}{2 \cos \theta} A_R - \frac{i\pi}{\lambda \cos \theta} \times \frac{\Delta n_s}{(\sqrt{\beta} e^{\Gamma z/2} + \frac{e^{-\Gamma z/2}}{\sqrt{\beta}})} A_D \\ \frac{dA_D}{dz} &= \frac{-\alpha}{2 \cos \theta} A_D - \frac{i\pi}{\lambda \cos \theta} \times \frac{\Delta n_s}{(\sqrt{\beta} e^{\Gamma z/2} + \frac{e^{-\Gamma z/2}}{\sqrt{\beta}})} A_R \end{aligned} \quad (2)$$

where α is the absorption constant at the reading wavelength, Γ is the coupling coefficient, $\beta = I_s/I_p$ is the writing beam intensity ratio, Δn_s is the saturation index modulation amplitude. By defining new variables,

$$\begin{aligned} B_i(z) &= A_i(z) \exp\left[\frac{\alpha z}{2 \cos \theta}\right] \quad i = R, D \\ z' &= \frac{2}{\Gamma} \tan^{-1} \left[\exp\left(\frac{\Gamma z \sqrt{\beta}}{2}\right) \right] \end{aligned} \quad (3)$$

we can obtain a pair of easily solvable equations,

$$\frac{dB_R}{dz'} = i\kappa B_D \quad \frac{dB_D}{dz'} = -i\kappa B_R \quad (4)$$

where $\kappa = \pi \Delta n_s / \lambda \cos \theta$ is the amplitude coupling constant for I_R and I_D . Combining the boundary conditions $A_R(0) = A_0$ and $A_D(0) = 0$ with Eq. (4), we can derive the diffraction efficiency

$$\eta = \exp\left\{-\frac{\alpha L}{\cos \theta}\right\} \times \sin^2 \left\{ \frac{2\kappa}{\Gamma} [\tan^{-1}(e^{\Gamma L/2} \sqrt{\beta}) - \tan^{-1}(\sqrt{\beta})] \right\} \quad (5)$$

If knowing the parameters of α , L , θ , κ and Γ , we can use Eq.(5) to fit the variation of the diffraction efficiency as the writing beam ratio.

We used Eq. (5) to fit our experimental data in Fig. 2 and Fig. 3. In the fitting, $\theta = 10.6^\circ$ and $L = 0.55\text{cm}$. α was experimentally measured to be 0.23cm^{-1} , κ and Γ were regarded as fitting variables. The theoretical fitting results are plotted by the solid curves in the figures. It can be seen that the theoretical results are coincident with the experimental data very well. In the fitting, we obtained the value of the fitting variables κ and Γ . In Fig. 2, for the extraordinarily polarized reading beam, $\kappa = 2.8\text{cm}^{-1}$ and $\Gamma = 8.3\text{cm}^{-1}$; for the ordinarily polarized reading beams, $\kappa = 0.6\text{cm}^{-1}$ and $\Gamma = 8.3\text{cm}^{-1}$. In Fig. 3, for the extraordinarily polarized reading beam, $\kappa = 2.8\text{cm}^{-1}$ and $\Gamma = 2.4\text{cm}^{-1}$; for the ordinarily polarized reading beams, $\kappa = 0.8\text{cm}^{-1}$ and $\Gamma = 2.4\text{cm}^{-1}$. So Γ value depends on the polarization of the writing beams. To verify the fitting results, we measured the actual value of Γ by two-wave-coupling method.¹⁸ The measured values are $\Gamma = 8.1\text{cm}^{-1}$ for the extraordinarily polarized writing beam and $\Gamma = 2.3\text{cm}^{-1}$ for the ordinarily polarized writing beam. They are in good agreement with the theoretical fitting values.

It also can be seen from above fitting results that the parameter κ strongly depends on the reading beam polarization and is independent of the writing beam polarization. As the reading beam is extraordinarily polarized, the parameter κ for two writing beam polarizations both are 2.8cm^{-1} . As the reading beam is ordinarily polarized, κ for the gratings written by extraordinarily polarized reading beams (0.6cm^{-1}) is nearly equal to that for the gratings written by ordinarily polarized reading beams (0.8cm^{-1}). The parameter κ for the extraordinarily polarized reading beam is almost five times that for the ordinarily polarized reading beam. This indicates that there is much more energy transferring from the reading beam to its diffraction beam for the case that the reading beam is with extraordinary polarization.

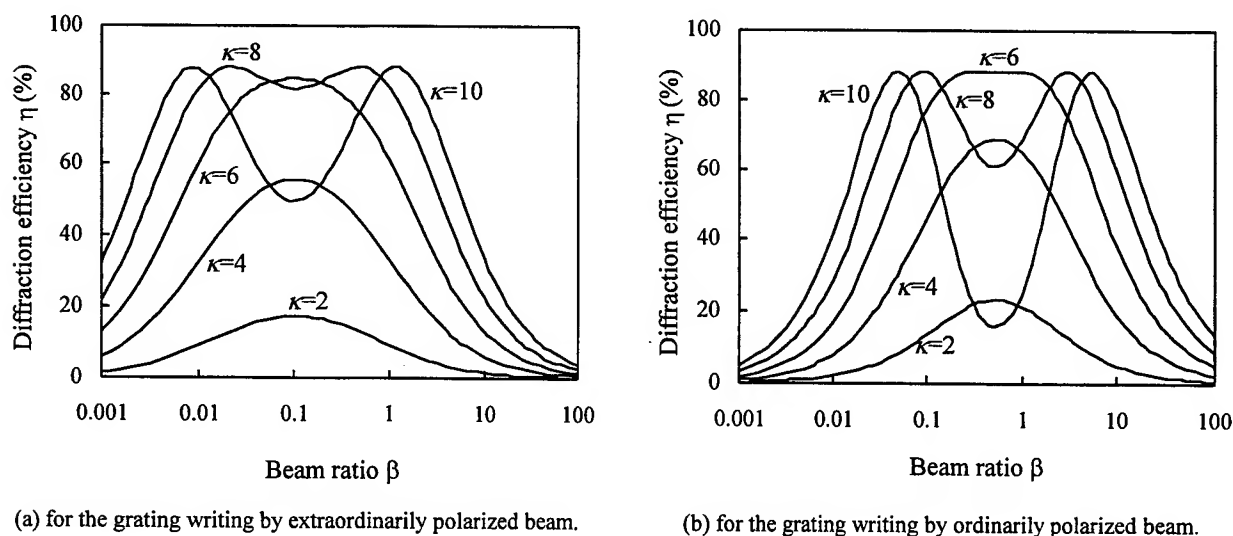


Fig. 5 Diffraction efficiency η as a function of the beam ratio β for different κ .

We also theoretically calculated the diffraction efficiency for different parameter κ . The results are plotted in Fig. 5, which shows that, as $\kappa < 6\text{cm}^{-1}$, the diffraction efficiency has single maximum and the maximum diffraction efficiency increases as the κ increase. As $\kappa > 6\text{cm}^{-1}$, the diffraction efficiency curves exhibit two peaks. The central position of the curves does not change with the variation of κ . However, the central position of the curves for the gratings written by extraordinarily polarized beams is different from that for the gratings written by ordinarily polarized beams. For the gratings written by extraordinarily polarized beams, the central position of the diffraction efficiency curves is at $\beta = 0.11$. For the gratings written by ordinarily polarized beams, it is at $\beta = 0.67$. The former has an obvious "left shift" with respect to the latter. This implies a much more intensive beam coupling occurs between the extraordinarily polarized writing beams.

4. CONCLUSIONS

We studied the variation of the diffraction efficiency of the volume grating in Ce:KNSBN photorefractive crystal as a function of writing beam ratio. It is found that due to the energy transfer effect between the reading beam and the diffracted beam, the diffraction efficiency behavior strongly depends on the reading beam polarization and the readout direction. In the selected direction, the diffraction efficiency for extraordinarily polarized reading beam obtains enhancement and can be fifteen times larger than that for the ordinarily polarized reading beam. Modified coupled-wave theory is used to fit the experimental data. The fitting is quite satisfied, and the fitting variables are experimentally verified to be correct. We also theoretically calculated the diffraction efficiency versus the parameter κ for different gratings. As $\kappa < 6\text{cm}^{-1}$, the diffraction efficiency has single maximum and the maximum diffraction efficiency increases as the κ increases. As $\kappa > 6\text{cm}^{-1}$, the diffraction efficiency curves exhibit two peaks. The central position of the curves does not change with the variation of κ . But the central position of the curves for the gratings written by extraordinarily polarized beams has an obvious "left shift" with respect to that for the gratings written by ordinarily polarized beams. This implies a much more intensive beam coupling occurs between the extraordinarily polarized writing beams. Our results present fundamental data for the applications of Ce:KNSBN crystal in holographic recording and optical information processing.

ACKNOWLEDGEMENT

This research was supported by The Chinese Nature Science Foundation. (Grant Number: 69677019).

REFERENCES

1. L. Solymar, D. J. Webb, and A. Grunnet-Jensen, *The Physics and Applications of Photorefractive Materials*, Clarendon, Oxford, 1996.
2. P. Yeh, *Introduction to photorefractive nonlinear optics*, New York, Wiley, 1993.
3. Francis T. S. Yu and Suganda Jutamulia, *Optical pattern recognition*, Cambridge University press, New York, 1998.
4. F. H. Mok, M. C. Tackitt, and H. M. Stoll, "Storage of 500 high-resolution holograms in a LiNbO_4 crystal," *Opt. Lett.* **16**, pp605-607, 1991.
5. H. Chen and Y. Xu, "Growth and some properties of undoped and doped $(\text{K}_{1-x}\text{Na}_x)_{0.4}(\text{Sr}_{1-y}\text{Ba}_y)_{0.8}\text{Nb}_2\text{O}_6$ (KNSBN) single crystals with tungsten-bronze structure," *J. Cryst. Growth.* **96**, pp357-362, 1989.
6. R. R. Neurgaonkar and W. K. Cory, "Progress in photorefractive tungsten bronze crystals," *J. Opt. Soc. Am. B* **3**, pp274-282, 1986.
7. Y. Tomita and J. Bergquist, "Photorefractive and thermooptic nonlinearities in potassium sodium strontium barium niobate single crystals," *Optoelectronics.* **8**, pp357-377, 1993.
8. X. Shen, J. Zhao, R. Wang, P. Yeh, S. Zhang, and H. Chen, "Photorefractive properties of Cu-doped KNSBN crystal with fluorine replacing oxygen," *Opt. Lett.* **23**, pp1253-1255, 1998.
9. Y. Tomita, J. Bergquist, and M. Shibata, "Photorefractive properties of undoped and Cu-doped potassium sodium strontium barium niobate crystals," *J. Opt. Soc. Am. B* **10**, pp94-99, 1993.
10. J. Xu, S. Liu, Y. Wu, G. Zhang, Y. Song, and H. Chen, "observation of self-pumped phase-conjugate wave in Cu; KNSBN crystal," *Opt. Commun.* **80**, pp239-241, 1991.
11. H. Xia, C. Wang, H. Chen, and X. Xu, "Photorefractive properties of manganese-modified potassium sodium strontium barium niobate crystal," *Phys. Rev.* **55**, pp1292-1294, 1997.
12. S. Bian, J. Zhang, X. Xu, W. Sun, Q. Jiang, H. Chen, and D. Sun, "Self-pumped phase conjugation of 18° -cut Ce-doped KNSBN Crystal at 632.8 nm," *Opt. Lett.* **18**, pp769-771, 1993.
13. S. Bian and J. Frejlich, "Actively stabilized holographic recording for the measurement of photorefractive properties of a Ti-doped KNSBN crystal," *J. Opt. Soc. Am. B* **12**, pp2060-2065, 1995.

14. Y. Li, S. Liu, M. Yang, K. Yang, K. Xu, and F. Hou, "Superior real-time holographic storage and properties in doped potassium sodium strontium barium niobate crystal," *Opt. Lett.* **22**, pp212-214, 1997.
15. H.Kogelnik, "Coupled wave theory for thick hologram gratings," *Bell.Syst.Tech.J.* **48**, pp2909-2947, 1969.
16. John H. Hong, and Ragini Saxena, "Diffraction efficiency of volume holograms written by coupled beams," *Opt. Lett.* **16**, pp180-182, 1991.
17. Yue Xue-feng, Shao Zong-shu, Chen Huan-chu, Wang Ying-su, "The maximum diffraction efficiency for holographic storage in photorefractive crystals" *Acta.Physica.Sinica*, **37**, pp2057-2061, 1988.
18. H.Y. Wang, M. Z. Tian, J. L. Lin, S. H. Huang, J. Q. Yu, H. C. Chen, Q. Z. Jiang, "Study of two-wave coupling in Cu:KNSBN using red light," *Opt. Commun.* **115**, pp563-567, 1995.

A test system for the embossed information's characteristics of 4X-density magneto optical disk

ZHOU Zuwang, CHEN Haiqing

Huazhong University of Science and Technology,
Department of Photoelectronics Engineering, Wuhan 430074, CHINA

ABSTRACT

The characteristic of embossed information is very important for magneto optical disk, which is used by the magneto optical driver to control the axial focusing and radial tracking servos on the information tracks and to search the sectors. It must be tested in the process of development and production of magneto optical disk. The characteristics of 4X-density magneto optical disk's embossed information are described in this thesis; the test method of the header signal and groove signal is discussed based on the international standard test condition. A test system has been designed which can measure the characteristics of embossed information of magneto optical disk, and a sample disk's test result is given in the end.

Keywords: Magneto optical disk, characteristics of embossed information, test system, data sampling.

1. INTRODUCTION

The technology of magneto-optic memory is a main branch of the computer data storage technology. Combined the advantage of the floppy's rewritable ability and the optical disk's large capacity, magneto disk is suitable for the application which need large capacity medium for data backup. The characteristic of embossed information is a very important parameter for magneto optical disk, which is used by the magneto optical driver to control the axial focusing and radial tracking servos on the information tracks and to search the sectors. The test system we developed in this thesis can be used to measure the embossed Information's characteristics of 4x-density magneto optical disk.

The characteristics of 4X-density magneto optical disk's embossed information are described in this paper, the test method of the header signal and groove signal is discussed based on the international standard test condition, and the test system's makeup and key technology are introduced. The test system is made up of a PC, a magneto optical disk driver and a data sampling card. The PC is used to control the system working flow, process data and display result. The magneto optical disk driver creates the signal we need to detect. The data sampling card processes and converts the signal and sends data to the PC.

2. EMBOSSED INFORMATION ANALYZING

The embossed information is the mark pre-stamped on the disk surface when producing, which include the pre-fluting spiral groove and the preformatted sector mark in the groove. The former is called groove signal used in the focusing and tracking servo for the magneto optical disk driver, and the later is called header signal. The sector's preformatted mark is similar to the floppy disk's sector mark, but it is finished when the disk is produced, not need user's formatting or reformatting, it is the real "hard" formatting.

The test items of magneto optical disk's embossed information include the header signal and groove signal. The test

condition and method must meet the requirement of the international standard ISO/IEC DIS 15041:1996, and the test system's optical system must have the identical performance with the reference driver. The reference driver's optical system is shown in Fig. 1.

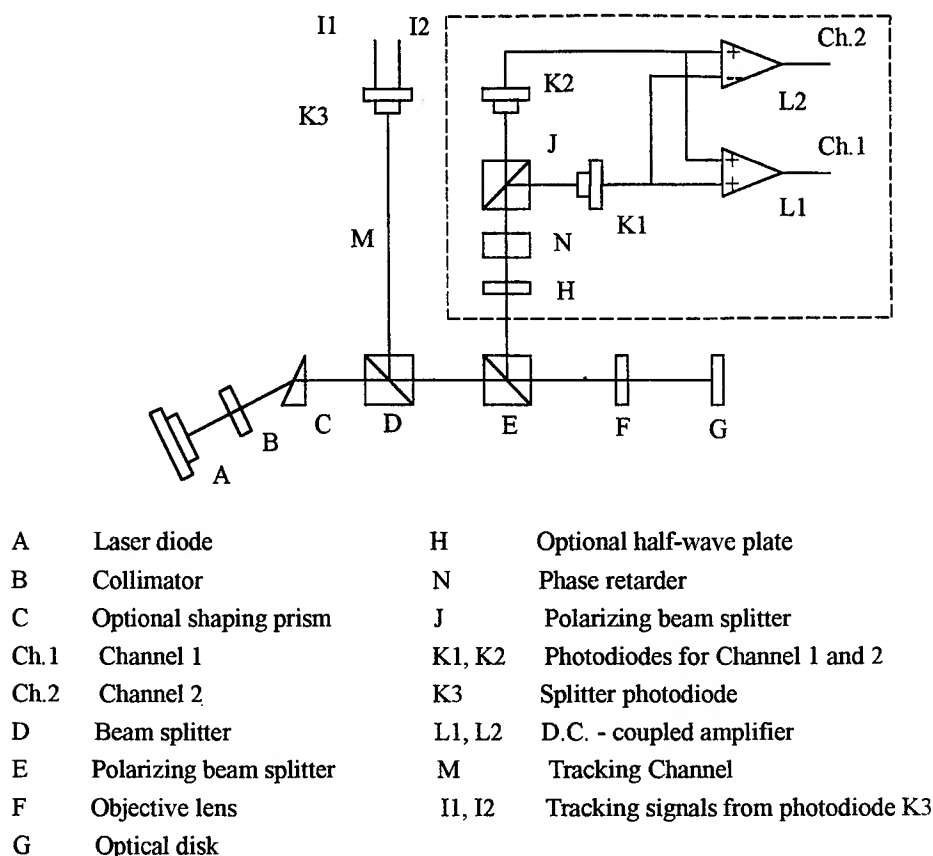


Fig.1. Optical system of the Reference Driver

In the absence of polarization changes in the disk, the polarizing beam splitter J shall be aligned to make the signal of detector K1 equal to that of detector K2. The direction of polarization in this case is called the neutral direction. Two read channels are provided to generate signals from the marks in the recording layer, the output of Channel 1 is the sum of the currents through photodiodes K1 and K2, which is used for reading embossed marks, using the diffraction of the optical beam by the marks. The output of Channel 2 is the difference between photodiode currents, which is used for reading user-written marks with the magneto-optical effect, using the rotation of the polarization of the optical beam due to the magneto-optical effect of the marks.

The Tracking channel of the driver provides the tracking error signals to control the servos for the axial and radial tracking of the optical beam, the radial tracking error is generated by a split photodiode detector K3 in the tracking channel.

2.1 Header signal measuring

The header signal obtained from the embossed marks in the recording layer is defined as the peak-to-peak value of the modulation of the signal in Channel 1 caused by the mark when the beam follows a recorded track. Fig. 2 shows the signal from sector headers in Channel 1.

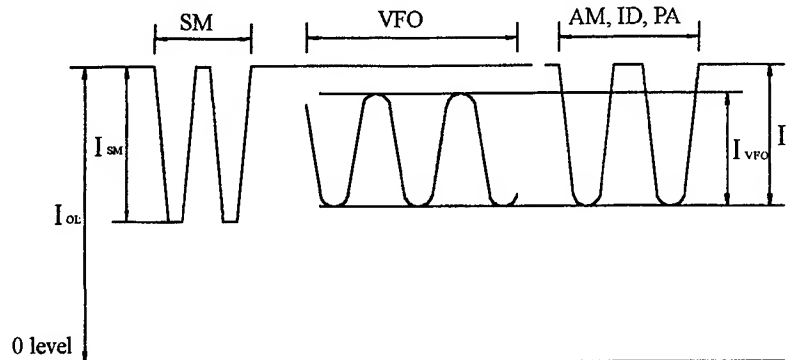


Fig.2. Signals from Headers in Channel 1

The Header signals include the signals from the marks in the Sector Mark (SM), VFO field, Address Mark (AM), ID field and Postamble (PA) field. For SM, measuring I_{SM} / I_{OL} , for VFO, measuring I_{VFO} / I_{OL} and I_{VFO} / I_{pmax} ; for AM and ID, measuring I_p / I_{OL} and I_{pmin} / I_{pmax} .

2.2 Groove signal measuring

Groove signal include cross-track signal, cross-track minimum signal and push-pull signal. The cross-track signal is the sinusoidal sum signal from Channel 1 in the Read Channel, when the focus of the optical beam crosses the tracks, and it can be used by the driver to locate the center of the track. The push-pull signal is the sinusoidal difference signal from the tracking channel, when the focus of the optical beam crosses the tracks, and it can be used by the driver for radial tracking. Fig. 3 and Fig. 4 show the signals from Channel 1 and tracking channel when the beam crosses the track. For cross-track signal, measuring $(I'_{OL} - I'_{OG}) / I'_{OL}$, for cross-track minimum signal, measuring $(I_1 + I_2)_{min} / (I_1 + I_2)_{OL}$, for push-pull signal, measuring $(I_1 - I_2)_{pp} / (I_1 + I_2)_{OL}$.

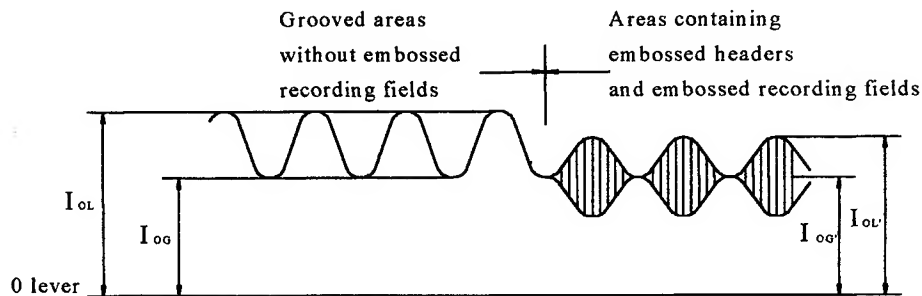


Fig.3. Signals from grooves in Channel 1

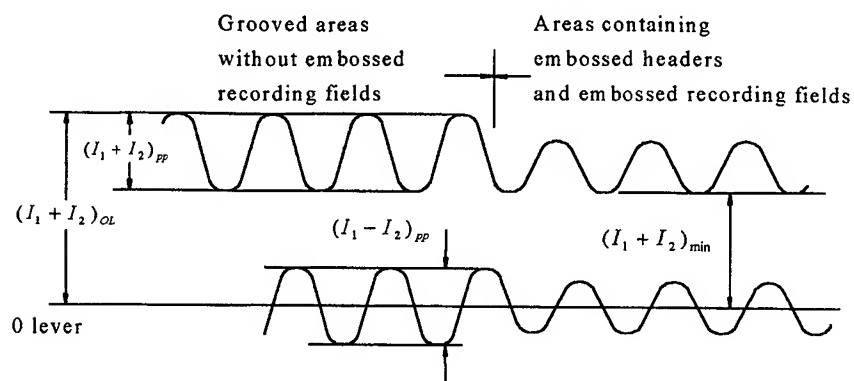


Fig.4. Signals from grooves in Channel 1

3. TEST SYSTEM IMPLEMENT

3.1 The structure of the test system

The test system for the embossed characteristic of 4X-density magneto optical disk is made up of two parts – host computer and slave machine. The former is made up of a 586 personal computer and the test control software, the later is made up of a magneto optical disk drive platform and the data sampling system. The host computer communicate with the slave machine through a RS232 cable and a SCSI cable, Fig. 5 shows the schematic diagram of the test system.

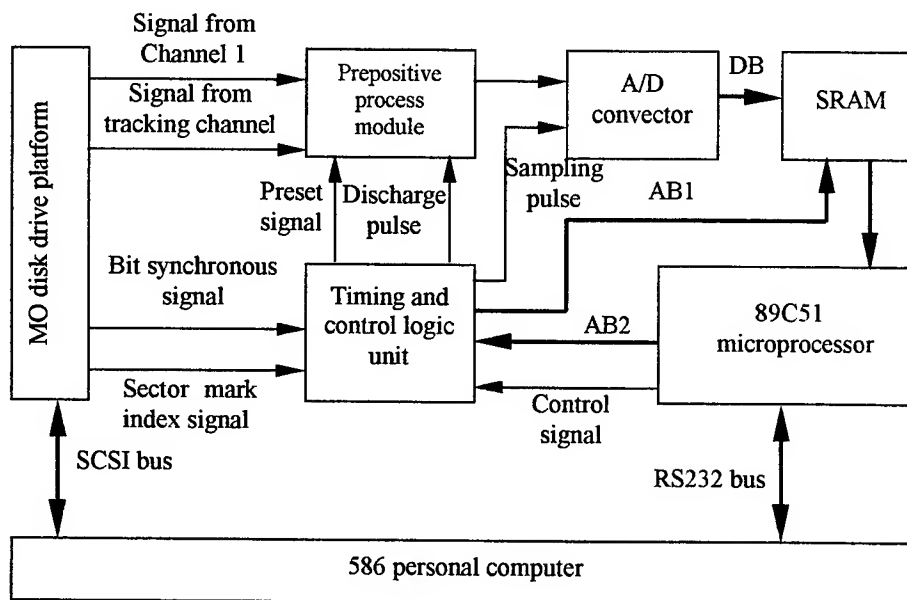


Fig.5. Test system's schematic diagram

When test system starts testing, the magneto optical disk driver drives the optical header to seek track or to cross track under the control of the host computer. Signals of Channel 1 and tracking Channel obtained from the driver platform are

transmitted to the sampling system, the prepositive process module finishes the signal's precise magnification, filtering and peak-to-peak sampling. The A/D converter transforms the signal to digital form and sent to the SRAM to store, waiting the host computer to read.

Timing and control logic unit finishes creating the sampling system's complex control timing and control signal. Because the signal to be tested is high speed and non-repeating, it must to be sampled in real time. The timing and control logic signal is so complex that if the timing and control module were realized by normal digital IC, it would need too many chips, and cause high power consumption, low reliability. This test system adopts a programmable logic device (PLD) ispLSI1024 to realize the required logic. The device has in-system programmable function, and it is very suitable for the system's design and debugging. The input of the timing and control logic unit includes the bit synchronization signals, sector mark index signal and the control signals from the microprocessor, the output includes sampling pulse, discharge pulse of peak-to-peak sampling, channel preset signal, and the address bus signal.

The microprocessor receives the instructions from the host computer and controls the timing and control logic unit, at the same time transports the sampling data stored in the memory to host computer for processing.

The control software of the host computer drives the magneto optical platform through a SCSI cable, communicates with the sampling system through a RS232 serial cable, sends out control instruments to sampling system and receives the sampling data from sampling system, and display the measuring result after data processing.

Prepositive process module includes amplification, filter, A/D converter, peak-to-peak value detector, and sector mark filter module. Fig.6 shows the prepositive process module's block diagram.

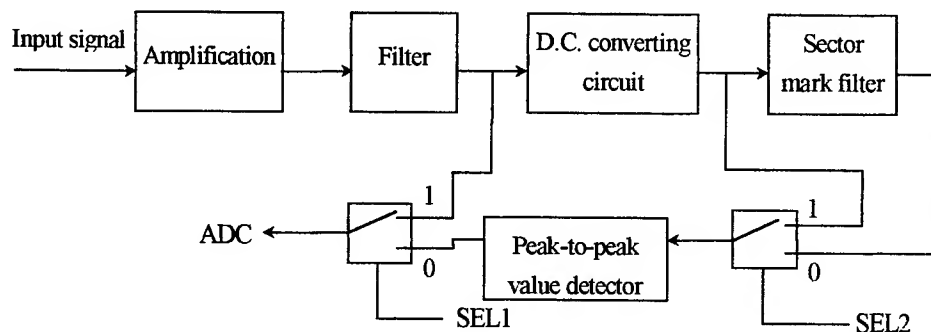


Fig.6. Prepositive process module's block diagram

The test system's inputs include the Channel 1 or tracking channel signals from the magneto optical driver. When the beam passes sector header areas, the output is the embossed signal of the sector mark. When the beam passes grooved areas without embossed recording Fields (see Fig.3), the output is I_{OL} . When the beam crosses the track, the output is the cross-track signal, so the output of the Channel 1 has different meaning under different condition.

For the three signals above, the task of the prepositive process module is not all same. Different input signal is processed by different channel of the module, the channel select is controlled by the two control signals (SEL1 and SEL2) of the PLD.

The input signal is amplified and filtered before entering different process channel. The output of Channel 1 is a pair of difference signal, it's peak-to-peak amplitude is about 500mv, but the input arrange of A/D converter used in the module is 0~2.5v, so the amplify multiple is set to 4. The filter's design must meet the input signal's frequency band, the input signal's frequency width is DC~20 MHz, so the low-pass filter's cut-off frequency must be wider than 20MHz.

For the sector mark signal and tracking signal, the peak-to-peak value must be measured according to the international standard test condition, so the peak-to-peak value detection circuit is added here. The valid range of the peak-to-peak value

detect module is 0.5~3.2v, but the range of the signal from the amplification circuit is 0~2.0v, so the direct current converting circuit is added between the two module above. When the optical beam scans on the preformatted areas of the information track, the preformatted sector mark will disturb the tracking signal, so for the measuring of tracking signal, sector header signal filtering circuit must be added in order to reduce the disturbance of the preformatted sector mark.

Timing and control logic circuit finishes producing complex control signal of all kinds of test states. Fig.7 shows the timing and control logic circuit's block diagram. The input and output pin's meaning is given below.

The input signals include:

- DETECT_EN: detect enable signal. After microcomputer sends detect command to the data sampling system and the microprocessor in the test system receives the command rightly, the microprocessor sends the signal to the timing and control logic unit. It is used by the PLD to decide the start time of detecting, and it is a pulse of width more than 2 μ s.
- SIGNAL_SEL: test select signal. The signal is send by the microprocessor, when it is low level, the test target is sector mark signal (includes I_{OL}), when it is high level, the test target is tracking signal.
- EX_CLK/4: the four-divided clock of the driver's bit clock. It is used as the sampling clock pulse.
- IN_CLK: the internal clock of the data sampling system. Its frequency is 500Hz and is used as the sampling pulse of low frequency signal such as tracking signal.
- FLAG: sector mark index signal. The signal is obtained from the driver, which is used to indicate the start position of the sector mark.
- COM_OUT: the output of the comparator. It is produced by the prepositive process circuit, and is used to produce the start pulse of tracking signal detecting.
- CPU_AB: the internal address signal of the microprocessor.

The output signals include:

- DETECT_OK: detect accomplishment signal. It is sent to the microprocessor indicating of success of sampling.
- SCLK: A/D converter sampling pulse. It has different frequency under different condition.
- SEL1, SEL2: channel select signal. When SEL1 is high level, the I_{OL} signal is selected to sample. When SEL1 is low level and SEL2 is low lever, the tracking signal is to detect. When SEL1 is low lever and SEL2 is high lever, the sector mark signal is selected to detect.
- DISCHARGE: discharge pulse. It is used by the peak-to-peak detect circuit.
- AB: internal address bus signal.

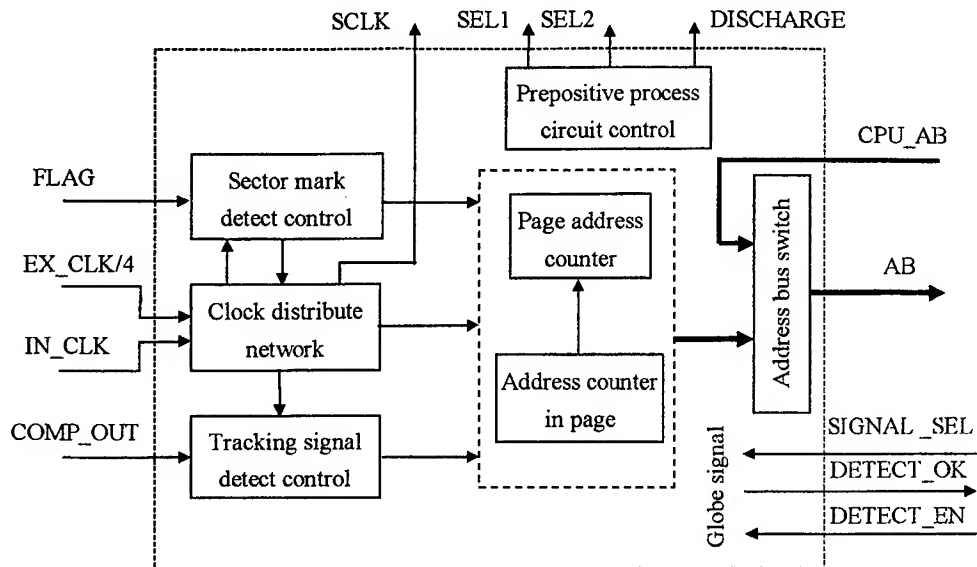


Fig.7. Timing and control logic control circuit's block diagram

3.2 Test procedure of header signal

The test process of sector's header signal operates as below: Before the test, user selects the header signal test track in the software interface, you can select either specified track or random track. When testing, the host computer send the header signal sampling command to the sampling system through RS232 bus, the sampling system presets the system as header signal sampling state after receiving the instruct. Secondly, the host computer drives the optical header to the specified track through the SCSI cable and does the read operation, and the steady sector mark signal could be obtained from the driver. When the test system receives the sector mark index signal, it triggers the A/D converter to sample the signal from every field of the sector mark. The test system can sample the specified track's all 17 sectors once an operation, the sampling data is stored in the static memory temporarily before transmitting to the host computer. The host computer receives the data and do calculation in the light of international standard ISO/IEC 15041:1996, finally the test result of SM, VFO, AM, ID of every sector mark is displayed on the screen.

3.3 Test procedure of groove signal

The test process of sector's groove signal operates as below: Before the test, user selects the groove signal test zone in the software interface, you can select either specified zone or random zone. When testing, the host computer send the groove signal sampling command to sampling system through RS232 bus, the sampling system presets the system as groove signal sampling state after receiving the instruct. Secondly, the host computer drives the optical header through the SCSI cable to the specified zone and does the cross-tracking operation, and the groove signal can be obtained at Channel 1 and tracking channel. At last the sampling system transmits the sampling data to the host computer, the host computer processes the data in the light of international standard ISO/IEC 15041:1996 and gets the test result of cross-track signal, cross-track minimum signal and push-pull signal.

We test a SONY 640M magneto optical disk sample using the test system, the test result is given below (see table 1), and test position is selected randomly by the control software. The test result indicates that test result completely meets the

international standard's requirement.

Table 1. SONY 640M sample disk test result

Test item	Test position	Test characteristic	Eligible range	Test value
Header signal	Track 16554 sector 1	I_{SM} / I_{OL}	0.45~0.95	0.711
		I_{VFO} / I_{OL}	0.18~0.90	0.287
		$I_{VFO} / I_{p \max}$	□0.30	0.404
		I_p / I_{OL}	0.18~0.90	0.585
		$I_{p \min} / I_{p \max}$	□0.30	0.893
Groove signal	Zone 10	$(I'_{OL} - I'_{OG}) / I'_{OL}$	0.20~0.60	0.472
		$(I_1 + I_2)_{\min} / (I_1 + I_2)_{OL}$	□0.15	0.539
		$(I_1 - I_2)_{pp} / (I_1 + I_2)_{OL}$	0.30~0.75	0.462

4. REFERENCE

1. Chen Xiaohong, Gao zhengping. Technology and principle of magneto optical memory. Chendu: Univ. of Electronic Science and Technology Press, 1994. 90~92(in Chinese)
2. ISO/IEC DIS 15041:1996 Information technology -- Data interchange on 90mm Optical Disk Cartridges Capacity -- 640 Megabytes per cartridge. 1996.

650nm AlGaInP Quantum Well Lasers for the application of DVD

Chen Lianghui *, Ma Xiaoyu *, Guo Liang*, Ma Jun♀, Ding Hongyu♀, Cao Qing*,
Wang Liming *, Zhang Guangzhe*, Yang Yali *, Wang Guohong *, Tan Manqing*,

* The Institute of Semiconductors, Chinese Academy of Sciences Beijing

♀Huayang Industrial (group) CO.LTD Huizhou China

ABSTRACT

Main application of 650nm band laser diodes are for digital versatile disk (DVD). We demonstrate here the 650nm AlGaInP LD grown by LP-MOCVD with the structure of selected buried ridge waveguide. Excellent performance of LD have been achieved such as threshold current, threshold current density as low as 20mA and 350A/cm² respectively at room temperature, the operating temperature up to 90 °C for the linear power output of 5mw. RIN is about -130db/Hz, The samples of LD have been certified by PUH manufacturers.

Key words: DVD, laser diode, visible, AlGaInP, MOCVD

1. INTRODUCTION

Optical storage is another important application of semiconductor lasers besides optical fiber communication, it is so popular that more devices needed and greater developing economical benefit predicted. Since 780nm semiconductor lasers used in CD instead of He-Ne Lasers, it has been rapidly developed. According to the statistics data, in 1998 more than 200 millions 780nm semiconductor lasers had been sold for optical storage, amount to 85 percent of the total sales of semiconductor lasers. Recently for high density optical storage, the semiconductor laser with shorter emitting wavelength are required because the size of light spots are proportional to the square of emitting wavelength of semiconductor laser. Digital Versatile Disc (DVD) with the light source of 650nm LD are suggested as an approach to enlarge the storage capacity.

In China, the VCD market is as large as 15 million sets per year in 1998, it can be expected that the market of DVD including DVD-ROM and Player is comparable with VCD and reach the amount of 10 million sets in the year of 2002. It is so important to develop high quality 650nm LD for DVD to fit the requirement of increasing month by month in China.

We show here the research results as follows: for 650nm LD, broad area threshold current density is about 350A/cm² and selected buried ridge waveguide LD is with threshold current as low as 20 mA at RT and operating temperature can be up to 90 °C. The astigmatism and RIN the relative noise RIN has been measured as 10 μm and 130 db/Hz respectively.

*Correspondence: Email: chenlh@red.semi.ac.cn;
Telephone: 86-10-62339535 Fax: 86-10-62324981

2. GaInP/AlGaInP Material Growth

Visible semiconductor laser can be fabricated by III-V compounds with mature technology, Energy band gap of ternary III-V compounds generally can be expressed as second power function of its composition factor x

$$E_g(x) = E_{g0} + bX + cX^2 \text{ (eV)} \quad (1)$$

where E_g is the lowest energy band gap of the binary compounds. for the energy range of direct band gap of $\text{Ga}_x\text{In}_{1-x}\text{P}$, it can be written as:

$$E_g(x) = 1.351 + 0.643X + 0.786X^2 \text{ (eV)} \quad (2)$$

For quaternary compounds AlGaInP, the varieties of energy band gap and crystal lattice constant versus its composition is shown in fig.1, from it we can select suitable composition of GaInP and AlGaInP in the direct band gap region matched with GaAs.

The crossover point between direct band Γ and indirect band X for $\text{In}_{0.49}(\text{Ga}_{1-x}\text{Al}_x)_{0.51}\text{P}$ occurs at 2.3 eV. If using compound material with this composition as active layer, it would lase at wavelength of 539nm, this would be the possible shortest emitting wavelength of this material system, but it will be difficulty to find material as confinement layer and barrier for heterojunction and quantum well.

Further research reveal that under a definite growth condition, $\text{Ga}_{0.5}\text{In}_{0.5}\text{P}$ has a strict order with one layer GaP over one layer InP along (111) direction, and this ordered $\text{Ga}_{0.5}\text{In}_{0.5}\text{P}$ has energy gap around 1.84 eV, rather than 1.92eV for disordered $\text{Ga}_{0.5}\text{In}_{0.5}\text{P}$.

Carriers effective mass plays an important role in semiconductors laser, it is related to state density, the larger the effective mass, the higher the injection current needed to reach population inversion, and the larger the threshold current. GaInP (AlGaInP) material has larger effective mass than GaAs (AlGaAs), so the threshold current density of GaInP(AlGaInP) visible semiconductor lasers can not be as low as that of GaAs(AlGaAs) lasers while technologies are at same level.

Besides, AlGaInP has a larger thermal receptivity, it is because of the large difference between masses of Ga atom and In atom. It causes strong disharmony of the lattice oscillation consequentially increasing the probability of phonon scattering and thermal resistivity. The thermal resistivity of $\text{Ga}_{0.5}\text{In}_{0.5}\text{P}$ is about 19 cm °C /w, in $\text{Al}_{0.5}\text{In}_{0.5}\text{P}$ the disharmony is stronger and thermal resistivity is larger, for $\text{Al}_x\text{Ga}_{1-x}\text{As}$ thermal resistivities less than 10cm°C /w for all composition compounds.

AlGaInP quaternary compounds can not be grown by LPE, for reason of large Al segregation coefficient in AlInP system. On the other hand, because the saturation pressure of phosphorous is too high, it can not be grown by normal MBE technology. Up to date GaInP/AlGaInP material can only be grown by GSMBE or MOCVD.

In this article, LP-MOCVD with horizontal reactor of AIX200 is used. 2 inches Si-doped (100) GaAs substrates with mis-orientation 6°-15° off towards (111)A were loaded on the graphite holder, which is heated by infrared lamp. The larger mis-orientation is beneficial to the shorter wavelength of laser

diode.^{4,5} The MO sources were TMIn, TMGa, and TMAI. The hydride sources are PH₃ and AsH₃. The doping sources were DEZn for the p-type layers and SiH₄ for the n-type layers. Carbon is selected as a p type of high concentration dopant special for ohmic contact top layer. The carrier gas is H₂ purified by Pd purifier. The growth temperature is about 680°C -720°C, the V/III ratio is in the range of 120-300, and growth rate can be controlled in the range of 1.8-4μm /hrs. The growth pressures were 50-100mbar. The lattice mismatch ($\Delta a/a$) of AlGaInP layer is about 1×10^{-3} .

3. The structure and fabrication of 650nm Laser Diode

In early stage, visible semiconductor lasers 1-3 are with the structure of InGaAlP /GaInP double heterojunction (DH), grown on Si-doped (001) GaAs substrate at 700°C, with unintentionally doped GaInP active layer and p-type, n-type AlGaInP used as upper and lower cladding layer, Fig.2 give out a typical gain guided and index guided laser structure. Injected current confinement of gain guided stripe laser is realized by the n-type GaAs blocking layer. Optical mode is defined by gain distribution induced by the injected current. Despite the gain guided lasers usually take multi-mode and large astigmatic, it could be accepted for some application with lax demand for the sake of its simple structure, simplified technology, high reliability and productivity, for instance the usage of laser pointer. Normally this type of devices is with lasing wavelength of 670nm-695nm.

Ridge waveguide is also a structure which has been widely used and posses a series of advantages such as low threshold current , high efficiency , simple processing , and low cost, but it can not fit to the application of DVD due to whose thermal conductivity and whose noise characteristics.

Index guided structure can realize stable transverse mode layout. Because its n-GaAs current blocking layer is grown selectively on the ridged double heterojunction, so called selectively buried ridge structure. The n-GaAs blocking layer also acts as a light absorbing layer and causes an effective refractive index difference along the junction plane. This kind of device can realize threshold current lower and operation temperature higher compared with gain guided laser, this transverse mode stabilized laser has less astigmatic which is dependent on the optical mode distribution built up by the laser structure. Fabrication of visible Semiconductor lasers with shorter wavelength as mentioned above, the application of DVD need lasers with wavelength as short as possible.

Generally three technical paths were taken to shorten the wavelength. Firstly using AlGaInP quaternary compound as active layer of DH lasers. Because it is very simple and easy to operate, during early stage a lot of research had been done. But practice reveals that visible lasers with AlGaInP active layer is difficult to operate at high temperature, this is because of the increasing of leakage current at high temperature. For 630nm lasers, the energy band gap of AlGaInP active layer has reached to 1.97eV. In such heterojunction, the conduction band offset between active layer and cladding layer is very small, more injected electrons flow over active layer getting into cladding layer. It is obvious that the shorter the lasing wavelength, the larger the electrons overflow. To overcome carriers overflow cladding layer with large energy band gap or high p-type doping level is needed. However experiments prove that Aluminum introduce more non-radiative centers into active layer thus raising the threshold current density. Secondly quantum well structure is employed in active layer. The third path is using mis-oriented GaAs substrates. The second and third measurement will be induced into design.

Fig.3 shows the schematic structure of our 650nm LD. The LD has a conventional buried ridge waveguide structure with three-step epitaxial growth. The multilayers containing Si-doped n-GaAs

buffer layer, Si-doped n-(Al_{0.55}Ga_{0.45})_{0.5} In_{0.5}P cladding layer ($n=5-8 \times 10^{17} \text{ cm}^{-3}$, $d=1.05 \mu\text{m}$), an undoped (Al_{0.55}Ga_{0.45})_{0.5} In_{0.5}P optical confinement layer for both of upper and lower, an undoped strained multi-quantum wells active layer, a Zn-doped p- (Al_{0.55}Ga_{0.45})_{0.5} In_{0.5}P cladding layer ($p=1-2 \times 10^{18} \text{ cm}^{-3}$, $d=0.25 \mu\text{m}$), a Zn-doped p-GaInP layer, a Zn-doped p-(Al_{0.55}Ga_{0.45})_{0.5} In_{0.5}P cladding layer ($p=1-2 \times 10^{18} \text{ cm}^{-3}$, $d=0.8 \mu\text{m}$), a Zn-doped p- Ga_{0.5}In_{0.5}P layer, and a Zn- doped p-GaAs layers were successively grown on a (100) 6°-15° off towards (111)A Si-doped n-GaAs substrate. Then, after depositing with SiO₂ or Si₃N₄, ridge stripes in the (011) direction were formed by chemical etching. In the second growth step, a Si-doped n-GaAs current blocking layer ($n=2 \times 10^{18} \text{ cm}^{-3}$, $d=1.2 \mu\text{m}$) was selectively grown on both sides of the stripes. In the 3rd growth step, a C-doped p-GaAs contact layer ($p=3 \times 10^{19} \text{ cm}^{-3}$, $d=2.2 \mu\text{m}$) was grown. The stripe width at the bottom of ridge is 4.5 μm . Ohmic contacts were formed with TiPtAu for p-side and Au-Ge-Ni for the n-side. The Lasers cavity is 300 μm long and with reflectivity of 15/85% coating, and are mounted on heat sink with configuration of p-side down.

4. The Performances of Lasers

Fig. 4 (a) shows the CW operating light output power against current characteristics of a typical 650nm DVD LD measured at temperatures ranging from 25~90°C. In the figure, the threshold current is as low as 25mA at 25°C, output power more than 10mW at $T_c=80^\circ\text{C}$ and more than 7.5mW at $T_c=90^\circ\text{C}$, respectively.

The lasing wavelength is 644nm at -10°C , 650.5nm at 25°C and 654.5nm at 7°C respectively, under 5mW shown in Fig 4(b). The beam divergences perpendicular and parallel to the junction are 8-12°, and 28-32°, respectively.

The 650nm DVD LDs reliability tests were performed at 70°C, APC 5mw, 1000hrs. The life time at 70°C, APC 5mW were about 4000-6000hrs.

5. SUMMARY

In conclusion, 650nm DVD LDs have been developed. Typical threshold current density is about 350A/cm², the threshold current as low as 20mA at 25°C, were achieved. The beam divergence is about 8-12°×28-32°. and operating temperature can be up to 90°C. The astigmatism and the relative noise (RIN) has been measured as 10 μm and 130 dB/Hz respectively. The specifications of LDs have essentially satisfied the requirement of DVD application by the certification of DVD pick-up manufacturers. The improvement of production capacity and yield are under way.

ACKNOWLEDGEMENTS

The authors wish to thank Mao Dongsheng for the facets coatings; Wang Yutian, Pan Guisheng, Zhang Xiaoyan, and Bian Jingyi for the measurements of X-ray, PL, and L-I characteristics; Ma Shuhong, Liu Dejun for PECVD and sputtering processing, Sun Xiuyan for processing assistance.

This work was supported by Chinese Academy of Sciences and Chinese Hi-Tech R& D Program (863 plan).

REFERENCES

1. Kobatashi,K., Kawata,S., et al Electron. Lett., 21, 931 1985.
2. Ikeda,M., Mors,Y., et al Appl. Phys. Lett., 47,1027,1985.
3. Fujii,H., Kobayashi,K., et al, Electron. Lett., Vol.23, pp.938-939 1987.
4. Hamada,H., et al, IEEE J. Quantum Electron., QE-27, pp. 1483-1488. 1991.
5. Xiaoyu,Ma., et al., Proceedings SPIE Semiconductor Lasers III, Vol.3547, P127-129, 1998.

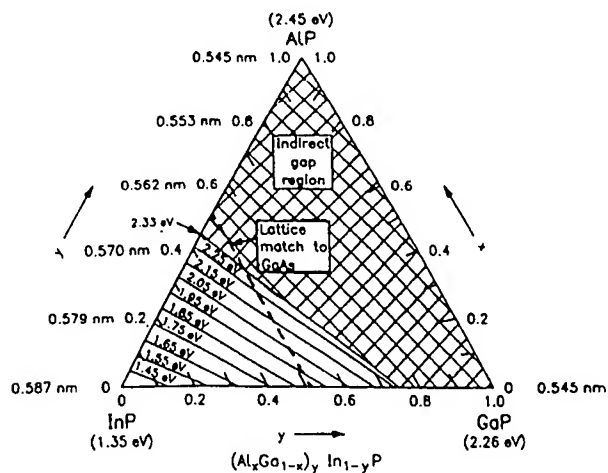


Fig. 1 Band gap and lattice constant of $(\text{Al}_x\text{Ga}_{1-x})_y\text{In}_{1-y}\text{P}$ versus x, y

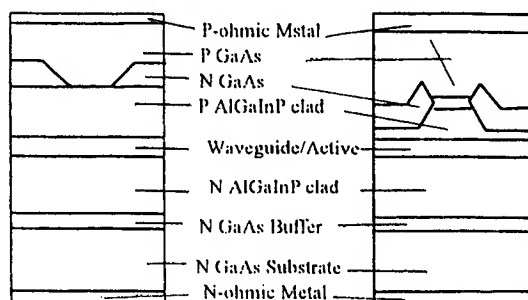


Fig. 2 InGaAlP Lasers (a) Gain guided
(b) SBR structure

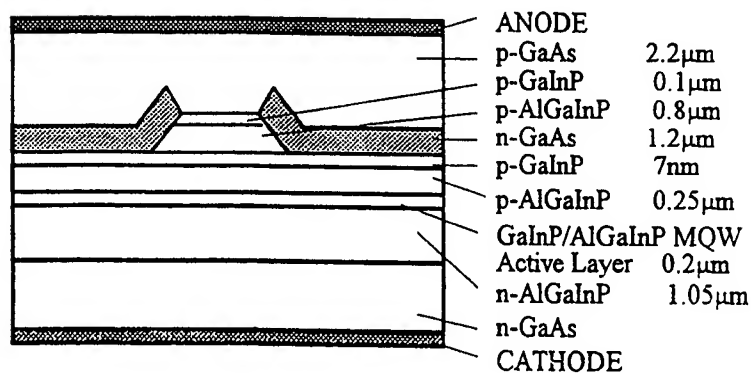


Fig. 3 The schematic structure of 635~650nm LD

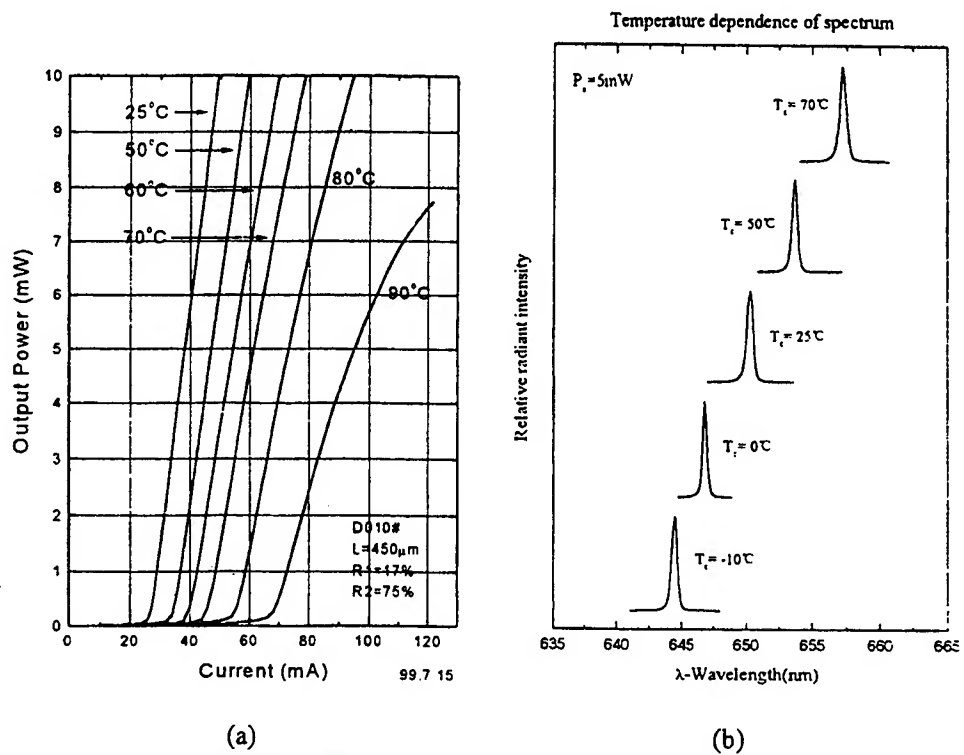


Fig.4 Temperature dependence of DVD grade LD
(a) P-I curves; (b) spectrum characteristics

SESSION 9

Nonlinear Optics

Optical nonlinearity of surface modified PbS and Cd_xPb_{1-x}S nanoparticles in the femtosecond regime

Heping Li^{a*}, B. Liu^b, C. H. Kam^a, Y. L. Lam^a, W. X. Que^a,
L. M. Gan^b, C. H. Chew^b, and G. Q. Xu^b

^aPhotonics Laboratory, School of Electrical and Electronic Engineering
Nanyang Technological University, Nanyang Avenue, S639798, Singapore

^bDepartment of Chemistry, National University of Singapore
Lower Kent Ridge Road, S119260, Singapore

ABSTRACT

We present an investigation of third-order optical nonlinearity in surface modified PbS and Cd_xPb_{1-x}S nanoparticles using the Z-scan technique with femtosecond laser pulses at 780-nm wavelength. The samples include PbS nanoparticles in microemulsion with PbS concentration range from $0.3 - 2.5 \times 10^{-3}$ M and Cd_xPb_{1-x}S nanoparticles in microemulsion with x from 0 to 1. An extended Z-scan theory based on the Huygens-Fresnel principle is employed to extract the nonlinear refraction index from the experimental Z-scan data with a large nonlinear phase shift. The nonlinear refractive index in PbS nanoparticle microemulsion is found to increase linearly with PbS concentration between 0.3×10^{-3} and 1.9×10^{-3} M. The highest concentration microemulsion gives a nonlinear refractive index of 1.8×10^{-11} cm²/W, which is approximately 4 orders of magnitude higher than those of commercially available bulk semiconductors, such as ZnS and CdS, measured at the same conditions. In Cd_xPb_{1-x}S nanoparticles, Cd_{0.33}Pb_{0.67}S exhibits relatively larger refractive nonlinearity. For all samples, nonlinear absorption remained unmeasurable up to 0.9 GW/cm². The observed large refractive nonlinearity in these nanoparticles may mainly be attributed to the optical Stark effect and contribution from the surface-trapped states in the nanoparticles.

Keywords: PbS, Cd_xPb_{1-x}S, Nanoparticles, Nonlinear refraction index, Z-scan technique

1. INTRODUCTION

Materials with large third-order optical nonlinearity and fast response time are essential for future optical device applications in optical computing, real time holography, optical correlators, and phase conjugators. The nanometer-sized semiconductor materials have been demonstrated to be such candidates since they exhibit large third-order optical nonlinearity based on the quantum size effect and interfacial effect. In recent years, quantum-confined semiconductor nanoparticles have been investigated extensively from the viewpoints of fundamental physics and applications to optoelectronic devices. In the quantum-confined regime, nanoparticles exhibit novel physical and chemical properties, especially nonlinear optical properties¹⁻³. For semiconductor nanoparticles coated by a layer of organic molecules on their surfaces, great enhancement of third-order optical nonlinear susceptibility has been predicted and observed in the single-photon resonance region⁴. Justus *et al.*^{5, 6} investigated the nonlinear optical properties of quantum-confined GaAs and InP micro-crystallites deposited in vycor glass, and significant enhancement of nonlinear optical response was observed. Yu *et al.*⁷ reported that the coated Bi₂O₃ nanoparticles have large third-order optical susceptibility, approximately two orders of magnitude greater than that of bulk Bi₂O₃, which was attributed to the contribution of the interfacial modification.

Unlike its second-order counterpart, the third-order susceptibility $\chi^{(3)}$, is a complex number whose real and imaginary components are responsible for self-focusing (or self-defocusing) and nonlinear absorption, respectively. Because of the potential photonic device applications of the third-order susceptibility, several methods have been developed for the characterization of $\chi^{(3)}$. These include nonlinear interferometry, wave mixing methods, Z-scan technique, and measurements of the far-field beam distortion, optical damage thresholds, and ellipse rotation. The Z-scan technique⁸, introduced by Sheik-

* Correspondence: Email: ehpli@ntu.edu.sg; Telephone: (65)790 6319; Fax: (65)791 2687

Bahae *et al.*, has been proven to have several advantages in the determination of third-order optical nonlinearities. The Z-scan technique is a simple yet sensitive single-beam method. It is capable of providing information not only on the magnitude but also on the sign of the third-order susceptibility for a given material. It can also distinguish between the real and imaginary parts of the third-order susceptibility ($Re\chi^{(3)}$ and $Im\chi^{(3)}$), which can result from the optical Kerr effect and two-photon absorption, respectively.

Recently, we successfully synthesized surface modified PbS and $Cd_xPb_{1-x}S$ nanoparticles using a microemulsion method. In this paper, we present an experimental investigation of the third-order optical nonlinearity in PbS and $Cd_xPb_{1-x}S$ nanoparticles using the Z-scan technique with 150-fs laser pulses at 780-nm wavelength. The results show that, for all samples, no nonlinear absorption occurs, and the sign of nonlinear refractive index n_2 in these nanoparticles is negative. We found that, with the increase of the input irradiance, the measured Z-scan traces with large purely refractive nonlinear index for these nanoparticles become asymmetric and differ from the usual dispersionlike (symmetric) Z-scan curve⁸, implying a large nonlinear-phase distortion in the nanoparticles. We have performed theoretical fitting to these Z-scan data using an extended Z-scan theory based on the Huygens-Fresnel principle. The obtained large refractive nonlinearity n_2 in these nanoparticles is mainly attributed to the optical Stark effect and contribution from the surface-trapped state in the nanoparticles.

2. EXPERIMENTAL

2.1 Sample Synthesis

The samples employed in this study include nanometer-sized PbS and $Cd_xPb_{1-x}S$ semiconductors, which were prepared by using a microemulsion method. A system containing the surfactant of poly(oxyethylene), nonyl phenol ether (NP-5) and 1-dodecanethiol, an oil phase of petroleum ether (PE), and an aqueous phase of salt solution was used. The colloidal PbS nanoparticles were prepared by mixing two NP5/dodecanthiol-PE microemulsions, one of $Pb(NO_3)_2$ and the other of $(NH_4)_2S$. The mixing is produced by rapid injection of variable volume of both microemulsions of the same concentration of reactant and the fixed water/surfactants ratio. A series of PbS nanoparticles with various concentrations was prepared in microemulsion based on the compositions: 2 wt % of aqueous phase and 98 wt % of organic phase consisting of the surfactants and petroleum ether as an oil phase in the weight ratio of 1:9, in which the mixed surfactants, i.e. NP-5 and 1-dodecanethiol are fixed at 4:1. The resultant PbS nanoparticles were thus stabilized by a surfactant of poly(oxyethylene), nonyl phenol ether (NP5) and capped by dodecanthiol. The samples for optical measurements are PbS nanoparticles in microemulsion with the PbS concentration range of $0.3 - 2.5 \times 10^{-3}$ M (mol/L) as well as $Cd_xPb_{1-x}S$ nanoparticles in microemulsion with x from 0 to 1, as listed in Tables 1 and 2 respectively. The particle size and crystalline structure were measured by transmission electron microscope (TEM) and selected area diffraction (SAD). The linear absorption spectra of these nanoparticles in microemulsion were recorded using UV-visible spectrophotometer.

Table 1. Measured n_2 values in PbS nanoparticle microemulsion with the PbS concentration range from $0.3 - 2.5 \times 10^{-3}$ M.

Sample	A1	A2	A3	A4	A5
PbS concentration ($\times 10^{-3}$ M)	0.31	0.62	1.3	1.9	2.5
$n_2 (\times 10^{-12} \text{ cm}^2/\text{W})$	0.26	0.86	2.2	4.7	18

Table 2. Measured n_2 values in $Cd_xPb_{1-x}S$ nanoparticles with x from 0 to 1.

Sample	B1	B2	B3	B4	B5	B6	B7
Fraction x	0	0.20	0.33	0.50	0.67	0.80	1
$n_2 (\times 10^{-12} \text{ cm}^2/\text{W})$	2.6	2.6	5.3	4.2	4.3	2.0	0.54

2.2 Z-Scan Measurement

A schematic of our Z-scan experimental set-up is shown in Fig. 1. The laser pulses at 780-nm wavelength were delivered by

a mode-locked Ti:sapphire laser operating at a repetition rate of 76 MHz. The FWHM pulse duration was 150 fs. The spatial profile of the laser beam was nearly a Gaussian distribution after a spatial filter. The minimum beam waist ω_0 of the focused laser beam was measured to be 28 μm . The linearly polarized pulses were divided by a beam-splitter into two parts: the reflected one was used as a reference to represent the incident light power; and the transmitted one was focused through the sample. Both the beams were recorded by two power probes (Newport 818 SL) simultaneously, and measured by a dual channel power meter (Newport 2832-C) which transferred the digitized signals to a computer. The sample was mounted on a computer-controlled translation stage that moved the sample along the Z-axis with respect to the focus of the lens. When measuring the nonlinear refraction, a 1.4-mm-diameter aperture was placed in front of the transmission detector. As a reference, we performed a Z scan on a sample of polycrystalline ZnSe, and obtained $n_2 = 2.3 \times 10^{-14} \text{ cm}^2/\text{W}$ ($1.0 \times 10^{-11} \text{ esu}$) and two-photon absorption coefficient $\beta = 3.8 \times 10^{-9} \text{ cm/W}$, which are in good agreement with the published results measured at the same conditions.⁹

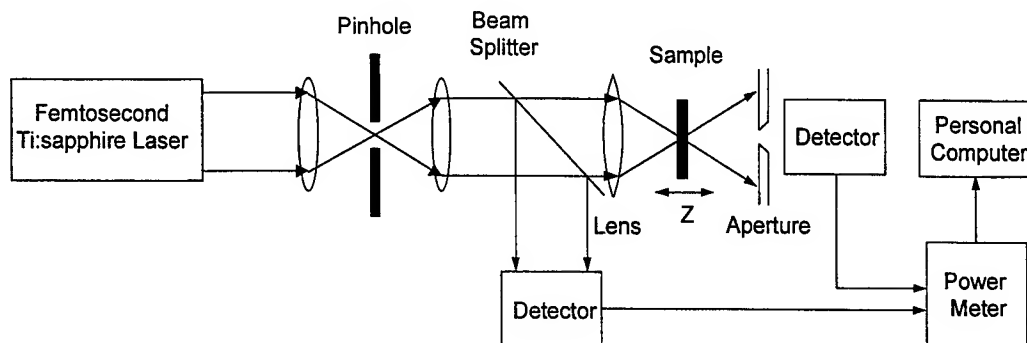


Fig.1 Experimental setup for Z-scan measurements

The nonlinear optical responses of the PbS and $\text{Cd}_x\text{Pb}_{1-x}\text{S}$ nanoparticles in microemulsion were investigated using the above-described Z-scan system. The samples were placed in a 1-mm-thick quartz cuvette, respectively. In our case, these samples satisfied the "thin sample" condition ($L < Z_0$, where L is the sample thickness, and Z_0 is the Rayleigh confocal parameter of the Gaussian beam)⁸. All the Z-scan measurements were carried out at room temperature. Our experimental error was about 20%, which mainly originated from the determination of the input irradiance distribution used in the experiment, i.e., beam waist, pulse width, and power calibration.

3. RESULTS AND DISCUSSION

Fig. 2 shows a typical TEM image and SAD pattern of the PbS nanoparticles in microemulsion. An average size of about 7

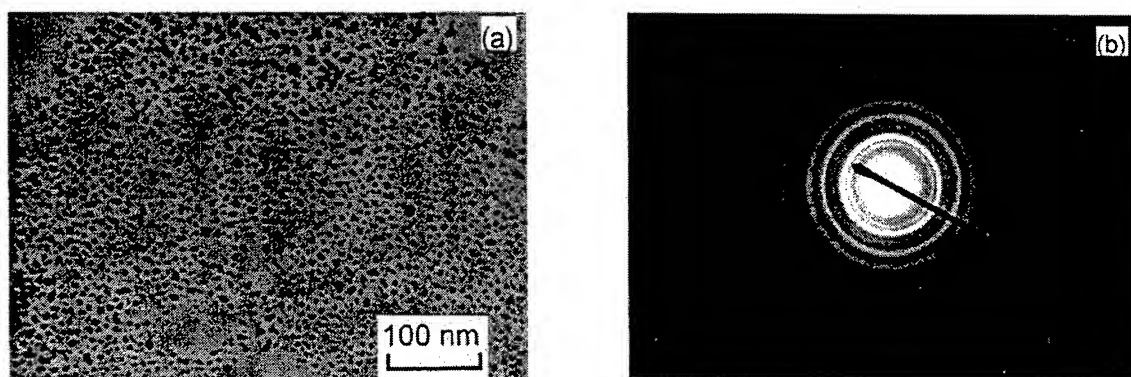


Fig. 2 (a) Transmission electron micrograph for PbS nanoparticles. (b) Electron diffraction pattern obtained from Fig. 2(a).

nm for these nanoparticles was observed, which is less than the bulk PbS exciton Bohr radius of 18 nm.¹⁰ The d-spacing calculated from the diffraction rings in Fig.2 establish a cubic rock salt structure for PbS particles. Compared with the standard value, all the diffraction rings are slightly broadened. This is due to the formation of nanocrystals. The linear absorption spectra of the PbS nanoparticle microemulsions (Samples A1-A5) are shown in Fig.3, which exhibits a blue shift in the absorption edges of the samples compared to bulk PbS. The results show that the onset of absorbance appears shifted to the longer wavelength with the increase of PbS concentration in the samples. The longer tail of the absorption band can be seen for the samples with high PbS concentration, which may be attributed to the size distribution of nanoparticles and defects on particle surface.

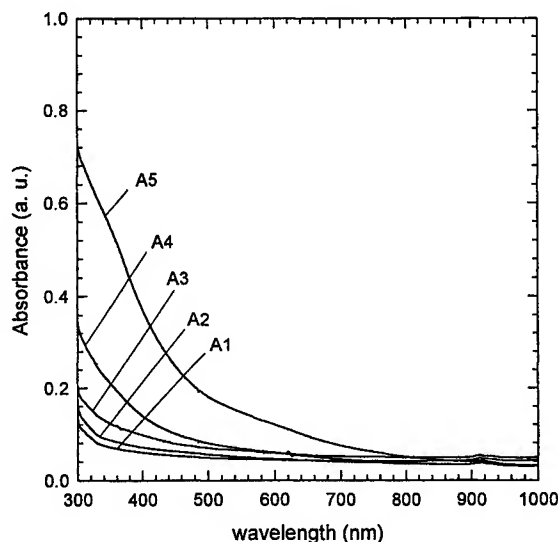


Fig. 3 The linear absorption spectra of PbS nanoparticle samples with PbS concentration range from $0.3 - 2.5 \times 10^{-3}$ M.

As an example, Fig.4 shows typical open-aperture and closed-aperture Z-scan results on the PbS nanocrystal microemulsion with 1.3×10^{-3} M (mol/L) PbS concentration, obtained with linearly polarized 780-nm femtosecond pulses at different irradiances. Note that all the input irradiances reported here are the peak irradiances at the focus within the sample. The measured open-aperture Z scans exhibit that Z-scan trace with the irradiance up to 0.9 GW/cm^2 is nearly flat, indicating that no two-photon absorption occurs in the sample at 780-nm wavelength. The measured closed-aperture Z scans show that the Z-scan traces at low irradiance level is symmetric about the focus $Z = 0$ (i.e., peak-valley symmetry), and the Z-scan traces become asymmetric with the increase of the input irradiance. The Z-scan trace at the irradiance of 155 MW/cm^2 in Fig.4 shows a severely asymmetric. Obviously the conventional Z-scan theory based on the small-phase-distortion approximation [i.e., the Gaussian decomposition (GD) method]⁸ does not fit the experimental data well. A Z-scan analysis based on the Huygens-Fresnel (H-F) principle will be used in present work as follows.

Consider a Z-scan experiment in which an incident laser beam with TEM_{00} Gaussian is propagating and is focused by a lens onto a thin sample. In the case of cubic nonlinearity and negligible nonlinear absorption, the irradiance at the exit surface of the sample may be obtained as:

$$I_t = I_i(r, t, z)e^{-\alpha L}, \quad (1)$$

where α is the linear absorption coefficient, L is the thickness of the sample, and z is the sample position. Here $I_i(r, t, z)$ is the irradiance within the sample. This irradiance is taken as a Gaussian in space and time, given by

$$I_i = \frac{I_0 \exp[-2(r/w)^2 - (t/t_0)^2]}{1 + (z/z_0)^2}, \quad (2)$$

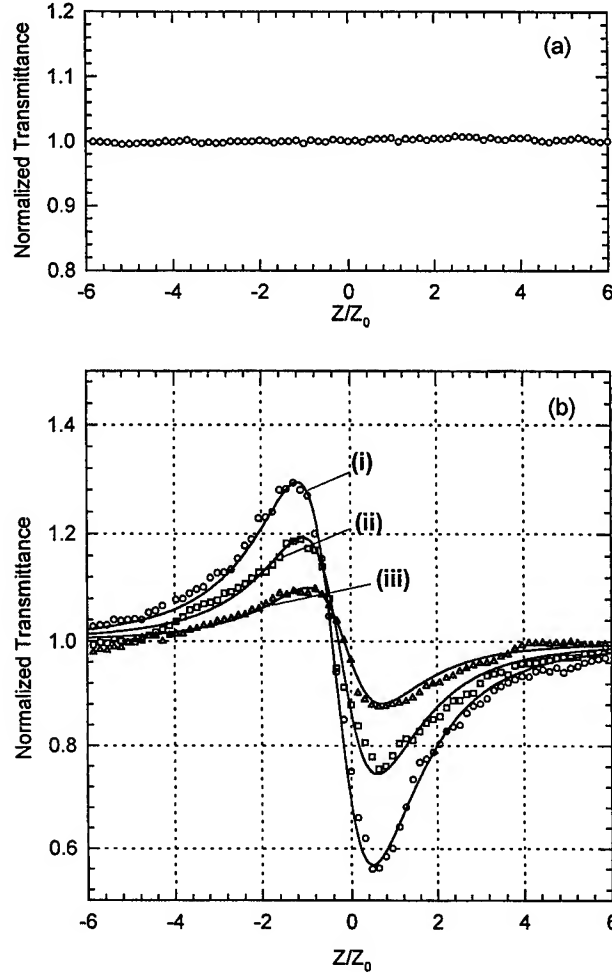


Fig. 4 Z-scan measurements on PbS nanoparticles in microemulsion (Sample A3). The open circles in (a) are measured without the aperture at the input irradiance of 500 MW/cm². The open circles, squares and triangles in (b) are measured with the aperture, respectively, at the input irradiances (i) 155, (ii) 95, and (iii) 47 MW/cm². The solid curves are the theoretical fits from Eq. (6).

where $z_0 = \pi w_0^2 / \lambda$, with w_0 the beam waist, r is the distance from the axis of the beam, and w is the radius of the beam at the z position. The nonlinear phase $\Delta\phi$ experienced by the beam may be derived as

$$\Delta\phi = \frac{\Delta\Phi_0}{1 + (z/z_0)^2} \exp(-2r^2/w^2) = \frac{kn_2 I_0 L_{eff}}{1 + (z/z_0)^2} \exp(-2r^2/w^2), \quad (3)$$

where $L_{eff} = [1 - \exp(-\alpha L)/\alpha]$, $\Delta\Phi_0$ is the on-axis nonlinear phase shift at the focus. The electric field at the exit surface of the sample is completely determined by Eqs. (1) and (3) [i.e., $E_s(r, t, z) \propto I^{1/2} \exp(i\Delta\phi)$].

The traditional Z-scan analysis is based on the GD method, which allows for calculation of the electric field in the plane of the aperture in front of the detector as a sum over infinite Gaussian beams. Based on this method, Sheik-Bahae *et al.* calculated the normalized transmittance through the aperture $T(z)$ under conditions of a small nonlinear phase shift, $|\Delta\Phi_0| < 1$, and small aperture. $T(z)$ is given by⁸

$$T(z) = 1 + \frac{4x\Delta\Phi_0}{(x^2+1)(x^2+9)} \quad (4)$$

with $x = z/z_0$. One can find that the last term of the right-hand side of Eq.(4) is an odd function of z , which indicates that the curve described by Eq.(4) is symmetric, crossing the axis $T(z) = 1$ at $z = 0$. Our measured Z-scan traces at high irradiance level, corresponding to large-nonlinear-phase shift, show an asymmetric characteristic. Hence, Eq.(4) is not applicable to this case.

In our numerical analysis, the electric field E_a at the aperture is obtained by applying an H-F propagation integral:¹¹

$$E_a(r, t, z) = \frac{2\pi}{i\lambda(d-z)} \exp\left[\frac{i\pi r^2}{\lambda(d-z)}\right] \int_0^\infty r' dr' E_s(r', t, z) \exp\left[\frac{i\pi r'^2}{\lambda(d-z)}\right] J_0\left[\frac{2\pi r r'}{\lambda(d-z)}\right], \quad (5)$$

where d is the distance between the aperture and the focal plane. The normalized transmittance $T(z, S)$ can be obtained as

$$T(z, S) = \frac{c\epsilon_0 n_0 \pi \int_{-\infty}^{\infty} dt \int_0^a |E_a(r, t, z)|^2 r dr}{S \int_{-\infty}^{\infty} P_i(t) dt}, \quad (6)$$

where $P_i(t) = \frac{\pi w_0^2}{2} I_0 \exp[-(t/t_0)^2]$ is the instantaneous input power, $S = 1 - \exp(-2r_a^2/w_a^2)$ is the aperture linear transmittance, with r_a and w_a denoting the aperture radius and the beam radius at the aperture in the linear regime, respectively.

It should be pointed out that Eq.(6) based on the H-F propagation integral is general and exact, which enables the calculation of $T(z)$ for any magnitude of nonlinear phase, as long as it keeps a Gaussian profile. Fig.5 shows the analytical curves resulting from GD theory Eq.(4) and Eq.(6) based on the H-F propagation integral for the nonlinear phase shift $\Delta\Phi_0$ equal to $-\pi/4, -\pi/2, -\pi, -3\pi/2$ and -2π . As $|\Delta\Phi_0|$ increases, we note that the Eq.(6)-predicted curves become asymmetric, and the point where it crosses the axis $T(z)=1$ moves away from the zero towards the negative portion of the axis. This trend is in agreement with our measured Z scans on PbS nanocrystals. In addition, it is interesting to note that, as represented in Fig. 5(a) for nonlinear phase shift larger than 4.93, the transmittance of Eq. (4) has a negative value, which is physically unacceptable.

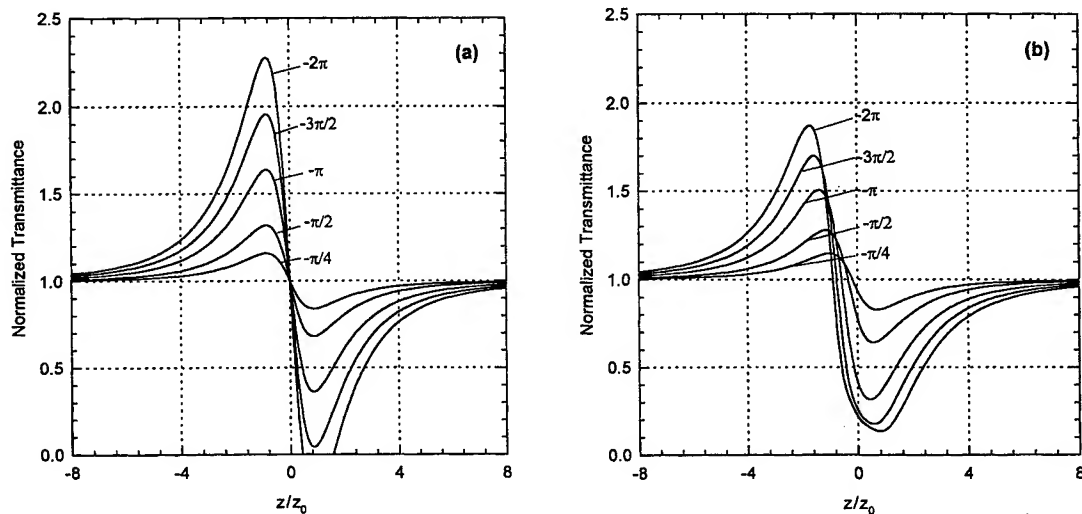


Fig. 5 Theoretical plots of closed-aperture Z-scan transmittance for purely nonlinear refraction: (a) the conventional small-phase-shift theory of Eq.(4) derived from Sheik-Bahae *et al.* and (b) the large nonlinear-phase-shift theory of Eq. (6) based on the Huygens-Fresnel principle.

By applying Eq.(6), we numerically calculated the normalized transmittance as a function of the z position using n_2 as a free parameter. The n_2 value can be extracted from the best fit. The solid lines in Fig.4 show the best fits to the experimental data at different input irradiances ranging from 30 – 200 MW/cm², which yield a range of n_2 values. We plot these n_2 values versus the input irradiances is shown in Fig.6. The results show that, in our experimental error, the measured n_2 is independent of the input irradiance, which confirms that the observed nonlinear refraction is the Kerr nonlinearity. Similar Z scans and analytical procedures have been carried out for the other samples. The measured n_2 values are summarized in Tables 1 and 2. It should be pointed out that nonlinear absorption was not observed for all samples, and the sign of their n_2 is negative, corresponding to a self-defocusing nonlinearity. We also conducted Z scans on the reagents used to synthesize these nanoparticles in microemulsion, and no nonlinearities are measurable, indicating that the PbS and Cd_xPb_{1-x}S nanoparticles give rise to the observed refractive nonlinearity in these microemulsions. The measured results also show that the n_2 value of the highest PbS-concentration microemulsion measured is 1.8×10^{-11} cm²/W, which is ~ 4 orders of magnitude higher than those of commercially available bulk materials such as CdS and ZnS measured at the same conditions¹⁰. For the samples of PbS nanoparticles, refractive nonlinearity n_2 is plotted against the PbS concentration in microemulsion in Fig.7 and can be seen to be approximately linear with the PbS concentration over the range of $0.3 - 1.9 \times 10^{-3}$ M. Therefore, we can conclude that the increase in the concentration of PbS nanoparticles is one of the ways to enhance the refractive nonlinearity of the composite. For Cd_xPb_{1-x}S nanoparticle samples, n_2 value is closely related to the fraction x in Cd_xPb_{1-x}S. It is found that Cd_{0.33}Pb_{0.67}S nanoparticles exhibits relatively larger refractive nonlinearity.

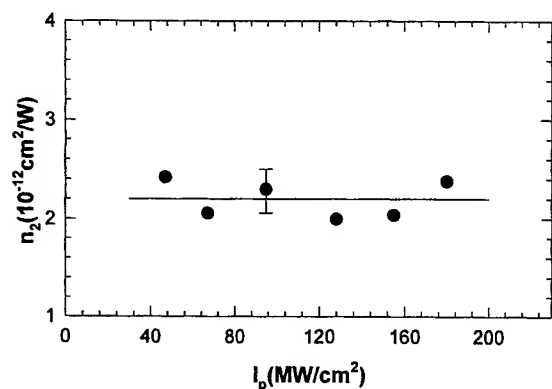


Fig. 6 Measured n_2 (filled circles) versus the input irradiance, I_p , for PbS nanoparticles in microemulsion (Sample A3). The solid line is a guide for the eye.

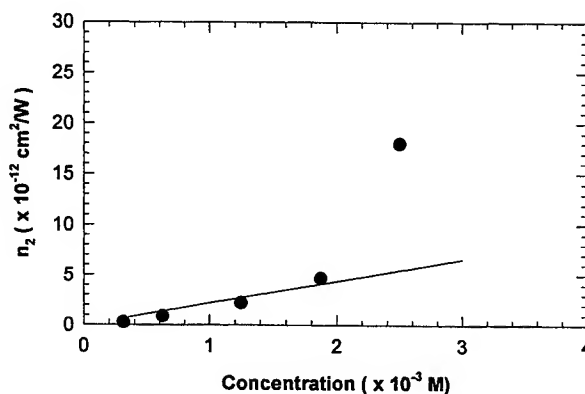


Fig.7 Measured n_2 (filled circles) plotted against PbS nanoparticle concentration in microemulsion.

Since the excitation frequency at 780 nm in our Z-scan measurement is below the absorption edge of the samples, the observed optical nonlinearity is nonresonant. The obtained large purely refractive nonlinearity of the PbS nanoparticles originates mainly from two mechanisms: (1) Optical Stark Effect (OSE). Cotter *et al.*² have confirmed that OSE makes the dominant contribution to the third-order refractive nonlinearity of quantum-confined semiconductor nanoparticles in the transparency region. Our experimental results agree to their conclusion, since our samples exhibit large refractive nonlinearity and negligible absorptive nonlinearity. As is already known, an interfacial polarization field will enhance OSE. Hence, we intentionally modified our nanoparticles with a layer of surfactant molecules forming an interface dipole layer on the surface of the nanoparticles, which may result in larger refractive nonlinearity. (2) Due to the high surface-to-volume ratio of the nanoparticles, there exist a number of surface-trapped states in the bandgap of the nanocrystals. These surface-trapped states, although of relatively low state density, could also significantly contribute to the optical nonlinearity¹². The direct excitation of these surface trapped states will generate photocarriers, which will also give a negative n_2 . In addition, due to the high repetition rate (76 MHz) of the laser pulses used in our Z-scan measurement, some slow nonlinear processes (e.g., thermal effect) may also be involved. Further investigation, such as femtosecond time-resolved nonlinearity experiment, is necessary to distinguish between these nonlinear mechanisms involved.

4. CONCLUSION

The third-order optical nonlinearity of surfaced modified PbS and $\text{Cd}_x\text{Pb}_{1-x}\text{S}$ nanoparticles in microemulsion has been studied using a Z-scan technique with femtosecond 780-nm pulses. An extended Z-scan theory was applied to extract the nonlinear refractive index n_2 from the experimental Z-scan data with a large nonlinear phase shift. The n_2 value of PbS nanoparticles in microemulsion was found to increase approximately linearly with the PbS concentration range from $0.3 - 1.9 \times 10^{-3}$ M. The sample of the highest PbS concentration in microemulsion gave a n_2 value of $1.8 \times 10^{-11} \text{ cm}^2/\text{W}$, which is about 4 orders of magnitude higher than those of commercially available bulk semiconductors, such as ZnS and CdS. For $\text{Cd}_x\text{Pb}_{1-x}\text{S}$ nanoparticles, $\text{Cd}_{0.33}\text{Pb}_{0.67}\text{S}$ was found to have relatively larger refractive nonlinearity. No nonlinear absorption was measurable up to $0.9 \text{ GW}/\text{cm}^2$ for these nanoparticles. The observed large refractive nonlinearity in these nanoparticles mainly originated from the optical Stark effect and contribution of the surface-trapped states of the nanoparticles. The experimental results show that these nanoparticles with large refractive nonlinearity and ultrafast response are potential materials for application in optical devices such as optical limiting and switching.

REFERENCES

1. N. Chestnoy, T.D. Harris, R. Hull, and L.E. Brus, "Luminescence and photophysics of CdS semiconductor clusters: the nature of the emitting electronic state", *J. Phys. Chem.* **90**, pp. 3393-3399, 1986.
2. D. Cotter, M. G. Burt, and R. J. Manning, "Below-band-gap third-order optical nonlinearity of nanometer-size semiconductor crystallites", *Phys. Rev. Lett.* **68**, pp. 1200-1203, 1992.
3. T. Takagahara, "Effects of dielectric confinement and electron-hole exchange interaction on excitonic states in semiconductor quantum dots", *Phys. Rev. B* **47**, pp. 4569 - 4584, 1993.
4. X. Ai, H. S. Fei, Y. G. Yang, L. Han and R. Nie, "Polar enhancement of nonlinear-optical properties of Fe_2O_3 microcrystallites", *J. Lumin.* **60&61**, pp. 364-367, 1994.
5. B. L. Justus, R. J. Touncci, and A. D. Berry, "Nonlinear optical properties of quantum-confined GaAs nanocrystals in vycor glass", *Appl. Phys. Lett.* **61**, pp. 3151-3153, 1992.
6. B. L. Justus, A. D. Campillo, D. G. Hendershot, and D. K. Gaskill, "Optical limiting in semiconductor nanocrystals in glass", *Opt. Commun.* **103**, pp. 405-409, 1993.
7. B. Yu, C. Zhu, and F. Gan, "Optical nonlinearity of Bi_2O_3 nanoparticles studied by Z-scan technique", *J. Appl. Phys.* **82**, pp. 4531-4537, 1997.
8. M. Sheik-Bahae, A. A. Said, T. H. Wei, D. J. Hagan, and E. W. Van Stryland, "Sensitive measurement of optical nonlinearities using a single beam," *IEEE J. Quantum Electron.*, **26**, pp. 760-769, 1990.
9. T. D. Krauss, and F. W. Wise, "Femtosecond measurement of nonlinear absorption and refraction in CdS, ZnSe and ZnS", *Appl. Phys. Lett.* **65**, pp. 1739-1741, 1994.
10. J. L. Machol, F. W. Wise, R. C. Patel, and D. B. Tanner, "Vibronic quantum beats in PbS microcrystallites", *Phys. Rev. B* **48**, pp. 2819- 2822, 1993.
11. J. D. Gaskill, *Linear Systems, Fourier Transforms, and Optics*, Wiley, New York, 1978.
12. F. Z. Henari, K. Morgenstern, W. J. Blau, V. A. Karavanskii, and V. S. Dneprovskii, "Third-order optical nonlinearity and all-optical switching in porous silicon", *Appl. Phys. Lett.* **67**, pp. 323-325, 1995.

Hyper-Rayleigh scattering and multi-photon fluorescence of Nanoscale CdS colloids in water

Xin WANG^a, Yu ZHANG^a, Degang FU^a, Zuhong LU^a, Yiping CUI^b

^aNational Lab. of Molecular and Biomolecular Electronics, Southeast Univ., Nanjing, 210096, China

^bLab. of Opto-electronic Technology, Southeast Univ., Nanjing, 210096, China

ABSTRACT

Optical nonlinearities of semiconductor nanoparticles are of great interest recently. Here the Hyper-Rayleigh scattering (HRS) technique is used to measure the second-order nonlinear optical (NLO) responses of nanoscale CdS Colloids with different surfaces in water. It shows that the HRS signals for CdS Colloids (about 5 nm in diameter) are very strong. The "per particle" first-order hyperpolarizability values β are estimated to fall in the range of 10^{-26} esu, and "per CdS unit" are in the range of 10^{-28} esu which is very large. And the β values are different for CdS nanoparticles with different surfaces. Further studies show that the CdS/SC(NH₂)₂ nanoparticle has strong multi-photon fluorescence (MPF) emission under the radiation of 1064 nm so the large signal at 532 nm is mainly from the MPF. But for Cd²⁺-rich and S²⁻-rich CdS nanoparticles the MPF are relatively weaker at 532 nm. These experiments reveal that the HRS or MPF signals are very sensitive to the changes of the nanoparticle surface and can provide useful information about the nanoparticle/solution interface. They also give the evidences proving that surface termination of the crystalline lattice that creates a condition of non-centrosymmetry is contributing to the large β value for CdS nanoparticles.

Keywords: CdS nanoparticle, semiconductor quantum dots, nanoparticle surface, nanoparticle/solution interface, Hyper-Rayleigh scattering (HRS), multi-photon fluorescence (MPF), two-photon fluorescence (TPF), first-order hyperpolarizability (β), second-order nonlinear optical property, nonlinear optics (NLO)

1. INTRODUCTION

With the development of modern integrated microelectronics and opto-electronics techniques, the functional components become smaller and smaller, so it is unavoidable to study the new properties and phenomena of low-dimensional materials and systems. During the last decade or two, research on nano-crystallite, often called "quantum crystallites" or "quantum dots", has developed into an active interdisciplinary field in materials science.¹⁻⁴ Semiconductor or metal nanoparticles exhibit interesting optical properties due to the confinement of the electronic wavefunctions, the drastically changed surface-to-volume ratio, and their surface conditions. The optical properties include linear absorption, fluorescence and electroluminescence as well as nonlinear optical (NLO) properties such as bleaching, electro-optic Stark effect, nonlinear absorption and nonlinear fluorescence. Many workers have reported that semiconductor^{2, 5-10} or metal¹¹⁻¹³ colloid particles doped Glasses, polymers or thin films show high optical nonlinearity, so they are attractive candidates for utilization in optical devices such as optical shutters, optical limiters, phase-conjugate mirrors and optical transistors. In particular, commercial glasses doped with micro-crystallites (100-1000Å) of CdS_xSe_{1-x} have been studied most extensively because of their strong nonlinearity, the absence of significant carrier diffusion, and their relatively fast response time.⁶⁻⁸ Up to the present time most of the studies in published papers about the NLO properties of quantum crystallites were concentrated on the third-order nonlinearity $\chi^{(3)}$ or γ . It is usually believed that the centrosymmetry or near-centrosymmetry structures of the ultra small particles eliminate their $\chi^{(2)}$ values to zero or near zero. And for a long time it remains a problem to directly study the second-order NLO properties of such nanoscale particles by conventional NLO techniques.

Recent advances in lasers and optical detection systems have led to the invention of several powerful methodologies for NLO properties probing and surface characterization. Among these, second-harmonic generation (SHG) which makes use of the second-order NLO effect has received much attention, because of its simplicity, surface specificity and versatility.¹⁴⁻¹⁵ SHG techniques have been widely applied to chemical and electrochemical interfaces (including monolayer or Langmuir-

* Correspondence: Email: wxzr@seu.edu.cn; Telephone: +86(25)3792245; Fax: +86(25)3619983

Blodgett film¹⁶), where they have proven useful for evaluating surface second-order nonlinear susceptibility, chemisorption, space charge properties, surface symmetry, surface dynamics, and molecular orientation.¹⁵ However, because of the finite coherence length for the required incident radiation, practical sample size limitation (lower limit, about an order of magnitude less than the wavelength of incident light) exists for this conventional coherent SHG approach.¹⁷ So the SHG technique can not be applied to the microscopic domain of nanoparticle. Another conventional NLO technique is called electric field induced second-harmonic generation (EFISHG). Just like SHG, it makes use of the coherent optical phenomenon, but additionally it needs an external static electric field to re-orient the chromophores so as to remove the centrosymmetry. This method is rather complicated and more importantly, it can neither be used for the chromophores that do not have a permanent dipole moment, nor the species with charge.¹⁸⁻¹⁹ For a nanoparticle it usually do not possess a stable permanent dipole moment so it can't be oriented, and it often has charges on the surface (according to the synthetic method) which might cause migration or even aggregation under the applied electric field.

Recently, a few workers make use of the newly developed Hyper-Rayleigh scattering (HRS), i.e. the incoherent harmonic light scattering technique to study the second-order NLO properties of metal colloid nanoparticle or insulator nanoparticle SiO_2 .¹⁷ We are also carrying out some studies on the second-order NLO properties of semiconductor nanoparticles especially the II-VI semiconductor nanoparticles.²⁰ Results of the initiatory work may prove that surface termination of the crystalline lattice creates a condition of non-centrosymmetry in a nanoparticle observable by HRS, so it can account for the large "per particle" first-order hyperpolarizability values β . Further studies show that the situation is more complicated and we will discuss it in section 3.2. As for the incoherent HRS technique we are using here, its model relies on the random fluctuations of the chromophore density or chromophore orientation, which instantaneously break the centrosymmetry of the isotropic media in the microscopic area of incident laser beam.²¹ So HRS technique is not constrained by the orientation, charge or size restrictions as mentioned above. In this paper, we report the new studies of II-VI semiconductor CdS colloids with different surfaces in water.

2. EXPERIMENT

Three kinds of CdS nanoparticles were prepared in aqueous solution by colloidal solution method. When a dilute Cd^{2+} solution is mixed with S^{2-} solution, solid CdS will be precipitated under thermal equilibrium because CdS is not so soluble in water. Here the starting materials were $\text{Cd}(\text{NO}_3)_2$ and Na_2S solution. For CdS nanoparticles with Cd^{2+} -rich or S^{2-} -rich surface, we did not add any stabilizing agent so the system was simple, and there were no disturbance signals from the stabilizing agents in the experiments. The molar ratio of Cd^{2+} : S^{2-} was 1:0.6 and 0.6:1 for Cd^{2+} -rich and S^{2-} -rich colloid respectively. Some of the excessive ions would be adsorbed onto the surfaces and they could prevent the aggregation to some extent, because of the repulsive force between the nanoparticles. The thiourea $\text{SC}(\text{NH}_2)_2$ was added to the Cd^{2+} -containing solution to prepare the $\text{SC}(\text{NH}_2)_2$ -rich CdS nanoparticle. The molar ratio of Cd^{2+} : S^{2-} : $\text{SC}(\text{NH}_2)_2$ was 1:0.6:4, the excessive $\text{SC}(\text{NH}_2)_2$ acted as not only surface modification molecule but also stabilizing agent. For controlling the particle size and preventing the aggregation, all the synthetic procedures were carried out at very quick mixing speed under low temperature and in stirred solutions. And the solution concentrations of CdS colloids were low to 3.75×10^{-4} M for all three samples. We will use CdS/ Cd^{2+} , CdS/ S^{2-} and CdS/ $\text{SC}(\text{NH}_2)_2$ to present the three samples in the following text. Before next experiments, all colloid samples were aged in darkness at cool room temperature. The aged time was six hours, one day and two days for CdS/ $\text{SC}(\text{NH}_2)_2$, CdS/ S^{2-} and CdS/ Cd^{2+} respectively. All the samples existed stable before and during the following experiments.

Figure 1 shows the UV-visible absorption spectra of the three CdS colloids and the transmission electron microscopy (TEM) image of the CdS/ $\text{SC}(\text{NH}_2)_2$. The absorption spectra for the three samples were almost the same, which indicated that they were almost the same of particle size and size distribution. It could be deduced from the absorption thresholds of the spectra that the particle sizes were about 5~6 nm.²⁰ The TEM image also revealed that the mean size of CdS/ $\text{SC}(\text{NH}_2)_2$ particle was about 5 nm in diameter and the size distribution was narrow, and for CdS/ S^{2-} and CdS/ Cd^{2+} the TEM images were similar. The transmission electron diffraction pattern showed that the CdS nanoparticle aggregations were in multicrystal form with the cubic zinc blende structure. To prove that these CdS samples had different surfaces we measured their fluorescence spectra. The fluorescence emission of naked CdS colloids CdS/ S^{2-} or CdS/ Cd^{2+} was very weak; the emission peak was about 620 nm. But for CdS/ $\text{SC}(\text{NH}_2)_2$ colloid, the fluorescence was much stronger and two new fluorescence emission peaks emerged around 400 nm: one was at 371 nm, the other was at 467 nm. From the fluorescence spectrum of CdS/ $\text{SC}(\text{NH}_2)_2$ colloid, we found that the intensities of the new peaks were much higher than its peak in the red area, which indicated that the surfaces were capped well with $\text{SC}(\text{NH}_2)_2$. In addition, we studied the concentrated powder samples from CdS/ $\text{SC}(\text{NH}_2)_2$ colloid by infrared (IR) absorption spectroscopy, which also proved the obvious existence of Cd-S coordinate linkages on the surface. So the three CdS samples were successfully synthesized with different surfaces and a small size of 5~6 nm.

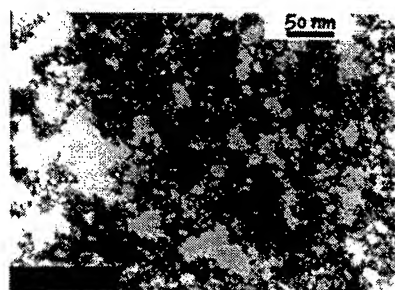
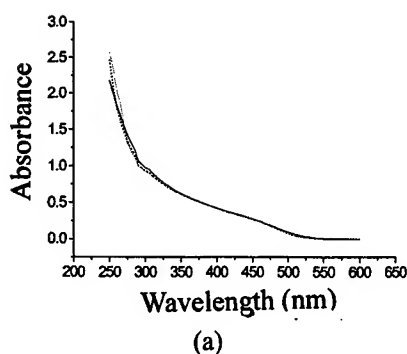


Figure 1. (a) The UV-visible absorption spectra of three CdS colloid samples in water with the same molar density of 3.75×10^{-4} M. (b) The TEM image of the CdS/SC(NH₂)₂ nanoparticle.

In the HRS experiments, samples with different concentration were obtained from the stock standard colloid solutions by successive dilutions. The measurements were performed by using a setup similar to K. Clays's (see Figure 2).²¹ The incident beam of a Q-switched Nd:YAG laser (Continuum Surelite II) at 1064 nm operating at 5 Hz with 8-10 ns pulse width was focused into a 5-cm glass cell with the pulse energy lower than 1 mJ. A 532 nm (12 nm bandwidth) interference filter was used at the entrance to the photomultiplier tube (PMT) to prevent any luminescence of the sample at other wavelength from reaching the detector. The signals from the PMT were analyzed with a microprocessor-based boxcar integrator (EG&G 4400, 4402) which was triggered by the Q-switch of the laser.

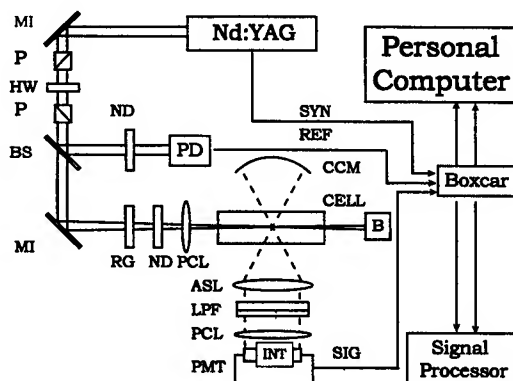


Figure 2. Setup for the HRS experiment

ASL: aspheric lens condenser,
B: beam-stop, BS: beam-splitter,
CCM: concave mirror,
HW: half-wave plate,
INT: interference filter,
LPF: low pass filter,
MI: mirror, ND: neutral density filter,
P: polarizer, PCL: plano-convex lens,
PD: fast photodiode,
PMT: photomultiplier tube,
REF: reference signal, RG: high pass filter,
SYN: synchronization signal.

For multi-photon fluorescence (MPF) experiment the setup was the same as the HRS setup but we replaced the 532 nm interference filter by a series of interference filters at different wavelengths in the range from 513 nm to 631 nm.

3. RESULTS AND DISCUSSION

3.1. Hyper-Rayleigh Scattering Experiment

HRS experiment allows for the direct assessment of sample's first-order hyperpolarizability β in multi-component systems if β for other components has been previously established. It is called the internal reference method (IRM). If the incident intensity is I^0 , then the frequency-doubled light ($I^{2\omega}$) observed for a two-component system can be described by eq (1) for low solute concentration¹⁹⁻²¹ as following:

$$I^{2\omega} = G (N_1 \langle \beta_1^2 \rangle + N_2 \langle \beta_2^2 \rangle) (I^0)^2. \quad (1)$$

In eq (1), N is number density of each component, G is a constant parameter for low solute concentration that encompasses collection efficiencies as well as local-field correction factors, subscriptions 1 and 2 denote solvent and analyte respectively, and the brackets indicate the orientational averaging. N_1 is constant for low solute concentration and the plot of N_2 vs. $I^{2\omega}/(I^0)^2$ yields a straight line of slope $G\langle \beta_2^2 \rangle$ and intercept $GN_1\langle \beta_1^2 \rangle$. So β_2 can be obtained from the slope divided by the

intercept when β_1 is known. To ascertain that the results of our measurements are consistent with the accepted data, we have calibrated our experiment by using para-nitroaniline (p-NA) dissolved in chloroform as the sample. And we obtained the β of p-NA to be 37×10^{-30} esu in the density lower than 2 mM, which was in satisfactory agreement with the literature value.²²

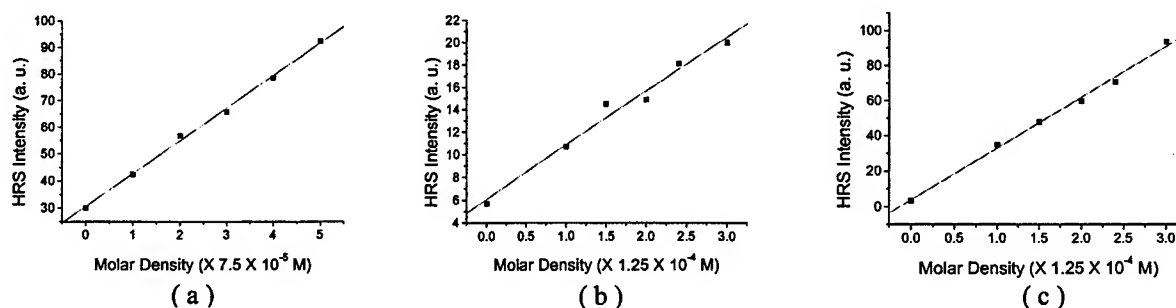


Figure 3. HRS intensities as function of molar densities for the CdS nanoparticles in water. (a) for CdS/Cd²⁺ colloid; (b) for CdS/S²⁻ colloid; (c) for CdS/SC(NH₂)₂ colloid.

Shown in Figure 3 are plots of the concentration dependence of the HRS intensity from CdS colloids at pH=5.6~6.0. As predicted by eq (1), the signals scaled linearly with the concentration of the colloids. From the linear fitting results, the value of β per CdS formula unit for CdS/Cd²⁺ (from Figure 3 (a)) was determined to be 3.1×10^{-28} esu by using water as an internal standard ($\beta_{\text{water}} = 0.56 \times 10^{-30}$ esu).¹⁷ This β value is very large in comparison with commonly studied organic chromophore. For example, it is larger than p-NA by about eight times. Similarly we obtained that the per Cd unit β value for CdS/S²⁻ was 3.3×10^{-28} esu (from Figure 3 (b)) and for CdS/SC(NH₂)₂ was 1.03×10^{-27} esu (from Figure 3 (c)).

The foregoing analysis assumed that the HRS signal originated from the collective effects of the nanoscale particle, especially from the surface molecules with highly non-symmetry because of imperfection or defect of the surface crystal lattice. So a "per particle" β value is more suitable for assessment. Here we estimated that one CdS nanoparticle of 5~6 nm contains about 1800 CdS units. So the "per particle" β values for CdS/Cd²⁺, CdS/S²⁻ and CdS/SC(NH₂)₂ were estimated to be 1.3×10^{-26} esu, 1.4×10^{-26} esu and 4.4×10^{-26} esu respectively. Considering the error in our measurement and if we deducted the error we could only say qualitatively that the β value of CdS/S²⁻ was slightly larger than that of CdS/Cd²⁺. We know that the two kinds of nanoparticles were synthesized under the same condition and by the same chemical method, and the mere difference was the kind of excess ion on their surfaces. So it proved that even small change of the surface conditions could give an observable influence on the HRS signal, i.e. the β value. And it is believable that the surface termination of the crystalline lattice that creates a condition of non-centrosymmetry contributes to the large β values for CdS nanoparticles by origin. But for CdS/SC(NH₂)₂ the β value was somehow too large. It could not result from the residual SC(NH₂)₂ in the solution, because we had measured the HRS signal from the no colloids-containing filtrate and found that the signal was negligible by comparing to that of the CdS colloids. So we carried on multi-photon fluorescence (MPF) experiments to verify if there existed MPF overlapping on the HRS signal at 532 nm wavelength.

3.2. Multi-photon Fluorescence Experiment

The multi-photon fluorescence (MPF) experiment was performed by replacing the 532 nm interference filter by a series of interference filters at different wavelengths (about 15 nm intervals) in the range from 513 nm to 631 nm. All the signals at each measure wavelengths were normalized according to the filters' bandwidths and transmittances, and the photomultiplier tube's spectral response characteristic. MPF is a kind of NLO phenomenon higher than the second order. For example, two-photon fluorescence (TPF) that absorbs two photons at once and emits one photon of higher frequency is the third-order NLO phenomenon.

Figure 4 shows the MPF emission spectra of CdS/Cd²⁺ and CdS/SC(NH₂)₂ colloids in water. The MPF spectrum of CdS/S²⁻ was similar to that of CdS/Cd²⁺. Because the bandwidth of each interference filter is about 15 nm, the MPF emission spectra were grossly measured and couldn't provide delicate substructures of the spectra. But it was still clear that the MPF spectral shapes were quite different from their linear fluorescence ones. The MPF peaks can reflect some new surface energy states, defect states and coupling modes with them or other states (acoustic mode is one example). For CdS/SC(NH₂)₂ colloid the

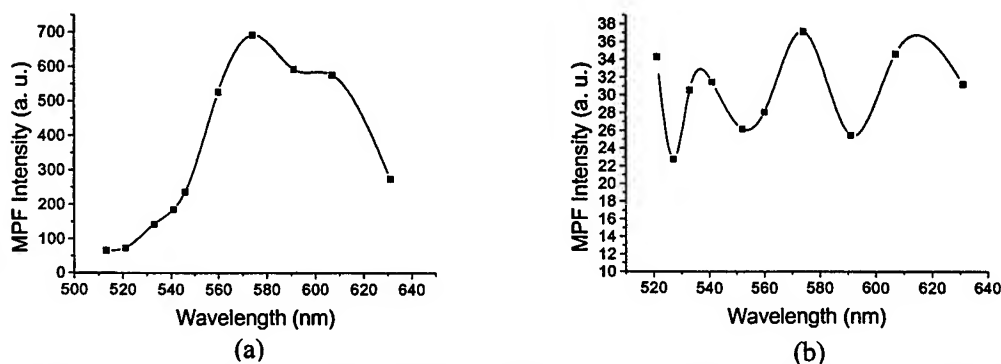


Figure 4. The multi-photon fluorescence emission spectra for the CdS colloids in water. (a) for CdS/SC(NH₂)₂ colloid; (b) for CdS/Cd²⁺ or CdS/S²⁻ colloid.

strong MPF at 532 nm overlapping the HRS signal might exceed it to about one order of magnitude. So when we cut off the MPF signal from the HRS signal, the "per particle" β value for CdS/SC(NH₂)₂ would decrease to 1.3×10^{-26} esu, assuming that the MPF was ten times of the HRS signal at 532 nm. For CdS/Cd²⁺ or CdS/S²⁻ the MPF also existed with a different spectrum shape than CdS/SC(NH₂)₂ (see Figure 4), and the fluorescence intensity was much weaker at the same concentration and incident laser intensity. We assumed that MPF at 532 nm was the same as HRS signal in amplitude, so the "per particle" β values for CdS/Cd²⁺ and CdS/S²⁻ decreased to 9.2×10^{-27} esu and 1.0×10^{-26} esu. If we want to get more precise β values for them, more detailed measurements of the MPF emission spectrum are needed with spectrum resolution high enough. And sometimes when MPF at 532 nm is very strong and not smoothly changing in the neighbor wavelengths, the true β value may not be able to be obtained through the mere HRS measurement. One reparative way to overcome the problem is to select a suitable incident wavelength to minimize the fluorescence at the second harmonic generation wavelength.

Because surface perturbations can be easily accomplished by changing the pH of the bulk solution with addition of acid or base, we also carried out pH-dependent experiment to study the relationship between surface condition and HRS intensity. We found that the HRS signal changed remarkably when the pH was different. From the absorption spectrum we excluded either particle aggregation or particle dissolution during our pH adjustment, so the change of HRS signal came from the change of the particle surface. It is well known that in solution the particles usually have electric-double-layer structure near their surfaces so we couldn't exclude that part of the signal might generate from the coupling with the $\chi^{(3)}$ effect, which combined the interfacial static electric field with two optical fields. We need further studies to clarify these relationships. From our present results and those of other researchers¹⁷, we can say that the signal arising from the "particle" first-order hyperpolarizability effect exists and takes more part than the double-layer-based $\chi^{(3)}$ effect.

4. CONCLUSIONS

We had synthesized three kinds of 5–6 nm CdS nanoparticles with different surfaces successfully. HRS technique, MPF spectroscopy and pH-dependent experiments were performed to study the NLO properties of them in water. Although the HRS signals are mixed with the MPF and the signals coupling with the $\chi^{(3)}$ responses, if we deduct these unwanted effects, we can see that the true HRS signals from the CdS nanoparticles are still very strong. Concentration-dependent measurements show that the "per particle" first-order hyperpolarizabilities β for CdS nanoparticles are very large (in the range of 10^{-26} esu) and the β are different for different surfaces. The results of these initiatory studies proved that surface termination of the crystalline lattice creates a condition of non-centrosymmetry in a nanoparticle and it is the origin of the large "per particle" β value.

In conclusion, HRS technique provide a new tool to study the second-order NLO properties and symmetry properties of nanoscale particles, which has many advantages over the conventional coherent SHG and EFISHG techniques. It also represents a powerful methodology for interrogating the surface chemistry and photo-physical properties of these materials because the HRS signal is extremely sensitive to the surface conditions of the nanoparticles. The large second-order NLO responses of the II-VI semiconductor nanoparticles suggest that they have considerable potential in NLO applications and opto-electronic devices. And we need more researches to investigate and improve the NLO properties of these nanoscale materials.

ACKNOWLEDGMENTS

We would like to thank Dr. Yaochun SHEN for helpful discussions and suggestions. Financial support by the National Science Foundation of China is gratefully acknowledged.

REFERENCES

1. G. D. Stucky and J. E. Mac Dougall, "Quantum confinement and host/guest chemistry: Probing a new dimension," *Science*, **247**, pp. 669-678, 1990.
2. D. Ricard, P. Roussignol, F. Hache, and C. Flytzanis, "Nonlinear optical properties of quantum confined semiconductor microcrystallites," *Phys. Stat. Sol. (b)*, **159**, pp. 275-285, 1990.
3. L. Brus, "Quantum crystallites and nonlinear optics," *Appl. Phys. A*, **53**, pp. 465-474, 1991.
4. H. Weller, "Quantized semiconductor particles: A novel state of matter for materials science," *Adv. Mater.* **5**(2), pp. 88-95, 1993.
5. R. K. Jain and R. C. Lind, "Degenerate four-wave mixing in semiconductor-doped glasses," *J. Opt. Soc. Am.* **73**(5), pp. 647-653, 1983.
6. K. W. DeLong, A. Gabel, C. T. Seaton, and G. I. Stegeman, "Nonlinear transmission, degenerate four-wave mixing, photodarkening, and the effects of carrier-density-dependent nonlinearities in semiconductor-doped glasses," *J. Opt. Soc. Am. B*, **6**(7), pp. 1306-1313, 1989.
7. S. S. Yao, C. Karaguleff, A. Gabel, R. Fortenberry, C. T. Seaton, and G. I. Stegman, "Ultrafast carrier and grating lifetimes in semiconductor-doped glasses," *Appl. Phys. Lett.* **46**, pp. 801-802, 1985.
8. P. Horan and W. Blau, "dispersion of the third-order optical nonlinearity in semiconductor-doped glasses," *Semicond. Sci. Technol.* **2**, pp. 382-384, 1987.
9. E. F. Hilinski, P. A. Lucas, and Y. Wang, "A picosecond bleaching study of quantum-confined cadmium sulfide microcrystallites in a polymer film," *J. Chem. Phys.* **89**(6), pp. 3435-3441, 1988.
10. Y. Wang, N. Herron, W. Mahler, and A. Suna, "Linear- and nonlinear-optical properties of semiconductor clusters," *J. Opt. Soc. Am. B*, **6**(4), pp. 808-813, 1989.
11. W. Schrof, S. Rozouvan, E. Van Keuren, D. Horn, J. Schmitt, and G. Decher, "Nonlinear optical properties of polyelectrolyte thin films containing gold nanoparticles investigated by wavelength dispersive femtosecond degenerate four wave mixing (DFWM)," *Adv. Mater.* **3**(4), pp. 338-341, 1998.
12. K. Fukumi, A. Chayahara, K. Kadono, T. Sakaguchi, and Y. Horino, "Gold nanoparticles ion implanted in glass with enhanced nonlinear optical properties," *J. Appl. Phys.* **75**(6), pp. 3075-3080, 1994.
13. L. Yang, K. Becker, F. M. Smith, R. H. Magruder III et al., "Size dependence of the third-order susceptibility of copper nanoclusters investigated by four-wave mixing," *J. Opt. Soc. Am. B*, **11**(3), pp. 457-461, 1994.
14. Y. R. Shen, "Surface properties probed by second-harmonic and sum-frequency generation," *Nature*, **337**, pp. 519-525, 1989.
15. Y. R. Shen, "Optical second harmonic generation at interfaces," *Annu. Rev. Phys. Chem.* **40**, pp. 327-350, 1989.
16. G. J. Ashwell, R. C. Hargreaves, C. E. Baldwin, G. S. Rahra, and C. R. Brown, "Improved second-harmonic generation from Langmuir-Blodgett films of hemicyanine dyes," *Nature*, **357**, pp. 393-395, 1992.
17. F. W. Vance, B. I. Lemon, J. A. Ekhooff, and J. T. Hupp, "Interrogation of nanoscale silicon dioxide/water interfaces via Hyper-Rayleigh scattering," *J. Phys. Chem. B*, **102**(11), pp. 1845-1848, 1998.
18. I. Ledoux, and J. Zyss, "Influence of the molecular environment in solution measurements of the second-order optical susceptibility for Urea and derivatives," *Chem. Phys.* **73**, pp. 203-213, 1982.
19. K. Clays, E. Hendrickx, M. Triest, T. Verbiest, A. Persoons, C. Dehu, and J.-L. Bredas, "Nonlinear optical properties of proteins measured by Hyper-Rayleigh scattering in solution," *Science*, **262**(26), pp. 1419-1422, 1993.
20. D.-G. Fu, M. Li, X. Wang, J.-Q. Cheng, Y. Zhang, Z.-H. Lu, J.-Z. Liu, and Y.-P. Cui, "The CdS nanoparticle with capped surface and its nonlinear optical properties studied by hyper-Rayleigh scattering," *Supramolecular Sci.* **5**(5-6), pp. 495-498, 1998.
21. K. Clays, and A. Persoons, "Hyper-Rayleigh scattering in solution," *Phys. Rev. Lett.* **66**(23), pp. 2980-2983, 1991. And references therein.
22. M. A. Pauley, H. -W. Guan, C. H. Wang, and Alex K. -Y. Jen, "Determination of first hyperpolarizability of nonlinear optical chromophores by second harmonic scattering using an external reference," *J. Chem. Phys.* **104**(20), pp. 7821-7829, 1996.

Two-wave mixing in stark geometry photorefractive quantum wells under a magnetic field

Y.F.Zhang*, J.M.Sun, M.H.Zhang, Z.G.Zhang, Q.Huang, and J.M.Zhou

Institute of Physics, Chinese Academy of Sciences, P.O.Box 603,

Beijing 100080, People's Republic of China.

ABSTRACT

Using a new method for measuring photorefractive two-wave mixing gain, we present the first experimental demonstration of nonreciprocal energy transfer during two-wave mixing under an external magnetic field. The nonreciprocal energy transfer is observed with mixing gains approaching 164 cm^{-1} exhibiting the characters of nonlinearity and saturation. A simple model of negative differential mobility and ultra fast carriers lifetime was proposed to explain these results.

Keywords: two-wave mixing gain, quantum wells, photorefractivity, magnetic field

1.INTRODUCTION

As a new coherent amplifying process in nonlinear optical field, nonreciprocal energy transfer between two coherent laser beams during two wave mixing in photorefractive not only makes photorefractive candidates for many new optical applications, such as coherent image processing and amplification,¹ but also provides important insights concerning the microscopic properties of photorefractive materials. For example, this technique has been employed in the study of simultaneous measurement of the photorefractive and absorptive grating gain coefficients in GaAs.² Its realization requires a photorefractive phase shift between the interference pattern and the resulting space charge distribution. Therefore it is normally forbidden by symmetry in longitudinal stark geometry photorefractive devices because the carrier transport is perpendicular to the holographic grating vector, and all optical changes respond locally to the illumination. Using moving gratings, I.Lahiri et al. present the first experiment demonstration of nonreciprocal energy transfer during two-wave mixing.³ Their method is based on the idea of breaking the symmetry by using the moving gratings. It suggests us that only if a photorefractive phase shift can be introduced, we can make it possible to observe energy transfer in two wave mixing.

The magnetic field has been used in the study of some photorefractive materials, such as to obtain hall mobilities of photoexcited electrons in sillenites and to show the anomalous room temperature conduction in GaAs grown by molecular beam epitaxy (MBE) at low temperature.^{4,5} But nobody before, to our knowledge, has ever exploited it in the stark geometry photorefractive device to create nonreciprocal energy transfer. The basic idea of our attempt is create this asymmetry by carrier moving under the magnetic field.

In this paper, we will illustrate the characteristics of incident light intensity dependent diffraction efficiency in stark geometry multiple quantum wells photorefractive device firstly, and then discuss the conventional methods of measuring two-wave mixing gain, point out their prerequisite is input intensity independence of diffraction efficiency. By introducing a new method for measuring photorefractive two-wave mixing gain and using an external magnetic field, we present the first experimental demonstration of nonreciprocal energy transfer. The nonreciprocal energy transfer is observed with mixing gains approaching 164 cm^{-1} exhibiting the characters of nonlinearity and saturation. At last, we proposed a simple model of negative differential mobility and ultra fast carriers lifetime to explain these results.

* Correspondence Email: mbe@aphy.iphy.ac.cn

2. EXPERIMENT

The samples used in our experiments were grown by MBE in V80H system at 380 °C. This as grown sample has resistivity of $10^7 \Omega \text{ cm}$.⁶ The structure, on the semi-insulating (001) GaAs substrate, is as follows: 500 nm GaAs buffer layer, 50 nm AlAs, and a 100 period multi-quantum wells of 4 nm $\text{Al}_{0.3}\text{Ga}_{0.7}\text{As}$ /8 nm GaAs which were sandwiched between 150 nm $\text{Al}_{0.3}\text{Ga}_{0.7}\text{As}$ cladding layers. After the substrate was removed using the selective lift-off technique, the epitaxial layer of $5 \times 5 \text{ mm}^2$ was put on a piece of glass on which the electrode and the insulating layer have been made by depositing with ITO and SiN_xO_y . The final step is bonding another electrode on the surface with epoxy. The device structure is shown schematically in figure 1.

2.1. Incident light intensity dependent diffraction efficiency

We have found in experiment that the electroabsorption, and therefore, the diffraction efficiency is determined not only on the characters of device, but also on the incident light intensity. Using the standard measurement setup, we studied the relation of the incident light intensity and the magnitude of electroabsorption and diffraction efficiency. The behavior of electroabsorption

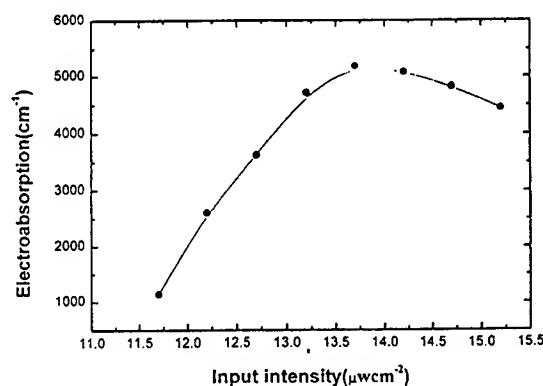
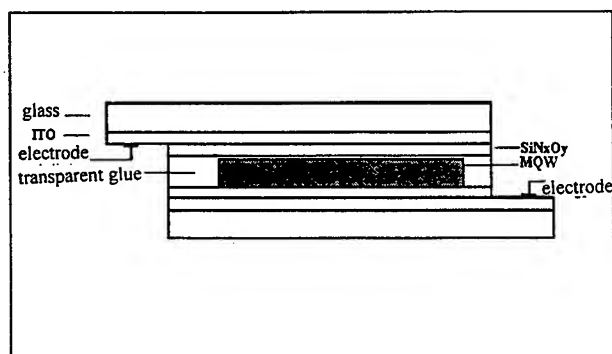


Fig.1. The structure of stark geometry photorefractive device Fig.2. The electroabsorption as a function of incident intensity

as a function of incident intensity is shown in Fig.2. As described above, the electroabsorption peaks at a certain intensity of incident light. We defined this value as the optimal incident intensity. Too large incident intensity will product too rapid generation rate of photocarriers, which will screen the changing applied field in no times, thus the electro-optic layer can not sense the change of external field. On the contrary, if too little intensity is imposed, it can not accumulate enough carriers in deep level due to their trapped lifetime. There is a finite intensity, which defined by us the optimal incident intensity, will lead to the maximum electroabsorption. In general, it is not only related to the characters of material itself, including concentration of deep centers in trap layers, carrier lifetime in electro-optic layer, but also connected with the external condition, such as the strength of applied field, wavelength of incident light, and etc. The optimal incident intensity of this sample is about $13.7 \mu\text{Wcm}^{-2}$.

2.2. Method of two-wave mixing gain measurement

In this section, we first describe the conventional methods of measuring mixing gain briefly, and point out its prerequisite is input intensity independence of diffraction efficiency. Which is not the case in stark geometry photorefractive multiple quantum wells. And then we introduce a new method of two-wave mixing gain measurement.

2.2.1. The discussion of the conventional methods

Two wave mixing gain in photorefractive medium has been studied extensively for its potential in many applications. Contrary to transverse geometry photorefractive device, it is normally no gain in stark geometry due to its symmetry. Because the carrier transport is perpendicular to the holographic grating vector and all optical changes respond locally to the illumination, therefore there is no phase shift between the interference pattern and the refractive index grating. In

I.Lahiri et al's paper,¹ an experimental investigation was carried out to obtain mixing gain in stark geometry photorefractive multiple quantum wells (MQW) using moving gratings. The definition of the two wave mixing gain, in terms of the gain factor γ_0 , is⁷

$$\gamma_0 = \frac{(1 + \beta) \exp \Gamma L}{\beta + \exp \Gamma L} \exp(-\alpha L), \quad (1)$$

where the parameter β is the input intensity ratio of the signal and pump beam, the gain factor γ_0 , defined as the effective signal beam amplification, and L is the interaction length, and α is the linearly absorption coefficient.

Experimentally, it is normally measured as the ratio of the intensity of signal beam after propagating through photorefractive material with and without coupling.⁸ In the case of longitudinal geometry, the electric field, interference pattern and a symmetry break down method that create phase shift, such as moving grating, are the three basic aspects product the two wave mixing gain. Therefore, there are three experimental schemes of measuring the mixing gain as follows: (1) modulate electric field, (2) chop the pump beam, and (3) modulate the running grating or the magnetic field.

The common experiment setup is a photodetector monitoring the signal beam intensity after propagating through the photorefractive material with and without pump beam. This in fact should be included the second method. The pump beam was chopped with a finite frequency, and the observed signal was fed into a lock-in amplifier and recorded by a microcomputer.

From the above illustrated, we can see that this method is based on the condition that the diffraction efficiency is independent on the total optical input power. Whereas, the situation in longitudinal geometry photorefractive quantum wells, is on the contrary as we illustrated above. The electroabsorption and therefore the diffraction efficiency are dependent crucially on the beam intensity, which determined the amount of carriers to screen the external electric field. This leads to the fact that the zero order beam also has contribution to the change of I_s when the reference beam I_r is chopped mechanically. We can obtain a so-called gain even if the two beams are non-coherent by this method, however, it is not true gain of two-wave mixing. Furthermore, the pump irradiant is often many times stronger than that of the signal, this effect is more serious. Therefore, this method will cause an obvious error in two wave mixing measurement.

In I.Lahiri's article, the gain is defined by the asymmetry in the transmitted intensity when both beams are copolarized,

$$\Gamma = \left(\frac{1}{2L} \right) \left[\left(\frac{I_1'' - I_1^\perp}{I_1^0} \right) - \left(\frac{I_2'' - I_2^\perp}{I_2^0} \right) \right], \quad (2)$$

where I'' is the transmitted intensity when the two writing beams are copolarized. I^\perp is the transmitted intensity when the two writing beams are cross-polarized. I^0 is the transmitted intensity when the electric field is turned off, L is the active crystal length, and the subscripts 1 and 2 refer to the two writing beams.

We consider firstly that I^\perp should be replaced by I''^0 , which is the transmitted intensity that when the interference pattern is still. Based on the author's definition, I^\perp is only the zero order transmitted intensity when the two writing beams cross-polarized, I''^0 is the output when two beams copolarized, which include the zero-order and symmetric first order. Secondly, I^\perp and I''^0 are also different because material will have different response to the redistribution of intensity even though the total input power is the same.

2.2.2. Advantages of our method

In contrast to the conventional two wave mixing experiment, The experimental setup is as follows. The Spectra-Physics model 3900s cw Ti: sapphire laser with intensity of $260 \mu\text{Wcm}^{-2}$, initially tuned to an operating wavelength of 842 nm and

splitted into two incident beams with the same intensity, referred reference and signal as I_r and I_s , respectively. They interfere on the device surface, say x-y plane, having both polarized perpendicular to the plane of incidence. Interacting with the photorefractive grating under the magnetic field along x-axis, up to 0.5 T, two beams are diffracted and give rise to beam coupling. The electric field across the photorefractive quantum wells, i.e., along z-axis, is modulated by a square pulse with single sided 50 % duty cycle at a repetition rate of 500 Hz. With this arrangement, the Hall field that creates the redistribution of the drift carriers is along the y direction. we utilized two photomultiplier tubes (PMT's) with 800 nm long pass filters for the detection of the transmitted and diffracted signals simultaneously, recorded by a TDS 360 oscilloscope. In order to obtain the energy transfer value, i.e., the mixing gain precisely, we measured the intensity difference between two beams with and without magnetic field, former one is reference as noise background, because the two beams could not make exact identical experimentally.

This technique has obvious advantages as compared with the conventional two-wave mixing technique. As is mentioned above, in photorefractive quantum wells there exists no phase shift because of the symmetry of the stark geometry. When the magnetic field is turned off, the intensity of the transmitted beams includes zero order beam, I_{s0} and I_{r0} , and first order diffraction, I_{s1} and I_{r1} , that is

$$I_{s,r} = I_{s0,r0} + I_{s1,r1} \quad (3)$$

When the magnetic field is turned on, because of the redistribution of the carriers in magnetic field, one beam is amplified and the other attenuated.

$$I_{sB,rB} = I_{s0B,r0B} + I_{s1B,r1B} \pm \text{energy transfer}, \quad (4)$$

where the subscript B refers to the magnetic field. The intensity of zero order beams would be changed when the magnetic field is turned on. However, the effect on both zero and first beams is equal due to the same intensity. Thus we can get the mixing gain correctly by calculating the difference between I_{sB} and I_{rB} .

3.RESULTS AND DISCUSSION

Figure 3 shows the magnitude of the mixing gain, which is a function of the amplitude of the applied voltage for the four different magnetic fields. From this graph the nonlinear behavior of the mixing gain for each given magnitude of the magnetic field was clear. We find that the gain increases rapidly with the voltage at beginning, reaches a peak and drops afterwards for larger voltage. We consider that the gain nonlinearity is dependent on carrier's velocity and invoke the negative differential conductivity to explain these results.

3.1. Nonlinearity

For simplified analysis, we consider that Δn is constant because it is slow vary with electric field. The increment of mixing gain indicates that the electric field across the electro-optic layer increases rapidly with the increasing voltage below 35 V. The maximum carrier deflective distance on cladding layer (equals to the radius of r), i.e., d in the Fig 2(b), increases with increasing field, because velocity increase within the range of the positive differential mobility. When the differential mobility dv/dE vanishes, the electron drift velocity saturates and the maximum mixing gain can be attained at this specific

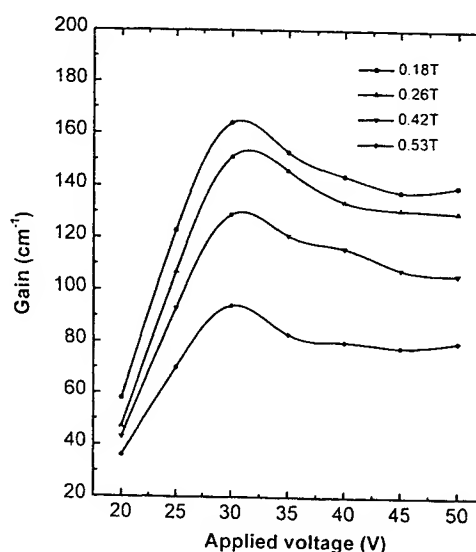


Fig.3 Mixing gain as a function of the applied voltage for four of magnetic field.

applied field. The slow decay contributes to the reduction of the averaged velocity of carriers, because the differential mobility changes to negative during the electric field increasing continuously.

The transport nonlinearity is important feature for the photorefractive effect. In transverse field, just this transport nonlinearity results in the photorefractive phase shift.⁹ In our experiment, it would be to reduce the response time of the photorefractive quantum wells by choosing the maximum drift velocity. Increasing the electric field continuously can increase the diffraction efficiency, but will increase the device response time because of the slower drift velocity.

The mixing gain is varying inversely with the magnitude of the magnetic field. When the magnetic field decreases from 0.53 T to 0.18 T, the mixing gain increases from 94 cm⁻¹ to 164 cm⁻¹. This is not surprising, since it is already known that the reduction in r with increasing field will lead to the reduction of drift distance d which would show by the decreasing of mixing gain. There is no contribution to the gain for the carriers which moving radius does not intercross with the cladding layer, because they can not be captured.

3.2. Saturation

Another noticeable phenomenon is the saturation of the mixing gain against the magnetic field. We can estimate the mixing gain maximum with the following parameters. The electroabsorption of the device under the operating conditions stated above approach 5000 cm⁻¹, which corresponds to a maximum change in the refractive index of 0.03, obtained through a Kramers-Kronig analysis. The electro-optic layer is 1.2 μm thick. Under the assumption of nonattenuation of light, we predict the peak mixing gain approaching 500 cm⁻¹ and producing a photorefractive phase shift of $\pi/10$ through the formula $2\pi \Delta n L \sin \phi / \lambda$. It is clear that this estimated value is much larger than that of our experimental results.

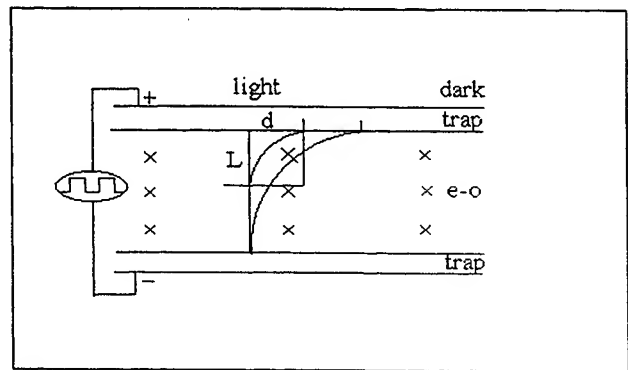


Fig.4 Deflection of carriers under magnetic field.

It is necessary to invoke the concept of carrier lifetime to explain the difference mentioned above. It was recognized that low temperature growth materials would have ultra fast carrier lifetimes because of the high defect densities. Whereas the sweep out time of carriers will last 33 ps even by using appropriately designed quantum wells.¹⁰ Therefore we can believe that there are only the carriers in the wells within a given distance of L nearby the cladding layer will contribute to the screening field. Using the relation $L = uE\tau$, and note that the relatively slow drift velocity of carriers in low temperature growth GaAs, yielding an upper limit for the cyclotron radius r of $r = L$. The magnetic field that corresponds to the radius $r = L$ can be named as a threshold magnetic field. The gain will not increase when the magnitude of the magnetic field decreases through threshold. The best way is to use AC magnetic field instead of constant one to do this experiment, and then we can obtain more information.

To identify the carrier lifetime responsible for the saturation of mixing gain, we note that a DLTS analysis shows carrier lifetime of our material to be 5 ps, which should produce about 120 nm distance. Thus, the experimental results is considered being agreement with our prediction although we omit many complex aspects of carrier transport, such as the periodic potential field of quantum wells and the nonuniformity of carrier distribution due to the attenuation of the light in our model.

In order to ascertain the data discussed above, we measured the gain at three other different grating periods. Within experimental uncertainties, they are in agreement with our prediction.

4. CONCLUSION

In this letter, we report the first experimental demonstration of two-wave mixing and nonreciprocal energy exchange in longitudinal field stark geometry photorefractive device under magnetic field, and describe a new method for measuring

photorefractive two wave mixing gain, which has evident advantages, compared with the conventional technique. Optical energy exchange is observed with mixing gains approaching 164 cm^{-1} with interesting nonlinear characters. A simple model, concerned negative differential mobility and ultra fast carrier lifetime was presented to explain this phenomenon, which not only qualitatively explains the characters of mixing gain, but also agrees with the experimental results in magnitude.

ACKNOWLEDGMENTS

This work is supported by the NSFC under Award No. 69896260.

REFERENCES

1. I.Lahiri, R.M.Brubaker, D.D.Nolte, and M.R.Melloch, "Two-wave mixing in stark geometry photorefractive quantum wells using moving gratings," *Appl.Phys.Lett.* **69**, pp.3414-3416, 1996.
2. S.L.Sochava, and S.I.Stepanov, "Optical excitation of Hall current in a GaAs crystal," *J.Appl.Phys.* **75**, pp.2941-2944, 1994.
3. J.P.Huignard, and A.Marrakchi, "Coherent signal beam amplification in two-wave mixing experiments with photorefractive $\text{Bi}_{12}\text{SiO}_{20}$ crystals," *Opt.Comm.* **38**, pp.249-254,1981.
4. G.D.Boyd, A.M.Fox, D.A.B.Miller, L.M.F.Chirovsky, L.A.D' Asaro, J.M.Kuo, R.F.Kopf, and A.L.Lentine, "33 ps optical switching of symmetric self-electro-optic effect devices," *Appl.Phys.Lett.* **57**, pp.1843-1845, 1990.
5. S.L.Sochava, K.Buse and E.Kratzig, "Photoinduced Hall-current measurements in photorefractive sillenites," *Phys.Rev.B.* **51**, pp.4684-4686, 1995.
6. W.Feng, Z.G.Zhang, Y.Yu, Q.Huang, P.M.Fu, and J.M.Zhou, "Resonant photorefractive AlGaAs/GaAs multiple quantum wells grown by molecular beam epitaxy at low temperature," *J.Appl.Phys.* **79**, pp.7404-7406, 1996.
7. Pochi.Yeh, "Two-wave mixing in nonlinear media," *IEEE J. Quan. Electron.* **25**,pp.484-519, 1989.
8. P.Gunter and J. -P.Huignard, *Photorefractive materials and their applications*, Springer-Verlag, Berlin, 1988
9. Q.N.Wang, R.M.Brubaker, and D.D.Nolte, "Photorefractive phase shift induced by hot-electron transport: multiple-quantum-well structures," *J.Opt.Soc.Am.B.* **11**, pp.1773-1779, 1994.
- 10.D.C.Look, D.C.Valters, M.O.Manasreh, J.R.Sizelove, C.E.Stutz, and K.R.Evans, "Anomalous Hall-effect results in low-temperature molecular-beam-epitaxial GaAs: Hopping in a dense EL2-like band," *Phys.Rev.B.* **42**, pp.3578-3581, 1990.

Soliton stability and compression in a system with nonlinear gain

Sofia C. V. Latas and Mário F. S. Ferreira

Department of Physics, University of Aveiro

3800 Aveiro, Portugal

ABSTRACT

The stability of soliton propagation in a system with spectral filtering, linear and nonlinear gain is numerically investigated. Different types of analytical solutions of the cubic complex Ginzburg-Landau equation, namely solutions with fixed amplitude and solutions with arbitrary amplitude, are presented. Then, the evolution equation is solved numerically assuming various input waveforms. Our results show that it will be possible to achieve relatively stable pulse propagation over long distances by the use of suitable combination of linear and nonlinear gains. However, truly stable propagation of arbitrary amplitude solitons can be achieved only in a system with purely nonlinear gain. A new soliton compression effect is demonstrated both for fixed-amplitude and arbitrary-amplitude solitons.

Keywords: Optical solitons, optical communication systems, nonlinear fiber optics, pulse compression

1. INTRODUCTION

Soliton-based optical communication systems are attracting considerable attention because of their potential for significantly increasing the capacity of long-haul lightwave systems. However, considering that several phenomena can affect soliton transmission through practical optical fibers, some control techniques must be considered. One of these techniques is based on spectral filtering. In fact, spectral filtering allows the soliton amplitude and frequency perturbations to be suppressed¹⁻⁴, as well as the interaction between solitons to be significantly reduced⁴⁻⁷. In the case of ultrashort solitons, the Raman induced soliton self frequency shift can also be suppressed by the action of narrow-band filters^{8,9}.

However, soliton propagation in a system with spectral filtering becomes eventually unstable due to amplification of linear radiation. This amplification is determined by the excess gain which must be provided to compensate for the loss that solitons suffer at wings of their spectrum. The amplified linear waves degrade the SN ratio and if their power grows comparable to that of the soliton, the soliton may be destroyed^{10,11}.

The instability caused by the accumulation and amplification of the background linear waves can be suppressed by sliding the center frequency of filters whereby the transmission line is made opaque to the linear waves^{4,12}. Another method consists of using nonlinear gain (the amplitude-dependent gain), which preferentially amplifies the soliton with large amplitudes while the linear waves with small amplitudes are unamplified or attenuated^{4,13,14}. Some examples of nonlinear gain mechanisms are fast saturable absorption, nonlinear polarization or nonlinear optical loop mirror switching.

In this paper we analyze the characteristics of pulse propagation in a transmission line where amplifiers having linear and nonlinear gains and narrow-band filters are periodically inserted. In Section 2 we present some exact analytical results concerning the pulse solutions of the evolution equation. In section 3 the evolution equation is solved numerically assuming various input waveforms with different phase profiles, as well as different values of the initial soliton amplitude and width. Finally, Section 4 summarizes the main conclusions.

2. EXACT ANALYTICAL RESULTS

The pulse propagation in optical fibers where linear and nonlinear amplifiers and narrow-band filters are periodically inserted may be described by the following modified nonlinear Schrödinger equation (NLSE) if the insertion period of these devices is sufficiently smaller than the dispersion distance¹³⁻¹⁵:

$$i \frac{\partial q}{\partial Z} + \frac{1}{2} \frac{\partial^2 q}{\partial T^2} + |q|^2 q = i\delta q + i\beta \frac{\partial^2 q}{\partial T^2} + i\epsilon q |q|^2 \quad (1)$$

where Z is the propagation distance, T is the retarded time, q is the normalized envelope of the electric field, β stands for spectral filtering ($\beta > 0$), δ is the linear gain or loss coefficient, ϵ accounts for nonlinear gain-absorption processes.

The above equation is known as the cubic complex Ginzburg-Landau equation (CGLE) and it is known in many branches of physics, including fluid dynamics, nonlinear optics and laser physics. This equation is rather general, as it includes dispersive and nonlinear effects, in both conservative and dissipative forms.

We will assume a stationary solution of Eq. (1) in the form:

$$q(T, Z) = a(T) \exp\{id \ln[a(T)] - i\omega Z\} \quad (2)$$

where $a(T)$ is a real function and d, ω are real constants. This is, obviously, a restriction because the chirp could have a more general functional dependence on T . By inserting Eq. (2) into Eq. (1), the following solution can be obtained for $a(T)$ ¹⁵⁻¹⁷:

$$a(T) = A \operatorname{sech}(BT) \quad (3)$$

where

$$A = \sqrt{\frac{B^2(2-d^2)}{2} + 3d\beta B^2} \quad (4)$$

$$B = \sqrt{\frac{\delta}{\beta d^2 + d - \beta}} \quad (5)$$

and d is given in the form:

$$d = \frac{3(1+2\epsilon\beta) - \sqrt{9(1+2\epsilon\beta)^2 + 8(\epsilon-2\beta)^2}}{2(\epsilon-2\beta)} \quad (6)$$

On the other hand, we have

$$\omega = -\frac{\delta(1-d^2+4\beta d)}{2(d-\beta+\beta d^2)} \quad (7)$$

Although the amplitude profile of the solution (3)-(5) is an hyperbolic secant as in the case of the NLS solitons, two important differences exist between the CGLE and the NLSE solitons. First, for CGLE pulses the amplitude and width are independently fixed by the parameters of (1), whereas for NLSE solitons $A=B$. The second difference is that the GL solitons are chirped.

The solution given by Eq. (3) has a singularity at $d - \beta + \beta d^2 = 0$, which takes place on the following line in the plane (β, ϵ) :

$$\epsilon = \epsilon_s = \frac{\beta}{2} \frac{3\sqrt{1+4\beta^2} - 1}{2+9\beta^2} \quad (8)$$

The Eq. (8) has the following limiting values:

$$\epsilon_s = \frac{\beta}{2}, \quad \text{for } \beta \ll 1 \quad (9a)$$

$$\epsilon_s = \frac{1}{3}, \quad \text{for } \beta \gg 1 \quad (9b)$$

It can be shown that for $\delta > 0$ the solution (3) exists and is stable below the curve (8). However, the background state is unstable. For $\delta < 0$ the solution (3) exists above the curve (8), but it is unstable^{15,17,18}.

If, β and ϵ satisfy the Eq. (8) and $\delta = 0$, a solution of the cubic CGLE with arbitrary amplitude exists, given by:

$$a(T) = C \sec h(DT) \quad (10)$$

where C is an arbitrary positive parameter and C/D is given by:

$$\frac{C}{D} = \sqrt{\frac{(2+9\beta^2)\sqrt{1+4\beta^2}(\sqrt{1+4\beta^2}-1)}{3\beta^2(3\sqrt{1+4\beta^2}-1)}} \quad (11)$$

We have also

$$d = \frac{\sqrt{1+4\beta^2}-1}{2\beta}, \quad \omega = -d \frac{1+4\beta^2}{2\beta} D^2 \quad (12)$$

It can be shown that the limiting value of the amplitude-width product A/B for the fixed-amplitude solitons coincide with the value C/D on the line (8). This shows that arbitrary amplitude solitons can be considered as a limiting case of fixed amplitude solitons when $\delta \rightarrow 0$. However, the arbitrary amplitude solitons have stability properties different from those for fixed amplitude solitons. In fact, arbitrary amplitude solitons are stable pulses, which propagate in a stable background because $\delta = 0$.

3. NUMERICAL SIMULATION OF PULSE PROPAGATION

In this section we consider the numerical simulation of pulse propagation, by solving Eq. (1) using the split-step Fourier method. The following initial waveforms are assumed:

$$(A) \quad q(Z=0, T) = A \operatorname{sech}(BT), \quad (13)$$

$$(B) \quad q(Z=0, T) = A \operatorname{sech}(BT) \exp\left[-id(BT)^2 / 2\right], \quad (14)$$

$$(C) \quad q(Z=0, T) = A \operatorname{sech}(BT) \exp(-id\phi), \quad (15)$$

where

$$\phi = \begin{cases} (BT)^2 / 2, & |BT| \leq 1 \\ |BT| - 1/2, & |BT| > 1 \end{cases} \quad (16)$$

The pulse (A) has the same amplitude and width as (2),(3) but has a constant phase. The pulse (B) has a linear frequency chirp whose rate is identical to that described by Eq.s (2) and (3) at the pulse center. In the case of pulse (C), the frequency chirp is limited to $\pm dB$ to approximate the tanh frequency chirp.

Fig. 1 illustrates the variation of the power at $T = 0$, $P_0 = |q(Z, T=0)|^2$ for $\beta = 0.15$ and $\beta = 0.3$ when the nonlinear gain is absent and the linear gain coefficient is such that the peak amplitude A given by Eq. (4) is unity. The background instability is significant for initial pulses (A) and (B), becoming clearly more pronounced for higher values of the filtering parameter β . In fact, the initial waveforms (A) and (B) correspond to different deviations from the stationary solution given by Eq.s (2) and (3). The background instability appears due to the amplification of the frequency components of the deviation within the gain bandwidth

$$\Omega \leq \sqrt{\frac{\delta}{\beta}} \quad (17)$$

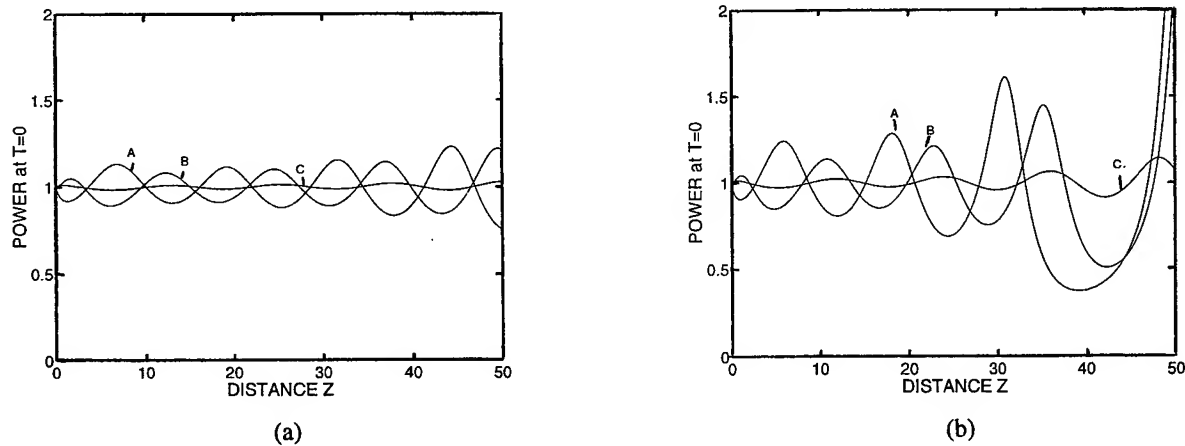


Fig. 1 - Evolution of power at $T = 0$ for $\beta = 0.15$ (a) and $\beta = 0.3$ (b) in the absence of nonlinear gain. The curves (A), (B) and (C) correspond to the initial pulse waveforms given by Eq.s (13)-(15).

Fig. 1 shows that merely giving a linear frequency chirp to the initial pulse is not effective to suppress the background instability. The period of oscillation of P_0 is approximately equal to $\Lambda = 2\pi / |\omega|$, indicating that the oscillation is caused by the interference of the pulse solution (2) and the background cw radiation. For the initial pulse (C), the oscillation amplitude is fairly reduced, because in this case the deviation from the stationary solution vanishes at the pulse wings as well as at the pulse center. This case shows that the instability in bandwidth-limited soliton transmission may be reduced by using initial pulses well matched to the stationary solution. However, this will be an unrealistically difficult task in real transmission systems.

Fig. 2 shows the effect of nonlinear gain on the evolution of the power P_0 for $\beta = 0.15$. The initial waveform of (A) with constant phase has been used and the linear gain coefficient δ is such that $A = 1$. It can be seen that the background instability appears when the nonlinear gain is smaller than about 0.05, whereas an almost monotonic growth is observed for $\epsilon > 0.08$. Between these regions of instabilities there is a range for the nonlinear gain coefficient within which relatively stable pulse propagation can be achieved.

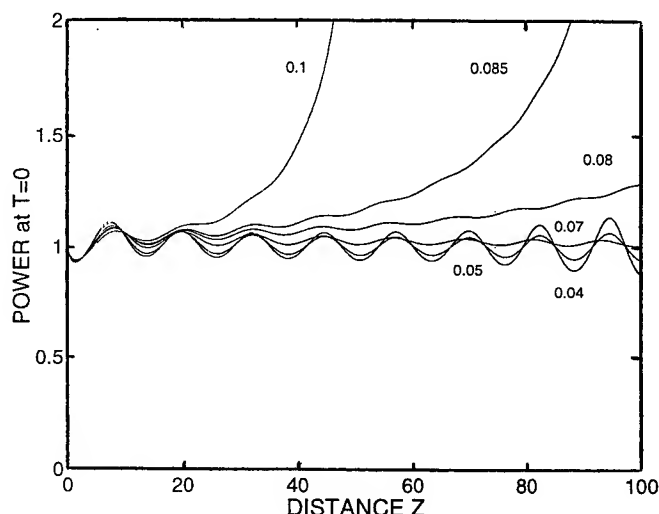


Fig. 2 - Evolution of the power at $T = 0$ for several values of the nonlinear gain coefficient.

Fig. 3 shows the evolution of the power at $T = 0$ for initial pulse amplitudes different from unity when the nonlinear gain coefficient is $\gamma = 0.07$. The initial pulse is given by $\eta \text{sech}(BT)$ with $\eta = 0.7, 0.9, 1.1$ and 1.3 . Although some initial fluctuations are observed, serious instabilities do not appear within the considered propagation distance. The fact that the pulse evolution is not very sensitive to the initial pulse amplitude is desirable for the present scheme to be used in long-distance transmission systems.

Fig. 4 shows the evolution of the power at $T = 0$ for an initial pulse amplitude $A = 1$ but different values of the initial inverse pulse width B . Also in this case we note that the pulse evolution is not very sensitive to the initial pulse width. In all cases considered in Fig. 4 the pulse evolves toward the stationary solution given by Eq. (2). Moreover, we can take advantage of this behaviour to get soliton compression. This possibility is illustrated in Fig. 5, where we show the evolution of the pulse full width at half-maximum (FWHM), normalized by its initial value, for the same cases of Fig. 4. Pulse compression is achieved for the cases $B = 0.4, 0.6$ and 0.8 , corresponding to values of the initial inverse pulse width lower than the stationary value ($B = 0.97$).

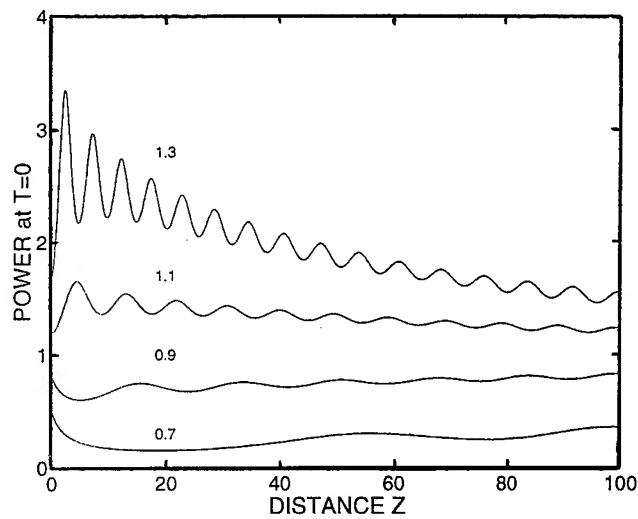


Fig.3 - Evolution of power at $T = 0$ for different values of the initial pulse amplitude.

The compression effect illustrated in Fig. 5 represents a new soliton compression technique, which must be added to other techniques already known^{19,20}. However, there is a fundamental difference between the new compression effect and the traditional one. In the last case, the compression mechanism is related to a fundamental property of the higher-order solitons. These solitons follow a periodic evolution pattern such that they go through an initial narrowing phase at the beginning of each period. By an appropriate choice of the fiber length, the input pulses can be compressed by a factor that depends on the soliton order N . On the other hand, the new compression effect reported in this paper applies to the fundamental soliton, which is of primary importance in the domain of optical communications. The final pulse width can be defined by an appropriate choice of the system parameters.

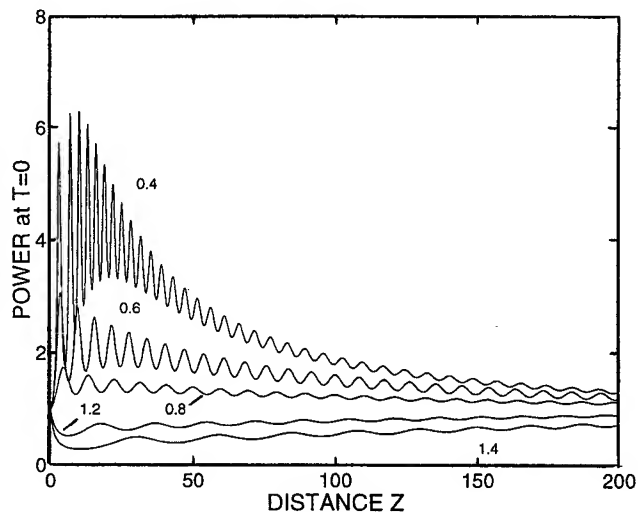


Fig. 4 - Evolution of the power at $T = 0$ for an initial pulse amplitude $A = 1$ but different values of the initial inverse pulse width B . The parameters $\beta = 0.15$ and $\varepsilon = 0.07$ are assumed.

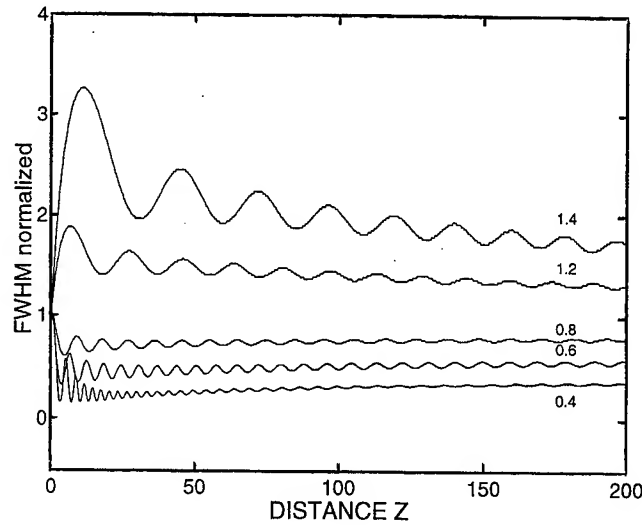


Fig. 5 - Evolution of the pulse full width at half-maximum (FWHM), normalized by its initial value, for the same cases of Fig. 4.

The stationary solutions considered in Figs 3-5 correspond to fixed-amplitude solitons, whose characteristics are independently determined by the parameters δ , β and ε . Since we assumed $\beta = 0.15$ and $\varepsilon = 0.07$, the linear gain was positive but relatively small ($\delta = 0.001735$), so that the background instability develops slowly. However, to guarantee a truly stable propagation, the linear gain must vanish and the nonlinear gain coefficient must be given by Eq. (8). As seen in Section 2, in this case the system supports the propagation of arbitrary amplitude solitons, described by Eqs (2) and (10)-(12). The amplitude-width product C/D for this type of solitons depends uniquely on the filtering parameter β , as seen from Eq. (11). An interesting question is the following: what happens in a system with purely nonlinear gain, when the initial amplitude-width product of the pulse does not satisfy that relation?

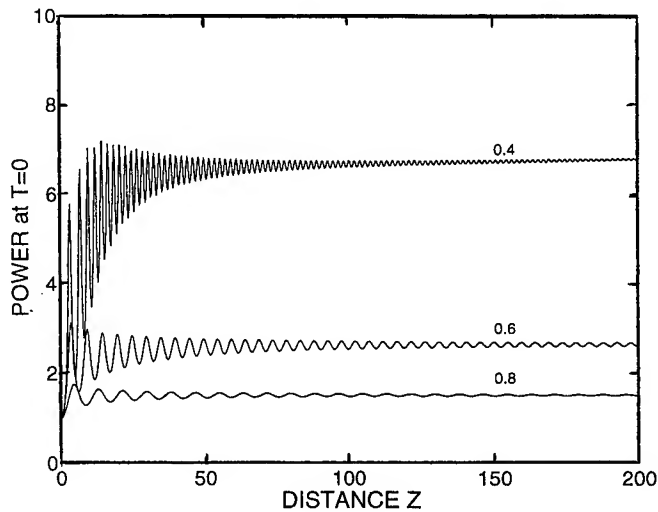


Fig. 6 - Evolution of the power at $T = 0$ for $\beta = 0.15$, $\delta = 0$, and $\varepsilon = \varepsilon_s$ (given by Eq. (8)). We assume $A = 1$ and $B = 0.4, 0.6$, and 0.8 .

Fig. 6 illustrates the evolution of the power at $T = 0$ for $\beta = 0.15$, $\delta = 0$, and $\varepsilon = \varepsilon_s$ (given by Eq. (8)). We assume $A = 1$ and $B = 0.4, 0.6$, and 0.8 . We observe that the power P_0 increases from its initial value $P_0 = 1$ and shows an oscillatory behaviour, which is more significant in the initial stage of propagation and for lower values of B at the input. On the other hand, the pulse width is reduced, as shown in Fig. 7. In the case $B = 0.4$, a soliton compression factor of about 6 is achieved. The oscillations observed in Figs 6 and 7 evidence that the forming steady-state pulses are chirped. On the other hand, the study of the final soliton shape shows the perfect $\text{sech}^2(BT)$ profile, while the amplitude-width product satisfy the relation (11). Fig. 8 shows the initial and the final pulse profiles corresponding the case $B = 0.4$.

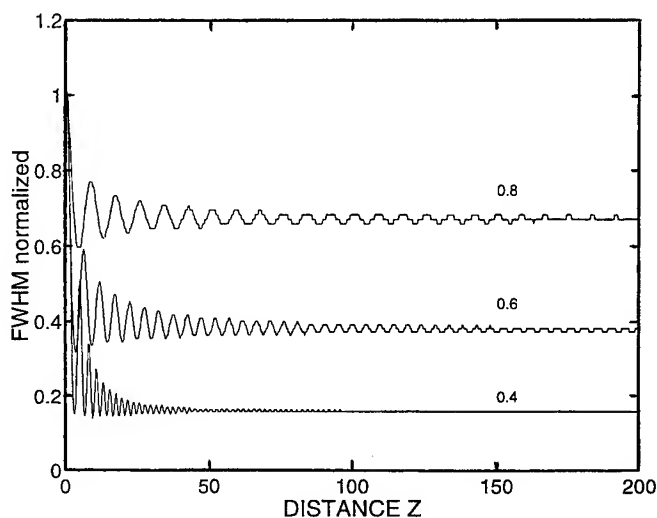


Fig. 7 - Evolution of the pulse full width at half-maximum (FWHM), normalized by its initial value, for the same cases of Fig. 8.

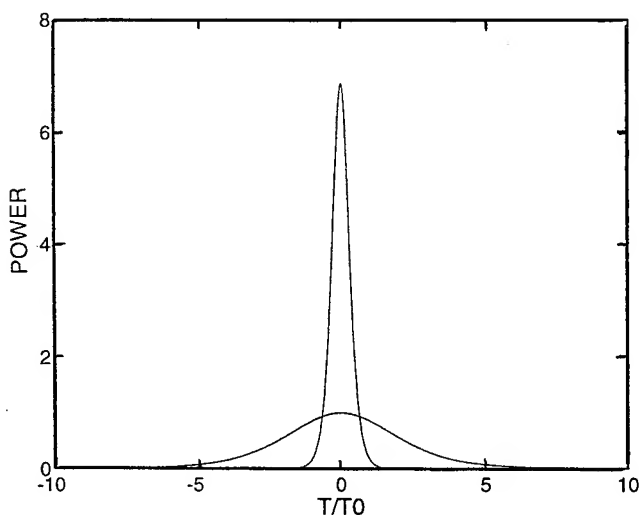


Fig. 8 - Initial and the final pulse profiles for $\beta = 0.15$, $\varepsilon = 0.07$, $A = 1$ and $B = 0.4$.

The very fact that arbitrary-amplitude pulses exist is important for many applications - for instance, fiber ring lasers and optical transmission lines. The results show that at some values of the parameters the system can be switched from the regime with hard excitation (fixed amplitude pulses) to the regime with soft excitation (arbitrary-amplitude pulses). On the other hand, the fact that the pulse evolution in the fixed-amplitude regime is not very sensitive to the initial pulse parameters and the possibility to achieve some degree of pulse compression in both regimes are very interesting features. This knowledge is important both for avoiding undesirable effects in the above referred devices and for designing new types of all-optical switches.

4. CONCLUSIONS

We have analyzed numerically the stability of soliton propagation in a system with spectral filtering, linear and nonlinear gain. Different types of analytical solutions of the cubic complex Ginzburg-Landau equation, namely solutions with fixed amplitude and solutions with arbitrary amplitude, were presented. The arbitrary-amplitude solutions correspond to stable solitons, which exist on special lines in the parameter space where solutions with fixed amplitude become singular.

The evolution equation was solved numerically assuming various input waveforms with different phase profiles, amplitudes and durations. Our results show that merely giving a linear frequency chirp to the initial pulse is not effective to suppress the background instability in bandwidth-limited soliton transmission. On the other hand, it will be possible to achieve relatively stable pulse propagation over long distances by the use of suitable combination of linear and nonlinear gains. However, truly stable propagation of arbitrary amplitude solitons can be achieved only in a system with purely nonlinear gain. A new soliton compression effect was demonstrated both for fixed-amplitude and arbitrary-amplitude solitons. In spite of the fact that the compression factor is not very high, this effect can be useful in some types of soliton systems, namely soliton lasers and optical transmission lines.

REFERENCES

1. A. Mecozzi, J. D. Moores, H. A. Haus, and Y. Lai, "Soliton transmission control," *Opt. Lett.*, **16**, pp. 1841-1843, 1991.
2. Y. Kodama and A. Hasegawa, "Generation of asymptotically stable optical solitons and suppression of the Gordon-Haus effect," *Opt. Lett.*, **17**, pp. 31-33, 1992.
3. H. Kubota and M. Nakazawa, "Soliton transmission control in time and frequency domains," *IEEE J. Quantum Electron.*, **29**, 2189-2197, 1993.
4. A. Hasegawa and Y. Kodama, "*Solitons in Optical Communications*", Oxford University Press, Oxford, 1995.
5. V. V. Afanasjev, "Interpretation of the effect of reduction of soliton interaction by bandwidth-limited amplification," *Opt. Lett.*, **18**, pp. 790-792, 1993.
6. M. F. Ferreira, "Analysis of soliton stability and interactions in a system with nonlinear gain," *SPIE Proc.*, **2994**, 349-357, 1997.
7. T. Okamawari and A. Hasegawa, "Analysis of soliton interaction by means of a perturbed inverse-scattering transform," *Phys. Rev. A*, **51**, pp. 3203-3220, 1995.
8. M. Nakazawa, K. Kurokawa, H. Kubota, and E. Yamada, "Observation of the trapping of an optical soliton by adiabatic gain narrowing and its escape," *Phys. Rev. Lett.*, **65**, 1881-1884, 1990.
9. M. F. Ferreira, "Analysis of femtosecond optical soliton amplification in fiber amplifiers," *Opt. Commun.*, **107**, 365-368, 1994.
10. Y. Kodama, M. Romagnoli, and S. Wabnitz, "Soliton stability and interactions in fibre lasers," *Electron. Lett.*, **28**, pp. 1981-1983, 1992.
11. M. Matsumoto and A. Hasegawa, "Numerical study of the reduction of instability in bandwidth-limited amplified soliton transmission," *Opt. Lett.*, **18**, 897-899, 1993.
12. L. F. Mollenauer, J. P. Gordon, and S. G. Evangelides, "The sliding-frequency guiding filter: An improved form of soliton jitter control," *Opt. Lett.*, **17**, pp. 1575-1577, 1992.

13. M. Matsumoto, H. Ikeda, T. Uda, and A. Hasegawa, "Stable soliton transmission in the system with nonlinear gain," *J. Lightwave Technol.*, **13**, pp. 658-665, 1995.
14. M. Matsumoto, "Stability analysis of bandwidth-limited soliton transmission", *Opt. Commun.*, **114**, 69-75, 1995.
15. J. M. Soto-Crespo, N. N. Akhmediev, and V. V. Afanasjev, "Stability of the pulselike solutions of the quintic complex Ginzburg-Landau equation," *J. Opt. Soc. Am. B*, **13**, 1439-1448, 1996.
16. N. R. Pereira, and L. Stenflo, "Nonlinear Schrödinger equation including growth and damping," *Phys. Fluids*, **20**, pp. 1733-1734, 1977.
17. M. F. Ferreira, M. V. Facão, and S. V. Latas, "Stable soliton propagation in a system with spectral filtering and nonlinear gain", accepted for publication in *Fiber and Integrated Optics*, Taylor & Francis, **18**, 1999.
18. M. F. Ferreira, "Stability conditions for soliton fiber lasers with nonlinear gain," *SPIE Proc.*, **2918**, 38-49, 1996.
19. K. Chan, and H. Liu, "Short pulse generation by higher order soliton-effect compression: effects of optical fiber characteristics", *IEEE J. Quantum Electron.*, **31**, 2226-2235, 1995.
20. G. P. Agrawal, "*Nonlinear Fiber Optics*", 2nd Ed., Academic Press, San Diego, 1995.

Self-focusing, Self-trapping and optical limiting of light beams in photorefractive $\text{Bi}_{12}\text{SiO}_{20}:\text{Fe}$ crystal

Sreeramana P. Aithal^{*a}, Prem P. Kiran^b, and Narayana D.Rao^b

^a Laser Physics and Quantum Optics Division, Physical Research Laboratory, Ahmedabad- 380 009, India

^b School of Physics, University of Hyderabad, Hyderabad - 500 046, India

ABSTRACT

Nonlinear absorption, 1-D self-focusing and 1-D self-trapping of optical beams are studied in 150 ppm Fe-doped $\text{Bi}_{12}\text{SiO}_{20}$ (BSO:Fe) crystal using single beam Z-scan technique in nano second regime using coherent and incoherent laser pulses without applying any external electric field across the crystal. When the crystal is placed in expanding beam one dimensional self-trapping is observed due to one dimensional self-focusing. The nonlinear absorption is also observed at high intensities due to trap assisted excited state absorption as well as two photon absorption. The ground state absorption and increased nonlinear absorption at 532 nm and 595 nm compared to pure BSO indicates the increased impurity traps in the crystal lattice due to iron incorporation. The studies reveal that incorporation of iron in BSO making it an excellent optical limiter.

Keywords: BSO:Fe crystal, self-focusing, self-trapping, optical limiting, Z-scan technique, excited state absorption, two-photon absorption.

1. INTRODUCTION

When a single light beam propagates in a photorefractive material, the inhomogeneous intensity profile produces an inhomogeneous change in the refractive index. The profile of the refractive index change is similar to a graded index lens and can focus (or defocus) the beam itself. If the light induced lens exactly compensates the diffraction of the beam, it leads to an invariant intensity profile along the beam propagation direction. This light profile is named as spatial soliton which has important applications for optical beam deflection, optical switching, guiding and routing and in all optical logic operations. The advantage of similar devices based on soliton propagation is associated with the fact that spatial solitons are self-guided beams giving rise to perfect waveguide structures which in turn can be used to guide another laser beam. PR materials show self-focusing at very low optical powers which makes them interesting for practical applications.^{1,2}

The dependence of the structure and the dimension of the scattered beam on the position of the crystal from the focusing point of the input beam is studied. The results show that the light induced scattering consists of basically of three parts : self-defocusing, self-focusing and speckle. The self-defocusing and self-focusing are caused due to light induced lensing. The speckle is caused mainly by the light induced fluctuation of the refractive index in the crystal. In 1997, Q.Sun et.al.³ showed that the fanning noise in $\text{LiNbO}_3:\text{Fe}$ crystal just depends on the diameter of incident light on the front crystal face and have poor relation with the thickness of the crystal and they also attributed it to that fanning noise is mainly caused by the amplification of the scattered light by the imperfections near the incident crystal face. The self-focusing can be used for self-trapping of optical beams.

Self-trapping of optical beams in nonlinear Kerr media is demonstrated by several investigators⁴⁻⁹ in which the diffraction of the propagating beam is exactly compensated by self-focusing (or self-defocusing) effect caused by the photoinduced change in refractive index. Alternately, in these cases, the propagation of light beam is in the form of so called spatial soliton

* Correspondence : Email : aithal @ prl.ernet.in; Telephone : 79-6462129-4758; Fax: 79-6301502

in which the beam shape is spatially confined and the transparent profile is preserved through out the media.¹⁰ However the index changes needed for Kerr-like spatial solitons require high intensities often exceeding 1 MW/cm^2 .

Self-trapping originates from a variation of the refractive index in a plane perpendicular to the propagation direction of an optical beam. If the refractive index change is positive, it can compensate for diffraction, and the light beam propagates without change in its diameter. This effect can be thermally because of light absorption,¹¹⁻¹² it can be due to nonlinear susceptibility,¹³ or it can be due to light induced changes in photorefractive crystals.¹⁴⁻¹⁵

In 1992, M. Sagev et al¹⁶ suggested a new type of spatial soliton that is associated with the photorefractive effect in the crystal. The intensity profile of the beam modulates the refractive index by means of photorefractive (PR) effect, which results in an exact compensation for the effects of diffraction and causes the light beam to propagate with an unvarying profile. These PR spatial solitons arise from the nonlocal PR effect rather than from the local Kerr-effect. They can be generated even at moderate light intensities since the efficiency of the PR effect is independent of the absolute light intensity.

Self-trapping of coherent, incoherent and white light beams is reported in the literature¹⁷⁻¹⁹ using ferroelectric oxide - strontium barium niobate crystal. One dimensional and two dimensional self-trapping is also achieved in same family crystals of Fe-doped KNbO_3 ²⁰⁻²¹ and Fe-doped LiNbO_3 ²²⁻²³ and in semiconductor like InP:Fe ²⁴ using only coherent light. The first observation of PR bright spatial soliton in cubic $\text{Bi}_{12}\text{TiO}_{20}$ (BTO) crystal of sillenite family is reported by M.D.I.Castillo et al²⁵ and subsequently, same group reported one dimensional dark soliton²⁶ as well as the observation of interaction forces between one dimensional spatial solitons.²⁷ In all these cases, the self-focusing in BTO is controlled by an external applied dc voltage and with external uniform illumination. All these cases a coherent light beam from He-Ne laser is used.

The light induced absorption due to the photoinduced charge transport has been studied in the field of photorefractive nonlinear optics because it plays an important role in the construction of passive optical limiters and optical threshold elements in the optical processing systems.²⁸⁻²⁹ Optical limiting devices are currently of interest for protecting sensors and eyes from high intensity laser light. The optical limiting function requires the optical output power to be clamped below a certain critical value as the incident optical power increases. An ideal limiter exhibits a linear transmission below threshold, but above threshold the transmitted output power is constant. Limiters for sensor protection demands broad-band response to long and short pulses, high linear transmission throughout its band-width, resistance to laser induced damage and stability of the material. Any limiter which is required to operate over a wide range of input levels must exhibit very high optical densities at the highest input levels, and this can only be achieved if the nonlinear effect extends across the whole of the laser pulse. Nonlinear material can interrupt the transmission of a powerful laser pulse, and limit the output to safe levels. The protection is self-activating and normal transmission is restored after the pulse. The optical limiting devices rely on one or more of the non-linear optical mechanisms, which includes Excited Saturation Absorption (ESA), Two-Photon Absorption (TPA), Non-linear refraction, Induced scattering and Photorefraction.³⁰ Out of these, ESA and TPA mechanisms can provide a response resembling that of an ideal optical limiter.

In photorefractive materials, at higher input intensities, the mechanism of charge carrier generation and transport processes involve impurity levels which lead to the greater possibility of the combined effect of trap assisted excited state absorption (TAESA) and TPA. Here the former is an accumulative non-linearity, which requires time for energy transfer from field to medium and hence can be in principle only depends on the input light fluence. ESA generally arises in a molecular system when the excited state absorption cross-section is larger than the ground state absorption cross-section. The later is an instantaneous non-linearity, which depends on the input light intensity, can be effective over broad band of the spectrum and for very short pulses. The process involves the absorption of a photon from the field to promote an electron from its initial state to a virtual intermediate state, followed by the absorption of second photon that takes the electron to its final state. The mechanism for TPA can be thought in terms of the three level reverse saturation absorption model for the case where the life time of the intermediate state approaches zero and the ground state absorption is extremely low. TPA can also act as a significant loss mechanism when a material is subjected to a strong beam of photon of energy $\hbar\omega$, with $\hbar\omega < E_g < 2\hbar\omega$, where E_g is the energy gap of the material.

Wide range of materials like semiconductors,³¹ Photorefractive materials,³² conjugated polymers³³ and dye solutions³⁴ with different mechanisms contributing for the optical limiting have been investigated. New approach of enhancing the optical power limiting by coupling effective TPA in one molecule and ESA in another molecule has been reported recently.³⁵

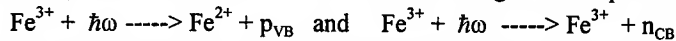
In this paper, we report the first experimental observation of photorefractive self-trapped one dimensional coherent and incoherent spatial solitons using self-focusing nonlinearity in another potential candidate of sillenite family, $\text{Bi}_{12}\text{SiO}_{20}$ (BSO) doped with 150 ppm iron as impurity. BSO:Fe shares the similar cubic structure as $\text{Bi}_{12}\text{TiO}_{20}$ with crystal class 23, has higher melting point (884 °C) and the transparency range (0.47 - 6 μm). It is one of the promising PR material for soliton observation because of its strong photorefractive properties like high sensitivity, fast response time, comparable electro-optic coefficient that of BTO and interesting photoconducting properties³⁶ due to the increased contribution to PR effect from the donor levels. To evaluate the potentiality of this crystal for soliton formation, we studied self-focusing and self-trapping in it. In this observation it has noted that the soliton retain its profile, which is independent of input power, instantaneous after input is switched on, independent on external applied dc electric field and can be observed at low light powers of less than 10 μW both cw and pulsed regime.

In BSO the standard photorefractive effect is based on the absorption of the photons by impurity levels. One can improve the performance by means of increasing the impurity levels by doping. Attard³⁷ predicted the Fermi level shift in BSO via photon induced trap occupation. The shift of Fermi level depends on the density of trap sites in the bandgap, the radiation induced occupation density, and the energy levels of the traps. Investigations reports that the photorefractive materials doped with iron leads to favorable photorefractive properties such as small response time and high sensitivity.³⁸

In this paper, we also studied the nonlinear absorption and optical limiting behavior of BSO:Fe exhibited due to combined effect of trap assisted excited state absorption and two photon absorption in the visible spectral range using nanosecond pulses at 532 nm and 595 nm. An excellent passive limiting behavior is demonstrated and consequently the precise role of the internal defects due to impurity centers exists in the crystal lattice is explained on the basis of a four level model. Theoretical curves are generated based on this simplified model to fit the experimental data to determine the accumulative ESA and instantaneous TPA coefficients.

2. THEORY

We assume all donor impurities are identical and have exactly the same energy state somewhere in the middle of the bandgap. These donor impurities are ionized by absorbing photons. As a result ionization electrons are generated in the conduction band leaving empty trap states behind, which are capable of capturing electrons. The impurities due to the presence of Fe atoms may be the form of Fe^{3+} or Fe^{2+} states. Photogeneration process produces Fe^{2+} and Fe^{3+} as



The nonlinear absorption processes by considering the combined effect of excited state absorption and two photon absorption can be explained using a four level model of valence band, impurity traps, conduction band and deep conduction band. The rate equations used to describe the processes are given below.

$$\left[\frac{dN_0}{dt} \right] = - \left[\sigma_0 I N_0 / \hbar\omega \right] - \left[\beta I^2 / 2\hbar\omega \right] + \left[N_1 / \tau_1 \right] + \left[N_3 / \tau_3 \right] \quad (1)$$

$$\left[\frac{dN_1}{dt} \right] = \left[\sigma_0 I N_0 / \hbar\omega \right] - \left[N_1 / \tau_1 \right] - \left[N_1 / \tau_{\text{ct}} \right] + \left[N_2 / \tau_2 \right] \quad (2)$$

$$\left[\frac{dN_2}{dt} \right] = \left[\beta I^2 / 2\hbar\omega \right] - \left[N_2 / \tau_2 \right] + \left[\sigma_1 I N_3 / \hbar\omega \right] \quad (3)$$

$$\left[\frac{dN_3}{dt} \right] = - \left[\sigma_1 I N_3 / \hbar\omega \right] - \left[N_3 / \tau_3 \right] + \left[N_1 / \tau_{\text{ct}} \right] \quad (4)$$

Intensity transmitted through the sample is given by

$$\left[\frac{dI}{dt} \right] = - \left[\sigma_0 I N_0 \right] - \left[\sigma_1 I N_3 \right] - \left[\beta I^2 \right] \quad (5)$$

with

$$I = I_{00} \left[\omega_0^2 / \omega^2(z) \right] * \exp \left[- \left(-t^2 / \tau_p^2 \right) \right] * \exp \left[- \left(2r^2 / \omega^2(z) \right) \right] \quad (6)$$

and

$$\omega(z) = \omega_0 \{ 1 + (z/z_0)^2 \}^{1/4} \quad ; \quad z_0 = (\pi \omega_0^2 / \lambda)$$

where σ_0 is the absorption cross-section from the valance band, β is the two photon absorption coefficient from the valance band to the conduction band and σ_1 is the excited state cross section from the trap levels to the conduction band, N_i 's are the corresponding populations in the different states, τ_i 's are the lifetimes of the excited states, z_0 is the Rayleigh range, ω_0 is the beam waist at focus, I is intensity as a function of r , t , and z , I_{00} is peak intensity at the focus of the Gaussian beam, τ_p is the input pulse width used, and $1/\tau_{CT}$ is the crossing rate to trap states from the conduction band. The differential equations are solved numerically using Runge-Kutta fourth order method. The differential equations are first de-coupled and then integrated over time, length, and along the radial direction. Assuming the input beam to be a Gaussian, the limits of integration for r , t , and z are varied from 0 to ∞ , $-\infty$ to $+\infty$, and 0 to L (length of the sample) respectively.

3. EXPERIMENTAL

3.1 Self-focusing and self-trapping :

We used single - beam Z-scan technique to investigate experimentally the self-focusing in BSO:Fe crystal for different light intensities, wavelengths, external electric field and additional homogeneous illuminations. The charge diffusion, which would produce an asymmetric electric field and refractive index profile leading to the one dimensional self-focusing is studied for different crystallographic axes. In this experiment a (110) configuration of BSO:Fe crystal, grown at University of Alabama, USA is used. The amount of iron incorporation in the crystal is determined by Inductive Coupled Plasma - Atomic Emission Spectroscopy (ICP-AES) which has shown that 150 ppm Fe is incorporated in the crystal as impurity. In principle, during the growth Fe can replace Bi as well as Si in BSO. But from ICP-AES study it is also found that the doped crystal grown from melt having no Si deficit. Hence it can be assumed that Fe atoms incorporated only on the Bi sites in our sample. The lattice parameters of both pure and doped BSO are studied using single crystal X-ray diffraction technique and the results shows that the lattice constants are slightly varied due to doping process with out change in crystal structure. The sample has dimensions of 6 mm X 5 mm X 3.5 mm and light propagated its strongest axis initially. The sample length corresponds to the diffraction length of a Gaussian beam with a characteristic waist radius $a_0 = 30 \mu\text{m}$ of the input beam used in the experiment ($n = 2.55$). An undoped BSO crystal bought from Fujian Catech Crystals Inc., China with dimensions of 10 mm X 10 mm X 5 mm, cut along <110> plane is also used for comparing the results. The basic apparatus consists of a cw He-Ne laser (632.8 nm) or second harmonic of pulsed Nd:YAG laser (532 nm) or incoherent dye laser pumped by second harmonic of Nd:YAG laser (peaked at 595 nm) as the incident beam source. The schematic diagram of the experimental set-up is shown in Fig. 1. The output beam from a laser is directed onto a spherical lens of focal length 12 cm and BSO:Fe crystal is placed along the focal length of the lens. The crystal is translated along the focal length of the lens (Z-scan) and the emergent beam is monitored on a screen placed 60 cm away from the focal point. The beam shape and diameter on the screen are measured using CCD and frame grabber assembly. The BSO:Fe crystal is placed in such a way that its c-axis is in the horizontal plane and along the direction of incoming focused light beam. The polarization of incoming beam could be varied using a polarization rotator but initially kept along the c-axis.

When the crystal is at focus ($Z = 0$), no change in the circular pattern of the output beam on the screen is observed. Only the diameter of the output beam is increased due to the diffraction of propagating beam through the material medium. When the crystal is translated away from the focus ($+z$ direction) the shape of the output beam started to become elliptical with a shrink along Y-axis due to one dimensional self-focusing. With increase in the translation of the crystal to the same direction, the ellipticity of the output beam is continuously increased. The intensity of the beam is also increased continuously at the centre of the spot. This made the output beam pattern elliptical with longer axis along X-direction. Same effect of self-focusing increased the size of the output beam when the crystal is translated towards the lens from the focus ($-z$ direction) and the intensity of the output beam at a give point is also gradually decreased. As a result the beam pattern on the screen became elliptical with longer axis along Y-direction. The above linear variation in intensity is observed only in case of low power cw beam, but with high input intensity pulsed beams the nonlinear absorption became apparent and the output intensity varied nonlinearly with same changes in the shape and ellipticity of the transmitted beam. Note that during these translations of the crystal along both sides of the focus, the size of the output beam along the x-axis has not been affected due to self-focusing or defocusing effects (by discarding the diffraction effects). This change in the ellipticity of the beam emerging from the crystal (A-axis) is plotted with the crystal position from the focus and is shown in Fig. 2. Fig. 3 shows the shapes of output beams on the screen along three crystallographic directions when the crystal is placed at different points

along z-direction (z-scan). When the light beam passed through the C and C^l axis the output beam shapes twisted 90° as shown in Fig. 3 (a) and (b), whereas no difference observed when the beam passes through A and A^l axis as well as B and B^l axis (Fig. 3 (c) and 3 (d)). The crystal gives rise to same output pattern due to one dimensional self-focusing with other input wavelengths (cw and pulsed). It is also found that the external uniform illumination as well as external dc electric field (up to 10 kV/cm²) could not change the nature of self-focusing and hence the shape of the output pattern on the screen. No elliptical shape in output pattern is observed in case of pure BSO during translation.

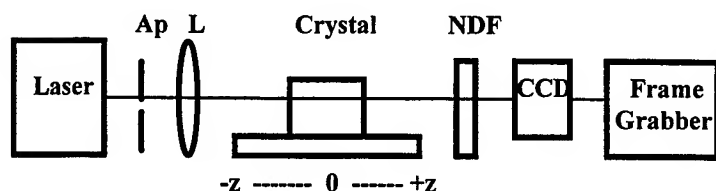


Fig. 1 : Schematic diagram of experimental set-up for self-focusing study.

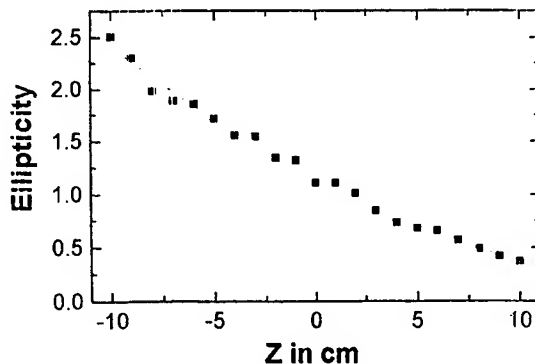


Fig. 2 : Plot of change in ellipticity of output beam with crystal position.

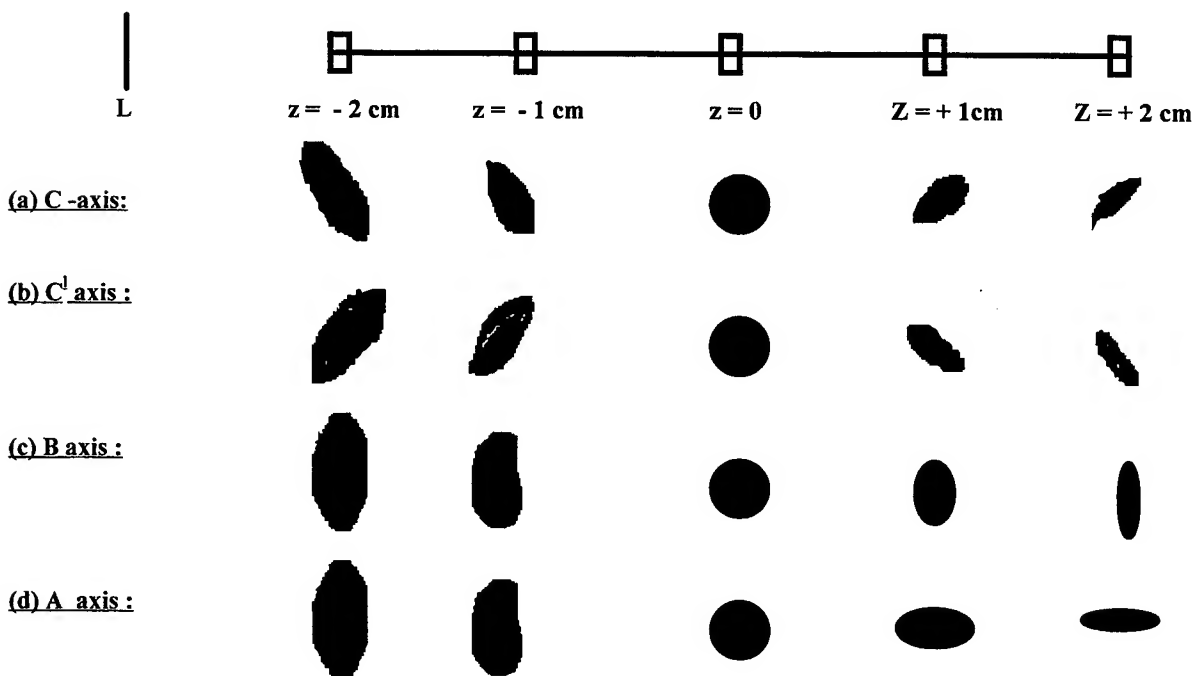


Fig. 3 : The shapes of output beam on the screen along three crystallographic directions when the crystal is placed at different points along z-direction (z-scan).

3.2 Nonlinear absorption studies :

A standard single-beam open aperture z-scan technique is used for measuring nonlinear absorption effect at different input intensities. Second harmonic (532 nm) from a 6 ns, 10 Hz, Q-switched Nd:YAG laser and Nd:YAG pumped Dye laser output at 595 nm are used for the study of nonlinear absorption. As like in self-focusing study, no external electric field is applied across the crystal. Laser beam is spatially filtered with a narrow aperture of 1 mm diameter and the beam profile is taken as

Gaussian for theoretical modeling. Neutral density filters are used for proper attenuation of the input beam. The laser beam is focused on to the crystal in Z-scan set-up with a lens of focal length 16 cm leading to a beam waist of 50 μm at the focal spot. Intensities are varied from 5 MW/cm^2 to 500 MW/cm^2 . A large diameter lens is used for collecting the transmitted light and focusing effectively on to a photo diode detector. Crystal is translated across the focal point to obtain the nonlinear absorption data. Normalized transmittance of BSO:Fe crystal is measured as a function of sample position from the focus at wavelengths 532 nm and 595 nm and are shown in Fig. 4 (a) and Fig. 4 (b) respectively. A significance decrease in normalized transmission is observed when the crystal approaches the focus ($z = 0$) and the decrease in the transmittance is found to be symmetric with respect to the focus. The solid lines in the figures represents the curve from our theoretical model calculated using equations (1) to (5). The absorption spectrum of BSO:Fe is depicted in Fig. 5 and is compared with pure

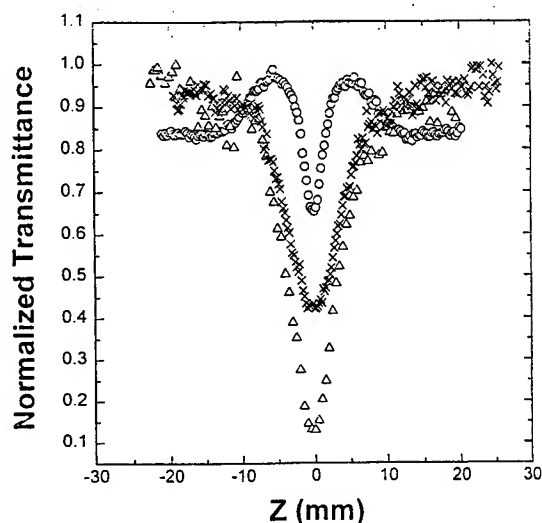


Fig. 4 (a) : Normalized transmittance of BSO:Fe at 532 nm at intensities 200 MW/cm^2 (Δ), 160 MW/cm^2 (\times), 105 MW/cm^2 (\circ).

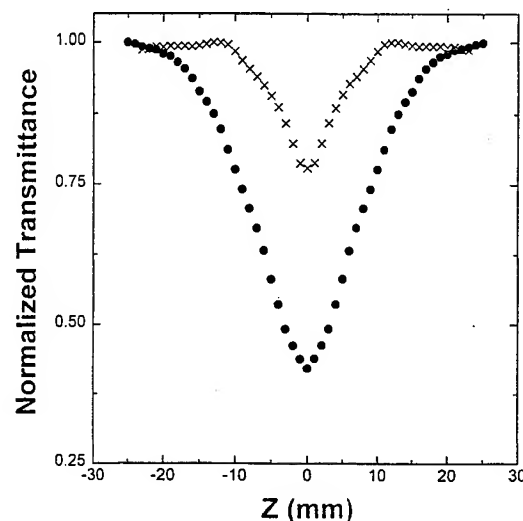


Fig. 4 (b) : Normalized transmittance of BSO:Fe at 595 nm. at intensities 200 MW/cm^2 (\circ) and 95 MW/cm^2 (\times).

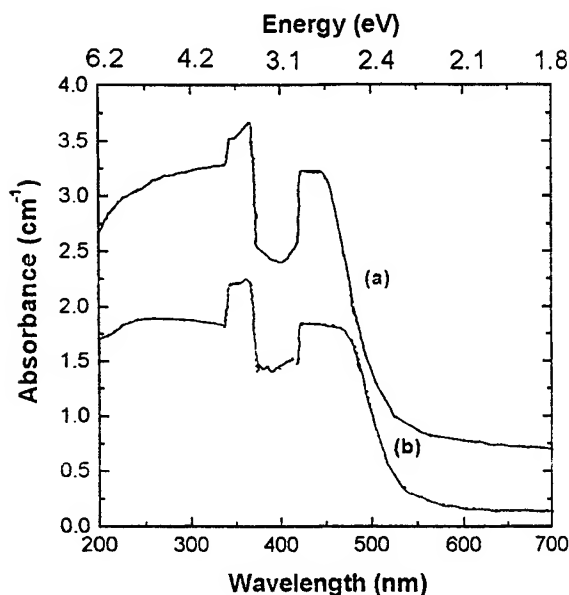


Fig. 5 : Absorption spectrum of (a) BSO:Fe and (b) BSO.

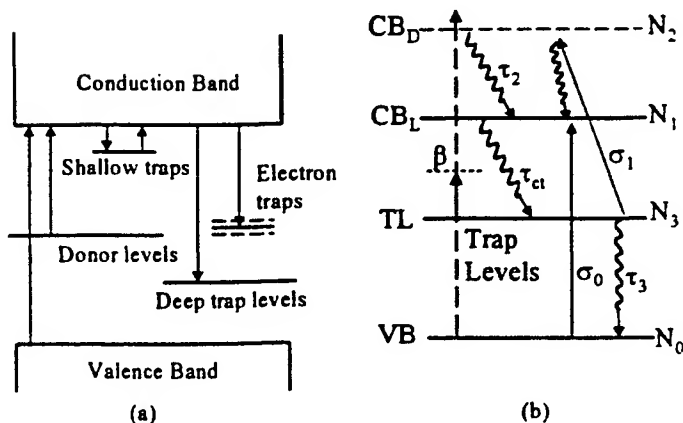


Fig. 6 : (a) Band energy diagram and (b) the equivalent four level model.

BSO crystal. The energy band structure and the equivalent four level energy level diagram used to explain the observed nonlinear absorption are shown in Fig. 6 (a) and 6 (b) respectively. Here all trap levels contribution due to impurities present in the crystal are assumed to be arising from a single level. The nonradiative decay times from the higher-lying manifolds are assumed to be sufficiently fast with respect to the laser pulse duration that there is no buildup of population in the conduction band (CB) and above. This assumption is justified because no saturation of the ESA is observed. The values of two photon absorption coefficient (β) and trap assisted excited state absorption coefficient (σ_1) are estimated at different input intensities using the equations (1) to (5) through least square fit of the experimental data and are given in table I.

3.3 Optical limiting studies :

The schematic diagram of the experimental set-up used to study the optical limiting characteristics of both the crystals is shown in Fig. 7. The laser pulses are focused at the center of the crystal by a 10 cm focal length, 2.5 cm diameter best-form lens, giving a waist spot size of 30 μm and 40 μm respectively with 532 nm and 595 nm light beams. The laser beam is spatially filtered with a narrow aperture of 1 mm diameter and the beam profile is taken as Gaussian. Neutral density filters are used for proper attenuation of the laser. No external electric field is applied across the crystal. Optical limiting studies as a function of input fluence is carried out at both wavelengths. The transmitted energy is collected by 5 cm diameter lens effectively on to a photodiode detector. This geometry afforded essentially total integrated energy detection to overcome any possible change in the spatial properties of the transmitted laser beam owing to self-focusing, self-defocusing, or thermal lens effects. Therefore, the measured transmission is only due to the net nonlinear absorption and not effects due to an induced refractive index change. Incident fluence is varied using the combination of neutral density filters. Using a beam splitter, focusing lens and photodetector combination, input fluence is also measured. The optical limiting response of BSO:Fe at 532 nm and at 595 nm are shown in Fig. 8 and is compared with that of pure BSO (Fig. 9). The linear transmission of the beam is also shown. The observed laser damage threshold in case of pure BSO is 1.69 GW/cm² at 532 nm and 0.92 GW/cm² at 595 nm and in case of BSO:Fe it is 2.54 GW/cm² at 532 nm and 1.57 GW/cm² at 595 nm (indicated by an arrow mark in the figures).

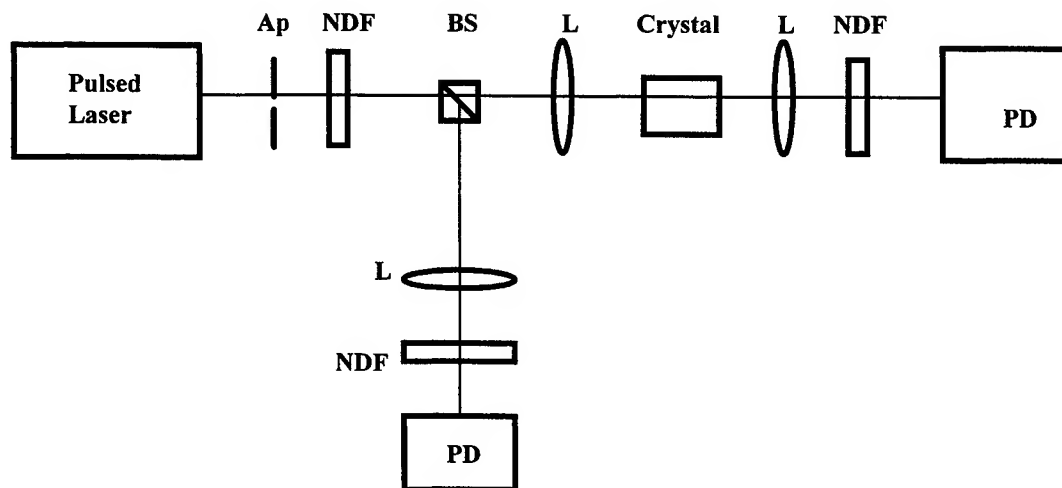


Fig. 7 : Schematic diagram of experimental set-up for optical limiting study. Ap - Aperture, NDF - Neutral density filter.

4. DISCUSSION

As seen from the plot of ellipticity versus the position of the crystal from the focus (Fig. 2), when the crystal is nearly 4 mm away from the focus towards +z direction, the size of the output beam on the screen along Y-axis becomes equal to the beam size on the screen without passing through the crystal. Thus one dimensional self-trapping is achieved by compensating the diffraction of the beam inside the crystal by one dimensional self-focusing of the beam. Here unlike reported earlier [7], no

external electric field is applied to control self-focusing effect, instead, we kept the crystal in a diverging field to control the self-focusing effect. This implies that one dimensional soliton can be produced very easily by placing the crystal in a divergent field and the position of the crystal in divergent beam depends on the size of the beam at the focus. The Z-scan study also shows that in BSO:Fe crystal the refractive nonlinearity is positive unlike LiNbO_3 and KNbO_3 . The observed prefocal transmittance minimum followed by a postfocal transmittance maximum is a signature of the positive refractive index nonlinearity.

The one-dimensional self-focusing in BSO:Fe can be explained by the band transport model. In this model, when the light beam propagating through the medium, the electrons from the donor iron impurities are excited from the donor level in the bandgap to the conduction band where they can migrate as free carriers. The free carriers migrate via diffusion or drift and are recaptured by the traps where they are transported from the conduction band back to the donor level. In the absence of external electric field the charge migration will be only in the form of diffusion, which would produce an asymmetric electric field and refractive index profile leading to the one dimensional self-focusing.

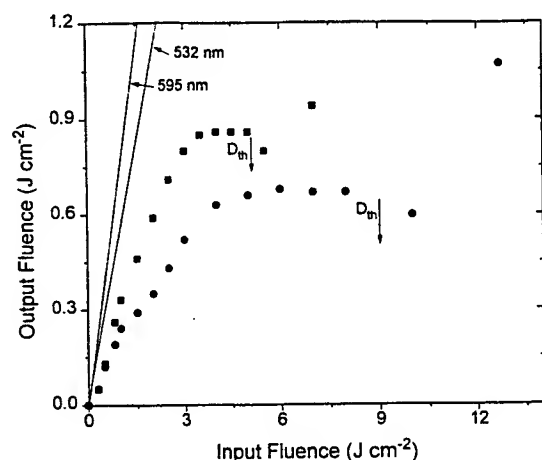


Fig. 8 : Optical limiting response of pure BSO at 532 nm (●) and at 595 nm (■). D_{th} - damage threshold.

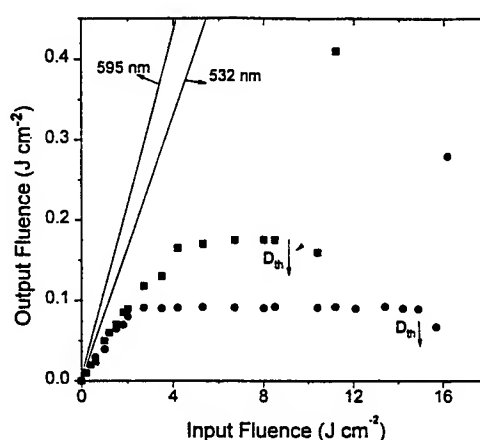


Fig. 9 : Optical limiting response of BSO:Fe at 532 nm (●) and at 595 nm (■).

Table I : β and σ_1 calculated at 532 nm and 595 nm at different intensities.

Wave length	Intensity (MW/cm^2)	β (cm/GW)	σ_1 (cm^2) * 10^{-20}
532 nm	200	92	0.68
	160	43	2.91
	105	13.6	17.3
595 nm	200	28.6	1.85
	95	26.2	9.72
	15	17.1	24.68

The absorption of both crystals is extending from 2.5 eV to 3.6 eV region. The origin of this absorption shoulder is still a subject of controversy. Silicon vacancy complex has been suggested by some to be the responsible defects, while others have proposed bismuth substituting for silicon. It is also suggested that 2.6 eV band in BSO is due to Fe^{2+} ions. It appears that all BSO crystals even undoped contain significant amount of Fe^{3+} ions which can easily change the valence state upon illumination. Therefore further incorporation of Fe atoms significantly increases the density of trap sites and the drift mobility of charge carriers is influenced strongly by the state of the traps. Due to the incorporation of iron to BSO crystal, a fraction of Fe atoms introduced probably occupies the Bi-vacancies and combines with their nearest neighbors in the same way as Bi-atoms. Thus isoelectrical impurities are created. Another fraction of Fe-atoms forms shallow donors. At high enough irradiation they generate free electrons into the conduction band and fill the deeper traps, causing a Fermi level shift to the bottom of the conduction band. On the other hand, the electrons generated may be captured on deep acceptors, playing the role of recombination centers which may be situated about 1.9 - 2.0 eV below the bottom of the conduction band. Thus it is found that the incorporation of Fe atoms in BSO lattice sites leads to appearance of new traps as well as creation of new "faster" recombination centers. The absorption spectrum of doped crystal shows a comparatively narrow peak at 2.1 eV as well as a broad absorption band extending into the infra-red side. The long tail in the absorption edge of both crystals goes all the way to 700 nm (1.8 eV). This implies that the crystals possess large number of trap sites, which would assist the material to become a good trap assisted reverse saturable absorber (TARSA). Thus at higher input intensities, due to nano second pulses the main contribution for optical limiting comes from TPA, assisted by TAESA. The observed nonlinear absorption which leads optical limiting can be explained qualitatively on the basis of four level model. At low intensities, the shallow traps are empty due to the thermal ionization. With increasing the intensity, however, the concentration of charge carriers in the conduction band (CB) increases and due to the recombination with shallow traps, the trap levels become active and the further excitation from the trap levels leads to TAESA, which takes the electrons back into deep CB. When the TAESA cross-section (σ_t) is greater than the single photon absorption cross section (σ_0), the RSA behavior enhances and it adds its contribution to optical limiting along with TPA. Further, the number of electrons going over from ground state to CB via TPA depends on the input laser intensity. Intuitively, at higher input power, TPA starts shooting up due to its fastness compared TAESA. The transfer of the conduction electrons to trap levels and the recombination with the valence band (VB) holes increases with the number density of excited electrons in the conduction band. Since excitation to CB is proportional to incident intensity, BSO thus forms a good RSA material. In case of doped BSO, due to the availability of more free electrons and also trap levels, the absorption effect is pronounced as compared to pure BSO. One can also see from the optical limiting curves that in both crystals the nonlinear absorption is stronger at 532 nm than at 595 nm, indicating the dominance of the electron transfer from the conduction band to the trap sites and then the excited state absorption from the trap sites. Higher damage threshold at 532 nm could be due to the creation of more charge carriers and their transport under local fields. The same reason accounts the higher damage threshold of doped BSO at both wavelengths. The additional traps and recombination centers due to iron incorporation to BSO makes it an excellent passive limiter with exceptionally high damage threshold in visible spectral region even with narrow optical pulses.

5. CONCLUSION

We have observed one dimensional self-focusing and self-trapping of both coherent and incoherent optical beams using photorefractive BSO:Fe crystal both for transmitted and reflected beam from the outer surface and this demonstration is independent on crystallographic directions, input beam polarization state, magnitude and direction of external applied electric field and external incoherent uniform background illumination. Moreover, the process is found to be instantaneous and there is no time lag between input beam irradiation and self-trapping. No such self-focusing is observed in pure BSO crystal. The nonlinear absorption and optical limiting behavior of BSO:Fe crystal are also studied and compared with that of pure BSO against a high power pulsed laser source with out application of any external electric field. Both crystals are found to have a very strong nonlinear absorption leading to optical limiting with major contribution from TPA assisted by ESA from the trap sites. The increased trap density due to 150 ppm iron incorporation to the crystal lattice sites improved the nonlinear absorption nature of the crystal. Furthermore, the improved characteristics of BSO:Fe both in absorption and damage threshold makes it an excellent optical limiter even for short pulse duration and high energy sources.

ACKNOWLEDGMENTS

We are thankful to Prof. M.D. Agarwal, Alabama A&M University, USA, for providing the doped BSO crystal and grateful to Prof. G. S. Agarwal for many useful discussions. Financial support from DST is acknowledged.

REFERENCES

1. M. Sagev and G. Stegeman "Self-trapping of optical beams," *Phys. Today*, **51**, pp. 42 - 48, 1998.
2. A.W. Snyder and F. Ladouceur "light guiding light," *Opt. & Photon. News*, February, pp. 35 - 39, 1999.
3. Q. Sun, S. Liu, G.Y. Zhang, G.Q. Zhang, Q. Fang, G. Tian, and J. Xu, "The dependence of fanning noise on beam size in $\text{LiNbO}_3\text{:Fe}$ crystals with different thickness," *Optik*, **105**, pp. 74 - 76, 1997.
4. R.Y. Chiao, E. Garmire, and C.H. Townes, "Self-trapping of optical beams," *Phys. Rev. Lett.* **13**, pp. 479 - 482, 1964.
5. J.E. Bjorkholm and A. Ashkin, "Cw self-focusing and self-trapping of light in sodium vapour," *Phys. Rev. Lett.* **32**, pp. 129 - 132, 1974.
6. H. Zhang, J. Dai, P. Wang, and L. Wu, "Self-focusing and self-trapping in a new types of Kerr media with large nonlinearities," *Opt. Lett.* **14**, pp. 695 - 696, 1989.
7. J.S. Aitchison, A.M. Weiner, Y. Silberberg, M.K. Oliver, J.L. Jackel, D.E. Leaird, E.M. Vogel and P.W.E. Smith, "Observation of spatial optical solitons in a nonlinear glass waveguide," *Opt. Lett.* **15**, pp. 471 - 473, 1990.
8. A. Barthelemy, C. Froehly, S. Maneuf, and F. Reynaud, "Experimental observation of beams self-deflection appearing with two-dimensional spatial soliton propagation in bulk Kerr material," *Opt. Lett.* **17**, pp. 844 - 846, 1992.
9. R.D.L. Fuente, A. Barthelemy, and C. Froehly, "Spatial-soliton-induced guided waves in a homogeneous nonlinear Kerr medium," *Opt. Lett.* **16**, pp. 793 - 795, 1991.
10. M. Hercher, *J. Opt. Soc. Am.* **54**, pp. 563, 1964.
11. M. Horowitz, R. Daisy, O. Werner, and B. Fischer, *Opt. Lett.* **17**, pp. 475 - 477, 1992.
12. M.D. I. Castillo, J.J.S. Mondragon, and S. Stepanov, *Opt. Lett.* **21**, pp. 1622 - 1624, 1996.
13. A. Barthelemy, C. Froehly, S. Maneuf, and F. Reynaud, *Opt. Lett.* **17**, pp. 844 - 846, 1992.
14. D.N. Christodoulides and M.I. Carvalho, *J. Opt. Soc. Am. B* **12**, pp. 1628, 1995.
15. N. Korneev, P.A.M. Aguilar, J.J.S. Mondragon, S. Stepanov, M. Klein, and B. Wechsler, *J. Mod. Opt.* **43**, pp. 311 - 321, 1996.
16. M. Sagev, B. Crosignani, A. Yariv, and B. Fischer, "Spatial solitons in photorefractive media," *Phys. Rev. Lett.* **68**, pp. 923 - 925, 1992.
17. G.C. Duree, J.L. Shultz, G.J. Salamo, M. Sagev, A. Yariv, B. Crosignani, P.D. Porto, E.J. Sharp, and R.R. Neurgaonkar, "Observation of self-trapping of an optical beam due to the photorefractive effect," *Phys. Rev. Lett.* **71**, pp. 533 - 535, 1993.
18. M. Mitchell and M. Sagev, "Self-trapping of incoherent white light," *Nature*, **387**, pp. 880- 883, 1997.
19. M. Shih, Z. Chen, M. Sagev, H. Lee, R.S. Feigelson and J.P. Wilde, "Waveguides induced by photorefractive screening solitons," *J. Opt. Soc. Am. B* **14**, pp. 3091 - 3101, 1997.
20. S. Lan, M. Shih and M. Sagev, "Self-trapping of one-dimensional and two-dimensional optical beams and induced waveguides in photorefractive KNbO_3 ," *Opt. Lett.* **22**, pp. 1467 - 1469, 1997.
21. R. Ryf, M. Wiki, G. Montemezzani, P. Gunter, and A.A. Zozulya, "Launching one- transverse dimensional photorefractive solitons in KNbO_3 crystals," *Opt. Comm.* **159**, pp. 339 - 348, 1999.
22. M. Taya, M. Bashaw, M.M. Fejer, M. Sagev, and G.C. Valey, "Observation of dark photovoltaic spatial solitons," *Phys. Rev. A*, **52**, pp. 3095 - 3100, 1995.
23. Z. Chen, M. Sagev, D.W. Wilson, R.E. Muller, and P.D. Maker, "Self-trapping of optical vortex by use of the bulk photovoltaic effect," *Phys. Rev. Lett.* **78**, pp. 2948 - 2950, 1997.
24. M. Chauvet, S.A. Hawkins, G.J. Salamo, M. Sagev, D.F. Bliss and G. Bryant, "Self-trapping of planar optical beams by use of the photorefractive effect in InP:Fe ," *Opt. Lett.* **21**, pp. 1333 - 1335, 1996.
25. M.D.I. Castillo, P.A.M. Aguilar, J.J.S. Mandragon, S.I. Stepanov, and V. Vysloukh, "Spatial solitons in photorefractive BTO with drift mechanism of nonlinearity," *Appl. Phys. Lett.* **64**, pp. 408 - 410, 1994.
26. M.D.I. Castillo, J.J.S. Mandragon, S.I. Stepanov, M.B. Klein and B.A. Wechsler, *Opt. Comm.* **118**, pp. 515 - 520, 1995.
27. G.S.G. Quirino, M.D.I. Castillo, V. Vysloukh, J.J.S. Mandragon, and S.I. Stepanov, G.L. Martinez, and G.E.T. Cisneros, "Observation of interaction forces between one dimensional spatial solitons in photorefractive crystals," *Opt. Lett.* **22**, pp. 154 - 156, 1997.
28. J.A. Hermann and J. Staromlynska, "Trends in optical switches, limiters and discriminators," *Int. J. Nonlin. Opt. Phys.*, **2**, pp. 271 - 275, 1993.
29. R. C. Hollins, "Materials for optical limiters," *Curr. Opin. in Solid State and Mat. Sci.*, **4**, pp. 189 - 196, 1999.
30. L.W. Tutt and T.F. Boggess, "A review of optical limiting mechanisms and devices using organics, fullerenes, semiconductors and other materials," *Prog. in Quant. Electr.* **17**, pp. 299 - 329, 1993.

31. M.S. Bahae, A.A. Said, T.H. Wei, D.J.Hagan, and V. Stryland, " Sensitive measurement of optical nonlinearities using a single beam," *IEEE J.Quantum Electron.* **26**, pp. 760 - 769, 1990.
32. M. Horowitz, B. Fischer, Y. Barad, and Y. Silberberg, Photorefractive effect in a BaTiO₃ crystal at 1.5 um wavelength regime by two-photon absorption," *Optics Lett.* **21**, pp. 1120 - 1123, 1996.
33. G.S. He, C. Weder, P. Smith, and P.N. Prasad, " Optical power limiting and stabilization based on a novel polymer compound," *IEEE J. Quan. Electron.* **34**, pp. 2279 - 2285, 1998.
34. T.J. Bunning, L.V. Natarajan, M.G. Schmitt, B.L. Epling, and R.L. Crane, "Optical limiting in solution of diphenyl polyenes," *Appl. Opt.* **30**, pp. 4341 - 4349, 1991.
35. M.P. Joshi, J. Swiatkiewicz, F. Xu, P.N. Prasad, B.A.Reinhardt and R. Kannan, " Energy transfer coupling of two -photon absorption and reverse saturable absorption for enhanced optical power limiting," *Opt. Lett.*, **23**, pp. 1742 - 1744, 1998.
36. D. Nesheva, Z. Aneva, and Z. Levi, "Some properties of BSO:Fe doped crystals," *J. Phys. Chem. Solids*, **55**, pp. 889 - 894, 1994.
37. A.E..Attard, "Fermi level shift in BSO via photon-induced trap level occupation," *J.Appl.Phy.* **71**, pp. 933 - 937, 1992 and Ref. therein.
38. A. Mazur, C. Veber, O.F. Schirmer, C. Kuper, and H. Hesse, "Light induced charge transport processes in photorefractive BaCaTiO₃ doped with iron," *J. Appl. Phys.*, **85**, pp. 6751 - 6757, 1999.

The Spectra Distribution Properties Of Ultraweak Photon Emission From Biological System and Its Applications in 21st Century*

Yanbin Zhu^{a#}, Zhaohui Zhu^b, Zhouyi Guo^a, Junfu Ma^a, Shaoshan Li^a, Zheng Bao^c,
Chao Bao^c

^asouth China Normal University, Guangzhou 510631, China.

^bSony semiconductor of America Design Engineering, Fremont, CA
94539, USA.

^cState Key Lab Of Modern Optical Instrumentation, Zhejiang Univesity,
Hangzhou 310027, China.

ABSTRACT

Using the theories of photon count statistic and test data of the ultraweak photon emission (UPE) from biological system, the biophoton field's spectra distribution properties were studied in this paper.

An experimental setup for testing UPE in different spectral region were designed. The test data proved UPE of living biological system exists in wide spectra region from UV-visible to infrared. Using the test data, we can obtain important conclusion that is UPE almost has nothing to do with wavelength. The conclusion has important significance for proving the bio-photon coherence.

In the end of this paper, the medical applications of UPE in 21st century were discussed simply.

Key words: Ultraweak photon emission(UPE), biophoton, photon count statistic, coherent state, Gaussian field, spectral region, spectra distribution

1. INTRODUCTION

Because of the ultraweak photon emission (UPE) from biological system gives the important information of metabolism and energy transformation of the living biological system including human, so that UPE's research will be to become an important research field in life science¹⁻⁶.

This paper presented the view point about the biophoton field elementally belong to Gaussian field, then from the coherent emission theory and some test data, we experimently proved the UPE from biological system indeed exist in a widely spectral region from UV-visible-infrared and obtained the conclusion about UPE of biosystem $f(\lambda) \approx \text{constant}$. In the end of paper, the medical applications of UPE in 21st century were discussed simply.

2. UPE'S SPECTRA DISTRIBUTION PROPERTIES

2.1. About biophoton coherence

F. A. Popp presented and builded the biophoton's coherent theory on 1988⁷. His theory could explain many experimental phenomenon which were not explained by chemistry luminescence theory. That means the biophoton field belongs to coherent light field.

On 1998, Zhu Yanbin et al. used the theories of photon count statistics to analyze the test data of UPE from four biological systems (they are respectively Soy-bean, Gonyaulax Polyedra, Thailand Firefly and Acetabularia Acetabulum shown in Fig. 1), then presented the biophoton field elementally belongs to Gaussian field and which was superposed at least by two independent parts of photon emission, one is coherent light field

of pure coherent state, another one is chaotic light field which is in heat balancing situation⁸.

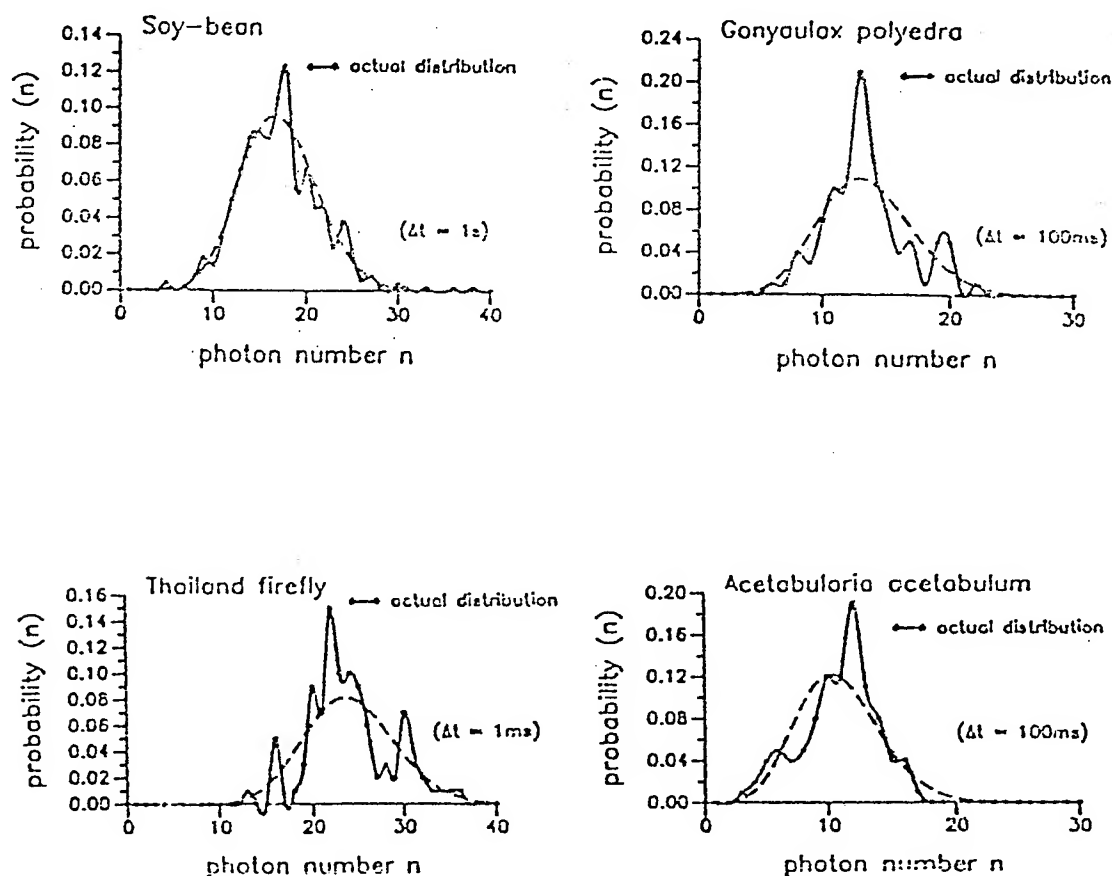


Fig.1 The photon count statistics of four biosystem⁷.

However above two view points both consider that the coherent light exist in UPE from biological systems and the coherent photon emission is most important life information carrer in biophoton field.

2.2. UPE's spectra distribution property.

Up to now, though all ultraweak photon emission test almost were down in UV and near UV's visible region, but according to the coherent state theory we could conjecture the ultraweak photon emission from biological system will also exist in near infrared's visible region and infrared region. So that we have to design the experimental setup for testing photon emission in different spectral region. Of course the range selected of spectral region was limited by the spectra sensitivity of experimental setup.

2.2.1. The experimental setup for testing UPE's spectra distribution properties.

A schematic diagram of the experimental setup for testing UPE's spectra distribution is shown in Fig.2

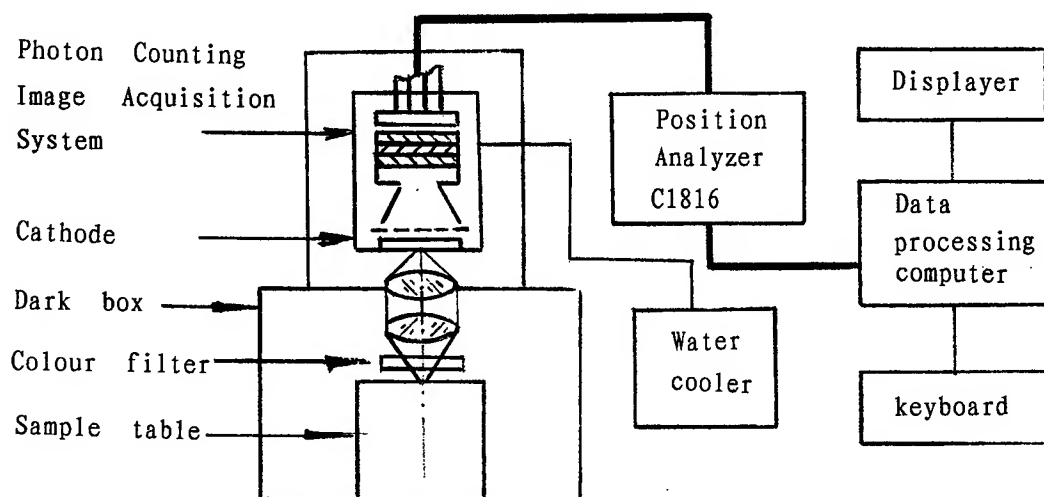


Fig.2 The experimental tetup for testing UPE's spectra distribution properties.

The experimental setup's spectra sensitivity region is from 300nm-1060nm. In testing UPE We selected three kinds of colour filter which action are to separate the all spectra region in to several parts as following:

- (1) All spectra region (From 300nm to 1060nm);
- (2) Visible-infrared region (From 400nm to 1060nm);
- (3) Red-infrared region (From 580nm to 1060nm).

2.2.2. The test results.

Two kinds of bio-sample were tested: Soybean Bud radicle and Greenbean radicle. The test results are shown in Fig.3 and Fig.4.

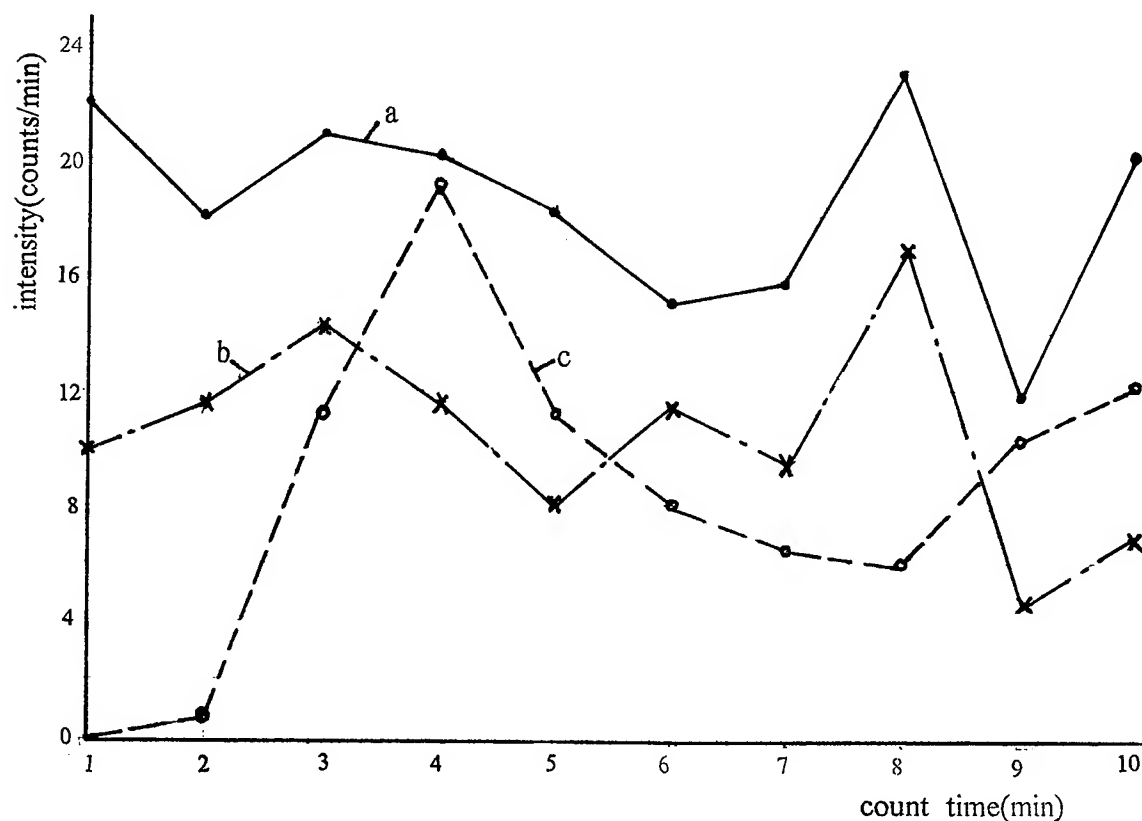


Fig. 3 UPE's intensity of soybean Bud radicle.
 Curve a--All spectra region;
 Curve b--Visible-infra region;
 Curve c--Red-infra region.

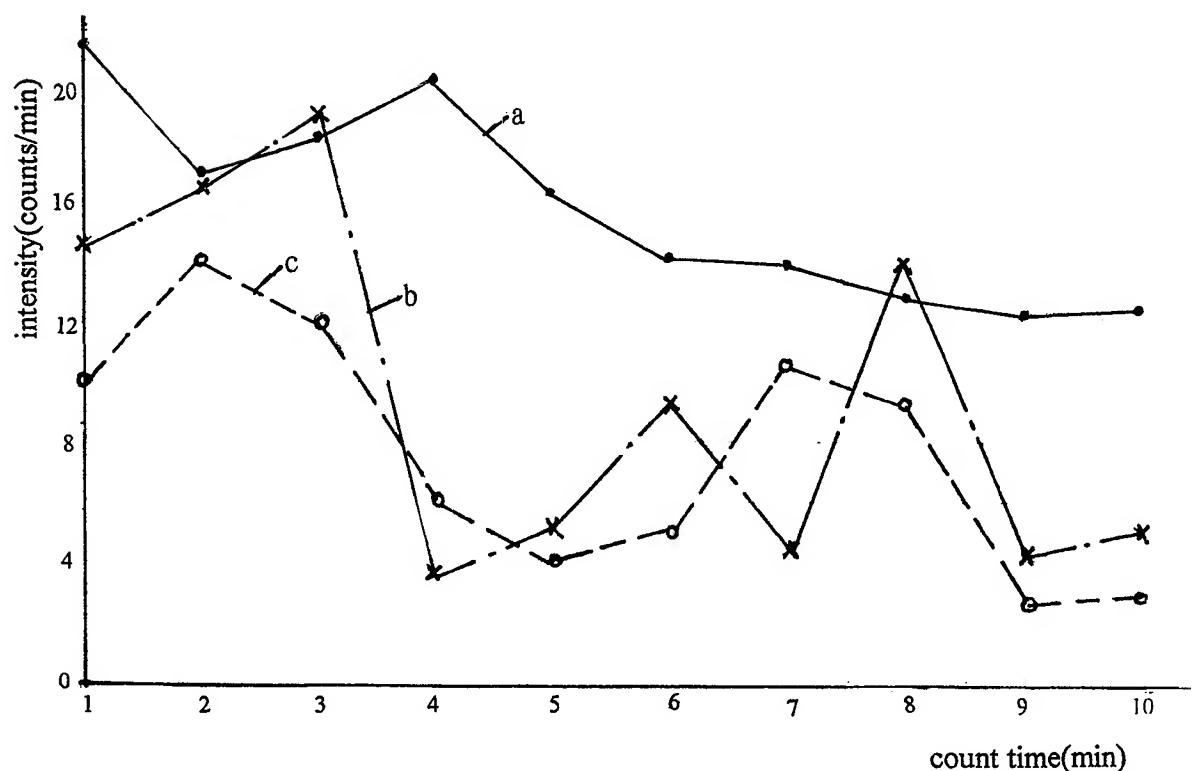


Fig.4. UPE's intensity of Greenbean radicle.
 Curve a--All spectra region;
 Curve b--Visible-infra region;
 Curve c--Red-infra region.

3. CONCLUSIONS AND SUMMARY

From Fig.3 and Fig.4 we can obtain the following conclusions:

1), First we calculated the UPE's average intensity of two finds of biosample in different spectra region shown as Table 1.

Table 1, UPE's average intensity in different spectra region

No	Spectra region	UPE's Average intensity (Counts/min)	
		Soybean	Greenbean
1	300nm to 1060nm	15.9	16.2
2	400nm to 1060nm	10.5	8.8
3	580nm to 1060nm	8	7.7

Then we can conjecture the UPE's average intensity in UV region (300-400nm region) by (1)-(2) and visible region (400-580nm region) by (2)-(3) in Table 1 for each biosample. The results conjectured are shown as Table 2.

Table 2, UPE's average intensity conjectured in uv region and visible region

Spectra region	UPE's Average intensity (Counts/min)	
	Soybean	Greenbean
300nm to 400nm	5.4	7.4
400nm to 580nm	2.5	1.1

Above data indicated that UPE indeed exists in wide spectra region from UV-visible to infrared.

2), UPE intensity indeed is very weak photon emission and its detection is very difficult. So up to now, through all UPE's test almost were down in UV and near UV's visible region. But according to above test results, we could conjecture UPE exists in a wide spectra region from UV-Visible-infra region. The key question is to design enough sensitive detecting system in wide spectra region particularly in infra spectra region.

3), Above test results also has an important significance to prove the coherence of biophoton field, that is UPE's intensity change are not too big in different wavelength region, so we can approximately consider that UPE of living biological system almost has nothing to do with wavelength λ , namely

$$f(\lambda) \approx \text{constant}. \quad (1)$$

K. H. Li has proved theoretically that if an exciting state exciplex opened want to keep the quasi-stability, a essential condition just is $f(\lambda) \approx \text{constant}^9$.

This conclusion also strongly supported the theory of biophoton field coherence.

4. UPE'S APPLICATION IN 21ST CENTURY

Now most people know that UPE of biological system carries much important information about metabolism, energy transformation, growth and health of the living animals and plants including human. Many experimental results showed, human's fingers, human's blood, human's brain etc. are the biophoton emission resources. So a new kind of diagnostic technology and device for human health status will produce in next century. A key technology is detecting the very weak coherent photons which exist in biophoton field. Because of the heat emission also exists in biophoton field, it will add much difficult in detection. At the same time, people also have to understand the relationship of UPE's, particularly coherent biophoton's emission rule and human health status.

Under the modern coherent photon technology develop by leaps and bounds, the high sensitive photon detector, particularly infra photon detector have got extremely improvement and the heat emission photons were filtered and disappeared in photon signal, UPE's medical application in 21st century will get new and fast development.

REFERENCES

1. Gurwitsch A.G, A historical review of the problem of mitogenetic radiation. *Experientia*, 1988, 44: 545-550
2. Colli L, Further Measurement on the bioluminescence of the seedlings.

Experientia, 1955, 11: 479-481

3. Chwirot W B, New indications of possible role of DNA in ultraweak photon emission from biological systems. J Plant physiology, 1986, 122 (1): 81-86
4. Slawinski J., Luminescence research and its relation to ultraweak cellradiation, Experientia, 1988 44: 559-571
5. Popp F A. Recent advances in biophoton research and its application. Singapore: World Scientific, 1992, Chapter 5, 157
6. Zhu Yanbin, Biophotonics and photon biology. Chinese Journal of Optoelectronics. Laser, 1997, 8 (2): 67-71
7. Popp F A, et al. Physical aspects of biophotons. Experientia, 1988, 44: 576-585
8. Zhu Yanbin, Photon count statistics and properties of biophoton emission, Acta Photonica Sinica, 1999, 1: 25-29
9. K.H. Li, Laser Elektro-Optik, 1981. 3, 32-35

*Supported by Guangdong Province Nature Science Fund and State Key Lab of Modern Optical Instrumentation, Zheying University.

*Correspondence: Email: Zhuyb@scnu.edu.cn; Telephone: 86-20-85212710.
Fax: 86-20-85213239.

SESSION 10

Poster Session

Amorphous SiCN films prepared by ECR-CVD technique for photoconductive detectors

D.H. Zhang^{*a}, Y. Gao^a, and J. Wei^b

^aSchool of Electrical and electronic Engineering, S2
Nanyang Technological University
Singapore 639798

^bGintic Institute of Manufacturing Technology
71 Nanyang Drive, Singapore 638075

ABSTRACT

Amorphous silicon-carbon-nitrogen (a-SiCN) films prepared using the industry-used electron cyclotron resonance chemical vapour deposition technique at room temperature for photoconductive detectors are systematically investigated. It is found that the film quality is sensitive to the preparation conditions. The deposition rate of the films is found to increase with the microwave power. It peaks at a ratio of silane to the mixture of silane, methane and nitrogen around 33% and at a radio frequency (RF) bias of 100 V. The optical energy band-gap of the films increases monotonically with the gas ratio but decreases with RF bias. The conductivity of the materials is also found to vary with the preparation conditions. The change in the energy band-gap and conductivity is associated with the change in the incorporation of carbon and nitrogen. The wavelength in the range of 0.65 to 0.45 micron could be detected by controlling the deposition conditions.

Key words: Electron cyclotron resonance, chemical vapor deposition, and photoconductive detector.

1. INTRODUCTION

Amorphous hydrogenated silicon carbon nitrogen (SiCN) alloys have been attracting great interest recently due to their new features compared to those of crystalline Si_3N_4 and SiC mixtures, and potential applications in microelectronics and coating technology. The preparation techniques reported for such alloys include laser vapor phase reaction of hexamethyldisilazane (HMDS) with ammonia¹, plasma polymerization of HMDS in an electronic discharge², reactive magnetron sputtering^{3,4}, plasma-assisted chemical vapour deposition (PACVD) using $\text{SiH}_4\text{-NH}_3\text{-C}_2\text{H}_4$ ^{5,6} or $[(\text{CH}_3)_2\text{N}]_3\text{SiN}_3$ ⁷ and laser ablation of a SiC target in nitrogen⁸ and electron cyclotron resonance plasma vapor deposition (ECRCVD)⁹. It is suggested that the promising features of the SiCN alloy are likely due to the more complicated Si, C, and N atomic chemical environments than a mixture of pure Si_3N_4 and SiC phase. Gomez et al. reported the structure properties and bonding formation⁹. To the best of our knowledge, little has been reported of the electrical and optical properties. In this paper we will concentrate on deposition rate, conductivity and transmission properties of the SiCN alloys deposited using an ECRCVD at room temperature under different conditions; which are useful for their potential applications in optoelectronic devices.

2. EXPERIMENTS

The SiCN alloys studied were fabricated using an industry-used ECRCVD system. There is an array of 8 electromagnets surrounding the chamber wall to control the shape of the plasma column so that uniform ion current density near the substrate can be produced. A load lock chamber and a high-speed turbomolecular pump are able to obtain a base pressure below 10^{-5} mTorr. The plasma was formed by introducing Ar and N mixture directly into the resonance zone whereas the reactive SiH_4 and CH_3 were introduced by a ring located closer to the substrate. The substrate holder is a metal box filled

* Correspondence: Email: edhzhang@ntu.edu.sg; Telephone: 65-7904841; Fax: 65-7920415

with liquid He to maintain a temperature around 20 °C. The deposition pressure was maintained at 6 mTorr in all experiments. Three kinds of substrates were simultaneously used for film deposition. They were cleaned ultrasonically before been introduced into the system and were further cleaned in Ar plasma for 5 mins to remove any residual oxide. Eleven samples were deposited under different conditions and the details are shown in Table I.

Table I. Preparation conditions of the A-SiCN alloy using ECRCVD technique.
The gas composition ratio is defined as $r = \text{SiH}_4/(\text{CH}_4 + \text{SiH}_4 + \text{N}_2)$.

Sample	r	Ar(sccm)	N ₂ (sccm)	CH ₄ (sccm)	SiH ₄ (sccm)	Microwave (w)	RF power (V)
6	9.0	100	70	30	10	1000	100
5	23.0	100	70	30	30	1000	100
4	33.3	100	70	30	50	1000	100
7	46.6	100	60	20	10	1000	100
3	83.3	100	10	10	10	1000	100
14	38.5	100	60	20	50	1000	0
9	38.5	100	60	20	50	1000	200
10	38.5	100	60	20	50	1000	300
11	38.5	100	60	20	50	1000	400
12	38.5	100	60	20	50	750	100
13	38.5	100	60	20	50	500	100

The film thickness was measured using a Dektak on a step formed by placing a mask on the substrate during deposition. The conductivity measurements were conducted in a custom-made vacuum chamber with the sample holder variable from -100 to 400 °C. The optical bandgaps of the alloys were extracted from the transmittance and reflectance data, measured by an ultraviolet to near infrared Perkin-Elmer Lambda spectrophotometer, using Tauc law.

3. RESULTS AND DISCUSSION

Fig. 1 shows the deposition rate dependence on the ratio r , defined as $\text{SiH}_4/(\text{SiH}_4 + \text{CH}_4 + \text{N}_2)$. The films were deposited at a RF bias of 100 V and a microwave power of 1000 W with the ratio r varied from 8 to 85%. As indicated in the figure, the deposition rate increases with r and reaches a maximum at an r of 33%. It then drops with a further increase in r . At a small r , silane content is relatively low. It is likely that the decomposition of silane enhances the deposition rate as the silane content increases. However, when the silane content is too high, some of the excess hydrogen decomposed from silane may etch the deposited film and recombine into silane and methane so as to reduce the deposition rate.

The effect of RF bias on the deposition rate is shown in Fig. 2. The films studied were prepared with the microwave power fixed at 1000 W and a ratio fixed at 38.5%. The deposition rate increases at low RF bias and then decreases with the increase in RF power after a maximum at 100 V. It is believed that the initial increase in the deposition rate is possibly due to the enhancement in the efficiency of decomposition of reacting gases. The decrease with the further increases of RF power is likely a result of bombardment of high-energy ions on the substrate.

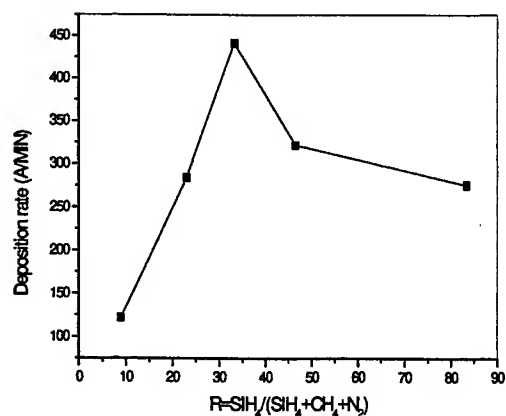


Fig. 1 Deposition rate as a function of gas-phase silane composition.

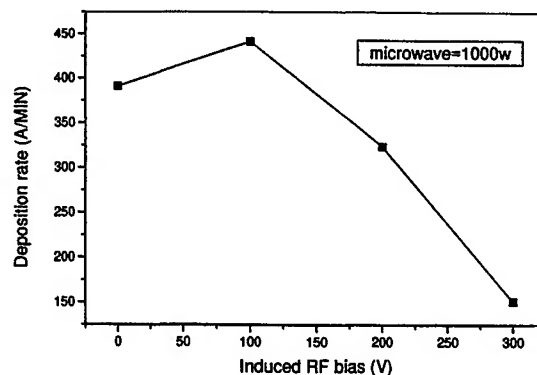


Fig. 2. Deposition rate versus RF bias.

In addition to the deposition rate, the effect of substrate is also studied by a scanning electron microscopy. The films studied were deposited on corning glass and silicon substrates at the same run. The micrographs are shown in Fig. 3 (a) and (b). It is seen that the film deposited on silicon substrate has some grains involved. The film deposited on glass substrate, however, is amorphous and there is a thin transfer layer between the amorphous layer and the substrate. This observation indicates that the substrate

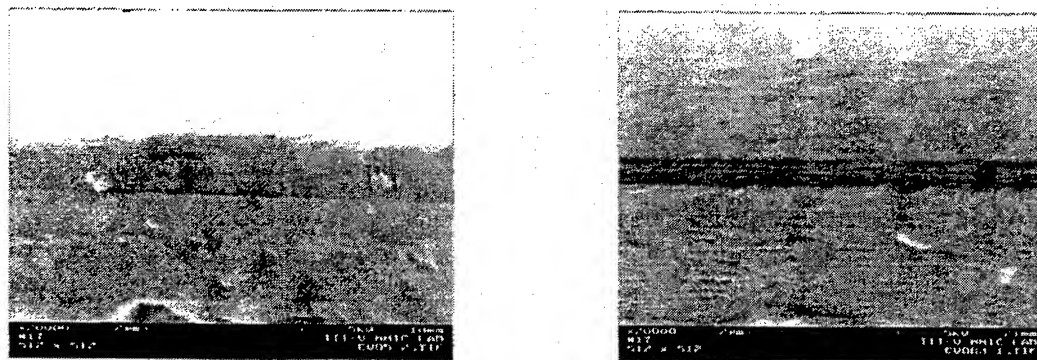


Fig. 3 Cross sectional micrograph of A-SiCN films deposited on (a) Si substrate and (b) glass substrate.

We now look at how the electrical properties of the SiCN alloy vary with the deposition conditions. Fig. 4 shows the conductivity as a function silane composition. It is interesting to find that the conductivity is in the range of 3.4×10^{-12} to $5.4 \times 10^{-11} \Omega\text{cm}^{-1}$ and does not change significantly over the composition range studied. This observation indicates that the amorphous SiCN alloys are basically insulating materials and nitrogen does not contribute carriers to the alloys for electrical conduction. The effect of RF power on the conductivity is shown in Fig. 5. The conductivity is about $4 \times 10^{-7} \Omega\text{cm}^{-1}$ for the films deposited at 0 RF bias. It drops drastically as the RF bias increases and goes up again at a RF bias of

300 V. The high conductivity at 0 RF bias responds well to a high deposition rate. It is believed that the significant difference in conductivity is not due to doping but a result of difference in the nature of structure.

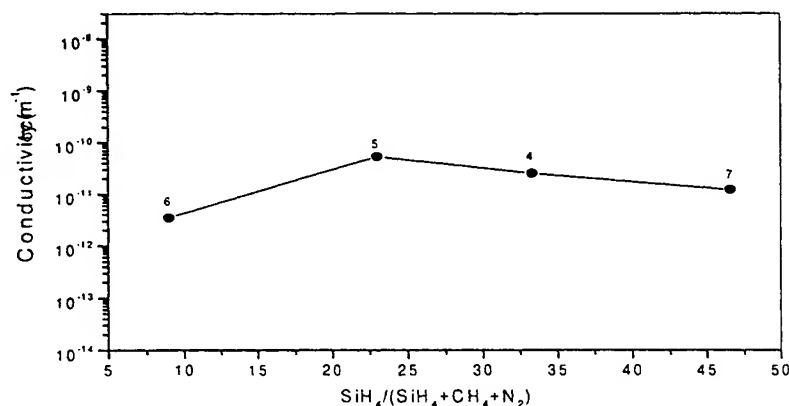


Fig. 4. Electrical conductivity of the a-SiCN films as a function of silane composition

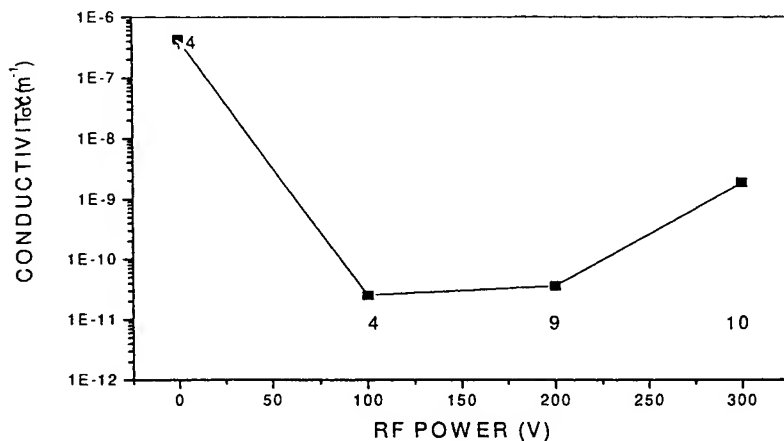


Fig. 5. Conductivity of the a-SiCN films as a function of RF bias.

Fig. 6 and 7 show the optical bandgap of the SiCN alloys as a function of silane composition and RF bias, respectively. The bandgap increases monotonically with silane composition while it decreases monotonically with RF bias. It is well known that the incorporation of hydrogen enhances the bandgap of the amorphous silicon based material by lowering the valence band of the material¹⁰. As the composition of silane increases, the concentration of the decomposed hydrogen increases rapidly. More and more hydrogen will be incorporated into the film as the silane composition increases, resulting in an increase in the bandgap. As far as the effect of RF bias is concerned, the drop in the bandgap is believed to be due to the high-energy hydrogen ions which not only etch the deposited film but also possibly recombine together with silicon and carbon ions to form silane and methane. The reduction of hydrogen due to the recombination will lead to a decrease in bandgap.

It is reported that the crystalline SiCN films deposited by microwave plasma enhanced chemical vapor deposition (MWCVD) at a high temperature (800 °C) exhibit a hexagonal structure, where the Si and C are substitutional elements in the network. The preliminary lattice parameters a and c are 5.4 and 6.7 Å, respectively¹¹. Such material can be used in coating applications. However, the amorphous SiCN films deposited by ECR CVD can not be regarded as a mixture of SiC and Si₃N₄ but as some intermediate state⁹. Our other results have drawn similar conclusion. It implies that the films deposited by ECR CVD method may not be suitable for coating application. We believe that the structure difference between the crystalline and amorphous SiCN films is mainly a result of substrate temperature. However, the amorphous SiCN films deposited by ECR CVD technique are possible to be used as detectors. The bandgap range from 1.9 to 2.8 eV obtained by varying silane ratio and RF bias could cover all visible range, including blue light.

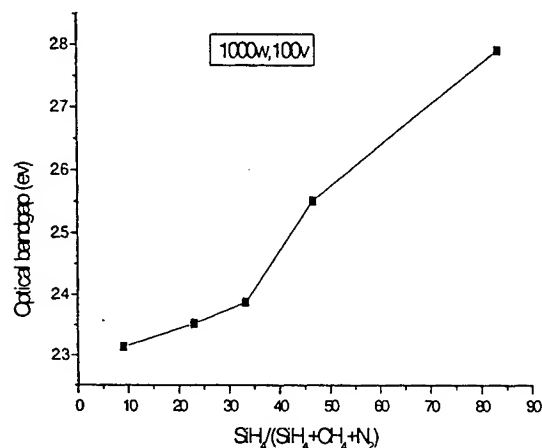


Fig. 6. Optical bandgap as a function of gas-phase silane composition.

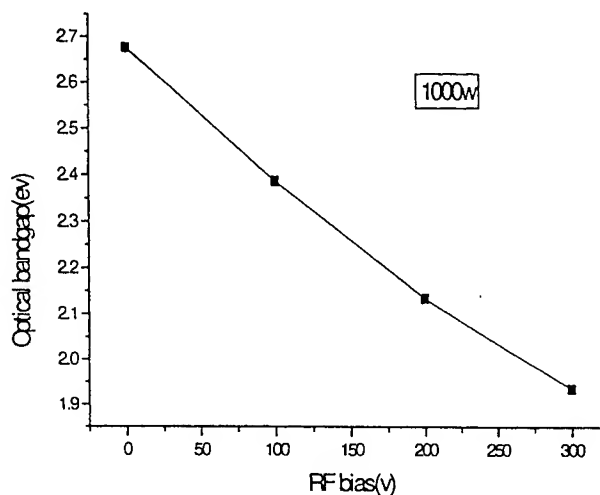


Fig. 7. Optical bandgap E_g as a function of RF bias.

4. CONCLUSION

In conclusion, the amorphous SiCN films deposited by ECR CVD technique were characterized. The deposition rate significantly varies with deposition conditions, such as silane ratio and RF bias. The structure of the amorphous SiCN alloy is not a mixture of SiC and Si₃N₄ but an intermediate state. They may be not suitable for coating applications. The variable bandgap in the range of 1.9 to 2.8 eV of the alloy by varying silane ratio and RF bias suggests possibly applications for detection of visible light.

References

1. W.F.A. Besling, P.J.J.M. van der Put and J. Schoonman, *J. Phys. Chem. Ref. Data* C5, 953, 1995.
2. K.W. Gertenberg, *Colloid Poly. Sci.* 268, 345, 1990.
3. N.V. Novikov, M.A. Voronkin and N.I. Zaika, *Diam. Relat. Mater.* 1, 580, 1992.
4. J. Wei, Y. Gao, D.H. Zhang, P. Hing and Z.Q. Mo, 1999.
5. K. Kamata, Y. Maeda and M. Moriyama, *J. Mater. Sci. Lett.* 5, 1051, 1986.
6. W. Zhang and J.T. Wang, *surf. Coat. Technol.* 50, 1, 1991.
7. H. Kitho and M. Muroyama, *Jpn. J. Appl. Phys.* 33, 7076, 1994.
8. A.L. Lee, H. Ong, F. Xiong and R.P.H. Chang, *Mater. Res. Soc. Symp Proc.* 356, 161 (1995).
9. F.J. Gomez, P. Prieto, E. Elizalde and J. Piqueras, *Appl. Phys. Lett.* 69, 773, 1996.
10. D.H. Zhang and D. Haneman, *J. Appl. Phys.* 66, 4958, 1989.
11. L.C. Chen, C.K. Chen, S.L. Wei, D.M. Bhusari, K.H. Chen, Y.F. Chen, Y.C. Jong and Y.S. Huang, *Appl. Phys. Lett.* 72, 2463, 1998.

Aligned $\text{In}_{0.5}\text{Ga}_{0.5}\text{As}$ quantum dots on laser patterned GaAs substrate

S.K. Park^{*a}, C.K. Hyon^a, B.D. Min^a, H.J. Kim^a, S.M. Hwang^a, E.K. Kim^a,
H.K. Lee^b, C. Lee^b, Y. Kim^c

^aSemiconductor Materials Laboratory, Korea Institute of Science and Technology, Seoul, Korea

^bDepartment of Electrical Engineering, Inha University, Incheon, Korea

^cDepartment of Physics, Donga University, Pusan, Korea

ABSTRACT

It has been studied the selective InGaAs quantum dots growth on laser-patterned GaAs substrate by atmospheric pressure metal organic chemical vapor deposition (APMOCVD). We have patterned the samples below etching threshold power density 8.84 MW/cm^2 by argon ion laser (514 nm). The depth and lateral size of the pattern are about 8 nm and 100 nm, respectively. The QDs (quantum dots) were grown on AlGaAs matrix. The formation of QDs on the matrix can be obtained a wider energy gap between the states of QDs and the matrix materials than on GaAs matrix. The buffer layer consisted of a 0.6 μm AlGaAs matrix layer and a 0.4 μm GaAs layer. AlAs mole fraction of $\text{Al}_x\text{Ga}_{1-x}\text{As}$ to realize graded refractive index is varied from 0.05 to 0.35. Structural and optical properties of InGaAs QDs were studied by scanning electron microscope (SEM), atomic force microscopy (AFM), and photoluminescence (PL). The QDs have a lateral size of about 20 nm and density of $3 \times 10^{10} \text{ cm}^{-2}$. Density and uniformity of QDs obtained on AlGaAs matrix are superior to on GaAs matrix. The PL peak of aligned InGaAs QDs is observed in the 900 nm.

Keywords: selective growth, InGaAs quantum dot, AlGaAs matrix, laser pattern

1. INTRODUCTION

The selective epitaxial growth is an attractive technique for achieving the arrangement of QWRs and QDs on the substrate. To present, the strained substrate¹ and the surface having step bunches² have been employed for the selective self-assembly of QWRs and QDs. Self organizing QDs due to S-K growth are affected by the strain of the underlying layer³⁻⁶. Therefore, if we can control the position of the surface strain of the underlying layers, the selective growth of self-organizing QDs can be realized on that surface.

Recent significant interest in the formation of quantum dots is the arrangement of the QDs using the various patterning techniques, e.g., photolithography, e-beam lithography, x-ray lithography, etc. The lithography techniques have demerits of many processes, complex, expensive cost, etc. But laser shallow etching technique has many merits of an easy controlling, decrease a number of process, cheap cost, no damage for substrates, and so on.

In this paper, InGaAs QDs were grown on laser-patterned GaAs substrate by APMOCVD. At first, we have investigated the laser etching of GaAs substrate at below a threshold etching power density. The laser-pattern technique was just used not to form the groove but to give a stress to substrates. In other words, we gave the difference of strain between patterned and not patterned substrates. InGaAs QDs were formed via S-K growth mode³⁻⁶ on the strained GaAs substrate. The QDs were selectively aligned along the patterned direction on the strain distributed GaAs surface. Structural and optical properties of InGaAs QDs were investigated.

2. EXPERIMENTS

2-1. Laser-Patterning

The GaAs substrates were cleaned with trichloroethylene - acetone - methanol - DI water. The samples were mounted in a vacuum chamber with a quartz window. The chamber was fixed on an electrically controlled X-Y-Z stage, and then evacuated down to 10^{-3} Torr by a rotary pump. An etching gas of CCl_2F_2 was introduced into the chamber through a needle valve at a pressure of 760 Torr. The irradiation was carried out with an argon ion laser operating at 514.5 nm. The beam was focused by a microscope objective lens (NA=0.4) down to a spot diameter of about $1.2 \mu\text{m}$ (at $1/e$ intensity) on the sample surface (see Fig. 1). The laser power density on the sample surface was fixed below the etching threshold power density of 8.84 MW/cm^2 . The beam was scanned on the sample by moving the chamber with a speed of $100 \mu\text{m/sec}$. The patterned profiles were observed by atomic force microscopy (AFM).

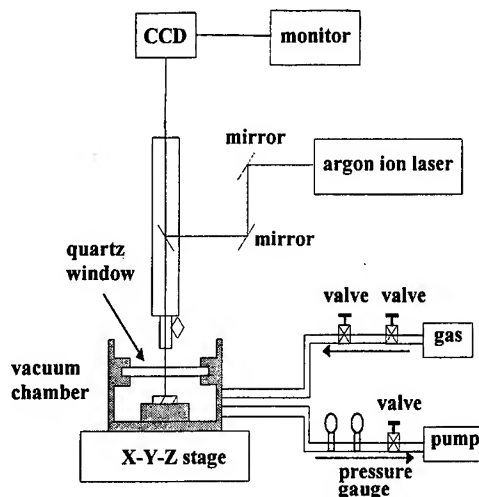


Fig. 1. A schematic diagram of laser pattern system.

2-2. Selective QDs Growth

Our growth system is atmospheric pressure MOCVD with a vertical quartz reactor. All the patterned samples were degreased in organic solvents, cleaned in de-ionized water and finally blown with nitrogen. The metal-organic sources for InGaAs quantum dots were trimethylgallium (TMG), AsH_3 (10% diluted in pure hydrogen) and trimethylindium (TMI). The source was carried with H_2 gas of 8000 SCCM. Figure 2 shows a schematic diagram of the sample structure. A 600 nm thickness $\text{Al}_x\text{Ga}_{1-x}\text{As}$ ($x=0.05\text{--}0.35$) matrix layer was grown at 650°C after deposition of a 400 nm thickness GaAs buffer layer at 650°C . $\text{In}_x\text{Ga}_{1-x}\text{As}$ ($x=0.5$) layer of 4.5 monolayer (nominally) was deposited onto the AlGaAs layer at 470°C . The growth temperature of 470°C was maintained to form QDs for 30 sec: interrupt time. The upper GaAs layer of 0.6 μm thickness was grown to protect the InGaAs QDs at 470°C . The temperature was raised to 650°C for two AlGaAs clad layers of 0.4 μm and 0.6 μm thickness, respectively. Finally, GaAs capping layer was grown at the same temperature.

Post-growth annealing was done in nitrogen gas using rapid thermal annealer at 800°C for 20 sec. Low-temperature (15K) photoluminescence spectra were obtained using 514 nm line of an argon ion laser. The spectra were detected using a germanium detector and lock-in techniques.

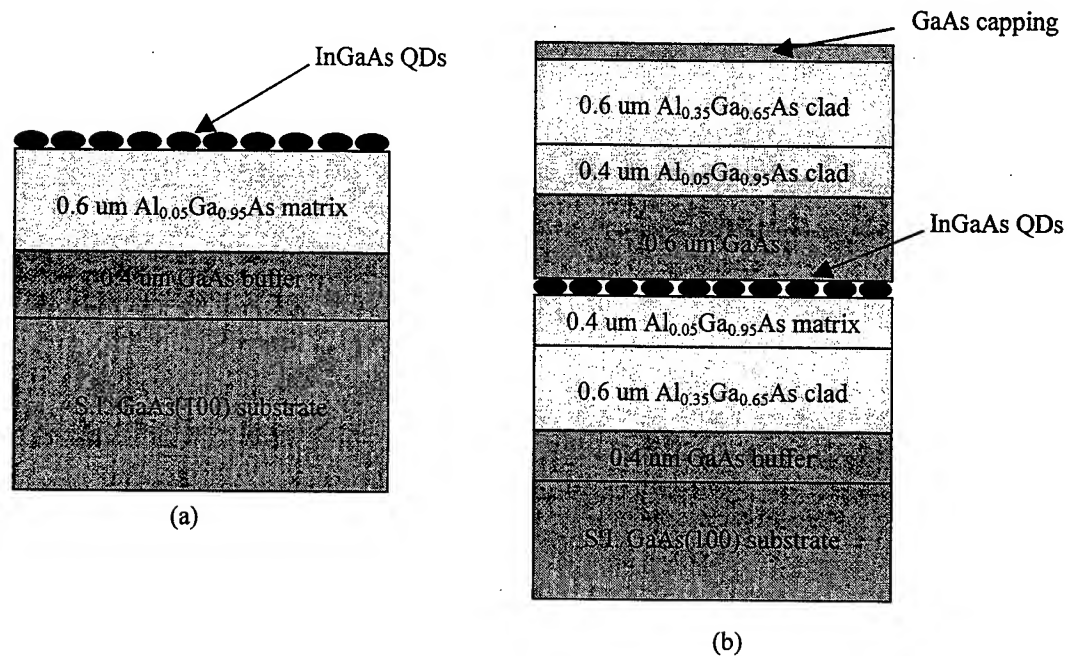


Fig. 2. A schematic diagram of the sample structures for (a) AFM and (b) PL measurements.

3. RESULTS AND DISCUSSION

3-1 . The Shallow Line Pattern

After laser patterning, we could not observe any patterned lines or spots but observe those patterns after conventional wet etching ($5\text{H}_2\text{SO}_4 : 1\text{H}_2\text{O}_2 : 1\text{DI}$ water) to prepare the sample for selective growth. Figure 3 shows the AFM image of the shallow etching pattern of GaAs substrate after wet etching.

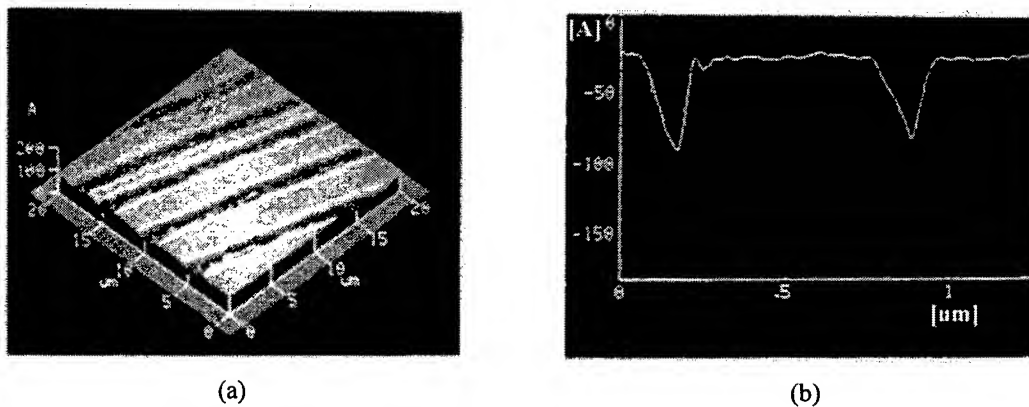


Fig. 3. (a) AFM image of the shallow etching pattern observed after conventional wet etching for selective growth. (b) Cross sectional analysis of (a) by surface profiler.

The depth and width of pattern are about 8 nm and 100 nm, respectively as shown Fig. 3. This pattern just can be obtained below etching threshold power density. Figure 4 shows the procedure of shallow etching process: (a) sample was exposed by laser irradiation in the reaction gas. (b) AsCl_3 and AsF_3 were volatilized in air. (c) weakened the surface of substrate. (d) shallow etching pattern was obtained after conventional wet etching.

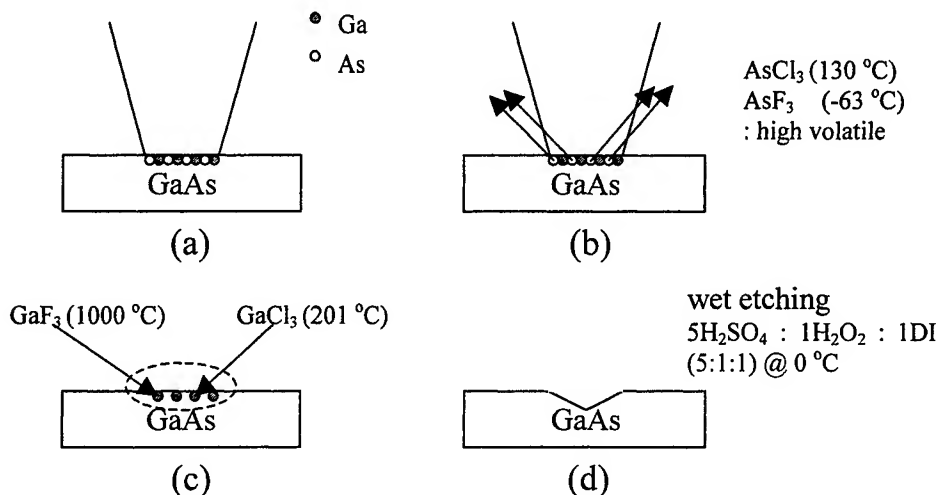


Fig. 4. The procedure of the shallow etching process: (a) sample was exposed by laser irradiation in the reaction gas. (b) AsCl_3 and AsF_3 were volatilized in air. (c) weakened the surface of substrate. (d) shallow etching pattern was obtained after conventional wet etching.

3-2. Selective Growth on Pattern Samples

Figure 5 shows AFM image of selectively formed InGaAs dots (QDs) grown on the laser patterned $\text{Al}_{0.05}\text{Ga}_{0.95}\text{As}$ matrix layer at growth temperature of 470 °C and interrupt time of 30 sec. As shown figure 5 (a), QDs was aligned along with shallow line pattern, which was obtained with laser irradiation even though the pattern was not shown clearly. But, the alignment was not good because there is not enough the difference of the strain between pattern and flat area. In other words, figure 5 (a) indicates that the GaAs substrate was not given enough strain because of low laser irradiation below etching threshold power density. For a while, figure 5 (b) shows the AFM image of the aligned QDs grown on the patterned sample with high power irradiation above etching threshold power density. The QDs aligned along with the ripple can be observed. The ripple was resulted from the excessive laser power density⁷. This result shows that the alignment of QDs can be controlled by the strain line formed with laser irradiation.

Figure 6 shows PL spectra for quantum dot samples grown under identical conditions (see Fig. 2 (b)). In order to recover many defects in each epilayers, the samples were treated by rapid thermal annealing at 800 °C for 20 sec. As shown Fig. 6, the quantum dot peak was broadened, decreased in the intensity and shifted to short wavelength. It is expected that there is two reasons -i.e. (a) ripening effect⁸ during a rapid thermal treatment. (b) inter-diffusion into clad upper or lower layers^{9,10}. The ripening effect results in the realignment of QDs toward line pattern and enlarged the lateral size of QDs. The effect causes the PL spectrum to broaden in the case of patterned sample¹⁰. It is also expected to occur an inter-diffusion of the In and Ga atoms not only at the interface between the QD and the AlGaAs matrix but also at the between QD and QD. The inter-diffusion induces a change in the dot composition resulting in a shallower confining potential and a blueshift in the emission¹⁰.

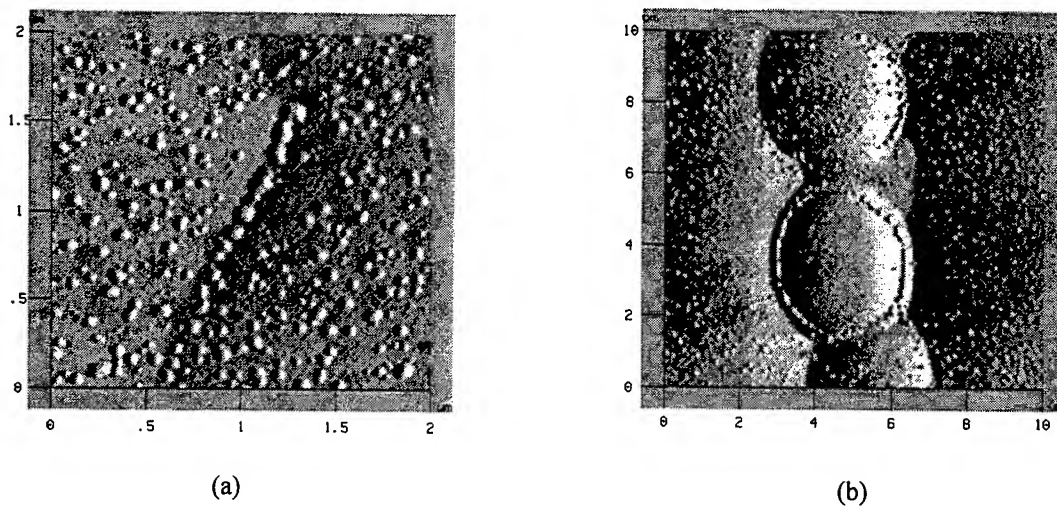


Fig. 5. The AFM image of the selective QDs growth onto laser patterned sample: (a) QDs on the shallow line (below threshold power density), (b) QDs on the ripple (above threshold power density).

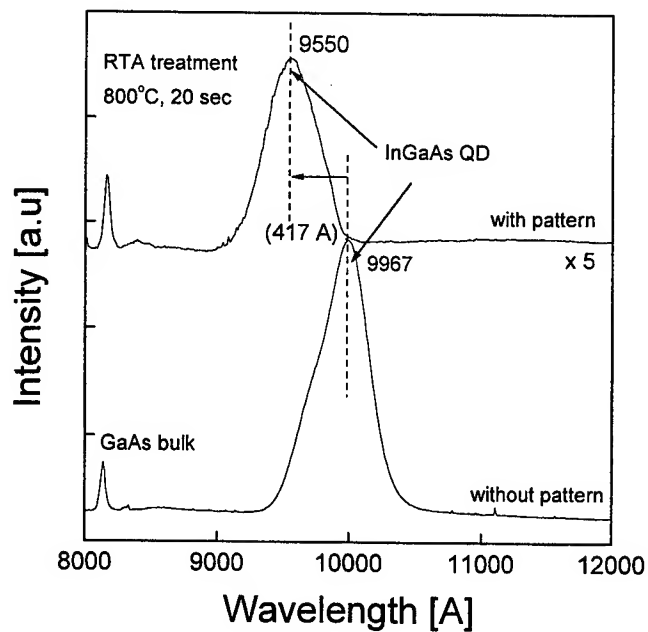


Fig. 6. Low-temperature PL spectra for quantum dot structures with and without shallow pattern.

4. CONCLUSIONS

The selective growth of self-organizing $\text{In}_{0.5}\text{Ga}_{0.5}\text{As}$ QDs was attempted on the patterned GaAs (100) substrate by means of APMOCVD. InGaAs QDs were grown on $\text{Al}_{0.05}\text{Ga}_{0.95}\text{As}$ matrix layer. The shallow pattern was formed by laser irradiation below etching threshold power density (8.84 MW/cm^2). The alignment of QDs along with shallow line pattern was obtained. The samples were annealed to recover many defects, which exists in each epilayers at 800°C for 20sec. The PL spectra of aligned InGaAs QDs were observed in the wavelength of 9550 \AA (with pattern) and 9967 \AA (without pattern), respectively. The reason of blueshift and breadth for QDs peak was supposed from the facts: (a) the realignment of QDs and the enlargement of QDs size in patterned area. (b) inter-diffusion of the In and Ga atoms not only at the interface between the QD and the AlGaAs matrix but also at the between QD and QD. Further study is essential for obtaining exact mechanism. This work presents the possibility of selective QDs growth on the patterned substrates using laser beam.

ACKNOWLEDGMENTS

This work was supported by the development program for the exemplary schools in information and communication from the Ministry of Information and Communication (MIC).

REFERENCES

1. D.S.L Mui, D. Leonard, L.A. Coldren, and P.M. Pertroff, Appl. Phys. Lett. **66**, 1620, 1995
2. M. Kitamura, N. Nishioka, and Y. Arakawa, Appl. Phys. Lett. **66**, 196, 1995
3. J. Tersoff, Phys. Rev. Lett. **76**, 1675, 1996
4. K. Yamaguchi, E. Waki, and H. Hasegawa, Jpn. J. Appl. Phys. **36**, L871, 1997
5. V.A. Shchukin, N.N. Ledentsov, P.S. Kopev, and D. Bimberg, Phys. Rev. Lett. **75**, 2968, 1995
6. W. Seifert, N. Carlsson, J. Johansson, M-E. Pistol, and L. Samuelson, J. Cryst. Growth. **170**, 39, 1997
7. M.S. Kim, C. Lee, S.K. Park, W.C. Choi, E.K. Kim, S.I. Kim, and S.K. Min, J. Elec. Mater. **26**, 436, 1997
8. K-N. Tu, J.W. Mayer, and L.C. Feldman, Electronic Thin Film Science for Electrical Engineers and Materials Scientists (Macmillan, New York, 1992)
9. R. Leon, Y. Kim, C. Jagadish, M. Gal, J.Zou, and D.J.H. Cockayne, Appl. Phys. Lett. **69**, 1888, 1996
10. S. Malik, C. Roberts, and R. Murray, Appl. Phys. Lett. **71**, 1987, 1997

*Correspondence: E-mail: skpark@kistmail.kist.re.kr, Telephone: 81-2-958-5742; FAX: 81-2-958-5739

Taguchi optimization for SU-8 photoresist and its applications in microfluidic systems

J. Zhang*, K.L Tan, L.J. Yang, H.Q. Gong, G. D. Hong, X. D. Wang and L. Q. Chen
Micromachine Laboratory, School of Mechanical and Production Engineering,
Nanyang Technological University
50 Nanyang Avenue, Singapore 639798

ABSTRACT

In this paper, the optimization and application results of SU-8 are reported. SU-8 is an ultra-thick, negative, epoxy-type, near UV photoresist based on EPON SU-8 resins from Microchem Crop. SU-8 is a highly photosensitive resist and its properties are greatly affected by the process parameters. The parameters, which have influence on the properties, were optimized by three level, L9 Orthogonal Array of Taguchi Method. Two kinds of photoresists, SU-8 5 and SU-8 50, and four parameters such as the prebake time, postbake time, exposure time and developing time were chosen to optimize. We found that there exist some minor differences between our results and the published data. This difference could be due to either the EPON SU-8 content or the fabrication conditions. According to the optimized data, for SU-8 5 and SU-8 50, many microstructures with thickness more than 100, 500 μ m and aspect ratio more than 20, 50 were obtained, respectively. All these were achieved without the introduction of GPL, a stronger developing solution. The positive photoresist AZ9260 with thickness more than 20micron were patterned as the sacrificial layer. Using SU-8 as the structural layer, we fabricated some micro-components such as micro-cantilevers, microchannels and micro-heatpipes. The primary experiments demonstrated that SU-8 could be used as the structural material for micro-components and even for some MicroElectroMechanical Systems.

Keywords: Taguchi parameter optimization, high aspect ratio, micro-components, microfluidic systems

1. INTRODUCTION

Photolithography is a well-established technique for resist patterning. For many years the development in this field was focused on how to get high resolution and printing accuracy. Due to the limitation of focus depth and diffraction effect, the maximum thickness of ordinary resists are only on the level of several microns. With the development of Micro Electro Mechanical Systems (MEMS), more and more interests are turned to how to pattern very thick photoresist layers since it has very good pattern transformation and can be used as the micro-moulds for electroplating, hot-embossing and even as the structural material. Some advanced lithography techniques like X-ray beam lithography also had been developed to obtain some high-aspect ratio of microstructures like PMMA, but some drawbacks such as complicated process and high cost of the synchrotron radiation sources limited their further applications.

Epon-based SU-8 was developed as a thick film resist by IBM mainly for MEMS applications. Up to now, SU-8 has proven to be a good candidate for the thick resist applications. The published papers had shown that SU-8 is very sensitive to the variations of processing parameters and conditions and hence difficult to be used properly in the microfabrication process. Unfortunately, no studies have demonstrated which processing parameters are most important or crucial in order to achieve good SU-8 microstructure up to now¹⁻³. At one hand, we guess these conditions may be due to the different SU-8 recipes (there are eight in the family). At another hand, SU-8 is sensitive to the processing environment and equipment used. For these reasons, it was necessary to perform optimization experiment to determine the values for the processing parameters.

In this paper, SU8 and SU8-50, two members of SU-8 series, are chosen because they can supply a wide thickness coverage. Taguchi method was used and four parameters such as the prebake time, postbake time, exposure time and developing time were chosen to optimize. The contribution of different factors to the quality is also list. Using this optimization result, some microstructures had been fabricated. All these confirmed our optimization.

* Correspondence: mzhangj@ntu.edu.sg; Tel: 65-7906994; Fax: 65-7911859(Inter) 7924062 (Local)

2. SU-8 NEGATIVE PHOTORESIST

EPON SU-8 has the highest epoxide functionality commercially available and can dissolve in an organic solvent GBL (gamma-butyrolactone). When coated on a substrate and exposed to ultraviolet light (365 to 436 nm), this epoxy resist can form a highly cross-linked matrix.⁴ Except for the high exposure sensitivity and the excellent adhesion, this resist system has three important attributes as follows, which make it suitable for thick-film applications. First, because of its low molecular weight of 7000 (± 1000), SU-8 can be dissolved in a variety of organic solvents such as propylene glycol methyl ether acetate (PGMEA), gamma-butyrolactone (GBL), or methyl iso-butyl ketone (MIBK) and provide solutions containing up to 85% solids by weight. Thickness of 500 μ m can be obtained easily even with a single spin coating. Second, this material has a very low optical absorption and high transparency in near-UV range. Thus, vertical sidewall profiles can be achieved and hence good dimensional control over the entire structure height could be realised. Third, because of its aromatic functionality and highly cross-linked matrix, the exposed resist is thermally and chemically stable, making it more suitable for some harsh application such as the prolonged plasma etching mask and electroplating processes than its counterpart such as PMMA. In addition, SU-8 has the capability to self-planarize during prebake and results in good contact between the mask and resist in contact lithography mode.

SU-8 5 and SU-8 50, two members of SU-8 series, were chosen in our experiment because they can supply a wide thickness variation. For a single time spin-coating, the thickness coverage can be adjusted from 10 to 350 μ m. For multi-layer coating, this coverage could be up to 1mm. This wide coverage of thickness almost could cover the whole MEMS applications.

3. TAGUCHI METHODOLOGY

In this study, Taguchi's statistical methods was employed to obtain the optimum range of process parameters. The appraisal standard is to gain the highest resolution and aspect ratio in microstructures. The four factors are selected for improving the characteristics including prebake time, exposure time, postbake time, and development time. Orthogonal Arrays (OA) selected for 3-level is L9 OA. The experiments were conducted as described by OA and the various parameter settings were shown in Tables 1. Analysis of variance (ANOVA) was used to interpret the experimental results and decided on which level of the factor need to use⁵. F-test was also performed to find the significant level of the factors. The significant factors with their respective levels were identified and set to the optimum. Once the optimum response was predicted, the confidence interval was then calculated. The final step of the Taguchi method was to conduct confirmation tests and verify the results obtained with the optimum parameter settings².

Table 1. Parameter settings of SU-8 photoresist for Taguchi optimization

SU8-5	Levels	Pre Bake (min)	Exposure (sec)	Post Bake(PEB) (min)	Develop (min)
40 μ m	1	12.5	28	20	5
	2	15	29	25	6
	3	20	30	30	7
30 μ m	1	10	17.5	15	4
	2	12.5	18.5	20	5
	3	15	19.5	25	6
13 μ m	1	8	10	15	3.5
	2	10	10.5	20	4
	3	15	11	22	5
SU8-50					
275 μ m	1	40	100	40	13
	2	50	105	50	16
	3	60	110	60	18
150 μ m	1	35	50	35	10
	2	45	52.5	45	12.5
	3	55	55	55	15
95 μ m	1	25	35	25	8
	2	35	40	35	10
	3	45	45	45	12

4. OPTIMIZATION EXPERIMENTS OF SU-8 NEGATIVE PHOTORESIST

This section describes the optimization experimental results of Epon SU8-5 and SU8-50 photoresist series. we know, there are a number of characteristics factors of SU-8 to consider, such as resolution, aspect ratio (side wall), mechanical properties like Young modulus, film stress, bonding strength and etc. It would not be a wise choice to optimize a large number of characteristics at the same time.

Three-level L9 orthogonal array were used to study the effects of four control factors (Pre bake time, Exposure time under $10\text{mW}/\text{cm}^2$, Post exposure baking time and Developing time), which have influence on the quality. With three different spin speeds, three different thickness could be obtained. Quality of the obtained photoresist structures were assessed on their resolution and aspect ratio. Readings for resolution are chosen from 5 different locations of the wafer with 3 highest reading taken out for optimization. And aspect ratio are obtained by the combination of SEM photo and profiler. All these are processed in 4 inch Silicon wafers with native oxide layer.

The optimization settings for resolution and aspect ratio with 3 different thicknesses, $40\mu\text{m}$, $30\mu\text{m}$, $13\mu\text{m}$, of SU8-5 and $275\mu\text{m}$, $150\mu\text{m}$, $95\mu\text{m}$ of SU8-50 are shown in tables 1-4. S/N ratio is applied to analyze the raw data. The change in the quality characteristic of a product under investigation, corresponding to a factor introduced in the experimental design, is the signal of the desired effect. However, when an experiment is conducted, numerous external factors not designed will involved into the experiment and influenced the outcome. These external factors are called the noise factors and their effect on the outcome of the quality characteristics under test is termed as noise. Thus, the signal to noise ratio measures the sensitivity of the quality characteristic, being investigated in a controlled manner, to some other external factors not under control. The aim of optimization experiment is always to determine the highest possible S/N ratio for the result. since a high S/N ratio implies that the signal is much higher than the random effect of the noise factor. In this experiment, S/N ratio of resolution is measured with the higher the better characteristic while the S/N ratio of aspect ratio is measured with the lower the better characteristic. (in the Table2-5, * stands for Represent Significant Factors, or RSF).

Table 2. Optimal setting of resolution for SU8-5 photoresist

Notation	Parameters	$40\mu\text{m}$		$30\mu\text{m}$		$13\mu\text{m}$	
		RAW DATA	S/N RATIO	RAW DATA	S/N RATIO	RAW DATA	S/N RATIO
PB	Pre bake	20min*	20min*	12.5min*	12.5min*	10min*	8min*
E	Expose	28sec*	30sec*	18.5sec*	18.5sec*	10sec*	10sec*
PEB	Post bake	30min	30min	25min*	25min	20min	20min
D	Develop	7min*	7min*	6min*	6min*	5min*	5min
99% Confidence Interval	Optimum	5.341	11.698	4.933	10.148	4.70	11.14
	C.I	± 0.463	± 0.485	± 0.619	± 4.025	± 0.506	± 0.841
Confirmation results		5.721	11.711	5.354	14.012	5.403	11.523

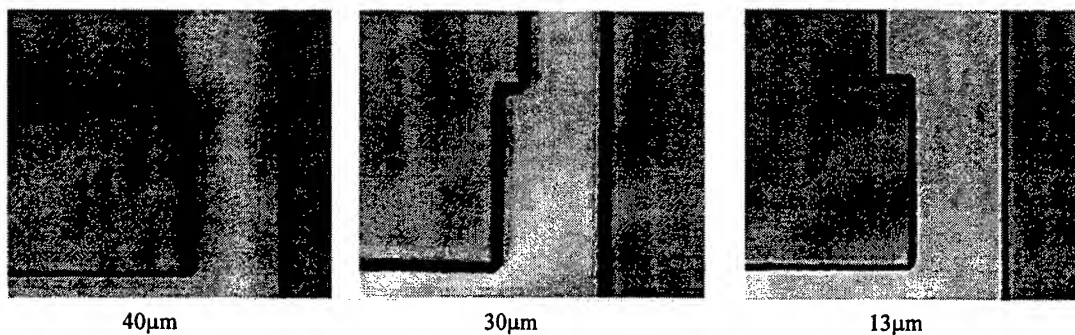


Figure 1. SEM photo shown the difference of resolution with different thickness t of SU8-5

Table 3. Optimal setting of aspect ratio for SU8-5 photoresist

Notation	Parameters	40 μ m		30 μ m		13 μ m	
		RAW DATA	S/N RATIO	RAW DATA	S/N RATIO	RAW DATA	S/N RATIO
PB	Pre bake	20min*	20min*	15min*	15min*	15min*	15min*
E	Expose	30sec*	30sec*	18.5sec*	18.5sec*	10.5sec*	10.5sec*
PEB	Post bake	30min*	30min*	20min*	20min	15min*	15min*
D	Develop	7min*	7min	6min*	6min*	5min*	5min
99% Confidence Interval	Optimum	7.333	-32.118	21.667	-36.294	50	-36.965
	C.I	± 6.636	6.922	± 5.960	± 4.859	± 6.193	± 2.758
Confirmation results		5.012	-28.213	16.314	-33.112	48.012	-32.564

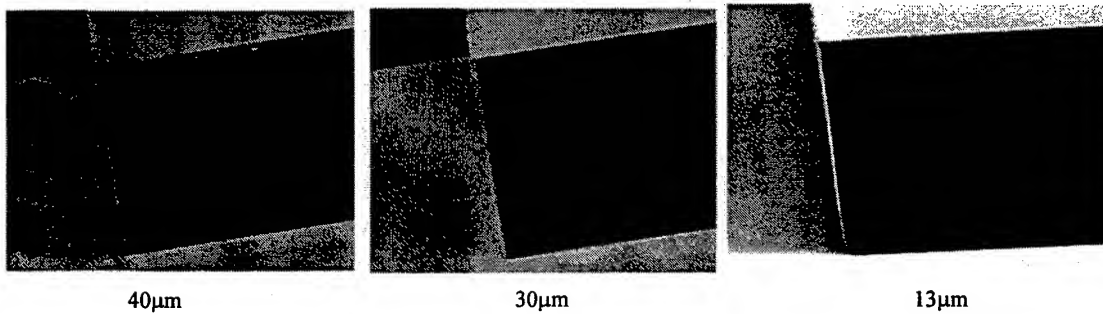


Figure 2. SEM photo shown the difference of aspect ratio with different thickness t of SU8-5

Table 4. Optimal setting of resolution for SU8-50 photoresist

Notation	Parameters	275 μ m		150 μ m		95 μ m	
		RAW DATA	S/N RATIO	RAW DATA	S/N RATIO	RAW DATA	S/N RATIO
PB	Pre bake	40min*	40min*	45min	45min*	25min*	25min*
E	Expose	100sec	100sec	52.5sec	52.5sec	40sec*	40sec*
PEB	Post bake	40min	40min*	55min*	55min*	25min*	25min*
D	Develop	18min*	18min*	15min*	15min*	10min*	8min
99% Confidence Interval	Optimum	4.904	10.993	3.833	8.344	5.133	9.948
	C.I	± 0.408	± 0.903	± 0.465	± 3.400	± 0.607	± 3.798
Confirmation results		4.9	11.02	4.8	11.431	5	11.872

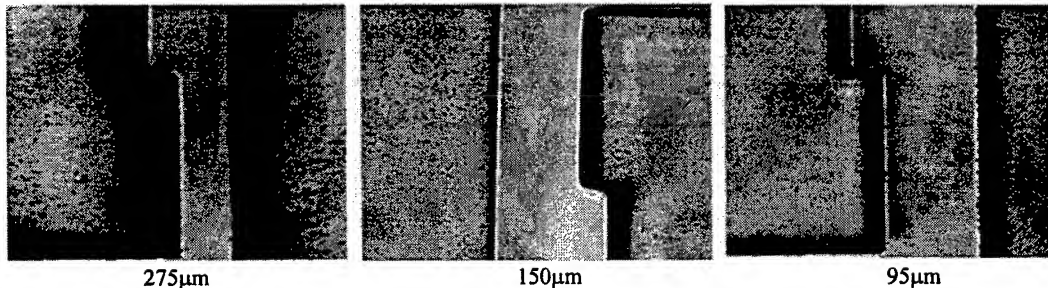


Figure 3. SEM photo shown the difference of resolution with different thickness t of SU8-50

Table 5. Optimal setting of aspect ratio for SU8-50 photoresist

Notation	Parameters	275 μ m		150 μ m		95 μ m	
		RAW DATA	S/N RATIO	RAW DATA	S/N RATIO	RAW DATA	S/N RATIO
PB	Pre bake	40min*	40min*	55min*	45min*	35min*	35min*
E	Expose	105sec*	105sec	50sec	50sec	45sec*	45sec*
PEB	Post bake	50min	50min*	55min*	52.5min*	45min*	45min*
--D	Develop	18min*	16min*	15min*	15min*	10min*	10min
99% Confidence Interval	Optimum	1.7e-15	-19.92	8.667	-27.939	2.333	-28.132
	C.I	± 4.526	± 15.261	5.241	4.464	6.193	6.944
Confirmation results		0.01	-12.541	3.01	-23.976	0.1	-23.475

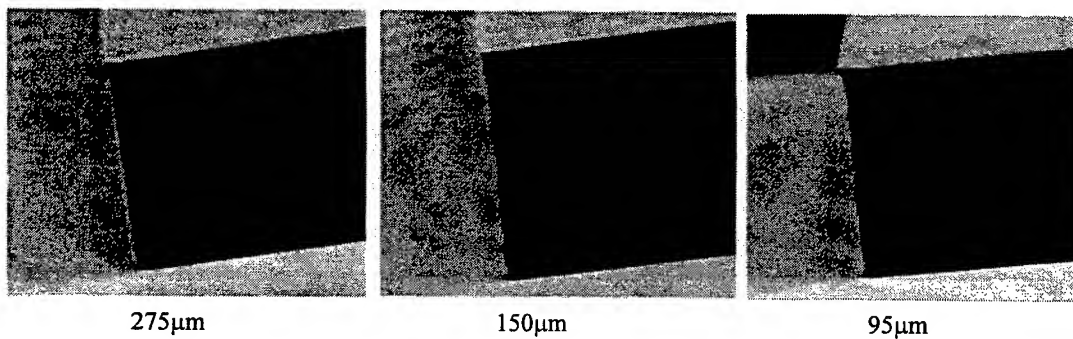


Figure 4. SEM photo shown the difference of aspect ratio with different thickness t of SU8-50

5. DISCUSSION

Through experiments, we can found that the parameter have great influence on the quality of obtained microstructures. But the contribution of these factors to the final result is varied in a very big range.

5.1 SU8-5

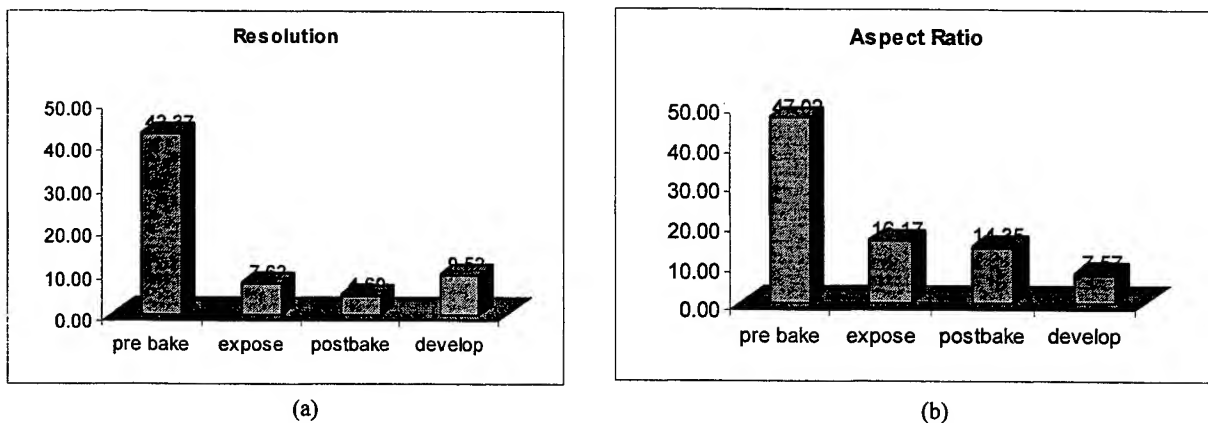


Figure 5. Percentage contribution of factors affecting resolution (a) and aspect ratio (b) of SU8-5

Based on ANOVA result, the contribution of four parameters to the resolution and aspect ratio are shown in Figure 5(a) and (b), respectively. From the Figure 5(a), we knew that the contribution of different factor to the final result is different, varying from Prebake 42.37% to postbake 4.6%. Prebake time is the most important factor to the resolution. From the Figure 5(b), we also found that prebake time 47.02% was the key factor. Therefore, for SU-8 5, good resolution and high aspect ratio can be obtained at the same time. Meantime, the experiment also showed that as the photoresist structure gets thicker, the importance of development time increased. The reason is that more SU-8 5 need to be developed, thus we required more precise control of the time. In addition, as the structure gets taller, it becomes more difficult for the developing solution to reach the photoresist below and the replacement of developing solution become more difficult, this will greatly reduced the efficiency of the developing solution.

5.2 SU8-50

The optimization result of SU-8 50 are shown in Figure 6(a) and (b). From the Figure 6(a), we knew that prebake time is highly significant factor (40.70%). Developing time is second important factor (22.06%). The trend of increasing significance of developing time is also seen with increasing thickness. Exposure time and post bake have little effect on the resolution of SU8-50.

From Figure 6(b), prebake time (27.52%), developing time (24.65%) and exposure time (24.17%) have almost identical influence on achieving higher aspect ratio. Once again, there also exists a trend that developing time will become more significant in thicker photoresist. From the optimized settings of resolution and aspect ratio of SU8-50, the thickness of 275 μ m and 150 μ m show almost similar settings but there are some differences in settings for the 95 μ m thickness. From the two optimizations of resolution and aspect ratio, it is found that pre bake time and developing time are highly significant. However, it is noted from the aspect ratio optimization, exposure time become more significant. This is because the aspect ratio of photoresist structure are more sensitive to exposure dosage as the difference between the three level setting of exposure time is only 1 to 2 seconds. This effect is also seen in SU8-5, aspect ratio optimization.

It is obvious that there exist some differences between the results of SU-8 5 and SU-8 50. The expose time and developing time play a more important role in SU-8 50 than in SU-8 5 in the case of getting high aspect ratio.

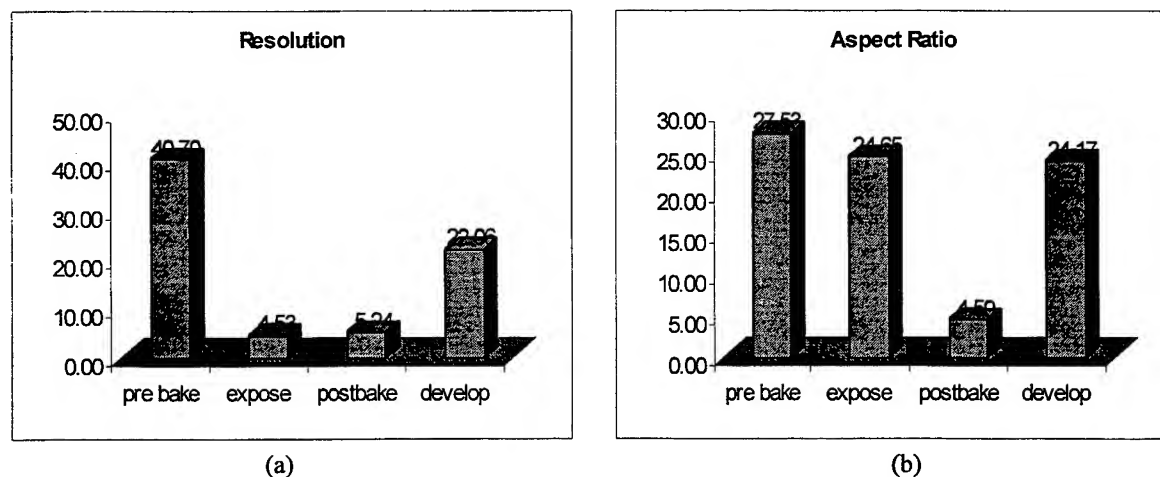


Figure 6. Percentage contribution of factors affecting resolution and aspect ratio of SU8-50

In conclusion, both SU8-5 and SU8-50 exhibit almost the same effect of the various factors. However, development time is more significant to the thicker SU8-50 photoresist in both the resolution and aspect ratio optimization.

6. APPLICATIONS OF SU-8 IN MICROFLUIDIC SYSTEMS

With the capabilities of SU-8, the application is very much like LIGA but of course with reduced resolution and aspect ratio. However, application that do not required ultra-high resolution can be done by SU-8 with a very low cost. SU-8 can be used as structural materials for fabrication of micro-channel in microfluidic system. These channel can be process easily

using SU-8 by UV photolithography. Both processing time and cost are reduced greatly comparing to LIGA technology. The main works are including:

- (1) Using AZ9260 positive photoresist as the sacrificial layer, employing two times exposure, embeded microchannel had been fabricated, shown in Figure 7.
- (2) Using single time exposure technique, micro-channels for microfluidic had been fabricated shown in Figure 8.

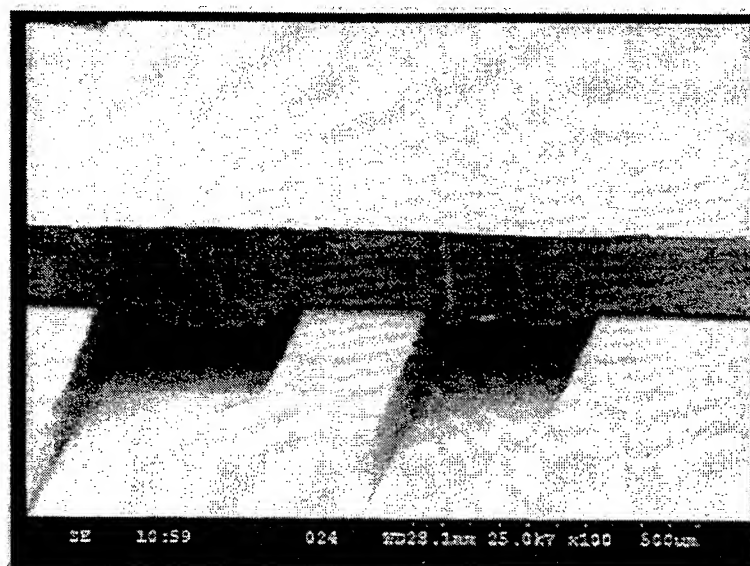


Figure 7. SEM photo of embeded micro-channel fabricated using SU-8 combining positive resist as sacrificial layer

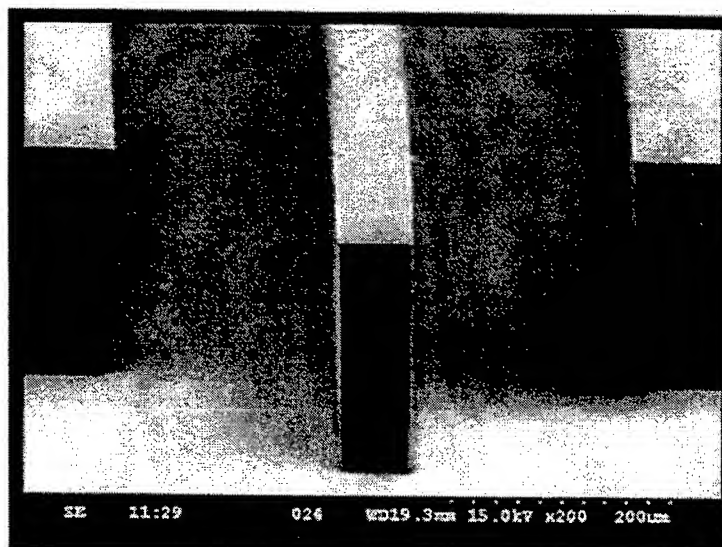


Figure 8. SEM photo of SU-8 microstructures for microfluidic system

7. Conclusion

Taguchi optimization technique has been applied to two commercially available SU-8, negative photoresist series, SU 8-5 and SU 8-50. From the experiment, it is found that all four control factors, prebake time, exposure time, postbake time and developing time, are significant in order to achieve high resolution and aspect ratio. Of the four factors, prebake time is the most significant factor for all the six thicknesses of photoresist. However, the significant of developing time increases with

increasing thickness. This is seen especially with SU8-50 photoresist. High aspect ratio and resolution photolithography of SU-8 photoresist has been developed. In this project, SU-8 is used to build the channels of microfluidic systems like micro heat pipe.

ACKNOWLEDGMENT

The author would like to thank all technicians of the Micromachine Lab in Nanyang Technological University for their help during the course of this project, without which the project would not have progressed as smoothly. Last but not least, everybody who has helped in one way or another but was not mentioned.

REFERENCES

1. Baeyre, J. Blosue, D. Wiberg, "Taguchi optimization for the processing of EPON SU-8 resist.", IEEE MEMS'98, pp. 218-222.
2. N.C. Labianca, J.D. Gelorme, K.Y. Lee, E.O Sullivan and J.M. Shaw, "High aspect ratio optical resist chemistry for MEMS application application" in Proc of the 4th Inter Symposium on Magnetic Materials, Processes and Devices, L.T Romankiw and D.A Ilberman, Eds, Chicago, IL, October 1993, The Electrochemical Society, vol. 95-18, pp. 386-396
3. M. Despont, H. Lorenz, N. Fahrni, J. Brugger, P. Renaud and P. Vettiger, " High aspect ratio ultra-thick, negative-tone near-UV photoresist for MEMS applications", in Proc IEEE, Tenth Annual International Workshop on Micro Electro Mechanical Systems, Nagoya, Japan, Jan 1997, pp.518-522
4. J.M Shaw, D Gelorme, N.C.LaBianca, WE. Conley and S.J. Holmes, " Negative photoresist for optical lithography", IBM Journal of R & D, 41 (1997).
5. Ross, Phillip J. Taguchi techniques for quality engineering : loss function, orthogonal experiments, parameter and tolerance design / Phillip J. Ross. New York : McGraw-Hill, c1996
6. Jorgenson. J. W, Lukacs, K.D. Science 1983, 222, 266-272.

Dynamics of diode-pumped microchip laser passively Q-switched with Cr:YAG

Weiyu Wang* Mali Gong Guofan Jin

Digital Photonics Lab, Dept. of Precision Instruments, Tsinghua Univ.

ABSTRACT

The reason for the instability of passively Q-switched lasers has been analyzed. Based on those reasons a novel model named pre-pumping passively Q switching is presented. The model we developed accounts for the properties of the lasing material, the saturable absorber, the pumping power and the resonator. With the aid of new factor f_p , we calculate the effects of pre-pumping mechanism on the pulse output energy. Like the model of Guohua Xiao the express we derived can be used to optimize the laser's performance.

Keywords: Passively Q-switched lasers, microchip laser, dynamics, instability

1. INTRODUCTION

Recently passively Q-switching by Cr⁴⁺ doped crystals have been reported for variety of systems. Cr⁴⁺:YAG is suitable for producing high-peak-power pulses of laser light with high pulse repetition rate due to its smaller saturation intensity and good heat conductivity¹. Although compared with coupled-cavity Q-switched lasers passively Q-switched lasers avoid high-speed high-voltage electronics their severe problems consist in the instability of pulse repetition rate and the jitter of pulse width. Their application fields are also reduced because of the difficulty in controlling pulse repetition rate.

Ding Yanhua² has reported the laser transversal and longitudinal mode structure as well as the pumping rate disturbance are the important reasons for instability of the output of a CW Nd:YAG laser passively Q-switched with Cr⁴⁺:YAG. The competition between multi-modes lead to the variety of output power from time to time. It has been demonstrated that passively Q-switched pulses under multi-modes oscillation appear to be envelope of pulse amplitude with no apparent periodicity³. However Ding did not give any calculation on the effects of instability caused by the wave of pumping power. Chen Wei⁴ indicated a kind of additional loss of Cr⁴⁺:YAG caused by laser intensity which increases with the circulating power in the cavity. The circulating power changes the Cr³⁺ into Cr⁴⁺ in Cr⁴⁺:YAG crystal which leads to the augment of concentration of Cr⁴⁺. Thus increases the intracavity loss. Wang Mingwei⁵ has explained the phenomena of envelope of pulse amplitude. He believes this modulation phenomena within Q-switched pulse is the result of beat frequency oscillation between different modes with relevant phases.

The theory of passively Q-switched lasers has been described since 1965. Szabo and Stein⁶ first derived the relevant rate equations for the passively Q-switched laser and presented some numerical results. Degnan⁷ demonstrated by applying the Lagrange multiplier method to the optimal coupling problem for the passively Q-switched laser, that simple analytical solutions could be obtained for all laser parameters of interest, e.g. optimum mirror reflectivity, output energy, pulsewidth, peak power, overall efficiency, etc. Later Guohua Xiao⁸ presented a generalized model of a passively Q-switched laser. It enables performance optimization including cases in which saturable absorber exhibits both ground and excited state absorption (ESA). However they did not describe the instability of passively Q-switched pulses theoretically. The goal of this article is to analyze and describe the dynamics of instability and provide a novel method to improve the stability.

Correspondence: Email: wangwy@post.pim.tsinghua.edu.cn

2. ANALYSIS

Population inversion and photon density versus time within a Q-switching period is shown in fig. 1. The time when a pulse begins to start can not keep constant due to the undulation of pumping power and variation of environment conditions. We assume that Q-switch is likely to open when the population inversion reaches some value between n_{th}^- and n_{th}^+ . Thus the region of $(n_{th}^- \sim n_{th}^+)$ is called critical region of inversion population density. The corresponding time region $(t_1 \sim t_2)$ is called the uncertainty of Q-switch. Obviously the two parameters above are very important to mark the stability of repetition rate. In order to reduce the scope of region $(t_1 \sim t_2)$, the following two measures are viable.

- 1) Utilize the stable pump source and keep the environment conditions constant. From the following derivation we can make it clear how the variation of pumping power effects the period of Q-switch.
- 2) A novel method named pre-pumping passively Q-switching is used to modulate the pumping power which make it very quickly for inversion population to pass the critical region of $(n_{th}^- \sim n_{th}^+)$.

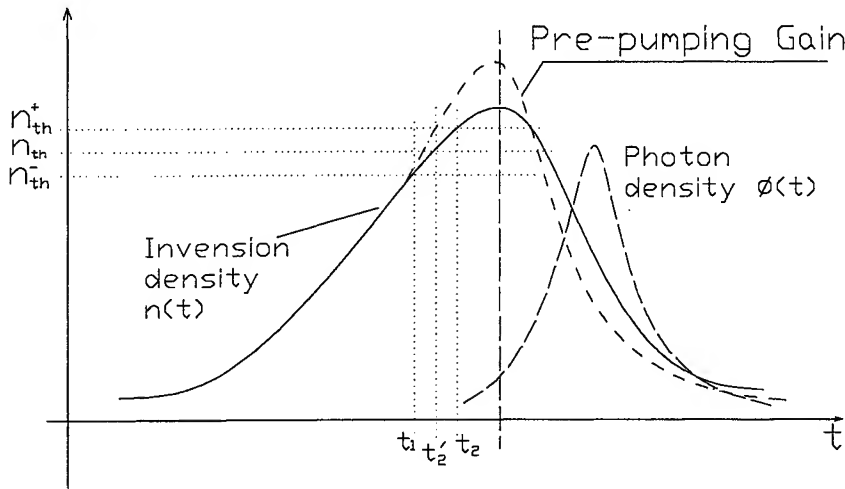


Fig. 1 Population inversion and photon density versus time

Because the pulse width is much smaller than the period of Q-switching, we neglect the effects of pulse width in the calculation of the period of Q-switching and assume $T \approx T'$ (Fig. 2)

According to the rate equations of passively Q-switched laser,

$$\frac{d\phi}{dt} = \frac{\phi}{t_r} [2\sigma n l - 2\sigma_{gs} n_{gs} l_s - 2\sigma_{es} n_{es} l_s - (\ln \frac{1}{R} + L)] \quad (1a)$$

$$\frac{dn}{dt} = R_a - \gamma \sigma c \phi n - \frac{n}{\tau_a} \quad (1b)$$

$$\frac{dn_{gs}}{dt} = -\sigma_{gs} c \phi n_{gs} \quad (1c)$$

$$\frac{dn_{es}}{dt} = \sigma_{gs} c \phi n_{gs} \quad (1d)$$

$$n_{gs} + n_{es} = n_0$$

(1e)

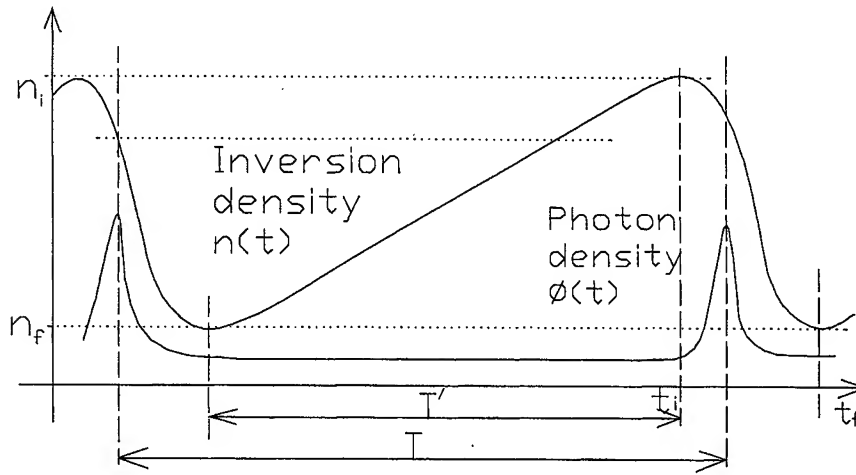


Fig. 2 Inversion density & photon density within one period of Q-switching

where ϕ is the intracavity photon density, σ is the stimulated emission cross section of the gain medium, n is the population inversion density of the gain medium, σ_{gs} , σ_{es} are the absorber ground, ESA cross section, respectively, l is the length of the gain medium, l_s is the saturable length along the cavity axis, $t_r = 2l/c$ is the cavity round-trip time, where c is the speed of light, R is the reflectivity of the output coupler, L is the nonsaturable intracavity round-trip dissipative optical loss, R_a is the pump rate, γ is the inversion reduction factor, τ_a is the lifetime of excited state, n_0 is the total population density.

In the range of T' , we have : $\phi \approx 0$, $d\phi/dt \approx 0$. Then (1b) can be simplified as:

$$\frac{dn}{dt} = Ra - \frac{n}{\tau_a} \quad (2)$$

After integral we got:

$$T' = \tau_a \ln \left(\frac{R_a \tau_a - n_f}{R_a \tau_a - n_i} \right) \quad (3)$$

With CW pumping, from a steady analysis⁷, Degnan presented the following equation:

$$T = \tau_a \ln \left(\frac{R_a \tau_a - \delta n_i}{R_a \tau_a - n_i} \right) \quad (4a)$$

$$\text{where, } \delta = 1 - \frac{f_a}{\gamma} (1 - e^{-\rho}) = 1 - \frac{f_a}{\gamma} \left(1 - \frac{n_f}{n_i} \right) \quad (4b)$$

$$\rho = \ln \left(\frac{n_i}{n_f} \right) \quad (4c)$$

Here δ is the fraction of the population inversion left over at the start of the next pump cycle for the repetitively Q-switched laser.

Notice when $f_a = \gamma$, equation (4) degenerates the same form as equation (3). But it is hard to be satisfied⁹, because it requires very long lifetime of intracavity photon. Although equation (3) is not accurate it can still be utilized to illustrate this question since it has the same form of equation (4).

From equation (3), we got

$$\frac{dT}{T} = \frac{-R_a \tau_a^2 (n_i - n_f)}{T(R_a \tau_a - n_f)(R_a \tau_a - n_i)} \frac{dR_a}{R_a} \quad (5a)$$

or in another format,

$$\frac{dT}{T} = \frac{-R_a \tau_a (n_i - n_f)}{\ln\left(\frac{R_a \tau_a - n_f}{R_a \tau_a - n_i}\right)(R_a \tau_a - n_f)(R_a \tau_a - n_i)} \frac{dR_a}{R_a} \quad (5b)$$

If we substitute δn_i instead of n_i , it will be the result of equation (4). In order to illuminate the effects more clearly we use the experiment data of reference³ to calculate. When the pump power is 1.5 times threshold, that is $R_a \tau_a = 1.5 n_b$, we got $n_f/n_i = 1/46953 \ll 1$ with a computer. Based on these facts we can make the following assumption: $n_i - n_f \approx n_i$ and $R_a \tau_a - n_f \approx R_a \tau_a$. From equation (5) we have $\frac{dT}{T} = -2 \frac{\tau_a}{T} \frac{dR_a}{R_a}$. Assuming the undulation of pump power is about 1%,

we got the laser repetition rate wave of -2.76% according to the relation above.

So we can make a conclusion that the relative alteration of laser repetition is larger than that of pump power within the ordinary range of pump power. And we can also acquire the following fact: the gain medium with longer excited state lifetime is more impressionable.

Obviously the response time of saturable absorber is another important parameter. According to the relation of response time τ and light intensity¹⁰:

$$\tau = \frac{\tau_s}{1 + I/I_s} \quad (6)$$

where, τ_s is the lifetime of excited state, I_s is the saturable intensity. Some saturable absorber with larger I_s or longer τ_s have longer response time which will leads to larger undulation of pulse repetition and pulse power.

3. DESIGN

According to the analysis above we plan to improve the stability of the frequency of passively Q-switched pulses with a passively Q-switched microchip laser pumped by pre-pumping mechanism. Following are the reasons: 1) The single-frequency microchip lasers whose mode spacing is greater than the medium-gain bandwidth can easily conquer the disadvantageous effects induced by multi-mode competition. 2) The mechanism of pre-pumping can effectively solve the problem caused by the undulation of pump power and the longer response time.

The mechanism of pre-pumping may be divided into three steps:

- 1) In the first step, inversion population in the gain-medium are pumped to some value close to the critical region of inversion population density with pump power lower than threshold.
- 2) In the second step, one high and narrow pumping pulse is superposed. Inversion population will arise and pass through critical region of inversion population very quickly under the additional pumping pulse which will greatly reduce the uncertainty of Q-switch (Fig. 1). Furthermore, because of the very high increase speed of inversion it will reach a higher inversion population during the switching time of Q-switch and thus make the energy of Q-

switched pulse higher than usual. But the addition part of pulse energy is very limited which will be shown in the following calculation. In order to avoid the disadvantage brought by pumping pulse we should keep the pumping pulse width shorter than the Q-switched pulse width.

- 3) The high pumping pulse and pre-pumping power are removed in the third step.

4. CALCULATION

Degnan and Guohua Xiao have neglected the terms R_a and n/τ_a of equation (1b) in solving the coupled differential equations from time t_i to t_f (Fig. 2). Because of the transcendental nature of the Q-switched laser equations, they can only give the intermediate analytical solutions. However with the aid of this simple analytical solutions passively Q-switched laser design could now be accomplished quickly using a series of general design curves and a simple hand calculator.

Because of the high pump pulse we can not neglect the term R_a of equation (1b) in the process of deriving analytical solutions. But we must make some necessary assumptions.

Equation (1b) can be written as:

$$\frac{dn}{dt} = R_a - \gamma\sigma c \phi n = \left(-\gamma\sigma c + \frac{R_a}{\phi n}\right) \phi n \quad (7)$$

Because ϕn may be very close to zero we have to simplified them and rewritten the item $R_a/\phi n$. During the period of t_i to t_f (Fig. 2) we can get the following expression approximately:

$$\frac{dn}{dt} \approx \frac{n_f - n_i}{2t_p} \quad (8)$$

Where t_p is the FWHM pulsewidth: $2t_p = t_f - t_i$

Combine (7) with (8) we get:

$$\phi n \approx \frac{n_f - n_i - 2R_a t_p}{-2\gamma\sigma c t_p} \quad (9)$$

Equation (7) can be simplified as:

$$\frac{dn}{dt} = R_a - \gamma\sigma c \phi n = \left(-\gamma\sigma c + \frac{2R_a \gamma\sigma c t_p}{n_i + 2R_a t_p - n_f}\right) \phi n \quad (1b')$$

Dividing (1b') by (1c) yields a relationship between n_{gs} and n_0 , i.e.,

$$\frac{dn}{dn_{gs}} = \frac{\gamma\sigma n}{\sigma_{gs} n_{gs}} \left(1 - \frac{2t_p R_a}{n_i + 2t_p R_a - n_f}\right) \quad (10)$$

Define the pumping factor f_p as: $f_p = \frac{2t_p R_a}{n_i + 2t_p R_a - n_f}$

To keep the parallels between the present analysis and that of ^{7,8} clear, the comparable parameters are given the same names. To enable one to keep track of which is which, the parameter α from this paper are primed twice.

$$\alpha'' = \frac{\sigma_{gs}}{\gamma\sigma(1 - f_p)} \quad (11)$$

Equation (10) can be integrated to yield

$$n_{gs} = n_0 \left(\frac{n}{n_i} \right)^{\sigma} \quad (12)$$

Following Degnan's approach, (1a), (1b'), (1e), (12), and (11) combine to give the relation between n_i and n_f , the initial and final population densities in the gain medium, as

$$n_i - n_f + \frac{\ln \frac{1}{R} + L'}{2sl} \ln \left(\frac{n_i}{n_f} \right) - \frac{l_s g}{l g_s} (1 - f_p) n_0 \left[1 - \left(\frac{n_f}{n_i} \right)^{\sigma} \right] = 0 \quad (13)$$

Where $L' = L + 2s_{ss} n_0 l$. If we order

$$g = g(1 - f_p)$$

Equation (13) then becomes

$$n_i - n_f + \frac{\ln \frac{1}{R} + L'}{2sl} \ln \left(\frac{n_i}{n_f} \right) - \frac{l_s g}{l g_s} n_0 \left[1 - \left(\frac{n_f}{n_i} \right)^{\sigma} \right] = 0 \quad (14)$$

Thus with the change to our primed parameters, Degnan's optimum design results, both formulae and graphs, can also be used to determine parameters of pre-pumping passively Q-switched lasers.

If we neglect the effects of pre-pumping mechanism, i.e. $f_p = 0$, equation (14) will become the same as ^{8, (4)} which is the case of Guohua Xiao's model including ESA.

In ¹², Koechner gives the total energy in the Q-switched pulse as

$$E = \frac{h A}{2 s g} \ln \left(\frac{1}{R} \right) \ln \left(\frac{n_i}{n_f} \right) \quad (15)$$

So the rate of n_i and n_f is very important for estimating pulse energy which is determined by (14). We have calculated the passively Q-switched lasers with the same parameters and compared the results of both Guohua Xiao's model and our model with a computer. As estimated above the output power of our model is slightly larger than that of Guohua Xiao.

5. CONCLUSION

We analyzed the reasons of instability of the passively Q-switched pulses and calculated the undulation of pulses frequency caused by the wave of pump power. The pre-pumping mechanism we developed can be used to improve stability of passively Q-switched laser and its effects on the output power has also been derived. The expression we deduced can also be used to optimize the laser's performance with pulse pump.

REFERENCES

1. H. J. Eichler, A. Haase, M. R. Kokta et al., "Cr⁴⁺:YAG as passive Q-switch for a Nd:YAlO oscillator with an average repetition rate of 2.7kHz, TEM₀₀ mode and 13W output", *Appl. Phys. B*, 58: pp.409~411, 1994
2. Ding Yanhua, Ouyang Bin, Xu Jun et al., "Stability and power improvement in passive Q-switching of CW Nd:YAG laser using Cr⁴⁺:YAG", *Chinese Journal of Lasers*, Vol. A24, No. 3, Mar., pp.197-201, 1997
3. J. J. Zayhowski and C. Dill III, "Diode-pumped passively Q-switched picosecond microchip lasers", *Opt. Lett.*, Vol. 19, No. 18, pp.1427-1429, 1994

4. Chen Wei, Xu Jun, Yang Xiangchun et. al., "Passive Q-switching for CW Nd:YAG laser by using Cr⁴⁺:YAG", *Chinese Journal of Lasers*, vol. A25, No. 1, Jan., pp.7-11, 1998
5. Wang Mingwei, Xing Qirong, Wang Qingyue, et. al., "Experiments research on CW Nd:YAG laser passively Q-switched by Cr⁴⁺:YAG", *Chinese Journal of Lasers*, vol. A25, No. 10, Oct., pp.872-875, 1998
6. A. Szabo and R. A. Stein, "Theory of laser giant pulsing by a saturable absorber", *J. Appl. Phys.*, vol. 36, pp. 1562-1566, 1965
7. John J. Degnan, "Optimization of Passively Q-Switched Lasers", *IEEE J. Quant. Elect.*, vol. 31, No. 11, pp.1890-1901, 1995
8. Guohua Xiao and Michael Bass, "A Generalized Model for Passively Q-Switched Lasers Including Excited State Absorption in the Saturable Absorber", *IEEE J. Quant. Elect.*, vol. 33, No. 1, pp.41-44, 1997
9. John J. Degnan, "Effects of Thermalization on Q-Switched Laser Properties", *IEEE J. Quant. Elect.*, vol. 34, No. 5, pp.887-898, 1998
10. W. Koechner, *Solid-State Laser Engineering*, Fourth Extensively Revised and Updated Edition, pp490, Springer, New York, 1996

Pulse control of passively Q-switched microchip laser with CW pumping modulation

Weiyu Wang* Mali Gong Guofan Jin

Digital Photonics Lab, Dept. of Precision Instruments, Tsinghua Univ., Beijing, 100084, China

ABSTRACT

In order to improve the stability of passively Q-switched lasers we put forward a kind of pre-pumping mechanism¹. Based on this mechanism we deduce an analytical expression which can be used to calculate or optimize the important parameters of passively Q-switched lasers. The analytical expression has been discussed in detail and the results can also be used in many cases of passively Q-switched lasers.

Keywords: Passively Q-switched lasers, pulse pump

1. INTRODUCTION

The theory of passively Q-switched lasers has been described since 1965. Szabo and Stein² first derived the relevant rate equations for the passively Q-switched laser and presented some numerical results. Degnan³ demonstrated by applying the Lagrange multiplier method to the optimal coupling problem for the passively Q-switched laser, that simple analytical solutions could be obtained for all laser parameters of interest, e.g. optimum mirror reflectivity, output energy, pulsewidth, peak power, overall efficiency, etc. Later Guohua Xiao⁴ presented a generalized model of a passively Q-switched laser. It enables performance optimization including cases in which saturable absorber exhibits both ground and excited state absorption (ESA). However they derive their analytical expression based on neglecting pump power during the switching time. This paper extends these results above and tries to solve many practical questions of pulse pumped passively Q-switched lasers.

Degnan introduced two constants which he calls γ and γ_s into his calculations. γ is the familiar quantity called a "degeneracy factor" by Koechner⁵, "2*" by Siegman⁶, "inversion deduction factor" by Degnan⁷. On the basis of models published by Hercher and Degnan, Guohua Xiao redefined the constant α' and γ_s' to mark the performance of the Q-switch and the saturable absorber. This paper modifies Guohua Xiao's constant α' to α'' and introduces a new constant f_p to describe the contribute of pulse pump. If we order the value of f_p as zero, our expression will become the same as that of Guohua Xiao.

The expression developed here can be applied to pulse pumping cases. With the help of numerical calculations we present graphs from which we can read the effects of parameters clearly.

2. THEORY

According to our pre-pumping mechanism we need to modulate the pumping power shown in Fig.1. Under this pre-pumping mechanism population inversion and photon density versus time within a Q-switching period is shown in Fig. 2. From Fig. 2 we can see very clearly the inversion density is different from that case of CW pumping. We must derive more accurate analytical expressions to match this case. Because we have derived the results in another paper¹ here we only write down the necessary expressions for discussing.

Correspondence: Email: wangwy@post.pim.tsinghua.edu.cn

According to the rate equations of passively Q-switched laser, we can write five coupled differential equations as following:

$$\frac{d\phi}{dt} = \frac{\phi}{t_r} [2\sigma n l - 2\sigma_{gs} n_{gs} l_s - 2\sigma_{es} n_{es} l_s - (\ln \frac{1}{R} + L)] \quad (1a)$$

$$\frac{dn}{dt} = R_a - \gamma \sigma c \phi n - \frac{n}{\tau_a} \quad (1b)$$

$$\frac{dn_{gs}}{dt} = -\sigma_{gs} c \phi n_{gs} \quad (1c)$$

$$\frac{dn_{es}}{dt} = \sigma_{es} c \phi n_{es} \quad (1d)$$

$$n_{gs} + n_{es} = n_0 \quad (1e)$$

where ϕ is the intracavity photon density, σ is the stimulated emission cross section of the gain medium, n is the population inversion density of the gain medium, σ_{gs} , σ_{es} are the absorber ground, ESA cross section, respectively, l is the length of the gain medium, l_s is the saturable length along the cavity axis, $t_r = 2l/c$ is the cavity round-trip time, where c is the speed of light, R is the reflectivity of the output coupler, L is the nonsaturable intracavity round-trip dissipative optical loss, R_a is the pump rate, γ is the inversion reduction factor, τ_a is the lifetime of excited state, n_0 is the total population density.

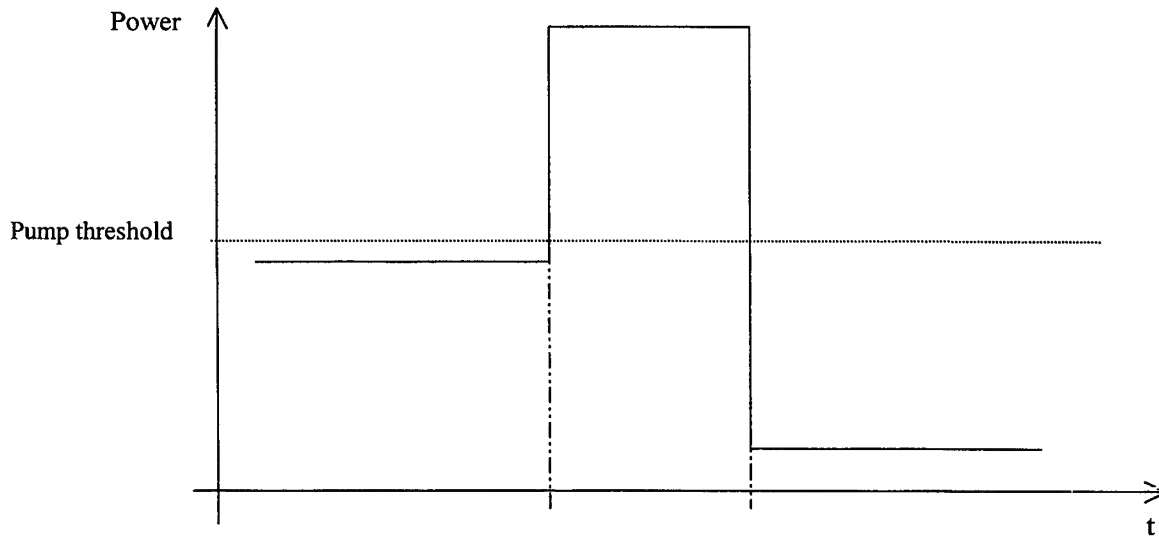


Fig. 1 Pump power versus time

Define the pumping factor f_p as:

$$f_p = \frac{2t_p R_a}{n_i + 2t_p R_a - n_f} \quad (2)$$

where t_p is the FWHM pulsewidth.

$$\alpha'' = \frac{\sigma_{gs}}{\gamma\sigma(1-f_p)} \quad (3)$$

Following Degnan's approach, the relation between n_i and n_f , the initial and final population densities in the gain medium can be written as:

$$n_i - n_f + \frac{\ln \frac{1}{R} + L'}{2\sigma l} \ln\left(\frac{n_i}{n_f}\right) - \frac{l_s \gamma}{l \gamma'_s} (1-f_p) n_0 \left[1 - \left(\frac{n_f}{n_i}\right)^{\alpha''}\right] = 0 \quad (4)$$

Where $L' = L + 2\sigma_{es} n_0 l$. If we order $\gamma' = \gamma(1-f_p)$. Equation (13) then becomes

$$n_i - n_f + \frac{\ln \frac{1}{R} + L'}{2\sigma l} \ln\left(\frac{n_i}{n_f}\right) - \frac{l_s \gamma'}{l \gamma'_s} n_0 \left[1 - \left(\frac{n_f}{n_i}\right)^{\alpha''}\right] = 0 \quad (5)$$

The parameter α'' is very important because it means how far the absorber is bleached compared to the depletion of the inversion density of the active material. Its value lies between zero and one. The larger α'' is, the higher the efficiency can reach. In another words it will spend more photons to bleach absorber if α'' is smaller and only a small part of the photons enter into the actual laser pulse. If we may neglect the pump energy (e.g. in CW pumping passively Q-switched lasers for its effect is too small) during the switching time, α'' can only be improved by selecting proper gain and absorber material since we can hardly improve the absorber ground cross section.

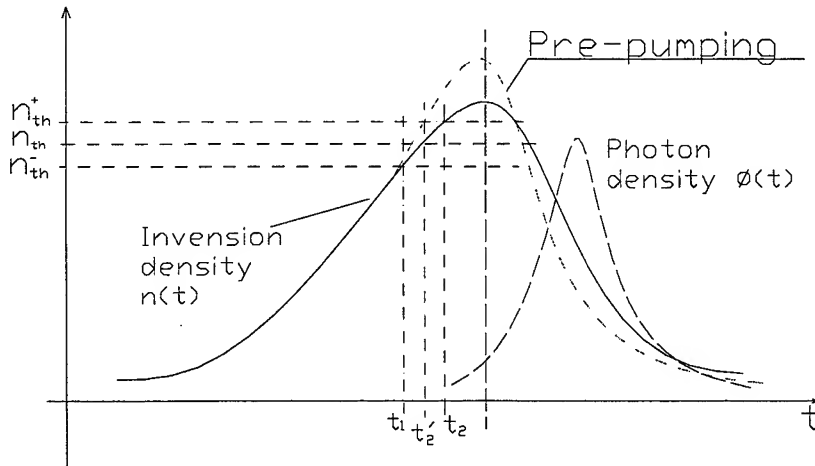


Fig. 2 Population inversion and photon density versus time

But considering the pulse pump effect during the switching time we may improve the α'' by factor f_p . The following analysis of equation (5) will demonstrate it. Here the inversion reduction factor γ is also changed to γ' which means the effect of pump energy during the switching time is absorbed in the reduction factor. Thus we need less inversion population to produce one photon. The value of f_p marks the effect brought by pump power in switching time. The factor f_p also ranges from zero to 1. If f_p equals to zero, equation (5) will become the same as Gouhua Xiao's model. If f_p equals to 1 (That is

impractical) which means $\alpha''=\infty$, equation (5) will become the same as the case of active Q-switched laser. Then we can draw a conclusion the efficiency of passively Q-switched laser is always smaller than that of active Q-switched laser.

3. RESULTS AND DISSCUSSION

The laser diode pumping has already proved to be comparatively better as the pump diode spectral output can be exactly tuned to match the highest peak of Nd:YAG absorption bands. This enable us to estimate accurately the initial inversion created by the diode laser pump elements. The electrical to optical conversion efficiency can also be measured to the accuracy of the energy meter.

For a system end-pumped by a Gaussian laser beam, we can write the pump rate as:

$$Ra = \frac{T_p \eta_p f_a P_p}{h\nu_p (Al)} [1 - \exp(-\alpha l)] [1 - \exp(-A/A_p)] \quad (6)$$

Where T_p is the transmission of the pump face at the pump wavelength (assumed to be near 1), η_p is the fraction of the energy in the pump band relaxing nonradiatively to the upper laser multiplet (also believed to be near 1 for the $^4F_{3/2}$ level in Nd:YAG), $h\nu_p$ is the energy of a pump photon, α is absorption coefficient of gain material (e.g. Nd:YAG), P_p is the pump power, $A_p = \pi\omega_p^2/2$ and $A = \pi\omega^2/2$ are the effective cross-sectional area of the Gausssian pump beam and laser beam area.

Besides equation (5) (constrain condition) and (6) (pump condition) we need to list the following equations to describe a passively Q-switched laser:

$$\text{Initial condition: } n_i = \frac{2\sigma_{gs} n_0 l_s + \ln \frac{1}{R} + L}{2\sigma l} \quad (7)$$

where n_i is initial inversion population.

$$\text{Output pulse energy: } E = \frac{h\nu A}{2\sigma\gamma} \ln \frac{1}{R} \ln \frac{n_i}{n_f} \quad (8)$$

$$\text{Output efficiency: } \eta_E = \frac{\ln \frac{1}{R} \ln \frac{n_i}{n_f}}{2\sigma n_i l} \quad (9)$$

First we numerically calculated the microchip passively Q-switched laser reported by J. Zayhowski and C.DIII⁸ to test our numerical algorithm. The results of the experiment and numerical calculation are listed in table 1. The errors between them are acceptable because many important parameters are not given accurately.

	Pump threshold (W)	Repetition rate (KHz)	Pulse Energy (μ J)
Experiment data	0.8	6	11
Numerical calculation	0.75	5.86	10.4

Table 1 Comparison of the experiment and numerical calculation

During the numerical calculation we did some research which could show the relation between the parameters and the performance of passively Q-switched lasers. Those relations are quite useful for the designers because they can adjust the parameters to reach their design targets (Table 2).

Parameters and their variation	Pulse Energy	Pump threshold	Repetition rate
Dissipative loss (L) ↗	↘	↗	↘
Ground-state cross section of SA (σ_{gs}) ↗	↗	↘	↘
Excite-state cross section of SA (σ_{es}) ↗	↘	→	↗
Absorption coefficient of gain medium ↗	→	↓	↑
Cross-sectional area of the pump beam (ω_p) ↘	→	↓	↑
Cross-sectional area of the laser beam (ω) ↘	↓	↘	↑
Stimulated emission cross section (σ) ↗	↓	↓	↑
Absorption coefficient of SA (α) ↗	↗	↗	↘

Table 2 The relation between the parameters and the performance of passively Q-switched lasers

Here, the symbol “↗” means “rise”, “↑” means “rise dramatically”, “↘” means “descend”, “↓” means “descend dramatically”, “→” means “keep constant approximately”. Some parameters are very important, e.g. ω , σ_{gs} , σ_{es} , and the absorption coefficient of gain medium. The performance of passively Q-switched laser is quite sensitive to the variation of them.

In order to compare the difference between Guohua Xiao's model and ours for an CW pumped microchip laser. We numerically calculated the same case with them respectively. We assume the length of its resonant cavity is equal to 1 millimeter (i.e. $l_s + l = 1\text{ mm}$). The mirror reflectivity varies from 95.5% to 99% and the length of the SA lies between 0.02 to 0.04 mm.

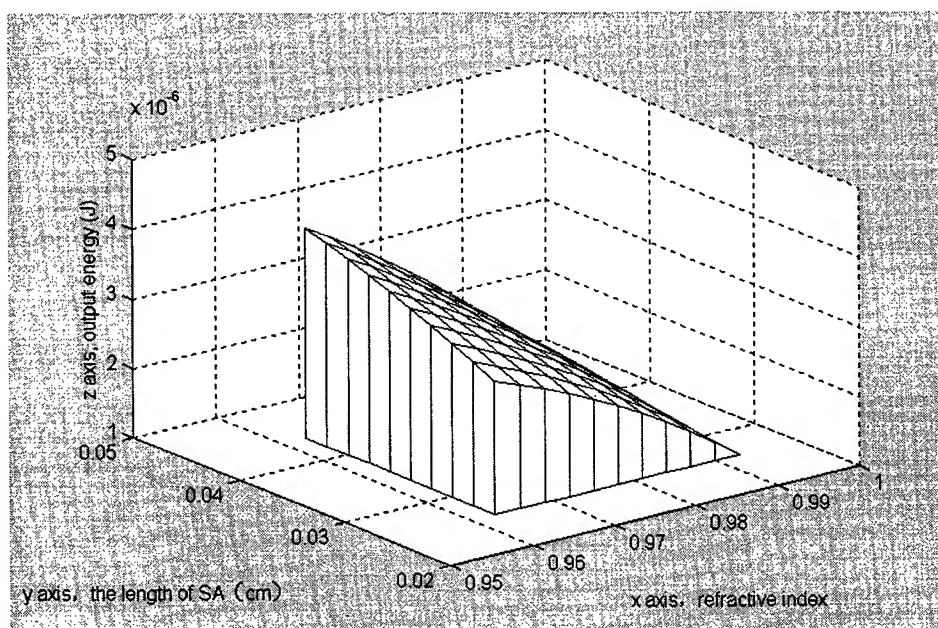


Fig. 3 Numerical calculation results with Guohua Xiao's model for CW pump

The results calculated by Guohua Xiao's model and ours are shown in Fig. 3 and Fig. 4 respectively. It can be seen that the shape of their 3D curves and values are almost the same. In fact the values of their output energy are so close that only the fifth number after decimal is different. This example shows our model is believable and the effects on the output energy brought by CW pump can be neglected (i.e. $f_p=0$ in our model).

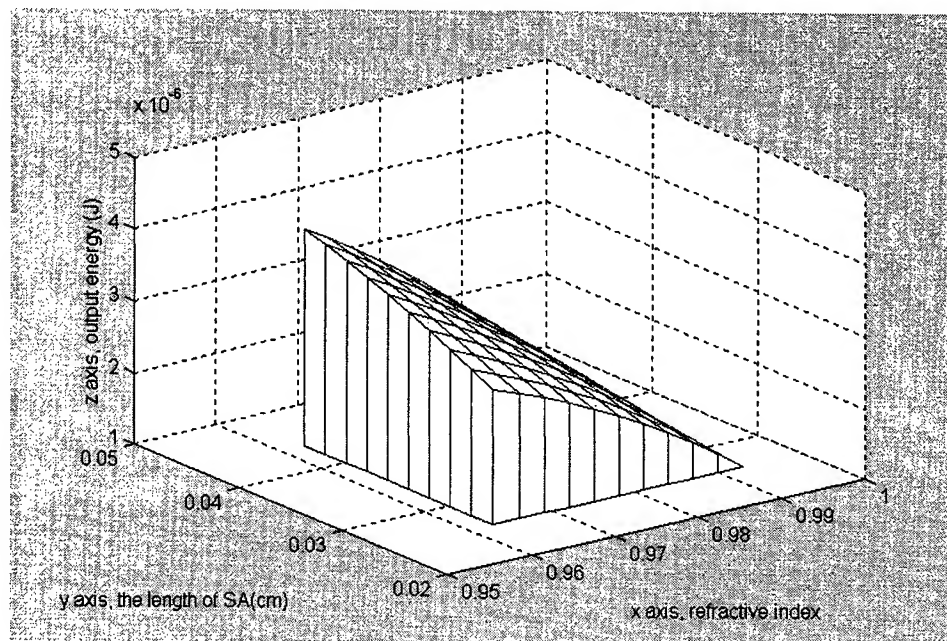


Fig. 4 Numerical calculation results with our model for CW pump

4. CONCLUSION

Based on our model including pump rate we analyzed the effects of pump during switching time. Numerical calculations have been done to show the creditability of this model. From those calculation we get some relation between important parameters and laser performance which can provide guidance for laser designers. By calculation we know pre-pumping mechanism will not influence the output energy greatly thus it is practical for us to improve stability of passively Q-switched laser with this mechanism.

REFERENCES

1. Weiyu Wang, Mali Gong, Guofan Jin, "Dynamics of diode-pumped microchip laser passively Q-switched with Cr:YAG", to be published.
2. A. Szabo and R. A. Stein, "Theory of laser giant pulsing by a saturable absorber", *J. Appl. Phys.*, vol. 36, pp. 1562-1566, 1965
3. John J. Degnan, "Optimization of Passively Q-Switched Lasers", *IEEE J. Quant. Elect.*, vol. 31, No. 11, pp.1890-1901, 1995
4. Guohua Xiao and Michael Bass, "A Generalized model for passively Q-switched lasers including excited state absorption in the saturable absorber", *IEEE J. Quant. Elect.*, vol. 33, No. 1, pp.41-44, 1997
5. W. Koechner, *Solid-State Laser Engineering*, Fourth Extensively Revised and Updated Edition, pp490, Springer, New

York, 1996

6. A. E. Siegman, *Lasers*, Ch26, Mill Valley, CA: Univ. Sci. Books, 1986
7. John J. Degnan, "Theory of the optimally coupled Q-switched Laser", *IEEE J. Quant. Elect.*, vol. 25, No. 2, pp.214-220, 1989
8. J. J. Zayhowski and C. Dill III, "Diode-pumped passively Q-switched picosecond microchip lasers", *Opt. Lett.*, Vol. 19, No. 18, pp.1427-1429, 1994

Quantum scale structures of nanocrystalline silicon films

Hong Yi Lin^a, Yan Na Gao^b, Bo Liao^a, Ying Zi Guo^a, Jing Hua Liu^a, Ying Xue Li^{*}

^aDept. of Electronic Engineering, Beijing Institute of Technology,

Beijing 100081, China

^bInstitute of microelectronics, Peking University,

Beijing 100871, China

ABSTRACT

Based on the growth process analysis of nanocrystalline silicon films, a fractal growth model named Diffusion and Reaction Limited Aggregation (DRLA) model is proposed, which is different from Diffusion Limited Aggregation (DLA) model. Nanocrystalline silicon films with quantum scale structures were prepared by PECVD method. Computer simulation of the DRLA model has been done, the results are in agreement with the experimental results. The relationship between structure of nanocrystalline silicon film and aggregation of nanocrystalline silicon film has also been discussed.

Keyword: Quantum structure, Nanocrystalline silicon films, Fractal aggregation, PECVD, Computer simulation

1. INTRODUCTION

Nanocrystalline silicon films are indicated a lot of important application in future with its excellent characterization, so it attracts scientist's and engineer extensive attention. We had prepared nanocrystalline Zinc oxide (nc-ZnO) films¹ with pillar-like structure and excellent piezoelectric effect. The grain size of Zinc oxide films is about 8-20 nm. The films have been applied to be fabricated integrated sensitive acceleration sensor. At present, the nanocrystalline silicon films² have been prepared by Plasma Enhanced Chemical Vapor Deposition (PECVD) technique with typical nanocrystalline structure. The experimental results show that the nanocrystalline silicon films have many excellent advantages^{3,4} such as high conductivity, high piezoresistivity, high light absorbance and so on. It is beneficial to manufacture force sensor (pressure sensor, acceleration sensor).

Since Witten and Sander^{5,6} proposed the model of Diffusion Limited Aggregation (DLA), Meakin⁷ improved on this model and proposed Kinetic Cluster Aggregation (KCA) model. Academic circles are very interested in the growth mechanism of films which is grown at far from the equilibrium system, especially, the fractal aggregation phenomenon of the films grown and crystallization have been paid special attention⁸.

In this paper, based on the growth process analysis of nanocrystalline silicon films, a fractal growth model called Diffusion and Reaction Limited Aggregation (DRLA) is proposed. It is different from Diffusion Limited Aggregation model. Computer simulation of the DRLA model has been done, the results are in agreement with the experimental results. The relationship between the structure of nanocrystalline silicon films which prepared by PECVD method and aggregation of nanocrystalline silicon films have also been discussed.

* Correspondence: Email: Liyy@ime.pku.edu.cn; Telephone: 086-010-62752549; Fax: 086-010-62571789

2. PREPARATION OF NANOCRYSTALLINE SILICON

Nanocrystalline silicon films were prepared by PECVD. Figure 1 shows the diagrammatic of the PECVD system. The reaction gas silane (SiH_4) is highly diluted by H_2 , the ratio of $\text{SiH}_4/(\text{SiH}_4+\text{H}_2)$ is about 1~2%, during deposition the pressure of gas is 200Pa, the frequency of radiofrequency electromagnetic field is 13.56MHz, the power density of radiofrequency electromagnetic field source is $0.44\text{W}/\text{cm}^2$. Temperature of substrate is $100\text{--}300^\circ\text{C}$, applied direct biased voltage is $0\text{--}400\text{V}$, typical value is -200V . The super fine grain size of nanocrystalline Si films is $3\text{--}9\text{nm}$.

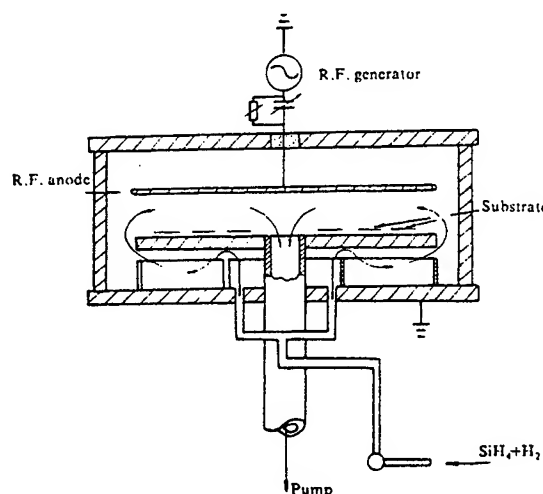


Fig. 1 PECVD system

3. TWO PHASES STRUCTURE OF NC-SI:H FILMS

The grain size of nano-Si:H films were measured by Raman Scattering Spectrum (RSS) and X-Ray Diffraction (XRD) technique.

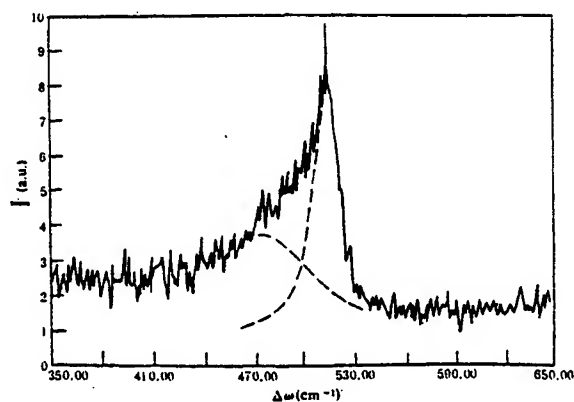


Fig. 2 Raman scattering spectrum of nc-Si:H film

Figure 2 shows the Raman scattering spectrum, a curve fitting at the spectrum peak to be done⁹, the result is indicated that the spectrum peak of curve contains two separated peaks. One peak located at 480cm^{-1} represents a disorder structure peak, and another peak located at 515cm^{-1} represents crystalline structure peak. The grain size of the nanocrystalline silicon can calculate by the formula⁶.

$$d = 2\pi \left(\frac{B}{\Delta W} \right)^{1/2}$$

Where B is constant, it is about $2.0\text{cm}^{-1}.\text{nm}^2$, ΔW is difference value between the crystalline peak of nanocrystalline films and the peak of bulk crystalline silicon located at 521.5cm^{-1} . After calculating we can get the average value of grain size is 3.2nm , and it is in agreement with the results of measured by X-ray diffraction. The fraction volume of crystalline phase is defined as

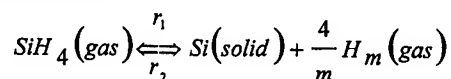
$$V_f = \frac{I_c}{I_c + I_d}$$

Where I_c and I_d is integral intensity of crystalline peak and integral intensity of disorder peak separately. Using equation (2) we can get the fraction volume of crystalline phase, $V_f=46\%$.

The power of radiofrequency source, the temperature of substrate and concentration of reaction gas in the deposition system of films are important factor for growth of nanocrystalline silicon films. In order to offer enough [H] radical, the reaction gas SiH_4 is highly diluted by hydrogen (H_2) in experiment, and a negative bias voltage is biased to chamber, so that reaction radical $[\text{SiH}_4]^+$ arrived at the surface of substrate to get appropriate energy, that is favorable to form proper crystalline component and repel effect of negative oxygen ion on growth of nanocrystalline Si film, and get a good quality films.

4. ANALYSIS OF FILM GROWTH KINETIC PROCESS

The plasma chemical reaction is a complex dynamic process in the chamber, this process can probably divide into three step: The first is the electron under effect of radio frequency electromagnetic field bombards a molecular of SiH_4 gas and generates plasma; The second is electron comes into complex collision with various particle of gas phase and forms various reactors; The third is when the interface reaction between gas phase and solid phase occur in the surface of substrate, a nucleation in a random site of substrate surface will appear and form aggregation cluster and then make nc-Si:H film to be grown. The interface reaction between gas phase and solid phase is a key factor for forming and growing of the thin films. It is shown by reaction equation of thermodynamic:



Where r_1 and r_2 is positive rate of reaction and inverse rate of reaction separately. When the silane suffer from bombarding of thermal electron in plasma, the silane will divide into $[\text{SiH}_n]$ radical and [H] radical which will accelerate growth of thin films and the collision between ions urge the inverse reaction to be occurred. The experimental results show that only the silane (SiH_4) is highly diluted by hydrogen(H_2), the Si-Si weak bond of being formed aggregation cluster in the surface will be etched by [H] radical and formed inverse reaction. So the growth process of nc-Si:H thin film is a dynamic process, that means growth of film and etching reaction coexist. It is important for growth of nanocrystalline silicon thin film.

5. FRACTAL AGGREGATION MODEL

On fractal growth mechanism of thin film has been described by some models, among them the Diffusion Limited Aggregation (DLA) model and Kinetic Cluster Aggregation (KCA) model have been considered to be representative model and to be applied to various field. Based on the analysis of growth kinetic of nc-Si:H thin film, a fractal growth model called Diffusion and Reaction Limited Aggregation (DRLA) model is proposed, the DRLA model point out emphatically that the diffusion motion of reaction particle and chemical etching reaction in films formed process coexist, just in the presence of the chemical etching reaction, the growing up of grain is limited and the nanocrystalline grains with quantum scale structure are formed.

The DRLA model is that in 640×480 dot matrix 100 particles of silicon with random distribution are acted as seeds, they are aggregation nucleus. Those random dots act as a random nucleus located at substrate in the PECVD system. Then generated 100 particles in matrix, among them atom of Si occupy 70% of total atoms number and atom of H occupy 30% of total atoms number. Those particles random walks in the matrix, called diffusion process. When the distance between silicon and a seed of Si being random distribution is one step, Si atom will aggregate with seed of Si and bonding. Therefore, each random nucleus are formation and all order aggregation cluster.

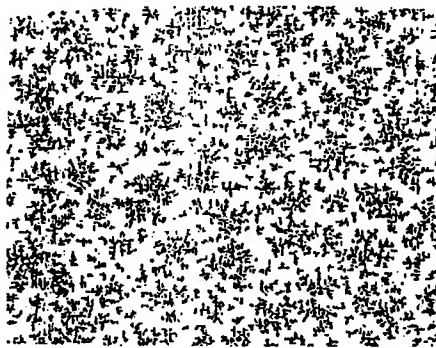


Fig.3 Fractal aggregation growth of nc-Si:H film by computer simulation



Fig.4 HREM image of nc-Si:H film

During this process, atom of H can be bonded with atom of Si in fixed condition, located in surface of each aggregation cluster and atom of H can etch these Si-Si weak bonds, to change it into moving particle and joining diffusion motion. In the whole process the ratio of Si and H is keep constant. According this model the simulation results is different from DLA model and KCA model. In this model an order area with clear and definite boundary is nanocrystalline grain and interface area which is mainly made up of H atom bonding with Si atom are formed.

Figure 3 shows an image of nc-Si:H film in growing one step by computer simulation, compare with the image (Figure 4) of nc-Si:H film measured by High Resolution Electronic Microscopy (HREM), they show better agreement. A direction of different stripe in Fig. 4 represents a different grain and a interface area between grains is formed. It is shown that many grains are separated by interface of many grains.

From statistical calculation of Fig. 3 we can get the average size of order area (crystalline phase) is 6.3nm, and average size of interface area (interface phase) is 1.9nm. A number of H atom occupy 28% of total atoms number. From the size of grain and the size of interface we can get the fraction volume of interface is about 48% of total atoms number and fraction volume of crystalline is about 52%.

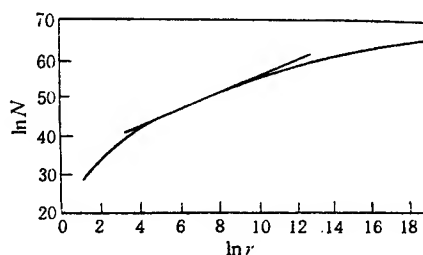


Fig. 5 Sandbox curve

Using Sandbox method^{10,11}, after statistical calculation for pixels of order area in the different scale show that there is a non-scale area, it was shown a linear area in the Fig.5 where slope of curve is exactly fractal dimension value of system D_f , in other words, the system of being self-similarity is a self-similarity fractal set. It may deduce that there are infinite level structure and infinite fine structure in the system, the shape of structure does not describe by traditional geometry terms. But it can be quantitatively described by fractal dimension in the fractal theory. From Fig.5 we can get the fractal dimension $D_f=1.81$. It is expected that this fractal dimension is different from it of DLA and KCA.

REFERENCE

1. X. Zhu, H. Gleiter, "X-ray diffraction studies of the structure of nanometer-sized crystalline materials," *Phys. Rev. B* **35**, pp. 9085-9090, 1987.
2. C. C. Dai, Z. H. Wang, "Mechanism for the nanometer scale modification on HOPG surface by scanning tunneling microscope," *Chinese Phys. Lett.* **10**, pp. 535-538, 1993.
3. H. Y. Lin, "Progress in nanoelectronics," *Acta Electronica sinica* **23**, pp. 59-64, 1995.
4. Y. L. He, Y. M. Chu, H. Y. Lin, "Microstructure and electron conduction mechanism of hydrogenated nanocrystalline silicon films," *Chinese Phys. Lett.* **10**, pp. 539-542, 1993.

5. H. Y. Lin , Y. X. Li, *Fractal Theory*, Beijing Institute of Technology, Beijing, 1992.
6. H. Y. Lin, W. W. Yu, X. H. Wu, "Fractal aggregation model of hydrogenated nanocrystalline silicon films," Chinese J. Of Semiconductors **16**, pp. 567-573, 1995.
7. H. Y. Lin, X. H. Wu, "Growth dynamics of nanocrystalline silicon films and its computer simulation," Acta Physica Sinica **45**, pp. 655-660, 1996.
8. H. Y. Lin, D. M. Yang, Y. X. Li, "Crystallization of hydrogenated amorphous silicon film and its fractal structure," Thin Film Phys and Appl. **1519**, pp. 210-213, 1991.
9. H. Y. Lin, Y. X. Li. "Investigation on surface stability of a new passivative," Microelectronics & Computer **1**, pp. 43-46, 1984.
10. H. Y. Lin, "Crystallization and fractal structure in hydrogenated amorphous silicon films," Chinese J. Of Semiconductors **11**, pp. 430-434, 1990.
11. H. Y. Lin , Y. X. Li , "Fractal structures in hydrogenated amorphous silicon films," Technical Digest of the International PVSEC-5, pp. 801-804, Kyoto , Japan, 1990.

The holographic storage property of In:Fe:LiNbO₃

Xu Wusheng*, Wang Rui, Li Minghua, Xu Yuheng

Department of Applied Chemistry, Harbin Institute of Technology, Harbin, China 150001

ABSTRACT

In₂O₃ and Fe₂O₃ were doped in LiNbO₃ and Czochralski method was used to grow In:Fe:LiNbO₃ crystals. The light scattering ability resistance, exponential gain coefficient, diffraction efficiency and response time of the crystals were measured. The light scattering ability resistance and response time of In:Fe:LiNbO₃ is one magnitude higher than Fe:LiNbO₃. In:Fe:LiNbO₃ was used as storage element to make the large capacity holographic storage and the holographic associative storage reality. The excellent results were gained.

Keywords: In:Fe:LiNbO₃, Czochralski method, two wave coupling, crystal growth, crystal polarizing, exponential gain coefficient, diffraction efficiency, response time, light scattering ability resistance, large capacity holographic storage, holographic associative storage

1. INTRODUCTION

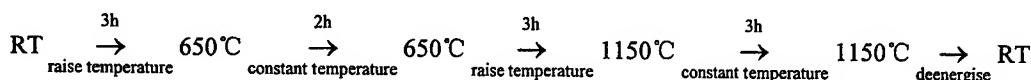
LiNbO₃ crystals belong to trigonal crystal system and 3m point group. They possess the electro-optic effect and nonlinear optical efficiency. But their photorefractive sensitivity is very poor. In order to improve the photorefractive sensitivity, Fe₂O₃ is doped in LiNbO₃ to grow Fe:LiNbO₃ crystal. Nevertheless the response time of the crystal is long and the light scattering ability resistance is poor. We doped In₂O₃ in Fe:LiNbO₃ to grow In:Fe:LiNbO₃ crystal.¹ Both light scattering ability resistance and the response rate of In:Fe:LiNbO₃ crystal are one magnitude higher than Fe:LiNbO₃ crystal. Its diffraction efficiency is higher, storage time is longer and thermal fixing is easier to process. In:Fe:LiNbO₃ crystal as storage media is superior to Fe:LiNbO₃ crystal. The large capacity storage experiment with In:Fe:LiNbO₃ was processed. Using In:Fe:LiNbO₃ crystals as storage medium and adopting the multi-angle and repeated using technology, the storage and recovery of 500~1000 digital pictures in one public cubage of the crystals were realized.²⁻⁹ Using In: Fe: LiNbO₃ crystals as storage elements and the phase conjugate reflectivity mirror of Ce:Fe:LiNbO₃ crystal as threshold organ, the optical holographic associative memory was achieved and the output pictures were clear, low noise and integrity.

2. CRYSTAL GROWTH

Using siliconit as heater, In:Fe:LiNbO₃ crystal was grown by Czochralski method.

2.1 Raw Material Preparation

The quality of Nb₂O₅ and Li₂CO₃ is 99%. The quality of Fe₂O₃ and In₂O₃ is spectra purity. The ratio of Li₂CO₃ to Nb₂O₅ is 48.6:51.4(mol ratio). The doped quantity of Fe₂O₃ and In₂O₃ is 0.05mol% and 1.8mol% respectively. The weight of Nb₂O₅, Li₂CO₃, Fe₂O₃, and In₂O₃ was calculated and weighed by analytical balance. For the sake of keeping congruent ratio, every component could not be lost during blending course. The raw materials were mixed in pulsator and shaken for twenty-two hours. Then the mixed symmetrical material was sintered and turned into In:Fe:LiNbO₃ polytropism. The technology is as follows.



where RT is room temperature. For CO₂ generated from Li₂CO₃ decomposes slowly, the material keeps constant temperature in 650°C for two hours, which can avoid other material is carried off by exsiliant CO₂ gas to destroy the congruent ratio. The chemical equation of Li₂CO₃ decompose is as follows.



Correspondence: Email: wushengx@yahoo.com

2.2 Crystal Growth Technology

The parameters of In:Fe:LiNbO₃ crystal growth include the temperature gradient, the crystal growth rate, the crystal rotation rate and the crystal polarization.

2.2.1 Temperature Gradient

The temperature gradient comprises axial direction and radial direction temperature gradient. The unit differential temperature above and under the melt level denotes axial direction temperature gradient. Selecting proper temperature gradient required the condition as following: (1) to generate the advisable degree of supercooling in the center of the melt surface; (2) to keep invariable temperature during crystal growth in order to make crystal shape controlled easily; (3) to make the thermal stress crystal endured small to avoid crack; (4) not to produce the component supercooling. Because the temperature gradient is the impetus of crystal growth, one important factor to grow highquality crystals is to select the proper temperature gradient. The proper axial direction temperature gradient to grow In:Fe:LiNbO₃ crystal is 35°C above the melt surface and 15°C under the melt surface.

2.2.2 Crystal Growth Rate

The time that the crystal growth face increases unit thickness along the normal direction is called the crystal growth axial rate. It includes both the mechanical lifting rate and the melt surface descending rate. The crystal growth rate depends on the temperature gradient, the crystal diameter, the material purity, the dopant species and the dopant quantity. When the condition above-mentioned is ascertained, the crystal growth rate has a maximum. If the growth rate exceeds the maximum, the component supercooling and varieties of crystal defects will appear. To grow crystal with 20mm~30mm diameter, the growth rate should be 1~2mm/h.

2.2.3 Crystal Rotation rate

The crystal quality depends on the flat degree of the solid-melt interface. The rotation rate is one of most important factors that influent the flat degree of the solid-melt interface. When crystal rotation rate is high, the solid-melt interface can turn flat from convex. When crystal rotation rate is low, the trend that the solid-melt interface turns concave decreases. The proper rotation rate is selected and the flat solid-melt interface will be gained. In our experiment, the crystal rotation rate is 20rpm~25rpm.

2.2.4 Crystal Polarization

In:Fe:LiNbO₃ crystal is ferroelectrics. It has a ferroelectric transition point (Curie point) between 1150°C and 1210°C. During crystal from high temperature through Curie point to low temperature, the crystal will turn into ferroelectric phase from paraelectric phase. In:Fe:LiNbO₃ crystal is one dimension ferroelectrics. In some temperature, the self-polarization exists, which intensity changes with the outer electric field adding on. The self-polarization of as-grown crystal has different directions and the crystal is multidomain crystal. When electromagnetic wave pass multidomain crystal, it will be scattered at domainwall, which will make the device property poor. So as-grown crystal must be polarized artificially so that the Ps turn direction along the c-axial and the crystal becomes the single domain crystal. In our experiment, the polarization current density is 5mA/cm² and the polarization temperature is 1200°C. After polarized, the HF and HNO₃ mixture liquid which ratio was 1:2 eroded the crystal piece. Using metallographical microscope to observe the piece, the In:Fe:LiNbO₃ crystal was polarized completely.

3. PHOTOREFRACTIVE PROPERTY OF IN:FE: LiNbO₃ CRYSTAL

3.1 Light Scattering Ability Resistance of In:Fe:LiNbO₃ Crystal¹⁰.

The light scattering ability resistance of In:Fe:LiNbO₃ crystal was observed by straightly observing transmission facula distortion method. Fig. 1 shows the experimental setup. Using Ar⁺ Laser of $\lambda=488.0\text{nm}$ as light source and output wavelength, the aggregate capacity was continuously regulated by spectroscope, the polarizing direction of the laser beam was parallel with c-axial of the crystal and the crystal was placed on the focal plane at the back of the convex lens. Using

following equation, the beam diameter D can be calculated by f that is the focal length of the convex lens and d that is the diaphragm diameter.

$$D = \frac{2f\lambda}{\pi d} \quad (1)$$

where λ is the wavelength of laser. The facula acreage S is gained.

$$S = \pi \left(\frac{D}{2}\right)^2 = \frac{(f\lambda)^2}{\pi d^2} \quad (2)$$

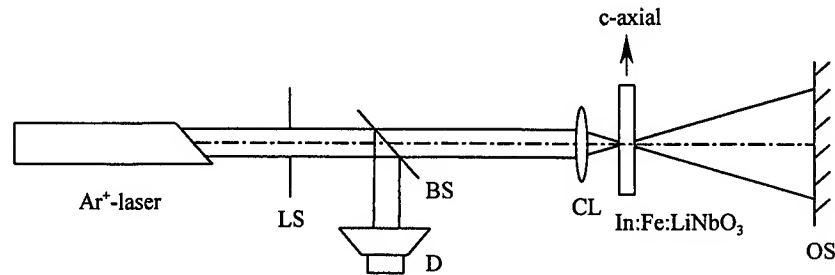


Fig. 1 Experimental setup of the light scattering ability resistance measuring: LS's, light shed; BS's, beam splitter; D's, detector; CL's, convex lens; OS's, observation screen.

When the laser power intensity is low, light scattering is unable to appear in the crystal and the facula on the screen is roundness. When the laser's power intensity achieves certain value, light scattering appears inside the crystal and the facula is elongated along c-axial of the crystal. That is to say the facula is distorted. The laser power intensity, which brings the distortion of the facula transited the crystal, is called the light scattering ability resistance of the crystal. Table 1 shows the experimental results.

Table 1. The results of light scattering ability resistance of crystals

Crystals	In:Fe:LiNbO ₃	Fe:LiNbO ₃	LiNbO ₃
Light scattering ability resistance(W/cm ²)	3.3×10^3	1.2×10^2	3.1×10^2

It is obvious in Table 1 that the light scattering ability resistance of In:Fe:LiNbO₃ is one magnitude higher than that of Fe:LiNbO₃.

3.2 The Exponential Gain Coefficient of In:Fe:LiNbO₃ Crystal

The exponential gain coefficient of two wave coupling in photorefractive crystal shows that the power of pump light is transmitted to that of signal light, which is the important parameter for reflecting the self-amplification ability of crystal material. Through discriminating the wave coupling equation, the formula to calculate the exponential gain coefficient is obtained.

$$I_1(\delta) = I_2(0) \frac{I_1(0) + I_2(0)}{I_1(0) + I_2(0) \exp(\Gamma \delta)} \exp[(\Gamma - \alpha)\delta] \quad (3)$$

$$I_2(\delta) = I_1(0) \frac{I_1(0) + I_2(0)}{I_1(0) + I_2(0) \exp(\Gamma \delta)} \exp(-\Gamma \delta) \quad (4)$$

where $I_1(0)$ and $I_2(0)$ is the incident light intensity when I is 0, Γ is the exponential gain coefficient, δ is the wafer thickness and α is the absorbance index of the crystal.

From equation (3), it is concluded that when $\Gamma > \alpha$ the signal I_1 obtain the exponent gain. Γ shows the per unit length gain induced by $\pi/2$ phase shift of grating component. Above equation indicates that energy exchange is produced during two beams coupling. One of two beams (signal light) is amplified for gaining energy and the other (pump light) is weakened because of its losing energy. When the optical absorption and the reflect on the front and back surfaces of the crystal are ignored, Γ shows as following equation.

$$\Gamma = \frac{1}{\delta} \ln \frac{I_1' I_2'}{I_1 I_2} \approx \frac{1}{\delta} \ln \frac{I_1'}{I_1} \quad (5)$$

where I_1' and I_2' (I_1 and I_2) is the transmission light intensity of signal light and pump light respectively when wave is coupled (not coupled).

The exponent gain coefficient for the crystal is measured by two wave coupling optical path. Fig. 2 shows the experimental schematic of two wave coupling.

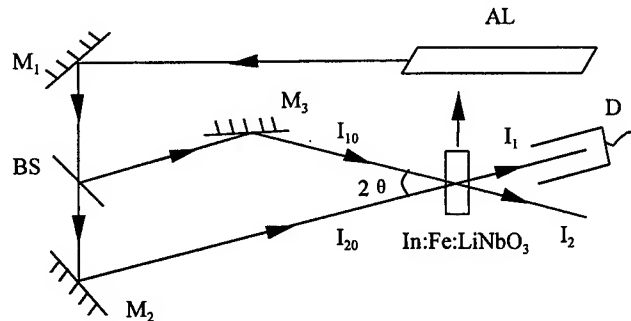


Fig. 2 Experimental schematic of two wave coupling: M_1 , M_2 and M_3 's, mirrors; BS's, beam splitter; AL's Ar⁺-laser; D's, detector; I_{10} and I_{20} 's, incident light; I_1 and I_2 's, emergent light.

Ar⁺-laser which wavelength is 488.0nm is used as light source. The polarization direction is located in incident plane. 2θ denotes the included angle between I_1 and I_2 , the incident light. The wafer thickness δ is 3mm. The light passes from x-plane of the wafer. I_{20} is 3.28W/cm² and β i.e. $I_{20}/I_{10}=2600$. Fig. 3 shows the experimental curve of Γ dependence on 2θ .

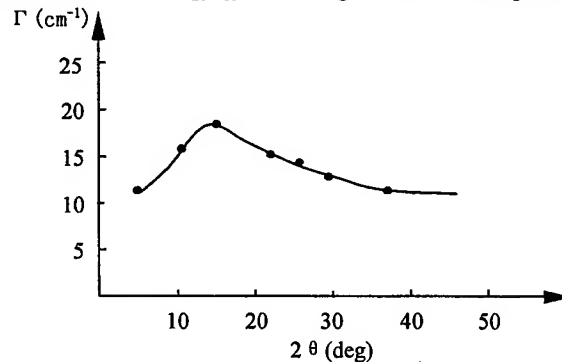


Fig. 3 Experimental curve of $\Gamma \sim 2\theta$

For $2\theta = 13.5^\circ$, the exponent gain coefficient Γ achieves the maximum 18cm^{-1} .

3.3 Diffraction Efficiency of In:Fe:LiNbO₃ Crystal

The diffraction efficiency of crystal is one of the most important parameters for holographic storage material. Using storage material with high diffraction efficiency, the clearer and more integrate record graphic can be obtained. Fig. 2 shows the experimental setup.

The definition of the diffraction efficiency is in the ratio of the diffracted intensity I_1' which is the refractive light of the pump light I_{20} through the grating at signal light I_1 to the signal light I_1 when there is no the grating, i.e., $\eta = I_1' / I_1 \times 100\%$. The e polarize light of Ar⁺ laser which wavelength λ is 488.0nm is separated into two beams by beam splitter. The two beams illuminate the crystal with included angle 2θ . The pump light intensity I_{20} and I_{10} is 1.82W/cm^2 and 0.85W/cm^2 separately. Fig. 4 shows the experimental curve of η dependent on 2θ .

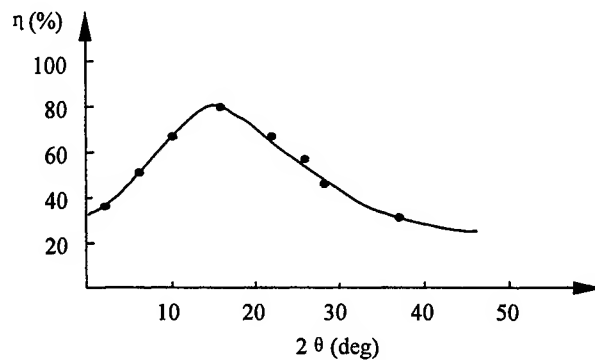


Fig. 3 Experimental curve of $\eta \sim 2\theta$

When 2θ is 15° , the maximum of diffraction efficiency η_{\max} is 84%.

3.4 Two Wave Coupling Response Time of In:Fe:LiNbO₃ Crystal

The definition of the response time is the time when incident light begin to illuminate the crystal to the time when the grating achieves $1-e^{-1}$ of the stable value. When the light intensity I_{20} and I_{10} is 1.82 and 0.85W/cm^2 respectively, the response time of In:Fe:LiNbO₃ τ_{In} is 18s and that of Fe:LiNbO₃ τ_{Fe} is 182s, i.e., the response time of In:Fe:LiNbO₃ is one magnitude higher than that of Fe:LiNbO₃.

4. LARGE CAPACITY STORAGE EXPERIMENT

The key of the high development of the information society is the high density of the information storage and the high speed of the data process. The crystal holographic storage system includes the prominent feature as following: (1) large capacity storage; (2) high-speed data transmission; (3) content addressing function; (4) high-speed addressing; (5) high degree of storage redundancy. Because the picture readout by the crystal memorizer is the optical reproduction of the original storage data, the further optical information processing can be carried out before it is transformed into the electronic signal. So the whole function of the storage system is enhanced greatly.

In Fig. 5, the experimental setup is showed. The incident parallel light of 514.5nm is separate into reference light and object light by polarizing spectroscopy PBS. The lens L_3 and L_4 is place in the same focus. The image shaped by the light modulator SLM locate in the crystal CR. The reference light arrives the record crystal via the lens L_1 , the reflect mirror M_1 and the lens L_2 , among of which L_1 and M_1 is fixed to the same delicate sliding platform S. The open and close of the electronic shutter SH_1 and SH_2 and the collection and treatment of CCD picture are controlled by the computer. The size of the record crystal is $15 \times 15 \times 15(\text{mm}^3)$. The c-axis of the crystal is in the plane of the crystal surface and the crossing angle with x-z and y-z plane is 45° . The intensity of the reference light and the object light can be adjustable agilely by rotating the $1/2$ wave plate in front of the polarizing spectroscopy. The most important factor to reality large capacity body

holographic storage is that the record material has enough dynamic range. Above experimental setup has been used to reality the storage and recovery of above 500 digital images in a public volume. The study is still under way.

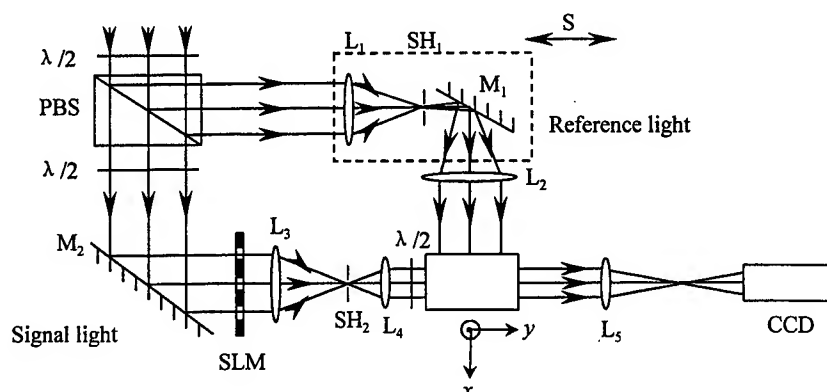


Fig. 5 Experimental setup: PBS's, polarizing spectroscopy; CR's, crystal; M's, reflect mirror; L's, lens; S's, delicate sliding platform; SH's, electronic shutter; SLM's, space light modulator; $\lambda/2$'s, 1/2 wave plate.

We have proceeded with the holographic associative storage experiment. In this experiment, He-Ne laser of $\lambda = 632.8\text{nm}$ is used as light source, the polarizing direction is in the incident plane (extraordinary light), In:Fe:LiNbO₃ crystal is used as the storage element, Ce:Mn:SBN is used as the threshold element which take the gaining and amplification effect, the included angle between the reference light and the object light is 13.2 degree and that between the pump light and signal light is 12.3 degree. Fig. 6 shows the index path of the holographic associative storage experiment.

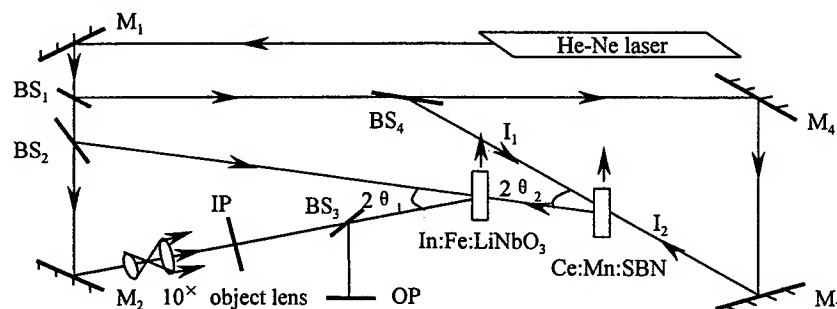


Fig. 6 Index path of the holographic associative storage experiment: M's, reflect mirror; BS's, beam splitter; IP's, input plane; OP's, output plane.

The ratio of two beams is 1:1. The pump light intensity I_1 and I_2 is 182 and 145mW/cm². Fig. 7(a) shows the stored image. When a part of the stored image is addressed (as in Fig. 7(b)), the integrate object is received in the output plane.

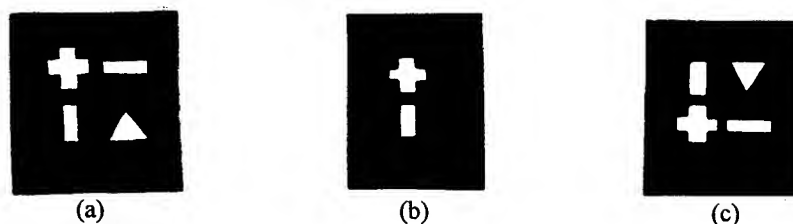


Fig. 7 The result of the holographic associative storage: (a) the stored image; (b) a part of image addressed; (c) output image of holographic associative storage.

5. CONCLUSION

In:Fe:LiNbO₃ crystals were grown by Czochralski method. The light scattering ability resistance, exponential gain coefficient, diffraction efficiency and response time of the crystals were measured. The light scattering ability resistance of In:Fe:LiNbO₃ is one magnitude higher than Fe:LiNbO₃. The exponential gain coefficient Γ is 18cm⁻¹ and the diffraction efficiency η is 84%. The response time is also one magnitude higher than Fe:LiNbO₃. In:Fe:LiNbO₃ was used as storage element to make the large capacity holographic storage and the holographic associative storage reality. The excellent results were gained.

ACKNOWLEDGMENTS

This study is supported by the National 863 Program of China (Code, 8635150010100).

REFERENCE

1. Zhang Jingwen, Li Minghua, and Xu Yuheng, "Very high photorefractive gain in two-beam coupling with thin Iron-doped LiNbO₃ crystal", *Chinese Phys. Lett.* **10**, pp. 227-230, 1993.
2. C.Perito, and C.Zaldo, "Determination of the lattice of Fe in photorefractive LiNbO₃", *Solid State Commun.* **83**, pp. 819-822, 1992.
3. C. Gu, J. Hong, I. Mcmichael, R. Saxena, and F. Mok, "Cross-talk-limited storage capacity of volume holographic memory", *J. Opt. Soc. Am. A* **9**, pp. 1978-1983, 1992.
4. M. C. Bashaw, J. F. Heanue, and A. Aharoni, "Cross-talk considerations for angular and phase encoded multiplexing in volume holography", *J. Opt. Soc. Am. B* **9**, pp. 1820-1836, 1994.
5. K. Crutis, and D. Psaltis, "Cross talk in phase encoded holographic memories", *J. Opt. Soc. Am. A* **10**, pp. 2547-2550, 1993.
6. C. Denz, G. Pauliat, and G. Roosen, "Volume hologram multiplexing using a deterministic phase encoding method", *Optics Communications* **85**, pp. 171-176, 1991.
7. J. Trisnadi, and S. Redfield, "Practical data reification of hologram multiplexing without beam movement", *Photonic Neural Networks* **1773**, SPIE, pp. 362-371, 1992.
8. G. A. Rakuljic, V. Leyva, and A. Yariv, "Optical data storage by using orthogonal wavelength-multiplexed volume holograms", *Opt. Lett.* **17**, pp. 1471-1473, 1992.
9. K. Curtis, A. Pu, and D. Psaltis. "Method for holographic storage using peristrophic multiplexing", *Opt. Lett.* **19**, pp. 993-995, 1994.
10. Li Minghua, Shun Shangwen, and Xu Yuheng, "Study on the properties of multiplier frequencies of Zn:LiNbO₃", *Application Laser* **15**, pp. 61-64, 1995.
11. Li Minghua, Wang Jiakang, and Xu Yuheng, "Study on the photorefractive effect of Eu:Fe:LiNbO₃ crystal", *Chinese Application Laser*, **15**, pp. 61-64, 1995.

Optical limiting properties of neutral nickel dithiolenes

Wei Lian Tan^a, Wei Ji^a, Jing Lin Zuo^b, Jun Feng Bai^b, Xiao Zeng You^b, Jin Hong Lim^c,
Sidney S. Yang^c, David J. Hagan^c and Eric W. Van Stryland^c

^a Department of Physics, National University of Singapore, Lower Kent Ridge Road,
Singapore 119260, Republic of Singapore

^b Coordination Chemistry Institute, State Key Laboratory of Coordination Chemistry,
Nanjing University, Nanjing 210093, P. R. China

^c School of Optics/CREOL, University of Central Florida, Orlando FL 32816-2700, USA

ABSTRACT

Wide applications of lasers have stimulated a great interest in development of optical limiting devices. These devices can be used to protect optical sensors from laser-induced damage because their transmission is high when they are exposed to low-power laser light, and their transmission becomes low when irradiated by intense laser beams. Here we report such a device based on nonlinear optical effects in two neutral nickel complexes with multi-sulfur 1,2 dithiolene ligands, [Ni(medt)₂] **1** (medt = 5,6-dihydro-6-methyl-1,4-dithiin-2,3-dithiolate) and [Ni(phdt)₂] **2** (phdt = 5,6-dihydro-5-phenyl-1,4-dithiin-2,3-dithiolate). The limiting device consisted of a focusing setup and a 1-mm-thick cell, which contained a benzene solution of one of the complexes. The limiting properties were investigated by both nanosecond and picosecond laser pulses. At 532 nm, the limiting thresholds of complexes **1** and **2** measured by the picosecond laser pulses with a (*f*/25) focusing geometry were determined to be ~0.3 J/cm². The linear absorption spectra of the two complexes also indicated that their limiting response should cover the visible and near-infrared region (up to 900 nm). All these results show their limiting performance is superior to the limiting effect in C₆₀. Picosecond time-resolved pump-probe and Z-scan experiments revealed that the observed limiting effects should originate from excited-state absorption and refraction.

Keywords: Nickel dithiolenes, picosecond, nanosecond, optical limiting, and pump-probe experiments

1. INTRODUCTION

In recent years, materials exhibiting strong nonlinear-optical behavior have been of considerable interest because of their applicability in a variety of optical devices.¹ In particular, optical limiters have received significant attention as a result of the growing needs for protection of both human eyes and optical sensors from intense laser beams. An ideal optical limiter should have the capability of being transparent at low-energy laser pulses and opaque at high energies. The most frequently reported materials are fullerenes (C₆₀),¹⁻⁶ and phthalocyanine complexes,⁷⁻¹⁰ which are generally regarded as the best candidate for optical-limiting applications. They are materials that exhibit strong reverse saturable absorption. For such materials, when irradiated by laser pulses, the electrons at the ground state are promoted to the excited singlet state by the ground state absorption in the material. Through inter-system crossing, a part of the electrons end up at the excited triplet state. Due to stronger absorption of the excited states, there is a decrease in the material transmission, thus leading to the desired limiting effect.

We note that there exists another class of materials, nickel complexes of 1,2-dithiolene ligands. These dithiolenes have been used as Q-switch dyes for near infrared lasers such as Nd:YAG lasers since the early seventies.¹¹ Recently, they have also been intensively investigated as optical-switching materials for optical

communications,¹²⁻¹⁵ molecular magnets, conductors and superconductors.¹⁶⁻²⁰ It is to our knowledge that no investigations have been carried out on the optical-limiting properties of dithiolene complexes. Here we report the observation of the optical-limiting effects in two neutral nickel complexes with multi-sulfur dithiolene ligands, [Ni(medt)₂](medt = 5,6-dihydro-6-methyl-1,4-dithiin-2,3-dithiolate) **1** and [Ni(phdt)₂](phdt = 5,6-dihydro-5-phenyl-1,4-dithiin-2,3-dithiolate) **2**. The observation has been carried out by nanosecond and picosecond laser pulses at wavelength of 532 nm. The mechanisms leading to the observed limiting effects are also investigated.

2. EXPERIMENTAL

The preparation of the two dithiolene complexes **1** and **2** was reported elsewhere.¹⁵ The structures of both complexes were identified from IR spectra and elemental analysis.⁸ The chemical structures of complexes **1** and **2** are shown schematically in Fig. 1. It can be seen that the four sulfur atoms surrounding the nickel atom yield a square planar coordination. The five-membered ring containing the nickel atom forms a delocalized π -electron system, making it favorable nonlinear-optical material.

The dithiolene complexes **1** and **2** were dissolved in benzene (C₆H₆) and contained in 1-mm-thick quartz cells for optical measurements. The electronic spectra of the two solutions were recorded with a spectrophotometer (Hitachi U-3410). The nonlinear-optical responses of the two solutions were measured with frequency-doubled, pulsed Nd:YAG lasers. The lasers were operated at a repetition rate of 10 Hz. The spatial profiles of the pulses were nearly Gaussian after passing through a spatial filter. Three types of experimental setup used for the nonlinear-optical measurements are described as follow:

- (1) The optical-limiting behavior was observed by measuring the nonlinear (energy-dependent) transmission of the two solutions with 532-nm laser pulses of 7-ns and 35-ps (FWHM) durations. The laser pulses were split into two parts: the reflected was used as a reference, and the transmitted was focused onto the sample. The transmitted pulses were focused onto the sample by using focusing geometry ($f/64$) and ($f/25$) for nanosecond and picosecond measurements respectively. The sample was placed at the focus where the spot radii of the pulses were $30 \pm 5 \mu\text{m}$ and $24 \pm 5 \mu\text{m}$ (FW1/e²M) for the 7-ns and 35-ps pulses, respectively. An aperture with a transmittance of 40% was placed in front of the transmission detector when the measurements were performed. Both the incident and transmitted pulse energies were monitored simultaneously by using two energy detectors (Rjp-735 energy probes, Laser Precision), which were connected to a computer by an IEEE interface.
- (2) The Z-scan setup^{21, 22} was similar to that used for the above measurements except that the sample was moved along the propagation direction (Z-axis) of the transmitted beam with respect to the focal plane. By keeping the incident pulse energy constant, the pulse energy transmission through the sample was measured with respect to the sample Z-position. The aperture was placed in front of the transmission detector in the closed-aperture Z-scans and removed in the open-aperture Z-scans.
- (3) The picosecond time-resolved pump-probe experimental setup was a standard arrangement, where the peak irradiance of the probe pulse is approximately 1% of that of the pump pulse. The pulse duration was 14 ps (HWHM). The probe pulse was focused to a spot size approximately one fourth as large as the pump pulse as to reduce the spatial averaging effects while sampling the largest nonlinearity. The spot size of the pump pulse was 100 μm . The pump pulse and the probe pulse were incident on the sample at an angle of 3° with respect to each other.

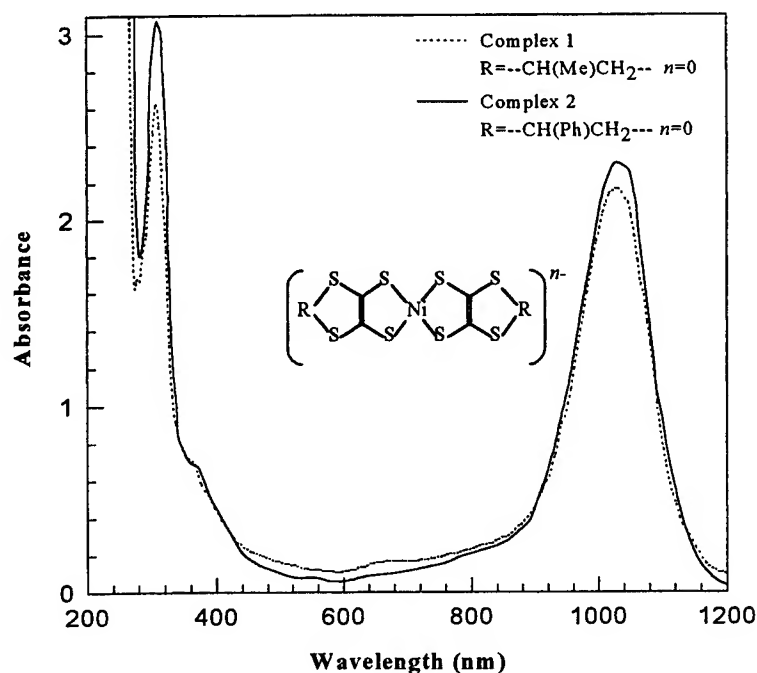


Fig. 1 Absorption spectra of complexes 1 (—) and 2 (—) in benzene solution with 1-mm optical path and concentration of $1.9 \times 10^{-4} \text{ M}$ for complex 1 and $6.1 \times 10^{-4} \text{ M}$ for complex 2. Inset shows the structures of the two complexes.

3. RESULTS AND DISCUSSION

The UV-visible absorption spectra of complexes 1 and 2 in benzene solution are depicted in Fig. 1. It is noticed that there is a relatively low absorption in the visible and near-IR region (400–900 nm) for both the complexes. The spectra are dominated by two intense absorption bands, one band is centered at around 1000 nm (π – π^* transition) and the other one at around 300 nm (ascribed to S→M charge transfer band).¹⁵ These indicate that both complexes have generally a broader transparent range than phthalocyanines (500–700 nm).⁷ Since a broad transparent range is an important criterion in the assessment of optical-limiting materials, the spectra of these nickel dithiolenes complexes have shown that their limiting response should cover a wider range thus are more superior than phthalocyanines complexes.

Fig. 2 shows the normalised transmittances of complexes 1 and 2 in benzene solution measured with the nanosecond and picosecond pulses. The linear transmittance of the two solutions was about 83% at 532 nm. The linear transmittance of both the solutions was about 33% when the aperture was used. At very low input fluences, the transmissions of the two solutions behave linearly. The transmittance begins to decrease rapidly as the incident fluence reaches about 0.1 J/cm^2 for both complexes 1 and 2. The limiting threshold is defined here as the incident fluence at which the transmittance falls to 50% of the linear transmittance. From Fig. 2, the limiting thresholds of complexes 1 and 2 are determined to be $\sim 0.3 \text{ J/cm}^2$ for the picosecond measurements and $\sim 2.0 \text{ J/cm}^2$ for the nanosecond measurements. It should be pointed out that the optical limiting responses were measured with the aperture placed in front of the transmission detector. It is known that such an aperture can enhance the limiting effect by blocking a part of the transmitted beam, which is expanded due to self-lensing effect in the high-power regime. The limiting effects were observed to deteriorate without the aperture, indicating that a self-lensing effect had enhanced the limiting effect in Fig. 2.

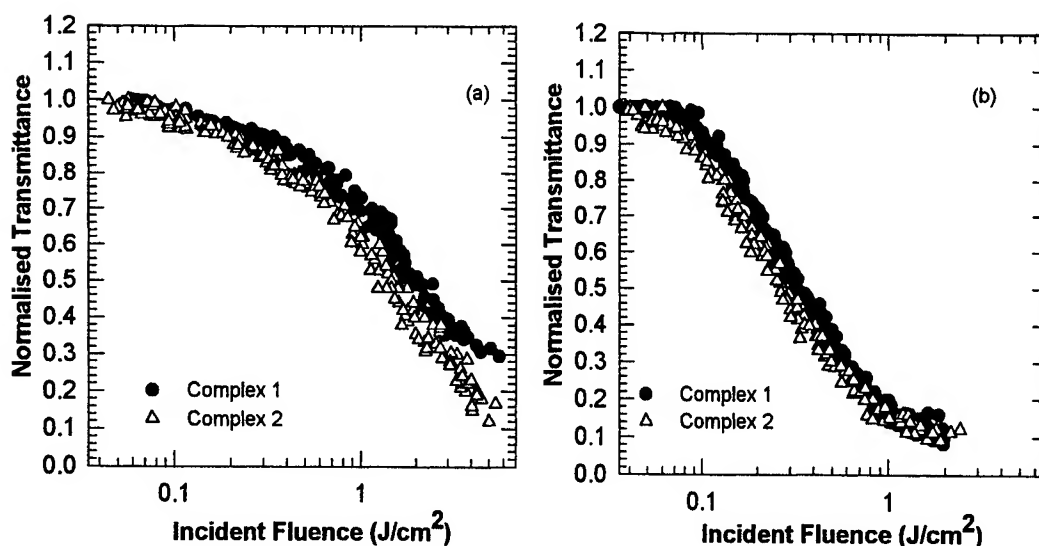


Fig. 2 Fluence-dependent transmittance of the complexes measured at 532 nm. (a) The filled circles (●) and the open triangles (△) were the data measured with 7-ns laser pulses for complexes 1 ($1.9 \times 10^{-4} \text{M}$) and 2 ($6.1 \times 10^{-4} \text{M}$), respectively. (b) The filled circles (●) and the open triangles (△) were the data measured with 35-ps laser pulses for complexes 1 ($1.9 \times 10^{-4} \text{M}$) and 2 ($6.1 \times 10^{-4} \text{M}$), respectively.

To gain insight on the mechanisms leading to the observed limiting effects, we performed the picosecond time-resolved pump-probe experiments and Z-scan measurements. The pump-probe experiments were conducted at the pump fluence of 0.06 J/cm^2 . The pump-probe results for complexes 1 and 2 are displayed in Fig. 3. The linear transmittance for complexes 1 and 2 was 67% and 85%, respectively. The ground-state absorption cross-sections, σ_0 , were measured to be $9.3 \times 10^{-18} \text{ cm}^2$ for 1 and $2.8 \times 10^{-18} \text{ cm}^2$ for 2 at 532 nm. The data in Fig. 3 are a typical behavior resulting from excited-state absorption. Based on a five-level model,²³ we fit the data with equation (1),

$$T(t) = T(0)b\exp(-t/\tau_T) + (1-b)\exp(-t/\tau_S), \quad (1)$$

where $T(t)$ is the normalised nonlinear transmittance; τ_T is the lifetime of the triplet state; τ_S is the lifetime of the singlet state and b is given by (2),

$$b = \frac{\sigma_2^\alpha - \sigma_0}{\sigma_1^\alpha - \sigma_0} \phi \quad (2)$$

where σ_1^α and σ_2^α are cross-sections of the excited singlet and triplet state, respectively and ϕ is the percentage of the total excited-state population that ends up in the triplet state and is given by τ_S/τ_{isc} . By the best fits, we determined that $\tau_T \geq 0.1 \mu\text{s}$ and $\tau_S = 0.8 \text{ ns}$ for 1; and $\tau_T \geq 0.1 \mu\text{s}$ and $\tau_S = 1.5 \text{ ns}$ for 2. We also found that $b = 0.23$ and 0.45 for complexes 1 and 2, respectively.

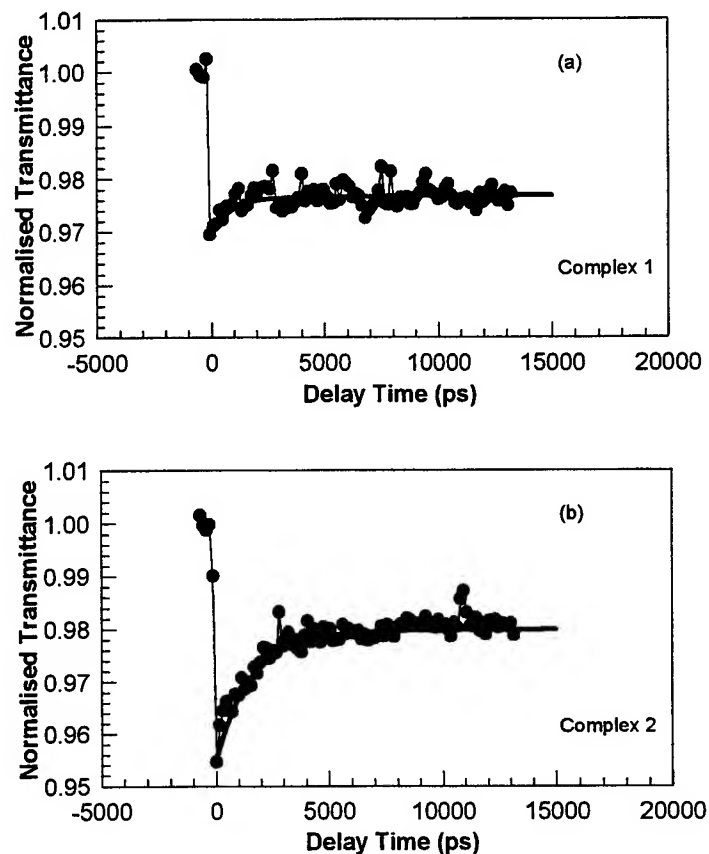


Fig. 3 Probe transmittance as a function of time delay for (a) complex 1 ($1.4 \times 10^{-3}\text{M}$) and (b) complex 2 ($6.2 \times 10^{-4}\text{M}$). The pump fluence was 0.06 J/cm^2 . The filled circles (\bullet) are the experimental data and the thick curves (—) are the theoretical fits.

In order to obtain the nonlinear cross-sections for these complexes, we conducted the Z-scan measurements. The Z-scan results for complexes 1 and 2 obtained from the nanosecond and picosecond measurements are shown in Fig. 4, which show a positive sign for the nonlinear refraction in complexes 1 and 2. This indicates that the laser beam propagating in both the complexes should undergo a self-focusing process. This self-focusing process can enhance limiting effectiveness as shown in our nonlinear transmission measurements. The positive sign of the refractive nonlinearities in the two complexes is similar to that found in metallophthalocyanines; and such nonlinearities are attributed to excited-state refraction.⁷ In Fig. 4, the solid curves are the best fitting by using the five-level model.²³ In the fittings, all the lifetimes used are those determined from the pump-probe data. The picosecond Z-scans measured with and without the aperture enabled us to unambiguously extract the absorptive cross-section, and refractive cross-section, (σ'_1) for the excited singlet state.⁷ Similarly, the nanosecond Z-scans enabled us to obtain the absorptive cross-section and refractive cross-section, (σ'_2) for the excited triplet state. These cross-sections are listed in Table 1 and compared favorably with those of silicon naphthalocyanines (SiNc) and chloro-aluminium phthalocyanines (CAP).⁷

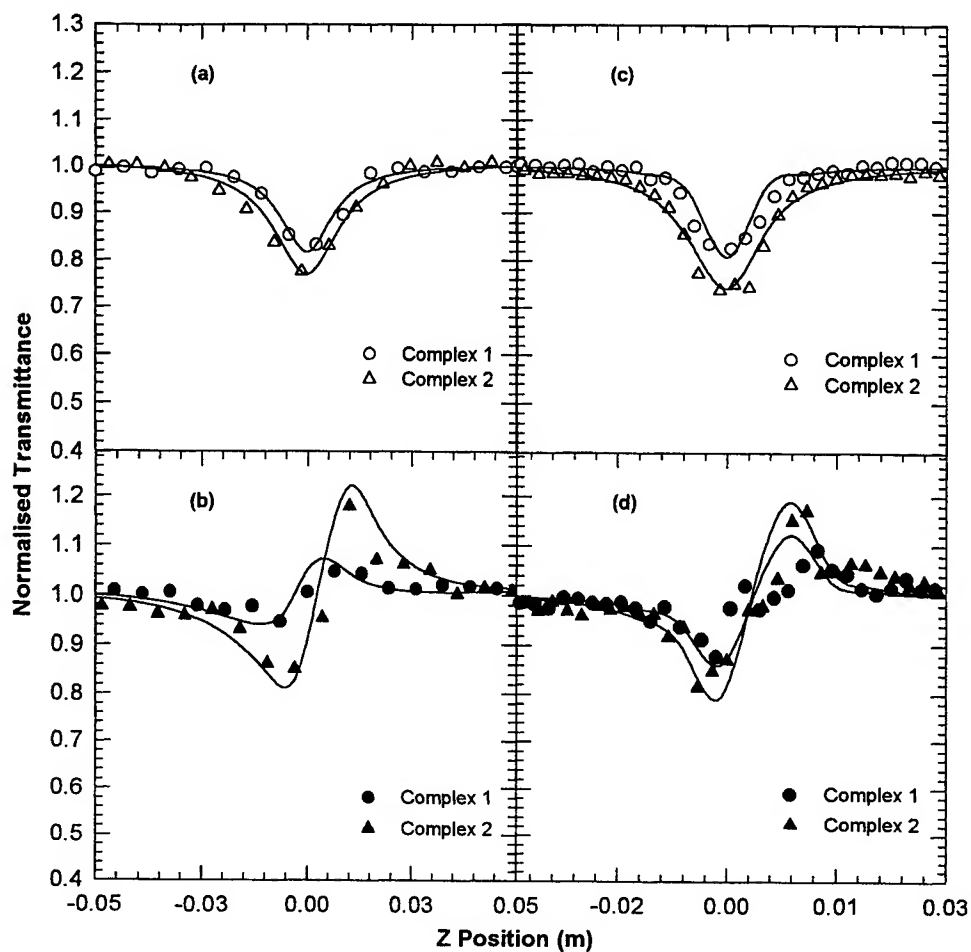


Fig. 4 Z-scan results for complexes 1 ($1.9 \times 10^{-4} \text{M}$) and 2 ($6.1 \times 10^{-4} \text{M}$). The data in (a) and (b) were obtained with the 7-ns pulses. The results in (c) and (d) were recorded with the 35-ps pulses. The input energies for the nanosecond and picosecond measurements were $25 \mu\text{J}$ and $5 \mu\text{J}$, respectively. The open circles (○) and open triangles (△) were the Z-scan data measured without the aperture and the filled circles (●) and filled triangle (▲) were those obtained from dividing the closed-aperture Z-scans by the open-aperture ones.

Table 1: Excited-state properties of nickel dithiolenes, phthalocyanines and naphthalocyanines

Sample	Pulse width	τ_T^c (μs)	τ_{isc}^d (ns)	τ_{SI}^e (ns)	$\sigma_1^{a,f}$ (10^{-17}cm^2)	$\sigma_2^{a,g}$ (10^{-17}cm^2)	$\sigma_1^{r,h}$ (10^{-17}cm^2)	$\sigma_2^{r,i}$ (10^{-17}cm^2)
CAP ^a	29 ps and 61 ps	N.A. ^b	18	7	2.3	N.A. ^b	1.8	N.A. ^b
SiNc ^a	29 ps and 61 ps	N.A. ^b	16	3.15	3.9	N.A. ^b	0.47	N.A. ^b
Complex 1	7 ns and 35 ps	≥ 0.1	13	0.85	5.0	2.2	2.0	1.8
Complex 2	7 ns and 35 ps	≥ 0.1	6	2	2.5	1.0	3.2	1.8

^a [7]; ^b Results not available; ^c Triplet state lifetime; ^d Inter-system crossing time; ^e Singlet state lifetime; ^f Singlet excited-state absorption cross-section; ^g Triplet excited-state absorption cross-section; ^h Singlet excited-state refraction cross-section; ⁱ Triplet excited-state refraction cross-section.

4. CONCLUSION

The optical-limiting and nonlinear-optical properties of two neutral nickel dithiolene complexes, [Ni(medt)₂] **1** and [Ni(phdt)₂] **2** have been observed with nanosecond and picosecond laser pulses. The observed nonlinear effects in the two complexes can be explained by excited-state absorption and refraction. These two complexes are shown to be promising for limiting applications in the visible and near infrared spectral region.

5. ACKNOWLEDGEMENT

We gratefully acknowledge the financial support of the National University of Singapore and the National Nature Science of P. R. China.

6. NOTES AND REFERENCES

^g For [Ni(medt)₂], IR spectra (KBr) ν/cm^{-1} : 1257(s), 1214(s), 1144(s), 1076(m), 873(m), 483(m). Anal. Calc. For C₁₀H₁₂S₈Ni: C, 26.85; H, 2.70; Ni, 13.12. Found: C, 27.02; H, 2.75; Ni, 13.07. For [Ni(phdt)₂], IR spectra (KBr) ν/cm^{-1} : 1234(s), 1174(s), 1134(s), 886(m), 873(m), 469(m). Anal. Calc. For C₂₀H₁₆S₈Ni: C, 42.03; H, 2.82; Ni, 10.27. Found: C, 42.30; H, 3.12; Ni, 9.99.

1. R. Crane, K. Lewis, E. W. Van Stryland, and M. Khoshnevis, *Materials for Optical Limiting I* (Material Research Society, Pittsburgh, 1994).
2. L. W. Tutt and A. Kost, *Nature* 356, 225 (1992).
3. D. G. McLean, R. L. Sutherland, M. C. Brant, D. M. Brandelik, P. A. Fleitz, and T. Pottenger, *Opt. Lett.*, 18, 858 (1993).
4. V. V. Golovlev, W. R. Garrett, and C. H. Chen, *J. Opt. Soc. Am. B* 13, 2801 (1996).
5. S. R. Mishra, H. S. Rawat, and S. C. Mehendale, *Appl. Phys. Lett.*, 71, 46 (1997).
6. S. Guha, W. T. Roberts, and B. H. Ahn, *Appl. Phys. Lett.*, 68, 3686 (1996).
7. T. H. Wei, D. J. Hagan, M. J. Sence, E. W. Van Stryland, J. W. Perry, and D. R. Coulter, *Appl. Phys. B*, 54, 46 (1992).
8. J. W. Perry, K. Mansour, S. R. Marder, K. J. Perry, D. Alvarez Jr, and I. Choong, *Opt. Lett.*, 19, 525 (1994).
9. J. S. Shirk, R. G. S. Pong, F. J. Bartoli, and A. W. Snow, *Appl. Phys. Lett.*, 63, 1880 (1993).
10. J. W. Perry, K. Mansour, I.-Y. S. Lee, X.-L. Wu, P. V. Bedworth, C. T. Chen, D. Ng, S. R. Marder, P. Miles, T. Wada, M. Tian, and H. Sasabe, *Science*, 273, 1533 (1996).
11. K. H. Drexhage and U. T. Müller-Westerhoff, *IEEE J. Quantum Electron.*, QE-8, 759 (1972).
12. C. S. Winter, C. A. S. Hill, and A. E. Underhill, *Appl. Phys. Lett.* 58, 107 (1991).
13. C. S. Winter, S. N. Oliver, R. J. Manning, J. D. Rush, C. A. S. Hill, and A. E. Underhill, *J. Mater. Chem.*, 2, 443 (1992).
14. C. S. Winter, R. J. Manning, S. N. Oliver, and C. A. S. Hill, *Opt. Commu.*, 90, 139 (1992).
15. J. L. Zuo, T. M. Tao, F. You, X. Z. You, H. K. Fun, and B. C. Yip, *J. Mater. Chem.*, 6, 1633 (1996).
16. P. Cassoux, L. Valade, H. Kobayashi, R. A. Clack, and A. E. Underhill, *Coord. Chem. Rev.*, 110, 115 (1991).
17. C. Faulmann, A. Errami, B. Donnadiou, I. Malfunt, J. P. Legros, P. Cassoux, C. Rovira, and E. Canadell, *Inorg. Chem.*, 35, 3856 (1996).
18. J. M. Williams, J. R. Ferraro, R. J. Thorn, K. D. Carlson, U. Geiser, H. H. Wang, A. M. Kini, M. H. Whangbo, *Organic Superconductors (including fullerenes)*, Prentice Hall, Englewood Cliffs, NJ, (1992).

19. P. Cassoux, L. Valade, in *Inorganic Materials*, D. W. Bruce, D. O. Hare, Eds, J Wiley & Sons, Chichester, England, (1996).
20. J. S. Miller, A. J. Epstein, *Angew. Chem. Int. Ed. Engl.*, 38, 385 (1994).
21. M. Sheik-Bahae, A. A. Said, and E. W. Van Stryland, *Opt. Lett.*, 14, 955 (1989).
22. M. Sheik-Bahae, A. A. Said, T. H. Wei, D. J. Hagan, and E. W. Van Stryland, *IEEE J. Quant. Electron.* 26, 760 (1990).
23. D. J. Hagan, T. Xia, A.A. Said, T. H. Wei, and E. W. Van Stryland, *International Journal of nonlinear optical Physics*, 2(4), 483 (1993).

Nonlinear optical response of inorganic metal clusters (μ_3 -MoSe₄)X₃(PPh₃)₃Cl (X = Cu, Ag)

Yuenan Xiong^a, Qianfeng Zhang^b, Xinquan Xin^b and Wei Ji^a

^aDepartment of Physics, National University of Singapore, Singapore 119260

^bState Key Laboratory of Coordination Chemistry, Coordination Chemistry Institute,
Nanjing University, Nanjing 210093, China

ABSTRACT

Optical limiting effects in cubane-like metal clusters (μ_3 -MoSe₄)X₃(PPh₃)₃Cl (X = Cu, Ag) dissolved in dichloromethane (CH₂Cl₂) have been studied by measurements of nonlinear transmission, nonlinear scattering, and pump-probe. The nonlinear transmission measurements show that there are strong optical limiting effects in these two cluster solutions; and the silver-containing cluster has larger limiting properties than the other. The nonlinear scattering results indicate that nonlinear scattering is responsible for the limiting action in both clusters. And the pump-probe experiments show that the nonlinear scattering is thermal in origin.

Keywords: Optical limiting, nonlinear scattering, pump probe, cubane like, inorganic cluster

1. INTRODUCTION

Inorganic metal clusters, like carbon black suspension (CBS), are promising candidates for broad-band optical limiting application from visible to IR region. During the past years we have synthesized a series of the coinage-metal/[MS₄]²⁻ (M = Mo, W) compounds and observed large optical nonlinearities in these clusters.¹⁻⁹ The structures of the clusters vary widely, including nest-shaped clusters,^{1,2} twenty-nuclear supracage-shaped clusters,³ twin nest-shaped clusters,⁴ butterfly-shaped clusters,⁵ cubane-like clusters,⁶⁻⁸ and hexagonal prism-shaped clusters.⁹ The strongest optical limiting effect has been observed in the prism-shaped cluster [Mo₂Ag₄S₈(PPh₃)₄], which is about ten times larger than that observed in C₆₀.^{9,10} However, the chemistry and optical nonlinear response of the corresponding selenide anions [MSe₄]²⁻ (M = Mo, W) and their related compounds have not been well-investigated.¹¹ It is also natural for ones to speculate that, similar to their sulfuric counterparts, Se-containing clusters may possess large nonlinear optical properties as well.

Here we report the nonlinear responses of two new transition-metal, Se-containing clusters, (μ_3 -MoSe₄)Cu₃(PPh₃)₃Cl (cluster I) and (μ_3 -MoSe₄)Ag₃(PPh₃)₃Cl (cluster II). They have been synthesized by using the low-heating solid-reaction method¹¹ and are of cubane-like structures and part of heteroselenometalates. With nanosecond laser pulses, the limiting effects in the two clusters have been measured and compared with C₆₀ and Se-containing cubane-like clusters. To study the limiting mechanism(s), we have also measured the angular distribution of scattered energy generated in the limiting process for the clusters. We have found that the total scattered energy should account for a large part in the total energy loss. Our pico-second time-resolved pump probe experiments have revealed that such nonlinear scattering is thermal in origin.

2. EXPERIMENT

Clusters I and II were synthesized and characterized using published methods.¹²⁻¹⁵ Results of their elemental analysis are C, 45.1; H, 3.12; P, 6.32; Cu, 13.6; Mo, 6.68% and: C, 42.1; H, 3.13; P, 6.12; Ag, 22.5; Mo, 5.97% respectively. Clusters I and II have the same cubane-like molecular configuration. The molecular structure of cluster I contains a highly distorted cubane-like {MoCu₃Se₃Cl}²⁺ cluster core with one Se²⁻ terminal ligand bound to Mo, and PPh₃ ligand bound to each Cu atom. In the core of {MoCu₃Se₃Cl}, both the Cu and Mo atoms are tetrahedrally coordinated. Each Cu center is bonded tetrahedrally to one P, one Cl and two Se atoms and the Mo center is bonded tetrahedrally to four Se atoms. In cluster II, all the Cu atoms are replaced by Ag atoms. However, two structures belong to different space groups, cluster I

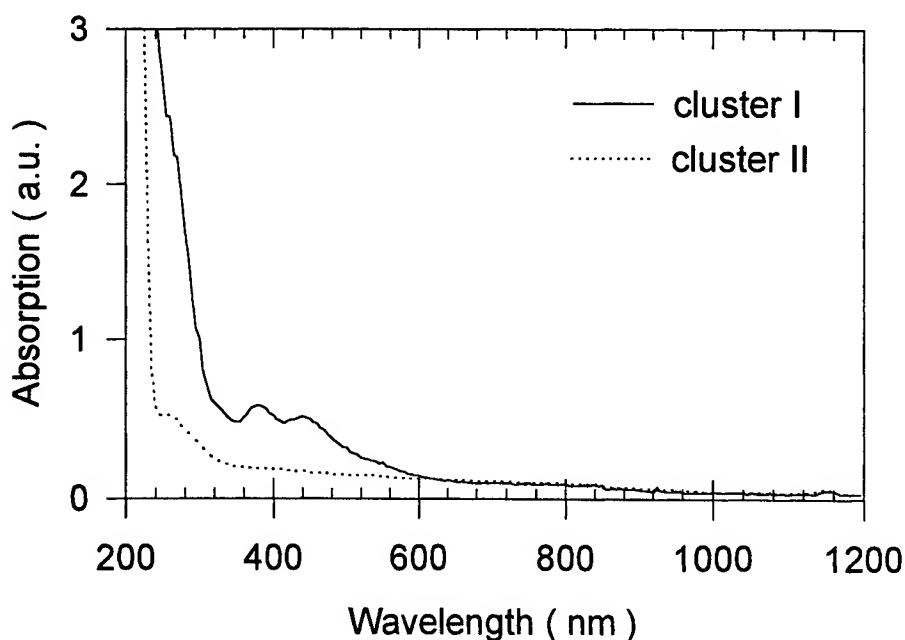


Fig. 1 Linear absorption spectra of cluster I ($(\mu_3\text{-MoSe}_4)\text{Cu}_3(\text{PPh}_3)_3\text{Cl}$) and cluster II ($(\mu_3\text{-MoSe}_4)\text{Ag}_3(\text{PPh}_3)_3\text{Cl}$) in CH_2Cl_2 with 1mm cell. The linear transmittance for cluster I and cluster II are 62% and 78% respectively.

crystallized in the orthorhombic $P2_12_12_1$ space group, while cluster II is of triclinic $P\bar{1}$ space group. Moreover, there is a large difference in M–Cl ($\text{M} = \text{Cu}, \text{Ag}$) bond distances. Cluster I presents two kinds of Cu–Cl bond distances: one short and two long bond distances. Cluster II has three long Ag–Cl bonds, which suggest that cluster II should have more distorted cubane-like cluster core than cluster I. The dichloromethane (CH_2Cl_2) solutions of clusters I and II were placed in 1-mm quartz cuvettes for optical measurements. The solutions were such prepared that they are of the same concentrations, 1 mmol/dm^3 .

In the nonlinear transmission and scattering experiments, linearly polarized, 7-ns pulses from a Q-switched frequency-doubled (532 nm) Nd:YAG laser were focused onto the sample with a 25-cm-focal-length mirror. The spatial profiles of the pulses were nearly Gaussian. The spot radius of the laser beam was measured by Z-scan technique to be about $30 \pm 5 \text{ }\mu\text{m}$ (half width at $1/e^2$ maximum). The laser was operated in single-shot condition, or 10-Hz repetition rate. The energy of the scattered light was measured under the same experiment except that the detector was positioned at different angles with respect to the optic axis. The angle was varied from 0 to 170 degree in increments of 10 degree. Since the orthogonal components of the scattered light are orders of magnitude lower in intensity as was observed in ref.16, depolarization of the input laser pulses could be neglected and hence no polarizer was used in front of the detector. The laser was originally horizontally polarized. Vertically polarized input pulses were obtained with a half-wave plate. Both the scattered light produced by the vertically and horizontally polarized input beams were measured.

The samples were also tested in a time-resolved pump-probe experiment with 532-nm pulses of 35-ps duration produced by a Q-switched, mode-locked, frequency-doubled Nd:YAG laser. We employed a standard pump-probe arrangement where the peak irradiance of the probe pulse was approximately 5% of that of the pump pulse.¹⁰ The pump and probe were orthogonally polarized to avoid interference and were incident at an angle of 10° with respect to each other. The probe was delayed relative to the pump pulse. Both the probe and pump were focused onto the cell with a beam waist of $75 \mu\text{m}$. In all the experiments, the incident and transmitted (or scattered) pulse energies were simultaneously recorded by two Laser Precision detectors, which were linked to a computer by an IEEE interface.^{8,9}

3. RESULTS

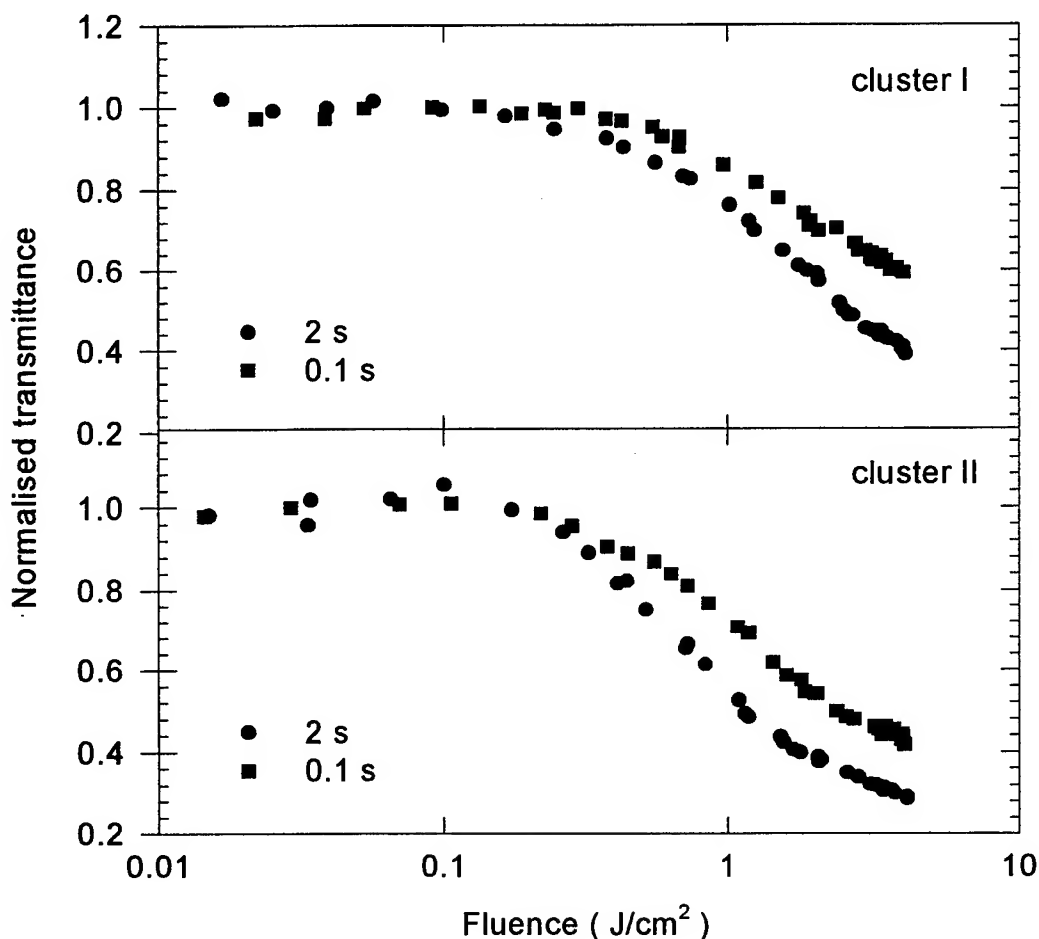


Fig.2 Optical limiting response to 7-ns, 532 nm laser pulses, with clusters I (upper graph) and II (lower graph) in dichloromethan (CH_2Cl_2) with 1-mm optical length: filled circle, single shot; filled box, 10 Hz. Linear transmittance is 62% for Cluster I and 78% for cluster II. Both samples have identical concentration.

The UV-visible absorption spectra of the clusters in CH_2Cl_2 solution are shown in Fig.1. Cluster I has two shoulders around 422 nm and 388 nm with a large absorption peak observed near 280 nm. Compared to cluster I, cluster II has a relatively flat absorption spectrum in the visible region with a fundamental absorption edge at 240 nm. This difference induces a relatively lower transmittance at 532 nm laser light for cluster I (62%) than for cluster II (78%) with the same concentration.

The optical limiting effects for cluster I and cluster II are depicted in Fig. 2. The transmittance is normalized to its linear transmittance measured when the fluence is low. The sample transmittance starts to drop as the input light fluence reaches about 0.1 J/cm^2 and become increasingly less transparent as the light fluence rises. The thresholds for these two samples in the single-shot condition are 1.8 and 0.8 J/cm^2 for cluster I and II, respectively. As the pulse repetition rate increases to 10 Hz, The samples became less effective in optical limiting and larger threshold values were observed. To testify their effectiveness as broad-band optical limiters, the 1064-nm-wavelength laser pulses from the nanosecond Nd:YAG laser have been used. At 1064 nm, the limiting threshold for cluster II is about three times larger than at 532 nm while cluster I does not possess the limiting effect anymore.

This less effectiveness at 1064-nm wavelength may be attributed to the obvious reduction in the linear-absorption coefficients (the linear transmittance for both the samples is about 98% at 1064 nm). Recent experiments on a hex-prism

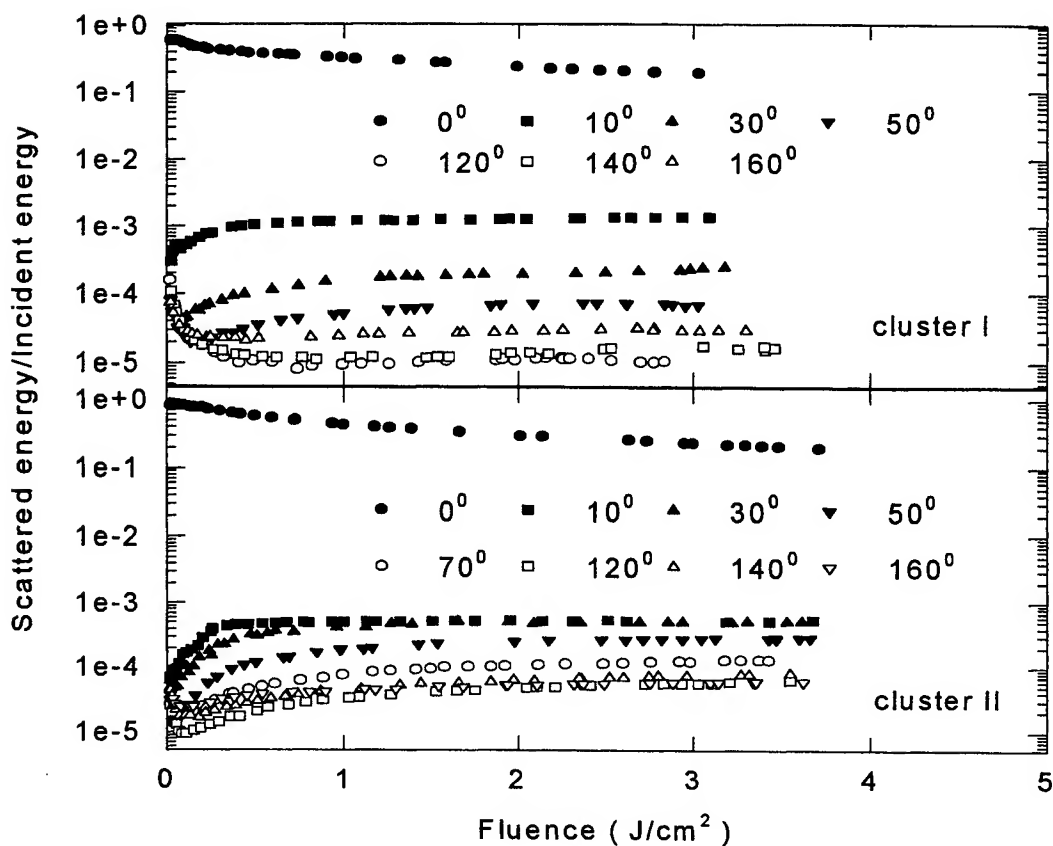


Fig.3 Ratios of scattered energy to input energy as a function of input fluence for cluster I (upper graph) and cluster II (lower graph). Input beam was vertically polarized. Plots of 0° corresponds to common optical limiting results.

Table I Limiting thresholds of clusters with cage-shaped structure measured at 532nm with 7-ns laser pulses.

Compound	Solvent	Linear transmission(%)	Limiting threshold/ Jcm^2	Ref.
C_{60}	Toluene	62	1.6	17
$[\text{NBu}^n_4]_3[\text{WCu}_3\text{Br}_4\text{S}_4]$	MeCN	70	1.1	8
$[\text{NBu}^n_4]_3[\text{WAg}_3\text{Br}_4\text{S}_4]$	MeCN	70	0.6	8
$[\text{NBu}^n_4]_3[\text{WAg}_3\text{BrI}_3\text{S}_4]$	MeCN	70	0.5	8
$[\text{NBu}^n_4]_3[\text{WAg}_3\text{BrCl}_3\text{S}_4]$	MeCN	70	0.6	8
$\text{Mo}_2\text{Ag}_4\text{S}_8(\text{PPh}_3)_4$	MeCN	92	0.1	9
$(\mu_3\text{-MoSe}_4)\text{Cu}_3(\text{PPh}_3)_3\text{Cl}$	CH_2Cl_2	62	1.8	This work
$(\mu_3\text{-MoSe}_4)\text{Ag}_3(\text{PPh}_3)_3\text{Cl}$	CH_2Cl_2	78	0.8	This work

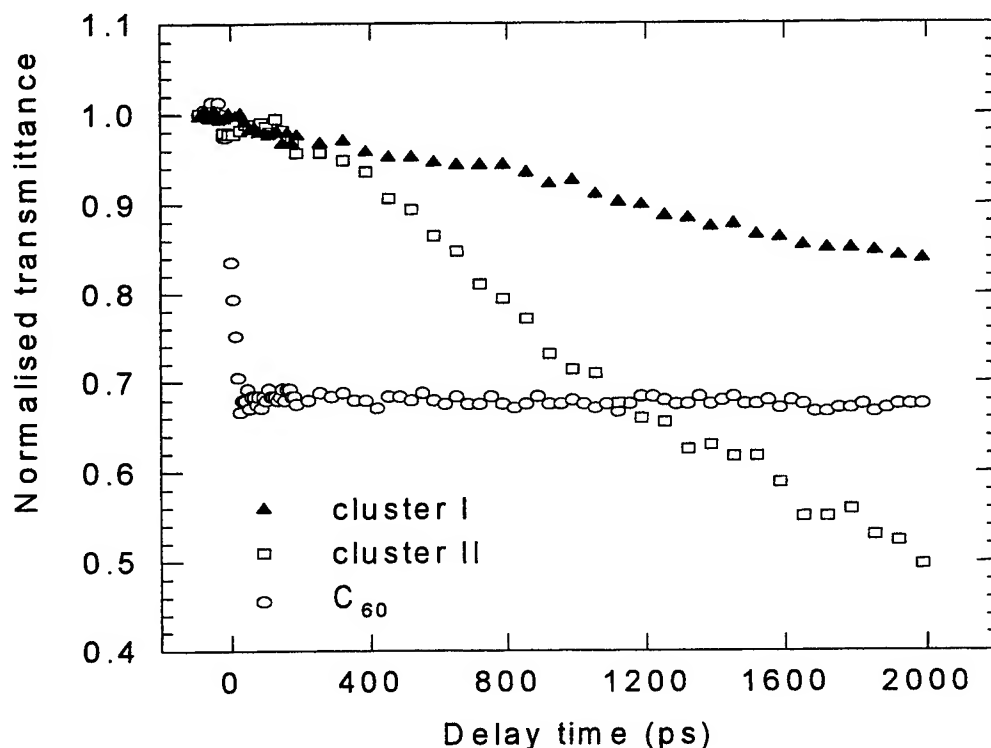


Fig.4 Normalized transmittance of the probe as a function of time delay for a pump fluence of 1.14 J/cm for various samples: C₆₀, open circle; cluster I, filled triangle; cluster II, open box.

cage shaped inorganic metal cluster Mo₂Ag₄S₈(PPh₃)₄ have indicated that the limiting effect originate from nonlinear scattering process, similar to that observed in carbon black suspension (CBS).^{10,16} In the nonlinear scattering process, the linear absorption initiates heating, which vaporize, and ionize the clusters. As a result, the clusters scatter light, leading to the limiting effect. At 1064 nm where the linear absorption becomes much smaller, the heating is less effective and so is nonlinear scattering, which leads to degrading of the limiting effect.

It is interesting to compare these two new clusters with other well-known optical limiting materials. Table 1 shows the limiting thresholds of cluster I and cluster II along with other cubane clusters, hexagonal prism-shaped clusters and C₆₀. All the silver-contained clusters have lower thresholds than those of the copper-contained clusters. This significant improvement of limiting capability by replacing skeleton Cu atoms with Ag atoms is consistent with the nonlinear scattering model,^{10,16} in which the plasmas may be more easily generated due to the fact that silver has a much lower sublimation temperature than copper.

The limiting data, along with the ratios of scattered to input energy measured at different angles, are shown in Figure 3, in which only the results obtained with vertically polarized input beams are presented. There is no nonlinear scattered light when the input fluence is less than 0.1 J/cm². With the input fluence exceeds 0.1 J/cm², nonlinear scattering appear. Similar results were obtained with horizontally polarized input light. An interesting phenomenon is that the angular distribution of scattered energy for these two clusters is quite different. For cluster I, at angles between 10° to 30°, the scattered energy increases with the increase of the input fluence; and at other angles, the scattered light behavior otherwise. But, for cluster II, the scattered energy is increased as the input fluence arises for all the angles. Furthermore, energy scattered into 10° angle is several times larger than that scattered into the adjacent 20° angles for cluster I while for cluster II there is only negligible difference, which means that the scattered light is more tightly confined in the forward direction for cluster I.

The pump-probe experimental results with a pump fluence of 1.14 J/cm² are given in Figure 4. The transmittance of the probe pulse is normalized to its linear transmittance. These two samples have identical concentrations. The response of the

C₆₀-toluene solution has also been tested in the same setup. The sharp drop of the probe signal is typical for C₆₀ due to excited single state absorption while the very slow recovery results from excited triplet state absorption, which can be explained by a five-energy-level model.¹⁷ Contrary to the response of C₆₀, clusters I and II have very small changes (about 2%) at zero delay time, which may be induced by excited state absorption, similar to C₆₀. The large changes take place at least ~0.2 ns and reach maximum at ~2.0 ns. These results are consistent with their poor limiting performance in our 35-ps nonlinear transmission measurements; and similar to the responses of CBS and metal cluster Mo₂Ag₄S₈(PPh₃)₄.¹⁰ The relatively slow responses for CBS and metal cluster Mo₂Ag₄S₈(PPh₃)₄ in the pump-probe experiments are explained by a model of direct heating of the microscopic sized particles by linear absorption. Subsequent to heating, the temperature can be increased to a point higher than the sublimation temperature of the molecules and then micro-plasmas are generated. Rapid expansion of the microscopic plasmas can effectively scatter the input light.¹⁰ From Figure 4, we can see that the maximum nonlinear transmission loss for cluster II is much higher than that of cluster I and C₆₀. Although the nonlinear response is much slower than C₆₀, the maximum nonlinear transmission for cluster II is much higher. This ns-responed nonlinearity is very effective for nanosecond optical limiting as we observed in the nanosecond experiments.

4. CONCLUSION

In summary, the optical limiting effects in two cubane-like clusters: (μ_3 -MoSe₄)Cu₃(PPh₃)₃Cl (I) and (μ_3 -MoSe₄)Ag₃(PPh₃)₃Cl (II) have been investigated. The limiting thresholds for both clusters are comparable to that of C₆₀. The picosecond time-resolved pump-probe experiment show a turn-on time for such limiting effects is about 2ns or longer. These results, along with the fact of very poor limiting with 35-ps laser pulses, imply that nonlinear scattering may play an important role in the nonlinear process. This assumption is confirmed by direct measurement of the scattered light.

ACKNOWLEDGEMENTS

We gratefully acknowledge the financial support of the National University of Singapore and the National Natural Foundation of China.

REFERENCES

- (a) W. Ji, P. Ge, Wei Xie, S. H. Tang and S. Shi, *J. Lumin.*, 66&67, 115, 1996; (b) S. Shi, W. Ji, W. Xie, T. C. Chong, H. C. Zeng, J. P. Lang and X. Q. Xin, *Mater. Chem. Phys.*, 39, 298, 1995.
- (a) Ge, P.; Tang, S. H.; Ji, W.; Shi, S.; Hou, H. W.; Long, D. L.; Xin, X. Q.; Lu, S. F.; Wu, Q. J. *J. Phys. Chem. B*, 101, 27, 1997. (b) Hou, H. W.; Xin, X. Q.; Shi, S. *Coord. Chem. Rev.* 153, 25, 1996.
- (a) W. Ji, W. Xie, S. H. Tang and S. Shi, *Mater. Chem. Phys.*, 43, 45, 1995. (b) S. Shi, W. Ji, and X. Q. Xin, *J. Phys. Chem.*, 99, 894, 1995.
- H. W. Hou, X. Q. Xin, J. Liu, M. Q. Chen and S. Shi, *J. Chem. Soc., Dalton Trans.*, 3211, 1994.
- Shi, S.; Ji, W.; Tang, S. H.; Lang, J. P.; Xin, X. Q. *J. Am. Chem. Soc.* 116, 3615, 1994.
- (a) Z. R. Chen, H. W. Hou, X. Q. Xin, B. Yu and S. Shi, *J. Chem. Phys.*, 99, 8717, 1995.
- (a) S. Shi, W. Ji, S. H. Tang, J. P. Lang and X. Q. Xin, *J. Am. Chem. Soc.*, 116, 3615, 1994; (b) S. Shi, W. Ji, J. P. Lang and X. Q. Xin, *J. Phys. Chem.*, 98, 3570, 1994.
- W. Ji; H. J. Du; S. H. Tang; S. Shi, *J. Opt. Soc. Am. B*, 12, 876, 1995.
- W. Ji, S. Shi, H. J. Du, P. Ge, S. H. Tang, X. Q. Xin, *J. Phys. Chem.* 99, 17297, 1995.
- (a) T. Xia, A. Dogariu, K. Mansour, D. J. Hagan, A. A. Said, and E. W. Van Stryland, and S. Shi, *J. Opt. Soc. Am. B*, 15, 1497, 1998. (b) O. Durand, V. Grolhier-Mazza, and R. Frey, *Opt. Lett.*, 23, 1471, 1998.
- (a) Li, J. G.; Xin, X. Q.; Zhou, Z. Y.; Yu, K. B. *J. Chem. Soc., Chem. Commun.* 250, 1991. (b) Lang, J. -P.; Xin, X. -Q. *J. Solid State Chem.* 108, 118, 1994.
- O'Neal, S. C.; Kolis, J. W. *J. Am. Chem. Soc.* 110, 1971, 1988.
- Zhang, Q. F.; Hong, M. C.; Su, W. P.; Cao, R.; Liu, H. Q. *Polyhedron*, 16, 1433, 1997.
- Stephens, R. D. *Inorg. Synth.* 19, 88, 1972.
- Zhang, Q. F.; Hong, M. C.; Liu, H. Q. *Trans. Met. Chem.* 22, 156, 1997.
- K. M. Nashold and D. P. Walter, *J. Opt. Soc. Am. B*, 12, 1228, 1995.
- D. G. McLean, R. L. Sutherland, M. C. Brant, D. M. Brandelik, P. A. Fleitz and T. Pottenger, *Opt. Lett.* 18, 858, 1993.

Dynamics of the $A^3\Pi_0$, $B^3\Pi_1$ and $C^1\Pi_1$ states of InCl by laser induced fluorescence

Yunjing Li, Meirong Lin*, Wenli Zou, Baozheng Zhang, and Wenju Chen

Institute of Modern Optics, Opto-electronic Information Science and Technology Laboratory,

EMC., Nankai University, Tianjin 300071, P. R. China

ABSTRACT

In this paper, we present the laser induced fluorescence spectra and the time-resolved spectra of the $A^3\Pi_0 \rightarrow X^1\Sigma^+$, $B^3\Pi_1 \rightarrow X^1\Sigma^+$ and $C^1\Pi_1 \rightarrow X^1\Sigma^+$ for InCl molecule in the ranges of 266.5-287.0nm and 332.0-373.0nm. It is the first time those radiative lifetimes of the $C^1\Pi_1$ and $B^3\Pi_1$ states have been measured by laser-induced fluorescence. From the time-resolved spectra under different pressures, we obtained the collision-free radiative lifetimes and quenching rate constants for InCl molecule: $A^3\Pi_0$ ($v'=0$), 370ns, $9.87 \times 10^{-11} \text{cm}^3 \text{molec}^{-1} \text{s}^{-1}$; $B^3\Pi_1$ ($v'=0$), 353ns, $1.985 \times 10^{-10} \text{cm}^3 \text{molec}^{-1} \text{s}^{-1}$; and $C^1\Pi_1$ ($v'=1$), 11ns. From the radiative lifetime and the Frank-Condon factors $q_{v',v''}$ for the $v'-v''$ transitions, the electronic transition moments $|\text{Re } \mathbf{P}|$ of $B^3\Pi_1$ and $C^1\Pi_1$ states have been obtained.

Keywords: laser induced fluorescence, collision-free lifetime, quenching rate constant

1. INTRODUCTION

The monohalides of the group IIIA play an important role in the development of new semiconductor devices in highfrequency and opto-electronic applications. The spectra of the InCl molecule have been well studied in emission and absorption over the spectral range 200-410nm^[1-15]. In recent years, the new observed transitions in blue-green bands that are predicted to develop into efficient laser systems. The observed strong and extensive bands of InCl have been arranged in different band systems designate as $A \leftrightarrow X$, $B \leftrightarrow X$ and $C \leftrightarrow X$ system, and the rovibrational constant of the electronic states of these three transitions are well-established^[1]. The $C^1\Pi_1$ state is the lower level of the potential laser medium and the upper level is a new state^[2].

The $B^3\Pi_1-X^1\Sigma^+$ system was first photographed by Wehrli and Miescher^[3] in absorption and the approximate vibrational constants were determined. The $C^1\Pi_1 \rightarrow X^1\Sigma^+$ transition falls within 265-282nm^[4]. Frosie^[5] found the $C^1\Pi_1(v=1)$ has predissociation and obtained the initial rovibrational constants. Perumalsamy^[6] suggested that the predissociation occurred above the $v=3$ level. Jones^[7] has observed more new bands up to $v=6$ in C state from microwave discharge absorption spectra. The accurate position of predissociation is not known in present.

Their time domain, however, has been little investigated. In this paper, we present the laser induced fluorescence spectrum and the time-resolve spectra of the $A^3\Pi_0 \rightarrow X^1\Sigma^+$, $B^3\Pi_1 \rightarrow X^1\Sigma^+$ and $C^1\Pi_1 \rightarrow X^1\Sigma^+$ for InCl molecule. At last we obtained the lifetime of the $A^3\Pi_0$, $B^3\Pi_1$ and $C^1\Pi_1$ and other parameters of the dynamic process.

* Correspondence: Email: spectroscopy @ 263. Net

2. EXPERIMENT

We use a pulsed Q-switched fourth harmonic YAG (Quantel YG580) operated at 4ns for the molecular excitation. The indium monochloride is produced by heating the indium trichloride (China, 99.999%) in the

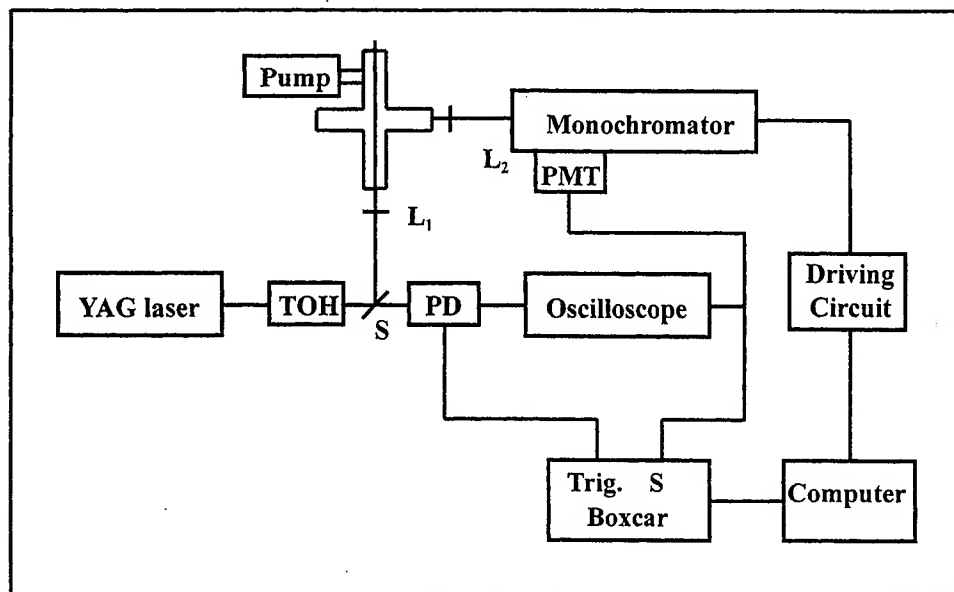


Figure 1. Schematic diagram of the experimental set-up

presence of an excess of metal indium (99.99%) under vacuum ($\times 10^{-5}$ Torr) in a quartz boat that is placed in the middle of a heat-pipe oven, equipped with UV quartz end windows. The reaction zone is heated from 250°C to 290°C by an electrical coil whose temperature is controlled by a digital temperature controller (WP-C80, precision $\pm 1^\circ\text{C}$) and measured by a NiCr-NiSi thermoelectric couple (precision $\pm 1^\circ\text{C}$). In order to avoid condensation of the vapor of InCl, the edge of the oven arm is cooled by water.

Figure 1 is the experimental set up. Fluorescence from InCl is detected perpendicular to the laser beam axis through a 0.5m monochromator equipped with a RCA 456 photomultiplier and then integrated by a Boxcar (Stanford SR250/200). A PC computer controls the scan of the monochromator and the data acquisition and the data are stored in it for farther process.

3. RESULTS AND DISCUSSION

3.1. The $C^1\Pi_1$ State

Figure 2 shows the laser induced fluorescence spectrum of the $C^1\Pi_1 \rightarrow X^1\Sigma^+$ system which is obtained using the 266nm laser, where several lines of the 1-1,1-2,1-3,1-4,1-5,1-6 and 1-7 bands are assigned based on the band frequency of Jones ^[3]. The wavelength of the seven bands are 268.4nm, 270.7nm, 273.0nm, 275.4nm,

277.7nm、280.2nm、282.5nm. To our knowledge, it is the first time to observe the transition from the $v'=1$ of $C^1\Pi_1$ state in emission which proved that the predissociation of $C^1\Pi_1$ state only occur above the $v'=1$.

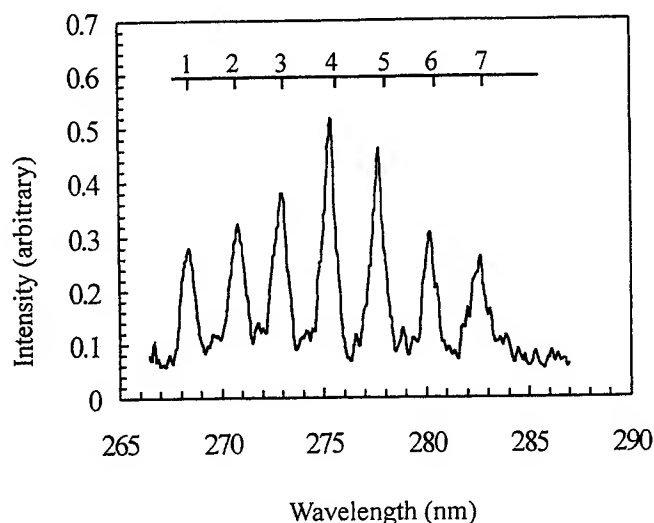


Figure 2. A section of the $C^1\Pi_1 \rightarrow X^1\Sigma^+$ electronic transition recorded by laser induced fluorescence

In order to obtain collision-free lifetime, we measured the time-resolved curves of 275.4nm band of $C^1\Pi_1(v'=1) \rightarrow X^1\Sigma^+(v''=4)$ under different pressures. Fluorescence decay curves show a monoexponential behavior characterized by a single lifetime.

Table 1. The lifetimes of $C^1\Pi_1(v'=1) \rightarrow X^1\Sigma^+(v''=4)$ under 250°C~290°C.

Temperature (°C)	250	260	270	280	290
pressure (mmhg)	0.144	0.211	0.305	0.436	0.614
lifetime (ns)	12	10	10	12	11

In order to eliminate the error of the time response of the instruments, the fluorescence decay curves are deconvoluted. Figure 3 shows a typical fluorescence decay curve of $C^1\Pi_1(v'=1) \rightarrow X^1\Sigma^+(v''=4)$ at 290°C, where the solid curve represents the observed fluorescence decay curve, the dotted line represents the deconvoluted fluorescence decay curve. The observed lifetime in figure 3 is 14ns and the deconvoluted is 11ns.

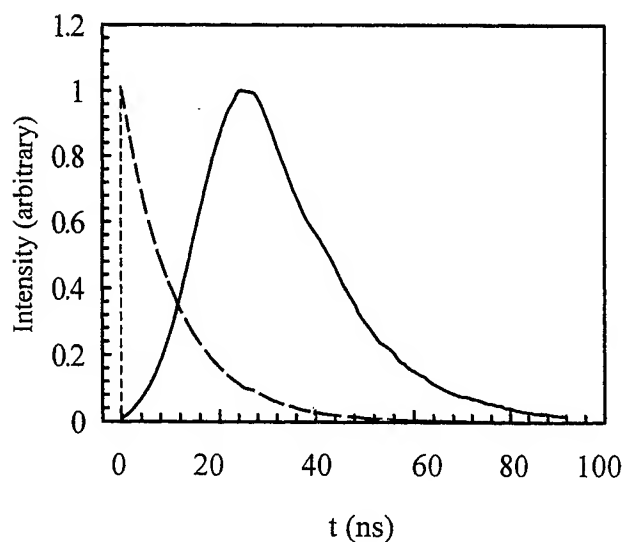


Figure 3. A typical fluorescence decay curve of $C^1\Pi_1(v'=1) \rightarrow X^1\Sigma^+(v''=4)$ at 290°C .
The solid curve represents the observed fluorescence decay curve.
The dotted line represents the deconvoluted fluorescence decay curve.

Table 1 shows the lifetimes of $C^1\Pi_1(v'=1) \rightarrow X^1\Sigma^+(v''=4)$ under $250^\circ\text{C} \sim 290^\circ\text{C}$. It can be seen from the table that the lifetimes under different pressures could not distinguished in our experimental precision scope. So we suppose the collision-free lifetime of the $C^1\Pi_1(v'=1)$ is approximately 11(1)ns.

3.2. The $A^3\Pi_0$ and $B^3\Pi_1$ State

We also obtain the laser induced fluorescence spectrum over 330-380nm as show in fig.4.

The $A^3\Pi_0$ state lies in $T_e=27767.0\text{cm}^{-1}$ and $B^3\Pi_1$ in $T_e=28563.6\text{cm}^{-1}$. According to the constants of the electronic state, we assigned the bands to $A^3\Pi_0 \rightarrow X^1\Sigma^+$ and $B^3\Pi_1 \rightarrow X^1\Sigma^+$ which are listed in table 2. The collision-free lifetime and quenching rate constant of $B^3\Pi_1$ state are determined in the range of total pressures from 0.21 to 0.86 Torr and extrapolated the curve to zero pressure.

Figure 5 shows a typical Stern-Volmer plot for emission from the $v'=0$ vibrational level of the InCl $B^3\Pi_1$ state, where inverse lifetimes are plotted against total pressure P_T giving quenching rate constants k_Q through

$$\frac{1}{\tau} = \frac{1}{\tau_0} + k_Q P_T \quad (1)$$

where τ_0 is the collision-free fluorescence radiative lifetime. As can be seen in figure 5, the Stern-Volmer plot is linear in the pressure interval studied. The collision-free lifetime is $\tau_0=353\text{ns}$ and quenching rate constant is $k_Q=1.985 \times 10^{-10} \text{mol}^{-1} \cdot \text{s}^{-1} \text{cm}^3$.

Table 2 The assignment of the bands of InCl in 330-375nm

No.	Band positions.(nm) (observation)	Band positions.(nm) (calculation) ^[6]	Assignment	
			$A^3\Pi_0 \rightarrow X^1\Sigma_0$	$B^3\Pi_1 \rightarrow X^1\Sigma_0$
1	338.2	338.25		(3,0)
2	339.8	339.92	(7,2)	
3	341.7	341.78		(4,2)
4	343.5	343.56	(6,2)	
5	345.9	345.94		(1,0)
6	347.3	347.34	(5,2)	
7	349.9	349.99		(0,0)
8	351.1	351.13	(5,3)	
9	353.6	353.63		(1,2)
10	355.7	355.72	(1,0)	
11	357.5	357.56		(1,3)
12	359.9	360.00	(0,0)	
13	361.2	361.25		(2,5)
14	363.8	363.85	(1,2)	
15	367.6	367.69	(2,4)	
16	371.8	371.89	(2,5)	

The electronic dipole moment $|\text{Re}|^2$ is a more fundamental measure of the transition probability than the reciprocal $1/\tau_R$. To consider any variation of transition probability with v' , or more precisely with r -centroid value, it is therefore useful to transform the τ_R value into the corresponding $|\text{Re}|^2$ value.

In this work, Frank-Condon factors and r -centroids have been calculated^[16,17] for the C-X and B-X systems. The spectroscopy constants for the B and C state are those given by Perumalsamy^[7]. The radiative lifetime τ_v of an excited vibrational level v' is related to the transition probabilities $A_{v'v''}$ by the following expression^[18]:

$$\frac{1}{\tau_v} = \sum_v A_{v v'} = \frac{64 \pi^4}{3 h} \sum_v |\text{Re}(\bar{r}_{v v'})|^2 q_{v v'} \nu^3_{v v'} \quad (2)$$

where ν , $q_{v v'}$ and $\bar{r}_{v v'}$ are, respectively, the transition frequency, Frank-Condon factor, and r-centroid of the (v', v'') band, and $|\text{Re}|^2$ is the square of the electronic transition moment.

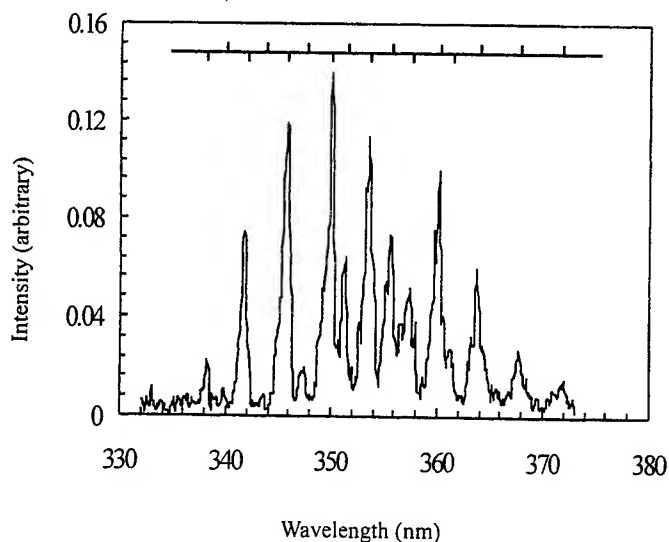


Figure 4. A section of the $A^3\Pi_0 \rightarrow X^1\Sigma^+$ electronic transition recorded by laser induced fluorescence

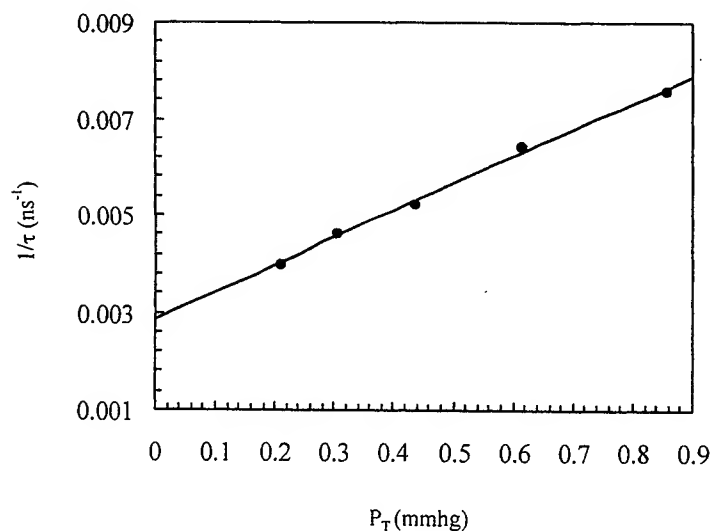


Figure 5. Stern-Volmer plot of the inverse lifetime (τ) against total pressure (P_T), for emission from the $A^3\Pi_0(v'=1) \rightarrow X^1\Sigma^+(v''=2)$ of InCl.

The range of r-centroids spanned by our interested progression is quite small, and $|\text{Re } \mu|$ can be approximately consider as a constant for emission from a single vibrational level ^[18]. Therefore equation (2) can be simplified as:

$$\frac{1}{\tau_v} = \frac{64\pi^4}{3h} |\text{Re } \mu|^2 \sum_v q_{vv} \nu^3_{vv} \quad (3)$$

Thus we can calculate $|\text{Re } \mu|$ from τ_v by evaluating the simple summation contained in equation (3). From the measured results of radiative lifetime and the molecular constants of the $B^3\Pi_1$ and $X^1\Sigma^+$ states, we estimate the electronic transition moment $|\text{Re } \mu|=0.40 \text{ D}^2$ for B state ($v=0$) and $|\text{Re } \mu|=5.95 \text{ D}^2$ for $C^1\Pi_1$ state ($v=1$). It is the first time that these values have been obtained.

Combining with our early result of $\tau_0=373\text{ns}$ and $|\text{Re } \mu|=0.42 \text{ D}^2$ of $A^3\Pi_0$ state, it could be found that the lifetime and electronic transition moment for $A^3\Pi_0$ and $B^3\Pi_1$ state are similar but smaller than those of the $C^1\Pi_1$ state. All these results give a significant support to study the dynamic process of InCl molecule.

4.ACKNOWLEDGMENTS

This work is supported by the National Science Foundation of China under Grant No.69878010.

5.REFERENCES

1. S. N. Vempati and W. E. Jones, "Spectroscopic investigation of InCl in the ultraviolet: constants of the $A^3\Pi_0$ state", *J. Mol. Spec.* **132**, pp. 458-466, 1988.
2. R. Venkatasubramantan, M. D. Saksena and M. Singh, "New visible emission spectra of GaBr, GaCl and InCl. Prospects of new laser transitions", *Chem. Phys. Lett.* **120**, pp. 367-372, 1993.
3. M. Wehrli and E. Miescher, "Spektroskopische untersuchung dampfförmiger indiumhalogenide", *Helvetica Physica Acta.* **7**, pp. 298, 1934.
4. E. Miescherin and M. Wehrli, "Die spektren der indiumhalogenide", *Helvetica Physica Acta.* **6**, pp. 256-259, 1933.
5. H. M. Froslie, J. G. Winans., "The absorption spectrum of InCl", *Phys. Rev.*, **72**, pp. 481, 1947.
6. K. Perumalsamy, S. B. Rai, K. N. Upadhyya and D. K. Rai, "Study of indium monochloride molecule", *Phys.*, **132C**, pp. 122-140, 1985.
7. W. E. Jones and T. D. Mclean, "Spectroscopic investigation of InCl in the ultraviolet: the $C^1\Pi-X^1\Sigma$ system", *J. Mol. Spec.* **150**, pp. 201-217, 1991.
8. R. F. Barrow, "Dissociation energies of the gaseous monohalides of boron, aluminium, gallium, indium, and thallium", *Transactions of the Faraday Society*, **56**, pp. 952, 1960.
9. A. H. Barrett and M. Mandel, "Microwave spectra of the Tl, In, and Ga monohalides", *Physical Review*, **109**, pp. 1572, 1958.
10. V. P. N. Nampoori and M. M. Patel, "A new band system of InCl molecule in the region 4100-3900Å", *Curri. Science*, **48**, pp. 532, 1979.
11. P. Younger, and J. G. Winans, "Molecular constants of InCl from absorption bands near 3600 angstroms", *J. Mole. Spect.* **4**, pp. 23-42, 1960.
12. J. Borkowska-Burnecka and W. Zyrnicki, "High-resolution study of InCl spectra", *Physica*, **115C**, pp. 415-418, 1983.
13. M. L. P. Rao, D. V. K. Rao, and P. T. Rao, "Rotational analysis of the A-X system of InCl molecule". *Spectroscopy Letters*, **9**, pp. 101-103, 1976.
14. Ashrafunnisa, D. V. K. Rao, and P. T. Rao. "Rotational analysis of $B^3\Pi_1-X^1\Sigma$ system of the InCl molecule". *Spectroscopy Letters*, **9**, pp. 9-17, 1976.

15. U. Wolf and E. Tiemann, "The potential curve for the $C^1\Pi$ state of InCl ", *Chemical Physical Letters*, **139**, pp. 191, 1987.
16. K. Perumalsamy, S. B. Rai and K. N. Upadhy, "On the $C^1\Pi-X^1\Sigma$ " system of the indium monochloride molecule and its dissociation energy", *Phys.*, **141C**, pp. 315-322, 1986.
17. Ashrafunnisa, D. V. K. Rao and P. T. Rao, "Frank-Condon factors and r-centroids of $^3\Pi-X^1\Sigma$ system of InCl molecule", *Current. Sci.*, **46**, pp. 179, 1977.
18. M. C. Heaven, "Fluorescence decay dynamics of the halogens and interhalogens", *Chem. Soc. Rev.*, **15**, pp. 405-448, 1986.

Plane Wave Quantity & Its Measurement of Plate working surface

Jun-Qi Liu^{*a}, Ya-Nan Liu^a, Lin-xiang Cao^b, Xiao-ming Zhao^a

^aDepartment of optics-Electronics, Xi'an Institute of Optics & Precision Mechanics(XIOPM)

Xi'an Shaanxi 710068, The people's public of China.

^bNorth-western polytechnical University, Xi'an Shaanxi 710072

The people's public of China.

ABSTRACT

This paper deals with the assay requirements and the method of plane Wave quantity of the plate working surface according to the National Standards of "Cast-Iron Plate" and "Rock Plate", derives, in detail, the detecting principle of plane wave detector and gives out the relationship between the partial plane error and the partial defect of the plate and the plane wave quantity. It also inquires into the relationship between the contact spot and 200 mm straight line wave and plane wave quantity.

Keyword: Plane wave detector, Principle application.

0. INTRODUCTION

At present, the method of node distance is mostly used to assay the plane degree of the working surface of plate. In fact, this method is to figure out the working surface error of the whole plate according to the assayed data of the specific points, therefore it cannot present a objective and detailed description about the whole picture of the working surface of the plate. So many factors may cause the partial plane error of the plate in the process of the manufacturing and repairing, such as the hardness and the homogeneity of the materials, the variations of temperature, the scraping skill, the distribution of the grinding force, the homogeneity of the wedge sand, the quality of the abrasive and other accidental factors. Partial wear and tear, scratch, impact injury and partial variation of temperature can also cause the partial plane error in the cause of using. So, as a way of complement, we must assay the partial plane error of the blank area besides the assayed points. The comprehensive and correct opinion of the plane degree of the working surface of the plate can be made out only by the comprehensive consideration, which is according to the results of these two methods.

The assay method and the technical requirement of partial plane error of the plate are formulated in the standards of each country (including assay regulations). In summary, there are contact speck and its homogeneity, smoothness, short node distance, linearity, the measuring error due to repeated reading and the change of curvature, and so on. It is ruled that "Assay the plane wave quantity of the plate working surface when checking up the contact spot can not carry out conveniently" in the National Standards GB4986~4987 of "Cast-Iron Plate" and "Rock Plate". Its value will not be greater than the value in "Table 1". The method of checking the plane wave quantity is given in the appendix of the standard.

Table1

Degree of accuracy	000	00	0	1	2	3
wave value of the working surface	2	4	8	16	32	80

Put the graphic plane wave detector in Figure 1 on the working surface of the plate, and then drag the detector along any straight direction. The distance is $d/2$, but it will not be less than 200mm. In the process of the dragging the Max and Min value will be read from the reading of the micrometer on the plane wave detector. The absolute value of the algebraic difference of these two will be the plane wave quantity of the plate-working surface.

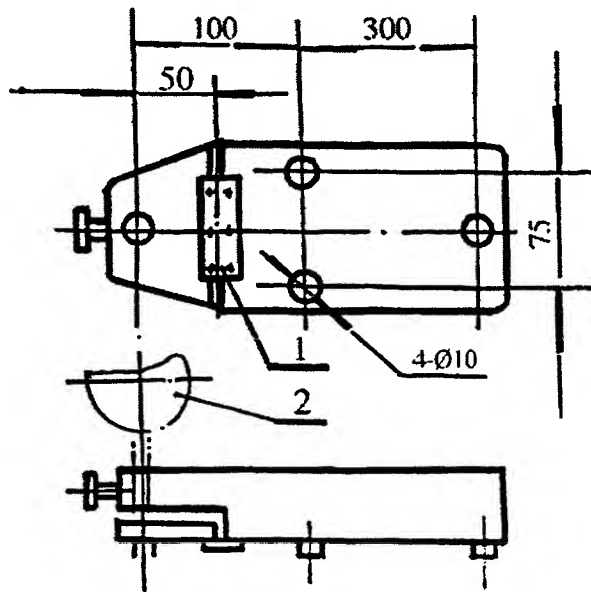


Figure 1 Instrument of plane wave quantity

1. Spring film 2. Measurement Watch

There are many advantages by using the plate wave quantity and their appropriate plate waves detector to assay the partial plane error. Such as the structure of the instrument is reasonable, and the working is credible and the usage method is convenient, and it can also figure out the value of the plate wave quantity. Comparing with other methods, this method is easier to carry out, the checking result is more accuracy, and it can reduce the checking issue and the examination clerk's labor intensity.

At present, the instrument of the assay, which is plate wave detector, is not yet widespread. The assay method is not spread. The main reason of this is short of thorough study about the detecting principle of plane wave detector. The explanations about the assayed data are not unified and lack relation to the contact spot. This paper gives a detail derivation about the detecting principle of plane wave detector and the relationship between the partial plane error and the partial defect of the plate and the plane wave quantity. And it also inquires the relationship between the contact spot and 200mm straight-line wave and plane wave quantity on the basis of this.

1. THE ASSAY PRINCIPLE & SIGNIFICANCE OF THE PLANE WAVE DETECTOR

1.1 Assumption

We can assume the following before we derive the principle of the plane wave detector:

1.1.1

The whole plane degree usually presents a single convexity or concavity or the type of saddle because the plane degree of the plate working surface is achieved by manual grind or scrape. So the cross line which is crossed by any section which is vertical with the plate working surface and the actual surface of the plate working surface usually appears the type of sine curve, and mostly it will not exceed a half wavelength.

1.1.2

The change of partial plane error, especial the partial plane error of the plate by scrape, is rather complex, but the partial plane error of the regular plate working surface will firstly not be greater than the plane degree of the whole plate and secondly be confined within a certain range such as about $1/3$ or $1/5$ of the whole plane degree.

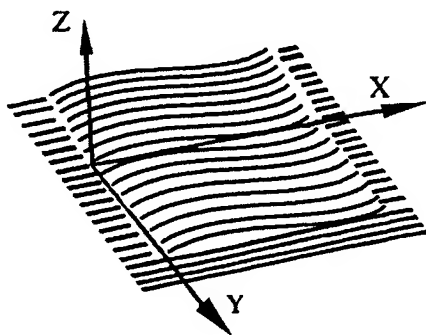


Figure 2 Actual of plane working surface

1.1.4

The edge of the scratch on the plate presents double peaks. It is treated as single peak.

1.1.5

The reading of the micrometer of plane wave detector $Z(x) \ll l$ (The "P" is the distance between the fixed points.).

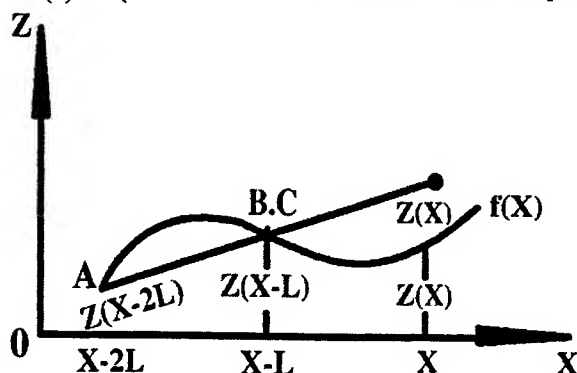


Figure 4 Principle of plane wave quantity

(Figure4) present actually the plane offset which is determined by x point and the three fixed points. In other words, the plane wave quantity represents the maximum angle deferent value of all tangent plane of which is formed by the three fixed points on the dragging direction of the plane wave detector in fact. The angle deference is transferred into linear value by the plane wave detector and showed by micrometer. The height change of each fixed point represents a new plane. So the value of $Z(x)$ is changed with its change. The transfer function is separately:

$$\begin{aligned} Z(x) &= z(A), \\ Z(x) &= -z(B) = -z(C), \end{aligned} \quad (1)$$

The reading of the plan wave detector $Z(x)$ is:

1.1.3

As above, we can regard the cross line which is crossed by any section which is vertical with the plate working surface and the actual surface as a sine curve, and it can be divided into horizontal (X) actual contour line and vertical (Y) actual contour line according to the difference of the sectional direction. Generally their types can be supposed as Figure 3. Figure 3(a) is actual contour line, and Figure 3(b) is that divided it into long period error and short period error. Short period error represents partial plane degree, which can be checked out separately.

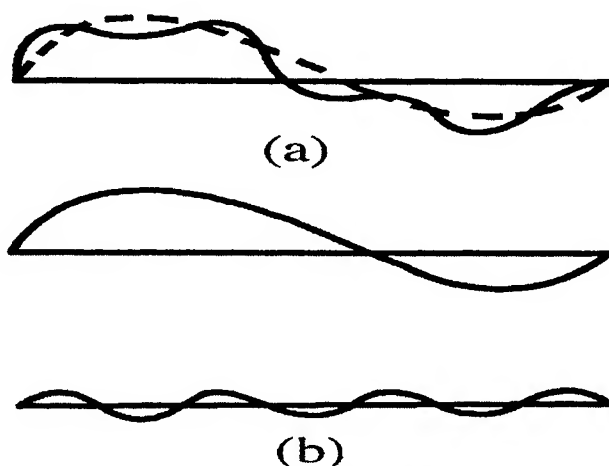


Figure 3 Actual control line of plane working surface

1.2 The Assay Principle

We will analyze the change and assay principle of plane wave detector's reading when the detector is dragged on several different type of surface.

1.2.1 Sine Function

The reading of the micrometer of plane wave detector $Z(x)$ (Figure4) present actually the plane offset which is determined by x point and the three fixed points. In other words, the plane wave quantity represents the maximum angle deferent value of all tangent plane of which is formed by the three fixed points on the dragging direction of the plane wave detector in fact. The angle deference is transferred into linear value by the plane wave detector and showed by micrometer. The height change of each fixed point represents a new plane. So the value of $Z(x)$ is changed with its change. The transfer function is separately:

$$\begin{aligned} Z(x) &= z(A), \\ Z(x) &= -z(B) = -z(C), \end{aligned} \quad (1)$$

The reading of the plan wave detector $Z(x)$ is:

$$Z(x) = z(x) - z(B) - z(C) + z(A), \quad (2)$$

If the actual contour line of the plane wave detector's dragging direction is a sine curve which amplitude is hx , wavelength is λx , as it is $Z(x) = hx \sin(2\pi x / \lambda x)$, and the curvature of the actual contour line which cross B, C fulcrums is no change and it is orthogonal with xoz plane, the reading of the plane wave detector's micrometer is :

$$\begin{aligned} Z(x) &= z(x) - z_y(x-l) + z(x-2l) \\ &= hx \sin(2\pi x / \lambda x) - 2hx \sin[2\pi(x-l) / \lambda x] + hx \sin[2\pi(x-2l) / \lambda x], \end{aligned} \quad (3)$$

If the actual contour line which cross B, C fulcrums is regarded as a sine curve which amplitude is hy , wavelength is λy , as it is $Z(y) = hy \cdot \sin(2\pi y / \lambda y)$, and there is creepage in y direction when the plane wave detector is dragged along x direction, the Formula (3) is transferred into:

$$Z(x) = hx \sin(2\pi x / \lambda x) - hLB \sin[2\pi(y-0.75l) / \lambda y] - hyC \sin[2\pi(y-0.75l) / \lambda y] + hx \sin[2\pi(x-2l) / \lambda x], \quad (4)$$

This is the analytic formula of the reading of the plane wave detector's micrometer. Its plane wave quantity δ is

$$\delta = |Z(x)_{\max} - Z(x)_{\min}|, \quad (5)$$

From Formula (3) and Formula (5) we can see:

When $l = \lambda$, $Z(x) = 0$, $\delta = 0$;

When $l = \lambda/2$, $Z(x)_{\max} = 4h$, $Z(x)_{\min} = -4h$, $\delta = 8h$;

When $l = \lambda/4$, $Z(x)_{\max} = 2h$, $Z(x)_{\min} = -2h$, $\delta = 4h$.

1.2.2

When the amplitude of horizontal and vertical actual contour line $hx = hy = 0$, it can be seen from Formula (4) and (5) that:

$$Z(x) = 0 \quad \delta = 0$$

which presents that the partial plane error $f = 0$ at this time.

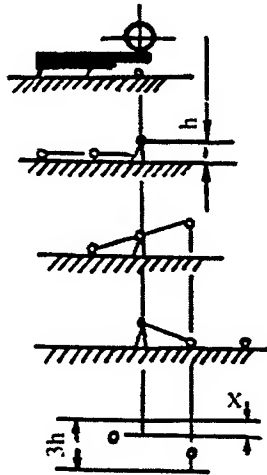


Figure 5

Perpendicular Scratch's measurement

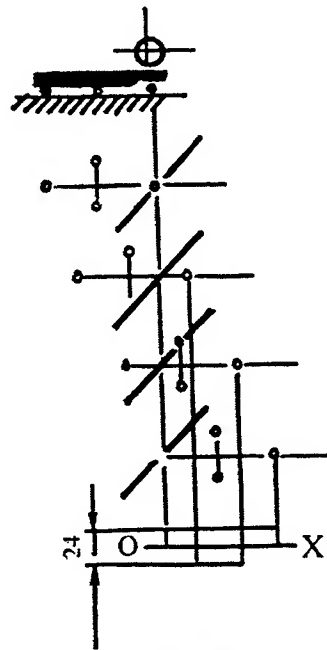


Figure 6

Level Scratch's measurement

1.2.3

When the wavelength of actual contour line $\lambda \geq d$ it can be seen from Formula (4) and (5) that:

$$Z(x) = 0 \quad \delta = 0,$$

which declares that the partial plane error present a single convexity or concavity. The partial plane error $f=2hx$.

1.2.4 Scratch

If there is a scratch that is vertical with the dragging direction of the plane wave detector, and the height of the scratch is h , the change quantity of the detector's reading is $3h$ (Figure 5).

The plane wave detector's reading doesn't have changes because the scratch on the rock plate cannot cause a heave and the $\phi 10\text{mm}$ fulcrum of the plane wave detector has the function of mechanical filtration.

If there is a scratch which appear a α angle with the dragging direction of the plane wave detector and the height of the scratch is h , the change quantity of the detector's reading is $2h$ (Figure 6).

2. THE EXPLANATION OF THE ASSAY RESULT

2.1

From the above analysis we can see that there is a certain relationship among the plane wave quantity δ and the partial plane degree f and linearity along the dragging direction h (scratch) or $2h$ (sine curve). In this paper we derive its mathematical expression under the certain assumption, but the results derived from the mathematical expression have some change with a certain range under different circumstance because the change of the partial plane degree is rather complex. In summary:

To sine curve $\delta = (0 \sim 4)f$ or $\delta = (0 \sim 4)2h$;

To scratch $\delta = (0 \sim 3)f$ or $\delta = (0 \sim 3)h$;

If the single convexity or concavity is regarded as long period error, as the whole plane degree and the scratch of the rock plate are not considered because they will not affect the usage, and exclude some accidental factors (such as $\lambda = l$), under the common circumstance it will be:

To sine curve $\delta = (2 \sim 4)f$ or $\delta = (0 \sim 4)2h$;

To scratch $\delta = (2 \sim 3)f$ or $\delta = (2 \sim 3)2h$;

On the basis of this we also consider the influence of the vertical sections' linearity error and the dragging direction is optional, so the explanation of the relationship between the plane wave quantity δ and the partial plane degree f when enacting the National Standards :

$$\delta = (3 \sim 4)f \quad (6)$$

is reasonable to some extent.

2.2

Take a $1600\text{mm} \times 1000\text{mm}$ regular 0 level scraped plate for example. There are more than 1.6 million contact spots. The number of checked points is 25 when it is assayed by the method of node distance, which is six per ten thousand. Many error information will be lost. So the assay of the whole plane degree can only confirm its long period error. The assay of the

partial plane error of short period error is similar. Now all the technique indexes of partial plane degree which include contact spot, smoothness, 200mm linearity, short node distance, the measure error caused by repeating reading and the plane wave quantity are all its substitute quantity. They all lack a quantitative and certain mathematical manipulation with partial plane degree.

The structure of the plane wave detector is simple and it adopts floating zero and continual measure and it can show the results directly. Because of the above reason we cannot expect that can acquire the certain value of the plate working surface's partial plane error with so simple appliance and by so simple measure.

2.3

Comparing to other substitute quantity of partial plane degree the plane wave detector has some advantage such as the structure of the instrument is reasonable, and the working is credible and the usage method is convenient, and it can also figure out the assay results, and it can effectively avoid the argument due to the assay which is carried out with sense organ. So it should be widely spread.

ACKNOWLEDGMENTS

For this project, ours working get support from research follows at Xi'an Institute of Optics & precision Mechanical (XIOPMZ) and North-western polytechnical University. We very thank them in here.

REFERENCES

1. Long-sheng Zhou , *measurement and control from precision plane* p3-13, machine industry publisher society, Beijing, 1987.
2. GB4986~1987-85, *Caste-Iron plate & Rock plate*, p9, Chinese standardization publisher society, Beijing, 1990.

* Correspondence: Telephone: (8629) 8498711(O), (8629) 8498676(H), Fax: (8629) 8484473

IMAGE CONVERTER TUBE USE IN VUV.UV.VISIBLE LIGHT

Xiao-qiu Zhang, Li-hong Niu, Mai-Xia Gong ,
Yua-Xing Zou, Jun-Qi Liu.

State Key Laboratory of Transient optics Technology, xi'an Institute of optics & precision Mechanics, xi'an Shaanxi 710068. The people's Republic of china.

ABSTRACT

Ultra high-speed streak cameras with image converter tubes play a very important role in the diagnosis of most experiments in laser fusion research.

The window materials of the image converter tube usually applied borosilicate glass, but it is only transparent for visible light. In order to apply in VUV.UV.visible light region for the tube, we used MgF_2 window material in the tube and exhibits excellent performance on the photocathode sensitivity and spectral response in the image converter tube.

Keywords: Image converter tube , streak camera, spectral response.

INTRODUCTION.

The Streak Camera has become one of the most versatile instruments for measurement of the dynamic behavior of luminous events. Its advantages are ability to determine optical temporal profiles directly with excellent time resolution and superior sensitivity. Recently , we have developed a streak camera utilizing a MgF_2 -window incorporated streak tube which has been modified for VUV.UV spectral range . The streak tube exhibits excellent performance on the photocathode sensitivity and spectral response.

1. STREAK CAMERA EXPERIMENTED SYSTEM

As shown in (Fig.1), the streak camera consists of a streak tube incorporating a MgF_2 window, input and output optics, a high voltage power supply ,a gating pulse generator and a push-pull circuit of generating sweeping voltage.

The light gain of the streak camera is controlled by changing the MCP voltage of the intensifier. The trigger pulse from the PIN diode is 5-40 $V_{pp}/50\ \Omega$, the image readout system using a CCD camera, easily gives access to a fast and automatic acquisition of the records. Fig.2 is a VUV. UV streak camera.

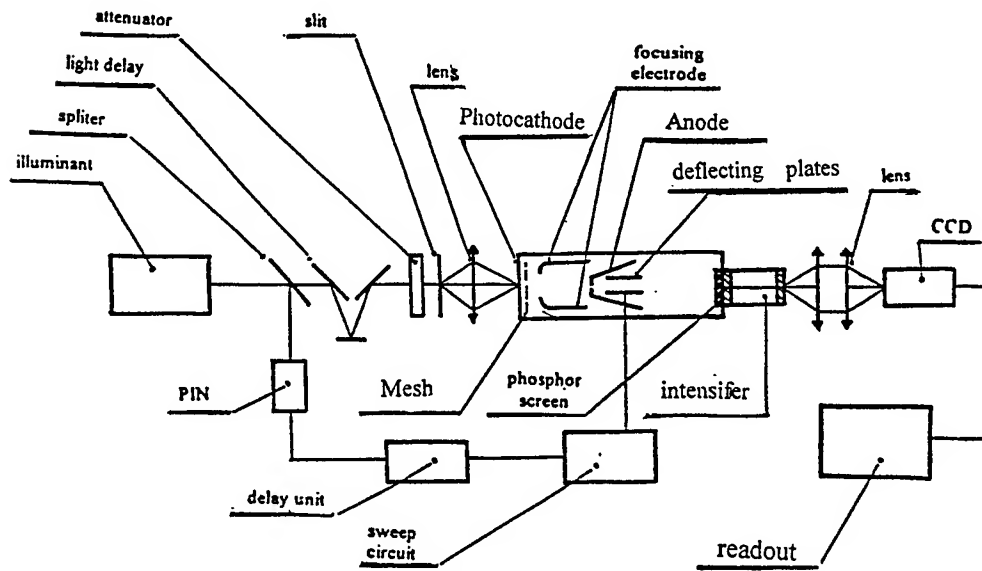


Figure 1 Block diagram of the streak camera.

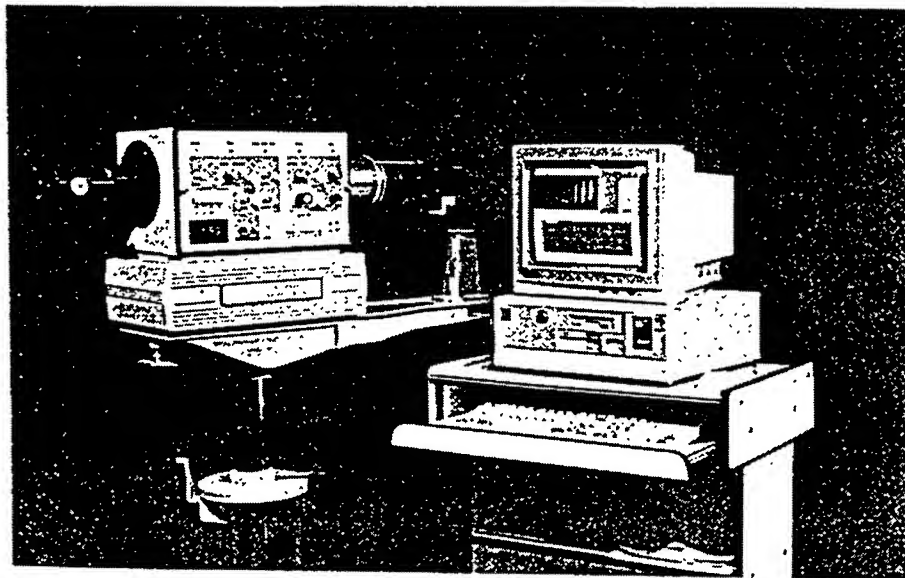


Figure 2 UV streak camera photo.

2.IMAGE CONVERTER TUBE

The image converter tube have four electrodes of axial symmetrical electron lens consisting of photocathode, accelerating mesh, focusing electrode and anode. The deflection system of the tube using parell plate deflector. Fig.3 shows a cross section of the image converter tube structure .

The performance characteristics of the image converter tube are shown in table 1.

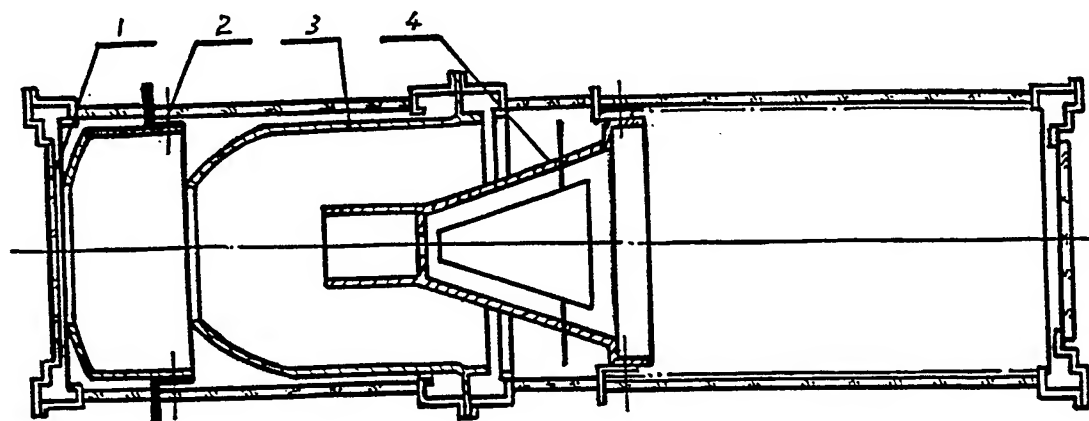


Figure 3 Cross section of the image converter tube structure .

1. photocathode ; 2. Mesh; 3. focusing electrode; 4. Anode;

Table 1 characteristics of the streak tube.

Categories	Specifications
1. window material	MgF ₂
2. photocathode type	S20
3.conductive substrate of the photocathode	Aluminium alloy film
4. Useful photocathode size	24mm Dia
5. Phosphor screen	P20
6. phosphor screen output windows material	Plane-parallel fibre optic faceplate
7. Useful Phosphor screen size	48mm Dia
8. Image magnification	1:2
9. spectral response	115~850nm
10.dynamic range	>200:1(slow sweep)
11.spatial resolution	>25lp/mm
12.Deflection sensitivity	40mm/kv
13.Light Gain of the external intensifier	>1×10 ⁴
each electrode potentials	
14.photocathode	-12kv
15.mesh	-10kv
16.focus	-11.2kv
17.anode	0v

3. PHOTOCATHODE OF THE IMAGE CONVERTER TUBE

In order to measure transient phenomena of VUV & UV spectral range, we used the MgF₂ window image converter tube. The plane MgF₂ window is sealed on the image tube by low melting point glass powder maintained at a temperature of about 460°C in Furnace. The image tube with MgF₂ window showed excellent detector in the spectral threshold. The transparency curve of MgF₂ window is shown in figure 4, the vacuum performance of MgF₂ window is very well. The active diameter of the MgF₂ window is 20mm. An electrical conductive film is applied by evaporating alloy aluminium wire before processing photocathode. The resultant coat of film has a resistivity of about 50ohm. It is resistant to multialkali metal vapour. The curve of the spectral transparency of the electrical conductive film is shown

(figure 5.). The semitransparent S_{20} photocathode has been proceed on the film.

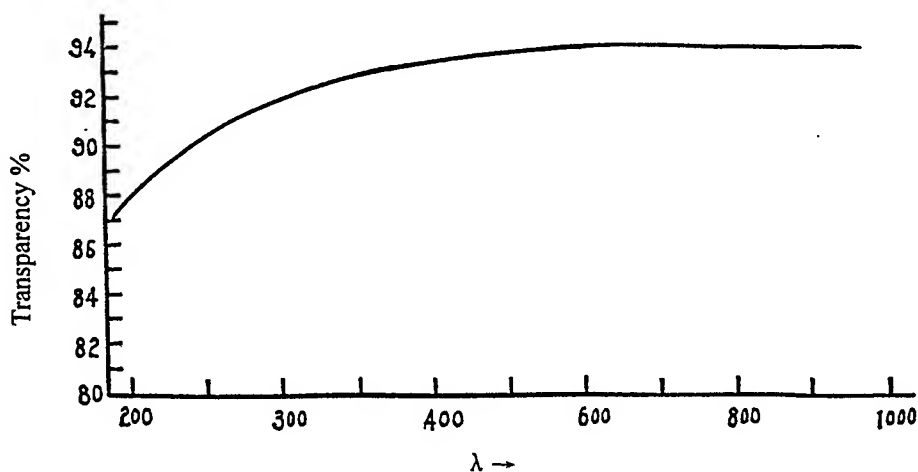


Figure 4 spectral transparency curve of MgF_2 window .

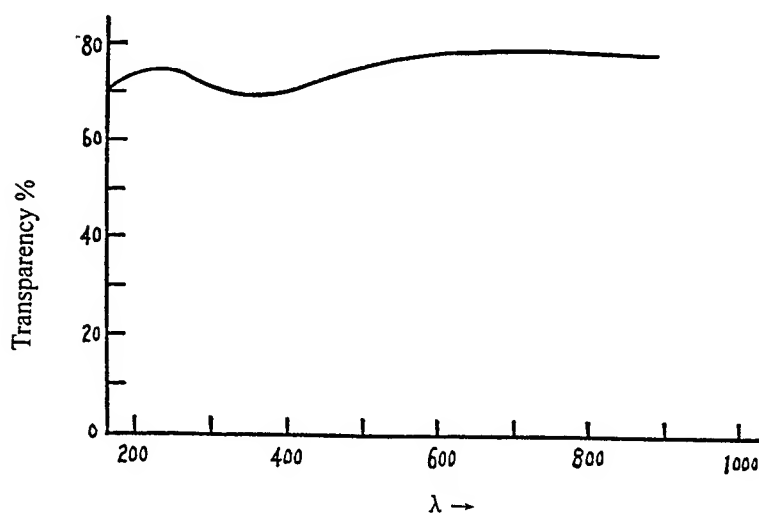


Figure 5 Curve of the spectral transparency of the electrical conductive film.

The measurement of the photocathode response is made by uniformly illuminating a 2.0cm diameter area of the photocathode with a distant lamp and by directly measuring the resulting photocurrent with an electrometer . A series of 20nm bandwidth filters are used to define several spectral regions throughout the wavelength interval 300-850nm. Curve of the spectral sensitivity of photocathode is shown in figure 6.

4. CONCLUSION

The streak camera with MgF_2 window image converter tube play a important role in the diagnosis of most experiments in Laser fusion research and Laser measurements. The measurements of the pulse width of KF laser (248nm) and XeCl laser (308nm) has been shown the excellent performance of the streak camera .

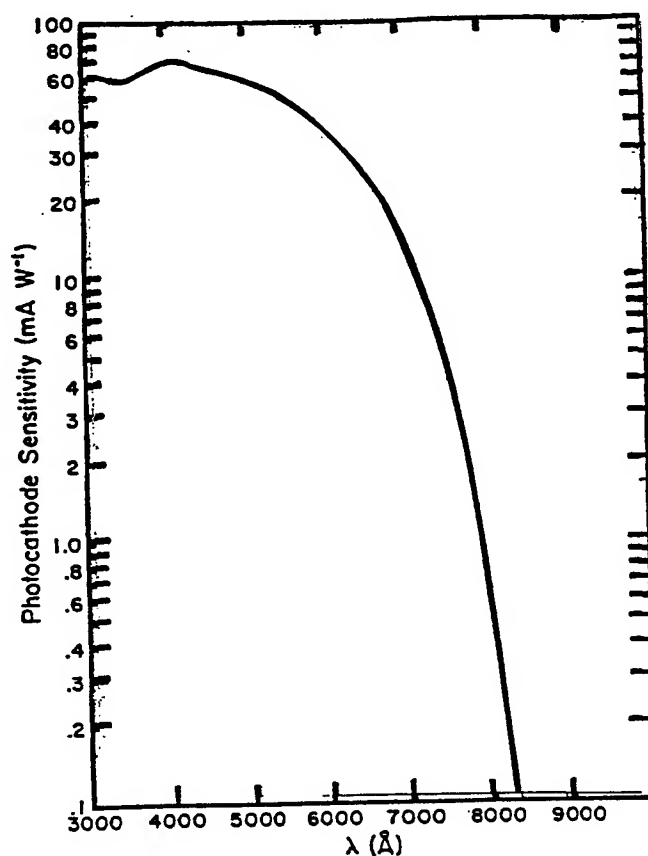


Figure 6 Curve of the spectral sensitivity of the photocathode .

ACKNOWLEDGMENTS

The authors wish to thank Directors of state Key laboratory of transient optics technology to support this work, also wish to thank ying Wu and yi-mei Xu to help for manufacture of streak tube. Special thank xiao-hui Guo and xiao-hong Bei for optical measurements of the image tube.

REFERENCE

1. X . Zhang, M.Gong, Z.Chang, "Picosecond soft x-ray streak camera" . 18th International congress on high speed photograph and photonics p102. 1988.
2. X.Hou ,X.Zhang, M.Gong, Z.Chang, "Picosecond x-ray streak camera improvement" , 19th International congress on high speed photograph and photnics p868,1990.
3. Z.Chang, X.Hou , X.Zhang, M.Gong, L. Niu, "Development of picosecond x-ray framing camera " , 19th International congress on high speed photograph and photonics, p614,1990.

correspondence, weiz@optics.opt.ac.cn Telephone (8629) 8498711. Fax : (8629)8498711

Optical Refractive Synchronization - Bit Error Rate Analysis And Measurement

J. R. Palmer
SilkRoad, Inc.
9707 Waples St., San Diego, Ca. 92121
U.S.A.

Abstract

The direction of this paper is to describe the analytical tools and measurement techniques used at SilkRoad to evaluate the optical and electrical signals used in *Optical Refractive Synchronization* for transporting SONET signals across the transmission fiber. Fundamentally, the direction of this paper is to provide an outline of how SilkRoad, Inc. transports a multiplicity of SONET signals across a distance of fiber > 100 Km without amplification or regeneration of the optical signal, i.e., one laser over one fiber.

Test and measurement data are presented to reflect how the SilkRoad technique of *Optical Refractive Synchronization* is employed to provide a zero bit error rate for transmission of multiple OC-12 and OC-48 SONET signals that are sent over a fiber optic cable which is >100Km. The recovery and transformation modules are described for the modification and transportation of these SONET signals.

Analytical Model

Basically, there are several techniques associated for the calculation of the Bit Error Rate, i.e., BER. The one commonly used is provided by the following formulation for the complimentary error function, commonly known as the Gaussian Error Integral. So that,^{(1),(2),(3),(4)}

$$2 * \text{BER} = \frac{2}{\sqrt{\pi}} \int_0^x e^{-t^2} dt = \frac{1.0}{2} \text{Erfc}(x) \quad (1)$$

where;

$$x = \frac{\sqrt{S}}{2\sqrt{2}N}$$

For the Optical SNR, we have,

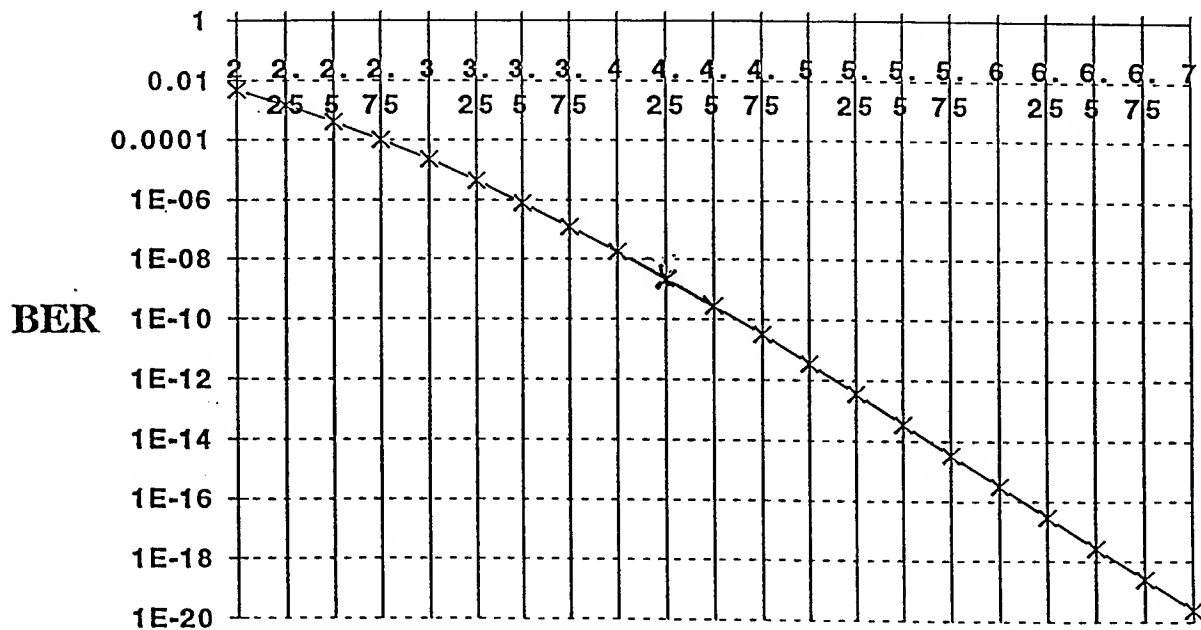
$$\frac{i \text{ sig}}{\sqrt{i N}} ; \frac{S}{N} = x^2 \cdot \sqrt{2} \quad \text{and } Y_{dB0} = 10 \text{ Log}_{(10)} [x^2 \cdot \sqrt{2}] \quad (2)$$

For the Electrical SNR, we have,

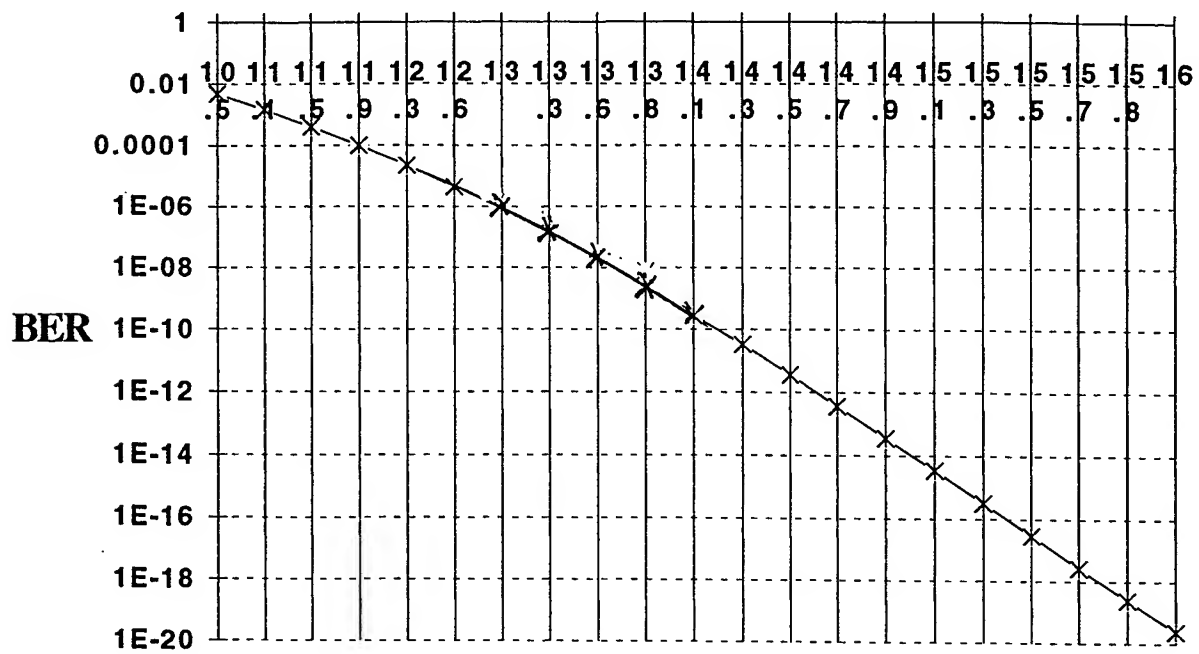
$$\frac{i^2 \text{ sig}}{\sqrt{i N}} ; \frac{S}{N} = [x^2 \cdot \sqrt{2}]^2 \quad \text{and } Y_{dB0} = 10 \text{ Log}_{(10)} [x^2 \cdot \sqrt{2}]^2 \quad (3)$$

Based on the equations above, we can plot BER as a function of the erfc value. Such that,

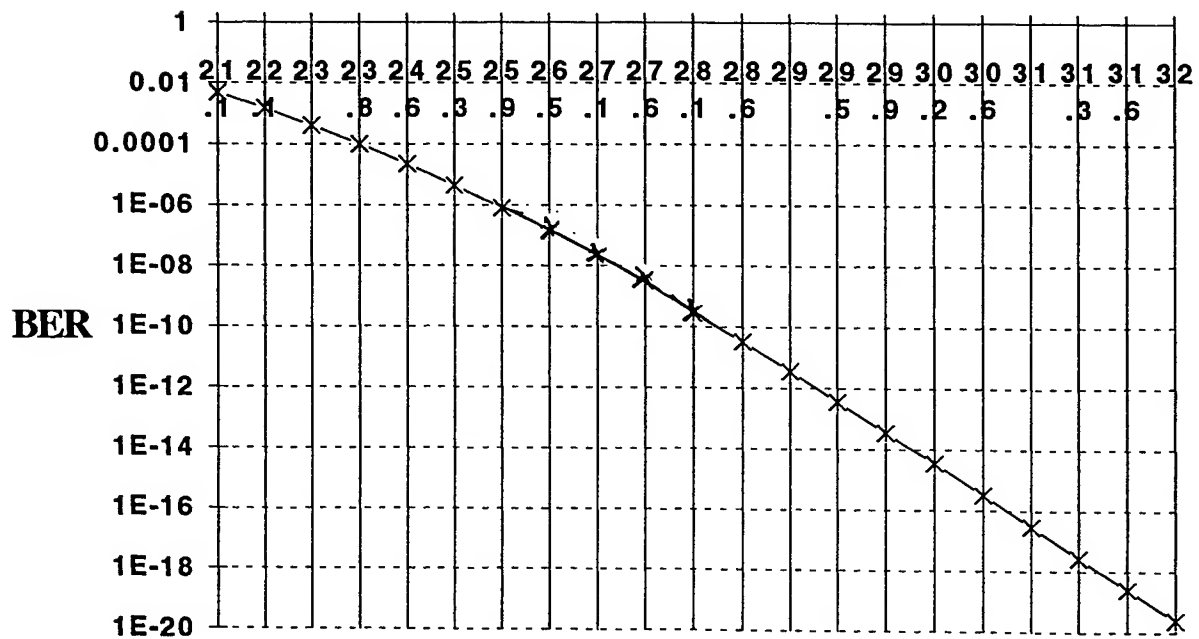
BER As a Function of the value of ERFC (x)
value of x



BER Versus The Optical Signal To Noise Ratio
S/N in dB



BER Versus The Electrical Signal To Noise Ratio
S/N in dB



(2)
 Silbey provides a somewhat broader set of definitions for defining the BER. He states, "The task of any processing circuitry is to determine with the minimum uncertainty, whether a 1 or a 0 was received. This is done by a threshold crossing device, or comparator, feeding a D-type flip-flop. The circuit operation is best explained by examining the eye diagrams at certain relevant points. . . the optimum threshold level is mid-way between the logic 1 and 0 levels." Sibley goes on to show the conditions of probability being equal for 0 and 1; then the noise has a Gaussian distribution,

(4)

$$P_{e011} = \frac{1.0}{\sqrt{2 \pi \sigma_{\text{off}}^2}} \int_{-\frac{V_T}{2}}^{\infty} e^{-\frac{(v - v_{\text{min}})^2}{2 \sigma_{\text{off}}^2}} dv \quad (5)$$

$$P_{e110} = \frac{1.0}{\sqrt{2 \pi \sigma_{\text{on}}^2}} \int_{-\infty}^{\frac{V_T}{2}} e^{-\frac{(v_{\text{max}} - v)^2}{2 \sigma_{\text{on}}^2}} dv$$

where;

σ_{on} and σ_{off} = r.m.s noise voltages at the comparator input

V_T = Threshold voltage

v_{max} , v_{min} = The received signal levels at the sensor

The optimum voltage lies midway between v_{min} and v_{max} . If V_T is biased to the left or right, it does so at the expense of either P_{e011} or P_{e110} .

With these assumptions in mind, then,

(6)

$$P_e = P_{e011}$$

$$= \frac{1.0}{\sqrt{(2 \pi \sigma^2)} V_T} \int_0^{\infty} e^{-\frac{(v - v_{\text{min}})^2}{2 \sigma^2}} dv$$

where;

$$\sigma_{\text{on}} = \sigma_{\text{off}} = \sigma$$

Changing variables, so that $t = \frac{(v - v_{\text{min}})}{\sigma}$ and

(7)

$$P_e = \frac{1.0}{\sqrt{2\pi}} \int_0^{\infty} e^{-\frac{Q^2}{2}} dt$$

where;

$$Q = \frac{V_T - v_{\min}}{\sigma}$$

$$V_T = \frac{v_{\max} + v_{\min}}{2}$$

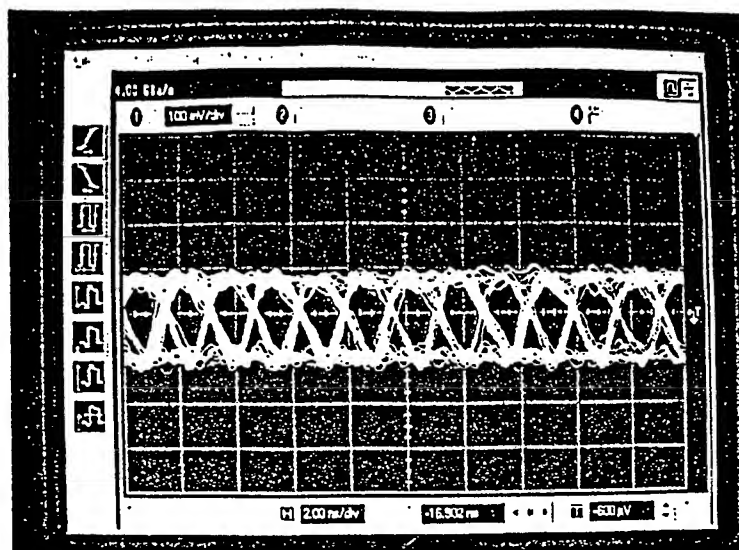
and

$$Q = \frac{v_{\max} - v_{\min}}{2\sigma}$$

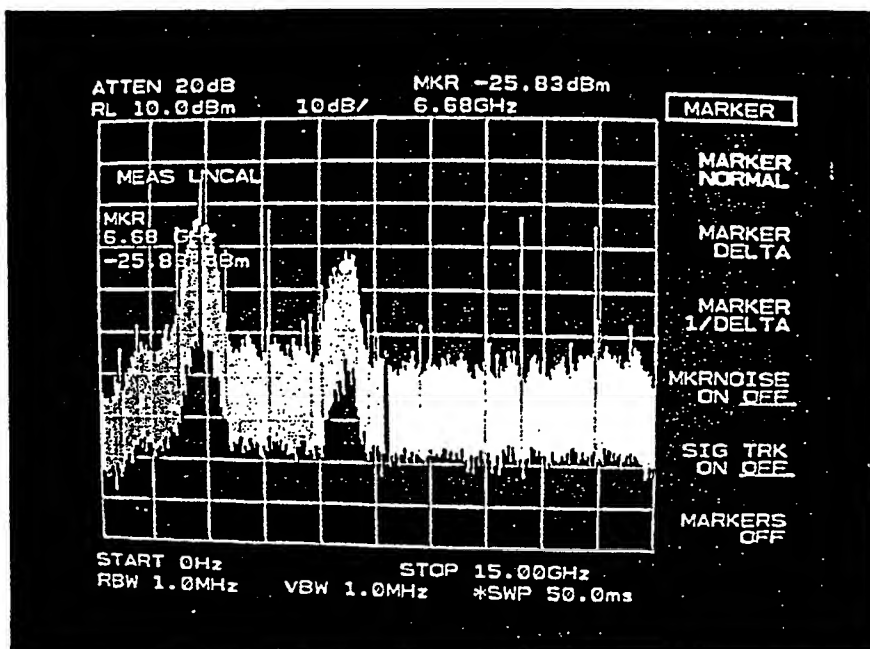
Consequently, if we know the signal voltage level and the r.m.s. noise voltage at the input, we can determine the error probability from Equation (7) which provides,

$$P_e = \frac{1.0}{2} \operatorname{erfc} \frac{Q}{\sqrt{2}}$$

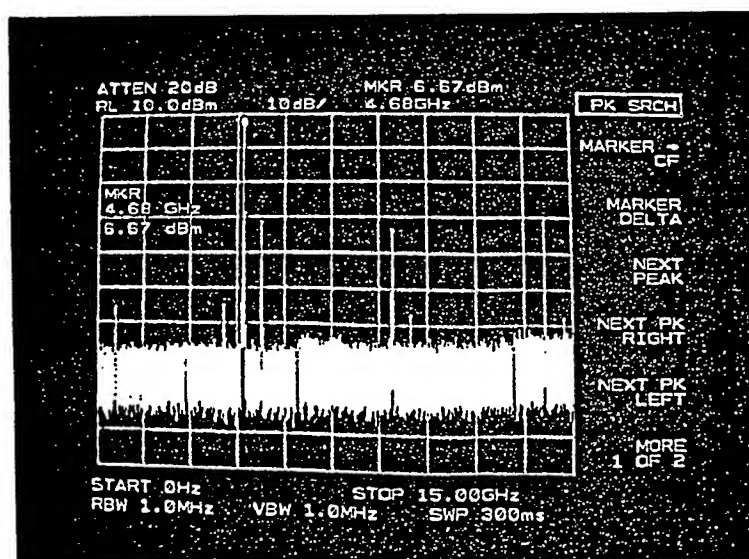
So, expressed in a different fashion, Sibley's technique is very much analogous to that shown for Eq. (1). SilkRoad employs a scheme wherein the square digital pulse is converted to a quasi analog signal by placing the clock frequencies in quadrature and sending the information through a proprietary digital to analog converter and sending this information onto the electroptical modulator which is then modulated onto the laser beam and subsequently sent down the fiber to the receiver where the process is reversed to homodyne the information from the clock frequencies and subsequently sent onto the customer's information network. The following photographs displays some of the equipment and description of the output signals that are used in the SilkRoad technique. It should be noted that experiments to date have refelected a zero (0) Bit Error Rate for over two hundred and fifty (250) hours of run time, running over >100 Km of fiber.



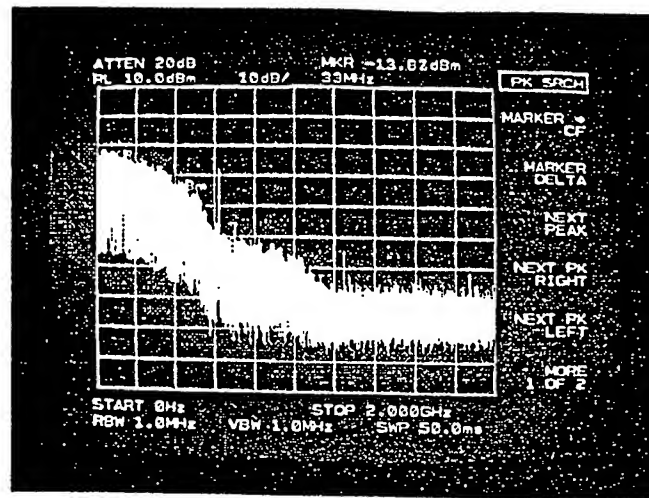
Out of Channel 1 to AMCC. Jan 26, 1999.



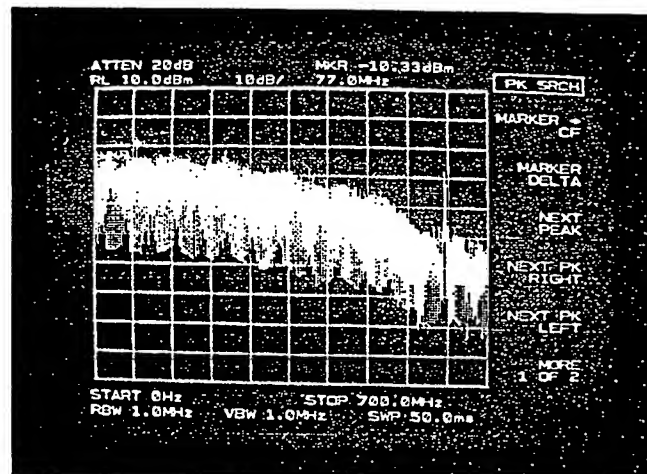
Levels out of Detector Module. The output levels from here are approximately the same as the level going to the Laser Modulator.



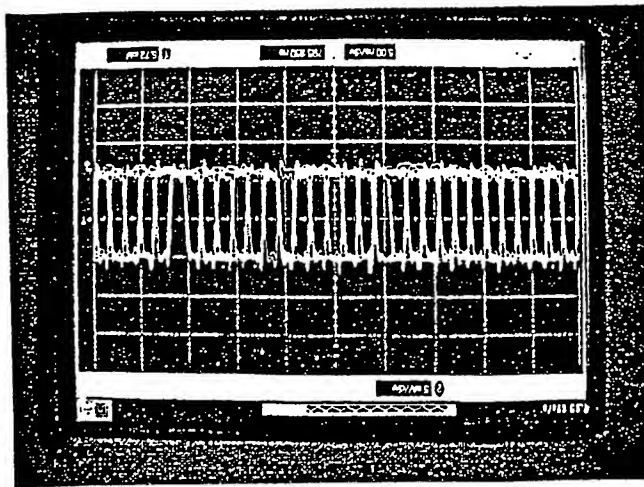
Bandpass Filter without K&L filter



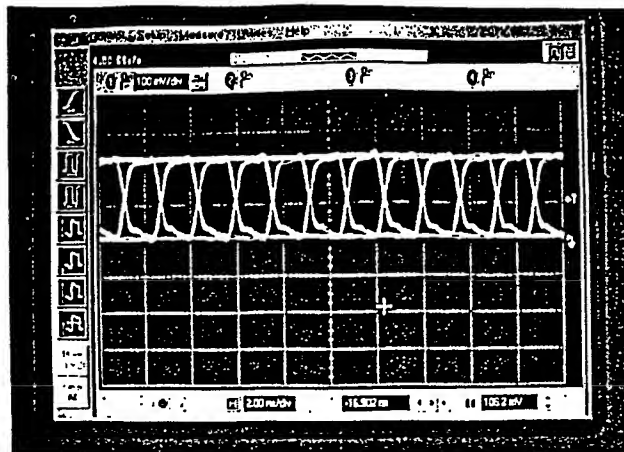
Upper Side Band of 622 MHz



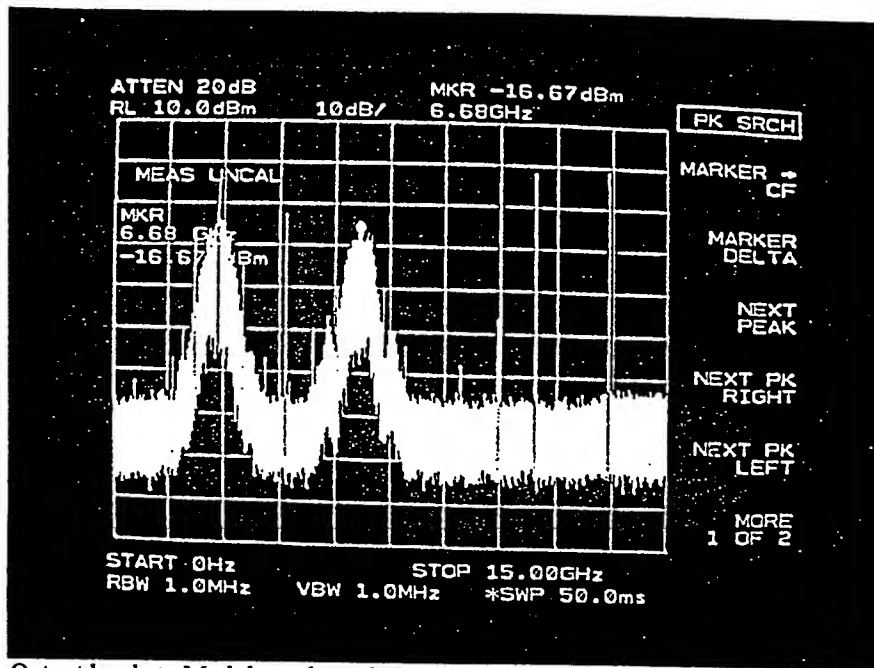
622 MHz Bandwidth



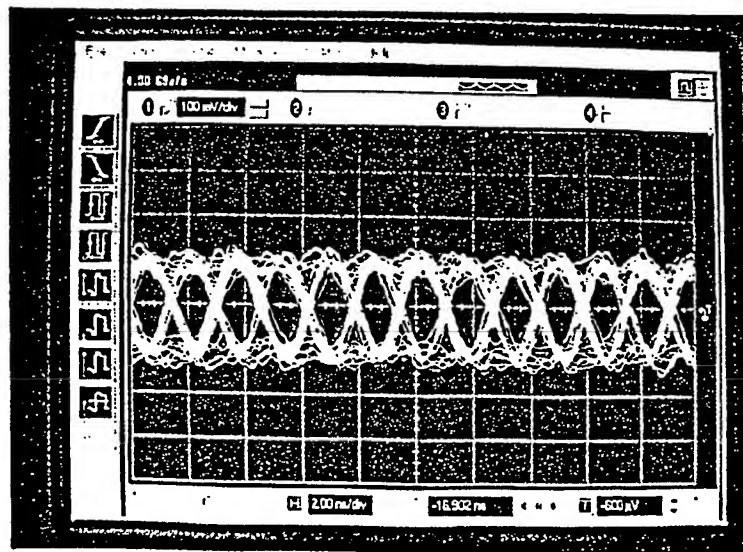
Output of Proprietary Analog to Digital Converter



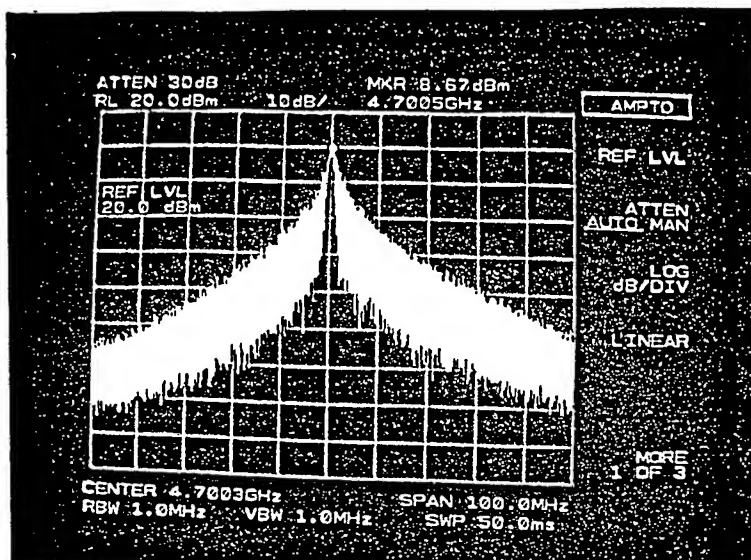
Channel 2 output from AMCC w/-10dB. Now about same as Channel 1. This will be fed into Harlan's output transmitter.



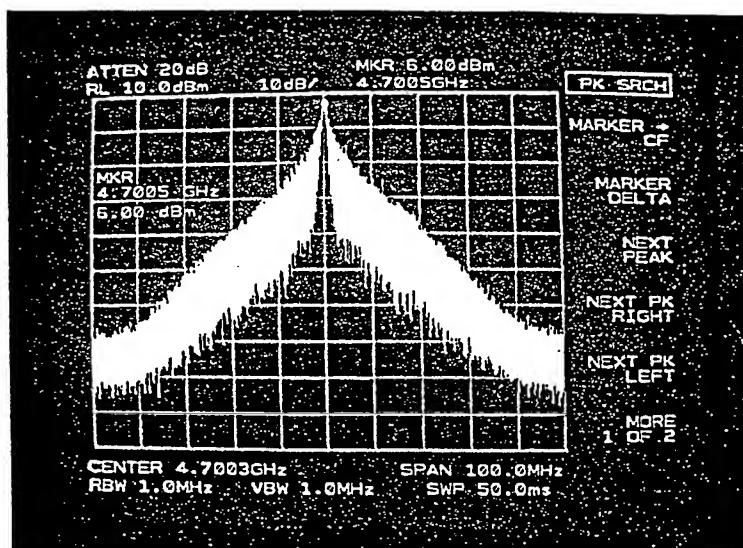
Output levels to Modulator through 8-way test combiner. The sideband to channel 1 is at -13dBm. The peak of the clocks are at -83dBm. The actual levels may be a bit higher since they are going through a 4-way in the actual module.



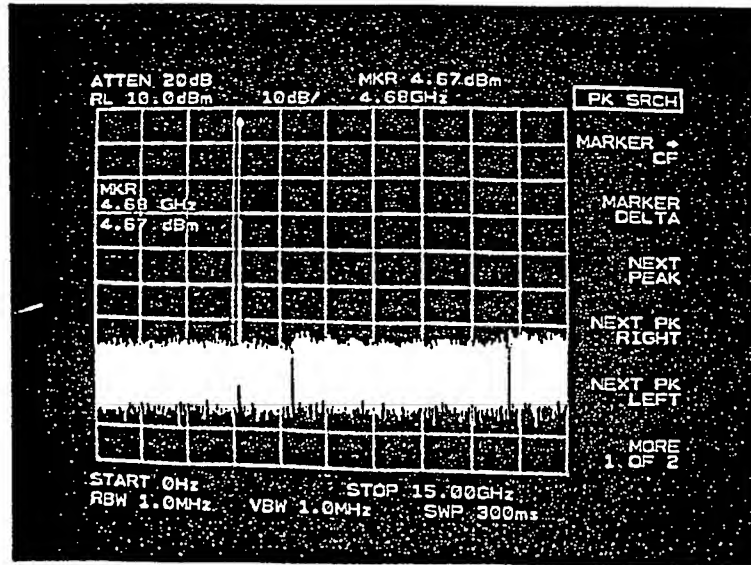
Out of Channel 2 to AMCC. Jan 26, 1999.



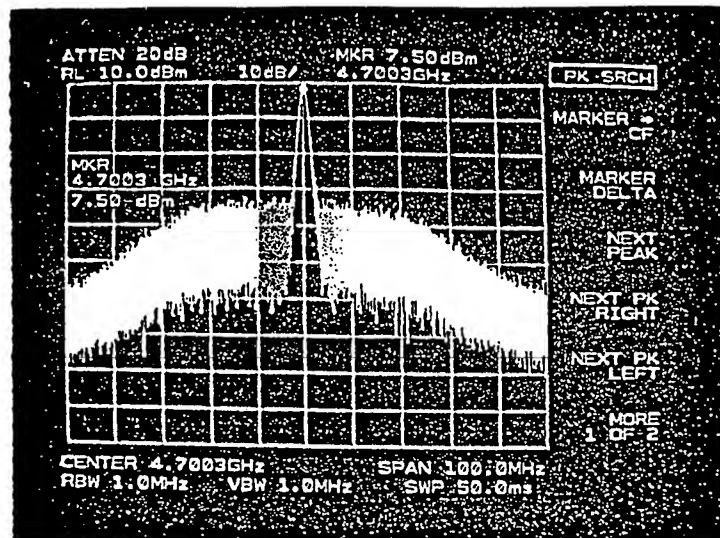
Bandpass Filter without K&L filter close-up span



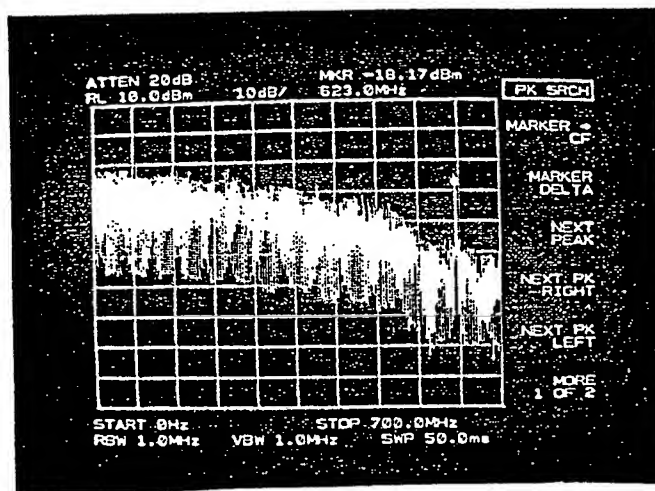
Bandpass Filter with K&L filter close-up span



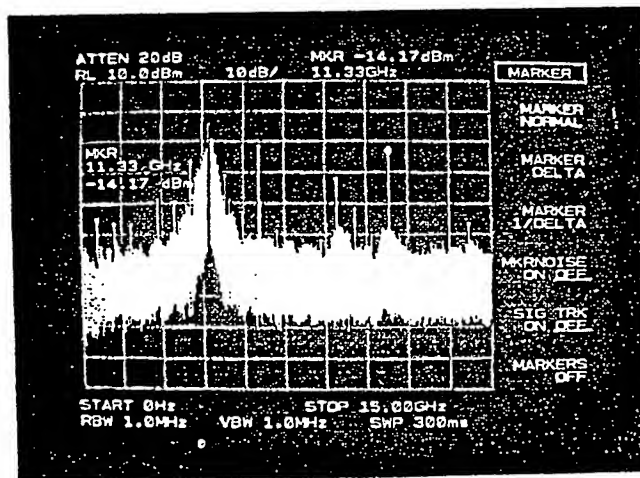
Bandpass filter with K&L filter



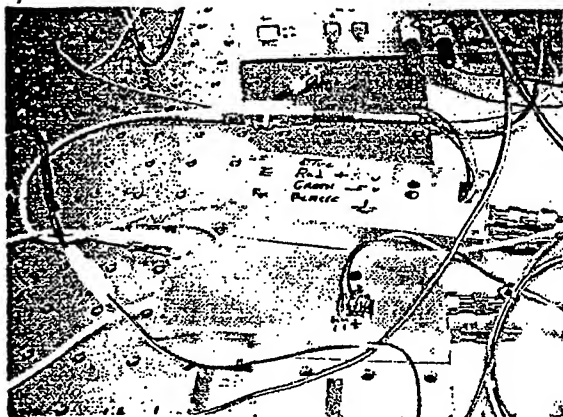
Tuneable Filter with Clock
Frequency at 4.7 GHz



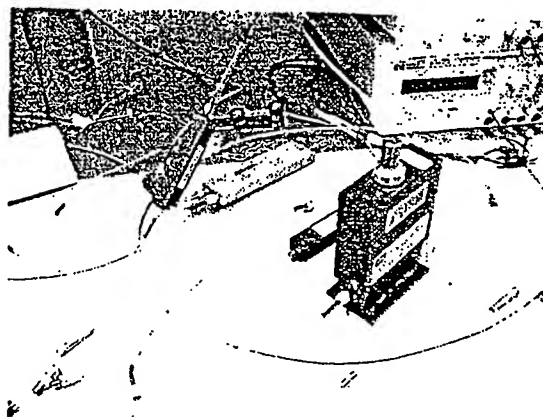
OC12 Spectrum Going Into Mixer



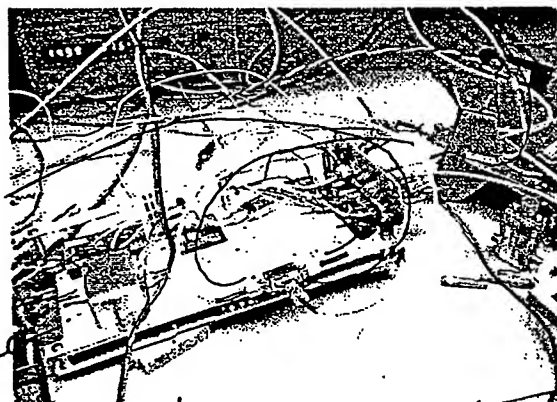
Clock Frequencies With OC12 Modulated Information



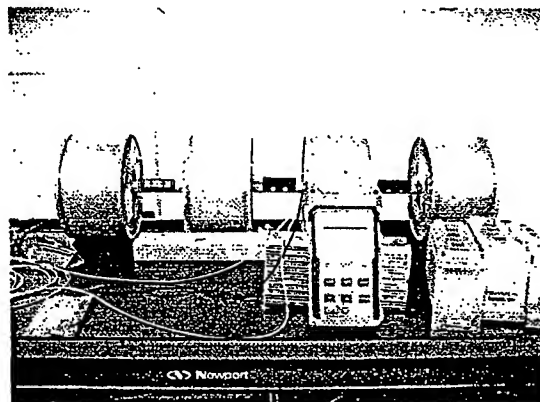
Analog to Digital & Digital to
Analog Signal



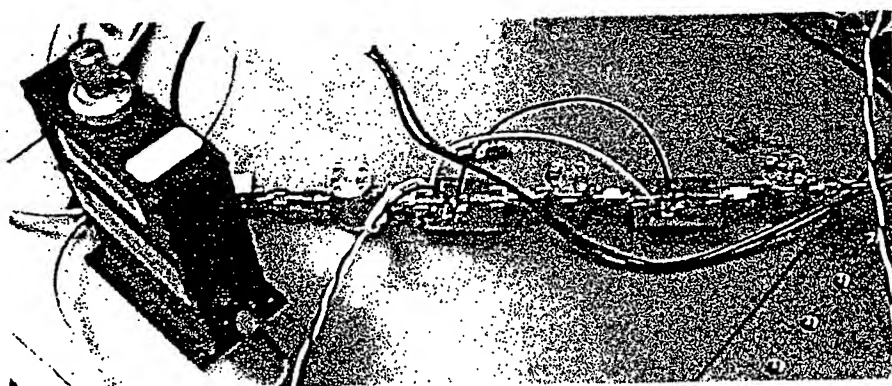
Trombone Filter with Phase Rotator



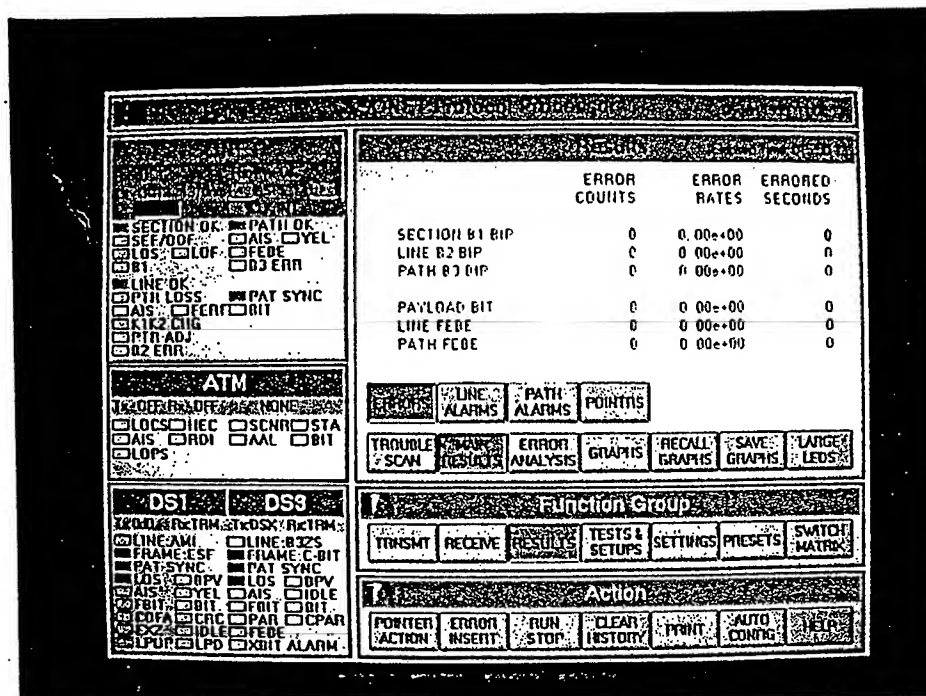
Transmitter Module



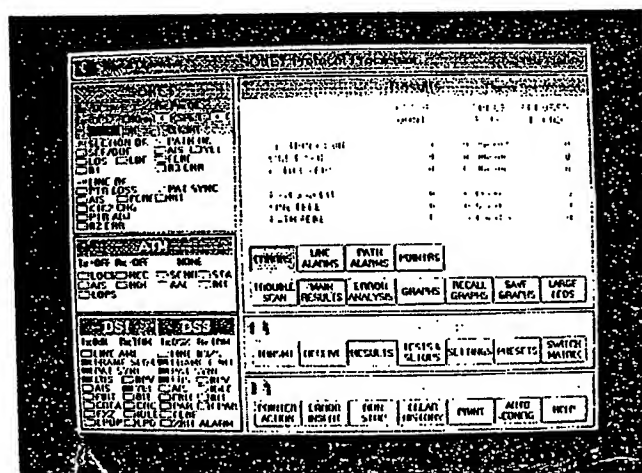
100 K True Wave Fiber



K & L Filter with Band Pass Filter & Amplifiers



System left on overnight January 5, 1998. This is channel 1 and 6. Non-active carrier receiver.



True Wave Sonet Signal Generator and Processor Showing 0 BER

References

1. J. R. Palmer, *High Power Laser Optics*, 2nd. ed., Pro Se Publications, San Diego, CA, 1997.
2. M. J. N. Sibley, *Optical Communications*, McGraw-Hill, Inc., New York, NY, 1990.
3. D. Derickson, ed., *Fiber Optic Test And Measurement*, Prentice Hall, Upper Saddle River, NJ, 1998.
4. R. Ramaswami and K. N. Sivaarajan, *Optical Networks: A Practical Perspective*, Morgan, Kaufmann Publishers, Inc., San Francisco, CA., 1998.

For Further Author Information:

Email: james.palmer@silkroadcorp.com
Telephone: (858) 457-6767
WebSite: <http://www.silkroadcorp.com>
Fax: (858) 457-6757
U.S.A.

Optical Refractive Synchronization - Bidirectional Information Transport Over A Single Wavelength-Single Laser For Distances >100Km-- Analysis And Measurement

J. R. Palmer

SilkRoad, Inc.
9707 Waples St, San Diego, CA, 92121

Abstract

The direction of this paper is to describe the experiments and analytical techniques used by SilkRoad, Inc. for sending 40 GHz of bandwidth, incorporating an eclectic body of data, over a single laser - single fiber over >100Km of optical fiber using the same wavelength in both directions. The paper will outline the various basic tenets of *Optical Refractive Synchronization* and the subsequent use of Ellipsometric Phase, based on these tenets, that allows a compilation of CATV, voice, video and SONET data to be transported in both directions without interference between the optical signals going in both directions over the single fiber.

The second portion of the paper will describe the test setup and measurement techniques that were used to validate the analytical models. Pictures of the Spectrum Analyzer data and the subsequent recovery of the eclectic information is then provided for all of the signals that have been transported.

Key Words: Optics, Polarized Light, Bandwidth, Fiber Optics, Ellipsometry

Introduction

There is great interest in the Telecommunications Technology arena to be able to conserve bandwidth and, subsequently, fiber space in the ground. In the early phases of information transport, up to and including today, information between point to point was enabled by the use of two fibers; one fiber

transporting information in each direction^[1]. There are some WDM (Wavelength Division Multiplexing) systems which are transporting information bidirectionally on a single fiber using two different

wavelengths^{[1],[2],[3]}. When using two different fibers it is not uncommon to have one or more EDFA (Erbium Doped Fiber Amplifier) in the fiber line between the two points. A common practice in terms of the EDFA when one uses two different wavelengths is to bifurcate the line so that one may use an EDFA in each direction and still take advantage of the optical isolation in the respective transmit direction.

In the case of *Optical Refractive Synchronization*, the line is also bifurcated, and for the same reason. However, unlike WDM, in the case of *Optical Refractive Synchronization*, we are using the same optical wavelength for transporting information in both directions. How the bifurcation is accomplished is described in the two experiments at the end of the paper.

Analysis

In this portion of the paper, we will undertake to describe the mathematical basis for the bi-directionality of the *Optical Refractive Synchronization*, that is employed with this technology. As we have outlined previously, *Optical Refractive Synchronization* is a compilation of optical techniques that are used

in concert to provide the coherency, line width and bandwidth^{[4],[5],[6]}. As we have suggested before, the laser cavity is maintained at a temperature such that the mirrors are controlled within $\pm 0.01^\circ\text{C}$ providing a single mode in the laser cavity. Additionally, the outcoupled laser beam is apodized to provide a TEM_{00} beam that is presented to the PM fiber attached to the laser and subsequently to the external modulator and on into the transmission fiber. As we have indicated before, this provides a Hermitian Gaussian temporal

distribution^[4]. There is a wisdom abroad that suggests that the single mode fiber will only support a TEM_{00} mode. This conventional wisdom needs to be challenged. The TEM_{00} is a function of the laser cavity and subsequent outcoupled mode of the laser. Laser Diodes are not known for outcoupling a TEM_{00} mode. Without apodization, a Diode Laser may very easily outcouple a TEM_{11} , or worse, which could be a single mode and which the single mode fiber will support. The problem with this mode, however, is that it will not travel very far down the single mode optical fiber. It may also provide a serious problem to modulation in the external modulator in attempting to generate the appropriate Laguerre Orders

for propagation^{[7],[8],[9]}. A good example of how the Laguerre Orders are distressed by the beam quality is shown in *Figure 2.0*. In *Optical Refractive Synchronization*, the Laser cavity is tightly controlled and is designed to provide only a single mode, which will also provide a very narrow line width^[10].

Optical Beam Quality Requirements For Launching Onto The Fiber Cable

Unfortunately, it would appear from the literature that the major concentration in the communications industry has been the electrical considerations. There is a dearth of consideration given to the very real concerns relative to the optical considerations. To that end, I feel that I should provide a brief outline of the optical considerations that are required to launch the laser beam transmitter onto the fiber optic cable. Actually, the following considerations should be applied whether in a guided wave or into free space.

There has been substantial discussion relative to beam quality and how it is to be quantified in the high power commercial laser arena and very little in commercial communications industry. In the very high power laser area, the concern has been mainly in how to provide a wave front that would provide a near diffraction limited Airy Disc in the far field. That is, how do we take the laser beam from the cavity and manipulate the beam quality and wave front so that the power of our laser is maximized in the far field to destroy a weapons platform at some distance away. Our problem in the high power commercial laser communications industry is not unlike that of the high power weaponry laser beams, in terms of wave front quality that has to be maintained. In the case of the high power commercial lasers, the user wants to maximize the laser power onto the workplace. In order to perform this function effectively, the wave front quality of the beam must be maintained from the laser cavity through the optical train and focused on the material to be processed. In the communications industry, we must also maintain beam quality or we risk the substantial loss of information that is contained in the modulation frequencies whether it be digital or analog. Fundamentally, we are talking about the diffraction image. "If the pupil function is a constant, i. e., if the transmission of the system is uniform over the aperture and the system is aberration - free, the illuminance distribution in the image becomes, in the far field,"^{[7],[9],[10]}

(1)

$$I = I_0 \left\{ e^{-\left(\frac{\rho^2}{2 R_0^2}\right)} \right\}$$

where:

$$R_0 = \{1.22 (N.A.) \lambda\}, \text{ cm}$$

= The un-aberrated Airy Disc radius at focus of the optic

$$\rho = \sqrt{2 \{1.22 (N.A.) \lambda\}^2 (0.1743533)} , \text{ cm}$$

= The central lobe of the un-aberrated Airy disc, cm

(Note: The central lobe carries 84% of the total flux density. The remainder is contained in the outer lobes.)

N. A. = Numerical Aperture

$$= \frac{\text{Focal Length}}{\text{Diameter of Optic}}$$

P = See Figure 3.0 - ordinate

q = See Figure 3.0 - abscissa

$\Sigma\sigma$ = Sum of defocus due to mirror train aberrations, cm

λ = Wavelength of the laser, cm

L = Total beam path length, cm

α = decollimation angle out of the laser cavity, radians

For the case where the optical component has a focus at infinity, the Numerical Aperture will equal, [9],[11]

$$N. A. = \frac{\text{diameter of the optic}}{2}$$

We must also accommodate the diffraction image of the multi modes of the laser beam coming out of the laser cavity. The central lobe begins to diminish in amplitude as the lobe begins to increase in radius because of the diffraction effects on the wave front quality. The diffraction for the laser mode is found from, [7],[9],[11]

$$\rho = \sqrt{2 \{1.22 (N.A.) \lambda [2P + q + 1]\}^2 (0.1743533)} , \text{ cm} \quad (2)$$

We must now take into consideration the diffraction effects caused by the figure error, ripple caused by cooling channels, and bowing caused by the axial temperature gradient across the optical component. These effects manifest themselves as a defocusing term (σ). The original equation, then, is expanded to include the defocusing term, such that, [7],[12],[13],[14]

$$\rho = \sqrt{2 \{1.22 (N.A.) \lambda [2P + q + 1] + \Sigma\sigma\}^2 (0.1743533)} , \text{ cm} \quad (3)$$

The last component to be included in our equation is the decollimation angle of the laser beam coming out of the laser cavity. Ideally, this decollimation angle will be very small. However, as the beam travel distance increases, say with a distributed system, this value can become a very real element in

the calculation. At large distances, for an un-aberrated Gaussian beam will provide an angular spread of a Gaussian beam is [15],[16]

$$\text{radians} = \frac{4 \lambda}{\pi D_o} \quad (4)$$

The final equation that includes all of the diffraction image manifestations that impose on the final work piece is found from, [7],[16]

$$\rho = \sqrt{2\{1.22 (N.A.) \lambda [2P + q + 1] + \Sigma \sigma\}^2 (0.1743533)} \quad (5)$$

The diameter of the laser beam at the focusing optic, after having passed through the beam path from the laser cavity, will follow from, [16]

$$D_{\beta}' = \frac{\sqrt{\left\{ \frac{\rho^2}{2 (0.1743533)} \right\}^2 2 D_{\beta}}}{(1.22 [2P + q + 1] \lambda D_o)} \quad (6)$$

where;

- D_{β} = Diameter of the laser beam at the laser cavity, cm
- d_w = Diameter of the beam waist at the focus of the work piece, cm
- D_{β}' = Diameter of the laser beam on the focusing optic, cm
- D_o = Diameter of the beam train optical components, cm

The beam waist diameter on the work piece becomes very important. The focusing optic will be expected to have a focal length of some value. All of the wave front aberrations that are presented to the focusing optic carry right on through the focusing system. If the energy in the central lobe of the wave front has been aberrated, i. e., diminished, the beam waist and concentration, or focusability, of the beam will be equally increased as to the waist diameter and subsequently diminished commensurately as to the concentration. The beam waist at the quasi focus of the refracting focusing lens will follow from, [7]

$$d_w = 2.44 \frac{f}{D_{\beta}'} \lambda [2P + q + 1] + \Sigma \sigma \quad (7)$$

It is not uncommon to use refracting optics to focus the beam. As the power of the laser increases, laser damage of the common materials used for refracting lens must be replaced by reflecting optical focusing systems. In both cases, there are additional aberrating third and fifth order terms that would come into play for the wave front aberration scheme. The focusing optics may be subject to Spherical aberration, Astigmatism and field curvature and coma. The most acute problem, however, is the first order term of defocus. We will see that many of these terms will reappear in our next analysis of the Laguerre Orders in the External Modulator.

In the early days of telecommunications, the basic technique for transporting information down the fiber was to modulate directly on the DFB laser. There are any number of real problems associated with modulating on the laser. And, with the inordinate increase in bandwidth requirements, it is no longer possible to use this technique. The previous standard for the industry was to use a laser that has a maximum continuous wave modulation on the order of 3.56 GHz. If the laser is pulsed modulated, this value can be boosted to 16 GHz. Suffice to say that 3.56 GHz will only allow for approximately one OC-48, when everything is properly in tune. The pulse modulation technique has any number of problems associated with the stability of the laser and the system. In any case, neither of the two techniques will provide what we will ultimately need for modulation bandwidth. Fundamentally, the system limit on the

diode laser is the cavity length that is used for most of these types of laser. Keiser^[17] states, "The basic limitation on the modulation rate of laser diodes depends on the carrier and photon lifetime parameters associated with the operation of the laser. These are the spontaneous and stimulated lifetimes and the photon lifetime. . . At room temperature the Radiative lifetime is about 1ns. . . The stimulated carrier lifetime depends on the optical density in the lasing cavity and is on the order of 10ps. The photon lifetime is the average lifetime that the photon resides in the cavity before being lost either by absorption or by emission

through the facets. In a Fabry-Perot cavity the photon lifetime is . . . typically 2ps." Senior^[18] supports Keiser in his contention when he states, "the limitations imposed by direct current modulation of semiconductor injection lasers currently restricts the maximum achievable modulation frequencies to a few Gigahertz. Furthermore, with most injection lasers, high speed current modulation also creates undesirable wavelength modulation which imposes problems for systems employing wavelength division multiplexing." When using a laser diode for high speed transmission systems, the modulation frequency can be no longer than the frequency of the relaxation oscillations of the laser field. The relaxation oscillation depends on both the spontaneous lifetime and the photon lifetime. Assuming a linear dependence of the optical gain on carrier density, the relaxation oscillation occurs approximately as shown

below,
[1],[17],[18],[19],[20]

(8)

$$f_o = \frac{1.0}{2\pi} \frac{1.0}{\sqrt{\tau_{sp} * \tau_{ph}}} \sqrt{\frac{I}{I_{th}} - 1.0}$$

where,

τ_{sp} = Spontaneous lifetime, $1.0(10^{-9})$ seconds

τ_{ph} = Photon lifetime, $2(10^{-15})$ seconds for a 300 - μ meter long laser

$$\sqrt{\frac{I}{I_{th}} - 1.0} = 1.0$$

From our calculation, we find that,

$$f_o = 3.56(10^9) \text{ Hz or approximately } 3.56 \text{ GHz}$$

Clearly, modulating directing onto the diode laser will not be applicable for our application. This brings me to the external optical modulator.

Knowing the electric and magnetic field amplitudes along the z axis, we can find what the amplitude and field strength distribution will be as we go from the z axis out towards the maximum radius

in the modulator channel. The geometry is shown by R. G. Walker, *et al.*,^{[9],[21]} and in several other bulletins of various manufacturers. The key to some of the modulator designs is to achieve a speed match

between the optical and electrical frequencies^{[21],[22]} I think the best statement of what is to be achieved is stated by R. G. Walker, *et al.* when they say, "the aim in traveling-wave design is to achieve a modulating voltage which propagates in exclusively the same direction and at precisely the same speed as the resultant modulation envelope on the optical wave, permitting the phase modulation to accumulate monotonically irrespective of frequency. Velocity mismatch causes phase walkoff between waves resulting, with

increasing frequency and distance, in the cancellation of initial modulation . . ."^[22] I think that most modulator designers would agree, for the most part, with this statement. However, there is a major constituent that is missing in all of the design criteria that one sees in the literature, viz., the imaginary part of the optical index at the various frequencies. Additionally, most all of the designs fail to include the distribution of the electric and magnetic field functions as it relates to the radius surrounding the z axis.

Probably the best evaluation relative to orbital angular momentum, following Beth^[23] is given by S. M. Barnett and L. Allen^[24] and by Allen, et al.,^[25] in describing the decomposed Laguerre-Gaussian modes into orbital and spin components associated with polarization as a function of nonparaxial light beams. Allen and his associates have noted that paraxial beams possessing cylindrical symmetry possess well defined angular momentum per unit energy flux and that, "... this angular momentum can be divided into orbital and spin components."^{[24],[25]} These two papers are the seminal work that has been done in this area. Allen, *et al.*, argue, "... it is, indeed, not possible to separate the total angular momentum of the photon field into and(sic) 'orbital' and 'spin' part (this would contradict gauge invariance); the best that can be done is to define the helicity operator. ... which is observable."^[25] However, Allen, *et al.*, show for Laguerre-Gaussian beams within the paraxial approximation that the z component of momentum is (± 1) for circularly polarized light and 0 for linearly polarized light. In this context, then, $E_{(\rho,\phi,z)}$ or $H_{(\rho,\phi,z)}$ is the complex scalar function, expressed in cylindrical polar coordinates, describing the distribution of the field amplitude of a Laguerre-Gaussian beam and is given by,

(9)

$$E_{(\rho,\phi,z)}^* = \frac{E}{\sqrt{1.0 + \frac{z^2}{2z_r^2}}} * \left(\frac{\rho\sqrt{2}}{W(z)} \right)^1 * L_p^1 \left(\frac{2\rho^2}{W^2(z)} \right) * e^{\left(-\frac{\rho^2}{W^2(z)} \right)} \\ * e^{\left(-\frac{k}{2} \frac{\sqrt{1.0 - \left(\frac{\lambda_{co}}{\lambda} \right)^2} \rho^2}{2(z^2 + z_r^2)} \right)} * e^{(\pm k l \phi)} * e^{(k^2 (2p + Q + 1.0) \tan^{-1}(\frac{z}{z_r}))}$$

where;

$$z = \text{Distance down the modulator, } \frac{c\tau}{n}$$

$$z_r = \text{Rayleigh range} = \left(\frac{c\tau}{n} \right) * \left\{ 1.0 + \left\{ \frac{\pi R_o^2}{\lambda * \left(\frac{c\tau}{n} \right)} \right\}^2 \right\}^{1/2} \quad [27]$$

$$W^2(z) = \left\{ R_o^2 \left\{ 1.0 + \left(\frac{\lambda \left(\frac{c\tau}{n} \right)}{\pi R_o} \right)^2 \right\} \right\}$$

$$R_o = 1.22 * N.A. * \lambda \quad [7]$$

The maximum $W(z)$ of the modulator will be ,

$$W(z) = \sqrt{x^2 + y^2} \quad [8]$$

The maximum $W(z)$ of the fiber will be the radius of the fiber.

$$\rho = \sqrt{2 * \left\{ 1.22 N.A. \lambda (2p + Q + 1.0) \right\}^2 * 0.1743533} \quad [7]$$

- l = Order number of the Laguerre Polynomial
 k = Imaginary component of the optical index for the wavelength of interest.
 k_1 = Imaginary component of the optical index for the electric frequency to be imposed on the light beam.
 c = Speed of Light in a vacuum, $\approx 3 (10^8) \frac{\text{Meters}}{\text{Seconds}}$
 n = Real part of the optical index of the material.
 n_1 = Real part of the optical index of the material at the electric frequency to be imposed on the light beam.
 τ = Time, seconds
 ϕ = Angle of incidence
 λ = Wavelength of interest, meters
 p = Radial zero fields of the Transverse modes of the laser.
 Q = Angular zero fields of the Transverse modes of the laser.
 note: see *Figure 3.0* for different TEM beam shapes.

$$[8],[26] L_p^1 \left(\frac{2^* \rho^2}{W(z)} \right) = e^{\left(\frac{2^* \rho^2}{W(z)} \right) (-1)} \frac{e}{p!} \frac{d^p}{dx^p} \left\{ e^{\left(\frac{2^* \rho^2}{W(z)} \right)} x^{pl} \right\}$$

For the magnetic field, we have a similar equation, however, the real and imaginary part of the optical index will have to reflect the value for the electric frequency that is placed on the imbedded electrodes and is subsequently

to be imposed on the light traversing the modulator, so that,

(10)

$$H_{(\rho, \phi, z)}^* = \frac{H}{\sqrt{1.0 + \frac{z^2}{2z_r}}} * \left(\frac{\rho \sqrt{2}}{W(z)} \right)^1 * L_p^1 \left(\frac{2^* \rho^2}{W(z)} \right) * e^{\left(-\frac{\rho^2}{W(z)} \right)}$$

$$\left(-\frac{k_1 \sqrt{1.0 - \left(\frac{\lambda_{co}}{\lambda} \right)^2} \rho^2}{2(z^2 + z_r^2)} \right) (\pm k_1 l \phi) \left(k_1^2 (2^* p + Q + 1.0) \tan^{-1} \left(\frac{z}{z_r} \right) \right)$$

$$x e^{...} * e^{...} * e^{...}$$

For all of the constituents of the equation, one would substitute n_1, k_1 for n and k at the optical frequency with the electric frequency values. It is not uncharacteristic for most electrical applications to assume that the value of $k_1 = 0$ ^[28]. This is not the case, however. I would argue that it may be quite small at microwave and lower frequencies; but, it is not zero. However, as the reader will view shortly, these values are not small at the very low frequencies. It is plain from the equations that the value of k_1 plays a significant part in the ability of the frequency to be modulated onto the light beam.

Additionally, what we find is that the different frequencies have a greater or lesser impact on the modulation as a function of the n_1 and k_1 of the modulator material at the radio frequency that is imposed.

Fundamentally, the electrodes in the modulator are set at right angles to the electric field vector. The magnetic field of the electrodes provide the traveling wave that is speed matched to the light frequency. The basic concept that I am proposing in this paper suggests that the magnetic field of the electrodes interacts with the different orders of the Laguerre-Gaussian photons as the elliptical path of each of the Laguerre-Gaussian orders passes through the magnetic field of the radio frequency on the imbedded electrodes. As each of the Laguerre-Gaussian orders passes through the magnetic field, each of the orders picks up frequencies in turn. Essentially, then, each of the clock frequencies, with their attendant modulated signals, becomes independently modulated onto different orders of the Laguerre-Gaussian, each having its own angular momentum, i.e., combinatorial orbit and spin. As such, each order of the Laguerre-Gaussian provides a means that circumscribes a different helicity and isolates one from the other.

This helicity gives rise to one of the more important aspects of the phenomena in that all of the orders are time dilated from one another as they are removed from the z axis. So that the time dilation goes according to, [29],[30],[31]

(11)

$$\Delta\tau = \tau_{(z)} * \frac{e^{(-kl\phi)}}{\sqrt{1.0 - \frac{v^2}{c^2}}}$$

where;

- l = The order number of the Laguerre-Gaussian
- k = Imaginary part of the optical index
- ϕ = The angle of incidence in radians
- v = Speed of light in the optical material, $\frac{c}{n}$
- c = Speed of light in a vacuum, $\approx 3 (10^8) \frac{\text{meters}}{\text{seconds}}$

Three Dimensional World - Optical Modulators Leaving Modulator-Into Fiber Waveguide

Now that we have introduced the modulation into the electrodes of the modulator and have modulated clock frequencies, with the attendant information frequencies, the beam must pass out of the modulator and into a fiber to be transported to the respective destinations.

Again, the modulated light beam comes into the fiber, once again changing from one optical index into another. Under most conditions, the index of refraction of the modulator will be substantially higher than that of the fiber into which the modulated signal is dumped. Again, there will be the interface issue of reflection, refraction and the change of phase angle with the transmission. We also have the addition of the amplitude increase because of the discontinuity between the two optical properties. The

relationship between the exit and entrance surface electric fields follows from, [4],[16],[32],[33],[34]

(12)

$$\frac{4 N_o^2}{(1 + N_o)^2} \quad \text{for } N = 1.0$$

$$\frac{4 * N_o * N}{(N_o + N)^2} \quad \text{for } N > 1.0$$

where;

N_o = High index of exit material

N = Low index of material that light exits into.

The values of $\sin \theta_1$ and $\sin \theta_o$ will take on different values, so that the transmission phase will again change as function of going down the z axis. As a result, the Laguerre-Gaussian values will also change as the Gaussian beam penetrates into the optical fiber. So, we now have *Eqs. (9)* for the z axis with an additional component reflecting the increase in the amplitude of the electric field. So that *Eqs. (9)* becomes,

(13)

$$\begin{aligned} \mathbf{E} = \mathbf{E}_o \mathbf{e}^{\left(-\frac{4 \pi k c \tau}{\lambda (\cos \theta_1) n}\right)} \mathbf{e}^{\left(k^2 * 2 * \pi \left\{ f_o * \tau - \frac{\sqrt{1.0 - \left(\frac{\lambda_{co}}{\lambda}\right)^2}}{\lambda} \right\} \frac{c \tau}{n}\right)} \\ \times \frac{2 * \sin \theta_1 * \cos \theta_o}{\sin (\theta_o + \theta_1) \cos (\theta_o - \theta_1)} * \left\{ \frac{4 * N_o * N}{(N_o + N)^2} \right\} \end{aligned}$$

$$\begin{aligned} \mathbf{H} = \mathbf{H}_o \mathbf{e}^{\left(-\frac{4 \pi k c \tau}{\lambda (\cos \theta_1) n}\right)} \mathbf{e}^{\left(k^2 * 2 * \pi \left\{ f_o * \tau - \frac{\sqrt{1.0 - \left(\frac{\lambda_{co}}{\lambda}\right)^2}}{\lambda} \right\} \frac{c \tau}{n}\right)} \\ \times \frac{2 * \sin \theta_1 * \cos \theta_o}{\sin (\theta_o + \theta_1) \cos (\theta_o - \theta_1)} * \left\{ \frac{4 * N_o * N}{(N_o + N)^2} \right\} \end{aligned}$$

and for $t_{(s)}$

$$\begin{aligned} \mathbf{E} = \mathbf{E}_o \mathbf{e}^{\left(-\frac{4 \pi k c \tau}{\lambda (\cos \theta_1) n}\right)} \mathbf{e}^{\left(k^2 * 2 * \pi \left\{ f_o * \tau - \frac{\sqrt{1.0 - \left(\frac{\lambda_{co}}{\lambda}\right)^2}}{\lambda} \right\} \frac{c \tau}{n}\right)} \\ \times \frac{2 * \sin \theta_1 * \cos \theta_o}{\sin (\theta_o + \theta_1)} * \left\{ \frac{4 * N_o * N}{(N_o + N)^2} \right\} \end{aligned}$$

$$\begin{aligned} \mathbf{H} = \mathbf{H}_o \mathbf{e}^{\left(-\frac{4 \pi k c \tau}{\lambda (\cos \theta_1) n}\right)} \mathbf{e}^{\left(k^2 * 2 * \pi \left\{ f_o * \tau - \frac{\sqrt{1.0 - \left(\frac{\lambda_{co}}{\lambda}\right)^2}}{\lambda} \right\} \frac{c \tau}{n}\right)} \\ \times \frac{2 * \sin \theta_1 * \cos \theta_o}{\sin (\theta_o + \theta_1)} * \left\{ \frac{4 N_o^2}{(1 + N_o)^2} \right\} \end{aligned}$$

The angle of ϕ_0 will change and consequently so will the helicity of the various orders of the Laguerre-Gaussian and the subsequent time dilation between the various orders. So that now, the Laguerre-Gaussian changes its shape and the value of ϕ_0 changes in accommodation to the difference in the index of refraction between the modulator and the anisotropic fiber that is to transmit the information. The new Laguerre-Gaussian will follow from,

$$E^*_{(\rho, \phi_0, z)} = \frac{E}{\sqrt{1.0 + \frac{z^2}{z_r^2}}} * \left(\frac{\rho \sqrt{2}}{W(z)} \right)^1 * L_p^1 \left(\frac{2^* \rho^2}{W^2(z)} \right) * e^{\left(-\frac{\rho^2}{W^2(z)} \right)} \quad (14)$$

$$\left(-\frac{k \sqrt{1.0 - \left(\frac{\lambda_{co}}{\lambda} \right)^2}}{2(z + z_r)} \right)^2 * e^{(\pm k l \phi_0)} * e^{(k^2 (2^* p + Q + 1.0) \tan^{-1} \left(\frac{z}{z_r} \right))}$$

There is yet another factor that comes into play with each of the interfaces that are encountered between the PM fiber going into the modulator and the modulator into the transport fiber, i.e., the scatter and absorption that takes place at each of these interfaces. Each optical component will have different flux density or fluence to contend with and, as such, will have different temperature gradients. Also, absorption and scattering from the coatings will be different for the various components which may have different reflectivities. For absorption, [4],[7],[16]

$$\sigma_{so} = \sum_{N=1}^{Nm} \left\{ 1 - R - \left[\frac{4(\psi)}{(\varphi) \left\{ \frac{\eta_L}{\eta_H} \right\}^{2N}} \right] \right\} \quad (15)$$

$$- \left[\frac{4 \pi \sigma^0 \{ 1.15 - 2.565(10^{-6})[5(10^3) - \lambda] \}^{2N}}{\lambda} \right]^2 \left\{ \frac{[1 - \left\{ \frac{\eta_L}{\eta_H} \right\}^{2N+1}]}{[\eta_H^2 - \eta_L^2]} \right\}^{-1}$$

where;

For low index material next to the substrate,

$$\psi = 1.0, \quad \varphi = \eta_s$$

For low index material next to the substrate,

$$\psi = \eta_s, \quad \varphi = \eta_H^2$$

η_s = Substrate index

η_H = High index of dielectric film

η_L = Low index of dielectric film

N = Number of high - low coating pairs

and for scatter, i. e., diffuse reflection, in a coated optic, [4],[7],[16]

$$\sigma_s = \sum_{N=1}^{Nm} \left[\frac{(4 \pi \sigma^0 \{ 1.0059(10^{-7}) [5(10)^3] - \lambda \})}{(\lambda)} \right]^{2N}$$

If the optical components are not coated with a quarter-wave stack of optical thin films, the average specular reflection from the optical surface at normal incidence in air will follow from, ^{[4],[7],[16]}

$$R_{1,2 \dots N} = \frac{(n-1)^2 + k^2}{(n+1)^2 + k^2} - \left[\frac{4 \pi \sigma^0 \{ \cos \theta \}}{\lambda} \right]^2 \quad (16)$$

where;

σ^0 = RMS Surface roughness, Å
 θ = Angle of incidence, radians
 λ = Wavelength of interest, Å

For the case where there is a splice, or any other type of interface between the waveguides in use, one may expect to see absorption and scatter which will also provide reflections with phase retardance that can interfere with the optical frequencies that are generated in the modulator.

Fundamentally, we have just shown how the electric field changes in both dimension and in amplitude. It is also important to note that as the electric field of the various orders of the Laguerre pass out of the External Modulator, and into the optical fiber for transmission, that approximately nineteen orders of the Laguerre are able to pass into the transmission fiber. The conventional wisdom has been, over the years, that the correct technique for evaluating the optical transmission into the fiber has been predicated ^{[35],[36],[37],[38]}

on the model of a truncated parabola as indicated by Marcuse and others. In this model, only the first order of the Laguerre will solve. However, the predicate in all of the models has been that one may use a standing wave model. In fact, this is not true. The optical fiber is, in fact, mildly bi-refrigent and, further, has a steep Lorentzian shape for the index change from the center to the outer radius of the fiber ^[39].

Using the Lorentzian model we find that the high orders of the Laguerre can pass through the transmission fiber as well ^[39]. So, the transmitted Laguerre Orders do not travel down the fiber as a standing wave. They are, in fact, elliptical in nature as a function of the modular and fiber's ^{[39],[40],[41],[42],[43]}

birefringence. What we have seen so far reflects how the light metamorphoses in its dimensions and time as it makes a transit from the laser on to the modulator and down the transmission optical fiber--in both directions.

Ellipsometric Phase Rotation In Bidirectionality

In the last segment we demonstrated how the coherent laser beam is traveling down the fiber in an elliptical orbit and at the same time is traveling a particular ellipsometric phase ^{[41],[43]}. Perhaps the most cogent statement relative to the bidirectionality used in *Optical Refractive Synchronization* is summarized in Nye's statement ^[42], "the nature of the medium is such that two circularly polarized waves of opposite hand and different velocity may be transmitted through it unchanged in form, that is, in their

state of polarization, while a plane wave may not be so transmitted.” We can determine the exact amount of angle of ellipsometric phase rotation from Equation (17), such that ^{[39],[40],[41],[42],[43]},

$$\frac{\phi}{l} = \rho = \frac{\pi^*(n_o - n_e)}{\lambda_o} \quad (17)$$

where;

- n_o = Real part of the high index
- n_e = Real part of the low index
- λ_o = Wavelength of interest, mm
- ϕ = Rotation in radians
- l = Length of travel, mm
- ρ = Rotary power

In a similar fashion when discussing the **standing wave phenomena**, Hardy and Perrin ^[44] state, “. . .for interference is observed between beams traveling in the opposite direction.” This problem would most surely be a factor if there were no rotary power to the two beams and they were in fact **standing waves**. As we have indicated above, clearly we do not have standing waves. Basically, because a photon has no rest mass, photons can exist in the same time and space. However, they cannot exist in the same ellipsometric phase ^[30]. For our particular problem, our wavelength is further separated by the use of splitters and combiners which are set out of phase such that each side of the splitter - combiner is out of phase by $\frac{\pi}{2}$. This phenomena is probably best described by the following expressions, such that ^{[45],[46],[47]},

for (p) polarized reflection; (18)

$$R_p = \frac{N_1 \cos \phi_o - N_o \cos \phi_1}{N_1 \cos \phi_o + N_o \cos \phi_1} \quad (19)$$

for (s) polarized reflection; (20)

$$R_s = \frac{N_o \cos \phi_o - N_1 \cos \phi_1}{N_o \cos \phi_o + N_1 \cos \phi_1} \quad (21)$$

for (p) polarized transmission; (22)

$$T_p = \frac{2*N_o \cos \phi_o}{N_1 \cos \phi_o + N_o \cos \phi_1} \quad (23)$$

for (s) polarized transmission; (24)

$$T_s = \frac{2*N_o \cos \phi_o}{N_o \cos \phi_o + N_1 \cos \phi_1}$$

These values can be recast such that, for transmission,

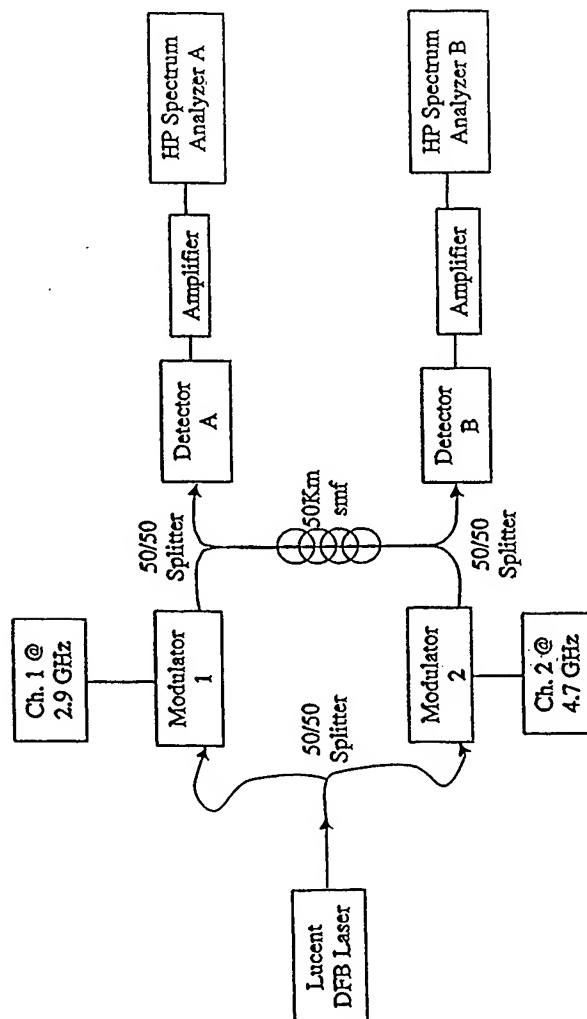
$$T_p = \frac{2*\sin \phi_1*\cos \phi_o}{\sin(\phi_o + \phi_1)*\cos(\phi_o - \phi_1)} \quad (25)$$

$$T_s = \frac{2 \sin \phi_1 \cos \phi_0}{\sin(\phi_0 + \phi_1)}$$

There is always a concern about reflections from the splitter-combiner such that it is manifested in *Equations (18) and (19)*. These reflections are mitigated by using ellipsometrically polarized isolators. In this fashion, the reflections from each side are minimized against imposing an aliasing signal onto the respective sensors.

Experiment With Subsequent Data

Experiment-----Number One



Goal: Observe if simultaneous two-way transmission of a single wavelength over a single fiber optic is possible without interference.

Introduction: The need for sending signals down a single fiber optic simultaneously in both directions is driven by specifications of redundancy within a fiber optic network. It is important to determine if two signals on similar carriers will interfere within the waveguide when traveling in opposite directions.

Setup: A schematic diagram of the setup is shown in Fig 1. Details of equipment specifications are shown in Appendix 2. The Lucent DFB laser in the Alpha Three transmitter is the 1550 light source. The output of the laser is split into two legs of fiber line with approximately 18 mW of power on each one. Each line is coupled into a separate UTP modulator. One is driven with a clock signals from channel one at 2.9 GHz and the other is driven with a clock signal from channel 2 at 4.7 GHz. The output of each modulator is fed through a splitter into opposite ends of 1550 nm single mode fiber 50 km long. The signals are then detected by separate detectors as shown in the figure. The signal from modulator 1 after passing through the fiber will appear in detector B. The signal from modulator 2 after passing through the fiber will appear in detector A. The output of each detector is amplified and monitored on a spectrum analyzer. Reflections are minimal and will be described later.

Bidirectionality: The signal transmitted from channel 1 after passing through the fiber is measured at detector B at ~14mV. The signal transmitted from channel 2 after passing through the fiber is measured at detector A at ~22mV. The difference, about 4 dB, is caused by a drive voltage on channel 2 that is about 3.5 dB greater than channel 1. In order to show that there is no interference of the two crossing signals, a separate experiment was carried out. Only one signal is sent down the fiber in one direction. No change in signal strength is observed between sending signals unidirectionally and bidirectionally.

Reflections: The signals from both channels also reflect and backscatter into the detectors. Sources of reflections are predominantly from the fiber surfaces on the splitters. The signal observed on detector A for Ch. 1 is ~2mV. The signal observed on detector B for Ch.2 is ~1.5mV.

Analysis: The Ch. 2 signal transmitting across the 50Km of fiber is about one order of magnitude larger than the reflected signal voltage from Ch. 1. That translates into a 20dB power difference between the transmitted and reflected signal. The transmitted

APPENDIX B

Equipment list:

Lucent laser 1550nm 10mW

Corning 5 smf

Firmionics detector HS-30

UTP (Uniphase) modulator AM150-002085

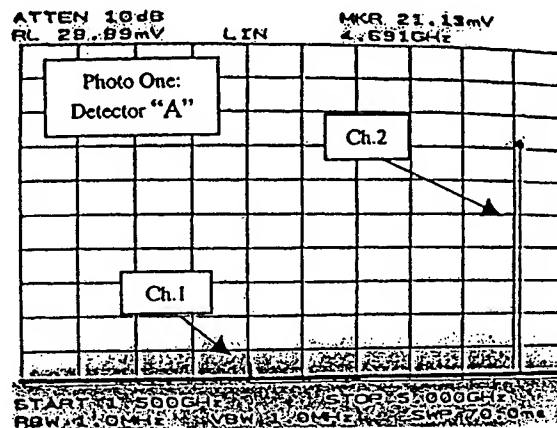
HP spectrum analyzer 8564E

JCA technologies amplifier jca218-344

Alpha Three Transmitter

signals should see about 13 dB loss in the 50Km of fiber and an additional 3dB loss for each splitter. The total loss for the transmitted power signal is about 20dB. The losses for the reflected signal should add up to about 40 dB or 0.01%, given the 20 dB differences seen in both signals.

Noise measurements: It was suggested by some that interference between the two signals in the fiber would increase the noise floor. No observed increase in the noise floor was measured between running a single channel or both simultaneously. The drive voltage on the modulators was moderate and on the order of 10mV or -30dBm.



Phase relationships: It was inferred by others that the phase is crucial. Therefore, the relative phase between signals was altered to observe any system performance changes. The legs on the dual port of the splitters adjacent to the 50Km of fiber were swapped to see if the $\pi/2$ phase shift has an effect on the system, but no significant change in system performance was measured. The phase shift appears to have no effect.

Path Lengths: The effect of changing the path length of the system was questioned in regards to unequal field strengths at different distances within the fiber. The attenuation in 50Km of fiber would cause an imperfect cancellation of the two waves. A shorter fiber would allow more perfect cancellation and extinguish the transmitted signals, if that was the correct model. The 50Km of fiber are replaced with a 1ft splice. This only increases the transmitted signal.

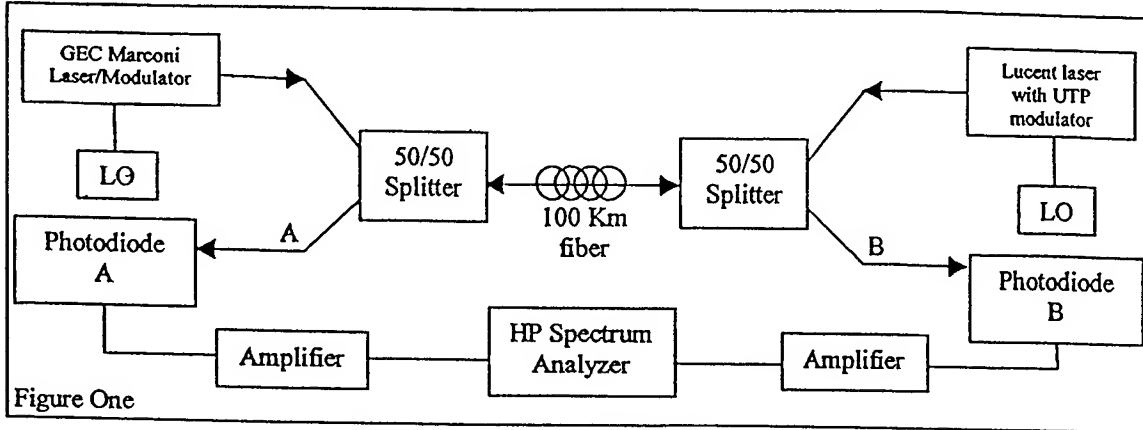
Conclusions: Simultaneous two-way transmission of a single wavelength over a single fiber optic is possible without interference. Efforts in the future will have to show if there is a limit to the amount of data transmitted due to noise in the system caused by reflections.

Experiment-----Number Two

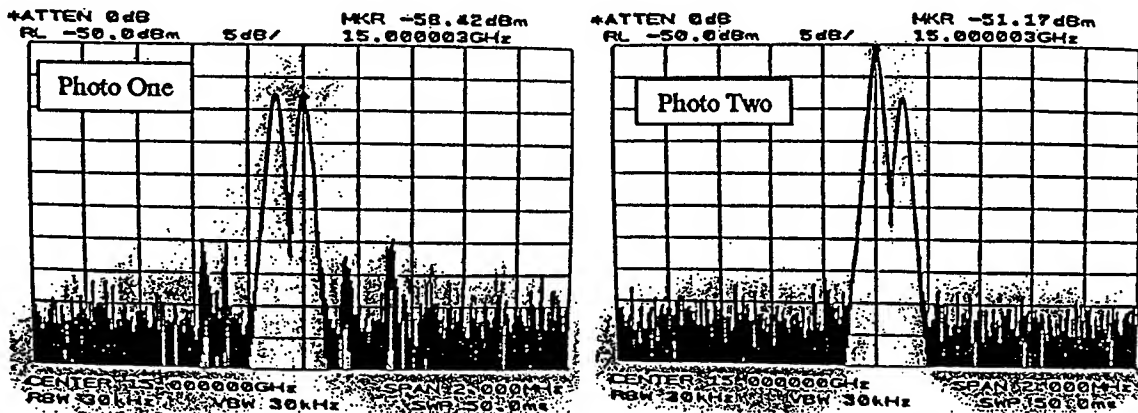
Equipment list:

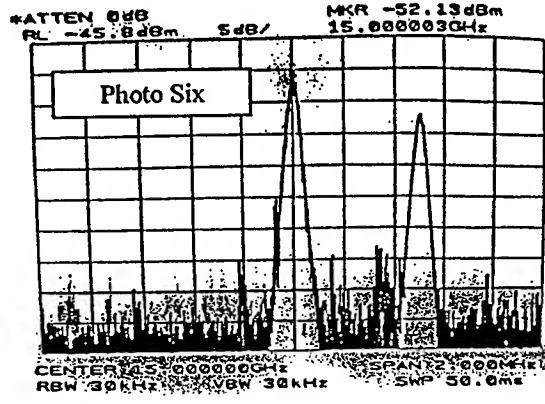
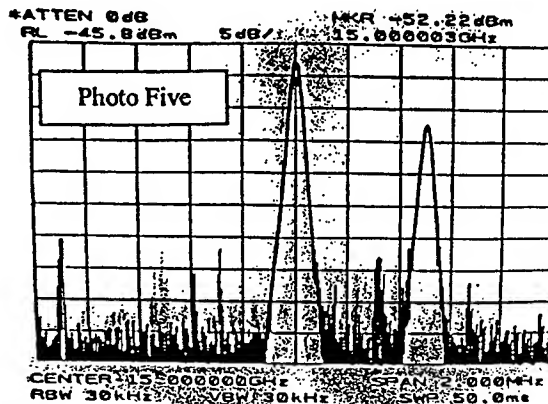
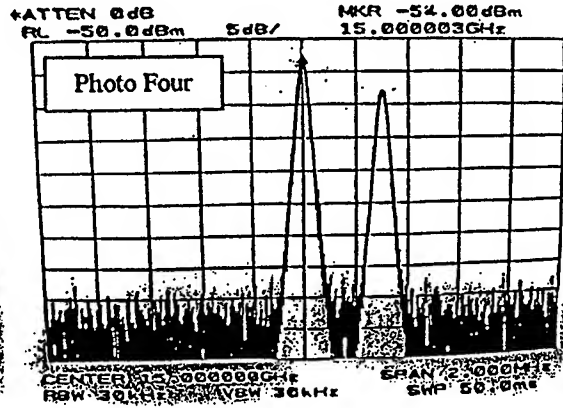
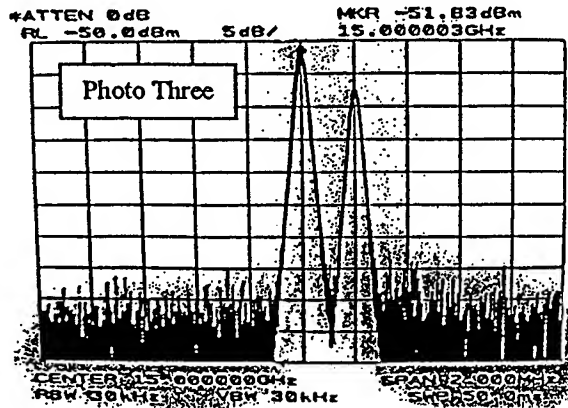
Lucent laser 1550nm 10mW
 GEC Marconi 1550nm 3mW
 UTP (Uniphase) modulator AM150-002085
 GEC Marconi modulator LT7726
 Firmionics detector HS-30
 JCA technologies amplifier jca218-344

AMP 50/50 splitter 107798-8
 Corning fiber 100km smf
 Semi-rigid cable dc-40GHz
 HP signal sweeper 83650A
 HP spectrum analyzer 8564E

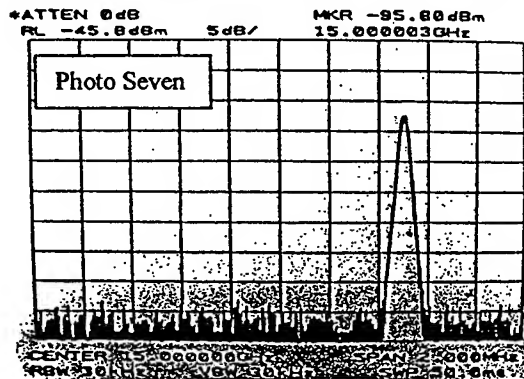


First Setup; Two 1550 nm lasers are used in this experiment. Signals in the 15GHz range are driven onto laser modulators. The signals are launched down the same fiber via 50/50 splitters, the signals are picked up by photodiodes on the other tail of the splitters (see Figure One). Both signals are transmitted over 100Km of fiber. The signals from the two photodiodes are monitored on a spectrum analyzer. Photos one through four show the resulting signals. The signal from the lucent laser is held at a static frequency of 15 GHz. The signal from the GEC Marconi laser modulator is swepted from 14.9999 GHz to 15.0003 GHz in 0.1 MHz increments and subsequently show no interference between the two beams.





It was, however, suggested that we show that what is being observed is not merely reflections off of the ends of the splitter outputs and not transmissions down the fiber. The connection in the system was broken at point A (Figure one) to show that if a reflection is being observed then the transmitted signal from the



Lucent laser will disappear and only the GEC signal will remain. Photo Five was taken before the connection at A was broken and photo Six was taken after. Obviously, if we were looking at transmitted signal it would no longer be observable. What we are seeing is a reflection in the coupler. The Lucent laser puts about 10 mW (10 dBm) out of the modulator. The glass to air interface accounts for approximately 4% of the power to be reflected, half of which will be seen on the photodiode leg of the coupler, that is 2% or 17dB down. A fairly strong signal when you consider that the transmitted signal drops 25 dB when traveling through 100 Km of fiber. A back of the envelope type calculation tells you that the reflected signal *should* be

stronger than the transmitted signal. Photo Seven was taken when the RF to the Lucent laser was shut off.

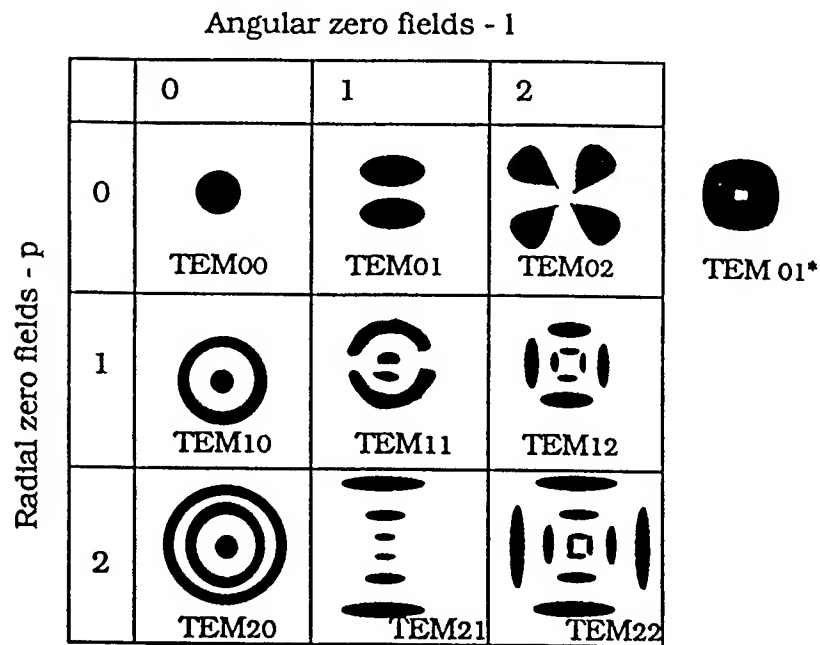


Figure 1.0- Radial And Angular Zero Fields

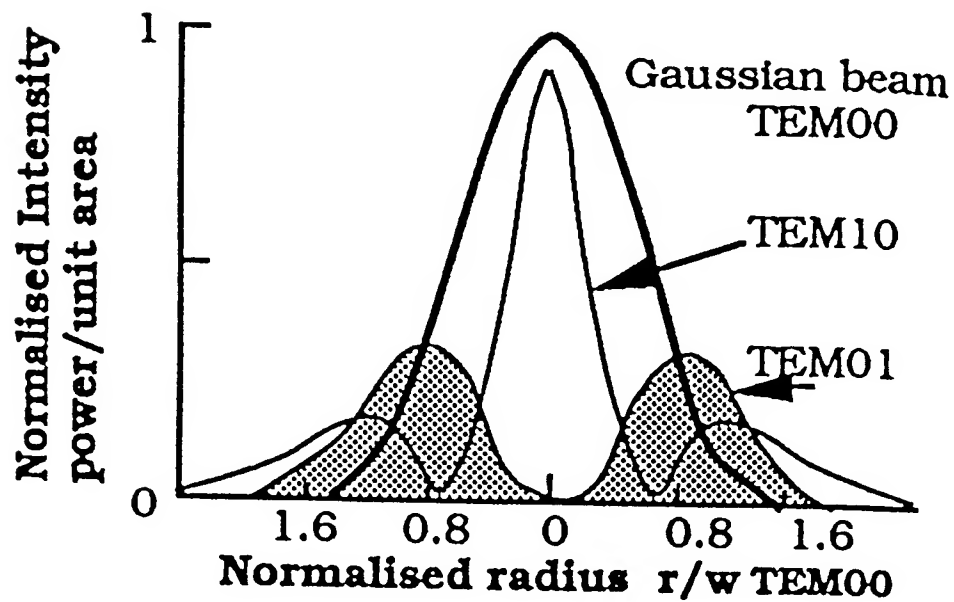


Figure 2.0- Outcoupled Laser Cavity Mode Patterns

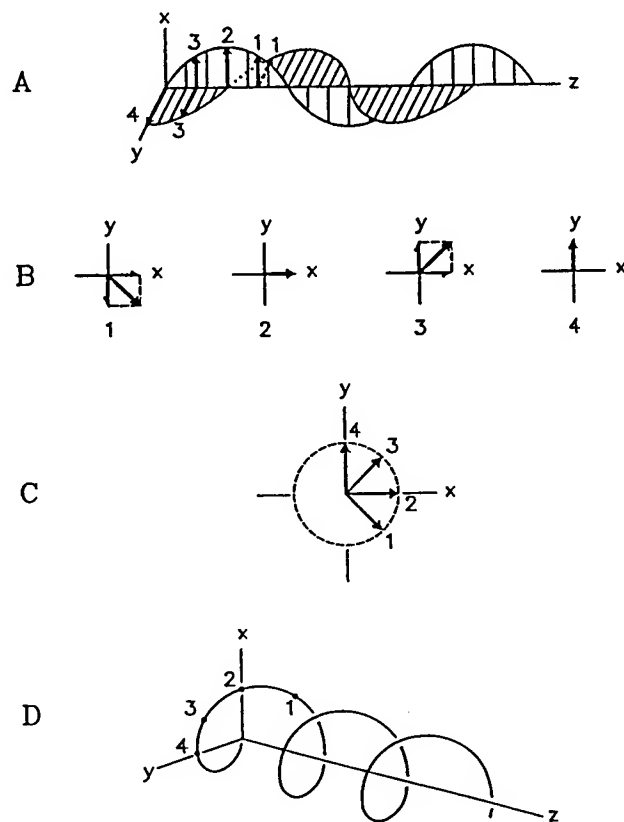


Figure 3.0- Circularly Polarized Light - Left Hand

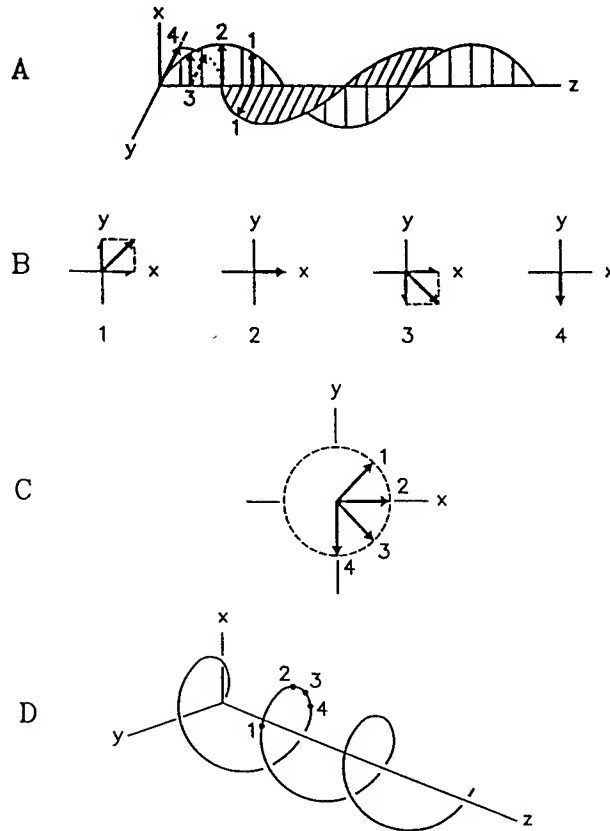


Figure 4.0- Circularly Polarized Light - Right Hand
A. orthogonal linear components with equal amplitudes and 90° relative phase shift; **B.** vector sums of the two components shown in A at points labeled 1 through 4; **C.** demonstration that the tip of the electric field maps out a circle when viewed along the propagation direction looking toward the light source; **D.** path at a single instant in time of the resultant electric field vector represented in A, B and C.

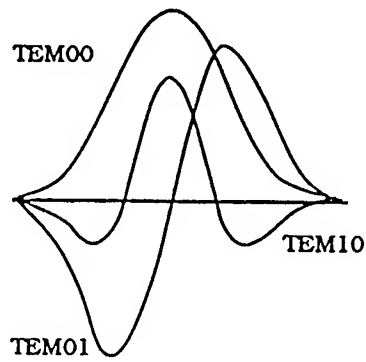


Figure 5.0- Intensity Distribution For Various Outcoupled Mode Patterns

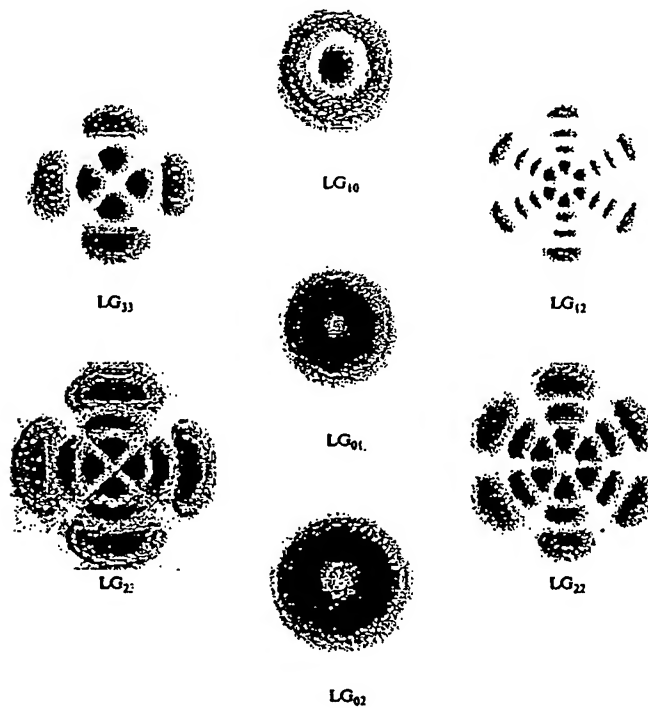


Figure 6.0- Laguerre Modes - Diffraction Patterns

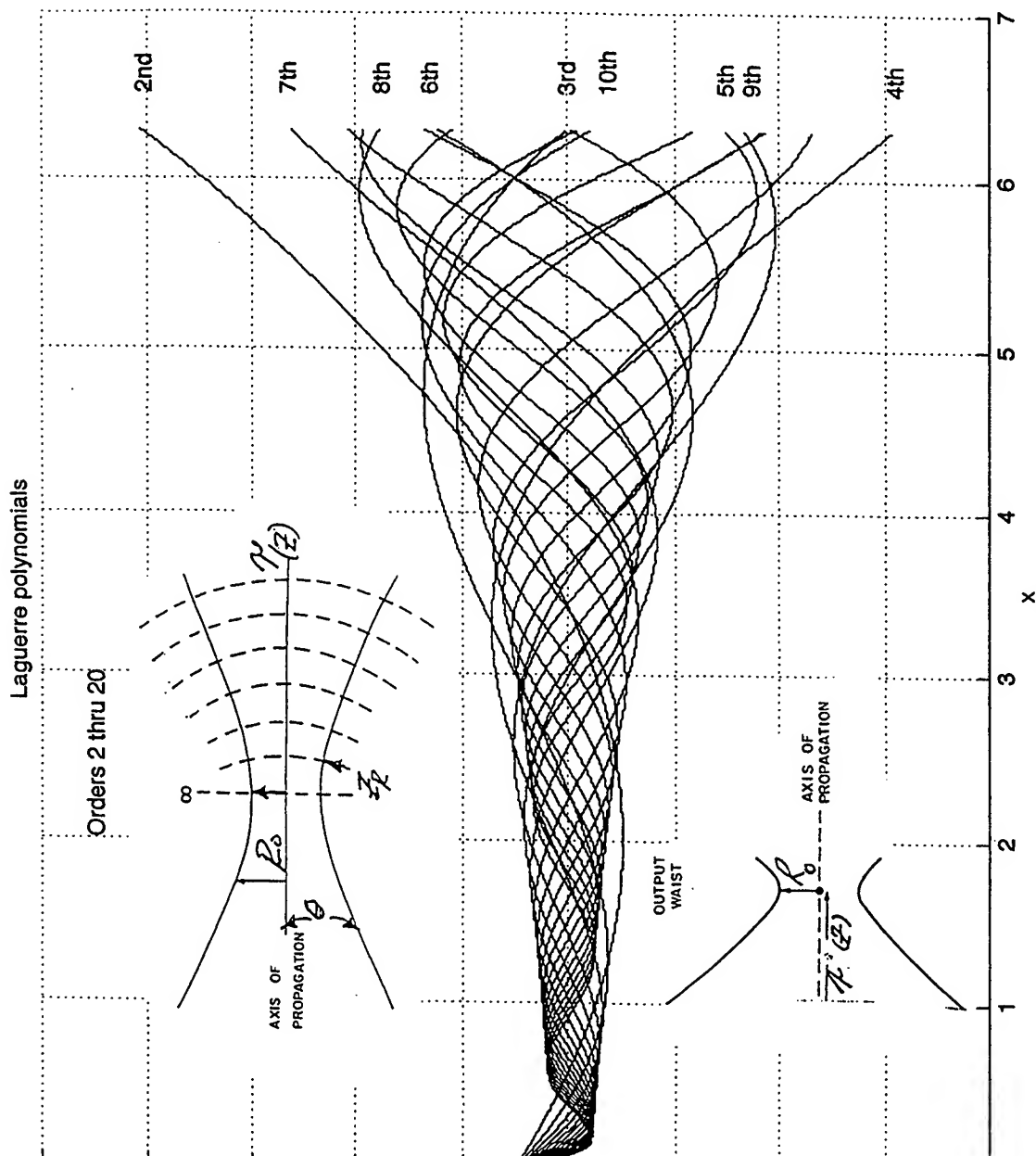
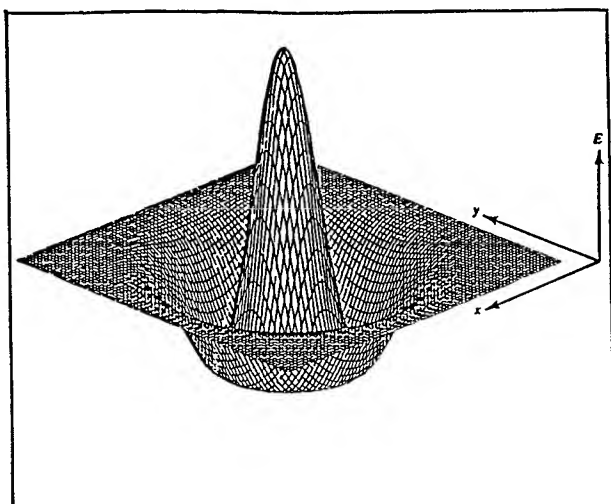
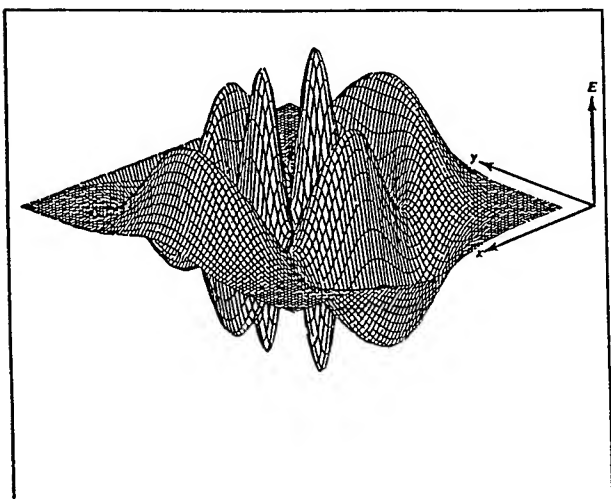
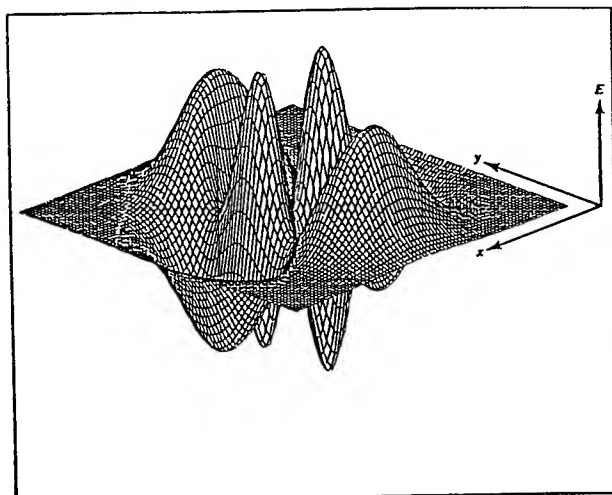


Figure 7.0- Laguerre Modes - Angular Momentum



**Figure 8.0 Three Dimensional Plots
Of The Field Distribution Of
Some Laguerre-Gaussian Laser Modes**



References

- 1.0 J. Gower, *Optical Communication Systems*, 2nd., ed., Prentice Hall, N.Y., N.Y., 1993.
- 2.0 J. Wilson and J. F. B. Hawkes, *Optoelectronics; An Introduction*, 2nd ed., Prentice Hall, N. Y., NY, 1989.
- 3.0 I. V. Kaminow and T. L. Koch, eds., *Optical Fiber Communications*, IIIA, Academic Press, N. Y., NY, 1997.
- 4.0 J. R. Palmer, "Optical Refractive Synchronization-Coherent Information In A Waveguide," *SPIE Vol. 3737, International Symposium On Optical Systems Design And Production*, Technical University of Berlin, German, May, 1999.
- 5.0 J. R. Palmer, "Optical Refractive Synchronization Frequency Sampling Ratio - - Amplitude Ratio Between The Clock Frequency And The Modulated Frequency," *International Symposium On Optoelectronics--6th Symposium Of Optoelectronics-Bucharest, Romania, September 1999*
- 6.0 J. R. Palmer, "Temperature And Dopant Concentration In Single Mode 5 Micron Diameter Optical Fiber -Cooling Through The Die - Implications For Laguerre Orders In Optical Refractive Synchronization," *International Symposium On Optoelectronics--6th Symposium Of Optoelectronics-Bucharest, Romania, September 1999*
- 7.0 J. R. Palmer, W. M. Steen and S. Martellucci, "Analytical Model For Aberrated Diffraction In High Power CW Laser Beam Trains; Laser Cavity To Work Piece," in *Laser Applications For Mechanical Industry*, S. Martellucci, A. N. Chester and A. M. Scheggi, eds., NATO Series E; Applied Sciences - Vol. 238, Dordrecht, The Netherlands, 1993.
- 8.0 W. M. Steen, *Laser Materials Processing*, 2nd. ed., Springer-Verlag, N.Y., N.Y., 1998.
- 9.0 W. G. Driscoll and W. Vaughan, eds., *Handbook Of Optics*, McGraw-Hill Book Co., N. Y., NY, 1978.
- 10.0 J. R. Palmer, *Verisimilitude-Homodyne Laser Transmitter - Receiver*, (Unpublished Paper).
- 11.0 A. C. Hardy and F. H. Perrin, *The Principles Of Optics*, McGraw-Hill Book Co., New York, NY., 1932.
- 12.0 O. Svelto and D. C. Hanna *Principles Of Lasers*, Plenum Press, New York, NY., 1982.
- 13.0 W. W. Duley, *CO₂ Lasers; Effects And Applications*, Academic Press, New York, NY., 1976.

- 14.0 W. W. Duley, *Effects Of High Power Laser Radiation*, Academic Press, New York, NY., 1971.
- 15.0 W. L. Wolfe and G. J. Zissis, eds., *The Infrared Handbook*, Office O Naval Research, Department Of The Navy, Washington, D.C., 1978.
- 16.0 J. R. Palmer, *High Power Laser Optics*, 2nd ed., *Pro Se* Publishing Co., San Diego, CA., 1996.
- 17.0 G. Keiser, *Optical Fiber Communications*, 2nd ed., McGraw-Hill, Inc., New York, NY, 1991.
- 18.0 J. M. Senior, *Optical Fiber Communications-Principles and Practice*, 2nd. ed., Prentice Hall, New York, NY., 1992.
- 19.0 J. R. Palmer, "Laser Change Of Phase When Reflecting From Objects With Rough Surfaces," Invited Paper presented at the Second University of Rome, II Unversita' di Roma 'Tor Vergata', July 1991.
- 20.0 J. R. Palmer, "Analytical Model For Phase Augmented Laser Beam," Invited Paper presented at Trinity College, Dublin, Ireland, December 1990.
- 21.0 R. G. Walker, M. J. Wale and C. Edge, *III-V Electro-Optic Modulators*, GEC-Marconi Materials and Technology Bulletin.
- 22.0 R. G. Walker, *High Speed III-V Semiconductor Intensity Modulators*, IEEE invited paper, 1991.
- 23.0 R. A. Beth, "Mechanical Detection And Measurement Of The Angular Momentum Of Light," *Physical Review*, Vol. 50, July 15, 1936.
- 24.0 S. M. Barnett and L. Allen, "Orbital Angular Momentum And Nonparaxial Light Beam," *Optics Communications*, Vol. 110, September 1994.
- 25.0 L. Allen, M. W. Beijersbergen, R. J. C. Spreeuw and J. P. Woerdman, "Orbital Angular Momentum Of Light And The Transformation Of Laguerre-Gaussian Laser Modes," *Physical Review "A"*, Vol. 45, NO. 11, June 1992.
- 26.0 F. R. Ruckdeschel, *BASIC Scientific Subroutines*, Vol. II, Byte/McGraw-Hill, Peterborough, NH, 1981.
- 27.0 K. Chang, ed., *Handbook Of Microwave And Optical Components, Vol. I--Microwave Passive And Antenna Components*, John Wiley & Sons, Inc., N.Y., N.Y., 1989.
- 28.0 F. Wooten, *Optical Properties Of Solids*, Academic Press, N.Y., N.Y., 1972.
- 29.0 D. Mermin, *Boojums All The Way Through*, Cambridge University Press, N.Y., N.Y., 1990.
- 30.0 A. P. French, *Special Relativity*, Thomas Nelson and Sons Ltd., Walton-on Thames, England, 1968.

- 31.0 T. Hey and P. Walters, *Einstein's Mirror*, Cambridge University Press, N.Y.,
N.Y., 1997.
- 32.0 M. Born and E. Wolf, *Principles Of Optics*, Pergamon Press, 5th ed., N.Y.,
N.Y., 1975.
- 33.0 R. M. Wood, *Laser Damage In Optical Materials*, Adam Hilger, Boston, MA,
1986.
- 34.0 C. M. Stickley, *NBS Special Publication*, No. 387, 1973.
- 35.0 H. Kogelnik, "Theory Of Dielectric Waveguides," *Integrated Optics*, T. Tamir, ed.,
Topics In Applied Physics, Vol. 7, 2nd ed., Springer-Verlag, New York, NY, 1985.
- 36.0 D. F. Nelson and J. McKenna, *J. Appl. Physics*, **38**, 4057, 1967.
- 37.0 J. R. Carruthers, I. P. Kaminow, and L. W. Stultz, *Appl. Opt.*, **13**, 2333, 1974.
- 38.0 D. Marcuse, *Light Transmission Optics*, Van Nostrand Reinhold Co., New York,
NY, 1972.
- 39.0 J. R. Palmer, "Temperature And Dopant Concentration In Single Mode 5 Micron
Diameter Optical Fiber -Cooling Through The Die - Implications For Laguerre Orders In Optical Refractive
Synchronization," *International Symposium On Optoelectronics--6th Symposium Of Optoelectronics
-Bucharest, Romania*, September, 1999.
- 40.0 E. E. Wahlstrom, *Optical Crystallography*, John Wiley and Sons, New York,
1949.
- 41.0 A. Yariv and P. Yeh, *Optical Waves In Crystals*, John Wiley and Sons, New York,
1984
- 42.0 J. F. Nye, *Physical Properties Of Crystals*, 2nd ed., Oxford University Press,
Oxford, England., 1985
- 43.0 E. A. Wood, *Crystals And Light*, 2nd. ed., Dover Publications, Inc., New York,
NY, 1977.
- 44.0 A. C. Hardy and F. H. Perrin, *The Principles Of Optics*, McGraw-Hill Book
Company, Inc., N. Y., NY, 1932.
- 45.0 R. M. A. Azzam and N. M. Bashaara, *Ellipsometry And Polarized Light*, North
Holland Publishing Co., N.Y., N.Y., 1979.
- 46.0 E. Collett, *Polarized Light-Fundamentals And Applications*, Marcel Dekker, Inc.,
N. Y. NY, 1993.
- 47.0 D. S. Kliger, J. W. Lewis and C. E. Randall, *Polarized Light In Optics And
Spectroscopy*, Academic Press, Inc., N. Y. , NY, 1990.

Author Index

- Aimez, Vincent, 168
 Aithal, Sreeramana P., 406
 Akutsu, Nakao, 46
 Asundi, Anand K., 98
 Bai, Jun Feng, 475
 Bao, C. L., 191
 Bao, Chao, 417
 Bao, Zheng, 417
 Beauvais, Jacques, 168
 Beerens, Jean, 168
 Bergh, Arpad A., 2
 Bhattacharya, Pallab K., 268
 Cao, Lin-xiang, 497
 Cao, Qing, 367
 Chan, Yuen Chuen, 162, 168
 Chau, Fook Siong, 109
 Chen, Haiqing, 359
 Chen, Jing Li, 54
 Chen, Lianghai, 367
 Chen, Long Qing, 440
 Chen, Minghua, 315
 Chen, Wenju, 489
 Chen, Xingzhong, 315
 Chen, YunQing, 232
 Chen, Zibiao, 290
 Cheng, Buwen, 326
 Cheng, Po-Hsiu, 215
 Cheng, Winchao, 147
 Chew, C. H., 376
 Chin, Mee Koy, 210
 Chin, Yuan-Chung, 124
 Chin, Yuan-Lung, 124
 Chollet, Franck A., 98
 Chou, Jung-Chuan, 124
 Chou, Yuan-Chin, 124
 Chu, Chen Fu, 79
 Chua, Soo Jin, 54, 63, 84
 Chung, Wen-Yaw, 124
 Cui, Yiping, 384
 Dai, Lun, 224, 232
 Das, Debendra Nath, 335
 Deppe, Dennis G., 12, 134
 Ding, Hongyu, 367
 Fang, Huimei, 79
 Fang, Wei, 232
 Feng, Ming-Shiann, 73
 Feng, Zhe Chuan, 54, 63, 84
 Ferreira, Mário F. S., 396
 Fleming, James G., 258
 Fu, Degang, 384
 Fu, Rulian, 351
 Gan, L. M., 376
 Gao, Yan Na, 462
 Gao, Yizhi, 315
 Gao, Yongsheng, 428
 Ghosh, Partha, 335
 Gong, Hai Qing, 440
 Gong, Mai-Xia, 503
 Gong, Ma Li, 448, 455
 Goto, Kenya, 344
 Graham, Luke A., 12
 Guan, Jiuhong, 351
 Gunawan, Oki, 162
 Guo, Jen-Da, 73
 Guo, Liang, 367
 Guo, Ying Zi, 462
 Guo, Zhouyi, 417
 Hagan, David J., 475
 Han, Seungoh, 117
 Hao, Mao Sheng, 63
 Ho, Seng Tiong, 210
 Hong, Guo Dong, 440
 Hosomi, Kazuhiko, 176
 Hou, Yong Tian, 46, 54, 84
 Hsiung, Shen-Kan, 124
 Hu, Xiaojun, 319
 Huang, Dexiu, 319
 Huang, H., 12
 Huang, Kai-Feng, 215
 Huang, Qi, 191, 390
 Huang, Yong-Zhen, 239
 Huda, Md. Q., 330
 Huffaker, Diana L., 12, 134
 Hwang, Sung Min, 434
 Hyon, C. K., 434
 Iga, Kenichi, 290, 344
 Islam, M. S., 330
 Islam, Mohammed N., 330
 Ji, Wei, 475, 483
 Jiang, Hong Xing, 224
 Jin, Changqin, 92
 Jin, Guofan, 448, 455
 Jing, Xiabin, 92
 Kam, Chan Hin, 278, 376
 Katsuyama, Toshio, 176
 Kim, Eun Kyu, 434
 Kim, Hyo Jin, 434
 Kim, Yong, 434
 Kiran, Prem P., 406
 Koch, Stephan W., 24
 Koyama, Fumio, 290, 344
 Kudryashov, Vladimir, 247
 Lai, Yinchieh, 215
 Lai, ZhiAn, 232

- Lam, Yee Loy, 162, 168, 376
 Latas, Sofia C. V., 396
 Lau, E. W. P., 84
 Lee, Cheon, 434
 Lee, Hong Kyu, 434
 Lee, Lye Huat, 162
 Lee, Paul, 247
 Lee, Shih-Chang, 73
 Lee, Sing, 247
 Lee, Tsin-Dong, 215
 Lee, Wei-I, 73
 Li, Chengfang, 147, 326
 Li, Guohua, 147
 Li, Heping, 376
 Li, Kun, 84
 Li, Ming Fu, 46, 84
 Li, Minghua, 468
 Li, P., 63
 Li, Shaoshan, 417
 Li, Ying Xue, 462
 Li, YueXia, 147
 Li, Yunjing, 489
 Liang, Baolai, 351
 Liao, Bo, 462
 Lim, Hwi Siong, 168
 Lim, Jin Hong, 475
 Lim, Tuan Kay, 278
 Lin, Hong Yi, 462
 Lin, J., 54
 Lin, Jing Yu, 224
 Lin, LiWie, 98
 Lin, Meirong, 489
 Lin, Shawn-Yu, 258
 Liu, AiQun, 98, 109
 Liu, B., 376
 Liu, Deming, 319
 Liu, Hongli, 351
 Liu, Jian, 147
 Liu, Jinghua, 462
 Liu, Jun-Qi, 497, 503
 Liu, Mahe, 247
 Liu, R., 183
 Liu, Xingyuan, 92
 Liu, Ya-Nan, 497
 Liu, Yun, 92
 Lu, Zuhong, 384
 Luo, Liping, 326
 Ma, Jun, 367
 Ma, Junfu, 417
 Ma, Xiao Yu, 232, 367
 Marest, Filip, 196
 Matsumoto, Koh, 46
 Meier, Torsten, 24
 Min, Byung Don, 434
 Miyamoto, Tomoyuki, 290
 Mu, Guoguang, 351
 Mukhopadhyay, Sourangshu, 335
 Muralidharan, Govindarajan, 153
 Mustapha, Mazlyn Mona, 297
 Ning, Yongqiang, 92
 Niu, Li-hong, 503
 Ooi, Boon Siew, 162, 168
 Ooi, C. H. Raymond, 278
 Ormondroyd, Richard F., 297
 Osotchan, T., 183
 Pak, Jungho, 117
 Palmer, James R., 508, 523
 Pan, Jin-Shan, 215
 Park, Gyoungwon, 134
 Park, Hojoon, 117
 Park, Se Ki, 434
 Pillai, A. Sivathanu, 36
 Qian, Yi, 232
 Qin, Wenbiao, 307
 Quan, Chenggen, 109
 Que, Wen Xiu, 376
 Rao, Narayana D., 406
 Sabarinathan, Jaysri, 268
 Sakai, Shiro, 63
 Schlenker, Dieter, 290
 Shchekin, Oleg B., 134
 Shen, Yumin, 232
 Shi, Xu, 183
 Shinada, Satoshi, 344
 Shirai, Masataka, 176
 Shkerdin, Gennady N., 196
 Siddiqui, Saiful A., 330
 Song, Aimin, 147
 Stiens, Johan H., 196
 Sugahara, Tomoya, 63
 Sun, J. M., 191, 390
 Sun, Tai-Ping, 124
 Tai, Kuochou, 215
 Tan, Khee Lip, 440
 Tan, Manqing, 367
 Tan, Tuck Lee, 247
 Tan, Wei Lian, 475
 Teo, Kie Leong, 46
 Tokunaga, Hiroki, 46
 Tsai, R. Y., 79
 Uchida, Kazuo, 46
 Van Stryland, Eric W., 475
 Vounckx, Roger A., 196
 Wang, Dajun, 232
 Wang, Fosong, 92
 Wang, Guohong, 367
 Wang, GuoZhong, 232
 Wang, Hongjie, 326
 Wang, Lijun, 92
 Wang, Liming, 367
 Wang, Lixiang, 92
 Wang, Qiming, 326
 Wang, Rui, 468
 Wang, RuoPeng, 224, 232
 Wang, S. C., 79
 Wang, W., 63

Wang, Weiyu, 448, 455
 Wang, Xiao Dong, 440
 Wang, Xin, 384
 Wang, Xinghua, 147
 Wang, Y. K., 79
 Wang, Zhaoqi, 351
 Wee, Andrew T. S., 84
 Wee, Teng Soon, 183
 Wei, J., 428
 Wen, Tzu-Chi, 73
 Wu, Dongjiang, 92
 Wu, Shengli, 92
 Xin, Xinquan, 483
 Xiong, Yuenan, 483
 Xu, G. Q., 376
 Xu, Lei, 315
 Xu, Shifa, 232
 Xu, Wusheng, 468
 Xu, Yuheng, 468
 Yang, Lin Jiang, 440
 Yang, Qifang, 307
 Yang, Qinqing, 326
 Yang, Sidney S., 475
 Yang, Yali, 367
 Yao, Minyu, 315
 Yeung, T. C. Au, 278
 Yoon, Soon Fatt, 183
 You, Xiao Zeng, 475
 Yu, Chongxiu, 307
 Yu, Jinzhong, 147, 326
 Zhang, Baozheng, 489
 Zhang, Bei, 224, 232
 Zhang, D. H., 183, 428
 Zhang, Guangzhe, 367
 Zhang, Jian, 440
 Zhang, Jianfeng, 315
 Zhang, Man Hong, 191, 390
 Zhang, P. H., 183
 Zhang, Qianfeng, 483
 Zhang, W. M., 183
 Zhang, X., 54
 Zhang, Xiao-qui, 503
 Zhang, Xu Ming, 109
 Zhang, Yan Feng, 191, 390
 Zhang, Yu, 384
 Zhang, Yu, 224
 Zhang, Zhi Guo, 390
 Zhao, Jiamin, 92
 Zhao, Xiao-ming, 497
 Zheng, LuDi, 98
 Zhou, Jun Ming, 191, 390
 Zhou, Weidong, 268
 Zhou, Yan, 162, 168
 Zhou, Zuwang, 359
 Zhu, Donghai, 268
 Zhu, Xing, 224, 232
 Zhu, Yanbin, 417
 Zhu, Zhaohui, 417
 Zou, Wenli, 489
 Zou, Yua-Xing, 503
 Zou, Z., 134
 Zuo, Jing Lin, 475